Advanced Series on Ocean Engineering — Volume 23

THEORY AND APPLICATIONS OF OCEAN SURFACE WAVES

Part 1: Linear Aspects

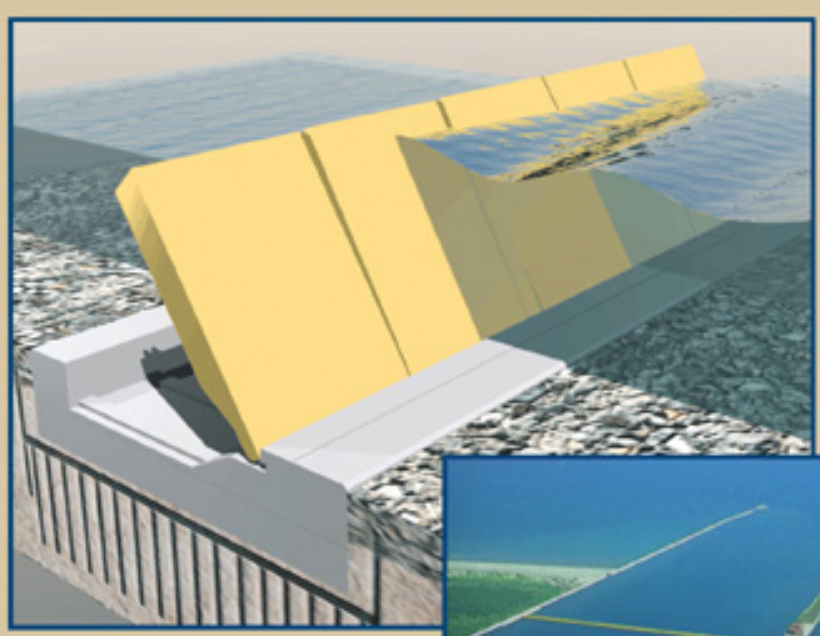

Chiang C. Mei
Michael Stiassnie
Dick K.-P. Yue

World Scientific

THEORY AND APPLICATIONS OF OCEAN SURFACE WAVES

Part 1: Linear Aspects

ADVANCED SERIES ON OCEAN ENGINEERING

Series Editor-in-Chief
Philip L- F Liu (*Cornell University*)

Vol. 9 Offshore Structure Modeling
by Subrata K. Chakrabarti (Chicago Bridge & Iron Technical Services Co., USA)

Vol. 10 Water Waves Generated by Underwater Explosion
by Bernard Le Méhauté and Shen Wang (Univ. Miami)

Vol. 11 Ocean Surface Waves; Their Physics and Prediction
by Stanislaw R Massel (Australian Inst. of Marine Sci)

Vol. 12 Hydrodynamics Around Cylindrical Structures
by B Mutlu Sumer and Jørgen Fredsøe (Tech. Univ. of Denmark)

Vol. 13 Water Wave Propagation Over Uneven Bottoms
Part I — Linear Wave Propagation
by Maarten W Dingemans (Delft Hydraulics)
Part II — Non-linear Wave Propagation
by Maarten W Dingemans (Delft Hydraulics)

Vol. 14 Coastal Stabilization
by Richard Silvester and John R C Hsu (The Univ. of Western Australia)

Vol. 15 Random Seas and Design of Maritime Structures (2nd Edition)
by Yoshimi Goda (Yokohama National University)

Vol. 16 Introduction to Coastal Engineering and Management
by J William Kamphuis (Queen's Univ.)

Vol. 17 The Mechanics of Scour in the Marine Environment
by B Mutlu Sumer and Jørgen Fredsøe (Tech. Univ. of Denmark)

Vol. 18 Beach Nourishment: Theory and Practice
by Robert G. Dean (Univ. Florida)

Vol. 19 Saving America's Beaches: The Causes of and Solutions to Beach Erosion
by Scott L. Douglass (Univ. South Alabama)

Vol. 20 The Theory and Practice of Hydrodynamics and Vibration
by Subrata K. Chakrabarti (Offshore Structure Analysis, Inc., Illinois, USA)

Vol. 21 Waves and Wave Forces on Coastal and Ocean Structures
by Robert T. Hudspeth (Oregon State Univ., USA)

Vol. 22 The Dynamics of Marine Craft: Maneuvering and Seakeeping
by Edward M. Lewandowski (Computer Sciences Corporation, USA)

Vol. 23 Theory and Applications of Ocean Surface Waves
Part 1: Linear Aspects
Part 2: Nonlinear Aspects
by Chiang C. Mei (Massachusetts Inst. of Technology, USA), *Michael Stiassnie* (Technion–Israel Inst. of Technology, Israel) and *Dick K. P. Yue* (Massachusetts Inst. of Technology, USA)

Vol. 24 Introduction to Nearshore Hydrodynamics
by Ib A. Svendsen (Univ. of Delaware, USA)

Advanced Series on Ocean Engineering — Volume 23

THEORY AND APPLICATIONS OF OCEAN SURFACE WAVES

Part 1: Linear Aspects

Chiang C. Mei
Ford Professor of Engineering
Massachusetts Institute of Technology, USA

Michael Stiassnie
David Hacohen and Hillel Dan Professor of Civil Engineering
Technion-Israel Institute of Technology, Israel

Dick K.-P. Yue
Professor of Mechanical and Ocean Engineering
Massachusetts Institute of Technology, USA

World Scientific

NEW JERSEY • LONDON • SINGAPORE • BEIJING • SHANGHAI • HONG KONG • TAIPEI • CHENNAI

Published by

World Scientific Publishing Co. Pte. Ltd.

5 Toh Tuck Link, Singapore 596224

USA office: 27 Warren Street, Suite 401-402, Hackensack, NJ 07601

UK office: 57 Shelton Street, Covent Garden, London WC2H 9HE

British Library Cataloguing-in-Publication Data
A catalogue record for this book is available from the British Library.

THEORY AND APPLICATIONS OF OCEAN SURFACE WAVES
Part 1: Linear Aspects

ISBN 981-238-893-1 — Set
ISBN 981-256-156-0 — Part 1
ISBN 981-256-158-7 — Part 2

ISBN 981-238-894-X (pbk) — Set
ISBN 981-256-157-9 (pbk) — Part 1
ISBN 981-256-159-5 (pbk) — Part 2

Printed in Singapore.

To: Caroline Mei, Hadassa Stiassnie and Eva Yue

This page intentionally left blank

Preface to the Expanded Edition

This is Part One of the expanded edition of *Applied Dynamics of Ocean Surface Waves* by CCM first published twenty two years ago by Wiley-Interscience. A corrected version was later published by World Scientific without essential changes. During the past two decades, many theoretical advances have been made by researchers throughout the world. Great strides have been made in analytical and numerical treatments for accurate predictions as well as physical understanding. In this new edition, the authors have added considerable new materials, hence the division to two separate parts.

Part One is restricted to the linear aspects. While nearly all the matierials in the first edition are kept, many new exercises are added. A major change is the addition of Chapter 7 on the multiple scattering by many scatterers on the seabed. Introductory aspects of Bragg resonance by periodic bars are first discussed. Important to coastal geomorphology, a complete understanding of longshore bars requires quantitative understanding of both the cause and the effect; it turns out that waves and bars affect each other in complicated ways. The formation and evolution of sandbars under waves is, however, a very slow process and involves the highly empirical science of sediment transport; we only discuss the linearized effects of rigid bars on the wave climate. Over a much larger scale of the continental shelf, bathymetric variations can be very irregular. Therefore we also present a new theory of the effects of scattering by random depth fluctuations. It is shown that the accumulation of incoherent scattering over an extended area results in energy removal from the averaged motion which is coherent. This physics is related to the phenomenon of Anderson localization in quantum physics.

In Chapter 8 on the dynamics of floating bodies, we have included a section on the trapped modes of the mobile gates designed for Venice lagoon, as a current application in coastal engineering.

The science of water waves has always been enriched by the use of mathematical tools. In order that a reader with only some familiarity with advanced calculus can make effective use of this book, we have continued the style of the previous edition by shunning the phrase "it can be shown that...". Often the mathematical steps of derivation are given in considerable detail. More advanced tools such as the techniques of asymptotic analysis are explained in the text. To highlight our objectives of bridging theory and applications, the title of this book has been changed.

Chiang C. Mei, Cambridge, Massachusetts, USA
Michael Stiassnie, Haifa, Israel
Dick K.-P. Yue, Cambridge, Massachusetts, USA

Preface to the First Edition

A substantial growth of knowledge in the dynamics of ocean surface waves has been witnessed over the past 20 years. While many advances have been stimulated by purely scientific inquiry in geophysics, the pace of progress has also been quickened by the increase in large engineering projects both offshore and along the coast. A major construction project now demands not only careful estimates of wave conditions near the site but also reliable predictions of the effects on and of the construction itself. With a view to bringing together scientific and engineering aspects of ocean waves, educational and research programs have naturally been established in a number of universities and industries.

This book is the outgrowth of my lecture notes for a two-semester course taught at M.I.T. since 1974 to graduate students in civil and ocean engineering, with occasional participants from physical oceanography. The aim of the book is to present selected theoretical topics on ocean-wave dynamics, including basic principles and applications in coastal and offshore engineering, all from the deterministic point of view. The bulk of the material deals with the linearized theory which has been well developed in the research literature. The inviscid linearized theory is covered in Chapters One to Five and again in Eight. Frictional effects caused directly or indirectly by viscosity are treated in Chapters Six, Nine, and Ten. A special effect of breaking waves on beaches is examined in Chapter Eleven. Chapters Ten and Eleven focus on the secondary effects of nonlinearity. The cases where nonlinearity is of primary importance are the subjects of Chapters Twelve and Thirteen, for shallow and deep waters, respectively. The last chapter (Fourteen) is on wave-induced stresses in a porous but deformable seabed, which is a problem vital to offshore engineering. In the construction of a gravity platform, the cost of the foundation alone can be as high as 40% of

the total. Under the influence of waves, the strength of a porous seabed is affected to varying degrees by fluid in the pores. Hence hydrodynamics is an essential part of the problem. In this chapter a well-known fluid-dynamic reasoning is applied to a soil model which includes fluid and solid phases. I hope the material will stimulate further interaction among researchers in different disciplines.

Most parts of this book have been used either for my own lectures or for self-paced reading by the students. Since contributions by mathematical scientists have always been prominent in this field, the use of certain analytical techniques which may be less familiar to many potential readers cannot be avoided. Therefore, considerable space is devoted to the informal explanation and demonstration of those techniques not customarily discussed in a course on advanced calculus. The derivations of most of the results are given in detail in order to reduce possible frustrations to those who are still acquiring the requisite skills. A few exercises are included; nearly all of them demand some effort. For additional exercises, I have usually suggested term papers based on the student's own survey of literature.

Studies on waves in general, and on water waves in particular, have always been enriched by cross fertilization among diverse fields of science and engineering, including physics, mathematics, oceanography, electrical engineering, and others. A conscientious effort has been made in this book to reflect this fact which I hope will induce more engineers and scientists to join their talents for further challenges of the sea.

Several important areas which are either beyond my own experience or have been treated in other books are not included here. The mechanisms of wave generation by wind and many aspects of resonant interactions have been admirably surveyed by Phillips (1977) and by LeBlond and Mysak (1978). On the statistical *description* of random sea waves, a detailed discussion of the basic aspects may be found in Price and Bishop (1974). For the statistical *mechanics* of sea waves one should consult Phillips (1977) and West (1981). The rapid advance on steep waves, spearheaded by M. S. Longuet-Higgins, is of obvious interest to engineers and oceanographers alike; the numerous papers by him and his associates on the subject cannot be matched for clarity and thoroughness. Waves due to advancing bodies belong to the realm of ship hydrodynamics; the definitive treatises by Stoker (1957), Wehausen and Laitone (1960), and Newman (1977), and all the past proceedings of the Naval Hydrodynamics Symposium should be consulted. Wave-induced separation around small bodies is at the heart of force prediction for offshore structures; it is a subject where

experiments play the leading role and has been expertly covered in a recent book by Sarpkaya and Issacson (1981). Storm surges are also omitted.

In a book containing many mathematical expressions, freedom from error can be strived for but is hard to achieve. I shall be grateful to readers who wish to inform me of any oversights that remain.

Chiang C. Mei
Cambridge, Massachusetts
July 1982

This page intentionally left blank

Acknowledgments

I would like to express my profound gratitude to the U.S. National Science Foundation (Program on Fluid Mechanics and Hydraulics) and to the U.S. Office of Naval Research (Programs on Fluid Mechanics and Ocean and Marine Technology). Without their sustained support, the list of new topics described herein would have been considerably shorter. Thanks are also due to my many student-collaborators at MIT. I have learned almost everything in this edition initially with them, and later from them. Finally, it is a pleasure to thank my wife Caroline, upon whose steady encouragement and editorial help I have always relied.

—*Chiang C. Mei*

M. Stiassnie's past and ongoing collaboration with Prof. Yehuda Agnon from the Technion and Prof. Lev Shemer from the Tel-Aviv University, is an essential factor in his scientific activities, and gives him great pleasure. Other significant contributors to the joint work, related to Zakharov's equation, include Dr. Michael Glozman, Dr. Jørgen Rasmussen, and the late Prof. Peter Bryant. Their collaboration is greatly appreciated.

—*Michael Stiassnie*

I would like to thank my many students, present and former, on whose work the material of Chapter 15 is based. I have learned a lot more from working with them than they could ever imagine. I am especially grateful to Dr. D.G. Dommermuth with whom I started on many of these exciting research directions; and to Dr. Yuming Liu who has been involved with me on all facets of the work and continues to be instrumental to many of our ongoing developments in these methods. Yuming also gave generously of his

time to help in the preparation of the manuscript for which I most grateful. Finally I want to acknowledge my former advisor, mentor and co-author, Professor Chiang C. Mei. From CC, I learned much of my hydromechanics. By his work and example, CC also taught me about dedication, excellence and the excitement of research. Thank you, CC.

— *Dick K.-P. Yue*

Contents

Part 2

Part 1

This page intentionally left blank

1 Introduction

Many types of waves involving different physical factors exist in the ocean. As in the elementary problem of a spring-mass system, all waves must be associated with some kind of restoring force. It is therefore convenient to make a crude classification of ocean waves according to the restoring force, as shown in Table 1.1.

Wind waves and swell, generated by local and distant storms, are the most directly experienced by mankind. Occurring less frequently but with occasionally disastrous consequences are the tsunamis which usually refer to long-period [$\sim O(1\text{ h})$] oscillations caused by large submarine earthquakes or landslides. Within the same broad range of time scales, waves can also exist as a result of human activities (ship motion, explosion, and so on). Since these waves are the most prominent on the water surface and their main restoring force is gravity, they are called the *surface gravity waves*. The shorter term, *surface waves*, is often used if the exclusion of surface capillary waves is understood.

Important in the science of oceanography are the internal gravity waves along the thermoclines which are horizontal layers of sharp density stratification beneath the sea surface. The associated wave motion is generally not pronounced on the surface except for some indirect signs of its presence. These waves contribute to the process of mixing and affect the eddy viscosity of ocean currents. Storm surges are the immediate consequence of local weather and can inflict severe damage to human life and properties by innundating the coast.

In nature, several restoring forces can be in effect at the same time, hence the distinction between various waves listed in Table 1.1 is not always very sharp.

Table 1.1: Wave Type, Physical Mechanism, Activity Region.

Wave Type	Physical Mechanism	Typical Period[a]	Region of Activity
Sound	Compressibility	10^{-2}–10^{-5} s	Ocean interior
Capillary ripples	Surface tension	$< 10^{-1}$ s	Air–water interface
Wind waves and swell	Gravity	1–25 s	
Tsunami	Gravity	10 min–2 h	
Internal waves	Gravity and density stratification	2 min–10 h	Layer of sharp density change
Storm surges	Gravity and earth rotation	1–10 h	Near coastline
Tides	Gravity and earth rotation	12–24 h	Entire ocean layer
Planetary waves	Gravity, earth rotation and variation of latitude or ocean depth	O(100 days)	

[a]In seconds (s), minutes (min), hours (h), and days.

This book will be limited to wave motions having time scales such that compressibility and surface tension at one extreme and earth rotation at the other are of little direct importance. Furthermore, the vertical stratification of sea water is assumed to be small enough within the depth of interest. Therefore, we shall only be concerned with the surface gravity waves, that is, wind waves, swell, and tsunamis. Discussions of all other waves listed in Table 1.1 can be found in the oceanographic treatises by Hill (1962) and LeBlond and Mysak (1978).

In this chapter we first review the basic equations of fluid motion and some general deductions for inviscid, irrotational flows. Linearized equations for infinitesimal waves are then derived. After introducing the general notions of propagating waves, we examine the properties of simple harmonic progressive waves on constant depth. An elementary discussion of group velocity will be given from both kinematic and dynamic points of view.

1.1 Review of Basic Formulation for an Incompressible Fluid of Constant Density

1.1.1 Governing Equations

In a wide variety of gravity-wave problems, the variation of water density is insignificant over the temporal and spatial scales of engineering interest.

The fundamental conservation laws are adequately described by the following Navier–Stokes equations:

$$\text{mass} : \nabla \cdot \mathbf{u} = 0\,, \tag{1.1.1}$$

$$\text{momentum} : \left(\frac{\partial}{\partial t} + \mathbf{u}\cdot\nabla\right)\mathbf{u} = -\nabla\left(\frac{P}{\rho} + gz\right) + \nu\nabla^2\mathbf{u}\,, \tag{1.1.2}$$

where $\mathbf{u}(\mathbf{x},t)$ is the velocity vector (u,v,w), $P(\mathbf{x},t)$ the pressure, ρ the density, g the gravitational acceleration, ν the constant kinematic viscosity, and $\mathbf{x} = (x,y,z)$ with the z axis pointing vertically upward.

One of the most important deductions from these equations is concerned with the vorticity vector $\boldsymbol{\Omega}(\mathbf{x},t)$ defined by

$$\boldsymbol{\Omega} = \nabla \times \mathbf{u}\,, \tag{1.1.3}$$

which is twice the rate of local rotation. By taking the curl of Eq. (1.1.2) and using Eq. (1.1.1), we can show that

$$\left(\frac{\partial}{\partial t} + \mathbf{u}\cdot\nabla\right)\boldsymbol{\Omega} = \boldsymbol{\Omega}\cdot\nabla\mathbf{u} + \nu\nabla^2\boldsymbol{\Omega}\,. \tag{1.1.4}$$

Physically, the preceding equation means that following the moving fluid, the rate of change of vorticity is due to stretching and twisting of vortex lines and to viscous diffusion (see, e.g., Batchelor, 1967). In water where ν is small ($\cong 10^{-2}$ cm^2/s) the last term in Eq. (1.1.4) is negligible except in regions of large velocity gradient and strong vorticity. A good approximation applicable in nearly all of the fluid is

$$\left(\frac{\partial}{\partial t} + \mathbf{u}\cdot\nabla\right)\boldsymbol{\Omega} = \boldsymbol{\Omega}\cdot\nabla\mathbf{u}\,. \tag{1.1.5}$$

An important class of problems is one where $\boldsymbol{\Omega} \equiv 0$ and is called the *irrotational flow*. Taking the scalar product of Eq. (1.1.5) and $\boldsymbol{\Omega}$, we have

$$\left(\frac{\partial}{\partial t} + \mathbf{u}\cdot\nabla\right)\frac{\boldsymbol{\Omega}^2}{2} = \Omega^2[\mathbf{e}_\Omega\cdot(\mathbf{e}_\Omega\cdot\nabla\mathbf{u})]\,,$$

where $\mathbf{e}_\Omega$ is the unit vector along $\boldsymbol{\Omega}$. Since the velocity gradient is finite in any physically realizable situation, the maximum of $\mathbf{e}_\Omega\cdot(\mathbf{e}_\Omega\cdot\nabla\mathbf{u})$ must be a finite value, $M/2$, say. The magnitude $\boldsymbol{\Omega}^2(\mathbf{x},t)$ following a fluid particle cannot exceed $\boldsymbol{\Omega}^2(\mathbf{x},0)e^{Mt}$. Consequently, if there is no vorticity anywhere at $t = 0$, the flow will remain irrotational for all time.

For an inviscid irrotational flow, the velocity $\mathbf{u}$ can be expressed as the gradient of a scalar potential Φ,

$$\mathbf{u} = \nabla\Phi\,. \tag{1.1.6}$$

Conservation of mass requires that the potential satisfies Laplace's equation

$$\nabla^2\Phi = 0\,. \tag{1.1.7}$$

If the velocity potential is known, then the pressure field can be found from the momentum equation (1.1.2). By using the vector identity

$$\mathbf{u}\cdot\nabla\mathbf{u} = \nabla\frac{\mathbf{u}^2}{2} - \mathbf{u}\times(\nabla\times\mathbf{u})$$

and irrotationality, we may rewrite Eq. (1.1.2), with $\nu = 0$, as

$$\nabla\left[\frac{\partial\Phi}{\partial t} + \frac{1}{2}|\nabla\Phi|^2\right] = -\nabla\left(\frac{P}{\rho} + gz\right).$$

Upon integration with respect to the space variables, we obtain

$$-\frac{P}{\rho} = gz + \frac{\partial\Phi}{\partial t} + \frac{1}{2}|\nabla\Phi|^2 + C(t)\,, \tag{1.1.8}$$

where $C(t)$ is an arbitrary function of t and can usually be omitted by redefining Φ without affecting the velocity field. Equation (1.1.8) is called the Bernoulli equation. The first term, gz, on the right-hand side of Eq. (1.1.8) is the hydrostatic contribution, whereas the rest is the hydrodynamic contribution to the total pressure P.

1.1.2 Boundary Conditions for an Inviscid Irrotational Flow

Two types of boundaries interest us: the air–water interface which will also be called the free surface, and the wetted surface of an impenetrable solid. Along these two boundaries the fluid is assumed to move only tangentially. Let the instantaneous equation of the boundary be

$$F(\mathbf{x}, t) = z - \zeta(x, y, t) = 0\,, \tag{1.1.9}$$

where ζ is the height measured from $z = 0$, and let the velocity of a geometrical point $\mathbf{x}$ on the moving free surface be $\mathbf{q}$. After a short time dt, the free surface is described by

$$F(\mathbf{x}+\mathbf{q}\,dt, t+dt) = 0 = F(\mathbf{x},t) + \left(\frac{\partial F}{\partial t} + \mathbf{q}\cdot\nabla F\right) dt + O(dt)^2\,.$$

In view of Eq. (1.1.9), it follows that

$$\frac{\partial F}{\partial t} + \mathbf{q}\cdot\nabla F = 0$$

for small but arbitrary dt. The assumption of tangential motion requires $\mathbf{u}\cdot\nabla F = \mathbf{q}\cdot\nabla F$ which, in turn, implies that

$$\frac{\partial F}{\partial t} + \mathbf{u}\cdot\nabla F = 0 \quad \text{on} \quad z=\zeta\,, \tag{1.1.10}$$

or, equivalently,

$$\frac{\partial \zeta}{\partial t} + \frac{\partial \Phi}{\partial x}\frac{\partial \zeta}{\partial x} + \frac{\partial \Phi}{\partial y}\frac{\partial \zeta}{\partial y} + \frac{\partial \Phi}{\partial z} \quad \text{on} \quad z=\zeta\,. \tag{1.1.11}$$

Equation (1.1.10) or (1.1.11) is referred to as the *kinematic* boundary condition. In the special case where the boundary is the wetted surface of a stationary solid S_B, $\partial\zeta/\partial t = 0$ and Eq. (1.1.10) reduces to

$$\frac{\partial \Phi}{\partial n} = 0 \quad \text{on} \quad S_B\,. \tag{1.1.12}$$

On the sea bottom B_0 at the depth $h(x,y)$, Eq. (1.1.9) becomes $z + h(x,y) = 0$ and Eq. (1.1.12) may be written

$$-\frac{\partial \Phi}{\partial z} = \frac{\partial \Phi}{\partial x}\frac{\partial h}{\partial x} + \frac{\partial \Phi}{\partial y}\frac{\partial h}{\partial y} \quad \text{on} \quad B_0\,. \tag{1.1.13}$$

On the air–water interface, both ζ and Φ are unknown, and it is necessary to add a *dynamical* boundary condition concerning forces.

For most of the topics of interest in this book, the wavelength is so long that surface tension is unimportant; the pressure just beneath the free surface must equal the atmospheric pressure P_a above. Applying Eq. (1.1.8) on the free surface, we have

$$-\frac{P_a}{\rho} = g\zeta + \frac{\partial \Phi}{\partial t} + \frac{1}{2}|\nabla\Phi|^2 \quad \text{on} \quad z=\zeta\,. \tag{1.1.14}$$

The two conditions, (1.1.11) and (1.1.14), may be combined into one in terms of Φ, by taking the total derivative of Eq. (1.1.14):

$$\left(\frac{\partial}{\partial t} + \mathbf{u}\cdot\nabla\right)\frac{P_a}{\rho} + \left(\frac{\partial}{\partial t} + \mathbf{u}\cdot\nabla\right)\left(\frac{\partial \Phi}{\partial t} + \frac{\mathbf{u}^2}{2} + g\zeta\right) = 0\,, \quad z=\zeta\,. \tag{1.1.15}$$

Using Eq. (1.1.11) and

$$\mathbf{u}\cdot\nabla\frac{\partial\Phi}{\partial t}=\frac{\partial}{\partial t}\frac{1}{2}\mathbf{u}^2\,,$$

we have from Eq. (1.1.15)

$$\frac{D}{Dt}\frac{P_a}{\rho}+\left[\frac{\partial^2\Phi}{\partial t^2}+g\frac{\partial\Phi}{\partial z}+\frac{\partial\mathbf{u}^2}{\partial t}+\frac{1}{2}\mathbf{u}\cdot\nabla\mathbf{u}^2\right]=0\,,\quad z=\zeta\,. \tag{1.1.16}$$

Furthermore, if $P_a=$ constant, the above condition becomes

$$\frac{\partial^2\Phi}{\partial t^2}+g\frac{\partial\Phi}{\partial z}+\frac{\partial}{\partial t}(\mathbf{u})^2+\frac{1}{2}\mathbf{u}\cdot\nabla\mathbf{u}^2=0\,,\quad z=\zeta\,, \tag{1.1.17}$$

which is essentially a condition for Φ. Not only do nonlinear terms appear in these boundary conditions, but the position of the free surface is also an unknown quantity. An exact analytical theory for water-wave problems is therefore almost impossible.

When the motion of the air above is significant, the atmospheric pressure cannot always be prescribed *a priori*; the motions of air and water are, in general, coupled. Indeed, the exchange of momentum and energy between air and sea is at the heart of the theory of surface-wave generation by wind. However, we shall limit our attention to sufficiently localized regions in the absence of direct wind action. Air can then be ignored for most purposes because of its comparatively small density.

1.2 Linearized Approximation for Small-Amplitude Waves

Let us assume that certain physical scales of motion can be anticipated *a priori*. In particular, let

$$\begin{pmatrix}\lambda/2\pi\\ \omega^{-1}\\ A\\ A\omega\lambda/2\pi\end{pmatrix}\quad\text{characterize}\quad\begin{pmatrix}x,y,z,h\\ t\\ \zeta\\ \Phi\end{pmatrix}, \tag{1.2.1}$$

where λ, ω, and A are the typical values of wavelength, frequency, and free-surface amplitude respectively. We have assigned the scale for Φ to be $A\omega\lambda/2\pi$ so that the velocity has the scale $A\omega$ which is expected near the

free surface. We now introduce dimensionless variables and denote them by primes as follows:

$$\begin{pmatrix} \Phi \\ x, y, z, h \\ t \\ \zeta \end{pmatrix} = \begin{pmatrix} A\omega\lambda\Phi'/2\pi \\ \lambda(x', y', z', h')/2\pi \\ t'/\omega \\ A\zeta' \end{pmatrix}. \tag{1.2.2}$$

When these variables are substituted into Eqs. (1.1.7), (1.1.11), (1.1.12) and (1.1.14), a set of dimensionless equations is obtained:

$$\nabla'^2\Phi' = \left(\frac{\partial^2}{\partial x'^2} + \frac{\partial^2}{\partial y'^2} + \frac{\partial^2}{\partial z'^2}\right)\Phi' = 0\,, \quad -h' < z' < \varepsilon\zeta'\,, \tag{1.2.3}$$

$$\frac{\partial\Phi'}{\partial n'} = 0\,, \quad z' = -h'\,, \tag{1.2.4}$$

$$\frac{\partial\zeta'}{\partial t'} + \varepsilon\left(\frac{\partial\Phi'}{\partial x'}\frac{\partial\zeta'}{\partial x'} + \frac{\partial\Phi'}{\partial y'}\frac{\partial z'}{\partial y'}\right) = \frac{\partial\Phi'}{\partial z'} \tag{1.2.5}$$

$$\text{on} \quad z' = \varepsilon\zeta'\,,$$

$$\frac{\partial\Phi'}{\partial t'} + \left(\frac{2\pi g}{\omega^2\lambda}\right)\zeta' + \frac{\varepsilon}{2}(\nabla'\Phi')^2 = -P_a' = -\frac{2\pi P_a}{\rho A\omega^2\lambda} \tag{1.2.6}$$

where $\varepsilon = 2\pi A/\lambda = 2\pi \times$ amplitude/wavelength = wave slope. Since the scales are supposed to reflect the physics properly, the dimensionless variables must all be of order unity; the importance of each term above is measured solely by the coefficients in front.[1]

Let us now consider small-amplitude waves in the sense that the wave slope is small: $\varepsilon \ll 1$. The free-surface boundary conditions can be simplified by noting that the unknown free surface differs by an amount of $O(\varepsilon)$ from the horizontal plane $z' = 0$. Thus, we can expand Φ' and its derivatives in a Taylor series:

[1] If the scales have been chosen properly, the normalized variables and their derivatives should indeed be of order unity. The relative importance of each term in an equation is entirely indicated by the dimensionless coefficient multiplying the term. If under certain conditions the solution of the approximate problem exhibits behavior which violates the original assumptions on the order of magnitude, then the scales initially chosen are no longer valid. New scales, hence new approximations, must be found to reflect the physics. It is not an exaggeration to say that estimating the scales is the first step toward the approximate solution of a physical problem.

As a procedural point, when the choices of the scales are limited so that only one dimensionless parameter appears, the formalism of nondimensionalization can often be omitted for brevity, although its essence must always be clearly understood.

$$f'(x', y', \varepsilon\zeta', t') = f'\Big|_0 + \varepsilon\zeta' \frac{\partial f'}{\partial z'}\Big|_0 + \frac{(\varepsilon\zeta')^2}{2!}\frac{\partial^2 f'}{\partial z'^2}\Big|_0 + O(\varepsilon^3)\,,$$

where $f|_0$ means $f(x, y, 0, t)$, etc. To the leading order of $O(1)$, the free-surface conditions become approximately

$$\begin{aligned} \frac{\partial \zeta'}{\partial t'} &= \Phi'_{z'} \\ & \qquad\qquad z' = 0\,. \\ \frac{\partial \Phi'}{\partial t'} + \frac{2\pi g}{\omega^2 \lambda}\zeta' &= -P'_a \end{aligned}$$

Only linear terms remain in these conditions which are now applied at a known plane $z' = 0$. Together with Eqs. (1.2.3) and (1.2.4) the approximate problem is completely linearized. Returning to physical variables, we have

$$\nabla^2 \Phi = 0\,, \qquad -h < z < 0\,, \tag{1.2.7}$$

$$\frac{\partial \Phi}{\partial n} = 0\,, \qquad z = -h\,, \tag{1.2.8}$$

$$\begin{aligned} \frac{\partial \zeta}{\partial t} &= \frac{\partial \Phi}{\partial z} \\ & \qquad\qquad z = 0\,. \\ \frac{\partial \Phi}{\partial t} + g\zeta &= -\frac{P_a}{\rho} \end{aligned} \tag{1.2.9, 1.2.10}$$

Furthermore, Eqs. (1.2.9) and (1.2.10) may be combined to give

$$\frac{\partial^2 \Phi}{\partial t^2} + g\frac{\partial \Phi}{\partial z} = -\frac{1}{\rho}\frac{\partial P_a}{\partial t}\,, \quad z = 0\,, \tag{1.2.11}$$

which can also be obtained by linearizing Eq. (1.1.16).

The total pressure inside the fluid can be related to Φ by linearizing the Bernoulli equation:

$$P = -\rho g z + p\,, \quad \text{where} \quad p = -\rho\frac{\partial \Phi}{\partial t} = \text{dynamic pressure}\,. \tag{1.2.12}$$

These conditions must be supplemented by initial conditions and the boundary conditions on the body and at infinity, if appropriate.

It is worthwhile to remark further on the assumption of zero viscosity in the context of linear approximation. Near a solid boundary, the potential theory allows a finite slip in the tangential direction, but in reality all velocity components must vanish. There must be a thin boundary layer to smooth the transition from zero to a finite value. Thus,

$$\frac{\partial}{\partial x_N} \gg \frac{\partial}{\partial x'_T}\,,\ \frac{\partial}{\partial x''_T}\,,$$

where x_N, x'_T, and x''_T form a locally orthogonal coordinate system with x_N normal to the solid surface and x'_T and x''_T tangential to it. It follows from the linearized momentum equation that the tangential velocity $\mathbf{u}_T$ satisfies

$$\frac{\partial \mathbf{u}_T}{\partial t} \cong \nu \frac{\partial^2 \mathbf{u}_T}{\partial x_N^2} - \frac{1}{\rho}\nabla_T p$$

inside the boundary layer. With the wave period as the time scale, the boundary-layer thickness δ must be of the order

$$\delta \sim \left(\frac{2\nu}{\omega}\right)^{1/2}.$$

For water, $\nu \cong 0.01$ cm^2/s; in model experiments the typical period is 1 s so that $\delta \sim 0.056$ cm, which is far too small compared with the wavelength of usual interest. In the ocean, swells of 10-s periods are common; $\delta \sim 0.17$ cm. But the boundary layer near the natural sea bottom is usually turbulent for most of the period. As will be discussed later, a typical experimental value of eddy viscosity is about 100ν; the thickness of the turbulent boundary layer for a 10-s period is then about $\leq O(10)$ cm, which is still quite small. Thus, the boundary-layer region is but a tiny fraction of a fluid volume whose dimensions are comparable to a wavelength, and the global influence on the wave motion is small over distances of several wavelengths or time of several periods.

1.3 Elementary Notions of a Propagating Wave

Let us consider a special form of the free surface

$$\zeta(x, y, t) = \mathrm{Re}\, A e^{i(\mathbf{k}\cdot\mathbf{x} - \omega t)} = A\cos(\mathbf{k}\cdot\mathbf{x} - \omega t)\,, \tag{1.3.1}$$

where i is the imaginary unit $(-1)^{1/2}$ and

$$\mathbf{k} = (k_1, k_2)\,, \quad \mathbf{x} \equiv (x, y)\,. \tag{1.3.2}$$

For the convenience of mathematical manipulation, the exponential form is often preferred, and for brevity the sign Re (the real part of) is often omitted, that is,

$$\zeta(x,y,t) = Ae^{i(\mathbf{k}\cdot\mathbf{x}-\omega t)} \tag{1.3.3}$$

is used to mean the same as Eq. (1.3.1). What sort of free surface does this expression describe?

To a stationary observer, ζ oscillates in time with the period $T = 2\pi/\omega$ between the two extremes A and $-A$. If we take a three-dimensional snapshot at a fixed t with ζ as the vertical ordinate and (x, y) as the horizontal coordinates, the variation of ζ in (x, y) describes a periodic topography. In a plane $y = \text{const}$, ζ is seen to vary periodically in the x direction between A and $-A$ with the spatial period $2\pi/k_1$. Similarly, in a plane $x = \text{const}$, ζ varies periodically in the y direction between A and $-A$ with the spatial period $2\pi/k_2$. Thus, along the x direction the number of crests per unit length is $k_1/2\pi$, and along the y direction the number of crests per unit length is $k_2/2\pi$.

Let us define the *phase function* S by

$$S(x,y,t) = k_1x + k_2y - \omega t = \mathbf{k}\cdot\mathbf{x} - \omega t\,. \tag{1.3.4}$$

For a fixed time, $S(x, y, t) = \text{const} = S_0$ describes a straight line with the normal vector

$$\mathbf{e}_k = \left(\frac{k_1}{k}, \frac{k_2}{k}\right), \quad \text{where} \quad k = (k_1^2 + k_2^2)^{1/2} = |\mathbf{k}|\,. \tag{1.3.5}$$

Along this straight line, the surface height is the same everywhere. In particular, the waves are the highest (crests) when $S_0 = 2n\pi$ and the lowest (troughs) when $S_0 = (2n + 1)\pi$. When S_0 increases by 2π, the surface height is repeated. Lines of different S_0 are parallel to each other if k_1 and k_2 are constant. We call these lines the *phase lines*. If we take a snapshot and cut a cross section along the direction $\mathbf{e}_k$, the profile of ζ is sinusoidal with the wavelength $\lambda = 2\pi/k$. Alternatively, we may say that the number of waves per unit length along the $\mathbf{k}$ direction is $k/2\pi$. Hence k is called the *wavenumber*, and $\mathbf{k}$ the *wavenumber vector* with k_1 and k_2 as its components. The maximum deviation A from the mean $z = 0$ is called the *amplitude*.

Let us follow a particular phase line $S = S_0$. As time t progresses, the position of the phase line changes. What is the velocity of the phase line? Evidently, if the observer travels with the same velocity $d\mathbf{x}/dt$, the phase line appears stationary, that is,

$$dS = \nabla S\cdot d\mathbf{x} + \frac{\partial S}{\partial t}\,dt = 0\,.$$

From Eq. (1.3.4) it follows that

$$\mathbf{k} = \nabla S = \mathbf{e}_k |\nabla S| \,, \tag{1.3.6a}$$

$$-\omega = \frac{\partial S}{\partial t} \,, \tag{1.3.6b}$$

and that

$$\mathbf{e}_k \cdot \frac{d\mathbf{x}}{dt} = \frac{-\partial S/\partial t}{|\nabla S|} = \frac{\omega}{k} \equiv C \,. \tag{1.3.7}$$

Thus, the speed at which the phase line advances normal to itself is ω/k, which is called the *phase speed* C. Equations (1.3.6a) and (1.3.6b) can be regarded as the definitions of ω and $\mathbf{k}$, that is, the frequency is the time rate, and the wavenumber is the spatial rate of phase change.

1.4 Progressive Water Waves on Constant Depth

For simple harmonic motion with frequency ω, linearity of the problem allows separation of the time factor $e^{-i\omega t}$ as follows:

$$\left.\begin{aligned} \zeta(x,y,t) &= \eta(x,y) \\ \Phi(x,y,z,t) &= \phi(x,y,z) \\ \mathbf{u}(x,y,z,t) &\to \mathbf{u}(x,y,z) \\ P(x,y,z,t) + \rho g z &= p(x,y,z) \end{aligned}\right\} e^{-i\omega t} \,. \tag{1.4.1}$$

Note that the same symbol $\mathbf{u}$ is used for both the fluid velocity and its spatial factor. The linearized governing equations (1.2.7) to (1.2.10) can be reduced to

$$\nabla^2 \phi = 0 \,, \quad -h < z < 0 \,, \tag{1.4.2}$$

$$\frac{\partial \phi}{\partial z} = 0 \,, \quad z = -h \,, \tag{1.4.3}$$

$$\frac{\partial \phi}{\partial z} + i\omega\eta = 0 \,, \tag{1.4.4}$$

$$z = 0 \,,$$

$$g\eta - i\omega\phi = \frac{-p_a}{\rho} \,, \tag{1.4.5}$$

where Eqs. (1.4.4) and (1.4.5) may be combined as

$$g\frac{\partial\phi}{\partial z} - \omega^2\phi = \frac{i\omega}{\rho}p_a\,, \quad z = 0\,. \tag{1.4.6}$$

Let us seek a two-dimensional solution which represents a progressive wave without direct atmospheric forcing, that is, $p_a = 0$ and

$$\eta = Ae^{ikx}\,. \tag{1.4.7}$$

The potential that satisfies Eqs. (1.4.2) and (1.4.3) is easily seen to be

$$\phi = B\cosh k(z+h)e^{ikx}\,.$$

To satisfy the free-surface conditions with $p_a = 0$, we require

$$B = -\frac{igA}{\omega}\frac{1}{\cosh kh}$$

and

$$\omega^2 = gk\tanh kh \tag{1.4.8}$$

so that

$$\phi = -\frac{igA}{\omega}\frac{\cosh k(z+h)}{\cosh kh}e^{ikx}\,. \tag{1.4.9}$$

Thus, for a given frequency ω the progressive wave must have the proper wavenumber given by Eq. (1.4.8). In dimensionless form

$$\omega\left(\frac{h}{g}\right)^{1/2} = (kh\tanh kh)^{1/2}\,.$$

The dimensionless frequency $\omega(h/g)^{1/2}$ and the dimensionless wavenumber kh vary as shown in Fig. 1.1. In particular, the limiting approximations are

$$\begin{aligned} &\omega \simeq (gh)^{1/2}k\,, \quad kh \ll 1\,,\\ &\omega \simeq (gk)^{1/2}\,, \quad\;\; kh \gg 1\,. \end{aligned} \tag{1.4.10}$$

Since $kh = 2\pi h/\lambda$ is essentially the depth-to-wavelength ratio, the terms *long waves* and *shallow-water waves* refer to $kh \ll 1$, while *short waves* and *deep-water waves* refer to $kh \gg 1$. For fixed h, shorter waves have higher frequencies. In shallow water, waves of a fixed frequency have shorter length in smaller depth since $k \simeq \omega/(gh)^{1/2}$.

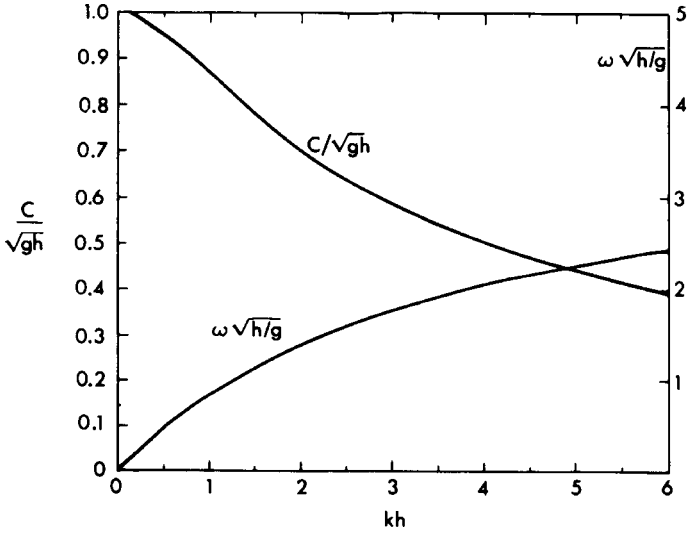

Figure 1.1: Dispersion curves for a progressive wave.

The phase speed C is given by

$$C = \frac{\omega}{k} = \left(\frac{g}{k}\tanh kh\right)^{1/2}, \tag{1.4.11}$$

which is plotted in dimensionless form in Fig. 1.1. For long and short waves the limiting relations are

$$\begin{aligned} C &= (gh)^{1/2}, \quad kh \ll 1, \\ C &= (g/k)^{1/2}, \quad kh \gg 1. \end{aligned} \tag{1.4.12}$$

In general, for the same depth, longer waves have faster speeds. It will be shown in Chapter Two that a localized initial disturbance can be thought of as a Fourier superposition of periodic disturbances with wavelengths ranging over a continuous spectrum. As time passes the longer waves lead the shorter waves. As the disturbances propagate outward the longest and shortest waves become further and further apart with intermediate waves marching in between. The phenomenon that waves of different frequencies travel at different speeds is called *dispersion.* Clearly, if the relation between ω and k for a sinusoidal wave is nonlinear, the medium is dispersive. Equation (1.4.8) or its equivalent, Eq. (1.4.11), is therefore called the *dispersion relation.*

From the linearized Bernoulli equation the dynamic pressure (without $-\rho g z$) is

$$\frac{p}{\rho} = i\omega\phi = gA\frac{\cosh k(z+h)}{\cosh kh}e^{ikx} = g\eta\frac{\cosh k(z+h)}{\cosh kh}\,. \tag{1.4.13}$$

The velocity field is

$$u = \frac{gkA}{\omega}\frac{\cosh k(z+h)}{\cosh kh}e^{ikx}\,, \tag{1.4.14}$$

$$v = 0\,, \tag{1.4.15}$$

$$w = -\frac{igkA}{\omega}\frac{\sinh k(z+h)}{\cosh kh}e^{ikx}\,. \tag{1.4.16}$$

For very deep water, $kh \gg 1$,

$$(\phi, u, v, w, p) = \left(-\frac{ig}{\omega}, \frac{gk}{\omega}, 0, -\frac{igk}{\omega}, \rho g\right) Ae^{kz}e^{ikx}\,, \tag{1.4.17}$$

and for very shallow water, $kh \ll 1$,

$$(\phi, u, v, w, p) = \left(-\frac{ig}{\omega}, \frac{gk}{\omega}, 0, 0, \rho g\right) Ae^{ikx}\,. \tag{1.4.18}$$

Several distinctive features of the shallow-water results deserve mentioning: (i) The dependence on z disappears; (ii) the vertical velocity is negligible; and (iii) the dynamic pressure is $\rho g\eta$ and the total pressure $P = \rho g(\zeta - z)$, which is hydrostatic in terms of depth below the free surface.

Finally, we know from Section 1.2 that when the spatial scale is $1/k$, the condition for linearization is $kA \ll 1$. Let us check the linearizing assumption again by comparing a nonlinear term with a linear term, both evaluated at the free surface $z = 0$. For arbitrary kh, we have from Eqs. (1.4.11) and (1.4.14)

$$\left(\frac{u\partial u/\partial x}{\partial u/\partial t}\right)_{z=0} \sim \left(\frac{uk}{\omega}\right)_{z=0} \sim \left(\frac{u}{C}\right)_{z=0} = \frac{kA}{\tanh kh} \quad \text{for all } kh\,.$$

Note that for $kh \ll 1$, the above ratio becomes A/h. Therefore, in shallow water the linearized theory is indeed a very restricted approximation.

1.5 Group Velocity

One of the most important concepts in dispersive waves is the group velocity, for which two views may be examined to understand its significance.

1.5.1 A Kinematic View

Suppose that there is a group of sinusoidal waves with a continuous but narrow range of wavelengths centered around $k = k_0$. The free-surface displacement may be represented by

$$\zeta = \int_{k_0-\Delta k}^{k_0+\Delta k} A(k) e^{i[kx-\omega(k)t]}\, dk\,, \quad \frac{\Delta k}{k_0} \ll 1\,, \tag{1.5.1}$$

where $A(k)$ is the wavenumber spectrum with ω and k satisfying the dispersion relation

$$\omega = \omega(k)\,. \tag{1.5.2}$$

By Taylor expansion we write

$$\omega = \omega[k_0 + (k-k_0)] = \omega(k_0) + (k-k_0)\left(\frac{d\omega}{dk}\right)_{k_0} + O(k-k_0)^2\,.$$

Denoting

$$\frac{k-k_0}{k_0} = \xi\,, \quad \omega_0 = \omega(k_0)\,, \quad \text{and} \quad \left(\frac{d\omega}{dk}\right)_0 = \left(\frac{d\omega}{dk}\right)_{k_0} \equiv C_g\,, \tag{1.5.3}$$

we have for sufficiently smooth $A(k)$ and to the crudest approximation

$$\begin{aligned}\zeta &\simeq A(k_0) e^{i(k_0 x-\omega_0 t)} \int_{-\Delta k/k_0}^{\Delta k/k_0} \{\exp[ik_0\xi(x-C_g t)]\} k_0\, d\xi \\ &= 2A(k_0)\frac{\sin \Delta k(x-C_g t)}{(x-C_g t)} e^{i(k_0 x-\omega_0 t)} = \tilde{A} e^{i(k_0 x-\omega_0 t)}\,,\end{aligned} \tag{1.5.4}$$

where

$$\tilde{A} = 2A(k_0)\frac{\sin \Delta k(x-C_g t)}{(x-C_g t)}\,. \tag{1.5.5}$$

Because of the factor $\exp[i(k_0 x - \omega_0 t)]$ in Eq. (1.5.4), ζ may be viewed as a locally sinusoidal wavetrain with a slowly modulated amplitude $\tilde{A}$. In particular, the envelope defined by $\tilde{A}$ is in the form of wave groups as shown in Fig. 1.2 and advances at the speed C_g. Therefore, C_g is called the *group*

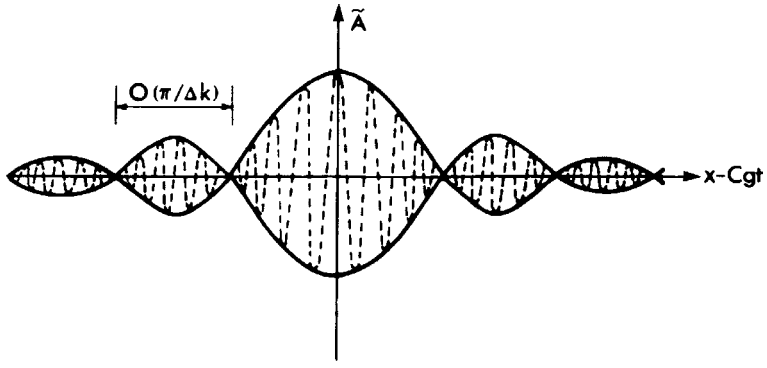

Figure 1.2: A group of waves within a narrow frequency band.

velocity. The distance between two adjacent nodes of an envelope, hence the modulation length scale of the amplitude, is roughly $\pi/\Delta k$ and is much greater than the length of the constituent waves $2\pi/k_0$.

For water waves on a constant depth, it follows by differentiating the dispersion relation (1.4.8) that

$$C_g = \frac{d\omega}{dk} = \frac{1}{2}\frac{\omega}{k}\left(1 + \frac{2kh}{\sinh 2kh}\right) = \frac{C}{2}\left(1 + \frac{2kh}{\sinh 2kh}\right). \tag{1.5.6}$$

For deep water $kh \gg 1$,

$$C_g \simeq \frac{1}{2}C \simeq \frac{1}{2}\left(\frac{g}{k}\right)^{1/2}, \tag{1.5.7}$$

while for shallow water, $kh \ll 1$,

$$C_g \simeq C \simeq (gh)^{1/2}. \tag{1.5.8}$$

Since the phase velocity exceeds the group velocity for general depths, the individual wave crests travel from the tail toward the front of a group.

It will be shown more generally in Section 2.4 that C_g is the velocity of any slowly varying envelope, Eq. (1.5.5) being a special case.

1.5.2 A Dynamic View: Energy Flux

Let us first compute the average energy in a uniform progressive wavetrain beneath a unit square of the free surface. Denoting the time average over a period by an overhead bar, we have the kinetic energy in the whole fluid column

$$\text{K.E.} = \frac{\rho}{2}\overline{\int_{-h}^{\zeta} [\mathbf{u}(\mathbf{x},t)]^2\, dz}$$

$$\cong \frac{\rho}{2}\int_{-h}^{0} \overline{\{[\operatorname{Re} u(\mathbf{x})e^{-i\omega t}]^2 + [\operatorname{Re} w(\mathbf{x})e^{-i\omega t}]^2\}}\, dz\,, \qquad (1.5.9)$$

where for second-order $O(kA)^2$ accuracy the upper limit has been replaced by $z = 0$, and $\mathbf{u}$ may be approximated by the first-order result, Eqs. (1.4.14) and (1.4.16). Note that for any two sinusoidal functions,

$$a = \operatorname{Re} Ae^{-i\omega t} \quad \text{and} \quad b = \operatorname{Re} Be^{-i\omega t}\,,$$

the following formula is true:

$$\overline{ab} = \frac{1}{T}\int_0^T dt\, ab = \frac{1}{2}\operatorname{Re}(AB^*) = \frac{1}{2}\operatorname{Re}(A^*B)\,, \qquad (1.5.10)$$

where $(\ )^*$ denotes the complex conjugate. The proof is left as an exercise. With Eqs. (1.4.14), (1.4.16), and (1.5.10), Eq. (1.5.9) becomes

$$\text{K.E.} = \frac{\rho}{4}\left(\frac{gk|A|^2}{\omega}\right)^2 \frac{1}{\cosh^2 kh}\int_{-h}^{0} [\cosh^2 k(z+h) + \sinh^2 k(z+h)]\, dz$$

$$= \frac{\rho}{4}\left(\frac{gk|A|}{\omega}\right)^2 \frac{\sinh 2kh}{2k\cosh^2 kh} = \frac{1}{4}\rho g|A|^2\,, \qquad (1.5.11)$$

where use is made of the following formula:

$$\int_0^{kh} \cosh^2\xi\, d\xi = \frac{1}{4}(\sinh 2kh + 2kh)\,, \qquad (1.5.12)$$

and the dispersion relation. On the other hand, the potential energy in the fluid column due to wave motion is

$$\text{P.E.} = \overline{\int_0^{\zeta} \rho g z\, dz} = \frac{1}{2}\rho g\overline{\zeta^2} = \frac{1}{4}\rho g|A|^2 \qquad (1.5.13)$$

since $\rho g\, dz$ is the weight of a thin horizontal slice whose height above the mean-free surface is z. The total energy is

$$E = \text{K.E.} + \text{P.E.} = \frac{1}{2}\rho g|A|^2. \qquad (1.5.14)$$

Note that the kinetic and potential energies are equal; this property is called the *equipartition of energy*. Let us consider a vertical cross section of unit

width along the crest. The rate of energy flux across this section is equal to the mean rate of work done by the dynamic pressure, that is,

$$\begin{matrix}\text{Rate of}\\ \text{energy flux}\end{matrix} = \begin{matrix}\text{Rate of}\\ \text{pressure working}\end{matrix} = \overline{\int_{-h}^{\zeta} p(\mathbf{x},t)u(\mathbf{x},t)\,dz} \cong -\rho\int_{-h}^{0}\overline{\Phi_t\Phi_x}\,dz\,, \tag{1.5.15}$$

which can be calculated to be

$$\text{Rate of energy flux} = -\frac{1}{2}\rho g A^2\left[\frac{1}{2}\frac{\omega}{k}\left(1+\frac{2kh}{\sinh 2kh}\right)\right] = EC_g\,. \tag{1.5.16}$$

Hence the group velocity has the dynamical meaning of the velocity of energy transport. In contrast, the phase speed is merely a kinematic quantity and is not always identifiable with the transport of any dynamical substance.

As an immediate application, consider a long wave tank of unit width with sinusoidal waves generated at one end. Many periods after the start of the wavemaker, the envelope is uniform almost everywhere except near the wave front which may look like Fig. 1.3. Since the rate of energy input by the wavemaker at the left (say at $x = 0$) is EC_g, the rate of lengthening of the wave region must be C_g. Thus the wave front must propagate at the group velocity. Details of the wave-front evolution will be discussed in Section 2.4.

Exercise 1.1

Consider a two-layered fluid system over a horizontal bottom. The lighter fluid above has the density of ρ, while the heavier fluid below has the density of ρ'. Let the free surface be at $z = 0$, the interface at $z = -h$, and the

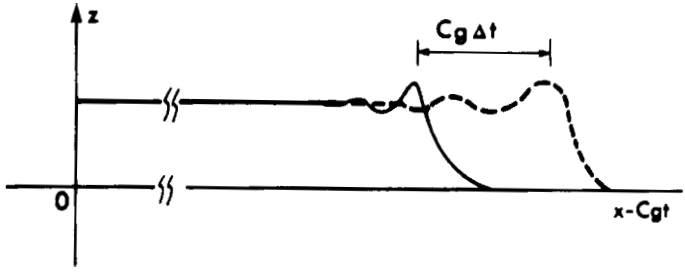

Figure 1.3: The envelope front of a sinusoidal wavetrain.

bottom at $z = -h'$. Show that a sinusoidal progressive wave must satisfy the dispersion relation:

$$\left(\frac{\omega^2}{gk}\right)^2 \{\rho' \coth kh \coth k(h'-h) + \rho\}$$

$$-\frac{\omega^2}{gk}\rho'\{\coth kh + \coth k(h'-h)\} + \rho' - \rho = 0\,.$$

Study the two possible modes corresponding to the two solutions ω_1^2 and ω_2^2 for the same k.

In particular, when $h' \sim \infty$ show that

$$\omega_1^2 = gk \quad \text{and} \quad \omega_2^2 = gk\frac{\rho' - \rho}{\rho' \coth kh + \rho} < \omega_1^2$$

and that the amplitude ratio of interface to free surface is

$$e^{-kh} \quad \text{and} \quad -\frac{\rho}{\rho' - \rho}e^{kh}$$

for the first and second mode, respectively. Plot the group velocity as a function of k for each mode.

Exercise 1.2: Capillary Waves

Surface tension on the free surface introduces a pressure difference between the atmospheric pressure P_a above and the water pressure P below. The difference is given by the Laplace formula (see, e.g., Landau and Lifshitz, 1959, p. 237 ff)

$$P - P_a \cong -T(\zeta_{xx} + \zeta_{yy})\,, \quad \text{on} \quad z \cong 0\,, \tag{1.5.17}$$

where the right-hand side is proportional to the surface curvature and T is the surface tension coefficient. For the water–air interface at 20°C, $T = 74$ dyn/cm in cgs units. Reformulate the boundary conditions on the free surface and study a plane progressive wave on deep water: $\Phi \propto e^{kz}e^{i(kx-\omega t)}$. Show that

$$\omega^2 = gk + \frac{Tk^3}{\rho}\,.$$

Show further that the phase velocity has a minimum value C_m which satisfies

$$\frac{C^2}{C_m^2} = \frac{1}{2}\left(\frac{\lambda}{\lambda_m} + \frac{\lambda_m}{\lambda}\right) = \frac{1}{2}\left(\frac{k_m}{k} + \frac{k}{km}\right),$$

where

$$\lambda_m = \frac{2\pi}{k_m} = 2\pi \left(\frac{T}{g\rho} \right)^{1/2} .$$

What are the numerical values of λ_m and C_m for water and air?

Discuss the variations of ω, C and C_g versus k or λ.

Propagation of Transient Waves in Open Water of Essentially Constant Depth

2

Disturbances generated by excitations of finite duration such as submarine earthquakes, landslides, explosions, and so on, produce transient waves. Because of dispersion, the propagation of transient water waves is considerably more complex than many other kinds of waves in nature. To facilitate a clear understanding of the physical consequences of dispersion, we will study in this chapter simple models of source mechanism and ocean depth for which detailed analyses are possible. In Sections 2.1 and 2.2 we will study the so-called Cauchy-Poisson problem of waves due to an impulsive source of some kind, with particular emphasis given to the behavior away from the source. Many practical issues concerning earthquake-induced waves in nature are omitted for simplicity. In Sections 2.3 and 2.4 the role of dispersion in slowly modulated wave groups will be investigated. The mathematical technique of multiple-scale expansions is introduced to arrive very directly at the asymptotic result for large time and to prepare the ground for later inclusion of nonlinearity.

2.1 Two-Dimensional Transient Problems

Let us consider an ocean of constant depth without other rigid boundaries. Assume that the disturbances on the free surface and at the bottom are independent of y. The problem can be formulated in the x, z plane. Thus, the velocity potential $\Phi(x, z, t)$ satisfies

$$\nabla^2\Phi = \frac{\partial^2\Phi}{\partial x^2} + \frac{\partial^2\Phi}{\partial z^2} = 0\,. \tag{2.1.1}$$

On the free surface the following conditions hold:

$$\frac{\partial \zeta}{\partial t} = \frac{\partial \Phi}{\partial z}\,, \qquad z = 0\,, \tag{2.1.2a}$$

$$\frac{\partial \Phi}{\partial t} + g\zeta = -\frac{P_a(x,t)}{\rho}\,, \quad z = 0\,, \tag{2.1.2b}$$

where $P_a(x,t)$ is prescribed. Let the seafloor be denoted by $z = -h + H(x,t)$. If the ground motion is known, continuity of normal velocity gives

$$\frac{\partial \Phi}{\partial z} = \frac{\partial H}{\partial t} + \frac{\partial \Phi}{\partial x}\frac{\partial H}{\partial x} \quad \text{on} \quad z = -h + H(x,t)\,. \tag{2.1.3}$$

Within the framework of linearization we assume that the amplitudes of H, $\partial H/\partial t$ and $\partial H/\partial x$ are small so that the quadratic term is negligible; hence

$$\frac{\partial \Phi}{\partial z} = \frac{\partial H}{\partial t} \equiv W(x,t) \quad \text{on} \quad z \cong -h\,. \tag{2.1.4}$$

Initial conditions must be further prescribed. To see what initial data are needed, let us employ the method of Laplace transform defined by

$$\bar{f}(s) = \int_0^\infty e^{-st} f(t)\, dt\,, \tag{2.1.5a}$$

$$f(t) = \frac{1}{2\pi i}\int_\Gamma e^{st}\bar{f}(s)\, ds\,, \tag{2.1.5b}$$

where Γ is a vertical line to the right of all singularities of $\bar{f}(s)$ in the complex s plane. The transforms of Eqs. (2.1.1) and (2.1.4) give

$$\nabla^2 \overline{\Phi}(x,z,s) = 0\,, \quad -h < z < 0\,, \tag{2.1.6}$$

$$\frac{\partial \overline{\Phi}}{\partial z} = \overline{W}(x,s)\,, \quad z = -h\,. \tag{2.1.7}$$

From Laplace transforms of conditions (2.1.2a, b) we obtain

$$-\zeta(x,0) + s\bar{\zeta}(x,s) = \frac{\partial \overline{\mathbf{\Phi}}(x,0,s)}{\partial z}\,, \tag{2.1.8}$$

$$-\Phi(x,0,0) + s\overline{\Phi}(x,0,s) + g\bar{\zeta}(x,s) = -\frac{\overline{P}_a(x,s)}{\rho}\,, \tag{2.1.9}$$

which can be combined to give

$$\frac{\partial \overline{\Phi}}{\partial z} + \frac{s^2}{g}\overline{\Phi} = -\frac{s\overline{P}_a}{\rho g} - \zeta(x,0) + \frac{s}{g}\Phi(x,0,0)\,, \quad z = 0\,. \tag{2.1.10}$$

From the above equation it is immediately clear that we only need to prescribe the initial data $\Phi(x,0,0)$ and $\zeta(x,0)$ on the free surface, but nowhere else, because time derivatives appear only in the free-surface conditions. A more mathematical study on the uniqueness of the initial-value problem has been made by Finkelstein (1953).

What is the physical significance of $\Phi(x,0,0)$? Assume that, before $t=0$, all is calm, but at $t=0$ an impulsive pressure $P_a(x,t)=I\delta(t)$ is applied on the free surface. Integrating Bernoulli's equation from $t=0-$ to $t=0+$, we obtain

$$\Phi(x,0,0+)-\Phi(x,0,0-)+\int_{0-}^{0+} g\zeta\,dt=-\frac{I}{\rho}\int_{0-}^{0+}\delta(t)\,dt=-\frac{I}{\rho}\,.$$

Since $\Phi(x,0,0-)=0$ and ζ must be finite, we obtain $\Phi(x,0,0+)=-I/\rho$. Thus, the initial value of $\boldsymbol{\Phi}$ represents physically an impulsive pressure acting on the free surface at an instant slightly earlier than $t=0+$.

Equations (2.1.6), (2.1.7), and (2.1.10) now define a boundary-value problem which formally resembles that of a simple harmonic case. For any finite t it is expected that no motion is felt at a great distance from the initial disturbance so that $\boldsymbol{\Phi}(x,t)\to 0$ as $|x|\to\infty$, which implies that $\overline{\boldsymbol{\Phi}}\to 0$ as $|x|\to\infty$. Since the region does not involve any finite bodies, the problem can be readily solved by applying the exponential Fourier transform with respect to x, defined by

$$\tilde{f}(k)=\int_{-\infty}^{\infty} e^{-ikx}f(x)\,dx\,,\quad f(x)=\frac{1}{2\pi}\int_{-\infty}^{\infty} e^{ikx}\tilde{f}(k)\,dk\,. \tag{2.1.11}$$

The Fourier–Laplace transform of Φ satisfies

$$\frac{d^2\tilde{\overline{\Phi}}}{dz^2}-k^2\tilde{\overline{\Phi}}=0\,,\quad -h<z<0\,, \tag{2.1.12}$$

$$\frac{d\tilde{\overline{\Phi}}}{dz}+\frac{s^2}{g}\tilde{\overline{\Phi}}=F(k,s)\,,\quad z=0\,, \tag{2.1.13}$$

$$\frac{d\tilde{\overline{\Phi}}}{dz}=\tilde{\overline{W}}\,,\quad z=-h\,, \tag{2.1.14}$$

where

$$F(k,s)\equiv-\frac{s\tilde{\overline{P}}_a(k,x)}{\rho g}-\tilde{\zeta}(k,0)+\frac{s}{g}\tilde{\Phi}(k,0,0)\,. \tag{2.1.15}$$

The general solution of Eq. (2.1.12) is

$$\tilde{\overline{\Phi}} = A\cosh k(z+h) + B\sinh k(z+h)\,.$$

The coefficients A and B are found from the boundary conditions (2.1.13) and (2.1.14) with the following result:

$$\tilde{\overline{\Phi}} = \frac{1/\cosh kh}{s^2 + gk\tanh kh} \times \left[gF\cosh k(z+h) + \frac{\tilde{\overline{W}}}{k}(s^2\sinh kz - gk\cosh kz) \right]. \qquad (2.1.16)$$

Clearly, the first and second addends in the brackets represent, respectively, all the disturbances on the free surface and on the bottom. Taking the inverse Fourier and Laplace transforms, we have, formally,

$$\Phi(x,z,t) = \frac{1}{2\pi}\int_{-\infty}^{\infty} dk\, e^{ikx}\frac{1}{2\pi i}\int_{\Gamma} ds\, e^{st}\tilde{\overline{\Phi}}(k,z,s)\,. \qquad (2.1.17)$$

To obtain the free-surface height we use Eq. (2.1.2b),

$$\zeta(x,t) = \frac{-P_a}{\rho g} - \frac{1}{g}\frac{\partial\Phi}{\partial t}(x,0,t) = \frac{-P_a}{\rho g} + \frac{1}{2\pi}\int_{-\infty}^{\infty} dk\, e^{ikx}\int_{\Gamma}\frac{ds}{2\pi i}e^{st}\frac{-s}{g}\tilde{\overline{\Phi}}(k,0,s)\,, \qquad (2.1.18)$$

where $\tilde{\overline{\Phi}}$ is given by Eq. (2.1.16). The task is now to extract information from Eqs. (2.1.17) and (2.1.18). Two special cases will be studied in the following subsections.

2.1.1 Transient Disturbance Due to an Initial Displacement on the Free Surface

Here we let

$$P_a(x,t) = W(x,t) = \Phi(x,0,0) = 0 \quad \text{and} \quad \zeta(x,0) \equiv \zeta_0(x) \neq 0\,, \qquad (2.1.19)$$

hence

$$\tilde{\overline{W}} = 0\,, \quad F = -\tilde{\zeta}_0(k)\,. \qquad (2.1.20)$$

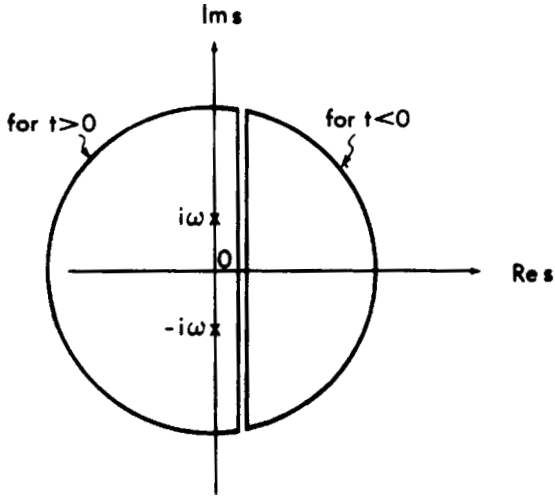

Figure 2.1: Contours for inverse Laplace transform.

Equation (2.1.18) gives the free-surface height

$$\zeta = \frac{1}{4\pi^2 i} \int_{-\infty}^{\infty} dk\, e^{ikx} \tilde{\zeta}_0(k) \int_\Gamma \frac{s e^{st}\, ds}{s^2 + gk \tanh kh}\,. \tag{2.1.21}$$

The s integral can be easily evaluated. The integrand has two imaginary poles at

$$s = \pm i\omega\,, \quad \text{with} \quad \omega = (gk \tanh kh)^{1/2}\,. \tag{2.1.22}$$

For $t < 0$ we introduce a closed semicircular contour in the right half s plane as shown in Fig. 2.1. Since the factor multiplying e^{st} in the integrand vanishes uniformly as $s \to \infty$, the line integral along the great semicircular arc is zero by Jordan's lemma. By Cauchy's residue theorem, the original s integral is zero, there being no singular points in the semicircle. Not suprisingly, then,

$$\zeta = 0\,, \quad t < 0\,. \tag{2.1.23}$$

For $t > 0$ we must choose a semicircle in the left half of the s plane. By Jordan's lemma again, the line integral along the semicircle vanishes, leaving only the residues for the two poles at $\pm i\omega$.

$$\frac{1}{2\pi i} \int_\Gamma \frac{s e^{st}\, ds}{s^2 + \omega^2} = \frac{1}{2\pi i} \int_\Gamma \frac{s e^{st}\, ds}{(s + i\omega)(s - i\omega)} = \cos \omega t\,, \quad t > 0\,.$$

Substituting into Eq. (2.1.21), we get

$$\zeta(x,t) = \frac{1}{2\pi}\int_{-\infty}^{\infty} dk\, e^{ikx}\cos\omega t\tilde{\zeta}_0(k)\,. \tag{2.1.24}$$

Clearly, $\cos\omega t$ is even in k. In general, we can split $\zeta_0(x)$ into even and odd parts with respect to x : ζ_0^e and ζ_0^o. It follows from the definition of Fourier transform that

$$\begin{aligned}\tilde{\zeta}_0(k) &= 2\int_0^{\infty} dx\cos kx\zeta_0^e(x) - 2i\int_0^{\infty} dx\sin kx\zeta_0^o(x)\\ &\equiv \tilde{\zeta}_0^e(k) + \tilde{\zeta}_0^o(k)\end{aligned}$$

where $\tilde{\zeta}_0^e$ is real and even in k and $\tilde{\zeta}_0^o$ is imaginary and odd in k.

For simplicity, let ζ_0 be even in x; Eq. (2.1.24) may now be written

$$\begin{aligned}\zeta(x,t) &= \frac{1}{\pi}\int_0^{\infty} dk\,\tilde{\zeta}_0^e\cos kx\cos\omega t\\ &= \frac{1}{2\pi}\,\mathrm{Re}\int_0^{\infty} dk\,\tilde{\zeta}_0^e[e^{i(kx-\omega t)} + e^{i(kx+\omega t)}]\,.\end{aligned} \tag{2.1.25}$$

The first and second terms in the brackets above represent right- and left-going waves, respectively.

For a better physical understanding, approximations are necessary. At large t we can employ the *method of stationary phase* devised by Kelvin. Heuristically, the idea is as follows.

Consider the integral

$$I(t) = \int_a^b f e^{itg}\,dk\,, \tag{2.1.26}$$

where f and g are smooth functions of k. When t is large, the phase tg of the sinusoidal part oscillates rapidly as k varies. If one plots the integrand versus k, there is very little net area under the curve due to cancellation unless there is a point at which the phase is stationary, that is,

$$g'(k) = 0\,, \quad k = k_0\,. \tag{2.1.27}$$

In the neighborhood of this stationary point the oscillating factor of the integrand of Eq. (2.1.26) may be written

$$e^{itg(k_0)}\exp\{it[g(k) - g(k_0)]\}\,.$$

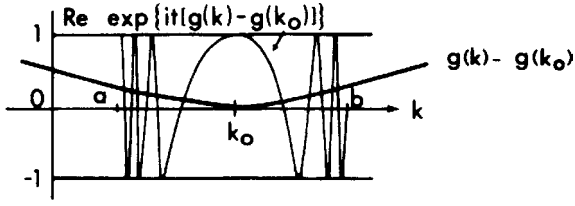

Figure 2.2: The real part of $\exp\{it[g(k) - g(k_0)]\}$.

The real part of $\exp\{it[g(k) - g(k_0)]\}$ varies slowly, as sketched in Fig. 2.2, while the imaginary part slowly touches the k axis at $k = k_0$. Therefore, a significant contribution to the integral can be expected from this neighborhood. If we approximate $g(k)$ by the first two terms of the Taylor expansion

$$g(k) \cong g(k_0) + \frac{1}{2}(k - k_0)^2 g''(k_0)\,,$$

then the integral may be written

$$I \cong e^{itg(k_0)} f(k_0) \int_{-\infty}^{\infty} dk \exp\left[\frac{1}{2} i(k - k_0)^2 t g''(k_0)\right],$$

where the limits (a, b) have been approximated by $(-\infty, \infty)$. Using the fact that

$$\int_{-\infty}^{\infty} e^{\pm itk^2}\, dk = \left(\frac{\pi}{t}\right)^{1/2} e^{\pm i\pi/4}\,,$$

we finally have

$$I \cong e^{itg(k_0)} f(k_0) \left(\frac{2\pi}{t|g''(k_0)|}\right)^{1/2} e^{\pm i\pi/4}\,, \tag{2.1.28}$$

where the $\pm$ sign is to be taken if $g''(k_0) \gtrless 0$. It can be shown by a more elaborate analysis that the error is of order $O(t^{-1})$. Also if there is no stationary point in the range (a, b), the integral is at most of order $O(t^{-1})$. This and other information can be found in Stoker (1957) or Carrier, Krook, and Pearson (1966).

Returning to Eq. (2.1.25), we need certain properties of the dispersion curve as sketched in Fig. 2.3. Consider $x > 0$. For the first integral

$$g(k) = k\frac{x}{t} - \omega\,,$$

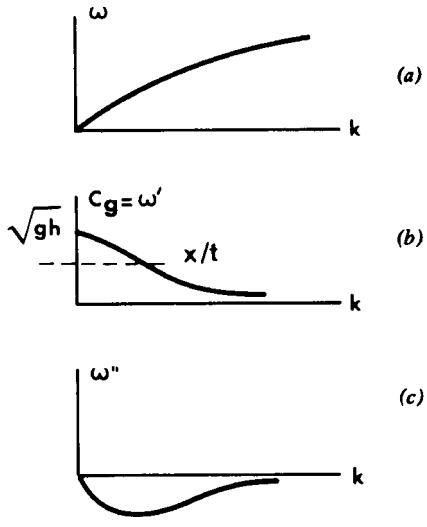

Figure 2.3: Variations of ω, ω', and ω'' with k.

it may be seen from Fig. 2.3(b) that there is a stationary point at

$$\frac{x}{t} = \omega'(k_0) = C_g(k_0) \quad \text{if} \quad \frac{x}{t} < (gh)^{1/2}\,. \tag{2.1.29}$$

In the same interval $(0, \infty)$ of k, there is no stationary point for the second integral. It follows from Eq. (2.1.28) that

$$\zeta \cong \frac{1}{2\pi}\tilde{\zeta}_0^e(k_0)\left[\frac{2\pi}{t|\omega''(k_0)|}\right]^{1/2} \cos\left[k_0 x - \omega(k_0)t + \frac{\pi}{4}\right] + O(t^{-1})\,,$$
$$x < (gh)^{1/2}t\,, \tag{2.1.30}$$

where use is made of the fact that $\omega''(k) < 0$ [Fig. 2.3(c)], and

$$\zeta \cong O(t^{-1})\,, \quad x > (gh)^{1/2}t\,. \tag{2.1.31}$$

Now let us examine the physics represented by Eq. (2.1.30). An observer moving at a certain speed x/t lower than $(gh)^{1/2}$ sees a train of sinusoidal waves of wavenumber k_0 [and frequency $\omega(k_0)$] whose group velocity equals x/t. The amplitude of the wavetrain decays as $O(t^{-1/2})$. For large x/t we see from Fig. 2.3(a) that k_0 is small, hence, a faster moving observer sees longer waves which are also of larger amplitude since $(|\omega''(k_0)|)^{1/2}$ is less.

The precise shape of $\zeta_0(x)$ affects $\tilde{\zeta}_0(k)$ and the amplitude of the dispersed waves. For example, if

$$\zeta_0(x) = \frac{Sb}{\pi(x^2 + b^2)}\,,$$

which is a symmetrical bump of area S and characteristic spread b, we find that

$$\tilde{\zeta}_0(k) = \tilde{\zeta}_0^e(k) = Se^{-|k|b}\,.$$

If the spread b is large, then $\tilde{\zeta}_0^e$ is not appreciable except for small k_0 or long leading waves. As b increases, the amplitude of a given k_0 decreases.

Summing up the views of many observers for the same t, we obtain a snapshot of the free surface (see Fig. 2.4). Thus, at a constant t, long waves are found toward the front and short waves toward the rear. Now consider the snapshot at a later time $t_2 > t_1$. Both observers have now moved to the right. The spatial separation, however, has increased. In particular, let $\xi_1 \approx \xi_2$ so that between them $k, \omega \approx$ const. The total extent of a monochromatic wavetrain with k, ω now stretches with increasing t, implying that wave crests are created in the course of propagation.

To follow a particular wave crest at its phase speed, an observer must travel at a varying speed since k_0 and $C(k_0)$ do not remain constant as the crest moves into new territory. However, if one moves at the group velocity of the waves of length $2\pi/k_0$, one only sees sine waves of this length catching

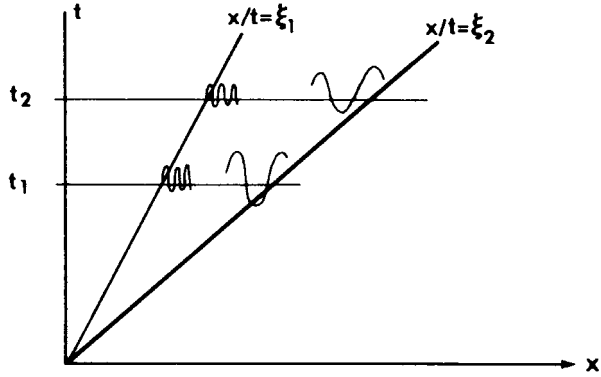

Figure 2.4: Space–time plot of dispersive waves between two moving observers.

up from behind and then running away toward the front, since their phase velocity exceeds the group velocity.

A similar picture exists for the left-going disturbance.

2.1.2 Energy Propagation, Group Velocity

Consider a rightward traveling disturbance only. Equation (2.1.30) holds for large t and represents a progressive wave with amplitude

$$A = \frac{\tilde{\zeta}_0^e(k_0)}{2\pi} \left(\frac{2\pi}{t|\omega''(k_0)|} \right)^{1/2} , \tag{2.1.32}$$

which decays slowly as $t^{-1/2}$.

The wave energy density of this progressive wave is approximately

$$E \approx \rho \frac{gA^2}{2} = \frac{1}{2}\rho g|\zeta|^2 = \frac{\rho g}{2} \left| \frac{\tilde{\zeta}_0^e(k_0)}{2\pi} \left(\frac{2\pi}{t|\omega''(k_0)|} \right)^{1/2} \right|^2$$

$$= \frac{\rho g|\tilde{\zeta}_0^e(k_0)|^2}{4\pi t|\omega''(k_0)|} . \tag{2.1.33}$$

At any given t, consider the waves between two observers moving at $C_{g_1} \equiv C_g(k_1)$ and $C_{g_2} \equiv C_g(k_2)$, that is, between the two rays

$$\frac{x_1}{t} = C_{g_1} \quad \text{and} \quad \frac{x_2}{t} = C_{g_2}$$

in the space–time diagram. The total wave energy between them is

$$\int_{x_1}^{x_2} E\, dx \cong \int_{x_1}^{x_2} \frac{\rho g|\tilde{\zeta}_0^e(k_0)|^2}{4\pi t|\omega''(k_0)|}\, dx . \tag{2.1.34}$$

Since $x = \omega'(k_0)t$ for fixed t and $\omega''(k_0) < 0$, we have

$$\frac{dx}{t} = \omega''(k_0)\, dk_0 = -|\omega''(k_0)|\, dk_0 . \tag{2.1.35}$$

Now for $x_2 > x_1$, $k_2 < k_1$ [see Figs. 2.3(a), (b)], Eq. (2.1.34) becomes

$$\int_{x_1}^{x_2} E\, dx \cong \rho g \int_{k_2}^{k_1} \frac{|\tilde{\zeta}_0^e(k_0)|^2}{4\pi}\, dk_0 = \text{const} , \tag{2.1.36}$$

which is constant in time. Therefore, the total energy of the waves between two observers moving at the local group velocities is conserved. This interpretation, due to Jeffreys and Jeffreys (1953), further strengthens the significance of the group velocity as discussed in Chapter One.

Whitham (1965) has shown that the asymptotic result by stationary phase for large x and t agrees with the so-called *geometrical optics theory*. From Eq. (2.1.29) we obtain, by differentiations with respect to x and t,

$$1 = \omega''(k)k_x t \quad \text{and} \quad 0 = \omega''(k)k_t t + \omega'$$

so that

$$k_x = \frac{1}{t\omega''(k)}\,, \quad k_t = -\frac{\omega'}{t\omega''(k)}\,. \tag{2.1.37}$$

It follows that

$$\frac{\partial k}{\partial t} + \omega' \frac{\partial k}{\partial x} = 0\,,$$

which may also be written

$$\frac{\partial k}{\partial t} + \frac{\partial \omega}{\partial x} = 0\,. \tag{2.1.38}$$

Since

$$dk = \frac{\partial k}{\partial t}\,dt + \frac{\partial k}{\partial x}\,dx\,,$$

we see from Eq. (2.1.37) that along the curve $dx/dt = C_g = \omega'$, $dk = 0$; hence k remains constant. Furthermore, by multiplying Eq. (2.1.33) with ω^{-1} and differentiating with respect to t and x, we obtain straightforwardly

$$\frac{\partial}{\partial t}\left(\frac{E}{\omega}\right) + \frac{\partial}{\partial x}\left(C_g \frac{E}{\omega}\right) = 0\,. \tag{2.1.39}$$

Both Eqs. (2.1.38) and (2.1.39) are basic results of the geometrical optics approximation and are of general validity for slowly varying, nearly periodic wavetrains as will be elaborated in Chapter Three.

2.1.3 Leading Waves Due to a Transient Disturbance

The fastest waves correspond to $k \simeq 0$ and move at the speed near $(gh)^{1/2}$. In the neighborhood of the wave front, $g'(k) \simeq x/t - (gh)^{1/2}$ is small, and the phase is nearly stationary. Furthermore, $\omega''(k) \simeq -(gh)^{1/2}h^2k$ is also very small and the approximation of Eq. (2.1.30) is not valid. A better approximation is needed (Kajiura, 1963).

Since $k \simeq 0$, we expand the phase function for small k as follows:

$$g(k) = k\frac{x}{t} - \omega(k) \simeq k\left(\frac{x}{t}\right) - (gh)^{1/2}\left(k - \frac{k^3h^2}{6} + \cdots\right)$$

$$= k\left[\frac{x}{t} - (gh)^{1/2}\right] + \frac{(gh)^{1/2}}{6}h^2k^3 + \cdots . \tag{2.1.40}$$

Near the leading wave, $x/t - (gh)^{1/2}$ can be zero; we must retain the term proportional to k^3. Again, only the first integral in Eq. (2.1.25) matters so that

$$\zeta = \frac{1}{2\pi}\int_0^\infty dk\,\tilde{\zeta}_0^e(k)\cos(kx - \omega t) + O\left(\frac{1}{t}\right)$$

$$\simeq \frac{1}{2\pi}\tilde{\zeta}_0^e(0)\int_0^\infty \cos\left\{k[x - (gh)^{1/2}t] + \left[\frac{(gh)^{1/2}h^2t}{6}\right]k^3\right\}dk\,,$$

where use is made of the fact that $\tilde{\zeta}_0^e$ is real. With the change of variables

$$Z^3 = \frac{2[x - (gh)^{1/2}t]^3}{(gh)^{1/2}h^2t} \quad \text{and} \quad k[x - (gh)^{1/2}t] = Z\alpha\,,$$

the integral above becomes

$$\zeta \sim \frac{(2)^{1/3}\tilde{\zeta}_0^e(0)}{2\pi((gh)^{1/2}h^2t)^{1/3}}\int_0^\infty d\alpha\cos\left(Z\alpha + \frac{\alpha^3}{3}\right),$$

which can be expressed in terms of Airy's function of Z:

$$\mathrm{Ai}(Z) \equiv \frac{1}{\pi}\int_0^\infty d\alpha\cos\left(Z\alpha + \frac{\alpha^3}{3}\right). \tag{2.1.41}$$

Thus, we have

$$\zeta \sim \left[\frac{2}{(gh)^{1/2}h^2t}\right]^{1/3}\frac{1}{2}\tilde{\zeta}_0^e(0)\,\mathrm{Ai}\left\{\left[\frac{2}{(gh)^{1/2}h^2t}\right]^{1/3}[x - (gh)^{1/2}t]\right\}. \tag{2.1.42}$$

$\mathrm{Ai}(Z)$ is oscillatory for $Z < 0$ and decays exponentially for $Z > 0$. Its variation is shown in Fig. 2.5.

The physical picture is as follows: For a fixed t, Z is proportional to $x - (gh)^{1/2}t$ which is the distance from the wave front $x = (gh)^{1/2}t$. At a fixed instant the amplitude is small ahead of the front, and the highest peak is at some distance behind. Toward the rear, the amplitude and the wavelength decrease. Since Z is proportional to $t^{-1/3}$, the snapshots at different

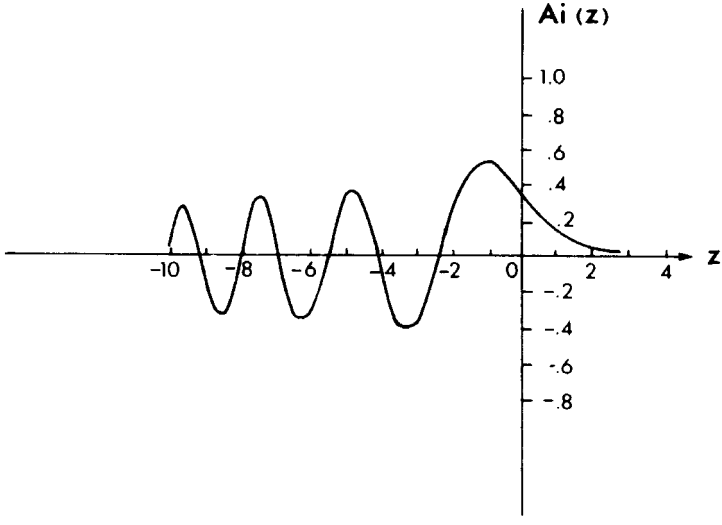

Figure 2.5: Leading wave due to a symmetrical surface hump or trough. The ordinate is $\zeta[(gh)^{1/2}h^2t/2]^{1/3}[\tilde{\zeta}_0^e(0)]^{-1}$, see Eq. (2.1.42).

times are of the same form except that the spatial scale is proportional to the factor $t^{1/3}$, meaning that the same wave form is being stretched out in time. During the evolution the amplitude decays as $t^{-1/3}$ while the rest of the wavetrain decays as $t^{-1/2}$. Thus, the head lives longer than the rest of the body. Note that the amplitude of the leading wave is proportional to $\tilde{\zeta}_0^e(0)$ which is equal to the total area of the initial displacement $\zeta_0^e(x)$.

2.1.4 Tsunami Due to Tilting of the Bottom

Tsunamis are the water waves generated by submarine earthquakes. If the seafloor displacement is known in the area of the earthquake, the water-wave problem is a purely hydrodynamic one. Unfortunately, direct measurements near the epicenter are too difficult to make, and a good deal of effort has been centered on using water-wave records measured at larger distances from the epicenter to infer roughly the nature of tectonic movement. Hence, there has been considerable theoretical studies on water waves due to a variety of ground movement.

Among the many features of tsunamis as recorded near a coast, two have been frequently (but not always) reported (Shepard, 1963). One feature is that the arrival of a tsunami is often preceded by the withdrawal of water

from the beaches, and the other is that the first crest may not be the largest. In this section we shall show an idealized model which reproduces these features qualitatively.

We shall assume that there is no disturbance on the free surface

$$\zeta(x,0) = \Phi(x,0) = P_a(x,0,t) = 0\,. \tag{2.1.43}$$

On the seafloor $z = -h$, the ground displacement $H(x,t)$ is prescribed. Thus, $W = \partial H/\partial t$ is known and the transformed solution follows from Eq. (2.1.16).

$$\tilde{\Phi} = \frac{\tilde{\overline{W}}}{k\cosh kh}\frac{s^2\sinh kz - gk\cosh kz}{s^2 + gk\tanh kh}\,. \tag{2.1.44}$$

The free-surface displacement is

$$\zeta = \frac{1}{2\pi}\int_{-\infty}^{\infty} dk \frac{e^{ikx}}{\cosh kh}\frac{1}{2\pi i}\int_{\Gamma} ds \frac{s\tilde{\overline{W}}e^{st}}{s^2+\omega^2}\,, \tag{2.1.45}$$

where $\omega = (gk\tanh kh)^{1/2}$, as before. We further restrict the ground motion to be a sudden displacement accomplished in an infinitesimal interval of time,

$$H(x,0-) = 0 \quad \text{but} \quad H(x,0+) = H_0(x)\,.$$

The ground velocity can be represented by a δ function

$$\frac{\partial\Phi}{\partial z} = W(x,t) = H_0(x)\delta(t)$$

so that $\tilde{\overline{W}} = \tilde{H}_0(k)$. The s integral can be immediately evaluated to give

$$\zeta = \frac{1}{2\pi}\int_{-\infty}^{\infty} dk \frac{\tilde{H}_0(k)}{\cosh kh}\frac{1}{2}[e^{i(kx+\omega t)} + e^{i(kx-\omega t)}]\,. \tag{2.1.46}$$

Again any $H_0(x)$ can be thought of as the sum of $H_0^o(x)$ and $H_0^e(x)$ which are odd and even in x, respectively. By linearity, the two parts may be treated separately first and their results superimposed later. It is easily shown that the even part $H_0^e(x)$ has effects very similar to the previous example of symmetrical initial displacement on the free surface, the only difference being the factor $(\cosh kh)^{-1}$ which cuts down the influence of the short waves. We shall, therefore, only focus our attention to the odd part.

Let us introduce

$$H_0^o(x) = \frac{dB}{dx} \tag{2.1.47}$$

so that $\tilde{H}_0^o(k) = ik\tilde{B}(k)$. Since $\tilde{H}_0^o(k)$ is odd, $\tilde{B}$ must be real and even in k; hence,

$$\begin{aligned}\zeta &= \frac{1}{2\pi}\int_{-\infty}^{\infty} dk \frac{e^{ikx}}{\cosh kh} ik\tilde{B}(k)\frac{1}{2}(e^{i\omega t}+e^{-i\omega t}) \\ &= \frac{1}{2\pi}\frac{d}{dx}\int_{-\infty}^{\infty} dk \frac{e^{ikx}}{\cosh kh}\tilde{B}(k)\frac{1}{2}(e^{i\omega t}+e^{-i\omega t}) \\ &= \frac{1}{2\pi}\frac{d}{dx}\,\mathrm{Re}\int_{0}^{\infty} dk \frac{e^{ikx}}{\cosh kh}\tilde{B}(k)(e^{i\omega t}+e^{-i\omega t})\,. \end{aligned} \tag{2.1.48}$$

For large t and away from the leading waves, the integrals can be dealt with by the stationary phase method just as before, and many of the same qualitative features should be expected. Let us only look at the neighborhood of the *leading waves* propagating to $x > 0$. Again, the second integral dominates and the important contribution comes from the neighborhood of $k \simeq 0$. Hence

$$\begin{aligned}&\mathrm{Re}\int_0^\infty dk \frac{e^{i(kx-\omega t)}}{\cosh kh}\tilde{B}(k) \\ &\quad\cong \mathrm{Re}\,\tilde{B}(0)\int_0^\infty dk\, e^{ikx}e^{-i\omega t} \\ &\quad\cong \mathrm{Re}\,\tilde{B}(0)\int_0^\infty dk\, \exp\left(i\left\{k[x-(gh)^{1/2}t]+\frac{1}{6}(gh)^{1/2}h^2k^3t\right\}\right) \\ &\quad= \pi\tilde{B}(0)\left[\frac{2}{(gh)^{1/2}h^2t}\right]^{1/3}\mathrm{Ai}\left\{\left[\frac{2}{(gh)^{1/2}h^2t}\right]^{1/3}[x-(gh)^{1/2}t]\right\},\end{aligned}$$

as discussed earlier. Differentiating with respect to x, we have

$$\begin{aligned}\zeta &\simeq \frac{\tilde{B}(0)}{2}\left[\frac{2}{(gh)^{1/2}h^2t}\right]^{1/3}\frac{d}{dx}\,\mathrm{Ai}\left\{\left[\frac{2}{(gh)^{1/2}h^2t}\right]^{1/3}[x-(gh)^{1/2}t]\right\} \\ &= \frac{\tilde{B}(0)}{2}\left[\frac{2}{(gh)^{1/2}h^2t}\right]^{2/3}\mathrm{Ai}'\left\{\left[\frac{2}{(gh)^{1/2}h^2t}\right]^{1/3}[x-(gh)^{1/2}t]\right\},\end{aligned} \tag{2.1.49}$$

where

$$\mathrm{Ai}'(Z) \equiv \frac{d}{dZ}\,\mathrm{Ai}(Z)\,.$$

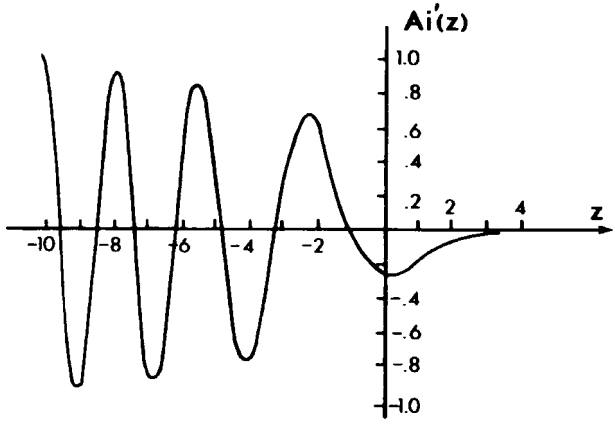

Figure 2.6: Leading wave due to antisymmetric ground tilt $\zeta[\tilde{B}(0)]^{-1}[(gh)^{1/2}h^2t/2]^{2/3}$, see Eq. (2.1.49).

The leading wave attenuates with time as $t^{-2/3}$ which is much faster than the case of a pure rise or fall (where $\zeta \sim t^{-1/3}$). This result is due to the fact that the ground movement is half positive and half negative, thereby reducing the net effect. The function $\mathrm{Ai}'(Z)$ behaves as shown in Fig. 2.6. Note that

$$\tilde{B}(0) = \int_{-\infty}^{\infty} B(x)\,dx = \int_{-\infty}^{\infty} dx \int_{-\infty}^{x} H_0^o(x')\,dx' = -\int_{-\infty}^{\infty} xH_0^o(x)\,dx\,.$$

Thus, if the ground tilts down on the right and up on the left, $\tilde{B}(0) > 0$ and the wave front propagating to the right is led by depression of water surface (hence withdrawal from a beach). The subsequent crests increase in amplitude. On the left side, $x < 0$, the wave front has the opposite phase and is led by a crest. If, however, the ground tilt is opposite in direction, that is, down on the left and up on the right, then the right-going wave front should be led by an elevation.

Kajiura pointed out that retaining the terms gk^3h^2 in $\omega(k)$ implies keeping dispersion to the lowest order, and the same results, Eqs. (2.1.42) and (2.1.49), may be obtained alternatively by invoking the long-wave approximation at the outset, which is clearly appropriate far away from the source. It will be shown in Chapter Twelve that such an approximation is given by the linearized Boussinesq equations which are, in one dimension, equivalent to

$$\frac{\partial^2\zeta}{\partial t^2} = gh\left(\frac{\partial^2\zeta}{\partial x^2} + \frac{h^2}{3}\frac{\partial^4\zeta}{\partial x^4}\right). \tag{2.1.50}$$

The vicinity of the tsunamic source has been examined by Kajiura (1963) and Momoi (1964a, b; 1965a, b).

Exercise 2.1

Show that by solving Eq. (2.1.50) exactly with the initial conditions

$$\zeta(x,0) = \tilde{\zeta}_0(0)\delta(x)\,, \quad \zeta_t(x,0) = 0\,,$$

the answer is given by Eq. (2.1.42).

Exercise 2.2: Cauchy–Poisson Problem for Capillary–Gravity Waves

Consider a free surface with capillarity (refer to Exercise 5.2, Section 1.5). Solve for the two-dimensional free-surface response to a localized initial elevation: $\zeta(x,0) = (b/\pi)(x^2+b^2)^{-1}$. Deduce the asymptotic result for large t and fixed x/t and describe the physical picture. Examine in particular the case where the stationary point is a zero of $\omega''(k)$.

Exercise 2.3: Waves on a Running Stream

Consider a river of constant depth h and uniform streaming velocity U. Formulate the linearized initial-boundary-value problem for the potential Φ of the disturbed flow defined by

$$\text{total velocity} = U\mathbf{i} + \nabla\Phi\,, \quad \mathbf{\Phi} = \Phi(x,z,t)\,,$$

where x, y, z refer to the coordinates fixed in space. Examine the effect of U on the dispersion relation $\omega = \omega(k;U)$ for a progressive wave.

If at $t = 0$, a localized impulsive pressure $P = P_0\delta(x)\delta(t)$ is applied externally on the free surface, find the asymptotic behavior of $\zeta(x,t)$ for large t and x including the wave front. Describe the physics and the effects of U.

Exercise 2.4: Alternative Method for Solving the Transient Problem

The initial-boundary-value problem of this sub-section and the general problem in Section 2.1 can be solved without Laplace transform and complex variables. Start by Fourier transform with respect to x, and get

$$\tilde{\phi} = A\sinh kz + B\cosh kz\,. \tag{2.1.51}$$

Show that the boundary condition at the seabed is

$$\tilde{\phi}_z = \tilde{W}\,, \quad z = -h\,. \tag{2.1.52}$$

Let the free surface be undisturbed initially,

$$\tilde{\phi}(k,0,0) = \tilde{\phi}_t(k,0,0) = 0\,. \tag{2.1.53}$$

Show from (2.1.52), (2.1.53) and (2.1.51) that

$$B_{tt} + \omega^2 B = \frac{-g\overline{W}}{\cosh kh}\,, \tag{2.1.54}$$

where $\omega = \sqrt{gk\tanh kh}$, subject to the initial conditions

$$B(k,0) = 0 \quad \text{and} \quad B_t(k,0) = 0\,, \tag{2.1.55}$$

which can be solved straightforwardly.

For the special case where $W(x,t) = H_0(x)\delta(t)$, integration across the delta function gives the impulsive vertical displacement

$$\int_{0-}^{0+} W\,dt = H_0(t)\,. \tag{2.1.56}$$

Show that (2.1.54) to (2.1.55) can be replaced by

$$B_{tt} + \omega^2 B = 0\,, \quad t > 0+\,, \tag{2.1.57}$$

$$B(k,0+) = 0 \quad \text{and} \quad B_t(k,0+) = \frac{-g\tilde{H}_0}{\cosh kh}\,. \tag{2.1.58}$$

Complete the solution and show finally that the free surface is given by (2.1.46).

2.2 Three-Dimensional Transient Response to Bottom Disturbances

If the source of disturbance is confined to a limited horizontal area, waves will propagate in all horizontal directions and the fluid motion will be three-dimensional. We illustrate only the case of a tsunami due to a sudden motion of the seafloor (Kajiura, 1963).

The governing equation for the velocity potential $\Phi(x,y,z,t)$ is the three-dimensional Laplace equation. Let there be no disturbance on the free surface at any time. On the bottom, the ground motion is two-dimensional:

$$\frac{\partial\Phi}{\partial z} = W(x,y,t)\,, \quad z = -h\,, \tag{2.2.1}$$

where W differs from zero only in a finite area. Furthermore,

$$\Phi,\ \nabla\Phi \to 0 \quad \text{as} \quad r = (x^2 + y^2)^{1/2} \to \infty\,. \tag{2.2.2}$$

One can solve the initial-boundary-value problem by Laplace transform with respect to t and two-dimensional Fourier transform with respect to x and y. Here a method by superposition of sources will prove to be quite efficient. Consider an impulsive disturbance concentrated at the origin $x = y = 0$, $z = -h$ at time $t = 0+$. Denote the potential response by $G(x, y, z, t)$; then

$$\frac{\partial G}{\partial z} = \delta(x)\delta(y)\delta(t - 0+)\,, \quad z = -h \tag{2.2.3}$$

instead of Eq. (2.2.1). Otherwise, G satisfies the same conditions as Φ, that is,

$$\nabla^2 G = 0\,, \tag{2.2.4}$$

$$G_{tt} + gG_z = 0\,, \quad z = 0\,, \tag{2.2.5}$$

$$G = G_t = 0\,, \quad t = 0\,, \quad z = 0\,, \tag{2.2.6}$$

$$G, \nabla G, \to 0\,, \quad r \to \infty\,, \quad t \text{ finite}\,. \tag{2.2.7}$$

Once $G(x, y, z, t)$ is found, Φ can be expressed immediately by

$$\Phi(x, y, z, t) = \int_0^t d\tau \int_{-\infty}^{\infty} dx' \int_{-\infty}^{\infty} dy'\, W(x', y', \tau) \times G(x - x', y - y', z, t - \tau)\,. \tag{2.2.8}$$

Physically, Eq. (2.2.8) represents the superposition of elemental impulsive sources whose intensity at $x = x'$, $y = y'$, $z = -h$, and $t = \tau$ is $W(x', y', \tau)\, dx'\, dy'\, d\tau$. We record here for later use that the Laplace transforms of Φ, W, and G are related by the convolution theorem as follows:

$$\overline{\Phi}(x, y, z, s) = \iint_{-\infty}^{\infty} dx'\, dy'\, \overline{W}(x', y', s)\overline{G}(x - x', y - y', z, s)\,. \tag{2.2.9}$$

$G(x, y, z, t)$ is considerably easier to construct because a point source has axial symmetry. Let us define $\delta(r)$ by

$$\delta(x)\delta(y) = \frac{\delta(r)}{2\pi r}$$

in the sense that the area integrals of both sides are equal, that is,

$$\int_0^{2\pi} d\theta \int_0^{\infty} \frac{r\,dr\,\delta(r)}{2\pi r} = 1 = \iint_{-\infty}^{\infty} dx\,dy\,\delta(x)\delta(y)\,.$$

Equation (2.2.3) may be rewritten

$$\frac{\partial G}{\partial z} = \frac{1}{2\pi r}\delta(r)\delta(t-0+)\,; \tag{2.2.10}$$

now the problem of G does not involve θ.

Because of axial symmetry, a Hankel transform with the Bessel function $J_0(kr)$ as the weighting function can be applied. Define the Hankel transform (see Sneddon, 1951) by

$$\hat{f}(k) = \int_0^{\infty} rJ_0(kr)f(r)\,dr\,, \tag{2.2.11a}$$

then the inverse transform is

$$f(r) = \int_0^{\infty} kJ_0(kr)\hat{f}(k)\,dk\,. \tag{2.2.11b}$$

Let us define the compound Laplace–Hankel transform of G by $\hat{\overline{G}}$

$$\hat{\overline{G}} = \int_0^{\infty} e^{-st}\,dt \int_0^{\infty} rJ_0(kr)G\,dr\,.$$

In polar coordinates,

$$\frac{1}{r}\frac{\partial}{\partial r}\left(r\frac{\partial G}{\partial r}\right) + \frac{\partial^2 G}{\partial z^2} = 0\,, \quad -h < z < 0\,,\ 0 \le r < \infty\,. \tag{2.2.12}$$

Applying Hankel transform to the first term, integrating by parts, using the boundary conditions at $r = 0$ and ∞, and invoking the differential equation satisfied by J_0, we can show that

$$\int_0^{\infty} dr\,rJ_0(kr)\left(\frac{1}{r}\frac{\partial}{\partial r}r\frac{\partial G}{\partial r}\right) = -k^2\hat{G}\,.$$

Thus, the Laplace–Hankel transform of Eq. (2.2.12) is

$$\frac{d^2}{dz^2}\hat{\overline{G}} - k^2\hat{\overline{G}} = 0\,. \tag{2.2.13}$$

The transform of the free-surface condition is

$$\hat{\overline{G}}_z + \frac{s^2}{g}\hat{\overline{G}} = 0\,, \tag{2.2.14}$$

and the transform of the bottom boundary condition (2.2.10) is

$$\hat{\overline{G}}_z = \frac{1}{2\pi}\,. \tag{2.2.15}$$

The solution to Eq. (2.2.13), subject to the boundary conditions (2.2.14) and (2.2.15), is

$$\hat{\overline{G}} = \frac{1}{2\pi}\frac{1}{s^2+\omega^2}\frac{s^2\sinh kz - gk\cosh kz}{k\cosh kh} \tag{2.2.16}$$

with $\omega^2 = gk\tanh kh$. Inverting the Hankel transform, we have

$$\overline{G}(r,z,s) = \int_0^\infty kJ_0(kr)\hat{\overline{G}}(k,z,s)\,dk\,, \quad r = (x^2+y^2)^{1/2}\,. \tag{2.2.17}$$

If the point disturbance is not at the origin but at some other point $\mathbf{r}'$, we must replace $|\mathbf{r}|$ by $|\mathbf{r}-\mathbf{r}'|$ so that

$$\overline{G}(|\mathbf{r}-\mathbf{r}'|,z,s) = \int_0^\infty kJ_0(k|\mathbf{r}-\mathbf{r}'|)\hat{\overline{G}}(k,z,s)\,dk\,, \tag{2.2.18}$$

where

$$\begin{aligned} x &= r\cos\theta\,, \quad y = r\sin\theta\,,\\ x' &= r'\cos\theta'\,, \quad y' = r'\sin\theta'\,,\\ |\mathbf{r}-\mathbf{r}'| &\equiv [(x-x')^2+(y-y')^2]^{1/2}\\ &= [r^2+r'^2-2rr'\cos(\theta-\theta')]^{1/2}\,. \end{aligned} \tag{2.2.19}$$

When Eq. (2.2.18) is substituted into Eq. (2.2.9), it follows that

$$\begin{aligned} \overline{\Phi}(r,\theta,z,s) = \int_0^\infty r'\,dr' \int_0^{2\pi} d\theta'\,\overline{W}(r',\theta',s)\\ \times \int_0^\infty kJ_0(k|\mathbf{r}-\mathbf{r}'|)\hat{\overline{G}}(k,z,s)\,dk\,. \end{aligned} \tag{2.2.20}$$

The potential Φ can then be obtained by Laplace inversion.

The Laplace transform of the free-surface displacement is

$$\begin{aligned} \bar{\zeta} = -\frac{s}{g}\overline{\Phi}\bigg|_{z=0} = \frac{1}{2\pi}\int_0^\infty r'\,dr' \int_0^{2\pi} d\theta'\,\overline{W}(r',\theta',s)\\ \times \int_0^\infty kJ_0(k|\mathbf{r}-\mathbf{r}'|)\frac{1}{\cosh kh}\frac{s}{s^2+\omega^2}\,dk\,. \end{aligned} \tag{2.2.21}$$

We now study a few specific cases.

2.2.1 Two-Dimensional Tsunami Due to Impulsive Bottom Displacement

In the special case of impulsive displacement

$$W(r,\theta,t) = \mathfrak{W}(r,\theta)\delta(t-0+)\,, \tag{2.2.22}$$

the Laplace transform is $\overline{W} = \mathfrak{W}(r,\theta)$. Inversion of the Laplace transform of Eq. (2.2.21) is immediate:

$$\zeta = \frac{1}{2\pi}\int_0^\infty r'\,dr' \int_0^{2\pi} d\theta'\,\mathfrak{W}(r',\theta') \times \int_0^\infty \frac{kJ_0(k|\mathbf{r}-\mathbf{r}'|)}{\cosh kh}\cos\omega t\,dk\,. \tag{2.2.23}$$

Further progress can be made by expressing $J_0(k|r-r'|)$ as a series with the aid of the famous addition theorem (Watson, 1958, pp. 358–359)

$$J_0(k[r^2+r'^2-2rr'\cos(\theta-\theta')]^{1/2}) = \sum_{n=0}^{\infty}\varepsilon_n J_n(kr)J_n(kr')\cos n(\theta-\theta')\,, \tag{2.2.24}$$

where ε_n is the Jacobi symbol ($\varepsilon_0 = 1, \varepsilon_n = 2, n = 1,2,3,\ldots$). Substituting (2.2.24) into (2.2.23) and denoting

$$\frac{1}{2\pi}\int_0^\infty r'\,dr\int_0^{2\pi} d\theta'\,\mathfrak{W}(r',\theta')J_n(kr')\begin{pmatrix}\cos n\theta'\\ \sin n\theta'\end{pmatrix} = \begin{pmatrix}W_n^c(k)\\ W_n^s(k)\end{pmatrix}, \tag{2.2.25}$$

we have

$$\zeta(r,\theta,t) = \sum_{n=0}\varepsilon_n\int_0^\infty kJ_n(kr)\frac{\cos\omega t}{\cosh kh} \times (W_n^c\cos n\theta + W_n^s\sin n\theta)\,dk\,. \tag{2.2.26}$$

In principle, given $\mathfrak{W}(r,\theta)$ we may perform the integration in Eq. (2.2.25) and obtain $W_n^s(k)$ and $W_n^c(k)$ so that the final solution can be obtained by numerical integration and summation.

To get some physical ideas we consider the following two simple examples:

(i) Axially symmetric displacement:

$$\mathfrak{W}(r,\theta) = W_0(r)\,. \tag{2.2.27}$$

Due to the orthogonality of $\{\cos n\theta\}$ and $\{\sin n\theta\}$, it follows that

$$W_0^c = \int_0^\infty rW_0(r')J_0(kr')\,dr = \hat{W}_0(k)\,, \quad n = 0\,,$$
$$W_n^c = 0\,, \quad W_n^s = 0 \quad \text{all} \quad n \neq 0\,.$$

We have, therefore,

$$\begin{aligned}\zeta(r,\theta,t) &= \int_0^\infty kJ_0(kr)\frac{\cos\omega t}{\cosh kh}\hat{W}_0(k)\,dk \\ &= \int_0^\infty r'J_0(kr')W_0(r')\,dr' \int_0^\infty kJ_0(kr)\frac{\cos\omega t}{\cosh kh}\,dk\,,\end{aligned} \tag{2.2.28}$$

which can be deduced directly by Hankel transform with $J_0(kr)$, without recourse to the source function G.

(ii) Displacement which is antisymmetric about the y axis:

$$\mathfrak{W}(r,\theta) = W_1(r)\cos\theta\,. \tag{2.2.29}$$

It is easy to show that

$$W_1^c = \frac{1}{2}\int_0^\infty rW_1J_1(kr')\,dr'\,, \quad W_n^c = 0 \quad \text{all} \quad n \neq 1\,, \quad W_n^s = 0 \quad \text{all} \quad n\,.$$

The integral is just the Hankel transform of W_1 with J_1 as the weighting function. Since $\varepsilon_1 = 2$, we have

$$\zeta(r,\theta,t) = \cos\theta \int_0^\infty kJ_1(kr)\frac{\cos\omega t}{\cosh kh}\,dk \int_0^\infty r'W_1(r')J_1(kr')\,dr'\,. \tag{2.2.30}$$

The above result can also be directly obtained by Hankel transform with the weighting function J_1.

In general, one may need many terms in the series of Eq. (2.2.26) to model a more general disturbance.

Let us examine the asymptotic behavior for large r and t for antisymmetric impulsive displacement only, leaving the symmetrical case as an exercise. Writing

$$F(k) = k\frac{\hat{W}_1}{\cosh kh} \quad \text{and} \quad \hat{W}_1(k) = \int_0^\infty rJ_1(kr)W_1(r)\,dr\,,$$

and using the identity

$$\begin{aligned} J_1(kr) &= \frac{1}{2\pi}\int_0^{2\pi} d\psi \exp[-i(\psi - kr\sin\psi)] \\ &= \frac{1}{\pi}\int_0^{\pi} d\psi \cos(\psi - kr\sin\psi)\,, \end{aligned} \tag{2.2.31}$$

which may be proved readily from the partial wave expansion, Appendix 4.A, Eq. (4.A.5), we may rewrite Eq. (2.2.30) as

$$\begin{aligned} \zeta(r,\theta,t) &= \cos\theta\ \mathrm{Re}\,\frac{1}{\pi}\int_0^{\pi} d\psi \int_0^{\infty} dk\, F(k)\cos(\psi - kr\sin\psi)e^{-i\omega t} \\ &= \cos\theta\ \mathrm{Re}\,\frac{1}{2\pi}\int_0^{\pi} d\psi \Bigg\{ e^{-i\psi}\int_0^{\infty} dk\, F(k)e^{ikr\sin\psi - i\omega t} \\ &\quad + e^{i\psi}\int_0^{\infty} dk\, F(k)e^{-ikr\sin\psi - i\omega t}\Bigg\}\,. \end{aligned} \tag{2.2.32}$$

Now consider the first double integral above

$$I_1 = \int_0^{\pi} d\psi\, e^{-i\psi}\int_0^{\infty} dk\, F(k)e^{it[k(r/t)\sin\psi - \omega_{(k)}]}\,. \tag{2.2.33}$$

The phase function depends on two variables, k and ψ, and a stationary phase point can be sought in the strip $k \geq 0$, $0 \leq \psi \leq \pi$ by equating to zero partial derivatives with respect to k and ψ simultaneously. A comprehensive account for higher-dimensional stationary phase methods may be found in Papoulis (1968). Let us take the obvious route of first keeping ψ fixed and finding the stationary phase contribution along k, and then repeating the process for ψ. Thus, for large t, fixed r/t and $\sin\psi$, one may apply the method of stationary phase

$$g(k) = k\frac{r}{t}\sin\psi - \omega(k)\,, \tag{2.2.34a}$$

$$g'(k) = \frac{r}{t}\sin\psi - \omega'(k)\,, \tag{2.2.34b}$$

$$g'' = -\omega''(k) > 0\,. \tag{2.2.34c}$$

There is a stationary point at the zero of $g'(k)$ since $\psi > 0$ in the range $0 < \psi < \pi$. The approximate value for the k integral is

$$\left(\frac{2\pi}{t|\omega''(k)|}\right)^{1/2} F(k) \exp\left\{it\left[k\frac{r}{t}\sin\psi - \omega(k)\right] + i\frac{\pi}{4}\right\},$$

where the stationary point k depends on ψ through Eq. (2.2.34b).

By a similar analysis, the remaining integral in Eq. (2.2.32) has no stationary point, hence is of the order $O(1/t)$. The integral I_1 becomes

$$I_1 = \int_0^\pi d\psi\, e^{i(-\psi+\pi/4)} \left[\frac{2\pi}{t|\omega''(k)|}\right]^{1/2} \times F(k) e^{it[k(r/t)\sin\psi - \omega(k)]} + O\left(\frac{1}{t}\right). \tag{2.2.35}$$

The ψ integral can be approximated once more by the method of stationary phase for large t and fixed r/t. The phase function and its first two derivatives are

$$f(\psi) = k\frac{r}{t}\sin\psi - \omega(k)\,, \tag{2.2.36a}$$

$$\frac{df}{d\psi} = k\frac{r}{t}\cos\psi + \frac{dk}{d\psi}\left[\frac{r}{t}\sin\psi - \omega'(k)\right], \tag{2.2.36b}$$

$$\frac{d^2f}{d\psi^2} = -k\frac{r}{t}\sin\psi + \frac{r}{t}\cos\psi\frac{dk}{d\psi} + \frac{d^2k}{d\psi^2}\left[\frac{r}{t}\sin\psi - \omega'(k)\right]. \tag{2.2.36c}$$

By the use of Eq. (2.2.34b), the point of stationary phase is clearly at $\psi = \pi/2$. Incorporating this result into Eqs. (2.2.36b) and (2.2.36c), we obtain

$$\frac{r}{t} - \omega'(k_0) = 0 \tag{2.2.37}$$

for the stationary point, now denoted by k_0, and

$$\left.\frac{d^2f}{d\psi^2}\right|_{\psi=\pi/2} = -k_0\frac{r}{t} < 0\,. \tag{2.2.38}$$

Equation (2.1.28) may be applied to Eq. (2.2.35), yielding

$$I_1 = -i\pi\left[\frac{2\pi}{t|\omega''(k_0)|}\right]^{1/2} F(k_0)\left(\frac{2}{\pi k_0 r}\right)^{1/2} e^{i[k_0 r - \omega(k_0)t]} + O\left(\frac{1}{t}\right).$$

The second double integral in Eq. (2.2.32) does not have a stationary point in $k \in [0, \infty]$, hence it is of $O(1/t)$. Finally, the total displacement is

$$\begin{aligned}\zeta(r,\theta,t) &= \cos\theta \ \mathrm{Re}\left\{\frac{-i}{2}\left(\frac{2\pi}{t|\omega''(k_0)|}\right)^{1/2}\right. \\ &\qquad \left.\times F(k_0)\left(\frac{2}{\pi k_0 r}\right)^{1/2} e^{i[k_0 r-\omega(k_0)t]}\right\} + O\left(\frac{1}{t}\right) \\ &= \frac{1}{2}\cos\theta\left[\frac{2\pi}{t|\omega''(k_0)|}\right]^{1/2} F(k_0)\left(\frac{2}{\pi k_0 r}\right)^{1/2} \\ &\qquad \times \sin[k_0 r-\omega(k_0)t] + O\left(\frac{1}{t}\right). \end{aligned} \tag{2.2.39}$$

The preceding result can also be obtained by using the asymptotic formula of $J_1(kr)$ for large kr,

$$J_1(kr) \simeq \left(\frac{2}{\pi kr}\right)^{1/2} \cos\left(kr - \frac{3\pi}{4}\right),$$

and then applying the method of stationary phase only once. However, the legitimacy of assuming large kr when k ranges from 0 to ∞ needs confirmation and we have taken a more cautious route here.

The physical features of dispersion are almost the same as in the one-dimensional case and need not be elaborated. It is only necessary to point out that the amplitude decay rate is different since for $r/t = \text{const}$

$$\zeta \simeq \frac{1}{2}\frac{1}{t}\cos\theta F(k_0)\left[\frac{2}{|\omega''(k_0)|}\right]^{1/2}\left(\frac{2}{k_0(r/t)}\right)^{1/2}\sin(k_0 r-\omega_0 t), \tag{2.2.40}$$

where k_0 depends on r/t according to Eq. (2.2.38). Thus, the individual waves found near $r/t = \text{const}$ decay at the rate of $O(1/t)$ which is due to the radial spreading of two-dimensional waves. The antisymmetric nature of the source is exactly carried over to the propagating waves by the factor $\cos\theta$; the wave is the greatest along the x direction $\theta = 0$, and insignificant along the axis of antisymmetry $\theta = \pi/2,\ 3\pi/2$.

For a more explicit result it is necessary to prescribe $W_1(r)$. For example, one may assume that

$$W_1(r) = \frac{A}{a}(a^2 - t^2)^{1/2}\,, \quad r < a\,, \\ = 0\,, \qquad\qquad\qquad r > a\,. \tag{2.2.41}$$

It can be inferred from a formula in Erdelyi (1954, II, p. 24, No. 25) that

$$\hat{W}_1(k) = \frac{A}{a}\int_0^\infty rJ_1(kr)(a^2 - r^2)^{1/2}\,dr \\ = \frac{A}{a}\left(\frac{\pi}{2}\right)^{1/2}\frac{a^2}{k}J_1^2\left(\frac{ka}{2}\right).$$

Hence

$$F(k) = \frac{k}{\cosh kh}\hat{W}_1 \\ = \left(\frac{\pi}{2}\right)^{1/2}\frac{Aa}{\cosh kh}J_1^2\left(\frac{ka}{2}\right), \tag{2.2.42}$$

which shows the effect of the size (a) of the source area. Through the Bessel function, $F(k)$ oscillates in ka, which is a manifestation of interference of waves from different parts of the source area.

2.2.2 Leading Waves of a Two-Dimensional Tsunami

Let us continue the antisymmetric example with the specific W_1 given by Eq. (2.2.41). In the zone of leading waves $kh \ll 1$, but for sufficiently large r, the leading wave must have some finite wavelength so that

$$kr \gg 1\,.$$

We may either express $J_1(kr)$ as an integral, Eq. (2.2.31), and carry out the stationary phase approximation for the ψ integral first, or take the asymptotic approximation of $J_1(kr)$ for large kr. Either way the result is

$$\zeta \simeq \cos\theta\ \mathrm{Re}\int_0^\infty dk\,F(k)\left(\frac{2}{\pi kr}\right)^{1/2} \\ \times\frac{1}{2}[e^{ikr - i\omega t - i3\pi/4} + e^{-ikr - i\omega t + i3\pi/4}]\,. \tag{2.2.43}$$

For leading waves $kh \ll 1$, only the first integrand matters and we can expand

$$\omega \cong (gh)^{1/2}\left(k - \frac{k^3h^2}{6}\right),$$

$$F(k) \cong Aa\left(\frac{\pi}{2}\right)^{1/2}\left(\frac{ka}{4}\right)^2 = \frac{Aa^3}{16}\left(\frac{\pi}{2}\right)k^2.$$

It follows that

$$\zeta \cong \frac{\cos\theta}{2}\frac{Aa^3}{16}\frac{1}{r^{1/2}}\,\mathrm{Re}\,e^{-i3\pi/4}\int_0^\infty dk\,k^{3/2} \times \exp\left(i\left\{k[r-(gh)^{1/2}t] + \frac{(gh)^{1/2}h^2k^3t}{6}\right\}\right). \tag{2.2.44}$$

This integral cannot be expressed in terms of known functions. Let us first rewrite it as follows:

$$\int_0^\infty = h^{-5/2}\int_0^\infty d(kh)(kh)^{3/2} \times \exp\left(i\left\{kh\left[\frac{r}{h} - \left(\frac{g}{h}\right)^{1/2}t\right] + \frac{(kh)^3}{6}\left(\frac{g}{h}\right)^{1/2}t\right\}\right) \tag{2.2.45}$$

and introduce the new variables (Kajiura, 1963, p. 549).

$$\frac{(kh)^3}{6}\left(\frac{g}{h}\right)^{1/2}t = u^6 \quad \text{or} \quad kh = u^2\left[\left(\frac{g}{h}\right)^{1/2}\frac{t}{6}\right]^{-1/3}.$$

Then the integral of Eq. (2.2.45) becomes

$$h^{-5/2}\left[\left(\frac{g}{h}\right)^{1/2}\frac{t}{6}\right]^{-5/6}\int_0^\infty du\,2u^4\,e^{i(u^2p+u^6)}, \tag{2.2.46}$$

with

$$p = \frac{r/h - (g/h)^{1/2}t}{[(g/h)^{1/2}t/6]^{1/3}}. \tag{2.2.47}$$

Equation (2.2.46) can be rewritten

$$-2h^{-5/2}\left[\left(\frac{g}{h}\right)^{1/2}\frac{t}{6}\right]^{-5/6}\frac{d^2}{dp^2}\int_0^\infty du\,e^{i(u^2p+u^6)},$$

whereupon Eq. (2.2.44) becomes

$$\zeta \cong \frac{\cos\theta}{2^{1/2}} \frac{Aa^3}{16r^{1/2}} h^{-5/2} \left(\left(\frac{g}{h} \right)^{1/2} \frac{t}{6} \right)^{-5/6} \times \frac{d^2}{dp^2} \operatorname{Re} \left[(1+i) \int_0^\infty du\, e^{i(u^2 p + u^6)} \right] . \tag{2.2.48}$$

For $p = 0$, that is, if the observer is exactly at $r = (gh)^{1/2}t$, the integral in Eq. (2.2.46) can be evaluated by letting $u^6 = \tau$,

$$\int_0^\infty du\, u^4 e^{iu^6} = \int_0^\infty d\tau \tau^{-1/6} e^{i\tau} = \Gamma\left(\frac{5}{6}\right) e^{i5\pi/12} .$$

For general p we follow Kajiura and define

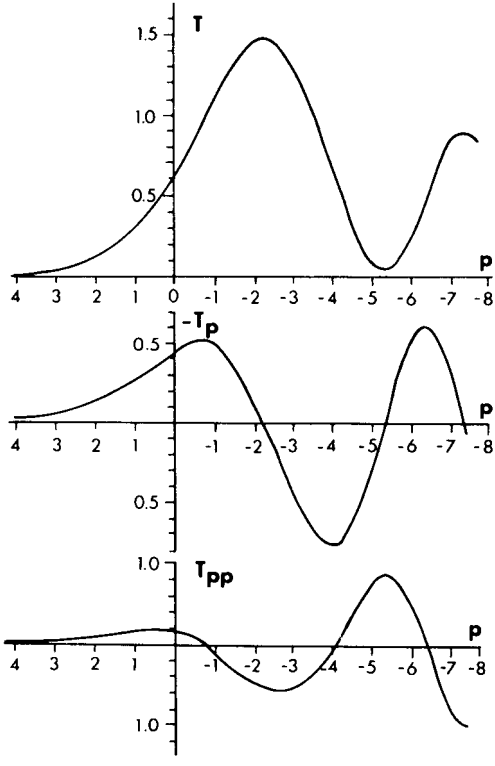

Figure 2.7: T, $-T_p$, and T_{pp} as functions of p (from Kajiura, 1963, *Bull. Earthquake Res. Inst.* Univ. Tokyo).

$$T(p) = \mathrm{Re}\left[(1+i)\int_0^\infty du\, e^{i(u^2 p + u^6)}\right], \tag{2.2.49}$$

then

$$\zeta = \cos\theta \frac{Aa^3}{16(2r)^{1/2}} \frac{T_{pp}}{h^{5/2}((g/h)^{1/2}t/6)^{5/6}}. \tag{2.2.50}$$

The variations of T, $-T_p$, and T_{pp} are plotted in Fig. 2.7. Since the coefficient of T_{pp} in Eq. (2.2.48) is proportional to

$$r^{-1/2}t^{-5/6} = \left(\frac{r}{t}\right)^{-1/2} t^{-4/3} \sim \left(\frac{r}{t}\right)^{5/6} r^{-4/3},$$

we conclude that near the wave front $r/t \cong (gh)^{1/2}$ the wave amplitude decays as $t^{-4/3}$ or $r^{-4/3}$. If $A < 0$, the ground tilts down on the right $-\pi/2 < \theta < \pi/2$ and up on the left. To an observer on the right the leading waves are a low trough followed by a high crest, similar to the two-dimensional case.

2.3 The Propagation of a Dispersive Wave Packet

Let us leave the idealized tsunamis and study the evolution of a slowly modulated wave group in order to achieve further understanding of dispersion. Consider a disturbance traveling to the right, which may be represented as a superposition of sinusoidal waves with a continuum of wavelengths:

$$\zeta(x,t) = \mathrm{Re}\int_{-\infty}^{\infty} \mathcal{A}(k) e^{i(kx-\omega(k)t)}\, dk. \tag{2.3.1}$$

The result may be generated by a wavemaker at $x \sim -\infty$ in a long tank from $t \sim -\infty$. The amplitude spectrum $\mathcal{A}(k)$ is determined by the initial disturbance (see Section 2.1). We shall leave $\omega(k)$ to be general so that the water wave is just a special case. Consider, in particular, a wave packet with a Gaussian envelope:

$$\zeta(x,0) = \mathrm{Re}\, A_0 e^{-ik_0 x} e^{-x^2/4\sigma^2}. \tag{2.3.2}$$

The amplitude spectrum is obtained by inverse Fourier transform

$$\begin{aligned}\mathcal{A}(k) &= \frac{1}{2\pi}\int_{-\infty}^{\infty}\zeta(x,0)e^{-ikx}\,dx \\ &= \frac{A_0}{2\pi}\int_{-\infty}^{\infty}e^{-i(k-k_0)x-x^2/4\sigma^2}\,dx \\ &= \frac{A_0}{2\pi}\int_{-\infty}^{\infty}e^{-[x/2\sigma+i(k-k_0)\sigma]^2-(k-k_0)^2\sigma^2}\,dx \qquad (2.3.3)\end{aligned}$$

after completing the square. Letting $u = x/2\sigma + i(k-k_0)\sigma$, we have further

$$\mathcal{A} = \frac{A_0}{2\pi}2\sigma e^{-(k-k_0)^2\sigma^2}\int_{\Gamma}e^{-u^2}\,du\,,$$

where the contour Γ is a straight line from $-\infty + i(k-k_0)\sigma$ to $\infty + i(k-k_0)\sigma$ in the complex u plane. Since e^{-u^2} is analytic in the strip between Γ and the real u axis, by Cauchy's theorem the contour can be replaced by the real axis. Using the well-known result

$$\int_{-\infty}^{\infty}e^{-u^2}\,du = \pi^{1/2}\,, \qquad (2.3.4)$$

we have

$$\mathcal{A}(k) = \frac{A_0\sigma}{\pi^{1/2}}e^{-(k-k_0)^2\sigma^2}\,. \qquad (2.3.5)$$

Thus, the wave profile at any t is

$$\zeta = \mathrm{Re}\,\frac{A_0\sigma}{\pi^{1/2}}\int_{-\infty}^{\infty}e^{-(k-k_0)^2\sigma^2+i(kx-\omega t)}\,dk\,. \qquad (2.3.6)$$

Let us study the behavior of the above integral when σk_0 is very large, that is, when the original envelope is very flat or the amplitude spectrum is very sharp near $k = k_0$. The integrand attenuates quickly away from $k = k_0$ so that one may approximate $\omega(k)$ by a few terms in the Taylor expansion:

$$\omega(k) = \omega_0 + (k-k_0)\omega_0' + \frac{1}{2}(k-k_0)^2\omega_0'' + \cdots\,,$$

where $\omega_0 \equiv \omega(k_0)$, $\omega_0' \equiv \omega'(k_0)$, and so on. After we let $u = k - k_0$, ζ becomes

$$\zeta \cong \mathrm{Re}\,\frac{A_0\sigma}{\pi^{1/2}}e^{i(k_0x-\omega_0t)}\cdot\int_{-\infty}^{\infty}e^{-(\sigma^2+i\omega_0''t/2)u^2+i(x-\omega_0't)u}\,du\,. \qquad (2.3.7)$$

Completing the squares and using Eq. (2.3.4), we get

$$\zeta \cong \mathrm{Re}\, A_0 \frac{e^{i(k_0 x - \omega_0 t)}}{[1 + \frac{i\omega_0'' t}{2\sigma^2}]^{1/2}} \exp\left\{ \frac{-(x - \omega_0' t)^2}{4\sigma^2[1 + (\frac{i\omega_0'' t}{2\sigma})^2]} \right\}. \tag{2.3.8}$$

Clearly, the envelope moves at the group velocity $C_g = \omega_0'$; its maximum is at $x = C_g t$ and attenuates as $t^{1/2}$ for large t. In addition, the length of the envelope, which is measured by

$$2\sigma \left(1 + \frac{i}{2}\frac{\omega_0'' t}{\sigma^2}\right)^{1/2},$$

increases as $t^{1/2}$ for large t. Therefore, the whole wave group flattens during propagation.

Compared with Eq. (1.5.4), Eq. (2.3.8) is an improved approximation. Several other observations are useful here. Let us regard Eq. (2.3.8) as slowly modulated sinusoidal waves. The energy contained in the entire wave group can be approximated by

$$\begin{aligned} &\frac{1}{2}\rho g A_0^2 \int_{-\infty}^{\infty} dx \left| \frac{\exp\{-(x - \omega_0' t)^2/4\sigma^2[1 + \frac{i\omega_0'' t}{2\sigma^2}]\}}{[1 + \frac{i\omega_0'' t}{2\sigma}]^{1/2}} \right|^2 \\ &\qquad \times \frac{\rho g A_0^2}{2} \int_{-\infty}^{\infty} dx \frac{\exp\{-(x - \omega_0' t)^2/2\sigma^2[1 + (\frac{\omega_0'' t}{2\sigma^2})^2]\}}{(1 + (\frac{\omega_0'' t}{2\sigma})^2)^{1/2}} \\ &= \frac{\rho g A_0^2}{2}\sqrt{2}\sigma \int_{-\infty}^{\infty} e^{-u^2}\, du = \frac{\rho g A_0^2}{2\sqrt{2}}\sqrt{\pi}\sigma\,, \end{aligned} \tag{2.3.9}$$

after an obvious change of variables. The total energy in the initial profile, Eq. (2.3.2), is

$$\frac{\rho g}{2} A_0^2 \int_{-\infty}^{\infty} e^{-x^2/2\sigma^2}\, dx = \frac{\rho g}{2(2)^{1/2}} A_0^2 \pi^{1/2} \sigma\,. \tag{2.3.10}$$

Thus energy is conserved, as it must be.

It may be noted that to the order σ^{-2} where σ^{-1} designates the slow rate of envelope modulation, the curvature of the dispersion curve ω'' is involved. To see that this is no accident, let us examine the elementary example of two wavetrains with slightly different wavelengths $k_+ = k + dk$ and $k_- = k - dk$ with $dk/k \ll 1$,

$$\zeta = A_0\{\exp[i(k_+ x - \omega_+ t)] + \exp[i(k_- x - \omega_- t)]\}\,, \tag{2.3.11}$$

where $\omega_\alpha = \omega(k_\alpha)$, $\alpha = 1, 2$. Expanding ω to $O(dk)^2$, we have

$$\omega_\pm = \left[\omega \pm \omega'\, dk + \frac{1}{2}\omega''(dk)^2 + \cdots\right]_k , \tag{2.3.12}$$

so that

$$\zeta \cong 2A_0 \cos[dk(x - C_g t)] \exp\left\{i\left(kx - \left[\omega + \frac{1}{2}\omega''(dk)^2\right] t\right)\right\}. \tag{2.3.13}$$

Over the space and time scale $O(dk)^{-1}$, the envelope modulates and moves at C_g; however, over the time scale $O(dk)^{-2}$, the phase, in particular the frequency, changes. This example suggests that there is a cascade of time scales $O(1), O(dk)^{-1}, O(dk)^{-2}, \ldots$, and so on.

Finally, for any amplitude spectrum sharply peaked around k_0 (the Gaussian spectrum (2.3.5) being a special case), Eq. (2.3.1) may be approximated by

$$\zeta(x, t) \cong \mathrm{Re}\left\{A(x, t) e^{i(k_0 x - \omega_0 t)}\right\}, \tag{2.3.14}$$

where

$$A(x, t) = \int_{-\infty}^{\infty} dk\, \mathcal{A}(k) \times \exp\left\{i\left[(k - k_0)x - \left[(k - k_0)\omega_0' + \frac{1}{2}(k - k_0)^2\omega_0''\right] t\right]\right\}. \tag{2.3.15}$$

It is readily verified that A satisfies the following differential equation:

$$\frac{\partial A}{\partial t} + \omega_0' \frac{\partial A}{\partial x} + \frac{1}{2}\omega_0'' \frac{\partial^2 A}{\partial x^2}. \tag{2.3.16}$$

Such a simple equation obviously makes subsequent analysis easy, as will be demonstrated in the next section. To prepare the ground for further extension to nonlinear problems where formally exact solutions are often not possible, we shall also rederive Eq. (2.3.16) by an alternative method directly from the governing equations, and not from the integral solution.

2.4 Slowly Varying Wavetrain by Multiple-Scales Analysis

2.4.1 Evolution Equation for the Wave Envelope

Let us incorporate the difference in scales as suggested at the end of Section 2.3 by formally introducing slow variables

$$\begin{aligned} x_1 &= \mu x\,, \quad x_2 = \mu^2 x, \ldots\,, \\ t_1 &= \mu t\,, \quad t_2 = \mu^2 t, \ldots\,, \end{aligned} \tag{2.4.1}$$

where $\mu \ll 1$ measures the ratio of two time scales, and then treating these variables in a perturbation analysis as if they were independent. This device may appear very artificial to the newcomer, but it has been shown to agree with other methods in old problems and to be an especially powerful tool for problems with weak nonlinearity. For a systematic exposition, see Cole (1968) and Nayfeh (1973).

Assume that

$$\begin{aligned} \Phi(x,z,t) &= \Phi(x, x_1, x_2, \ldots; z; t, t_1, t_2, \ldots)\,, \\ \zeta(x,t) &= \zeta(x, x_1, x_2, \ldots; t, t_1, t_2, \ldots)\,. \end{aligned} \tag{2.4.2}$$

Derivatives with respect to x and t must now be replaced by

$$\frac{\partial}{\partial x} \to \frac{\partial}{\partial x} + \mu\frac{\partial}{\partial x_1} + \mu^2\frac{\partial}{\partial x_2} + \cdots\,, \tag{2.4.3}$$

so that

$$\frac{\partial^2}{\partial x^2} \to \frac{\partial^2}{\partial x^2} + 2\mu\frac{\partial^2}{\partial x \partial x_1} + \mu^2\left(\frac{\partial^2}{\partial x_1^2} + 2\frac{\partial^2}{\partial x \partial x_2}\right) + \cdots\,. \tag{2.4.4}$$

Similar replacements must be made for time derivatives, while z derivatives remain the same. We now restrict ourselves to slowly varying sinusoidal waves and assume a perturbation series as follows:

$$\Phi = (\psi_0 + \mu\psi_1 + \mu^2\psi_2 + \cdots)e^{i(kx-\omega t)}\,, \tag{2.4.5}$$

where

$$\psi_\alpha = \psi_\alpha(x_1, x_2, \ldots; z; t_1, t_2, \ldots)\,, \quad \alpha = 0, 1, 2, \ldots\,. \tag{2.4.6}$$

Substituting Eq. (2.4.4) to Eq. (2.4.6) into Laplace's equation and separating by powers of μ, we obtain

$$O(\mu^0): \quad -k^2\psi_0 + \frac{\partial^2\psi_0}{\partial z^2} = 0\,, \tag{2.4.7a}$$

$$O(\mu): \quad -k^2\psi_1 + \frac{\partial^2\psi_1}{\partial z^2} = -2ik\frac{\partial\psi_0}{\partial x_1}\,, \tag{2.4.7b}$$

$$O(\mu^2): \quad -K^2\psi_2 + \frac{\partial^2\psi_2}{\partial z^2} = -\left(2ik\frac{\partial\psi_1}{\partial x_1} + \frac{\partial^2\psi_0}{\partial x_1^2} + 2ik\frac{\partial\psi_0}{\partial x_2}\right). \tag{2.4.7c}$$

Similarly, the free-surface boundary condition gives

$$O(\mu^0): \quad g\frac{\partial\psi_0}{\partial z} - \omega^2\psi_0 = 0\,, \tag{2.4.8a}$$

$$O(\mu^1): \quad g\frac{\partial\psi_1}{\partial z} - \omega^2\psi_1 = 2i\omega\frac{\partial\psi_0}{\partial t_1}\,, \tag{2.4.8b}$$

$$O(\mu^2): \quad g\frac{\partial\psi_2}{\partial z} - \omega^2\psi_2 = 2i\omega\frac{\partial\psi_1}{\partial t_1} - \left(\frac{\partial^2\psi_0}{\partial t_1^2} - 2i\omega\frac{\partial\psi_0}{\partial t_2}\right). \tag{2.4.8c}$$

On the bottom we have

$$\frac{\partial\psi_0}{\partial z} = \frac{\partial\psi_1}{\partial z} = \frac{\partial\psi_2}{\partial z} = 0\,, \quad z = -h\,. \tag{2.4.9a, b, c}$$

It is obvious that the solution for ψ_0 governed by Eqs. (2.4.7a), (2.4.8a), and (2.4.9a) is simply

$$\psi_0 = -\frac{igA}{\omega}\frac{\cosh k(z+h)}{\cosh kh}\,, \quad A = A(x_1, x_2, \ldots; t_1, t_2, \ldots) \tag{2.4.10}$$

with $\omega^2 = gk\tanh kh$. The amplitude A is thus far undetermined. Now ψ_1 is governed by the inhomogeneous boundary-value problem (2.4.7b), (2.4.8b), and (2.4.9b). Since the homogeneous version of the boundary-value problem has ψ_0 as a nontrivial solution, the inhomogeneous problem must satisfy a solvability condition,[1] which follows by applying Green's theorem to ψ_0 and ψ_1:

[1] This condition is related to a very general mathematical theorem called *Fredholm alternative*. In the context of boundary-value problems the theorem can be stated as follows (see, e.g., Garabedian, 1964): "Either the inhomogeneous boundary-value problem is solvable whatever the forcing terms may be, or the corresponding homogeneous problem has one or more eigenfunctions (nontrivial solutions). In the first case the inhomogeneous solution is unique. In the second case the inhomogeneous problem is solvable if and only if the forcing terms are orthogonal to all the eigenfunctions of the homogeneous problem."

In our problem, ψ_0 is the eigenfunction to the homogeneous problem and ψ_1 is the solution to the inhomogeneous problem; Eq. (2.4.12) is the "orthogonality" condition.

$$\int_{-h}^{0} dz \left[\psi_0 \left(\frac{\partial^2 \psi_1}{\partial z^2} - k^2 \psi_1 \right) - \psi_1 \left(\frac{\partial^2 \psi_0}{\partial z^2} - k^2 \psi_0 \right) \right]$$

$$= \left[\psi_0 \frac{\partial \psi_1}{\partial z} - \psi_1 \frac{\partial \psi_0}{\partial z} \right]_{-h}^{0} . \tag{2.4.11}$$

If Eqs. (2.4.7a, b) are used on the left, and Eqs. (2.4.8a, b) and (2.4.9a, b) are used on the right, we get, from the preceding theorem,

$$-\frac{\partial A}{\partial x_1} \left[\frac{gk}{\omega} \frac{1}{\cosh^2 kh} \int_{-h}^{0} \cosh^2 k(z+h)\, dz \right] = \frac{\partial A}{\partial t_1} .$$

In view of Eq. (1.5.12), it follows that

$$\frac{\partial A}{\partial t_1} + C_g \frac{\partial A}{\partial x_1} = 0 . \tag{2.4.12}$$

The solution can be easily verified to be $A(x_1 - C_g t_1)$, implying that the envelope propagates at the group velocity without change of form. This general result includes Eq. (1.5.5), as a special case. In addition, it also applies to the front of a gradually started and steadily maintained wavetrain as anticipated in Section 1.5.2.

Before proceeding to the next order, let us digress for an immediate application. When sinusoidal disturbances are generated in a localized region, there is a mathematical ambiguity in the boundary condition at infinity in the steady-state formulation. For example, merely stating that the disturbance should remain finite (in one dimension) or die out (in two or three dimensions) at infinity does not guarantee the uniqueness of the solution; a much stronger condition must be imposed. Within the strict limits of a steady-state formulation this condition is usually stated as follows: "A locally generated sinusoidal disturbance must propagate outward to infinity". This important statement is called the *radiation condition.* A justification, even for a special case, is certainly desirable.

Let us regard the steady state as the limit of $t \to \infty$ of an initial-value problem. In particular, consider the one-dimensional waves in the domain $x > 0$ due to the sinusoidal oscillation of a wavemaker at $x = 0$. Let the amplitude of the sinusoidal wave near $x = 0$ vary slowly from 0 at $t \sim -\infty$ to a constant A_0 at $t \sim +\infty$ according to some law $A(t) = \overline{A}(t_1)$, see Fig. 2.8. We then expect the solution at any $x_1 > 0$ to be given by Eq. (2.4.10) with $A(x,t) = \overline{A}(t_1 - x_1/C_g)$. By causality, the wave amplitude vanishes at sufficiently large x_1 for any finite t; hence $A(x,t) \cong \overline{A}(-x_1/C_g) \downarrow 0$ as $x_1 \uparrow +\infty$. In view of Fig. 2.8 this is possible

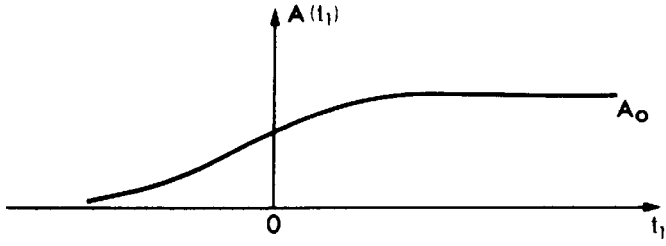

Figure 2.8: Slow rise of amplitude near the wavemaker.

only if $C_g > 0$. Since C_g and k are of the same sign, we must have $k > 0$, which implies from Eq. (2.4.5) that $\psi_0 e^{i(kx-\omega t)}$ propagates to the right, that is, *outgoing*.

In principle, the radiation condition can be deduced from an initial-value problem without the assumption of a slow start. However, the required analysis is long (see Stoker, 1956, 1957).

The permanence of form implied by Eq. (2.4.12) is only true on the scale $O(\mu^{-1})$, that is, with respect to x_1 and t_1. Let us pursue the next order to observe changes over a longer distance or time $O(\mu^{-2})$, that is, with respect to x_2 and t_2.

First, we leave it to the reader to show that the inhomogeneous solution for ψ_1 is

$$\psi_1 = -\frac{gQ \text{ sh Q}}{\omega k \text{ ch kh}} \frac{\partial A}{\partial x_1}, \quad \text{with} \quad Q \equiv k(z+h), \quad \text{sh} \equiv \sinh \quad \text{and} \quad \text{ch} \equiv \cosh. \tag{2.4.13}$$

The boundary conditions are satisfied because of Eq. (2.4.12). A homogeneous solution is omitted because it can be considered as contained in ψ_0. Substituting Eqs. (2.4.10) and (2.4.13) into the right-hand sides of Eqs. (2.4.7c) and (2.4.8c), we obtain

$$\frac{\partial^2 \psi_2}{\partial z^2} - k^2 \psi_2 = \frac{2ig}{\omega} \frac{\partial^2 A}{\partial x_1^2} \frac{Q \text{ sh } Q}{\text{ch } kh} + \frac{ig}{\omega} \left(\frac{\partial^2 A}{\partial x_1^2} + 2ik \frac{\partial A}{\partial x_2} \right) \frac{\text{ch}}{\text{ch}} \frac{Q}{kh}, \tag{2.4.14a}$$

$$\frac{\partial \psi_2}{\partial z} - \frac{\omega^2}{g} \psi_2 = i \left(\frac{2h \text{ sh } kh}{\text{ch } kh} C_g + \frac{C_g^2}{\omega} \right) \frac{\partial^2 A}{\partial x_1^2} + 2 \frac{\partial A}{\partial t_2}, \quad z = 0, \tag{2.4.14b}$$

$$\frac{\partial \psi_2}{\partial z} = 0, \quad z = -h. \tag{2.4.14c}$$

In arriving at Eq. (2.4.14b), use is made of Eq. (2.4.12). Now the argument of solvability can be repeated which, after lengthy but straightforward algebra, gives a surprisingly simple result:

$$\frac{\partial A}{\partial t_2} + C_g \frac{\partial A}{\partial x_2} = \frac{i}{2}\omega'' \frac{\partial^2 A}{\partial x_1^2}\,, \tag{2.4.15}$$

where

$$\omega'' = \frac{d^2\omega}{dk^2} = \frac{C_g}{k}(1 - 2kh \text{ th } kh) - \frac{C_g^2}{\omega} + \frac{C}{2k}(2kh \text{ cth } 2kh - 1)$$

$$= \frac{-g}{4\omega k\sigma}\{T^2 - 2khT(1-T^2) + (kh)^2(1-T^2)^2 + 4(kh)^2T^2(1-T^2)\}\,,$$

with th $\equiv$ tanh, cth $\equiv$ cotanh and $T \equiv \tanh kh$ for brevity.

The two orders (2.4.12) and (2.4.15) may be combined, and the small parameter μ may be dropped to give

$$\frac{\partial A}{\partial t} + C_g \frac{\partial A}{\partial x} = \frac{i}{2}\omega'' \frac{\partial^2 A}{\partial x^2}\,, \tag{2.4.16}$$

which governs the slow modulation of the envelope and is exactly Eq. (2.3.16).

In terms of the coordinate system moving at C_g, that is, with the group

$$\xi = x - C_g t\,,$$

Eq. (2.4.16) becomes the Schrödinger equation in quantum mechanics,

$$\frac{\partial A}{\partial t} = \frac{i\omega''}{2}\frac{\partial^2 A}{\partial \xi^2}\,. \tag{2.4.17}$$

This equation involves only one space coordinate and is, therefore, easier to deal with than the boundary-value problem involving x and z. Let us apply it to a new example.

2.4.2 Evolution of the Front of a Wavetrain

Consider a sinusoidal disturbance originated from a wavemaker which is switched on at some earlier time and is maintained steadily afterward. Ultimately, at a fixed station, a steady sinusoidal motion is attained. It is interesting to examine the development of the wave front. This problem was first studied by Wu (1957) for an oscillating point pressure suddenly started at $t = 0$ on the surface of an infinitely deep water with surface tension. The same problem, without surface tension, was later studied by

Miles (1962). The transient wave front caused by a vertical plate rolling in the free surface was also examined by Mei (1966a). The approach of all these authors was to start from an exact solution and then to perform an asymptotic approximation of the integral representation for large x and t. The mathematics contained some subtleties in that the major contribution came from near the pole of a principal-valued integral.

Let us use Eq. (2.4.17) which should be applicable for the wave front once it is far enough from the source of disturbance. The precise history of the starting process is not important. We now seek the solution to satisfy the boundary conditions that

$$A \to 0 \quad \text{as} \quad \xi \to \infty\,, \tag{2.4.18a}$$

$$A \to A_0 \quad \text{as} \quad \xi \to -\infty\,, \tag{2.4.18b}$$

that is, the envelope changes from the constant A_0 behind the wave front to zero ahead of the front. No restriction is made on kh.

The boundary-value problem defined by Eqs. (2.4.17) and (2.4.18a, b) can be solved by the similarity method familiar in boundary-layer theory or heat conduction. Since Eq. (2.4.17) resembles the heat equation, we anticipate a similarity solution of the form

$$A = A_0 f(\gamma) \quad \text{where} \quad \gamma = -\frac{\xi}{t^{1/2}}\,. \tag{2.4.19}$$

It follows from Eq. (2.4.17) that

$$f'' - \frac{i\gamma}{|\omega''|} f' = 0\,, \tag{2.4.20}$$

with the boundary conditions

$$f \to 1\,, \quad \gamma \sim \infty\,, \tag{2.4.21a}$$

$$f \to 0\,, \quad \gamma \sim -\infty\,. \tag{2.4.21b}$$

Equation (2.4.20) may be integrated to give

$$f = C \int_{-\infty}^{\gamma} \exp\left(\frac{iu^2}{2|\omega''|}\right) du\,,$$

which satisfies Eq. (2.4.21b). To satisfy Eq. (2.4.21a), we insist that

$$1 = C \int_{-\infty}^{\infty} \exp\left(\frac{iu^2}{2|\omega''|}\right) du\,.$$

Since

$$\int_0^\infty e^{i\tau^2} d\tau = \frac{\pi^{1/2}}{2} e^{i\pi/4}\,, \tag{2.4.22}$$

we obtain

$$C = e^{-i\pi/4}(2\pi|\omega''|)^{-1/2}\,,$$

and the solution

$$\frac{A}{A_0} = e^{-i\pi/4}(2\pi|\omega''|)^{-1/2} \int_{-\infty}^{\gamma} du\, \exp\left(\frac{iu^2}{2|\omega''|}\right). \tag{2.4.23}$$

The above result may be expressed alternatively

$$\begin{aligned}\frac{A}{A_0} &= e^{-i\pi/4}(2\pi|\omega''|)^{-1/2} \left[\int_{-\infty}^{0} + \int_0^{\gamma}\right] du \exp\left(\frac{iu^2}{2|\omega''|}\right) \\ &= \frac{1}{2} + e^{-i\pi/4}(2\pi|\omega''|)^{-1/2} \int_0^{\gamma} du \exp\left(\frac{iu^2}{2|\omega''|}\right)\end{aligned} \tag{2.4.24}$$

after the use of Eq. (2.4.22). Introducing $u^2/|\omega''| = \pi\upsilon^2$, we get

$$\begin{aligned}\frac{A}{A_0} &= \frac{1}{2} + \frac{e^{-i\pi/4}}{2^{1/2}} \int_0^{\beta} e^{i\pi\upsilon^2/2}\, d\upsilon \\ &= \frac{e^{-i\pi/4}}{2^{1/2}} \left[\frac{1+i}{2} + \int_0^{\beta} d\upsilon \left(\cos\frac{\pi\upsilon^2}{2} + i\sin\frac{\pi\upsilon^2}{2}\right)\right],\end{aligned} \tag{2.4.25}$$

where

$$\beta = -\xi(\pi|\omega''|t)^{-1/2}\,. \tag{2.4.26}$$

Since

$$C(\beta) = \int_0^{\beta} \cos\frac{\pi\upsilon^2}{2}\, d\upsilon \tag{2.4.27a}$$

and

$$S(\beta) = \int_0^{\beta} \sin\frac{\pi\upsilon^2}{2}\, d\upsilon \tag{2.4.27b}$$

are the Fresnel cosine and sine integrals, Eq. (2.4.25) may be written

$$\frac{A}{A_0} = \frac{e^{-i\pi/4}}{2^{1/2}} \left\{\left[\frac{1}{2} + C(\beta)\right] + i\left[\frac{1}{2} + S(\beta)\right]\right\}. \tag{2.4.28}$$

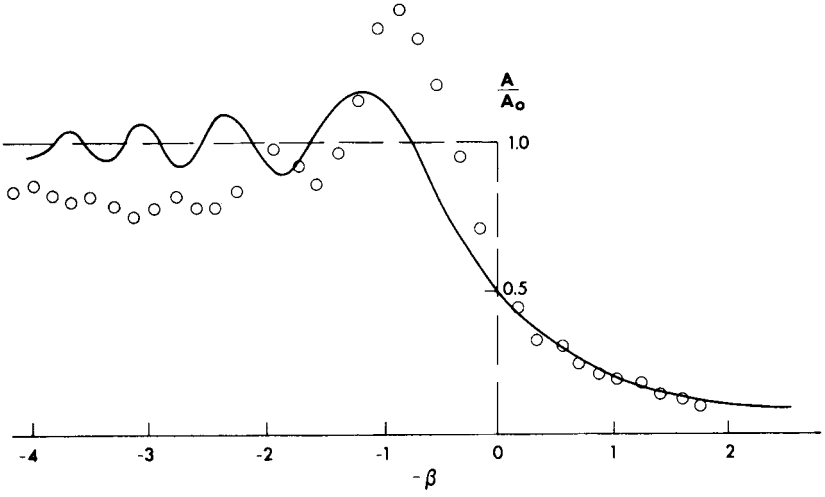

Figure 2.9: Comparison of theory (Miles, 1962) with experiments. The amplitude is measured at 160 ft from the wavemaker; frequency is $\omega = 5.52$ rad/s (from Longuet–Higgins, 1974a, *Proceedings*, *Tenth Symposium on Naval Hydrodynamics*. Reproduced by permission of U.S. Office of Naval Research).

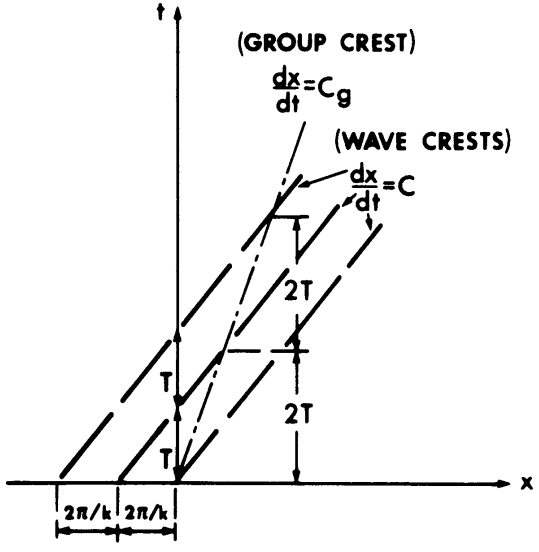

Figure 2.10: Effect of group velocity versus phase velocity in deep water $C_g = C/2$; the time interval is $2T$ between two successive instants when a wave crest coincides with the envelope crest.

The magnitude $|A/A_0|$ is given by

$$\left|\frac{A}{A_0}\right| = \frac{1}{2^{1/2}}\left\{\left[\frac{1}{2}+C(\beta)\right]^2+\left[\frac{1}{2}+S(\beta)\right]^2\right\}^{1/2}, \tag{2.4.29}$$

which is plotted in Fig. 2.9. It is interesting that Eq. (2.4.29) also describes the variation across a shadow boundary in a diffraction problem which will be examined later. To an observer fixed at x which is far from the wavemaker, the envelope first grows monotonically to $A_0/2$ when $t = x/C_g$, then approaches the steady-state limit A_0 in an oscillatory manner. The transition region stretches out with time as $t^{1/2}$. Longuet–Higgins (1974a) has performed experiments which support this theory qualitatively. Some quantitative discrepancy exists which is likely related to nonlinear effects. In particular, for sufficiently high amplitude the observed crests break at the first peak of the envelope. Since the envelope velocity in deep water is one-half of the crest velocity, the time interval between two successive crests arriving at the peak of the envelope is two wave periods (see Fig. 2.10). If the waves at the peak are high enough to break, one finds the time interval between two successive breakers to be $2T$. This phenomenon can be observed in white caps (Donelan, Longuet–Higgins, and Turner, 1972).

Refraction by Slowly Varying Depth or Current

3

When a train of plane monochromatic waves enters a zone of slowly varying depth, the wavenumber can be expected to change with depth in accordance with Eq. (1.4.8), Chapter One, resulting in a gradual change in the phase velocity. In general, the spacings between equal phase lines and the amplitude of crests and troughs will vary from place to place. Similar changes can also occur for waves riding on a current whose intensity varies in horizontal directions. These phenomena, which are related mainly to the variation in phase velocity, are of course well known in optics and acoustics and are called *refraction*. In this chapter, we develop an approximate *ray theory* (or *geometrical optics theory*) for the effects of varying depth (Sections 3.1–3.4) and of varying current (Sections 3.6 and 3.7) on the propagation of infinitesimal waves. The evolution equations will be deduced by the so-called WKB method which is a special version of the multiple-scales method. While these equations are normally solved numerically for practical problems, we shall extract from them physical insights through a variety of analytical examples. A brief discussion is also made, for varying depth only, on the local remedy needed when the ray approximation fails. In a numerical treatment of natural topography, this failure can be overcome more straightforwardly by incorporating diffraction in the so-called *mild-slope equation*, which we derive in Section 3.5. Other more mathematical aspects not treated here can be found in the excellent surveys of Meyer (1979a) for varying depth and Peregrine (1976) for varying current.

3.1 Geometrical Optics Approximation for Progressive Waves Over a Gradually Varying Bottom

We assume that the typical wavelength is much less than the horizontal length scale of depth variation. A small parameter can be introduced as follows:

$$\mu = O\left(\frac{\nabla h}{kh}\right) \ll 1\,. \tag{3.1.1}$$

To be more general, let us allow slow modulation in time too, which may be the result of initial conditions. Following Keller (1958), we introduce the slow coordinates

$$\bar{x} = \mu x\,, \quad \bar{y} = \mu y\,, \quad \bar{t} = \mu t\,. \tag{3.1.2}$$

The linearized governing equations become

$$\mu^2(\Phi_{\bar{x}\bar{x}} + \Phi_{\bar{y}\bar{y}}) + \Phi_{zz} = 0\,, \quad -h(\bar{x},\bar{y}) < z < 0\,, \tag{3.1.3}$$

$$\mu^2\Phi_{\bar{t}\bar{t}} + g\Phi_z = 0\,, \quad z = 0\,, \tag{3.1.4}$$

$$\Phi_z = -\mu^2(\Phi_{\bar{x}}h_{\bar{x}} + \Phi_{\bar{y}}h_{\bar{y}})\,, \quad z = -h(\bar{x},\bar{y})\,. \tag{3.1.5}$$

The second key step, typical of WKB, is to introduce the following expansion in anticipation that waves are progressive:

$$\Phi = [\phi_0 + (-i\mu)\phi_1 + (-i\mu)^2\phi_2 + \cdots]e^{iS/\mu}\,, \tag{3.1.6}$$

where

$$\phi_j = \phi_j(\bar{x},\bar{y},z,\bar{t}\,) \quad \text{for} \quad j = 0,1,2,\ldots\,; \quad \text{and} \quad S = S(\bar{x},\bar{y},\bar{t}\,)\,.$$

The intuitive basis for this assumption is that while wave amplitude varies with the slow coordinates $\bar{x}$, $\bar{y}$, $\bar{t}$, the phase varies with the fast coordinates $(\bar{x},\bar{y},\bar{t}\,)\mu^{-1}$. By straightforward differentiation we get

$$\begin{aligned}
\mu^2\Phi_{\bar{t}\bar{t}} = -(-i\mu)^2\Phi_{\bar{t}\bar{t}} = -\{&S_{\bar{t}}^2(\phi_0 + (-i\mu)\phi_1 + (-i\mu)^2\phi_2 + \cdots) \\
&+ (-i\mu)[S_{\bar{t}\bar{t}}(\phi_0 + (-i\mu)\phi_1 + \cdots) + 2S_{\bar{t}}(\phi_{0\bar{t}} + (-i\mu)\phi_{1\bar{t}} + \cdots)] \\
&+ (-i\mu)^2(\phi_{0\bar{t}\bar{t}} + \cdots)\}e^{iS/\mu}\,,
\end{aligned}$$

$$\overline{\nabla}\Phi = \left\{[\overline{\nabla}\phi_0 + (-i\mu)\overline{\nabla}\phi_1 + \cdots] + \frac{i\overline{\nabla}S}{\mu}[\phi_0 + (-i\mu)\phi_1 + \cdots]\right\}e^{iS/\mu}\,,$$

$$\mu^2\overline{\nabla}\cdot\overline{\nabla}\phi = -(-i\mu)^2\overline{\nabla}\cdot\overline{\nabla}\phi = -(-i\mu)^2$$
$$\cdot\left\{[\overline{\nabla}^2\phi_0 + (-i\mu)\overline{\nabla}^2\phi_1 + \cdots] + [\overline{\nabla}\phi_0 + (-i\mu)\overline{\nabla}\phi_1 + \cdots]\right.$$
$$\cdot\frac{i\overline{\nabla}S}{\mu} + \frac{1}{-i\mu}[\overline{\nabla}\cdot\phi_0\overline{\nabla}S + (-i\mu)\overline{\nabla}\cdot(\phi_1\overline{\nabla}S) + \cdots]$$
$$\left.+\left(\frac{i\overline{\nabla}S}{\mu}\right)^2[\phi_0 + (-i\mu)\phi_1 + \cdots]\right\}e^{iS/\mu}\,.$$

Let us define

$$\mathbf{k} = \overline{\nabla}S \tag{3.1.7a}$$

and

$$\omega = -S_{\bar{t}}\,, \tag{3.1.7b}$$

which represent the local wavenumber vector and frequency, respectively. Substituting Eqs. (3.1.7) into Eqs. (3.1.3)–(3.1.5) and separating the orders, we obtain at $O(-i\mu^0)$

$$\phi_{0zz} - k^2\phi_0 = 0\,, \quad -h < z < 0\,, \tag{3.1.8}$$

$$\phi_{0z} - \frac{\omega^2}{g}\phi_0 = 0\,, \quad z = 0\,, \tag{3.1.9}$$

$$\phi_{0z} = 0\,, \quad z = -h\,; \tag{3.1.10}$$

and at $O(-i\mu)$

$$\phi_{1zz} - k^2\phi_1 = \mathbf{k}\cdot\overline{\nabla}\phi_0 + \overline{\nabla}\cdot(\mathbf{k}\phi_0)\,, \quad -h < z < 0\,, \tag{3.1.11}$$

$$\phi_{1z} - \frac{\omega^2}{g}\phi_1 = -\frac{[\omega\phi_{0\bar{t}} + (\omega\phi_0)_{\bar{t}}]}{g}\,, \quad z = 0\,, \tag{3.1.12}$$

$$\phi_{1z} = \phi_0\mathbf{k}\cdot\overline{\nabla}h\,, \quad z = -h\,. \tag{3.1.13}$$

Equations (3.1.8)–(3.1.10) and (3.1.11)–(3.1.13) define two boundary-value problems governed by ordinary differential equations. The solution to Eqs. (3.1.8)–(3.1.10) is, formally,

$$\phi_0 = -\frac{igA}{\omega}\frac{\cosh k(z+h)}{\cosh kh}\,, \tag{3.1.14}$$

with

$$\omega^2 = gk \tanh kh \,. \tag{3.1.15}$$

Thus, $\omega(\bar{x}, \bar{y}, \bar{t}\,)$ and $k(\bar{x}, \bar{y}, \bar{t}\,)$ are related to the local depth $h(\bar{x}, \bar{y})$ by the same dispersion relation as if h were constant. The amplitude $A(\bar{x}, \bar{y}, \bar{t}\,)$ is still arbitrary.

To get a condition on A we examine the solvability of ϕ_1 by applying Green's formula [Eq. (2.4.11)] to ϕ_0^* and ϕ_1. Making use of all conditions (3.1.8)–(3.1.10) and (3.1.11)–(3.1.13), we get

$$\int_{-h}^{0} dz\, \phi_0^* [(\mathbf{k} \cdot \overline{\nabla}\phi_0) + \overline{\nabla} \cdot (\mathbf{k}\phi_0)]$$

$$= -\frac{1}{g} \{\phi_0^* [\omega\phi_{0\bar{t}} + (\omega\phi_0)_{\bar{t}}]\}_{z=0} - |\phi_0|^2_{z=-h} \mathbf{k} \cdot \overline{\nabla} h \,.$$

By Leibniz's rule

$$D \int_b^a f\, dz = \int_b^a Df\, dz + (Da)(f)_{z=a} - (Db)(f)_{z=b} \,, \tag{3.1.16}$$

where D is either $\partial/\partial\bar{t}$, $\partial/\partial\bar{x}$, or $\partial/\partial\bar{y}$; the integral on the left and the last term on the right can be combined to give

$$\overline{\nabla} \cdot \int_{-h}^{0} dz\, \mathbf{k}|\phi_0|^2 + \frac{1}{g} \frac{\partial}{\partial\bar{t}} [\omega|\phi_0|^2]_{z=0} = 0 \,.$$

By the use of Eqs. (3.1.14) and (3.1.15), and the definitions of E and C_g [Eqs. (1.5.14) and (1.5.6), Chapter One] which are still valid here except that they are functions of ($\bar{x}$, $\bar{y}$, and $\bar{t}$), it is easy to verify that

$$\overline{\nabla} \cdot \left(\frac{E}{\omega} \mathbf{C}_g \right) + \frac{\partial}{\partial\bar{t}} \left(\frac{E}{\omega} \right) = 0 \,. \tag{3.1.17}$$

In the classical mechanics of oscillators, a similar ratio of energy to frequency is called *action* and is also found to be invariant when properties of the oscillator change slowly (adiabatically). Hence E/ω has come to be known as the *wave action* and Eq. (3.1.17) states its conservation while being transported by the group velocity.

In summary, the phase function of slowly varying water waves is governed by Eq. (3.1.15) with k and ω given by Eq. (3.1.7). S is thus governed by a highly nonlinear first-order partial differential equation which is called

the *eikonal equation* in optics. Once the phase is found, the amplitude is solved from the wave action equation (3.1.17).

Let us also note that definition (3.1.7) implies

$$\overline{\nabla} \times \mathbf{k} = 0 \tag{3.1.18}$$

$$\frac{\partial \mathbf{k}}{\partial \bar{t}} + \overline{\nabla}\omega = 0\,. \tag{3.1.19}$$

The one-dimensional version of Eq. (3.1.19)

$$\frac{\partial k}{\partial \bar{t}} + \frac{\partial \omega}{\partial \bar{x}} = 0 \tag{3.1.20}$$

is most easily interpreted physically. By definition, k is the number of equal phase lines per unit distance, hence the *density* of equal phase lines. By definition also, ω is the number of equal phase lines passing a fixed station, hence the *flux* of equal phase lines. Between the two stations $\bar{x}$ and $\bar{x} + d\bar{x}$, the net rate of out-flux of phase lines is $(\partial\omega/\partial\bar{x})\,d\bar{x}$, while the rate of decrease of phase lines in the control volume is $-(\partial k/\partial\bar{t})\,d\bar{x}$. It is clear that Eq. (3.1.20) is simply a law of wave-crest conservation.

In the next few sections we shall confine ourselves to strictly sinusoidal waves and study several examples which have their analogs in optics (Luneberg, 1964). Since the purpose of deducing approximate equations is already achieved, there is no need to distinguish the slow variables from the physical variables. All bars will now be removed.

Exercise 3.1: Slow Modulation of Waves in a Two-layered Sea

A two-layer ocean with densities ρ and ρ' has a slowly varying bottom $z = -h(x, y)$. The interface is at $z = 0$, while the mean free surface is at $z = h'$. Invoke the rigid-lid approximation and analyze a progressive train of internal waves by WKB approximation. Show that at the leading order $O(\mu^0)$ energy is $E = \frac{1}{2}\Delta\rho g A^2$ with $\Delta\rho = \rho - \rho'$, while the dispersion relation and group velocity are, respectively,

$$\omega^2 = \frac{\Delta\rho g k}{\rho' \coth kh' + \rho \coth kh}\,,$$

$$C_g = \frac{C}{2}\left[1 + \frac{\omega^2}{g\Delta\rho}(\rho' h' \operatorname{csch}^2 kh' + \rho h \operatorname{csch}^2 kh)\right].$$

From the solvability condition at $O(\mu)$, show that Eq. (3.1.17) is also true.

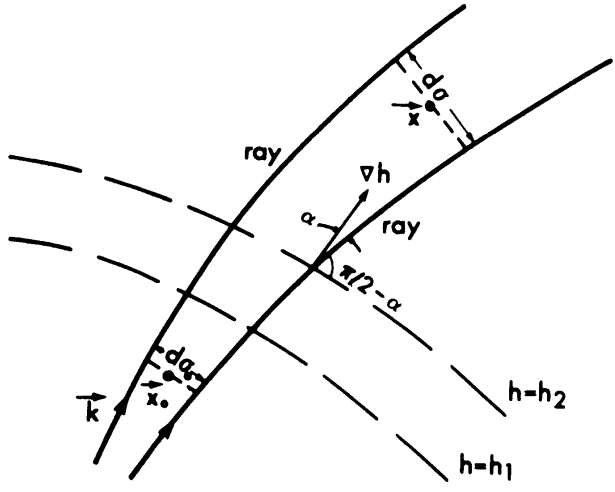

Figure 3.1: A ray channel and depth contours.

3.2 Ray Theory for Sinusoidal Waves, Fermat's Principle

If the waves are steady, $\partial/\partial t = 0$, then Eq. (3.1.19) implies that $\omega = \text{const}$. The problem involves waves purely sinusoidal in time. From Eq. (3.1.17) the amplitude variation is governed by

$$\nabla \cdot (E\mathbf{C}_g) = 0\,. \tag{3.2.1}$$

Imagine the x-y plane to be filled with $\mathbf{k}$ vectors which vary with position in magnitude and direction. Starting from a given point, let us draw a curve which is tangent to the local $\mathbf{k}$ vector at every point along the curve. Such a curve is called a wave *ray* and is always orthogonal to the local crests or phase lines $S = \text{const}$. From different starting points different rays can be drawn. Two adjacent rays form a ray channel. Consider a segment of a ray channel whose widths at the two ends are $d\sigma_0$ and $d\sigma$ (Fig. 3.1). Integrate Eq. (3.2.1) along the closed contour formed by the boundaries of the ray segment. From the Gauss divergence theorem and the fact that $\mathbf{C}_g$ is tangent to the ray, it follows that the energy fluxes through both ends are the same

$$EC_g d\sigma = (EC_g d\sigma)_0 = \text{const}\,. \tag{3.2.2}$$

The variation of amplitude along a ray then follows the law

$$\frac{A}{A_0} = \left[\frac{(C_g)_0}{C_g}\frac{d\sigma_0}{d\sigma}\right]^{1/2}, \tag{3.2.3}$$

where the ratio $d\sigma/d\sigma_0$ is called the *ray separation factor*.

The problem now is to find the rays, or their orthogonals, which are just the phase lines $S(x, y) = \text{const}$. Once the rays are located and the amplitude at station $\mathbf{u^x 0}$ is known, the amplitude at any other station along the ray is found immediately.

Taking the square of Eq. (3.1.7a), we obtain a nonlinear partial differential equation for S:

$$|\nabla S|^2 = k^2 \quad \text{or} \quad \left(\frac{\partial S}{\partial x}\right)^2 + \left(\frac{\partial S}{\partial y}\right)^2 = k^2\,, \tag{3.2.4}$$

the right-hand side being known from the dispersion relation. Equation (3.2.4) is called the *eikonal* equation which can be treated in a most general way by the method of characteristics. We present below a more elementary approach.

Let $y(x)$ represent a particular ray; its slope must be given by

$$y' = \frac{dy}{dx} = \frac{\partial S}{\partial y}\Big/\frac{\partial S}{\partial x}\,.$$

It follows from Eq. (3.2.4) that

$$(1 + y'^2)^{1/2} = \frac{k}{\partial S/\partial x} \quad \text{and} \quad \frac{ky'}{(1 + y'^2)^{1/2}} = \frac{\partial S}{\partial y}\,.$$

The derivative of the second equation above gives

$$\begin{aligned}
\frac{d}{dx}\frac{ky'}{(1 + y'^2)^{1.2}} &= \frac{\partial^2 S}{\partial y \partial x} + \frac{\partial^2 S}{\partial y^2}y' \\
&= \left(\frac{\partial^2 S}{\partial y \partial x}\frac{\partial S}{\partial x} + \frac{\partial^2 S}{\partial y^2}\frac{\partial S}{\partial y}\right)\Big/\frac{\partial S}{\partial x} \\
&= \left[\frac{1}{2}\frac{\partial}{\partial y}(\nabla S)^2\right]\Big/\frac{\partial S}{\partial x} \\
&= \left(\frac{\partial k}{\partial y}\right)(1 + y'^2)^{1/2}
\end{aligned}$$

or

$$\frac{d}{dx}\left[\frac{ky'}{(1+y'^2)^{1/2}}\right] = (1+y'^2)^{1/2}\frac{\partial k}{\partial y} \quad \text{with} \quad k = k(x, y(x))\,. \tag{3.2.5}$$

Equation (3.2.5) is a nonlinear ordinary differential equation for the ray $y(x)$. Once the initial point is known, the ray path can be solved numerically.

Before discussing specific examples, it is interesting to establish the correspondence between Eq. (3.2.5) and the celebrated *Fermat's principle* which states: "If P_0 and P_1 are two points on a ray and

$$L = \int_{P_0}^{P_1} k\, ds \tag{3.2.6}$$

is an integral along a certain path joining P_0 and P_1, then L is an extremum if and only if the path coincides with the ray." It is well known in the calculus of variations (see Hildebrand, 1964 p. 355ff) that the functional

$$L = \int_{P_0}^{P_1} F[x, y(x), y'(x)]\, dx \tag{3.2.7}$$

is extremum if and only if F satisfies the following Euler's equation:

$$\frac{d}{dx}\left(\frac{\partial F}{\partial y'}\right) = \frac{\partial F}{\partial y}\,. \tag{3.2.8}$$

If we let

$$L = \int_{P_0}^{P_1} k(1+y'^2)^{1/2} dx$$

and identify

$$F = k(1+y'^2)^{1/2}\,,$$

then Eq. (3.2.5) is precisely Euler's equation for Fermat's principle.

We have now seen that the eikonal equation and Fermat's principle are but two ways of expressing the same thing. Let us consider a few cases where the ray geometry can be easily found. Indeed, all the cases have their counterparts in optics (Luneberg, 1964).

3.3 Straight and Parallel Depth Contours

3.3.1 Geometry of Rays

Let all the contours be parallel to the y axis so that $h = h(x)$ and $k = k(x)$. The Euler equation (3.2.5) gives

$$\frac{d}{dx}\frac{ky'}{(1+y'^2)^{1/2}} = 0\,, \tag{3.3.1}$$

implying that

$$\frac{ky'}{(1+y'^2)^{1/2}} = K = \text{const}\,. \tag{3.3.2}$$

Since

$$\frac{y'}{(1+y'^2)^{1/2}} = \frac{dy}{ds} = \sin\alpha\,, \tag{3.3.3}$$

where α is the angle between the ray and the positive x axis, Eq. (3.3.2) is easily recognized as the well-known Snell's law:

$$k\sin\alpha = K = k_0\sin\alpha_0 \quad \text{or} \quad \frac{\sin\alpha}{C} = \frac{\sin\alpha_0}{C_0} \tag{3.3.4}$$

where k_0 and α_0 refer to a known point (x_0, y_0) on the ray. Solving for y' from Eq. (3.3.2), we have

$$\frac{dy}{dx} = \frac{\pm K}{(k^2 - K^2)^{1/2}}\,. \tag{3.3.5}$$

The above result can also be arrived at more simply. Indeed, Eq. (3.3.4) is just the consequence of Eq. (3.1.18) with $\partial/\partial y = 0$, while Eq. (3.3.5) follows from the geometrical definition of a ray:

$$\frac{dy}{dx} = \frac{k\sin\alpha}{k\cos\alpha}\,.$$

The equation of the ray is, upon integration,

$$y - y_0 = \pm\int_{x_0}^{x}\frac{K\,dx}{[k^2(x) - K^2]^{1/2}}\,. \tag{3.3.6}$$

Clearly, a ray can exist only where $k^2 > K^2$.

On the other hand, since a wave phase line is orthogonal to the rays, its slope must be given by

$$\frac{dy}{dx} = \mp\frac{1}{K}(k^2 - K^2)^{1/2}\,.$$

The equation of the phase line is therefore

$$\mp Ky = \int^x dx(k^2 - K^2)^{1/2} + \text{const}\,.$$

A good deal can be learned from Eqs. (3.3.5) and (3.3.6) without restricting $k(x)$ to any explicit form. The following cases give some idea of the possible varieties.

Case 1: Plane Wave Incident on a Ridge or a Beach

Let a plane incident wave approach from the left, $x \sim -\infty$. The incident rays are all parallel and enter the ridge at $x = x_0 < 0$ at the angle α_0. Since $k_0 \sin\alpha_0 = K < k$ everywhere, the square root $(k^2 - K^2)^{1/2}$ is always real, and since $dy/dx > 0$, the positive sign is to be taken in Eqs. (3.3.5) and (3.3.6). As h decreases, k increases, and dy/dx decreases; thus, when a ray passes over the ridge, it first becomes increasingly normal to the depth contours. After the peak is passed, the ray then turns away from the normal. The ray path is sketched in Fig. 3.2.

As a limiting case, let the summit of the ridge rise above the mean water level, resulting in a beach on either side. Consider a ray with $k = k_0$ at $x = x_0$ approaching from the left at the incidence angle α_0. The ray turns toward the depth contours and finally strikes the shorelines perpendicularly since $k \uparrow \infty$ for $h \downarrow 0$.

The following choice of k, due to Pocinki (1950), is a special model for a beach which begins at $x = a$ and ends at the shoreline $x = b$.

$$\frac{k}{k_0} = 1\,, \quad x < a\,,$$

$$\frac{k}{k_0} = \frac{1 - a/b}{1 - x/b}\,, \quad a < x < b\,.$$

Substituting into Eq. (3.3.5), we get

$$\frac{dy}{dx} = \frac{(1 - x/b)[(\sin\alpha_0)/(1 - a/b)]}{\{1 - [(\sin\alpha_0)/(1 - a/b)]^2(1 - x/b)^2\}^{1/2}}\,, \quad a > x > b\,.$$

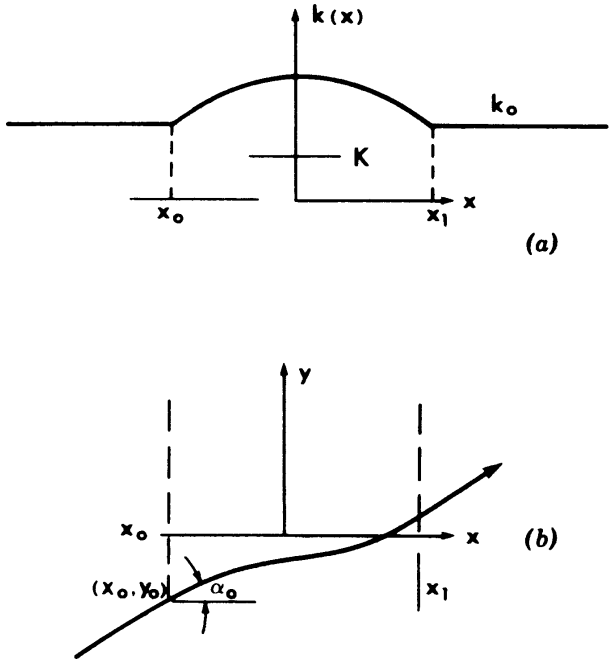

Figure 3.2: An incident ray passing over a submarine ridge. (a) Variation of $k(x)$ for a ridge; (b) an incident ray with $K < k_0 = k_{\min}$.

Let

$$\beta = \frac{\sin\alpha_0}{1 - a/b}\,, \quad \xi = 1 - \frac{x}{b}\,, \quad \eta = \frac{y}{b}\,,$$

then the ray differential equation becomes

$$d\eta = \frac{-\beta\xi d\xi}{(1-\beta^2\xi^2)^{1/2}} = \frac{1}{\beta} d(1-\beta^2\xi^2)^{1/2}$$

which is easily integrated to give

$$\xi^2 + (\eta - \eta_c)^2 = \frac{1}{\beta^2}$$

or

$$(x-b)^2 + (y-y_c)^2 = \frac{(b-a)^2}{\sin^2\alpha_0}\,.$$

Hence, the rays are a family of circular arcs centered at $x = b$ and $y = y_c$. The parameter y_c is related to the coordinate y_0 where the ray

intersects the contour $x = a$. By letting $x = a$ and $y = y_0$ in the last formula, we find

$$y_c = y_0 - (b - a)\cot\alpha_0 .$$

Case 2: Wave Trapping on a Ridge

If $k_{\max} > K = k_0 \sin\alpha_0 > k_{\min}$ [Fig. 3.3(a)], then rays can exist only in the region $b < x < a$, where $k > K$. Let such a ray originate from x_0 at the angle α_0 with $0 < \alpha_0 < \frac{1}{2}\pi$. From x_0 to a, $dy/dx > 0$ and y is given by Eq. (3.3.6) with the positive sign. The ray approaches the point $x = a$ and $y = y_a$ where

$$y_a = y_0 + \int_{x_0}^{a} \frac{K\,dx}{(k^2 - K^2)^{1/2}} .$$

For a sufficiently smooth bottom where k can be expanded as a Taylor series near $x = a$,

$$k^2 = K^2 + (x - a)(k^2)'_a + \cdots \quad \text{if} \quad (k^2)'_a \equiv (k^2)'|_{x=a} \neq 0 , \tag{3.3.7}$$

the integral is finite. The slope dy/dx is, however, infinite; hence the line $x = a$ is the envelope of all the rays and is called a *caustic*. Because of the crossing of the adjacent rays, the equation for the amplitude variation (3.2.3) ceases to be valid. A more refined treatment in the neighborhood of a caustic will be described in Section 3.3.3. After the point (a, y_a), $dy/dx < 0$; the ray turns back and is described by Eq. (3.3.6) with the negative sign until it reaches the line $x = b$, which is another caustic enveloping all rays. Thus, the ray bounces back and forth within the two caustics while advancing in the positive y direction [Fig. 3.3(b)]. No simple harmonic waves with the stated K are possible outside the range $b < x < a$. This phenomenon is called *wave trapping*.

External excitation of the trapped waves is possible by meteorological forcing on the free surface (atmospheric pressure or wind). For such high values of $K(> k_{\min})$ there is no simple harmonic wave away from the ridge. It is not possible to excite the ridge wave by a simple harmonic incident wave from either side of the ridge, according to the linearized mechanism. This does not, however, rule out the excitation of transient waves from outside sources.

Case 3: Submarine Trough

For a trough connecting two sides of equal depth, $k(x)$ varies as shown in Fig. 3.4(a). If an incident wave is such that $K = k_0 \sin\alpha_0 = K_2 < k_{\min}$,

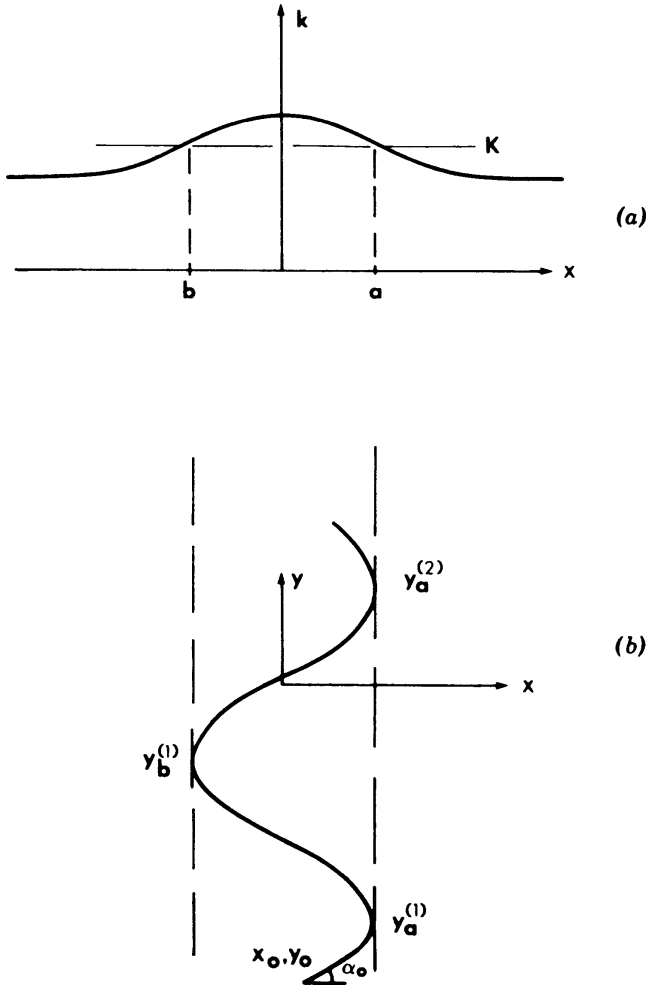

Figure 3.3: Wave trapping on a ridge: (a) variation of k over a ridge; (b) a trapped ray with $k_{\max} > K > k_{\min}$.

it will simply bend first toward, then away from the axis of the trough and pass the trough to the right side as shown in Fig. 3.4(b). However, if $K = K_1$ is sufficiently large, then no rays can exist in the region where $k < K$ and the line $x = x_1$ where $k(x_1) = K_1$ is a caustic. The ray must then turn around to the same side where it started. For fixed $k_0 > k_{\min}$, a sufficiently large value of K may be achieved if the incidence angle α_0 is sufficiently close to $\frac{1}{2}\pi$. The incident ray then makes a small acute angle to

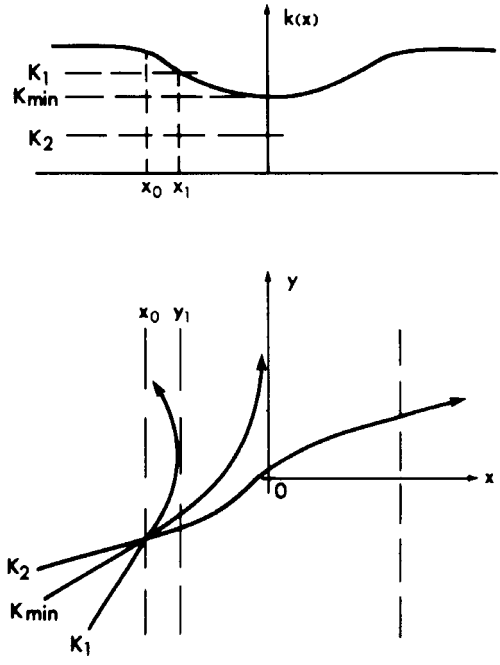

Figure 3.4: Wave rays over a submarine trough.

the contours; this is called *glancing* incidence. At the critical value $k_0 \sin \alpha_0 = k_{\min}$, the incident ray becomes asymptotically parallel to the depth contours.

3.3.2 Amplitude Variation

In this simple case, $\partial/\partial y = 0$ and Eq. (3.2.1) can be integrated to give

$$EC_g \cos\alpha = \frac{1}{2}\rho g A^2 C_g \cos\alpha = \text{const}\,. \tag{3.3.8}$$

Let the subscript $(\ )_0$ denote values at the reference depth h_0, then the amplitude ratio is

$$\begin{aligned} \frac{A}{A_0} &= \left[\frac{(C_g)_0 \cos\alpha_0}{C_g \cos\alpha}\right]^{1/2} \\ &= \left[\frac{k\cos\alpha_0}{k_0\cos\alpha}\frac{(1+2kh/\sinh 2kh)_0}{1+2kh/\sinh 2kh}\right]^{1/2}. \end{aligned} \tag{3.3.9}$$

In very shallow water, $\cos\alpha \to 1$, $C_g \simeq C \simeq (gh)^{1/2}$ and

$$\frac{A}{A_0} \simeq (C_{g_0}\cos\alpha_0)^{1/2}(gh)^{-1/4}\,, \tag{3.3.10}$$

hence the amplitude increases with decreasing depth. The 1/4 power dependence is often called Green's law. Combined with the shortening of the wavelength [$k \simeq \omega(gh)^{-1/2}$], the local wave slope increases with decreasing depth as $kA \propto h^{-3/4}$. For sufficiently small depth, the small-amplitude assumption underlying the linearized theory ceases to be valid and nonlinear effects become important. For a beach of constant slope the assumption that $(dh/dx)kh^{-1} \ll 1$ inherent in the WKB method also breaks down ultimately. Under certain conditions to be elaborated in Chapter Twelve, incident progressive waves may break in very shallow water. For normal incidence on a plane beach, experiments by Eagleson (1956) confirm Eq. (3.3.9) almost up to the first line of breaking.

3.3.3 The Neighborhood of a Straight Caustic

The inadequacy of the ray approximation may be remedied near a straight caustic with reasonable ease. In terms of the stretched variables defined by Eq. (3.1.2) we let the $\bar{y}$ axis be the caustic, and the incident and reflected rays be to the left. Then near $\bar{x} = 0$ we may approximate

$$k^2 \cong K^2 - \gamma\bar{x} \quad \text{with} \quad \gamma > 0 \tag{3.3.11}$$

provided that dk/dx does not vanish at $\bar{x} = 0$. It follows that

$$k_1 = (-\gamma\bar{x})^{1/2} \quad \text{and} \quad \int k_1 d\bar{x} = -\frac{2}{3}\gamma^{1/2}(-\bar{x})^{3/2} \tag{3.3.12}$$

where k_1 is the x component of $\mathbf{k}$. According to the ray approximation (3.3.9), we have

$$A = A_0\left(\frac{C_g k_1}{k}\right)_0^{1/2}\left(\frac{K}{C_g}\right)_{\bar{x}=0}^{1/2}(-\gamma\bar{x})^{-1/4} \equiv \tau(-\gamma\bar{x})^{-1/4}\,. \tag{3.3.13}$$

The free surface to the left of the caustic is

$$\eta = \tau(-\gamma\bar{x})^{-1/4}e^{iK\bar{y}/\mu} \times\left\{\exp\left[-i\frac{\gamma^{1/2}}{\mu}\frac{2}{3}(-\bar{x})^{3/2}\right] + R\exp\left[i\frac{\gamma^{1/2}}{\mu}\frac{2}{3}(-\bar{x})^{3/2}\right]\right\} \tag{3.3.14}$$

where the first term in { } is the incident wave and the second term is the reflected wave whose complex amplitude R is yet unknown.

From the above result the amplitude increases without bound as $\bar{x} \to 0$. An improved local theory near the caustic must therefore retain the highest derivative of the amplitude with respect to $\bar{x}$. Substituting

$$\Phi = \frac{-igX(\bar{x})}{\omega} \frac{\cosh k(z+h)}{\cosh kh} \exp\left(\frac{iK\bar{y}}{\mu} - \frac{i\omega\bar{t}}{\mu}\right) \tag{3.3.15}$$

into Eq. (3.1.3) and keeping the leading terms and the highest derivatives with respect to $\bar{x}$, we get

$$\mu^2 X_{\bar{x}\bar{x}} + (k^2 - K^2)X \cong 0\,. \tag{3.3.16}$$

Now $k^2 - K^2$ changes sign at $\bar{x} = 0$, being positive for $\bar{x} < 0$ and negative for $\bar{x} > 0$. The solution is oscillatory for $\bar{x} < 0$ and monotonic for $\bar{x} > 0$. The point $\bar{x} = 0$ is called a *turning point* in mathematical physics. Invoking Eq. (3.3.11), we have from Eq. (3.3.16)

$$\mu^2 X_{\bar{x}\bar{x}} - \gamma\bar{x}X \cong 0\,, \tag{3.3.17}$$

which is a good approximation in the region $\bar{x} = O(\mu)^{2/3}$, that is, $x = O(\mu^{-1/3})$. With the new variable

$$\sigma = \gamma^{1/3}\bar{x}\mu^{-2/3}\,, \tag{3.3.18}$$

Eq. (3.3.17) becomes the Airy equation

$$X_{\sigma\sigma} - \sigma X = 0 \tag{3.3.19}$$

whose general solution is

$$X = a\,\mathrm{Ai}(\sigma) + b\,\mathrm{Bi}(\sigma)\,. \tag{3.3.20}$$

The Airy function Ai has already been plotted in Fig. 2.5, Chapter Two. It is also known that for large $|\sigma|$:

$$\mathrm{Ai}(\sigma) \sim \frac{1}{2\pi^{1/2}}\sigma^{-1/4}\exp\left(-\frac{2}{3}\sigma^{3/2}\right), \quad \sigma \sim \infty\,, \tag{3.3.21a}$$

$$\sim \frac{1}{\pi^{1/2}}(-\sigma)^{-1/4}\sin\left[\frac{2}{3}(-\sigma)^{3/2} + \frac{\pi}{4}\right], \quad \sigma \sim -\infty\,, \tag{3.3.21b}$$

and

$$\mathrm{Bi}(\sigma) \sim \frac{1}{\pi^{1/2}}\sigma^{-1/4}\exp\left[\frac{2}{3}(\sigma^{3/2})\right], \quad \sigma \sim \infty\,, \tag{3.3.22a}$$

$$\sim \frac{1}{\pi^{1/2}}\sigma^{-1/4}\cos\left[\frac{2}{3}(-\sigma)^{3/2}+\frac{\pi}{4}\right], \quad \sigma \sim -\infty\,. \tag{3.3.22b}$$

If there are no other caustics or solid boundaries within the region $\bar{x} = O(\mu^{2/3}) > 0$, the solution $\mathrm{Bi}(\sigma)$ must be discarded; hence

$$\eta = a\,\mathrm{Ai}(\sigma)e^{iK\bar{y}/\mu}\,. \tag{3.3.23}$$

The coefficient a and the amplitude R of the reflected wave must be found by matching Eq. (3.3.23) with Eq. (3.3.14) for $-\sigma \gg 1$. With Eq. (3.3.21b) we rewrite Eq. (3.3.23)

$$\eta \cong \frac{a}{2i\pi^{1/2}}\left(-\frac{\gamma^{1/3}}{\mu^{2/3}}\bar{x}\right)^{-1/4}\left\{\exp\left[i\frac{2}{3}\frac{\gamma^{1/2}}{\mu}(-\bar{x})^{3/2}+\frac{i\pi}{4}\right]\right.$$
$$\left.-\exp\left[-i\frac{2}{3}\frac{\gamma^{1/2}}{\mu}(-\bar{x})^{3/2}-\frac{i\pi}{4}\right]\right\}e^{ik\bar{y}/\mu} \tag{3.3.24}$$

for $\sigma \sim -\infty$. Equations (3.3.14) and (3.3.24) are now required to match, hence

$$a = -2\pi^{1/2}ie^{i\pi/4}\tau(\gamma\mu)^{-1/6} \tag{3.3.25a}$$

and

$$R = -e^{i\pi/2}\,. \tag{3.3.25b}$$

For a given incident wave at $\bar{x} = \bar{x}_0$, τ is known. The coefficient a can be found at once. It is interesting that the largest amplitude is now finite and occurs before the caustic is reached. The reflected wave has the same amplitude as the incident wave but differs from the latter in phase by $\frac{1}{2}\pi$.

For a submarine trough there can be two parallel caustics. If the distance between them is not too great, the residual effect of $\mathrm{Ai}(\sigma)$ from the left caustic may penetrate the right caustic, inducing a transmitted wave. The details involve a similar treatment of the right caustic with both Ai and Bi used. Another case where $dk^2/d\bar{x} = 0$ but $d^2k^2/d\bar{x}^2 \neq 0$ is more complicated but may be analyzed in principle by modifying Eq. (3.3.11).

The approximate treatment of the caustic region presented in this subsection is of the boundary-layer type well known in viscous flow theory. An

alternative procedure is to seek a single representation which is uniformly valid everywhere. Such theories have been developed in other physical contexts for curved caustics (see Ludwig, 1966; Nayfeh, 1973) and have been applied to water waves (Chao, 1971). Experimental confirmation of this kind of theory is also available for simple topography and sufficiently small amplitudes (Chao and Pierson, 1972).

3.4 Circular Depth Contours

This class of problems was first studied by Arthur (1946) for water waves; analogous examples are also known in optics (Luneberg, 1964).

3.4.1 Geometry of Rays

In cylindrical polar coordinates (r, θ), the water depth, and hence the magnitude of the wavenumber vector, depend only on r, that is, $h = h(r)$, $k = k(r)$. To get Euler's equation for the ray we start from Fermat's principle and extremize the integral

$$L = \int k(r)(1 + r^2\theta'^2)^{1/2}\, dr \tag{3.4.1}$$

where $\theta' \equiv d\theta/dr$. Euler's equation is then

$$\frac{d}{dr}\left\{\frac{\partial}{\partial\theta'}[k(1 + r^2\theta'^2)^{1/2}]\right\} = 0\,,$$

or

$$\frac{kr^2\theta'}{(1 + r^2\theta'^2)^{1/2}} = \text{const} = \kappa \tag{3.4.2}$$

along a ray where κ is a constant characterizing the ray. Solving for θ', we obtain

$$\frac{d\theta}{dr} = \frac{\pm|\kappa|}{r(k^2r^2 - \kappa^2)^{1/2}}\,. \tag{3.4.3}$$

This differential equation can be integrated formally to give

$$\theta - \theta_0 = \pm|\kappa| \int_{r_0}^{r} \frac{dr}{r(k^2r^2 - \kappa^2)^{1/2}}\,, \tag{3.4.4}$$

where r_0 and θ_0 refer to a known point passed by the ray.

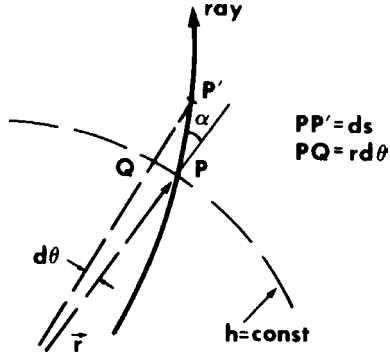

Figure 3.5: A smooth bottom with circular contours.

What is the significance of the constant κ? With the help of Fig. 3.5, Eq. (3.4.2) may be rewritten

$$\kappa = kr\frac{r\,d\theta}{(dr^2 + r^2\,d\theta^2)^{1/2}} = kr\frac{r\,d\theta}{ds} = kr\sin\alpha \tag{3.4.5}$$

where α is the angle between the ray and the normal (radius) vector to the depth contour intersected by the ray. If at the point r_0, θ_0 the incidence angle is $\alpha = \alpha_0$, then

$$\kappa = k_0 r_0 \sin\alpha_0\,. \tag{3.4.6}$$

Thus, the constant κ is determined by the initial position and direction of the ray.

In contrast to the case of straight and parallel contours, r appears on the right-hand side of Snell's law (3.4.5) as an additional factor. To help understand this difference, let us examine in an elementary way a bottom having a stepwise depth variation with radial symmetry, that is,

$$k = k_i = \text{const}\,, \quad r_{i-1} \le r \le r_i\,, \quad i = 1, 2, 3\,.$$

Here the subscripts 1, 2, 3 designate the regions and not the vector components. Consider a ray passing through regions 1, 2, and 3 (see Fig. 3.6). The ray in region i leaves the discontinuity at $r = r_{i-1}$ at the angle α_{i-1} and is incident on $r = r_i$ at the angle α_i', being a straight line segment in between. Applying Snell's law at the junction $r = r_1$, we obtain

$$k_1 \sin\alpha_1' = k_2 \sin\alpha_1\,. \tag{3.4.7}$$

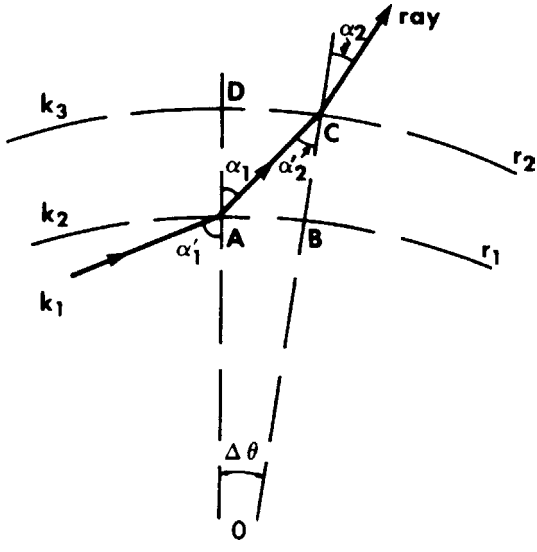

Figure 3.6: Circular step bottom.

It is important to note that $\alpha_1 \neq \alpha_2'$; in fact, it is evident from Fig. 3.6 that

$$\sin\alpha_1 = \frac{CD}{AC} = \frac{r_2\Delta\theta}{AC}\,, \quad \sin\alpha_2' = \frac{AB}{AC} = \frac{r_1\Delta\theta}{AC}\,,$$

hence

$$r_1 \sin\alpha_1 = r_2 \sin\alpha_2'\,. \tag{3.4.8}$$

Combining Eq. (3.4.8) with Eq. (3.4.7), we have

$$k_1 r_1 \sin\alpha_1' (= k_2 r_1 \sin\alpha_1) = k_2 r_2 \sin\alpha_2'\,.$$

Clearly, the same argument can be extended for many successive rings so that $k_n r_n \sin\alpha_n' = \text{const}$ which is the discontinuous version of Eq. (3.4.5). Thus, the appearance of r is due to the *curvature* of the depth contours.

From Eq. (3.4.4), it is clear that rays only exist in the regions where $k^2 r^2 > \kappa^2$. The critical radius at which

$$k^2 r^2 = \kappa^2\,, \quad r = r_*\,. \tag{3.4.9}$$

will be denoted by r_* and the corresponding θ by θ_* with

$$\theta_* - \theta_0 = \pm \int_{r_0}^{r_*} \frac{|\kappa|\, dr}{r(k^2r^2 - \kappa^2)^{1/2}}\,. \tag{3.4.10}$$

From Eq. (3.4.3), $dr/d\theta = 0$ at (r_*, θ_*); the ray is either the closest to, or the farthest from, the origin. The proper choice of sign in the preceding formula can be made by considering the sign of $dr/d\theta$ as will be illustrated in later examples.

Let us also deduce the equation for the constant-phase lines. Denoting the ray by $r = f(\theta)$ and the constant-phase line by $r = g(\theta)$, we use the fact that the two are orthogonal to obtain

$$\nabla[r - f(\theta)] \cdot \nabla[r - g(\theta)] = 0$$

or

$$g' = -\frac{r^2}{f'}\,.$$

Since

$$f'(\theta) = \pm\frac{r}{\kappa}(k^2r^2 - \kappa^2)^{1/2},$$

the differential equation for a phase line is

$$\frac{dr}{d\theta} = \mp\frac{\kappa r}{(k^2r^2 - \kappa^2)^{1/2}}\,, \tag{3.4.11}$$

which may be integrated to give

$$\kappa\theta \pm \int \frac{dr}{r}(k^2r^2 - \kappa^2)^{1/2} = \text{const}\,. \tag{3.4.12}$$

Several types of k are now examined for the physical implications:

Case 1: $0 < kr < \infty$ and kr is monotonic in r

In very shallow water, $k \sim h^{-1/2}$; we have $kr \to 0$ when $r \to 0$ as long as $rh^{-1/2} \to 0$. A submerged circular shoal falls into this category. Let the point $P_0(r_0, \theta_0)$ be the initial point. Then

$$\theta - \theta_0 = -|\kappa| \int_{r_0}^{r} \frac{dr}{r(k^2r^2 - \kappa^2)^{1/2}}\,, \tag{3.4.13}$$

where the negative sign is chosen since $d\theta/dr < 0$. This equation is valid until the point P_* is reached where $r = r_*$ is minimum. Beyond this point the ray is given by

$$\theta - \theta_* = \int_{r_*}^{r} \frac{|\kappa|\, dr}{r(k^2r^2 - \kappa^2)^{1/2}}\,, \tag{3.4.14}$$

where the positive sign is chosen. Since the ray is obviously symmetrical about the radius vector $\theta = \theta_*$, we may incorporate both branches of the ray into one equation,

$$|\theta - \theta_*| = \int_{r_*}^{r} \frac{|\kappa|\, dr}{r(k^2r^2 - \kappa^2)^{1/2}}\,. \tag{3.4.15}$$

The geometry is shown in Fig. 3.7.

Suppose that there is a plane wave incident from $x \sim -\infty$ toward a circular shoal. Beyond $r = r_0$, the bottom is assumed to be horizontal so that $k = k_0$ for $r > r_0$. The incident rays are originally parallel to the x axis. Among them, those rays which are initially outside the strip $|y| \le r_0$ do not intersect the circle $r = r_0$ and advance without deflection. Consider a ray initially within the strip $-r_0 < y < 0$ entering the shoal at the angle α_0 with respect to the radius vector; it first bends toward, and then away from, the center after a minimum r_*. Since the ray must be symmetrical about the minimum radius vector $\theta = \theta_*$, the angle between the outgoing ray and the radius vector at the point of departure must be $\pi - \alpha_0$ (see Fig. 3.7). Let the total angle by which the ray is deflected be β. It is clear that

$$\beta = \pi - \alpha_0 + \theta_0'$$

where θ_0' is the direction of the point at which the ray leaves the shoal:

$$\theta_0' - \theta_* = \int_{r_*}^{r_0} \frac{|\kappa|\, dr}{r(k^2r^2 - \kappa^2)^{1/2}}\,.$$

Similarly, rays entering the shoal from $0 < y < r_0$ bend first toward, and then away from, the center of the shoal. Thus, on the lee side of the shoal, rays from opposite sides of the x axis intersect, and the progressive waves associated with these rays interfere. In particular, at any point on the positive x axis, the resulting amplitude is twice that associated with a single ray because of symmetry. At a point not on the x axis, the intersecting rays may interfere either destructively or constructively, depending on the wave phases.

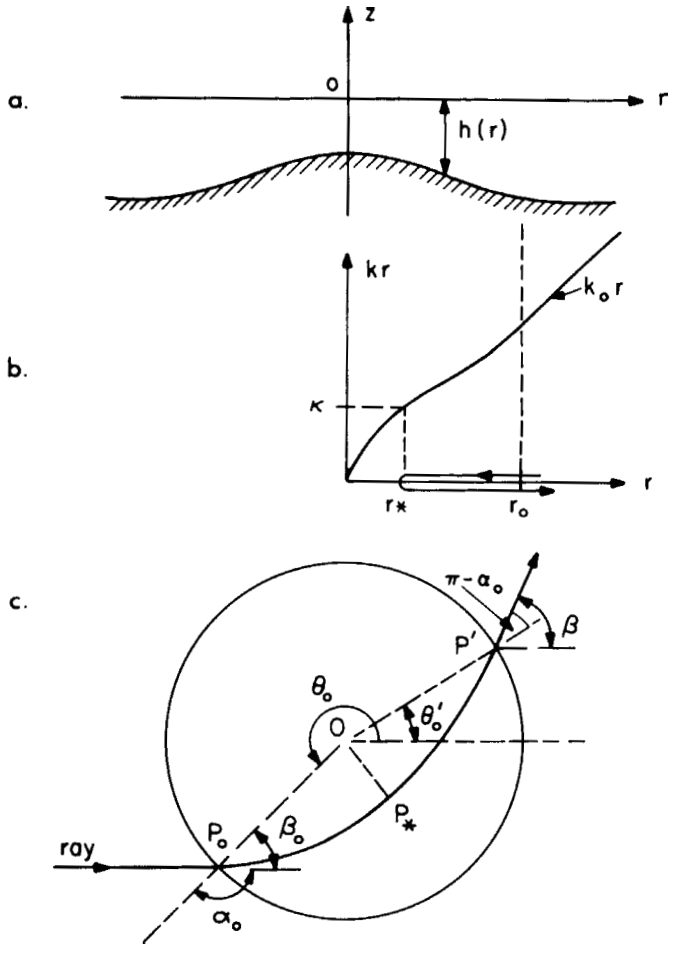

Figure 3.7: Submerged shoal: (a) side view of topography; (b) variation of kr versus r; (c) ray geometry.

Consider rays from the same side of the x axis, say, $-r_0 < y < 0$. Since there is no deflection and $\beta = 0$ for the two extreme values of $\alpha_0 : \pi$ (normal incidence) and $\pi/2$ (glancing incidence), and since $\beta > 0$ for intermediate values of α_0, there must be a positive maximum for β. Similarly, a ray entering the upper half of the shoal must have a negative maximum for β. It follows that the bundle of rays from the same side of the x axis must intersect one another in addition to intersecting those from the other side. A cusp-like caustic will develop on the lee side of the shoal, and a local

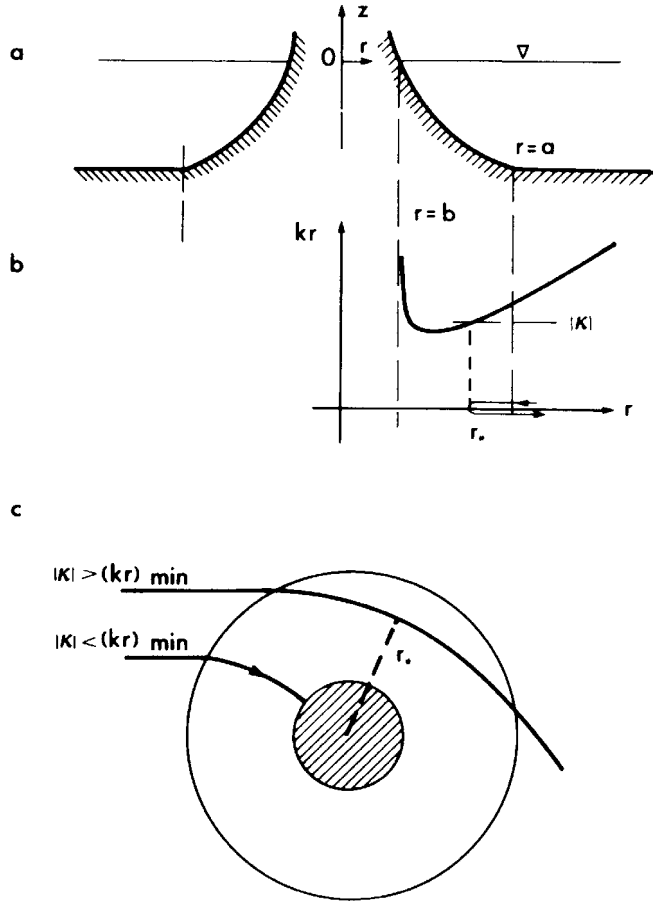

Figure 3.8: Circular island: (a) side view of topography; (b) kr versus r; (c) ray geometry.

remedy more complicated than that in Section 3.3.3 can be constructed to yield finite amplitude.

Case 2: kr first decreases to a minimum, then increases

Here is a case of a circular island with the shoreline at $r = b$ (see Fig. 3.8). Let $h \downarrow 0$ as $r - b \downarrow 0$, then $k \downarrow h^{-1/2}$ from the dispersion relation, and $kr \uparrow bh^{-1/2}$. At large r, $kr \to k_0 r$. All the incident rays intersecting the outer circle $r = a$ have $|\kappa|$ less than $k_0 a$. Those sufficiently close to the island axis satisfy $\kappa^2 < (kr)^2_{\min}$ so that they reach the shore eventually. However, those farther from the axis satisfy $(kr)_{\min} < \kappa^2 < (k_0 a)^2$ and

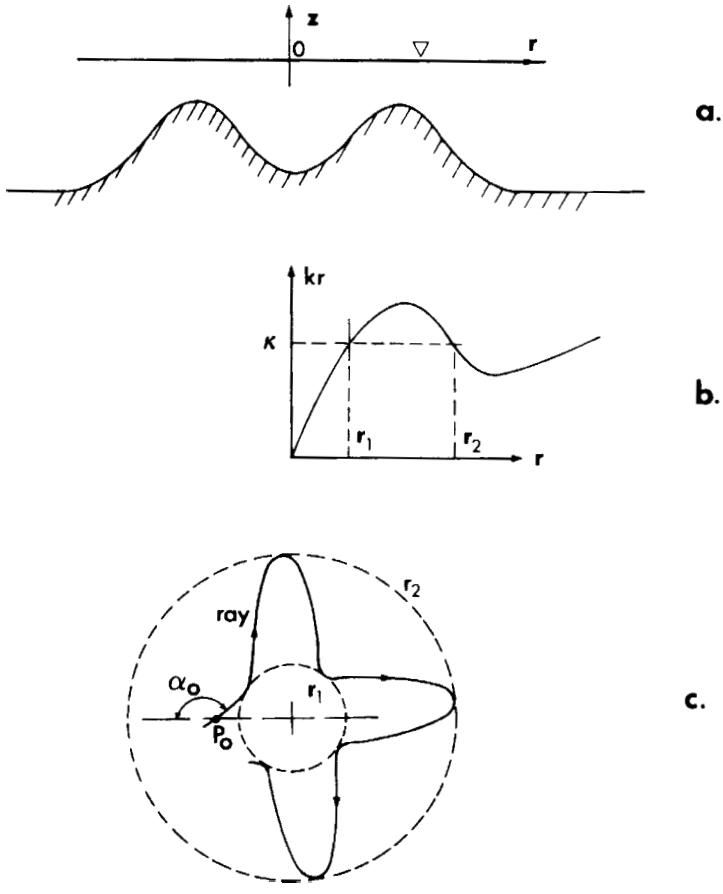

Figure 3.9: Trapped waves on a ring-shaped ridge: (a) side view of topography; (b) kr versus r; (c) ray geometry.

will be repelled by the island without reaching the shore. The critical ray is one which has such an entry angle that $\alpha_0 = \alpha_0^C$, where $|\sin\alpha_0^C| = (kr)_{\min}/k_0 r_0$. A more explicit example will be given shortly.

Case 3: Wave trapping on a ring-shaped ridge

If the depth variation is as shown in Fig. 3.9(a), then a local maximum kr is possible at some finite r. A ray originating at r_0, θ_0, with an inclination $\alpha_0 < \pi$, is given at first by

$$\theta - \theta_0 = \int_{r_0}^{r} \frac{|\kappa|\, dr}{r(k^2 r^2 - \kappa^2)^{1/2}}$$

so that $dr/d\theta > 0$ until $r = r_1$, $\theta = \theta_1'$. The ray then bends back to larger r with

$$\theta - \theta_1' = \int_{r_1}^{r} \frac{-|\kappa|\, dr}{r(k^2r^2 - \kappa^2)^{1/2}}$$

and advances clockwise, undulating between two caustic circles $r = r_1$ and $r = r_2$. Previous arguments show that the ray is symmetrical about the radius vector $\theta = \theta_1'$ and θ_2', and so on. Clearly, the configuration of the ray is repeated after every angular period:

$$\Delta\theta = 2|\kappa| \int_{r_1}^{r_2} \frac{dr}{r(k^2r^2 - \kappa^2)^{1/2}}\,.$$

Furthermore, if $\Delta\theta$ is a rational multiple of 2π, the ray will return to its original point and form a closed curve. Thus, the condition

$$\frac{\Delta\theta}{2\pi} = \frac{n}{m}\,, \quad m, n = 1, 2, 3, \ldots$$

determines the "eigenvalues" of free oscillation trapped on the ridge. Direct meteorological or transient incident waves may excite these modes, which may pose potential hazards to ocean structures built on the ridge.

3.4.2 Amplitude Variation

Consider the ray separation factor for a plane wave incident on a circular zone of refraction $r \le r_0$. Let the incident rays be parallel to the negative x axis as before. We note from Fig. 3.7 that

$$\theta_0 = \pi + \beta_0$$

where $\beta_0 = \pi - \alpha_0$. It follows from Eq. (3.4.4) that

$$\theta = \pi + \beta_0 \pm \int_{r_0}^{r} \frac{|\kappa|\, dr}{r(k^2r^2 - \kappa^2)^{1/2}}\,, \tag{3.4.16}$$

where

$$|\kappa| = k_0 r_0 |\sin\alpha_0| = k_0 r_0 |\sin\beta_0|\,,$$

and a refracted ray is characterized by its point of entry r_0, θ_0, or β_0. Consider two neighboring rays of slightly different incident angles β_0 and $\beta_0 + d\beta_0$. From Fig. 3.10 we have, at any circle $r < r_0$,

$$d\sigma = \overline{AB}\cos\beta = r\, d\theta \cos\beta = r\cos\beta\, d\beta_0 \left(\frac{\partial\theta}{\partial\beta_0}\right)_{r=\text{const}}$$

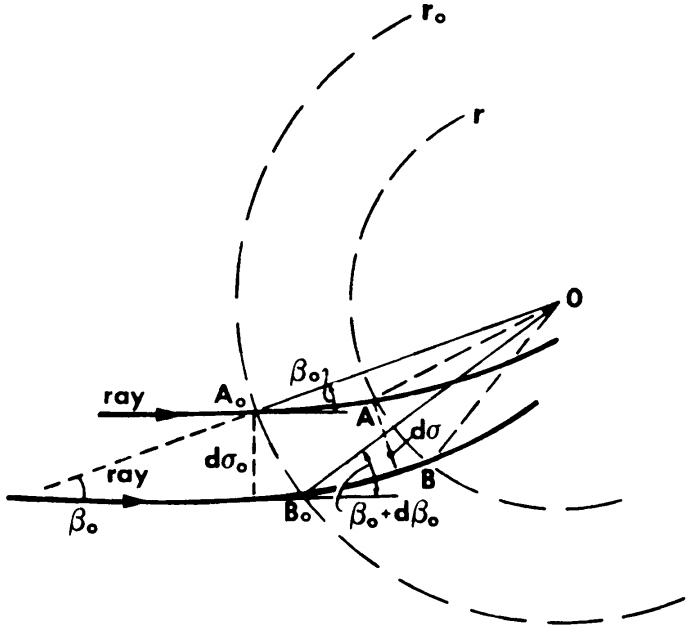

Figure 3.10: Geometry of a ray channel for circular depth contours.

because $d\theta$ is measured along the circle of radius r. Now at the initial circle $r = r_0$, $d\theta = d\beta_0$ and

$$d\sigma_0 = \overline{A_0 B_0} \cos\beta_0 = r_0 \, d\beta_0 \cos\beta_0 \, .$$

Hence the separation factor is

$$\frac{d\sigma}{d\sigma_0} = \frac{r\cos\beta}{r_0 \cos\beta_0} \left(\frac{\partial\theta}{\partial\beta_0} \right)_{r=\text{const}} .$$

Since $kr\sin\beta = \kappa = \text{const}$ and

$$\cos\beta = \left(1 - \left(\frac{\kappa}{kr} \right)^2 \right)^{1/2} ,$$

we have

$$\frac{d\sigma}{d\sigma_0} = \left\{ r \left[1 - \left(\frac{\kappa}{kr} \right)^2 \right]^{1/2} \left(\frac{\partial\theta}{\partial\beta_0} \right)_{r=\text{const}} \right\} (r_0 \cos\beta_0)^{-1} \qquad (3.4.17)$$

where $\partial\theta/\partial\beta_0$ may be obtained from Eq. (3.4.16).

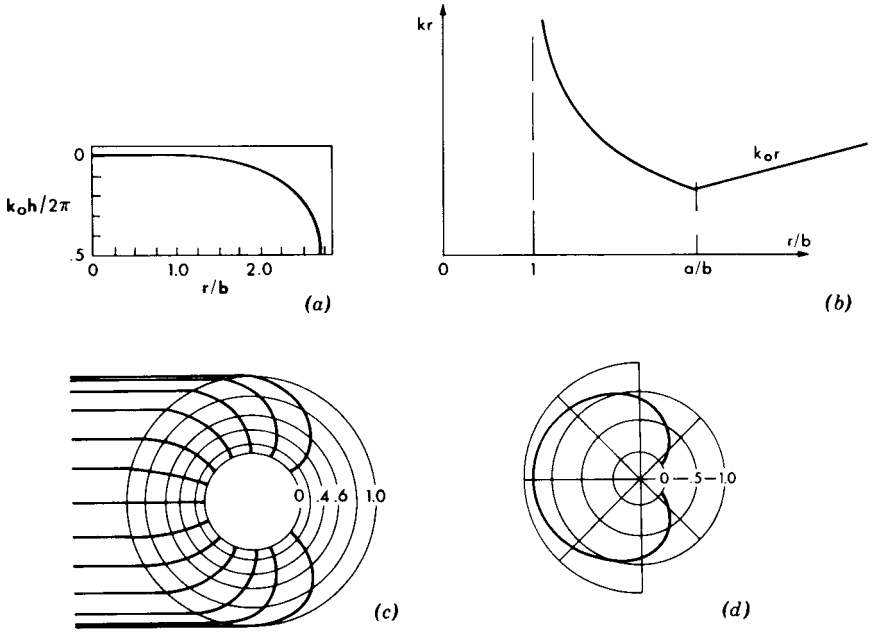

Figure 3.11: A circular island (Pocinki, 1950): (a) bottom profile; (b) kr versus r; (c) ray geometry; (d) polar plot of $(d\sigma_0/d\sigma)^{1/2}$ at the shore $r = b$.

Example: A Circular Island (Pocinki, 1950)

Take

$$\begin{aligned} kr &= k_0 a \cdot \frac{\ln(a/b)}{\ln(r/b)}\,, \qquad b < r < a\,, \\ &= k_0 r\,, \qquad\qquad\quad a < r\,, \end{aligned} \tag{3.4.18}$$

so that the shoreline is at $r = b$ and the toe of the island is at $r = a$. The variation is shown in Fig. 3.11(a). Near the shore $r = b$ where the depth is small, $h \sim k^{-2} \sim r^2 \ln^2 r/b$ and $dh/dr \sim 0$ as $r \to b$. The beach is therefore very flat. It is evident that in this case all the rays entering the island toe eventually intersect the shoreline at right angles.

With this choice of k, the ray equation is easily integrated:

$$\pm(\theta - \theta_0) = \int_{r=a}^{r=r} \frac{\ln(r/b) d[\ln(r/b)] k_0 a |\sin\alpha_0|}{[(k_0 a)^2 \ln^2(a/b) - (k_0 a)^2 \sin^2\alpha_0 \ln^2(r/b)]^{1/2}} \tag{3.4.19}$$

where the $+(-)$ sign is chosen for those rays entering the shoal in the second (third) quadrant. Letting

$$D = \frac{\ln(a/b)}{\sin\beta_0}\,, \quad \rho = \ln\frac{r}{b}\,, \tag{3.4.20}$$

we rewrite and integrate Eq. (3.4.19)

$$\begin{aligned}\pm(\theta-\theta_0) &= \int_{\ln(a/b)}^{\ln(r/b)} \frac{\rho\,d\rho}{(D^2-\rho^2)^{1/2}} \\ &= \left(D^2-\ln^2\frac{a}{b}\right)^{1/2} - \left(D^2-\ln^2\frac{r}{b}\right)^{1/2}\,, \end{aligned} \tag{3.4.21}$$

or, equivalently,

$$\ln\frac{r}{b} = \left\{D^2 - \left[\pm(\theta-\theta_0) - \left(D^2-\ln^2\frac{a}{b}\right)^{1/2}\right]^2\right\}^{1/2}\,.$$

Dividing throughout by $\ln(a/b)$, we have, finally,

$$\frac{\ln(r/b)}{\ln(a/b)} = \left\{\csc^2\beta_0 - \left[\pm\frac{\theta-\theta_0}{\ln(a/b)} - \cot\beta_0\right]^2\right\}^{1/2}\,, \quad \theta_0 = \pi+\beta_0 \tag{3.4.22}$$

which has been plotted by Pocinki, 1950 [see Fig. 3.11(c)].

Let (r_b, θ_b) be the point where the outermost ray entering the shoal in the third quadrant ($\beta_0 = \frac{1}{2}\pi$, i.e., $\theta_0 = \frac{3}{2}\pi$) intersects the shore. Since $\sin\beta_0 = 1$ and $\cot\beta_0 = 0$, we have from Eq. (3.4.21)

$$\theta_b - \frac{3\pi}{2} = \ln\frac{a}{b}\,.$$

Since $\theta_b > 3\pi/2$ the plus sign has been chosen. Similarly, the outermost ray which enters the shoal in the second quadrant ($\beta_0 = -\pi/2, \theta_0 = \pi/2$) intersects the shore at the point $r = b$ and

$$\theta_b' = \frac{\pi}{2} - \ln\frac{a}{b}\,.$$

If $\ln(a/b) < \pi/2$, there is a portion of the shoreline within the range $-[\pi/2 - \ln(a/b)] < \theta < \pi/2 - \ln(a/b)$ which is shielded from the incident waves; this range has been called the *lee shore* by Arthur (1946).

If $\ln(a/b) > \pi/2$, the rays from one side of the axis cross those from the other side in the lee of the island. The resulting wave amplitude can be computed by superposition and proper account of the phases. At the value $\ln(a/b) = \pi/2$ or $a/b \cong 4.81$, the outermost rays from both sides meet the shore at $\theta = 0$; the lee shore then disappears.

To find the separation factor, consider again the rays entering from the third quadrant. Differentiating Eq. (3.4.21) in accordance with Eq. (3.4.17), we get

$$\frac{\partial}{\partial\beta_0}\left(D^2-\ln^2\frac{r}{b}\right)^{1/2}=D\frac{\partial D}{\partial\beta_0}\left(D^2-\ln^2\frac{r}{b}\right)^{-1/2},$$

so that

$$\frac{\partial\theta}{\partial\beta_0}=1-D\frac{\partial D}{\partial\beta_0}\left[\left(D^2-\ln^2\frac{a}{b}\right)^{-1/2}-\left(D^2-\ln^2\frac{r}{b}\right)^{-1/2}\right].$$

Now from the definition equation for D we find

$$\frac{\partial D}{\partial\beta_0}=-\cos\beta_0\ln\frac{a}{b}\sin^{-2}\beta_0\,.$$

It follows after a little algebra that

$$\frac{\partial\theta}{\partial\beta_0}=\left\{1+\frac{\ln(a/b)}{\sin^2\beta_0}\left[1-\frac{\cos\beta_0}{(1-R^2\sin^2\beta_0)^{1/2}}\right]\right\}, \tag{3.4.23}$$

where

$$R\equiv\frac{\ln(r/b)}{\ln(a/b)}\,.$$

The separation factor is therefore

$$\frac{d\sigma}{d\sigma_0}=\frac{r\cos\beta}{a\cos\beta_0}\frac{\partial\theta}{\partial\beta_0}=\frac{r[1-(k_0a)^2\sin^2\beta_0/(kr)^2]^{1/2}}{a\cos\beta_0}\left(\frac{\partial\theta}{\partial\beta_0}\right) \tag{3.4.24}$$

with $\partial\theta/\partial\beta_0$ given by Eq. (3.4.23). The inverse square root of Eq. (3.4.24) is plotted for $r=b$ in Fig. 3.11(d).

The approach presented in Sections 3.3 and 3.4 is a semi-inverse one in that some convenient form of k is assumed and the depth variation must be found from the dispersion relation. Thus, for different frequencies the same k corresponds to different depths. The more direct problem of prescribing ω and $h(\mathbf{x})$ must usually be solved by numerical methods. This is not a difficult task for straight or circular contours. For general contours computer methods have been developed by Skovgaard, Jonsson, and Bertelsen (1976) who also incorporated the additional effects of bottom friction.

Over a general topography, caustics of various kinds are possible. Although a local remedy or uniformly valid approximation is still possible in principle (Ludwig, 1966), incorporation in a numerical refraction program

becomes cumbersome in practice. In the next section an approximate equation will be deduced for slowly varying depth but without the assumption of rays, as implied by Eq. (3.1.6). Since the new equation can be effectively solved by modern numerical methods, the intricate theory of caustics can be circumvented altogether for general topography and will not be pursued here.

Exercise 3.2: Spiral Wave in a Circular Basin (Mei, 1973)

For simulating an infinitely long plane beach in a laboratory, a circular basin with a drum-like wavemaker at the center has been suggested (Dalrymple and Dean, 1972). Outgoing waves of a single frequency are generated by the wavy motion of the drum circumference proportional to $\exp[i(m\theta - \omega t)]$. By the ray approximation, the wave field far away from the drum is approximately given by

$$\Phi = \frac{-igA(r)}{\omega}\frac{\cosh\, k\,(z+h)}{\cosh\, kh}\, e^{iS}\,, \quad \eta = A(r)\, e^{iS}\,,$$

where $k(r)$ and $h(r)$ are slowly varying in r and satisfy the familiar dispersion relation, and the phase function S is

$$S = \int^r \alpha dr + m\theta\,,$$

where m is a large integer and $m/r = O(1)$.

Show first that the components of the wavenumber vector in the radial and in azimuthal directions are $k_r = \alpha$ and $k_\theta = m/r$, and $\alpha^2 + (m/r)^2 = k^2$. Sketch a few wave crests.

Assuming that energy flux between two closely adjacent rays is conserved, derive the following formula

$$EC_g r\frac{\alpha}{k} = \text{constant}\,.$$

Discuss the qualitative behavior of A as r for the following cases.

(i) If the beach has the constant slope s so that $h = s(R - r)$ where R denotes the radius of the shore, show that A increase with r in the manner

$$A \propto [R^{1/2} s(R-r)]^{-1/4}\,.$$

(ii) If $h \sim r^{-n}$ as r increases, show that $A \sim r^{(n-2)/4}$ for large r. If the breaking criterion $A \cong 0.8h$ (known empirically for straight beaches) is accepted, are there any values for n for which spiral waves will not break as $h \downarrow 0$?

3.5 An Approximate Equation Combining Diffraction and Refraction on a Slowly Varying Bottom — The Mild-Slope Equation

A merit of the ray approximation is to reduce a three-dimensional problem to many one-dimensional problems along ray channels. Yet, near a caustic, additional consideration must be given to variations transverse to a ray. Hence the problem is, at least locally, two dimensional in the horizontal plane. There are also situations where the problem is basically two dimensional, as for instance the obstruction of incident waves by a vertical cylinder on a slowly varying seabed. These two-dimensional effects are related to *diffraction* which will be studied more extensively later in this book. It is therefore desirable to obtain an approximation which accounts for slow depth variations and allows rapid horizontal variations associated with diffraction.

In the case of constant depth, the velocity potential may be written

$$\phi = -\frac{ig\eta}{\omega} f \,, \tag{3.5.1}$$

where

$$f = \frac{\cosh k(z+h)}{\cosh kh} \quad \text{and} \quad \omega^2 = gk \tanh kh \,. \tag{3.5.2}$$

From Laplace's equation, $\eta(\mathbf{x}, y)$ is found to satisfy the two-dimensional Helmholtz equation

$$\nabla^2 \eta + k^2 \eta = 0 \tag{3.5.3}$$

which describes diffraction. It is plausible to expect that for slowly varying depth, Eqs. (3.5.1) and (3.5.2) still apply with k and h referring to their local values. Based on this idea, Berkhoff (1972) deduced a convenient equation for $\eta(x, y)$. Various derivations of the same result have been reported by Schonfeld (1972), Jonsson and Brink-Kjaer (1973), Smith and Sprinks (1975), and Lozano and Meyer (1976). Here we present the arguments of Smith and Sprinks.

The exact governing equations for ϕ may be written

$$\frac{\partial^2 \phi}{\partial z^2} + \nabla^2 \phi = 0 \,, \quad -h \le z \le 0 \,; \quad \nabla = \left(\frac{\partial}{\partial x}, \frac{\partial}{\partial y} \right) , \tag{3.5.4a}$$

$$\frac{\partial\phi}{\partial z} - \frac{\omega^2}{g}\phi = 0\,, \quad z = 0\,, \tag{3.5.4b}$$

$$\frac{\partial\phi}{\partial z} = -\nabla h \cdot \nabla\phi\,, \quad z = -h\,, \tag{3.5.4c}$$

while f satisfies Eqs. (3.1.8)–(3.1.10). Considering Eq. (3.5.4a) as an ordinary differential equation in z, and applying Green's formula for ϕ and f, we get, upon using Eqs. (3.5.4a)–(3.5.4c) and (3.1.8)–(3.1.10),

$$\int_{-h}^{0} (k^2\phi f + f\nabla^2\phi)\,dz = -(f\nabla h \cdot \nabla\phi)_{-h}\,. \tag{3.5.5}$$

Now we invoke Eqs. (3.5.1) and (3.5.2) and note that

$$\nabla\phi = -\frac{ig}{\omega}\left(f\nabla\eta + \eta\frac{\partial f}{\partial h}\nabla h\right),$$

$$\nabla^2\phi = -\frac{ig}{\omega}\left(f\nabla^2\eta + 2\frac{\partial f}{\partial h}\nabla\eta\cdot\nabla h + \eta\frac{\partial^2 f}{\partial h^2}(\nabla h)^2 + \eta\frac{\partial f}{\partial h}\nabla^2 h\right).$$

Equation (3.5.5) may be written

$$\int_{-h}^{0}\left\{f^2\nabla^2\eta + 2f\frac{\partial f}{\partial h}\nabla\eta\cdot\nabla h + \eta f\frac{\partial^2 f}{\partial h^2}(\nabla h)^2 + \eta f\frac{\partial f}{\partial h}\nabla^2 h + k^2\eta f^2\right\}dz$$

$$= -\nabla h\cdot\nabla\eta f^2\Big|_{-h} - \eta(\nabla h)^2 f\frac{\partial f}{\partial h}\Big|_{-h}\,. \tag{3.5.6}$$

By Leibniz' rule, the first two terms on the left of Eq. (3.5.6) may be combined with the first term on the right, yielding

$$\nabla\cdot\int_{-h}^{0} f^2\nabla\eta\,dz + \int_{-h}^{0} k^2 f^2\eta\,dz$$

$$= -f\frac{\partial f}{\partial h}\Big|_{-h}\eta(\nabla h)^2 - \int_{-h}^{0}\eta f\frac{\partial^2 f}{\partial h^2}(\nabla h)^2\,dz - \int_{-h}^{0}\eta f\frac{\partial f}{\partial h}\nabla^2 h\,dz\,.$$

Since $\nabla h/kh = O(\mu) \ll 1$ and $\nabla\eta/k\eta = O(1)$, every term on the right-hand side of Eq. (3.5.6) is of $O(\mu^2)$ relative to the left-hand side and may be omitted. Upon integration and using Eq. (1.5.12), Chapter One, we obtain, finally,

$$\nabla\cdot(a\nabla\eta) + k^2 a\eta = 0\,, \tag{3.5.7}$$

where

$$a = gh\frac{\tanh kh}{kh}\frac{1}{2}\left(1+\frac{2kh}{\sinh 2kh}\right) = CC_g\,, \tag{3.5.8}$$

In the special case of arbitrary constant kh, Eq. (3.5.7) reduces to the Helmholtz equation (3.5.3). On the other hand, for small but variable depth $kh \ll 1$, Eq. (3.5.7) reduces to

$$\nabla\cdot(h\nabla\eta) + \frac{\omega^2}{g}\eta = 0 \tag{3.5.9}$$

which will be shown in Chapter Four to be valid even if $\nabla h/kh = O(1)$. Therefore, Eq. (3.5.7) provides a two-dimensional approximation of the three-dimensional problem for the whole range of wavelengths as long as the seabed slope is small, and is now known as the *mild-slope* equation (Jonsson and Skovgaard, 1979).

By the simple transformation

$$\eta = a^{-1/2}\xi\,, \tag{3.5.10}$$

Eq. (3.5.7) may be rewritten

$$\nabla^2\xi + \kappa^2\xi = 0\,, \tag{3.5.11}$$

where

$$\kappa^2(x,y) = k^2 - \frac{\nabla^2 a}{2a} + \frac{|\nabla a|^2}{4a^2}\,. \tag{3.5.12}$$

Equation (3.5.11) is well known in the acoustics of inhomogeneous media, with κ being the index of refraction. Many approximate analytical techniques exist in classical physics for special classes of κ^2. For coastal problems, numerical techniques are required. In Chapter Four one such technique will be described for Eq. (3.5.9); the necessary modification for Eq. (3.5.7) or (3.5.11) is straightforward and has been carried out by Houston (1981). By reducing the three-dimensional problem to two, the computational effort needed for practical problems is obviously much reduced.

There have been several extensions of the mild-slope approximation, aiming either at steeper slopes of very large characteristic length scales or at shorter irregularities such as sand bars, (Kirby, 1986; Chamberlain and Porter 1995; Porter and Staziger, 1995, Miles and Chamberlain, 1998; Agnon and Pelinovsky, 2001).

The simplest extension of Chamberlain and Porter is to keep all terms in (3.5.6.a) without discarding terms of the order $O(\nabla^2 h, (\nabla h)^2)$. The result is still of the form of (3.5.7),

$$\nabla \cdot (a \nabla \eta) + b\eta = 0 \tag{3.5.13}$$

where

$$a = CC_g\,, \quad \text{and} \quad b = k^2 a + gU\nabla^2 h + gV(\nabla h)^2\,, \tag{3.5.14}$$

with

$$U = \int_{-h}^{0} f \frac{\partial f}{\partial h}\, dz\,, \tag{3.5.15}$$

and

$$V = \frac{\partial U}{\partial h} - \int_{-h}^{0} \left(\frac{\partial f}{\partial h}\right)^2 dz\,. \tag{3.5.16}$$

From the definition of f, we get

$$\frac{\partial f}{\partial h} = \frac{1}{\cosh kh} \frac{\partial k}{\partial h} \left[z \sinh k(z+h) - \frac{\sinh kh \sinh kz}{k} \right] \tag{3.5.17}$$

and

$$\frac{\partial k}{\partial h} = -\frac{2k^2}{2kh + \sinh 2kh}\,. \tag{3.5.18}$$

We leave it as an exercise to show that

$$U = \frac{\sinh 2kh - 2kh \cosh 2kh}{4 \cosh^2 kh (2kh + \sinh 2kh)} \tag{3.5.19}$$

and

$$\begin{aligned} V = {} & \frac{k[(2kh)^4 + 4(2kh)^3 \sinh 2kh - 9 \sinh 2kh \sinh 4kh]}{12 \cosh^2 kh (2kh + \sinh 2kh)^3} \\ & + \frac{k[kh(kh + \sinh 2kh)(\cosh^2 2kh - 2\cosh 2kh + 3)]}{\cosh^2 kh (2kh + \sinh 2kh)^3}\,. \end{aligned} \tag{3.5.20}$$

With these coefficients, the result is called the modified mild-slope equation (MMSE), which can be just as easily solved numerically as (3.5.7). The advantage of doing only two-dimensional computations for three-dimensional problems is preserved.

A still better approximation by Massel (1993) and Porter and Staziger (1995) is to admit not only the propagating mode but also evanescent modes in the velocity potential

$$\psi = -\frac{ig}{\omega}\sum_{n=0}^{\infty}\xi_n(x)f_n(z,h(x))\,, \quad \text{where} \quad f_n(z,h(x)) = \frac{\cos k_n(z+h)}{\cos k_n h}\,. \tag{3.5.21}$$

The first term in the series $n = 0$ corresponds to the propagating mode with $f_0 = f$ defined by (3.5.2). For $n = 1, 2, \ldots$, k_n are the real roots of the equation

$$-\omega^2 = gk_n \tan k_n h\,, \quad (n-1/2)\pi \le k_n h \le n\pi\,, \tag{3.5.22}$$

and correspond to the evanescent modes.

Repeating for each m the procedure of weighted vertical averaging via Green's formula, we obtain a matrix equation coupling all modal amplitudes:

$$\nabla\cdot(a_l\nabla\xi_l) + \sum_{m=0}^{\infty}\{(b_{ml}-b_{lm})\nabla h\cdot\nabla\xi_m + [b_{m,l}\nabla^2 h + c_{ml}(\nabla h)^2 + d_{ml}]\xi_m\} = 0\,, \tag{3.5.23}$$

where

$$a_l = \int_{-h}^{0} f_l^2 dz\,, \quad b_{m,l} = \int_{-h}^{0} f_l\frac{\partial f_m}{\partial h}dz$$

$$c_{ml} = \frac{db_{ml}}{dh} - \int_{-h}^{0}\frac{\partial f_m}{\partial h}\frac{\partial f_l}{\partial h}dz\,, \quad d_{ml} = \int f_l\frac{\partial^2 f_m}{\partial z^2}dz\,.$$

More explicit formulas for these coefficients can be straightforwardly worked out, and are given by Porter and Staziger (1995).

In numerical computations, it is necessary to truncate the series (3.5.21). The numerical task of solving the matrix equation with two dimensional discretization is likely less laborious than the fully three-dimensional discretization needed otherwise. For a two-dimensioal example of scattering by a long slope connecting two horizontal shelves, Porter and Staziger have indeed demonstrated improved accuracy by comparing with calculations with the simplest mild-slope approximation.

3.6 Geometrical Optics Approximation for Refraction by Slowly Varying Current and Depth

In addition to depth variation, the presence of current in the ocean affects the propagation of waves. Of practical interest in coastal problems are the tidal currents near a river inlet or a harbor entrance. During flood tides the current and the waves are in the same direction, resulting in the lengthening of waves and reduction of wave heights. However, during ebb tides the waves are shortened and steepened by the opposing current, often to the extent of inducing breaking (see aerial photograph of Humboldt Bay, California, Johnson, 1947). If there are submarine bars in the entrance channel of a harbor, the combined effect of shoaling and current over the bars can create significant choppiness on the sea surface and therefore present hazards to navigation. Entrance channels to many harbors on the northern Pacific coast of the United States are rarely passable for small fishing boats during ebb tides in the winter (Issacs, 1948). The best time for passage is at the end of the flood tide when the water depth is the greatest and current speed is the least.

In this section we shall lay the theoretical foundation for the combined effects of currents and depth on small-amplitude waves. In particular, attention will be focused on strong currents which affect waves but are not affected by waves. We shall also assume, as is frequently the case in nature, that the characteristic time and distance of the current are very much greater than those of the waves. A systematic theory of this class of problems began with Longuet–Higgins and Stewart (1961) and Whitham (1962), while important extensions have been made by Bretherton and Garrett (1968), and Phillips (1977). A different derivation of the basic equations will be presented below by extending the WKB formalism of Section 3.2.

To describe the magnitude of a quantity in this section, reference to the characteristic wavelength $2\pi/k$ and wave period $2\pi/\omega$ (which are related by the dispersion relation) is always implied. It will be assumed that the depth h varies slowly in horizontal coordinates x_i $(i = 1, 2)$, while the current varies slowly both in x_i and t. The long length and time scales are L and T such that

$$(\omega T)^{-1} \sim (kL)^{-1} \sim \frac{h}{L} = O(\mu) \ll 1\,. \tag{3.6.1}$$

While the horizontal velocity components of the strong current U_i are $O(gh)^{1/2}$, and the small wave velocities u_i and w are $O[(kA)(gh)^{1/2}]$, we shall for brevity speak of U_i, h, and so on, as being $O(1)$, and u_i and w as being $O(kA)$. Similarly, the operators $\partial/\partial t$ and $\partial/\partial x_i$ $(i = 1, 2)$ are $O(\mu)$ when acting on a current-related quantity and $O(1)$ when acting on a wave-related quantity, for example,

$$\frac{\partial U_i}{\partial t}, \frac{\partial U_j}{\partial x_i}, \frac{\partial h}{\partial x_i} \cdots \sim O(\mu)\,;$$

$$\frac{\partial u_i}{\partial x_j}, \frac{\partial w}{\partial x_i}, \ldots \sim O(kA)\,;$$

and

$$\frac{\partial}{\partial z} = O(1)$$

on all quantities.

Consider first the current $\mathbf{U} = (U_i, W)$ without waves. If dissipation is ignored, then the governing equations are

$$\frac{\partial U_i}{\partial x_i} + \frac{\partial W}{\partial z} = 0\,, \tag{3.6.2}$$

$$\frac{\partial U_i}{\partial t} + U_j \frac{\partial U_i}{\partial x_j} + W \frac{\partial U_i}{\partial z} = -\frac{1}{\rho}\frac{\partial P}{\partial x_i}\,, \quad i = 1, 2\,, \tag{3.6.3}$$

$$\frac{\partial W}{\partial t} + U_j \frac{\partial W}{\partial x_j} + W \frac{\partial W}{\partial z} = -\frac{1}{\rho}\frac{\partial P}{\partial z} - g\,. \tag{3.6.4}$$

Because of Eq. (3.6.1) and continuity, the vertical current velocity is small, $W = O(\mu)$. It follows from Eq. (3.6.4) that the pressure is nearly hydrostatic

$$P = \rho g(\bar{\zeta} - z) + O(\mu^2) \tag{3.6.5}$$

where $\bar{\zeta}$ is the associated free-surface displacement. On the free surface and at the sea bottom, the kinematic boundary conditions are

$$W = \frac{\partial \bar{\zeta}}{\partial t} + U_j \frac{\partial \bar{\zeta}}{\partial x_j}\,, \quad z = \bar{\zeta}(x_i, t)\,, \tag{3.6.6}$$

$$W = -U_j \frac{\partial h}{\partial x_j} \quad z = -h(x_i)\,. \tag{3.6.7}$$

Now the vorticity vector has the following horizontal components:

$$\Omega_1 = \frac{\partial W}{\partial x_2} - \frac{\partial U_2}{\partial z}\,, \quad \Omega_2 = \frac{\partial U_1}{\partial z} - \frac{\partial W}{\partial x_1}\,. \tag{3.6.8}$$

The term $\partial W/\partial x_j$ above is $O(\mu^2)$; thus, as long as

$$\Omega_j \leqq O(\mu^2)\,, \tag{3.6.9}$$

U_j is independent of z to the order $O(\mu^2)$, that is,

$$\frac{\partial U_j}{\partial z} = O(\mu^2)\,. \tag{3.6.10}$$

Equation (3.6.9) will be assumed. Recall, however, that the vertical vorticity component is allowed to be of the order $O(\mu)$. With Eq. (3.6.10) the horizontal momentum equations may be approximated by

$$\frac{\partial U_i}{\partial t} + U_j \frac{\partial U_i}{\partial x_j} = -g\frac{\partial \bar{\zeta}}{\partial x_i} + O(\mu^2 U_i)\,. \tag{3.6.11}$$

Integrating the continuity equation vertically from $z = -h$ to $z = \bar{\zeta}$ and using Eqs. (3.6.6) and (3.6.7), we obtain

$$\frac{\partial \bar{\zeta}}{\partial t} + \frac{\partial}{\partial x_i}[U_i(\bar{\zeta} + h)] = 0\,. \tag{3.6.12}$$

Equations (3.6.5), (3.6.11), and (3.6.12) constitute the so-called Airy's theory of finite-amplitude long waves which will be discussed more extensively in Chapter Twelve. For present purposes, U_i and $\bar{\zeta}$ will be assumed to be known. We merely point out that the free-surface displacement $\bar{\zeta}$ is of the order $O(h)$. In the special case of steady current, $\partial/\partial t = 0$, Eq. (3.6.11) may be rewritten

$$U_j \frac{\partial}{\partial x_j}\left(\frac{U_i U_i}{2} + g\bar{\zeta}\right) = 0\,,$$

which implies

$$\bar{\zeta} = -\frac{U_i U_i}{2g} + \text{const} \tag{3.6.13}$$

along a streamline.

Consider next the wave fluctuations that are superposed on the current. The velocity components (u_i, w) and the pressure p of the wave field are

less than their counterparts in the current by the factor $O(kA)$. Continuity requires that

$$\frac{\partial u_i}{\partial x_i} + \frac{\partial w}{\partial z} = 0\,. \tag{3.6.14}$$

The momentum equations may be linearized by omitting $O(kA)^2$. We further discard linearized terms of $O(\mu^2 kA)$ or less, that is, $w\partial U_i/\partial z$ and $u_i \partial W/\partial x_i$, and obtain

$$\frac{\partial u_i}{\partial t} + U_j \frac{\partial u_i}{\partial x_j} + W\frac{\partial u_i}{\partial z} + u_j \frac{\partial U_i}{\partial x_j} = -\frac{1}{\rho}\frac{\partial p}{\partial x_i}\,, \tag{3.6.15}$$

$$\frac{\partial w}{\partial t} + U_j \frac{\partial w}{\partial x_j} + W\frac{\partial w}{\partial z} + w\frac{\partial W}{\partial z} = -\frac{1}{\rho}\frac{\partial p}{\partial z}\,. \tag{3.6.16}$$

The remaining terms contain $O(kA)$ and $O(\mu kA)$. By differentiating Eqs. (3.6.15) and (3.6.16) and adding the results, we have

$$\frac{\partial^2 p}{\partial x_i \partial x_i} + \frac{\partial^2 p}{\partial z^2} = -2\rho\left(\frac{\partial u_i}{\partial x_j}\frac{\partial U_j}{\partial x_i} + \frac{\partial w}{\partial z}\frac{\partial W}{\partial z}\right) \tag{3.6.17}$$

after omitting again terms of $O(\mu^2 kA)$. Equation (3.6.17) will be treated as the governing equation for p.

At the sea bottom the wave field also has no normal velocity

$$w = -u_j \frac{\partial h}{\partial x_j}\,, \quad z = -h(x_i)\,. \tag{3.6.18}$$

It is desirable to infer from this condition a boundary condition for p. Differentiating Eq. (3.6.18) with respect to x_j and noting that w and u_i are already evaluated on $z = -h(x_i)$, we get

$$\frac{\partial w}{\partial x_j} - \frac{\partial h}{\partial x_j}\frac{\partial w}{\partial z} = -\frac{\partial u_i}{\partial x_j}\frac{\partial h}{\partial x_i} + O(\mu^2 kA)\,.$$

With this result, Eq. (3.6.16) may be rewritten

$$\begin{aligned} -\frac{1}{\rho}\frac{\partial p}{\partial z} &= -\frac{\partial u_j}{\partial t}\frac{\partial h}{\partial x_j} + \left(U_j\frac{\partial h}{\partial x_j} + W\right)\frac{\partial w}{\partial z} - U_j\frac{\partial u_i}{\partial x_j}\frac{\partial h}{\partial x_i} - w\frac{\partial U_j}{\partial x_j} \\ &= -\frac{\partial h}{\partial x_i}\left(\frac{\partial u_i}{\partial t} + U_j\frac{\partial u_i}{\partial x_j}\right) + O(\mu^2 kA) \\ &= \frac{\partial h}{\partial x_i}\frac{1}{\rho}\frac{\partial p}{\partial x_i} + O(\mu^2 kA) \end{aligned} \tag{3.6.19}$$

after invoking Eqs. (3.6.7), (3.6.15), and (3.6.18).

On the free surface, the exact kinematic boundary condition states that

$$\frac{\partial}{\partial t}(\bar{\zeta}+\zeta)+(U_j+u_j)\frac{\partial}{\partial x_j}(\bar{\zeta}+\zeta)=W+w \quad \text{on} \quad z=\bar{\zeta}+\zeta\,.$$

Upon linearizing and using Eq. (3.6.6), we get

$$\frac{\partial\zeta}{\partial t}+U_j\frac{\partial\zeta}{\partial x_j}+u_j\frac{\partial\bar{\zeta}}{\partial x_j}=w+\zeta\frac{\partial W}{\partial z} \quad \text{on} \quad z=\bar{\zeta}\,. \tag{3.6.20}$$

The dynamic condition is that the total pressure does not vary as one follows the fluid motion along the free surface

$$\frac{\partial p}{\partial t}+(U_j+u_j)\frac{\partial p}{\partial x_j}+(W+w)\frac{\partial p}{\partial z}$$
$$+\left[\frac{\partial}{\partial t}+(U_j+u_j)\frac{\partial}{\partial x_j}+(W+w)\frac{\partial}{\partial z}\right]\rho g(\bar{\zeta}-z)=0\,,\quad z=\bar{\zeta}+\zeta\,.$$

With the help of Eq. (3.6.6) the above equation can be linearized to give

$$\frac{\partial p}{\partial t}+U_j\frac{\partial p}{\partial x_j}+W\frac{\partial p}{\partial z}+\rho g\left(u_j\frac{\partial\bar{\zeta}}{\partial x_j}-w-\zeta\frac{\partial W}{\partial z}\right)$$
$$=O(kA)^2\,,\quad z=\bar{\zeta}\,. \tag{3.6.21}$$

In order to express this boundary condition for p only, we shall differentiate Eq. (3.6.21) and make use of Eqs. (3.6.16) and (3.6.20). Again, it must be realized that

$$\frac{\partial}{\partial x_i}W(x_i,\bar{\zeta},t)=\left[\frac{\partial}{\partial x_i}W(x_j,z,t)+\frac{\partial\bar{\zeta}}{\partial x_i}\frac{\partial}{\partial z}W(x_j,z,t)\right]_{z=\bar{\zeta}} \tag{3.6.22a}$$

and

$$\frac{\partial}{\partial t}W(x_i,\bar{\zeta},t)=\left[\frac{\partial}{\partial t}W(x_i,z,t)+\frac{\partial\bar{\zeta}}{\partial t}\frac{\partial}{\partial z}W(x_i,z,t)\right]_{z=\bar{\zeta}}\,. \tag{3.6.22b}$$

With this kind of care the following boundary condition is obtained on the free surface:

$$\left(\frac{\partial}{\partial t}+U_j\frac{\partial}{\partial x_j}\right)^2 p+2W\frac{\partial}{\partial z}\left(\frac{\partial p}{\partial t}+U_j\frac{\partial p}{\partial x_j}\right)$$
$$-g\frac{\partial\bar{\zeta}}{\partial x_j}\frac{\partial p}{\partial x_j}+g\frac{\partial p}{\partial z}=0\,,\quad z=\bar{\zeta} \tag{3.6.23}$$

where derivatives with respect to t and x_i are taken before letting $z=\bar{\zeta}$.

We now introduce the slow variables $\bar{x}_i = \mu x_i$ and $\bar{t} = \mu t$, so that $U_j = U_j(\bar{x}_i, \bar{t})$, $\bar{\zeta} = \bar{\zeta}(\bar{x}_i, \bar{t})$, and $h = h(\bar{x}_i)$, and assume the WKB expansions

$$p(x_i, z, t) = [p_0 + (-i\mu)p_1 + \cdots]e^{iS/\mu}\,, \tag{3.6.24a}$$

$$u_i(x_i, z, t) = [u_{0_i} + (-i\mu)\mu_{1_i} + \cdots]e^{iS/\mu}\,, \tag{3.6.24b}$$

and so on, where

$$\begin{aligned} p_0 &= p_0(\bar{x}_i, z, \bar{t}\,)\,, \quad u_{0_i} = \mu_{0_i}(\bar{x_i}, z, \bar{t}\,) \\ S &= S(\bar{x}_i, \bar{t}\,)\,, \quad \text{and so on}\,. \end{aligned} \tag{3.6.25}$$

When Eqs. (3.6.24a) and (3.6.24b) are substituted into Eqs. (3.6.17), (3.6.19), and (3.6.23), a sequence of perturbation equations results. At the order $O(\mu^0)$ we have simply

$$\frac{\partial^2 p_0}{\partial z^2} - k^2 p_0 = 0\,, \quad -h < z < \bar{\zeta}\,, \tag{3.6.26}$$

$$\frac{\partial p_0}{\partial z} - \frac{\sigma^2}{g} p_0 = 0\,, \quad z = \bar{\zeta}\,, \tag{3.6.27}$$

$$\frac{\partial p_0}{\partial z} = 0\,, \quad z = -h\,, \tag{3.6.28}$$

where

$$\sigma = \omega - U_j k_j\,, \tag{3.6.29}$$

with

$$k_i \equiv \frac{\partial S}{\partial \bar{x}_i}\,, \quad \omega \equiv -\frac{\partial S}{\partial \bar{t}}\,, \quad k_i k_i = k^2\,.$$

We shall call ω the *absolute* and σ the *intrinsic* frequency, respectively. From these definitions, it is clear that

$$\frac{\partial k_i}{\partial \bar{t}} + \frac{\partial \omega}{\partial \bar{x}_i} = 0\,, \tag{3.6.30}$$

that is, wave crests are conserved, and

$$\frac{\partial k_i}{\partial \bar{x}_j} = \frac{\partial k_j}{\partial \bar{x}_i}\,, \tag{3.6.31}$$

that is, $\mathbf{k}$ is irrotational. The solution to Eqs. (3.6.26)–(3.6.28) is

$$p_0 = \rho g A \frac{\cosh k(z+h)}{\cosh k\bar{h}} \tag{3.6.32}$$

where $A = A(\bar{x}_i, \bar{t})$, $\bar{h} = \bar{\zeta} + h$ is the total mean depth, and

$$\sigma^2 = gk \tanh k\bar{h}\,. \tag{3.6.33}$$

It may be shown from the horizontal momentum equation (3.6.15) that

$$u_{0_i} = \frac{k_i p_0}{\rho\sigma}\,. \tag{3.6.34}$$

Let us denote the group velocity relative to the current by

$$C_g = \left.\frac{\partial\sigma}{\partial k}\right|_{\bar{h}} = \frac{1}{2}\frac{\sigma}{k}\left(1 + \frac{2k\bar{h}}{\sinh 2k\bar{h}}\right) \tag{3.6.35}$$

and

$$C_{g_i} = C_g \frac{k_i}{k}\,.$$

Two useful results on wave kinematics may be deduced at this stage. Differentiating Eq. (3.6.29) with respect to time and using Eqs. (3.6.30) and (3.6.31), we find

$$\frac{\partial\omega}{\partial\bar{t}} + (U_i + C_{g_i})\frac{\partial\omega}{\partial\bar{x}_i} = k_i\frac{\partial U_i}{\partial\bar{t}} + \left.\frac{\partial\sigma}{\partial\bar{h}}\right|_k \frac{\partial\bar{h}}{\partial\bar{t}}\,. \tag{3.6.36}$$

When the current is steady, the absolute frequency ω does not change for an observer traveling at the absolute group velocity $\mathbf{U} + \mathbf{C}_g$. Alternatively, one may start from Eq. (3.6.30) and get

$$\frac{\partial k_i}{\partial\bar{t}} + (U_j + C_{g_j})\frac{\partial k_i}{\partial\bar{x}_j} = -k_j\frac{\partial U_i}{\partial\bar{x}_j} - \left.\frac{\partial\sigma}{\partial\bar{h}}\right|_k \frac{\partial h}{\partial\bar{x}_i} \tag{3.6.37}$$

after using the irrotationality of $\mathbf{k}$ [cf. Eq. (3.6.31)]. In principle, Eq. (3.6.37) may be solved numerically for the rays which are everywhere tangent to the local $\mathbf{k}$ vector.

We must now seek information regarding the variation of the wave amplitude $A(\bar{x}_i, \bar{t})$. To this end the order $O(\mu)$ problem is needed,

$$\frac{\partial^2 p_1}{\partial z^2} - k^2 p_1 = \frac{\partial}{\partial\bar{x}_j}(k_j p_0) + k_j\frac{\partial p_0}{\partial\bar{x}_j} + 2\rho\left(k_j u_{0_i}\frac{\partial U_j}{\partial\bar{x}_i} + k_i u_{0_i}\frac{\partial U_j}{\partial\bar{x}_j}\right), \quad -h < z < \bar{\zeta} \tag{3.6.38}$$

$$g\frac{\partial p_1}{\partial z} - \sigma^2 p_1 = -\frac{\partial}{\partial \bar{t}}(\omega p_0) - \omega\frac{\partial p_0}{\partial \bar{t}} - 2U_j\left[\omega\frac{\partial p_0}{\partial \bar{x}_j} - \frac{\partial}{\partial \bar{t}}(k_j p_0)\right]$$
$$+ U_i U_j\left[\frac{\partial}{\partial \bar{x}_j}(k_i p_0) + k_i\frac{\partial p_0}{\partial \bar{x}_j}\right] + \left(\frac{\partial U_i}{\partial \bar{t}} + U_j\frac{\partial U_i}{\partial \bar{x}_j}\right)k_i p_0$$
$$- 2\left(\frac{\partial \bar{\zeta}}{\partial \bar{t}} + U_j\frac{\partial \bar{\zeta}}{\partial \bar{x}_j}\right)(\omega - U_i k_i)\frac{\partial p_0}{\partial z}$$
$$- g\frac{\partial \bar{\zeta}}{\partial \bar{x}_j}k_j p_0\,, \quad z = \bar{\zeta} \tag{3.6.39}$$

and

$$\frac{\partial p_1}{\partial z} = k_j\frac{\partial h}{\partial \bar{x}_j}p_0\,, \quad z = -h\,. \tag{3.6.40}$$

In Eq. (3.6.39), the derivatives of p_0 with respect to $\bar{t}$ and $\bar{x}_i$ are taken before letting $z = \bar{\zeta}(\bar{x}, \bar{t}\,)$. Making use of Eq. (3.6.22), we may condense the right-hand side of Eq. (3.6.39) to

$$-\frac{\partial}{\partial \bar{t}}(\omega p_0) - \omega\frac{\partial p_0}{\partial \bar{t}} - 2U_j\left[\omega\frac{\partial p_0}{\partial \bar{x}_j} - \frac{\partial}{\partial \bar{t}}(k_j p_0)\right]$$
$$+ U_i U_j\left[\frac{\partial}{\partial \bar{x}_j}(k_i p_0) + k_i\frac{\partial p_0}{\partial \bar{x}_j}\right] + p_0\left[k_j\frac{\partial U_j}{\partial \bar{t}} + k_i U_j\frac{\partial U_i}{\partial \bar{x}_j}\right] - g k_j p_0\frac{\partial \bar{\zeta}}{\partial \bar{x}_j}$$

where p_0 is now evaluated at $z = \bar{\zeta}$ first before derivatives are taken with respect to $\bar{t}$ and $\bar{x}_i$. Applying Green's formula to p_0 and p_1, we then get, after a little rearrangement,

$$\frac{\partial}{\partial \bar{t}}\left(\frac{E}{\sigma}\right) + \frac{\partial}{\partial \bar{x}_i}\left[(U_i + C_{g_i})\frac{E}{\sigma}\right] + \frac{2E}{\sigma^2}\left[\frac{\partial \sigma}{\partial \bar{t}} + (U_i + C_{g_i})\frac{\partial \sigma}{\partial \bar{x}_i}\right]$$
$$+ \frac{2E}{\sigma}\frac{\partial U_i}{\partial \bar{x}_j}\left[\frac{C_g}{C}\frac{k_i k_j}{k^2} + \left(\frac{C_g}{C} - \frac{1}{2}\right)\delta_{i\cdot j}\right] = 0 \tag{3.6.41}$$

where $E = \frac{1}{2}\rho g A^2$. As will be discussed more extensively in Chapter Eleven, the quantity

$$S_{ij} = E\left[\frac{C_g}{C}\frac{k_i k_j}{k^2} + \left(\frac{C_g}{C} - \frac{1}{2}\right)\delta_{ij}\right] \tag{3.6.42}$$

is a component of the *radiation stress tensor* associated with averaged momentum fluxes in a sinusoidal wavetrain. Equation (3.6.41) may thus be rewritten

$$\left\{\frac{\partial}{\partial \bar{t}}\left(\frac{E}{\sigma}\right)+\frac{\partial}{\partial \bar{x}_i}\left[(U_i+C_{g_i})\frac{E}{\sigma}\right]\right\}$$
$$+\left\{\frac{2E}{\sigma^2}\left[\frac{\partial \sigma}{\partial \bar{t}}+(U_i+C_{g_i})\frac{\partial \sigma}{\partial \bar{x}_i}\right]+\frac{2}{\sigma}S_{ij}\frac{\partial U_i}{\partial \bar{x}_j}\right\}=0\,. \qquad (3.6.43)$$

It can be shown (Bretherton and Garrett, 1968) by differentiating Eq. (3.6.33), and using Eqs. (3.6.36), (3.6.37) and (3.6.12), that quantities in the second pair of curly brackets in Eq. (3.6.43) vanish identically, therefore,

$$\frac{\partial}{\partial \bar{t}}\left(\frac{E}{\sigma}\right)+\frac{\partial}{\partial \bar{x}_i}\left[(U_i+C_{g_i})\frac{E}{\sigma}\right]=0\,. \qquad (3.6.44)$$

The *wave action* defined with the intrinsic frequency σ is again conserved! Using the same identity, we may also rewrite Eq. (3.6.43)

$$\frac{\partial E}{\partial \bar{t}}+\frac{\partial}{\partial \bar{x}_i}[(U_i+C_{g_i})E]+\frac{1}{2}S_{ij}\left(\frac{\partial U_i}{\partial \bar{x}_j}+\frac{\partial U_j}{\partial \bar{x}_i}\right)=0 \qquad (3.6.45)$$

after noting that $S_{ij}=S_{ji}$. This result was first deduced by Longuet–Higgins and Stewart (1961) and means physically that work done to the current strain by the radiation stress tends to reduce wave energy.

As in Section 3.1 the ordering parameter μ may be dropped from the final results and the original coordinates restored.

Equation (3.6.44) forms the starting point for further analysis. In principle, one computes $\mathbf{k}$ first; Eq. (3.6.44) is then integrated along the path of the convected ray for the wave amplitude. There are some numerical techniques for this purpose (see Dingemans, 1978 for a survey). We shall only examine a few analytical examples in subsequent sections.

The law of wave-action conservation is a very general result valid in many different physical contexts involving slowly varying media. In fact Eq. (3.6.44) has been deduced for general non-dissipative dynamical systems by Bretherton and Garrett (1968) by applying WKB expansions to a variational principle involving a Lagrangian. The same result can be obtained even more rapidly by first averaging the Lagrangian and then taking the variations. These approaches require that the problem be first formulated as a variational principle; this is not always a trivial task. For a comprehensive treatment of the averaged Lagrangian method, the more advanced reader should consult Whitham (1974).

3.7 Physical Effects of Simple Steady Currents on Waves

When current and waves are both steady, $\partial/\partial t = 0$, we get from Eqs. (3.6.29) and (3.6.30)

$$\omega = \text{const} = \sigma + \mathbf{U}\cdot\mathbf{k}\,. \tag{3.7.1}$$

Let $y = y(x)$ be the equation for a ray. With Eq. (3.7.1), Eq. (3.2.5) may be solved numerically by first noting that

$$\mathbf{U}\cdot\mathbf{k} = (U_1 + U_2 y')k(1+y_2')^{-1/2}\,. \tag{3.7.2}$$

The wave amplitude may be obtained from

$$\nabla\cdot\left[(\mathbf{U}+\mathbf{C}_g)\frac{E}{\sigma}\right] = 0\,. \tag{3.7.3}$$

Clearly, in addition to rays which follow $\mathbf{k}$, one must construct curves that are everywhere tangential to the local absolute group velocity $\mathbf{U}+\mathbf{C}_g$.

The implication of Eq. (3.7.1) is best seen through the simplest example of a uniform current.

3.7.1 Uniform Current on Constant Depth

With the help of Galilean transformation

$$\mathbf{x}' = \mathbf{x} - \mathbf{U}t\,, \tag{3.7.4}$$

a progressive wave in the rest frame may be written

$$e^{i(\mathbf{k}\cdot\mathbf{x}-\omega t)} = e^{i[\mathbf{k}\cdot(\mathbf{x}'+\mathbf{U}t)-\omega t]} = e^{i[\mathbf{k}\cdot\mathbf{x}'-(\omega-\mathbf{k}\cdot\mathbf{U})t]}\,. \tag{3.7.5}$$

Thus in the moving frame the effective frequency is

$$\sigma = \omega - \mathbf{k}\cdot\mathbf{U} = \omega - Uk\cos\alpha \tag{3.7.6}$$

where α denotes the angle between $\mathbf{k}$ and $\mathbf{U}$. We observe immediately that $\sigma \gtrless \omega$ if $|\alpha| \gtrless \pi/2$; this result is the well-known Doppler's effect.

Let us orient our coordinate system such that $\mathbf{k} = (k, 0)$ with $k > 0$. Equation (3.6.33) may be rewritten

$$\omega - kU\cos\alpha = \pm\hat{\sigma}(k) = \pm(gk\tanh k\bar{h})^{1/2}\,. \tag{3.7.7}$$

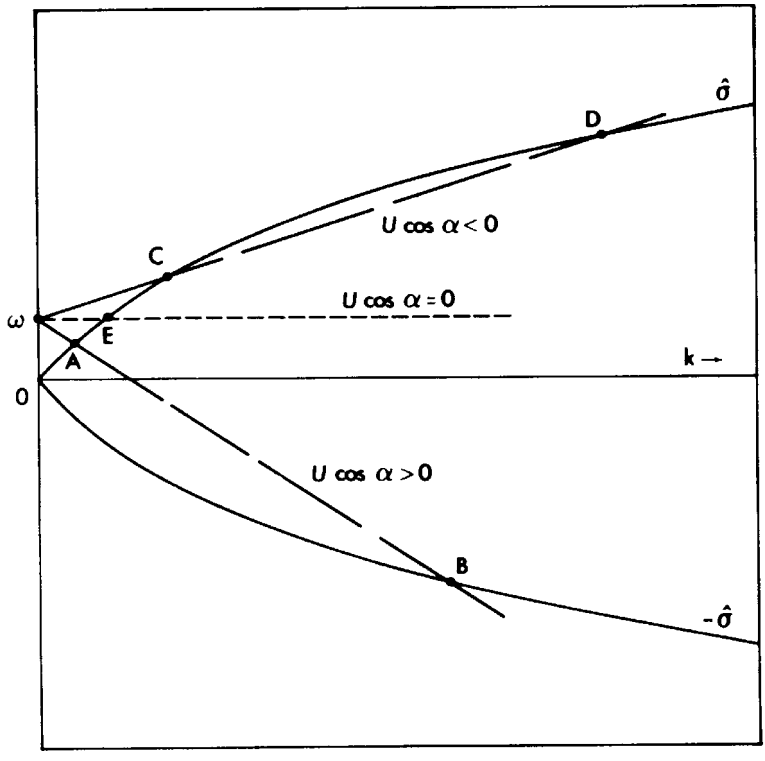

Figure 3.12: Graphical solution of Eq. (3.7.7).

This dispersion relation can be solved graphically from the intersection of the straight line $y = \omega - kU\cos\alpha$ and the curves $y = \pm\hat{\sigma}(k)$ as shown in Fig. 3.12. When $\alpha = \pm\pi/2$, the current has no effect on waves (see point E).

For $U\cos\alpha > 0$, there are two solutions corresponding to the points A and B. In comparison with the waves without current (point E), the waves represented by A are lengthened, and their intrinsic phase and group velocities are increased. The opposite is true for the waves represented by B. In particular, the intrinsic phase and group velocities are negative, but they are both less than $U\cos\alpha$ in magnitude. Hence the crests and wave energy are swept along by the fast current.

For $U\cos\alpha < 0$, the current has a component opposing the waves. If $-U\cos\alpha > (g\bar{h})^{1/2}$, no waves of any length are possible. For a smaller

$-U\cos\alpha$ there is a threshold such that only one solution exists for any given ω. At this threshold, the net velocity of energy transport vanishes,

$$C_g + U\cos\alpha = 0\,. \tag{3.7.8}$$

Thus, although the crests appear to propagate upstream ($\sigma/k > 0$), energy is held stationary in space.

For still smaller $-U\cos\alpha$, two solutions exist. The waves represented by point C satisfy

$$\frac{\sigma}{k} > C_g > -U\cos\alpha\,,$$

hence both the crests and wave energy move upstream. The waves represented by D satisfy

$$\frac{\sigma}{k} > -U\cos\alpha > C_g\,.$$

Now wave energy is swept downstream while the crests move upstream. This type of wave owes its existence to the finite curvature of the σ-curve, hence to dispersion.

3.7.2 Oblique Incidence on a Shear Current Over Constant Depth

Let the shear current be in the positive y direction,

$$U_1 = 0\,, \quad U_2 = V(x) > 0\,. \tag{3.7.9}$$

The associated $\bar{\zeta}$ may be taken to be zero. Since $\partial/\partial y = 0$, $k_2 = k\sin\alpha =$ const from Eq. (3.6.31). The direction of the ray is determined from

$$k_1 = [k^2(x) - k_2^2]^{1/2}\,, \tag{3.7.10}$$

where

$$\omega - V(x)k_2 = (gk\tanh kh)^{1/2}\,. \tag{3.7.11}$$

The equation of the ray is similar to Eq. (3.3.6)

$$y - y_0 = \pm\int_{x_0}^{x} \frac{dx\,k_2}{(k^2(x) - k_2^2)^{1/2}}\,. \tag{3.7.12}$$

Assume that V increases from zero for $x < 0$ to a peak at $x = 0$, and decreases to zero for $x > 0$ as shown in Fig. 3.13. Consider first waves

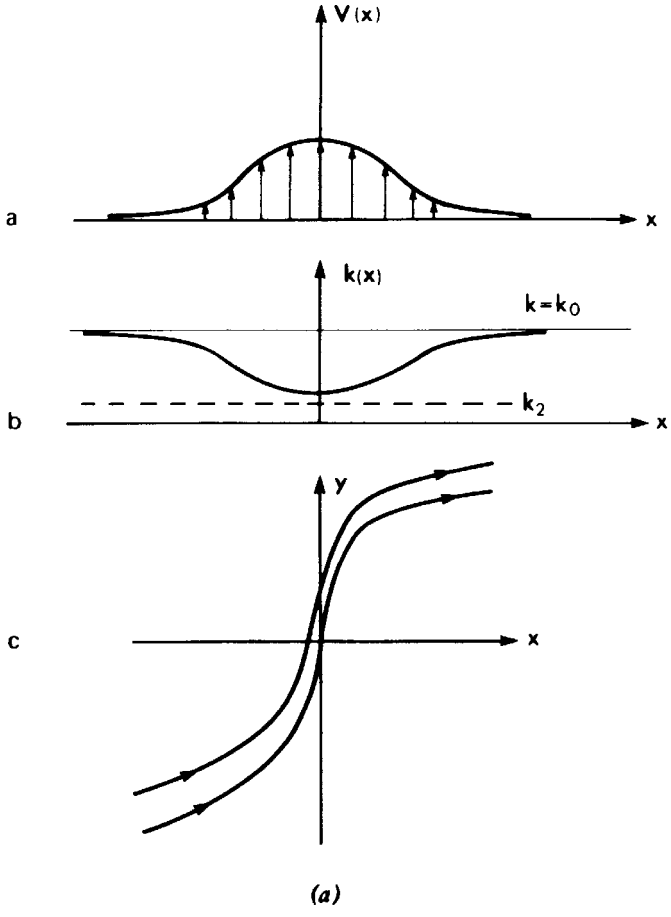

Figure 3.13a: $0 < k_2 < k_{\min}$: rays pass through a shear current after deflection.

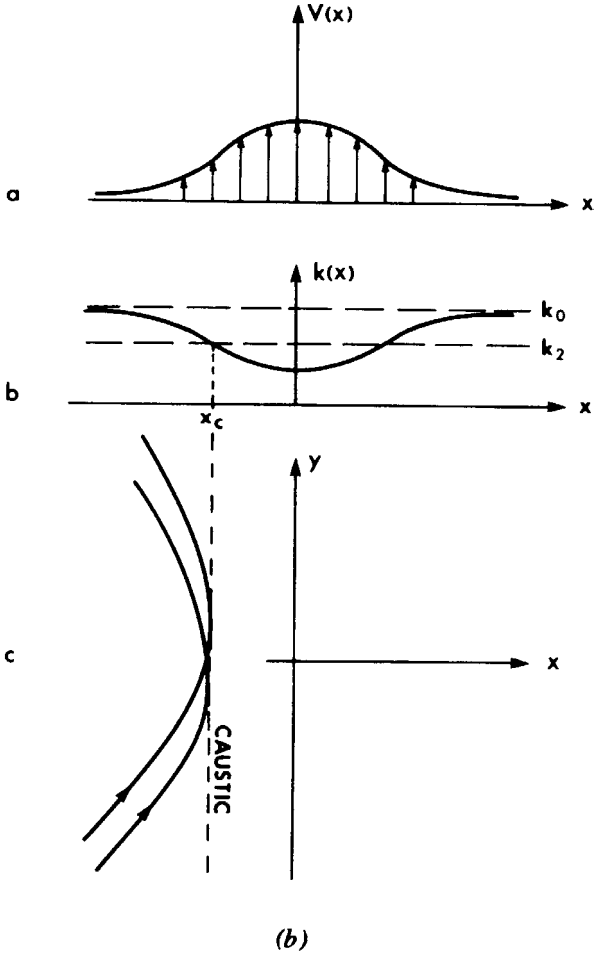

Figure 3.13b: $k_0 > k_2 > k_{\min}$: rays are bent back by a shear current.

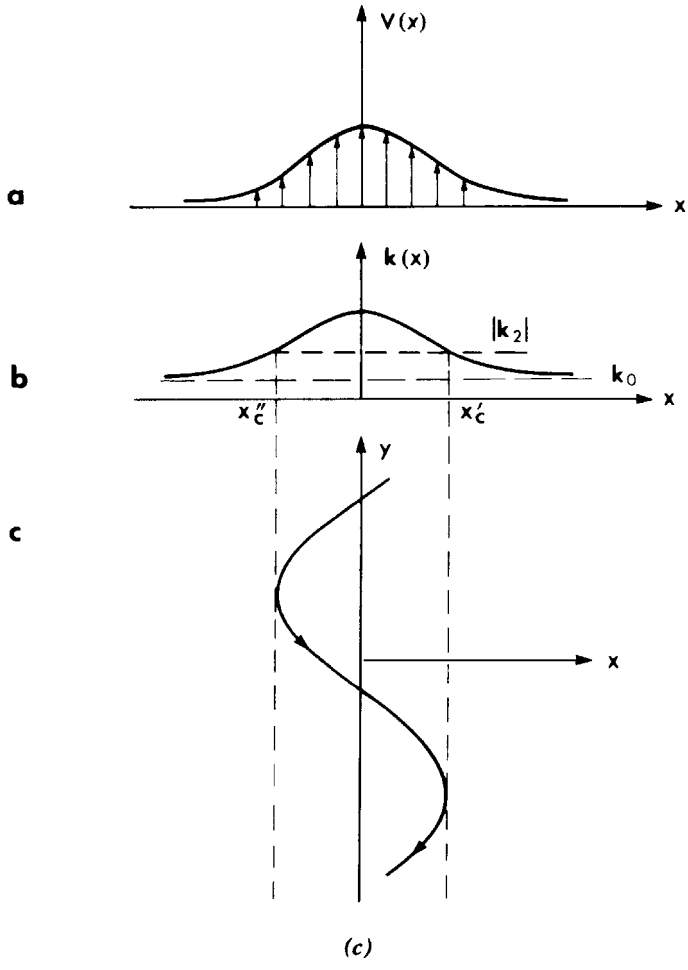

Figure 3.13c: $k_2 < 0$ and $k_0 < |k_2| < k_{\max}$: rays are trapped in a shear current.

propagating with the current, that is, $k_2 > 0$. The variation of $k(x)$ implied by Eq. (3.7.11) is qualitatively shown in Figs. 3.13(a) and 3.13(b). If $0 < k_2 < k_{\min}$, then a ray can penetrate the current [see Fig. 3.13(a)]. If, however, $0 < k_{\min} < k_2$, the square root in Eq. (3.7.12) is real only for $x < x_c$. Rays incident from outside must bend backward after touching the caustic at $x = x_c$, where $k_1 = 0$. These geometrical varieties resemble those over the submarine trough in Section 2.3. If the waves propagate against

the same current, $k_2 < 0$, the variation of $k(x)$ is shown in Fig. 3.13(c) in accordance with

$$\omega + V|k_2| = (gk \tanh kh)^{1/2} . \tag{3.7.13}$$

Now rays can exist only within the current when $k_0 < k_2 < k_{\max}$, that is, they can be trapped near the current peak. This situation resembles the submarine ridge in Section 2.3.

From the wave-action equation (3.7.3) the amplitude variation can be found

$$\frac{k_1 E C_g}{k(\omega - V k_2)} = \left[\frac{k_1 E C_g}{k(\omega - V k_2)}\right]_0 = \text{const} .$$

It follows that

$$\frac{A^2}{A_0^2} = \frac{C_{g0} \cos \alpha_0}{C_g \cos \alpha} \frac{\omega - V k_2}{\omega - V_0 k_2} . \tag{3.7.14}$$

In the special case of deep water, $kh \gg 1$, more explicit results may be obtained. In particular, Eq. (3.7.11) gives

$$\omega - V k_2 = (gk)^{1/2} . \tag{3.7.15}$$

With the further simplification that $V_0 = 0$, Eq. (3.7.14) becomes

$$\frac{A^2}{A_0^2} = \frac{\cos \alpha_0 [1 - (V/C_0) \sin \alpha_0]^2}{\{1 - (\sin^2 \alpha_0 / [1 - (V/C_0) \sin \alpha_0]^4\}^{1/2}} . \tag{3.7.16}$$

Figure 3.14 gives the amplitude ratio for various values of incidence angle α_0 and local current strength V/C_0.

Along a caustic, $\alpha = \pm\pi/2$ in Eq. (3.7.14) and the amplitude cannot be correctly predicted by the ray approximation. Local improvement can be effected in the manner of Section 2.3.3. McKee (1974) and Peregrine and Smith (1975) have given a detailed treatment of various types of caustics in a current in the context of linearized theory. Smith (1976) further included nonlinearity in order to accommodate fairly large amplitudes. These highly theoretical investigations have been stimulated by the *giant waves* in Agulhas Current, as vividly described in the introduction of Smith's paper:

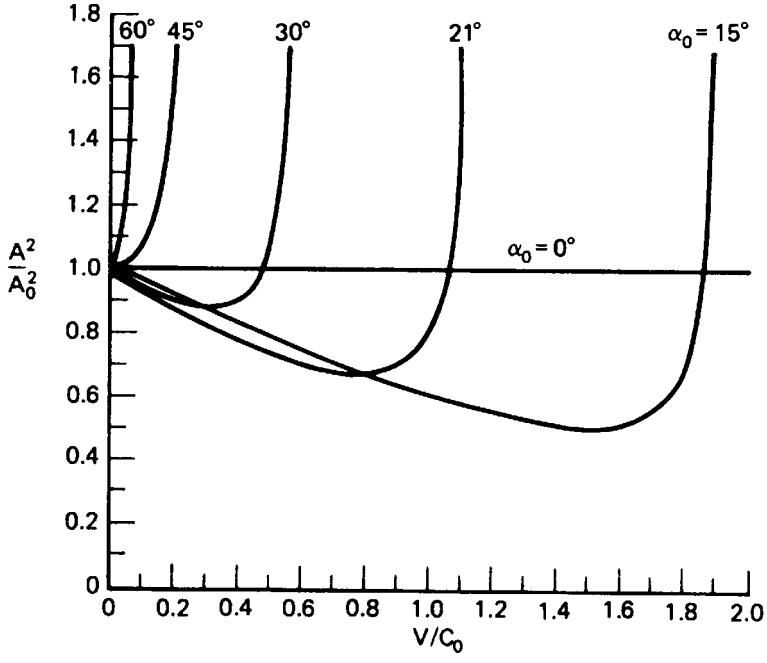

Figure 3.14: Wave amplitude versus current velocity for various angles of incidence α.

During the closure of the Suez Canal a number of ships, particularly oil tankers, have reported extensive damage caused by giant waves off the south-east coast of South Africa (Mallory, 1974). Two particularly unfortunate vessels were the *World Glory*, which broke in two and sank in June 1968, and the *Neptune Sapphire*, which lost 60 m of its bow section in August 1973. We can only speculate that giant waves may account for many ships which have been lost without trace off this coast. When returning from the Persian Gulf the tankers take advantage of the rapid Agulhas Current, and all except one of the eleven incidents listed by Captain Mallory (1974) involved vessels riding on the current. By examining weather charts, Mallory showed that when the incidents occurred the dominant wind-produced waves were opposed by the current.

Smith's account suggests that the situation depicted in Fig. 3.13(c) is likely encountered in nature.

In recent years there has been intensive interest in the role of nonlinearity in giant waves, now also called freak waves or rogue waves. Much focus has been directed to the side-band instability mechansism to be studied in Chapter Thirteen (see, e.g., Onorato et al., 2001; Trulsen and Dysthe, 1997).

3.7.3 Colinear Waves and Current

Assume that both waves and current are parallel to the x axis and the current speed changes in x:

$$U_1 = U(x)\,, \quad U_2 = 0\,, \quad \mathbf{k} = (k, 0)\,. \tag{3.7.17}$$

This kind of current, which must be accompanied by a vertical velocity component to satisfy continuity, Eq. (3.6.2), is called *upwelling* (or *downwelling*). Again $\omega = \text{const}$ so that

$$\omega = kU + \sigma = k_0 U_0 + \sigma_0 = \text{const} \tag{3.7.18}$$

where $(\,)_0$ signifies the value at a reference point. Defining C and C_0, which are the phase velocities with respect to the moving fluid, by

$$C^2 = \left(\frac{\sigma}{k}\right)^2 = \frac{g}{k}\tanh k\bar{h}\,, \quad C_0^2 = \left(\frac{\sigma_0}{k_0}\right)^2 = \frac{g}{k_0}\tanh k_0\bar{h}_0\,, \tag{3.7.19}$$

we have from Eq. (3.7.18)

$$\frac{k}{k_0}\left(\frac{U}{C_0} + \frac{C}{C_0}\right) = \frac{U_0}{C_0} + 1\,. \tag{3.7.20}$$

On the other hand, from Eq. (3.7.19)

$$\frac{C^2}{C_0^2} = \frac{k_0}{k}\frac{\tanh k\bar{h}}{\tanh k_0\bar{h}_0} \tag{3.7.21}$$

which is an implicit equation for k/k_0 in terms of C/C_0. Equations (3.7.20) and (3.7.21) can be combined to give

$$\frac{C^2}{C_0^2} = \frac{(U/C_0 + C/C_0)}{(U_0/C_0 + 1)}\frac{\tanh k\bar{h}}{\tanh k_0\bar{h}_0}\,. \tag{3.7.22}$$

Solving C/C_0 formally from Eq. (3.7.22) by pretending that k is constant, we get

$$\frac{C}{C_0} = \frac{1}{2T}\left[1 + \left(1 + 4T\frac{U}{C_0}\right)^{1/2}\right] \tag{3.7.23}$$

where

$$T = \left(1 + \frac{U_0}{C_0}\right)\frac{\tanh k_0\bar{h}_0}{\tanh k\bar{h}}\,. \tag{3.7.24}$$

Clearly, there is a critical current velocity at which the square root in Eq. (3.7.23) vanishes, that is,

$$U = -\frac{C_0}{4T} \tag{3.7.25a}$$

which implies that

$$\frac{C}{C_0} = \frac{1}{2T} \tag{3.7.25b}$$

and

$$U = -\frac{C}{2}\,. \tag{3.7.25c}$$

When $-U$ is greater than $C/2$, C/C_0 is complex and no unidirectional propagation is possible.

Consider the limit of deep water $k\bar{h}$, $k_0\bar{h}_0 \gg 1$, and $U_0 = 0$. Equation (3.7.23) reduces to

$$\frac{C}{C_0} = \frac{1}{2}\left[1 + \left(1 + 4\frac{U}{C_0}\right)^{1/2}\right]. \tag{3.7.26}$$

Thus, a current following the waves ($U > 0$) increases the phase velocity and lengthens the waves. On the other hand, an opposing current ($U < 0$) reduces the phase velocity and shortens the waves. The critical speed is at $U = -C/2 = -C_0/4$.

For arbitrary depth, the wavelength has been calculated for an extensive range of current and depth by Jonsson, Skovgaard, and Wang (1970). Figure 3.15 shows a few sample results computed by Brevik and Aas (1980) who also conducted some experiments which confirmed the present theory.

As for the amplitude, Eq. (3.7.3) gives

$$(C_g + U)\frac{E}{\sigma} = \text{const}$$

so that

$$\frac{A^2}{A_0^2} = \frac{\sigma}{\sigma_0}\frac{C_{g0} + U_0}{C_g + U}\,, \tag{3.7.27}$$

which becomes unbounded when $U = -C_g$. For deep water, $C_g \to \frac{1}{2}C$, $\sigma \to g/C$; Eq. (3.7.27) may be written

$$\frac{A^2}{A_0^2} = \frac{C_0}{C}\frac{C_0/2 + U_0}{C/2 + U} = \frac{C_0}{C}\frac{\frac{1}{2} + U_0/C_0}{\frac{1}{2}C/C_0 + U/C_0}\,, \quad k\bar{h} \gg 1\,. \tag{3.7.28}$$

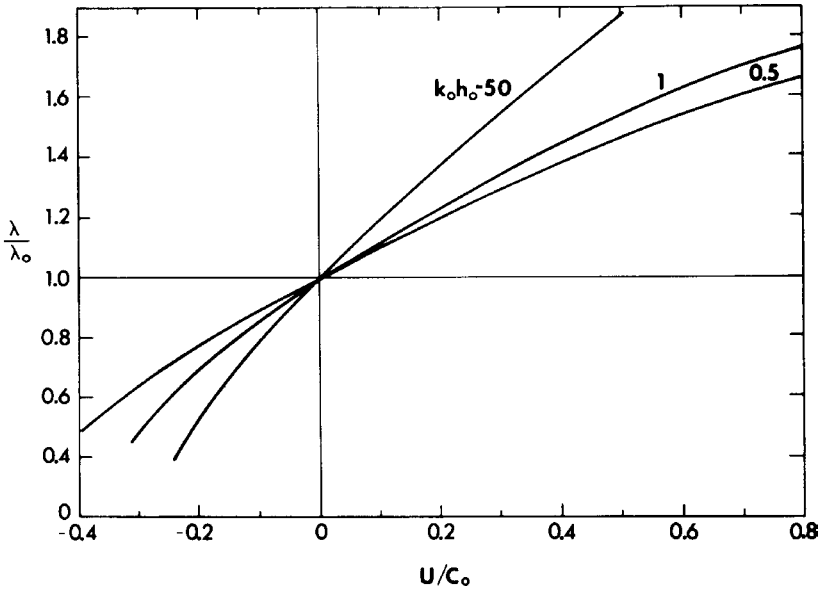

Figure 3.15: Change of wavelength due to colinear current (from Brevik and Aas, 1980, *Coastal Engineering*. Reproduced by permission of Elsevier Scientific Publishing Co.).

By using Eq. (3.7.26), C/C_0 may be eliminated to give

$$\frac{A^2}{A_0^2} = \frac{\frac{1}{2} + U_0/C_0}{U/C_0 + \frac{1}{2}[\frac{1}{2} + \frac{1}{2}(1 + 4U/C_0)^{1/2}]} \frac{1}{[\frac{1}{2} + \frac{1}{2}(1 + 4U/C_0)^{1/2}]}, \quad k\bar{h} \gg 1 . \tag{3.7.29}$$

Again, when the critical current speed $U = -\frac{1}{2}C = -\frac{1}{4}C_0$ is reached, the wave amplitude becomes infinite. This prediction is often used to infer breaking and is the idea behind the so-called *hydraulic breakwater*. In fact, the ray approximation ceases to be valid here. A more refined linear theory accounting for reflection near the critical speed can be found in Peregrine (1976). Nonlinear effects, however, can also be important and have been, to some extent, explored by Crapper (1972).

Numerical results for A/A_0 can be obtained straightforwardly for arbitrary $k\bar{h}$, by obtaining the mean surface height from Eq. (3.6.13), then solving for k from Eq. (3.7.22). Finally, Eq. (3.7.27) gives A/A_0. Figure 3.16 shows some sample results for $U_0 = 0$ by Brevik and Aas (1980), who also performed some experiments which supported the theory here.

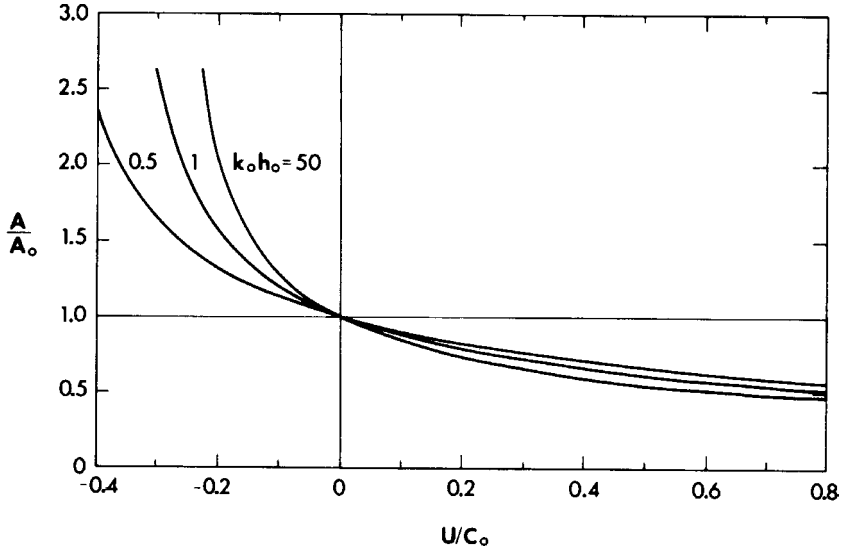

Figure 3.16: Change of wave amplitude due to colinear current (from Brevik and Aas, 1980, *Coastal Engineering*. Reproduced by permission of Elsevier Scientific Publishing Co.).

More extensive computations have been reported by Jonsson, Skovgaard and Wang (1970).

For the purpose of computing practical cases where the slow variations of depth and current can be quite arbitrary, Eq. (3.5.7) has been generalized by Booij (1981) using the elegant theory of Lagrangian. Both refraction and diffraction are included. Actual computations can, however, be expensive and further approximation must be added.

This page intentionally left blank

Long Waves of Infinitesimal Amplitude Over Bottom with Appreciable Variations

4

When a propagating wave enters a region where the fractional change of depth within a wavelength is significant, the phenomenon of scattering occurs in which reflection becomes appreciable. The simple ray theory which ignores reflection is no longer adequate. Before discussing the scattering of dispersive waves, let us examine similar problems for long waves in shallow water where dispersion is not important. For mathematical simplicity we shall deal largely with discontinuous depth variation. An interesting aspect of varying depth is wave trapping, that is, the phenomenon whereby waves are effectively confined in a part of the ocean. This topic has been discussed for short waves in Chapter Three. Long-wave trapping problems associated with sloping beaches, continental shelves, and oceanic ridges will be discussed here by way of several simple models such as a rectangular sill or shelf, and a uniformly sloping beach, and so on. In addition, several general aspects of the scattering matrix will be studied. Since only a few continuous variations can be solved analytically with a good deal of algebra, approximate or numerical methods are needed and will be discussed at the end of this chapter.

4.1 Formulation of Linearized Long-Wave Theory

4.1.1 Governing Equations

In Section 1.4 we have observed that for infinitesimal waves on constant depth, water motion in long waves is essentially horizontal, implying that the vertical variation is weak and the pressure is hydrostatic. This observation has been reaffirmed in Section 3.6 in the derivation of the nonlinear

equations for large-scale currents which are just long waves of finite amplitudes. Thus, long-wave motions are approximately two dimensional.

Linearizing Eqs. (3.6.11) and (3.6.12), Chapter Three, for infinitesimal amplitudes

$$\frac{|\zeta|}{h} \ll 1\,, \tag{4.1.1}$$

and changing the notations from $\mathbf{U}$ to $\mathbf{u}$ and from $\bar{\zeta}$ to ζ, we have for mass conservation

$$\frac{\partial \zeta}{\partial t} + \nabla \cdot (h\mathbf{u}) = 0\,, \tag{4.1.2}$$

and for momentum conservation

$$\frac{\partial \mathbf{u}}{\partial t} = -g\nabla\zeta\,. \tag{4.1.3}$$

The total pressure is still hydrostatic:

$$P = \rho g(\zeta - z)\,. \tag{4.1.4}$$

Eliminating $\mathbf{u}$ from Eqs. (4.1.2) and (4.1.3), we obtain

$$g\nabla \cdot (h\nabla\zeta) = \frac{\partial^2 \zeta}{\partial t^2} \tag{4.1.5}$$

which is a hyperbolic partial differential equation with variable coefficients.

If the waves are sinusoidal in time with radian frequency ω, we may separate time and space dependences by

$$\begin{aligned} \zeta \;&=\; \eta(x,y)e^{-i\omega t}\,, \\ \mathbf{u}(x,y,t) \;&\rightarrow\; \mathbf{u}(x,y)e^{-i\omega t}\,. \end{aligned} \tag{4.1.6}$$

From Eqs. (4.1.2) and (4.1.3) the spatial factors are related by

$$i\omega\eta = \nabla \cdot (h\mathbf{u})\,, \tag{4.1.7}$$

$$\mathbf{u} = -\frac{ig}{\omega}\nabla\eta\,, \tag{4.1.8}$$

and

$$\nabla \cdot (h\nabla\eta) + \frac{\omega^2}{g}\eta = 0\,. \tag{4.1.9}$$

For constant depth ($h = \text{const}$), Eq. (4.1.5) becomes the classical wave equation

$$\nabla^2\zeta = \frac{1}{gh}\frac{\partial^2\zeta}{\partial t^2}\,, \tag{4.1.10}$$

while Eq. (4.1.9) becomes the Helmholtz equation

$$\nabla^2\eta + k^2\eta = 0\,, \quad k = \frac{\omega}{(gh)^{1/2}}\,. \tag{4.1.11}$$

If the lateral boundary is a rigid vertical wall, the boundary condition must be such that the normal flux vanishes. It follows from Eq. (4.1.8) that

$$\frac{\partial\zeta}{\partial n} = 0 \quad \text{or} \quad \frac{\partial\eta}{\partial n} = 0, \tag{4.1.12}$$

which implies that the free-surface height is either a maximum or a minimum. If the boundary is a relatively steep beach and if the waves are not steep enough to break (see Section 10.5), Eq. (4.1.12) may be modified to

$$\lim_{h\to 0} h\mathbf{u}\cdot\mathbf{n} = 0 \quad \text{or} \quad \lim_{h\to 0} h\frac{\partial\zeta}{\partial n} = 0\,. \tag{4.1.13}$$

On the other hand, the boundary condition along a rubble-mound breakwater or a mild beach with breaking waves cannot be easily stated because dissipation on these boundaries is a nonlinear process which is difficult to describe mathematically.

Finally, an appropriate condition must be specified at infinity.

To reinforce the above heuristic argument, let us give a more formal derivation for Eqs. (4.1.1) and (4.1.4) by taking the long-wave limit of the general linearized theory. The reasoning follows that of Friedrichs (1948a) for nonlinear long waves and is partially similar to that of Section 3.1. Let us normalize all variables according to the scales anticipated on physical grounds:

$$\begin{gathered}(x', y') = k(x, y)\,, \quad z' = \frac{z}{h_0}\,, \quad h' = \frac{h}{h_0}\,,\\ t' = [k(gh_0)^{1/2}]t\,, \quad \zeta' = \frac{\zeta}{A_0}\,, \quad \Phi = \frac{1}{k}\frac{A}{h_0}(gh_0)^{1/2}\phi\,,\end{gathered} \tag{4.1.14}$$

where $\omega \sim (gh_0)^{1/2}k$. The normalization for t and Φ is suggested by Eq. (1.2.2), Chapter One. The dimensionless governing equations are precisely Eqs. (3.1.3)–(3.1.5), Chapter Three, if $(^-)$ is replaced by $(\ )'$ everywhere. For brevity the primes will be omitted from here on.

Let us introduce the series

$$\phi = \phi_0 + \mu^2\phi_2 + \mu^4\phi_4 + \cdots . \tag{4.1.15}$$

At the order $O(\mu^0)$ we have

$$\frac{\partial^2\phi_0}{\partial z^2} = 0\,, \quad -h < z < 0\,, \tag{4.1.16}$$

$$\frac{\partial\phi_0}{\partial z} = 0\,, \quad z = 0, -h\,, \tag{4.1.17}$$

so that $\phi_0 = \phi_0(x, y, t)$. At the order $O(\mu^2)$ we have

$$\frac{\partial^2\phi_2}{\partial z^2} = -\nabla^2\phi_0\,, \quad -h < z < 0\,, \tag{4.1.18}$$

$$\frac{\partial\phi_2}{\partial z} = -\frac{\partial^2\phi_0}{\partial t^2}\,, \quad z = 0\,, \tag{4.1.19}$$

$$\frac{\partial\phi_2}{\partial z} = -\nabla h\cdot\nabla\phi_0\,, \quad z = -h\,. \tag{4.1.20}$$

Application of Green's formula [Eq. (2.4.11), Chapter Two] to ϕ_0 and ϕ_2 gives a solvability condition for ϕ_2,

$$\nabla\cdot(h\nabla\phi_0) = \frac{\partial^2\phi_0}{\partial t^2}\,. \tag{4.1.21}$$

If the physical variables are restored and the linearized Bernoulli equation $g\zeta = \Phi_t$ is used, then Eq. (4.1.21) leads to Eq. (4.1.5).

4.1.2 Quasi-One-Dimensional Waves in a Long Channel of Slowly Varying Cross Section

For a long channel of rectangular cross section with width much less than the length longitudinal scale, the lateral variation is expected to be much less significant than that of the longitudinal variation. Intuitively, this is true because the boundary conditions of zero normal flux on the banks of a narrow channel imply that the transverse variation of ζ is negligible everywhere. The motion should be describable by a one-dimensional equation; a heuristic derivation is given below.

Let x be the longitudinal axis, y the transverse axis, $b(x)$ the width, and $h(x, y)$ the depth. Let $y = a_1(x)$ and $a_2(x)$ be the banks, then

$$b = a_2 - a_1\,, \quad \text{Area } A = \int_{a_1}^{a_2} h\,dy\,. \tag{4.1.22}$$

Integrating the continuity equation (4.1.2) from one bank to the other, we have

$$\int_{a_1}^{a_2} \frac{\partial \zeta}{\partial t}\,dy + \frac{\partial}{\partial x}\int_{a_1}^{a_2} hu\,dy \left[h\left(v - u\frac{da}{dx}\right)\right]_{y=a_1}^{y=a_2} = 0\,,$$

where use is made of the Leibniz rule. The integrated terms vanish along both banks, hence,

$$\frac{\partial \zeta}{\partial t} + \frac{1}{b}\frac{\partial Au}{\partial x} = 0\,. \tag{4.1.23}$$

When the transverse variations of ζ and u are ignored, the momentum equation reads approximately

$$\frac{\partial u}{\partial t} = -g\frac{\partial \zeta}{\partial x}\,. \tag{4.1.24}$$

Combining Eqs. (4.1.23) and (4.1.24), we have

$$\frac{\partial}{\partial x}\left(A\frac{\partial \zeta}{\partial x}\right) - \frac{b}{g}\frac{\partial^2 \zeta}{\partial t^2} = 0\,. \tag{4.1.25}$$

For sinusoidal waves $\zeta = \eta e^{-i\omega t}$, the governing equation is

$$\frac{\partial}{\partial x}\left(A\frac{\partial \eta}{\partial x}\right) + \frac{\omega^2 b}{g}\eta = 0\,, \tag{4.1.26}$$

which is of the well-known Stürm–Liouville type. It should be emphasized that so far the wavelength and the longitudinal scale of channel geometry are considered to be of the same order.

Exercise 4.1

Use Friedrichs' method to deduce Eq. (4.1.25) by a perturbation analysis.

4.1.3 Further Remarks on the Radiation Condition

Recall from Section 2.4 that for steady sinusoidal problems, it is necessary to impose the radiation condition that waves due to localized disturbances propagate outward. An equivalent approach is to begin with an initial-value problem and to regard the steady state as the limit of $t \to \infty$. Another alternative is to insist on a steady-state formulation but to include a small damping, which may be either real or fictitious, and then to require that

the simple harmonic solution vanish at infinity. When damping is allowed to diminish at the end, the ultimate result satisfies the radiation condition also. The artifice of fictitious damping is due to Rayleigh.

In shallow water, one may imagine bottom friction to be the physical source of damping. Let the friction force be modelled by $2\varepsilon\mathbf{u}$, where ε is a small positive coefficient. The momentum equation reads

$$\frac{\partial \mathbf{u}}{\partial t} = -g\nabla\zeta - 2\varepsilon\mathbf{u}\,. \tag{4.1.27}$$

which can be combined with the continuity equation (4.1.2) to give

$$\nabla \cdot gh\nabla\zeta - 2\varepsilon\frac{\partial \zeta}{\partial t} = \frac{\partial^2 \zeta}{\partial t^2}\,. \tag{4.1.28}$$

For simple harmonic motion Eq. (4.1.28) becomes

$$\nabla \cdot gh\nabla\eta + (\omega^2 + 2i\varepsilon\omega)\eta = 0\,, \tag{4.1.29}$$

which may be written

$$\nabla \cdot gh\nabla\eta + (\omega + i\varepsilon)^2\eta = 0 \tag{4.1.30}$$

for small ε. The boundary condition at infinity is that η must be bounded. The ultimate steady state is then the limit of the solution when $\varepsilon \downarrow 0$.

Instead of the physical or pseudophysical approach of introducing damping, a mathematically equivalent way is to say that η satisfies

$$\nabla \cdot gh\nabla\eta + \omega'^2\eta = 0\,, \tag{4.1.31}$$

where ω' is complex with a small but positive imaginary part.

To see the implication of "damping" or complex ω', consider one-dimensional scattering by a localized obstacle. In the zones of constant h the scattered wave is

$$e^{ik'|x|} \quad \text{or} \quad e^{-ik'|x|}\,,$$

where

$$k' = k + i\varepsilon(gh)^{-1/2} \tag{4.1.32}$$

with $k = \omega(gh)^{-1/2}$. For the solution to be bounded as $|x| \to \infty$, $e^{-ik'|x|}$ must be discarded. In the limit of $\varepsilon \downarrow 0$, the disturbance becomes

$$\eta^S \sim e^{ik|x|}\,, \quad k|x| \gg 1\,, \tag{4.1.33}$$

which implies outgoing waves. Hence the complex ω' implies the radiation condition. As is easily verified, the radiation condition can be expressed

$$\left(\frac{\partial}{\partial x} \mp ik\right)\eta^S \to 0\,, \quad |kx| \to \infty\,. \tag{4.1.34}$$

In two-dimensional scattering by localized objects, the solution in a sea of constant depth can be constructed by superposition of the following terms:

$$\left\{\begin{array}{l} H_n^{(1)}(k'r) \\ H_n^{(2)}(k'r) \end{array}\right\}\left\{\begin{array}{l} \sin n\theta \\ \cos n\theta \end{array}\right\}.$$

Because of the asymptotic behavior of the Hankel functions

$$\left\{\begin{array}{l} H_n^{(1)}(k'r) \\ H_n^{(2)}(k'r) \end{array}\right\} \sim \left(\frac{2}{\pi kr}\right)^{1/2} \exp\left[\pm i\left(k'r - \frac{\pi}{4} - \frac{n\pi}{2}\right)\right], \tag{4.1.35}$$

$H_n^{(2)}$ must be discarded when k' is complex with a positive real part. At the limit of $\varepsilon \downarrow 0$, the general solution for the scattered waves may be written

$$\eta^S = \sum_{n=0}^{\infty}(\alpha_n \cos n\theta + \beta_n \sin n\theta)H_n^{(1)}(kr)\,. \tag{4.1.36}$$

For $kr \gg 1$, η^S behaves as

$$\begin{aligned}\eta^S &\simeq \left[\sum(\alpha_n \cos n\theta + \beta_n \sin n\theta)e^{-in\pi/2}\right]\left(\frac{2}{\pi kr}\right)^{1/2} e^{ikr - i\pi/4} \\ &\equiv A(\theta)\left(\frac{2}{\pi kr}\right)^{1/2} e^{-ikr - i\pi/4}\end{aligned} \tag{4.1.37}$$

which is again an outgoing wave. Equation (4.1.37) is therefore the radiation condition for two-dimensional scattering by finite objects. Alternatively, this condition may be expressed

$$(kr)^{1/2}\left(\frac{\partial}{\partial r} - ik\right)\eta^S \to 0\,, \quad kr \gg 1\,. \tag{4.1.38}$$

We hasten to emphasize that Eq. (4.1.38) is much stronger than the mere requirement that $\eta^S \downarrow 0$ at infinity.

The above remarks suggest a simple routine for constructing transient solutions from simple harmonic solutions. If the disturbance begins at some

finite time, then $\zeta \to 0$ as $t \to -\infty$. With damping we expect $\zeta \to 0$ also as $t \to +\infty$. Thus, the Fourier transform may be applied

$$\eta = \frac{1}{2\pi} \int_{-\infty}^{\infty} \zeta(\mathbf{x}, t) e^{i\omega t}\, dt\,. \tag{4.1.39}$$

The transform of Eq. (4.1.28) is just Eq. (4.1.29) and the boundary-value problem is precisely the one for damped harmonic disturbance $\eta(\mathbf{x}, \omega')$. Consequently, the transient disturbance may be obtained by inversion

$$\zeta(\mathbf{x}, t) = \int_{-\infty}^{\infty} \eta(\mathbf{x}, \omega') e^{-i\omega t}\, d\omega, \tag{4.1.40}$$

which amounts to linear superposition of damped simple harmonic solutions. Since $\omega' = \omega + i\varepsilon$, Eq. (4.1.40) may be rewritten

$$\begin{aligned} \zeta(\mathbf{x}, t) &= e^{\varepsilon t} \int_{-\infty}^{\infty} \eta(\mathbf{x}, \omega') e^{-i\omega' t}\, d\omega \\ &= e^{\varepsilon t} \int_{-\infty+i\varepsilon}^{\infty+i\varepsilon} \eta(\mathbf{x}, \omega') e^{-i\omega' t}\, d\omega'\,. \end{aligned} \tag{4.1.41}$$

The inviscid solution is simply the limit of $\varepsilon \downarrow 0$, with the understanding that the Fourier integral in Eq. (4.1.41) is along a path slightly above the real axis in the complex ω' plane. Now that the final goal has been achieved, one can forget the artifice of damping and simply say that $\zeta(\mathbf{x}, t)$ is the Fourier integral of the simple harmonic solution which satisfies the radiation condition

$$\zeta(\mathbf{x}, t) = \int_{-\infty}^{\infty} \eta(\mathbf{x}, \omega) e^{-i\omega t}\, d\omega\,, \tag{4.1.42}$$

where the path of integration must be slightly above the real ω axis.

The ideas in this subsection can be generalized to the three-dimensional case of arbitrary kh.

4.2 Straight Depth Discontinuity — Normal Incidence

4.2.1 The Solution

Consider a simple ocean where the depth changes discontinuously at $x = 0$, and $h = h_1$ for $x < 0$ and $h = h_2$ for $x > 0$, where h_1 and h_2 are unequal

constants. Two incident waves of frequency ω arrive from $x \sim \pm\infty$. From each wavetrain some energy is transmitted beyond the step and some is reflected backward, creating scattered waves propagating away from the step. The problem is to find the transmitted and the reflected waves.

The wave on either side of $x = 0$ satisfies

$$\frac{\partial \zeta}{\partial t} + \frac{\partial}{\partial x}(hu) = 0 \tag{4.2.1}$$

and

$$\frac{\partial u}{\partial t} + g\frac{\partial \zeta}{\partial x} = 0\,, \tag{4.2.2}$$

where $\zeta = (\zeta_1, \zeta_2)$, $u = (u_1, u_2)$, and $h = (h_1, h_2)$ for $x < 0$, $x > 0$, respectively. We must now find matching conditions at $x = 0$. Subject to further scrutiny let us assume for the moment that Eqs. (4.2.1) and (4.2.2) are valid even across the depth discontinuity and can be integrated with respect to x from $x = 0_-$ to $x = 0_+$. Since the interval of integration is infinitesimal and $\partial\zeta/\partial t$ and $\partial u/\partial t$ are finite, the first terms of Eqs. (4.2.1) and (4.2.2) do not contribute to the result, so that

$$\lim_{x\to 0_-} h_1 u_1 = \lim_{x\to 0_+} h_2 u_2\,, \tag{4.2.3}$$

$$\lim_{x\to 0_-} \zeta_1 = \lim_{x\to 0_+} \zeta_2\,. \tag{4.2.4}$$

These conditions (Lamb, 1932) relate ζ and the flux uh across the discontinuity.

For simple harmonic motion we use Eq. (4.1.9) so that the spatial factors satisfy

$$\frac{d^2\eta_m}{dx^2} + k_m^2\eta_m = 0\,, \quad m = 1, 2 \tag{4.2.5}$$

with

$$k_m = \frac{\omega}{(gh_m)^{1/2}}\,. \tag{4.2.6}$$

The spatial part of the velocity is given by

$$u_m = -\frac{ig}{\omega}\frac{d\eta_m}{dx}\,. \tag{4.2.7}$$

The matching conditions at the junction are

$$\eta_1 = \eta_2\,, \tag{4.2.8a}$$

$$h_1 \frac{\partial \eta_1}{\partial x} = h_2 \frac{\partial \eta_2}{\partial x}\,. \tag{4.2.8b}$$

To complete the formulation we must add the radiation condition that the disturbance caused by the incident wave can only be outgoing. Thus, if there is only one incident wave from the left (or right), the waves on the right (left) side must be only right- (or left-) going. More generally, we assume that there are incident waves coming from both infinities $A_- e^{ik_1 x}$ and $B_+ e^{-ik_2 x}$. The general solution should be of the following form:

$$\eta_1 = A_- e^{ik_1 x} + B_- e^{-ik_1 x} \quad \text{for} \quad x < 0 \tag{4.2.9}$$

and

$$\eta_2 = B_+ e^{-ik_2 x} + A_+ e^{ik_2 x} \quad \text{for} \quad x > 0\,. \tag{4.2.10}$$

The amplitudes of the incident waves A_- and B_+ are known and those of the scattered waves A_+ and B_- are to be found. Applying the matching conditions (4.2.8a) and (4.2.8b), we obtain

$$A_+ + B_+ = A_- + B_-\,,$$

$$k_1 h_1 (A_- - B_-) = k_2 h_2 (-B_+ + A_+)\,,$$

which are readily solved to give

$$B_- = \frac{(k_1 h_1 - k_2 h_2) A_- + 2 k_2 h_2 B_+}{k_1 h_1 + k_2 h_2}\,, \tag{4.2.11}$$

$$A_+ = \frac{2 k_1 h_1 A_- - (k_1 h_1 - k_2 h_2) B_+}{k_1 h_1 + k_2 h_2}\,. \tag{4.2.12}$$

The results may be written more compactly in matrix form as

$$\{A^S\} = [S]\{A^I\} \tag{4.2.13}$$

with

$$\{A^I\} = \begin{Bmatrix} A_- \\ B_+ \end{Bmatrix}, \quad \{A^S\} = \begin{Bmatrix} A_+ \\ B_- \end{Bmatrix}, \tag{4.2.14}$$

and

$$[S] = (k_1h_1 + k_2h_2)^{-1} \begin{bmatrix} 2k_1h_1 & -(k_1h_1 - k_2h_2) \\ k_1h_1 - k_2h_2 & 2k_2h_2 \end{bmatrix}$$

$$= \begin{bmatrix} T_1 & R_2 \\ R_1 & T_2 \end{bmatrix}. \tag{4.2.15}$$

The matrix $[S]$ is called the *scattering matrix*.

To understand the meaning of T_1, T_2, R_1, and R_2, let there be an incident wave from the left only so that $A_- \neq 0$ and $B_+ = 0$. It is clear that

$$\frac{A_+}{A_-} = T_1 = \frac{2k_1h_1}{k_1h_1 + k_2h_2}, \tag{4.2.16a}$$

$$\frac{B_-}{A_-} = R_1 = \frac{k_1h_1 - k_2h_2}{k_1h_1 + k_2h_2}. \tag{4.2.16b}$$

Thus, T_1 and R_1 can be defined, respectively, as the *transmission* and *reflection* coefficients when the incident wave originates from the side of $h = h_1$. T_2 and R_2 are similarly defined for an incident wave from h_2. Since $k_mh_m = \omega(h_m/g)^{1/2}$, we have

$$T_1 = \frac{2(h_1)^{1/2}}{(h_1)^{1/2} + (h_2)^{1/2}} = \frac{2}{1 + (h_2/h_1)^{1/2}}, \tag{4.2.17a}$$

$$R_1 = \frac{(h_1)^{1/2} - (h_2)^{1/2}}{(h_1)^{1/2} + (h_2)^{1/2}} = \frac{1 - (h_2/h_1)^{1/2}}{1 + (h_2/h_1)^{1/2}}. \tag{4.2.17b}$$

The variation of T_1 and R_1 with the depth ratio is shown in Fig. 4.1. Note that the phase of the reflected wave does not change when the incident wave is from the deeper side, but changes by π when it is from the shallower side. We leave it as an exercise to prove that the energy transported by the scattered waves (reflected and transmitted) equals the energy transported by the incident wave. For very shallow shelf, $h_2/h_1 \ll 1$,

$$T_1 = 2\left[1 - \left(\frac{h_2}{h_1}\right)^{1/2}\right] \quad R_1 = 1 - 2\left(\frac{h_2}{h_1}\right)^{1/2}. \tag{4.2.18}$$

The reflection coefficient $R_1 \cong 1$, so that the sum of the incident and reflected waves represents essentially a standing wave with an antinode of amplitude $2A^I$ at $x = 0$. It must be cautioned that nonlinear effects so far ignored here can be very important for small enough h_2. Although

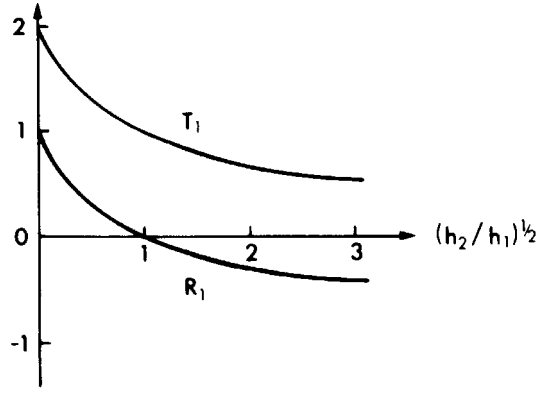

Figure 4.1: Transmission (T_1) and reflection (R_1) coefficients for a step shelf with normally incident waves.

the transmitted wave amplitude increases to twice the incident wave amplitude due to the decrease in depth h_2, very little energy gets through because the rate of energy flux is $T_1^2 C_g \propto (h_2)^{1/2}$. In the extreme case of $h_2/h_1 \gg 1$ the reflection coefficient $R_1 = -1$, so that the total wave system in $x < 0$ is also a standing wave but with a node at $x = 0$.

Exercise 4.2: A Shelf with a Parabolic Transition

Consider a shelf of depth h_1 in the region $x < x_1$ connected to an ocean of greater depth h_2 in the region $x > x_2$. In the transition $x_1 < x < x_2$, the depth is given by $h = ax^2$ with $h_1 = ax_1^2$, $h_2 = ax_2^2$, and $x_2 - x_1 \gg h_1$ or h_2. Let a train of long-period waves be incident normally from the ocean. Show that the scattering coefficients are

$$T = \frac{ib}{\mu^{1/2}\Delta} \quad \text{and} \quad R = i \sinh\left(\frac{b}{2}\ln\frac{1}{\mu}\right) \frac{\exp[-2i(\omega^2/ga)^{1/2}]}{\Delta},$$

where

$$b = \left(1 - 4\frac{\omega^2}{ga}\right)^{1/2}, \quad \mu = \frac{x_1}{x_2},$$

and

$$\Delta = 2\left(\frac{\omega^2}{ga}\right)^{1/2} \sinh\left(\frac{b}{2}\ln\frac{1}{\mu}\right) + ib\cosh\left(\frac{b}{2}\ln\frac{1}{\mu}\right).$$

Plot the results and examine the effects of ω^2/ga and μ (Kajiura, 1961).

4.2.2 Justification of the Matching Conditions at the Junction

Although the conditions of matching Eqs. (4.2.8a) and (4.2.8b) are intuitively reasonable, they are deduced on the basis of Eqs. (4.2.1) and (4.2.2), which are valid only when the vertical motion is negligible compared with the horizontal and when $\partial/\partial x$ is small. However, these assumptions are no longer valid in the neighborhood of the step. Is our theory in Section 4.2.1 still valid? This question was the subject of a paper by Bartholomeuz (1958) who started from a formulation for arbitrary kh and proved rigorously that the result of the foregoing section is the correct asymptotic limit of $k_m h_m \to 0$. His argument was very lengthy and involved some very difficult mathematics. We present below a simpler argument via the *matched asymptotics method*, which is a slightly elaborated version of the boundary-layer approximation in Section 3.3.3, and has been used effectively in many long-wave problems by Ogilvie (1960), Tuck (1975), and others.

As a start we divide the physical region into a *near field* and a *far field* according to the dominant scales in each region. For example, the length scale on the incident side far away from the junction is the wavelength $1/k_1$, hence

$$\eta_1 = A(e^{ik_1 x} + Re^{-ik_1 x}) \tag{4.2.19}$$

properly describes the waves. This region of $O(k_1^{-1})$ is a far field. In the eyes of a far-field observer, the neighborhood of the step appears so small that the first few terms of the Taylor expansion of Eq. (4.2.19) sufficiently approximate the free surface there, hence

$$\eta_1 = A[1 + R + (1 - R)ik_1 x] + O(k_1 x)^2 \quad \text{as} \quad k_1 x \to 0\,. \tag{4.2.20}$$

To another similar observer on the transmission side of the far field, the wave is described by

$$\eta_2 = ATe^{ik_2 x}\,, \tag{4.2.21}$$

which tends to

$$\eta_2 = AT(1 + ik_2 x) + O(k_2 x)^2 \tag{4.2.22}$$

in the neighborhood of the step. For shallow water the Bernoulli equation gives

$$\phi = \frac{-ig}{\omega}\eta\,,$$

so that

$$\phi_1^{\text{far}} \to \frac{-ig}{\omega}A[(1+R)+(1-R)ik_1x]\,, \quad k_1x \to 0\,, \tag{4.2.23}$$

$$\phi_2^{\text{far}} \to \frac{-ig}{\omega}AT(1+ik_2x)\,, \quad k_2x \to 0\,. \tag{4.2.24}$$

Now the neighborhood of the step constitutes a near field where the motion is two dimensional and the characteristic scale is the local depth $h(h_1$ or $h_2)$. The equation of motion and the boundary condition on the step are

$$\frac{\partial^2\phi}{\partial x^2}+\frac{\partial^2\phi}{\partial z^2}=0\,, \tag{4.2.25}$$

$$\frac{\partial\phi}{\partial n}=0\,. \tag{4.2.26}$$

Although the exact linearized boundary condition on the free surface is

$$\frac{\partial\phi}{\partial z}-\frac{\omega^2}{g}\phi=0\,, \tag{4.2.27}$$

the two terms above are in the ratio

$$\frac{\omega^2\phi/g}{(\partial\phi/\partial z)}=O\left(\frac{\omega^2 h}{g}\right)=O(k^2h^2)\,.$$

Hence condition (4.2.27) is approximately

$$\phi_z \cong 0 \tag{4.2.28}$$

with an error of $(kh)^2$. Physically, Eq. (4.2.28) implies that the near-field observer is oblivious of the long-scale waves and sees, at any instant, a

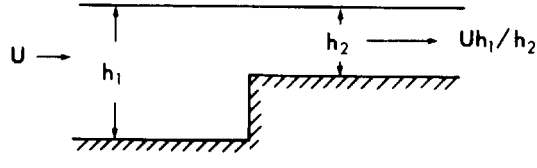

Figure 4.2: Near field of a step shelf.

current passing a confined channel with a step as in Fig. 4.2. The formal solution to this simplified potential flow problem can, in principle, be obtained by conformal mapping or other means.

Thus far, the near- and far-field solutions contain coefficients yet undetermined. The next step of the matched asymptotics method is to require that these solutions be joined smoothly in intermediate regions, which appear to be very near the junction to the far-field observer but very far from the junction to the near-field observer; in other words,

$$\phi^{\text{far}}|_{|kx|\ll 1} = \phi^{\text{near}}|_{|x/h|\gg 1} + O(kh)^2 \,. \tag{4.2.29}$$

Before carrying out the matching, let us write down the far-field (outer) approximation of ϕ^{near}:

$$\begin{aligned} \phi^{\text{near}} &= C - DUh_1 + Ux \,, \qquad && \frac{x}{h_1} \sim -\infty \\ &= C + DUh_1 + U\frac{h_1}{h_2}x \,, && \frac{x}{h_2} \sim +\infty \,. \end{aligned} \tag{4.2.30}$$

Note in particular that the additive constants at $x \sim \pm\infty$ are different by $2DUh_1$; in fact, D is related to the unknown constant U as follows. By continuity, we have at any x,

$$Uh_1 = \int_{-h}^{0} \frac{\partial\phi}{\partial x}\, dz = \frac{\partial}{\partial x}\int_{-h}^{0} \phi\, dz - \frac{\partial h}{\partial x}\phi(x,-h)$$

which gives, after integration from x_1 to x_2 where $-x_1/h_1$ and $x_2/h_2 \gg 1$,

$$\left[\int_{-h}^{0} \phi\, dz\right]_{x_1}^{x_2} = Uh_1(x_2 - x_1) + \int_{x_1}^{x_2} \frac{\partial h}{\partial x}\phi(x,-h)\, dx \,. \tag{4.2.31}$$

Since Eq. (4.2.30) applies at x_1 and x_2, the left-hand side of Eq. (4.2.31) may be written

$$C(h_2 - h_1) + DUh_1(h_1 + h_2) + Uh_1(x_2 - x_1) \,,$$

whereas the right-hand side of Eq. (4.2.31) may be written

$$Uh_1(x_2 - x_1) + C(h_2 - h_1) + \int_{-\infty}^{\infty} \frac{\partial h}{\partial x}[\phi(x,-h) - C]\, dx \,.$$

Substituting these into Eq. (4.2.31), we get

$$D = \frac{1}{h_1 + h_2}\int_{-\infty}^{\infty} dx \frac{\partial h}{\partial x}\frac{\phi(x,-h) - C}{Uh_1} \,. \tag{4.2.32}$$

Since $\phi - C$ must be of the order of Uh_1, D is a dimensionless number of order unity and depends only on the geometry of the near field. The explicit value of D can be worked out for a rectangular step as in Section 4.2.3.

Supposing that the near field and hence D are already known in terms of C and U, let us match Eqs. (4.2.23) and (4.2.24) with Eq. (4.2.30). By equating the coefficients of like powers of x, we get

$$C - Uh_1 D = -\frac{igA}{\omega}(1+R)\,,$$

$$U = -\frac{igA}{\omega}(1-R)ik_1\,,$$

$$C + Uh_1 D = -\frac{igA}{\omega}T\,,$$

$$U\frac{h_1}{h_2} = -\frac{igA}{\omega}Tik_2\,.$$

These equations can be solved for R, T, U, and C; the results are

$$R = -\frac{1 - s + 2iDk_1h_1}{1 + s - 2iDk_1h_1}\,, \tag{4.2.33}$$

$$T = \frac{2s}{1 + s - 2iDk_1h_1}\,, \tag{4.2.34}$$

$$h_1U = -\frac{igA}{\omega}ik_2h_2\frac{2s}{1 + s - 2iDk_1h_1}\,, \tag{4.2.35}$$

and

$$C = -\frac{igA}{\omega}\frac{2s - iDk_1h_1}{1 + s - 2iDk_1h_1}\,, \tag{4.2.36}$$

where

$$s \equiv \frac{k_1h_1}{k_2h_2}\,. \tag{4.2.37}$$

Since D is real and of order unity [see Eq. (4.2.32)], it only affects the phases of R, T, U, and C but may be ignored for their magnitudes, with an error of $O(kh)^2$. This conclusion is consistent with Bartholomeuz (1958) and was deduced in this manner by Tuck (1976). Thus, the simple requirements of Eq. (4.2.8) are justified.

Exercise 4.3: Flux Condition at the Junction of a Floating Body
If there is a ship with a draft $z = -H(x)$, show that Eq. (4.2.32) is generalized to

$$Uh_1D = \frac{1}{h_1 + h_2}\int_{-\infty}^{\infty} dx \times \left\{-\frac{\partial h}{\partial x}[\phi(x_1, -h) + C] + \frac{\partial H}{\partial x}[\phi(x_1, -H) + C]\right\}.$$

4.2.3 The Near Field for a Rectangular Step

In general, the near field of an abrupt transition must be solved numerically as a classical problem of steady potential flow. For a rectangular step, the solution can be achieved analytically by the theory of complex functions (see Milne-Thomson, 1967).ındexMilne-Thomson, 1967 Let us introduce the complex variable $z = x + jy$ and the complex velocity potential $W(z)$ with $\phi(x, y) = \mathrm{Re}_j W(z)$. Note that the imaginary unit here is denoted by j in order to be distinguished from the unit i used for time variation. Although both i and j are $(-1)^{1/2}$, each is to be regarded as real with respect to the other when they appear together. In particular the real velocity potential is to be interpreted by

$$\begin{aligned}\Phi(x, y, t) &= \mathrm{Re}_i \mathrm{Re}_j W(z) e^{-i\omega t} = \mathrm{Re}_i e^{-i\omega t}\,\mathrm{Re}_j(\phi + j\psi)\\ &= \mathrm{Re}_i e^{-i\omega t}\phi = \mathrm{Re}_i e^{-i\omega t}(\phi_1 + i\phi_2)\\ &= \phi\cos\omega t + \phi_2 \sin\omega t\,,\end{aligned}$$

where ϕ_1 and ϕ_2 are real with respect to both i and j.

The physical strip in the z plane can be mapped to the upper half of the ζ plane, as shown in Fig. 4.3, by the Schwarz–Christoffel formula

$$\frac{dz}{d\zeta} = \frac{K}{\zeta}\left(\frac{\zeta - 1}{\zeta - c^2}\right)^{1/2}. \tag{4.2.38}$$

Clearly, the complex potential $W = \phi + j\psi$ is a source of strength Uh_1 at the origin of the ζ plane,

$$W = \frac{Uh_1}{\pi}\ln\zeta + \mathrm{const}\,. \tag{4.2.39}$$

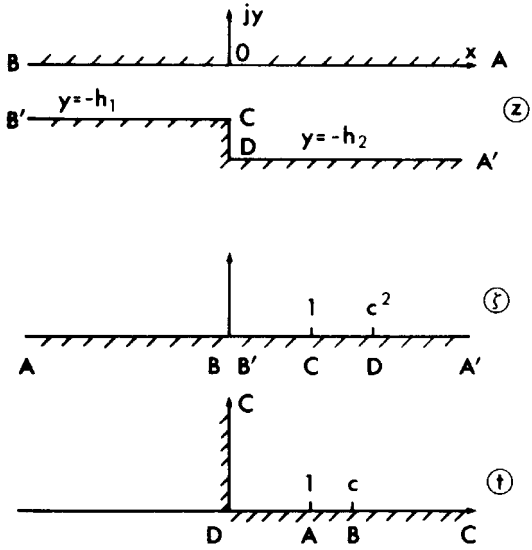

Figure 4.3: Mapping of the physical strip in the z plane to the upper half of the ζ plane.

To fix K and c^2 we note that the complex velocity is

$$\frac{dW}{dz} = \frac{dW}{d\zeta} \Big/ \frac{dz}{d\zeta} = \frac{Uh_1}{\pi K} \left(\frac{\zeta - c^2}{\zeta - 1} \right)^{1/2} .$$

Since $\zeta \sim \infty$ near A, $dW/dz \cong Uh_1/\pi K = Uh_1/h_2$, hence

$$K = \frac{h_2}{\pi} .$$

Near B, $\zeta \sim -0$ and $dW/dz \cong Uh_1 c/\pi K = U$, hence

$$c = \frac{h_2}{h_1} .$$

To integrate Eq. (4.2.38) we introduce a t plane by

$$\zeta = \frac{t^2 - c^2}{t^2 - 1} \tag{4.2.40a}$$

or

$$t = \left(\frac{\zeta - c^2}{\zeta - 1} \right)^{1/2} , \tag{4.2.40b}$$

which maps the upper half ζ plane to the first quadrant of t as shown in Fig. 4.3. Taking the logarithmic derivative of Eq. (4.2.40) and combining with Eq. (4.2.38), we can integrate z in terms of t, with the result

$$z + jh_1 = \frac{h_2}{\pi}\left(\frac{1}{c}\ln\frac{t-c}{t+c} - \ln\frac{t-1}{t+1}\right), \tag{4.2.41}$$

where the constant jh_1 is chosen so that the images of point C are as shown in the z and t planes.

Now putting Eq. (4.2.40a) into Eq. (4.2.39), we get

$$W = \frac{Uh_1}{\pi}\ln\frac{t^2-c^2}{t^2-1}. \tag{4.2.42}$$

For a given t in the first quadrant, we can find z from Eq. (4.2.41) and the corresponding W from Eq. (4.2.42). Now the near-field solution is complete.

The asymptotic approximations in the neighborhoods of A and B are needed. Let t approach the point B from the left, $t \to c - 0$, then

$$z + jh_1 \cong \frac{h_2}{\pi}\left[\frac{1}{c}\ln(t-c) - \frac{1}{c}\ln 2c - \ln\frac{c-1}{c+1}\right]$$

and

$$W \cong \frac{Uh_1}{\pi}\left[\ln(t-c) + \ln\frac{2c}{c^2-1}\right].$$

After $\ln(t-c)$ is eliminated, it follows that

$$W \cong Uz + \frac{Uh_1}{\pi}\left[j\pi + \ln 2c + c\ln\frac{c-1}{c+1} + \ln\frac{2c}{c^2-1}\right]. \tag{4.2.43}$$

Let t approach A from the right, then

$$z + jh_1 \cong \frac{h_2}{\pi}\left[\frac{1}{c}\left(\ln\frac{c-1}{c+1} + j\pi\right) - \ln(t-1) + \ln 2\right]$$

and

$$W \cong \frac{Uh_1}{\pi}[\ln(c^2-1) + j\pi - \ln 2 - \ln(t-1)].$$

Eliminating $\ln(1-t)$, we get

$$W \cong \frac{Uh_1 z}{h_2} + \frac{Uh_1}{\pi}\left[\ln(1-c^2) - 2\ln 2 + j\pi - \frac{1}{c}\ln\frac{c-1}{c+1}\right]. \tag{4.2.44}$$

We may now subtract the additive constants of Eqs. (4.2.43) and (4.2.44) to give

$$2D = \frac{1}{\pi}\left[\frac{c^2+1}{c}\ln\frac{c+1}{c-1} - 2\ln\frac{4c}{c^2-1}\right] \tag{4.2.45}$$

which was given by Tuck (1976) and confirms the order estimate of D in Section 4.2.2.

Exercise 4.4: Scattering by a Submerged Thin Barrier (Siew and Hurley, 1977)

Consider the scattering of infinitesimal long waves normally incident toward a long and thin plate horizontally submerged in a sea of constant depth H. The plate has the width $\ell = 2a$ and is fixed at depth $z = -c$. A steady train of sinusoidal waves of frequency σ and wavenumber k arrives from $x = -\infty$. The depth is small and the plate is wide so that we can assume that $kH \ll 1$ and $k\ell = O(1)$. Verify, by matched asymptotics, the approximate reflection and transmission coefficients R and T to the leading order in kH, as given below:

$$R = S\left\{\frac{\sigma\ell}{\sqrt{gH}}\sin\Omega - 2\sqrt{\frac{c}{H}}(1-\cos\Omega)\right\} \tag{4.2.46}$$

and

$$T = S\left\{2i\left[\sin\Omega + \frac{\sigma\ell}{b}\sqrt{\frac{c}{g}}\right]\right\}, \tag{4.2.47}$$

where

$$\begin{aligned} S = 1\Big/\Bigg\{&2\sqrt{\frac{c}{H}}(1-\cos\Omega) + \frac{\sigma\ell}{b}\sqrt{\frac{H}{g}}\left(1+\frac{c}{H}\right)\sin\Omega \\ &+ 2i\left(\sin\Omega + \frac{\sigma\ell}{b}\sqrt{\frac{c}{g}}\cos\Omega\right)\Bigg\} \end{aligned} \tag{4.2.48}$$

$$\Omega = \frac{\sigma\ell}{\sqrt{cg}}, \quad \text{and} \quad b = H - c\,.$$

The time factor $e^{-i\sigma t}$ is assumed. Discuss R vs $k\ell$ for $c/H = 0$ and for nonzero but small c/H.

Can you derive the same answer by just using the linearized long-wave approximation everywhere with some crude but physically plausible junction conditions?

4.3 Straight Depth Discontinuity — Oblique Incidence

Consider a plane wavetrain arriving at an angle θ_1 with respect to the depth discontinuity (Fig. 4.4). Let the y axis be the discontinuity and x be normal to it. The depths on two sides are h_1, $x < 0$ and h_2, $x > 0$, where $h_1 \neq h_2$ in general.

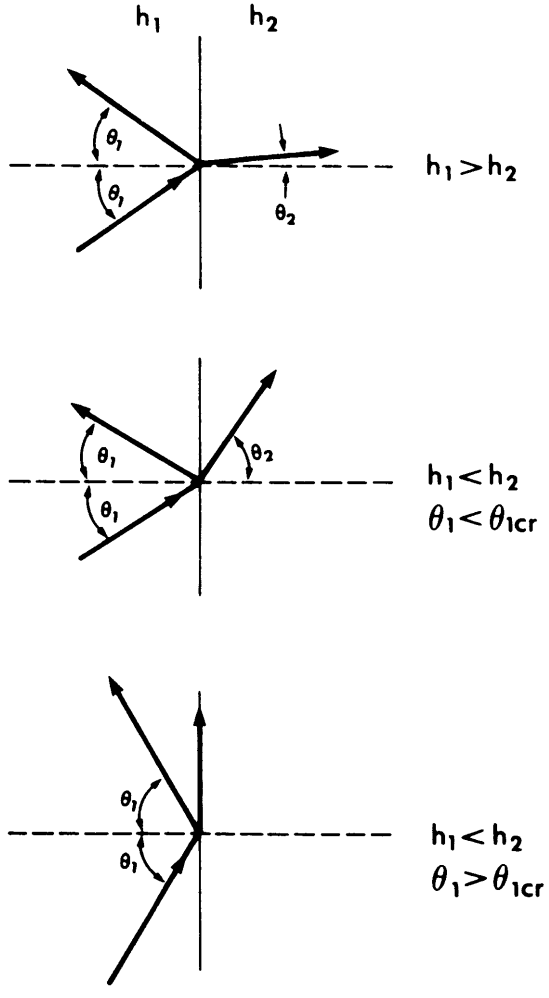

Figure 4.4: Directions of wave vectors at a step.

Let the incident wave come from $x \to -\infty$,

$$\eta_1 = Ae^{i(\alpha_i x+\beta y)} \quad \text{so that} \quad \alpha_1^2+\beta^2 = k_1^2\,. \tag{4.3.1}$$

The incident wavenumber vector is inclined at the angle

$$\theta_1 = \tan^{-1}(\beta/\alpha_1) \tag{4.3.2}$$

with respect to the x axis. The solutions should be of the following form:

$$\eta_1 = A(e^{i\alpha_1 x}+Re^{-i\alpha_1 x})e^{i\beta y}\,, \quad \alpha_1^2+\beta^2=k_1^2\,, \quad x<0\,, \tag{4.3.3}$$

$$\eta_2 = ATe^{i(\alpha_2 x+\beta y)}\,, \quad \alpha_2^2+\beta^2=k_2^2\,, \quad x>0\,, \tag{4.3.4}$$

so that on the left side there is a reflected wave toward the left, and on the right side a transmitted wave toward the right. The reflection and transmission coefficients R and T must be determined by matching the surface height and the volume flux at $x=0$. Substituting Eqs. (4.3.3) and (4.3.4) into Eqs. (4.2.8a) and (4.2.8b), we obtain

$$1+R=T\,, \tag{4.3.5a}$$

$$h_1(i\alpha_1 - Ri\alpha_1) = h_2 i\alpha_2 T\,. \tag{4.3.5b}$$

The solutions for R and T are formally the same as for normal incidence if we replace k_1 and k_2 by α_1 and α_2 in Eqs. (4.2.16) and (4.2.17), that is,

$$T = \frac{2\alpha_1 h_1}{\alpha_1 h_1+\alpha_2 h_2} \tag{4.3.6a}$$

$$R = \frac{\alpha_1 h_1-\alpha_2 h_2}{\alpha_1 h_1+\alpha_2 h_2}\,. \tag{4.3.6b}$$

Certain features of the solution deserve attention. The directions of the incident and transmitted waves are given by

$$\tan\theta_1 = \frac{\beta}{(k_1^2-\beta^2)^{1/2}} \tag{4.3.7}$$

and

$$\tan\theta_2 = \frac{\beta}{(k_2^2-\beta^2)^{1/2}}\,. \tag{4.3.8}$$

For $h_1 > h_2$, $k_1 < k_2$, hence $\theta_1 > \theta_2$. If the transmission side is the shallower of the two, the wavenumber vector of the transmitted wave is directed more closely to the x axis than to the incident wave vector. On the other hand,

if $h_1 < h_2$ so that the incident side is the shallower, then $\theta_1 < \theta_2$ and the transmitted wave turns away from the normal x axis. This result is just the phenomenon of refraction discussed in Chapter Two for slowly varying depth, and the transmitted wave may be called the refracted wave. For a fixed frequency, k_1 and k_2 are fixed by h_1 and h_2. If we increase β toward k_1 (i.e., increase the angle of incidence), a stage will be reached such that $k_2 = \beta$ because $k_2 < k_1$. At this stage, $\theta_2 = \pi/2$ and the transmitted wave propagates along the discontinuity ($\alpha_2 = 0$). The critical angle of incidence is

$$(\theta_1)_{\rm cr} = \tan^{-1}\frac{k_2}{\alpha_1} = \tan^{-1}\frac{k_2}{(k_1^2 - k_2^2)^{1/2}}\,. \tag{4.3.9}$$

Since $\alpha_2 = 0$, the reflection coefficient is $R = 1$; hence there is total reflection. The transmitted wave has crests parallel to the x axis with equal amplitude along the crests.

What happens when β increases further? $\alpha_2 = (k_2^2 - \beta^2)^{1/2}$ becomes imaginary, and $\tan\theta_2$ loses meaning. Let us go back to the original solution and rewrite $\alpha_2 = i\gamma_2$, $\gamma_2 = (\beta^2 - k_2^2)^{1/2}$ so that γ_2 is real and positive:

$$\eta_2 = a_1 T e^{-\gamma_2 x} e^{i\beta y}\,. \tag{4.3.10}$$

The general solution actually contains $e^{\gamma_2 x}$ and $e^{-\gamma_2 x}$; we take only $e^{-\gamma_2 x}$ for the bounded solution at $x \sim \infty$. Thus,

$$T = \frac{2\alpha_1 h_1}{\alpha_1 h_1 + i\gamma_2 h_2} \tag{4.3.11a}$$

$$R = \frac{\alpha_1 h_1 - i\gamma_2 h_2}{\alpha_1 h_1 + i\gamma_2 h_2}\,. \tag{4.3.11b}$$

Clearly $|R| = 1$, so that reflection is perfect. With Eqs. (4.3.11) the solution may be renormalized to give

$$\eta_1 = A\cos(\alpha_1 x + \delta)e^{i\beta y}\,, \tag{4.3.12}$$

$$\eta_2 = A\frac{\alpha_1 h_1}{(\alpha_1^2 h_1^2 + \gamma_2^2 h_2^2)^{1/2}} e^{-\gamma_2 x} e^{i\beta y}\,, \tag{4.3.13}$$

where δ is a phase angle

$$\tan\delta = \frac{\gamma_2 h_2}{\alpha_1 h_1}\,.$$

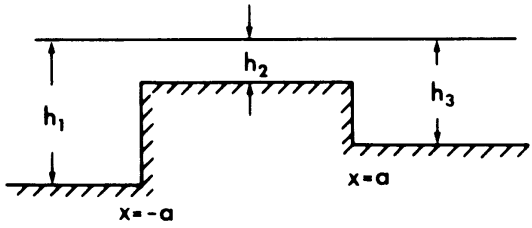

Figure 4.5: A submerged ridge.

This solution requires a new interpretation. On the deep side, $x > 0$, the transmitted wave propagates along the y axis with the amplitude exponentially attenuating away from the maximum at $x = 0$. The larger the angle β, the faster the attenuation.

4.4 Scattering by a Shelf or Trough of Finite Width[1]

Consider an ocean bottom with a stepwise variation of depth as shown in Fig. 4.5. An obliquely incident wave of unit amplitude arrives from $x \sim -\infty$. What are the effects of the finite size of the step?

The general solution over each flat region can be written

$$\eta_1 = e^{i\beta y}(e^{i\alpha_1(x+a)} + R'e^{-i\alpha_1(x+a)}), \quad x < -a, \tag{4.4.1}$$

$$\eta_2 = e^{i\beta y}(Ae^{i\alpha_2 x} + Be^{-i\alpha_2 x}), \quad -a < x < a, \tag{4.4.2}$$

$$\eta_3 = T'e^{i\beta y}e^{i\alpha_3(x-a)}, \quad x > a. \tag{4.4.3}$$

We may define

$$R = R'e^{-2i\alpha_1 a} \tag{4.4.4}$$

as the reflection coefficient, and

$$T = T'e^{-i(\alpha_1+\alpha_3)a} \tag{4.4.5}$$

as the transmission coefficient. The coefficients A, B, R', and T' must be found by matching η and $h\,\partial\eta/\partial x$ at the two edges.

[1]This problem is analogous to the problem of a square-well potential in quantum mechanics (see Bohm, 1951, p. 242ff).

Matching at $x = -a$, we get

$$1 + R' = Ae^{-i\alpha_2 a} + Be^{i\alpha_2 a} \tag{4.4.6}$$

and

$$\alpha_1 h_1(1 - R') = \alpha_2 h_2(Ae^{-i\alpha_2 a} - Be^{i\alpha_2 a}) , \tag{4.4.7}$$

whereas matching at $x = a$, we get

$$Ae^{i\alpha_2 a} + Be^{-i\alpha_2 a} = T' \tag{4.4.8}$$

and

$$\alpha_2 h_2(Ae^{i\alpha_2 a} - Be^{-i\alpha_2 a}) = \alpha_3 h_3 T' . \tag{4.4.9}$$

The simultaneous equations (4.4.6)–(4.4.9) remain to be solved. The bookkeeping may be simplified with the following new substitutions:

$$s_{\mu\nu} = \frac{\alpha_\mu h_\mu}{\alpha_\nu h_\nu} \quad \text{with} \quad \mu, \nu = 1, 2, 3 \text{ (no summation)} . \tag{4.4.10}$$

Equations (4.4.6)–(4.4.9) become

$$Ae^{-i\alpha_2 a} + Be^{i\alpha_2 a} = 1 + R' , \tag{4.4.11}$$

$$Ae^{-i\alpha_2 a} - Be^{i\alpha_2 a} = s_{12}(1 - R') , \tag{4.4.12}$$

$$Ae^{i\alpha_2 a} + Be^{-i\alpha_2 a} = T' , \tag{4.4.13}$$

$$Ae^{-i\alpha_2 a} - Be^{-i\alpha_2 e} = s_{32} T' . \tag{4.4.14}$$

From Eqs. (4.4.13) and (4.4.14) we can express A and B in terms of T' or T:

$$A = \frac{1}{2} T' e^{-i\alpha_2 a}(1 + s_{32}) , \tag{4.4.15}$$

$$B = \frac{1}{2} T' e^{i\alpha_2 a}(1 - s_{32}) . \tag{4.4.16}$$

Eliminating A and B from Eqs. (4.4.11) and (4.4.12), we can solve for R' and T':

$$R' = \frac{e^{-2i\alpha_2 a}[-(1 - s_{12})(1 + s_{32}) + (1 + s_{12})(1 - s_{32})e^{2i\alpha_2 a}]}{\Delta} , \tag{4.4.17}$$

$$T' = \frac{4s_{12}}{\Delta}\,, \tag{4.4.18}$$

where

$$\Delta = (1+s_{12})(1+s_{32})e^{-2i\alpha_2 a} - (1-s_{12})(1-s_{32})e^{2i\alpha_2 a}\,. \tag{4.4.19}$$

Finally, A and B can be obtained from Eqs. (4.4.15) and (4.4.16) with the help of Eq. (4.4.18).

For physical implications let us examine a special case where the depths on both sides of the step are equal, $h_1 = h_3$. We now have $\alpha_1 = \alpha_3$, so that

$$s_{12} = s_{32} = \frac{\alpha_1 h_1}{\alpha_2 h_2} \equiv s = \frac{h_1}{h_2}\left(\frac{\omega^2/gh_1 - \beta^2}{\omega^2/gh_2 - \beta^2}\right)^{1/2}\,. \tag{4.4.20}$$

Note that $s > 1$ if the center region is a shelf and $s < 1$ if it is a trough. The transmission and reflection coefficients are

$$T' = \frac{4s}{(1+s)^2 e^{-2i\alpha_2 a} - (1-s)^2 e^{2i\alpha_2 a}}\,, \tag{4.4.21}$$

$$R' = \frac{-(1-s^2)(e^{-i\alpha_2 a} - e^{i\alpha_2 a})}{(1+s)^2 e^{-2i\alpha_2 a} - (1-s)^2 e^{2i\alpha_2 a}}\,. \tag{4.4.22}$$

The energy of the transmitted and reflected waves are proportional to

$$\begin{pmatrix} |T'|^2 \\ |R'|^2 \end{pmatrix} = \begin{pmatrix} |T|^2 \\ |R|^2 \end{pmatrix} = \begin{pmatrix} 4s^2 \\ (1-s^2)^2 \sin^2 2\alpha_2 a \end{pmatrix} \times [4s^2 + (1-s^2)^2 \sin^2 2\alpha_2 a]^{-1}\,. \tag{4.4.23}$$

It is straightforward to show that $|R|^2 + |T|^2 = 1$, which means that the energy of the scattered waves is the same as the energy of the incident waves. An important physical feature is that $|R|^2$ and $|T|^2$ vary periodically with $2\alpha_2 a$. In particular, for $2\alpha_2 a = n\pi$, $n = 0, 1, 2, 3, \ldots$, that is, $4a/\lambda_2 = 0, 1, 2, 3, \ldots$, where $\lambda_2 = 2\pi/\alpha_2$, $|R|^2 = 0$, and $|T|^2 = 1$ so that there is total transmission and the shelf is transparent to the incident wave. Minimum transmission and maximum reflection occur when $\sin^2 2\alpha_2 a = 1$ or

$$2\alpha_2 a = \left(n - \frac{1}{2}\right)\pi\,, \quad n = 1, 2, 3, \ldots$$

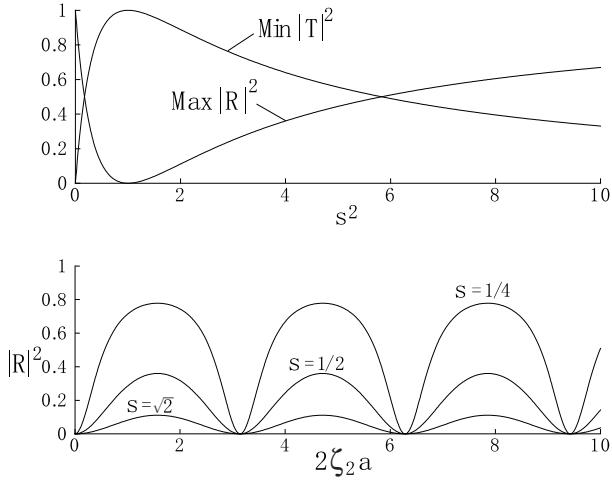

Figure 4.6: Properties of $|T|^2$ and $|R|^2$. Top: Effects of varying $s = \alpha_1 h_1/\alpha_2 h_2$. Bottom: Effects of varying $2\alpha_2 a$ for several s.

that is,

$$\frac{4a}{\lambda_2} = \frac{1}{2}, \frac{3}{2}, \frac{5}{2}, \ldots .$$

The corresponding values are

$$\min |T|^2 = \frac{4s^2}{(1+s^2)^2}\,, \tag{4.4.24}$$

$$\max |R|^2 = \frac{(1-s^2)^2}{(1+s^2)^2} \tag{4.4.25}$$

whose dependence on s^2 is shown in Fig. 4.6(a). The dependence of $|T|$ and $|R|$ on $2\alpha_2 a$ is oscillatory as shown in Fig. 4.6(b).

The wave on the shelf is obtained by substituting Eq. (4.4.21) into Eqs. (4.4.15) and (4.4.16) with $s_{12} = s_{32} = s$, that is,

$$A = \frac{1}{2}T'(1+s)e^{-i\alpha_2 a}\,, \quad B = \frac{1}{2}T'(1-s)e^{i\alpha_2 a} \tag{4.4.26}$$

and then into Eq. (4.4.2). Omitting the intermediate steps, we give the final result:

$$\eta_2 = \frac{2s[(1+s)e^{i\alpha_2(x-a)} + (1-s)e^{-i\alpha_2(x-a)}]}{(1+s)^2 e^{-2i\alpha_2 a} - (1-s)^2 e^{2i\alpha_2 a}} \tag{4.4.27}$$

so that the square of the envelope is

$$|\eta_2|^2 = \frac{4s^2[\cos^2 \alpha_2(x-a) + s^2 \sin^2 \alpha_2(x-a)]}{4s^2 + (1-s^2)^2 \sin^2 2\alpha_2 a}\,. \tag{4.4.28}$$

The free surface within $-a < x < a$ is composed of two wavetrains traveling in opposite directions, resulting in interference and a partially standing wave with amplitude varying along x. In particular, at the edge $x = a$,

$$|\eta_2|^2 = \frac{4s^2}{4s^2 + (1-s^2)^2 \sin^2 2\alpha_2 a}\,, \quad x = a \tag{4.4.29}$$

so that the interference is destructive, that is, $|\eta_2|^2$ is the smallest, when $2\alpha_2 a = (n-\frac{1}{2})\pi$, and constructive, that is, $|\eta_2|^2$ is the largest, when $2\alpha_2 a = n\pi$. Since the fluid at $x = a$ acts as a piston for the motion in the region of $x > a$, its amplitude of motion determines the amplitude of the transmitted wave.

The features of interference just deduced mathematically can also be explained physically. When a wave first strikes the edge at $x = -a$, part of the wave is transmitted into $-a < x < a$ and part is reflected. Upon reaching the edge at $x = a$, the transmitted wave undergoes the same scattering process, whereupon part of the wave is transmitted to $x > a$ and part is reflected toward the edge $x = 0$. This back-and-forth process of transmission and reflection is repeated indefinitely for all the waves of the periodic train. The total left-going wave in $x < -a$ is the sum of the reflected waves from $x = -a$ and all the transmitted waves from $-a < x < a$ to $x < -a$, whereas the total right-going wave in $x > a$ is the sum of all the transmitted waves from $-a < x < a$ to $x > a$. Now if $4a$ is an integral multiple of wavelength λ_2, each time a typical wave crest completes a round trip, being reflected from $x = a$ to $x = -a$ and back to $x = a$, its phase is changed by π twice. Therefore, all the crests which arrive at $x = a$ at the same time after different numbers of round trips $\ldots, -2, -1, 0, 1, 2, \ldots$ have the same phase; they interfere *constructively* and the total amplitude at $x = a$ is consequently the larger. On the other hand, if $4a$ is an odd multiple of half-wavelength $\lambda_2/2$, then after a round trip a typical wave crest is opposite in phase with the other crests which lag or lead by an odd number of round trips. This interference is *destructive*, resulting in the smallest net amplitude at $x = a$.

Furthermore, taking the x derivative of $|\eta_2|^2$, we find $\partial|\eta_2|^2/\partial x \propto \sin 2\alpha_2(x-a)$ so that the intensity $|\eta_2|^2$ is extremum at $2\alpha_2(x-a) = n\pi$,

that is, $x-a=\frac{1}{2}n\lambda_2$. It follows from Eq. (4.4.28) that the extremum values are

$$\text{Extr}\,|\eta_2|^2=\frac{4s^2}{4s^2+(1-s^2)^2\sin^2 2\alpha_2 a}\quad\text{if}\quad n=\text{even}\,,$$

and

$$\text{Extr}\,|\eta_2|^2=\frac{4s^2}{4s^2+(1-s^2)^2\sin^2 2\alpha_2 a}\quad\text{if}\quad n=\text{odd}\,.$$

In both cases the extremum values are the largest when $2\alpha_2 a$ are integer multiples of π. Thus, the peaks of T versus $2\alpha_2 a$ coincide with the peak response in the region $-a<x<a$.

Finally, we consider the limit of a short step $\alpha_2 a\downarrow 0$. By Taylor's expansion of Eq. (4.4.23), it follows that

$$|T|^2=1-\frac{(1-s^2)^2}{s^2}(\alpha_2 a)^2+O(\alpha_2 a)^4\,,$$

$$|R|^2=\frac{(1-s^2)^2}{s^2}(\alpha_2 a)^2+O(\alpha_2 a)^4\,.$$

Thus, a barrier much shorter than the wavelength is quite transparent to incident waves. In nature, real fluid effects introduce flow separation, hence dissipation, and change the above conclusion in important ways.

4.5 Transmission and Reflection by a Slowly Varying Depth

There are certain special depth profiles (linear, parabolic) for which analytical solutions are possible (Kajiura, 1961). The mathematics involved is straightforward but can be tedious. For slowly varying bottoms, it is possible to derive some general but approximate results which are physically revealing.

For a depth varying with the scale that is much longer than the local wavelength, the classical WKB approximation is a natural starting point. Assuming one-dimensional topography, that is, $h=h(x)$, the equation of motion is, from Eq. (4.1.26),

$$\frac{d}{dx}\left(gh\frac{d\eta}{dx}\right)+\omega^2\eta=0\,. \tag{4.5.1}$$

Consider a wave propagating in the positive x direction,

$$\eta = A(\bar{x})e^{iS(\bar{x})/\mu}\,, \tag{4.5.2}$$

where $\bar{x} = \mu x$ with μ being a small parameter characterizing the bottom slope. As in Section 2.1, we denote

$$k(\bar{x}) = \frac{1}{\mu}\frac{dS}{dx} = \frac{dS}{d\bar{x}}\,. \tag{4.5.3}$$

Substituting the derivatives of η into Eq. (4.5.1), we get

$$(-ghk^2 + \omega^2)A + \mu\left\{g\frac{dh}{d\bar{x}}ikA + gh\left[ik\frac{dA}{d\bar{x}} + ih\frac{d(kA)}{d\bar{x}}\right]\right\}$$
$$+ \mu^2\left(g\frac{dh}{d\bar{x}}\frac{dA}{d\bar{x}} + gh\frac{d^2A}{d\bar{x}^2}\right) = 0\,.$$

From $O(\mu^0)$ the dispersion relation follows

$$\frac{\omega^2}{g} = k^2 h\,, \tag{4.5.4}$$

while from $O(\mu)$ we have, after some simple manipulations,

$$\frac{d}{dx}(khA^2) = 0$$

so that

$$(khA^2) = \text{const} \equiv E_0^2 \equiv (khA^2)_{x\sim-\infty}\,. \tag{4.5.5}$$

In terms of E_0 the leading-order solution is

$$\eta = \frac{E_0}{(kh)^{1/2}}e^{iS/\mu} = \frac{E_0}{(kh)^{1/2}}\exp\left[\frac{i}{\mu}\int^{\bar{x}} k(\bar{x})\,d\bar{x}\right], \tag{4.5.6}$$

where E_0^2 is proportional to the energy flux of the wave incident from $x \sim -\infty$.

It is possible to superimpose waves traveling in both directions so that the general solution is

$$\eta \cong \frac{1}{(kh)^{1/2}}(E_0 e^{iS/\mu} + F_0 e^{-iS/\mu})\,, \tag{4.5.7}$$

where F_0^2 is proportional to the incident wave energy from the right,

$$F_0^2 = (khA^2)_{x\sim+\infty}\,.$$

The solution (4.5.6) or (4.5.7) gives no account of reflection. Extensions of the preceding analysis to weak reflection were developed in other physical contexts by Bremmer (1951) and others and applied to shallow-water waves by Ogawa and Yoshida (1959). For a very good summary see Kajiura (1961) or Wait (1962); their reasoning is followed here.

Beginning from the mass and momentum equations, it is convenient to define $uh = Q$ so that

$$i\omega\eta = \frac{dQ}{dx}\,, \tag{4.5.8}$$

$$i\omega Q = gh\frac{d\eta}{dx}\,. \tag{4.5.9}$$

From Eq. (4.5.7) the discharge to the leading order is given by

$$i\omega Q \cong ig(kh)^{1/2}(E_0 e^{iS/\mu} + F_0 e^{-iS/\mu})\,, \tag{4.5.10}$$

the omitted term being $O(\mu)$. We now follow Bremmer and replace E_0 and F_0 in Eqs. (4.5.7) and (4.5.10) with two unknown functions E and F, that is,

$$\eta = \frac{1}{(kh)^{1/2}}(Ee^{iS/\mu} + Fe^{-iS/\mu})\,, \tag{4.5.11}$$

$$i\omega Q = ig(kh)^{1/2}(Ee^{iS/\mu} - Fe^{-iS/\mu})\,, \tag{4.5.12}$$

which are now taken as the exact solution to Eqs. (4.5.8) and (4.5.9). Upon substitution we obtain a pair of equations governing E and F:

$$\frac{dE}{dx}e^{iS/\mu} - \frac{dF}{dx}e^{-iS/\mu} = -\frac{\mu}{(kh)^{1/2}}\frac{d(kh)^{1/2}}{d\bar{x}}(Ee^{iS/\mu} - Fe^{-iS/\mu})$$

and

$$\frac{dE}{dx}e^{iS/\mu} - \frac{dF}{dx}e^{-iS/\mu} = \frac{\mu}{(kh)^{1/2}}\frac{d(kh)^{1/2}}{d\bar{x}}(Ee^{iS/\mu} + Fe^{-iS/\mu})\,.$$

The derivatives dE/dx and dF/dx can be solved to give

$$\frac{dE}{dx} = \frac{\mu}{(kh)^{1/2}}\frac{d(kh)^{1/2}}{d\bar{x}}Fe^{-2iS/\mu}\,, \tag{4.5.13a}$$

$$\frac{dF}{dx} = \frac{\mu}{(kh)^{1/2}}\frac{d(kh)^{1/2}}{d\bar{x}}Ee^{2iS/\mu}\,, \tag{4.5.13b}$$

which are still exact. We now introduce the perturbation expansions

$$E = E_0 + \mu E_1 + \mu^2 E_2 + \cdots ,$$

$$F = F_0 + \mu F_1 + \mu^2 F_2 + \cdots .$$

Direct substitution yields

$$\frac{dE_0}{dx} = \frac{dF_0}{dx} = 0 ,$$

$$\frac{dE_{n+1}}{dx} = \left[\frac{d}{d\bar{x}} \ln(kh)^{1/2} \right] F_n e^{-2iS/\mu} ,$$

and

$$\frac{dF_{n+1}}{dx} = \left[\frac{d}{d\bar{x}} \ln(kh)^{1/2} \right] E_n e^{2iS/\mu} ,$$

which can be integrated to give

$$E_0 = \text{const} , \quad F_0 = \text{const} , \tag{4.5.14a}$$

$$E_{n+1} = \int_{-\infty}^{x} \left[\frac{d}{d\bar{x}} \ln(kh)^{1/2} \right] F_n e^{-2iS/\mu} \, dx , \tag{4.5.14b}$$

$$F_{n+1} = \int_{\infty}^{x} \left[\frac{d}{d\bar{x}} \ln(kh)^{1/2} \right] E_n e^{2iS/\mu} \, dx . \tag{4.5.14c}$$

The lower limits of integration are chosen such that

$$E_n(-\infty) = 0 , \quad F_n(\infty) = 0 , \quad n = 1, 2, 3, \ldots .$$

From now on the parameter μ may be set to unity and $\bar{x}$ restored to x. The solution is complete.

As a special case, let $F_0 = 0$ so that the incident wave is from left to right. Then,

$$E = E_0 + \mu E_1 + \mu^2 E_2 + \mu^3 E_3 + \cdots , \quad x \sim +\infty \tag{4.5.15}$$

represents the transmitted wave, while

$$F = \mu F_1 + \mu^2 F_2 + \cdots , \quad x \sim -\infty \tag{4.5.16}$$

represents the reflected wave. To $O(\mu)$ the reflection coefficient is

$$R_1 = \left(\frac{F_1}{E_0} \right)_{x \sim -\infty} = - \int_{-\infty}^{\infty} dx \left[\frac{d}{dx} \ln(kh)^{1/2} \right] e^{2iS/\mu} . \tag{4.5.17}$$

The integrals can be carried out by quadrature once ω and $h(x)$ are prescribed.

To gain some physical understanding let us assume that h differs slightly from a constant h_0,

$$h = h_0[1 + q(x)]\,, \quad q \ll 1\,, \tag{4.5.18}$$

then

$$\frac{\omega^2}{g} = k^2 h_0(1+q)$$

and

$$k = \frac{\omega}{(gh_0)^{1/2}}(1+q)^{-1/2} \cong k_0\left(1 - \frac{q}{2}\right)$$

so that

$$kh \cong k_0 h_0\left(1 + \frac{q}{2}\right).$$

Expanding the logarithm, we get

$$\frac{d}{dx}\ln(kh)^{1/2} \cong \frac{1}{4}\frac{dq}{dx}$$

and

$$\int_0^x k\,dx \cong k_0 x\,.$$

Thus, for small perturbations the reflection is approximately

$$R_1 = -\int_{-\infty}^{\infty} \frac{1}{4}\frac{dq}{dx} e^{2ik_0 x}\,dx\,. \tag{4.5.19}$$

Let us consider several special cases where the depth changes from one constant to another. If the depth changes discontinuously by an amount Δh_0, that is,

$$q = \Delta H(x)\,, \quad H(x) = \text{Heaviside function} \tag{4.5.20}$$

where $\delta \ll 1$, we have

$$R_1 = -\frac{1}{4}\Delta \tag{4.5.21}$$

which is constant. The above result can also be deduced as a limit of Eq. (4.2.17), even though a discontinuity is not consistent with the assumption of slow variation.

If the depth changes linearly from $x = -\frac{1}{2}L$ to $x = +\frac{1}{2}L$ by an amount Δ, then

$$q = \left(\frac{\Delta}{L}\right) x\,, \tag{4.5.22}$$

so that

$$R_1 = -\frac{\Delta}{4}\int_{-L/2}^{L/2} \frac{e^{ik_0 x}\,dx}{L} = -\frac{\Delta}{4}\frac{\sin k_0 L}{k_0 L} \tag{4.5.23}$$

which oscillates with $k_0 L$; the envelope diminishes as $k_0 L \to \infty$.

Finally, if the transition is infinitely smooth and can be represented by an error function of x, then

$$\frac{d}{dx}q = \frac{\Delta}{\pi^{1/2}L}e^{-x^2/L^2} \tag{4.5.24}$$

is Gaussian so that

$$R_1 = -\frac{\Delta}{4\pi^{1/2}L}\int_{-\infty}^{\infty} e^{-(x/L)^2}e^{2ik_0 x}\,dx = -\frac{\Delta}{4}e^{-k_0^2 L^2}\,. \tag{4.5.25}$$

Note that for this case R_1 diminishes exponentially in $(k_0 L)^2$.

The preceding examples differ from one another significantly in their rates of attenuation with respect to $k_0 L$; the smoother profile attenuates faster with increasing $k_0 L$. This fact can be proven more generally from Eq. (4.5.17) (Felsen and Marcuvitz, 1973). Let h, hence k also, be different from constant only within the range $x_1 < x < x_2$ with $x_2 - x_1 = L$. We rewrite Eq. (4.5.17)

$$R_1 = -\int_{x_1}^{x_2} e^{2iS}\frac{d}{dx}\ln(kh)^{1/2}\,dx\,.$$

If dh/dx is finite at the end points $x = x_1$, x_2 but d^2h/dx^2 is not, we can integrate by parts once to get

$$R_1 = -\left\{e^{2iS}\frac{1}{2ik}\left[\frac{d}{dx}\ln(kh)^{1/2}\right]\right\}_{x_1}^{x_2} + \int_{x_1}^{x_2} dx\, e^{2iS}\frac{d}{dx}\left\{\frac{1}{2ik}\left[\frac{d}{dx}\ln(kh)^{1/2}\right]\right\}.$$

From the integrated term above it is clear that $R_1 = O(k_0 L)^{-1}$, which agrees with Eq. (4.5.23). If d^2h/dx^2 is finite at the ends but d^3h/dx^3 is not, then the last integral above can be partially integrated once more to

give a term that is of the order $O(k_0L)^{-2}$. More generally, if d^nh/dx^n is finite at both ends, then $R_1 = O(k_0L)^{n-1}$. If the profile is infinitely smooth which implies that $x_1 \to -\infty$ and $x_2 \to \infty$, then R_1 decays faster than any algebraic power of k_0L_0.

The result that reflection depends strongly on the smoothness at two points invites mathematical curiosity, since such a local property can hardly be so influential from the physical standpoint. Indeed Eq. (4.5.25) implies that the reflection coefficient is transcendentally small for infinitely smooth topographies. In a highly mathematical paper, Meyer (1979b) abandoned the WKB approximation and showed the reflection coefficient to be of the form $\exp[-\alpha(k_0L)^{1/2}]$ instead for both a Gaussian ridge and a shelf of hyperbolic-tangent profile. Since the improvement is concerned only with a small quantity, we do not pursue the matter further here. The interested reader may consult Meyer's paper for details and references.

4.6 Trapped Waves on a Stepped Ridge

As shown in Section 4.3, certain sinusoidal waves may exist at a depth discontinuity, but are unable to propagate from shallow to deep water. Let us study what can happen on a shelf with two edges at a finite distance $2a$ apart. It will be found that *eigenfrequencies* exist which correspond to modes trapped over the shelf. These modes are analogous to the so-called *bound states* in a square-well potential in quantum mechanics and to *Love waves* in a layered elastic half-space. Indeed, the analyses of trapped long waves (Snodgrass, Munk, and Miller, 1962; Longuet–Higgins, 1967) can be borrowed from any standard treatise on quantum mechanics (e.g., Bohm, 1951).

Consider the geometry of Fig. 4.5 with $h = h_2$ over the ridge $-a < x < a$; the general solution is

$$\eta_2 = (Be^{i\alpha_2 x} + Ce^{-i\alpha_2 x})e^{i\beta y} \tag{4.6.1}$$

where $\alpha_2 = (k_2^2 - \beta^2)^{1/2}$. We are only interested in the solution which attenuates to zero at infinities on either side of the ridge; hence

$$\eta_1 = Ae^{\gamma_1(x+a)}e^{i\beta y}\,, \quad x < -a\,, \tag{4.6.2}$$

and

$$\eta_3 = De^{-\gamma_1(x-a)}e^{i\beta y}\,, \quad x > a\,, \tag{4.6.3}$$

where $\gamma_1 = (\beta^2 - k_1^2)^{1/2}$. It is assumed that

$$k_2 > \beta > k_1 \quad \text{or} \quad \beta(gh_1)^{1/2} > \omega > \beta(gh_2)^{1/2}\,. \tag{4.6.4}$$

The coefficients A, B, C, and D are as yet arbitrary. Continuity of η and $h\partial\eta/\partial x$ at $x = \pm a$ gives four conditions

$$A = Be^{-i\alpha_2 a} + Ce^{i\alpha_2 a}\,, \tag{4.6.5}$$

$$\gamma_1 h_1 A = i\alpha_2 h_2 (Be^{-i\alpha_2 a} - Ce^{i\alpha_2 a})\,, \tag{4.6.6}$$

$$D = Be^{i\alpha_2 a} + Ce^{-i\alpha_2 a}\,, \tag{4.6.7}$$

$$-\gamma_1 h_1 D = i\alpha_2 h_2 (Be^{i\alpha_2 a} - Ce^{-i\alpha_2 a})\,. \tag{4.6.8}$$

For a nontrivial solution the coefficient determinant of the simultaneous Eqs. (4.6.5)–(4.6.8) must vanish:

$$(\gamma_1 h_1 - i\alpha_2 h_2)^2 e^{-2i\alpha_2 a} - (\gamma_1 h_1 + i\alpha_2 h_2)^2 e^{2i\alpha_2 a} = 0 \tag{4.6.9}$$

which can be manipulated to give

$$\tan 2\alpha_2 a = \frac{2\gamma_1 h_1 \alpha_2 h_2}{(\alpha_2 h_2)^2 - (\gamma_1 h_1)^2}\,. \tag{4.6.10}$$

Let

$$\frac{\gamma_1 h_1}{\alpha_2 h_2} = \tan\delta\,, \tag{4.6.11}$$

then Eq. (4.6.10) becomes

$$\tan 2\alpha_2 a = \frac{2\tan\delta}{1 - \tan^2\delta} = \tan 2\delta\,,$$

hence

$$\delta = \frac{1}{2} n\pi + \alpha_2 a\,. \tag{4.6.12}$$

Taking the tangent of both sides of Eq. (4.6.12), we get

$$\tan\delta = \frac{\gamma_1 h_1}{\alpha_2 h_2} = \begin{pmatrix} \tan\alpha_2 a \\ -\cot\alpha_2 a \end{pmatrix}, \quad \begin{pmatrix} n = \text{even} \\ n = \text{odd} \end{pmatrix}, \tag{4.6.13}$$

or

$$\frac{h_1}{h_2}\frac{(\beta^2 - k_1^2)^{1/2}}{(k_2^2 - \beta^2)^{1/2}} = \begin{pmatrix} \tan(k_2^2 - \beta^2)^{1/2} a \\ -\cot(k_2^2 - \beta^2)^{1/2} a \end{pmatrix}, \quad \begin{pmatrix} n = \text{even} \\ n = \text{odd} \end{pmatrix}.$$

Since

$$k_2^2 = \frac{\omega^2}{gh_2} \quad \text{and} \quad k_1^2 = \frac{\omega^2}{gh_1} = \frac{h_2}{h_1}k_2^2\,,$$

Eq. (4.6.13) may be expressed in terms of k_2 alone,

$$\frac{h_1}{h_2}\frac{[\beta^2 - (h_2/h_1)k_2^2]^{1/2}}{(k_2^2-\beta^2)^{1/2}} = \begin{pmatrix} \tan(k_2^2-\beta^2)^{1/2}a \\ -\cot(k_2^2-\beta^2)^{1/2}a \end{pmatrix}, \quad \begin{pmatrix} n=\text{even} \\ n=\text{odd} \end{pmatrix}. \tag{4.6.14}$$

By the change of variables

$$\xi = a(k_2^2-\beta^2)^{1/2} = \alpha_2 a\,, \tag{4.6.15}$$

we obtain

$$a\left(\beta^2 - \frac{h_2}{h_1}k_2^2\right)^{1/2} = \left[k_2^2a^2\left(1-\frac{h_2}{h_1}\right) - \xi^2\right]^{1/2}$$

so that Eq. (4.6.14) becomes

$$\frac{(h_2/h_1)\xi}{(\xi_*^2-\xi^2)^{1/2}} = \begin{pmatrix} \cot\xi \\ -\tan\xi \end{pmatrix}, \quad \begin{pmatrix} n=\text{even} \\ n=\text{odd} \end{pmatrix}, \tag{4.6.16}$$

with

$$\xi_*^2 = k_2^2a^2\left(1-\frac{h_2}{h_1}\right) = \frac{(\omega a)^2}{gh_2}\left(1-\frac{h_2}{h_1}\right). \tag{4.6.17}$$

For a given ω and geometry, ξ_* is fixed; ξ is solved from Eq. (4.6.16), and the eigenwavenumber a_2 follows from Eq. (4.6.15). Let us consider odd and even n separately.

n odd: The eigenvalues can be found graphically and correspond to intersections of the curve $y_1 = \tan\xi$ with the curve

$$y_2 = -\frac{h_2}{h_1}\frac{\xi}{(\xi_*^2-\xi^2)^{1/2}}$$

as shown in Fig. 4.7(a). The $y_2(\xi)$ curve is odd in ξ, passes through the origin, and approaches $\pm\infty$ as ξ approaches $\pm\xi_*$.

From the same figure it is clear that the roots appear in pairs $\pm\xi_n$ and only $+\xi_n$ needs to be considered. For $\frac{1}{2}\pi < \xi_* < \frac{3}{2}\pi$ there is one mode with $\frac{1}{2}\pi < \xi_1 < \pi$. For $\frac{3}{2}\pi < \xi_* < \frac{5}{2}\pi$ there are two modes ξ_1 and ξ_3, with

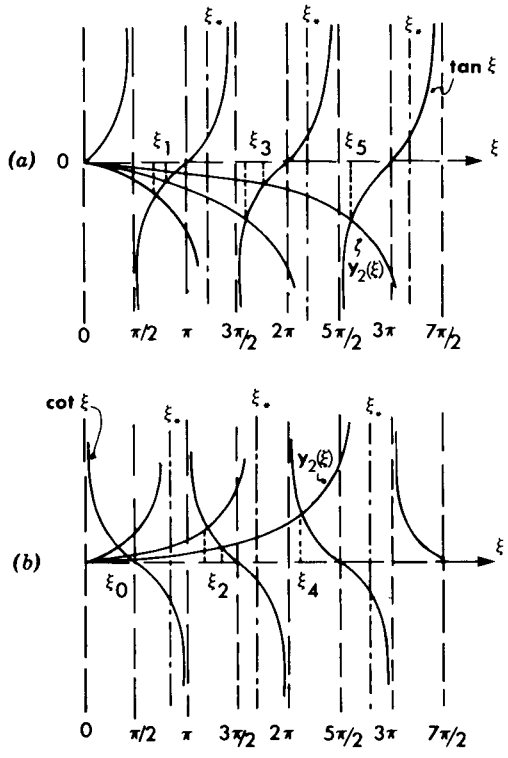

Figure 4.7: Graphic solution of eigenvalues: (a) odd n, (b) even n.

$\frac{3}{2}\pi < \xi_3 < 2\pi$. In general, if $(n - \frac{1}{2})\pi < \xi_* < (n + \frac{1}{2})\pi$, there are n modes $\xi_1, \xi_3, \ldots, \xi_{2n-1}$ (n odd) with the mth root in the range

$$\left(m - \frac{1}{2}\right)\pi < \xi_m < m\pi\,.$$

Thus, there is a new trapped mode for every increase of ξ_* by π, which can be achieved by increasing ωa or decreasing shelf depth h_2 for a fixed h_2/h_1.

n even: We need to examine the intersections of $y_1 = \cot\xi$ with

$$y_2 = \frac{h_2}{h_1}\frac{\xi}{(\xi_*^2 - \xi^2)^{1/2}}\,.$$

The intersections are shown in Fig. 4.7(b). For $0 < \xi_* < \pi$ there is one trapped mode, $\pm\xi_0$ with $0 < \xi_0 < \frac{1}{2}\pi$; for $\pi < \xi_* < 2\pi$ there are two modes

$\pm\xi_0$ and $\pm\xi_2$, with $\pi < \xi_2 < \frac{3}{2}\pi$. In general, for $(n+1)\pi > \xi_* > n\pi$ there are $n+1$ modes: $\xi_0, \xi_2, \ldots, \xi_{2n}$.

Summarizing, the roots ξ_n form a sequence $\xi_0 < \xi_1 < \xi_2 < \cdots$; the corresponding eigenwavenumbers also form an increasing sequence $\alpha_0 < \alpha_1 < \alpha_2 < \alpha_3 < \cdots$.

What are the free surfaces of these modes like? From Eqs. (4.6.5) and (4.6.6), we have

$$\frac{B}{C} = -e^{2i\alpha_2 a}\left(\frac{\gamma_1 h_1 + i\alpha_2 h_2}{\gamma_1 h_1 - i\alpha_2 h_2}\right) = -e^{2i\alpha_2 a}\frac{\tan\delta + i}{\tan\delta - i}$$

$$= e^{2i\alpha_2 a}\frac{\cos\delta - i\sin\delta}{\cos\delta + i\sin\delta} = e^{2i(\alpha_2 a - \delta)} = e^{in\pi}\,. \tag{4.6.18}$$

The last equality follows from Eq. (4.6.12). For n = even, $B = C$; from Eqs. (4.6.5) and (4.6.7), $A = D$, and the displacement is proportional to $\cos\alpha_2 x$, see Eqs. (4.6.1)–(4.6.3). Hence n = even corresponds to an even mode. Similarly, for n = odd, $B = -C$ and $A = -D$; the displacement is proportional to $\sin\alpha_2 x$ and odd in x. The first few modes are sketched in Fig. 4.8.

The even modes can be regarded alternatively as the trapped modes on an idealized continental shelf of width a with $x = 0$ being the coastline. As an approximate model for the California Shelf, Miles (1972) has taken $h_2 = 600$ m, $h_1 = 3600$ m, and $\xi_* = 2.19\pi$ which for $a = 70$ km

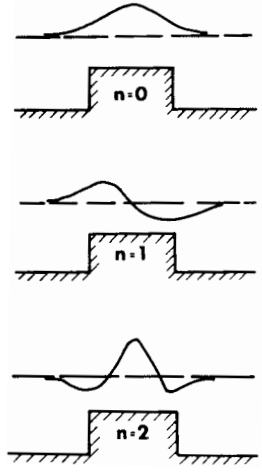

Figure 4.8: Trapped modes on a ridge.

corresponds to $T = 2\pi/\omega = 27.78$ min $= \frac{1}{6} \times 10^4$ s. The three trapped modes are at $\xi_0 \cong \frac{1}{2}\pi$, $\xi_2 \cong 1.45\pi$, and $\xi_4 \cong 2.15\pi$, so that $2\pi/\alpha_0 = 280$ km, $2\pi/\alpha_2 = 96$ km, and $2\pi/\alpha_4 = 65$ km, which can be important to resonate the so-called Helmholtz mode in a harbor, a subject to be discussed in the next chapter. For the same ω and β there is no solution that corresponds to imaginary γ_1; no propagation in the x direction is possible. It follows that trapped waves over an infinitely long ridge or shelf of finite width cannot be excited by sinusoidal incident waves according to linearized theory. However, excitation is possible by transient waves, wind stress, or on a ridge (or shelf) of finite length. Furthermore, nonlinear mechanisms of excitation cannot be ruled out.

Exercise 4.5: Waves Trapped in a Jet-Like Stream

In Chapter Three the presence of a variable current is seen to be similar to a variable depth in influencing waves. Examine shallow-water long waves in a strong current $U = 0$, $V = V(x)$, on a sea of variable depth $z = -h(x)$. Show that the equations for the wave perturbations are

$$\frac{\partial \zeta}{\partial t} + V\frac{\partial \zeta}{\partial y} + \frac{\partial uh}{\partial x} + h\frac{\partial v}{\partial y} = 0\,, \tag{4.6.19}$$

$$\zeta\frac{\partial \mathbf{u}}{\partial t} + V\frac{\partial \mathbf{u}}{\partial y} + u\frac{\partial V}{\partial x}\mathbf{e}_y = -g\nabla \tag{4.6.20}$$

where the current set-down is zero.

Assume

$$\begin{pmatrix} \zeta(x,y,t) \\ \mathbf{u}(x,y,t) \end{pmatrix} = \begin{pmatrix} \hat{\zeta}(x) \\ \hat{\mathbf{u}}(x) \end{pmatrix} e^{i(\beta y - \omega t)}\,, \tag{4.6.21}$$

and show that

$$(h\hat{\zeta}')' + \frac{2\beta V' h}{\omega - \beta V}\hat{\zeta}' + \left[\frac{(\omega - \beta V)^2}{g} - \beta^2 h\right]\hat{\zeta} = 0\,. \tag{4.6.22}$$

Thus, if $V(x) > 0$ within a finite strip $|x| < a$ and vanishes outside, and if $\beta < 0$ (waves oppose the current), waves satisfying the condition

$$\frac{\omega^2}{gh} < \beta^2 < \frac{(\omega - \beta V)^2}{gh} \tag{4.6.23}$$

will be trapped in the current.

For the special case where $h = \text{const}$ for all x, $V = \text{const}$ if $|x| < a$ and $V = 0$ if $|x| > a$, study the eigenvalues β of the trapped waves. Analyze also a scattering problem where $\beta^2 < \omega^2/gh$.

4.7 Some General Features of One-Dimensional Problems — Trapped Modes and the Scattering Matrix

4.7.1 A Qualitative Discussion of Trapped Waves

Let us discuss qualitatively the existence of trapped modes for a continuous one-dimensional topography $h = h(x)$. Substituting $\zeta = X(x)\exp[i(\beta y - \omega t)]$ into Eq. (4.1.5), we obtain

$$(hX')' + \left(\frac{\omega^2}{g} - \beta^2 h\right) X = 0\,. \tag{4.7.1}$$

The qualitative features may be studied in the so-called *phase plane* of X and Y, where Y is defined by

$$Y = hX' \quad \text{or} \quad X' = \frac{1}{h}Y\,. \tag{4.7.2}$$

Equation (4.7.1) may be written

$$Y' + \left(\frac{\omega^2}{g} - \beta^2 h\right) X = 0\,. \tag{4.7.3}$$

Division of Eq. (4.7.3) by Eq. (4.7.2) gives

$$\frac{dY}{dX} = \frac{-(\omega^2/g - \beta^2 h)X}{(1/h)Y} \tag{4.7.4}$$

which is a first-order equation in X and Y with x as the parameter. In the phase plane the solution to Eq. (4.7.4) is represented by a trajectory. Assume that $h(x)$ approaches a finite constant at infinity, that is,

$$h(x) \to h_\infty\,, \quad |x| \to \infty\,,$$

and assume further that

$$\beta^2 h_0 < \frac{\omega^2}{g} < \beta^2 h_\infty \tag{4.7.5}$$

so that there are two points (x_1, x_2) at which

$$\frac{\omega^2}{g} = \beta^2 h(x_l)\,, \quad l = 1, 2$$

(see Fig. 4.9). In the theory of differential equations, these two points are called the *turning points* on opposite sides of which the solution behaves

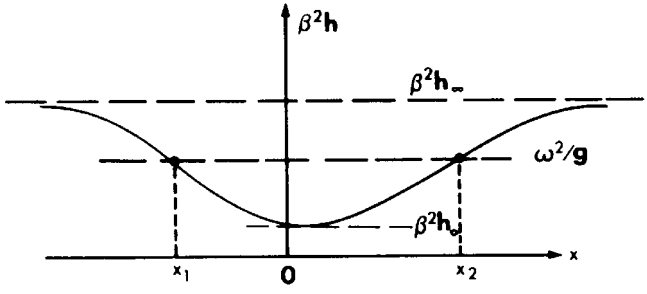

Figure 4.9: Variation of $\beta^2 h$ with x for a submarine ridge.

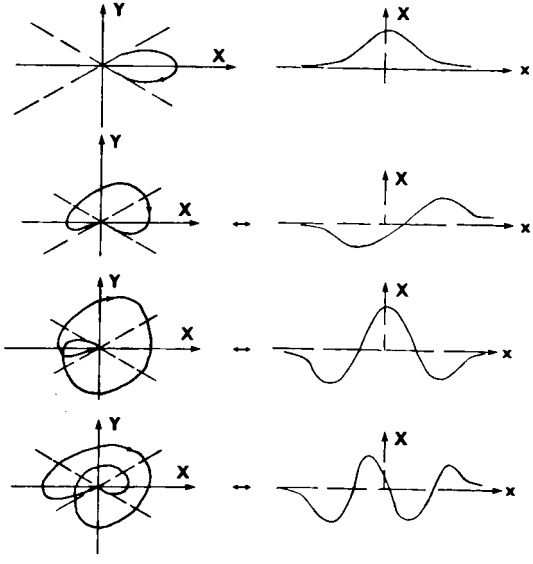

Figure 4.10: The solution trajectories in the phase plane (left) and the corresponding free surface (right) for the first few trapped modes. Dash lines in the phase planes are $Y = \pm H h_\infty^{1/2} x$. Arrows along the phase-plane curves show the direction of increasing x.

differently. In the ranges $x > x_2$ and $x < x_1$, the factor $h(\omega^2/g - \beta^2 h)$ is negative, and the solution $X(x)$ is monotonic in x. In particular, for large x

$$h\left(\beta^2 h - \frac{\omega^2}{g}\right) \to h_\infty\left(\beta^2 h_\infty - \frac{\omega^2}{g}\right) \equiv h_\infty H^2 > 0$$

so that $X \propto e^{-H|x|}$. In the phase plane the solution point (X, Y) approaches the origin as $x \to \mp\infty$ along the straight lines $Y = \pm H h_\infty^{1/2} X$ which are integrals of the limiting form of Eq. (4.7.4). Within the range $x_1 < x < x_2$, the coefficient $h(\omega^2/g - \beta^2 h)$ is positive and the solution $X(x)$ is in general oscillatory in x. The trajectory in the phase plane can wind around the origin and cross the X, Y axes. Several possible solutions are sketched in Fig. 4.10 for both the phase plane and the physical plane. Thus, a wavy surface exists only in the range (x_1, x_2) and decays exponentially outside it; this feature is precisely the characteristics of trapped waves. If $\omega^2/g > \beta^2 h_\infty$, there is no monotonic region and the entire fluid can have wave-like motion; waves are no longer trapped. If $\omega^2/g < \beta^2 h_0$, there is no periodic wave anywhere.

4.7.2 The Scattering Matrix $[S(\alpha)]$

Consider oblique incidence on a submarine ridge with $h(x) \to h_\infty$ as $|x| \to \infty$. We rewrite Eq. (4.7.1)

$$(aX')' + \left(\frac{\omega^2}{g h_\infty} - \beta^2 a\right) X = 0 \quad \text{with} \quad a(x) = \frac{h}{h_\infty}, \tag{4.7.6a}$$

or, since $\omega^2/g h_\infty = \alpha^2 + \beta^2$,

$$(aX')' + [\alpha^2 + \beta^2(1 - a)]X = 0 \tag{4.7.6b}$$

which is a Stürm–Liouville equation. By the transformation $X = a^{-1/2}\xi$, Eq. (4.7.6b) becomes the time-independent Schrödinger equation in quantum mechanics:

$$\xi'' + [\lambda - U(x)]\xi = 0$$

where

$$\lambda = -\beta^2, \quad -U = h^{-1}\left(\alpha^2 + \beta^2 + \frac{3}{4}\frac{h'^2}{h} - \frac{1}{2}\frac{h'}{h} - \frac{h''}{2}\right).$$

Many general properties of Schrödinger's equation are known in quantum scattering theory. We shall only discuss a few of these properties with

respect to Eq. (4.7.6). For a more extensive study reference should be made to Roseau (1952) and Sitenko (1971).

Let us consider a general scattering problem whose asymptotic behavior is

$$X \sim A_- e^{i\alpha x} + B_- e^{-i\alpha x}\,, \quad x \sim -\infty\,, \tag{4.7.7a}$$

$$\sim A_+ e^{i\alpha x} + B_+ e^{-i\alpha x}\,, \quad x \sim +\infty\,. \tag{4.7.7b}$$

Thus, A_- and B_+ correspond to the incoming waves from the left and the right, respectively, and A_+ and B_- correspond to the scattered waves toward the right and the left, respectively.

Let us also define $f_1(x,\alpha)$ to be the solution to the left-scattering problem

$$f_1(x,\alpha) \sim \frac{1}{T_1} e^{i\alpha x} + \frac{R_1}{T_1} e^{-i\alpha x}\,, \quad x \sim -\infty\,, \tag{4.7.8a}$$

$$\sim e^{i\alpha x}\,, \quad x \sim +\infty\,, \tag{4.7.8b}$$

and $f_2(x,\alpha)$ to be the solution to the right-scattering problem

$$f_2 \sim e^{-i\alpha x}\,, \quad x \sim -\infty\,, \tag{4.7.9a}$$

$$\sim \frac{1}{T_2} e^{-i\alpha x} + \frac{R_2}{T_2} e^{i\alpha x}\,, \quad x \sim +\infty\,. \tag{4.7.9b}$$

In quantum mechanics f_1 and f_2 are called *Jost functions*. Now f_1 and f_2 are linearly independent solutions since their Wronskian

$$W(f_1, f_2) \equiv f_1 f_2' - f_2 f_1' = -\frac{2i\alpha}{T_1} \quad (\text{from } x \sim -\infty)$$

$$= -\frac{2i\alpha}{T_2} \quad (\text{from } x \sim +\infty)$$

does not vanish in general. As a by-product the preceding equation implies at once

$$T_1 = T_2\,, \tag{4.7.10}$$

that is, the right and left transmission coefficients are equal even if $h(x)$ is not symmetrical. Also, due to the linear independence of f_1 and f_2 we may express X in Eqs. (4.7.7) as a linear combination,

$$X = Cf_1 + Df_2 \,. \tag{4.7.11}$$

Comparing the asymptotic values of Eqs. (4.7.11) and (4.7.7), we get

$$\frac{C}{T_1} = A_- \,, \quad C\frac{R_1}{T_1} + D = B_- \,,$$

$$C + D\frac{R_2}{T_2} = A_+ \,, \quad D\frac{1}{T_2} = B_+ \,.$$

A_+ and B_- may be solved by eliminating C and D,

$$A_+ = T_1 A_- + R_2 B_+ \,, \quad B_- = R_1 A_- + T_2 B_+$$

which may be expressed in matrix form:

$$\begin{pmatrix} A_+ \\ B_- \end{pmatrix} = [S] \begin{pmatrix} A_- \\ B_+ \end{pmatrix} \tag{4.7.12a}$$

with

$$[S] = \begin{bmatrix} T_1 & R_2 \\ R_1 & T_2 \end{bmatrix} . \tag{4.7.12b}$$

As before, $[S]$ is the *scattering matrix*, or S matrix, which is the generalization of Eqs. (4.2.13) and (4.2.15) for a very special depth profile.

4.7.3 Trapped Modes as Imaginary Poles of $[S(\alpha)]$

In the result for a rectangular shelf let us replace $\gamma_1 = -i\alpha_1$, so that the eigenvalue condition (4.6.9) becomes

$$(1+s)^2 e^{-2i\alpha_2 a} - (1-s)^2 e^{2i\alpha_2 a} = 0 \quad \text{with} \quad s = \frac{\alpha_1 h_1}{\alpha_2 h_2} \,.$$

In view of Eqs. (4.4.21) and (4.4.22) the above equation amounts to the vanishing of the denominators of R and T of the scattering problem, that is, the trapped modes correspond to the positive imaginary poles of R and T in the complex α plane. That the two physically different problems should be so connected mathematically arouses curiosity. We now give a general theory for arbitrary $h(x)$ as long as $h \to h_\infty$ when $|h| \to \infty$.

The Jost solutions $f_1(x,\alpha)$ and $f_1(x,-\alpha)$ are linearly independent since their Wronskian

$$W[f_1(x,\alpha), f_1(x,-\alpha)] = f_1(x,\alpha)f_1'(x,-\alpha) - f_1(x,-\alpha)f_1'(x,\alpha)$$
$$= -2i\alpha$$

does not vanish after using the asymptotic values at $x \sim +\infty$. Any solution such as $f_2(x,\alpha)$ can be expressed as a linear superposition of $f_1(x,\alpha)$ and $f_1(x,-\alpha)$. From the behavior at $x \sim \infty$, it is easy to see that

$$f_2(x,\alpha) = \frac{R_2}{T_2} f_1(x,\alpha) + \frac{1}{T_2} f_1(x,-\alpha)$$

or

$$T_2 f_2(x,\alpha) = R_2 f_1(x,\alpha) + f_1(x,-\alpha)\,. \tag{4.7.13}$$

Differentiating the preceding equation with respect to x, we have

$$T_2 f_2'(\alpha,x) = R_2 f_1'(x,\alpha) + f_1'(x,-\alpha)\,. \tag{4.7.14}$$

Let us solve T_2 and R_2 from Eqs. (4.7.13) and (4.7.14):

$$T_2 = -\frac{2i\alpha}{W\{f_1(x,\alpha), f_2(x,\alpha)\}}\,,$$

$$R_2 = \frac{W\{f_1(x,-\alpha), f_2(x,\alpha)\}}{W\{f_1(x,\alpha), f_2(x,\alpha)\}}\,.$$

If there are poles for T_2, they must correspond to the zeroes of

$$W\{f_1(x,\alpha), f_2(x,\alpha)\} = 0\,.$$

Let the poles be denoted by α_n. First, they must also be the poles of R_2, hence of $[S(\alpha)]$. Second, at these poles $1/T_2 = 0$ and $R_2/T_2 =$ finite so that f_2 behaves asymptotically as

$$f_2 \sim e^{-i\alpha_n x}\,, \quad x \sim -\infty\,,$$
$$\sim \left(\frac{R_2}{T_2}\right)_{\alpha_n} e^{i\alpha_n x}\,, \quad x \sim +\infty\,. \tag{4.7.15}$$

Assume that these poles are complex with positive imaginary parts so that f_2 decays exponentially to zero as $|x| \to \infty$, that is,

$$\alpha_n = \delta_n + i\gamma_n\,, \quad \gamma_n > 0\,.$$

From Eq. (4.7.6) it is simple to derive

$$[a(XX^{*\prime} - X^*X')]' = 2i(\operatorname{Im}\alpha^2)|X|^2\,. \tag{4.7.16}$$

Now letting $X = f_2$, integrating both sides of Eq. (4.7.16) from $-\infty$ to ∞, and using the exponential behavior at $|x| \to \infty$, we get

$$\operatorname{Im}\alpha_n^2 \int_{-\infty}^{\infty} |f_2|^2\, dx = 0$$

which implies

$$\operatorname{Im}\alpha_n^2 = 0 \quad \text{or} \quad \delta_n = 0\,. \tag{4.7.17}$$

Thus, the poles are purely imaginary and the trapped modes are *monotonically* decaying at large x.

For such an eigenvalue $\alpha_n = i\gamma_n$, the eigenfunction X may be taken to be real. Multiplying Eq. (4.7.6a) by X and integrating by parts, we get

$$\int_{-\infty}^{\infty} a(X')^2\, dx + \int_{-\infty}^{\infty} \left(\beta^2 a - \frac{\omega^2}{gh_\infty}\right) X^2\, dx = 0\,.$$

Since $(\beta^2 a - \omega^2/gh_\infty) \to (\beta^2 - \omega^2/gh_\infty) > 0$ as $x \to \pm\infty$, the above equality implies that $\beta^2 a - \omega^2/gh_\infty < 0$ for some range of x; otherwise X is trivially zero. The condition (4.7.5) for the existence of trapped modes is again confirmed.

4.7.4 Properties of $[S(\alpha)]$ for Real α

Returning to Eqs. (4.7.7) for the scattering problem, we now examine some other properties of the S matrix. Consider α to be real, then from Eqs. (4.7.6) and its complex conjugate, it can be shown that

$$a(XX^{*\prime} - X^*X') = \text{const}\,. \tag{4.7.18}$$

Equating the asymptotic values of the left-hand side at $x \sim -\infty$ and $x \sim +\infty$, we get

$$|A_+|^2 + |B_-|^2 = |A_-|^2 + |B_+|^2, \tag{4.7.19}$$

which states that the energy of the incoming waves equals the energy of the outgoing waves. In view of Eq. (4.7.12a), Eq. (4.7.19) may be written

$$|A_+|^2 + |B_-|^2 = \{A_+, B_-\} \begin{Bmatrix} A_+^* \\ B_-^* \end{Bmatrix}$$

$$= \{A_-, B_-\}[S]^T[S^*] \begin{Bmatrix} A_-^* \\ B_+^* \end{Bmatrix}$$

where $[S]^T$ is the transpose of $[S]$. It follows that

$$[S]^T[S^*] = I = \begin{bmatrix} 1 & 0 \\ 0 & 1 \end{bmatrix} \tag{4.7.20}$$

which is called the *unitary* property of the S matrix. By the definition of $[S]$, Eq. (4.7.20) implies

$$\begin{bmatrix} T_1 & R_1 \\ R_2 & T_2 \end{bmatrix} \begin{bmatrix} T_1^* & R_2^* \\ R_1^* & T_2^* \end{bmatrix} = \begin{bmatrix} 1 & 0 \\ 0 & 1 \end{bmatrix}, \tag{4.7.21}$$

which yields three independent relations:

$$|T_1|^2 + |R_1|^2 = 1 \tag{4.7.22a}$$

$$|T_2|^2 + |R_2|^2 = 1 \tag{4.7.22b}$$

$$T_1 R_2^* + R_1 T_2^* = 0\,. \tag{4.7.22c}$$

Equations (4.7.22a) and (4.7.22b) again represent energy conservation. Because of Eq. (4.7.10), Eq. (4.7.22c) implies that

$$|R_1| = |R_2|\,. \tag{4.7.23}$$

From Eqs. (4.7.7), the asymptotic behavior of the complex conjugate of X is

$$X^* \sim A_-^* e^{-i\alpha x} + B_-^* e^{i\alpha x}\,, \quad x \sim -\infty\,, \tag{4.7.24a}$$

$$\sim A_+^* e^{-i\alpha x} + B_+^* e^{i\alpha x}\,, \quad x \sim +\infty\,. \tag{4.7.24b}$$

By comparison with Eqs. (4.7.7) it is clear that A_-^*, B_-^*, A_+^*, and B_+^*, may be substituted for B_-, A_-, B_+, and A_+, respectively, so that Eq. (4.7.12a) may be written

$$\begin{Bmatrix} B_+^* \\ A_-^* \end{Bmatrix} = [S] \begin{Bmatrix} B_-^* \\ A_+^* \end{Bmatrix} \tag{4.7.25a}$$

or

$$\begin{Bmatrix} B_+ \\ A_- \end{Bmatrix} = [S^*] \begin{Bmatrix} B_- \\ A_+ \end{Bmatrix}. \tag{4.7.25b}$$

On the other hand, we rewrite the solution X [Eqs. (4.7.7)] as

$$X \sim B_- e^{i(-\alpha)x} + A_- e^{-i(-\alpha)x}, \quad x \sim -\infty, \tag{4.7.26a}$$

$$B_+ e^{i(-\alpha)x} + A_+ e^{-i(-\alpha)x}, \quad x \sim +\infty, \tag{4.7.26b}$$

which can be regarded as a problem with ω replaced by $(-\omega)$ and α replaced by $-\alpha$. Now B_- and A_+ are the incoming waves and A_- and B_+ are the outgoing waves. By analogy to Eq. (4.7.12), we get

$$\begin{Bmatrix} B_+ \\ A_- \end{Bmatrix} = [S(-\alpha)] \begin{Bmatrix} B_- \\ A_+ \end{Bmatrix}. \tag{4.7.27}$$

Upon comparing Eqs. (4.7.25b) and (4.7.27), we conclude that

$$[S^*(\alpha)] = [S(-\alpha)]. \tag{4.7.28}$$

In summary, Eq. (4.7.18), which is a consequence of Green's formula, has led to considerable information regarding the far fields. This approach will be further explored in Chapter Eight.

Exercise 4.6: A Channel with Changing Width

Consider a channel which has a varying cross section only in the finite part of x and approaches constant width and depth at infinities: $(b, h) \to (b_1, h_1)$ as $x \sim -\infty$, and $\to (b_2, h_2)$ as $x \to +\infty$. Let (R_1, T_1) and (R_2, T_2) be the left- and right-scattering coefficients, respectively. Show that

$$k_1 A_1 (1 - |R_1|^2) = k_2 A_2 |T_1|^2, \quad \text{where} \quad A_1 = b_1 h_1 \quad \text{and} \quad A_2 = b_2 h_2, \tag{4.7.29a}$$

$$\frac{T_1}{T_2} = \frac{k_1 A_1}{k_2 A_2}, \tag{4.7.29b}$$

and

$$|R_1| = |R_2| \tag{4.7.30a}$$

$$|T_1 T_2| = 1 - |R_2|^2 \,. \tag{4.7.30b}$$

4.8 Edge Waves on a Constant Slope

As a special case of continuous depth variation we consider a straight and long beach with constant slope (Eckart, 1951). Let the mean shoreline coincide with the y axis, and let water be in the region $x > 0$. The bottom is described by

$$z = -h = -sx \,, \quad x > 0, \; s = \text{const} \,. \tag{4.8.1}$$

Because the coefficients are constant in y and t, we try the solution

$$\zeta = \eta(x) e^{i(\beta y - \omega t)} \,. \tag{4.8.2}$$

Equation (4.1.9) then gives

$$x\eta'' + \eta' + \left(\frac{\omega^2}{sg} - \beta^2 x \right) \eta = 0 \,. \tag{4.8.3}$$

By the following transformation

$$\xi = 2\beta x \,, \quad \eta = e^{-\xi/2} f(\xi) \,. \tag{4.8.4}$$

Eq. (4.8.3) may be rewritten

$$\xi f'' + (1 - \xi) f' + \left[\frac{\omega^2}{2\beta sg} - \frac{1}{2} \right] f = 0 \tag{4.8.5}$$

which belongs to the class of confluent hypergeometric equations (more specifically Kummer's equation, see Abramowitz and Stegun, 1972). In general, there are two homogeneous solutions, one of which is singular at the shoreline $\xi = 0$ and must be discarded. Nontrivial solutions which render η finite at $\xi = 0$ and zero as $\xi \to \infty$ exist when ω corresponds to the following discrete values:

$$\frac{\omega^2}{2\beta sg} = n + \frac{1}{2} \,, \quad n = 0, 1, 2, 3, \ldots \,. \tag{4.8.6}$$

The associated eigenfunctions are proportional to Laguerre polynomials

$$L_n(\xi) = \frac{(-)^n}{n!}\left[\xi^n - \frac{n^2}{1!}\xi^{n-1} + \frac{n^2(n-1)^2}{2!}\xi^{n-2} - \frac{n^2(n-1)^2(n-2)^2}{3!}\xi^{n-3} + \cdots + (-)^n n!\right]; \qquad (4.8.7)$$

for example, $L_0 = 1$, $L_1 = 1-\xi$, $L_2 = 1-2\xi+\frac{1}{2}\xi^2$, and so on. The first few modes are plotted in Fig. 4.11 with the higher mode attenuating faster in the offshore direction. Because these eigenfunctions correspond to modes that are appreciable only near the shore, they are called *edge waves*. These eigenfunctions are orthonormal in the following sense:

$$\int_0^\infty e^{-\xi} L_n L_m d\xi = \delta_{nm}\,. \qquad (4.8.8)$$

For $m = n$ Eq. (4.8.8) implies that each mode has a finite energy.

Edge waves are of interest in coastal oceanography because the largest amplitude, hence the largest run-up, occurs at the shore. They are also believed to be responsible for rip currents near the shore when the shorter

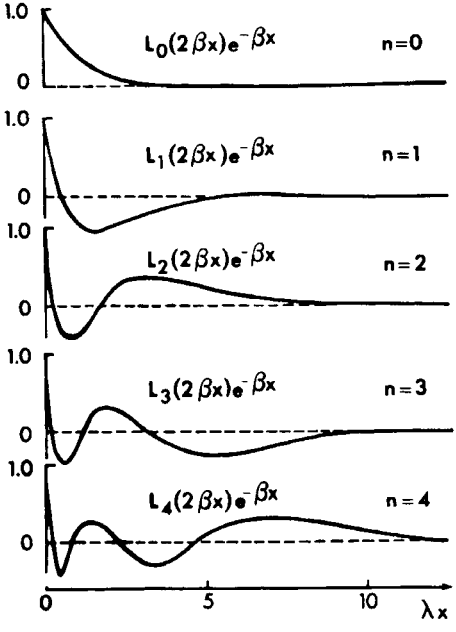

Figure 4.11: Profiles of some edge wave modes.

breaking waves are present. For large beach angles, similar edge waves were discovered by Stokes (1847); the complete edge- wave spectrum which includes both discrete and continuous parts was discovered by Ursell (1952).

Several mechanisms for generating edge waves are possible in nature. On a large scale (typical wavelength 200 miles, period 6 h, amplitude 3 ft) edge waves can be excited by wind stress directly above the water. Munk, Snodgrass, and Carrier (1956) and Greenspan (1958) have studied the effect of pressure deviation in a storm traveling parallel to the coast; their results are relevant to storm surges. Smaller-scale edge waves can be excited by a nonlinear mechanism of subharmonic resonance (Guza and Bowen, 1976; Minzoni and Whitham, 1977) as will be discussed in Chapter Twelve. Medium-scale edge waves of periods 1–5 min can also be excited by a long group of short swells through a nonlinear mechanism, which will be further commented on in Chapter Thirteen.

4.9 Circular Bottom Contours

4.9.1 General Aspects

Next in complexity to straight and parallel contours is the topography with concentric circular contours. In polar coordinates (r, θ), $h = h(r)$, the long-wave equation becomes

$$\nabla^2 \eta + \frac{h'}{h}\frac{\partial \eta}{\partial r} + \frac{\omega^2}{gh}\eta = 0\,, \tag{4.9.1}$$

with

$$\nabla^2 = \frac{\partial^2}{\partial r^2} + \frac{1}{r}\frac{\partial}{\partial r} + \frac{1}{r^2}\frac{\partial^2}{\partial \theta^2}\,. \tag{4.9.2}$$

Let us consider, for integer n,

$$\eta = R(r)e^{i(n\theta - \omega t)} \tag{4.9.3}$$

so that R satisfies

$$R'' + \left(\frac{1}{r} + \frac{h'}{h}\right)R' + \left(\frac{\omega^2}{gh} - \frac{n^2}{r^2}\right)R = 0 \tag{4.9.4}$$

or

$$(hrR')' + \left(\frac{\omega^2}{g} - \frac{n^2 h}{r^2}\right) rR = 0\,. \tag{4.9.4'}$$

Now the behavior of R will be exponential or oscillatory according to

$$\frac{\omega^2}{gn^2} \gtrless \frac{h}{r^2}: \quad \begin{matrix}\text{oscillatory} \\ \text{exponential}\end{matrix}\,. \tag{4.9.5}$$

Consider a submerged island with monotonically increasing h, $0 < h(0) < h(r) < h(\infty)$. For a fixed n, h/r^2 behaves as shown in Fig. 4.12. The solution is oscillatory outside a critical circle $r = r_0$ where

$$\frac{\omega^2}{g} = \left(\frac{n^2 h}{r^2}\right), \quad r = r_0\,. \tag{4.9.6}$$

In comparison with one-dimensional topography, the factor $1/r^2$ drastically changes the situation and perfect trapping is no longer possible.

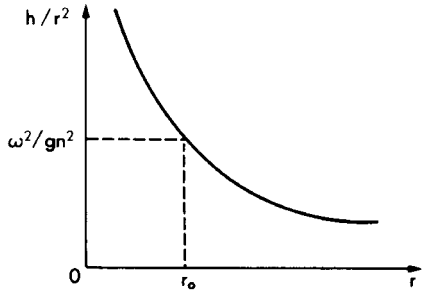

Figure 4.12: h/r^2 versus r for a submerged island.

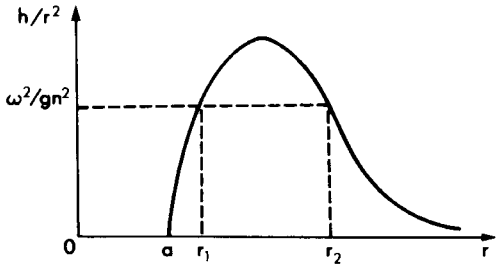

Figure 4.13: h/r^2 versus r for an island with shoreline radius a.

Consider an island with a shore at $r = a$ so that $h(r) = 0$ for $0 < r < a$ and increases monotonically for $r > a$. Then $n^2 h/r^2$ behaves as shown in Fig. 4.13. For $\omega^2/gn^2 < \max(h/r^2)$, the free surface is oscillatory near the shore $a < r < r_1$, exponentially attenuating in the region $r_1 < r < r_2$, and oscillatory again outside ($r > r_2$). Therefore, the island slope acts as a barrier of finite thickness to trap waves of sufficiently low frequency, or waves of fixed ω but sufficiently large n. For a large n, the barrier appears thicker and is more effective in trapping energy, which means less energy leakage. These facts have important consequences on the resonance of trapped waves over a submarine seamount by externally incident waves.

Longuet–Higgins (1967) considered a special example of a stepped circular sill where

$$\begin{aligned} h &= h_1\,, \quad 0 < r < a \\ &= h_2\,, \quad r > a \quad \text{with} \quad \frac{h_1}{h_2} < 1 \end{aligned} \tag{4.9.7}$$

as shown in Fig. 4.14(a). The variation of h/r^2 is shown in Fig. 4.14(b). For sufficiently low ω or high n there is also an annular region $r_1 < r < a$ over the sill where oscillations occur. This annulus of oscillations surrounds a central core of monotonic motion ($0 < r < r_1$) and is separated from the oscillating ocean ($r > r_2$) by a barrier $a < r < r_2$. If h_1/h_2 is very small, the barrier is high so that trapping is very effective, though still imperfect, and resonance of higher modes near the edge over the sill can be severe.

This mechanism of energy trapping is of practical interest in offshore engineering where geological conditions may dictate the site of construction to be on a seamount. The inherent danger of such a site is not always evident to the designer. During a tour of a Texas tower on Brown's Bank, off the east coast of the United States, a party of inspectors, caught by a Nor'easter, saw the storm waves moving the iron collars up and down the piles by as much as 100 ft and threatening to break up the structure. These collars weighed several tons each and were installed to protect the feet of the piles. This phenomenon was believed to be an evidence of the resonant mechanism discussed here (Meyer, 1970).

In the following subsection, we describe further details of Longuet–Higgins' example for which the analytical solution is relatively simple. For other smooth circular topographies, a WKB approximation is possible. However, for still more general two-dimensional topography, numerical methods are inevitable.

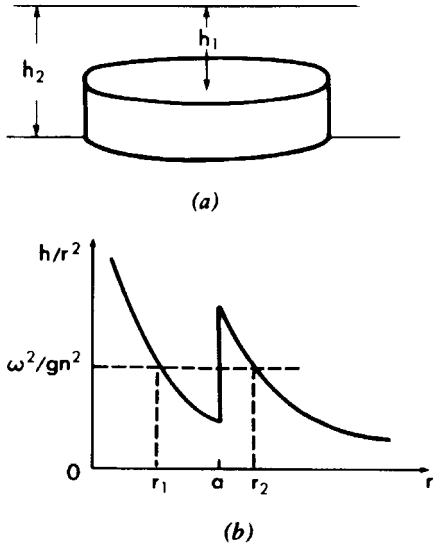

Figure 4.14: A submerged circular sill: (a) geometry; (b) h/r^2 versus r.

4.9.2 Scattering of Plane Incident Waves by a Circular Sill

Consider the circular sill as shown in Fig. 4.14. The top of the sill is at the depth $z = -h_2$. The adjacent water is assumed to be of constant depth h_1. For simple harmonic waves with frequency ω, the wavenumber is $k_2 = \omega/(gh_2)^{1/2}$ in the region above the sill $r < a$ and is $k_1 = \omega/(gh_1)^{1/2}$ around the sill $r > a$. Let the incident wave approach from $x \sim -\infty$ with unit amplitude so that

$$\eta^I = e^{ik_1 x}\,. \tag{4.9.8}$$

In the region $r > a$, there must be radiated (scattered) waves which propagate away to $r \sim \infty$. Hence if

$$\eta_1 = \eta^I + \eta^R\,, \tag{4.9.9}$$

η^R must satisfy, in polar coordinates,

$$\nabla^2\eta^R + k_1^2\eta^R = \frac{1}{r}\frac{\partial}{\partial r}\left(r\frac{\partial\eta^R}{\partial r}\right) + \frac{1}{r^2}\frac{\partial^2\eta^R}{\partial\theta^2} + k_1^2\eta^R = 0 \tag{4.9.10}$$

and must be outgoing as $r \to \infty$. Above the sill the displacement satisfies

$$\nabla^2\eta_2 + k_2^2\eta_2 = \frac{1}{r}\frac{\partial}{\partial r}\left(r\frac{\partial\eta_2}{\partial r}\right) + \frac{1}{r^2}\frac{\partial^2\eta_2}{\partial\theta^2} + k_2^2\eta_2 = 0\,. \tag{4.9.11}$$

At the edge of the sill $r = a$, the pressure and the flux must be matched:

$$\eta_1 = \eta_2\,, \qquad r = a\,. \tag{4.9.12}$$

$$h_1\frac{\partial\eta_1}{\partial r} = h_2\frac{\partial\eta_2}{\partial r}\,, \tag{4.9.13}$$

By separation of variables, it is easy to show that the general solution to Eqs. (4.9.10) and (4.9.11) must consist of linear combinations of Bessel functions, that is,

$$\eta_R \sim \cos n\theta[J_n(k_1r), Y_n(k_1r)]\,,$$

$$\eta_2 \sim \cos n\theta[J_n(k_2r), Y_n(k_2r)]\,.$$

In Appendix 4.A it will be shown that the incident wave can be expanded as a series of *partial waves*, each with an angular dependence of $\cos n\theta$, $n = 0, 1, 2, \ldots$,

$$e^{ikx} = e^{ikr\cos\theta} = \sum_0^\infty \varepsilon_n(i)^n \cos n\theta J_n(kr) \tag{4.9.14}$$

where ε_n are the Jacobi symbols defined by $\varepsilon_0 = 1$, $\varepsilon_n = 2$, for $n = 1, 2, \ldots$.

We propose the following solution for η:

$$\eta_1 = \sum_0^\infty \varepsilon_n(i)^n \cos n\theta[J_n(k_1r) + B_nH_n^{(1)}(k_1r)]\,, \quad r > a\,, \tag{4.9.15}$$

$$\eta_2 = \sum^\infty \varepsilon_n(i)^n \cos n\theta[A_nJ_n(k_2r)]\,, \quad r < a\,, \tag{4.9.16}$$

where A_n and B_n are to be determined. In Eq. (4.9.16) only J_n's have been kept to ensure boundedness at the center $r = 0$. In Eq. (4.9.15), only $H_n^{(1)}$'s have been kept so that the scattered waves are outgoing. Since $H_n^{(2)}$ is never used here, we shall omit the superscript on the Hankel functions and write simply

$$H_n(k_2r) \equiv H_n^{(1)}(k_2r)\,. \tag{4.9.17}$$

The coefficients A_n and B_n must be chosen so that the matching conditions at $r = a$, Eqs. (4.9.12) and (4.9.13), are satisfied; thus

$$A_n J_n(k_2 a) = J_n(k_1 a) + B_n H_n(k_1 a)\,,$$

$$k_2 h_2 A_n J_n'(k_2 a) = k_1 h_1 [J_n'(k_1 a) + B_n H_n'(k_1 a)]\,,$$

where primes denote derivations with respect to the argument.

In terms of

$$s = \frac{k_2 h_2}{k_1 h_1} \quad \left(= \left(\frac{h_2}{h_1} \right)^{1/2} = \frac{k_1}{k_2} \right), \quad \upsilon = k_2 a\,, \tag{4.9.18}$$

the solutions for A_n and B_n are

$$A_n = \frac{-[J_n(s\upsilon) H_n'(s\upsilon) - J_n'(s\upsilon) H_n(s\upsilon)]}{\Delta_n} = \frac{-2i}{\pi s \upsilon \Delta_n} \tag{4.9.19a}$$

and

$$B_n = \frac{J_n(\upsilon) J_n'(s\upsilon) - s J_n'(\upsilon) J_n(s\upsilon)}{\Delta_n}\,, \tag{4.9.19b}$$

where

$$\Delta_n \equiv -J_n(\upsilon) H_n'(s\upsilon) + s J_n'(\upsilon) H_n(s\upsilon)\,. \tag{4.9.19c}$$

Use has been made of the Wronskian identity:

$$J_n(\zeta) H_n'(\zeta) - J_n'(\zeta) H_n(\zeta) = \frac{2i}{\pi \zeta} \tag{4.9.20}$$

which may be verified by writing the Bessel equation in Stürm–Liouville form and by using the asymptotic behavior of J_n and H_n. When Eqs. (4.9.19a)–(4.9.19c) are substituted into Eqs. (4.9.15) and (4.9.16), the solution for η is fully determined.

The modal responses over the sill have been calculated by Longuet–Higgins (1967), as shown in Fig. 4.15. Note that for the lowest mode $n = 0$, the resonant amplification ratio is nearly 8, while increasing n leads to much higher and sharper resonant peaks. Of course, the narrowness of a peak implies that the corresponding mode is difficult to excite unless the incident wavetrain is precisely tuned. If the tuning is good, then a weak but persistent incident wave can cause a large response. This feature can also be anticipated from Fig. 4.14 where a larger n leads to a thicker outer barrier which makes it hard to acquire energy from the incident waves. On the other hand, once the energy is trapped within the outer barrier, it does not escape easily. These features have further ramifications in the

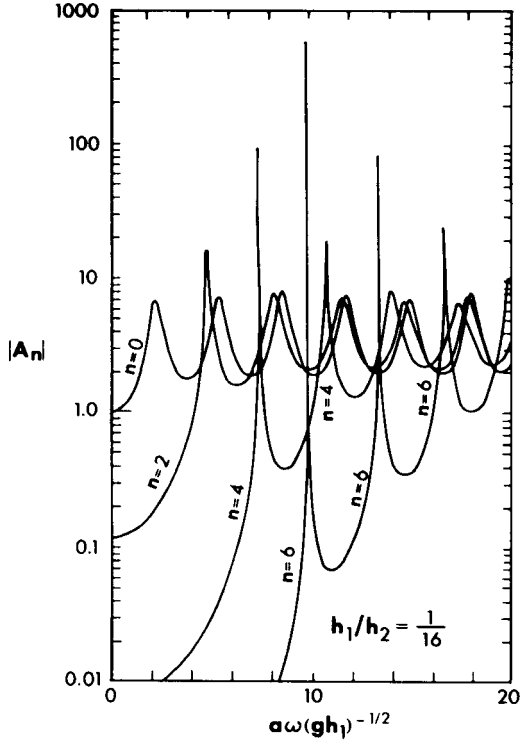

Figure 4.15: Graph of A_n for $h_1/h_1 = 1/16$ and $n = 0$, 2, 4, and 6, giving the amplitude of the response as a function of the frequency of the incident wave (from Longuet–Higgins, 1967, *J. Fluid Mech.* Reproduced by permission of Cambridge University Press).

transient excitation by short-lived incident waves,[2] as will be described in Chapter Five for the similar problem of harbor resonance. The large numerical values of some of the amplification factors suggest that nonlinear and/or frictional effects may also be important near these resonant peaks, when the incident waves are steady.

Exercise 4.7: Scattering by a Circular Platform

A large circular platform of radius R is fixed on the mean free surface $z = 0$ in a shallow sea of constant mean depth h. A plane incident wave of long period ω arrives from $x \sim \infty$. Find the scattered waves and the

[2]Longuet–Higgins (1967) studied the special case of an impulsive incident wave proportional to $\delta(x - (gh_1)^{1/2}t)$.

hydrodynamic pressure under the platform. Impose crude but physically reasonable junction conditions at $r = R$.

4.10 Head-Sea Incidence on a Slender Topography — The Parabolic Approximation

Before embarking on a general numerical method, let us describe the approximate analysis of a slender island or a sill attacked by waves incident along the longitudinal axis of the topography (head-sea incidence). A crucial aspect of this method was originated in electromagnetics and has been further developed in acoustics (see Tappert, 1977, for a review). The present adaptation is based on the work of Mei and Tuck (1980) and the critical appraisal by Bigg (1982). Similar ideas have also been extended to deep-water waves (Haren and Mei, 1981) and to weakly nonlinear waves (Yue and Mei, 1980, see Section 12.8).

Consider first an island with vertical sides in a shallow sea of constant depth h. The length L of the island is assumed to be much greater than the half-breadth B and the incident wavelength $2\pi/k$, namely,

$$\frac{B}{L} = \mu \ll 1 \quad \text{and} \quad kL = \omega L(gh)^{-1/2} \gg 1\,. \tag{4.10.1}$$

For head-sea incidence on a slender obstacle, the waves should roughly remain propagating forward with the amplitude modulated slowly in both horizontal directions, that is,

$$\eta(x, y) = A(x, y)e^{ikx} \tag{4.10.2}$$

where A varies slowly in x and y. Substituting Eq. (4.10.2) into (4.1.11), we get

$$2ikA_x + A_{yy} + A_{xx} = 0\,. \tag{4.10.3}$$

Now the length scale of A along x is L, $2ikA_x/A_{xx} = O(kL)$, hence A_{xx} is of secondary importance. In order to get something nontrivial, we retain A_{yy}; the implied length scale along y is then $O[L(kL)^{-1/2}]$. Let us introduce the *outer* length scales as follows:

$$X = \frac{x}{L}\,, \quad Y = y/(\mu^{\alpha/2}L)\,, \tag{4.10.4}$$

and express

$$\eta = A(X,Y)e^{iKX\mu^{-\alpha}} \tag{4.10.5}$$

with $kL = K\mu^{-\alpha}$ and $K = O(1)$; the leading order approximation to Eq. (4.10.3) is

$$2iKA_X + A_{YY} = 0 \tag{4.10.6}$$

with a relative error $O(\mu^\alpha)$. This equation is called the *parabolic approximation* and the region defined by Eq. (4.10.4) will be referred to as the parabolic region. Because of the resemblance to the heat equation, the following initial and boundary conditions

$$A = 1 \quad x = 0,\ |y| < \infty\,, \tag{4.10.7}$$

$$A \to 1 \quad x > 0,\ |y| \uparrow \infty \tag{4.10.8}$$

are natural, where the incident wave amplitude has been taken to be unity. The usual radiation condition is relevant to the region where $O(x,y) = L$ which lies outside the parabolic region, however.

Assuming symmetry about the x axis, we need be concerned only with the side $y > 0$. The no-flux condition on the island wall then requires

$$\frac{\partial \eta}{\partial y} = \frac{dW}{dx}\frac{\partial \eta}{\partial x} \quad \text{on} \quad y = W(x)\,. \tag{4.10.9}$$

Letting

$$W(x) = Bb(x)\,, \quad 0 < b < 1 \tag{4.10.10}$$

and using Eq. (4.10.5), we get, in terms of the normalized variables,

$$\frac{\partial A}{\partial Y} = iK\mu^{1-\alpha/2}b'A\,, \quad \text{on} \quad Y = \mu^{1-\alpha/2}b(x) \tag{4.10.11}$$

with a relative error of $O(\mu^\alpha)$. With $\alpha = 2$, both sides of Eq. (4.10.11) are balanced

$$\frac{\partial A}{\partial Y} = iKb'A \quad \text{on} \quad Y = b(x)\,. \tag{4.10.12}$$

The initial-boundary-value problem as defined by Eqs. (4.10.6), (4.10.7), (4.10.8) and (4.10.12) can be solved in general by numerical methods for heat conduction in one dimension (Y). Here X plays the role of time, and the computation marches forward in X over discrete steps much greater than a wavelength, hence is much more economical than the direct numerical solution of the Helmholtz equation. For the special case of a parabolic

half-body, $b = \sqrt{X}$, the approximate problem can be solved quickly by the method of similarity as in Section 2.4; the result is:

$$A = 1 + \frac{iK}{2}\left(\int_{\infty}^{Y/\sqrt{X}} e^{iK\xi^2/2}d\xi\right)\left(e^{iK/2} + \frac{iK}{2}\int_{1}^{\infty} e^{iK\xi^2/2}d\xi\right)^{-1} . \tag{4.10.13}$$

Thus, the amplitude along the island remains constant. Without the slenderness assumption the parabolic cylinder can be solved exactly in terms of parabolic coordinates (see Jones, 1964, p. 467).

We now turn to a sill whose top is submerged at the depth $h_0 < h$. Let the half-breadth B be much smaller than $\mu^{\alpha/2}$ (i.e., $\alpha < 2$); the sill appears practically as a thin line to the *outer* observer in the parabolic region, causing a distributed flux $\partial A/\partial Y = V(X)$ along the X axis with $V \neq 0$, for $0 < X < 1$, and $V = 0$, for $X > 1$. This problem resembles the heat conduction in a semi-infinite rod with the variation of heat flux prescribed at one end. The solution is formally

$$A(X,Y) = 1 - \frac{1+i}{2(\pi K)^{1/2}}\int_0^X \frac{d\xi V(\xi)}{(X-\xi)^{1/2}} \exp\frac{iKY^2}{2(X-\xi)}, \quad 0 < X < 1 . \tag{4.10.14}$$

Near the sill the appropriate *inner* variables are

$$X = \frac{x}{L}, \quad \overline{Y} = \frac{y}{\mu L} . \tag{4.10.15}$$

Assume the inner solution to be of the form

$$\eta = A(X,\overline{Y})e^{iKX\mu^{-\alpha}} , \tag{4.10.16}$$

then outside the sill this solution must satisfy Eq. (4.1.11) which yields

$$\frac{\partial^2 A}{\partial \overline{Y}^2} + \mu^{2-\alpha}2iK\frac{\partial A}{\partial X} + \mu^2\frac{\partial^2 A}{\partial X^2} = 0 , \quad \overline{Y} > b(X) . \tag{4.10.17}$$

Omitting terms of order $O(\mu^{2-\alpha})$, we get

$$A = B + C(\overline{Y} - b) . \tag{4.10.18}$$

Over the sill, the governing Helmholtz equation is of the same form as Eq. (4.1.11) but k^2 must be replaced by $k_0^2 = \omega^2/gh_0$. Substitution of Eq. (4.10.16) then gives

$$\frac{\partial^2 A}{\partial \overline{Y}^2} + K^2 \left(\frac{h}{h_0} - 1 \right) \mu^{2(1-\alpha)} A = O(\mu^{2-\alpha} A) \,. \tag{4.10.19}$$

The solution which is symmetric about the X axis is

$$A = \overline{A} \cos \left[K \left(\frac{h}{h_0} - 1 \right)^{1/2} \mu^{2(1-\alpha)} \overline{Y} \right], \quad 0 < \overline{Y} < b \,, \tag{4.10.20}$$

where $\overline{A}(X)$ is the amplitude along the axis. Requiring the inner solutions (4.10.18) and (4.10.20) to be continuous and to have equal normal flux across $\overline{Y} = b$, we get, to the leading order,

$$B = \overline{A} \cos \left[\mu^{1-\alpha} K \left(\frac{h}{h_0} - 1 \right)^{1/2} b \right] \tag{4.10.21}$$

and

$$-h_0 \overline{A} \mu^{1-\alpha} K \left(\frac{h}{h_0} - 1 \right)^{1/2} \sin \left(\mu^{1-\alpha} K \left(\frac{h}{h_0} - 1 \right)^{1/2} b \right) = hC \,. \tag{4.10.22}$$

We now match the inner approximation of Eq. (4.10.14) for small Y

$$A(X, Y) \cong 1 - \frac{1+i}{2(\pi K)^{1/2}} \int_0^X \frac{d\xi V(\xi)}{(X-\xi)^{1/2}} + VY + \cdots \,, \quad Y \gg 1 \,, \tag{4.10.23}$$

with the outer approximation of Eq. (4.10.20) for large $\overline{Y} \gg 1$,

$$A \cong B + C\overline{Y} \,, \tag{4.10.24}$$

yielding

$$B = 1 + \frac{1+i}{2(\pi K)^{1/2}} \int_0^X \frac{d\xi V(\xi)}{(X-\xi)^{1/2}} \tag{4.10.25}$$

and

$$C = V \mu^{1-\alpha/2} \,. \tag{4.10.26}$$

From Eqs. (4.10.21), (4.10.22), (4.10.25), and (4.10.26), B, C, and $\overline{A}$ may be eliminated to give

$$\frac{1+i}{2(\pi K)^{1/2}} \int_0^X \frac{d\xi V(\xi)}{(X-\xi)^{1/2}} = 1 + Z(X) V(X) \,, \tag{4.10.27}$$

where

$$Z(X) = \frac{h\mu^{\alpha/2}}{h_0 K(h/h_0 - 1)^{1/2}} \cot\left[\mu^{1-\alpha} K \left(\frac{h}{h_0} - 1\right)^{1/2} b\right]. \qquad (4.10.28)$$

We insist that $Z = O(1)$ to make all terms in Eq. (4.10.27) of equal order of magnitude, thus,

$$\alpha = 2/3 \quad \text{and} \quad \frac{h}{h_0} = \mu^{-2/3}, \qquad (4.10.29)$$

that is, the sill must be much shallower than the surrounding sea bottom.

The flux V can be solved numerically from the integral equation (see Mei and Tuck, 1980); afterward, the amplitude $\overline{A}$ along the sill axis can be calculated.

Bigg (1982) has evaluated the present theory against numerical solutions of the full Helmholtz equation. He cautions that Eq. (4.10.27) can be used only when Eq. (4.10.29) is met and $\overline{A}$ and V do not change rapidly over the sill. Numerically, when K increases to the value such that

$$\cot\left[\mu^{1-\alpha} K \left(\frac{h}{h_0} - 1\right)^{1/2} b_{\max}\right] = 0,$$

V and $\overline{A}$ become unbounded at the station where the sill is the widest. Although this suggests resonance over the sill, the results are grossly invalid. Several numerical examples reported by Mei and Tuck (1980) are unacceptable for these reasons. We present in Fig. 4.16 the center-line amplitude along a parabolic sill with pointed ends for a range of parameters where Eq. (4.10.27) is reliable. The wave amplitude outside the sill follows from Eq. (4.10.14) and is omitted.

The parabolic approximation has been applied to short waves propagating over a slowly varying bottom. For example, Radder (1979) has examined a submerged circular shoal, neglecting the bending of rays. Diffraction around curved rays has been studied by Liu and Mei (1976a) in the shadow boundary created by the tip of a long breakwater (see Section 10.7 for the limiting case of straight rays). Extensions by Lozano and Liu (1980) can now deal with the local curvature of rays and the neighborhood of a focus. Booij (1981) has treated the combined effects of varying current and depth. As this approximation expedites numerical computations, it deserves to be further developed for practical problems.

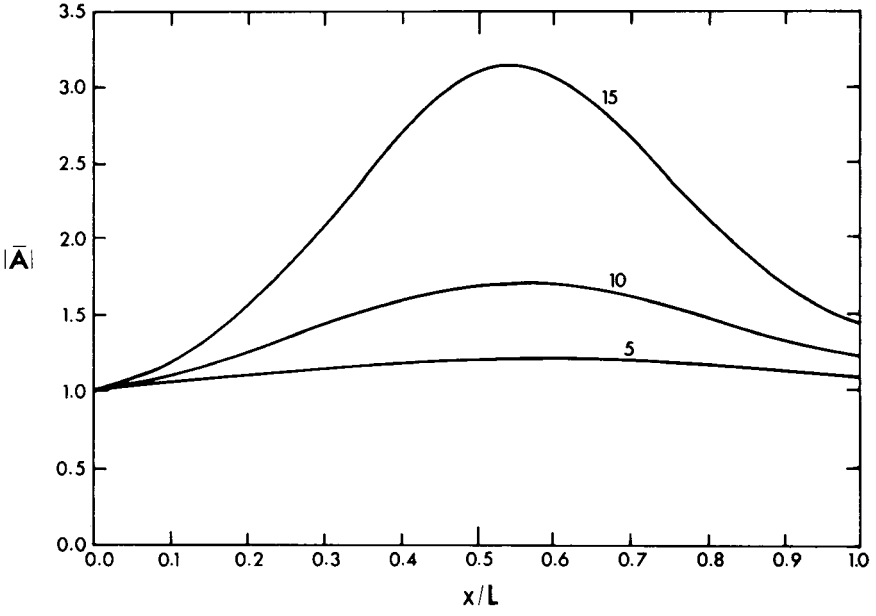

Figure 4.16: Variation of wave amplitude along the centerline of a submerged sill in head seas. The sides of the sill are a pair of parabolas $y/L = \pm\mu x(L-x)/L^2$. Numbers next to each curve indicate the value of $kL = \omega L(gh)^{-1/2}$ of the incident wave. $\mu = 0.05$, $h/h_0 = 9$.

4.11 A Numerical Method Based on Finite Elements

4.11.1 Introduction

The topography of the coastal region is seldom simple. To predict the water response to wave excitations, it is desirable to have a method which is capable of treating arbitrary geometry and depth. The *method of finite elements* is particularly suitable to fill this need because the element sizes and shapes can be freely varied to discretize the region of irregularity. After scoring spectacular successes in structural mechanics, this method has been extended to a variety of water-wave problems. While further refinements are still being made, recent advances have already found applications in actual design and planning on a large scale. We therefore devote this section to describing some essentials in the context of long waves, emphasizing those aspects which are unique to exterior problems. For the standard aspects of the theory of finite elements, the reader is referred to many excellent texts, for example, Zienkiewicz (1971) and Tong and Rossettos (1976).

A common procedure of the finite-element method for a linear boundary-value problem involves the following key steps:

1 Express the boundary-value problem as a variational principle where a certain functional is stationary.

2 Discretize the region into finite elements (such as triangles, quadrilaterals, and so on, for two-dimensional problems).

3 Select interpolating functions which approximate the solution inside the finite elements (linear, quadratic, and so on). The interpolating functions involve unknown coefficients.

4 For each element, perform the necessary differentiation and integration called for in the functional. For linear problems the functional is quadratic and can be expressed as a bilinear form in the unknown coefficients.

5 Assemble the element bilinear forms so that the total functional is expressed as a global bilinear form.

6 Extremize the functional with respect to each unknown coefficient and obtain a set of linear algebraic equations for the coefficients.

7 Solve the equations for the coefficients.

8 Compute quantities of physical interest.

Variational principles are not always easy to derive nor do they exist for all physical problems. A more general and straightforward approach is the so-called Galerkin weak formulation which will be touched upon in Chapter Eight for two- and three-dimensional problems with vertical variation. For problems of our interest, it can be shown that the variational formulation is equivalent to the weak formulation. Both formulations involve derivatives of order lower than those present in the original differential equation; therefore, they allow the use of a class of interpolating functions which are less differentiable (hence more general).

Usually the problems in structural mechanics involve a region of finite extent (a plate, a shell, a machine part, an airplane fuselage, and so on), whereas those in fluid mechanics often involve a theoretically infinite region. One may, of course, attempt to use a large but finite exterior boundary on which the condition at infinity is applied. After a numerical solution is completed for this finite region, a new and more remote boundary is introduced and the calculation is repeated. This procedure is continued until further expansion gives rise to negligible corrections to the solution. For wave problems the exterior boundary must be at least several wavelengths away from the bodies to give any degree of accuracy, while within each wavelength there must be sufficient grid points for good resolution.

Thus, in order to study a wide range of wavelengths, one must use either a different grid for each narrow range of wavelengths or a single but enormous total region dictated by the longest waves, with very fine grids dictated by the shortest waves. Clearly, neither alternative is economical and many artificial devices such as fictitious damping have been proposed.

To study diffraction by an island where the water depth is constant except in the vicinity of the island, Berkhoff (1972) divided the fluid into two regions by a circle which surrounds the island but is in the domain of constant depth. Only the interior of the circle is discretized into finite elements, while the solution in the exterior is represented by a continuous distribution of sources along the circle. The source solution is analytic and satisfies exactly the governing equation and the boundary condition at infinity. The source strength along the circle is unknown, however, and must be solved along with the interior of the circle by requiring the continuity of pressure and normal velocity across the circle. Different types of interpolating functions are used in different regions; hence the method may be called a *hybrid-element method* (HEM). The element with an analytical interpolating function is called the *superelement*, after Tong, Pian, and Lasry (1973).

Considerable freedom remains in the manner of enforcing the continuity of pressure and normal velocity between the finite elements and the superelement. An optimal choice is to cast the two matching conditions as *natural* boundary conditions in a variational principle, so that they are automatically satisfied in the numerical procedure. This variational approach has been successfully used for two-dimensional scattering and radiation problems (Chen and Mei, 1974a, b; Bai and Yeung, 1974), two-dimensional ship waves (Mei and Chen, 1976), three-dimensional scattering problems (Yue, Chen, and Mei, 1976, 1978), as well as for wave problems involving fluid-structure interactions (Mei, Foda, and Tong, 1979). The procedure of Chen and Mei is described below.

4.11.2 The Variational Principle

We assume that complicated topography, such as large structures, curved coastlines, varying depths, and so on, are localized within a closed contour C, as shown in Fig. 4.17. Beyond C, the depth is everywhere constant, and the fluid region is denoted by $\overline{\Omega}$. The incident plane wave is in the direction θ_I:

$$\eta^I = Ae^{ikr\cos(\theta-\theta_I)} = A\sum_{n=0}^{\infty}\varepsilon_n i^n J_n(kr)\cos n(\theta-\theta_I)\,. \tag{4.11.1}$$

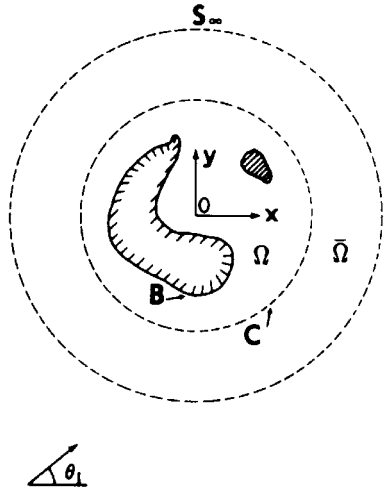

Figure 4.17: Definitions.

Within $\overline{\Omega}$, the scattered wave, denoted by $\bar{\eta}^S$, must satisfy the Helmholtz equation and the radiation condition and may be represented exactly by the Fourier–Bessel expansion

$$\bar{\eta}^S = \alpha_0 H_0(kr) + \sum_{n=1}^{\infty} H_n(kr)(\alpha_n \cos n\theta + \beta_n \sin n\theta) \tag{4.11.2}$$

where H_n's are Hankel functions of the first kind. The expansion coefficients α_n, $n = 0, 1, 2, \ldots$, and β_n, $n = 1, 2, 3, \ldots$, are to be found. The total displacement in $\overline{\Omega}$ will be denoted by $\bar{\eta}$ $(= \eta^I + \bar{\eta}^S)$. The region $\overline{\Omega}$ is the *superelement*.

Let the fluid region within C be denoted by Ω and the corresponding displacement by η. Then η must satisfy Eq. (4.1.9) in Ω and Eq. (4.11.3) on B. Across C the pressure and normal velocity must be continuous:

$$\eta = \bar{\eta}\,, \quad \frac{\partial \eta}{\partial n} = \frac{\partial \bar{\eta}}{\partial n} \quad \text{on} \quad C\,. \tag{4.11.3}$$

We shall now show that the stationarity of the functional

$$J(\eta, \bar{\eta}) = \iint_{\Omega} \frac{1}{2}\left[h(\nabla\eta)^2 - \frac{\omega^2}{g}\eta^2\right] dA + \int_C h\left[\left(\frac{1}{2}\bar{\eta}^S - \eta^S\right)\frac{\partial \bar{\eta}}{\partial n} - \frac{1}{2}\bar{\eta}^S \frac{\partial \eta^I}{\partial n}\right] ds, \tag{4.11.4}$$

where $\eta^S \equiv \eta - \eta^I$, is equivalent to the boundary-value problem defining η in Ω and $\bar{\eta}^S$ in $\overline{\Omega}$. To prove the equivalence, we take the first variation of J:

$$\delta J = \iint_\Omega \left[h\nabla\eta \cdot \nabla\delta\eta - \frac{\omega^2}{g}\eta\delta\eta \right] dA + \int_C h \left[\left(\frac{1}{2}\delta\bar{\eta}^S - \delta\eta^S \right) \frac{\partial\bar{\eta}}{\partial n} + \left(\frac{1}{2}\bar{\eta}^S - \eta^S \right) \frac{\partial\delta\bar{\eta}}{\partial n} - \frac{1}{2}\delta\bar{\eta}^S \frac{\partial\eta^I}{\partial n} \right] ds\,.$$

By partial integration and Gauss' theorem, the first term above may be written

$$\iint_\Omega h\nabla\eta \cdot \nabla\delta\eta\, dA = \iint_\Omega [\nabla \cdot (h\delta\eta\nabla\eta) - \delta\eta\nabla \cdot (h\nabla\eta)]\, dA = -\iint_\Omega \delta\eta\nabla \cdot (h\nabla\eta)\, dA + \int_C h\delta\eta \frac{\partial\eta}{\partial n}\, ds + \int_B h\delta\eta \frac{\partial\eta}{\partial n}\, ds\,.$$

Since η^I is known, $\delta\eta^I = 0$ and

$$\delta\bar{\eta}^S = \delta\bar{\eta} \quad \text{and} \quad \delta\eta^S = \delta\eta\,.$$

It follows that

$$\begin{aligned} \delta J = &- \iint_\Omega \delta\eta \left[\nabla \cdot (h\nabla\eta) + \frac{\omega^2}{g}\eta \right] dA \\ &+ \int_C h \left[\left(\frac{1}{2}\delta\bar{\eta} - \delta\eta \right) \frac{\partial\bar{\eta}}{\partial n} + \left(\frac{1}{2}\bar{\eta}^S - \eta^S \right) \frac{\partial\delta\bar{\eta}}{\partial n} \right. \\ &\left. - \frac{1}{2}\delta\bar{\eta} \frac{\partial\eta^I}{\partial n} + \delta\eta \frac{\partial\eta}{\partial n} \right] ds + \int_B h\,\delta\eta \frac{\partial\eta}{\partial n}\, ds \\ = &- \iint_\Omega \delta\eta \left[\nabla \cdot (h\nabla\eta) + \frac{\omega^2}{g}\eta \right] dA \\ &+ \int_C h \left[\delta\eta \left(\frac{\partial\eta}{\partial n} - \frac{\partial\bar{\eta}}{\partial n} \right) - \frac{\partial\delta\bar{\eta}}{\partial n}(\eta^S - \bar{\eta}^S) \right] ds \\ &+ \frac{1}{2}\int_C h \left[\delta\bar{\eta} \frac{\partial\bar{\eta}^S}{\partial n} - \bar{\eta}^S \frac{\partial\delta\bar{\eta}}{\partial n} \right] ds + \int_B h\delta\eta \frac{\partial\eta}{\partial n}\, ds\,. \end{aligned} \tag{4.11.5}$$

The next to the last integral in the preceding equation is equal to

$$I(C) = \frac{h}{2}\int_C \left[\delta\bar{\eta}^S \frac{\partial\bar{\eta}^S}{\partial n} - \bar{\eta}^S \frac{\partial\delta\bar{\eta}^S}{\partial n} \right] ds\,.$$

Now apply Green's formula to $\bar{\eta}^S$ and $\delta\bar{\eta}^S$ for the region $\overline{\Omega}$. Since both $\bar{\eta}^S$ and $\delta\bar{\eta}^S$ satisfy the Helmholtz equation exactly, the above integral I is unchanged if C is replaced by a circle C_∞ of great radius. Along C_∞, both $\bar{\eta}^S$ and $\delta\bar{\eta}^S$ satisfy the radiation condition (4.1.38); hence

$$I(C_\infty) = 0\,, \quad \text{implying } I(C) = 0\,.$$

With I removed from Eq. (4.11.5), it is clear that if Eqs. (4.1.9), (4.1.13b), (4.11.3a), and (4.11.3b) are satisfied by η, then

$$\delta J = 0\,. \tag{4.11.6}$$

Conversely, if $\delta J = 0$, it is necessary that η satisfies Eq. (4.1.9) in Ω as the Euler equation, Eq. (4.1.13b) on B, and Eqs. (4.11.3a) and (4.11.3b) on C as the *natural* boundary conditions. The equivalence is thus proved.

The stationary functional involves integrals in and on the boundaries of Ω and may be used as the basis for obtaining an approximate solution in Ω. The method of finite elements is only one of the possibilities.

4.11.3 Finite-Element Approximation

Let us discretize the integrals in Eq. (4.11.4) by dividing the water area in Ω into a network of finite elements whose sizes should be much less than both the typical wavelength and the scale of local topographical variation. Since the integrands in Eq. (4.11.4) contain only first-order derivatives of η, it is only necessary to require the continuity of η in the finite-element domain. For simplicity we choose the three-node triangular elements, within each of which η is approximated by linear interpolating functions

$$\eta^2(x,y) = \sum_{i=1}^{3} N_i^2 \eta_i^e = \underset{1\times 3}{\{N^e\}^T}\ \underset{3\times 1}{\{\eta^e\}} \tag{4.11.7}$$

where superscripts e represent quantities associated with an element. Here $\{\ \}$ denotes a column vector and the superscript T denotes the transpose; hence $\{\ \}^T$ is a row vector. The underlying products indicate the dimensions of a matrix, for example, 1×3 means that the matrix has 1 row and 3 columns. More explicitly,

$$\{\eta^e\}^T = (\eta_1^e, \eta_2^e, \eta_3^e) \tag{4.11.8a}$$

$$\{N^e\}^T = (N_1^e, N_2^e, N_3^e) \tag{4.11.8b}$$

where

$$N_i^e(x,y) = \frac{a_i + b_i x + c_i y}{2\Delta^e}\,, \quad i = 1,2,3 \tag{4.11.9a}$$

$$a_1 = x_2^e y_3^e - x_3^e y_2^e\,, \quad b_1 = y_2^e - y_3^e\,, \quad c_1 = x_3^e - x_2^e \tag{4.11.9b}$$

$$\begin{aligned}\Delta^e &= \text{area of element } e \\ &= \frac{1}{2}\begin{vmatrix} 1 & x_1^e & y_1^e \\ 1 & x_2^e & y_3^e \\ 1 & x_3^e & y_3^e \end{vmatrix}.\end{aligned} \tag{4.11.9c}$$

Other coefficients $a_{2,3}$, $b_{2,3}$, and $c_{2,3}$ may be obtained by permutation while x_i, y_i, and the coefficient η_i^e represent, respectively, the x, y coordinates and the value of η^e at node i. Let the depth within an element be approximated by a plane,

$$h^2(x,y) = \sum_{i=1}^{3} N_i^2 h_i^e = \underset{1\times 3}{\{N^e\}^T}\,\underset{3\times 1}{\{h^e\}}\,, \tag{4.11.10}$$

h_i^e being the water depth at node i. When integration is performed for the area integral, we obtain

$$\begin{aligned} I_1 &= \iint_\Omega \frac{1}{2}\left[h(\nabla\eta)^2 - \frac{\omega^2}{g}\eta^2\right] dA \\ &= \frac{1}{2}\sum_{e\in\Omega} \underset{1\times 3}{\{n^e\}^T}\,\underset{3\times 3}{[K_1^e]}\,\underset{3\times 1}{\{\eta^e\}}, \end{aligned} \tag{4.11.11}$$

where the element stiffness matrix $[K_1^e]$ has the components

$$K_{1_{ij}}^e = h_\beta^e \iint_e N_\beta^e \frac{\partial N_i^e}{\partial x_\alpha}\frac{\partial N_j^e}{\partial x_\alpha}\,dx\,dy - \frac{\omega^2}{g}\iint_e N_i^e N_j^e\,dx\,dy\,. \tag{4.11.12}$$

When Eq. (4.11.9) is substituted into (4.11.12), the integrals over any triangle e can be evaluated explicitly as

$$\begin{aligned}\iint_e N_i^e N_j^e\,dx\,dy &= \frac{1}{6}\Delta^e\,, \quad i = j \\ &= \frac{1}{2}\Delta^e\,, \quad i \neq j\,,\end{aligned} \tag{4.11.13a}$$

$$\iint_e \frac{\partial N_i^e}{\partial x_\alpha}\frac{\partial N_j^e}{\partial x_\alpha}\,dx\,dy = \frac{1}{4\Delta^e}(b_i b_j + c_i c_j)\,, \tag{4.11.13b}$$

$$h_\beta^e \iint_e N_\beta^e \frac{\partial N_i^e}{\partial x_\alpha}\frac{\partial N_j^e}{\partial x_\alpha}\,dx\,dy = \frac{h_1^e + h_2^e + h_3^e}{12\Delta^e}(b_i b_j + c_i c_j)\,. \tag{4.11.13c}$$

The element stiffness matrix $[K_1^e]$ is symmetric. Now assemble all the element nodal displacements and define a total nodal displacement vector $\{\eta\}$ with E components where E is the total number of nodes in and on the boundaries of Ω. In so doing, the element nodal points must be reindexed to take into account the fact that the same node can belong to several adjacent elements. The element stiffness matrices must be assembled accordingly to give a total stiffness matrix $[K_1]$. Finally, I_1 is written

$$I_1 = \frac{1}{2} \underset{1\times E}{\{\eta\}^T} \underset{E\times E}{[K_1]} \underset{E\times 1}{\{\eta\}} \,. \tag{4.11.14}$$

Because $[K_1^e]$ is symmetric for all elements, $[K_1]$ is also symmetric.

The line integral in Eq. (4.11.4) may be written as follows:

$$\begin{aligned}
&\int_C h \left[\left(\frac{1}{2}\bar{\eta}^S - \eta^S \right) \left(\frac{\partial \bar{\eta}^S}{\partial n} + \frac{\partial \eta^I}{\partial n} \right) - \frac{1}{2}\bar{\eta}^S \frac{\partial \eta^I}{\partial n} \right] ds \\
&\quad = \int_C h \frac{1}{2}\bar{\eta}^S \frac{\partial \bar{\eta}^S}{\partial n}\, ds - \int_C h(\eta - \eta^I) \frac{\partial \bar{\eta}^S}{\partial n}\, ds - \int_C h(\eta - \eta^I) \frac{\partial \eta^I}{\partial n}\, ds \\
&\quad = \frac{1}{2} \int_C h\bar{\eta}^S \frac{\partial \bar{\eta}^S}{\partial n}\, ds - \int_C h\eta \frac{\partial \bar{\eta}^S}{\partial n}\, ds - \int_C h\eta \frac{\partial \eta^I}{\partial n}\, ds \\
&\qquad \underset{I_2}{} \qquad\qquad \underset{I_3}{} \qquad\qquad \underset{I_4}{} \\
&\qquad + \int_C h\eta^I \frac{\partial \bar{\eta}^S}{\partial n}\, ds + \int_C h\eta^I \frac{\partial \eta^I}{\partial n}\, ds \,.
\end{aligned} \tag{4.11.15}$$

$\underset{I_5}{}$ $\underset{I_6}{}$

For simplicity, C is assumed to be a circle of radius R. For computational purposes we truncate the series (4.11.1) and (4.11.2) at the term m. With Eq. (4.11.2), the line integral I_2 can be evaluated analytically by invoking the orthogonality of sines and cosines:

$$I_2 = \frac{\pi}{2} kRh \left[2\alpha_0^2 H_0 H_0' + \sum_{n=1}^{m} (\alpha_n^2 + \beta_n^2) H_n H_n' \right],$$

where

$$H = H_n^{(1)}(kR)\,, \quad H_n' \equiv \left[\frac{d}{d(kr)} H_n^{(1)}(kr) \right]_{r=R}$$

and R is the radius of C. Note that h on and outside C has been assumed to be constant. Define the column vector

$$\underset{1\times M}{\{\mu\}}$$

such that

$$\underset{1\times M}{\{\mu\}^T} = \{\alpha_0, \alpha_1, \beta_1, \alpha_2, \beta_2, \ldots, \alpha_m, \beta_m\}$$

with $M = 2m + 1$, and $[K_2]$ the diagonal matrix

$$\underset{M\times M}{[K_2]} = \pi kRh \ \mathrm{diag}\{2H_0'H_0, H_1'H_1, H_1'H_1, \ldots, H_m'H_m, H_m'H_m\}\,.$$

The integral I_2 can now be written

$$I_2 = \frac{1}{2} \underset{1\times M}{\{\mu\}^T} \underset{M\times M}{\{K_2\}} \underset{M\times 1}{\{\mu\}} \ . \tag{4.11.16}$$

For integrals I_3 and I_4, we define for convenience the subset $\{\hat{\eta}\}$ of $\{\eta\}$ which lies on C (see Fig. 4.18)

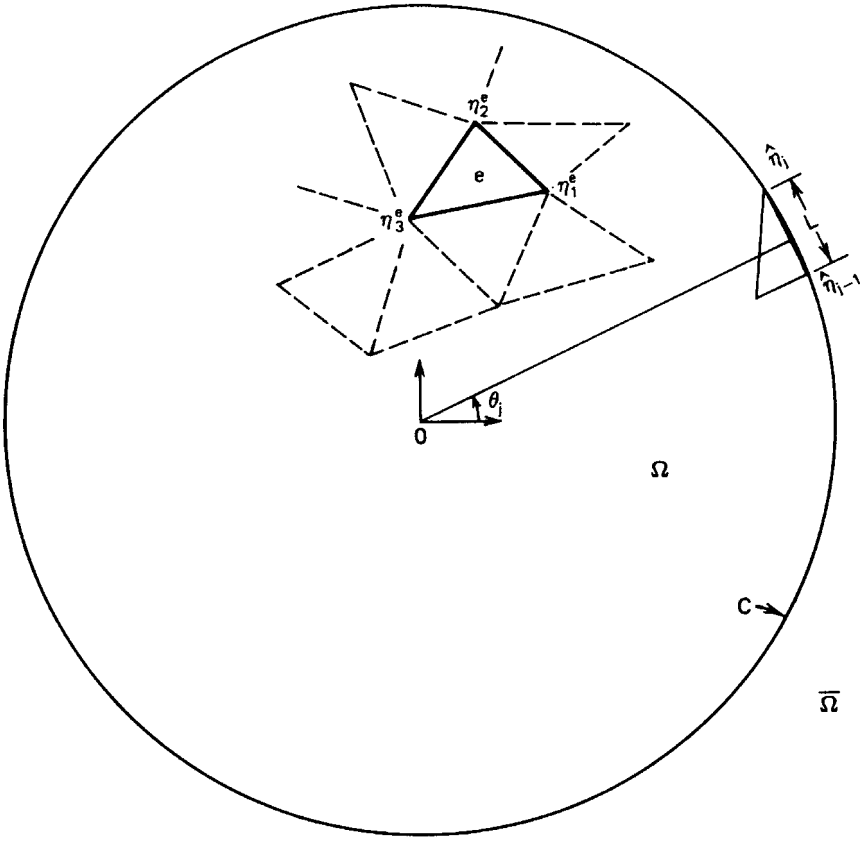

Figure 4.18: Typical boundary and interior elements.

$$\underset{1\times P}{\{\hat{\eta}\}^T} = \{\hat{\eta}_1, \hat{\eta}_2, \ldots, \hat{\eta}_P\}\,.$$

Approximating the line integral over C by the sum of the integrals along the straight elements $\hat{\eta}_p\hat{\eta}_1, \hat{\eta}_1\hat{\eta}_2, \ldots, \hat{\eta}_{p-1}\hat{\eta}_p$, η by its linear interpolations, and $\bar{\eta}^S$ by its value at the center of each arc element on C, namely, at $\theta = \theta_j$ (see Fig. 4.18), we obtain

$$I_3 \cong -\frac{1}{2}kh\sum_{j=1}^{p} L_j(\hat{\eta}_{j-1} + \hat{\eta}_j)\left[\alpha_0 H_0' + \sum_{n=0} H_n'(\alpha_n \cos n\theta_j + \beta_n \sin n\theta_j)\right]$$

where L_j^e is the length of the element segment j. This may be written in matrix form

$$I_3 = \underset{1\times P}{\{\hat{\eta}\}^T}\ \underset{P\times M}{[K_3]}\ \underset{M\times 1}{\{\mu\}} \tag{4.11.17}$$

where $[K_3]$ is a fully populated $P \times M$ matrix

$$\underset{P\times M}{\{K_3\}} = -\frac{kh}{2} \times \begin{bmatrix} 2H_0'L_1 \cdots H_n'(\cos n\theta_P + \cos n\theta_1)L_1 & H_n'(\sin n\theta_P + \sin n\theta_1)L_1 \cdots \\ 2H_0'L_2 \cdots H_n'(\cos n\theta_1 + \cos n\theta_2)L_2 & H_n'(\sin n\theta_1 + \sin n\theta_2)L_2 \cdots \\ \vdots \quad \vdots & \vdots \\ 2H_0'L_P \cdots H_n'(\cos n\theta_{P-1} + \cos n\theta_P)L_P & H_n'(\sin n\theta_{P-1} + \sin n\theta_P)L_P \cdots \end{bmatrix} \tag{4.11.18}$$

in which $n = 1, 2, \ldots, m$.

Similarly, the integral I_4 is obtained:

$$I_4 = -\frac{1}{2}kh\sum_{j=1}^{P} L_j[i\cos(\theta_j - \theta_I)]\exp[ikR\cos(\theta_j - \theta_I)]\cdot(\hat{\eta}_{j-1} + \hat{\eta}_j)$$

$$\equiv -\{Q_4\}^T\{\hat{\eta}\} \tag{4.11.19}$$

where

$$\{Q_4\}^T = \frac{1}{2}kh\{(q_P - q_1)L_1, (q_1 + q_2)L_2, \ldots, (q_{P-1} + q_P)L_P\}\,,$$

$$q_j = i\cos(\theta_j - \theta_1)\exp[ikR\cos(\theta_j - \theta_I)]\,, \quad j = 1, 2, \ldots, P\,.$$

Finally, the integral I_5 can be evaluated analytically to give

$$I_5 = -\underset{1\times M}{\{Q_5\}^T}\ \underset{M\times 1}{\{\mu\}} \tag{4.11.20}$$

where

$$\underset{1\times M}{\{Q_5\}^T} = 2\pi Rkh\{J_0H_0', \ldots, i^m J_m H_m' \cos m\theta_I, i^m J_m H_m' \sin m\theta_I\}\,.$$

I_6 is a known constant and drops out upon extremization, hence it is of no interest.

Now we summarize the functional

$$\begin{aligned} J = {} & \frac{1}{2}\{\eta\}^T[K_1]\{\eta\} + \frac{1}{2}\{\mu\}^T[K_2]\{\mu\} + \{\hat{\eta}\}^T[K_3]\{\mu\} \\ & - \{Q_4\}^T\{\hat{\eta}\} - \{Q_5\}^T\{\mu\}\,. \end{aligned} \tag{4.11.21}$$

Since J is stationary, we require that

$$\frac{\partial J}{\partial \eta_j} = 0\,, \quad j = 1, 2, \ldots, E$$

and

$$\frac{\partial J}{\partial \mu_j} = 0\,, \quad j = 1, 2, \ldots, M$$

which leads to a set of linear algebraic equations

$$\begin{aligned} [K_1]\{\eta\} + [K_3]\{\mu\} &= \{Q_4\}\,, \\ [K_2]\{\mu\} + [K_3]^T\{\hat{\eta}\} &= \{Q_5\}\,. \end{aligned} \tag{4.11.22}$$

Elimination of $\{\mu\}$ gives a matrix equation for $\{\eta\}$

$$\begin{aligned} [K]\{\eta\} \equiv {} & [[K_1] - [K_3][K_2]^{-1}[K_3]^T]\{\eta\} \\ = {} & \{Q_4\} + [K_3][K_2]^{-1}\{Q_5\}\,. \end{aligned} \tag{4.11.23}$$

The resultant matrix $[K]$ is symmetric; only half of its elements need to be stored in the computer.

By heuristic reasoning and numerical experiments in which comparisons with analytic solutions were made in several cases, the following empirical rules on the element size have been found:

1 The element size should be everywhere less than 10% of the incident wavelength.

2 At the neighborhood of sharp curvature, elements smaller than the radius of curvature should be used locally, otherwise local but not global errors can result.

The number of coefficients M needed in the superelement is easy to decide by trial and error; it usually increases for shorter waves.

To minimize the bandwidth of $[K]$, the numbering of nodes should be proceeded first along one ring, then along the next ring either toward or from C. When this is done, the semibandwidth is then roughly equal to the number of nodes on C and is independent of the number of series coefficients in the superelement. Because of the symmetry and bandedness of the matrix, the numerical solution of the algebraic equation is particularly efficient. Clearly, the smaller the circle C, the smaller the bandwidth, and the amount of computation is usually reduced even though more coefficients may be required in the superelement.

It should be remarked that the contour C need not be a circle; for an arbitrarily shaped contour numerical integration of the line integrals along C is needed and $[K_2]$ is full.

An interesting application of the hybrid-element method has been made by Houston (1978) on the response near the Hawaiian Islands to tsunamis caused by earthquakes near Chile in 1960 and Alaska in 1964. Based on a two-dimensional linearized long-wave equation including the earth's curvature, Houston used initial data estimated from the permanent displacement of the fault and calculated the waves up to a depth of 5000 m near the islands. The calculated wave history (shown in Fig. 4.19) was then Fourier analyzed into 18 harmonics with periods ranging from 14.5 min to 260 min.

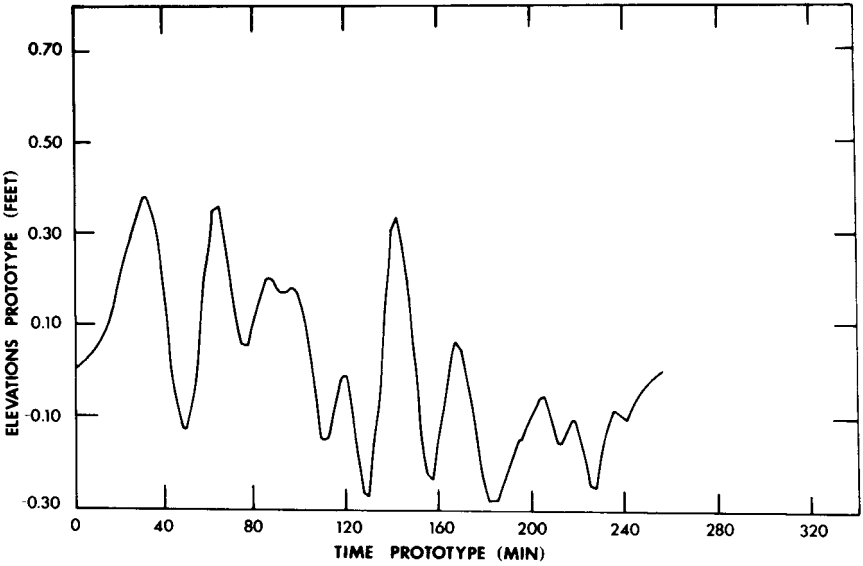

Figure 4.19: Calculated transient incident waves for 1964 Alaskan earthquake (from Houston, 1978, *J. Phys. Ocean.* of American Meteorological Society).

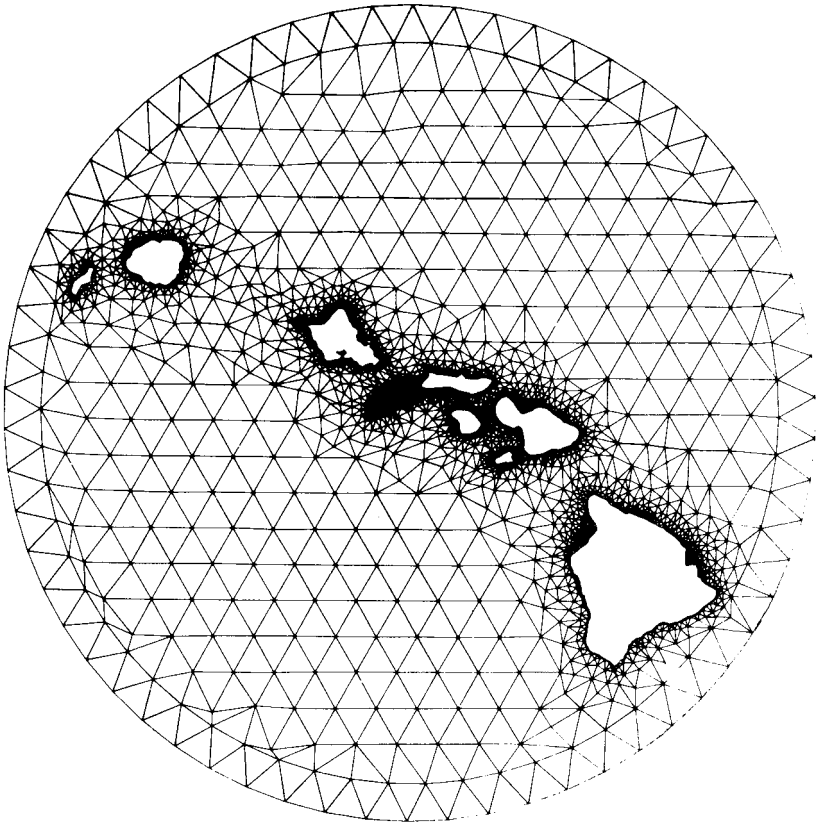

Figure 4.20: Typical finite-element grid surrounding Hawaiian islands (from Houston, 1978, *J. Phys. Ocean.* of American Meterorological Society).

These harmonics were used as the incident waves. With the finite-element grid shown in Fig. 4.20 which has roughly 2500 nodes, the harmonic responses were calculated and superimposed in accordance with Eq. (2.56) to give the transient response at three wave stations: Kahului of Maui, Honolulu of Oahu, and Hilo of Hawaii. The agreement between theory and records is excellent. Figure 4.21 shows a sample comparison for the Alaskan earthquake with a 500-mile-long fault. The theoretical reason that the linear shallow-water equation is adequate for tsunami transocean propagation will be discussed in Chapter Twelve. This kind of calculation is useful for planning policies for tsunami flood insurance and can be applied to improve the speed and accuracy of tsunami warning systems.

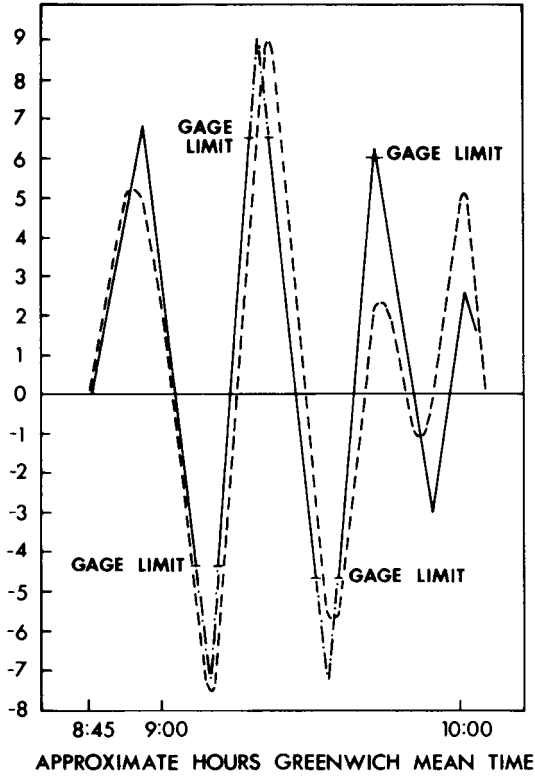

Figure 4.21: Calculated (dashed curve) versus measured (solid curve) tsunami records at Kahului, Maui for 1964 Alaskan earthquake (from Houston, 1976, *J. Phys. Ocean.* of American Meteorological Society).

Appendix 4.A Partial Wave Expansion of the Plane Wave

Consider the product of the Taylor series expansions of $e^{zt/2}$ and $e^{-zt/2}$

$$\begin{aligned} e^{z(t-1/t)/2} &= e^{zt/2}e^{-z/2t} \\ &= \left[\sum_{n=0}^{\infty} \frac{1}{n!}\left(\frac{zt}{2}\right)^n\right]\left[\sum_{m=0}^{\infty} \frac{1}{m!}\left(-\frac{z}{2t}\right)^m\right]. \end{aligned} \tag{4.A.1}$$

Carrying out the multiplication and collecting the coefficients of the term t^n, we find that

$$e^{z(t-1/t)/2} = \sum_{n=-\infty}^{\infty} t^n \left[\frac{(z/2)^n}{n!} - \frac{(z/2)^{n+2}}{1!(n+1)!} + \frac{(z/2)^{n+4}}{2!(n+2)!} + \cdots (-1)^r \frac{(z/2)^{n+2r}}{r!(n+r)!} \cdots \right].$$

Now the series in the brackets above is just the Bessel function of order n, $J_n(z)$; hence

$$e^{z(t-1/t)/2} = \sum_{n=-\infty}^{\infty} t^n J_n(z)\,. \tag{4.A.2}$$

If we substitute $t = ie^{i\theta}$ into Eq. (4.A.2), then

$$e^{iz\cos\theta} = \sum_{-\infty}^{\infty} e^{in(\theta+\pi/2)} J_n(z)\,. \tag{4.A.3}$$

Now let us combine pairs of terms with equal but opposite n's and use the fact that

$$J_{-n}(z) = (-1)^n J_n(z)\,.$$

Equation (4.A.3) can be written in an alternate form:

$$e^{iz\cos\theta} = \sum_{0}^{\infty} \varepsilon_n \cos n\theta (i)^n J_n(z) \tag{4.A.4}$$

where the Jacobi symbols have been used.

For a plane wave, we let $z = kr$ in Eq. (4.A.4) and get

$$e^{ikx} = e^{ikr\cos\theta} = \sum_{0}^{\infty} \varepsilon_n \cos n\theta i^n J_n(kr)\,. \tag{4.A.5}$$

Harbor Oscillations Excited by Incident Long Waves

5

5.1 Introduction

A harbor is a partially enclosed basin of water connected through one or more openings to the sea. Conventional harbors are built along a coast where a shielded area may be provided by natural indentations and/or by breakwaters protruding seaward from the coast, as sketched in Fig. 5.1.

Although a variety of external forcings can be responsible for significant oscillations within a harbor, the most studied forcing is caused by incident

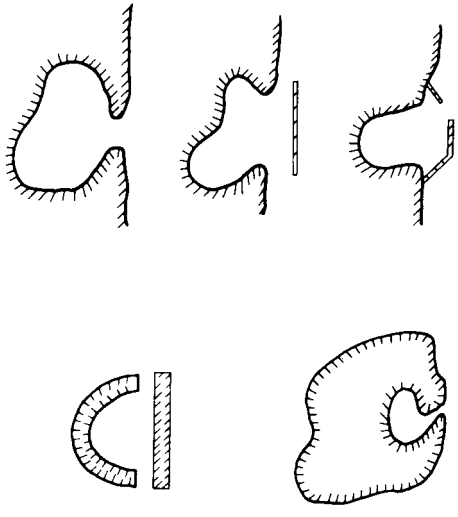

Figure 5.1: Variety of harbor configurations.

tsunamis which have typical periods from a few minutes to an hour and are originated from distant earthquakes. If the total duration of the tsunami is sufficiently long, oscillations excited in the harbor may persist for days, resulting in broken mooring lines, damaged fenders, hazards in berthing and loading or navigation through the entrance, and so on. Sometimes incoming ships have to wait outside the harbor until oscillations within subside, causing costly delays.

To understand roughly the physical mechanism of these oscillations, consider a harbor with the entrance in line with a long and straight coastline. Onshore waves are partly reflected and partly absorbed along the coast. A small portion is, however, diffracted through the entrance into the harbor and reflected repeatedly by the interior boundaries. Some of the reflected wave energy escapes the harbor and radiates to the ocean again, while some stays inside. If the wavetrain is of long duration, and the incident wave frequency is close to a standing-wave frequency in the closed basin, resonance will occur in the basin so that a relatively weak incident wave can induce a large response in the harbor.

The peak amplitude at resonance can be limited by a number of mechanisms:

1 Radiation damping, associated with energy escaped seaward from the harbor entrance.
2 Frictional loss near the basin boundary and the harbor entrance.
3 Loss due to wave breaking on shallow beaches.
4 Finite-amplitude effects of energy transfer into higher harmonics.

Among these mechanisms, radiation damping is the most understood theoretically and was first treated in a pioneering paper by Miles and Munk (1961) for a rectangular harbor. Frictional losses occur along harbor boundaries and near breakwater tips at the entrance; these losses are harder to estimate and vary widely according to the property of the boundary. Reliable estimates require empirical information which is difficult to obtain by model tests because of the scale effects. Breaking is a phenomenon associated mostly with wind-generated waves on mild beaches and is not amenable to full treatment by theory. Fortunately, for very long tsunamis, breaking is usually unimportant.

In this chapter we shall ignore frictional and breaking losses and only include the effects of radiation damping. After the formulation, three elements of the harbor problem are discussed separately: standing waves in a basin, the concept of radiation damping, and diffraction through a gap.

Next, for sinusoidal inputs and constant depth, we shall study the full problem coupling the ocean with harbors of various simple plan forms. Transients will be considered for a narrow bay. At the end of the chapter the general hybrid-element method of Section 4.11 will be modified for harbors of arbitrary depth and shape.

5.2 Formulation for Harbor Oscillation Problems

For simplicity we make the following assumptions on the fluid motion: (i) inviscid fluid, (ii) irrotational flow, (iii) infinitesimal waves amplitude, (iv) very long wavelength compared to depth, and (v) lateral boundaries are perfectly reflective and vertical throughout the sea depth. The governing equations derived in Section 4.1 are applicable; for convenience they are recalled here. For transient motion the displacement satisfies the field equation

$$g\nabla \cdot (h\nabla\zeta) = \frac{\partial^2 \zeta}{\partial t^2} \tag{5.2.1}$$

with the no-flux condition

$$h\frac{\partial \zeta}{\partial n} = 0 \tag{5.2.2}$$

on the lateral walls. For simple harmonic motion the spatial amplitude η of the free-surface displacement satisfies the field equation

$$\nabla \cdot (h\nabla\eta) + \frac{\omega^2}{g}\eta = 0 \tag{5.2.3}$$

subject to the no-flux condition

$$h\frac{\partial \eta}{\partial n} = 0 \tag{5.2.4}$$

on the lateral walls. For constant depth, Eq. (5.2.1) reduces to the classical wave equation, while Eq. (5.2.3) reduces to the Helmholtz equation

$$\nabla^2\eta + k^2\eta = 0 \tag{5.2.5}$$

where $\omega = (gh)^{-1/2}k$.

The radiation condition for sinusoidal motion can be stated explicitly if the topography far away from the harbor is simple. Consider a harbor on a coastline which is also perfectly reflective. Let Ω denote the region which includes the harbor and all the complex topography nearby, and let $\overline{\Omega}$ be

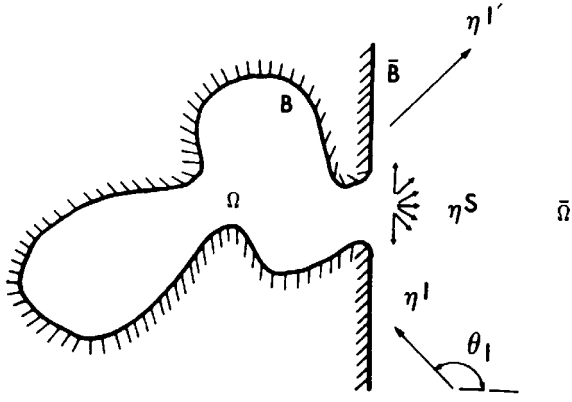

Figure 5.2: Definition sketch.

the remaining part of the ocean in which $h = \text{const}$ and the coastline $\overline{B}$ is straight (see Fig. 5.2). A plane incident wave may be expressed by

$$\eta^I = A \exp[ik(x \cos\theta_I + y \sin\theta_I)] \tag{5.2.6}$$

where A, k, and the direction θ_I are prescribed. The complete wave system in the ocean $\overline{\Omega}$ may be split as

$$\eta = \eta^I + \eta^{I'} + \eta^S, \tag{5.2.7}$$

where $\eta^{I'}$ denotes the reflected wave due to the straight coast without the local topography near the harbor, while η^S denotes the wave scattered by the local topography and radiated by the piston action at the entrance. Let the y axis coincide with the straight portion of the coast $\overline{B}$; the reflected wave is

$$\eta^{I'} = A \exp[ik(-x \cos\theta_I + y \sin\theta_I)] \tag{5.2.8}$$

so that on $\overline{B}$

$$\frac{\partial}{\partial x}(\eta^I + \eta^{I'}) = 0\,. \tag{5.2.9}$$

Then the radiated/scattered wave cannot have any normal flux along the straight coast:

$$\frac{\partial}{\partial x}\eta^S = 0 \quad \text{on} \quad \overline{B}\,. \tag{5.2.10}$$

Furthermore, η^S must be outgoing at large distances,

$$(kr)^{1/2}\left(\frac{\partial}{\partial r}-ik\right)\eta^S \to 0\,, \quad kr\to\infty\,. \tag{5.2.11}$$

In the case of an offshore harbor many wavelengths away from a coast, one may simply omit the reflected wave $\eta^{I'}$ from Eq. (5.2.7). For other coastal configurations, or nonconstant depth in $\overline{\Omega}$, an explicit description of η^I and $\eta^{I'}$ may be a difficult task in itself.

When the depth is constant everywhere in Ω and in $\overline{\Omega}$, and all walls are vertical, the three-dimensional potential for arbitrary kh may be expressed as

$$\phi(x,y,z)=\frac{-ig\eta}{\omega}\frac{\cosh k(z+h)}{\cosh kh}\,.$$

Recall from Section 3.5 that η also satisfies the horizontal Helmholtz equation except that ω and k are related by $\omega^2=gk\tanh kh$. Since the walls are vertical, the normal vector is in the horizontal plane, and the boundary condition is $\partial\eta/\partial n=0$ on side walls. Thus, the boundary-value problems for long and short waves are formally the same. This mathematical analogy enables one to perform harbor experiments in deep water where nonlinear effects are easier to avoid.

5.3 Natural Modes in a Closed Basin of Simple Form and Constant Depth

As a preliminary, it is useful to discuss the typical features of standing waves in a closed basin. For simplicity, we assume the depth to be constant. The boundary-value problem for η, which may now be taken as real, is defined by the homogeneous equations (5.2.5) and (5.2.4), and admits nontrivial solutions only when k equals certain eigenvalues. The corresponding ω's are called the *natural* (*or eigen*) *frequencies* and the corresponding η's the *natural* (*or eigen*) *modes*. Two elementary examples are discussed below.

5.3.1 A Rectangular Basin

Let the lateral boundaries of the basin be $x=0,a$ and $y=0,b$. The eigensolutions to Eq. (5.2.5) are found by separation of variables

$$\eta=A_{nm}\cos\frac{n\pi x}{a}\cos\frac{m\pi y}{b} \tag{5.3.1}$$

with $n, m = 0, 1, 2, 3, \ldots$. The corresponding eigenvalues are

$$k = k_{nm} = \left[\left(\frac{n\pi}{a} \right)^2 + \left(\frac{m\pi}{b} \right)^2 \right]^{1/2} . \tag{5.3.2}$$

The natural periods are

$$T_{nm} = 2\pi/\omega_{nm} \tag{5.3.3}$$

where ω_{nm} are related to k_{nm} via the dispersion relation

$$\omega_{nm}^2 = ghk_{nm}^2 . \tag{5.3.4}$$

If $a > b$, the lowest mode ($n = 1$, $m = 0$) has the lowest frequency and the longest period and is referred to as the *fundamental mode*. The corresponding motion is one dimensional.

If the ratio between the two sides is a rational number, that is, $a = pL$, $b = qL$ (p, q = integers),

$$k_{nm} = \left[\left(\frac{m}{p} \right)^2 + \left(\frac{n}{q} \right)^2 \right]^{1/2} \frac{\pi}{L} ,$$

there are more than one set of (n, m) which correspond to the same eigenfrequency. This situation is called *degeneracy*.

Let us illustrate the spatial structure of the mode $(n, m) = (1, 1)$, that is,

$$\eta_{11} = A_{11} \cos \frac{\pi x}{a} \cos \frac{\pi y}{b} .$$

At the boundaries $x = 0, a$, and $y = 0, b$, the amplitude is maximum. On the other hand, the amplitude is zero along the *nodal lines* $x = a/2$ or $y = b/2$, which divide the basin into four rectangles. At a given instant two adjacent rectangles are opposite in phase. Thus, if two regions are above the mean water level, the other two are below and vice versa. In Fig. 5.3 the contour lines are shown.

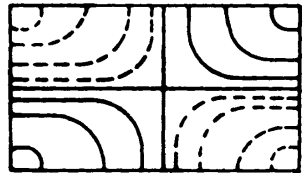

Figure 5.3: Free-surface contours of natural mode $\cos(\pi x/a) \cos(\pi y/b)$ in a rectangular basin.

For higher modes (n, m), the free surface is also similarly divided by n nodal lines along $x/a = \frac{1}{2}\pi,\ \frac{3}{2}\pi, \ldots, (n - \frac{1}{2})\pi$, as well as m nodal lines along $y/b = \frac{1}{2}\pi,\ \frac{3}{2}\pi, \ldots, (m - \frac{1}{2})\pi$.

5.3.2 A Circular Basin

Let the radius of the basin be a; polar coordinates (r, θ) may be chosen so that the origin is at the center. The governing Helmholtz equation may be written in the form of Eq. (4.9.10), Chapter Four. On the wall, $r = a$, the normal radial velocity component vanishes. Hence

$$\frac{\partial \eta}{\partial r} = 0\,. \tag{5.3.5}$$

A solution to the Helmholtz equation is, by separation of variables,

$$\eta = J_m(kr)(A_m \cos m\theta + B_m \sin m\theta) \tag{5.3.6}$$

where A_m and B_m are arbitrary constants. To satisfy the boundary condition we must have

$$J'_m(kr)|_{r=a} = J'_m(ka) = 0\,. \tag{5.3.7}$$

Now $J'_m(z)$ is an oscillatory function of z having an infinite number of zeroes. Denoting the nth zero of J'_m by j'_{mn} : $J'_m(j'_{mn}) = 0$, we have the eigenvalues

$$k_{mn} = \frac{j'_{mn}}{a}\,, \quad n = 1, 2, 3, \ldots\,,\ m = 0, 1, 2, 3, \ldots\,. \tag{5.3.8}$$

The corresponding eigensolutions or natural modes are

$$\eta_{mn} = J_m(k_{mn}r)(A_{mn} \cos m\theta + B_{mn} \sin m\theta)\,. \tag{5.3.9}$$

To illustrate the structure of a particular mode, we consider the free-surface variation for $\eta_{mn} = J_m(k_{mn}r) \cos m\theta$ with n, m fixed. Clearly, $\cos m\theta = 1$ when $m\theta = 0, 2\pi, 4\pi, \ldots, 2m\pi$, and -1 when $m\theta = \pi, 3\pi, 5\pi, \ldots, (2m-1)\pi$. Thus, $\theta = 0, \pi/m, 2\pi/m, 3\pi/m, \ldots$ are antinodal lines where the surface displacement is the greatest along a circle of given r. On the other hand, $\theta = \pi/2m, 3\pi/2m, 5\pi/2m, \ldots$ are the nodal lines where the displacement is zero. For a fixed θ, the curve $J_m(k_{mn}r)$ crosses the zero line exactly $n - 1$ times within the range $r < a$ so that there are $n - 1$ nodal rings; this fact is the consequence of the general Stürm's oscillation theorem in the theory of ordinary differential equations. The partition of the free surface into

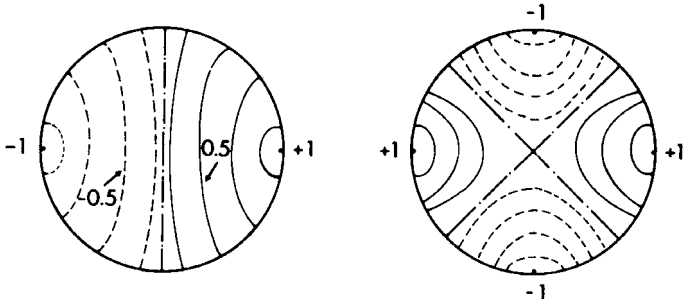

Figure 5.4: Contour lines of two natural modes in a circular basin: $J_1(k_{11}r)\cos\theta$ and $J_2(k_{21}r)\cos 2\theta$.

Table 5.1: Values of j'_{mn} such that $J'_m(j'_{mn}) = 0$.

n \ m	0	1	2	3	4	5
1	0	1.84118	3.05424	4.20119	5.31755	6.41562
2	3.83171	5.33144	6.70713	8.01524	9.28240	10.51986
3	7.01559	8.53632	9.96947	11.34592	12.18190	13.98719
4	10.17346	11.70600	13.17037	14.58525	15.96411	17.31284

ups and downs is illustrated in Fig. 5.4. The values of these zeroes are available in Abramowitz and Stegun (1972) and are tabulated in Table 5.1. In ascending order, the indices (n, m) of the zeroes are $(0, 1)$, $(1, 1)$, $(2, 1)$, $(0, 2)$, (3.1), (4.1), (1.2), ... For mass conservation, the mode $(0, 0)$ cannot exist in a completely closed basin.

5.4 Concept of Radiation Damping — A Model Example

An important feature of wave diffraction in an infinite medium is that oscillations which originate from a finite region experience damping even when the medium is conservative. This damping is associated with the energy carried away to infinity by outgoing waves and is called *radiation damping*. To gain some idea about it let us study a very instructive model example of Carrier (1970) which has the physical features typical of a vibrating system coupled with propagating waves.

Consider a semi-infinite channel of uniform depth h and width b, Fig. 5.5. At $x = 0$ there rests a gate of mass M which is allowed to

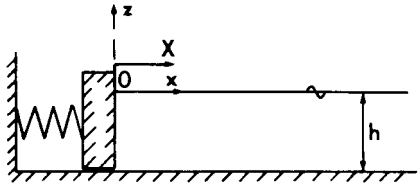

Figure 5.5: A spring-supported mass against water waves.

slide along the channel without friction. The gate is supported by a spring with elastic constant K. Assuming for simplicity that there is no leakage at $x = 0$, we wish to find the displacement $Xe^{-i\omega t}$ of the gate when there is an incident shallow-water wave of amplitude A and frequency ω from $x \sim +\infty$.

The water surface can be represented by

$$\begin{aligned}\zeta = \eta e^{-i\omega t} &= A(e^{-ikx} + Re^{ikx})e^{-i\omega t} \\ &= A[e^{-ikx} + e^{ikx} + (R-1)e^{ikx}]e^{-i\omega t}\,. \end{aligned} \tag{5.4.1}$$

In the last brackets above the second term stands for the reflected wave when the gate is held stationary, and the third term stands for the radiated wave due to the induced motion of the gate.

The equation of motion of the gate is

$$-M\omega^2 X = -KX = pbh \tag{5.4.2}$$

where p is the hydrodynamic pressure per unit area at $x = 0$:

$$p = \rho g \eta = \rho g A(1 + R)\,. \tag{5.4.3}$$

Equations (5.4.2) and (5.4.3) can be combined to give

$$A(1 + R) = \frac{K - M\omega^2}{\rho g b h} X\,. \tag{5.4.4}$$

At $x = 0$ the fluid velocity $u(0) = (-ig/\omega)\eta_x(0)$ must equal the gate velocity $-i\omega X$, thus,

$$u(0) = -i\omega X = \frac{gkA}{\omega}(-1 + R)\,. \tag{5.4.5}$$

It is easy to deduce the solution from Eqs. (5.4.4) and (5.4.5)

$$\frac{X}{2A} = \frac{\rho g b h}{-K + M\omega^2 + i(\omega^2/k)\rho b h}$$

$$= \frac{\rho g b h}{-K + M\omega^2 + i\omega(gh)^{1/2}(\rho b h)}\,. \tag{5.4.6}$$

The radiated wave amplitude is

$$R - 1 = -2i\omega \left(\frac{h}{g}\right)^{1/2} \frac{X}{2A}\,.$$

Equation (5.4.6) may be compared with the usual mass–spring–dashpot system. Except for a constant of proportionality, the denominator in Eq. (5.4.6) may be called the *impedance*. The imaginary part (proportional to ρbh) of the impedance plays the role of damping. To see this let us consider the system to be unforced. A nontrivial free vibration can still be described by Eq. (5.4.6) with $A = 0$ if we insist that the denominator vanishes, that is,

$$-K + M\omega^2 + i\omega(gh)^{1/2}(\rho b h) = 0, \tag{5.4.7}$$

which is an eigenvalue condition with complex solutions for ω:

$$\omega = \pm \left\{ \omega_0^2 - \left[\frac{(gh)^{1/2}\rho b h}{2M}\right]^2 \right\}^{1/2} - \frac{i(gh)^{1/2}\rho b h}{2M}$$

where $\omega_0 = K/M$. Inserting either solution in the time factor $\exp(-i\omega t)$, we see that the oscillation decays exponentially at the rate proportional to

$$\frac{(gh)^{1/2}\rho b h}{2M}\,. \tag{5.4.8}$$

To trace the physical source of this damping, let us calculate the rate of work done by the radiated wave averaged over a cycle

$$\overline{\dot{E}}_{\text{rad}} = \frac{1}{2}\,\text{Re}\,[p_{\text{rad}} u^*]_{x=0} b h$$

$$= \frac{1}{2} b h\,\text{Re}\,\rho g A(R-1)(-i\omega X)^*$$

$$= \frac{1}{2}\rho\frac{\omega^3}{k}|X|^2 = \frac{1}{2}\rho b h(\omega^2(gh)^{1/2})|X|^2$$

after using Eq. (5.4.5) and $\omega = (gh)^{1/2}k$. This positive-definite quantity is clearly associated only with the damping term so that damping is due to

the rate of work imparted by the radiated waves to the fluid. Therefore, we refer to the imaginary term in Eq. (5.4.6) as the *radiation damping*.

The response (5.4.6) may be written either as a function of ω:

$$\frac{X}{2A} = \left(\frac{\rho g b h}{M}\right)\left[\omega^2 - \frac{K}{M} + \frac{i\omega(gh)^{1/2}\rho b h}{M}\right]^{-1}, \tag{5.4.9}$$

or as a function of k:

$$\frac{X}{2A} = \left(-\frac{\rho b}{M}\right)\left(k^2 - \frac{K}{Mgh} + \frac{ik\rho b h}{M}\right)^{-1}. \tag{5.4.10}$$

In the complex k plane there are two poles located at

$$\pm\tilde{k} + i\hat{k} \tag{5.4.11}$$

with

$$\tilde{k} = k_0\left[1 - \left(\frac{\rho b h^2}{M}\right)^2 \frac{Mg}{4Kh}\right]^{1/2},$$

$$k_0 \equiv \frac{\omega_0}{(gh)^{1/2}} \equiv \left(\frac{K}{M}\right)^{1/2} \frac{1}{(gh)^{1/2}}, \tag{5.4.12}$$

and

$$\hat{k} = -\frac{\rho b h}{2M} < 0. \tag{5.4.13}$$

Equation (5.4.10) then becomes

$$\frac{X}{2A} = \left(\frac{\rho b}{M}\right)(k - \tilde{k} - i\hat{k})^{-1}(k + \tilde{k} - i\hat{k})^{-1}. \tag{5.4.14}$$

For small damping the two poles are only slightly below the real axis. In the physical problem, ω and k are both positive and real; the only pole of physical meaning is $\tilde{k}+i\hat{k}$. In its neighborhood, $|X|$ is large and Eq. (5.4.14) may be approximated by

$$\frac{X}{2A} \cong \left[\left(\frac{\rho b}{M}\right)\frac{1}{2\tilde{k}}\right](k - \tilde{k} - i\hat{k})^{-1}. \tag{5.4.15}$$

The maximum of $|X/2A|^2$ is

$$\left|\frac{X}{2A}\right|^2_{\max} = (\tilde{k}h)^{-2} \cong (k_0 h)^{-2}$$

which is attained near $k \cong \tilde{k}$. When $k - \tilde{k} = \pm\hat{k}$, the square response drops to one-half of the peak value, therefore $\hat{k}$ is a measure of the width of the response curve ($|X/2A|^2$ versus k). As in electric circuit theory, we may define the *quality factor* $\mathscr{Q}$ by

$$\mathscr{Q} = -\frac{\tilde{k}}{\hat{k}} \cong \frac{\rho b h}{2M}\left(\frac{M}{K}\right)^{1/2}(gh)^{1/2}\,. \tag{5.4.16}$$

As the radiation damping $\hat{k}$ decreases, $\mathscr{Q}$ decreases; the peak width of the response curve decreases, hence the shape of the curve sharpens. As is seen from Eq. (5.4.8), $\mathscr{Q}\omega_0$ also corresponds to the rate of damping of free oscillations.

5.5 Diffraction Through a Narrow Gap

A harbor entrance is often just an opening along an otherwise long and thin breakwater. Transmission of waves through the opening is of obvious interest. For analytical simplicity, we assume that the breakwater is thin, vertical, and perfectly reflective, and the depth is constant so that the problem has an exact acoustical analogy.

Referring to Fig. 5.6, we consider normal incidence from $x > 0$. On the incidence side, $x > 0$, the total wave system consists of the incident wave, the reflected wave from a solid wall, and disturbances due to the fluid motion along the gap. On the transmission side, $x < 0$, there are only disturbances due to the motion along the gap. The gap acts as a piston in a baffle wall and radiates waves to infinity on both sides.

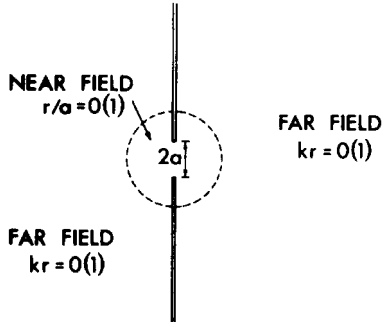

Figure 5.6: A gap between two breakwaters.

While the boundary-value problem can be solved approximately for any gap width by the integral-equation method, we shall apply the method of *matched asymptotic expansions*, which is particularly convenient for a gap whose width is much less than the wavelength (Buchwald, 1971).

The intuitive ideas of the method have been explained in Section 4.2.2. Briefly, when various parts of the physical domain are governed by vastly different scales, we approximate the equations and the boundary conditions according to the local scales and seek solutions valid in these separate regions. The solution in one region usually does not satisfy the boundary conditions in the other, resulting in some indeterminancy. By the requirement that they match smoothly in some intermediate region, this indeterminancy is removed and the solution is obtained to a desired order.

Let us define the *far field* to be the region which is a few wavelengths away from the gap,

$$kr = O(1) \quad \text{(the far field)}\,. \tag{5.5.1}$$

Clearly, $1/k$ is the proper scale and all terms in the Helmholtz equation are equally important. At great distances from the gap, the radiated waves must satisfy the Helmholtz equation and the radiation condition. However, to the far-field observer, the gap is a very small region in the neighborhood of the origin. The radiated wave may be represented by superimposing solutions which are singular at the origin and cause no flux along the y axis:

$$\eta_{\pm}^{R} = \frac{\omega Q^{\pm}}{2g} H_0^{(1)}(kr) + \frac{\omega \mu^{\pm}}{2g} H_1^{(1)}(kr) \sin\theta + \cdots\,, \quad x \gtrless 0\,. \tag{5.5.2}$$

The total far-field solutions on both sides of the gap are

$$\eta_{+} = 2A \cos kx + \eta_{+}^{R}\,, \quad x > 0\,, \quad \text{and} \quad \eta_{-} = \eta_{-}^{R}\,, \quad x < 0\,. \tag{5.5.3}$$

From the first term in the series of Eq. (5.5.2), the flux out of a semicircle of small radius around the origin is, for $x \lessgtr 0$,

$$\text{flux} = \lim_{r \to 0} \pi r \left(\frac{-ig}{\omega} \frac{\omega Q^{\pm}}{2g} \right) \frac{\partial}{\partial r} H_0^{(1)}(kr) = Q^{\pm}\,.$$

Hence, the first term of Eq. (5.5.2) represents a source with a discharge rate of $Q^{\pm}$ into the half-plane $x \gtrless 0$. The subsequent terms represent doublet, quadrupole, ..., and so on.

Near the junction, the length scale is the gap width; hence we may define a *near field* where

$$\frac{r}{a} = O(1)\,. \tag{5.5.4}$$

In this region

$$\frac{k^2\eta}{\nabla^2\eta} = O(ka)^2$$

so that the flow is essentially governed by the Laplace equation

$$\nabla^2\eta = 0 \tag{5.5.5}$$

with a relative error of order $O(ka)^2$. The no-flux condition must be satisfied on the solid walls. The radiation condition is no longer relevant and has to be discarded. Now Eq. (5.5.5) and the no-flux condition define a usual potential flow problem with time as a parameter only. Since η is harmonic, it may be taken as the real part of an analytic function W of the complex variable $z = x + jy$, that is,

$$\eta = \mathrm{Re}_j W(z) \tag{5.5.6}$$

where Re_j means the real part with respect to j, with i regarded as real. The solution of Eqs. (5.5.5) and (5.2.4) becomes the search for $W(z)$ that is analytic in the z plane with

$$\mathrm{Im}_j W(z) = \text{constant on the solid walls}\,. \tag{5.5.7}$$

For simple geometries, the solution is most effectively found by the technique of conformal mapping. In the present case, we use the Joukowski transformation in the airfoil theory

$$z = -\frac{ja}{2}\left(\tau + \frac{1}{\tau}\right) \tag{5.5.8}$$

to map the z plane outside the two breakwaters onto the upper half-plane of τ (see Fig. 5.7). In particular, the image of the solid wall ABD is the negative real τ axis, and the image of $A'B'D'$ is the positive real τ axis. To satisfy the condition that $\mathrm{Im}_j W = 0$ on $A'B'D'$ and $\mathrm{Im}_j W = \text{const}$ on ABD, we adopt the solution

$$W(z) = C + M\ln\tau + C_1\tau + C_2\tau^2 + \cdots + C_{-1}\tau^{-1} + C_{-2}\tau^{-2} + \cdots \tag{5.5.9}$$

where the coefficients are real with respect to j but may be complex with respect to i. The coefficients $Q^{\pm}$ and $\mu^{\pm}$ in Eq. (5.5.2), as well as C, M, and C_1, C_{-1}, and so on, will be found by matching the near and far fields.

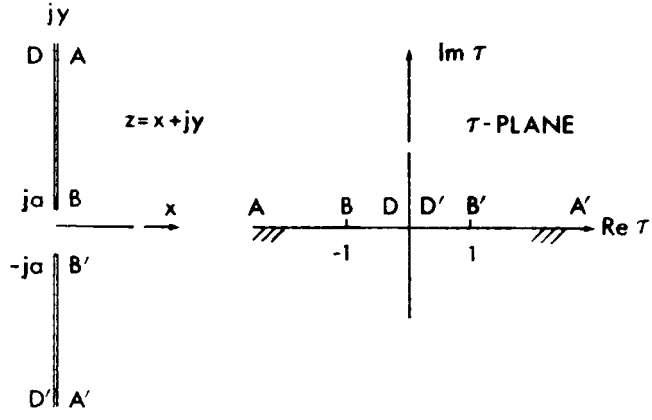

Figure 5.7: Mapping of the near field from the z plane (physical) to the upper half of the τ plane.

Let us require that in an intermediate region, which appears to be close to the origin to the far-field observer ($kr \ll 1$), while very far away from the near-field observer ($r/a \gg 1$), the near- and far-field solutions should match smoothly. For $kr \ll 1$, the *inner expansion* of the total far field is

$$\eta_+ = 2A + \frac{i\omega Q^+}{g}\left(-\frac{i}{2} + \frac{1}{\pi}\ln\frac{\gamma kr}{2}\right) - \frac{\omega\mu^+}{2g}\frac{1}{r}\sin\theta + \cdots O(kr)^2\ln kr\,, \quad x > 0 \tag{5.5.10}$$

$$\eta_- = +\frac{i\omega Q^-}{g}\left(-\frac{i}{2} + \frac{1}{\pi}\ln\frac{\gamma kr}{2}\right) - \frac{\omega\mu^-}{2g}\frac{1}{r}\sin\theta + \cdots O(kr)^2\ln kr\,, \quad x < 0 \tag{5.5.11}$$

where $\ln\gamma$ = Euler's constant = 0.5772157.... To approximate the near-field solution for $r/a \gg 1$, we must distinguish the two sides $x < 0$ and $x > 0$. On the side of $x > 0$, the region of $|z|/a \gg 1$ corresponds to $|\tau| \gg 1$ in the τ plane so that

$$\tau = \frac{2jz}{a}\left[1 + O\left(\frac{r}{a}\right)^{-2}\right] \tag{5.5.12}$$

from Eq. (5.5.8). If this is substituted into Eq. (5.5.6), the *outer expansion* of the near field η is obtained,

$$\eta \simeq \mathrm{Re}_j W \simeq \mathrm{Re}_j \left(C + M \ln \frac{2jz}{a} + C_1 \left(\frac{2jz}{a} \right) + \cdots + C_{-1} \left(\frac{a}{2jz} \right) + \cdots \right)$$

$$= C + M \ln \frac{2r}{a} - C_1 \left(\frac{2y}{a} \right) + \cdots - C_{-1} \left(\frac{a}{2r} \right) \sin\theta + \cdots \tag{5.5.13}$$

On the side of $x < 0$, the region of $|z|/a \gg 1$ corresponds to the origin in the τ plane. Hence from Eq. (5.5.8)

$$\tau = \frac{a}{2jz} \left[1 + O\left(\frac{z}{a} \right)^{-2} \right], \tag{5.5.14}$$

and the *outer expansion* of the near field is

$$\eta \simeq \mathrm{Re}_j W \simeq \mathrm{Re}_j \left\{ C + M \ln \frac{a}{2jz} + C_1 \left(\frac{a}{2jz} \right) + \cdots + C_{-1} \left(\frac{2jz}{a} \right) + \cdots \right\}$$

$$= C - M \ln \frac{2r}{a} - C_1 \left(\frac{a}{2r} \right) \sin\theta + \cdots - C_{-1} \left(\frac{2y}{a} \right) + \cdots . \tag{5.5.15}$$

We now equate Eqs. (5.5.10) and (5.5.13) to match η_+. From the coefficients of like terms several algebraic relations are found,

$$(\text{const}): \quad 2A + \frac{i\omega Q^+}{g} \left[-\frac{i}{2} + \frac{1}{\pi} \ln \frac{\gamma k}{2} \right] = C + M \ln \frac{2}{a} \tag{5.5.16a}$$

$$(\ln r): \quad \frac{i\omega Q^+}{\pi g} = M \tag{5.5.16b}$$

$$(y): \quad C_1 = 0 \tag{5.5.16c}$$

$$\left(\frac{1}{r} \sin\theta \right): \quad C_{-1} = \frac{\omega \mu^+}{ga} . \tag{5.5.16d}$$

Matching η_- by equating Eqs. (5.5.11) and (5.5.15) similarly, we obtain

$$(\text{const}): \quad \frac{i\omega Q^-}{g} \left(-\frac{i}{2} + \frac{1}{\pi} \ln \frac{\gamma k}{2} \right) = C - M \ln \frac{2}{a} \tag{5.5.17a}$$

$$(\ln r): \quad \frac{i\omega Q^-}{\pi g} = -M \tag{5.5.17b}$$

$$(y): \quad C_{-1} = 0 \tag{5.5.17c}$$

$$\left(\frac{1}{r} \sin\theta \right): \quad C_1 = \frac{\omega \mu^-}{ga} . \tag{5.5.17d}$$

Observe immediately that

$$C_1 = C_{-1} = 0\,, \tag{5.5.18a}$$

$$\mu^+ = \mu^- = 0\,. \tag{5.5.18b}$$

It can be shown that poles of higher order are likewise zero so that only the source is important at the leading order. Thus C_n, $n = \pm 2, \pm 3, \ldots$, are also zero and no nonzero powers of τ are needed in the inner solution to the present accuracy. These facts will be used in future analysis without further verification.

There are now only four unknowns remaining: $Q^{\pm}$, M, and C which can be solved to give

$$-\frac{i\omega Q^+}{g} = +\frac{i\omega Q^-}{g} = \frac{A}{-\frac{1}{2}i + (1/\pi)\ln(\gamma ka/4)}\,, \tag{5.5.19a}$$

$$M = +\frac{i\omega Q^+}{\pi g} = -\frac{i\omega Q^-}{\pi g}\,, \tag{5.5.19b}$$

$$C = A\,. \tag{5.5.19c}$$

Combination of Eq. (5.15.19a) with Eq. (5.5.2) yields, finally,

$$\eta_{\pm}^R \cong \frac{\pm i\frac{1}{2}AH_0^{(1)}(kr)}{-\frac{1}{2}i + (1/\pi)\ln(\gamma ka/4)}\,. \tag{5.5.20}$$

Expanding the Hankel function for large kr, we have

$$\eta_{\pm}^R = \pm A\mathfrak{A}\left(\frac{2}{\pi kr}\right)^{1/2} e^{ikr - i\pi/4} \tag{5.5.21}$$

where

$$\mathfrak{A} = \left(1 + \frac{2i}{\pi}\ln\frac{\gamma ka}{4}\right)^{-1}\,. \tag{5.5.22}$$

The function $-\ln z$ approaches infinity very slowly as z diminishes. For example, $-\ln z = 2.0, 4.6, 6.9, \ldots$ for $z = 10^{-1}$, 10^{-2}, 10^{-3}, and so on. Thus, $-\ln(\gamma ka/4)$ is really not so large for practical ranges of ka, and $|\mathfrak{A}|$ diminishes slowly as ka decreases, as shown below:

ka	1	0.1	0.01	0.001
$\lvert\mathfrak{A}\rvert$	0.8890	0.4506	0.2786	0.1995 .

The persistence of transmission for very small ka is a typical result in potential theory and should be modified by real fluid effects of viscosity and separation at the tips.

To the present degree of approximation, the near field is dominated by a constant and a term proportional to $\ln r$. Physically, the former term represents a uniform rise and fall of the free surface and the latter indicates that the gap acts as a source to one side and a sink of equal magnitude to the other.

In closing, it should be mentioned that for arbitrary ka the diffraction problem can be solved by a number of approximate methods based on the method of integral equations. As ka increases the radiated wave amplitude $\mathscr{A}$ has a more complicated dependence on θ. As will be shown later, significant resonance in a harbor occurs when the wavelength is at least comparable to the harbor dimensions, which usually far exceeds the width of the harbor entrance. Hence, we shall not discuss the gap problem further here.

5.6 Scattering by a Long and Narrow Canal or a Bay

5.6.1 General Solution

Let us consider a narrow canal of width $2a$ open to the ocean. The geometry is depicted in Fig. 5.8. For long waves, $ka \ll 1$, the far field in the canal can only be one dimensional, this being a special case of Section 4.1.2. Therefore, the general far-field solution in the canal is

$$\eta_c = Be^{-ikx} + De^{ikx}, \quad x < 0 \tag{5.6.1}$$

with the inner expansion

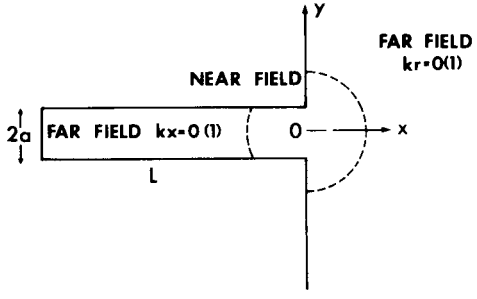

Figure 5.8: A narrow bay.

$$\eta_c = (B+D) + ik(-B+D)x + \cdots O(kx)^2 \quad \text{for} \quad |kx| \ll 1\,. \tag{5.6.2}$$

The far-field solution in the ocean is, as before,

$$\eta_0 \cong 2A\cos kx + \frac{\omega Q}{2g} H_0^{(1)}(kr) \tag{5.6.3}$$

with the inner expansion

$$\eta_0 = 2A + \frac{\omega Q}{2g}\left(1 + \frac{2i}{\pi}\ln\frac{\gamma kr}{2}\right) + O(kr)\,, \quad kr \ll 1\,. \tag{5.6.4}$$

The near-field problem is that of a potential flow past a right-angled estuary; see Fig. 5.9. By the Schwarz–Christoffel transformation the physical region in the complex z plane ($z = x + jy$) can be mapped onto the upper half of the τ plane by

$$z = \frac{2a}{\pi}\left[-j(\tau^2-1)^{1/2} + \ln\frac{\tau}{(\tau^2-1)^{1/2}+j}\right] \tag{5.6.5}$$

(Kober, 1957, p. 155) with the images shown in Fig. 5.9. For single valuedness the square root $(\tau^2-1)^{1/2}$ is defined in the τ plane with a cut along the real axis $-1 \le \operatorname{Re}\tau \le 1$, and the branch is chosen so that $(\tau^2-1)^{1/2} \to \tau$ as $|\tau| \to \infty$. The logarithmic function $\ln\tau$ is defined with a cut along the positive real axis.

The near-field approximation has to be analytic in τ as before,

$$\eta = \operatorname{Re}_j W(\tau) = \operatorname{Re}_j(M\ln\tau + C) \tag{5.6.6}$$

with M and C real in j. Its outer expansion must be calculated by distinguishing the two sides $x \gtrless 0$. On the ocean side, $x > 0$, large $|z|/a$

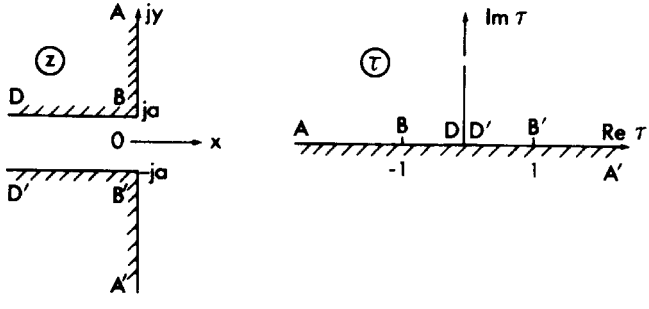

Figure 5.9: Mapping of the near field from the z plane to the upper half of the τ plane.

corresponds to large $|\tau|$ (see Fig. 5.9). By expanding the right-hand side of Eq. (5.6.5), we have

$$z = \frac{2a}{\pi}\left[-j\tau + O\left(\frac{1}{\tau}\right)\right], \quad -j\tau = \frac{\pi z}{2a}\left[1 + O\left(\frac{a}{z}\right)^2\right], \quad x > 0\,. \tag{5.6.7}$$

Substituting Eq. (5.6.7) into Eq. (5.6.6), we obtain the outer expansion of the near field

$$\eta \cong \mathrm{Re}_j M \ln\frac{j\pi z}{2a} + C = M\ln\frac{\pi r}{2a} + C\,, \quad x > 0\,. \tag{5.6.8}$$

On the canal side, $x < 0$, large $|z/a|$ corresponds to small $|\tau|$. Since from Eq. (5.6.5)

$$\begin{aligned}\frac{\pi z}{2a} &= 1 + \ln\tau - \ln 2j + O(\tau)^2 \\ &= \ln\frac{e\tau}{2j} + O(\tau)^2 \quad \text{or} \quad \tau \cong \frac{2j}{e}e^{\pi z/2a}\,, \quad -\frac{x}{a} \gg 1\,,\end{aligned}$$

we have

$$\ln\tau \cong \frac{\pi z}{2a} - \ln\frac{e}{2j}\,, \tag{5.6.9}$$

the error being exponentially small for $x/a \to -\infty$. The outer expansion of the near-field solution is, therefore,

$$\eta \cong M\frac{\pi x}{2a} - M\ln\frac{e}{2} + C\,, \quad x < 0\,. \tag{5.6.10}$$

Matching of the inner and outer solutions on the canal side $x < 0$ gives

$$B + D = C - M\ln\frac{e}{2}\,, \tag{5.6.11a}$$

$$ik(-B + D) = \frac{\pi M}{2a}\,. \tag{5.6.11b}$$

Similarly, on the ocean side we obtain by matching Eqs. (5.6.4) and (5.6.8)

$$2A + \frac{\omega}{2g}Q\left(1 + \frac{2i}{\pi}\ln\frac{\gamma k}{2}\right) = C + M\ln\frac{\pi}{2a}\,, \tag{5.6.11c}$$

$$\frac{iQ\omega}{\pi g} = M\,. \tag{5.6.11d}$$

Thus far, there are four algebraic equations for five unknowns: B, D, C, M, and Q; A being prescribed. One more condition is needed which depends on the constraints at the far end of the canal. The following possibilities are of physical interest:

1 Wave scattering into an infinitely long channel with no reflection from the far end. Since only left-going waves are possible, $D = 0$, so that the channel solution is

$$\eta_c = Be^{-ikx}\,. \tag{5.6.12}$$

2 Wave incident from the far end of the channel and transmitted into the ocean. In this case D is given and $A = 0$.

3 Wave scattering into a long bay of length L where the far end $x = -L$ is highly reflective. Here we impose

$$\frac{\partial \eta_c}{\partial x} = 0\,, \quad x = -L\,.$$

The appropriate outer solution is

$$\eta_c = E\cos k(x+L)\,, \tag{5.6.13}$$

so that

$$B = \frac{1}{2}Ee^{-ikL}, \quad D = \frac{1}{2}Ee^{ikL}\,. \tag{5.6.14}$$

The corresponding inner expansion is

$$\eta_c = E[\cos kL - (\sin kL)kx] + O(kx)^2\,. \tag{5.6.15}$$

The algebraic problems for the unknown coefficients can now be solved for each case. For instance, for the first problem (wave scattered into a long canal), we get

$$\frac{\omega Q}{2g} = \frac{2Aka}{[1 + ka + (2ika/\pi)\ln(2\gamma ka/\pi e)]}\,, \tag{5.6.16}$$

$$B = \frac{-2A}{[1 + ka + (2ika/\pi)\ln(2\gamma ka/\pi e)]}\,. \tag{5.6.17}$$

Again, C is concerned with the near field only and will not be recorded. Equation (5.6.16) gives the strength of the source radiating waves back to the infinite ocean and Eq. (5.6.17) gives the amplitude of the transmitted wave.

Exercise 5.1

Complete the solution for problem 2, wave propagation from the channel into the ocean, and discuss the result.

5.6.2 An Open Narrow Bay

The case of a narrow bay of finite length, that is, problem 3 above, illustrates many common features of harbor resonance, hence a detailed analysis is given here. A complete analysis was first given by Miles and Munk (1961) whose approximation at the entrance was slightly different from matched asymptotics (Ünlüata and Mei, 1973).

By combining Eq. (5.6.14) with Eqs. (5.6.11a)–(5.6.11d), we obtain the bay response η_c and the discharge Q through the bay entrance:

$$\eta_c = \frac{2A\cos k(x+L)}{\cos kL + (2ka/\pi)\sin kL \ln(2\gamma ka/\pi e) - ika\sin kL} \tag{5.6.18}$$

$$\frac{\omega Q}{2g} = \frac{2Aika\sin kL}{\cos kL + (2ka/\pi)\sin kL \ln(2\gamma ka/\pi e) - ika\sin kL} \tag{5.6.19}$$

where η_c refers to the far-field motion away from the entrance by a distance much greater than $2a$ but much less than the wavelength. Relative to the standing wave amplitude $2A$, an amplification factor $\mathcal{A}$ may be defined,

$$\mathcal{A} = \frac{1}{\cos kL + (2ka/\pi)\sin kL \ln(2\gamma ka/\pi e) - ika\sin kL} \tag{5.6.20}$$

so that

$$\eta_c = 2A\,\mathcal{A}\cos k(x+L)\,. \tag{5.6.21}$$

The plot of $|\,\mathcal{A}\,|^2$ versus kL will be called the *response curve*, with ka being a parameter.

Since $ka \ll 1$, the response curve has a peak near the zeroes of $\cos kL$, that is,

$$\cos kL \cong 0\,, \quad kL \cong k_n L = \left(n + \frac{1}{2}\right)\pi\,, \quad n = 0, 1, 2, \ldots\,.$$

Because of the small terms of $O(ka)$ in Eq. (5.6.20), the resonant peaks are slightly shifted from these crude values. A better approximation is obtained by letting

$$k = k_n + \Delta$$

and expanding for small Δ:

$$\cos kL = -L\Delta \sin k_n L + O(\Delta^3)\,, \quad \sin kL = \sin k_n L + O(\Delta^2)\,.$$

In the neighborhood of the nth resonant peak, the amplification factor is

$$\begin{aligned} \mathcal{A} &\cong \frac{1}{-\sin k_n L[L\Delta - (2k_n a/\pi)\ln(2\gamma k_n a/\pi e) + ik_n a]} \\ &\cong \frac{1}{(-1)^{n+1}[(k-\tilde{k}_n)L + ik_n a]}\,, \end{aligned} \tag{5.6.22}$$

with

$$\tilde{k}_n \equiv k_n \left(1 + \frac{2}{\pi}\frac{a}{L}\ln\frac{2\gamma k_n a}{\pi e}\right), \tag{5.6.23}$$

which may be compared with Eq. (5.4.15) for the model example. Clearly, the peak is at $k = \tilde{k}_n$ and the shift of the peak is given by

$$(\tilde{k}_n - k_n) = \frac{2}{\pi}\frac{k_n a}{L}\ln\frac{2\gamma k_n a}{\pi e} < 0\,. \tag{5.6.24}$$

Around the peak, the square of the amplification factor is

$$|\,\mathcal{A}\,|^2 = \frac{1}{|(k-\tilde{k}_n)L|^2 + (k_n a)^2}\,, \tag{5.6.25}$$

while the peak value is

$$|\,\mathcal{A}\,|_{\max} = \frac{1}{k_n a} = \frac{1}{(n+\frac{1}{2})\pi a/L}\,. \tag{5.6.26}$$

Thus, the height of successive resonant peaks decreases with the mode number n.

For mode n, the plot of $\mathcal{A}$ versus kL is approximately symmetrical about the peak. At the values

$$(k-\tilde{k}_n)L = \pm k_n a\,,$$

$|\,\mathcal{A}\,|^2$ is reduced by half. Thus, $k_n a$ is a measure of both the peak height and the half-width of the resonance curve. The corresponding wave profile in the bay is roughly proportional to

$$\cos\left[\left(n+\frac{1}{2}\right)\pi\left(\frac{x}{L}+1\right)\right].$$

In particular, at the lowest mode $n = 0$, the bay length is about one-quarter of the wavelength so that the harbor entrance is very close to the first node.

Compare two bays of equal length L but different width $2a$. The narrower harbor has the small shift $(k_n - \tilde{k}_n)L$ and the resonant peak is sharper and higher. In the limit of $ka \to 0$ the radiation damping diminishes to zero and the peak height becomes infinite. Since the width of the resonant peak in the response diagram also diminishes with a, the incident wave must be precisely tuned to the peak frequency in order to resonate the harbor. If the tuning is slightly off, the response is greatly reduced. The feature that the resonant response increases with narrowing entrance does not always agree with practical experience and is one aspect of the *harbor paradox* termed by Miles and Munk (1961). This paradox can be removed by considering friction at the harbor entrance and/or nonlinearity, both of which will be considered in later chapters.

From Eq. (5.6.19) the discharge per unit depth at the harbor entrance Q, which is essentially the amplitude of the radiated waves, is also maximum at a resonant peak. The maximum values of Q are obtained by letting the real part in the denominator vanish so that

$$\max |Q| = \frac{4Ag}{\omega_n}$$

where $\omega_n = k_n(gh)^{1/2}$. The resonant discharge is smaller for a higher mode.

Notice that at the nth peak the free surface has an apparent node at $x = l$ so that

$$\cos \tilde{k}_n(l + L) = 0\,,$$

or

$$(k_n + \Delta)(l + L) = \left(n + \frac{1}{2}\right)\pi\,,$$

or

$$\frac{l}{L} \cong -\frac{\Delta}{k_n} = -\frac{2}{\pi}\frac{a}{L}\ln\frac{2\gamma k_n a}{\pi e} > 0\,,$$

which decreases with a/L and with n. Thus, the effective length of the bay is greater than the actual L. This increase in length can be thought of as the added inertia of the ocean water near the entrance.

The analytical result Eq. (5.6.20) is accurate as long as ka is small. For a special case treated by finite elements and shown later in Fig. 5.23, the present theory is quantitatively satisfactory only for the lowest (quarter wavelength) mode.

Exercise 5.2

Study the mutual influence of two straight and narrow canals of finite lengths opened perpendicularly to the same straight coast. Consider the angle of incidence to be arbitrary (Mei and Foda, 1979, where a mathematically similar problem of elastic SH waves incident on open cavities is treated).

Exercise 5.3

Study the oscillation in a semicircular canal of narrow width $2a$, with both ends open to the same straight coast. Consider the angle of incidence to be arbitrary (Mei and Foda, 1979).

Exercise 5.4: A Modeling Effect in Harbor Resonance (Rogers and Mei, 1978)

In harbor experiments the ocean is limited by the finite size of the test basin. Typically, the wavemaker is at a finite distance L' from the coast. Show by the method of images that the effect of the wavemaker at $x = L'$ can be approximately accounted for by letting the far-field solution in the ocean be

$$\eta = 2A\cos kx + \frac{\omega Q}{2g}\left\{H_0^{(1)}(kr) + \sum_{n=1}^{\infty}[H_0^{(1)}(k|\mathbf{r} - 2nL'\mathbf{e}_x|) + H_0^{(1)}(k|\mathbf{r} + 2nL'\mathbf{e}_x|)]\right\}$$

for $0 < x < L'$ and $kL' \neq m\pi$. Near the entrance for $kr \ll 1$ the correction due to finite L' is

$$e = \frac{\omega Q}{g}\sum_{n=1}^{\infty} H_0^{(1)}(2nkL')\,.$$

For large kL', the Hankel functions may be replaced by their asymptotic approximations so that

$$e \cong \frac{\omega Q}{g}\left(\frac{2}{\pi}\right)^{1/2} e^{-i\pi/4}\sum_{n=1}^{\infty}\frac{e^{inZ}}{(nZ)^{1/2}}\,,$$

$$Z = 2kL'\,.$$

For $Z = 2kL' \gg 1$ the series can be approximated by an integral in the following manner:

$$\sum_{n=1}^{\infty} f(n) = \sum_{n=1}^{\infty} f(n)\Delta n \quad (\text{since } \Delta n = 1)$$

$$= \sum_{n=1}^{\infty} f(\sigma Z) Z \Delta\sigma \quad \text{with} \quad \frac{n}{Z} = \sigma$$

$$\cong \int_{1/Z}^{\infty} f(\sigma Z) Z \, d\sigma \, .$$

Express the integral as a Fresnel integral and show that $e \sim O(kL')^{-3/2}$, hence give your own criterion on how large a wave tank should be to model an infinite ocean.

Exercise 5.5: Resonance in a Canal Connecting Two Seas

A straight and narrow canal of width $2a$ and length L connects two seas. Assume for simplicity that the coasts are vertical cliffs parallel to the y axis, the centerline of the canal is along the x axis, and the water deph is constant everywhere. Let a simple harmonic long wavetrain approach from $x \sim -\infty$ normally. Find the response in most of the canal except near the entrances. Discuss the physics. (You may use the crude method of matching averages of the far fields across the entrances.)

5.7 A Rectangular Harbor with a Narrow Entrance

In addition to the physical features deduced in Section 5.6, a harbor with comparable dimensions in both horizontal directions has a new mode of oscillation where the free surface within the harbor rises and falls in unison. This phenomenon is familiar in acoustics and may be demonstrated by a simple analysis. In reference to Fig. 5.10, consider a basin of surface area S open to the infinite ocean through a channel of length L and width a, where L is assumed to be sufficiently long so that the added hydrodynamic

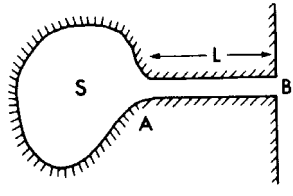

Figure 5.10

length is negligible by comparison. Let the free-surface amplitude at A be ζ and the velocity in the channel be U. Continuity requires that

$$\frac{\partial \zeta}{\partial t} S = -Uah\,.$$

When resonance occurs in the basin, ζ is small at the estuary B; the pressure gradient between A and B is approximately

$$-\frac{\Delta p}{\Delta x} = \frac{p_A - p_B}{L} = \frac{\rho g \zeta}{L}\,.$$

The momentum equation for the channel water is

$$\frac{\partial U}{\partial t} = \frac{g\zeta}{L}\,.$$

Combining the mass and momentum equations by eliminating U, we get

$$S\frac{\partial^2 \zeta}{\partial t^2} + gh\frac{a}{L}\zeta = 0\,,$$

which resembles a mass–spring system and has a natural mode with the natural frequency

$$\omega = \left(\frac{gha}{SL}\right)^{1/2}\,.$$

The corresponding characteristic wavenumber is, in dimensionless form, $kS^{1/2} = (a/L)^{1/2}$ and is very small. This mode of oscillation is called the *Helmholtz mode* in acoustics and the *pumping mode* in harbor engineering literature. Clearly, the existence of the Helmholtz mode is associated with the finite harbor area. Since the narrow bay in Section 5.6 corresponds to an oscillation with a spring but without mass, there is no Helmholtz mode.

We now turn to the special example of a rectangular harbor for a detailed analysis. This example was first studied by Miles and Munk (1961) with revisions by Garrett (1970). Use of matched asymptotics was made by Ünlüata and Mei (1973). Let the sides of the harbor be B and L as shown in Fig. 5.11. The harbor entrance is a gap in an otherwise thin and straight breakwater aligned with the coast. The gap width is assumed to be small compared to the wavelength $ka \ll 1$.

Assuming for simplicity that the incidence is normal, the outer solution for the ocean is again given by Eq. (5.6.3):

$$\eta_0 = 2A\cos kx - \frac{i\omega}{g} Q_0 \left[\frac{i}{2} H_0^{(1)}(kr)\right], \quad r^2 = x^2 + y^2 \tag{5.7.1}$$

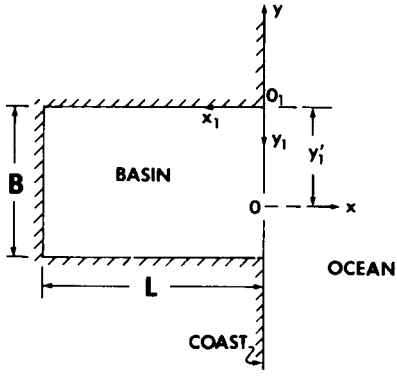

Figure 5.11: A rectangular harbor behind a straight coast.

where the coordinate system has its origin at the center of the entrance. The inner expansion of η_0 is recorded here for convenience,

$$\eta_0 = 2A + i\frac{\omega}{g}Q_0\left(\frac{-i}{2} + \frac{1}{\pi}\ln\frac{\gamma k}{2}\right) + i\frac{\omega}{g\pi}Q_0 \ln r + O(kr\ln kr)\,. \qquad (5.7.2)$$

The inner solution near the entrance is the potential flow past a gap and has the following two-term outer expansion [cf. Eqs. (5.5.13) and (5.5.15)]:

$$\eta_E = C \mp M\ln\frac{a}{2} + M\begin{pmatrix} +\ln r \\ -\ln r \end{pmatrix}, \quad \begin{matrix} x > 0 \\ x < 0 \ (x_1 > 0) \end{matrix}\,. \qquad \begin{matrix} (5.7.3a) \\ (5.7.3b) \end{matrix}$$

To describe the interior of the harbor, it is convenient to use a different coordinate system (x_1, y_1) where the origin coincides with a corner of the basin so that

$$x = -x_1\,, \quad y = y_1' - y_1\,, \quad r_1^2 = x_1^2 + (y_1 - y_1')^2\,. \qquad (5.7.4)$$

The center of the harbor entrance is at $y_1 = y_1'$ (see Fig. 5.11).

5.7.1 Solution by Matched Asymptotic Expansions

Let it be understood that *in the harbor* the coordinate system (x_1, y_1) is used. However, for brevity, the subscripts $(\ )_1$ will be omitted.

To the leading order the outer solution for the harbor is the field due to a pulsating source of unknown strength Q_H at the point $x = 0$, $y = y'$. Let $G(x, y; y')$ be the solution corresponding to

$$\nabla^2 G + k^2 G = 0\,, \tag{5.7.5a}$$

$$\frac{\partial G}{\partial y} = 0\,, \quad 0 < x < L,\ y = 0, B\,, \tag{5.7.5b}$$

$$\frac{\partial G}{\partial x} = 0\,, \quad x = L\,, \tag{5.7.5c}$$

$$= \delta(y - y')\,, \quad x = 0\,, \quad 0 < y < B\,. \tag{5.7.5d}$$

Since G represents the solution for a point source of unit discharge, it follows that

$$\eta_H = \frac{i\omega}{g} Q_H G(x, y; y') \tag{5.7.6}$$

is the desired outer solution in the harbor basin. The function of G is a kind of Green's function; its solution is derived in Appendix 5.A. We only give the following result:

$$G(x, y; y') = \sum_{n=0}^{\infty} X_n(x) Y_n(y) Y_n(y') \tag{5.7.7}$$

where

$$X_n(x) = \frac{\varepsilon_n \cos K_n(x - L)}{K_n B \sin K_n L}\,, \tag{5.7.8a}$$

$$Y_n(y) = \cos\left(\frac{n\pi y}{B}\right), \tag{5.7.8b}$$

$$K_n = \left[k^2 - \left(\frac{n\pi}{B}\right)^2\right]^{1/2}, \tag{5.7.8c}$$

and ε_n is again the Jacobi symbol. The inner expansion, however, needs a little work. The series for G converges slowly as it stands since

$$K_n \sim i\left(\frac{n\pi}{B}\right)$$

for n large, and

$$\frac{\varepsilon_n \cos K_n(x - L)}{K_n B \sin K_n L} = -\frac{2\cosh[n\pi(x - L)/B]}{n\pi \sinh(n\pi L/B)} = O\left(\frac{1}{n^3}\right)$$

$$= -\frac{2}{n\pi} e^{-n\pi x/B} + O\left(\frac{1}{n^3}\right).$$

The nth term dies out only as fast as $1/n$. A usual trick to speed up the convergence is to try summing the series composed of the leading approximation of each term:

$$\tilde{G} = \sum_{1}^{\infty} -\frac{2}{n\pi} e^{-n\pi x/B} Y_n(y) Y_n(y') \,. \tag{5.7.9}$$

The remaining series

$$X_0 Y_0(y) Y_0(y') + \sum_{n=1}^{\infty} \left(X_n + \frac{2}{n\pi} e^{-n\pi x/B} \right) Y_n(y) Y_n(y') \tag{5.7.10}$$

then converges much faster (as $1/n^3$) (see Kantorovich and Krylov, 1964, p. 79ff for examples of this technique). The summation turns out to be possible and is detailed in Appendix 5.B; we only give the following result:

$$\tilde{G} = \frac{1}{2\pi} \ln |1 - e^{-Z_s}|^2 \, |1 - e^{-Z_s'}|^2 \,, \tag{5.7.11}$$

where

$$Z_s = \frac{\pi}{B}[x + j(y - y')] \,, \quad Z_s' = \frac{\pi}{B}[x + j(y + y')] \,. \tag{5.7.12}$$

Note that Z_s is the normalized complex distance from the field point (x, y) to the source $(0, y')$, and Z_s' is the normalized complex distance from (x, y) to the mirror image of the source located at $(0, -y')$. Very close to the mouth, $r/B \ll 1$, we have $|Z_s| \ll 1$. Since

$$\begin{aligned} Z_s' &= Z_s + \frac{2j\pi y'}{B} \,, \\ 1 - e^{-Z_s} &= Z_s[1 + O(Z_s)] \,, \\ 1 - e^{-Z_s'} &= (1 - e^{-2j\pi y'/B})[1 + O(Z_s)] \,, \end{aligned} \tag{5.7.13}$$

it follows that

$$\begin{aligned} |1 - e^{-Z_s}|^2 &= \left(\frac{\pi r}{B}\right)^2 \left[1 + O\left(\frac{r}{B}\right)\right] , \\ |1 - e^{-Z_s'}|^2 &= 4 \sin^2 \frac{\pi y'}{B} \left[1 + O\left(\frac{r}{B}\right)\right] . \end{aligned} \tag{5.7.14}$$

Substituting these formulas into Eq. (5.7.11), we get

$$\tilde{G} = \frac{1}{\pi} \ln \left(\frac{2\pi r}{B} \sin \frac{\pi y'}{B} \right) + O\left(\frac{r}{B}\right) \tag{5.7.15}$$

which is logarithmically singular as $r \to 0$. This result is expected since $r = 0$ is the source point. From Eq. (5.7.15) the flux through an infinitesimal half-circle surrounding the source point on the side $x > 0$ is unity. Thus, $\tilde{G}$ represents the singular part of the Green function, and the residual series in Eq. (5.7.10) must be regular at the source point $r = 0$. The leading inner expansion of G is, therefore,

$$G(x, y; y') \cong \frac{1}{\pi} \ln \left(\frac{2\pi r}{B} \sin \frac{\pi y'}{B} \right) + F \,, \tag{5.7.16}$$

where F is the value of the residual series evaluated at the source point

$$F = \sum_{n=1}^{\infty} \left(\frac{\varepsilon_n \cos K_n L}{K_n B \sin K_n L} + \frac{2}{n\pi} \right) Y_n(y') Y_n(y') + \frac{\cos kL}{kB \sin kL} \,. \tag{5.7.17}$$

Finally, the inner expansion of the outer solution is

$$\eta_H \cong i \frac{\omega}{g} Q_H \left[\frac{1}{\pi} \ln \left(\frac{2\pi}{B} \sin \frac{\pi y'}{B} \right) + F \right] + i \frac{\omega}{g} \frac{Q_H}{\pi} \ln r \,. \tag{5.7.18}$$

Now we can perform the matching. On the ocean side the constant terms and the $\ln r$ terms in Eqs. (5.7.2) and (5.7.3a) must match separately; two equations are obtained

$$C - M \ln \frac{a}{2} = 2A + i \frac{\omega}{g} Q_0 \left(\frac{-i}{2} + \frac{1}{\pi} \ln \frac{\gamma k}{2} \right) \tag{5.7.19}$$

and

$$M = i \frac{\omega}{g} \frac{Q_0}{\pi} \,. \tag{5.7.20}$$

Similarly, by matching Eqs. (5.7.3b) and (5.7.18) on the harbor side $x < 0$ ($x_1 > 0$), we obtain

$$C + M \ln \frac{a}{2} = i \frac{\omega}{g} Q_H \left[\frac{1}{\pi} \ln \left(\frac{2\pi}{B} \sin \frac{\pi y'}{B} \right) + F \right] , \tag{5.7.21}$$

$$-M = i \frac{\omega}{g} \frac{Q_H}{\pi} \,. \tag{5.7.22}$$

These four algebraic equations (5.7.19)–(5.7.22) can be easily solved for the unknowns C, Q_0, Q_H, and M. An immediate result is that $Q_0 = -Q_H$ which could have been anticipated on grounds of continuity. The most important result is

$$i\frac{\omega}{g}Q_0 = \frac{-i\omega Q_H}{g} = -2A\left[\frac{-i}{2} + F - I\right]^{-1}, \tag{5.7.23}$$

where

$$I = \frac{1}{\pi}\ln\left[\frac{4B}{(\pi\gamma ka^2\sin(\pi y'/B))}\right]. \tag{5.7.24}$$

Finally, the far-field solution in the harbor is

$$\eta_H = \frac{-2A}{-i/2 + F - I}\sum_n X_n(x)Y_n(y)Y_n(y') \tag{5.7.25}$$

which can be used to calculate numerically the harbor response at almost all points except within a small region of order $O(a)$ from the entrance.

5.7.2 Resonant Spectrum and Response for Non-Helmholtz Modes

In order to enhance the physical understanding of the numerical results to be presented later, it is useful to examine the formulas (5.7.23) and (5.7.25) approximately.

When the incident wavenumber k is close to one of the natural modes of the closed basin, $k_{nm} = [(n\pi/B)^2 + (m\pi/L)^2]^{1/2}$, resonance should be expected. In the neighborhood of k_{nm} let

$$k = k_{nm} + \Delta \tag{5.7.26}$$

and assume that

$$\frac{\Delta}{k_{nm}} \ll 1\,. \tag{5.7.27}$$

From Eq. (5.7.8c) we have

$$K_nL = L\left[(k_{nm}+\Delta)^2 - \left(\frac{n\pi}{B}\right)^2\right]^{1/2}$$

$$\cong m\pi + \frac{k_{nm}L^2\Delta}{m\pi}, \quad n = 0,1,2,\ldots,\ m = 1,2,3,\ldots \tag{5.7.28a}$$

or

$$\cong L(2k_{n0}\Delta)^{1/2} \quad m = 0,\ n = 1,2,3,\ldots\,. \tag{5.7.28b}$$

Note that $\sin K_n L$ is nearly zero for either Eq. (5.7.28a) or (5.7.28b). In the series for G or F the nth term is much greater than all the rest. The dominant term of the series F is

$$F \cong \frac{\varepsilon_n \cos K_n L}{K_n B \sin K_n L} \cos^2 \frac{n\pi y'}{B} \cong \frac{c}{\Delta}, \quad \text{with} \quad c = \frac{\varepsilon_n \varepsilon_m}{2k_{nm} BL} \cos^2 \frac{n\pi y'}{B} \tag{5.7.29}$$

when at least one of the indices n or m is not zero, whereas G is approximated by

$$X_n Y_n(y) Y_n(y') \cong \frac{c}{\Delta} \frac{\cos(m\pi/L)(x-L)}{\cos m\pi} \frac{Y_n(y)}{Y_n(y')}.$$

Equation (5.7.25) gives the harbor response

$$\eta_H \cong \frac{-2A}{-i/2 + c/\Delta - I(k_{nm})} \frac{c}{\Delta} \frac{\cos(m\pi/L)(x-L)}{\cos m\pi} \frac{Y_n(y)}{Y_n(y')} \tag{5.7.30}$$

where

$$I(k_{nm}) \equiv [I(k)]_{k=k_{nm}} \tag{5.7.31}$$

is logarithmically large for small $k_{nm}a$. It is important to point out that when $\Delta = 0$, that is, $k = k_{nm}$, the right-hand side of Eq. (5.7.30) approaches

$$-2A \frac{\cos(m\pi/L)(x-L)}{\cos m\pi} \frac{Y_n(y)}{Y_n(y')}$$

which is not large. Thus, the resonant mode does not coincide with the natural mode of the closed basin. The amplification factor $\mathcal{A}$ for mode (n, m) can be defined by

$$\frac{\eta_H}{2A} = \mathcal{A} \frac{\cos(m\pi/L)(x-L)}{\cos m\pi} \frac{Y_n(y)}{Y_n(y')}, \tag{5.7.32a}$$

where

$$\mathcal{A} = \frac{c/I}{\Delta - c/I + \frac{1}{2} i\Delta/I}. \tag{5.7.32b}$$[1]

Equation (5.7.32b) has the same form as Eq. (5.4.15) for the model example. Therefore, the term $i\Delta/2I$ is associated with radiation damping

[1] Note that $\mathcal{A}$ has a simple pole in the complex k plane; the pole is located slightly below the real k axis.

which depends on the frequency shift Δ. Consider the square of the modal amplification factor

$$|\mathcal{A}|^2 = \frac{(c/I)^2}{(\Delta - c/I)^2 + \Delta^2/4I^2}\,. \tag{5.7.33}$$

The minimum of the denominator occurs at

$$\Delta_{\text{peak}} = \frac{c}{I}\left(1 + \frac{1}{4I^2}\right)^{-1} \cong \frac{c}{I}\,.$$

Hence, the resonant wavenumber is slightly greater than the natural value k_{nm},

$$\tilde{k}_{nm} \cong k_{nm} + \frac{c}{I}\,. \tag{5.7.34}$$

The correction c/I decreases as the width of the harbor mouth decreases. The peak value of $|\mathcal{A}|^2$ is

$$|\mathcal{A}|^2_{\max} \cong 4I^2\,. \tag{5.7.35}$$

It is easy to check that when

$$\Delta \cong \frac{c}{I} \pm \frac{c}{2I^2}\,,$$

the square response is reduced to half the peak value. Thus, $c/2I^2$ is essentially the half-width of the resonant peak in the plot of $|\mathcal{A}|^2$ versus k. By the definition of I, a reduction of the entrance width results in an increase in I, hence an increase in $\mathcal{A}_{\max}$ and a decrease in the width of the resonant peak. Although narrowing the harbor entrance reduces the change of precise tuning for resonance, the peak response, if perfectly tuned, is heightened. This behavior is related to the radiation damping which corresponds to the term $i\Delta/I$ in Eq. (5.7.32). Being proportional to $c/2I^2$ at resonance, the radiation damping diminishes sharply as a decreases. Thus, energy escapes the harbor with greater difficulty, and amplification is understandably more severe. This result is again likely at variance with the intuition of the designer who would normally narrow the entrance for better protection and is a feature of the *harbor paradox*. Note that the sharpening of a resonant peak is such that the area under the curve is roughly

$$|\mathcal{A}|^2_{\max}\frac{c}{2I^2} = 2c \tag{5.7.36}$$

which is independent of the entrance width and decreases with higher resonant mode (increasing n or m) (Garrett, 1970). If the incident waves are a

stationary random process with the spectrum $S_I(k)$, it may be shown that the mean-square response in the harbor is proportional to

$$\int_0^\infty S_I(k)|\mathcal{A}(k)|^2\,dk$$

as in the case of simple oscillators. To this integral the resonant peak at k_{nm} makes a contribution approximately equal to the product of $S_I(k_{nm})$ and the area of the $|\mathcal{A}|^2$ curve under the peak. Equation (5.7.36) then implies that the mean-square response is unchanged as the harbor entrance narrows. This result is another feature of the *harbor paradox*.

By combining Eq. (5.7.29) with Eq. (5.7.23) the discharge per unit depth near a resonant peak through the harbor entrance is found

$$\frac{i\omega Q_0}{g} = \left(\frac{-2A}{-i/2 + c/\Delta - I}\right). \tag{5.7.37}$$

Note that when the entrance width a vanishes, $k = k_{nm}$ and $Q_0 = 0$ so that pressure is transmitted across the entrance but mass is not. At resonance the quantity $\omega Q_0/\mathrm{g}$ is simply $4A$; the corresponding averaged current velocity through the entrance U_E is

$$|U_E| = \left|\frac{Q_0}{2a}\right|_{\max} = \frac{2gA}{\omega_{nm}a} = \frac{gAT_{nm}}{\pi a} \tag{5.7.38}$$

where ω_{nm} is a resonant frequency $= (gh)^{1/2}k_{nm}$, and T_{nm} is the corresponding period. As a numerical example we take $a = 200$ m, $A = 0.2$ m, and $T_{nm} = 10$ min, then

$$|U_E| = 6 \text{ m/s}\,.$$

If the local breakwater thickness is estimated to be 10 m, the maximum local Reynolds number is 6×10^7. As the flow is oscillatory, the instantaneous Reynolds number varies from 0 to $O(10^8)$. In reality there must be a significant energy loss due to vortex shedding and turbulence. Equation (5.7.38) also shows that $|U_E|$ is inversely proportional to the entrance width a, suggesting that for narrower entrance width real fluid effects should be more important. Dissipation at the entrance will be pursued in Chapter Six.

5.7.3 The Helmholtz Mode

The preceding analysis [in particular, Eq. (5.7.28)] does not apply when $n = m = 0$ so that $k_{00} = 0$. Since X_0 and Y_0 are constants, the free surface

rises and falls in unison throughout the basin, and hence corresponds to the *Helmholtz* or the *pumping mode*. From Eq. (5.7.8c) we have

$$\Delta = k \quad \text{and} \quad K_n = k = \Delta \tag{5.7.39}$$

instead of Eq. (5.7.28). The leading terms in the series for F and G are associated with the term $n = 0$, and the harbor response is

$$\eta_H \cong \frac{-2A}{-i/2 + 1/k^2BL - I} \frac{1}{k^2BL} \,. \tag{5.7.40}$$

The resonant wavenumber $\tilde{k}_{00}$ is approximately given by the root of the transcendental equation

$$\frac{1}{k^2BL} - I = 0 \quad \text{or} \quad k^2BL = \frac{1}{I} \,, \quad k \equiv \tilde{k}_{00} \,, \tag{5.7.41}$$

since I depends on k. As a decreases, I increases so that k decreases. The square amplification factor is

$$|\mathfrak{A}|^2 = \frac{(1/k^2BL)^2}{\frac{1}{4} + (1/k^2BL - I)^2} \,. \tag{5.7.42}$$

The peak value of $|\mathcal{A}|^2$ is approximately $4I^2$ when Eq. (5.7.41) is satisfied. The half-width of the peak is obtained by letting

$$\frac{1}{k^2BL} - I = \pm\frac{1}{2} \quad \text{or} \quad k - \tilde{k}_\infty = \pm\frac{1}{4} \frac{1}{(BLI^3)^{1/2}} \,. \tag{5.7.43}$$

As a decreases, $\mathcal{A}^2_{\max}$ increases and the width of the peak decreases. However, the area under the peak of the curve of $|\mathcal{A}|^2$ versus k is proportional to

$$\frac{1}{4} \frac{4I^2}{(BLI^3)^{1/2}} = \left(\frac{I}{BL}\right)^{1/2} \,, \tag{5.7.44}$$

which increases, although mildly, with decreasing a. The severity of the harbor paradox is worse for the Helmholtz mode than for non-Helmholtz modes, suggesting that friction loss is more important at the entrance, as will be discussed in detail in Chapter Six.

5.7.4 Numerical Results and Experiments

The response of a square harbor has been computed from Eq. (5.7.25) for a wide range of wavenumbers by Ünlüata and Mei (1973); these results

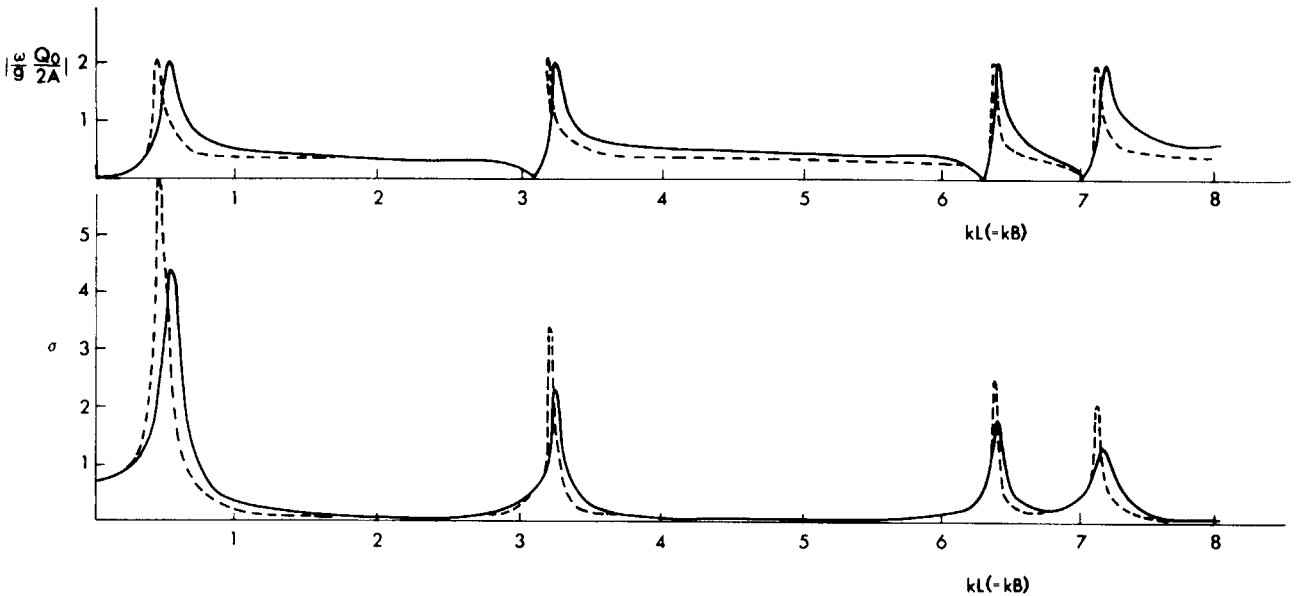

Figure 5.12: Root mean square response σ and normalized flux intensity $|(\omega/g)(Q_0/2A)|$ at the harbor mouth. $2a/B = 3 \times 10^{-2}$ (solid curve); $2a/B = 0.585 \times 10^{-2}$ (dashed curve). σ is defined in Eq. (5.9.5).

are consistent with those of Miles (1971) who used a different approximate analysis. Two different entrance widths are studied; see Fig. 5.12. The effects of reducing a are clearly in agreement with the analysis in Sections 5.7.2 and 5.7.3.

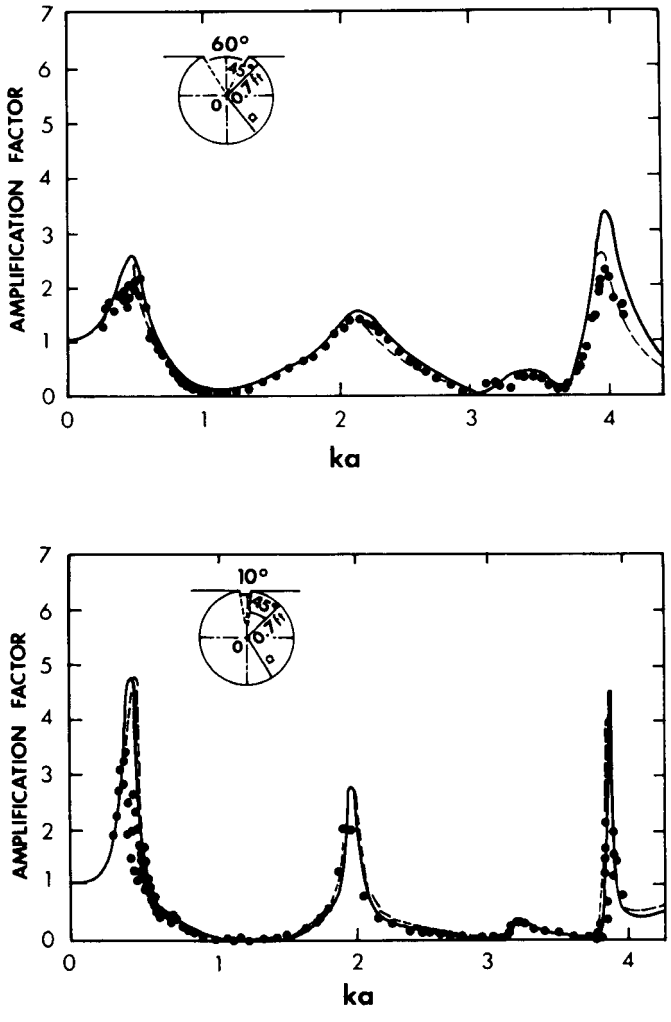

Figure 5.13: Response curve at $r = 0.7$ ft. $\theta = 45°$ of a circular harbor of radius = 0.75 ft. Solid and dashed curves are by two different theories; ◯: experiment. (a) 60° opening; (b) 10° opening (from Lee, 1971, *J. Fluid Mech.* Reproduced by permission of Cambridge University Press).

Approximate analytical theories for a circular harbor have been worked out by Miles (1971) and Lee (1971). In addition, Lee performed experiments which were in excellent agreement with the linear theory. The only significant discrepancy appeared for the lowest resonant peaks, near which friction was likely important; see Fig. 5.13. It should be pointed out that Lee's experiments were made in very deep water, $kh \gg 1$, and comparison with the long-wave theory was based on the analogy for linear theories with constant depth and vertical side walls. However, in the laboratory, nonlinearity cannot be easily avoided in shallow water, and discrepancies between shallow-water experiments and the linearized long-wave theory can be expected to be large.

5.7.5 Effects of Finite Entry Channel

For a harbor with a single basin, Carrier, Shaw, and Miyata (1971) found that the finite length of the entry channel, or the finite thickness of the breakwater at the entrance, has qualitatively the same effect as a narrowed entrance. This conclusion can also be proven analytically by matched asymptotics. For a junction whose thickness $2d$ is of the same order of magnitude as the width $2a$, the near-field solution can be pursued by means of the Schwarz–Christoffel transformation. The results have been given by Davey (1944) in terms of elliptic integrals and have been used by Guiney, Noye, and Tuck (1972) for the transmission of deep-water waves through a narrow slit. Ünlüata and Mei (1973, in the context of harbor oscillations) and Tuck (1975, in a survey of wave transmission through small holes) have shown that all results obtained for a thin gap can be reinterpreted for a thick-walled gap if an effective width a_e is introduced to replace the actual width. The effective width a_e is given parametrically (through v) by the following relations:

$$\frac{a_e}{a} = 2pv^{1/2}\,, \quad \frac{d}{a} = -\frac{p}{2}(K'v'^2 - 2K' - 2E') \tag{5.7.45}$$

where

$$p = (2E - v'^2K)^{-1}, \qquad v' = (1 - v^2)^{1/2}$$

$$\left.\begin{matrix} E = E(v) \\ K = K(v) \end{matrix}\right\} = \text{complete elliptic integrals of the } \left\{\begin{matrix} \text{first} \\ \text{second} \end{matrix}\right\} \text{ kind}$$

$$E' \equiv E(v')\,, \quad K' \equiv K(v')\,.$$

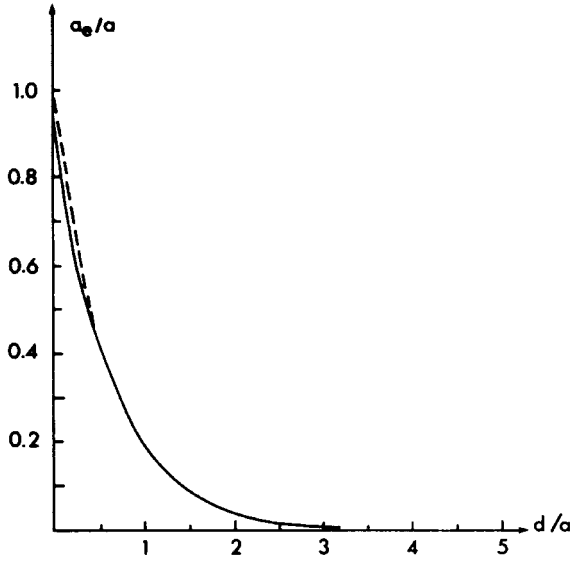

Figure 5.14: The ratio a_e/a of effective width to actual width of a junction as a function of the thickness-to-width ratio d/a. Equation (5.7.45): solid curve; Eq. (5.7.46): dashed curve (from Mei and Ünlüata, 1978).

We caution that the symbols E and K are conventional in the literature of elliptic integrals and do not have the same meaning as similar symbols used elsewhere in this section.

Details of the analysis leading to Eq. (5.7.45) are rather complicated and can be found in Ünlüata and Mei (1973). We simply state that a_e/a decreases monotonically with d/a. A rather explicit approximation to Eq. (5.7.45), valid for large d/a, is

$$\frac{a_e}{a} \cong \frac{8}{\pi} \exp\left[-\left(\frac{\pi d}{2a} + 1\right)\right] \tag{5.7.46}$$

which is very accurate for $d/a > 0.5$. In fact, even for $d/a = 0$, Eq. (5.7.46) gives a fairly good result: $a_e/a = 0.937$, as shown in Fig. 5.14.

5.8 The Effect of Protruding Breakwater

The coastline near the harbor entrance is often not a straight line, due either to the natural topography or to breakwaters protruding seaward. The latter

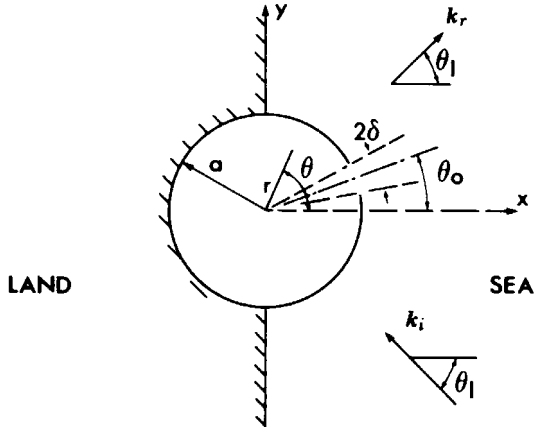

Figure 5.15: A circular harbor with protruding breakwater.

is a common configuration for new and small harbors on shallow coasts. Physically, the protrusion alters the scattered waves when the harbor mouth is closed; therefore, the forcing agent at the mouth is different from that of a straight coastline. The radiation pattern is also altered, for now the harbor mouth is like a loudspeaker mounted on a protrusion from a baffle wall. The shape of the protrusion and the location of the harbor mouth become new factors which must be considered in design and/or operations.

To illustrate the effects of protrusion, we follow Mei and Petroni (1973) and consider a circular harbor with half of its area indented behind a straight coast. The breakwater is a semicircular arc with an opening centered at $\theta = \theta_0$. The harbor mouth subtends an angle 2δ. The geometry is shown in Fig. 5.15.

5.8.1 Representation of Solution

Consider the representation of the solution outside the harbor. We shall account for the straight coast first, then the semicircular breakwater, and finally the harbor mouth. Let the incidence angle be θ_I as shown in Fig. 5.15.

A perfectly reflective coast along the y axis introduces a reflected wave $\eta^{I'}$ in addition to the incoming wave η^I. In terms of partial waves, the sum is

$$\eta^I + \eta^{I'} = A[e^{-ikr\cos(\theta+\theta_I)} + e^{ikr\cos(\theta-\theta_I)}]$$
$$= A\sum_m \varepsilon_m[(-i)^m \cos m(\theta+\theta_I) + (i)^m \cos m(\theta-\theta_I)]J_m(kr)$$
$$= 2A\sum_m \varepsilon_m \left(\cos\frac{m\pi}{2}\cos m\theta_I \cos m\theta + i\sin\frac{m\pi}{2}\sin m\theta_I \sin m\theta\right)$$
$$\times J_m(kr)\,, \quad m = 0, 1, 2, \ldots\,. \tag{5.8.1}$$

It is easy to verify that there is no normal velocity on the y axis, that is,

$$\frac{1}{r}\frac{\partial}{\partial\theta}(\eta^I + \eta^{I'}) = 0\,, \quad \theta = \pm\frac{\pi}{2}\,. \tag{5.8.2}$$

The presence of a solid circular cylinder centered at the origin creates scattered waves radiating outward to infinity. Thus, we must add to Eq. (5.8.1) terms which are proportional to $H_m(kr)\left(\begin{smallmatrix}\cos m\theta\\ \sin m\theta\end{smallmatrix}\right)$, where H_m are the Hankel functions of the first kind. The coefficients must be chosen so that the sum of $\eta^I + \eta^{I'}$ and the scattered η^S satisfy

$$\frac{\partial\eta^0}{\partial r} = 0\,, \quad r = a\,, \tag{5.8.3}$$

where

$$\eta^0 = \eta^I + \eta^{I'} + \eta^S \tag{5.8.4}$$

is the solution to the diffraction problem for a circular peninsula on a straight coast. The result is

$$\eta^0(r,\theta) = A\sum_m 2\varepsilon_m \left(\cos\frac{m\pi}{2}\cos m\theta_I \cos m\theta + i\sin\frac{m\pi}{2}\sin m\theta_I \sin m\theta\right)$$
$$\times \left[J_m(kr) - \frac{J_m'(ka)}{H_m'(ka)}H_m(kr)\right], \quad r \geq a \tag{5.8.5}$$

in which $(\ )'$ denotes differentiation with respect to the argument. Note that the boundary condition on the coastline is still satisfied. The preceding solution can be thought of as two plane waves incident symmetrically from the opposite sides of the y axis and scattered by a circular cylinder in an open sea. The acoustic counterpart for one incident wave is well known (Morse and Feshbach, 1953, Vol. II, pp. 1387ff).

To complete the wave field outside the harbor, we must further correct for the piston action at the harbor entrance. The corresponding displacement can be formally given as

$$\eta^R = \sum_m \frac{H_m(kr)}{kaH'_m(ka)}(A_m \cos m\theta + B_m \sin m\theta)\,, \quad R \geq a \tag{5.8.6}$$

in which A_m and B_m are to be found.

In summary, the total field outside the harbor is

$$\eta_0 = \eta^0 + \eta^R\,, \quad r \geq a\,, \quad |\theta| < \frac{1}{2}\pi\,. \tag{5.8.7}$$

The displacement inside the harbor, η_H, must satisfy the Helmholtz equation so that the formal solution is

$$\eta_H(r,\theta) = \sum_m \frac{J_m(kr)}{kJ'_m(ka)}(C_m \cos m\theta + D_m \sin m\theta) \tag{5.8.8}$$

in which C_m and D_m are yet unknown.

5.8.2 Reduction to an Integral Equation

The unknown coefficients A_m, B_m, C_m, and D_m must be fixed so that the surface height (i.e., pressure) and the normal surface slope (i.e., normal velocity) are continuous at every point of the harbor entrance

$$\eta_0 = \eta_H\,, \tag{5.8.9}$$

$$\frac{\partial \eta_0}{\partial r} = \frac{\partial \eta_H}{\partial r}\,, \quad r = a\,, \quad |\theta - \theta_0| \leq \delta\,. \tag{5.8.10}$$

Let the surface slope in the radial direction at the entrance be formally $F(\theta)$

$$\frac{\partial \eta_0}{\partial r} = \frac{\partial \eta_H}{\partial r} = F(\theta) \tag{5.8.11}$$

which differs from zero only across the entrance $|\theta - \theta_0| \leq \delta$. Applying Eq. (5.8.11) to Eq. (5.8.8) and using the theory of Fourier series, we can express the coefficients C_m and D_m as

$$C_m = \frac{\varepsilon_m}{2\pi}\int_M F(\theta')\cos m\theta'\, d\theta'\,, \tag{5.8.12a}$$

$$D_m = \frac{\varepsilon_m}{2\pi}\int_M F(\theta')\sin m\theta'\, d\theta'\,, \tag{5.8.12b}$$

in which M stands for harbor *mouth*.

Now apply Eq. (5.8.11) to Eq. (5.8.7). Some care is required for A_m and B_m as the conditions $\partial\eta_0/\partial\theta = 0$ on $\theta = \pm\pi/2$, and $r > a$ must

not be violated. The physical region outside the harbor is to the right of $x = 0$ (i.e., $|\theta| < \pi/2$). However, as far as the outside of the harbor is concerned, the problem is equivalent to an offshore circular harbor with two mouths symmetrically located with respect to the y axis, attacked by two symmetrically incident waves at the angles θ_I and $\pi - \theta_I$. The corresponding boundary condition is then

$$\frac{\partial \eta_0}{\partial r} = \frac{\partial \eta^R}{\partial r} = F(\theta)\,, \quad 0 \le \theta \le 2\pi\,, \quad r = a \tag{5.8.13a}$$

where

$$F(\theta) = F(\pi - \theta)\,. \tag{5.8.13b}$$

With this condition the no-flux condition on the coast (y axis) is assured by symmetry.

Applying Eq. (5.8.13) to Eq. (5.8.6) for the complete range of $0 \le \theta \le 2\pi$, and using the symmetry property of $F(\theta)$, Eq. (5.8.13b), we obtain the Fourier coefficients

$$A_m = \frac{\varepsilon_m}{\pi} \cos^2 \frac{m\pi}{2} \int_M d\theta' F(\theta') \cos m\theta'\,, \tag{5.8.14a}$$

$$B_m = \frac{\varepsilon_m}{\pi} \sin^2 \frac{m\pi}{2} \int_M d\theta' F(\theta') \sin m\theta'\,. \tag{5.8.14b}$$

Thus, $A_m = 0$ for $m =$ odd, and $B_m = 0$ for $m =$ even.

In terms of the surface slope, $F(\theta)$, we get from Eqs. (5.8.6) and (5.8.7)

$$\eta_0 = \eta^0 + a \sum_m \frac{\varepsilon_m}{\pi} \frac{H_m(kr)}{kaH'_m(ka)} \left[\cos^2 \frac{m\pi}{2} \cos m\theta \int_M du\, F(u) \cos mu \right.$$

$$\left. + \sin^2 \frac{m\pi}{2} \sin m\theta \int_M du\, F(u) \sin mu \right], \quad r > a\,, \tag{5.8.15}$$

and from Eq. (5.8.8)

$$\eta_H = a \sum_m \frac{\varepsilon_m}{2\pi} \frac{J_m(kr)}{kaJ'_m(ka)} \left[\cos m\theta \int_M du\, F(u) \cos mu \right.$$

$$\left. + \sin m\theta \int_M du\, F(u) \sin mu \right], \quad r < a\,. \tag{5.8.16}$$

Finally, condition (5.8.9) is invoked to match the surface displacement for all points at the harbor entrance $r = a$, $|\theta - \theta_0| \le \delta$, leading to an integral equation for $F(\theta)$,

$$\int_M du\, F(u)K(\theta|u) = \frac{1}{a}\eta^0(a,\theta)\,, \quad |\theta-\theta_0| \le \delta \tag{5.8.17a}$$

in which the kernel K is

$$\begin{aligned} K(\theta|u) = K(u|\theta) &= \sum_m \frac{\varepsilon_m}{2\pi}\frac{J_m(ka)}{kaJ'_m(ka)}(\cos m\theta\cos mu + \sin m\theta \sin mu) \\ &\quad - \sum_m \frac{\varepsilon_m}{\pi}\frac{H_m(ka)}{kaH'_m(ka)} \\ &\quad \times \left(\cos^2\frac{m\pi}{2}\cos m\theta\cos mu + \sin^2\frac{m\pi}{2}\sin m\theta\sin mu\right). \end{aligned} \tag{5.8.17b}$$

Note the important property that the kernel is symmetric with respect to the interchange of u and θ.

The Wronskian identity (4.9.20), Chapter Four, can be used to rewrite the right-hand side of (5.8.17a)

$$\begin{aligned} \frac{1}{a}\eta^0(a,\theta) = \frac{A}{a}\sum_m \frac{2i}{\pi ka}\frac{2\varepsilon_m}{H'_m(ka)}\Bigg(&\cos\frac{m\pi}{2}\cos m\theta_I\cos m\theta \\ &+ i\sin\frac{m\pi}{2}\sin m\theta_I\sin m\theta\Bigg), \quad |\theta-\theta_0| < \delta\,. \end{aligned} \tag{5.8.18}$$

The crux of the problem is to solve $F(\theta)$ from Eq. (5.8.17) for every θ within $|\theta-\theta_0| \le \delta$. This can be done by a variety of numerical procedures, most of which lead to a set of finite algebraic equations. Alternatively, by recasting the integral equation as a variational principle, one may obtain a simple but optimal approximation whose numerical accuracy is best for narrow mouths, as has been demonstrated in the straight-coast problem by Miles and Munk (1961). The latter approach is adopted below.

5.8.3 Approximate Solution by Variational Method

It can be shown that solving the integral equation (5.8.17) is equivalent to finding the extremum of the following functional (the proof is given in Appendix 5.C):

$$J[F(\theta)] = \frac{1}{2}\iint_M F(\theta)K(\theta|u)F(u)\,d\theta\,du - \frac{1}{a}\int_M \eta^0(a,\theta)F(\theta)\,d\theta\,. \tag{5.8.19}$$

Although this variational principle can be used as the basis of the finite-element approximation, we take a less numerical approach and assume F to possess a certain form with a multiplicative parameter f_0, that is,

$$F(\theta) = f_0 f(\theta) \tag{5.8.20}$$

with $f(\theta)$ prescribed; then

$$J = \frac{f_0^2}{2} \iint_M f(\theta) K(\theta|u) f(u)\, d\theta\, du - \frac{f_0}{a} \int_M \eta^0(a,\theta) f(\theta)\, d\theta\,. \tag{5.8.21}$$

For J to be stationary, f_0 must be chosen such that $dJ/df_0 = 0$; thus

$$f_0 = \frac{(1/a)\int_M \eta^0(a,\theta) f(\theta)\, d\theta}{\int_M \int f(\theta) K(\theta|u) f(u)\, d\theta\, du}\,. \tag{5.8.22}$$

One reasonable choice for $f(\theta)$ is that

$$f = \frac{1}{\pi}[\delta^2 - (\theta - \theta_0)^2]^{-1/2} \tag{5.8.23}$$

which has the correct singularity at the tips and is particularly appropriate for a narrow mouth ($\ll$ wavelength). Intuitively, in the neighborhood of the narrow mouth, the term $k^2\eta$ can be neglected from the Helmholtz equation and Eq. (5.8.23) should be a good quasistatic approximation. For a wide mouth, Eq. (5.8.23) is not adequate and other methods must be used.

The identity

$$\frac{1}{\pi} \int_{\theta_0-\delta}^{\theta_0+\delta} [\delta^2 - (\theta - \theta_0)^2]^{-1/2} \begin{pmatrix} \cos m\theta \\ \sin m\theta \end{pmatrix} d\theta = \begin{pmatrix} \cos m\theta_0 \\ \sin m\theta_0 \end{pmatrix} J_0(m\delta) \tag{5.8.24}$$

changes the numerator of Eq. (5.8.22) to

$$\begin{aligned} \frac{A}{a} N &\equiv \frac{1}{a} \int_M \eta^0(a,\theta) f(\theta)\, d\theta \\ &= \frac{A}{a} \sum_m \frac{2i}{\pi k a} \frac{2\varepsilon_m J_0(m\delta)}{H_m'(ka)} \\ &\quad \times \left(\cos\frac{m\pi}{2} \cos m\theta_I \cos m\theta_0 + i \sin\frac{m\pi}{2} \sin m\theta_I \sin m\theta_0 \right). \end{aligned} \tag{5.8.25}$$

Since η^0 is the wave pressure at the entrance in the absence of the opening, N is a weighted average of the forcing pressure. Note in particular the reciprocity between θ_0 and θ_I, that is, N is symmetrical with respect to the interchange of θ_0 and θ_I. Furthermore, the denominator of Eq. (5.8.22) is

$$\begin{aligned} D &\equiv \int_M \int f(\theta) K(\theta|u) f(\theta)\, d\theta\, du \\ &= \sum_m \frac{\varepsilon_m}{2\pi} \frac{J_m(ka) J_0^2(m\delta)}{ka J'_m(ka)} \\ &\quad - \sum_m \frac{\varepsilon_m}{2\pi} \frac{H_m(ka) J_0^2(m\delta)}{ka H'_m(ka)} (1 + \cos m\pi \cos 2m\theta_0)\,. \end{aligned} \tag{5.8.26}$$

The first series in Eq. (5.8.26) appears also in the case of a straight coast but the second series is now different. Substituting Eqs. (5.8.20) and (5.8.23) into Eq. (5.8.16), and using Eqs. (5.8.22) and (5.8.24)–(5.8.26), we obtain the harbor response

$$\eta_H = A \frac{N}{D} \sum_m \frac{\varepsilon_m}{2\pi} \frac{J_0(m\delta)}{ka J'_m(ka)} J_m(kr) \cos[m(\theta - \theta_0)]\,. \tag{5.8.27}$$

The necessary numerical calculations merely involve summation of series.

Qualitative behavior of η_H near the natural modes can be examined analytically as seen in previous sections, and can be found in Mei and Petroni (1973).

5.8.4 Numerical Results

The excitation N at the mouth is plotted as a function of ka for several values of incidence angle θ_I and mouth position θ_0, in Fig. 5.16. In contrast with a straight coast, the most important new feature is the fluctuation with respect to ka, due to the complicated diffraction process. For a given ka and θ_I which characterize the incident wave, it is possible to orient the harbor mouth θ_0 so that the forcing is small.

Let us define

$$A_m = \frac{N}{D} \frac{\varepsilon_m}{2} \frac{J_0(m\delta) J_m(ka)}{ka J'_m(ka)} \tag{5.8.28}$$

as the amplification factor for the modes with angular dependence $\cos m(\theta - \theta_0)$. Near a zero of $J'_m(ka)$, that is, $ka \cong j'_{ms}$, $s = 1, 2, \ldots$, A_m is large and

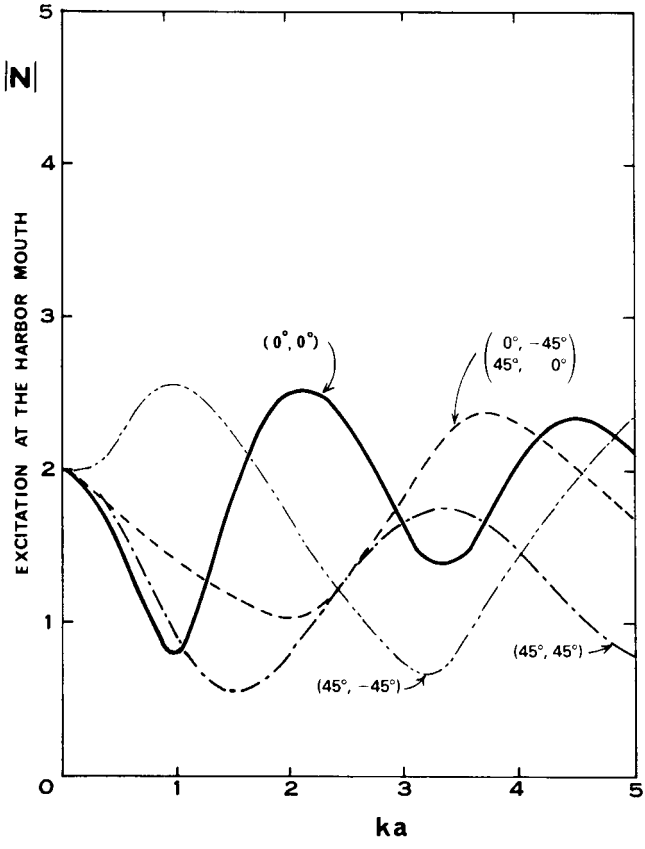

Figure 5.16: Excitation at the harbor mouth for an opening $2\delta = 10°$. Numbers in a parenthesis show (θ_0, θ_I) in degrees (from Mei and Petroni, 1973, *J. Waterway, Port, Coastal and Ocean Div.* Reproduced by permission of American Society of Civil Engineers).

the standing wave mode (m, s) is resonated. From Section 5.3 the first few values of j'_{ms} are 0 $(0,1)$, 1.84118 $(1,1)$, 3.05424 $(2,1)$, 3.83171 $(0,2)$, 4.20119 $(3,1)$, 5.33144 $(1,2)\ldots$, where the numbers in the parentheses refer to the index pair (m, s). Note that the mode $(0,1)$ corresponds to the Helmholtz mode. Because of radiation damping, D is complex. The peak frequency is slightly shifted and A_m is finite at resonance. Figure 5.17 is a typical plot for $|A_m|$.

For any given set of ka, a, θ_0, and δ, the free-surface displacement at the point (r, θ) within the harbor can be calculated as soon as the amplification factors A_m are calculated. As a convenient measure of the overall response,

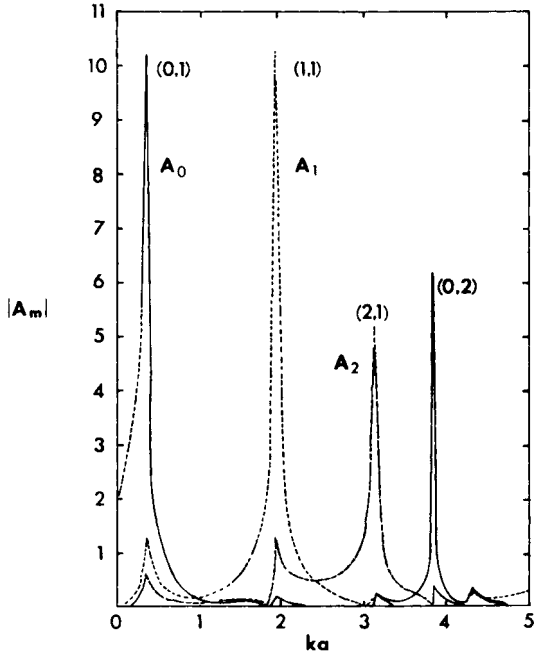

Figure 5.17: Amplification coefficient for mode m with $2\delta = 10°$, $\theta_0 = 0°$, $\theta_I = 0°$ (from Mei and Petroni, 1973, *J. Waterway, Port, Coastal and Ocean Div.* Reproduced by permission of American Society of Civil Engineers).

the mean-square elevation, averaged spatially over the entire area of the basin, is useful. From Eq. (5.8.27), the mean square

$$\begin{aligned}\overline{|\eta_H|^2} &= \frac{1}{\pi a^2}\int_0^{2\pi} d\theta \int_0^a dr\, r|\eta_H|^2 \\ &= \frac{A^2}{\pi a^2 k^2}\sum_m \frac{|A_m|^2}{J_m^2(ka)}\frac{2\pi}{\varepsilon_m}\int_0^{ka} zJ_m^2(z)\,dz \\ &= \frac{4A^2}{(ka)^2}\sum_m \frac{1}{\varepsilon_m}\frac{|A_m|^2}{J_m^2(ka)}\sum_{n=0}^{m}(m+2n+1)J_{m+2n+1}^2(ka) \qquad (5.8.29)\end{aligned}$$

is obtained. The last integral is evaluated with the help of an identity in Abramowitz and Stegun (1972, p. 484).

For the following range of parameters: wavelength, $0 < ka < 5$; half-opening angle of harbor entrance, $\delta = 5°$; entrance position, $\theta_0 = 0°$, $45°$; and the direction of incidence, $\theta_I = 0°$, $\pm 45°$, the root mean square of the harbor response $(|\eta_H|^2)^{1/2}$ is shown in Figs. 5.18(a)–5.18(e).

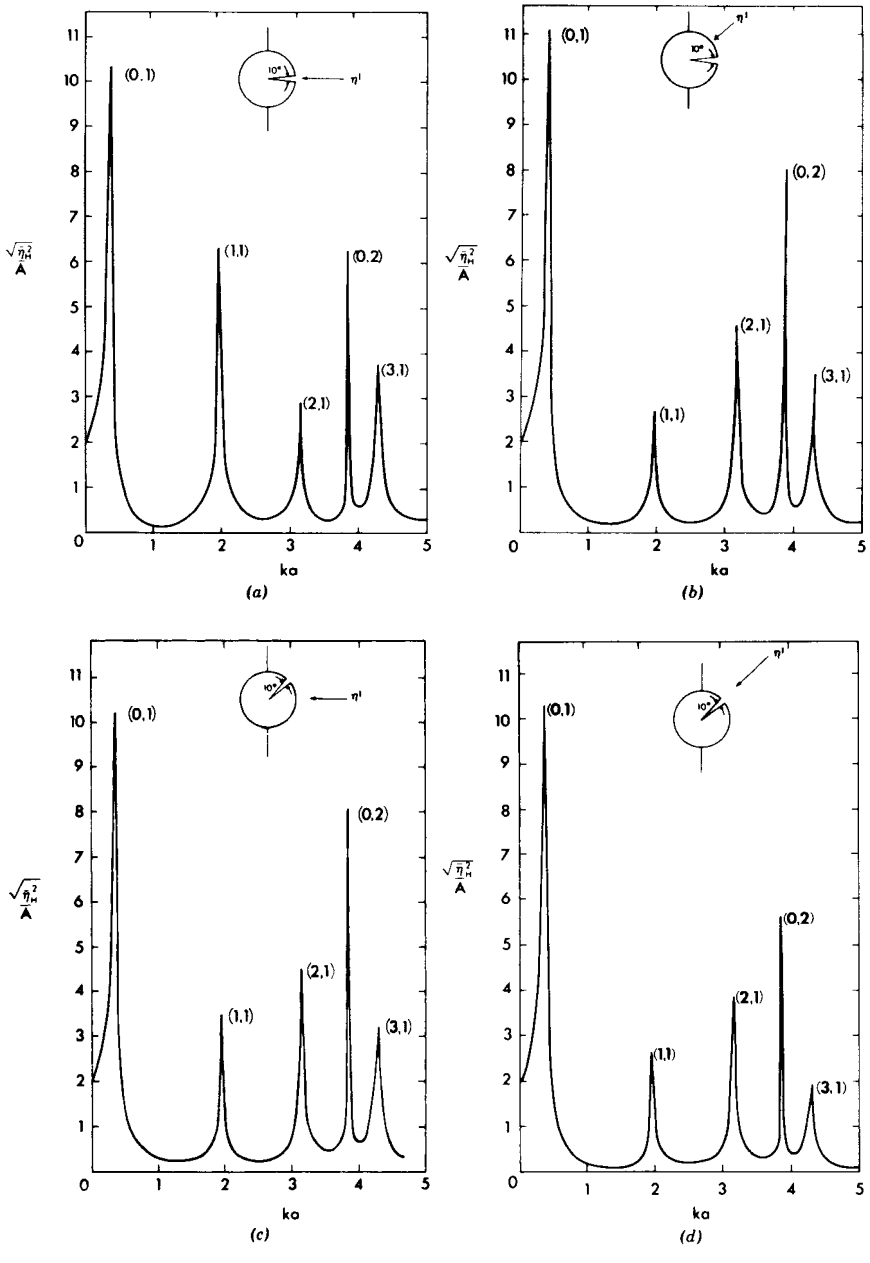

Figure 5.18: Mean harbor response for $2\delta = 10°$. (*a*) $\theta_0 = 0°$, $\theta_I = 0°$; (*b*) $\theta_0 = 0°$, $\theta_I = -45°$; (*c*) $\theta_0 = 45°$, $\theta_I = 0°$; (*d*) $\theta_0 = 45°$, $\theta_I = -45°$. (*e*) $\theta_0 = 45°$, $\theta_I = 45°$.

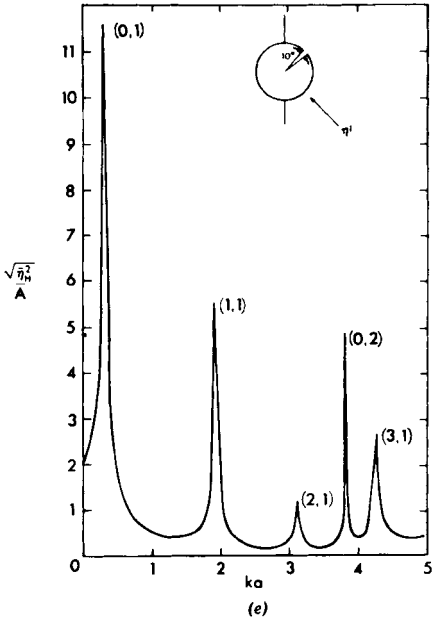

Figure 5.18: (*Continued*)

Qualitatively, the response curves look the same in all cases with the peaks occurring at the expected places. However, the heights of the peaks differ quantitatively for different values of θ_0 and θ_I. As an example, consider the resonant mode $(2,1)$ near $ka = 3.1$. The peak heights decrease according to the order $(\theta_0 = 45°,\ \theta_I = 0)$, $(\theta_0 = 45°,\ \theta_I = -45°)$, $(\theta_0 = 0,\ \theta_I = 0)$, and $(\theta_0 = 45°,\ \theta_I = 45°)$; the forcing N at the mouth is also in the same order as shown in Fig. 5.17. Thus, if the design wavelength is close to a particularly dangerous mode, proper siting of the entrance can reduce the input and the response.

Note that the Helmholtz mode is hardly affected by θ_0 and θ_I; this result is consistent with Fig. 5.16 where $N \approx 2$ for small ka.

Comparing Figs. 5.18(b) (for $\theta_0 = 0$; $\theta_I = -45°$) and 5.18(c) (for $\theta_0 = 45°$, $\theta_I = 0°$), we see that the modes with $m = 0, 2$, namely, $(0,1)$, $(0,2)$, and $(2,1)$, have the same peak height. This equality occurs because N is symmetric with respect to the interchange of θ_0 and θ_I [cf. Eq. (5.8.25)], while D is independent of θ_I [cf. Eq. (5.8.26)] and has the same value for the two sets of θ_0 and m.

Local responses may be calculated from Eq. (5.8.27) but are not pursued here.

5.9 A Harbor with Coupled Basins

The total area of some harbors consists of two large basins connected by a narrow passage; the Long Beach Harbor in California is such an example. Several new features arise because of the added degree of freedom. For two equal circular basins with centers lying on a line normal to the coast, numerical and laboratory experiments were first conducted by Lee and Raichlen (1972) whose results showed a systematic doubling of resonant peaks in contrast to a harbor with only one basin. Further analytical studies were made by Mei and Ünlüata (1978) for narrow openings, using the method of matched asymptotics as in Section 5.7. Though straightforward, the analysis is necessarily lengthy and we only summarize here the approximate results for two equal rectangular basins. The configuration is shown in Fig. 5.19 where the widths of the harbor entrance and the inter-basin opening are denoted by $2a_1$ and $2a_2$, respectively.

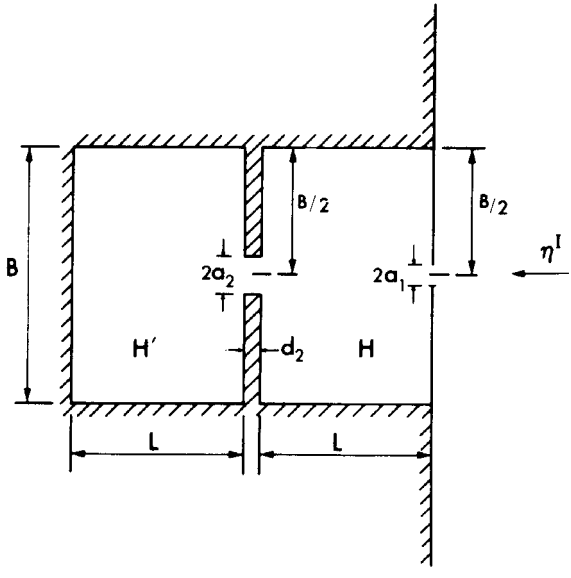

Figure 5.19: A harbor with two basins.

Corresponding to the natural mode k_{nm} of a closed basin with n and m not both zero, there are two resonant peaks $\tilde{k}^{+}_{nm}$ and $\tilde{k}^{-}_{nm}$ with

$$\tilde{k}^{\pm}_{nm} \cong k_{nm} + c \left\{ \frac{1}{I'} + \frac{1}{2I} \pm \left[\left(\frac{1}{I'} \right)^2 + \left(\frac{1}{2I} \right)^2 \right]^{1/2} \right\}_{k=k_{nm}} , \tag{5.9.1}$$

where

$$c = \frac{\varepsilon_n \varepsilon_m}{2 k_{nm} BL} , \tag{5.9.2}$$

and

$$I = \frac{1}{\pi} \ln \frac{4B}{\pi \gamma k a_1^2} , \tag{5.9.3a}$$

$$I' = \frac{1}{\pi} \ln \frac{B^2}{\pi^2 a_2^2} . \tag{5.9.3b}$$

The separation between the two peaks is

$$\tilde{k}^{+}_{nm} - \tilde{k}^{-}_{nm} \cong 2c \left[\left(\frac{1}{I'} \right)^2 + \left(\frac{1}{2I} \right)^2 \right]^{1/2} . \tag{5.9.4}$$

When either a_1 or a_2 increases, I or I' decreases, hence the peaks move further apart. Corresponding to k_{00}, there are also two Helmholtz modes with similar dependence on the openings.

If we define σ_H^2 as the mean-square amplification factor of the outer basin

$$\sigma_H^2 = \frac{1}{2BL} \int_0^L dx \int_0^B dy \frac{|\eta_H|^2}{4A^2} , \tag{5.9.5}$$

and define $\sigma_H^{2\prime}$ similarly for the inner basin, it can be shown that

$$\frac{(\tilde{\sigma}_H^{2\prime})^+}{(\tilde{\sigma}_H^2)^+} \cong \frac{(\sigma_H^2)^-}{(\tilde{\sigma}_H^{2\prime})^-} \cong \left\{ \frac{1}{\beta} \left[\left(\beta^2 + \frac{1}{4} \right)^{1/2} - \frac{1}{2} \right] \right\}^2_{k_{nm}} \tag{5.9.6}$$

where $\beta \equiv I/I'$ increases with decreasing harbor entrance ($2a_1$) or increasing inter-basin opening ($2a_2$). Since β lies between 0 and ∞, the following ordering is true

$$(\tilde{\sigma}_H^{2\prime})^- > (\tilde{\sigma}_H^2)^- > (\tilde{\sigma}_H^2)^+ > (\tilde{\sigma}_H^{2\prime})^+ . \tag{5.9.7}$$

For very large β, the ratios of mean squares in Eq. (5.9.6) tend to unity; the basin responses for both peaks are equalized. However, for small β these ratios become as small as 2β; the contrast of the basin responses then increases for both modes $\tilde{k}^{\pm}_{nm}$. In particular this implies that the inner basin becomes less protected for the lower mode $\tilde{k}^{-}_{nm}$. Clearly, this is a *paradox* associated with the coupling of basins in the context of the inviscid theory.

For the pair of Helmholtz modes corresponding to k_{00}, the ordering relation and the dependence on β is qualitatively the same. In addition, the two basins are out of phase for $\tilde{k}^{+}_{00}$ but in phase for $\tilde{k}^{-}_{00}$.

Numerical results based on the matched asymptotic theory are shown in Fig. 5.20 for two equal square basins. The width of the harbor entrance is fixed at $2a_1/B = 3 \times 10^{-2}$. In Fig. 5.20($a$) we take $a_1 = a_2$ and the breakwaters have zero thickness. Within the computed range $0 < kB < 8$, the distinct natural modes of one basin H or H' are: $k_{01}B = \pi = 3.1415$,

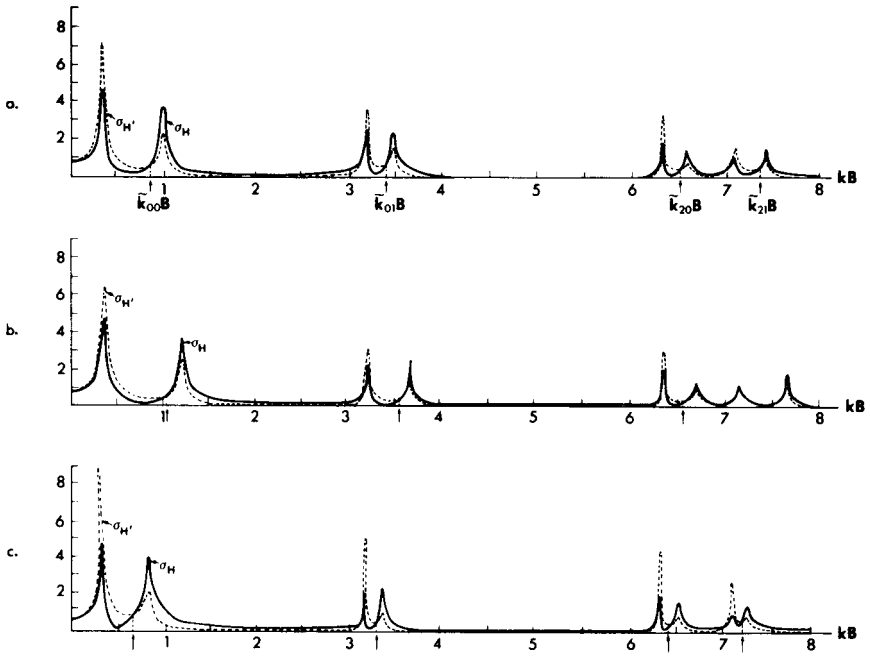

Figure 5.20: Root mean square responses of two identical square basins: Outer basin: solid curve; inner basin: dashed curve. $2a_1/B = 3 \times 10^{-2}$. ($a$) $a_1 = a_2$, $d_l = d_2 = 0$; (b) $a_2 = 4a_1$, $d_1 = d_2 = 0$; (c) $a_1 = a_2$, $d_1 = 0$, $d_2 = 2a_1$ (from Mei and Ünlüata, 1978, *J. Eng. Math.*, Reproduced by permission of Sijthoff and Noordhoff).

$k_{02}B = k_{20}B = 2\pi = 6.2833$, $k_{21}B = \sqrt{5}\pi = 7.0248$, which correspond to the second, third, and fourth pairs of peaks, respectively, the first pair being the Helmholtz modes. Clearly, the ordering of the first three pairs of peaks obey Eq. (5.9.7). The ordering of the last pair of peaks is only in partial agreement with Eq. (5.9.7) because the parameter $\tilde{k}a$ is no longer sufficiently small (> 0.107).

In Fig. 5.20(b) the inter-basin opening is changed to $a_2 = 4a_1$; the thickness of all breakwaters is still zero. Let us examine the lowest three pairs of peaks. In comparison with Fig. 5.20(a) the separation between a pair $\tilde{k}^{\pm}$ is indeed increased, and for the same mode the difference between the response of the basins is reduced, in accordance with Eq. (5.9.6). Note that for the fourth and highest pair of peaks the ordering rule Eq. (5.9.7) has deteriorated further, for now $\tilde{k}a_2 > 0.426$.

In Fig. 5.20(c) we keep $a_1 = a_2$ but increase the thickness of the breakwaters which divide the two basins, from zero to $d_2 = 2a_1$. In accordance with the results in Section 5.7.5 the effective width a_{2e} is reduced. In comparison with Fig. 5.20(a) the highest pair of peaks now obey the ordering rule since ($\tilde{k}a_{2e}$) is reduced to ~ 0.027. Moreover, the separation between pairs of peaks at $\tilde{k}^{\pm}$ decreases, while for the same mode ($\tilde{k}^{+}$ or $\tilde{k}^{-}$) the difference between the resonant responses of the basins is increased.

These features are consistent with the numerical and experimental findings of Lee and Raichlen (1972).

5.10 A Numerical Method for Harbors of Complex Geometry

For harbors of constant depth but arbitrary plan form, numerical solutions have been obtained by Hwang and Tuck (1970) and Lee (1971) by the method of integral equations. Extension of integral equations for varying depth is rather complicated and expensive (Lautenbacher, 1970; Mattioli, 1978). The hybrid-element method (HEM) discussed in Section 4.11 can be modified to account for the coastline and other special features of harbors and is particularly well-suited for variable harbor depth.

The coastline causes a reflected wave and modifies the scattered waves. Assume for simplicity that all topographical irregularities are within a contour C, and the coast is otherwise straight and coincides with the x axis, as shown in Fig. 5.21. In the superelement $\overline{\Omega}$ outside C, the depth is assumed to be a constant. Now the total wave in $\overline{\Omega}$ must consist of an incident

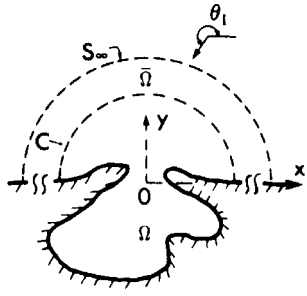

Figure 5.21: Harbor with a straight coast.

wave, a reflected wave due to the straight coast, and a scattered wave. Thus,

$$\eta = \eta^I + \eta^S \,,$$

where

$$\begin{aligned} \eta^I &= e^{ikr\cos(\theta-\theta_I)} + e^{ikr\cos(\theta+\theta_I)} \\ &= 2\sum_{n=0}^{\infty} \varepsilon_n (i)^n J_n(kr)\cos n\theta_I \cos n\theta \,, \end{aligned} \tag{5.10.1}$$

and

$$\eta^S = \sum_{n=0}^{\infty} \alpha_n H_n(kr)\cos n\theta \quad \text{so that} \quad \frac{1}{r}\frac{\partial \eta}{\partial \theta} = 0 \,, \quad \theta = 0, \pi \,. \tag{5.10.2}$$

The same stationary functional (4.11.4), Chapter Four, still holds as long as one uses η^I and η^S as given here. The computational procedure remains the same.

Figure 5.22 shows the finite-element grid for a rectangular bay which was already studied by using matched asymptotics in Section 5.6.2. The response at the inland end of the bay is shown in Fig. 5.23 for comparison with experiments performed in rather deep water. Discrepancy near the lowest peak suggests the importance of friction losses at the entrance.

If there is a thin breakwater, the velocity near the tip is very high so that local gradients are large. It is inefficient to increase the number of finite elements around the tip because ordinary interpolating functions cannot represent the singularity adequately. However, the hybrid-element idea can again be applied by inserting a circular disc Ω' centered at the

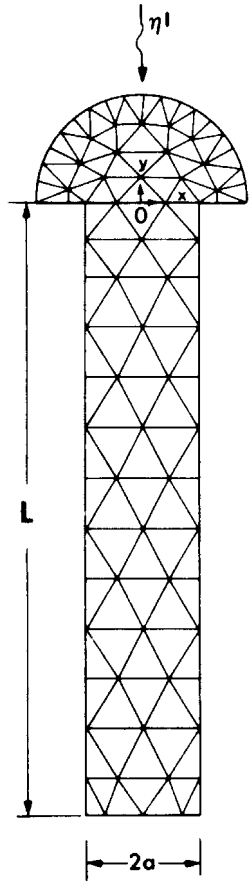

Figure 5.22: Network of finite elements for a rectangular bay (from Mei and Chen, 1975, *Proc., Symp. on Modelling Techniques.* Reproduced by permission of American Society of Civil Engineers).

tip (see Fig. 5.24). Within Ω', an analytical solution η' is used so that the singular behavior is accounted for exactly. The functional of Eq. (4.11.4), Chapter Four, must be modified by adding the following integral:

$$-\int_{C'} \left(\frac{1}{2}\eta' - \eta\right) \frac{\partial \eta'}{\partial \eta}\, ds\,, \tag{5.10.3}$$

where C' is the boundary of Ω', and $\mathbf{n}$ is the unit normal to C' pointing out of Ω'. Matching of η and $\partial\eta/\partial n$ is guaranteed as natural boundary conditions.

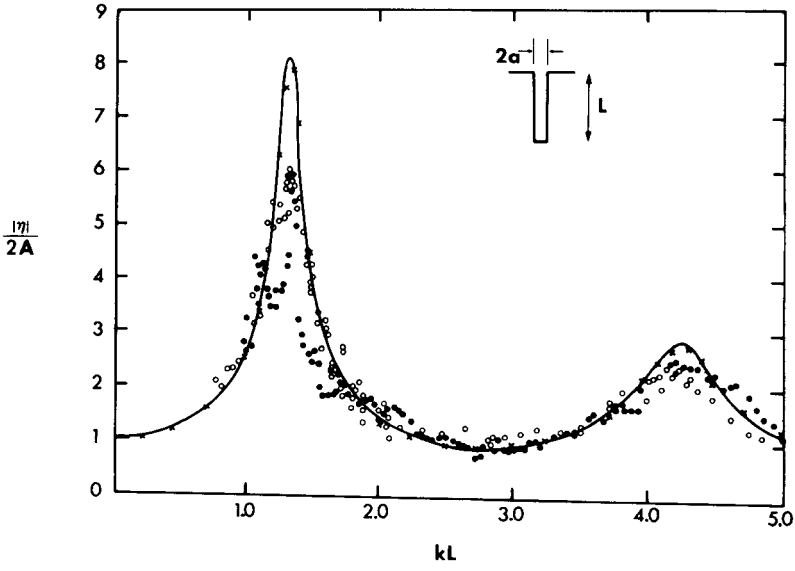

Figure 5.23: Amplification factor $|\eta|/2A$ at the inner end of an open rectangular bay. Solid curve: solution by integral equation (Lee, 1971); $\times\times\times$: solution by hybrid elements; ○○○: experiment by Lee (1971); ●●●: experiment by Ippen and Goda (1963). In both experiments, $2a = 2.38$ in., $L = 12.25$ in., and $h = 10.13$ in (from Mei and Chen, 1975, *Proc., Symp. on Modelling Techniques*. Reproduced by permission of American Society of Civil Engineers).

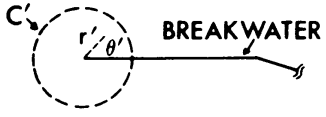

Figure 5.24: Neighborhood of the tip of a thin breakwater.

For a thin breakwater the curve C' may be taken as a circle small enough so that the depth within is approximately constant. The proper form of η' is

$$\eta' = \sum_{n=0}^{\infty} \gamma_n J_{n/2}(kr') \cos \frac{n\theta'}{2}\,, \tag{5.10.4}$$

where r' and θ' are the local polar coordinates shown in Fig. 5.24. Equation (5.10.4) satisfies the Helmholtz equation and the no-flux conditions on the walls:

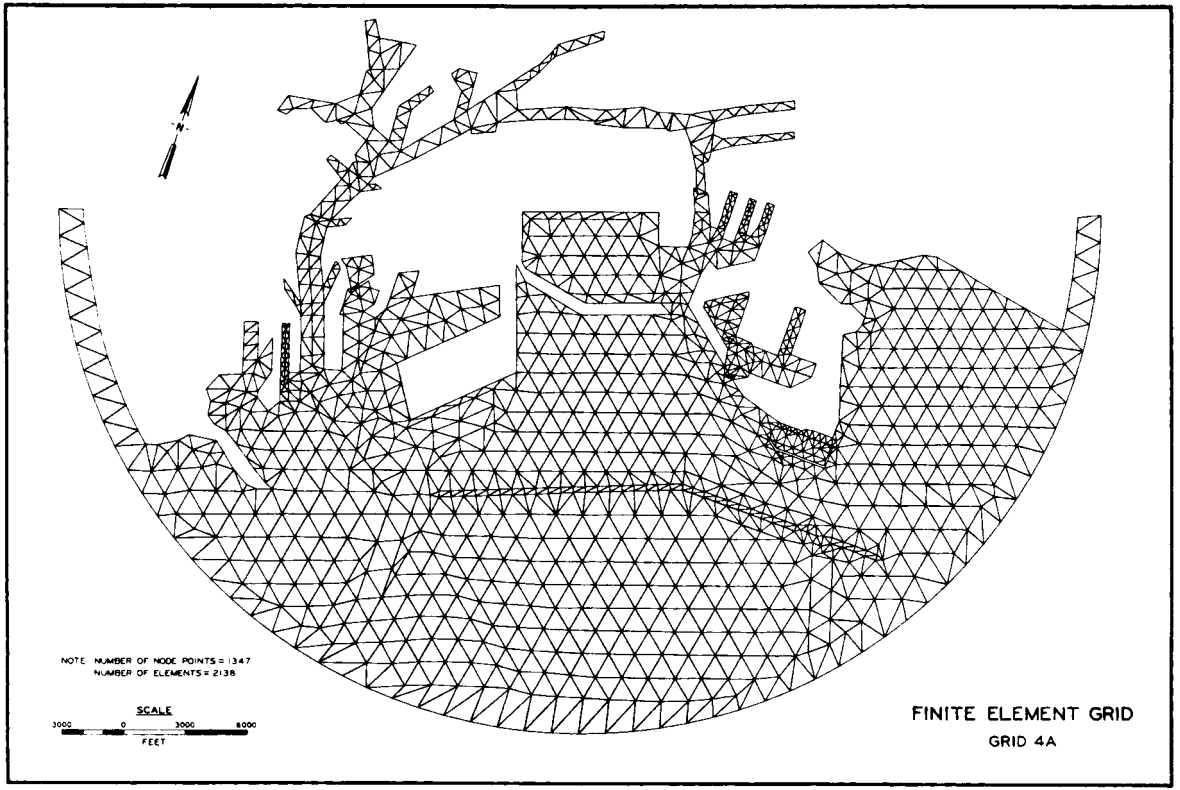

Figure 5.25: Finite-element grid for Long Beach Harbor (from Houston, 1976, *Report, U.S. Army Waterways Experiment Station*).

$$\frac{1}{r'}\frac{\partial \eta}{\partial \theta'} = 0 \quad \text{on} \quad \theta' = 0, 2\pi\,. \tag{5.10.5}$$

In addition, since

$$J_{1/2}(kr') = \left(\frac{2}{kr'}\right)^{1/2} \sin kr'\,,$$

Eq. (5.10.4) has the right singular behavior. For other wedge-shaped corners with the wedge angle equaling a rational multiple of 2π, analytical representation similar to Eq. (5.10.4) can also be obtained (Chen and Mei, 1974a, b).

Because of the versatility in treating arbitrary depth and boundary shape, the *hybrid element method* is a very powerful method for harbor studies. Indeed, its inception was in response to the proposed but later aborted offshore harbor project for the New Jersey Public Service Gas and Electric Company (Kehnemuyi and Nichols, 1973). Houston (1976) has made use of it in planning new piers and terminals in Long Beach Harbor; a sample finite-element grid is shown in Fig. 5.25.

5.11 Harbor Response to Transient Incident Wave

In Section 4.1.3 we have pointed out that the transient response in shallow water can be obtained by Fourier integration of the simple harmonic response. Let us now apply this procedure to the transient response in a harbor. Our analysis is adapted from Carrier (1970) who treated the elementary model of Section 5.4 in detail.

Let the transient incident wave be described by

$$\zeta^I(x,t) = \int_{-\infty}^{\infty} d\omega A_0(\omega) e^{-ikx - i\omega t} \tag{5.11.1}$$

where $A_0(-\omega) = A_0^*(\omega)$ for real ζ^I. The incident/reflected wave system due to the straight coastline at $x = 0$ must be

$$\zeta^I + \zeta^{I'} = \int_{-\infty}^{\infty} d\omega 2A_0(\omega)(\cos kx) e^{-i\omega t}\,. \tag{5.11.2}$$

The harbor response may be written

$$\zeta_H = 2\int_{-\infty}^{\infty} d\omega A_0(\omega) e^{-i\omega t} \eta_H(x,y,\omega) \tag{5.11.3}$$

where η_H is the frequency response to an incident wavetrain of unit amplitude. The path of integration should be slightly above the real axis so that $\zeta_H \to 0$ as $t \to -\infty$. Although all previous results were for positive and real ω and k, the results for negative and real ω can be inferred from the former by changing the sign of i, implying that

$$\eta_H(\mathbf{x}, -\omega) = \eta_H^*(\mathbf{x}, \omega)\,. \tag{5.11.4}$$

Note first that to obtain the transient response by Fourier superposition it is, in principle, necessary to know $\eta_H(x, y, \omega)$ for the entire range of frequencies $-\infty < \omega < \infty$. This knowledge would require a numerical solution unrestricted for narrow entrance. Fortunately, tsunami inputs are usually of long periods and the harbor response is significant only in the lowest few modes; inaccuracy in the high-frequency range should not be essential. Therefore, it is reasonable to expect that the approximate long-wave theory developed in previous sections may be used without incurring gross error.

Consider a transient wave packet with a carrier frequency ω_0 and a slowly varying Gaussian envelope so that at $x = 0$

$$\zeta^I + \zeta^{I'} = 4Be^{-\Omega^2 t^2} \cos\omega_0 t\,, \quad x = 0\,, \tag{5.11.5}$$

where

$$\frac{\omega_0}{\Omega} \gg 1\,. \tag{5.11.6}$$

The peak of the envelope strikes the coast at $t = 0$. The amplitude spectrum is easily found:

$$A_0(\omega) = \frac{B}{\pi^{1/2}} \frac{1}{2\Omega} \left\{ \exp\left[-\left(\frac{\omega - \omega_0}{2\Omega} \right)^2 \right] + \exp\left[-\left(\frac{\omega + \omega_0}{2\Omega} \right)^2 \right] \right\}.$$

Making use of Eq. (5.11.4), we can verify that

$$\zeta_H = \frac{B}{\pi^{1/2}} \frac{1}{\Omega} \operatorname{Re} \int_{-\infty}^{\infty} \left\{ \exp\left[-\left(\frac{\omega - \omega_0}{2\Omega} \right)^2 \right] \right\} \eta_H(\mathbf{x}, \omega) e^{-i\omega t}\, d\omega\,,$$

or, equivalently,

$$\zeta_H = \frac{B}{\pi^{1/2}} \frac{1}{K} \operatorname{Re} \int_{-\infty}^{\infty} \left\{ \exp\left[-\left(\frac{k - k_0}{2K} \right)^2 \right] \right\} \eta_H(\mathbf{x}, k) e^{-ik\tau}\, dk\,, \tag{5.11.7}$$

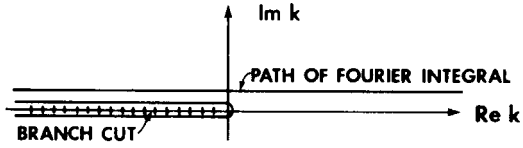

Figure 5.26: The complex plane for Fourier integral.

where

$$(k, k_0, K) = (\omega, \omega_0, \Omega)(gh)^{-1/2} \quad \text{and} \quad \tau = (gh)^{1/2} t\,. \tag{5.11.8}$$

Equation (5.11.6) implies that

$$\frac{K}{k_0} \ll 1\,, \tag{5.11.9}$$

so that the important part of the spectrum is narrow.

For simplicity only the rectangular bay in Section 5.5.2 is discussed here, but the analysis is much the same for other harbors where analytical solutions are available (see Carrier, 1970; Risser, 1976). Let us confine our attention to the point $x = -L$, that is, the landward end of the bay:

$$\zeta_H = \frac{B}{K\pi^{1/2}} \operatorname{Re} \int_{-\infty}^{\infty} \mathcal{A}(k) \exp\left[-\frac{(k-k_0)^2}{4K^2} - ik\tau\right] dk\,, \tag{5.11.10}$$

where

$$\mathcal{A} = \left[\cos kL + \frac{2ka}{\pi} \sin kL \ln \frac{2\gamma ka}{\pi e} - ika \sin kL\right]^{-1} \tag{5.11.11}$$

is the amplification factor from Eq. (5.6.20). The preceding integral can be evaluated numerically. However, an analytical study for the present simple case here is both physically informative and useful in guiding numerical work. First of all, $\mathcal{A}(k)$ has a logarithmic branch point at $k = 0$. Since the path of integration is slightly above the real k axis, the branch cut must lie beneath the path and may be chosen as shown in Fig. 5.26. As a check recall that for negative and real ω one may replace i by $-i$ in Eq. (5.6.20) with the result

$$\mathcal{A}(\omega) = \left[\cos kL + \frac{2ka}{\pi} \sin kL \ln \frac{2\gamma ka}{\pi e} + ika \sin ka\right]^{-1}\,,$$
$$k = \omega(gh)^{-1/2} < 0\,. \tag{5.11.12}$$

Equation (5.11.12) can also be obtained from Eq. (5.6.20) by replacing k by $ke^{i\pi}$ (not by $ke^{-i\pi}$). This particular choice of phase is consistent with the position of the branch cut.

Next, note that $\mathcal{A}(k)$ has poles in the lower half of the complex k plane at

$$\bar{k}_n = \pm\tilde{k}_n + i\hat{k}_n\,, \quad \hat{k}_n < 0\,,$$

where $\tilde{k}_n$ corresponds to the nth resonant mode and $\hat{k}_n$ to the radiation damping rate.

The integral in Eq. (5.11.10) can be analyzed by the asymptotic *method of steepest descent*. Leaving the general exposition to many existing texts on applied mathematics (e.g., Carrier, Krook, and Pearson, 1966), we shall only explain this method for the problem at hand. Consider the phase function of the exponential in Eq. (5.11.10)

$$g(k) = -\frac{(k-k_0)^2}{4K^2} - ik\tau \tag{5.11.13}$$

as an analytic function of k. Let $k = \alpha + i\beta$, then the contour lines of $\mathrm{Re}\, g$ and $\mathrm{Im}\, g$ are given by

$$\mathrm{Re}\, g = \text{const}: \quad (\alpha - k_0)^2 - (\beta + 2K^2\tau)^2 = \text{const} \tag{5.11.14a}$$

$$\mathrm{Im}\, g = \text{const}: \quad (\alpha - k_0)(\beta + 2K^2\tau) = \text{const} \tag{5.11.14b}$$

which are hyperbolas; contours of $\mathrm{Re}\, g$ are as shown in Fig. 5.27 for $\tau < 0$ and Fig. 5.28 for $\tau > 0$. The center of the hyperbolas is the point S where

$$k = k_0 - 2iK^2\tau = k_0 - 2iK\Omega t\,. \tag{5.11.15}$$

Relative to the point S, the topography of $\exp(\mathrm{Re}\, g)$ falls both to the east and west and rises both to the north and south; point S is therefore called the *saddle point*.[2] Because g is analytic, the contours of $\mathrm{Im}\, g$ are orthogonal to $\mathrm{Re}\, g = \text{const}$ and are the paths along which $\exp(\mathrm{Re}\, g)$ changes most rapidly; we call these the paths of the *steepest descent*. The strategy is to deform the original path to the steepest path so that the integrand is of significant magnitude only over a small stretch of the path.

Before the peak strikes the harbor mouth, $\tau < 0$, the saddle point is in the first quadrant. A closed rectangular contour is introduced in Fig. 5.27 with a horizontal path I_1 passing from the west valley over the saddle and down to the east valley. The integral along the two short vertical stretches

[2]In the most general situation a saddle point is defined by $dg/dz = 0$. Recall that an analytic function cannot have an extremum in the region of analyticity.

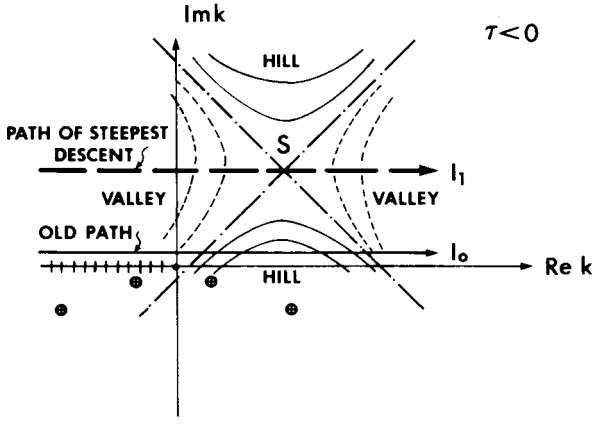

Figure 5.27: Topography near the saddle point for $\tau < 0$ (before the pulse strikes the coast). Vertical scale is exaggerated, $-2K^2\tau \ll k_0$, $K/k_0 \ll 1$.

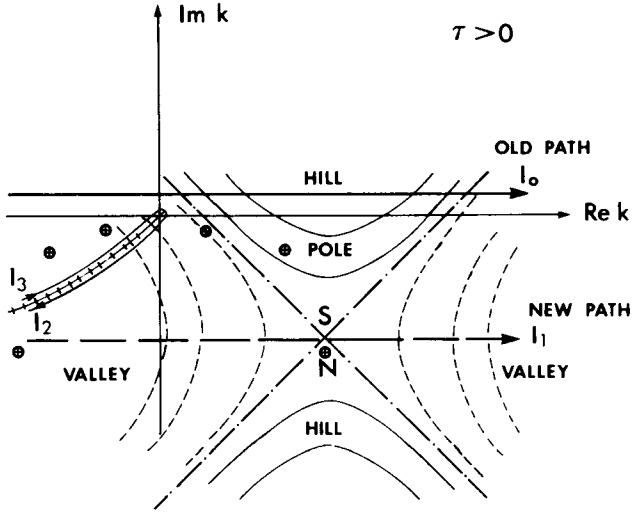

Figure 5.28: Topography near the saddle point for $\tau > 0$ (after the pulse strikes the coast). Branch cuts I_2 and I_3 follow the steepest path. N refers to a resonant pole.

at $\mathrm{Re}\, k \to \pm\infty$ vanishes because of the exponential in the integrand. By Cauchy's theorem, $I_0 = I_1$. Now along path I_1, $\mathrm{Im}\, g = 0$ and $\mathrm{Re}\, g$ drops off most rapidly on both sides of S; I_1 is a path of the *steepest descent*. Clearly, the most important contribution is from the neighborhood of S itself, where the rate of change of $\mathrm{Re}\, g$ is zero. Along I_1, let

$$\sigma = k - k_0 + 2iK^2\tau\,, \tag{5.11.16}$$

then

$$\zeta_H = \frac{B}{K\pi^{1/2}}\ \mathrm{Re}\left\{ e^{-K^2\tau^2 - ik_0\tau} \int_{-\infty}^{\infty} d\sigma \exp\left(-\frac{\sigma^2}{4K^2}\right) \mathcal{A}\Big|_{k=k_0-2iK^2\tau+\sigma} \right\}. \tag{5.11.17}$$

Because of the Gaussian factor $\exp(-K^2\tau^2)$ we need only confine our attention to $K\tau = O(1)$. Since $K/k_0 \ll 1$, the leading term in Eq. (5.11.17) is

$$\begin{aligned}\zeta_H &\cong \frac{B}{K\pi^{1/2}}\ \mathrm{Re}\left\{ e^{-K^2\tau^2 - ik_0\tau}\, \mathcal{A}(k_0) \int_{-\infty}^{\infty} d\sigma \exp\left(-\frac{\sigma^2}{4K^2}\right) \right\} \\ &= 2B\ \mathrm{Re}\left\{ \mathcal{A}(k_0) e^{-\Omega^2 t^2} e^{-i\omega_0 t} \right\}, \quad t,\ \tau < 0\,. \end{aligned} \tag{5.11.18}$$

Thus, before the peak of the envelope strikes, the harbor responds passively with the same carrier frequency and similar envelope as the input.

Equation (5.11.18) is valid whenever the saddle point is at a distance greater than $O(K)$ from a pole of $\mathcal{A}(k)$. Now all the poles of $\mathcal{A}(k)$ correspond to resonances and have negative imaginary parts, $\hat{k}_n < 0$. If the lowest resonant mode has a $-\hat{k}_1 > O(K)$, that is, when the duration of the incident wave packet is much greater than the radiation damping time scale, Eq. (5.11.18) is valid up to $t = 0$ when the peak of the incident wave envelope strikes the coast. If the envelope is infinitely long, the peak of the envelope arrives at the coast only asymptotically in time. The input is effectively sinusoidal and the steady-state response is obtained by letting $\Omega \to 0$, while keeping t finite in Eq. (5.11.18); the result is, of course, already known.

After the peak of the incident packet strikes the coast, τ becomes positive and the saddle point S moves to the fourth quadrant. The most interesting case is when

$$k_0 = \tilde{k}_N\,, \tag{5.11.19}$$

that is, the incident wave has the same frequency as one of the lowest resonant modes N. For $K\tau \leq O(1)$ so that the wave packet is still appreciable, there is a time interval when S is just above the Nth pole, that is, $2K^2\tau < -\hat{k}_N$. In order to shift the integration path to a horizontal line passing through S, we must account for the contributions from the branch cut and from the poles lying above S and corresponding to modes with lower frequencies than the incident wave. Referring to Fig. 5.28, let us deform the branch cut so that it follows a path of the steepest descent. By Cauchy's theorem

$$\zeta_H = \zeta_H(I_1) + \zeta_H(I_2) + \zeta_H(I_3) - \frac{B}{K\pi^{1/2}} \operatorname{Re} 2\pi i \sum_n \text{ residues}\,, \tag{5.11.20}$$

where $\zeta_H(I_\alpha)$ stands for Eq. (5.11.10) with I_α as the integration path. Along I_2 and I_3 which are the steepest paths, the neighborhood of $k = 0$ contributes the most to the integral. Because of the exponentially small factor $\exp(-k_0^2/4K^2)$, the corresponding integrals $\zeta_H(I_2)$ and $\zeta_H(I_3)$ are not important.

The residue for mode n can be obtained by first using Eq. (5.6.22) which is valid near the pole

$$\mathfrak{A} \cong (-1)^{n+1} \frac{1}{(k - \tilde{k}_n)L + ik_n a} \tag{5.11.21}$$

$$= \frac{1}{(-1)^{n+1}L} \frac{1}{k - (\tilde{k}_n + i\hat{k}_n)} \quad \text{with} \quad \hat{k}_n = -\frac{k_n a}{L} < 0\,, \tag{5.11.22}$$

where $\tilde{k}_n$ is given by Eq. (5.6.23). The residue is

$$\frac{B}{K\pi^{1/2}} \frac{-2\pi i}{(-)^{n+1}L} e^{-i\tilde{k}_n\tau} e^{\hat{k}_n\tau} \exp\left[-\frac{(\tilde{k}_n - k_0 + i\hat{k}_n)^2}{4K^2}\right], \tag{5.11.23}$$

which is also exponentially small for all $n \neq N$.

We now examine the term $\zeta_H(I_1)$. Extra care is needed since the saddle point S is close to the pole $\tilde{k}_N + i\hat{k}_N$. Again using Eq. (5.11.22) we obtain from Eq. (5.11.10) that

$$\zeta_H(I_1) = \frac{B}{K\pi^{1/2}} \operatorname{Re} \int_{I_1} \frac{\exp[-(k - k_0)^2/4k^2 - ik\tau]}{[k - (\tilde{k}_N + i\hat{k}_N)](-)^{N+1}L}\, dk$$

which can also be written

$$\zeta_H(I_1) \cong \frac{B}{K\pi^{1/2}} \operatorname{Re} \frac{e^{-K^2\tau^2} e^{-i\tilde{k}_N \tau}}{(-)^{N+1} L} \int_{-\infty}^{\infty} \frac{e^{-\sigma^2/4K^2}\, d\sigma}{\sigma - i(2K^2\tau + \hat{k}_N)} \tag{5.11.24}$$

after the use of Eqs. (5.11.16) and (5.11.19). The integral above may be evaluated exactly (Carrier, 1970) as is detailed in Appendix 5.D. In particular, for $2K^2\tau + \hat{k}_N < 0$, the saddle point S is still above the pole,

$$\zeta_H(I_1) \cong \frac{B}{K\pi^{1/2}} \operatorname{Re} \frac{-i\pi e^{-\tilde{k}_N \tau}}{(-)^{N+1} L} \left\{ e^{\hat{k}_N^2/4K^2} e^{\hat{k}_N \tau} \left[1 + \operatorname{erf}\left(\frac{2K^2\tau + \hat{k}_N}{2K} \right) \right] \right\}. \tag{5.11.25}$$

When time has increased further so that $2K^2\tau + \hat{k}_N$ is positive, the integral along I_1 becomes

$$\zeta_H(I_1) = \frac{B}{K\pi^{1/2}} \operatorname{Re} \frac{-i\pi e^{-\tilde{k}_N \tau}}{(-)^{N+1} L} \left\{ e^{\hat{k}_N^2/4K^2} e^{\hat{k}_N \tau} \left[1 + \operatorname{erf}\left(\frac{2K^2\tau + \hat{k}_N}{2K} \right) \right] \right\} \tag{5.11.26}$$

(see Appendix 5.D). We must now add the residue from pole N:

$$\operatorname{Re} \frac{-2iB\pi^{1/2}}{(-)^{N+1} KL} e^{i\hat{k}_N \tau} e^{\hat{k}_N \tau} e^{\hat{k}_N^2/4K^2}, \tag{5.11.27}$$

which follows from Eq. (5.11.23). The combined result is also given by Eq. (5.11.25). It is evident that the bay is excited at the frequency of mode N and attenuates according to the time scale of radiation damping $\propto |\hat{k}_N|^{-1}$. The maximum amplitude in the bay increases with increasing duration of the incident wave group (decreasing K). For a shorter wave group (larger K) the maximum not only is smaller but also occurs earlier.

The preceding analysis can be extended to harbor basins which are truly two dimensional. There the Helmholtz mode has the lowest resonant frequency and damping rate and may be excited by a simple pulse with nearly zero carrier frequency $\omega \approx 0$. Carrier and Shaw (1969) integrated numerically the harmonic response to get the transient response in a rectangular harbor with $B = 600$ ft, $L = 100$ ft, and $h = 21$ ft, which approximately represents Barber's Point Harbor in Oahu, Hawaii. For a very long pulse (pulse duration is 6.4 times the Helmholtz mode period), they found the response to be passive as shown in Fig. 5.29(a). The reason is that the

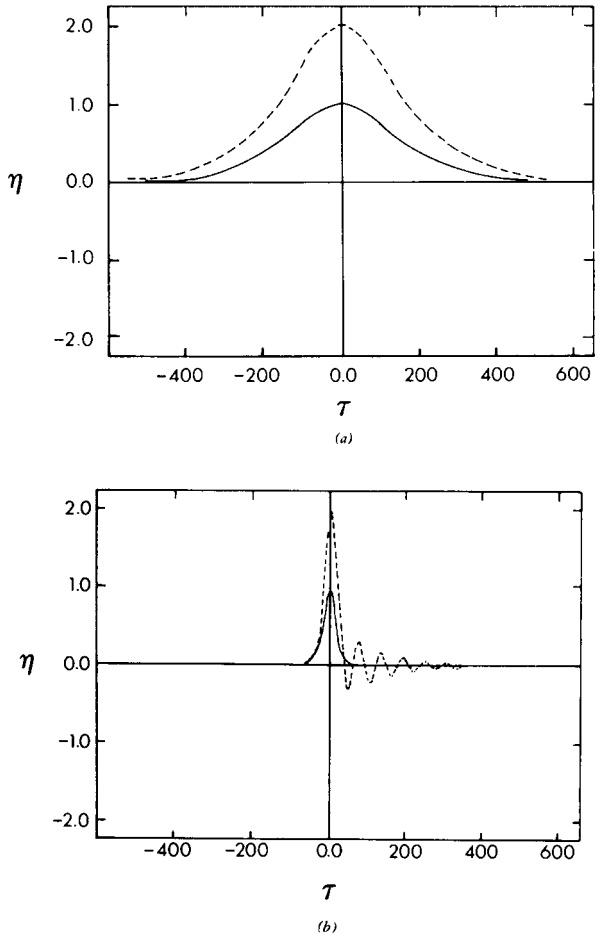

Figure 5.29: Transient responses to a single-crested wave: (a) long pulse, (b) short pulse. Solid curve: incident wave; dashed curve: harbor reponse (from Carrier and Shaw, 1969, *Tsunamis in the Pacific Ocean* edited by W. M. Adams. Reproduced by permission of University Press of Hawaii).

Fourier spectrum of a flat pulse is very sharp with $k_0 = 0$ and very small K; the residue from the Helmholtz pole is very small. However, for a very short pulse, the Helmholtz mode is excited, as shown in Fig. 5.29(b). This excitation occurs because the Fourier spectrum of a short incident pulse is quite broad (K large) so that the terrain near the saddle is mild, and the residue from the Helmholtz pole is considerable. Finally, Fig. 5.30 shows the response of the Helmholtz mode excited by an incident wave packet.

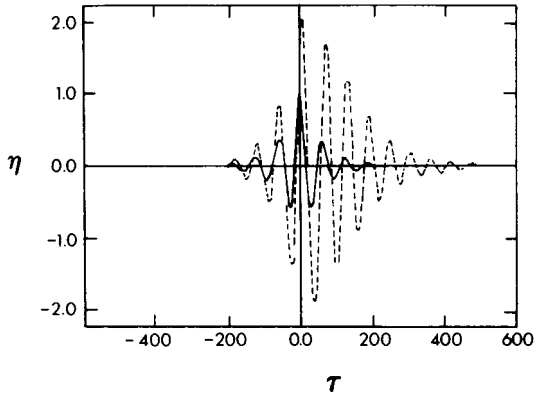

Figure 5.30: Transient response to a wave packet (from Carrier and Shaw, 1969, *Tsunamis in the Pacific Ocean* edited by W. M. Adams. Reproduced by permission of University Press of Hawaii).

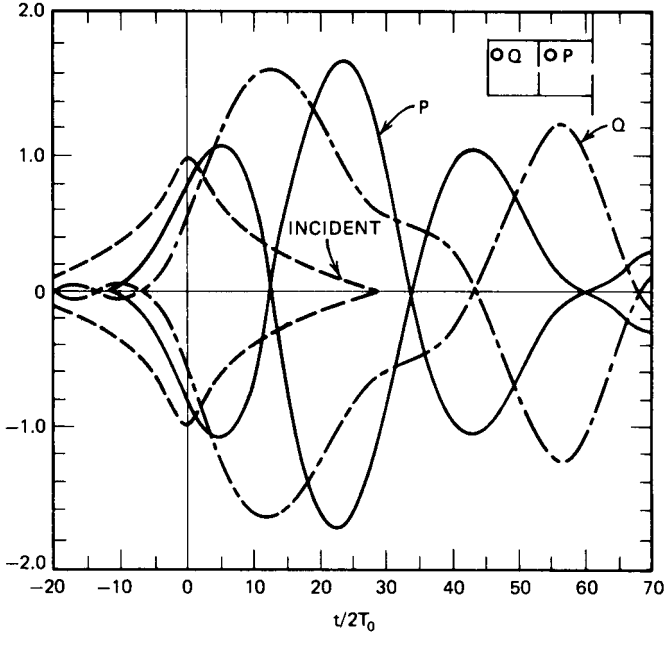

Figure 5.31: Sample transient responses in two identical square basins coupled in series. $2a_1 = 2a_2 = 3B \times 10^{-2}$, $k = 3.289 \times 10^{-3}$, $T_0 = 136$ s. Only the envelopes are shown (from Risser, 1976).

The growth to resonance for $t < 0$ and the reverberation and attenuation for $t > 0$ are qualitatively consistent with the analytical predictions of a narrow bay.

For two coupled square basins, analytical and numerical studies have been carried out by Risser (1976). In Fig. 5.31(a) a sample result by Risser is shown for the harbor system of Fig. 5.19(a) with $h = 20$ m and $B = L = 1000$ m. The carrier frequency of the wave packet is assumed to be $kB = 3.289$ which corresponds to the third lowest peak ($k_{01}^{-}B$ or $k_{10}^{-}B$). In physical terms the incident wave period is $T_0 = 136$ s. For a wave packet of duration $= 30T_0$, the envelopes of the responses at points P and Q as marked in the inset of Fig. 5.31 are shown. It is interesting that there is an oscillatory interchange of energy between the two basins and that the inner basin can have slightly higher response than the outer.

Appendix 5.A The Source Function for a Rectangular Basin

In this appendix we deduce the source function $G(x, y; y')$ which satisfies the Helmholtz equation

$$(\nabla^2 + k^2)G = 0 \tag{5.A.1}$$

and the boundary conditions

$$\frac{\partial G}{\partial y} = 0 \quad \text{on} \quad y = 0, B,\ 0 < x < L\,, \tag{5.A.2}$$

$$\frac{\partial G}{\partial x} = \begin{cases} 0\,, & x = L\,, \qquad (5.A.3) \\ \delta(y - y')\,, & x = 0\,. \qquad (5.A.4) \end{cases}$$

Thus, G represents a source on the wall at $x = 0$, $y = y'$.

We assume the solution to be in the form

$$G = \sum_{n=0}^{\infty} X_n(x) \cos \frac{n\pi y}{B}\,, \tag{5.A.5}$$

and note that it satisfies the zero-flux condition (5.A.2). Upon substituting Eq. (5.A.5) into Eq. (5.A.1), we have

$$\left(\frac{d^2}{dx^2} + K_n^2\right) X_n = 0\,, \tag{5.A.6}$$

wherein

$$K_n^2 = k^2 - \left(\frac{n\pi}{B}\right)^2 . \tag{5.A.7}$$

The solution of Eq. (5.A.6) satisfying Eq. (5.A.3) is simply

$$X_n = A_n \cos K_n(x - L) . \tag{5.A.8}$$

To determine the unknown coefficients A_n in Eq. (5.A.8), we first substitute Eq. (5.A.8) into Eq. (5.A.5) and invoke the condition (5.A.4):

$$\sum_{n=0}^{\infty} A_n K_n \sin K_n L \cos \frac{n\pi y}{B} = \delta(y - y') . \tag{5.A.9}$$

Second, we multiply both sides of Eq. (5.A.9) by $\cos(n\pi y/B)$ and integrate with respect to y from 0 to B. By means of the orthogonality relation

$$\int_0^B \cos \frac{n\pi y}{B} \cos \frac{m\pi y}{B}\, dy = \frac{B\delta_{mn}}{\varepsilon_n}$$

where

$$\varepsilon_0 = 1 , \quad \varepsilon_n = 2 , \quad n = 1, 2, 3, \ldots , \tag{5.A.10}$$

the coefficients are found to be

$$A_n = \frac{\varepsilon_n}{BK_n \sin K_n L} \cos\left(\frac{n\pi y'}{B}\right) . \tag{5.A.11}$$

Finally, the source function is given by

$$G(x, y; y') = \sum_{n=0}^{\infty} \frac{\varepsilon_n}{BK_n \sin K_n L} \cos K_n(x - L) \cos \frac{n\pi y}{B} \cos \frac{n\pi y'}{B} . \tag{5.A.12}$$

Appendix 5.B Summation of the $\tilde{G}$ Series

The series to be summed is

$$\tilde{G} = \sum_{n=1}^{\infty} \tilde{G}_n , \tag{5.B.1}$$

where

$$\tilde{G}_n = \tilde{X}_n(x) Y_n(y) Y_n(y') \tag{5.B.2}$$

and

$$\tilde{X}_n = -\frac{2}{n\pi} e^{-n\pi x/B}\,, \tag{5.B.3}$$

$$Y_n = \cos\frac{n\pi y}{B}\,. \tag{5.B.4}$$

We let

$$\xi = \frac{\pi x}{B}\,, \quad \eta = \frac{\pi y}{B}\,, \quad \eta' = \frac{\pi y_0}{B}\,, \tag{5.B.5}$$

and note, by using trigonometric identities, that

$$\begin{aligned} Y_n(y)Y_n(y') &= \cos n\eta \cos n\eta' \\ &= \frac{1}{4}\{[e^{-jn(\eta-\eta')} + e^{-jn(\eta-\eta')}] + *\}\,, \end{aligned} \tag{5.B.6}$$

where $(*)$ denotes the complex conjugate of the preceding terms in curly parentheses. Upon substituting Eqs. (5.B.6) and (5.B.3) into Eq. (5.B.2), we have

$$\tilde{G} = -\frac{1}{2}\left[\left(\frac{e^{-nZ_s}}{n} + \frac{e^{-nZ'_s}}{n}\right) + *\right], \tag{5.B.7}$$

where

$$Z_s = \xi + j(\eta - \eta')\,, \quad Z'_s = \xi + j(\eta + \eta')\,. \tag{5.B.8}$$

The substitution of Eq. (5.B.7) into Eq. (5.B.1) yields four infinite series, each of which can be summed in closed form by the following formula (Collin, 1960, p. 579):

$$\sum_{n=1}^{\infty} \frac{e^{-ns}}{n} = -\ln(1 - e^{-s})\,, \tag{5.B.9}$$

yielding the result that

$$\tilde{G} = \sum_{n=1}^{\infty} \tilde{G}_n = \frac{1}{2\pi}\{[\ln(1 - e^{-Z_s}) + \ln(1 - e^{-Z'_s})] + *\} \tag{5.B.10}$$

or

$$\tilde{G} = \frac{1}{2\pi} \ln\{|1 - e^{-Z_s}|^2\ |1 - e^{-Z'_s}|^2\}\,. \tag{5.B.11}$$

Appendix 5.C Proof of a Variational Principle

The functional J is defined as

$$J = \frac{1}{2}\int_M \int F(\theta)K(\theta|\theta')F(\theta')\,d\theta\,d\theta' - \frac{1}{a}\int_M F(\theta)\eta^0(\theta)\,d\theta \tag{5.C.1}$$

in which $F(\theta)$ is the solution to the integral equation

$$\int_M F(\theta')K(\theta|\theta')\,d\theta' = \frac{1}{a}\eta^0(\theta)\,, \quad \theta \text{ in } M \tag{5.C.2}$$

with a symmetric kernel

$$K(\theta|\theta') = K(\theta'|\theta)\,. \tag{5.C.3}$$

Let us now prove that Eq. (5.C.2) is equivalent to the vanishing of the first variation of J, that is,

$$\delta J = 0\,. \tag{5.C.4}$$

Let an approximate solution be denoted by $\overline{F}$ which differs from the true solution F by δF, that is,

$$\overline{F} = F + \delta F\,. \tag{5.C.5}$$

Thus, the approximate value of J is

$$\begin{aligned}
\overline{J} &= \frac{1}{2}\int_M \int (F+\delta F)K(F'+\delta F')\,d\theta\,d\theta' - \frac{1}{a}\int_M (F+\delta F)\eta^0\,d\theta \\
&= \frac{1}{2}\int_M \int [FF' + F'(\delta F) + F(\delta F')]K\,d\theta\,d\theta' \\
&\quad - \frac{1}{a}\int_M (F+\delta F)\eta^0\,d\theta + O(\delta F)^2 \\
&= J + \frac{1}{2}\int_M \int (F'\delta F + F\delta F')K\,d\theta\,d\theta' - \frac{1}{a}\int_M \delta F\eta^0\,d\theta + O(\delta F)^2
\end{aligned} \tag{5.C.6}$$

in which the shorthand notation $F' = F(\theta')$ is used. The first variation of J is

$$\delta J = \overline{J} - J = \frac{1}{2}\int_M \int (F'\delta F + F\delta F')K\,d\theta\,d\theta' - \frac{1}{a}\int_M \delta F\eta^0\,d\theta\,. \tag{5.C.7}$$

Due to the symmetry of K [cf. Eq. (5.C.3)],

$$\int_M \int F' \delta F K \, d\theta \, d\theta' = \int_M \int F \delta F' K \, d\theta \, d\theta' \,, \tag{5.C.8}$$

it follows that

$$\delta J = \int_M d\theta F \int_M d\theta' \left[F(\theta') K(\theta|\theta') - \frac{1}{a} \eta^0(\theta') \right]. \tag{5.C.9}$$

Thus, the integral equation (5.C.2) implies Eq. (5.C.4). Conversely, if Eq. (5.C.4) is true for small but arbitrary δF, then Eq. (5.C.2) must be true.

Appendix 5.D Evaluation of an Integral

Carrier (1970) has given the following result:

$$\begin{aligned} J &= \int_{-\infty}^{\infty} \frac{d\sigma \, e^{-\sigma^2/4K^2}}{\sigma + i\gamma} \\ &= -(\text{sgn } \gamma) i\pi e^{\gamma^2/4K^2} \left[1 - \text{erf} \left(\frac{|\gamma|}{2K} \right) \right], \end{aligned} \tag{5.D.1}$$

which can be derived by contour integration (Risser, 1976). Consider first that $\gamma > 0$, and introduce $z = \sigma + i\gamma$. It follows that

$$J = \int_{-\infty + i\gamma}^{\infty + i\gamma} \frac{dz}{z} \exp \left[-\frac{(z^2 - 2i\gamma z - \gamma^2)}{4K^2} \right]. \tag{5.D.2}$$

The pole is now at the origin of the z plane while the path of integration is above the real z axis. By Cauchy's theorem, the integration path can be replaced by the real z axis indented above the origin.

Now break the integral into two parts: a principal-valued integral J_p

$$J_p = e^{\gamma^2/4K^2} \fint_{-\infty}^{\infty} \frac{dz}{z} e^{-(z^2 - 2i\gamma z)4K^2} \,, \tag{5.D.3}$$

and an integral along the indentation

$$J_\varepsilon = e^{\gamma^2/4K^2} \lim_{\varepsilon \to 0} \int_{\theta=\pi}^{\theta=0} \frac{d\varepsilon e^{i\theta}}{\varepsilon e^{i\theta}} = i\pi e^{\gamma^2/4K^2} \,. \tag{5.D.4}$$

Denoting the principal-valued integral in (5.D.3) by F,

$$F = \fint_{-\infty}^{\infty} \frac{dz}{z} e^{-(z^2-2i\gamma z)/4K^2}\,, \tag{5.D.5}$$

we find

$$\begin{aligned}
\frac{\partial F}{\partial \gamma} &= \frac{i}{2K^2}\int_{-\infty}^{\infty} dz\, e^{-(z^2-2i\gamma z)/4K^2} \\
&= \frac{i}{2K^2}\int_{-\infty}^{\infty} dz\, e^{-(z-i\gamma)^2/4K^2} e^{-\gamma^2/4K^2} \\
&= \frac{i}{2K^2} 2K\pi^{1/2} e^{-\gamma^2/4K^2} \\
&= \frac{i\pi^{1/2}}{K} e^{-\gamma^2/4K^2}\,.
\end{aligned} \tag{5.D.6}$$

When $\gamma = 0$, the integrand in Eq. (5.D.5) is odd in z; hence $F(\gamma = 0) = 0$. We may integrate Eq. (5.D.6) to get

$$\begin{aligned}
F &= \frac{i\pi^{1/2}}{K}\int_0^{\gamma} e^{-\gamma^2/4K^2}\, d\gamma \\
&= i\pi \frac{2}{\pi^{1/2}} \int_0^{\gamma/2K} e^{-\sigma^2}\, d\sigma \\
&= i\pi\ \mathrm{erf}\left(\frac{\gamma}{2K}\right).
\end{aligned} \tag{5.D.7}$$

Adding up J_p and J_ε, we get

$$J = J_p + J_\varepsilon = -i\pi e^{\gamma^2/4K^2}\left[1 - \mathrm{erf}\left(\frac{\gamma}{2K}\right)\right]. \tag{5.D.8}$$

If $\gamma < 0$, we write $\gamma = -|\gamma|$ which amounts to replacing i by $-i$ in the integrand of Eq. (5.D.1), hence the change of sign.

This page intentionally left blank

Effects of Head Loss at a Constriction on the Scattering of Long Waves: Hydraulic Theory

6

In the idealized theory of wave scattering in an inviscid fluid, it is usually assumed that the fluid flow is always tangential to the solid boundary of a wall or a structure. In reality, however, an adverse pressure gradient and viscosity can decelerate the fluid near a sharp convex corner, forcing the flow to separate and to form eddies of high vorticity and causing significant energy loss. This natural tendency is the basis of perforated panels on room walls to absorb sound energy. Jarlan (1965) introduced this idea to coastal engineering and patented the design of a caisson breakwater which has a perforated front wall but a solid back wall. Dissipation is enhanced by the water jets falling through the holes when the surface elevations on both sides differ. Breakwaters of similar types have been constructed at Baie Comeau Harbor and Chandler Harbor in Quebec, Canada, and at Roscoff Harbor in France (Richey and Sollitt, 1969). A more recent and dramatic example is the North Sea Ekofisk oil storage tank which is surrounded by a circular perforated breakwater with a diameter of approximately 92 m in water of 70 m (Gerwick and Hognestad, 1973). A breakwater consisting of a row of circular piles of 2 m diameter spaced with 0.5 cm gaps has been in use in Osaka Harbor, Japan (Hayashi, Kano and Shirai, 1966).

In all these designs, flow separation due to sudden contraction and expansion is the primary physical feature. Now flow separation around a small cylinder is a related subject important in offshore structures and much experimental research has been done for isolated cylinders with smooth or sharpedged boundaries (see, for example, Sarpkaya and Issacson, 1981). It is known from the experiments that the Strouhal number $U/\omega a$ (or equivalently the Keulegan–Carpenter number UT/a for the pioneering work of G. H. Keulegan and L. H. Carpenter, 1956, on oscillatory flows) is an

important parameter, where U is the velocity amplitude and a the body dimension. According to Graham (1980), there appears to be at least two distinct regimes within the range of $2 < UT/a < 100$. For $UT/a > 20$ (the number depends on the cylinder cross-section), a limited wake containing a number of vortices extends downstream of the point of separation. With increasing UT/a, the wake lengthens and resembles more and more the steady stream situation of a Kármán vortex street. However, for $UT/a < 20$, vortices are shed from the separation points of the cylinder; each vortex is swept back by the reverse flow to the other side of the cylinder to pair up with a successive vortex of the opposite sign. This vortex pair is then convected away from the body at large angles ($\sim 45°$) to the incident flow. A friction loss formula which is quadratic in the local velocity [see Eq. (6.1.17) later] is satisfactory only for high values of UT/a. Unfortunately, a similar criterion is still lacking for gaps and holes. Since the Keulegan–Carpenter number can be rather large[1] for usual breakwater dimensions and wave periods, the quadratic loss formula provides at least a crude estimate until more experimental data become available. For one-dimensional scattering problems, such a semiempirical theory has been developed by Hayashi, Kano, and Shirai (1966), Terrett, Osorio, and Lean (1968), and others. Their reasoning has been further elaborated by Mei, Liu, and Ippen (1974) as described below.

6.1 One-Dimensional Scattering by a Slotted or Perforated Breakwater

6.1.1 The Field Equations

We limit ourselves to the study of small-amplitude waves in shallow water. Since the local velocity in the neighborhood of a sudden constriction can be large, let us include nonlinearity and begin with the equations of Airy, already given as Eqs. (3.5.11) and (3.5.12), Chapter Three:

$$\frac{\partial \zeta}{\partial t} + \nabla \cdot (\zeta + h)\mathbf{u} = 0 \tag{6.1.1}$$

[1]For tsunamis past a breakwater, we may take $U = 1$ m/s, $T = 3600$ s, and $a =$ breakwater thickness $= 10$ m, then $UT/a = 360$. For wind waves attacking a perforated breakwater we take $U = 3$ m/s for the velocity through the holes, $T = 10$ s, $a = 0.5$ m, then $UT/a = 60$.

$$\frac{\partial \mathbf{u}}{\partial t} + \mathbf{u} \cdot \nabla \mathbf{u} = -g \nabla \zeta \,. \tag{6.1.2}$$

Consider a thin barrier with vertical slots of width $2b$. The center-to-center spacing between any adjacent slots is $2a$. Periodicity allows us to consider a channel whose side walls coincide with the center lines of two adjacent vertical piles, as sketched in Fig. 6.1. The water depth h is assumed to be constant. The incoming wave is long, of low amplitude, and normally incident; hence it must satisfy

$$\frac{\partial \zeta}{\partial t} + h \frac{\partial u}{\partial x} = 0 \,, \tag{6.1.3}$$

$$\frac{\partial u}{\partial t} + g \frac{\partial \zeta}{\partial x} = 0 \,, \tag{6.1.4}$$

which are the limits of Eqs. (6.1.1) and (6.1.2) for $A/h \ll 1$. More explicitly, the incident wave may be written

$$\zeta^I = \frac{1}{2} A [e^{i(kx - \omega t)} + e^{-i(kx - \omega t)}] \,, \tag{6.1.5}$$

$$u^I = \frac{gk}{\omega} \zeta^I \,. \tag{6.1.6}$$

It is assumed that the incident wave is not only long compared to the depth, but is even longer compared to the channel width, so that $ka \ll 1$.

Referring to Fig. 6.1, let the region at a distance $O(k^{-1})$ away from the constriction be called the *far field*. Because $ka \ll 1$, the flow is one dimensional and governed by Eqs. (6.1.3) and (6.1.4) on both sides of the barrier. Their solutions must be joined across the barrier by certain matching conditions which depend on the *near field*, defined as the neighborhood of $O(a)$ around the barrier.

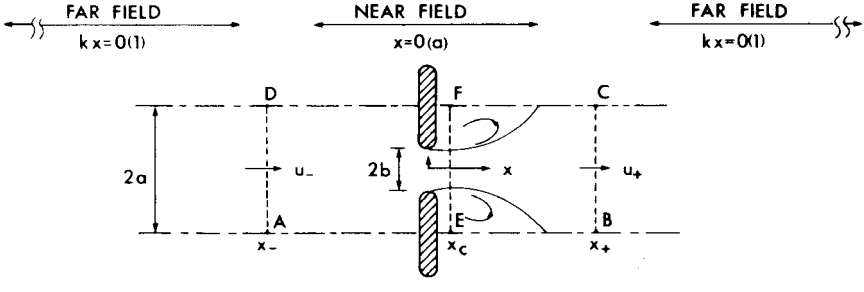

Figure 6.1: Near and far fields.

6.1.2 The Matching Conditions and the Near Field

For sufficiently sharp constriction and moderate amplitude, flow is separated downstream of the barrier. A jet is formed which expands and collides with jets from adjacent slots to create two eddy zones. Further downstream the flow becomes nearly one dimensional again. We denote the outer limits of the near field by x_- and x_+ as shown in Fig. 6.1. The geometry is reversed with the reversal of flow direction.

In this complex near field the continuity equation (6.1.1) may be simplified. Even when the gaps or holes are absent, the wave amplitude can be $2A$ at most, hence ζ may be neglected relative to h. Furthermore, between x_- and x_+ the horizontal length scale is a, $\zeta = O(A)$, $t = O(\omega^{-1})$, and $u \geqq O((A/h)(gh)^{1/2})$; it follows that

$$\frac{\partial \zeta}{\partial t} \Big/ \nabla \cdot (h\mathbf{u}) \leqq O(ka) \ll 1 \,.$$

The continuity equation (6.1.1) becomes

$$\nabla \cdot \mathbf{u} \cong 0 \,. \tag{6.1.7}$$

Outside the region of turbulent eddies the inviscid momentum equation applies. Since the velocity through the slots can be large, we retain the convective inertia term, that is, the entire Eq. (6.1.2) which is valid outside the eddy zone.

We now take the hydraulic approach by examining the differences of the cross-sectional averages between x_- and x_+. Upon integrating Eq. (6.1.7), it is obvious that

$$u_- S = u_c S_c = u_+ S \,, \tag{6.1.8}$$

where S is the gross area of the channel. S_c is the area at the *vena contracta* and is related to the net opening area S_0 by the empirical discharge coefficient c

$$S_c = c S_0 \,; \tag{6.1.9}$$

u_c is the mean velocity at the *vena contracta*.

Outside the eddy zone, it is consistent with Eq. (6.1.2) to take $\mathbf{u}$ as irrotational so that $\mathbf{u} = \nabla\Phi$. A Bernoulli equation then holds:

$$\frac{\partial \Phi}{\partial t} + \frac{\mathbf{u}^2}{2} + g\zeta = \text{const} \,. \tag{6.1.10}$$

Applying Eq. (6.1.10) between x_- and x_c which is at the *vena contracta*, see Fig. 6.1, we get

$$\frac{\partial}{\partial t}(\Phi_c - \Phi_-) + \frac{1}{2}(u_c^2 - u_-^2) + g(\zeta_c - \zeta_-) = 0\,, \tag{6.1.11}$$

assuming that at both stations the transverse variation is negligible.

Downstream of the barrier we apply global momentum conservation to the control volume $EBCF$ in Fig. 6.1. In the wake of the solid barrier the mean-fluid velocity is negligible and the free-surface height, hence the dynamic pressure, is essentially uniform in y, and is equal to that in the jet. Thus, the pressure force along EF is $\rho g \zeta_c S$. The balance of total momentum requires that

$$\rho g S(\zeta_c - \zeta_+) + \rho(u_c^2 S_c - u_+^2 S) = \rho \frac{\partial}{\partial t} \int_{x_c}^{x_+} S_J u \, dx\,, \tag{6.1.12}$$

where S_J is the cross-section area of the jet. Subtracting Eq. (6.1.12) from Eq. (6.1.11) and invoking Eq. (6.1.8), we get

$$(\zeta_- - \zeta_+) = \frac{1}{2g} u_+^2 \left(\frac{S}{cS_0} - 1\right)^2 + \frac{1}{g}\frac{\partial}{\partial t}\left[\int_{x_-}^{x_c} u \, dx + \int_{x_c}^{x_+} u \left(\frac{S_J}{S}\right) dx\right], \tag{6.1.13}$$

where the first integral above follows from the definition of Φ. If we introduce the loss coefficient f

$$f = \left(\frac{S}{cS_0} - 1\right)^2\,, \tag{6.1.14}$$

and the length L

$$L u_+ = \int_{x_-}^{x_c} u \, dx + \int_{x_c}^{x_+} u \left(\frac{S_J}{S}\right) dx\,, \tag{6.1.15}$$

Eq. (6.1.13) may be rewritten

$$\zeta_- - \zeta_+ = \frac{f}{2g} u_+^2 + \frac{L}{g}\frac{\partial u_+}{\partial t}\,, \quad u_+ > 0\,. \tag{6.1.16}$$

If the argument is repeated for $u_+ < 0$, a negative sign appears in front of the first term on the right of Eq. (6.1.16). Accounting for both flow directions, we have

$$\zeta_- - \zeta_+ = \frac{f}{2g} u_+ |u_+| + \frac{L}{g}\frac{\partial u_+}{\partial t}\,. \tag{6.1.17}$$

Once the coefficients f and L are determined empirically, Eqs. (6.1.8) and (6.1.17) provide the boundary conditions for the far-field solutions on two sides of the barrier. Since the far-field length scale is $O(k^{-1})$, these matching conditions can be approximately applied to the far-field solutions by letting $x \to \pm 0$.

If there is a solid wall at $x = l$, as in the case of a caisson with one wall perforated, the boundary condition $\partial\zeta_+/\partial x = 0$ at $x = l$ must be added. If the region extends to $x \to \pm\infty$, then the scattered waves must be outgoing from $x = 0$ (radiation condition). In practice, the width of the caisson l is typically of order $O(10$ m$)$ and is shorter than a design wavelength. Use of Eqs. (6.1.9) and (6.1.17) for the perforated wall is therefore not entirely legitimate from a theoretical point of view.

As an aside, a formula may be deduced for the force acting on the solid barrier. Consider the fluid in $ABCD$ and outside the body and its wake. The net effect of pressure distribution on the upstream face of the body and in its wake is to produce a force $-F$ against the fluid in the control volume. Hence from momentum balance

$$S[\rho g(\zeta_- - \zeta_+) + \rho(u_-^2 - u_+^2)] - F = \rho \frac{\partial}{\partial t}\left[\int_{x_-}^{0} dx\, uS + \int_{0}^{x_+} dx\, uS_J\right].$$

It follows from Eqs. (6.1.8), (6.1.15), and (6.1.17) that

$$F = S\left[\rho g(\zeta_- - \zeta_+) - \rho L \frac{\partial u_+}{\partial t}\right] = \frac{1}{2}\rho f S u_+ |u_+| \,. \tag{6.1.18}$$

6.1.3 The Coefficients f and L

It is well-known that in steady flows past sharp-edged orifices, the discharge coefficient c (thus f) depends primarily on the orifice geometry, if the Reynolds number is sufficiently high so that separation is a clear-cut feature. For a sharp-edged orifice, an empirical formula is

$$c = 0.6 + 0.4\left(\frac{S_0}{S}\right)^3 . \tag{6.1.19}$$

For thick or rounded edges, the discharge coefficient c is much closer to unity. According to this formula, c varies between 0.6 and 1. As the passing fluid slows down, the frequency of vortex shedding decreases. Thus, f and c should vary with the instantaneous velocity and acceleration, hence with Reynolds and Strouhal numbers. Since comprehensive experimental data

on f and c are not available for this kind of oscillatory flow, the steady-state values are customarily used in the engineering literature. On the other hand, the length L is the most difficult to estimate. While Hayashi et al. (1966) neglected L altogether, Terrett et al. (1968) chose a constant value to fit the experiments. In the absence of separation, the boundary-value problem is linear; the corresponding length, denoted by L_0 herein, can be calculated by a two-dimensional theory. In fact, for long waves, L_0 is related to the transmission and reflection coefficients T and R as will now be shown. In the far field where the flow is one dimensional, the free-surface displacement is given by

$$\zeta_- = Ae^{i(kx-\omega t)} + ARe^{-i(kx-\omega t)}\,, \quad x < 0\,, \tag{6.1.20}$$

$$\zeta_+ = ATe^{i(kx-\omega t)}\,, \qquad x > 0\,. \tag{6.1.21}$$

Evaluating ζ_- at x_-, ζ_+ at x_+, and noting that $|kx_-|$, $kx_+ \ll 1$, we obtain

$$\zeta_- - \zeta_+ \simeq A(1 + R - T)e^{-i\omega t}\,. \tag{6.1.22}$$

At x_+ the velocity field on the right is

$$u_+ = \frac{gk}{\omega}\zeta_+ \simeq \frac{gk}{\omega}ATe^{-i\omega t}\,. \tag{6.1.23}$$

With Eq. (6.1.23), Eq. (6.1.22) may be written in the form

$$\begin{aligned}\zeta_- - \zeta_+ &= \left[\frac{T-(1+R)}{ikT}\right]\frac{1}{g}\frac{\partial u_+}{\partial t}\\ &= \frac{L_0}{g}\frac{\partial u_+}{\partial t}\,,\end{aligned} \tag{6.1.24}$$

where L_0 is given by

$$L_0 = \left[\frac{T-(1+R)}{ikT}\right]. \tag{6.1.25}$$

After multiplying by $\rho g S$, we can interpret Eq. (6.1.24) as Newton's second law for a mass of $\rho S L_0$, subject to the net force $\rho g S(\zeta_- - \zeta_+)$; the effect of the orifice is equivalent to adding a mass of $\rho S L_0$ at the section $x = 0$. The transmission and reflection coefficients must be found by a locally two-dimensional theory. Now long waves of small amplitude are exactly analogous to sound waves; analytical results known for several acoustic orifices (a slot in a rectangular duct, a circular hole in a circular pipe, and

so on) may be applied here. As an example, for a thin two-dimensional slot, we have

$$\frac{L_0}{2a} \simeq \frac{1}{\pi} \ln \frac{1}{2} \left(\tan \frac{\pi b}{4a} + \cot \frac{\pi b}{4a} \right), \quad ka \ll 1 \tag{6.1.26}$$

(Morse and Ingard, 1968). Note that for long waves L_0 depends on k in the above approximation. The derivation of this formula is left as an exercise of matched asymptotics. In the limits of small and large gaps, we get

$$\begin{aligned} &\frac{L_0}{2a} \simeq \frac{1}{\pi} \ln \frac{2}{\pi} \frac{a}{b} = \frac{1}{\pi} \ln \frac{2}{\pi} \frac{S}{S_0}, \quad \frac{b}{a} \ll 1, \\ &\frac{L_0}{2a} \sim \frac{\pi}{8} \left(\frac{a-b}{a} \right)^2; \quad \frac{a-b}{a} \ll 1. \end{aligned} \tag{6.1.27}$$

Even for quite large S/S_0, $\ln(S/S_0)$ remains practically of $O(1)$; the ratio

$$\frac{L_0}{g\zeta} \frac{\partial u_+}{\partial t} = O(kL_0) \tag{6.1.28}$$

is very small for long waves. Thus, $\zeta_- \simeq \zeta_+$ and the constriction is ineffective. This result is related to the deduction in Section 5.5 that the transmission coefficient is nearly unity in the irrotational theory, unless S/S_0 is an enormous number.

With separation, L is obviously less tractable theoretically. Compared with the unseparated flow, separation reduces the curvature of the local streamlines around the gap. The local acceleration, which is responsible for the hydrodynamic reaction and hence the apparent mass, should be reduced also. In other words, we can expect the inviscid L_0 to be the upper bound of L. Now compare the inertia term to the friction loss term in Eq. (6.1.17)

$$\alpha = \frac{(L/g)(\partial u_+/\partial t)}{(f/2g)u_+|u_+|} = O\left(\frac{kL}{\frac{1}{2}fA/h} \right) = O\left(\frac{2kaL/2a}{\frac{1}{2}fA/h} \right).$$

Using L_0 in Eq. (6.1.26) for L, one sees that the aforementioned ratio is only important for relatively short waves. As the area ratio S/S_0 increases, $L/2a \sim \ln(S/S_0)$ and $f \sim (S/S_0)^2$, so that the preceding ratio diminishes rapidly as

$$\alpha \simeq \frac{(4/\pi)ka \ln(2/\pi)(S/S_0)}{f(A/h)(S/S_0)^2}. \tag{6.1.29}$$

Table 6.1: Ratio α according to Eq. (6.1.29).

a(m)	b(m)	$\frac{b}{a}$ or $\frac{S_0}{S}$	$\frac{L}{2a}$	f	$\frac{1}{2}\frac{fA}{h}$	α
1	0.5	0.5	0.22	1	00.5	0.1332
1	0.025	0.025	2.32	1.521	76	0.0018

Thus, for small gaps or holes, friction loss dominates for small but practical wave amplitudes. As a numerical example, assume that $A = 1$ m, $h = 10$ m, $T = 2\pi/\omega = 10$ s, $k = \omega/(gh)^{1/2} = 0.06/\text{m}$, and $c = 1$. For the perforated breakwater of the North Sea oil storage tank, $S/S_0 \simeq 2$ with hole diameter ≈ 1 m. We may take for estimates $a = 1$ m and $b = 0.5$ m as the equivalent channel and gap widths, respectively. For the Osaka pile breakwater, the values are close to $a = 1$ m, $b = 25$ mm, and $S/S_0 = 40$. The apparent orifice length is calculated according to Eq. (6.1.26) and the ratio α by Eq. (6.1.29) as given in Table 6.1. Note that even for wind waves, α is quite small and diminishes for larger amplitudes or longer waves, or both. Thus, in practical calculations there is an ample range of circumstances in which the inertia term can be ignored altogether.

Exercise 6.1

Use comformal mapping and matched asymptotics to verify Eq. (6.1.26).

6.1.4 Equivalent Linearization

The quadratic friction term in Eq. (6.1.17) makes the entire problem nonlinear, and the response to a simple harmonic input should contain many harmonics. If the response is dominated by the first harmonic as the input, as should be checked *a posteriori*, then the so-called *equivalent linearization* may be applied. Let the friction term be expressed in a linear form $c_e u$, that is,

$$\zeta_- - \zeta_+ = c_e u\,, \tag{6.1.30}$$

where c_e denotes the equivalent friction coefficient. We shall choose c_e in such a way that the mean square of the error

$$e = \frac{f}{2g} u|u| - c_e u \tag{6.1.31}$$

is minimum. Averaged over a period, the mean square is

$$\overline{e^2} = \overline{\left(\frac{f}{2g}u|u|\right)^2} - \frac{f}{g}c_e\overline{u^2|u|} + c_e^2\overline{u^2}\,. \tag{6.1.32}$$

The minimum occurs when $\overline{\partial e^2}/\partial c_e = 0$, which determines the optimal c_e

$$c_e = \frac{f}{2g}\frac{\overline{u^2|u|}}{\overline{u^2}}\,. \tag{6.1.33}$$

The equivalent friction coefficient now depends on u, and is not known before the solution is completed. Alternatively, Eq. (6.1.33) can be obtained by requiring that the nonlinear friction force and the equivalent linear friction give the same energy loss per period. Approximating u by a simple harmonic, that is,

$$u \cong \frac{1}{2}(U_0 e^{-i\omega t} + U_0^* e^{-i\omega t}) = |U_0|\cos\omega(t+\tau) \tag{6.1.34}$$

where τ is the phase of U_0, that is, $U_0 = |U_0|e^{-i\omega\tau}$, we have

$$\begin{aligned}
\overline{u^2} &= \frac{\omega}{2\pi}\int_0^{2\pi/\omega} |U_0|^2\cos^2\omega(t+\tau)dt \\
&= |U_0|^2\frac{1}{2\pi}\int_0^{2\pi}\cos^2\sigma d\sigma = \frac{1}{2}|U_0|^2 \\
\overline{u^2|u|} &= \frac{1}{2\pi}\int_0^{2\pi}\cos^2\sigma|\cos\sigma||U_0|^3 d\sigma = \frac{4}{3\pi}|U_0|^3\,.
\end{aligned}$$

It follows that

$$c_e = \frac{f}{2g}\frac{8}{3\pi}|U_0|\,, \tag{6.1.35}$$

which depends on the amplitude of the motion.

6.1.5 Approximate and Exact Solutions

We first derive the approximate solution by using Eq. (6.1.30) instead of Eq. (6.1.17). The solution can be written in the following form:

$$\begin{aligned}
\zeta_- &= Ae^{-i\omega t}[e^{+ikx} + Re^{-ikx}]\,, \\
u_- &= \frac{gk}{\omega}Ae^{-i\omega t}[e^{+ikx} - Re^{-ikx}]\,,
\end{aligned} \qquad x < 0 \tag{6.1.36}$$

$$\begin{aligned} \zeta_+ &= ATe^{-i\omega t+ikx}\,, \\ u_+ &= \frac{gk}{\omega}ATe^{-i\omega t+ikx}\,, \end{aligned} \qquad x>0\,. \tag{6.1.37}$$

Invoking continuity of velocity (6.1.8), we obtain

$$T=\frac{\omega}{gk}\frac{U_0}{A}=\frac{U_0}{(A/h)(gh)^{1/2}} \tag{6.1.38}$$

$$R=1-T=1-\frac{\omega}{gk}\frac{U_0}{A}\,. \tag{6.1.39}$$

Applying the head-loss condition (6.1.30), we have

$$A=\left(\frac{c_e}{2}+\frac{\omega}{gk}\right)U_0$$

which becomes

$$A=\frac{\omega}{gk}U_0+\frac{2}{3\pi}\frac{f}{g}U_0|U_0| \tag{6.1.40}$$

upon inserting Eq. (6.1.35). The phases of U_0 and A_0 are equal and may be taken to be zero, that is, $U_0=|U_0|$. Equation (6.1.40) is a quadratic equation for U_0, which may be solved:

$$U_0=\frac{A}{h}(gh)^{1/2}T=\frac{A}{h}(gh)^{1/2}\frac{(1-2\beta)^{1/2}-1}{\beta} \tag{6.1.41}$$

where $\beta=(4/3\pi)(fA/h)$ (Hayashi et al., 1966).

For small-amplitude waves or a wide opening, β is much less than unity. Taylor expansion of the right-hand side of Eq. (6.1.41) gives

$$U_0=\frac{A}{h}(gh)^{1/2}\left[1-\frac{1}{2}\beta+O(\beta^2)\right].$$

Thus,

$$\begin{aligned} c_e &\cong \frac{f}{2g}\frac{8}{3\pi}\left(\frac{A}{h}(gh)^{1/2}\right)\left(1-\frac{1}{2}\frac{4}{3\pi}\frac{fA}{h}\right), \\ T &\cong \left(1+\frac{1}{2}\beta\right), \quad R\cong\frac{1}{2}\beta\,. \end{aligned} \tag{6.1.42}$$

For small openings, $S_0/S \ll 1$, f is large according to Eq. (6.1.14); Eq. (6.1.41) may be approximated for large β by

$$U_0 = \frac{A}{h}(gh)^{1/2}\left(\frac{2}{\beta}\right)^{1/2} = \left(\frac{3\pi}{2f}gA\right)^{1/2}$$

$$\cong \left(\frac{3\pi}{2}\right)^{1/2}\frac{cS_0}{S}(gA)^{1/2}. \tag{6.1.43}$$

The above limit may be deduced more directly as follows. By assuming that the reflection is nearly total, one has a standing wave with amplitude $2A$ on the side $x < 0$. The maximum difference of the free surfaces on both sides is $2A$ which gives the discharge velocity $(4gA)^{1/2}$ through a tiny hole, according to Torricelli's law. The discharge velocity defined by averaging over the gross area of S is then $U_0 = (4gA)^{1/2}S_0/S$, which corresponds to $c = 2\sqrt{2}/(3\pi)^{1/2} = 0.92$ in Eq. (6.1.43), the theoretical range of c being $0.6 < c < 1$. Finally, the corresponding transmission coefficient is

$$T \cong \left(\frac{2}{\beta}\right)^{1/2} = \left(\frac{3\pi}{2}\frac{h}{fA}\right)^{1/2}$$

$$= \left(\frac{3\pi}{2}\frac{h}{A}\right)^{1/2}\frac{cS_0}{S}. \tag{6.1.44}$$

The scattering coefficients T and R are plotted in Figs. 6.2(a) and 6.2(b).

Özsoy (1977) compared the experiments of Hayashi et al. (1966) for a closely spaced pile breakwater with the theory of this section. With f given by Eq. (6.1.14), he found that the agreement in transmission and reflection coefficients was rather good (Figs. 6.2(a) and 6.2(b)). Özsoy also performed experiments for vertical slots in a thin barrier ($b/a = 0.052$, 0.103, 0.162, 0.441, and $d/2b \leqq 0.133$ where $d =$ thickness, $2b =$ slot width, and $2a = 0.87$ m). The empirical coefficient f has a significant scatter for a fixed b/a (see Fig. 6.3), suggesting that other parameters such as the Strouhal number might be important. Further information of interest may be found in Özsoy.

The present problem with the nonlinear boundary condition (6.1.17) without $(L/g)(\partial u/\partial t)$ has been solved exactly by Mei, Liu, and Ippen (1974). We include it here to show that although odd higher harmonics exist, the fundamental harmonic dominates in practice and is quite accurately given by the method of equivalent linearization.

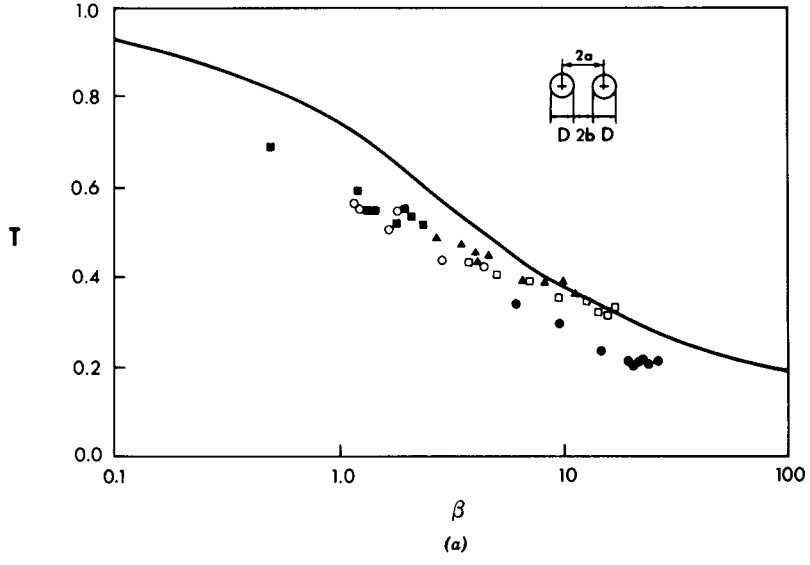

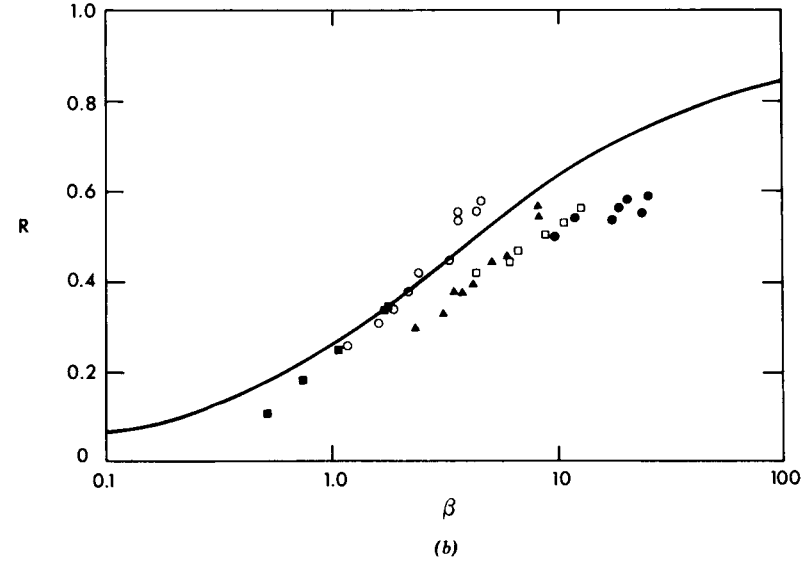

Figure 6.2: Comparison of theory (solid curve), Eqs. (6.1.14) and (6.1.41), with experiments by Hayashi et al. (1966). Experiments were performed for various b/a : (● : 0.055; □ : 0.075; ▲ : 0.091; ◯ : 0.141; ■ : 0.182). $(a)T$; $(b)R$ (from Özsoy, 1977).

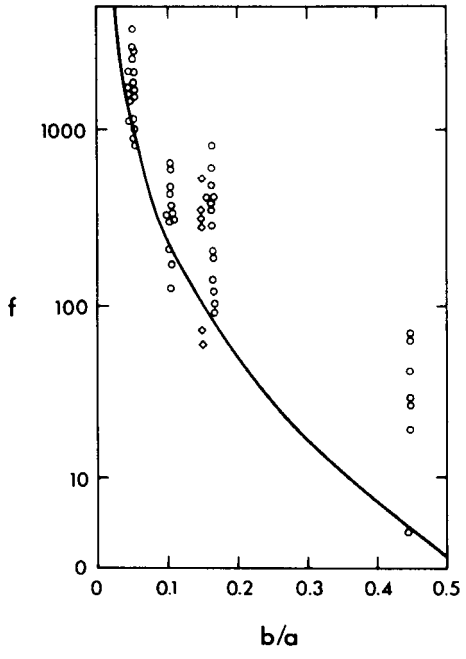

Figure 6.3: The friction coefficient as a function of b/a. (From Özsoy, 1977).

Due to the nonlinear boundary condition we propose the solution

$$\zeta_- = \zeta_I + \frac{1}{2}\sum_{-\infty}^{\infty} A_m e^{-im(kx+\omega t)}\,, \tag{6.1.45}$$

$$u_- = u_I - \sum_{-\infty}^{\infty} \frac{gk}{2\omega} A_m e^{im(kx+\omega t)}\,, \tag{6.1.46}$$

for $x < 0$, and

$$\zeta_+ = \frac{1}{2}\sum_{-\infty}^{\infty} B_m e^{im(kx-\omega t)}\,, \tag{6.1.47}$$

$$u_+ = \frac{gk}{2\omega}\sum_{-\infty}^{\infty} B_m e^{im(kx-\omega t)}\,, \tag{6.1.48}$$

for $x > 0$. By time averaging the governing conditions, it may be shown that $\bar{\zeta}$ is zero if $\bar{u}$ is assumed to be zero at one end. Thus, there is no zeroth harmonic in the series above. For every harmonic we require that

$$A_{-m} = A_m^*\,, \quad B_{-m} = B_m^*\,, \tag{6.1.49}$$

so that all physical quantities are real.

By matching the velocity according to Eq. (6.1.8), it follows that

$$\begin{aligned} B_m &= -A_m \qquad \text{for} \quad m \neq 1\,, \\ B_1 &= A_1 + A \quad \text{for} \quad m = 1\,. \end{aligned} \tag{6.1.50}$$

Since

$$\begin{aligned} \zeta_- &= \frac{\omega}{gk}\left(u_I + \frac{gk}{2\omega}\sum A_m e^{-im\omega t}\right) \\ &= \frac{\omega}{gk}\left[2u_I - \left(u_I - \frac{gk}{2\omega}\sum A_m e^{-im\omega t}\right)\right] \\ &= \frac{\omega}{gk}(2u_I - u_+)\,, \end{aligned}$$

at $x = 0-$, and

$$\zeta_+ = \frac{\omega}{gk}u_+\,,$$

at $x = 0+$, it follows from Eq. (6.1.17) with $L = 0$ that

$$\frac{f}{2g}u_+|u_+| + 2\frac{\omega}{gk}u_+ = 2\frac{\omega}{gk}u_I = 2A\cos\omega t\,.$$

Clearly, the signs of u_+ and u_I are the same, that is, u_+ and $u_I(O,t)$ are always in phase. The above equation then gives

$$\frac{f}{2g}|u_+|^2 + \frac{2\omega}{gk}|u_+| = 2A|\cos\omega t|\,. \tag{6.1.51}$$

In terms of the dimensionless variable W defined by

$$u_+(0,t) = A\frac{gk}{\omega}W = \frac{A}{h}(gh)^{1/2}W(t)\,, \tag{6.1.52}$$

the solution to Eq. (6.1.51) is

$$|W| = \frac{(1 + 2\beta'|\cos\omega t|)^{1/2} - 1}{\beta'}\,, \tag{6.1.53}$$

where

$$\beta' = \frac{fA}{2h} = \frac{3\pi}{8}\beta\,. \tag{6.1.54}$$

When W is expressed as a Fourier series

$$W = \frac{1}{2}\sum T_m e^{-im\omega t}\,, \tag{6.1.55}$$

the Fourier coefficient must be

$$\frac{T_m}{2} = \frac{1}{2\pi}\int_0^{2\pi} d\tau\, e^{im\tau}\ \mathrm{sgn}(\cos\tau)|W(\tau)|\,.$$

The results are

$$T_m = 0\,, \quad m = 2, 4, 6, \ldots, \text{even}\,, \tag{6.1.56}$$

$$\frac{1}{2}T_m = \frac{2}{\pi}\left[\frac{(-1)^{(m+3)/2}}{\beta m} - \frac{M_m(\beta')}{\beta'}\right], \quad m = 1, 3, 5, \ldots, \text{odd}\,, \tag{6.1.57}$$

where

$$M_m(\beta') = \int_0^{\pi/2} d\tau\ \cos m\tau(1 + 2\beta'\cos\tau)^{1/2}\,, \tag{6.1.58}$$

which may be expressed in elliptic integrals but is readily integrated numerically.

By combining Eqs. (6.1.46), (6.1.50), (6.1.52), and (6.1.55), we get

$$B_m = AT_m\,, \tag{6.1.59}$$

so that T_m is the transmission coefficient of the mth harmonic. The reflected coefficient for the mth harmonic is

$$R_1 = 1 - T_1\,, \quad R_m = -T_m\,, \tag{6.1.60}$$

where $A_m = AR_m$. Table 6.2 shows the calculated first and third harmonics by the exact theory, and the first harmonic by the equivalent linearization for $1 < \beta < 5$. The smallness of the third harmonic and the efficiency of the approximate theory are evident.

Exercise 6.2

Consider a caisson breakwater which is composed of two parallel walls $x = 0$ and $x = l$. The wall $x = 0$ faces the incoming waves normally and is perforated with the area ratio S_0/S. Use the equivalent linear friction formula (6.1.30) to find the reflection coefficient. Discuss the effect of l.

Table 6.2: Transmission coefficients as a function of $\beta' = fA/2h$, T_m : mth harmonic.

	T_1		T_3
β'	Exact	Approximate	Exact
0.0	1	1	0
0.1	0.9601	0.9608	−0.0052
0.2	0.9271	0.9290	−0.0120
0.3	0.8978	0.8975	−0.0169
0.4	0.8719	0.8712	−0.0207
0.5	0.8486	0.8476	−0.0238
0.6	0.8276	0.8262	−0.0264
0.7	0.8084	0.8067	−0.0285
0.8	0.7907	0.7888	−0.0304
0.9	0.7744	0.7722	−0.0319
1.0	0.7593	0.7569	−0.0332
2.0	0.6498	0.6459	−0.0400
3.0	0.5813	0.5766	−0.0418
4.0	0.5326	0.5275	−0.0421
5.0	0.4954	0.4902	−0.0418

6.2 Effect of Entrance Loss on Harbor Oscillations

In Chapter Five where real fluid effects were ignored, the resonant response in a harbor was found to increase for decreasing entrance width. However, experiments by Lee (1971) confirmed this trend only for a relatively wide entrance and showed the reduction of the entrance width ultimately reduced the peak response. This discrepancy suggests the importance of friction loss at the harbor entrance. Indeed, Japanese engineers have successfully utilized friction to diminish tsunami effects in Ofunato Bay by narrowing the entrance with two transverse breakwaters. In a research conducted for the Ofunato project, Ito (1970) and Horikawa and Nishimura (1970) found experimentally that entrance friction practically eliminated the quarter-wave mode in the long bay. They also developed a theoretical model which incorporated the hydraulic loss formula (6.1.17) without the apparent inertia, that is,

$$\zeta_- - \zeta_+ = \frac{f}{2g} u|u| \,. \tag{6.2.1}$$

While more experimental information is needed for two-dimensional problems with a constriction, the simple formula (6.2.1) with an estimated

constant f appears to yield reasonable global predictions. Based on the same assumptions, Ünlüata and Mei (1975) studied the problem analytically for the simple rectangular harbor with a centered entrance, and Miles and Lee (1975) for the Helmholtz mode of general harbor shape. The theory of Ünlüata and Mei, simplified by ignoring all higher harmonics, is presented below.

6.2.1 The Boundary-Value Problem

For analytical convenience we consider a rectangular harbor with a centered entrance as depicted in Fig. 5.11, Chapter Five.

In the ocean $x > 0$, we separate the radiated waves from the normally incident and reflected waves

$$\eta_0 = 2A \cos kx + \eta^R \,. \tag{6.2.2}$$

The radiated wave η^R satisfies

$$\nabla^2 \eta^R + k^2 \eta^R = 0 \,, \tag{6.2.3}$$

$$\frac{\partial \eta^R}{\partial x} = 0 \,, \qquad |y| > a \qquad \text{on} \quad x = 0 \,, \tag{6.2.4}$$

$$\frac{\partial \eta^R}{\partial x} = \frac{i\omega}{g} U(y) \,, \quad |y| < a \tag{6.2.5}$$

and must behave as outgoing waves at infinity. The velocity across the harbor entrance is denoted by $U(y) = |U(y)| e^{-i\omega\tau}$ where τ is the phase of U. In the harbor $x < 0$, the displacement amplitude η_H is governed by

$$\nabla^2 \eta_H + k^2 \eta_H = 0 \,, \tag{6.2.6}$$

$$\frac{\partial \eta_H}{\partial x} = 0 \,, \qquad x = -L, \ |y| < B \tag{6.2.7}$$

$$\frac{\partial \eta_H}{\partial y} = 0 \,, \qquad y = \pm \frac{1}{2} B, \ -L < x < 0 \tag{6.2.8}$$

$$\frac{\partial \eta_H}{\partial x} = 0 \,, \qquad a < |y| < \frac{B}{2} \,, \qquad x = 0 \,. \tag{6.2.9}$$

$$= \frac{i\omega}{g} U(y) \,, \quad |y| < a \,, \tag{6.2.10}$$

Together, Eqs. (6.2.9) and (6.2.10) imply the continuity of normal velocity across the entrance. In addition we have at $x = 0$, $|y| < a$,

$$\eta_H - \eta_0 = c_e U\,, \quad c_e = \frac{8}{3\pi}\frac{f}{2g}|U|\,. \tag{6.2.11}$$

The solution can be formally written as a superposition of sources:

$$\eta_0 = \int_{-a}^{a} U(y')G_0(x, y|y')\,dy' + 2A\cos kx\,, \tag{6.2.12}$$

$$\eta_H = \int_{-a}^{a} U(y')G_H(x, y|y')\,dy'\,, \tag{6.2.13}$$

where the source functions are

$$G_0 = -\frac{i\omega}{g}\frac{i}{2}H_0^{(1)}(kr)\,, \tag{6.2.14}$$

$$G_H = -\frac{i\omega}{g}\left[\frac{\cos k(x+L)}{kB\sin kL} + 2\sum_{n=1}^{\infty}\frac{\cos K_n(x+L)}{K_nB\sin K_nL}\cos\frac{2n\pi y}{B}\cos\frac{2n\pi y'}{B}\right], \tag{6.2.15}$$

with $K_n = [k^2 - (2n\pi/B)^2]^{1/2}$. Equations (6.2.14) and (6.2.15) are essentially the same as Eqs. (5.7.1) and (5.7.7), Chapter Five, except for a factor $-i\omega/g$. Substituting Eqs. (6.2.12) and (6.2.13) into Eq. (6.2.11), we get

$$\begin{aligned}\int_{-a}^{a} M(y|y')U(y)\,dy - 2A = c_eU(y) &= \frac{f}{2g}\frac{8}{3\pi}|U|U \\ &= \frac{f}{2g}\frac{8}{3\pi}|U|^2e^{-i\omega\tau}\end{aligned} \tag{6.2.16}$$

where

$$M(y|y') = G_H(0, y|y') - G_0(0, y|y')\,. \tag{6.2.17}$$

Equation (6.2.16) is a nonlinear integral equation which can be solved numerically for $U(y)$. Because of the uncertainties in f, we shall be contented with a gross estimate by assuming that U is constant in y for $|y| < a$ and try to satisfy Eq. (6.2.16) only on the average, that is,

$$U\iint_{-a}^{a} M(y|y')\,dy\,dy' - 4aA = a\frac{f}{g}\frac{8}{3\pi}|U|^2e^{-i\omega\tau}\,. \tag{6.2.18}$$

For a small gap in a perfect fluid, $U(y)$ is well approximated by $(\text{const})(a^2 - y^2)^{-1/2}$. With flow separation, however, $U(y)$ should no longer be singular at the tips. For this reason and for mathematical simplicity, a uniform velocity distribution is adopted. Needless to say, this approximation cannot give the correct U in detail, and the inaccuracy is not easy to ascertain. Since it is already known that the harbor response for a narrow entrance is related to the total flux through the entrance, a gross global error is not likely to occur using this approximation. With

$$\frac{2a^2\omega}{g} D = -\iint_{-a}^{a} M \, dy \, dy' \,, \tag{6.2.19}$$

and $S \equiv 4/3\pi$, Eq. (6.2.18) may be rearranged as follows:

$$-\left(\frac{f}{\omega a} S|U|\right)^2 + \left(\frac{f}{\omega a} S|U|\right) D = \frac{2fA}{h} \frac{S}{(ka)^2} \exp(-i\omega\tau) \,, \tag{6.2.20}$$

where use has been made of $\omega^2 = gk^2h$. Taking the square of the magnitude, we get

$$W^4 + 2(\operatorname{Re} D)W^3 + |D|^2 W^2 - \left[\frac{4\beta}{(ka)^2}\right]^2 = 0 \,, \tag{6.2.21}$$

in which $\operatorname{Re} D$ is the real part of D,

$$W = \frac{fS}{\omega a}|U| \,, \quad \text{and} \quad \beta = \frac{fA}{2h} S = \frac{2fA}{3\pi h} \,. \tag{6.2.22}$$

Equation (6.2.21) is a quartic equation for W, which can be solved numerically. Afterward the phase $\omega\tau$ follows from Eq. (6.2.20) and the solution for U is complete. Finally, the value of U is substituted into Eq. (6.2.13) to give the harbor response.

6.2.2 Local and Mean Square Response in the Harbor

From Eqs. (6.2.13) and (6.2.16), the response at a point (x, y) in the harbor is

$$\eta_H(x, y) = \frac{(A/a) \int_{-a}^{a} G_H(x, y|y') \, dy'}{(1/4a^2) \iint_{-a}^{a} M(y|y') \, dy \, dy' - (fS/2ga)|U|} \,. \tag{6.2.23}$$

Since the integral

$$\frac{1}{2a}\int_{-a}^{a} G_H\, dy' = -\frac{i\omega}{g}\left[\frac{\cos k(x+L)}{kb\sin kL} + 2\sum_{n=1}^{\infty}\frac{\cos K_n(x+L)}{K_nB\sin K_nL}\frac{\sin n\alpha}{n\alpha}\cos\frac{2n\pi y}{B}\right], \tag{6.2.24}$$

in which

$$\alpha \equiv \frac{2\pi a}{B}, \tag{6.2.25}$$

is the response to an oscillating piston with uniform velocity $1/2a$ at the entrance (thus, unit total discharge per unit depth), the remaining factor

$$Q \equiv \frac{2A}{(1/4a^2)\iint_{-a}^{a} M\, dy\, dy' - fS|U|/2ga} \tag{6.2.26}$$

in Eq. (6.2.23) represents the amplitude of the discharge across the entrance.

We introduce the normalized mean square response as follows:

$$\sigma^2 = \frac{1}{2}\frac{1}{BL}\int_{-L}^{0} dx\int_{-B/2}^{B/2} dy\left|\frac{\eta_H}{2A}\right|^2 = \frac{1}{2}\frac{|Q/2A|^2}{BL}\int_{-L}^{0} dx\int_{-B/2}^{B/2} dy\left|\frac{1}{2a}\int_{-a}^{a} dy'\, G_H\right|^2. \tag{6.2.27}$$

After evaluating all the integrals, one obtains

$$\sigma^2 = \frac{1}{4}\left|\frac{Q}{2A}\frac{\omega}{g}\right|^2 F, \tag{6.2.28}$$

in which

$$F = \frac{1}{(kB\sin kL)^2}\left(1+\frac{\sin 2kL}{2kL}\right) + 2\sum_{n=1}\left(\frac{(\sin n\alpha)/n\alpha}{K_nB\sin K_nB}\right)^2\left(1+\frac{\sin K_nL}{2K_nL}\right). \tag{6.2.29}$$

Various aspects of these general formulas are examined in the following subsections.

6.2.3 Approximations for Narrow Entrance

As may be anticipated intuitively, the effect of head loss is most important for narrow entrances and near resonant peaks. Hence further considerations will be restricted to $ka \ll 1$.

By a common technique of improving the convergence of a series, it can be shown that

$$\frac{1}{4a^2}\iint_{-a}^{a} M\,dy\,dy' \simeq -\frac{i\omega}{g}\left(-\frac{i}{2}+F-I\right)+O(k^2a^2\ln ka)\,, \qquad (6.2.30)$$

in which

$$F \equiv \frac{\cot kL}{kB}+2\sum_{n=1}^{\infty}\left(\frac{\cot K_nL}{K_nB}+\frac{1}{2n\pi}\right)\left(\frac{\sin n\alpha}{n\alpha}\right)^2\,, \qquad (6.2.31)$$

and

$$I = -\left(\ln\frac{\pi ka^2\gamma}{4B}+\ln 16-3\right), \qquad (6.2.32)$$

with $\ln\gamma = 0.5772157 =$ Euler's constant. Details of the derivation are given in Appendix 6.A. The approximate discharge per unit depth is

$$Q \simeq \frac{2A}{-(i\omega/g)[-\frac{1}{2}i(1+W)+F-I]}\,, \quad W=\frac{fS|U|}{a\omega}\,, \qquad (6.2.33)$$

which can be combined with Eq. (6.2.28) for the approximate σ and with Eq. (6.2.23) for the approximate η_H. The result should be compared with Eq. (5.7.23), Chapter Five.

The effect of head loss enters the theory explicitly only through the factor $W = fS|U|/\omega a$ in the entrance discharge Q [cf. Eq. (6.2.33)]. In the absence of friction ($f = 0$), the resonance features in the harbor have been studied in Chapter Five. In particular, the term $-\frac{1}{2}i$ in brackets in Eq. (6.2.33) (with $W = 0$) corresponds to radiation damping. Clearly, the term $(-\frac{1}{2}i)(1+W)$ corresponds to the sum of radiation and friction damping at the entrance. For a narrow entrance and $f = W = 0$, radiation damping should be weak so that resonance occurs near the natural modes of the completely closed basin, that is,

$$k = k_{mn} = \left[\left(\frac{m\pi}{L}\right)^2+\left(\frac{2n\pi}{B}\right)^2\right]^{1/2}, \quad m=0,1,2,3,\ldots;\ n=0,1,2,3,\ldots\,. \qquad (6.2.34)$$

Now, when $W \neq 0$ but

$$W \leqq O(1)\,, \tag{6.2.35}$$

the friction loss, and thus the total damping, is also weak; the resonant peaks should still be near k_{mn} and the neighborhoods of the resonant peaks can be examined in the manner of Section 5.7. For brevity, only the peaks themselves, when they are well isolated, are studied in the next subsection.

6.2.4 Small Radiation and Friction Damping

Near the natural mode $k = k_{mn}$, the magnitude of Q is, from Eq. (6.2.33),

$$|Q| = \frac{2A(\omega/g)^{-1}}{[|\frac{1}{2}(1+W)|^2 + (F-I)^2]^{1/2}}\,. \tag{6.2.36}$$

Since F is large for $k \simeq k_{mn}$ and I is logarithmically large for small ka^2/B, the maxima of $|Q|$ occur approximately where

$$F - I = 0\,, \tag{6.2.37}$$

provided that $W \leqq O(1)$. Let $\tilde{}$ denote quantities evaluated at the resonant peaks. In particular, the real roots of Eq. (6.2.37) will be designated by $\tilde{k}_{mn}$. Since F and I are independent of f, the locations of the resonant peaks are not strongly affected by friction losses. The corresponding maximum discharge is

$$|\tilde{Q}| = \left(\frac{4A(\omega/g)^{1/2}}{1+W}\right)_{\omega=\tilde{\omega}_{mn}}\,. \tag{6.2.38}$$

Since

$$|\tilde{Q}|_{f=0} = \left(\frac{4A}{\omega/g}\right)_{\omega=\tilde{\omega}_{mn}} \tag{6.2.39}$$

for $f = 0$, the reduction ratio for peak discharge at the entrance is

$$\frac{|\tilde{Q}|}{|\tilde{Q}|_{f=0}} = \frac{1}{(1+W)_{\omega=\tilde{\omega}_{mn}}}\,. \tag{6.2.40}$$

In view of Eq. (6.2.28), Eq. (6.2.40) is also the reduction ratio for the root mean square response at resonance since F and the resonant wavenumbers are approximately independent of f.

The value of W at resonance remains to be found. From Eqs. (6.2.30) and (6.2.19) it follows that for a narrow entrance and at resonance

$$\frac{2a^2\omega}{g} D = -\iint_{-a}^{a} M\, dy\, dy' \simeq \frac{2a^2\omega}{g}\,, \quad \text{or} \quad D \simeq 1\,. \tag{6.2.41}$$

Hence,

$$\omega\tau = 0 \tag{6.2.42}$$

from Eq. (6.2.20) and W can be solved from Eq. (6.2.21):

$$W = \frac{fS|U|}{\omega a} = \frac{1}{2}\left[-1 + \left(1 + \frac{16\beta}{(ka)^2}\right)^{1/2}\right]_{k=\tilde{k}_{mn}} \tag{6.2.43}$$

in which $\beta = 2fA/3\pi h$ [cf. Eq. (6.2.22)]. Note that the original condition (6.2.35) implies that

$$\frac{16\beta}{(ka)^2} \leq O(1)\,. \tag{6.2.44}$$

After Eq. (6.2.43) is substituted into Eq. (6.2.40), the reduction factor is found to be

$$\frac{\tilde{\sigma}}{\tilde{\sigma}_{f=0}} \cong \frac{\tilde{Q}}{\tilde{Q}_{f=0}} = \left(\frac{2}{1 + (1 + 16\beta/(ka)^2)^{1/2}}\right)_{k=\tilde{k}_{mn}}, \tag{6.2.45}$$

where the value of $\tilde{k}_{mn}$ may be estimated by the natural wavenumbers of the closed basin when n and m are not both zero (non-Helmholtz mode). For the Helmholtz mode, $\tilde{k}_{00}$ may be estimated by the inviscid value.

It can be concluded from Eq. (6.2.45) that the reduction of resonant peaks by entrance loss is more pronounced for increasing $16\beta/(\tilde{k}a)^2$, that is, for (i) larger f, (ii) larger amplitude, (iii) longer waves or lower resonant modes, or (iv) narrower entrance. The wisdom in the Ofunato breakwater design is evident. Items (iii) and (iv) are also consistent with the experimental observations by Lee (1971) for a circular harbor.

With regard to the parameter $16\beta/(\tilde{k}a)^2$, it should be pointed out that the loss coefficient f may depend on the Strouhal and Reynolds numbers and on the geometry of the breakwater tips at the entrance. Ito (1970) suggests that the empirical value $f = 1.5$ gives reasonable results for the Ofunato tsunami breakwater. For reference, note that when $A = 0.5$ m, $h = 10$ m and f is taken to be 1, then $\beta = 10^{-2}$. Now take a square basin with $B = L$; the lowest few natural modes of the closed basin are:

$$k_{10}L = \pi\,, \quad k_{01}L = k_{20}L = 2\pi\,, \quad \text{and} \quad k_{11}L = 5^{1/2}\pi\,.$$

For a narrow entrance with $2a/B = 3 \times 10^{-2}$, the reduction factor and the parameter $16\beta/(\tilde{k}a)^2$ are listed in Table 6.3 for a range of β no greater than 10^{-2}. The values marked with a † violate the assumption that $16\beta/(\tilde{k}a)^2 \leq$

Table 6.3: Reduction factor according to Eq. (6.2.45).

m, n		(0, 0)	(1, 0)	(2, 0), (0, 1)	(1,1)
$\tilde{k}B$		0.55	π	2π	$\sqrt{5}\pi$
$\tilde{k}a = \frac{2a}{B}\frac{\tilde{k}B}{2}$		0.825×10^{-2}	4.71×10^{-2}	9.42×10^{-2}	10.53×10^{-2}
	$\beta = 10^{-2}$	2350^a	72.1^a	18.0^a	14.43^a
	$\beta = 10^{-3}$	23.5^a	0.721	0.18	1.44
$\frac{16\beta}{(\tilde{k}a)^2}$	$\beta = 10^{-4}$	23.5^a	0.721	0.18	0.144
	$\beta = 10^{-5}$	2.35	0.0721	0.018	0.0144
	$\beta = 10^{-2}$	0.04^a	0.209^a	0.373^a	0.406^a
	$\beta = 10^{-3}$	0.122^a	0.517	0.748	0.781
$\frac{\tilde{\sigma}}{\tilde{\sigma}_{f=0}}$	$\beta = 10^{-4}$	0.336^a	0.865	0.959	0.966
	$\beta = 10^{-5}$	0.707	0.983	0.996	0.996

[a]From Mei, Liu, and Ippen (1974). *J. Waterway, Port, Coastal and Ocean Division.* Reproduced by permission of the American Society of Civil Engineers.

$O(1)$ and the calculated reduction factor is not reliable quantitatively; a different approximation is needed.

6.2.5 Large Friction Damping

Table 6.3 shows that the value of $16\beta/(\tilde{k}a)^2$ can be very large for the lowest resonant mode or for narrow entrance. From Eq. (6.2.21) the value of $W = fS|U|/\omega a$ is also large and can be approximated to the leading order by

$$W \simeq \frac{(4\beta)^{1/2}}{ka} \tag{6.2.46}$$

or

$$|U| \simeq \left(\frac{2gA}{fS}\right)^{1/2}. \tag{6.2.47}$$

Note that the velocity U is proportional to $(2gA)^{1/2}$, as in the elementary Torricelli's law. The corresponding discharge per unit depth through the entrance is

$$|Q| \simeq 2a \left(\frac{2gA}{fS} \right)^{1/2} , \tag{6.2.48}$$

which diminishes with the entrance width $2a$. Combining this result with Eq. (6.2.28), it may be concluded that sufficiently large head loss removes the harbor paradox, that is, the response ultimately diminishes with the entrance width.

6.2.6 Numerical Results for General W

As shown in Table 6.3, the assumption of small friction damping $W \leq O(1)$ is not appropriate for the Helmholtz mode, and an accurate solution of W from the quartic equation (6.2.21) is necessary. Since the real part of D is proportional to the total damping, the coefficients of W^4, W^3, and W^2 in Eq. (6.2.21) are positive; one and only one real and positive solution can exist. After solving for W numerically the root mean square response for the fundamental harmonic can be calculated from Eq. (6.2.28) without the assumption of $ka \ll 1$. The normalized flux and the root mean square response are plotted in Fig. 6.4 for the range $0 < kL < 8$ for $\beta = 10^{-2}, 10^{-4}$ and 0. For comparison, the inviscid theory which predicts the harbor paradox is also shown. In Figs. 6.5 and 6.6, the amplification ratios

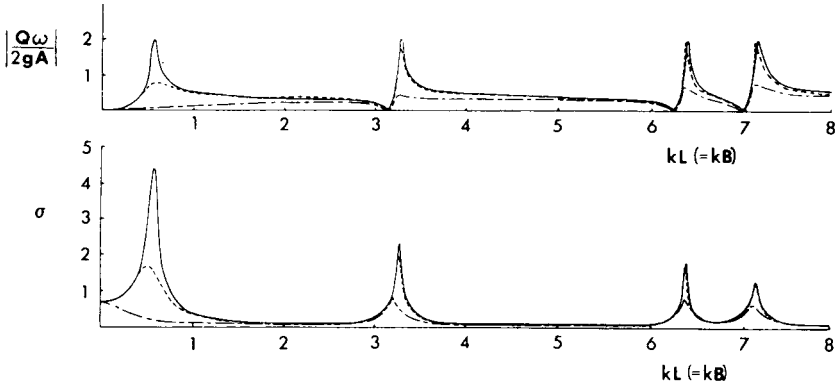

Figure 6.4: Root mean square response σ and the normalized flux intensity $|Q\omega/2gA|$ of the fundamental harmonic as function of $kL(= kB)$. Normalized entrance width $2a/B = 3 \times 10^{-2}$. $\beta = 0$: solid curve; $\beta = 10^{-4}$: dashed curve, $\beta = 10^{-2}$: dash–dot curve (from Ünlüata and Mei, 1975, *J. Waterway, Port, Coastal and Ocean Division.* Reproduced by permission of American Society of Civil Engineers).

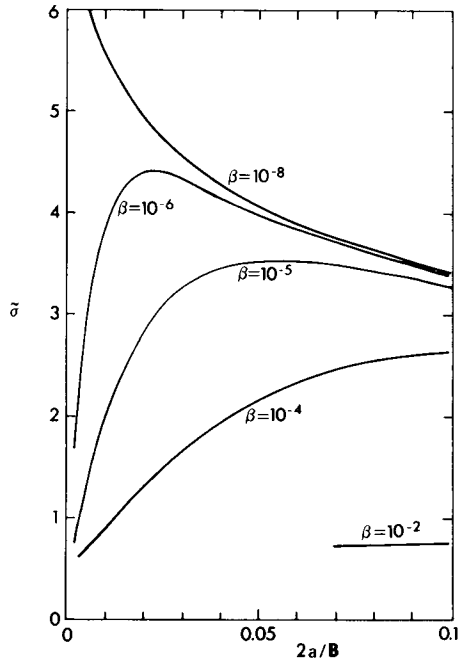

Figure 6.5: Mean resonant amplification $\tilde{\sigma}$ of the fundamental harmonic for the Helmholtz mode (from Ünlüala and Mei, 1975, *J. Waterway, Port, Coastal and Ocean Division*. Reproduced by permission of American Society of Civil Engineers).

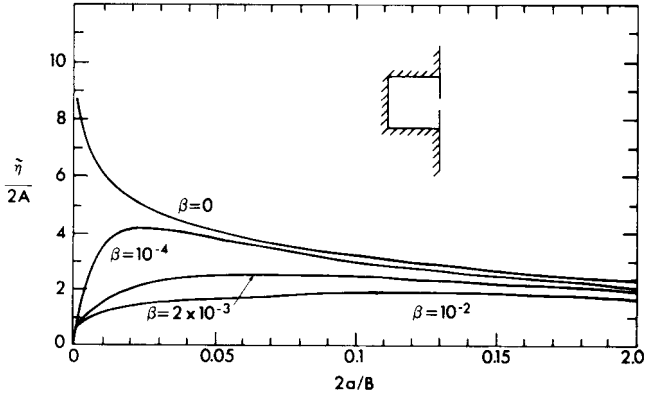

Figure 6.6: Resonant amplification $\tilde{\eta}$ of the fundamental harmonic at the corner $x = -B$, $y = \frac{1}{2}B$ for the first mode $k_{01}B = \pi$ (or $\eta \propto \cos(\pi(x+L)/L)$ (from Ünlüata and Mei, 1975, *J. Waterway, Port, Coastal and Ocean Division*. Reproduced by permission of American Society of Civil Engineers).

for the Helmholtz mode ($m = n = 0$) and for the mode $m = 1$, $n = 0$ are plotted as functions of the normalized entrance width $2a/B$. Again, the harbor response reduces with $2a/B$ for a fixed β.

Appendix 6.A Approximations of an Integral for $ka \ll 1$

The integral in question is

$$\frac{1}{4a^2}\iint_{-a}^{a} dy\,dy' M(y|y') = \frac{1}{4a^2}\iint_{-a}^{a} [G_H(0,y,y') - G_0(0,y|y')]\,dy\,dy'$$
$$= \mathscr{J}_H - \mathscr{J}_O\,. \tag{6.A.1}$$

From Eq. (6.2.14) it follows that

$$\mathscr{J}_O \equiv \frac{1}{4a^2}\iint_{-a}^{a} G_0(0,y|y')\,dy\,dy'$$
$$= \frac{1}{4a^2}\frac{i\omega}{g}\left(-\frac{i}{2}\right)\int_{-a}^{a} H_0^{(1)}(k|y-y'|)\,dy\,dy'\,,$$
$$= \frac{\omega}{2g}\iint_{-1/2}^{1/2} H_0^{(1)}[(2ka)|\xi-\xi'|]\,d\xi\,d\xi'\,, \tag{6.A.2}$$

after the transformation $y = 2a\xi$, $y' = 2a\xi'$. Approximating $H_0^{(1)}$ for small ka, one has

$$\mathscr{J}_O = \frac{\omega}{2g}\int_{-1/2}^{1/2}\left[1 + \frac{2i}{\pi}\ln(\gamma ka|\xi-\xi'|)\right]d\xi\,d\xi' + O(ka)^2\ln(ka)\,, \tag{6.A.3}$$

where $\ln\gamma = 0.5772157 =$ Euler's constant. Thus,

$$\mathscr{J}_O = \frac{\omega}{2g}\left[\left(1 + \frac{2i}{\pi}\ln\gamma ka\right) + \frac{2i}{\pi}\int_{-1/2}^{1/2}\ln|\xi-\xi'|\,d\xi\,d\xi'\right] \tag{6.A.4}$$

$$= \frac{\omega}{2g}\left[1 + \frac{2i}{\pi}\left(\ln\gamma ka - \frac{3}{2}\right)\right] + O[(ka)^2\ln ka]\,, \tag{6.A.5}$$

where the following identity has been used:

$$\iint_{-1/2}^{1/2}\ln|\xi-\xi'|\,d\xi\,d\xi' = -\frac{3}{2}\,. \tag{6.A.6}$$

From Eq. (6.2.15) it follows that

$$\begin{aligned}\mathscr{J}_H &= \frac{1}{4a^2}\iint_{-a}^{a} G_H(0,y|y')\,dy' \\ &= -\frac{i\omega}{g}\frac{1}{4a^2}\iint_{-a}^{a} dy\,dy'\left(\frac{\cot kL}{kB}+2\sum_{n=1}^{\infty}\frac{\cot K_nL}{K_nB}\cos\frac{2n\pi y}{B}\cos\frac{2n\pi y'}{B}\right) \\ &= -\frac{i\omega}{g}\left[\frac{\cot kL}{kB}+2\sum_{n=1}^{\infty}\frac{cotK_nL}{K_nB}\left(\frac{\sin n\alpha}{n\alpha}\right)^2\right], \qquad (6.A.7)\end{aligned}$$

where $\alpha \equiv 2\pi a/B$. Consider the series above. Since the harbor dimensions have been assumed to be comparable to the incident wavelength, we must have

$$\alpha = \frac{2\pi a}{B} \ll 1\,.$$

Now for large n, the nth term in the last series of Eq. (6.A.7) approaches

$$\frac{\cot K_nL}{K_nB}\left(\frac{\sin n\alpha}{n\alpha}\right)^2 \to -\frac{1}{2n\pi}\left(\frac{\sin n\alpha}{n\alpha}\right)^2;$$

the series, to be denoted by Σ, may be written

$$\begin{aligned}\Sigma = &-\frac{1}{\pi}\sum_{n=1}^{\infty}\frac{1}{n}\left(\frac{\sin n\alpha}{n\alpha}\right)^2 \\ &+2\sum_{n=1}^{\infty}\left(\frac{\cot K_nL}{K_nB}+\frac{1}{2n\pi}\right)\left(\frac{\sin n\alpha}{n\alpha}\right)^2. \qquad (6.A.8)\end{aligned}$$

The second series on the right-hand side above now converges rapidly; its sum with the remaining term in Eq. (6.A.1) will be denoted by F;

$$F = \frac{\cot kL}{kB}+2\sum_{n=1}^{\infty}\left(\frac{\cot K_nL}{K_nB}+\frac{1}{2n\pi}\right)\left(\frac{\sin n\alpha}{n\alpha}\right)^2. \qquad (6.A.9)$$

The first series on the right-hand side of Eq. (6.A.8) may be approximately summed in closed form. By the following rearrangement,

$$F' \equiv -\frac{1}{\pi}\sum_{1}^{\infty}\frac{1}{n}\left(\frac{\sin n\alpha}{n\alpha}\right)^2 = \frac{1}{2\pi\alpha^2}\sum_{1}^{\infty}\frac{1}{n^3}(\cos 2n\alpha - 1)\,,$$

it can be found from Collin (1960, p. 579) that

$$\sum_1^\infty \frac{\cos nz}{n^3} = \frac{z^2}{2}\ln z - \frac{3}{4}z^2 + O(z^4) + \sum_1^\infty \frac{1}{n^3}\,.$$

Hence

$$\begin{aligned} F' &= \frac{1}{2\pi\alpha^2}\left[\frac{(2\alpha)^2}{2}\ln 2\alpha - \frac{3}{4}(2\alpha)^2 + O(\alpha)^4\right] \\ &= \frac{1}{\pi}\left(\ln 2\alpha - \frac{3}{2}\right)[1 + O(\alpha^2)] \\ &= \frac{1}{\pi}\left(\ln\frac{4\pi a}{B} - \frac{3}{2}\right)\left[1 + O\left(\frac{2\pi a}{B}\right)^2\right]. \end{aligned}$$

Substituting into Eq. (6.A.8) and combining with Eqs. (6.A.7) and (6.A.9), one gets

$$\begin{aligned} &\frac{1}{4a^2}\int_{-a}^{a} M\,dy\,dy' \\ &\quad = \mathscr{J}_H - \mathscr{J}_O \\ &\quad \simeq -\frac{i\omega}{g}\left\{F + \frac{1}{\pi}\left(\ln\frac{4\pi a}{B} - \frac{3}{2}\right) + O[(ka)^2\ln ka] - \frac{i}{2} + \frac{1}{\pi}\left(\ln\gamma ka - \frac{3}{2}\right)\right\} \\ &\quad = -\frac{i\omega}{g}\left\{-\frac{i}{2} + F + \left[\ln\left(\frac{\pi k a^2\gamma}{4B}\right) + \ln 16 - 3\right] + O(ka)^2\ln(ka)\right\}. \end{aligned} \tag{6.A.10}$$

Since $\ln 16 - 3 = -0.2274$ and $ka^2/B \ll 1$, the square bracket is negative and will be denoted by

$$I = -\left[\ln\left(\frac{\pi k a^2\gamma}{4B}\right) + \ln 16 - 3\right]. \tag{6.A.11}$$

In summary, the integral in Eq. (6.A.1) is

$$\begin{aligned} &\frac{1}{4a^2}\iint_{-a}^{a} M(y|y')\,dy\,dy' \\ &\qquad \simeq -\frac{i\omega}{g}\left(-\frac{i}{2} + F - I\right) + O(k^2a^2\ln ka)\,. \end{aligned} \tag{6.A.12}$$

Multiple Scattering by Seabed Irregularities

7

Proper account for bathymetric variations is an important task in constructing wave-forcasting models for coastal waters. For slowly varying depth, the ray (or WKB) and mild-slope approximations are useful tools to deal with refraction and diffraction in many practical situations. For abrupt depth changes involving one or a few obstacles, effective numerical schemes have been well developed to give the details of wave scattering near the obstacles. In cases where the bottom irregualarities extend over many wavelengths, i.e., tens or hundreds of kilometers, however, one must deal with multiple scattering. In nature both the waves and the depth variations can be highly irregular. A comprehensive wave model should account for the scattering of random waves by randomly irregular bathymetry, in addtion to viscous dissipation. Early works on this topic are due to Hasselmann (1966) and Long (1973).

As a first step towards physical understanding of multiple scattering, we shall examine in this chapter two types of bathymetry and monochromatic waves. Specifically, two linearized theories will be discussed: (i) Bragg scattering by a periodic bathymetry (Section 7.1–Section 7.3), and (ii) scattering by random roughness (Section 7.4–Section 7.6). Extensions to narrow-banded nonlinear waves can be found in Mei and Hancock (2003) and Pihl, Mei and Hancock (2002). Ardhuin and Herbers (2002) have studied the effects of Bragg mechanism on the scattering of random waves over random bottom. More work is needed.

7.1 Field Evidence of Periodic Longshore Bars

Longshore sand bars are often found along gentle beaches. The number of bars can range from a few to dozens and the spacing from tens to hundreds of meters, see Table 7.1. The bar amplitudes can be as high as a meter. Figure 7.1 shows a sample profile in Chesapeake Bay, Maryland, USA, recorded by accoustic sounding (Dolan, 1983; Dolan and Dean, 1985). An aerial photograph of longshore bars at Ecambia Bay Florida is shown in Chapter 10.

Scientifically, it is natural to ask what effects the presence of long-shore bars may have on the wave climate. Of course how these sand bars are generated is of interest to coastal morphodynamics. Indeed the first laboratory study of bar formation on a beach was motivated by military needs, and was conducted by Keulegan (1943) as a classified project in preparation for the Normandy landing of Allied troops at the end of the second World War. As will be discussed in Chapter 10, waves can induce a circulation in

Table 7.1: Records of sand bars in US.

	Beach slope	No. of bars	Bar spacing (m)
Lake Michigan	0.0072–0.012	3–4	39–321
Cape Cod	0.0014–0.0029	6–8	40–105
Alaskan Artic	30.0041–0.0057	4–5	141–479
Chesapeake Bay	0.0017–0.0052	4–17	12–70

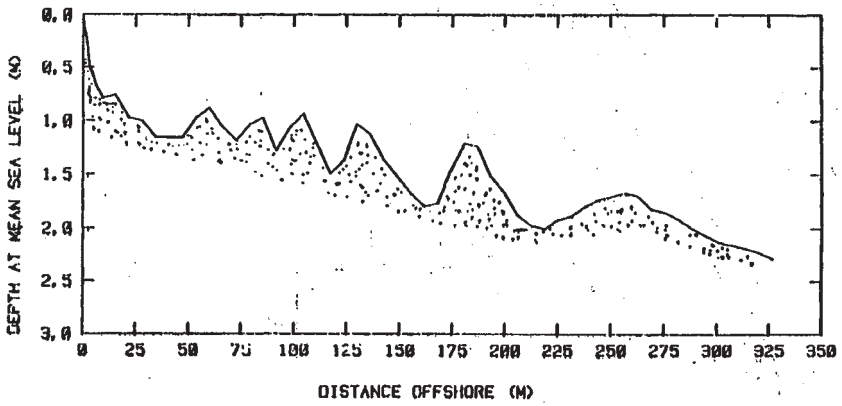

Figure 7.1: Bar profile at Scientists Cliff, Chesapeake Bay, by Dolan, 1983 .

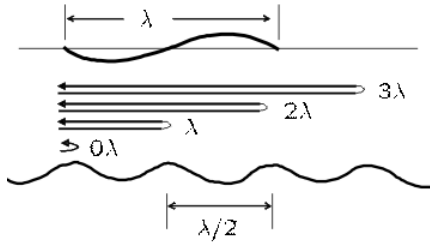

Figure 7.2: Bragg resonance as the result of constructive interference.

the bed boundary layer and transport sand particles from wave antinodes to nodes, hence to form bars. A fuller explanation requires the combination of the hydrodynamics of waves boundary layers and the dynamics of sediment motion. The latter subject is very complicated and theoretical understanding is meager. In this chaper we shall only examine the effects of rigid bars on waves.

If the bar amplitudes are small, $D \ll h$, one might expect their effects on a train of progressive waves to be small and apply a straightforward second-order analysis so that the effect on waves will appear at the order $kA(KD)$ (Davis (1982), see Exercise 7.2). The situation is different however if the incident waves are twice as long as the bar spacing, i.e., $K = 2k$; then the phenomenon of Bragg resonance occurs and the reflection by many small and periodic bars can be very strong. The source of this resonance is due to constructive interference of incident and reflected waves and is well known in x-ray diffraction by crystaline materials. Referring to Fig. 7.2 where a number of bars of wavelength λ_b are fixed on a horizontal bed, we consider the propagation of a train of waves incident from the left. Every wave crest passing over a bar will be mostly transmitted toward the next bar ahead and sends a weak reflected wave towards the bar behind. At any given bar, the maximum amplitude of the left-going wave is the sum of all left-going wave crests, each of which is the consequence of reflection by the nth bar on the right. Therefore, each of these wave crests has traveled the distance of $2n\lambda_b$. When $2\lambda_b$ equals the surface wavelength, λ, all these reflected wave crests are in phase upon arrival at the same bar and reinforce one another, resulting in strong (resonant) reflection. Thus many small bars can give rise to strong reflection if the Bragg resonance condition is met.

Let us now describe a theory of Bragg resonance. Since many bars must be involved in order for this phenomenon to be appreciable, the total region

of bars must be much greater than the typical bar length or wavelength. Second, since reflection is strong, incident and reflected waves must be allowed to be comparable in order. Let us also allow slow variation in mean depth $h(x, y)$. Therefore, the WKB approximation[1] in Section 2.1 will be used.

7.2 Evolution Equations for Bragg-Scattering

Let the seabed be describd by $z = -h(x, y)+\epsilon\delta(x, y)$, where $\epsilon\delta(x, y)$ denotes the bar profile with $\epsilon \ll 1$ signifying the order of magnitude of both the mean beach slope and the bar slope. The exact kinematic condition on the seabed reads,

$$\Phi_z = \nabla(-h + \epsilon\delta) \cdot \nabla\Phi\,, \quad z = -h + \epsilon\delta\,, \tag{7.2.1}$$

where ∇ denotes the horizontal gradient. Expanding about $z = -h$, we get

$$\Phi_z + \epsilon\delta\Phi_{zz} + O(\epsilon^2) = \nabla(-h + \epsilon\delta) \cdot \nabla\Phi + O(\epsilon^2)\,, \quad z = -h\,. \tag{7.2.2}$$

Since $\Phi_{zz} = -\nabla^2\Phi$, we get the approximate condition,

$$\Phi_z = -\nabla h \cdot \nabla\Phi + \epsilon\nabla \cdot (\delta\nabla\Phi)\,, \quad z = -h\,. \tag{7.2.3}$$

Introducing slow coordinates $x_1 = \epsilon x, y_1 = \epsilon y, t_1 = \epsilon t$, we recall from Section 3.1 the governing Laplace equation:

$$\epsilon^2\nabla_1^2\Phi + \Phi_{zz} = 0\,, \quad -h < z < 0, \tag{7.2.4}$$

where

$$\nabla_1 = \frac{\partial^2}{\partial x_1^2} + \frac{\partial^2}{\partial y_1^2} \tag{7.2.5}$$

is the horizontal Laplacian. The free-surface condition becomes

$$g\Phi_z + \epsilon^2\Phi_{t_1t_1} = 0\,, \quad z = 0\,. \tag{7.2.6}$$

On the mean seabed we have

$$\Phi_z = -\epsilon^2\nabla_1 h \cdot \nabla_1\Phi + \epsilon^3\nabla_1 \cdot (\delta\nabla_1\Phi)\,, \quad z = -h\,. \tag{7.2.7}$$

We assume the seabed to have parallel contours so that $h = h(x_1)$ and $\delta = \delta(x_1)$. Anticipating strong reflection, let us start with the following

[1]Equivalently, the multiple-scale method can be employed to yield the same results.

WKB expansion where both incident and reflected waves are allowed at the leading order

$$\begin{aligned}\Phi &= \Phi^{(0)} + \epsilon\Phi^{(1)} + O(\epsilon^2)\\ &= (\psi^+ + i\epsilon\gamma^+ + \cdots)e^{iS_+/\epsilon} + (\psi^- + i\epsilon\gamma^- + \cdots)e^{iS_-/\epsilon} + *\,, \end{aligned} \tag{7.2.8}$$

where

$$S_\pm = \pm \int \alpha\, dx_1 + \beta y_1 - \omega t_1 \tag{7.2.9}$$

is ϵ times the wave phase of incident and reflected waves. The local wavenumber components α, β are related to the local wavenumber vector $\mathbf{k}$ and local angle of incidence θ by

$$\mathbf{k}_\pm = (\pm\alpha, \beta)\,, \quad \alpha = k\cos\theta\,, \quad \beta = k\sin\theta\,. \tag{7.2.10}$$

The leading-order solution is the sum of incident and reflected waves, as in Section 2.1,

$$\psi^\pm = -\frac{igA^\pm}{2\omega}\frac{\cosh k(z+h)}{\cosh kh} \tag{7.2.11}$$

with

$$\omega^2 = gk\tanh kh\,. \tag{7.2.12}$$

At the next order $O(\epsilon)$ we assume the bars to be parallel to the depth contours

$$\delta = \frac{D}{2}\left[\exp\left(\frac{2i}{\epsilon}\int \alpha\, dx_1\right) + \exp\left(-\frac{2i}{\epsilon}\int \alpha\, dx_1\right)\right], \tag{7.2.13}$$

where $D(x_1, y_1)$ is the bar amplitude. Using (7.2.13) in (7.2.7) we get, after some algebra,

$$\begin{aligned}\Phi_z^{(1)} &= -i\nabla_1 h\cdot(\mathbf{k}_+\psi^+ e^{iS_+/\epsilon} + \mathbf{k}_-\psi^- e^{iS_-/\epsilon}) + *\\ &\quad \frac{D}{2}(\alpha^2 - \beta^2)(\psi^- e^{iS_+/\epsilon} + \psi^+ e^{iS_-/\epsilon}) + * + \text{non-resonating terms}\,. \end{aligned} \tag{7.2.14}$$

Only terms proportional to $\exp(iS_\pm/\epsilon)$ (hence to the homogeneous solutions) are written explicitly above, as they may force resonance. Other less important terms are grouped as the non-resonant terms. Assuming

$$\Phi^{(1)} = i\gamma^+ e^{iS_+} + c.c. + i\gamma_- e^{iS_-} + c.c. + \cdots \tag{7.2.15}$$

and separating the coefficients of incident and reflected waves, we get two inhomogeneous boundary-value problems for $\gamma^{\pm}$:

$$\gamma^{\pm}_{zz} - k^2\gamma^{\pm} = \mathbf{k}_{\pm}\cdot\nabla_1\psi^{\pm} + \nabla_1\cdot(\mathbf{k}_{\pm}\psi_{\pm})\,, \quad -h < z < 0 \tag{7.2.16}$$

$$\gamma^{\pm}_{z} - \frac{\omega^2}{g}\gamma^{\pm} = -\frac{2\omega}{g}\psi^{\pm}_{t_1}\,, \quad z = 0 \tag{7.2.17}$$

$$\gamma^{\pm}_{z} = \nabla_1 h\cdot(\mathbf{k}_{\pm}\psi^{\pm}) + \frac{iD}{2}(\alpha^2-\beta^2)\psi^{\mp}\,, \quad z = -h\,. \tag{7.2.18}$$

Since $\psi^{\pm}$ are the homogeneous solutions of (7.2.16), (7.2.17) and (7.2.18), Green's formula can be used:

$$\begin{aligned}\int_{-h}^{0}[\psi^{\pm}(\gamma_{zz}-k^2\gamma^{\pm}) - \gamma^{\pm}(\psi^{\pm}_{zz}-k^2\psi^{\pm})]\,dz \\ = [\psi^{\pm}\gamma^{\pm}_{z} - \gamma^{\pm}\psi^{\pm}_{z}]_{z=0} - [\psi^{\pm}\gamma^{\pm}_{z} - \gamma^{\pm}\psi^{\pm}_{z}]_{z=-h}\,.\end{aligned} \tag{7.2.19}$$

Use of the governing equations for $\psi^{\pm}$ and $\gamma^{\pm}$ yields the following evolution equations for $A^{\pm}$ as solvability conditions,

$$\frac{\partial}{\partial t_1}\left(\frac{(A^{+})^2}{2}\right) + \nabla_1\cdot\left[\mathbf{C}^{+}_{g}\left(\frac{(A^{+})^2}{2}\right)\right] = -i\Omega_o A^{+}A_{-}\cos 2\theta \tag{7.2.20}$$

$$\frac{\partial}{\partial t_1}\left(\frac{(A^{-})^2}{2}\right) + \nabla_1\cdot\left[\mathbf{C}^{-}_{g}\left(\frac{(A^{-})^2}{2}\right)\right] = -i\Omega_o A^{+}A_{-}\cos 2\theta \tag{7.2.21}$$

where C^{+}_{g} and C^{-}_{g} defined by

$$\mathbf{C}^{\pm}_{g} = C_g\frac{\mathbf{k}_{\pm}}{k} \tag{7.2.22}$$

are the group velocities of the incident and reflected waves, respectively, and Ω_o is defined by

$$\Omega_o = \frac{gkD}{4\cosh^2 kh} = \frac{\omega kD}{2\sinh 2kh}, \tag{7.2.23}$$

which has the dimension of frequency. Use has been made of $\alpha^2-\beta^2 = k^2\cos 2\theta$. Thus, under Bragg resonance, the incident and reflected waves are coupled; the coupling coefficient Ω_o is proportional to the bar amplitude.

For brevity we shall change A^{+} to A and A^{-} to B from here on. Because h, k, C_g depends only on x_1, we have

$$\frac{\partial A}{\partial t_1} + C_g \cos\theta \frac{\partial A}{\partial x_1} + \frac{\partial (C_g \cos\theta)}{\partial x_1} \frac{A}{2} + C_g \sin\theta \frac{\partial A}{\partial y_1} = -i\Omega_o B \cos 2\theta \tag{7.2.24}$$

$$\frac{\partial B}{\partial t_1} - C_g \cos\theta \frac{\partial B}{\partial x_1} - \frac{\partial (C_g \cos\theta)}{\partial x_1} \frac{B}{2} + C_g \sin\theta \frac{\partial B}{\partial y_1} = -i\Omega_o A \cos 2\theta \,. \tag{7.2.25}$$

In the simplest case where the mean depth h and D are constants, then so are C_g and θ. The two equations can be easily reduced to one

$$\left(\frac{\partial}{\partial t_1} + C_g \frac{\partial}{\partial y_1} \right)^2 A - (C_g^2 \cos^2\theta) \frac{\partial^2 A}{\partial x_1^2} + (\Omega_o \cos^2\theta) A = 0 \tag{7.2.26}$$

which also governs B.

For normal incidence, $\theta = \partial/\partial y_1 = 0$, A and B are coupled by

$$A_{t_1} + C_g A_{x_1} = -i\Omega_o B \tag{7.2.27}$$

$$B_{t_1} - C_g B_{x_1} = -i\Omega_o A \tag{7.2.28}$$

which can be combined to give the Klein-Gordon equation for A and B,

$$A_{t_1 t_1} - C_g^2 A_{x_1 x_1} + \Omega_o^2 A = 0 \,. \tag{7.2.29}$$

It is easy to check by considering a propagating wave solution that the envelopes A and B are dispersive themselves.

In the next subsection, explicit solutions for constant mean depth will be analyzed.

Exercise 7.1

Use (7.2.24) and (7.2.25) to show that

$$\frac{\partial}{\partial t_1} \left(\frac{|A|^2}{2} \right) + \nabla_1 \cdot \left[\mathbf{C}_g^+ \left(\frac{|A|^2}{2} \right) \right] = -i\Omega_o A^* B \cos 2\theta + * \tag{7.2.30}$$

$$\frac{\partial}{\partial t_1} \left(\frac{|B|^2}{2} \right) + \nabla_1 \cdot \left[\mathbf{C}_g^- \left(\frac{|B|^2}{2} \right) \right] = i\Omega_o A^* B \cos 2\theta + * \tag{7.2.31}$$

whose sum gives

$$\frac{\partial}{\partial t_1} (|A|^2 + |B|^2) + \nabla_1 \cdot (\mathbf{C}_g |A|^2 + \mathbf{C}_g^- |B|^2) = 0 \,. \tag{7.2.32}$$

Thus rigid bars do not add or remove energy from, and merely transfer energy between, incident and reflected waves.

Exercise 7.2: Solution for Nonresonant Scattering (Davies, 1982)

Consider only constant mean depth h and use the linearized boundary condition on the bed

$$\frac{\partial \Phi}{\partial z} = \frac{\partial}{\partial x}\left(\delta \frac{\partial \Phi}{\partial x}\right), \quad z = -h\,. \tag{7.2.33}$$

Let the bar profile be

$$\delta = \epsilon D \cos Kx = \frac{\epsilon D}{2}(e^{iKx} + e^{-iKx}) \tag{7.2.34}$$

with $\epsilon \ll 1$ and $KL \gg 1$.

Carry out a perturbation analysis by letting

$$\Phi = \Phi_0 + \epsilon \Phi_1 + \cdots\,. \tag{7.2.35}$$

Show that at the leading order $O(\epsilon^0)$, the solution is simply

$$\Phi_0 = -\frac{igA}{2\omega}\frac{\cosh k(z+h)}{\cosh kh} e^{ikx - i\omega t} + *\,. \tag{7.2.36}$$

Show at the next order $O(\epsilon)$, that the governing equations are

$$\frac{\partial^2 \Phi_1}{\partial x^2} + \frac{\partial^2 \Phi_1}{\partial z^2} = 0\,, \quad h < z < 0 \tag{7.2.37}$$

$$g\frac{\partial \Phi_1}{\partial z} + \frac{\partial^2 \Phi_1}{\partial t^2} = 0 \quad z = 0 \tag{7.2.38}$$

$$\begin{aligned}\frac{\partial \Phi_1}{\partial z} &= \frac{D}{2}\frac{\partial}{\partial x}\left\{(e^{iKx} + e^{-iKx})\frac{gkA}{2\omega}\frac{1}{\cosh kh}[e^{ikx - i\omega t} + e^{-ikx + i\omega t}]\right\} \\ &= \frac{gkAD}{4\omega \cosh kh}[i\alpha_+ e^{i\alpha_+ x - i\omega t} - i\alpha_- e^{-i\alpha_- x + i\omega t} + *]\end{aligned} \tag{7.2.39}$$

on $z = -h$, where $\alpha_\pm = K \pm k$. Verify the following solution

$$\Phi_1 = f_+(z) e^{i\alpha_+ x - i\omega t} + f_-(z) e^{-i\alpha_- x + i\omega t} \tag{7.2.40}$$

with

$$\begin{aligned} f_\pm(z) = {} & \frac{igkAD}{4\omega \cosh kh} \\ & \times \left[\frac{\alpha_\pm - \frac{\omega^2}{g}\tanh \alpha_\pm h}{\frac{\omega^2}{g} - \alpha_\pm \tanh \alpha_\pm + h}\cosh \alpha_\pm (z+h) + \sinh \alpha_\pm (z+h)\right]. \end{aligned}$$

Observe that if $\alpha_- = k$, i.e., $K = 2k$, then $e^{-i\alpha_- x + i\omega t} = e^{-ikx - i\omega t}$ is a reflected wave. The associated amplitude is unbounded. By expanding $\alpha_- = k + O(\epsilon)$, show that $\epsilon\Phi_1$ blows up as ϵx. The theory here breaks down.

7.3 Normal Incidence

In a laboratory experiment, Heathershaw (1982) installed 10 bars of amplitude $D = 5$ cm and wavelength 100 cm on the bottom of a long wave flume. Incident waves of length $2\pi/k = 200$ cm were sent from one side of the bar patch. On the transmission side, waves are essentially absorbed by breaking on a gentle beach. Sizable reflection coefficients were measured along many stations over the bar patch. This experiment gives the first observed evidence of strong reflection by periodic bars. Let us apply the present theory to a more general case where the normally incident wave is slightly detuned from perfect resonance.

Let the bars of wavenumber $2k$ be located in $0 < x_1 < L$ and the incident wavetrain be slightly detuned from resonance, so that the wave frequency is $\omega + \epsilon\Omega$ and the wavenumber is $k + \epsilon K$, where $\Omega = O(\omega)$ and $K = O(k)$. Since $\omega + \epsilon\Omega$ and $k + \epsilon K$ must be related by the dispersion relation,

$$\Omega = K\frac{d\omega}{dk} = KC_g\,. \tag{7.3.1}$$

The detuned incident wave

$$\zeta = A_o \exp[i(k + \epsilon K)x - (\omega + \epsilon\Omega)t], \quad x_1 < 0\,, \tag{7.3.2}$$

can be alternatively written as

$$\zeta = A(x_1, t_1)e^{ikx - i\omega t}\,, \quad x_1 < 0\,, \tag{7.3.3}$$

where

$$A(x_1, t_1) = A_o e^{iK(x_1 - C_g t_1)}\,, \quad x_1 < 0\,. \tag{7.3.4}$$

When such a wavetrain passes a patch of periodic bars, A and B must vary with x_1 and t_1 according to (7.2.27) and (7.2.28).

To the left and to the right of the bars, the governing equations are simply

$$A_{t_1} + C_g A_{x_1} = 0\,, \quad B_{t_1} - C_g B_{x_1} = 0\,, \quad x_1 < 0\,, \quad \text{and} \quad x_1 > L\,. \tag{7.3.5}$$

We shall assume further that $B = 0$ for $x_1 > L$. Over the bars (7.2.27) and (7.2.28) or (7.2.29) hold. In order that pressure ($\propto \Phi$) and horizontal velocity ($\propto \Phi_x$) are continuous at $x_1 = 0, L$, A and B must be continuous at $x_1 = 0, L$. Since the solutions must be of the form

$$(A, B) = A_0(T(x_1), R(x_1))e^{-i\Omega t_1}\,, \quad 0 < x_1 < L\,. \tag{7.3.6}$$

T and R are governed by

$$T_{x_1x_1} + \frac{(\Omega^2 - \Omega_0^2)}{C_g}T = 0\,, \quad 0 < x_1 < L\,. \tag{7.3.7}$$

Several cases can be distinguished according to the sign of $\Omega^2 - \Omega_0^2$:

7.3.1 Subcritical Detuning: $0 < \Omega < \Omega_0$

Let

$$QC_g = (\Omega_0^2 - \Omega^2)^{1/2} \tag{7.3.8}$$

then

$$T(x_1) = \frac{iQC_g \cosh Q(L - x_1) + \Omega \sinh Q(L - x_1)}{iQC_g \cosh QL + \Omega \sinh QL} \tag{7.3.9}$$

and

$$R(x_1) = \frac{Q \sinh Q(L - x_1)}{iQC_g \cosh QL + \Omega \sinh QL}\,. \tag{7.3.10}$$

On the incidence side the reflection coefficient is just $R(0)$ and on the transmission side the transmission coefficient is $T(L)$. Clearly the dependence on L and x_1 is monotonic. In the limit of $L \to \infty$, it is easy to find that

$$T(x_1) = e^{-Qx_1}\,, \quad R(x_1) = \frac{Q}{iQC_g + \Omega}e^{-Qx_1}\,. \tag{7.3.11}$$

Thus all waves are localized in the range $x_1 < O(1/Q)$.

7.3.2 Supercritical Detuning: $\Omega > \Omega_0$

Let

$$PC_g = (\Omega^2 - \Omega_0^2)^{1/2} \tag{7.3.12}$$

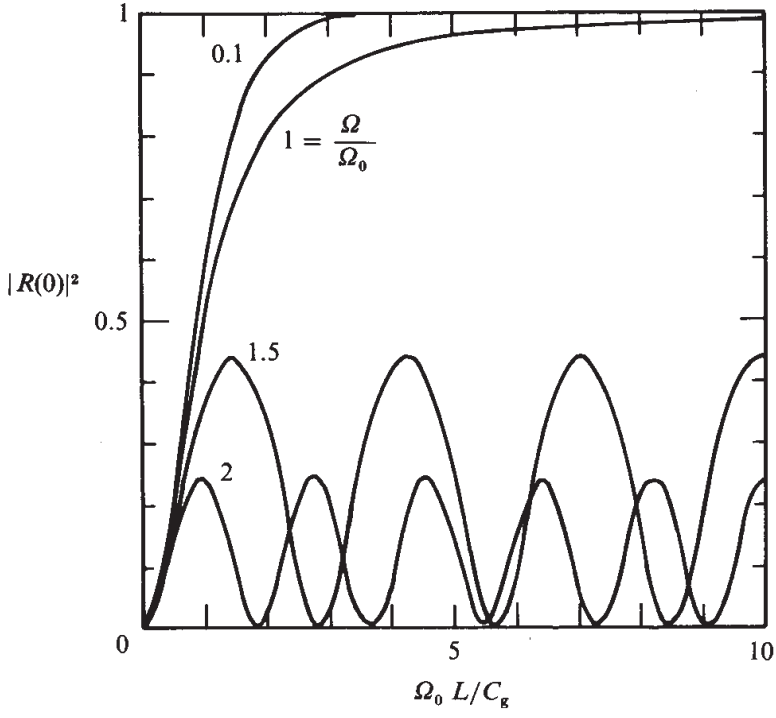

Figure 7.3: Effects of detuning on the reflection coefficient (from Mei (1985), *J. Fluid Mech.* Reproduced by permission of Cambridge University Press).

then the transmission and reflection coefficients are:

$$T(x_1) = \frac{PC_g \cos P(L-x_1) - i\Omega \sin P(L-x_1)}{PC_g \cos PL - i\Omega \sin PL} \tag{7.3.13}$$

and

$$R(x_1) = \frac{-iQ_0 \sin P(L-x_1)}{PC_g \cos PL - i\Omega \sin PL}\,. \tag{7.3.14}$$

The dependence on L and x_1 is clearly oscillatory. Thus Ω_0 is the cut-off frequency marking the transition of the spatial variation. Figure 7.3 shows the dependence of the reflection coefficient $R(0)$ on the width of the bar patch for various ratios of Ω/Ω_0. For subcritical detuning complete reflection can occur for sufficiently large L. For supercritical detuning there can be windows of strong transmission.

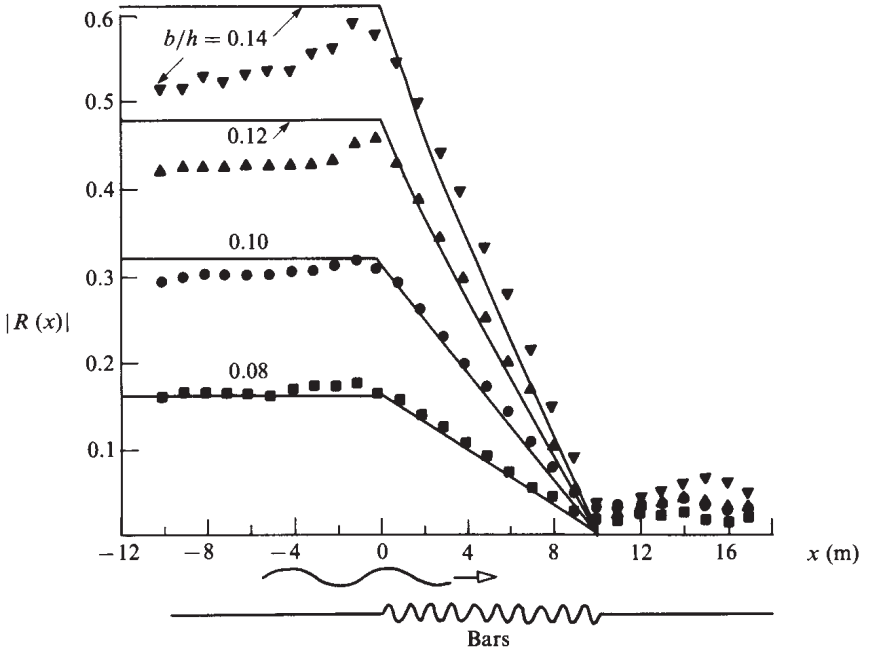

Figure 7.4: Comparison of theory with measurements by Heathershaw, 1982 (from Mei (1985), *J. Fluid Mech.* Reproduced by permission of Cambridge University Press).

In the special case of perfect resonance, we get from (7.3.9) and (7.3.10) that

$$T(x_1) = \frac{A}{A_o} = \frac{\cosh \frac{\Omega_o(L-x_1)}{C_g}}{\cosh \frac{\Omega_o L}{C_g}}\,,$$
$$R(x_1) = \frac{B}{A_o} = -\frac{i \sinh \frac{\Omega_o(L-x)}{C_g}}{\cosh \frac{\Omega_o L}{C_g}}\,. \tag{7.3.15}$$

Clearly both coefficients decrease monotonically from $x_1 = 0$ to $x_1 = L$. These results agree quite well with the experiments of Heathershaw, as shown in Fig. 7.4, and therefore confirm that enough small bars can generate strong reflection, especially in very shallow water.

Further theory and experiments demonstrating the linear effects of cut-off frequency when the incident wave is detuned are discussed in Hara and Mei (1987).

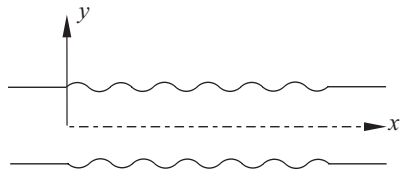

Figure 7.5: A channel with wavy banks.

Exercise 7.3: Bragg Resonance by a Corrugated River Bank

An infinitely long river has constant depth h and constant averaged width $2a$. In the stretch $0 < x < L$ where $kL \gg 1$, the banks are slightly sinusoidal about the mean so that

$$y = \pm a \pm B \sin Kx\,, \quad KB \equiv \epsilon \ll 1 \tag{7.3.16}$$

see Fig. 7.5. Let a train of monochromatic waves be incident from $x \sim -\infty$,

$$\zeta = \frac{A}{2} e^{i(kx-\omega t)} \tag{7.3.17}$$

where $kh, ka = O(1)$. Develop a uniformly valid linearized theory to predict Bragg resonance. Can the corrugated boundary be used to reflect waves as a breakwater? Discuss your results for various parameters that can affect the function as a breakwater.

Suggested steps: Assume

$$\phi = -\frac{ig\eta(x,y)}{\omega} \frac{\cosh k(z+h)}{\cosh kh} \tag{7.3.18}$$

and show that

$$\left(\frac{\partial^2}{\partial x^2} + \frac{\partial^2}{\partial y^2} \right) \eta + k^2 \eta = 0 \tag{7.3.19}$$

and

$$\omega^2 = gk \tanh kh\,. \tag{7.3.20}$$

Show that the no-flux boundary condition on the upper bank can be approximated by

$$\frac{\partial \eta}{\partial y} + \delta \frac{\partial^2 \eta}{\partial y^2} = \frac{\partial \delta}{\partial x} \frac{\partial \eta}{\partial x} + \cdots\,, \quad y = a\,, \tag{7.3.21}$$

where $\delta = B \sin Kx$. Try a uniformlly valid approximation by assuming

$$\eta = [\psi_0^+ + i\epsilon\psi_1^+ + \cdots]e^{ikx-i\omega t} + [\psi_0^- + i\epsilon\psi_1^- + \cdots]e^{-ikx-i\omega t} \tag{7.3.22}$$

where ψ's depend on the slow coordinate $X = \epsilon x$.

Exercise 7.4: Bars on a Sloping Beach (Mei, Hara and Naciri, 1988)

Consider a patch of longshore bars of uniform amplitude D on a plane beach with gentle slope. The bars are spread in the region $-L < x_1 < 0$ while the shore at $x_1 = L_1$ absorbs all the incident wave energy. To solve the evolution equations let

$$A\sqrt{C_g} = \hat{A}e^{-i\Omega t_1}\,, \quad B\sqrt{C_g} = \hat{B}e^{-i\Omega t_1}\,. \tag{7.3.23}$$

Show, after suitable normalization, that the coupled equations can be reduced to a Stürm-Liouville equation for $\hat{B}$:

$$\frac{d}{dx_1}\left[p(x_1)\frac{d\hat{B}}{dx_1}\right] - q(x)\hat{B} = 0\,, \quad -1 < x_1 < 0 \tag{7.3.24}$$

subject to the boundary conditions

$$\hat{B} = 0\,, \quad x_1 = 0 \tag{7.3.25}$$

$$\frac{d\hat{B}}{dx_1} + r\hat{B} = b\,, \quad x_1 = -1 \tag{7.3.26}$$

where

$$p(x_1) = -\left(\frac{C_g}{\Omega_o L}\right), \quad q(x_1) = \frac{\Omega_o L}{C_g}\left[\left(\frac{\Omega}{\Omega_o}\right)^2 - 1\right] + i\frac{d}{dx_1}\frac{\Omega}{\Omega_o}$$

$$r(x_1) = i\left(\frac{\Omega_o L}{C_g}\frac{\Omega}{\Omega_o}\right)_{-1}, \quad b(x_1) = i\left[\frac{\Omega_o L}{C_g}\hat{A}\right]_{-1}. \tag{7.3.27}$$

Use MATLAB to study the numerical solution. Discuss the effects of L/L_1.

Exercise 7.5: Effects of Oblique Incidence (Mei, 1985)

Consider a bar field occupying the semi-infinite region $0 < x_1 < \infty$. A detuned sinusoidal wavetrain arrives from $x_1 \sim -\infty$. Let the envelopes of the incident and reflected waves be

$$A = A_o \exp\{i[K(x_1\cos\theta + y_1\sin\theta) - \Omega t_1]\} \tag{7.3.28}$$

$$B = B_o \exp\{i[K(-x_1\cos\theta + y_1\sin\theta) - \Omega t_1]\} \tag{7.3.29}$$

in $x_1 < 0$ and

$$A = A_o \exp\{i[px_1 + Ky_1 \sin\theta) - \Omega t_1]\} \tag{7.3.30}$$

$$B = B_o \exp\{i[-px_1 + K(y_1 \sin\theta) - \Omega t_1]\} \tag{7.3.31}$$

over the bar field ($x > 0$). Show first that

$$p^2 C_g^2 = \Omega_0^2 \cos^2\theta \left[\left(\frac{\Omega}{\Omega_0} \right)^2 - \left(\frac{\cos 2\theta}{\cos\theta} \right)^2 \right] \tag{7.3.32}$$

and that

$$R = \frac{B_0}{A_0} = \frac{\cos^2\theta}{\cos^2 2\theta} \left\{ \frac{\Omega}{\Omega_0} - \left[\left(\frac{\Omega}{\Omega_0} \right)^2 - \left(\frac{\cos 2\theta}{\cos\theta} \right)^2 \right]^{1/2} \right\}. \tag{7.3.33}$$

Discuss the dependence of R on the angle of incidence and on the detuning parameter Ω/Ω_0.

Exercise 7.6: Effects of Shore Reflection on Waves Over Offshore Bars (Yu and Mei, 2000a)

Let there be many sinusoidal bars in the range $0 < \bar{x} < L$,

$$\delta = \frac{1}{2} D e^{2ikx} + \frac{1}{2} D^* e^{-2ikx}$$

where $D = |D| e^{i\theta_D}$ is complex and D^* its complex conjugate. A train of slightly detuned incident waves arrive from $\bar{x} \sim -\infty$. Due to partial reflection at the shoreline somewhere along $\bar{x} > L$, the reflection coefficient R_L at $\bar{x} = L$ is finite. Let the incident and reflected wave amplitudes over the bars be $A_0 T(\bar{x})$ and $A_0 R(\bar{x})$ respectively. Show that for sub-critical detuning $0 < \Omega < \Omega_0$, T and R are given by

$$T(x_1) = \frac{-iQC_g \cosh Q(L - x_1) - \Omega \sinh Q(L - x_1) + \Omega_0 \widetilde{R}_L \sinh Q(L - x)}{iQC_g \cosh QL + \Omega \sinh QL + \Omega_0 \widetilde{R}_L \sinh QL} \tag{7.3.34}$$

$$R(x_1) e^{i\theta_D}$$

$$= -\frac{[iQC_g \cosh Q(L - x_1) + \Omega \sinh Q(L - x_1)]\, \widetilde{R}_L + \Omega_0 \sinh Q(L - x_1)}{iQC_g \cosh QL + \Omega \sinh QL + \Omega_0 \widetilde{R}_L \sinh QL} \tag{7.3.35}$$

where

$$\Omega_0 = \frac{|D|\omega k}{2\sinh(2kh)}, \quad QC_g = \sqrt{\Omega_0^2 - \Omega^2}$$

and R_L is a known complex constant and

$$\widetilde{R}_L = R_L e^{i\theta_D} = |R_L| e^{i(\theta_L + \theta_D)}$$

Show that with $\widetilde{R}_L \neq 0$ the variation of $|T|$ (or $|R|$) over the bar patch has three different possible trends, depending on the magnitude and phase of $\widetilde{R}_L$.

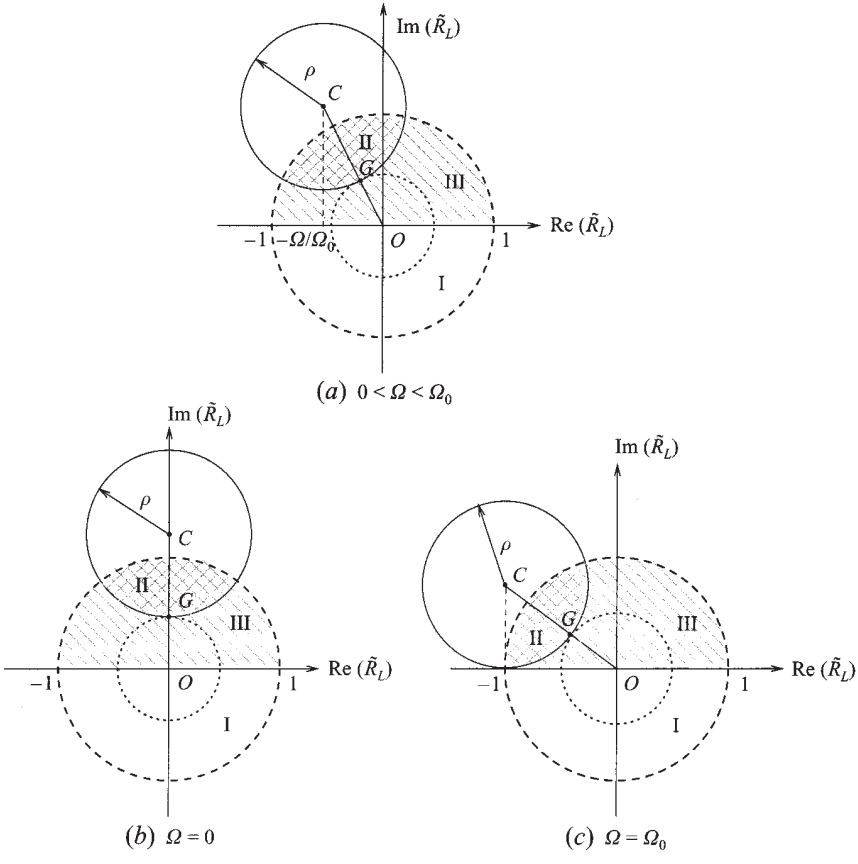

Figure 7.6: Complex plane of $\widetilde{R}_L$ for subcritical detuning. Region 1 (semi-circle in the upper half plane: $|T|$ and $|R|$ decrease monotonically shoreword. Region II (doubly hatched): $|T|$ and $|R|$ increase monotonically shoreward. Region III (singly hatched): $|T|$ and $|R|$ first decrease then increase shoreward (from Yu and Mei (2000), *J. Fluid Mech.* Reprinted by permission of Cambridge University Press).

With reference to Fig. 7.6, show that the three trends corresponds to the three regions in the unit circle in the complex plane of $\widetilde{R}_L$. In particular (i) Region I (lower half plane): Both incident and reflected waves decrease monotonically onshore. Thus the shore is sheltered by the bars. (ii) Region II (doubly hatched): Both incident and reflected waves increase monotonically shoreward. In this case, the bars make things worse for the shoreline. In the complex plane of $\widetilde{R}_L$, Fig. 7.6, this region corresponds to the doubly hatched area defined by the intersection of the unit circle and the circle $\mathcal{C}$ of radius

$$\varrho = \frac{QC_g/\Omega_0}{\sinh 2QL}$$

centered at the complex point

$$C : -\frac{\Omega}{\Omega_0} + i\frac{QC_g}{\Omega_0}\coth 2QL\,.$$

Finally, Region III (singly hatched): Both incident and reflected waves decrease first then increase onshore. This correspnonds to the singly hatched area in the upper half of the unit circle.

We now turn to the randomly rough seabed.

7.4 Randomly Rough Seabed–Envelope Equation

In many branches of physics there is an extensive literature on the propagation of infinitesimal sinusoidal waves in randomly inhomogeneous media (see Ishmaru, 1980). In one-dimensional propagation through a large region of disorder, multiple scattering is known to yield a complex change in the wavenumber k of which the real part corresponds to a change of wavenumber and the imaginary part to spatial attenuation (Keller, 1964). In solid-state physics this phenomenon was found to be important by Anderson (1958), who explained the transition of randomly inhomogeneous metals from a conductor to an insulator, and is known as Anderson localization. In contrast to periodic inhomogeneities where Bragg resonance causes strong scattering only for certain discrete frequencies, attenuation (localization) by disorder is effective for a broad range of incident wave frequencies.

The study of localization of water waves by bathymetric disorder was stimulated by the experiments of Belzons et al. (1988) for long waves of infinitesimal amplitude in shallow water of constant mean depth with

discontinuous step of random amplitudes and lengths. They found that, in addition to boundary-layer friction at the bottom and vortex shedding around sharp corners, radiation damping due to multiple scattering indeed led to spatial attenuation for all frequencies. Relevant theories have been given by Devillard et al. (1988), Nachbin (1997) and Nachbin and Papanicolau (1992).

Random depth variations of gentle slope in water of finite mean depth have been studied for infinitesimal waves by Pelinofsky et al. (1998), and for weakly nonlinear waves by Kawahara (1976), Mei and Hancock (2003), and Pihl et al. (2002). We present the linearized version of Mei and Hancock and restrict our attention to two-dimensional motion in a sea of constant mean depth. The characteristic length ℓ of the random perturbations is taken to be comparable to the wavelength $2\pi/k$ and to the mean depth h, i.e., $kh, k\ell = O(1)$. The root-mean-square amplitude of the irregularities σ is small so that $k\sigma = O(\epsilon) \ll 1$, and the horizontal extent of randomness is very long, $\sim 2\pi/\epsilon^2 k$. Under these scale assumptions it will be shown that the attenuation distance is inversely proportional to the root-mean-square amplitude of the disorder. For weakly nonlinear waves in finite depth, the envelope equation was first found by Kawahara (1976). Detailed analysis of physical effects may be found in Mei and Hancock (2003) and Pihl, Mei and Hancock (2002). Transient nonlinear waves over a shallow seabed with random roughness will be discussed in Chapter Thirteen.

Let the seabed be $z = -h + b(x)$, where b is a real random function of x of zero mean and order $kb = O(\epsilon) = O(kA)$. We further assume that b is non-zero over a large domain $kx = \epsilon^{-2}$, i.e., $kx_2 = \epsilon^2 = O(1)$. Omitting the Laplace's equation and the familiar linearized boundary condition on the free surface, we start with the seabed condition,

$$\phi_z = b_x \phi_x \,, \quad z = -h + b(x) \,. \tag{7.4.1}$$

Let us first approximate this condition to $O(\epsilon^3)$,

$$\phi_z + b\phi_{zz} + \frac{b^2}{2}\phi_{zzz} + \cdots = b_x(\phi_x + b\phi_{xz} + \cdots) \tag{7.4.2}$$

which can be rewritten as

$$\begin{aligned} \phi_z &= b\phi_{xx} + \frac{b^2}{2}\phi_{xxz} + b_x(\phi_x + b\phi_{xz} + \cdots) \\ &= (b\phi_x)_x + \frac{1}{2}(b^2\phi_{xz})_x + \cdots \quad z = -h \,. \end{aligned} \tag{7.4.3}$$

After introducing the multiple-scale expansions

$$\phi = \phi_0 + \epsilon\phi_1 + \epsilon^2\phi + \cdots , \tag{7.4.4}$$

where ϕ_n are functions of x, x_2 and z, pertubation equations are obtained. They are, at the leading order $O(\epsilon^0)$,

$$\phi_{0_{xx}} + \phi_{0_{zz}} = 0 , \quad -h < z < 0 \tag{7.4.5}$$

$$\phi_{0_z} - \frac{\omega^2}{g}\phi_0 = 0 , \quad z = 0 , \tag{7.4.6}$$

$$\phi_{0_z} = 0 , \quad z = -h; \tag{7.4.7}$$

at the next order $O(\epsilon)$:

$$\phi_{1_{xx}} + \phi_{1_{zz}} = 0 , \quad -h < z < 0 \tag{7.4.8}$$

$$\phi_{1_z} - \frac{\omega^2}{g}\phi_1 = 0 , \quad z = 0 , \tag{7.4.9}$$

$$\phi_{1_z} = (b(x)\phi_{0_x})_x , \quad z = -h \tag{7.4.10}$$

and at $O(\epsilon^2)$:

$$\phi_{2_{xx}} + \phi_{2_{zz}} = -2ik\phi_{0_{x_2}} , \quad -h < z < 0 \tag{7.4.11}$$

$$\phi_{2_z} - \frac{\omega^2}{g}\phi_2 = 0 , \quad z = 0 , \tag{7.4.12}$$

$$\phi_{2_z} = (b(x)\phi_{1_x})_x + \frac{1}{2}(b^2(x)\phi_{0_{xz}})_x = (b(x)\phi_{1_x})_x , \quad z = -h \tag{7.4.13}$$

after using (7.4.7).

We shall focus on the evolution of the simple progressive wave at the leading order

$$\phi_0(x, z) = -\frac{igA(x_2)}{\omega}\frac{\cosh k(z+h)}{\cosh kh}e^{ikx} . \tag{7.4.14}$$

Uneffected directly by disorder, this solution is deterministic and represents a coherent wave.

At the next order the forcing at the seabed is random, hence the response is random (incoherent). Let us solve the inhomogeneous problem via a

Green's function $G(x,z;x')$, defined as the response to a unit source on the seabed. The defining equations are

$$G_{xx}+G_{zz}=0\,,\quad -h<z<0 \tag{7.4.15}$$

$$G_z-\frac{\omega^2}{g}G=0\,,\quad z=0\,, \tag{7.4.16}$$

$$G_z=\delta(x-x')\,,\quad z=-h \tag{7.4.17}$$

and the radiation condition at infinities. By the method of exponential Fourier transform, it is straightforward to find

$$G(x,z)=\frac{1}{2\pi}\int_C d\alpha\, e^{i\alpha(x-x')}\frac{-\frac{\omega^2}{g}\sinh\alpha z-\alpha\cosh\alpha z}{\alpha\left(\alpha\sinh\alpha h-\frac{\omega^2\cosh\alpha h}{g}\right)}\,. \tag{7.4.18}$$

To satisfy the radiation condition, we take the integration path C to be the real axis of the complex α plane, but indented above the real pole at $\alpha=-k$ and below another real pole at $\alpha=k$, where k is the positive real root of the dispersion relation. The integrand also has imaginary poles at $\pm ik_n$ which are the positive real roots of

$$\omega^2=gik_n\tanh ik_nh=-gk_n\tan k_nh\,,\quad n=1,2,3,\ldots\,. \tag{7.4.19}$$

By residue calculus it can be shown that, at $z=-h$,

$$G(|x-x'|,-h)=-\frac{i\frac{\omega^2}{gk}e^{ik|\xi|}}{\frac{\omega^2h}{g}+\sinh^2kh}-\sum_n\frac{\frac{\omega^2}{gk_n}e^{-k_n|x-x'|}}{\frac{\omega^2h}{g}-\sin^2k_nh}\,, \tag{7.4.20}$$

which is symmetric with respect to the interchange of x and x'. Details are left as an exercise.

By using Green's theorem, the solution for ϕ_1 is found to be

$$\begin{aligned}\phi_1(x,z)&=\int_{-\infty}^{\infty}(b(x')\phi_{0_{x'}})_{x'}G(x,-h;x')\,dx'\\&=\frac{gkA}{\omega\cosh kh}\int_{-\infty}^{\infty}[b_{x'}(x')+ikb(x')]e^{ikx'}G(|x-x'|,z)\,dx'\end{aligned} \tag{7.4.21}$$

which is a random function of x. Denoting the ensemble average of a random function R by $\langle R\rangle$, it is clear that $\langle\phi_1(x,z)\rangle\equiv 0$.

Now we take the ensemble average of the problem at $O(\epsilon^2)$ and get from ((7.4.11), (7.4.12), (7.4.13)) or (7.4.21)

$$\langle\phi_2\rangle_{xx} + \langle\phi_2\rangle_{zz} = -2ik\phi_{0_{x_2}}\,, \quad -h < z < 0 \tag{7.4.22}$$

$$\langle\phi_2\rangle_z - \frac{\omega^2}{g}\langle\phi_2\rangle = 0\,, \quad z = 0\,, \tag{7.4.23}$$

$$\begin{aligned}\langle\phi_2\rangle_z &= \left\langle (b(x)\phi_{1_x})_x + \frac{1}{2}(b^2(x)\phi_{0_{xz}})_x \right\rangle \\ &= \langle (b(x)\phi_{1_x})_x \rangle\,, \quad z = -h\,.\end{aligned} \tag{7.4.24}$$

With the help of (7.4.21), the boundary condition (7.4.13) becomes

$$\begin{aligned}\langle\phi_2\rangle_z = \left\langle \frac{\partial}{\partial x}\left\{ b(x)\left(\frac{gkA}{\omega\cosh kh}\right)\int_{-\infty}^{\infty}[b_{x'}(x') + ikb(x')]e^{ikx'}\right.\right. \\ \left.\left.\times\, G(|x-x'|,-h)\,dx'\right\}\right\rangle.\end{aligned} \tag{7.4.25}$$

To solve for $\langle\phi_2\rangle$, we let

$$\langle\phi_2\rangle = e^{ikx}F(x,x_2,z), \tag{7.4.26}$$

then from the Laplace equation:

$$F_{zz} - k^2F = -\frac{2gk}{\omega}\frac{\partial A}{\partial x_2}\frac{\cosh k(z+h)}{\cosh kh}\,, \quad -h < z < 0\,, \tag{7.4.27}$$

and on the free surface,

$$F_z - \frac{\omega^2}{g}F = 0\,. \tag{7.4.28}$$

On the seabed, (7.4.21) gives

$$\begin{aligned}\frac{\partial\langle\phi_2\rangle}{\partial z} = e^{ikx}F_z = \frac{gkA}{\omega\cosh kh} \\ \times\left\langle\frac{\partial}{\partial x}\left\{b(x)\int_{-\infty}^{\infty}[b_{x'}(x') + ikb(x')]e^{ikx'}G(|x-x'|,-h)\,dx'\right\}\right\rangle\end{aligned} \tag{7.4.29}$$

or

$$\frac{\partial F}{\partial z} = \frac{gkA}{\omega \cosh kh} e^{-ikx} \times \left\langle \frac{\partial}{\partial x} \left\{ b(x) \int_{-\infty}^{\infty} [b_{x'}(x') + ikb(x')] e^{-ikx'} G(|x - x'|, -h)\, dx' \right\} \right\rangle . \tag{7.4.30}$$

Let us assume stationarity and define the correlation function

$$\langle b(x)b(x') \rangle = \sigma^2 \gamma(|x - x'|) = \sigma^2 \gamma(\xi) \tag{7.4.31}$$

where $\xi = |x - x'|$ and $\sigma(x_2)$ is the root-mean-square amplitude of the disorder. We assume for generality that the length scale (the correlation length ℓ) is of the order of the incident wavelength. Note that the disorder is characterized by both σ and ℓ; large σ or small ℓ corresponds to strong disorder.

Since

$$\langle b_x(x)b(x') \rangle = \langle b(x)b(x') \rangle_x = \sigma^2 \frac{d\gamma}{d\xi} ,$$

the boundary condition (7.4.30) can be manipulated to the form

$$\frac{\partial \langle F \rangle}{\partial z} = i\beta A \cosh kh \tag{7.4.32}$$

where

$$\beta = \frac{gk^2\sigma^2}{\omega \cosh^2 kh} \left\{ \int_{-\infty}^{\infty} \left\{ \left(\frac{d}{d\xi} - ik \right)^2 \gamma \right\} e^{-ik\xi} G(|\xi|, -h)\, d\xi \right. . \tag{7.4.33}$$

The last integral is a complex constant.

Now the inhomogeneous boundary-value problem defined by (7.4.27), (7.4.28) and (7.4.32) also has the homogeneous solution $f(z) = \cosh k(z + h)/\cosh kh$. Appying Green's formula to f and $\langle F \rangle$ we get, after using their governing equations,

$$C_g \frac{\partial A}{\partial x_2} = \frac{i\beta A}{2 \cosh kh} . \tag{7.4.34}$$

This is the evolution equation for the envelope A of the coherent wave as affected by disorder through its statistical correlation.

In Appendix 7.A, the complex coefficient $\beta = \beta_r + i\beta_i$ is evaluated analytically in terms of the Fourier transform of the correlation function. For the special case of Gaussian correlation

$$\gamma(\xi) = \exp(-\xi^2/\ell_G^2)\,, \tag{7.4.35}$$

where ℓ_G is the Gaussian correlation length. The result is

$$\frac{\beta_r}{\omega} = \frac{(\sigma/\ell_G)^2(k\ell_G)^2}{2\cosh^2 kh}\left\{\frac{2+\frac{\sqrt{\pi}k\ell_G}{2}e^{-(k\ell_G)^2}\mathrm{erfi}(k\ell_G)}{\frac{\omega^2 h}{g}+\sinh^2 kh}\right.$$
$$\left. + \sum_{n=1}^{\infty}\frac{2-k_n\ell_G\sqrt{\pi}\ \mathrm{Re}\left\{\exp(\frac{\ell_G^2}{4}(k_n+ik)^2)\mathrm{erfc}(\frac{\ell_G}{2}(k_n+ik))\right\}}{\frac{\omega^2 h}{g}-\sin^2 k_n h}\right\}, \tag{7.4.36}$$

and

$$\frac{\beta_i}{\omega} = \frac{(\sigma k)^2}{\cosh^2 kh(\frac{\omega^2 h}{g}+\sinh^2 kh)}\frac{\sqrt{\pi}k\ell_G}{4}(1+e^{-(k\ell_G)^2})\,. \tag{7.4.37}$$

The task is now to discuss the solution to (7.4.34) and the physical implications.

7.5 Change of Wave Amplitude by Disorder

The solution to (7.4.34) is

$$A = A(0)e^{-\beta_i x_2/C_g}\exp\left(i\frac{\beta_r x_2}{C_g}\right). \tag{7.5.1}$$

The magnitude of A decays exponentially in space. The localization distance can be defined by

$$L_{loc} = \frac{C_g}{\epsilon^2\beta_i}\,. \tag{7.5.2}$$

Substituting (7.4.37) into (7.5.2) yields

$$\frac{L_{loc}}{h} = \frac{(2kh+\sinh 2kh)^2}{2\sqrt{\pi}\epsilon^2 kh(\sigma/\ell_G)^2(k\ell_G)^3(1+e^{-(k\ell_G)^2})}\,. \tag{7.5.3}$$

The localization length L_{loc} is plotted in Fig. 7.7. Either large σ (strong disorder) or large σ/ℓ_G (steep roughness) leads to short localization distances and fast attenuation.

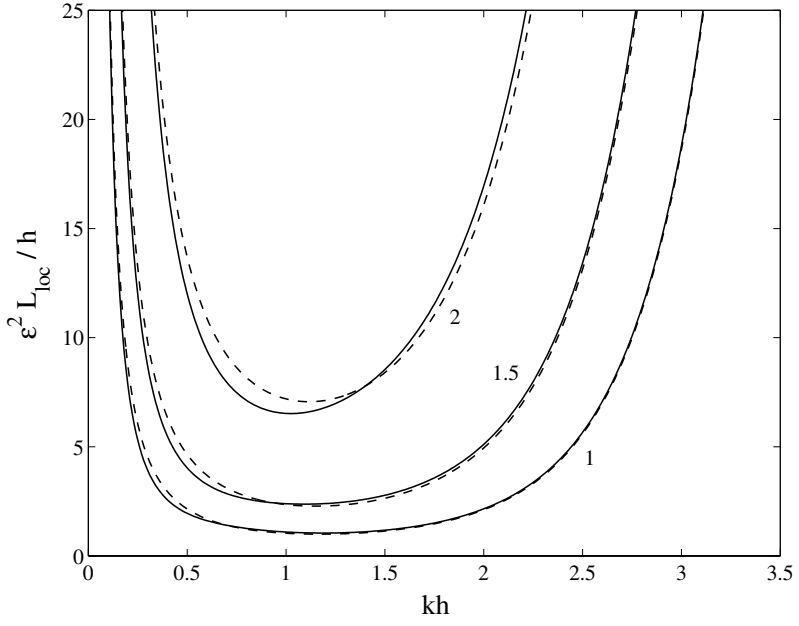

Figure 7.7: Localization length to depth ratio $\epsilon^2 L/h$ corresponding to the Gaussian [solid line, Eq. (7.5.3)] and exponential [broken line, Eq. (7.5.4)] correlations, for $B/\ell = 1$ and various $k\ell$, where $\ell = \ell_G$ or ℓ_E. Numbers adjacent to curves indicate the corresponding value of $k\ell$ (from Mei and Handcock (2003), *J. Fluid Mech.* Reproduced by permission of Cambridge University Press).

If the correlation length to depth ratio ℓ_G/h and the steepness σ/ℓ_G of the random topography are held fixed, then L_{loc}/h becomes infinite as $kh \to 0$ and as $kh \to \infty$. Thus long waves are only affected by the mean depth h and not by the relatively short bottom roughness, while short waves do not feel the bottom at all.

The product $k\ell_G = 2\pi\ell_G/\lambda$ represents the ratio of correlation length to wavelength. If kh and the mean steepness of the roughness, σ/ℓ_G, are held fixed, then $L_{loc}/h \propto \mathcal{F}(k\ell_G)$ where $\mathcal{F}(x) = x^{-3}(1 + e^{-x^2})^{-1}$ is a monotonically decreasing function for $x > 0$. Therefore, as $k\ell_G$ increases (longer roughness relative to the wavelength), the localization length L_{loc} decreases, indicating stronger attenuation. For $k\ell_G \ll 1$, waves are too long relative to the correlation length to be affected by the random bed roughness. On the other hand, for $k\ell_G \gg 1$, the waves are very short relative to the correlation length and are thus strongly attenuated.

To see whether localization is sensitive to the precise form of the correlation function, Mei and Hancock (2003) have also examined the exponential correlation function

$$\gamma(\xi) = \exp\left(-\frac{|\xi|}{\ell_E}\right). \tag{7.5.4}$$

The corresponding localization distance is found to be

$$\frac{L_{loc}}{h} = \frac{(2kh + \sinh 2kh)^2(1 + 4(k\ell_E)^2)}{8\varepsilon^2 kh(\sigma/\ell_E)^2(k\ell_E)^3(1 + 2(k\ell_E)^2)}\,. \tag{7.5.5}$$

The length ℓ_E is chosen to be $\ell_E = \sqrt{\pi}\ell_G/2$ so that the two correlation functions have the same total area. As seen in Fig. 7.7, only minor differences exist between the two correlations.

In the experiments by Belzons et al. (1988), the depth irregularities are discontinuous with the step heights comparable in order of magnitude to the depth itself. Vortex shedding at the step corners appear important. Despite these geometrical differences, the predictions are consistent with their measured data. Conclusive checks must await new experiments for small-amplitude randomness, common in many oceanographic situations.

7.6 Change of Wavenumber by Disorder

In view of (7.5.1), disorder leads to an increase in wavenumber through β_r,

$$\Delta k = (\Delta k)_{RD} \equiv \frac{\epsilon^2}{C_g}\beta_r\,. \tag{7.6.1}$$

Figure 7.8 shows that $(\Delta k)_{RD}$ is positive for all kh, and hence randomness shortens the wavelength. Since $dC_g/dk = \omega'' < 0$ and $dC/dk = (C_g - C)/k < 0$, randomness also reduces the group and phase speeds. If σ/h is fixed, decreasing ℓ/h is equivalent to increasing σ/ℓ, implying steeper random roughness, which is seen to shorten the waves. For fixed roughness (σ, ℓ), $(\Delta k)_{RD}$ decreases with increasing kh in general, since short waves are less affected by the bottom. As a last remark, since the change of wavenumber is a function of k, randomness modifies the dispersive character of the coherent wave.

The theory of this section has been extended to narrow-banded and weakly nonlinear waves. If the region of random irregularities spreads in two horizontal directions (x, y), the slow modulation must be described

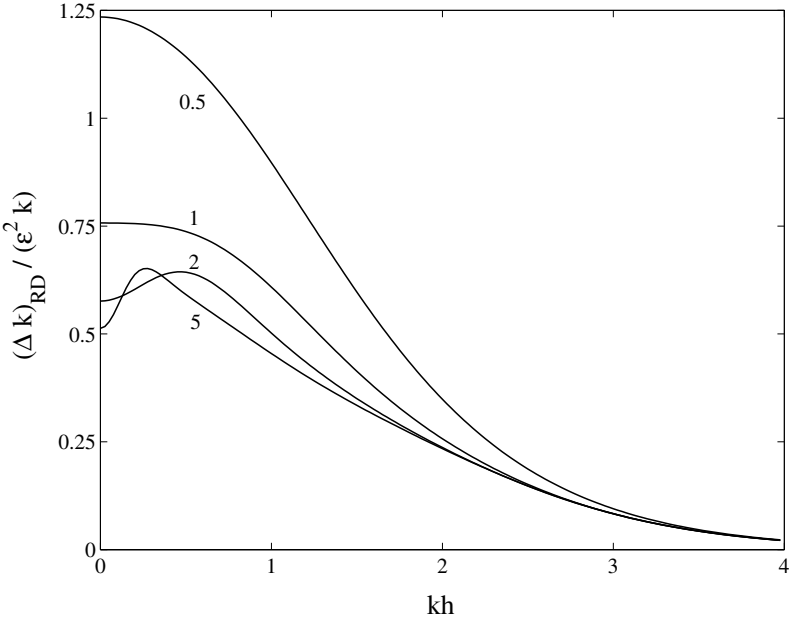

Figure 7.8: Normalized increase in wavenumber $\Delta k_R D/\epsilon^2 k$ due to Gaussian disorder vs kh, for $\sigma/h = 1$ and various ℓ_G/h (from Mei and Hancock (2003), *J. Fluid Mech.* Reproduced by permission of Cambridge University Press).

by $x_1 = \epsilon x, y_1 = \epsilon y, t_1 = \epsilon t; x_2 = \epsilon^2 x$. The coherent wave amplitude is governed by the following evolution equation,

$$\left(\frac{\partial}{\partial t_1}+C_g\frac{\partial}{\partial x_1}\right)A+i\epsilon\left\{-\frac{1}{2}\frac{d^2\omega}{dk^2}\frac{\partial^2 A}{\partial x_1^2}-\frac{C_g}{2k}\frac{\partial^2 A}{\partial y_1^2}+\alpha_1|A|^2A-\alpha_2 A-\beta A\right\}=0\,, \tag{7.6.2}$$

which is coupled to the potential of a long wave ϕ_{10}, with

$$\alpha_1 = \frac{\cosh 4kh + 8 - 2\tanh^2 kh}{16\sinh^4 kh} \tag{7.6.3}$$

and

$$\alpha_2 = \frac{k^2}{2\omega\cosh^2 kh}\frac{\partial\phi_{10}}{\partial t_1} - k\frac{\partial\phi_{10}}{\partial x_1}\,. \tag{7.6.4}$$

In the limit of two dimensions, the amplitude equation can be reduced to the nonlinear Schrödinger form, which was first deduced by Kawahara (1976).

Without the effects of disorder ($\beta = 0$) the equation will be discussed at length in Chapter Fourteen. Effects of disorder on nonlinear waves are discussed in Mei and Hancock (2003) and Pihl, Mei and Hancock (2002). The propagation of long waves over a shallow seabed with random perturbations will be discussed in Chapter Twelve.

In summary, we have examined in this chapter two complementary mechanisms of multiple scattering by bottom perturbations of gentle slope $O(\epsilon)$. For spatially periodic irregularities, Bragg resonance is effective over the distance $O(1/\epsilon k)$. On the other hand, for random irregularities localization becomes important over the distance $O(\epsilon^2 k)$. For oceanographic applications it would be useful to predict how bathymetric variations affect nonlinear random waves. Both mechanisms are likely important. A promising first step has been initiated by Ardhuin and Herbers (2002) who show that the Bragg mechanism also affects random waves propagating over a random seabed. Comprehensive wave forecasting models for a very large region will likely require the account of localization by disorder.

Appendix 7.A Explicit Evaluation of the Coefficient β

Substituting the Green's function (7.4.20) into (7.4.33) yields

$$\frac{\beta}{\omega} = \frac{(kB)^2}{2\cosh kh}\left\{\frac{\mathcal{I}_0}{\frac{\omega^2 h}{g} + \sinh^2 kh} + \sum_{n=1}^{\infty}\frac{k}{k_n}\frac{\mathcal{I}_n}{\frac{\omega^2 h}{g} - \sin^2 k_n h}\right\}, \qquad (7.A.1)$$

where

$$\mathcal{I}_0 = -\frac{i}{k}\int_{-\infty}^{\infty}\left\{\left(\frac{d}{d\xi} - ik\right)^2 \gamma\right\} e^{-ik\xi + ik|\xi|}\, d\xi\,, \qquad (7.A.2)$$

$$\mathcal{I}_n = -\frac{1}{k}\int_{-\infty}^{\infty}\left\{\left(\frac{d}{d\xi} - ik\right)^2 \gamma\right\} e^{-ik\xi - k_n|\xi|}\, d\xi\,. \qquad (7.A.3)$$

Note that $\frac{2n-1}{2}\pi < k_n h < n\pi$, and as $n \to \infty$, $k_n h \sim n\pi$. Thus $\lim_{n\to\infty} \sin k_n h = 0$.

Assume that $\gamma(\xi)$ is real and even in ξ, has the maximum value $\gamma(0) = 1$ and decays exponentially as $|\xi| \to \infty$. Equations (7.A.2) and (7.A.3) can be simplified to

$$\mathcal{I}_0 = ik \int_0^\infty (e^{2ik\xi} + 1)\gamma(\xi)\, d\xi + 2\,, \tag{7.A.4}$$

$$\mathcal{I}_n = -\frac{2}{k}\,\mathrm{Re}\left\{ \int_0^\infty e^{-(k_n + ik)\xi} \left(\frac{d}{d\xi} - ik \right)^2 \gamma(\xi)\, d\xi \right\}. \tag{7.A.5}$$

Note that $\mathcal{I}_n$ is real. Taking the real and imaginary parts of (7.A.1) and substituting (7.A.4) and (7.A.5) gives

$$\frac{\beta_r}{\omega} = \frac{(kB)^2}{2\cosh kh} \left\{ \frac{\mathrm{Re}\,(\mathcal{I}_0)}{\frac{\omega^2 h}{g} + \sinh^2 kh} + \sum_{n=1}^{\infty} \frac{k}{k_n} \frac{\mathcal{I}_n}{\frac{\omega^2 h}{g} - \sin^2 k_n h} \right\}, \tag{7.A.6}$$

$$\frac{\beta_i}{\omega} = \frac{(kB)^2}{2\cosh kh} \frac{\mathrm{Im}\,(\mathcal{I}_0)}{\frac{\omega^2 h}{g} + \sinh^2 kh}\,. \tag{7.A.7}$$

Taking the real and imaginary parts of (7.A.4) gives

$$\begin{aligned}
\mathrm{Re}\,(\mathcal{I}_0) &= 2 - k \int_0^\infty \gamma(\xi) \sin(2k\xi)\, d\xi\,, \\
\mathrm{Im}\,(\mathcal{I}_0) &= k \int_0^\infty \gamma \cos(2k\xi)\, d\xi + k \int_0^\infty \gamma d\xi \\
&= \frac{k}{2} \int_{-\infty}^\infty \gamma \cos(2k\xi)\, d\xi + \frac{k}{2} \int_{-\infty}^\infty \gamma d\xi \\
&= \frac{k}{2} \int_{-\infty}^\infty \gamma(\xi) e^{-2ik\xi} d\xi + \frac{k}{2} \int_{-\infty}^\infty \gamma(\xi)\, d\xi \\
&= \frac{k}{2} (\hat{\gamma}(2k) + \hat{\gamma}(0))\,,
\end{aligned}$$

where $\hat{\gamma}(k)$ is the Fourier transform of $\gamma(\xi)$. Hence (7.A.7) can be rewritten as

$$\frac{\beta_i}{\omega} = \frac{(kB)^2 k(\hat{\gamma}(2k) + \hat{\gamma}(0))}{4\cosh kh(\frac{\omega^2 h}{g} + \sinh^2 kh)}\,. \tag{7.A.8}$$

This result was first obtained by Pelinofsky et al. (1998).

For the special case of Gaussian correlation

$$\gamma(\xi) = e^{-\xi^2/\ell_G^2}\,, \tag{7.A.9}$$

(7.A.4) gives

$$\mathcal{I}_0 = \frac{i\sqrt{\pi}k\ell_G}{2}(1+e^{-(k\ell_G)^2}) + \frac{\sqrt{\pi}k\ell_G}{2}e^{-(k\ell_G)^2}\ \mathrm{erfi}\,(k\ell_G) + 2\,, \tag{7.A.10}$$

$$\mathcal{I}_n = \frac{k_n}{k}\ \mathrm{Re}\left\{2 - \sqrt{\pi}k_n\ell_G \exp\left(\frac{\ell_G^2}{4}(k_n+ik)^2\right)\mathrm{erfc}\left(\frac{\ell_G}{2}(k_n+ik)\right)\right\}\,, \tag{7.A.11}$$

where $\mathrm{erfi}\,(x) = i\ \mathrm{erf}\,(ix)$ is a real-valued function. It is straightforward to show that for large n, $\mathcal{I}_n \propto 1/n^2$, so that the sum in β_r converges. With these results we finally get

$$\frac{\beta_r}{\omega} = \frac{(\sigma/\ell)^2(k\ell)^2}{2\cosh^2 kh}\left\{\frac{2+\frac{\sqrt{\pi}k\ell}{2}e^{-(k\ell)^2}\ \mathrm{erfi}\,(k\ell)}{\frac{\omega^2 h}{g}+\sinh^2 kh}\right.$$
$$\left. + \sum_{n=1}^{\infty}\frac{2 - k_n\ell\sqrt{\pi}\ \mathrm{Re}\left\{\exp(\frac{\ell^2}{4}(k_n+ik)^2)\ \mathrm{erfc}\,(\frac{\ell}{2}(k_n+ik))\right\}}{\frac{\omega^2 h}{g}-\sin^2 k_n h}\right\} \tag{7.A.12}$$

and

$$\frac{\beta_i}{\omega} = \frac{(\sigma k)^2}{\cosh^2 kh(\frac{\omega^2 h}{g}+\sinh^2 kh)}\frac{\sqrt{\pi}k\ell}{4}(1+e^{-(k\ell)^2})\,. \tag{7.A.13}$$

This page intentionally left blank

Floating Body Dynamics: Diffraction and Radiation by Large Bodies

8

8.1 Introduction

Ships, buoys, barges, floating docks, breakwaters, submersibles supporting oil drilling rigs, and so on, are all structures whose safety and performance depend on their response to waves. In a calm sea, the body weight, the buoyancy force, and possible forces from external constraints such as tension legs, keep the body in static equilibrium. In waves, the presence of a sufficiently large body causes diffraction (scattering) of waves. The body must absorb some of the incident wave momentum and therefore must suffer a dynamic force. If the constraints, such as the mooring lines, are not sufficiently rigid, the body oscillates, hence further radiates waves, and experiences reacting forces from the surrounding fluid and from the constraint. Since the reacting forces depend on the motion of the body itself, the body, the constraint, and the surrounding water are dynamically coupled in the presence of incoming waves.

In modern offshore oil exploration, the gravity-type structure is frequently used in relatively shallow seas. This massive structure sits on the sea bottom and serves both as a storage tank and a support for the drilling deck above the sea level. The intensity of wave pressure has a direct effect on the stability of the seabed near the structure. Moreover, wave forces on the structure are transmitted to the seabed, causing stresses and deformation in both solids. Thus, the design of gravity structure involves the dynamic interaction of three media (water, structure, and seabed). A comprehensive discussion involving all three elements at once is too complex to be discussed here; we shall limit ourselves to the interaction of water with a rigid body.

First, a few remarks must be made on what is a *large* body. Excluding local corners, there are at least three relevant length scales in wave–body interaction: the characteristic body dimension a, the wavelength $2\pi/k$, and the wave amplitude A. Among these scales two ratios may be formed, for example, ka and A/a. If $ka \geqq O(1)$, a body is regarded as large; its presence alters the pattern of wave propagation significantly and produces diffraction. Ships, submersibles, and underwater storage tanks fall into this category. For small bodies ($ka \ll 1$), such as the structural members of a drilling tower, diffraction is of minor importance. When A/a is sufficiently large, the local velocity gradient near the small body augments the effect of viscosity and induces flow separation and vortex shedding, leading to the so-called *form drag*. At present, the inviscid linearized diffraction theory has been fairly well developed for $A/a \ll 1$ and $ka = O(1)$ with considerable experimental confirmation. The case of $A/a \geqq O(1)$ and $ka \ll 1$ has been the subject of intensive experimental studies (Sarpkaya and Issacson, 1981), but is not easily describable on purely theoretical ground. The intermediate case of $A/a \geqq O(1)$ and $ka = O(1)$ involves both separation and nonlinear diffraction and is the most difficult and least explored area of all.

It is useful to recall from the classical viscous flow theory why A/a plays a role in flow separation. If a circular cylinder of radius a starts to accelerate from rest with a uniform acceleration b, the inviscid flow just outside the cylinder is potential and is given by

$$U(x,t) = t2b\sin\theta\,, \tag{8.1.1}$$

where U is the tangential velocity along the cylinder and θ is the angle of a point along the cylinder measured from the forward stagnation point. From the solution of the viscous boundary layer along the cylinder surface, it is known that the boundary layer begins to separate at the rear stagnation point $\theta = \pi$ after the critical time t_c

$$t_c = \left(1.04\frac{a}{b}\right)^{1/2} \tag{8.1.2}$$

(Schlichting, 1968, p. 407). If the acceleration is continued, the rear region of separation expands toward the forward stagnation point; eddies are generated and shed downstream. The above information may be used to give an order-of-magnitude estimate for an oscillating cylinder in a calm fluid or an oscillating flow around a stationary cylinder. Let the amplitude of the oscillating velocity be U_0 so that the acceleration is $b = O(\omega U_0)$. The separation time is

$$t_c = O\left(\left(\frac{a}{\omega U_0}\right)^{1/2}\right). \tag{8.1.3}$$

Over a period $2\pi/\omega$, there is no separation if

$$\frac{2\pi}{\omega} < t_c \quad \text{or} \quad \frac{2\pi}{\omega} < c\left(\frac{a}{\omega U_0}\right)^{1/2} \quad \text{where} \quad c = O(1)\,. \tag{8.1.4}$$

This criterion may be rewritten in terms of the Strouhal number, which is just $1/2\pi$ times the Keulegan–Carpenter number U_0T/a:

$$\frac{U_0}{\omega a} < \left(\frac{c}{2\pi}\right)^2. \tag{8.1.5}$$

Since $U_0 = O(\omega A)$ in water waves where A is the wave amplitude, the criterion may be expressed

$$\frac{A}{a} < \left(\frac{c}{2\pi}\right)^2. \tag{8.1.6}$$

Thus, the parameter A/a governs the phenomenon of separation. Keulegan and Carpenter (1956) found experimentally that for a circular cylinder the value $A/a = 1$ is sufficiently large for flow separation and form drag is important. Since A is also the measure of the particle orbit in waves, a convenient rule of thumb is that no separation occurs if the orbital diameter is much less than the cylinder diameter.

Although large floating or submerged structures must often be designed to withstand storm waves with typical amplitudes as high as 15 m, the diffraction of large amplitude waves is still a challenging task in computatinoal dydrodynamics. On the other hand, wave–body interaction at infinitesimal amplitudes is a richly developed subject, which has been serving the field of naval architecture with great success. Its applications in offshore technology have have been wide-spread. An acquaintance with the elements of linearized theory is now an essential first step to the rational design of a costly new project. Some aspects of this are expounded here.

In Section 8.2 the governing equations for a partially constrained floating rigid body are derived for a body of arbitrary shape. The equations of static equilibrium and of small-amplitude motion are obtained as the zeroth- and the first-order approximations, respectively. The main body of this chapter is devoted to simple harmonic motions. Thanks to linearity, the fluid motion may be decoupled from that of the rigid body. A survey of the theoretical aspects of wave scattering and radiation is given in Sections 8.3–8.6 which include the derivations of the general reciprocity theorems for a single body.

The principles of a versatile numerical method of hybrid elements which extends the method described in Chapter Four are then briefly described in Section 8.7, followed by some remarks on the alternative methods of integral equations in Section 8.8. Applications of the theoretical tools are demonstrated via the topic of wave-power absorption in Section 8.9. As another application, wave trapping near a storm barrier designed for Venice, Italy, is discussed in Section 8.10. General formulas for the second-order drift forces are deduced in Section 8.11 by using the first-order results. Finally, we develop in Section 8.12 the general relationships between the simple harmonic response and the responses to transient waves.

8.2 Linearized Equations of Motion for a Constrained Floating Body

Details of the derivation presented below are due to John (1949) whose formal approach not only leads systematically to the complete first-order theory but also shows how higher-order extension may be made.

As in the case of the free surface, there are *kinematic* and *dynamic* conditions on the wetted body surface S_B, relating the motions of the body and of the surrounding water.

8.2.1 The Kinematic Condition

Let the instantaneous position of S_B be described by $z = f(x, y, t)$. Continuity of normal velocity requires that

$$\Phi_x f_x + \Phi_y f_y + f_t = \Phi_z \,, \quad z = f(x, y, t) \,. \tag{8.2.1}$$

For small-amplitude motions, we expand f in powers of the wave slope $\varepsilon = kA$ which is expected to characterize the body motion also,

$$z = f^{(0)}(x, y) + \varepsilon f^{(1)}(x, y, t) + \varepsilon^2 f^{(2)}(x, y, t) + \cdots \,, \tag{8.2.2}$$

where $f^{(0)}(x, y)$ corresponds to the rest position of S_B, that is, $S_B^{(0)}$. Likewise the velocity potential may also be expanded:

$$\Phi = \varepsilon \Phi^{(1)} + \varepsilon^2 \Phi^{(2)} + \cdots \,. \tag{8.2.3}$$

Since the body motion is small, any function evaluated on S_B may be expanded about $S_B^{(0)}$, that is, $z = f^{(0)}(x, y)$. To the order $O(\varepsilon)$, Eq. (8.2.1) gives

$$\phi_x^{(1)} f_x^{(0)} + \phi_y^{(1)} f_y^{(0)} + f_t^{(1)} = \phi_z^{(1)} \quad \text{on} \quad z = f^{(0)}(x, y)\,. \tag{8.2.4}$$

It is necessary to find $f^{(1)}$. Let the center of rotation of the rigid body be Q which has the following moving coordinate:

$$\mathbf{X}(t) = \mathbf{X}^{(0)} + \varepsilon \mathbf{X}^{(1)}(t) + \varepsilon^2 \mathbf{X}^{(2)}(t) + \cdots\,, \quad \mathbf{X} = (X, Y, Z)\,, \quad \text{and so on}\,, \tag{8.2.5}$$

where $\mathbf{X}^{(0)}$ is the rest position of Q independent of t. For generality, Q need not coincide with the center of mass of the body. We introduce $\bar{\mathbf{x}}$ to be the coordinate system fixed with the body such that $\bar{\mathbf{x}} = \mathbf{x}$ when the body is at its rest position. If the angular displacement of the body is $\varepsilon \boldsymbol{\theta}^{(1)}(t)$ with the components $\varepsilon\alpha$, $\varepsilon\beta$, and $\varepsilon\gamma$ about axes parallel to x, y, and z, then the two coordinate systems $\mathbf{x}$ and $\bar{\mathbf{x}}$ are related, to the first order, by

$$\mathbf{x} = \bar{\mathbf{x}} + \varepsilon[\mathbf{X}^{(1)} + \theta^{(1)} \times (\bar{\mathbf{x}} - \mathbf{X}^{(0)})] + O(\varepsilon^2)\,. \tag{8.2.6}$$

To the same accuracy $\bar{\mathbf{x}}$ may be solved in terms of $\mathbf{x}$ to give

$$\bar{\mathbf{x}} = \mathbf{x} - \varepsilon[\mathbf{X}^{(1)} + \boldsymbol{\theta}^{(1)} \times (\mathbf{x} - \mathbf{X}^{(0)})] + O(\varepsilon^2)\,, \tag{8.2.7a}$$

or, in component form,

$$\bar{x} = x - \varepsilon[X^{(1)} + \beta(z - Z^{(0)}) - \gamma(y - Y^{(0)})]\,, \tag{8.2.7b}$$

$$\bar{y} = y - \varepsilon[Y^{(1)} + \gamma(x - X^{(0)}) - \alpha(z - Z^{(0)})]\,, \tag{8.2.7c}$$

$$\bar{z} = z - \varepsilon[Z^{(1)} + \alpha(y - Y^{(0)}) - \beta(x - X^{(0)})]\,. \tag{8.2.7d}$$

Since $\mathbf{x} = \bar{\mathbf{x}}$ at rest by definition, the following is true:

$$\bar{z} = f^{(0)}(\bar{x}, \bar{y})\,. \tag{8.2.8}$$

Upon substituting Eq. (8.2.7) into Eq. (8.2.8), expanding about $S_B^{(0)}$, and then comparing the result with Eq. (8.2.2), we get

$$\begin{aligned} f^{(1)} = {} & Z^{(1)} + \alpha(y - Y^{(0)}) - \beta(x - X^{(0)}) \\ & - f_x^{(0)}[X^{(1)} + \beta(z - Z^{(0)}) - \gamma(y - Y^{(0)})] \\ & - f_y^{(0)}[Y^{(1)} + \gamma(x - X^{(0)}) - \alpha(z - Z^{(0)})]\,. \end{aligned} \tag{8.2.9}$$

Finally, the combination of Eqs. (8.2.9) and (8.2.4) yields the first-order kinematic condition:

$$
\begin{aligned}
-\boldsymbol{\Phi}_x^{(1)} f_x^{(0)} - \boldsymbol{\Phi}_y^{(1)} f_y^{(0)} + \boldsymbol{\Phi}_z^{(1)} \\
&= -f_x^{(0)}[X_t^{(1)} + \beta_t(z - Z^{(0)}) - \gamma_t(y - Y^{(0)})] \\
&\quad - f_y^{(0)}[Y_t^{(1)} + \gamma_t(x - X^{(0)}) - \alpha_t(z - Z^{(0)})] \\
&\quad + Z_t^{(1)} + \alpha_t(y - Y^{(0)}) - \beta_t(x - X^{(0)})\,. \qquad (8.2.10)
\end{aligned}
$$

There are more compact ways of expressing Eq. (8.2.10). Since the unit normal vector $\mathbf{n}$ pointing into the body is

$$
\mathbf{n} = (-f_x^{(0)}, -f_y^{(0)}, 1)[1 + (f_x^{(0)})^2 + (f_y^{(0)})^2]^{-1/2}\,, \qquad (8.2.11)
$$

Eq. (8.2.10) may be written

$$
\begin{aligned}
\frac{\partial \boldsymbol{\Phi}^{(1)}}{\partial n} &= \mathbf{X}_t^{(1)} \cdot \mathbf{n} + [\boldsymbol{\theta}_t^{(1)} \times (\mathbf{x} - \mathbf{X}^{(0)})] \cdot \mathbf{n} \\
&= \mathbf{X}_t^{(1)} \cdot \mathbf{n} + \boldsymbol{\theta}_t^{(1)} \cdot [(\mathbf{x} - \mathbf{X}^{(0)}) \times \mathbf{n}]\,. \qquad (8.2.12)
\end{aligned}
$$

Alternatively, we may introduce the six-dimensional generalized displacement vector $\{X_\alpha\}$ and the generalized normal vector $\{n_\alpha\}$ defined by

$$
\{X_\alpha\}^T = \{X^{(1)}, Y^{(1)}, Z^{(1)}, \alpha, \beta, \gamma\} = \{\mathbf{X}^{(1)}, \boldsymbol{\theta}^{(1)}\}\,, \qquad (8.2.13a)
$$

$$
\begin{aligned}
\{n_\alpha\}^T &= \{n_1, n_2, n_3, -[n_2(z - Z^{(0)}) - n_3(y - Y^{(0)})]\,, \\
&\quad - [n_3(x - X^{(0)}) - n_1(z - Z^{(0)})]\,, \\
&\quad - [n_1(y - Y^{(0)}) - n_2(x - X^{(0)})]\} \\
&= \{\mathbf{n}, (\mathbf{x} - \mathbf{X}^{(0)}) \times \mathbf{n}\}\,, \qquad (8.2.13b)
\end{aligned}
$$

where $\{\ \}$ denotes a column vector and $\{\ \}^T$ its transpose, and the subscript α ranges over $1, 2, \ldots, 6$. Equation (8.2.12) becomes

$$
\frac{\partial \Phi^{(1)}}{\partial n} = \sum_{\alpha=1}^{6} (X_\alpha)_t n_a = \{X_t\}^T \{n\}\,. \qquad (8.2.14)
$$

Exercise 8.1

Show that the order $O(\varepsilon^2)$ correction to the kinematic boundary condition is

$$
\begin{aligned}
\phi_x^{(2)} f_x^{(0)} + \phi_y^{(2)} f_y^{(0)} + f_t^{(2)} &= \phi_z^{(2)} - (\phi_x^{(1)} f_x^{(1)} + \phi_y^{(1)} f_y^{(1)}) \\
&\quad + f^{(1)}(\phi_{zz}^{(1)} - \phi_{xz}^{(1)} f_x^{(0)} - \phi_{yz}^{(1)} f_y^{(0)})\,.
\end{aligned}
$$

However, to get $f^{(2)}$ it is necessary to improve Eq. (8.2.6) which is good only for infinitesimal rotation. For finite rotation, the concept of Euler's angles is needed (Goldstein, 1950, Chapter 4).

We turn next to the dynamic conditions.

8.2.2 Conservation of Linear Momentum

Let M be the mass of the entire floating body, part of which may be above the free surface, and $\mathbf{x}^c(t)$ be the position of the center of mass. Conservation of linear momentum requires that

$$M\mathbf{x}^c_{tt} = \iint_{S_B} P\mathbf{n}\, dS - Mg\mathbf{e}_3 + \mathbb{F}\,, \tag{8.2.15}$$

where S_B is the instantaneous wetted body surface. $\mathbb{F}$ denotes the constraining force from external support, such as mooring lines, tension legs, and so on, and consists also of a static and a dynamic part:

$$\mathbb{F}(t) = \mathbb{F}^{(0)} + \varepsilon\mathbb{F}^{(1)}(t) + \cdots\,. \tag{8.2.16}$$

Up to the first order, Eq. (8.2.7) applies to $\mathbf{x}^c(t)$ so that

$$\mathbf{x}^c = \bar{\mathbf{x}}^c + \varepsilon[\mathbf{X}^{(1)} + \boldsymbol{\theta}^{(1)} \times (\bar{\mathbf{x}}^c - \mathbf{X}^{(0)})] + O(\varepsilon^2)\,.$$

The left-hand side of Eq. (8.2.15) becomes

$$M\mathbf{x}^c_{tt} = \varepsilon M[\mathbf{X}^{(1)}_{tt} + \boldsymbol{\theta}^{(1)}_{tt} \times (\bar{\mathbf{x}}^c - \mathbf{X}^{(0)})] + O(\varepsilon^2)\,. \tag{8.2.17}$$

On the right-hand side of Eq. (8.2.15), the linearized Bernoulli equation

$$P = -\rho g f - \varepsilon\rho\boldsymbol{\Phi}^{(1)}_t + O(\varepsilon^2) \tag{8.2.18}$$

is used in the first integral. The second term above gives

$$-\varepsilon \iint_{S^{(0)}_B} \rho\boldsymbol{\Phi}^{(1)}_t \mathbf{n}\, dS + O(\varepsilon^2)\,, \tag{8.2.19}$$

where S_B has been approximated by $S^{(0)}_B$. To consider the buoyancy term $-\rho g f$ we assume for simplicity that the horizontal cross section of the body decreases in area with depth, although all the final results can be shown to remain valid for more complex geometries. Now on the instantaneous body surface S_B,

$$\mathbf{n}\, dS = (-f_x, -f_y, 1)\, dx\, dy\,,$$

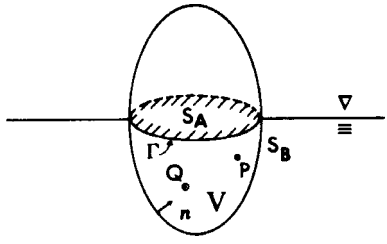

Figure 8.1: A floating body.

and the domain of integration S_B may be replaced by the part of the water surface cut out by S_B, that is, S_A (see Fig. 8.1). The vertical component of buoyancy is

$$-\rho g \iint_{S_B} f n_3 \, dS = -\rho g \iint_{S_A} (f^{(0)} + \varepsilon f^{(1)}) \, dx \, dy \, .$$

Since S_A differs from its equilibrium counterpart $S_A^{(0)}$ by $O(\varepsilon)$, and since $f^{(0)} = 0$ in the equilibrium free surface, the surface S_A may be replaced by $S_A^{(0)}$ with an error of $O(\varepsilon^2)$. By partial integration, we have

$$\iint_{S_A^{(0)}} f_x^{(0)} \, dx \, dy = \oint_\Gamma [f^{(0)}]_{x_-}^{x_+} \, dy \, ,$$

where Γ is the edge of $S_A^{(0)}$, that is, the water line, and x_+ and x_- refer to the points on Γ intersected by a line of constant y. Since $f^{(0)} = 0$ on Γ, the right-hand side integral in the equation above vanishes; it follows by using Eq. (8.2.9) that

$$-\rho g \iint_{S_B} f n_3 \, dS = -\rho g \iint_{S_A^{(0)}} f^{(0)} \, dx \, dy - \varepsilon \rho g \iint_{S_A^{(0)}} \times [Z^{(1)} + \alpha(y - Y^{(0)}) - \beta(x - X^{(0)})] \, dx \, dy + O(\varepsilon^2) \, . \tag{8.2.20}$$

The first integral on the right is just the submerged volume $V^{(0)}$ (static displacement). When Eqs. (8.2.17), (8.2.19), and (8.2.20) are combined with Eq. (8.2.15), terms of different orders may be separated. At the zeroth order, we have

$$Mg = \rho g V^{(0)} + \mathbb{F}_3^{(0)} \, , \tag{8.2.21}$$

which is just Archimedes' law.

Let $A^{(0)}$ be the area of $S_A^{(0)}$ and

$$I_1^A = \iint_{S_A^{(0)}} (x - X^{(0)})\, dx\, dy\,, \quad I_2^A = \iint_{S_A^{(0)}} (y - Y^{(0)})\, dx\, dy \tag{8.2.22}$$

be the moments of inertia of the cut plane $S_A^{(0)}$, then the linearized z momentum equation at $O(\varepsilon)$ is

$$M[Z_{tt}^{(1)} + \alpha_{tt}(\bar{y}^c - Y^{(0)}) - \beta_{tt}(\bar{x}^c - X^{(0)})]$$
$$= -\rho \iint_{S_B^{(0)}} \boldsymbol{\Phi}_t^{(1)} n_3\, dS + \mathbb{F}_3^{(1)} - \rho g(I_2^A \alpha - I_1^A \beta + Z^{(1)} A^{(0)})\,. \tag{8.2.23a}$$

If the floating body is totally immersed, $S_A^{(0)}$ vanishes and buoyancy does not affect the dynamic equilibrium.

Consider next the x and y components. Note that

$$\rho g \iint_{S_B} f n_1\, dS = -\rho g \iint_{S_B} f f_x\, dx\, dy$$
$$= -\rho g \oint_\Gamma \left[\frac{1}{2} f^2\right]_{x_-}^{x_+} dy = O(\varepsilon^2)\,,$$

and

$$\rho g \iint_{S_B} f n_2\, dS = -\rho g \iint_{S_A} f f_y\, dx$$
$$= -\rho g \oint_\Gamma \left[\frac{1}{2} f^2\right]_{y_-}^{y_+} dx = O(\varepsilon^2)\,.$$

Thus, buoyancy has a negligible effect in the horizontal directions. It follows from Eq. (8.2.15) that at the first order

$$M[X_{tt}^{(1)} + \beta_{tt}(\bar{z}^c - Z^{(0)}) - \gamma_{tt}(\bar{y}^c - Y^{(0)})]$$
$$= -\rho \iint_{S_B^{(0)}} \boldsymbol{\Phi}_t^{(1)} n_1\, dS + \mathbb{F}_1^{(1)}\,, \tag{8.2.23b}$$

$$M[Y_{tt}^{(1)} + \gamma_{tt}(\bar{x}^c - X^{(0)}) - \alpha_{tt}(\bar{z}^c - Z^{(0)})]$$
$$= -\rho \iint_{S_B^{(0)}} \boldsymbol{\Phi}_t^{(1)} n_2\, dS + \mathbb{F}_2^{(1)}\,. \tag{8.2.23c}$$

The zeroth-order (static) balance of horizontal momentum is trivially satisfied.

8.2.3 Conservation of Angular Momentum

Let V_b be the volume of the whole body including the part above the free surface. The rate of change of angular momentum of the body about the axes passing through the fixed origin 0 is

$$\frac{d\mathbf{L}}{dt} = \frac{d}{dt}\iiint_{V_b} \mathbf{x} \times \mathbf{x}_t \, dm = \iiint_{V_b} \mathbf{x} \times \mathbf{x}_{tt} \, dm \,,$$

where dm is the body mass per unit volume and $\mathbf{x}(t)$ denotes the instantaneous position of a point in the rigid body. Conservation of angular momentum requires that

$$\iiint_{V_b} \mathbf{x} \times \mathbf{x}_{tt} \, dm = \iint_{S_B} \mathbf{x} \times P\mathbf{n} \, dS + \mathbf{x}^c \times (-Mg\mathbf{e}_3) + \mathbf{T} \,, \qquad (8.2.24)$$

where $\mathbf{T}$ is the constraining torque due to external influences. Note that by definition $\mathbf{x}^c$ is the center of mass of the body, that is,

$$\iiint_{V_b} \mathbf{x} \, dm = M\mathbf{x}^c \,. \qquad (8.2.25)$$

The equation of linear momentum (8.2.15) may be rewritten

$$\iiint_{V_b} \mathbf{x}_{tt} \, dm = \iint_{S_B} P\mathbf{n} \, dS - Mg\mathbf{e}_3 + \mathbb{F} \,. \qquad (8.2.26)$$

Taking the cross product of $\mathbf{X}$ with Eq. (8.2.26) and subtracting the result from Eq. (8.2.24), we get

$$\begin{aligned} \frac{d\mathbf{L}^Q}{dt} \equiv \iiint_{V_b} (\mathbf{x} - \mathbf{X}) \times \mathbf{x}_{tt} \, dm &= \iint_{S_B} (\mathbf{x} - \mathbf{X}) \times P\mathbf{n} \, dS \\ &+ (\mathbf{x}^c - \mathbf{X}) \times (-Mg\mathbf{e}_3) + (\mathbf{T} + \mathbb{F} \times \mathbf{X}) \end{aligned} \qquad (8.2.27)$$

which represents the conservation of angular momentum with respect to the center of rotation Q.

Consider the zeroth-order balance. The left-hand side of Eq. (8.2.27) is ineffective. On the right-hand side, the constraining torque is simple:

$$\begin{aligned} \mathbf{T} + \mathbb{F} \times \mathbf{X} = (&\mathbf{T}^{(0)} + \mathbb{F}^{(0)} \times \mathbf{X}^{(0)}) \\ &+ \varepsilon(\mathbf{T}^{(1)} + \mathbb{F}^{(1)} \times \mathbf{X}^{(0)} + \mathbb{F}^{(0)} \times \mathbf{X}^{(1)}) + O(\varepsilon^2) \,. \end{aligned}$$

For convenience we denote

$$\mathfrak{T}^{(0)} = \mathbf{T}^{(0)} + \mathbb{F}^{(0)} \times \mathbf{X}^{(0)} \quad \text{and} \quad \mathfrak{T}^{(1)} = \mathbf{T}^{(1)} + \mathbb{F}^{(1)} \times \mathbf{X}^{(0)} ,$$

so that

$$\mathbf{T} + \mathbb{F} \times \mathbf{X} = \mathfrak{T}^{(0)} + \varepsilon \mathfrak{T}^{(1)} + \varepsilon \mathbb{F}^{(0)} \times \mathbf{X}^{(1)} . \tag{8.2.28}$$

When Eq. (8.2.28) is substituted into Eq. (8.2.27), it is easily seen that to the zeroth order

$$-\rho g \iint_{S_B^{(0)}} (\bar{\mathbf{x}} - \mathbf{X}^{(0)}) \times \mathbf{n} f^{(0)} \, dS + (\bar{\mathbf{x}}^c - \mathbf{X}^{(0)}) \times (-Mg\mathbf{e}_3) + \mathcal{J}^{(0)} = 0 . \tag{8.2.29}$$

Being over the rest surface $S_B^{(0)}$, $\bar{\mathbf{x}}$ in the integral above may be replaced by $\mathbf{x}$. Using the argument leading to Eq. (8.2.20), we may write the x component of the same integral as

$$-\rho g \left[\iint_{S_A^{(0)}} (y - Y^{(0)}) f^{(0)} \, dx \, dy + \iint_{S_A^{(0)}} f^{(0)} (f^{(0)} - Z^{(0)}) f_y^{(0)} \, dx \, dy \right] .$$

The second integral above vanishes after partial integration in y. On the other hand, since $f^{(0)} = -\int_{f^{(0)}}^{0} dz$ the first integral may be rewritten

$$\rho g \iiint_{V^{(0)}} (y - Y^{(0)}) \, dx \, dy \, dz \equiv \rho g I_2^V \equiv \rho g V^{(0)} (y^V - Y^{(0)}) , \tag{8.2.30}$$

where $V^{(0)}$ is the static submerged volume, I_2^V its first moment about the plane $y = Y^{(0)}$, and y^V the y coordinate of the *center of buoyancy*. In terms of these symbols, we get from Eq. (8.2.29)

$$\rho g I_2^V - Mg(y^c - Y^{(0)}) + \mathfrak{T}_1^{(0)} = 0 . \tag{8.2.31}$$

Similarly, for the y component we may define I_1^V and x^V by

$$\rho g I_1^V \equiv \rho g V^{(0)} (x^V - X^{(0)}) \equiv \rho g \iiint_{V^{(0)}} (x - X^{(0)}) \, dx \, dy \, dz , \tag{8.2.32}$$

and obtain

$$-\rho g I_1^V + Mg(\bar{x}^c - X^{(0)}) + \mathfrak{T}_2^{(0)} = 0 . \tag{8.2.33}$$

If there is no external contraint, $\mathfrak{T}^{(0)} \equiv 0$; we must have $Mg = \rho g V^{(0)}$. It follows from Eqs. (8.2.31) and (8.2.33) that $x^c = x^V$ and $y^c = y^V$, that is, the centers of mass and of buoyancy must lie on the same vertical line.

We leave it for the reader to verify that the z component of the integral in Eq. (8.2.29) vanishes identically so that the corresponding static balance is trivial:

$$\mathfrak{T}_3^{(0)} = 0\,. \tag{8.2.34}$$

Now consider the order $O(\varepsilon)$. On the left-hand side of Eq. (8.2.27) we may replace $\mathbf{x} - \mathbf{X}$ by $\bar{\mathbf{x}} - \mathbf{X}^{(0)}$ and invoke Eq. (8.2.6):

$$\mathbf{x}_{tt} = \varepsilon[\mathbf{X}_{tt}^{(1)} + \boldsymbol{\theta}_{tt}^{(1)} \times (\bar{\mathbf{x}} - \mathbf{X}^{(0)})]\,.$$

Equation (8.2.27) becomes

$$\frac{dL^Q}{dt} \equiv \varepsilon\Bigg\{ \left[\iiint_{V_b} (\bar{\mathbf{x}} - \mathbf{X}^{(0)})\, dm\right] \times \mathbf{X}_{tt}^{(1)} + \boldsymbol{\theta}_{tt}^{(1)} \iiint_{V_b} (\bar{\mathbf{x}} - \mathbf{X}^{(0)})^2\, dm$$

$$- \left[\boldsymbol{\theta}_{tt}^{(1)} \cdot \iiint_{V_b} (\bar{\mathbf{x}} - \mathbf{X}^{(0)})\right] (\bar{\mathbf{x}} - \mathbf{X}^{(0)})\, dm \Bigg\}\,. \tag{8.2.35}$$

Let us define the first and second moments of inertia as follows:

$$I_1^b = \iiint_{V_b} (\bar{x} - X^{(0)})\, dm \equiv M(\bar{x}^c - X^{(0)})\,,$$

$$I_{11}^b = \iiint_{V_b} (\bar{x} - X^{(0)})^2\, dm\,, \tag{8.2.36}$$

$$I_{12}^b = \iiint_{V_b} (\bar{x} - X^{(0)})(\bar{y} - Y^{(0)})\, dm\,.$$

Other moments $I_2^b, I_3^b, I_{22}^b, \ldots, I_{33}^b, \ldots$, and so on, are similarly defined. In terms of these moments, the left-hand side of Eq. (8.2.27) becomes, in component form,

$$\frac{dL_1^Q}{dt} = \varepsilon\{I_2^b Z_{tt}^{(1)} - I_3^b Y_{tt}^{(1)} + (I_{22}^b + I_{33}^b)\alpha_{tt} - I_{21}^b \beta_{tt} - I_{31}^b \gamma_{tt}\}\,,$$

$$\frac{dL_2^Q}{dt} = \varepsilon\{I_3^b X_{tt}^{(1)} - I_1^b Z_{tt}^{(1)} + (I_{33}^b + I_{11}^b)\beta_{tt} - I_{32}^b \gamma_{tt} - I_{12}^b \alpha_{tt}\}\,, \tag{8.2.37}$$

$$\frac{dL_3^Q}{dt} = \varepsilon\{I_1^b Y_{tt}^{(1)} - I_2^b X_{tt}^{(1)} + (I_{11}^b + I_{22}^b)\gamma_{tt} - I_{13}^b \alpha_{tt} - I_{23}^b \beta_{tt}\}\,.$$

There are no terms of zeroth order.

On the other hand, the right-hand side of Eq. (8.2.27) gives

$$
\begin{aligned}
&-\varepsilon \iint_{S_B^{(0)}} \rho \boldsymbol{\Phi}_t^{(1)} (\mathbf{x} - \mathbf{X}^{(0)}) \times \mathbf{n}\, dS \\
&\quad - \rho g \left\{ \iint_{S_B} f(\mathbf{x} - \mathbf{X}) \times \mathbf{n}\, dS - \iint_{S_B^{(0)}} f^{(0)} (\mathbf{x} - \mathbf{X}^{(0)}) \times \mathbf{n}\, dS \right\} \\
&\quad + \varepsilon [\boldsymbol{\theta}^{(1)} \times (\bar{\mathbf{x}}^c - \mathbf{X}^{(0)})] \times (-Mg\mathbf{e}_3) + \varepsilon (\mathfrak{T}^{(1)} + \mathbb{F}^{(0)} \times \mathbf{X}^{(1)}) \,. \qquad (8.2.38)
\end{aligned}
$$

These terms represent torques of various physical origin: the first integral is due to hydrodynamics, the second from buoyancy, and the third from inertia, while the remaining terms are from the constraint. We now treat them separately.

Hydrodynamic Torque

The generalized normal (8.2.13b) enables us to express the components of the hydrodynamic torque

$$
-\varepsilon \iint_{S_B^{(0)}} \rho \boldsymbol{\Phi}_t^{(1)} n_\alpha \, dS \,, \quad \alpha = 4, 5, 6 \,. \qquad (8.2.39)
$$

Buoyancy Torque

Written in component form, the buoyancy torque is

$$
\begin{aligned}
&-\rho g \iint_{S_B} f(\mathbf{x} - \mathbf{X}) \times \mathbf{n}\, dS \\
&\quad = -\rho g \iint_{S_B} f \{ [(y - Y) n_3 - (z - Z) n_2] \, \mathbf{e}_1 \\
&\qquad + [(z - Z) n_1 - (x - X) n_3] \mathbf{e}_2 + [(x - X) n_2 - (y - Y) n_1] \mathbf{e}_3 \} \, dS \\
&\quad = -\rho g \iint_{S_A} f \{ [(y - Y) + (f - Z) f_y] \, \mathbf{e}_1 + [-(f - Z) f_x - (x - X)] \mathbf{e}_2 \\
&\qquad + [-(x - X) f_y + (y - Y) f_x] \mathbf{e}_3 \} \, dx \, dy \,.
\end{aligned}
$$

After partial integration and noting $f = \varepsilon f^{(1)}$ on the edge of S_A, we find that the terms with f_x and f_y are of order $O(\varepsilon^2)$; hence

$$
-\rho g \iint_{S_B} f(\mathbf{x} - \mathbf{X}) \times \mathbf{n}\, dS = -\rho g \iint_{S_A} [f(y - Y)\mathbf{e}_1 - f(x - X)\mathbf{e}_2] \, dx \, dy \,. \qquad (8.2.40)
$$

The second integral in { } of Eq. (8.2.38) obviously takes a form similar to Eq. (8.2.40). Consider the x component of the same { }:

$$
\begin{aligned}
\{\ \} &= -\rho g \iint_{S_A} f(y-Y)\,dx\,dy - \rho g \iint_{S_A^{(0)}} f^{(0)}(y-Y^{(0)})\,dx\,dy \\
&= -\varepsilon\rho g \iint_{S_A^{(0)}} [f^{(1)}(y-Y^{(0)}) - f^{(0)}Y^{(1)}]\,dx\,dy \\
&= -\varepsilon\rho g \iint_{S_A^{(0)}} [Z^{(1)} + \alpha(y-Y^{(0)}) - \beta(x-X^{(0)})](y-Y^{(0)})\,dx\,dy \\
&\quad + \varepsilon\rho g \iint_{S_A^{(0)}} f_x^{(0)}[X^{(1)} + \beta(z-Z^{(0)}) - \gamma(y-Y^{(0)})](y-Y^{(0)})\,dx\,dy \\
&\quad + \varepsilon\rho g \iint_{S_A^{(0)}} f_y^{(0)}[Y^{(1)} + \gamma(x-X^{(0)}) - \alpha(z-Z^{(0)})](y-Y^{(0)})\,dx\,dy \\
&\quad + \varepsilon\rho g Y^{(1)} \iint_{S_A^{(0)}} f^{(0)}\,dx\,dy\,.
\end{aligned}
$$

After partial integration, the second integral above vanishes; the third and fourth integrals combine to give

$$
\begin{aligned}
&-\varepsilon\rho g \iint_{S_A^{(0)}} f^{(0)}[\gamma(x-X^{(0)}) - \alpha(z-Z^{(0)})]\,dx\,dy \\
&\qquad = +\varepsilon\rho g \iiint_{V^{(0)}} [\gamma(x-X^{(0)}) - \alpha(z-Z^{(0)})]\,dx\,dy\,dz\,,
\end{aligned}
$$

where use is made of $f^{(0)} = -\int_{f^{(0)}}^{0} dz$. Introducing the second moments

$$
\begin{aligned}
I_{22}^A &= \iint_{S_A^{(0)}} (y-Y^{(0)})^2\,dx\,dy\,, \\
I_{12}^A &= \iint_{S_A^{(0)}} (x-X^{(0)})(y-Y^{(0)})\,dx\,dy\,, \quad \text{and so on}\,,
\end{aligned}
\tag{8.2.41}
$$

we get the x component of the buoyancy torque:

$$
-\varepsilon\rho g[Z^{(1)}I_2^A + \alpha I_{22}^A - \beta I_{12}^A - \gamma I_1^V + \alpha I_3^V]\,, \tag{8.2.42}
$$

and, by similar arguments, the y component:

$$
-\varepsilon\rho g[Z^{(1)}I_1^A + \alpha I_{21}^A - \beta I_{11}^A - \beta I_3^V + \gamma I_2^V]\,. \tag{8.2.43}
$$

There is no z component.

Inertia Torque

Expanding the triple vector product in Eq. (8.2.38), we get

$$\begin{aligned}&\mathbf{e}_1(-Mg)[\gamma(\bar{x}^c - X^{(0)}) - \alpha(\bar{z}^c - Z^{(0)})]\\ &\quad + \mathbf{e}_2(Mg)[\beta(\bar{z}^c - Z^{(0)}) - \gamma(\bar{y}^c - Y^{(0)})]\,.\end{aligned} \tag{8.2.44}$$

Constraining Torque

$$\begin{aligned}&\mathbf{e}_1(\mathfrak{T}_1^{(1)} + \mathbb{F}_2^{(0)} Z^{(1)} - \mathbb{F}_3^{(0)} Y^{(1)}) + \mathbf{e}_2(\mathfrak{T}_2^{(1)} + \mathbb{F}_3^{(0)} X^{(1)} - \mathbb{F}_1^{(0)} Z^{(1)})\\ &\quad + \mathbf{e}_3(\mathfrak{T}_3^{(1)} + \mathbb{F}_1^{(0)} Y^{(1)} - \mathbb{F}_2^{(0)} X^{(1)})\,.\end{aligned} \tag{8.2.45}$$

Equations (8.2.39) and (8.2.42)–(8.2.45) may be combined with Eq. (8.2.38) and then with Eq. (8.2.37) to give the conservation equations of angular momentum as follows:

x component:

$$\begin{aligned}&I_2^b Z_{tt}^{(1)} - I_3^b Y_{tt}^{(1)} + (I_{22}^b + I_{33}^b)\alpha_{tt} - I_{21}^b \beta_{tt} - I_{13}^b \gamma_{tt}\\ &\quad = -\rho \iint_{S_B^{(0)}} \mathbf{\Phi}_t^{(1)} n_4 \, dS - \rho g\{Z^{(1)} I_2^A + \alpha(I_{22}^A + I_3^V) - \beta I_{12}^A - \gamma I_1^V\}\\ &\qquad + Mg[\alpha(\bar{z}^c - Z^{(0)}) - \gamma(\bar{x}^c - X^{(0)})] + \mathfrak{T}_1^{(1)} + \mathbb{F}_2^{(0)} Z^{(1)} - \mathbb{F}_3^{(0)} Y^{(1)}\,,\end{aligned} \tag{8.2.46a}$$

y component:

$$\begin{aligned}&I_3^b X_{tt}^{(1)} - I_1^b Z_{tt}^{(1)} + (I_{33}^b + I_{11}^b)\beta_{tt} - I_{32}^b \gamma_{tt} - I_{12}^b \alpha_{tt}\\ &\quad = -\rho \iint_{S_B^{(0)}} \mathbf{\Phi}_t^{(1)} n_5 \, dS + \rho g\{Z^{(1)} I_1^A + \alpha I_{21}^A + \beta(-I_{11}^A - I_3^V) + \gamma I_2^V\}\\ &\qquad + Mg[(\bar{z}^c - Z^{(0)})\beta - (\bar{y}^c - Y^{(0)})\gamma] + \mathfrak{T}_2^{(1)} + \mathbb{F}_3^{(0)} X^{(1)} - \mathbb{F}_1^{(0)} Z^{(1)}\,,\end{aligned} \tag{8.2.46b}$$

z component:

$$\begin{aligned}&I_1^b Y_{tt}^{(1)} - I_2^b X_{tt}^{(1)} + (I_{11}^b + I_{22}^b)\gamma_{tt} - I_{13}^b \alpha_{tt} - I_{23}^b \beta_{tt}\\ &\quad = -\rho \iint_{S_B^{(0)}} \mathbf{\Phi}_t^{(1)} n_6 \, dS + \mathfrak{T}_3^{(1)} + \mathbb{F}_1^{(0)} Y^{(1)} - \mathbb{F}_2^{(0)} X^{(1)}\,.\end{aligned} \tag{8.2.46c}$$

Equations (8.2.23) and (8.2.46) can be regarded as the dynamic boundary conditions for the fluid problem. In the original derivation of John (1949, 1950), the reference point Q is assumed to coincide with the center of mass. The minor extension presented here is due to Serman (1978).

8.2.4 Summary of Dynamic Equations for a Floating Body in Matrix Form

The linear system of Eqs. (8.2.22) and (8.2.46) can be summarized in matrix form in terms of the generalized coordinates (8.2.13a)

$$[M]\{\ddot{X}\} + [C]\{X\} = -\rho \iint_{S_B^{(0)}} dS\, \mathbf{\Phi}_t^{(1)}\{n\} + \{\mathbb{F}\}\,, \tag{8.2.47}$$

where an overhead dot denotes the time derivative and $\{\mathbb{F}\}$ is the generalized dynamic force of constraint:

$$\{\mathbb{F}^{(1)}, \mathfrak{T}^{(1)} + \mathbb{F}^{(0)} \times \mathbf{X}^{(1)}\}^T\,. \tag{8.2.48}$$

The mass matrix $[M]$ and the buoyancy restoring force matrix $[C]$ are given, respectively, by Eqs. (8.2.49) and (8.2.50) shown on the next page.

It is obvious that the matrix $[M]$ is symmetric. If the center of mass coincides with the center of rotation, then $\bar{\mathbf{x}}^c - \mathbf{X}^{(0)} = 0$, and many terms in $[M]$ and $[C]$ vanish identically. Furthermore, when there is no constraint, $I_1^V = I_2^V = 0$ by Eqs. (8.2.31) and (8.2.33); $[C]$ is also symmetric.

In some situations the constraining force $\mathbb{F}^{(1)}$ and torque $\mathcal{T}^{(1)}$ may depend on the body displacement; equations governing the dynamics of the constraints must then be added.

The Two-Dimensional Limit

For a long horizontal cylinder with normally incident waves from one side, the motion can be described in the cross-sectional plane of x and z. It is only necessary to restrict our attention to unit length in the y direction.

For the rigid body there are only two translational modes x and z and one rotational mode β about the y axis. The relevant generalized coordinates are 1, 3, and 5. For a right-handed coordinate system, the negative y axis points out of the paper so that positive rotations are clockwise.

$$[M] = \begin{bmatrix} M & 0 & 0 & 0 & M(\bar{z}^c - Z^{(0)}) & -M(\bar{y}^c - Y^{(0)}) \\ 0 & M & 0 & -M(\bar{z}^c - Z^{(0)}) & 0 & M(\bar{x}^c - X^{(0)}) \\ 0 & 0 & M & M(\bar{y}^c - Y^{(0)}) & -M(\bar{x}^c - X^{(0)}) & 0 \\ 0 & -M(\bar{z}^c - Z^{(0)}) & M(\bar{y}^c - Y^{(0)}) & (I^b_{22} + I^b_{33}) & -I^b_{21} & -I^b_{13} \\ M(\bar{z}^c - Z^{(0)}) & 0 & -M(\bar{x}^c - X^{(0)}) & -I^b_{12} & I^b_{33} + I^b_{11} & -I^b_{32} \\ -M(\bar{y}^c - Y^{(0)}) & M(\bar{x}^c - X^{(0)}) & 0 & -I^b_{13} & -I^b_{23} & I^b_{11} + I^b_{22} \end{bmatrix}. \tag{8.2.49}$$

$$[C] = \begin{bmatrix} 0 & 0 & 0 & 0 & 0 & 0 \\ 0 & 0 & 0 & 0 & 0 & 0 \\ 0 & 0 & \rho g A & \rho g I^A_2 & -\rho g I^A_1 & 0 \\ 0 & \mathbb{F}^{(0)}_3 & \rho g I^A_2 - \mathbb{F}^{(0)}_2 & \begin{pmatrix} \rho g (I^A_{22} + I^V_3) \\ -Mg(\bar{z}^c - Z^{(0)}) \end{pmatrix} & -\rho g I^A_{12} & \begin{pmatrix} -\rho g I^V_1 \\ +Mg(\bar{x}^c - X^{(0)}) \end{pmatrix} \\ -\mathbb{F}^{(0)}_3 & 0 & -\rho g I^A_1 + \mathbb{F}^{(0)}_1 & -\rho g I^A_{21} & \begin{pmatrix} +\rho g (I^A_{11} + I^V_3 \\ -Mg(\bar{z}^c - Z^{(0)}) \end{pmatrix} & \begin{pmatrix} -\rho g I^V_2 \\ +Mg(\bar{y}^c - Y^{(0)}) \end{pmatrix} \\ \mathbb{F}^{(0)}_2 & -\mathbb{F}^{(0)}_1 & 0 & 0 & 0 & 0 \end{bmatrix}. \tag{8.2.50}$$

The linear momentum equations are reduced to

$$M[X_{tt}^{(1)} + \beta_{tt}(\bar{z}^c - Z^{(0)})] = -\rho \int_{S_B^{(0)}} \mathbf{\Phi}_t^{(1)} n_1 \, dS + \mathbb{F}_1^{(1)} , \tag{8.2.51a}$$

$$M[Z_{tt}^{(1)} + \beta_{tt}(\bar{x}^c - X^{(0)})] = -\rho \int_{S_B^{(0)}} \mathbf{\Phi}_t^{(1)} n_3 \, dS + \mathbb{F}_3^{(1)} + \rho g I_1^A \beta - \rho g Z^{(1)} A , \tag{8.2.51b}$$

and the angular momentum about the y axis is

$$\begin{aligned} & I_3^b X_{tt}^{(1)} - I_1^b Z_{tt}^{(1)} + (I_{33}^b + I_{11}^b)\beta_{tt} \\ & \quad = -\rho \int_{S_B^{(0)}} \mathbf{\Phi}_t^{(1)} n_5 \, dS + \rho g \{ Z^{(1)} I_1^A - \beta (I_{11}^A + I_3^V) \} \\ & \qquad + Mg(\bar{z}^c - Z^{(0)})\beta + \mathfrak{J}_2^{(1)} + \mathbb{F}_3^{(0)} X^{(1)} - \mathbb{F}_1^{(0)} Z^{(1)} , \end{aligned} \tag{8.2.52}$$

where

$$\begin{aligned} I_1^A &= \int_{S_A^{(0)}} (x - X^{(0)}) \, dx , \quad I_1^b = \iint_{V_b} (x - X^{(0)}) \, dm , \\ I_{11}^A &= \int_{S_A^{(0)}} (x - X^{(0)})^2 \, dx , \quad I_{11}^b = \iint_{V_b} (x - X^{(0)})^2 \, dm , \\ I_3^V &= \iint_{V^{(0)}} (z - Z^{(0)}) \, dx \, dz . \end{aligned} \tag{8.2.53}$$

In the expressions above, A is the length of the water line S_A, that is, the segment of the x axis which is displaced by the body, V is the submerged cross-section area, and V_b is the entire body cross section. The corresponding matrix equation is

$$\begin{aligned} & [M] \frac{d^2}{dt^2} \begin{Bmatrix} X^{(1)} \\ Z^{(1)} \\ \beta \end{Bmatrix} + [C] \begin{Bmatrix} X^{(1)} \\ Z^{(1)} \\ \beta \end{Bmatrix} \\ & \quad = -\rho \int_{S_B^{(0)}} dS \, \mathbf{\Phi}_t^{(1)} \begin{Bmatrix} n_1 \\ n_3 \\ n_5 \end{Bmatrix} + \begin{Bmatrix} \mathbb{F}_1^{(1)} \\ \mathbb{F}_3^{(1)} \\ \mathfrak{T}_2^{(1)} + \mathbb{F}_3^{(0)} X^{(1)} - \mathbb{F}_1^{(0)} Z^{(0)} \end{Bmatrix} , \end{aligned} \tag{8.2.54}$$

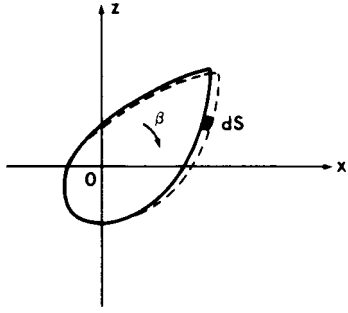

Figure 8.2

where

$$[M] = \begin{bmatrix} M & 0 & M(\bar{z}^c - Z^{(0)}) \\ 0 & M & -M(\bar{x}^c - X^{(0)}) \\ M(\bar{z}^c - Z^{(0)}) & -M(\bar{x}^c - X^{(0)}) & I_{11}^b + I_{33}^b \end{bmatrix} \tag{8.2.55}$$

and

$$[C] = \begin{bmatrix} 0 & 0 & 0 \\ 0 & \rho g A & -\rho g I_1^A \\ -\mathbb{F}_3^{(0)} & -\rho g I_1^A + \mathbb{F}_1^{(0)} & \begin{pmatrix} \rho g(I_{11}^A + I_3^V) \\ -Mg(\bar{z}^c - Z^{(0)}) \end{pmatrix} \end{bmatrix}, \tag{8.2.56}$$

where the inertia terms refer to the unit length of the cylinder.

So far our derivation has been rather formal so that no first-order term could escape our attention. For the relatively simple case of two dimensions, it is instructive to reexamine some of the terms heuristically. Consider the buoyancy torque caused by rotation β. Referring to Fig. 8.2 for the boundary element dS, a positive (clockwise) β will induce an added buoyancy force of the magnitude

$$\begin{aligned} &-\rho g[\boldsymbol{\theta}^{(1)} \times (\mathbf{x} - \mathbf{X}^{(0)})] \cdot \mathbf{n}\, dS \\ &\quad = -\beta[(z - Z^{(0)})n_1 - (x - X^{(0)})n_3]\rho g\, dS \end{aligned} \tag{8.2.57}$$

in the vertical direction. The corresponding restoring moment is

$$-\rho g \beta \int_{S_B^{(0)}} [(z - Z^{(0)})n_1 - (x - X^{(0)})n_3](x - X^{(0)})\, dS\,.$$

Since $n_1\,dS = -dz$ and $n_3\,dS = dx$, this moment can also be expressed

$$-\rho g\beta\left[\int_{S_B^{(0)}}(x-X^{(0)})(z-Z^{(0)})\,dz+\int_{S_B^{(0)}}(x-X^{(0)})^2\,dx\right]. \qquad (8.2.58)$$

Noting that $(x-X^{(0)}) = \int_{X^{(0)}}^{x} dx$, we may rewrite the first integral in Eq. (8.2.58) as

$$\iint_{V^{(0)}}(z-Z^{(0)})\,dx\,dz = I_3^V\,,$$

and the second integral in Eq. (8.2.58) as

$$\int_{S_B^{(0)}}(x-X^{(0)})^2\,dx = I_{11}^A\,.$$

Thus, Eq. (8.2.58) gives the first β terms on the right of Eq. (8.2.52) and the appearance of I_3^V and I_{11}^A is verified by an elementary consideration.

In subsequent sections all superscripts (0) and (1) will be omitted for brevity.

8.3 Simple Harmonic Motion

8.3.1 Decomposition into Diffraction and Radiation Problems

As in simpler vibrating systems governed by linear ordinary differential equations with constant coefficients, the most basic task is to study the frequency response to a simple harmonic excitation. Furthermore, it is convenient to decouple the hydrodynamics from the body dynamics by the following device (Haskind, 1944). Let us introduce the complex amplitude

$$\{\mathbf{\Phi}, \dot{X}_\alpha\}^T = \mathrm{Re}\,\{\phi, V_\alpha\}^T e^{-i\omega t}\,, \qquad (8.3.1)$$

where V_α denotes the amplitude of the generalized body velocity, and the decomposition

$$\phi = \phi^D + \sum_\alpha V_\alpha \phi_\alpha\,, \quad \alpha = 1,2,\ldots,6\,. \qquad (8.3.2)$$

The potential ϕ^D is governed by the following conditions:

$$\nabla^2\phi^D = 0 \qquad \text{in the fluid}\,, \tag{8.3.3}$$

$$\frac{\partial\phi^D}{\partial z} - \frac{\omega^2}{g}\phi^D = 0 \qquad \text{on} \quad S_F \ (z=0)\,, \tag{8.3.4}$$

$$\frac{\partial\phi^D}{\partial z} = 0 \qquad \text{on} \quad B_0 \ (z=-h, \text{ sea bottom})\,, \tag{8.3.5}$$

$$\frac{\partial\phi^D}{\partial n} = 0 \qquad \text{on} \quad S_B \ (\text{body surface})\,, \tag{8.3.6}$$

$$\phi^D - \phi^I \qquad \text{outgoing at infinity}\,. \tag{8.3.7}$$

ϕ^I represents the incident wave potential. Thus, ϕ^D represents the *diffraction* potential when the body is held stationary in incoming waves. Using the generalized normal introduced in Eq. (8.2.4), we define ϕ_α to satisfy Eqs. (8.3.3)–(8.3.5) and

$$\frac{\partial\phi_\alpha}{\partial n} = n_\alpha \qquad \text{on} \quad S_B\,, \tag{8.3.8}$$

$$\phi_\alpha \qquad \text{outgoing at infinity}\,. \tag{8.3.9}$$

It is obvious that the total potential ϕ of Eq. (8.3.2) satisfies

$$\frac{\partial\phi}{\partial n} = \sum_\alpha V_\alpha n_\alpha \quad \text{on} \quad S_B\,, \tag{8.3.10}$$

hence $\mathbf{\Phi}$ satisfies Eq. (8.2.14). Each ϕ_α corresponds to a generalized mode of forced motion with unit body velocity and is a *radiation* potential.

The advantage of the decomposition is that the component problems for ϕ^D and ϕ_α involve only hydrodynamics and can be solved separately first. The results are then used in Eq. (8.2.47) or (8.2.54) to determine the body motion. The solution of ϕ^D and ϕ_α is usually the most difficult part of the entire task.

For very large structures, elastic deformation due to wave forces may be appreciable. If the motion of the body surface is decomposed into real-valued normal modes, then decomposition can still be introduced with suitable reinterpretation of the generalized normal n_α.

We shall always assume that sufficiently far from the body or variable depth, the sea bottom is horizontal at the depth h. We further assume a

plane incident wave propagating in the direction $\theta = \theta_I$; the corresponding potential is

$$\phi^I = \frac{-igA}{\omega} \frac{\cosh k(z+h)}{\cosh kh} e^{ikr\cos(\theta-\theta_I)} . \tag{8.3.11}$$

8.3.2 Exciting and Restoring Forces; Added Mass and Radiation Damping for a Body of Arbitrary Shape

We now introduce some general definitions applicable to a body of arbitrary shape.

The αth component of the generalized hydrodynamic force on the body is

$$\mathscr{F}_\alpha = \iint_{S_B} p n_\alpha \, dS = \mathrm{Re}\left(F_\alpha e^{-i\omega t}\right), \tag{8.3.12}$$

where

$$F_\alpha = i\rho\omega \iint_{S_B} \phi n_\alpha \, dS . \tag{8.3.13}$$

Substituting Eq. (8.3.2) into Eq. (8.3.13), we get

$$F_\alpha = i\rho\omega \iint_{S_B} \phi^D n_\alpha \, dS + \sum_\beta i\rho\omega V_\beta \iint_{S_B} \phi_\beta n_\alpha \, dS . \tag{8.3.14}$$

We also denote

$$\begin{aligned} F_\alpha^D &= i\rho\omega \iint_{S_B} \phi^D n_\alpha \, dS , \\ f_{\beta\alpha} &= i\rho\omega \iint_{S_B} \phi_\beta n_\alpha \, dS \end{aligned} \tag{8.3.15}$$

so that

$$F_\alpha = F_\alpha^D + \sum_\beta V_\beta f_{\beta\alpha} . \tag{8.3.16}$$

The vector $\{F_\alpha^D\}$ is the *exciting force* on a stationary body due to diffraction, while the matrix $[f_{\beta\alpha}]$ is called the *restoring force* matrix. The component $f_{\beta\alpha}$ represents the hydrodynamic reaction in direction α due to

the normal mode β. Consider the effect of the β mode only. The restoring force is, without summing over β,

$$\begin{aligned}
&\mathrm{Re}\,(V_\beta f_{\beta\alpha} e^{-i\omega t}) \\
&\quad = \mathrm{Re}\,[(\mathrm{Re}\, f_{\beta\alpha} + i\,\mathrm{Im}\, f_{\beta\alpha}) V_\beta e^{-i\omega t}] \\
&\quad = \mathrm{Re}\left[\left(i\rho\omega \iint_{S_B} \mathrm{Re}\,\phi_\beta n_\alpha\, dS - \rho\omega \iint_{S_B} \mathrm{Im}\,\phi_\beta n_\alpha\, dS\right) \cdot V_\beta e^{-i\omega t}\right] \\
&\quad = -\left(\rho \iint_{S_B} \mathrm{Re}\,\phi_\beta n_\alpha\, dS\right) \mathrm{Re}\,\frac{d}{dt}(V_\beta e^{-i\omega t}) \\
&\qquad -\left(\rho\omega \iint_{S_B} \mathrm{Im}\,\phi_\beta n_\alpha\, dS\right) \mathrm{Re}\,(V_\beta e^{-i\omega t}) \\
&\quad = -\left(\rho \iint_{S_B} \mathrm{Re}\,\phi_\beta n_\alpha\, dS\right) \ddot{X}_\beta - \left(\rho\omega \iint_{S_B} \mathrm{Im}\,\phi_\beta n_\alpha\, dS\right) \dot{X}_\beta\,.
\end{aligned} \tag{8.3.17}$$

The first integral above is proportional to the body acceleration and is the hydrodynamic inertia. We therefore call the matrix

$$[\mu]: \quad \mu_{\beta\alpha} = \rho \iint_{S_B} \mathrm{Re}\,\phi_\beta n_\alpha\, dS = \frac{1}{\omega}\,\mathrm{Im}\, f_{\beta\alpha} \tag{8.3.18}$$

the *added mass matrix*. The second integral in Eq. (8.3.17) is proportional to the body velocity and is expected to lead to damping, as will be shown. We call the matrix

$$[\lambda]: \quad \lambda_{\beta\alpha} = \rho\omega \iint_{S_B} \mathrm{Im}\,\phi_\beta n_\alpha\, dS = -\mathrm{Re}\, f_{\beta\alpha} \tag{8.3.19}$$

the *radiation damping matrix*. In terms of these matrices the restoring force due to all six modes is expressed as

$$\mathscr{F}_\alpha^R = -\sum_\beta \mu_{\beta\alpha}\ddot{X}_\beta - \sum_\beta \lambda_{\beta\alpha}\dot{X}_\beta\,, \quad \text{so that} \quad \mathscr{F}_\alpha = \mathscr{F}_\alpha^D + \mathscr{F}_\alpha^R\,. \tag{8.3.20}$$

To justify the name "damping matrix" for $[\lambda]$, let us consider the average rate of work done *by* the body *to* the fluid over a period:

$$\overline{\dot{E}} = -\sum_\alpha \overline{\mathscr{F}_\alpha^R \dot{X}_\alpha} = \sum_{\alpha,\beta} \mu_{\beta\alpha}\overline{\ddot{X}_\beta \dot{X}_\alpha} + \sum_{\alpha,\beta} \lambda_{\beta\alpha}\overline{\dot{X}_\beta \dot{X}_\alpha}\,. \tag{8.3.21}$$

Because $\mu_{\alpha\beta} = \mu_{\beta\alpha}$, which will be proven later, the first term may be written

$$\frac{1}{2}\sum_{\alpha,\beta}\mu_{\beta\alpha}\overline{(\ddot{X}_\beta\dot{X}_\alpha + \dot{X}_\alpha\ddot{X}_\beta)} = \frac{1}{2}\sum_{\alpha,\beta}\mu_{\beta\alpha}\overline{\frac{d}{dt}\dot{X}_\beta\dot{X}_\alpha} = 0\,, \tag{8.3.22}$$

which vanishes due to periodicity. Thus,

$$\overline{\dot{E}} = \sum_{\alpha,\beta}\lambda_{\beta\alpha}\overline{\dot{X}_\beta\dot{X}_\alpha} \tag{8.3.23}$$

and $[\lambda]$ is associated with the energy given away by the oscillating body, hence the name *radiation damping*.

Finally, with these definitions, the matrix equation for the rigid body (8.2.47) may be written

$$[-\omega^2([M]+[\mu]) + [C] - i\omega[\lambda]]\{\xi\} = \{F^D\} + \{\mathbb{F}\}\,, \tag{8.3.24}$$

where $\{\xi\}$ is the amplitude of $\{X\}$:

$$\{X\} = \mathrm{Re}\,\{\xi\}e^{-i\omega t}\,. \tag{8.3.25}$$

From Eqs. (8.2.49) and (8.2.50), $[M]$ and $[C]$ are known from the equilibrium geometry of the body. Solutions of the hydrodynamic boundary-value problems then give $[\mu]$, $[\lambda]$, and $\{F^D\}$. Once the information for the constraint is known, Eq. (8.3.24) may be solved for $\{\xi\}$.

8.4 Formal Representations of Velocity Potential when h = Constant

8.4.1 Away from the Body

Let all the geometrical departures (bodies, topography, etc.) from a sea of constant depth be confined in an imaginary vertical cylinder of finite size. In the exterior of this cylinder the general solution can be represented analytically in the form of an eigenfunction expansion, as shown below.

Two Dimensions

By separation of variables, $\phi = \psi(x)f(z)$, it is easy to show that $\psi(x) = e^{\pm ikx}$ and that

$$f'' - k^2 f = 0\,, \quad -h < z < 0 \tag{8.4.1a}$$

$$f' - \sigma f = 0\,, \quad z = 0\,, \tag{8.4.1b}$$

$$f' = 0\,, \quad z = -h \tag{8.4.1c}$$

with $\sigma = \omega^2/g$. This is an eigenvalue problem of the Stürm–Liouville type. The solution is proportional to $\cosh k(z+h)$ and the eigenvalue condition for k is the usual dispersion relation

$$\sigma = k \tanh kh\,. \tag{8.4.2}$$

Let us examine Eq. (8.4.2) graphically. There is a pair of real roots which are familiar; see Fig. 8.3. Both of these roots $\pm k$ correspond to the same normalized eigenfunction; hence only the positive real root needs to be

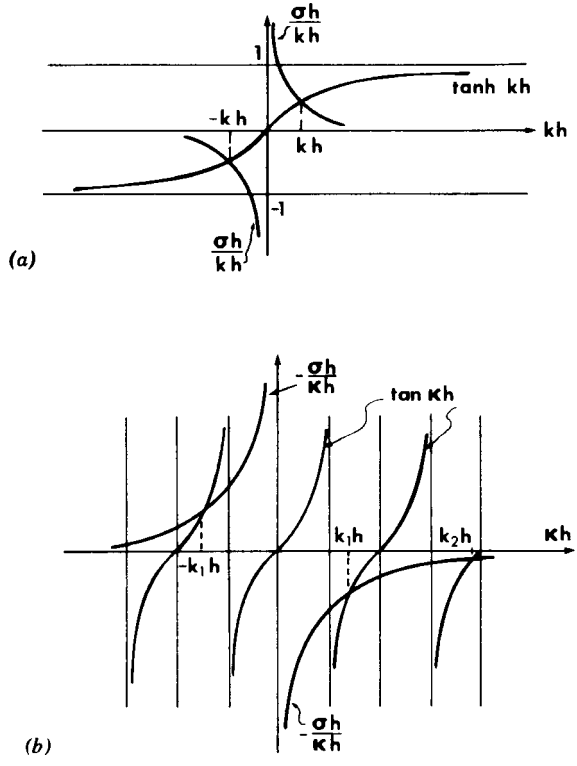

Figure 8.3: Graphical solution of dispersion relation: (a) real solutions and (b) imaginary solutions.

considered in the future. For later convenience, we introduce the normalized eigenfunction:

$$f_0(z) = \frac{\sqrt{2}\cosh k(z+h)}{(h+\sigma^{-1}\sinh^2 kh)^{1/2}} \quad \text{so that} \quad \int_{-h}^{0} f_0^2(z)\,dz = 1\,. \tag{8.4.3}$$

In addition, there are also imaginary eigenvalues $k = i\kappa$ corresponding to the real solutions of

$$\sigma = -\kappa \tan \kappa h\,. \tag{8.4.4}$$

Graphically, these roots are the intersections of $-\sigma h/\kappa h$ and $\tan\,\kappa h$, as shown in Fig. 8.3(b). Since $\tan \kappa h$ has infinitely many branches, there is an infinite number of discrete roots $\kappa = \pm k_n$. Again it is only necessary to consider positive k_n. From Fig. 8.3(b), it is evident that

$$\frac{\pi}{2} < k_1 h < \pi\,, \quad \frac{3\pi}{2} < k_2 h < 2\pi\,, \quad \left(n - \frac{1}{2}\right)\pi < k_n h < n\pi\,. \tag{8.4.5}$$

As n becomes large, $k_n h$ approaches $n\pi$. The corresponding normalized eigenfunctions are

$$f_n(z) = \frac{\sqrt{2}\cos k_n(z+h)}{(h-\sigma^{-1}\sin^2 k_n h)^{1/2}}\,, \quad \int_{-h}^{0} f_n^2\,dz = 1\,. \tag{8.4.6}$$

By straightforward integration and by using the eigenvalue condition (8.4.2) or (8.4.4), it can be shown that distinct eigenfunctions are orthogonal to one another, that is,

$$\int_{-h}^{0} f_m(z) f_n(z)\,dz = \delta_{mn}\,, \quad m,n = 0,1,2,\ldots\,. \tag{8.4.7}$$

Kreisel (1949) has proven that the set $\{f_n\}$, $n = 0,1,2,\ldots$, is complete so that any function $G(z)$ in the interval $z \in [-h,0]$ can be represented by a Fourier series based on $\{f_n\}$. Consequently, one can use the series

$$\phi(x,z) = a_0 f_0(z) e^{\pm ikx} + \sum_{n=1}^{\infty} b_n f_n(z) e^{\mp k_n x} \quad \begin{cases} x_+ < x < \infty \\ x_- > x > -\infty \end{cases} \tag{8.4.8}$$

to represent the potential of a radiated or scattered wave. The first term corresponds to the propagating mode, while the series terms are only of local importance and are called the *evanescent* modes.

Three-Dimensional Eigensolutions in Cylindrical Polar Coordinates

The Laplace equation in polar coordinates is

$$\frac{1}{r}\frac{\partial}{\partial r}\left(r\frac{\partial\phi}{\partial r}\right)+\frac{1}{r^2}\frac{\partial^2\phi}{\partial\theta^2}+\frac{\partial^2\phi}{\partial z^2}=0\,. \tag{8.4.9}$$

The eigensolution corresponding to the real and the imaginary eigenvalues are

$$\left\{\begin{matrix}H_m^{(1)}(kr)\\H_m^{(2)}(kr)\end{matrix}\right\}\left\{\begin{matrix}\cos m\theta\\\sin m\theta\end{matrix}\right\}f_0(z)\,,\quad m=0,1,2,3,\ldots$$

$$\left\{\begin{matrix}I_m(k_nr)\\K_m(k_nr)\end{matrix}\right\}\left\{\begin{matrix}\cos m\theta\\\sin m\theta\end{matrix}\right\}f_n(z)\,,\quad n=1,2,3,\ldots \tag{8.4.10}$$

where $H_m^{(1)}$ and $H_m^{(2)}$ are the Hankel functions of the first and second kinds, and I_m and K_m are the modified Bessel functions of the first and second kinds, respectively. The most general representation which satisfies the radiation condition at infinity is

$$\begin{aligned}\phi=&\sum_m H_m^{(1)}(kr)(\alpha_{0m}\cos m\theta+\beta_{0m}\sin m\theta)f_0(z)\\&+\sum_m\sum_n K_m(k_nr)(\alpha_{nm}\cos m\theta+\beta_{nm}\sin m\theta)f_n(z)\,.\end{aligned} \tag{8.4.11}$$

Because of the exponential attenuation with r, terms associated with $K_m(k_nr)$ are the evanescent modes.

From the general representations (8.4.8) and (8.4.11) we may express the radiation condition in more explicit mathematical forms as follows:

Two Dimensions: For $\phi=\phi^S\equiv\phi^D-\phi^I$, or ϕ_α

$$\phi\to-\frac{ig\mathcal{A}_\pm}{\omega}\frac{\cosh k(z+h)}{\cosh kh}e^{\pm ikx}\quad\text{as}\quad kx\to\pm\infty\,, \tag{8.4.12}$$

or equivalently

$$\frac{\partial\phi}{\partial x}\mp ik\phi\to0\quad\text{as}\quad kx\to\pm\infty\,. \tag{8.4.13}$$

Three Dimensions: With the asymptotic formula for $H_m^{(1)}$, the wave potential can be written

$$\phi \sim -\frac{ig}{\omega}\sum_m H_m^{(1)}(kr)(\alpha'_{0m}\cos m\theta + \beta'_{0m}\sin m\theta)\frac{\cosh k(z+h)}{\cosh kh}$$

$$\sim \left\{\sum_m (\alpha'_{0m}\cos m\theta + \beta'_{0m}\sin m\theta)e^{-im\pi/2}\right\}$$

$$\cdot(-)\frac{ig}{\omega}\left(\frac{2}{\pi kr}\right)^{1/2} e^{ikr-i\pi/4}\frac{\cosh k(z+h)}{\cosh kh}\,. \tag{8.4.14}$$

Let us denote the quantity inside { } above by $\mathcal{A}(\theta)$; then

$$\phi \sim \frac{-ig\mathcal{A}(\theta)}{\omega}\left(\frac{2}{\pi kr}\right)^{1/2} e^{ikr-i\pi/4}\frac{\cosh k(z+h)}{\cosh kh}\,, \quad kr\to\infty\,. \tag{8.4.15}$$

$\mathcal{A}(\theta)$ represents the angular variation of the radially spreading wave. By differentiation, the above statement can be expressed alternatively as

$$(kr)^{1/2}\left(\frac{\partial\phi}{\partial r} - ik\phi\right) \to 0\,, \quad kr\to\infty \tag{8.4.16}$$

just as the case for shallow water waves.

Exercise 8.2

In a sea of constant depth, a row of equally spaced, identical bodies symmetrical about their axes parallel to x are fixed along the y axis. A train of plane waves is incident in the direction of positive x. Formulate the problem. Find the most general expressions for the velocity potential on the reflection and transmission sides. Give the explicit forms of the evanescent and the propagating modes. What is the effect of spacing on the number of propagating modes?

8.4.2 The Entire Fluid Domain

A formal solution for the whole fluid domain is possible by the use of Green's theorem and the so-called Green function.

For two twice-differentiable functions f and g, Green's theorem is

$$\iiint_\Omega (f\nabla^2 g - g\nabla^2 f)\,d\Omega = \iint_{\partial\Omega}\left(f\frac{\partial g}{\partial n} - g\frac{\partial f}{\partial n}\right)dS\,, \tag{8.4.17}$$

where Ω is a closed volume, $\partial\Omega$ its boundary, and $\mathbf{n}$ a unit normal to $\partial\Omega$ and outward from Ω.

The Green function $G(\mathbf{x}|\mathbf{x}_0)$ is defined to be the potential at any field point $\mathbf{x}$ due to an oscillating source of unit strength at $\mathbf{x}_0$. The governing conditions for G are

Two Dimensions: $\mathbf{x} = (x, z)$, $\mathbf{x}_0 = (x_0, z_0)$

$$\left(\frac{\partial^2}{\partial x^2} + \frac{\partial^2}{\partial z^2}\right) G = \delta(x - x_0)\delta(z - z_0) \quad \text{in the fluid}\,, \tag{8.4.18}$$

$$\frac{\partial G}{\partial z} - \sigma G = 0\,, \quad \sigma = \frac{\omega^2}{g},\ z = 0\,, \tag{8.4.19}$$

$$\frac{\partial G}{\partial z} = 0\,, \quad z = -h\,, \tag{8.4.20}$$

$$\frac{\partial G}{\partial x} \mp ikG = 0\,, \quad k|x - x_0| \sim \infty\,. \tag{8.4.21}$$

Three Dimensions: $\mathbf{x} = (x, y, z)$, $\mathbf{x}_0 = (x_0, y_0, z_0)$. Equations (8.4.19) and (8.4.20) are still valid but Eqs. (8.4.18) and (8.4.21) must be replaced by

$$\left(\frac{\partial^2}{\partial x^2} + \frac{\partial^2}{\partial y^2} + \frac{\partial^2}{\partial z^2}\right) G = \delta(x - x_0)\delta(y - y_0)\delta(z - z_0)\,, \tag{8.4.22}$$

$$(kr)^{1/2}\left(\frac{\partial G}{\partial r} - ikG\right) \to 0\,, \quad kr \sim \infty\,. \tag{8.4.23}$$

The depth h is constant everywhere and the differentiations refer to $\mathbf{x}$ only.

Postponing the details of G, let us first apply Green's theorem to a radiation or a scattering potential and to the Green function, that is, $f = \phi$ where $\phi = \phi^R$ or ϕ^S and $g = G$. Consider only the three-dimensional case and let Ω be the control volume bounded by the free surface S_F, the body surface S_B, the sea bottom B_0, and a vertical circular cylinder S_∞ of great radius surrounding the body. For simplicity, the sea bottom for the radiation or the scattering problem is assumed to be horizontal everywhere, but it is not difficult to extend to the case where the bottom irregularity is confined in a finite region near the body. It follows from Eq. (8.4.17) that

$$\iiint_{\Omega} (\phi \nabla^2 G - G \nabla^2 \phi)\, d\Omega$$
$$= \left\{ \iint_{S_F} + \iint_{S_B} + \iint_{B_0} + \iint_{S_\infty} \right\} \left(\phi \frac{\partial G}{\partial n} - G \frac{\partial \phi}{\partial n} \right) dS\,.$$

The field equations for ϕ and G and the property of the δ function reduce the left-hand side to simply $\phi(\mathbf{x}_0)$. Because of the boundary conditions on ϕ and G, the surface integrals on S_F, B_0, and S_∞ vanish. Thus the preceding equation becomes

$$\phi(\mathbf{x}_0) = \iint_{S_B} \left(\phi \frac{\partial G}{\partial n} - G \frac{\partial \phi}{\partial n} \right) dS\,, \quad \mathbf{x}_0 \in \Omega,\ \notin S_B\,. \tag{8.4.24}$$

Now the Green function is symmetric with respect to the interchange of $\mathbf{x}$ and $\mathbf{x}_0$, that is,

$$G(\mathbf{x}|\mathbf{x}_0) = G(\mathbf{x}_0|\mathbf{x})\,. \tag{8.4.25}$$

This fact may be proven straightforwardly by introducing another Green function with the source at $\mathbf{x}'$, $G(\mathbf{x}|\mathbf{x}')$, and applying Green's formula to $G(\mathbf{x}|\mathbf{x}_0)$ and $G(\mathbf{x}|\mathbf{x}')$. With Eq. (8.4.25) one can interchange $\mathbf{x}_0$ and $\mathbf{x}$ in Eq. (8.4.24) to get

$$\phi(\mathbf{x}) = \iint_{S_B} \left[\phi(\mathbf{x}_0) \frac{\partial G}{\partial n_0} - G \frac{\partial \phi(\mathbf{x}_0)}{\partial n_0} \right] dS_0\,, \quad \mathbf{x} \in \Omega,\ \notin S_B\,. \tag{8.4.26}$$

Thus, if ϕ and $\partial\phi/\partial n$ are known on the body surface, $\phi(\mathbf{x})$ is known everywhere. But in practice only the normal velocity $\partial\phi/\partial n$ is prescribed on the body, while $\phi(\mathbf{x}_0)$ is not known *a priori*. The representation (8.4.26) is therefore only formal.

While other applications of Eq. (8.4.26) will be discussed later, we shall derive here an asymptotic approximation of ϕ for $kr \gg 1$. For this purpose we need to obtain G explicitly. For three dimensions, one form of G is cited below, while further information may be found in Appendix 8.A.

$$G(\mathbf{x}|\mathbf{x}_0) = -\frac{i}{2} \frac{\sigma^2 - k^2}{h(k^2 - \sigma^2) + \sigma} \cosh k(z_0 + h) \cosh k(z + h) H_0^{(1)}(kR)$$
$$+ \frac{1}{\pi} \sum_{n=1}^{\infty} \frac{k_n^2 + \sigma^2}{h(k_n^2 + \sigma^2) - \sigma} \cos k_n(z_0 + h) \cos k_n(z + h) K_0(k_n R)\,, \tag{8.4.27}$$

where

$$R = [(x - x_0)^2 + (y - y_0)^2]^{1/2} .$$

For $kR \gg 1$ it is sufficient to keep the propagating mode only which may be written

$$G(\mathbf{x}|\mathbf{x}_0) \cong C_0 \cosh k(z+h) \cosh k(z_0+h) \left(\frac{2}{\pi kR}\right)^{1/2} e^{ikR - i\pi/4} , \qquad (8.4.28)$$

where C_0 is a constant coefficient

$$C_0 = \frac{(-\frac{1}{2}i)(\sigma^2 - k^2)}{h(k^2 - \sigma^2) + \sigma} . \qquad (8.4.29)$$

Using polar coordinates

$$(x, y) = r(\cos\theta, \sin\theta) , \quad (x_0, y_0) = r_0(\cos\theta_0, \sin\theta_0)$$

and approximating R for $r \gg r_0$

$$R = [r^2 + r_0^2 - 2rr_0 \cos(\theta - \theta_0)]^{1/2} \cong r - r_0 \cos(\theta - \theta_0) ,$$

we get

$$G(\mathbf{x}|\mathbf{x}_0) \cong C_0 \cosh k(z + h) \cosh k(z_0 + h) \times \left(\frac{2}{\pi kr}\right)^{1/2} e^{ikr} e^{-ikr_0 \cos(\theta - \theta_0)} e^{-i\pi/4} . \qquad (8.4.30)$$

Substituting this into Eq. (8.4.26), we get

$$\phi(\mathbf{x}) \cong C_0 \cosh^2 kh \frac{\cosh k(z + h)}{\cosh kh} \left(\frac{2}{\pi kr}\right)^{1/2} e^{ikr - i\pi/4} \iint_{S_B} dS_0 \times \left(\phi \frac{\partial}{\partial n_0} - \frac{\partial \phi}{\partial n_0}\right) \frac{\cosh k(z_0 + h)}{\cosh kh} e^{-ikr_0 \cos(\theta - \theta_0)} , \qquad (8.4.31)$$

which can also be written in the form of Eq. (8.4.15). This result gives a relation between the far-field amplitude $\mathcal{A}(\theta)$ and the values of ϕ and $\partial\phi/\partial n_0$ on S_B:

$$\mathcal{A}(\theta) = \frac{i\omega}{g} C_0 \cosh^2 kh \iint_{S_B} dS_0 \left(\phi \frac{\partial}{\partial n_0} - \frac{\partial \phi}{\partial n_0}\right) \times \frac{\cosh k(z_0 + h)}{\cosh kh} e^{-ikr_0 \cos(\theta - \theta_0)} . \qquad (8.4.32)$$

When ϕ and $\partial\phi/\partial n$ are known on the body, $\mathcal{A}(\theta)$ is obtainable by quadrature. In Russian literature the integral above is used to define the so-called Kochin's H function.

For two dimensions the Green function may be expressed as

$$\begin{aligned} G(\mathbf{x}|\mathbf{x}_0) = -\frac{i}{k}\left(h+\frac{1}{\sigma}\sinh^2 kh\right)^{-1} e^{ik|x-x_0|} \\ \times \cosh k(z_0+h)\cosh k(z+h) \\ + \sum_{n=1}^{\infty}\frac{1}{k_n}\left(h-\frac{1}{\sigma}\sin^2 k_n h\right)^{-1} e^{-k_n|x-x_0|} \\ \times \cos k_n(z_0+h)\cos k_n(z+h)\,. \end{aligned} \tag{8.4.33}$$

The full derivation is given in Appendix 8.A. For $|kx| \gg 1$, only the propagating mode needs to be kept and Eq. (8.4.26) may be written

$$\begin{aligned} \phi(\mathbf{x}) \cong -\frac{i}{k}\frac{\cosh^2 khe^{\pm ikx}}{h+(1/\sigma)\sinh^2 kh}\frac{\cosh k(z+h)}{\cosh kh} \\ \times \int_{S_B} dS_0\left(\phi\frac{\partial}{\partial n_0}-\frac{\partial\phi}{\partial n_0}\right)e^{\mp ikx_0}\frac{\cosh k(z_0+h)}{\cosh kh}\,. \end{aligned} \tag{8.4.34}$$

The wave amplitude at $x \sim \pm\infty$ is

$$\begin{aligned} \mathcal{A}_{\pm} = \frac{\omega}{gk}\frac{\cosh^2 kh}{h+(1/\sigma)\sinh^2 kh}\int_{S_B} dS_0 \\ \times\left(\phi\frac{\partial}{\partial n_0}-\frac{\partial\phi}{\partial n_0}\right)e^{\mp ikx_0}\frac{\cosh k(z_0+h)}{\cosh kh}\,. \end{aligned} \tag{8.4.35}$$

In this form $\mathcal{A}_{\pm}$ is essentially the two-dimensional Kochin H function.

We now leave generalities behind for a specific solution.

8.5 Scattering by a Vertical Cylinder with Circular Cross Section

There are only a few geometries in the theory of water-wave diffraction where exact analytical solutions have been found. One of them is a vertical cylinder of circular cross section, extending from the sea bottom to the free surface. Without loss of generality, we take the incident wave to arrive from $x \sim -\infty$, as given by Eq. (8.3.11). The orthogonality property (8.4.7)

can be used to show that only the propagating mode matters and the evanescent modes vanish identically.[1] Consequently, the total potential can be expressed

$$\phi = -\frac{ig}{\omega}\eta(x,y)\frac{\cosh k(z+h)}{\cosh kh}\,, \tag{8.5.1}$$

where η is the free-surface displacement and satisfies the two-dimensional Helmholtz equation. The free surface of the incident wave is, in terms of partial waves,

$$\begin{aligned}\eta^I &= Ae^{ikx} = Ae^{ikr\cos\theta}\\ &= A\sum_{m=0}^{\infty}\varepsilon_m(i)^m J_m(kr)\cos m\theta\,.\end{aligned} \tag{8.5.2}$$

The total free-surface displacement is given by

$$\eta = A\sum_{m=0}^{\infty}\varepsilon_m(i)^m\left\{J_m(kr) - H_m(kr)\frac{J'_m(ka)}{H'_m(ka)}\right\}\cos m\theta\,, \tag{8.5.3}$$

where $H_m \equiv H_m^{(1)}$ and $H'_m(s) \equiv dH_m/ds$ for the sake of brevity. The dynamic pressure may be calculated as

$$p(r,\theta,z) = i\omega\rho\phi = \rho g\eta\frac{\cosh k(z+h)}{\cosh kh}\,. \tag{8.5.4}$$

In general, the pressure at any point on the cylinder can be calculated by summing up the infinite series

$$\begin{aligned}p(a,\theta,z) &= \rho gA\frac{\cosh k(z+h)}{\cosh kh}\\ &\quad\times\sum_{m=0}^{\infty}\varepsilon_m(i)^m\left\{J_m(ka) - H_m(ka)\frac{J'_m(ka)}{H'_m(ka)}\right\}\cos m\theta\,.\end{aligned} \tag{8.5.5}$$

In view of the Wronskian identity Eq. (8.9.20), Chapter Four, the pressure may be rewritten

$$p(a,\theta,z) = \rho gA\frac{\cosh k(z+h)}{\cosh kh}\sum_{m=0}^{\infty}\frac{2(i)^{(m+1)}\varepsilon_m\cos m\theta}{\pi kaH'_m(ka)}\,. \tag{8.5.6}$$

The series also represents the normalized free-surface displacement around the cylinder. For small ka, the pressure p is rather uniform around the

[1] This result holds for a vertical cylinder of arbitrary cross section.

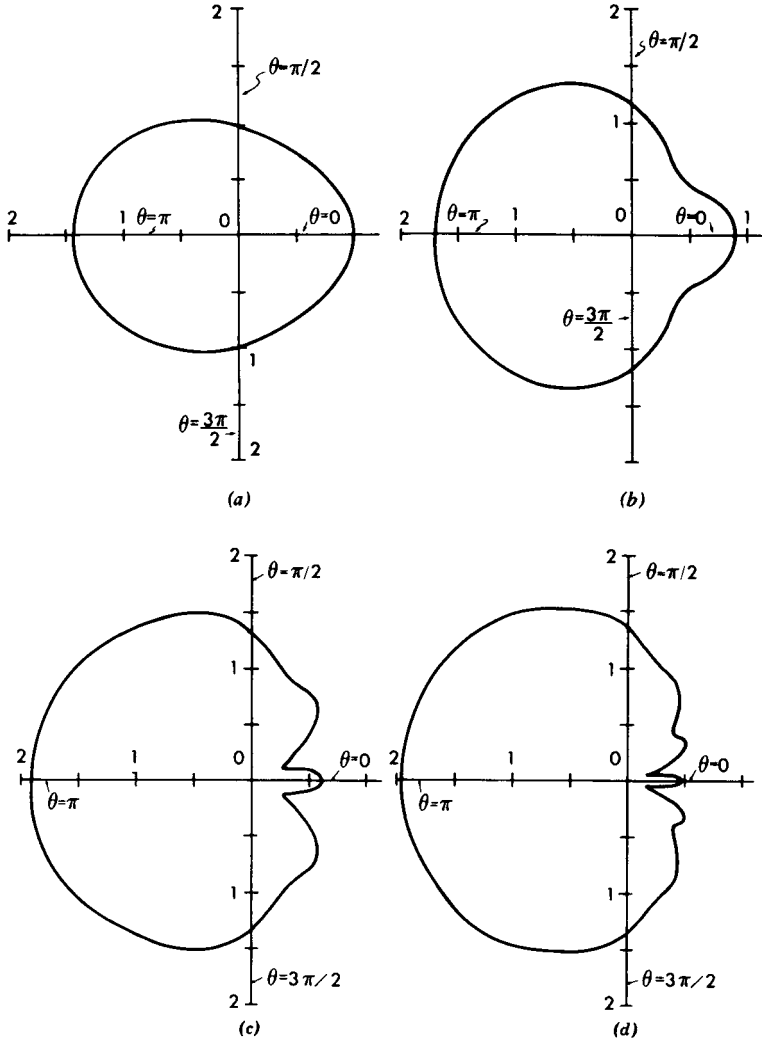

Figure 8.4: Polar distribution of run-up on a circular cylinder extending the entire sea depth. Incident wave is in the direction $\theta = 0$. (*a*) $ka = 0.5$, (*b*) $ka = 1.0$, (*c*) $ka = 3.0$, and (*d*) $ka = 5.0$.

cylinder. As ka increases, the variation becomes more complex, as shown in Fig. 8.4.

Let us integrate the pressure on the cylinder. On a horizontal slice of a unit height, the force in the direction of wave propagation is

$$\frac{dF_x}{dz} = -a \int_0^{2\pi} p(a, \theta, z) \cos\theta \, d\theta \, .$$

By the orthogonality of cosines, only the term $m = 1$ in the series of Eq. (8.5.6) remains,

$$\frac{dF_x}{dz} = \frac{4A}{ka} \frac{\rho g a}{H_1'(ka)} \frac{\cosh k(z+h)}{\cosh kh} \, . \tag{8.5.7}$$

The total horizontal force on the cylinder is then

$$F_x = \int_{-h}^{0} \frac{dF_x}{dz} \, dz = \frac{4\rho g A a h}{ka H_1'(ka)} \frac{\tanh kh}{kh} \, . \tag{8.5.8}$$

The total moment about an axis parallel to y passing through the bottom of the cylinder is

$$\begin{aligned} M_y &= -\int_{-h}^{0} (z+h) \frac{dF_x}{dz} \, dz \\ &= -\frac{4\rho g A a h^2}{ka H_1'(ka)} \frac{kh \sinh kh - \cosh kh + 1}{(kh)^2 \cosh kh} \, , \end{aligned} \tag{8.5.9}$$

which is positive counterclockwise. Formulas (8.5.8) and (8.5.9) were first given by McCamy and Fuchs (1954). To show the dependence of F_x and M_y on ka, it is only necessary to plot the magnitude and the phase of the factor $[kaH_1'(ka)]^{-1}$:

$$\left| \frac{1}{kaH_1'(ka)} \right| = (ka)^{-1} \{ [J_1'(ka)]^2 + [Y_1'(ka)]^2 \}^{-1/2} \, , \tag{8.5.10}$$

and the phase $\tan\delta = Y_1'(ka)/J_1'(ka)$; see Fig. 8.5.

Let us introduce the inertia and drag coefficients per unit height, analogous, respectively, to the added mass and damping coefficients in the restoring forces on a body in forced radiation, as defined in more general terms in Section 8.3.2. For a unit horizontal slice of the cylinder we write

$$\mathrm{Re}\left(\frac{dF_x}{dz} e^{-i\omega t} \right) = \rho \pi a^2 (C_M \dot{U} + \omega C_D U) \, , \tag{8.5.11}$$

where U is the velocity of the incident wave at $x = 0$ in the absence of the cylinder,

$$U = \mathrm{Re} \frac{\partial \phi^I}{\partial x} e^{-i\omega t} = \frac{gkA}{\omega} \frac{\cosh k(z+h)}{\cosh kh} \cos\omega t \, . \tag{8.5.12}$$

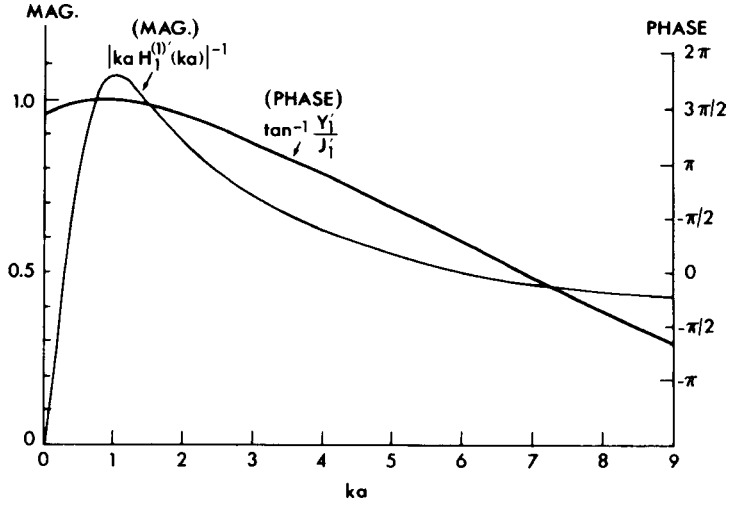

Figure 8.5: Magnitude and phase of the factor $(kaH_1')^{-1}$, which describes the dependence of force and moment on ka [cf. Eqs. (8.5.8) and (8.5.9)].

From Eq. (8.5.7) it can be deduced that

$$\mathrm{Re}\left(\frac{dF_x}{dz}e^{-i\omega t}\right) = \frac{4\rho g a A}{ka|H_1'(ka)|^2}\frac{\cosh k(z+h)}{\cosh kh}[J_1'(ka)\cos\omega t - Y_1'(ka)\sin\omega t]\,.$$

Upon comparing with Eq. (8.5.11), we obtain

$$C_M = \frac{4}{\pi}\frac{Y_1'(ka)}{(ka)^2|H_1'(ka)|^2}\,, \tag{8.5.13a}$$

$$C_D = \frac{4}{\pi}\frac{J_1'(ka)}{(ka)^2|H_1'(ka)|^2}\,. \tag{8.5.13b}$$

The inertia coefficient is plotted in Fig. 8.6. It is important that even in the absence of viscosity the cylinder experiences a drag (damping) force, which is due to the transport of energy toward infinity by scattered waves.

For a small cylinder we have approximately

$$C_M \cong 2 \tag{8.5.14}$$

and

$$C_D \cong \frac{\pi(ka)^2}{2}\,. \tag{8.5.15}$$

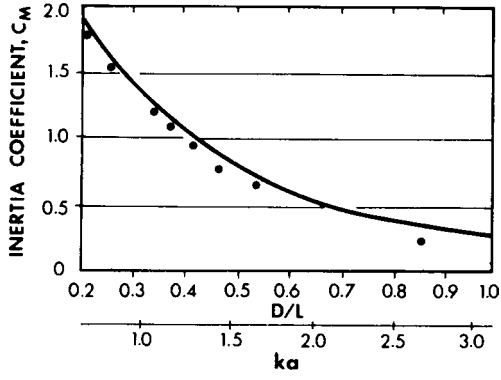

Figure 8.6: Inertia coefficient C_M by Eq. (8.5.13a) and by experiment (from Charkrabarti and Tam, 1975, *J. Ship Res.* Reproduced by permission of the Society of Naval Architects and Marine Engineers).

Thus, the drag coefficient due to waves is very small; in reality, viscous effects including vortex shedding are much more dominant. Note also that the apparent mass is twice that of the accelerating circular cylinder in an otherwise calm fluid without a free surface. To help understand this limit, we examine the neighborhood of the cylinder where $r = O(a)$. By keeping only the two most important terms, $m = 0$, 1, in Eq. (8.5.3), we find

$$\begin{aligned}\phi &\simeq -\frac{igA}{\omega}\frac{\cosh k(z+h)}{\cosh kh}\left\{1 + ik\left(r + \frac{a^2}{r}\right)\cos\theta\right\} \\ &= -\frac{igA}{\omega}\frac{\cosh k(z+h)}{\cosh kh}\left\{1 + ik\left(x + \frac{a^2}{r}\cos\theta\right)\right\}. \qquad (8.5.16)\end{aligned}$$

At a fixed z, this is just the potential for an oscillating flow past a stationary circular cylinder. The first term, ikx, corresponding to the incident wave in the absence of the cylinder, gives half of C_M, while the scattered waves, due to the presence of the cylinder, gives the other half.

Not too close to the small cylinder, the amplitude of the scattered wave is, from Eq. (8.5.3),

$$\begin{aligned}\frac{\eta^S}{A} &= -H_0(kr)\frac{J_0'(ka)}{H_0'(ka)} - 2iH_1(kr)\frac{J_1'(ka)}{H_1'(ka)}\cos\theta + O(ka)^3 \\ &= \frac{\pi}{2}(ka)^2\left\{-\frac{i}{2}H_0(kr) - H_1(kr)\cos\theta\right\} + O(ka)^3. \qquad (8.5.17)\end{aligned}$$

The scattered wave therefore consists of a radially symmetric wave and a dipole-like wave; their amplitudes are, however, very small ($O(ka)^2$). Correspondingly, the damping force given by Eq. (8.5.15) is small.

The linearized theory here has been checked experimentally by Charkrabarti and Tam (1975), as shown in Fig. 8.6 for the coefficient C_M. Their measurements were taken for a cylinder of radius $a = 40.5$ in. in water depth of $h = 47.25$ in. The range of wave period was 1.0 to 3.5 s, while the incident wave amplitude was under 4.5 in.; the corresponding range of kA was $0.1 < kA < 0.38$, which included some steep waves. There was a good agreement between theory and experiment for $0.2 < ka < 0.65$. For still smaller radius or larger waves, viscous effect and flow separation became dominant which greatly affected both C_M and C_D.

Exercise 8.3

Solve the problem of a vertical circular cylinder forced to *sway* in the x direction, or to *roll* about the axis $x = 0$, $z = c$. The boundary condition on the cylinder is

$$\frac{\partial \phi}{\partial r} = U \cos\theta\,, \quad \text{sway}$$

or

$$\frac{\partial \phi}{\partial r} = \Omega(c - z)\cos\theta\,, \quad \text{roll}\,.$$

Find the added inertia and the damping force matrices by numerical summation of the series.

Exercise 8.4

Let a plane wavetrain be incident from $x \sim -\infty$ toward a vertical cylinder whose cross section is described by $r = a[1 + \varepsilon\xi(\theta)]$ with $\varepsilon \ll 1$. Show that, on a unit horizontal slice at height z,

(a) the in-line wave force is

$$f_x \cong -a \int_0^{2\pi} d\theta \{[p^{(0)} + \varepsilon(\xi p^{(0)} + p^{(1)})]\cos\theta + \varepsilon\xi' p^{(0)} \sin\theta\}_{r=a}\,;$$

(b) the transverse wave force is

$$f_y \cong -\varepsilon a \int_0^{2\pi} d\theta \{[\xi p^{(0)} + p^{(1)}]\sin\theta - \xi' p^{(0)} \cos\theta\}_{r=a}\,; \text{ and}$$

(c) the moment about the z axis is

$$m_z \cong \varepsilon a^2 \int_0^{2\pi} d\theta\, \xi' p^{(0)}(a,\theta)\,,$$

where $p = p^{(0)} + \varepsilon p^{(1)} + \cdots$.

For a slightly elliptical cylinder whose major axis is inclined at the angle α with the x axis, solve for $p^{(1)}$ explicitly and find f_x, f_y, and m_z.

8.6 General Identities for the Diffraction and Radiation of Simple Harmonic Waves

As seen in Section 4.7.4 and in many other wave problems, there are certain very general identities relating quantities of practical interest. These identities are useful for several reasons. First, they facilitate the theoretical understanding of the physical problem. Second, they provide necessary checks for an analytical or numerical theory. Third, they minimize the task of computing those quantities related by them. For constant h, many of these identities have been derived individually for a long time (Wehausen, 1971). Here we shall follow the systematic approach of Newman (1976) by selecting exhaustively various pairings of ϕ^D and ϕ_α for f and g in Green's formula (8.4.17).

Let f and g be any two velocity potentials ϕ and ψ, and let the bounding surface $\partial\Omega$ be divided into the free surface S_F, the bottom B_0, the body S_B, and a vertical circular cylinder S_∞ with an arbitrarily large radius. The volume integral in Eq. (8.4.17) clearly vanishes. By invoking the appropriate boundary conditions, neither the sea bottom B_0 nor the free surface S_F gives any contribution to the surface integral; therefore,

$$\iint_{S_B+S_\infty} \left(\phi \frac{\partial \psi}{\partial n} - \psi \frac{\partial \phi}{\partial n}\right) dS = 0\,. \tag{8.6.1}$$

If we take $f = \phi$ but $g = \psi^*$ where $(\,)^*$ denotes the complex conjugate and use the fact that ψ^* satisfies the conjugate of the equations governing ψ, it follows that

$$\iint_{S_B+S_\infty} \left[\phi \frac{\partial \psi^*}{\partial n} - \psi^* \frac{\partial \phi}{\partial n}\right] dS = 0\,. \tag{8.6.2}$$

Further information may be obtained by specifying the boundary conditions on S_B and S_∞. A general result used repeatedly later is that the

surface integral of S_∞ in Eq. (8.6.1) vanishes if ϕ and ψ are outgoing waves at infinity and satisfy Eq. (8.4.16),[2] that is,

$$\iint_{S_\infty} \left(\phi \frac{\partial \psi}{\partial n} - \psi \frac{\partial \phi}{\partial n} \right) dS = 0 \,. \tag{8.6.3}$$

As a consequence, Eq. (8.6.1) gives

$$\iint_{S_B} \left(\phi \frac{\partial \psi}{\partial n} - \psi \frac{\partial \phi}{\partial n} \right) dS = 0 \,. \tag{8.6.4}$$

We now specify ϕ and ψ even further.

8.6.1 Relations between Two Radiation Problems and their Consequences

Let $\phi = \phi_\alpha$ and $\psi = \phi_\beta$ be the radiation potentials for two normal modes. Since they both satisfy Eq. (8.4.16), Eq. (8.6.4) applies. If use is made of the boundary condition on the body, we have

$$\iint_{S_B} \phi_\beta n_\alpha \, dS = \iint_{S_B} \phi_\alpha n_\beta \, dS \,. \tag{8.6.5}$$

In view of the definitions in Eqs. (8.3.15), (8.3.18), and (8.3.19), the restoring force, the added mass, and the damping matrices must be symmetric:

$$f_{\beta\alpha} = f_{\alpha\beta} \,, \quad \mu_{\alpha\beta} = \mu_{\beta\alpha} \,, \quad \lambda_{\alpha\beta} = \lambda_{\beta\alpha} \,. \tag{8.6.6}$$

It should be stressed that there is no restriction on the symmetry of the body.

Recall that the average rate of work done by the body to water as given by Eq. (8.3.23) was deduced after using the symmetry of $\lambda_{\alpha\beta}$. Now the working rate can be alternatively obtained in terms of the total radiation potential $\phi^R = \Sigma V_\alpha \phi_\alpha$ as follows:

$$\begin{aligned} \overline{\dot{E}} &= -\frac{\mathrm{Re}}{2} \left[i\omega\rho \iint_{S_B} \phi^R \frac{\partial \phi^{R*}}{\partial n} \, dS \right] = \frac{\omega\rho}{2} \,\mathrm{Im} \iint_{S_B} \phi^R \frac{\partial \phi^{R*}}{\partial n} \, dS \\ &= \frac{\omega\rho}{2} \frac{1}{2i} \iint_{S_B} \left[\phi^R \frac{\partial \phi^{R*}}{\partial n} - \phi^{R*} \frac{\partial \phi^R}{\partial n} \right] dS \,. \end{aligned}$$

[2] Alternatively, one may regard Eq. (8.6.3) as the weak radiation condition on ϕ if ψ satisfies the strong condition (8.4.16). An application of the weak condition is discussed in Section 13.12.

From Eq. (8.6.2) the integral over S_B is the negative of a similar integral over S_∞; hence

$$\overline{\dot{E}} = \frac{\rho\omega i}{4} \iint_{S_\infty} \left[\phi^R \frac{\partial \phi^{R*}}{\partial n} - \phi^{R*} \frac{\partial \phi^R}{\partial n} \right] dS \,. \tag{8.6.7}$$

If the asymptotic expressions of ϕ^R and ϕ^{R*}, that is, Eq. (8.4.15) and its complex conjugate, are used in Eq. (8.6.7), we get

$$\overline{\dot{E}} = \frac{i\rho\omega}{4} \int_0^{2\pi} \int_{-h}^{0} \left[-\frac{ig}{\omega} \left(\frac{2}{\pi kr} \right)^{1/2} \right]^2 2ik |\mathcal{A}^R(\theta)|^2 \frac{\cosh^2 k(z+h)}{\cosh^2 kh} r \, d\theta \, dz \,, \tag{8.6.8}$$

which is non-negative. Therefore, the radiation condition is consistent with the physical fact that energy can only flow from the rigid body to water when the body is forced externally to move.[3] Let us now return to Eq. (8.3.23). Since $\dot{X}_\alpha$ and $\dot{X}_\beta$ can be arbitrarily prescribed, the non-negativeness of $\dot{E}$ implies that the damping matrix is positive semidefinite. As a corollary, the diagonal terms of $[\lambda]$, λ_{11}, λ_{22}, and λ_{33}, are each individually positive semidefinite.

The radiation damping rate may also be related to the radiated amplitude in the far field. Putting $\phi = \phi_\alpha$ and $\psi^* = \phi^*_\beta$ in Eq. (8.6.2), we get

$$\iint_{S_B} (\phi_\alpha n_\beta - \phi^*_\beta n_\alpha) \, dS = - \iint_{S_\infty} \left(\phi_\alpha \frac{\partial \phi^*_\beta}{\partial n} - \phi^*_\beta \frac{\partial \phi_\alpha}{\partial n} \right) dS \,.$$

By virtue of the symmetry relation (8.6.5), the left side is seen to be

$$2i \, \mathrm{Im} \iint_{S_B} \phi_\alpha n_\beta \, dS = \frac{2i\lambda_{\alpha\beta}}{\rho\omega} \,.$$

It follows after using the radiation condition that

$$\lambda_{\alpha\beta} = -\frac{\rho\omega}{2i} \iint_{S_\infty} \left(\phi_\alpha \frac{\partial \phi^*_\beta}{\partial n} - \phi^*_\beta \frac{\partial \phi_\alpha}{\partial n} \right) dS = \rho\omega k \iint_{S_\infty} \phi_\alpha \phi^*_\beta \, dS \,. \tag{8.6.9a}$$

In particular we have

$$\lambda_{\alpha\alpha} = -\rho\omega \, \mathrm{Im} \iint_{S_\infty} \phi_\alpha \frac{\partial \phi^*_\alpha}{\partial n} \, dS = \rho\omega k \iint_{S_\infty} |\phi_\alpha|^2 \, dS > 0 \tag{8.6.9b}$$

[3] There are special cases where an oscillating body does not radiate any energy for a particular frequency (e.g., Bessho, 1965; Frank, 1967a; Kyozuka and Yoshida, 1981).

for $\alpha = \beta$. The right-hand side of Eqs. (8.6.9a) and (8.6.9b) may be expressed in terms of far-field amplitudes, as shown below.

Two Dimensions

According to Eq. (8.4.12), the asymptotic behavior of ϕ_α is

$$\phi_\alpha \sim -\frac{ig\mathcal{A}_\alpha^\pm}{\omega} e^{\pm ikx} \frac{\cosh k(z+h)}{\cosh kh}\,, \quad x \sim \pm\infty\,, \tag{8.6.10}$$

where $\mathcal{A}_\alpha^\pm$ have the dimension of time. The right-hand side of Eq. (8.6.9a) consists of two integrals on $S_\infty^\pm$ at $x \sim \pm\infty$. By straightforward substitution, it can be shown that

$$\lambda_{\alpha\beta} = \rho g C_g (\mathcal{A}_\alpha^- \mathcal{A}_\beta^{-*} + \mathcal{A}_\alpha^+ \mathcal{A}_\beta^{+*})\,. \tag{8.6.11}$$

Three Dimensions

The asymptotic behavior is, from Eq. (8.4.15),

$$\phi_\alpha = -\frac{ig\mathcal{A}_\alpha(\theta)}{\omega} \frac{\cosh k(z+h)}{\cosh kh} \left(\frac{2}{\pi kr}\right)^{1/2} e^{ikr - i\pi/4}\,. \tag{8.6.12}$$

We leave it as an exercise to show from Eq. (8.6.9a) that

$$\lambda_{\alpha\beta} = \frac{2}{\pi k} \rho g C_g \int_0^{2\pi} \mathcal{A}_\alpha(\theta) \mathcal{A}_\beta^*(\theta)\, d\theta\,. \tag{8.6.13}$$

8.6.2 Relations between Two Diffraction Problems

Let $\phi = \phi^{(1)}$ and $\psi = \phi^{(2)}$ be two diffraction problems corresponding to different angles of incidence. As the normal velocity vanishes on the body, the surface integral on S_B in Eq. (8.6.1) vanishes. It follows that

$$\iint_{S_\infty} \left(\phi^{(1)} \frac{\partial \phi^{(2)}}{\partial n} - \phi^{(2)} \frac{\partial \phi^{(1)}}{\partial n}\right) dS = 0\,. \tag{8.6.14}$$

For the same reason, Eq. (8.6.2) gives

$$\iint_{S_\infty} \left(\phi^{(1)} \frac{\partial \phi^{(2)*}}{\partial n} - \phi^{(2)*} \frac{\partial \phi^{(1)}}{\partial n}\right) dS = 0\,. \tag{8.6.15}$$

A special case of Eq. (8.6.15) is obtained by letting $\phi^{(1)} = \phi^{(2)} = \phi$; then

$$\mathrm{Im} \iint_{S_\infty} \phi \frac{\partial \phi^*}{\partial n} \, dS = 0 \,. \tag{8.6.16}$$

The left side is proportional to the pressure work done on the surface S_∞. Hence Eq. (8.6.16) states the conservation of energy. Let us examine these results in terms of the far-field amplitudes.

Two Dimensions

Let $\phi^{(1)}(\phi^{(2)})$ be the diffraction potential with an incident wave from left (right) to right (left). The asymptotic potentials are

$$\phi^{(1)} \sim \begin{cases} e^{ikx} + R_1 e^{-ikx} \\ T_1 e^{ikx} \end{cases} \cdot \left(-\frac{igA}{\omega} \right) \frac{\cosh k(z+h)}{\cosh kh} \,, \quad \begin{matrix} x \sim -\infty \,, \\ x \sim \infty \,, \end{matrix} \tag{8.6.17}$$

and

$$\phi^{(2)} \sim \begin{cases} T_2 e^{-ikx} \\ e^{-ikx} + R_2 e^{ikx} \end{cases} \cdot \left(-\frac{igA}{\omega} \right) \frac{\cosh k(z+h)}{\cosh kh} \,, \quad \begin{matrix} x \sim -\infty \,, \\ x \sim +\infty \,. \end{matrix} \tag{8.6.18}$$

Let $S_\infty^\pm$ be two vertical lines at $x \sim \pm\infty$. Then on $S_\infty^\pm$, $\partial/\partial n = \pm \partial/\partial x$. Upon substitution of Eqs. (8.6.17) and (8.6.18) into Eq. (8.6.14), we obtain, after a little algebra,

$$T_1 = T_2 \tag{8.6.19}$$

(Kreisel, 1949). The transmission coefficient is independent of the direction of the incident wave even though the body may not possess any symmetry at all! It should be emphasized that this result does not imply the equality of two problems and their solutions; only the far fields are involved here. Performing similar computations, we get from Eq. (8.6.15)

$$R_1 T_2^* + R_2^* T_1 = 0 \tag{8.6.20}$$

(Meyer, 1955; Newman, 1965), and from Eq. (8.6.16) for a single diffraction problem

$$|R^2| + |T^2| = 1 \,. \tag{8.6.21}$$

Further inferences may be made. Using Eq. (8.6.19), Eq. (8.6.20) leads to

$$|R_1| = |R_2| \tag{8.6.22}$$

which was first obtained by Kreisel (1949) in a different way. Let δ_1^T and δ_2^R be the phase angles of the transmission and reflection coefficients as defined by

$$T_j = |T_j| e^{i\delta_j^T}\,, \quad R_j = |R_j| e^{i\delta_j^R}\,, \quad j = 1, 2\,. \tag{8.6.23}$$

It follows from Eqs. (8.6.19) and (8.6.20) that

$$\delta_1^T = \delta_2^T\,, \tag{8.6.24}$$

and

$$\delta_1^R + \delta_2^R = \delta_1^T + \delta_2^T \pm \pi \tag{8.6.25}$$

(Newman, 1965). In the special case of a symmetric body, $\delta_1^R = \delta_2^R$ and $\delta_1^T = \delta_2^T$; hence

$$\delta_1^R = \delta_1^T \pm \frac{\pi}{2}\,. \tag{8.6.26}$$

Equations (8.6.19)–(8.6.22) are extensions of similar results in Section 4.7.4 for long waves.

Three Dimensions

$$\phi^{(l)} \cong -\frac{igA}{\omega}\frac{\cosh k(z+h)}{\cosh kh} \times \left[e^{ikr\cos(\theta-\theta_l)} + \left(\frac{2}{\pi kr}\right)^{1/2} \mathcal{A}_l^S(\theta) e^{ikr - i\pi/4}\right], \quad l = 1, 2 \tag{8.6.27}$$

where $\mathcal{A}_l^S$ denotes the normalized scattered wave amplitude due to the incident wave in the direction θ_l. Substitution of Eq. (8.6.27) into Eqs. (8.6.14), (8.6.15), and (8.6.16) yields three relations governing $\mathcal{A}_l^S(\theta)$. Let us illustrate the analysis for the energy conservation theorem only. Due to Eq. (8.6.27), the left-hand side of Eq. (8.6.16) reads

$$2i\,\mathrm{Im}\int_0^{2\pi} d\theta \int_{-h}^{0} dz \frac{\cosh^2 k(z+h)}{\cosh^2 kh}\left(\frac{gA}{\omega}\right)^2 r \times \left[e^{ikr\cos(\theta-\theta_l)} + \left(\frac{2}{\pi kr}\right)^{1/2} \mathcal{A}_l^S e^{ikr - i\pi/4}\right] \times \left[-ik\cos(\theta-\theta_l) e^{-ikr\cos(\theta-\theta_l)} - ik\left(\frac{2}{\pi kr}\right)^{1/2} \mathcal{A}_l^{S^*} e^{-ikr + i\pi/4}\right].$$

After multiplying out the integrand and omitting a constant factor, we get

$$-\operatorname{Im} i \int_0^{2\pi} d\theta \left\{ \frac{2}{\pi} |\mathcal{A}_l^S(\theta)|^2 + kr \cos(\theta - \theta_l) \right.$$
$$+ \left(\frac{2}{\pi} kr\right)^{1/2} \mathcal{A}_l^S \cos(\theta - \theta_l) e^{ikr[1-\cos(\theta-\theta_l)]} e^{-i\pi/4}$$
$$\left. + \left(\frac{2}{\pi} kr\right)^{1/2} \mathcal{A}_l^{S^*} e^{-ikr[1-\cos(\theta-\theta_l)]} e^{i\pi/4} \right\} = 0\,. \tag{8.6.28}$$

The term proportional to kr vanishes by periodicity. The fourth term may be combined with the third upon using the identity $\operatorname{Im} if = \operatorname{Im} if^*$; the combination gives

$$e^{-i\pi/4} \left(\frac{2}{\pi} kr\right)^{1/2} \int_0^{2\pi} d\theta\, \mathcal{A}_l^S e^{ikr[1-\cos(\theta-\theta_l)]} [1 + \cos(\theta - \theta_l)]\,, \tag{8.6.29}$$

which can be approximated for $kr \gg 1$ by the method of stationary phase. The stationary phase points occur at

$$\frac{\partial}{\partial\theta}[1 - \cos(\theta - \theta_l)] = \sin(\theta - \theta_l) = 0 \quad \text{or} \quad \theta = \theta_l,\ \theta_l + \pi \tag{8.6.30}$$

within the interval $[0, 2\pi]$. In the neighborhood of the first stationary phase point the integrand in Eq. (8.6.29) is roughly

$$e^{ikr(\theta-\theta_l)^2/2} 2\mathcal{A}_l^S(\theta_l)\,. \tag{8.6.31}$$

When the limits are approximated by $(-\infty, \infty)$, the integral in Eq. (8.6.29) can be evaluated:

$$\mathcal{A}_l^S(\theta_l) \int_{-\infty}^{\infty} e^{ikr\theta^2/2}\, d\theta = \left(\frac{2\pi}{kr}\right)^{1/2} e^{i\pi/4} \mathcal{A}_l^S(\theta_l) \quad \text{as} \quad kr \gg 1\,. \tag{8.6.32}$$

Near the second stationary point the integrand of Eq. (8.6.29) vanishes. Finally, Eq. (8.6.28) becomes

$$\frac{1}{\pi} \int_0^{2\pi} |\mathcal{A}_l^S(\theta)|^2\, d\theta = -2\ \operatorname{Re} \mathcal{A}_l^S(\theta_l) \tag{8.6.33}$$

which was first derived by Maruo (1960). Similar relations are well known in quantum mechanics and other physical contexts as the *optical theorem*. Since $|\mathcal{A}_l^S(\theta)|^2\, d\theta$ is a measure of the scattered energy within the wedge $(\theta, \theta + d\theta)$, the integral on the left of Eq. (8.6.33) is a measure of the total

scattered energy and is a feature of the body. The theorem implies that the total energy scattered can be alternatively obtained from the scattered wave amplitude in the forward direction alone. This result is important in experiments if the total scattered energy is of interest, as is the case in many branches of physics.

By a similar analysis for Eq. (8.6.14), and using the approximation

$$\int_0^{2\pi} \mathcal{A}_l^S(\theta) e^{-i\pi/4}[1-\cos(\theta-\theta_2)] e^{ikr[1+\cos(\theta-\theta_2)]}\, d\theta$$

$$= 2\left(\frac{2\pi}{kr}\right)^{1/2} \mathcal{A}_1^S(\theta_2+\pi) \quad \text{for} \quad kr \gg 1\,,$$

we get

$$\mathcal{A}_1^S(\theta_2+\pi) = \mathcal{A}_2^S(\theta_1+\pi)\,. \tag{8.6.34}$$

In particular, if $\theta_1 = 0$ and $\theta_2 = -\pi$, then $\mathcal{A}_1^S(0) = \mathcal{A}_2^S(\pi)$; this coincides with Eq. (8.6.19) which relates the transmission coefficients in two dimensions. In general, Eq. (8.6.35) states that the amplitude of the first scattered wave toward the second incident wave is equal to the amplitude of the second scattered wave toward the first incident wave.

We leave it for the reader to show from Eq. (8.6.15) that

$$-\pi[\mathcal{A}_1^S(\theta_2) + \mathcal{A}_2^{S*}(\theta_1)] = \int_0^{2\pi} d\theta \mathcal{A}_1^S(\theta)\mathcal{A}_2^{S*}(\theta) \tag{8.6.35}$$

of which Eq. (8.6.33) is just a special case.

Exercise 8.5

Show that for a two-dimensional rigid body induced to oscillate by an incident wave A from $x \sim -\infty$,

$$1 = \left|R + \frac{A_-}{A}\right|^2 + \left|T + \frac{A_+}{A}\right|^2 \tag{8.6.36}$$

in which R and T are the reflection and transmission coefficients when the body is held stationary, while A_+ and A_- are induced wave amplitudes toward $x \sim +\infty$ and $x \sim -\infty$, respectively.

Exercise 8.6

Consider a variable bottom which changes from one constant depth to another, that is, $h(x) \to h_+$ or h_- as $x \sim \infty$ or $-\infty$. A train of waves

is incident obliquely from the left. What should the far-field expressions be for ϕ on both sides of the transition? Define the reflection (R) and transmission (T) coefficients, and derive an energy relation for R and T.

8.6.3 One Diffraction Problem and One Radiation Problem

Haskind–Hanaoka Theorem

There is a remarkable theorem due independently to Haskind (1957) and Hanaoka (1959), and popularized by Newman (1960), which relates the αth generalized component of the exciting force (due to diffraction) on a fixed body to the radiation potential of the αth normal mode of the same body; specifically,

$$\begin{aligned} F_\alpha^D &= i\omega\rho \iint_{S_B} \left(\phi^I \frac{\partial \phi_\alpha}{\partial n} - \phi_\alpha \frac{\partial \phi^I}{\partial n} \right) dS \\ &= -i\omega\rho \iint_{S_\infty} \left[\phi^I \frac{\partial \phi_\alpha}{\partial n} - \phi_\alpha \frac{\partial \phi^I}{\partial n} \right] dS \,. \end{aligned} \tag{8.6.37}$$

By definition,

$$\begin{aligned} F_\alpha^D &= \iint_{S_B} p n_\alpha \, dS \\ &= i\omega\rho \iint_{S_B} (\phi^I + \phi^S) n_\alpha \, dS \\ &= i\omega\rho \iint_{S_B} (\phi^I + \phi^S) \frac{\partial \phi_\alpha}{\partial n} \, dS \,. \end{aligned} \tag{8.6.38}$$

Because ϕ^S and ϕ_α are outgoing at infinity, Eq. (8.6.4) applies so that

$$F_\alpha^D = i\omega\rho \iint_{S_B} \left(\phi^I \frac{\partial \phi_\alpha}{\partial n} + \phi_\alpha \frac{\partial \phi^S}{\partial n} \right) dS \,. \tag{8.6.39}$$

By the boundary condition $\partial\phi^S/\partial n = -\partial\phi^I/\partial n$, the first equality in Eq. (8.6.37) follows at once; the second equality then follows by letting $\phi = \phi^I$ and $\psi = \phi^S$ in Eq. (8.6.1).

We leave it for the reader to deduce from the proper asymptotic expressions the following explicit formulas:

Two Dimensions:

$$F_\alpha^D = -2\rho g A \mathcal{A}_\alpha^- C_g \,. \tag{8.6.40}$$

Three Dimensions:

$$F_\alpha^D = -\frac{4}{k}\rho g A \mathcal{A}_\alpha(\theta_I + \pi) C_g \,. \tag{8.6.41}$$

In both cases the exciting force is related to the wave amplitude in the direction opposite to the incident waves.

Exercise 8.7

Show from Eqs. (8.6.13) and (8.6.41) that in three dimensions the damping coefficients and the exciting force are related by

$$\lambda_{\alpha\alpha} = \frac{k/8\pi}{\rho g C_g |A|^2} \int_0^{2\pi} |F_\alpha^D(\theta)|^2 \, d\theta \,. \tag{8.6.42}$$

Bessho–Newman Relations

A still less obvious identity between radiation and scattering problems was discovered by Bessho (1967) for two dimensions, rediscovered and extended for three dimensions by Newman (1975, 1976).

Assuming that the normal velocity on S_B has the same phase everywhere, we may always redefine time so that

$$\frac{\partial \phi^R}{\partial n} = V_n = \text{real} \quad \text{or} \quad \frac{\partial}{\partial n}(\phi^R - \phi^{R*}) = 0 \quad \text{on} \quad S_B \,. \tag{8.6.43}$$

Because $\phi^I + \phi^S$ satisfies the same condition on S_B, it follows from Eq. (8.6.1) that

$$\iint_{S_\infty} \left[(\phi^R - \phi^{R*}) \frac{\partial}{\partial n}(\phi^I + \phi^S) - (\phi^I + \phi^S) \frac{\partial}{\partial n}(\phi^R - \phi^{R*}) \right] dS = 0 \,. \tag{8.6.44}$$

By applying Eq. (8.6.3) to ϕ^R and ϕ^S, we may rewrite Eq. (8.6.44)

$$\iint_{S_\infty} \left[(\phi^R - \phi^{R*}) \frac{\partial \phi^I}{\partial n} - \phi^I \frac{\partial}{\partial n}(\phi^R - \phi^{R*}) \right] dS$$
$$= \iint_{S_\infty} \left(\phi^{R*} \frac{\partial \phi^S}{\partial n} - \phi^S \frac{\partial \phi^{R*}}{\partial n} \right) dS \,. \tag{8.6.45}$$

Equation (8.6.45) relates the far fields of ϕ^R and ϕ^S. More explicit implications follow.

Two Dimensions: By letting S_∞ be a large rectangular box and using Eq. (8.6.10) in Eq. (8.6.45), the two-dimensional Bessho–Newman relation can be obtained:

$$A_- + RA_-^* + TA_+^* = 0\,. \tag{8.6.46}$$

Consider now the special case of a body which is symmetrical about its vertical plane and is executing either a symmetric mode (heave) or an antisymmetric mode (roll or sway). For the symmetric mode, we have

$$A_+ = A_- = A_s = |A_s|e^{i\delta_s}\,, \tag{8.6.47}$$

and for the antisymmetric mode

$$A_+ = -A_- = |A_a|e^{i\delta_a}\,. \tag{8.6.48}$$

Substituting Eqs. (8.6.47) and (8.6.48) in turn into Eq. (8.6.46), we get

$$R + T = -e^{2i\delta_s}\,, \quad R - T = -e^{2i\delta_a}\,. \tag{8.6.49}$$

Since both roll and sway are antisymmetric modes, we have the striking result that the phases of their radiated waves must satisfy

$$\delta_1 = \delta_5 \pm \pi\,. \tag{8.6.50}$$

Furthermore, for the same body and bottom geometry one may obtain the scattering coefficients R and T by solving two radiation problems (for two modes, say). With the help of the Haskind–Hanaoka relation for exciting forces, it is possible to obtain all the important global quantities in both radiation and scattering problems by solving the radiation problems alone!

Three Dimensions: Use of the asymptotic formulas for ϕ^S and ϕ^R transforms the right-hand side of Eq. (8.6.45) to:

$$C2i\frac{2}{\pi}\int_0^{2\pi} d\theta \mathcal{A}^S(\theta)\mathcal{A}^{R*}(\theta)\,, \tag{8.6.51}$$

where C is a constant multiplier. For the left-hand side of Eq. (8.6.45) we observe first that

$$\iint_{S_\infty} \left(\phi^R \frac{\partial \phi^I}{\partial n} - \phi^I \frac{\partial \phi^R}{\partial n} \right) dS$$

$$= Ci(kr)^{1/2} \frac{2}{\pi} \int_0^{2\pi} d\theta \, \mathcal{A}^R [1 - \cos(\theta - \theta_I)] e^{ikr[\cos(\theta - \theta_I) + 1]}$$

$$= 4iC\mathcal{A}^R(\theta_I + \pi) \tag{8.6.52}$$

after using Eq. (8.6.34); then by similar reasoning,

$$\iint_{S_\infty} \left(\phi^{R*} \frac{\partial \phi^I}{\partial n} - \phi^I \frac{\partial \phi^{R*}}{\partial n} \right) dS = 4iC\mathcal{A}^{R*}(\theta_I) \,. \tag{8.6.53}$$

Finally, from Eq. (8.6.45) we get the three-dimensional Bessho–Newman relations:

$$-\mathcal{A}^{R*}(\theta_I) + \mathcal{A}^R(\theta_I + \pi) = \frac{1}{\pi} \int_0^{2\pi} \mathcal{A}^{R*} \mathcal{A}^S \, d\theta \,. \tag{8.6.54}$$

Consider the special case of a body with rotational symmetry about the z axis. Without loss of generality we let $\theta_I = 0$. Now only three modes are distinct, that is, sway ($\alpha = 1$), heave ($\alpha = 3$), and roll about the y axis ($\alpha = 5$).

$$\mathcal{A}_\alpha(\theta) = (\text{const}) \cos\theta \,, \quad \alpha = 1, 5 \,,$$

$$\mathcal{A}_3(\theta) = \text{const} \,. \tag{8.6.55}$$

For sway, we expect that $\mathcal{A}^R = \mathcal{A}_1(0) \cos\theta$. It follows from Eq. (8.6.54) that

$$-\mathcal{A}_1^*(0) - \mathcal{A}_1(0) = \frac{1}{\pi} \mathcal{A}_1^*(0) \int_0^{2\pi} \mathcal{A}^S \cos\theta \, d\theta \,, \tag{8.6.56}$$

or

$$-1 - \frac{\mathcal{A}_1(0)}{\mathcal{A}_1^*(0)} = \frac{1}{\pi} \int_0^{2\pi} \mathcal{A}^S \cos\theta \, d\theta \,. \tag{8.6.57}$$

For roll, we also expect $\mathcal{A}^R = \mathcal{A}_5(0) \cos\theta$ although $\mathcal{A}_1(0) \neq \mathcal{A}_5(0)$. Equation (8.6.57) also applies if $\mathcal{A}_1(0)$ is replaced by $\mathcal{A}_5(0)$; therefore

$$\frac{\mathcal{A}_1(0)}{\mathcal{A}_1^*(0)} = \frac{\mathcal{A}_5(0)}{\mathcal{A}_5^*(0)} \,. \tag{8.6.58}$$

If we denote the phase angle of $\mathcal{A}_\alpha(0)$ by δ_α, that is, $\mathcal{A}_\alpha(0) = |\mathcal{A}_\alpha(0)|e^{i\delta_\alpha}$, then the phase angles due to sway and roll are related by

$$\delta_1 = \delta_5 \pm \pi. \tag{8.6.59}$$

This result was first shown for a circular cylinder by Garrett (1970) and generalized in the present manner by Newman (1976). From Eq. (8.6.41) the phases of the sway exciting force and the roll exciting moment must also satisfy Eq. (8.6.59). Similar results hold for a two-dimensional body symmetrical about its vertical axis.

For the heave mode, $\mathcal{A}^R = \mathcal{A}_3$, which is independent of θ. A similar application of Eq. (8.6.55) gives

$$e^{2i\delta_3} - 1 = \frac{i}{\pi}\int_0^{2\pi} \mathcal{A}^S(\theta)\, d\theta\,. \tag{8.6.60}$$

All the general identities discussed in this section have been generalized for N bodies (Srokosz, 1980). These identities are useful in theoretical argument and can be used to check the correctness of calculations or to reduce the numerical work of calculating certain global quantities. Nevertheless, they do not change the basic need of an efficient technique for solving the typical hydrodynamic boundary-value problem; hence the next section.

8.7 Numerical Solution by Hybrid Element Method

Two primary classes of numerical methods have been well developed for diffraction problems of this chapter. One class is based on finite elements, and the other on integral equations. In each class, there are variations in details, but the general spirits are exemplified by the two methods discussed briefly here and in the next section. Further information may be found in the survey by Mei (1978), Susbielles and Bratu (1981), Sarpkaya and Issacson (1981), and Yeung (1982). In particular, the second and third references contain the numerical and experimental results of a variety of geometries.

In this section we shall extend the hybrid element method of Section 4.11 for long waves in shallow water to water of arbitrary depth. As before, one of the main ideas is to employ the finite-element approximation near the body and analytical representation everywhere else. As the first step we must establish the variational principle which only involves integrals over a finite domain surrounding the body.

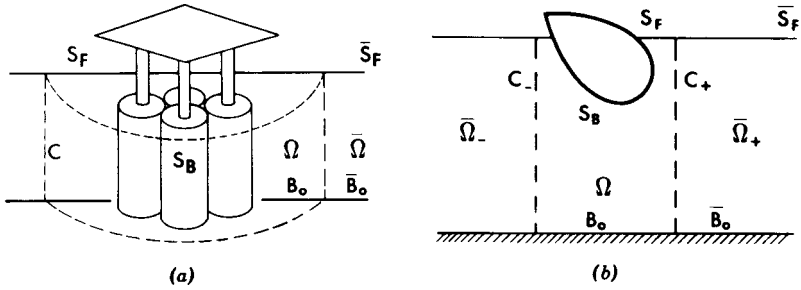

Figure 8.7: Division of fluid regions in the hybrid element method: (a) three dimensional; (b) two dimensional.

With reference to Fig. 8.7(a) let all bodies and bottom irregularities be localized within a vertical cylinder C of finite size. Beyond C the ocean depth is assumed to be constant everywhere. Overhead bars will be used to distinguish quantities outside C (i.e., in the superelement $\overline{\Omega}$) from those within C (i.e., in Ω). Let $\bar{\phi}$ satisfy *exactly* the Laplace equation, the boundary conditions on the free surface $\overline{S}_F$ and on the bottom $\overline{B}_0$, and the radiation condition at infinity. Since nothing is yet specified on C, $\bar{\phi}$ is so far unknown but may be formally represented in a variety of ways. One way is to use Green's function and express $\bar{\phi}$ as the superposition of sources on C with unknown source strength. Another way is to use eigenfunction expansions with unknown coefficients as in Eq. (8.4.8) for two dimensions and Eq. (8.4.11) for three dimensions. The latter course will be adopted here.

8.7.1 The Variational Formulation

Taking the radiation problem for demonstration, we shall show that the stationarity of the functional

$$J(\phi,\bar{\phi}) = \frac{1}{2}\iiint_{\Omega}(\nabla\phi)^2\,d\Omega - \frac{\omega^2}{2g}\iint_{S_F}\phi^2\,dS$$
$$- \iint_{S_B} V\phi\,dS + \iint_C \left(\frac{1}{2}\bar{\phi} - \phi\right)\frac{\partial\bar{\phi}}{\partial n}\,dS \qquad (8.7.1)$$

implies, and is implied by, the original boundary-value problem. Equating the first variation to zero, we get,

$$\delta J = 0 = \iiint_{\Omega} \nabla\phi \cdot \nabla(\delta\phi)\, d\Omega - \frac{\omega^2}{g} \iint_{S_F} \phi\delta\phi\, dS$$
$$- \iint_{S_B} V\delta\phi\, dS + \iint_{C} (\bar{\phi} - \phi)\frac{\partial\delta\bar{\phi}}{\partial n}\, dS$$
$$+ \frac{1}{2}\iint_{C}\left(\delta\bar{\phi}\frac{\partial\bar{\phi}}{\partial n} - \bar{\phi}\frac{\partial\delta\bar{\phi}}{\partial n}\right) dS - \iint_{C} \delta\phi\frac{\partial\bar{\phi}}{\partial n}\, dS \qquad (8.7.2)$$

after some arrangement. Since $\delta\bar{\phi}$ satisfies the same conditions as $\bar{\phi}$, it may be shown by applying Green's formula to $\delta\bar{\phi}$ and $\bar{\phi}$ over $\overline{\Omega}$ that the last integral in Eq. (8.7.2) vanishes identically. By partial integration and Gauss' theorem, the first integral in Eq. (8.7.2) may be transformed to surface integrals, leading to the following:

$$\delta J = 0 = -\iiint_{\Omega} \delta\phi\nabla^2\phi\, d\Omega + \iint_{S_F} \delta\phi\left(\frac{\partial\phi}{\partial z} - \frac{\omega^2}{g}\phi\right) dS$$
$$+ \iint_{B_0} \delta\phi\frac{\partial\phi}{\partial n}\, dS + \iint_{S_B} \delta\phi\left(\frac{\partial\phi}{\partial n} - V\right) dS$$
$$+ \iint_{C} (\bar{\phi} - \phi)\frac{\partial\delta\bar{\phi}}{\partial n}\, dS + \iint_{C} \delta\bar{\phi}\left(\frac{\partial\phi}{\partial n} - \frac{\partial\bar{\phi}}{\partial n}\right) dS\,. \qquad (8.7.3)$$

In order for $\delta J = 0$ for arbitrary $\delta\phi$ and $\delta\bar{\phi}$, it is both necessary and sufficient that Laplace's equation be satisfied as the Euler–Lagrange equation, while all the other boundary conditions on S_F, S_B, and B_0, including the continuity of ϕ and $\partial\phi/\phi n$ across C, must be satisfied as *natural conditions*. Thus, the stationarity of J is equivalent to the boundary-value problem for the radiation potential.

Equation (8.7.2) without the last integral may be stated in another way. Since only first derivatives are involved, ϕ and $\delta\phi$ need only be piecewise linear in Ω. In mathematical language, ϕ and $\delta\phi$ are said to be in the Sobolev space $H^1(\Omega)$ defined by

$$f \in H^1(\Omega) \quad \text{if} \quad \iiint_{\Omega} [(\nabla f)^2 + f^2]\, d\Omega < \infty\,.$$

Being analytic functions, $\bar{\phi}$ and $\delta\bar{\phi}$ are said to be in the space $C^\infty(\Omega)$. Thus, Eq. (8.7.2) may be stated as follows: Find $\phi \in H^1(\Omega)$ and $\bar{\phi} \in C^\infty(\Omega)$ such that for every $\psi \in H^1(\Omega)$:

$$- \iiint_{\Omega} \nabla\phi \cdot \nabla\psi \, d\Omega + \frac{\omega^2}{g} \iint_{S_F} \phi\psi \, dS + \iint_{S_B} V\psi \, dS + \iint_{C} \frac{\partial\bar{\phi}}{\partial n}\psi \, dS = 0 \,, \tag{8.7.4}$$

and for every $\bar{\psi} \in C^{\infty}(\Omega)$:

$$\iint_{C} (\phi - \bar{\phi}) \frac{\partial\bar{\psi}}{\partial n} \, dS = 0 \,, \tag{8.7.5}$$

where we have written

$$\psi \equiv \delta\phi \,, \quad \bar{\psi} = \delta\bar{\phi} \,. \tag{8.7.6}$$

Equations (8.7.4) and (8.7.5) constitute the *weak formulation* of the problem (Aranha, Mei, and Yue, 1979).

Finally, the reader may verify that the proper functional for the diffraction problem is

$$J(\phi, \bar{\phi}) = \frac{1}{2} \iiint_{\Omega} (\nabla\phi)^2 \, d\Omega - \frac{\omega^2}{2g} \iint_{S_F} \phi^2 \, dS + \iint_{C} \left[\left(\frac{\bar{\phi}^S}{2} - \phi^S \right) \frac{\partial\bar{\phi}^S}{\partial n} - \bar{\phi}^S \frac{\partial\phi^I}{\partial n} \right] dS \,, \tag{8.7.7}$$

where $\phi^S = \phi - \phi^I$ and $\bar{\phi}^S = \bar{\phi} - \phi^I$.

Exercise 8.8

Use Eq. (8.7.7) to deduce the expansion coefficients in Eq. (8.5.3) for the circular cylinder, by making the entire fluid domain the superelement $\overline{\Omega}$.

8.7.2 The Approximate Solution

Equation (8.7.2) is now most convenient for setting up the discrete approximation. For simplicity, we shall demonstrate for the two-dimensional problem in the vertical plane. As shown in Fig. 8.7(b) there are now two superelements, $\overline{\Omega}_-$ and $\overline{\Omega}_+$, to the left of C_- and to the right of C_+, respectively. In $\overline{\Omega}_-$ and $\overline{\Omega}_+$ we take,

$$\bar{\phi}^+ = A_0^{\pm} e^{\pm ikx} f_0^{(z)} + \sum_n A_n^{\pm} e^{\pm k_n x} f_n(z) \,, \quad \mathbf{x} \in \overline{\Omega}_{\pm} \,. \tag{8.7.8}$$

The region Ω is divided into triangles to form a network with N nodes. Let us introduce the pyramid function $F_i(x, z)$ which is linear in x and z in

each triangle, has the value 1 at the node (x_i, z_i), and vanishes at all other nodes, that is,

$$F_i(x_j, z_j) = \delta_{ij}\,. \tag{8.7.9}$$

Clearly, F_i is in $H^1(\Omega)$. We now express

$$\phi = \sum_{j=1}^{n} \phi_j F_j(x, z)\,, \tag{8.7.10a}$$

$$\psi = \sum_{i=1}^{N} \psi_i F_i(x, z)\,, \tag{8.7.10b}$$

where ϕ_j is the nodal potential, ψ_i is the nodal weight, and

$$\bar{\psi}^{\pm} = B_0^{\pm} e^{\pm ikx} f_0(z) + \sum_{n=1}^{\infty} B_n^{\pm} e^{\mp k_n x} f_n(z)\,. \tag{8.7.11}$$

Substituting into Eq. (8.7.4), we get from various integrals

$$\begin{aligned}
\iint_{\Omega} \nabla\phi \cdot \nabla\psi \, d\Omega &= \sum_i \sum_j \psi_i \left(\iint_{\Omega} \nabla F_i \cdot \nabla F_j \, d\Omega \right) \phi_j \\
&= \{\psi\}^T [K_1] \{\phi\}\,, \qquad (8.7.12a) \\
-\frac{\omega^2}{g} \int_{S_F} \phi\psi \, dS &= \sum_i \sum_j \psi_i \left(\int_{S_F} F_i F_j \, dS \right) \phi_j \\
&= \{\psi^F\}^T [K_2] \{\phi^F\}\,, \qquad (8.7.12b) \\
-\int_{S_B} V\psi \, dS &= -\sum_i \psi_i \left(\int_{S_B} V F_i \, dS \right) \\
&= -\{\psi^B\}^T \{V\}\,. \qquad (8.7.12c)
\end{aligned}$$

After truncating the series (8.7.8) and (8.7.11) after M terms, we have

$$\bar{\phi}^{\pm} = \sum_{j=0}^{M-1} \bar{\phi}_j^{\pm} f_j(z)\,, \tag{8.7.13a}$$

$$\bar{\psi}^{\pm} = \sum_{j=0}^{M-1} \bar{\psi}_j^{\pm} f_j(z)\,, \tag{8.7.13b}$$

$$\frac{\partial \bar{\phi}^{\pm}}{\partial n} = \sum_{j=0}^{M-1} \sigma_j^{\pm} k_j \bar{\phi}_j^{\pm} f_j(z)\,, \tag{8.7.13c}$$

$$\frac{\partial \bar{\psi}^{\pm}}{\partial n} = \sum_{j=0}^{M-1} \sigma_j^{\pm} k_j \bar{\psi}_j^{\pm} f_j(z)\,, \tag{8.7.13d}$$

where $\sigma_0^{\pm} = \pm i$, $\sigma_j^{\pm} = \mp 1$, and $j = l, 2, 3, \ldots$. If (ϕ_i^+, ψ_i^+) denote the N_+ nodal values on C_+, the remaining integrals on C_+ in Eq. (8.7.4) become

$$\begin{aligned}\int_{C_+} \frac{\partial \bar{\phi}}{\partial n} \psi \, dS &= \sum_{i=1}^{N_+} \sum_{j=1}^{M-1} \psi_i^+ \left(\int_{C_+} \sigma_j^+ k_j f_j F_i dz \right) \bar{\phi}_j^+ \\ &= \{\psi^+\}^T [K_3^+] \{\bar{\phi}^+\}\,, \end{aligned} \tag{8.7.14a}$$

$$\begin{aligned}\int_{C_+} \phi \frac{\partial \bar{\psi}}{\partial n} \, dS &= \sum_{i=1}^{N_+} \sum_{j=1}^{M-1} \phi_i^+ \left(\int_{C_+} \sigma_j^+ k_j f_j F_i \, dz \right) \bar{\psi}_j^+ \\ &= \{\phi^+\}^T [K_3^+] \{\bar{\psi}^+\} = \{\bar{\psi}^+\}^T [K_3^+]^T \{\phi^+\}\,, \end{aligned} \tag{8.7.14b}$$

$$\begin{aligned}\int_{S_+} \bar{\phi} \frac{\partial \bar{\psi}}{\partial n} \, dS &= \sum_{i=1}^{M-1} \sum_{j=1}^{M-1} \bar{\psi}_i^+ \left(\int_{S_+} \sigma_j^+ k_i f_i f_j dz \right) \bar{\phi}_j^+ \\ &= \sum_{i=1}^{M-1} \sum_{j=1}^{M-1} \bar{\psi}_i^+ (\sigma_j^+ k_i \delta_{ij}) \bar{\phi}_j^+ = \{\bar{\psi}^+\}^T [K_4^+] \{\bar{\phi}^+\}\,. \end{aligned} \tag{8.7.14c}$$

Similar expressions may be obtained for integrals along C_-.

Using Eqs. (8.7.12) and (8.7.14), we assemble Eqs. (8.7.4) and (8.7.5) to give

$$\{\psi\}^T [K] \{\phi\} = \{\psi\}^T \{V\}\,, \tag{8.7.15}$$

where the transpose of the column vector $\{\phi\}$ is arranged as follows

$$\{\phi\}^T = \{\{\bar{\phi}^-\}^T, \{\phi^-\}^T, \{\tilde{\phi}\}^T, \{\phi^+\}^T, \{\bar{\phi}^+\}^T\}$$

with $\{\tilde{\phi}\}$ corresponding to the nodes inside Ω and on S_B. The column vector $\{\psi\}$ is arranged similarly. The column vector $\{V\}$ has nonzero entries only for the nodes on S_B. The global stiffness matrix $[K]$ is of the following form:

$$\begin{bmatrix} [K_4^-][K_3^-]^T & & & \\ [K_3^-] & & & \\ & [K_1]+[K_2] & & \\ & & & [K_3^+] \\ & & & [K_3^+]^T[K_4^+] \end{bmatrix}$$

which is symmetric. Since $\{\psi\}$ is arbitrary,

$$[K]\{\phi\} = \{V\} \tag{8.7.16}$$

which may be solved numerically.

To minimize the bandwidth of $[K]$, it is desirable to number the nodes downward along a vertical line, followed by the nodes on the next vertical line..., and to let $\{\bar{\phi}^-\}$ and $\{\bar{\phi}^+\}$ occupy the top and bottom positions, respectively, of the column vector $\{\phi\}$. In this arrangement, the semibandwidth is roughly equal to the number of nodes on a vertical line, that is, N_+ or N_-. Further details may be found in Bai and Yeung (1974) for two dimensions and Yue, Chen, and Mei (1976) for three dimensions.

When the sea depth becomes infinite, the eigenfunction expansion becomes inefficient and it is more advantageous to localize the finite element in all three dimensions and to employ Green's function for $\bar{\phi}$. These modifications have been accomplished by Seto and Yamamoto (1975) and Lenoir and Jami (1978).

8.7.3 A Theoretical Property of the Hybrid Element Method

In the weak formulation, let us choose among all admissible functions $\psi = \phi^*$. Equation (8.7.4) yields

$$-\iiint_\Omega |\nabla\phi|^2\, d\Omega + \frac{\omega^2}{g}\iint_{S_F} |\phi|^2\, dS + \iint_{S_B} V\phi^*\, dS + \iint_C \frac{\partial\bar{\phi}}{\partial n}\phi^*\, dS = 0\,. \tag{8.7.17}$$

Since the first two integrals are purely real, we must have

$$\mathrm{Im}\iint_{S_B} V\phi^*\, dS = -\mathrm{Im}\iint_C \phi^*\frac{\partial\bar{\phi}}{\partial n}\, dS\,. \tag{8.7.18}$$

From $C^\infty(\overline{\Omega})$ let us choose $\bar{\psi} = \partial\bar{\phi}^*/\partial n$; Eq. (8.7.5) then implies

$$\iint_C \phi \frac{\partial \bar{\phi}^*}{\partial n}\, dS = \iint_C \bar{\phi} \frac{\partial \bar{\phi}^*}{\partial n}\, dS\,. \tag{8.7.19}$$

Using the complex conjugate of Eq. (8.7.19) in Eq. (8.7.18), we get

$$\mathrm{Im} \iint_{S_B} V\phi^*\, dS = -\mathrm{Im} \iint_C \bar{\phi}^* \frac{\partial \bar{\phi}}{\partial n}\, dS\,. \tag{8.7.20}$$

But this is formally the statement of energy conservation that the rate of work done by the body is equal to the rate of energy flux through the cylinder C. The remarkable point is that ϕ^* and $\bar{\phi}$ (and $\bar{\phi}^*$) correspond to the approximate solution whose accuracy depends on the discretization and the number of terms in the truncated series. Therefore, the present hybrid element method, which imposes continuity on C in a special way according to Eq. (8.7.5), preserves energy conservation. This property was observed in numerical experiments by Yue and Mei and proven by Aranha; it implies that the energy theorem *cannot* be used as a way to check the discretization error. Indeed, by proper selections of ϕ, ψ, and $\bar{\psi}$ one can further prove that *all* the global identities deduced in Section 8.6 are preserved in the weak formulation. Aranha, Mei, and Yue (1979) also gave numerical evidence of these properties by treating a given problem with two vastly different finite-element grids. They showed that while the two grids gave quite different answers at any point, the global identities were satisfied to an extremely high degree with a minute round-off error. Therefore, the relations in Section 8.6 are not *sufficient* to guarantee an accurate solution, although they are *necessary*, when the present hybrid element method is employed. Similar caution is warranted when other numerical methods are used.

8.7.4 A Numerical Example

As an application of the hybrid element method, we shall show some sample numerical results for a floating two-dimensional cylinder with the cross section of a tear drop. This cylinder was used by Salter as a device to extract energy from water waves, a topic which will be further discussed in Section 8.9. Here we shall only give the hydrodynamical quantities (Mynett, Serman, and Mei, 1979).

A sample finite-element grid for Salter's cam is shown in Fig. 8.8. Note that the lines C_+ and C_- are as close as one element away from the body.

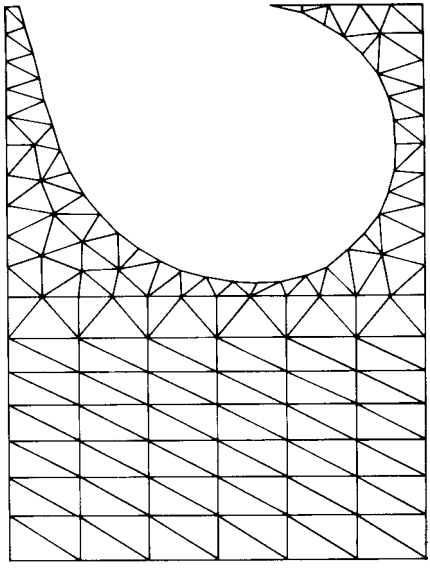

Figure 8.8: Sample finite-element grid for Salter's cam.

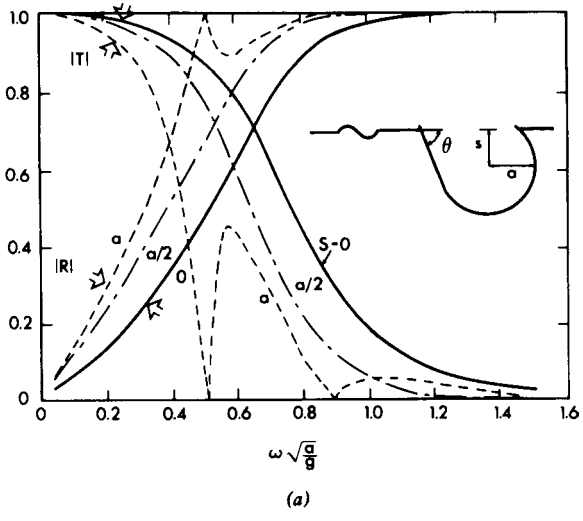

Figure 8.9: Sample computed results for schematized Salter cam with $\theta = \frac{1}{4}\pi$, $h = 4a$. (a) Transmission and reflection coefficients; (b) sway exciting force $\hat{F}_1^D = F_1^D/\rho g A a$; ($c$) heave exciting force $\hat{F}_3^D = F_3^D/\rho g A a$; ($d$) roll exciting moment $\hat{F}_5^D = F_5^D/\rho g A a^2$; ($e$) roll inertia and damping coefficients, $\hat{\mu}_{55} = \mu_{55}/\rho a^4$, $\hat{\lambda} = {}_{55} = \lambda_{55}(\rho a^4(g/a)^{1/2})^{-1}$ (from Mynett et al., 1979, *Appl. Ocean Res.* Reproduced by permission of CML Publications).

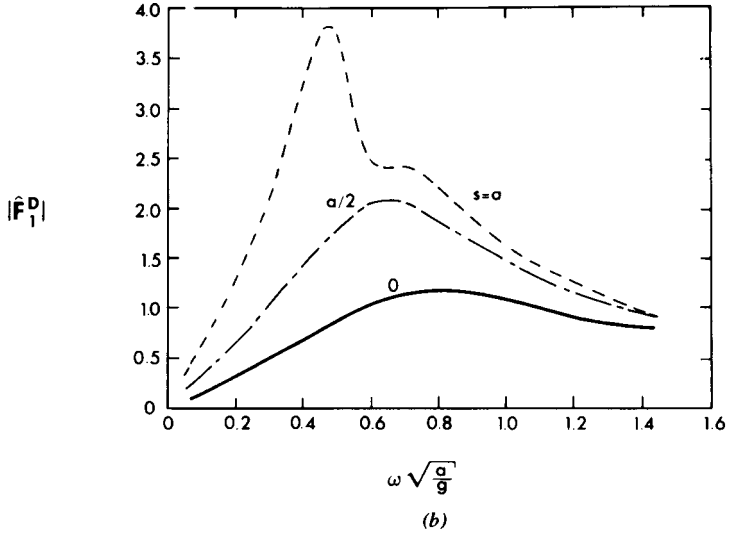

(b)

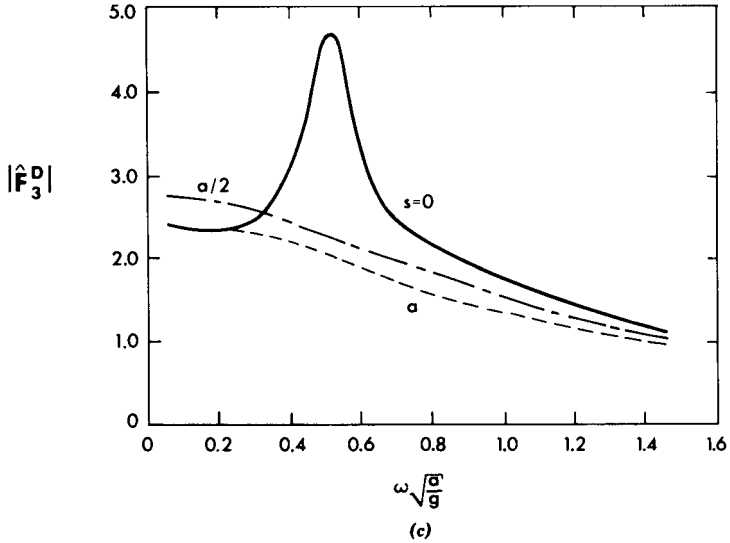

(c)

Figure 8.9 (*Continued*)

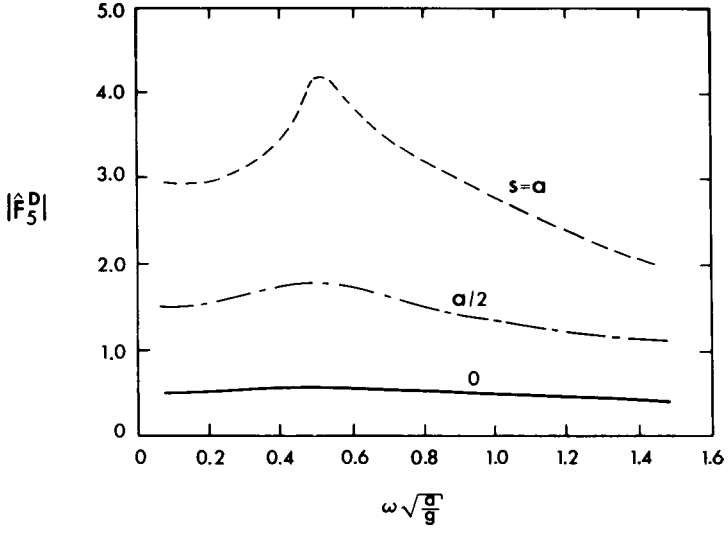

(d)

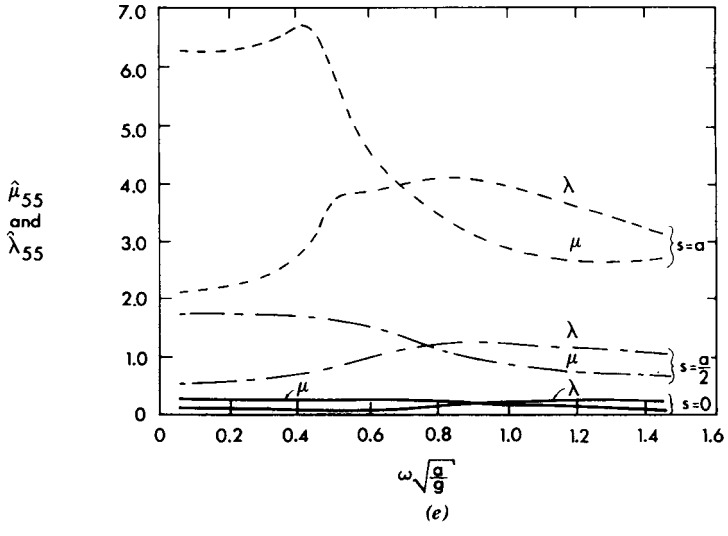

(e)

Figure 8.9 (*Continued*)

The results shown in Figs. 8.9(a)–8.9(e) correspond to a schematized Salter cam with a circular stern of radius a and a straight bow slanted at an angle $\theta = \pi/4$. The water depth is kept at a constant $h = 4a$.

For the diffraction problem the reflection and transmission coefficients are given in Fig. 8.9(a) for three depths of submergence, $s = 0$, $a/2$, and a. As $\omega(a/g)^{1/2}$ increases beyond 1, $|T| \to 1$ and $|R| \to 0$. Figures 8.9(b)–8.9(d) give the exciting forces F_1^D (horizontal), F_3^D (vertical), and F_5^D (moment about the y axis). Note that the largest forces occur around $\omega(a/g)^{1/2} = 1$.

For the radiation problem, the real quantities λ_{ij} and μ_{ij} are shown in Fig. 8.9(e).

For three-dimensional examples and programming details, reference is made to Yue, Chen, and Mei (1976).

8.8 Remarks on the Numerical Methods by Integral Equations

8.8.1 The Integral Equations

Another powerful numerical technique for diffraction is the method of integral equations via Green's function, which was introduced in Section 8.4.2. Let us consider three dimensions and recall that

$$\phi(\mathbf{x}_0) = \iint_{S_B} \left(\phi \frac{\partial G}{\partial n} - G \frac{\partial \phi}{\partial n} \right) dS \quad \text{if} \quad \mathbf{x}_0 \in \Omega \text{ but not on } S_B \,. \tag{8.8.1}$$

If $\mathbf{x}_0$ is on S_B, we must proceed with caution and exclude from Ω a small hemisphere Ω_ε centered at $\mathbf{x}_0$ as shown in Fig. 8.10.

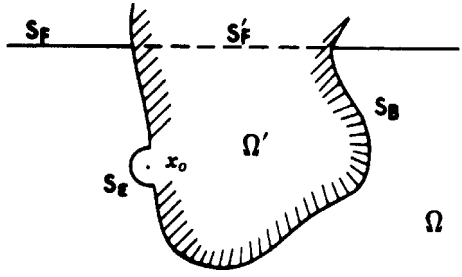

Figure 8.10

Let the surface of the ε-sphere be denoted by S_ε. Application of Green's theorem to ϕ and G over Ω (excluding Ω_ε) leads to

$$\iint_{S_B+S_\varepsilon} \left(\phi\frac{\partial G}{\partial n} - G\frac{\partial \phi}{\partial n}\right) dS = 0\,, \tag{8.8.2}$$

where the integral over S_B is to be interpreted as the principal value, a circular patch of radius ε being excluded. Over S_ε, ϕ is nearly constant and equal to $\phi(x_0)$, and $\partial G/\partial n$ is much greater than G. Integrating the polar form of Eq. (8.4.22) for small r where $r = |\mathbf{x} - \mathbf{x}_0|$, we get

$$\frac{\partial G}{\partial r} \sim \frac{1}{4\pi r^2}\,, \quad r \to 0\,. \tag{8.8.3}$$

Therefore, the integral over the hemisphere S_ε is

$$\lim_{\varepsilon\to 0} \iint_{S_\varepsilon} \left(\phi\frac{\partial G}{\partial n} - G\frac{\partial \phi}{\partial n}\right) dS = -\lim_{\varepsilon\to 0} \phi(\mathbf{x}_0) \iint_{S_\varepsilon} \frac{\partial G}{\partial r}\, dS = -\frac{1}{2}\phi(\mathbf{x}_0)\,. \tag{8.8.4}$$

Putting Eq. (8.8.4) into Eq. (8.8.2), we get

$$\frac{1}{2}\phi(\mathbf{x}_0) = \iint_{S_B} \left(\phi\frac{\partial G}{\partial n} - G\frac{\partial \phi}{\partial n}\right) dS\,, \quad \mathbf{x}_0 \text{ on } S_B\,. \tag{8.8.5}$$

Since $\partial\phi/\partial n$ is prescribed in a diffraction or radiation problem, Eq. (8.8.5) is a Fredholm integral equation of the second kind for $\phi(\mathbf{x}_0)$ ($\mathbf{x}_0 \in S_B$). By dividing S_B into discrete panels and approximating ϕ in each panel by a constant ϕ_i and then carrying out the integration, one obtains a system of algebraic equations for ϕ_i, $i = 1, 2, \ldots, N$, which can be solved for ϕ_i. Afterward, ϕ at any other point is given by Eq. (8.8.1) or (8.8.5).

In practice, higher-order interpolating functions may be used within each panel. More important, when $\mathbf{x}$ and $\mathbf{x}_0$ are close, the integration in Eq. (8.8.5) must be carried out to high accuracy; indeed, analytic integration is often necessary. While the advantage of this method is that the number of unknowns is usually small, being the ϕ_i on S_B, evaluation of the integrals in order to get the matrix coefficients is a laborious task both for the worker and for the computer (Jawson and Symm, 1977).

A closely related approach is the method of source distribution where one represents the potential everywhere in Ω by

$$\phi(\mathbf{x}_0) = \iint_{S_B} \gamma G\, dS_0 \tag{8.8.6}$$

with γ unknown. The boundary condition on the body requires that

$$\lim_{\mathbf{x}\to\mathbf{x}_0} \iint_{S_B} \gamma \frac{\partial G}{\partial n_0}\, dS_0 = U(\mathbf{x}_0) \tag{8.8.7}$$

as $\mathbf{x}$ approaches S_B from without. To carry out the limiting process we indent S_B inward by a hemispherical surface S_ε. Since,

$$\frac{\partial G}{\partial n_0} = -\frac{\partial G}{\partial r} \cong -\frac{1}{4\pi r^2} \tag{8.8.8}$$

on S_ε, we get the limit

$$-\frac{1}{2}\gamma(\mathbf{x}_0) + \iint_{S_B} \gamma \frac{\partial G}{\partial n}\, dS = U(\mathbf{x}_0)\,. \tag{8.8.9}$$

This integral equation has the same kernel as Eq. (8.8.5).

8.8.2 Irregular Frequencies

The type of integral equations (8.8.5) or (8.8.9) is known to possess the so-called *irregular frequencies* and nontrivial eigensolutions if S_B intersects the free surface. The numerical consequence is that the approximate matrix equation becomes ill-conditioned. This drawback is strictly a feature of the kernel and does not imply that the original diffraction or radiation problem has eigensolutions, as is well known in acoustics (Lamb, 1932, Sec. 290). In the context of a floating body in water waves, John (1950) was the first to call attention to irregular frequencies, while Frank (1967b) gave the first numerical evidence.

To see the origin of irregular frequencies we consider first a fictitious problem for the interior of S_B, that is, Ω' which intersects the free surface over the portion S'_F. Let the interior potential ϕ' satisfy

$$\nabla^2\phi' = 0 \quad \text{in} \quad \Omega'\,, \tag{8.8.10}$$

$$\frac{\partial \phi'}{\partial z} - \sigma\phi' = 0 \quad z = 0 \text{ on } S'_F\,. \tag{8.8.11}$$

Using the same Green's function G as before which is defined everywhere in $\Omega + \Omega'$, and applying Green's theorem to ϕ' and G over Ω', we get

$$-\phi'(\mathbf{x}_0) = \iint_{S_B} \left(\phi' \frac{\partial G}{\partial n} - G\frac{\partial \phi'}{\partial n}\right) dS\,, \quad \mathbf{x}_0 \in \Omega',\ \text{not on } S_B\,. \tag{8.8.12}$$

The minus sign on the left is due to the fact that the unit normal $\mathbf{n}$ is from Ω to Ω'. It is also easy to deduce that

$$\begin{bmatrix} -\frac{1}{2}\phi'(\mathbf{x}_0) \\ 0 \end{bmatrix} = \iint_{S_B} \left(\phi' \frac{\partial G}{\partial n_0} - G \frac{\partial \phi'}{\partial n_0} \right) dS_0 \quad \text{if} \quad \mathbf{x}_0 \begin{bmatrix} \text{on } S_B \\ \in \Omega \end{bmatrix}. \qquad \begin{matrix} (8.8.13a) \\ (8.8.13b) \end{matrix}$$

Now subtracting Eq. (8.8.13b) from Eq. (8.8.1), we get

$$\phi(\mathbf{x}_0) = \iint_{S_B} \left[(\phi - \phi') \frac{\partial G}{\partial n} - \left(\frac{\partial \phi}{\partial n} - \frac{\partial \phi'}{\partial n} \right) G \right] dS \quad \mathbf{x}_0 \text{ in } \Omega \text{ but not on } S_B \,. \tag{8.8.14}$$

If we impose that

$$\phi' = \phi \quad \text{on} \quad S_B \tag{8.8.15}$$

as the boundary condition for the interior problem, we recover the source representation (8.8.6) upon defining

$$\gamma = - \left(\frac{\partial \phi}{\partial n} - \frac{\partial \phi'}{\partial n} \right)_{S_B} . \tag{8.8.16}$$

Therefore, Eq. (8.8.6) and the integral equation (8.8.9) are related to the interior problem defined by Eqs. (8.8.10) and (8.8.11) and the Dirichlet condition (8.8.15). It may be shown that this interior problem has eigensolutions defined by the homogeneous problem

$$\nabla^2 \psi_m = 0 \quad \text{in} \quad \Omega' \,, \tag{8.8.17}$$

$$\frac{\partial \psi_m}{\partial z} - \sigma_m \psi_m = 0 \quad \text{on} \quad S'_F \,, \tag{8.8.18}$$

$$\psi_m = 0 \quad \text{on} \quad S_B \,, \tag{8.8.19}$$

where $\sigma_m = \omega_m^2/g$ and ω_m is the mth eigenfrequency. If $\omega = \omega_m$, the inhomogeneous problem for ϕ' does not have a unique solution. It follows from Eq. (8.8.16) that the source distribution is not unique; hence the integral equation method must fail. The irregular frequencies are precisely the eigenfrequencies of the fictitious interior problem with the Dirichlet condition on S_B.

A simple example serves to confirm the theoretical discussion above. Let a vertical circular cylinder in shallow water pulsate uniformly in all

directions. The potential satisfying the Helmholtz equation, the radiation condition, and

$$\frac{\partial \phi}{\partial r} = U \quad \text{on} \quad r = a \tag{8.8.20}$$

is easily found to be

$$\phi = \frac{(U/k)H_0^{(1)}(kr)}{H_0^{(1)\prime}(ka)}\,. \tag{8.8.21}$$

On the other hand, the Green function is

$$G = \frac{i}{4}H_0^{(1)}(kR)\,, \quad R^2 = r^2 + r_0^2 - 2rr_0\cos(\theta - \theta_0) \tag{8.8.22}$$

which may be expanded to

$$G = \frac{i}{4}\sum_{n=0}^{\infty} \varepsilon_n J_n(kr)H_n^{(1)}(kr_0)\cos n(\theta - \theta_0) \tag{8.8.23}$$

by the addition theorem. The integral equation for the source strength is

$$\begin{aligned} -U &= -\lim_{r_0 \to a} a\int_0^{2\pi}\left[\gamma\frac{\partial G}{\partial n_0}\right]_{r=a} d\theta \\ &= -\frac{i}{4}\gamma ka\int_0^{2\pi} d\theta \sum_n^{\infty} \varepsilon_n J_n(ka)H_n^{(1)\prime}(ka)\cos n(\theta - \theta_0) \\ &= -\frac{i}{4}2\pi\gamma kaJ_0(ka)H_0^{(1)\prime}(ka)\,. \end{aligned} \tag{8.8.24}$$

Hence

$$\gamma = -\frac{2iU}{\pi ka}[J_0(ka)H_0^{(1)\prime}(ka)]^{-1}\,. \tag{8.8.25}$$

Formally, we may substitute Eq. (8.8.25) into Eq. (8.8.6)

$$\phi(r,\theta) = a\int_0^{2\pi}\gamma G\, d\theta_0 \tag{8.8.26}$$

to recover Eq. (8.8.21). However, γ is clearly infinite at the zeroes of $J_0(ka)$, that is, at the eigenfrequencies of the interior Dirichlet problem.

There are ways to avoid irregular frequencies in solving these integral equations. Usually one introduces additional artificial unknowns and more conditions so as to improve the conditioning of the matrix equations. There are other integral equation methods which do not employ Green's function

and hence do not share the same difficulties, for example, Yeung (1975). References may be made to Mei (1978) or Yeung (1982) and the literature cited therein.

In contrast, the hybrid element method of Section 8.7 does not seem to have irregular frequencies. Indeed, Aranha has shown theoretically that for long waves the method gives unique solutions for all ω (see Aranha et al., 1979). Yue (private communication) has experimented numerically for three-dimensional floating boxes of rectangular and circular shapes; no irregular frequencies have been encountered. By combining finite elements with singularity distributions, Lenoir and Jami (1978) have also devised a hybrid method which is free of irregular frequencies.

8.9 Power Absorption by Floating Bodies

8.9.1 Introduction

To demonstrate the applications of the theory developed in this chapter, we shall discuss the subject of wave-power absorption by floating bodies.

The power flux within a unit crest length of a plane sine wavetrain in deep water is $\frac{1}{2}\rho g A^2 C_g = \rho g^2 A^2 T/8\pi$. By this simple formula the available power for 10-s-period swells is estimated below.

Amplitude A (m)	Wave Power (kW/m)
0.5	10
1	40
5	1000

If $A = 1$ m, the power along 25 km of the sea coast is 1000 MW and is comparable to the capacity of a typical conventional power plant. Of course, this estimate must be reduced by directivity of the wave spectrum and varies widely with season and locale. Although the economic feasibility and environmental consequences of wave power are still matters of contention, technical potentials and challenges have already spurred serious research in several countries (see Jansson, Lunde, and Rindby, 1979). Contemplated applications include small-scale power supplies for desolate islands, remote lighthouses, and desalinization of sea water (Pleass, 1978), and so on, or, more optimistically, integration with conventional power plants in a large grid system. Continued depletion of oil and gas resources

will eventually force mankind to pursue alternative energy sources such as wave power.

That power can be extracted from sea waves is readily seen by modifying the elementary example discussed in Section 5.4.

If a damper (i.e., a power takeoff device) is attached to the block shown in Fig. 5.5, Chapter Five, power is fed into the damper by the oscillating block. By proper adjustment of the spring and the damping rate, the net radiated waves to the right can be made to vanish so that all the incident wave power is removed by the damper. A detailed analysis for long waves can be worked out in the same manner as in Section 5.4. For better realism the spring may be replaced by a finite body of water filling the space between the block and the shore, if the distance between them is suitably chosen.

A large variety of designs have been proposed (see McCormick, 1981). In most of them the energy converter (turbine, generator) is on or directly connected to the structure. The designs may be classified into three types according to the gross geometry of the structure. With respect to plane incident waves, these are (a) beam–sea absorbers, (b) omnidirectional absorbers, and (c) head–sea absorbers. A beam–(head-) sea absorber is an elongated device with the longitudinal axis parallel (perpendicular) to the incident wave crests. A special case of the omnidirectional absorber is a *point absorber* which can be a buoy or a resonant water column whose diameter is much smaller than the dominant wavelength.

Beam–Sea Absorbers

To save construction material, it is natural to use floating bodies whose draft is less than the water depth. Consider a cylinder which is symmetrical about its vertical axis and is allowed to have two modes of motion: heave and sway (or roll). Let R and T be the reflection and transmission coefficients, respectively, when the body is held fixed. The induced heave (sway) creates radiation potentials which are symmetric (antisymmetric) with respect to the vertical axis. The corresponding normalized radiated wave amplitudes at infinity are A_s (A_a) at $x \sim +\infty$ and A_s $(-A_a)$ at $x \sim -\infty$. If the induced motion is controlled (e.g., by dampers and springs) so that $R + A_s - A_a = 0$ and $T + A_s + A_a = 0$, then all the incident wave energy is absorbed.

By using a cam with a cross section in the shape of an inclined tear drop, Salter (1974) demonstrated that roll mode alone is sufficient to give high efficiency. This is partly due to the fact that for sufficiently short waves

or large cylinder $T \approx 0$ and $|R| \approx 1$. Because of the inclined bow and the circular stern, the nodding cam radiates larger waves to the incidence than to the transmission side. By controlling the phase and magnitude of A_-, it is possible to make $R + A_-$ very small, leaving a large fraction of incident power for extraction. This device has been christened the *duck*, because of its pointed beak, round tail, and nodding motion.

Many other varieties of design are possible. For example, one may hinge one end of a floating pontoon on a sea wall and install a converter (e.g., a torsional damper) at the hinge. Proper control of the pontoon size and motion will enable complete removal of incident wave energy also. Instead of a fixed hinge, several pontoons may be hinged in a series and moored only at the bow; energy may then be extracted from the relative rotation of adjacent pontoons about the hinges. This is the two-dimensional version of the raft invented by G. Hagen (1975) and C. Cockerell (Wooley and Platts, 1975). Another device makes use of the fact that a submerged stationary circular cylinder does not reflect normally incident waves, while the transmitted waves only suffer a phase shift (Ursell, 1950). If the same cylinder is made to move along a circular orbit around its axis, then wave radiation will be in one direction only (Ogilvie, 1963). Because of these properties, a buoyant circular cylinder tied to a pair of taut moorings can be controlled to absorb all the incident wave energy (Evans et al., 1979).

There are also designs involving pneumatic mechanisms for power take-off. For example, the oscillating water column of the National Engineering Laboratory, United Kingdom, has a line of caissons moored to the sea floor. The interior of the caisson is an air–water chamber open to the sea through a slot below the free surface on the incidence side. With proper chamber dimensions, the water level within may be tuned to resonance, thereby producing high-pressure air capable of driving, through a rectifier, a turbine in a duct.

Omnidirectional Absorbers

An extensively studied point absorber is a small vertical cylindrical buoy moored to the sea bottom (Budal and Falnes, 1975; Falnes and Budal, 1978). Work is done by the heaving buoy relative to the mooring rod or line. When properly tuned, energy can be absorbed from a sizable width of the wave crest much larger than the diameter of the buoy.

Another variety makes use of a resonant tube which can be either totally or partially submerged (Simon, 1981; see also Lighthill, 1979a for the beam–sea version).

The so-called dam–atoll (Wirt and Higgins, 1979) uses a submerged circular island to focus the incoming wave rays to the top of the island, where special vanes guide the high water down to a vertical shaft which houses a turbine.

Head–Sea Absorbers

In contrast to the beam–sea absorbers, a slender body pointed normally to the wave crests suffers relatively small horizontal wave forces. The differences among various slender head–sea absorbers lie primarily in the details of power takeoff. In the floating raft system of G. Hagen and C. Cockerel1 each raft has several pontoons connected by hinges, and energy is derived from the relative rotation about the hinges. The Kaimei ship of M. Masuda (1979) has a series of vertical chambers open along the keel to the sea. In each chamber there is a turbine which is driven by the oscillatory water column. The system of M. J. French (1979) has many flexible air bags mounted on a slender floating frame. The varying pressure from the passing waves compresses the bags which then act as pumps to circulate air in a pipe connected to a turbine.

When the power converter is physically a part of the main structure placed in the sea, costs for energy storage and transmission to land are important concerns. To circumvent these costs, Mehlum and Stamnes (1979) introduced a submerged (beam–sea) lens along a line parallel to the incoming wave crests. Each section of the lens is designed to induce little reflection but to cause different phase lag in the transmitted wave. After passing the lens, the wave crests become concave and converge toward a focal point where a converter is installed. The lateral dimensions of the lens are comparable to other beam–sea devices.

While a recent survey of the large literature can be found in Falnes (2002), we analyze a few simple devices below.

8.9.2 A Two-Dimensional Beam–Sea Absorber — Salter's Cam (Duck)

Consider normal incidence and an infinitely long cam with a rigid shaft. The problem is two dimensional. Let $\overline{X}$ and $\overline{Z}$ denote the mean position of the center of the shaft (point Q), ξ_1 and ξ_3 the translations of the shaft, and ξ_5 the rotation about the shaft.

The equations of the cam are given by Eq. (8.3.24). There is now a reacting force due to the energy generator which transforms the mechanical

energy of waves to another form. For generality, we assume that the generator exerts a force on the cam

$$(\omega^2\mu'_{\alpha\beta} - C'_{\alpha\beta} + i\omega\lambda'_{\alpha\beta})\xi_\beta\,, \quad \alpha,\beta = 1,3,5 \tag{8.9.1}$$

which is partly inertial ($\mu'_{\alpha\beta}$), partly elastic ($C'_{\alpha\beta}$), and partly damping ($\lambda'_{\alpha\beta}$). These primed matrices are the characteristics of the energy generator. If the force in the αth direction due to ξ_β is nonzero, off-diagonal terms of the matrices do not vanish, meaning that modes of the generator can be coupled. The equations of motion of the cam are, therefore,

$$\begin{aligned}[-\omega^2(M_{\alpha\beta} + \mu_{\alpha\beta} + \mu'_{\alpha\beta}) + (C_{\alpha\beta} + C'_{\alpha\beta}) - i\omega(\lambda_{\alpha\beta} + \lambda'_{\alpha\beta})]\xi_\beta \\ = F^D_\alpha + \mathbb{F}_\alpha\,,\end{aligned} \tag{8.9.2}$$

where F^D_α is the exciting force due to diffraction and $\mathbb{F}_\alpha$ the constraining force on the shaft, where the matrices $[M]$, $[C]$, $[\mu]$, and $[\lambda]$ have been defined in Sections 8.2 and 8.3.

When the shaft is fixed, $\xi_1 = \xi_3 = 0$, there is only one degree of freedom, that is, ξ_5 (roll). If we assume that the friction between the cam and the shaft is also included in $\lambda'_{\alpha\beta}$ of Eq. (8.9.1), then $\mathbb{F}_5 = 0$ and Eq. (8.9.2) may be simplified to

$$[-\omega^2\mathscr{M}_{55} + \mathscr{C}_{55} - i\omega(\lambda_{55} + \lambda'_{55})]\xi_5 = F^D_5\,, \tag{8.9.3}$$

where

$$\begin{aligned}\mathscr{M}_{55} &= M_{55} + \mu_{55} + \mu'_{55}\,,\\ \mathscr{C}_{55} &= C_{55} + C'_{55}\,.\end{aligned}$$

The solution is obvious. The known value of ξ_5 can be substituted into the remaining momentum equations:

$$\begin{aligned}[-\omega^2(M_{\alpha5} + \mu_{\alpha5} + \mu'_{\alpha5}) + (C_{\alpha5} + C'_{\alpha5}) - i\omega(\lambda_{\alpha5} + \lambda'_{\alpha5})]\xi_5 \\ = F^D_\alpha + \mathbb{F}_\alpha\,, \quad \alpha = 1,3\end{aligned} \tag{8.9.4}$$

to determine the constraining force $\mathbb{F}_\alpha$, which is the negative of the force exerted by the cam on the shaft.

Equation (8.9.4) is formally identical to that describing a simple harmonic oscillator. Clearly, the power extracted is

$$\overline{\dot{E}} = \frac{1}{2}\lambda'_{55}\omega^2|\xi_5|^2$$

$$= \frac{1}{2}\frac{\lambda'_{55}\omega^2|F_5^D|^2}{(\mathscr{C}_{55} - \mathscr{M}_{55}\omega^2)^2 + (\lambda_{55} + \lambda'_{55})^2\omega^2}\,. \tag{8.9.5}$$

We emphasize that this total power removed from the waves includes both usable and wasted power due to friction and generator loss, and so on. If the incident wave frequency and the cam geometry are both fixed, then μ_{55}, λ_{55}, and F_5^D are fixed. Let us suppose that the cam inertia M_{55} and the damping rate λ'_{55} can be adjusted to maximize the power output. Therefore we require that

$$\frac{\partial\overline{\dot{E}}}{\partial\lambda'_{55}} = 0 \quad \text{and} \quad \frac{\partial\overline{\dot{E}}}{\partial(\mathscr{M}_{55} - \mathscr{C}_{55}\omega^2)} = 0\,, \tag{8.9.6}$$

leading to the optimizing criteria

$$\mathscr{C}_{55} - \mathscr{M}_{55}\omega^2 = 0 \tag{8.9.7}$$

and

$$\lambda'_{55} = \lambda_{55}\,. \tag{8.9.8}$$

According to the first criterion, the cam must be tuned to resonance, which is intuitively reasonable. The second criterion means that the effective extraction rate must equal the effective radiation damping rate, which is a result not easily anticipated. Substituting Eqs. (8.9.7) and (8.9.8) into Eq. (8.9.5), we get the optimum power

$$\overline{\dot{E}}_{\text{opt}} = \frac{|F_5^D|^2}{8\lambda_{55}}\,. \tag{8.9.9}$$

By means of Eq. (8.6.11) and the Haskind–Hanaoka relation (8.6.40), the right-hand side of Eq. (8.9.9) may be represented in terms of the far-field amplitudes $\mathcal{A}^{\pm}$ due to unit roll:

$$\overline{\dot{E}}_{\text{opt}} = \frac{\frac{1}{2}\rho g A^2 C_g}{1 + |\mathcal{A}^+|^2/|\mathcal{A}^-|^2}\,. \tag{8.9.10}$$

Since the numerator is the power flux of the incident wave per unit crest length, the optimum efficiency is

$$E_{\text{ff}}^{\text{opt}} = \left(1 + \frac{|\mathcal{A}^+|^2}{|\mathcal{A}^-|^2}\right)^{-1}\,. \tag{8.9.11}$$

This formula (Evans, 1976; Mei, 1976; Newman, 1976) gives the maximum possible efficiency for energy removed from the waves. Through $\mathcal{A}^{\pm}$, $E_{\rm ff}^{\rm opt}$ is a function of frequency and the cam geometry. For a body symmetrical about its vertical axis, $|\mathcal{A}^{+}| = |\mathcal{A}^{-}|$; the maximum ideal efficiency is at most $\frac{1}{2}$. As $|\mathcal{A}^{+}|/|\mathcal{A}^{-}|$ decreases, this efficiency increases toward unity; this can be achieved by an asymmetrical cam, and Salter's cam with its circular stern and inclined bow certainly conforms with this principle.

Using the damping and added mass coefficients calculated by numerical solutions of the requisite scattering and radiation problems, Mynett, Serman, and Mei (1979) have obtained the following results for Salter's model cam profile shown in Fig. 8.8 which is slightly different from the profile used for Figs. 8.9(a)–8.9(d). The depth of water is kept at $h = 4a$, where a is the radius of the cam stern.

Figure 8.11 shows the efficiency curves for a variety of extraction rates. Note first that if the cam is so small that for a given design frequency the resonance corresponds to $\hat{\omega} < 0.5$ where $\hat{\omega} = \omega(a/g)^{1/2}$, then not only is the peak efficiency low but the bandwidth of the efficiency curve is narrow.

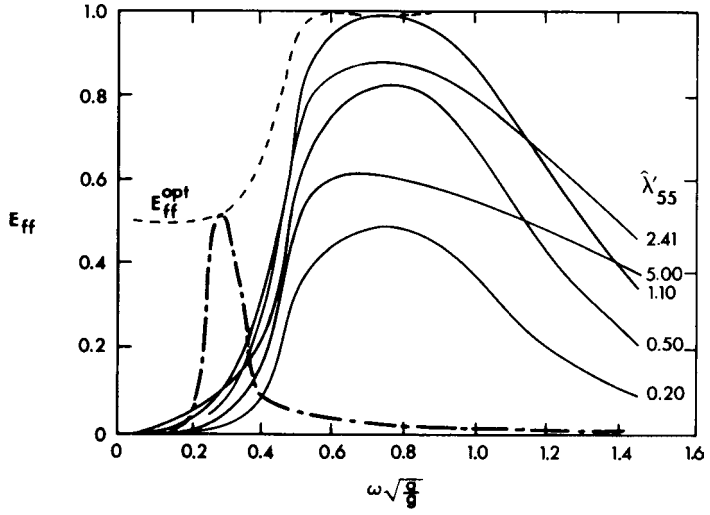

Figure 8.11: Efficiencies of Salter's cam on a fixed shaft. Optimum efficiency $E_{ff}^{\rm opt}$. Solid curve: Inertia is optimized at $\omega(a/g)^{1/2} = 0.7$ ($\hat{I}_{55} = I_{55}/\rho a^4 = 1.9$) but extraction rates vary from below to above optimum ($\hat{\lambda}'_{55} = 1.10$) where $\hat{\lambda}'_{55} = \lambda_{55}/\rho a^4 (g/a)^{1/2}$. Dash–dot curve: inertia and extraction rates are optimized at $\omega(a/g)^{1/2} = 0.25$ with $\hat{I}_{55} = 13$, and $\hat{\lambda}'_{55} = 0.4$ (from Mynett et al., 1979, *Appl. Ocean Res.* Reproduced by permission of CML Publications).

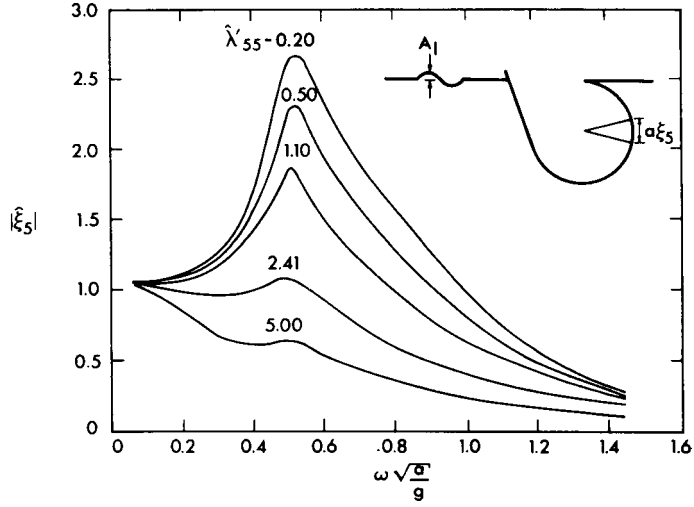

Figure 8.12: Normalized amplitude of roll angle $\hat{\xi}_5 \equiv (a\xi_5)/A$, corresponding to solid curves in Fig. 8.11 (from Mynett et al., 1979, *Appl. Ocean Res.* Reproduced by permission of CML Publications).

The sharpness is associated with the rapid decrease of radiation damping (see Fig. 8.9(e) for the qualitative trend).

For a sufficiently large cam the bandwidth of the efficiency curve easily spans over a range $k_0 < k < 2k_0$ which is the range in which most of the wind wave energy lies. Thus, Salter's cam with one degree of freedom is excellent in efficiency. Figure 8.12 gives the roll amplitude for various damping rates.

The major drawback of a cam on a fixed axis is the large wave force which must be endured by the shaft [Figs. 8.13(a) and 8.13(b)]. The maximum vertical and horizontal forces at resonance are of the order ($5\rho gaA$) per unit cam length. Let $a = 10$ m, $A = 1$ m, and $\rho g = 10^4$ kg/m^2-s. The peak force can be $f \sim 50$ tons/m. This large force is inevitable on any rigidly supported beam–sea absorber of similar draft.

Because a rigid support is costly, there are now attempts to allow for a flexible support with provisions to utilize each mode of motion for power production. For this purpose an intricate automatic control system is needed which is capable of varying the impedance of the power-takeoff mechanism in order to maximize the efficiency according to the changing sea spectrum. Indeed, Salter (1979) has developed a system with a

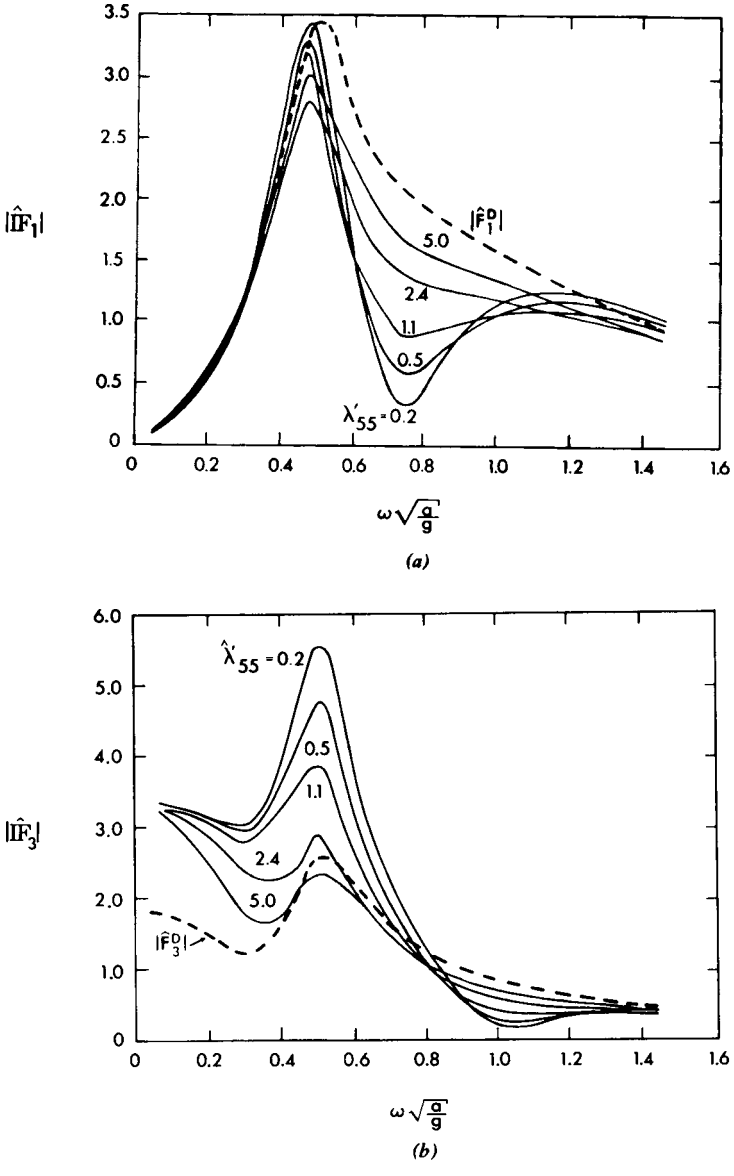

Figure 8.13: Normalized forces $\hat{F} = F/\rho g A a$. Solid curves correspond to solid curves in Fig. 8.11. (a) Horizontal exciting force $\hat{F}_1^D$ and horizontal constraining force $\hat{\mathbb{F}}_1$; (b) vertical exciting force $\hat{F}_3^D$ and vertical constraining force $\hat{\mathbb{F}}_3$ (from Mynett et al., 1979, *Appl. Ocean Res.* Reproduced by permission of CML Publications).

string of ducks which are slackly moored. Precessing gyros, controlled by microprocessors, are sealed within each duck. Energy is extracted from the precession relative to the moving duck. While automatic control may be a technologically innovative solution of some difficult problems unique to the sea, strong sentiments exist which prefer the use of simple devices at the expense of low efficiency.

8.9.3 Optimum Efficiency of Three-Dimensional Absorbers

A complete study of three-dimensional absorbers regarding optimum and off-optimum performances, wave forces, and so on, requires considerable numerical computations for the scattering and radiation problems (see, e.g., Simon, 1981; Thomas, 1981). The detailed results vary with the design. We shall limit our discussion here to certain features regarding the optimum efficiency without specifying the power-takeoff system (Newman, 1976, 1979; Budal, 1977).

First, the power extracted by a body must equal the rate of work done by the dynamic pressure in water to the body, that is,

$$\overline{\dot{E}} = \iint_{S_B} p\overline{\frac{\partial \Phi}{\partial n}}\, dS = \frac{i\omega\rho}{4} \iint_{S_B} \left(\phi \frac{\partial \phi^*}{\partial n} - \phi^* \frac{\partial \phi}{\partial n}\right) dS$$

$$= -\frac{i\omega\rho}{4} \iint_{S_\infty} \left[\phi \frac{\partial \phi^*}{\partial n} - \phi^* \frac{\partial \phi}{\partial n}\right] dS\,. \tag{8.9.12}$$

Let the total potential be decomposed to three parts: incident, scattered, and radiated:

$$\phi = \phi^I + \phi^S + \phi^R\,. \tag{8.9.13}$$

Let us define $\mathcal{A}$ to be the amplitude factor of the total outgoing waves:

$$\phi^S + \phi^R = -\frac{igA\mathcal{A}}{\omega} \frac{\cosh k(z+h)}{\cosh kh} \left(\frac{2}{\pi kr}\right)^{1/2} e^{i(kr-\pi/4)}\,. \tag{8.9.14}$$

It follows after familiar use of stationary phase that

$$\overline{\dot{E}} = \frac{\rho g A^2}{k} C_g \left\{-\frac{1}{\pi} \int_0^{2\pi} d\theta |\mathcal{A}(\theta)|^2 - 2\ \mathrm{Re}\mathcal{A}(0)\right\} \tag{8.9.15}$$

which is a generalized optical theorem.

We further define the *absorption* (or *capture*) width as the ratio of the absorbed power to the incident power per unit width of the crest, that is,

$$W = \overline{\dot{E}} \left(\frac{1}{2} \rho g A^2 C_g \right)^{-1} , \tag{8.9.16}$$

then the following dimensionless ratio

$$kW = -\frac{2}{\pi} \int_0^{2\pi} d\theta |\mathcal{A}(\theta)|^2 - 4 \, \mathrm{Re}\mathcal{A}(0) \tag{8.9.17}$$

is clearly a measure of efficiency. For greatest efficiency, it is necessary to maximize the total scattered and radiated waves in the forward direction $\theta = 0$.

Newman has also deduced useful expressions for $\overline{\dot{E}}$ and kW in terms of the radiation potentials only. To anticipate the behavior of articulated rafts or deformable bodies, he assumes that the normal velocity of the body surface can be expressed as the sum of real-valued normal modes $f_\alpha(x, y, z)$ on S_B, that is,

$$\frac{\partial \phi^R}{\partial n} = A \sum_\alpha V_\alpha f_\alpha(x, y, z) \quad \text{on} \quad S_B \, , \tag{8.9.18}$$

with V_α being complex constants. The total potential can then be decomposed as

$$\Phi = A e^{-i\omega t} \left(\phi^D + \sum_\alpha V_\alpha \phi_\alpha \right) , \tag{8.9.19}$$

where

$$\frac{\partial \phi^D}{\partial n} = 0 \, , \quad \text{on} \quad S_B \, , \tag{8.9.20}$$

$$\frac{\partial \phi_\alpha}{\partial n} = f_\alpha \, , \quad \text{on} \quad S_B \, , \tag{8.9.21}$$

The extracted energy is

$$\begin{aligned} \overline{\dot{E}} &= \iint_{S_B} p \overline{\frac{\partial \Phi}{\partial n}} \, dS = \frac{1}{2} \rho \omega A^2 \, \mathrm{Re} \iint_{S_B} i \left(\phi^D + \sum_\alpha V_\alpha \phi_\alpha \right) \left(\sum_\beta V_\beta^* f_\beta \right) dS \\ &= \frac{1}{2} \rho \omega A^2 \, \mathrm{Re} \left\{ i \sum_\alpha V_\alpha^* \iint_{S_B} \phi^D f_\alpha \, dS + i \sum_\alpha \sum_\beta V_\alpha V_\beta^* \iint_{S_B} \phi_\alpha f_\beta \, dS \right\} . \end{aligned} \tag{8.9.22}$$

For the first series above, the Haskind–Hanaoka theorem applies,

$$\iint_{S_B} \phi^D f_\alpha \, dS = \frac{4ig}{\omega k} C_g \mathcal{A}_\alpha(\pi) \,, \tag{8.9.23}$$

which is simply Eq. (8.6.41) when n_α is replaced by f_α. Furthermore, the restoring force matrix is symmetric, that is,

$$\iint_{S_B} \phi_\alpha f_\beta \, dS = \iint_{S_B} \phi_\beta f_\alpha \, dS \,. \tag{8.9.24}$$

Now the double series in Eq. (8.9.22) may be manipulated by interchanging the indices to give

$$\begin{aligned} &\mathrm{Re}\, i \sum_\alpha \sum_\beta V_\alpha V_\beta^* \iint_{S_B} \phi_\alpha f_\beta \, dS \\ &\qquad = -\mathrm{Re} \sum_\alpha \sum_\beta V_\alpha V_\beta^* \left(\mathrm{Im} \iint_{S_B} \phi_\alpha f_\beta \, dS \right) . \end{aligned}$$

Again by using the symmetry theorem (8.9.24), we obtain

$$\begin{aligned} \mathrm{Im} \iint_{S_B} \phi_\alpha f_\beta \, dS &= \frac{1}{2i} \iint_{S_B} \left(\phi_\alpha \frac{\partial \phi_\beta^*}{\partial n} - \phi_\beta^* \frac{\partial \phi_\alpha}{\partial n} \right) dS \\ &= \frac{-1}{2i} \iint_{S_\infty} \left(\phi_\alpha \frac{\partial \phi_\beta^*}{\partial n} - \phi_\beta^* \frac{\partial \phi \alpha}{\partial n} \right) dS \\ &= \frac{2gC_g}{\pi \omega k} \int_0^{2\pi} d\theta \, \mathcal{A}_\alpha(\theta) \mathcal{A}_\beta^*(\theta) \end{aligned}$$

which agrees with Eq. (8.6.13); therefore,

$$\begin{aligned} &\mathrm{Re}\, i \sum_\alpha \sum_\beta V_\alpha V_\beta^* \iint_{S_B} \phi_\alpha f_\beta \, dS \\ &\qquad = -\frac{2gC_g}{\pi \omega k} \int_0^{2\pi} d\theta \left| \sum_\alpha V_\alpha \mathcal{A}_\alpha(\theta) \right|^2 . \end{aligned} \tag{8.9.25}$$

When Eqs. (8.8.24) and (8.9.25) are put in Eq. (8.9.22), the extracted power becomes

$$\overline{\dot{E}} = -\frac{1}{2} \rho g A^2 \frac{C_g}{k} \left[\frac{2}{\pi} \int_0^{2\pi} d\theta \left| \sum_\alpha V_\alpha \mathcal{A}_\alpha \right|^2 + \mathrm{Re}\, 4 \sum_\alpha V_\alpha \mathcal{A}_\alpha^*(\pi) \right] \tag{8.9.26}$$

which is expressed only in terms of the radiation potentials. Accordingly, the efficiency is

$$kW = -\frac{2}{\pi}\int_0^{2\pi} d\theta \left| \sum_\alpha V_\alpha \mathcal{A}_\alpha(\theta) \right|^2 - 4 \text{ Re} \sum_\alpha V_\alpha \mathcal{A}_\alpha^*(\pi)\,. \tag{8.9.27}$$

If there is only one degree of freedom, the summation sign can be removed from Eq. (8.9.27). To maximize the efficiency the second term in Eq. (8.9.27) must be real and negative, that is,

$$V_\alpha \mathcal{A}_\alpha^*(\pi) = -|V_\alpha|\ |\mathcal{A}_\alpha(\pi)|\,.$$

The maximum value is

$$(kW)_{\text{opt}} = \frac{2\pi |\mathcal{A}_\alpha(\pi)|^2}{\int_0^{2\pi} |\mathcal{A}_\alpha(\theta)|^2\, d\theta}\,, \tag{8.9.28a}$$

which occurs when

$$|V_\alpha| = \frac{\pi |\mathcal{A}_\alpha(\pi)|}{\int_0^{2\pi} |\mathcal{A}_\alpha(\theta)|^2\, d\theta}\,. \tag{8.9.28b}$$

Equation (8.9.28) is the three-dimensional counterpart of Eq. (8.9.11) and implies that for one degree of freedom, focusing the radiated waves in the opposite sense of the incident wave can increase efficiency. We now seek more specific results.

Omnidirectional Absorbers

Consider an absorber which is an axially symmetric rigid body about an upright axis. There are only three modes $\alpha = 1$, 3, and 5. Substituting Eq. (8.6.55) into Eq. (8.9.26) and integrating, we get

$$\begin{aligned}\overline{\dot{E}} = -\frac{1}{k}\rho g A^2 C_g \{ &|V_1\mathcal{A}_1(0) + V_5\mathcal{A}_5(0)|^2 + 2|V_3\mathcal{A}_3(0)|^2 \\ &- 2 \text{ Re}\,[V_1\mathcal{A}_1^*(0) + V_5\mathcal{A}_5^*(0) + 2 \text{ Re}\,[V_3\mathcal{A}_3^*(0)]\}\,.\end{aligned} \tag{8.9.29}$$

For maximum $\overline{\dot{E}}$ we must orchestrate the motion so that $V_1\mathcal{A}_1^*(0) + V_5\mathcal{A}_5^*(0)$ is real and positive while $V_3\mathcal{A}_3^*(0)$ is real and negative. The optimum criteria are

$$V_1\mathcal{A}_1^*(0) + V_5\mathcal{A}_5^*(0) = 1 \quad \text{and} \quad V_3\mathcal{A}_3^*(0) = -\frac{1}{2}\,. \tag{8.9.30}$$

The corresponding optimum absorbed power and efficiency are

$$\overline{\dot{E}}_{\rm opt} = \frac{3}{2k}\rho g A^2 C_g\,, \tag{8.9.31a}$$

$$kW_{\rm opt} = 3\,. \tag{8.9.31b}$$

When all three modes are optimized, the absorption width is about $\frac{1}{2}\lambda$, *independent* of the body size. If the axially symmetric buoy only heaves (such as a small buoy), Eq. (8.9.28) shows that $kW_{\rm opt} = 1$ which is one-third of the possible maximum when all three are optimized. These results may be confirmed in another way. Recall that the incident wave may be expanded as

$$Ae^{ikx} = A\sum_{n=0}^{\infty} \varepsilon_n (i)^n J_n(kr)\cos n\theta\,.$$

In the far field the nth partial wave mode may be approximated by

$$\varepsilon_n i^n \cos n\theta \frac{A}{2}\left(\frac{2}{\pi kr}\right)^{1/2} \times \left\{\exp\left[i\left(kr - \frac{\pi}{4} - \frac{n\pi}{2}\right)\right] + \exp\left[-i\left(kr - \frac{\pi}{4} - \frac{n\pi}{2}\right)\right]\right\}$$

which consists of both outgoing and incoming parts. Supposing that the body is only allowed to heave, its induced motion in the fluid can only be axially symmetric, that is, isotropic. With proper orchestration the radiated wave can be combined with the isotropic mode ($n = 0$) of the scattered wave to cancel the outgoing part of the isotropic mode in the incident wave. The converging part of the incident isotropic mode is available for absorption; the corresponding rate of energy influx through a circular cylindrical surface around the body is $\frac{1}{2}\rho g A^2 C_g/k$, which implies an absorption width of $W = 1/k$. Similarly, if the body can only sway or roll, the radiated wave is proportional to $\cos\theta$ only and can be used to cancel the outgoing part of the partial wave mode with $n = 1$. The energy influx from the converging part is then $\rho g A^2 C_g/k$, which implies $W = 2/k$.

It is interesting that the value of the optimum efficiency does not depend on the size of the buoy, suggesting that a small buoy can be as efficient as a larger one. However, a small buoy can only achieve the same optimum by oscillating at a very large amplitude, which may be demonstrated for the case of heave only $V_3 \neq 0$, $V_1 = V_5 = 0$. By the Haskind–Hanaoka theorem, Eq. (8.6.41), $\mathcal{A}_3(0)$ may be expressed in terms of the exciting force F_3^D

$$\mathcal{A}_3(0) = -\frac{k}{4} F_3^D (\rho g C_g A)^{-1} . \tag{8.9.32}$$

For a small buoy, F_3^D may be estimated by ignoring both diffraction and the spatial variation of pressure around the buoy, yielding

$$F_3^D \cong \rho g A \pi a^2 , \tag{8.9.33}$$

where a is the radius of the buoy at the water plane. Putting Eq. (8.9.33) into Eq. (8.9.32) and then into Eq. (8.9.30), we get

$$\mathcal{A}_3 = -\frac{\pi k a^2}{4 C_g} , \tag{8.9.34a}$$

$$AV_3 = \frac{2}{\pi} \frac{A}{a} \frac{C_g}{ka} . \tag{8.9.34b}$$

Thus, for diminishing ka the heave velocity AV_3 must become very large for optimum absorption.

Furthermore, from Eq. (8.6.13) the radiation damping coefficient may be calculated:

$$\lambda_{33} \cong \frac{\rho g a^4 k}{4 C_g} \tag{8.9.35}$$

which also diminishes with ka. By considerations similar to Section 8.9.2, the response curve of a small heaving buoy must be very sharply peaked. In order to achieve high efficiency for the broad frequency spectrum of sea waves, it is necessary to tune a small heaving buoy to optimum conditions for nearly every frequency in that spectrum. The following tuning method by phase control has been demonstrated in the laboratory by Falnes and Budal (1978) and Budal et al. (1979). A small buoy is used so that the resonant frequency is always far above the incident wave frequency. In order to maximize the power output, an electronic circuit is introduced to alternately lock or free the buoy so that its heave velocity is roughly in phase with the exciting force. Note that for a small buoy the exciting force is in phase with the incident wave surface, scattering being negligible. Wave height measured instantaneously in front of the buoy can be signaled back for optimum phase control.

In large-scale applications, it is natural to envision an array of point absorbers. The total system is in general no longer omnidirectional and interference among neighboring buoys can either enhance or reduce the overall efficiency. Budal (1977), Falnes and Budal (1978), Budal et al. (1979), and

Falnes (1980) have made a number of important theoretical and experimental contributions to this topic. In particular, Budal studied a single row of N small and identical buoys equally spaced at the distance d between centers, with the incident wave inclined at the angle α with respect to the line of centers. He assumed that all the buoys only heaved at equal amplitude, but different phase. When $kd = 0(1)$, he used an approximation for weak interaction and showed the total capture width to be

$$kW = Nq\,, \tag{8.9.36a}$$

with q being the interaction factor

$$q = \left[1 + \frac{2}{N}\sum_{n=1}^{N}(N-n)\cos(nkd\sin\alpha)J_0(nkd)\right]^{-1}\,. \tag{8.9.36b}$$

When $d \to \infty$, $q \to 1$; the total capture width is the sum of the individual capture width of N isolated bodies. Figure 8.14 shows the interference factor for normal incidence $\alpha = 0$ and for $N = 2$, 10, and ∞. Clearly, interference can be constructive so as to augment the capture width. In the limit of $N \to \infty$,

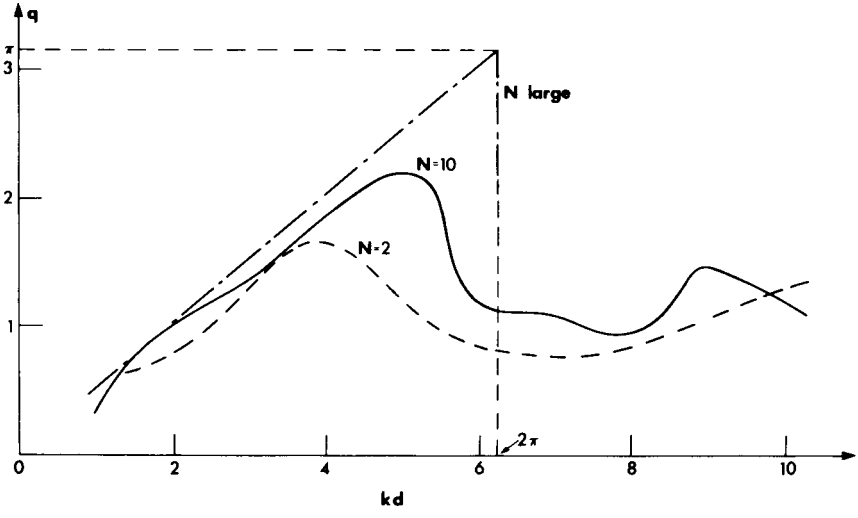

Figure 8.14: The interaction factor q [Eq. (8.9.36b)] for normal incidence and for two, ten, and an infinite number of bodies in a row. For small kd, Eq. (8.9.36b) is invalid. All bodies move with equal amplitudes (from Budal, 1977, *J. Ship Res.* Reproduced by permission of The Society of Naval Architects and Marine Engineers).

$$W = \frac{Nd\cos\alpha}{2} \quad \text{for} \quad kd < \frac{2\pi}{1+\sin\alpha}\,,$$

implying that the row of buoys absorbs half of the power incident on the projected length $Nd\cos\alpha$. Budal further studied two parallel rows and showed that all the incident power on the projected length could be absorbed.

Srokosz (1979) (see also Evans, 1979, and Falnes, 1980) relaxed the constraint of Budal and allowed the N point absorbers to have unequal motions. The optimum interaction factor q was found to be greater than that given by (8.9.36b) for low value of kd but the difference diminished for sufficiently large kd. For two absorbers the unconstrained result is

$$q = \frac{1 - J_0(kd)\cos(kd\sin\alpha)}{1 - J_0^2(kd)}\,. \tag{8.9.36c}$$

A sample comparison is shown in Fig. 8.15. Note that for long waves $kd \to 0$ the unconstrained theory gives different q for different incidences. These limits are of doubtful practical significance since the predicted amplitude of optimum motion would be infinite and inconsistent with the assumption of linearity.

A Head–Sea Absorber: Hagen–Cockerell Raft

Newman (1979) has made a penetrating study of the optimum efficiency of a slender Hagen–Cockerell raft which has fore-and-aft symmetry. Following him we let the longitudinal axis of the slender body be the x axis. In general, the vertical displacement Z of the raft may be decomposed into a number of modes $f_\alpha(x)$:

$$Z(x,t) = A\sum_\alpha Z_\alpha f_\alpha(x) e^{-i\omega t}\,, \tag{8.9.37}$$

where Z_α and f_α are dimensionless and f_α is real. Let us consider deep water only. $\mathcal{A}_\alpha(\theta)$ may be related to the potential on the body by Eq. (8.4.32) which becomes, in the limit of $kh \to \infty$,

$$\mathcal{A}_\alpha(\theta) = -\frac{\omega k}{2g}\iint_{S_B} dS\left(\phi_\alpha\frac{\partial}{\partial n} - \frac{\partial\phi_\alpha}{\partial n}\right) e^{kz}\exp(-ikx\cos\theta - iky\sin\theta)\,. \tag{8.9.38}$$

For a slender body with beam and draft small compared to the wavelength, ky, $kz \ll 1$ on S_B and the term $\partial\phi_\alpha/\partial n$ above dominates so that

$$\mathcal{A}_\alpha(\theta) \cong -\frac{\omega k}{2g}\iint_{S_B} dS\frac{\partial\phi_\alpha}{\partial n} e^{-ikx\cos\theta}\,.$$

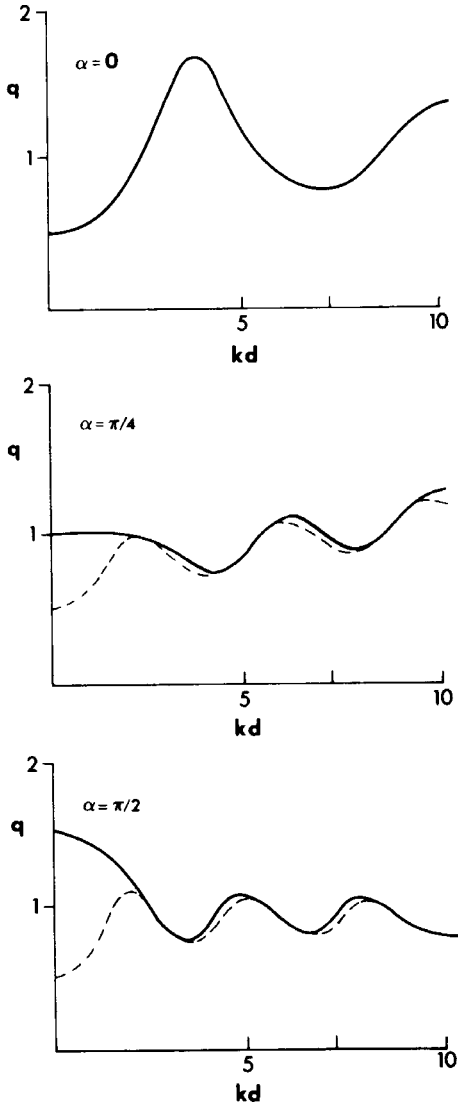

Figure 8.15: The interaction factor for two bodies at various incidences: (a) $\alpha = 0$ normal incidence; (b) $\alpha = \frac{1}{4}\pi$ oblique incidence; (c) $\alpha = \frac{1}{2}\pi$ waves along the line of axis of bodies. Dashed curve: Budal's theory requiring two bodies moving at equal amplitude; solid curve: Srokoz's theory without Budal's constraint (from Srokosz, 1979).

On the body

$$dS\frac{\partial\phi_\alpha}{\partial n} = -i\omega f_\alpha n_z\, dx[(dy)^2 + (dz)^2]^{1/2} = -i\omega f_\alpha\, dx\, dy\,,$$

hence

$$\mathcal{A}_\alpha(\theta) \cong -\frac{i}{2}k^2 \int_{-l/2}^{l/2} dx\, b(x) f_\alpha(x) e^{-ikx\cos\theta}\,, \tag{8.9.39}$$

where l is the body length. Assume for simplicity that $b = \text{const}$ and end effects are minor; Eq. (8.9.39) may be written

$$\mathcal{A}_\alpha(\theta) = -\frac{i}{2}K^2\left(\frac{2b}{l}\right)\int_{-1}^{1} dX f_\alpha(X) e^{-iKX\cos\theta} \tag{8.9.40}$$

after introducing $X = 2x/l$ and $K = \frac{1}{2}kl$. Clearly, $\mathcal{A}_\alpha(\theta)$ is a function of $\cos\theta$. For a body with fore-and-aft symmetry, the motion can always be decomposed into modes which are either even or odd in X. Let f_α be even in X when α is an even integer, then

$$\mathcal{A}_\alpha(\theta) = -iK^2\left(\frac{2b}{l}\right)\int_0^1 dX f_\alpha(X)\cos(KX\cos\theta) \tag{8.9.41}$$

is even in $\cos\theta$ and imaginary. Similarly, let f_α be odd in X when α is an odd integer, then

$$\mathcal{A}_\alpha(\theta) = K^2\left(\frac{2b}{l}\right)\int_0^1 dX f_\alpha(X)\sin(KX\cos\theta) \tag{8.9.42}$$

is odd in $\cos\theta$ and real. For varying b, the product bf_α may be considered as the effective modal shape.

The even and odd symmetry of $\mathcal{A}_\alpha$ implies that the absorption width may be decomposed into even and odd parts also:

$$kW = kW^e + kW^o\,, \tag{8.9.43}$$

where

$$kW^e = -\frac{2}{\pi}\int_0^{2\pi} d\theta\left|\sum_\alpha Z_\alpha\mathcal{A}_\alpha(\theta)\right|^2 - 4\ \mathrm{Re}\sum_\alpha[Z_\alpha\mathcal{A}_\alpha^*(\pi)]\,, \tag{8.9.44}$$

with a similar formula for kW^o.

To extract energy from heave or pitch the raft must be dynamically coupled with a stationary structure which must endure a large wave force.

For the sake of reducing structural costs, a slack mooring is likely preferable in design. One can then expect no absorption from these rigid body modes $\alpha = 0,\ 1$; therefore

$$kW_0 = -\frac{2}{\pi}\int_0^\infty d\theta |Z_0\mathcal{A}_0(\theta)|^2 - 4\ \mathrm{Re}\,[Z_0\mathcal{A}_0^*(\pi)] = 0\,, \tag{8.9.45}$$

and a similar relation $kW_1 = 0$ holds. Subtracting Eq. (8.9.45) from kW^e, we get

$$kW^e = -\frac{2}{\pi}\int_0^{2\pi} d\theta \left|\sum_\alpha{}' Z_\alpha\mathcal{A}_\alpha(\theta)\right|^2 - 4\ \mathrm{Re}\sum_\alpha{}' \{Z_\alpha\mathcal{A}_\alpha^*(\pi)\}$$
$$-\frac{4}{\pi}\ \mathrm{Re}\int_0^{2\pi} d\theta Z_0^*\mathcal{A}_0^*(\theta)\sum_\alpha{}' Z_\alpha\mathcal{A}_\alpha(\theta)\,, \quad \alpha = 2, 4, 6, \ldots \tag{8.9.46}$$

where $\alpha = 0$ is excluded from the sum $\sum'$. Recall first that $\mathcal{A}_\alpha$ is real for all even α. For optimum performance at higher modes $\alpha \geqq 2$, the phases must be such that $Z_\alpha\mathcal{A}_\alpha^*$ is real and negative. Now $\alpha = 0$ is a passive mode with $Z_0 = O(1)$ at most. Since $\mathcal{A}_0 = O(2b/l)$ from Eq. (8.9.41), Eq. (8.9.45) implies that $\mathrm{Re}\,(Z_0\mathcal{A}_0) = O(2b/l)^2$. Consequently, the last term in Eq. (8.9.46) may be neglected with a relative error of $O(2b/l)$. Thus,

$$kW^e \cong -\frac{2}{\pi}\int_0^{2\pi} d\theta \left|\sum_\alpha{}' Z_\alpha\mathcal{A}_\alpha(\theta)\right|^2 - 4\ \mathrm{Re}\sum_\alpha{}' \{Z_\alpha\mathcal{A}_\alpha(\pi)\}^*\,. \tag{8.9.47}$$

A similar result may be obtained for kW^o.

If there is only one even or odd mode, the summation sign may be removed from Eq. (8.9.47). For optimum efficiency one must have

$$Z^e\mathcal{A}^{e^*}(\pi) = |Z^e|\mathcal{A}^e(\pi)|e^{i\pi}$$

so that

$$kW^e = -\frac{2}{\pi}|Z^e|^2\int_0^{2\pi} d\theta|\mathcal{A}^e(\theta)|^2 + 4|Z^e|\ |\mathcal{A}^e(\pi)|\,. \tag{8.9.48}$$

A similar expression holds for the odd mode. Equations (8.9.28a) and (8.9.28b) hold for $(kW^e)_{\mathrm{opt}}$ and $(kW^o)_{\mathrm{opt}}$ when $\mathcal{A}_\alpha$ is replaced by $\mathcal{A}^e$ and $\mathcal{A}^o$, respectively.

Now consider an articulated raft made up of three pontoons with two hinges located at $x = \pm\frac{1}{2}al$ (i.e., $X = \pm a$). There can only be four independent modes of transverse motion. Hence, aside from heave and pitch, there are only one even and one odd mode. The following modal shapes can be shown to be orthogonal to heave and pitch:

$$f^e = \begin{cases} 1\,, & |X| < a \\ 1 - \dfrac{2(|X| - a)}{(1-a)^2}\,, & a < |X| < 1 \end{cases} \tag{8.9.49a}$$

$$f^o = \frac{\pm a[2 + (a^2 - 3)|X|]}{(2+a)(1-a)^2}\,, \quad \pm a \lessgtr X \lessgtr \pm 1\,. \tag{8.9.49b}$$

The corresponding maximum displacements are

$$f^e_{\max} = f^e(1) = \frac{1+a}{1-a} \tag{8.9.50a}$$

$$f^o_{\max} = \begin{cases} f^o(a) = a\,, & a < \sqrt{2} - 1 \\ f^o(1) = \dfrac{a(1+a)}{(2+a)(1-a)}\,, & a > \sqrt{2} - 1 \end{cases}. \tag{8.9.50b}$$

A power-takeoff mechanism can, in principle, be designed for each mode. Now the amplitude functions may be evaluated explicitly:

$$\mathcal{A}^e = \frac{2iK^2 b}{l}\left\{\frac{1+a}{1-a}\frac{\sin(K\cos\theta)}{K\cos\theta} + \frac{2}{(1-a)^2(K\cos\theta)^2} \times [\cos(K\cos\theta) - \cos(Ka\cos\theta)]\right\} \tag{8.9.51a}$$

and

$$\mathcal{A}^o = \frac{K^2 b}{l}\left\{\frac{-2a}{(2+a)(1-a)^2 K\cos\theta}\left[\frac{2\sin(Ka\cos\theta)}{Ka\cos\theta} + (a^2 - 3) \times \frac{\sin(K\cos\theta)}{K\cos\theta} + (1-a^2)\cos(K\cos\theta)\right]\right\}. \tag{8.9.51b}$$

These functions may be substituted into Eq. (8.9.48) for the optimum absorption widths which are plotted as solid lines in Fig. 8.16. Although $W/l \uparrow \infty$ as $k \downarrow 0$, it may be shown that kW approaches a finite limit for long waves. Nevertheless Z^e and Z^o become unbounded, implying violent

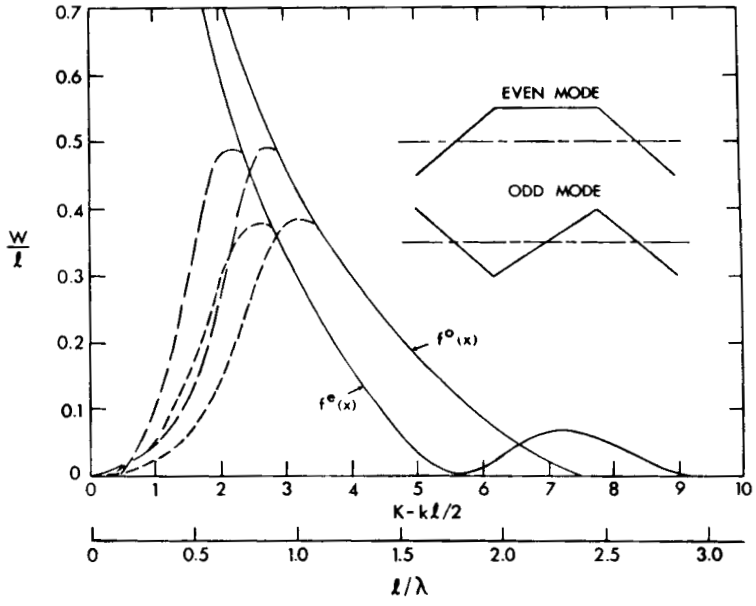

Figure 8.16: Absorption width ratios W/l for hinged raft ($a = 0.4$) with the modes f^e and f^o of optimum amplitude and phase. Broken curves are for the limited displacements defined by Eq. (8.9.52) (from Newman, 1979, *Appl. Ocean Res.* Reproduced by permission of CML Publications).

motion. A further condition that the vertical displacement must not exceed a certain limit,

$$\beta = \frac{|Z^{e,o}|b}{l} < 0.2 \quad \text{or} \quad 0.4\,, \tag{8.9.52}$$

may be imposed on Eq. (8.9.48) for the maximum absorption width. The corresponding curves for $(W/l)_{\text{opt}}$ are shown in Fig. 8.16 by long dashes for $\beta < 0.4$ and short dashes for $\beta < 0.2$. These constraints can be enforced by electronically controlling the impedances. The total optimum power is the sum of the contributions from the two modes. Within the practical range of $0.2 < a < 0.6$ the optimum W/l is insensitive to a.

Further studies on the impedance of the power-takeoff mechanism at the hinges have been made by Haren and Mei (1980). They have shown that it is necessary to have negative springs and even negative damping at the forward hinge so that the induced raft motion can radiate large waves in the forward direction. This result is in accordance with Eq. (8.9.15) since

the scattered wave is negligible. Heuristically, the radiated waves should be made to cancel the diverging part of as many partial wave modes in the incident wave as possible. For "infinite" absorption width the radiated waves must have the following far field:

$$\eta^R \cong -\left(\frac{2}{\pi kr}\right)^{1/2} e^{i(kr-\pi/4)} \frac{A}{2} \sum_{n=0} \varepsilon_n (i)^n e^{-in\pi/2} \cos n\theta$$

$$= -\left(\frac{2}{\pi kr}\right)^{1/2} e^{i(kr-\pi/4)} \frac{A}{2} \delta(\theta)\,.$$

The δ-function dependence implies forward focusing. Of course, this limit cannot be achieved in practice for a raft of finite length.

Finally, Newman (1980, private communication) has also extended the slender body theory to the Kaimei ship with a discrete number of resonant chambers.

For a survey of many other theoretical aspects of wave-power absorption, reference should be made to Evans (1981) and Falnes (2002).

8.10 Trapped Modes Near a Mobile Storm Barrier

Venice is a small island city in a lagoon approximately 50 km long and 5 km wide. During much of the last century excessive pumping of groundwater in the neighboring mainland district of Maghera has caused severe land subsidence. Compounded by the gradual rise of the sea-level, the elevation of Venice is now so low that storm tides entering the lagoon from the Adriatic innundate the city at the average frequency of once a week. As a measure to hault further decay of this fabled city, storm barriers have been designed to span the four inlets of Venice Lagoon: Lido-Tiporti, Lido-Saint Nicolo, Malamocco and Chioggia. Each barrier consists of a series of $19 \sim 20$ hollow steel gates all of which are unconnected to one another but hinged along a common axis on the seabed. In calm weather the gates rest horizontally on the seabed so as not to obstruct shipping traffic or to impair the scenic view of the area. In stormy weather, all gates will be raised by buoyancy to an inclination of about 50° from the horizon, and hence will act as a dam for keeping upto 2 meters of high water outside the lagoon. The gates are otherwise free to swing to and fro so that only a small portion of the wave force is transmitted to the weak foundation. An artist's sketch is shown in Fig. 8.17.

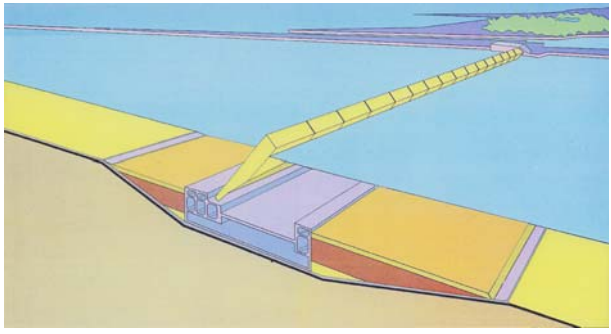

Figure 8.17: Artist's sketch of Venice storm barrier (courtesy of Consorzio Venezia Nuova).

Each inlet has a pair of long and parallel jetties of O(1 km) length extending normally seaward. At the early stage of design, laboratory experiments for gates spanning the full width of a wide channel revealed an unexpected phenomenon when the incident waves are long-crested and monochromatic. At certain frequencies, neighboring gates did not oscillate in unison but in opposite directions at half the incident-wave frequency (Consorzio Venezia Nuova, 1988; Varisco, 1992). The out-of-phase motion due to subharmonic forcing poses a possible threat to diminish the intended function of the barrier as a dam.

As will be shown in Chapter Twelve, edge waves trapped on a sloping beach can be excited subharmonically by normally incident waves. Inspired by this possible analogy, Mei et al. (1994) showed theoretically that trapped waves exist as natural modes along an articulated barrier composed of a series of vertical gates spanning across the middle of an infinitely long channel. They also showed experimentally for the same geometry that a natural mode can indeed be resonated by incident waves of twice the frequency. Focussing at first on the most undesirable mode where neighboring gates move in opposite directions, a nonlinear theory has been carried out by Sammarco et al. (1997a, b) for the amplitude of the gate oscillations at and near resonance long after the arrival of monchromatic and bichromatic incident waves. For calculating the same eigenmode for inclined gates including the complex geometry of housing, a hybrid-element method has later been developed by Liao and Mei (2000). Calculations of all the eigenmodes involving many inclined gates across a long channel have been worked out by Li and Mei (2003). Since the Venice barriers face a large

open water on the lagoon side, without the jetties, trapping is not perfect. Sychronous excitation by a linear mechanism is also possible. A linear theory has been carried out and applied by Adamo and Mei (2004) to predict the statistical responses to random incident waves. Related works have been reported by Vittori et al. (1996), Vittori (1997, 1998) who have studied a more idealized model where the barrier consists of gates of infinitesimal width.

Waves can also be trapped near periodic and fixed structures with finite separation (Evans et al. (1994) and Porter and Evans (1999).) In contrast the gaps between neighboring gates of Venice barrier are very small (a few centimeters), and it is the articulatedness that allows wave trapping. As an application of the tools introduced in this chapter, we shall describe below the theory of trapped modes for vertical gates in an infinitely long channel.

8.10.1 The Two-Gate Mode in an Infinitely Long Barrier

Let us first consider the simplest and the worst mode with just two gates per period in an otherwise infinitely long barrier. Let the horizontal displacement of the gates in the period $-a < y < a$ be described by

$$-(z+h)\theta(y)e^{-i\omega t} \tag{8.10.1}$$

with

$$\theta(y) = 1\,, \quad -a/2 < y < a/2\,; \tag{8.10.2}$$

$$-1\,, \quad -a < y < -a/2\,, \quad \text{and} \quad a/2 < y < a. \tag{8.10.3}$$

Using eigenfunction expansions, the most general solution in a long rectangular channel of width $2a$ consists of not only long-crested propagating and evanescent modes,

$$e^{-i\omega t}\left\{A_0 e^{\pm ikx}\cosh(k(z+h)) + \sum_{n=1}^{\infty} A_n e^{\mp k_n x}\cos(k_n k(z+h))\right\} + c.c.$$

but also short-crested propagating modes,

$$e^{-i\omega t}\sum_{m=1}^{\overline{m}} \cos\frac{m\pi y}{a} A_{m0} e^{\pm i\alpha_{m0}x}\cosh(k(z+h)) + c.c.$$

and short-crested evanescent modes,

$$e^{-i\omega t}\sum_{m=\overline{m}+1}^{\infty}\cos\frac{m\pi y}{a}A_{m0}e^{\pm i\alpha_{m0}x}\cosh(k(z+h))$$
$$+e^{-i\omega t}\sum_{m=1}^{\infty}\cos\frac{m\pi y}{a}\sum_{n=1}^{\infty}A_{mn}e^{\mp\alpha_{mn}x}\cos(k_n(z+h))+c.c.$$

Here k and k_n are the real roots of the following dispersion relations

$$\omega^2=gk\tanh kh\,;\quad \omega=-gk_n\tan k_nh,\ n=1,2,3,\ldots,$$

with

$$\alpha_{m0}=\sqrt{k^2-\left(\frac{m\pi}{a}\right)^2},\quad \alpha_{mn}=\sqrt{\left(\frac{m\pi}{a}\right)^2+k_n^2}.$$

$\overline{m}$ is the largest integer m for which α_{m0} is real, i.e., for all $m\geq\overline{m}+1$, $\pm i\alpha_{m0}=\mp\sqrt{(m\pi/a)^2-k^2}$ is real. To construct trapped modes we must exclude all propagating waves. First the frequency must be low enough

$$k<\frac{\pi}{a}\tag{8.10.4}$$

so that no short-crested propagating modes can exist, hence $\overline{m}=0$. To ensure the absence of the long-crested propagating wave, $A_0=0$, we must also require that

$$\int_{-a}^{a}\theta(y)\,dy=0\tag{8.10.5}$$

which also guarantees the absence of all long-crested evanescent modes, i.e., $A_n=0$ for all n.

Let the vertical sides of the gates be $x=\pm b$, the trapped mode potential is therefore

$$\phi^{\pm}=\mp i\omega\sum_{m=1}^{\infty}b_m\cos\frac{m\pi y}{a}\left[\frac{D_0}{\alpha_{m0}C_0}e^{\mp\alpha_{m0}(x\mp b)}\cosh Q\right.$$
$$\left.+\sum_{n=1}^{\infty}\frac{D_n}{\alpha_{mn}C_n}e^{\mp\alpha_{mn}(x\mp b)}\cos Q_n\right]e^{-i\omega t}+c.c.\tag{8.10.6}$$

where $Q = k(z+h)$ and $Q_n = k_n(z+h)$. The coefficients are obtained by matching the normal velocities of the gate and of the adjacent fluid:

$$b_m = \frac{1}{a}\int_{-a}^{a} \theta(y)\cos\frac{m\pi y}{a}\,dy = \frac{4}{m\pi}\sin\frac{m\pi}{2}\,. \tag{8.10.7}$$

$$C_0 = \frac{1}{2k}\left(q + \frac{1}{2}\sinh 2q\right), \quad D_0 = \frac{1}{k^2}(q\sinh q - \cosh q + 1) \tag{8.10.8}$$

where $q = kh$, and

$$C_n = \frac{1}{2k_n}\left(q_n + \frac{1}{2}\sin 2q_n\right), \quad D_n = \frac{1}{k_n^2}(q_n\sin q_n + \cos q_n - 1) \tag{8.10.9}$$

where $q_n = k_n h$. The corresponding free-surface height is

$$\zeta^{\pm} = \pm\frac{\omega^2}{g}\sum_{m=1}^{\infty} b_m\cos\frac{m\pi y}{a}\left[\frac{D_0}{\alpha_{m0}C_0}e^{\mp\alpha_{m0}(x\mp b)}\cosh q + \sum_{n=1}^{\infty}\frac{D_n}{\alpha_{mn}C_n}e^{\mp\alpha_{mn}(x\mp b)}\cos q_n\right]e^{-i\omega t} + c.c. \tag{8.10.10}$$

To determine ω we apply Newton's law to the gate at the center of the modal period,

$$I\ddot{\theta} + C\theta = -2\int_{-a/2}^{a/2} dy\int_{-h}^{0}\rho[\phi_t^+]_{x=b}(z+h)\,dz\,, \tag{8.10.11}$$

where I is the moment of inertia of the gate, and C is the restoring moment due to buoyancy, both of which can be determined from the material and construction of the gate. The right-hand side of (8.10.11) can be found from (8.10.6) to be $\omega^2 I_a\theta_1 e^{-i\omega t}$, where

$$I_a(\omega) = \frac{16\rho a}{\pi^2}\sum_{m=1}^{\infty}\sum_{n=0}^{\infty}\frac{D_n^2\sin^2 m\pi/2}{\alpha_{mn}C_n m^2} \tag{8.10.12}$$

is the hydrodynamic moment of inertia which is a function of ω and of the parameters kh and a. Combining (8.10.11) with (8.10.12) we get the eigenvalue condition for ω:

$$\omega^2(I + I_a(\omega)) = C\,. \tag{8.10.13}$$

This is a transcendental equation for the eigenfrequency ω. Once solved numerically, the free surface height of the eigenmode is given by (8.10.10).

As shown in Fig. 8.18, predictions are confirmed by laboratory experiments with two vertical gates in a long channel, for a range of water depths and several gate inertias (Mei et al., 1994). The same experiments also give evidence of subharmonic resonance by incident wave of twice the frequency.

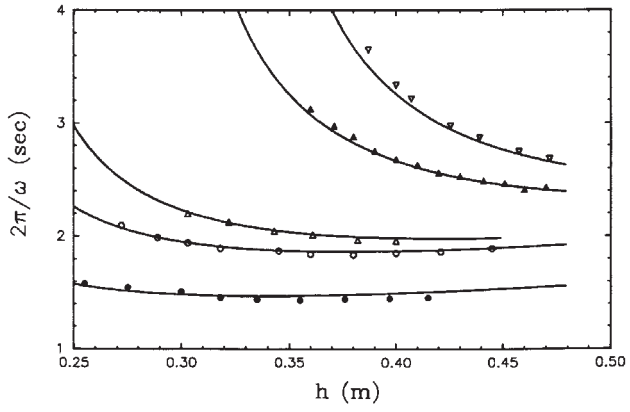

Figure 8.18: Measured and predicted eigenfrequencies for various gate buoyancy torque C, moment of inertia I and water depth h. C was varied by attaching styrofoams on the front and back of the gates. I was changed by attaching extra weight on the top (from Mei et al., 1994, *Proc. Roy. Soc. Lond.* Reproduced by permission of The Royal Society).

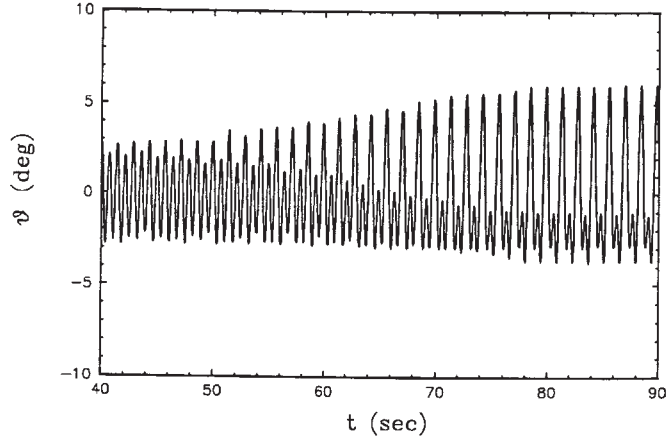

Figure 8.19: Time-series record of gate oscillations induced by incident waves at the frequency twice that of the eigenfrequency (from Mei et al., 1994, *Proc. Roy. Soc. Lond.* Reproduced by permission of The Royal Society).

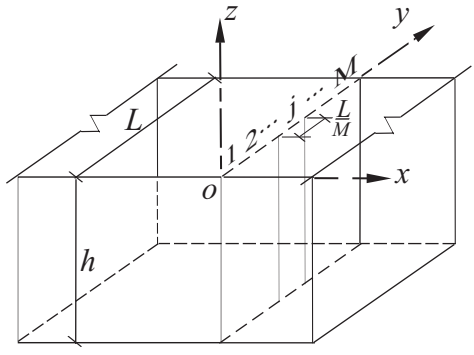

Figure 8.20: Sketch of M gates spanning a channel of total width L.

Figure 8.19 shows the time series of a gate motion. In the beginning, all the gates oscillate in phase and at the same frequency as the incident waves. After a long time, neighboring gates oscillate more vigorously in opposite phases at one-half of the incident-wave frequency, implying subharmonic resonance.

8.10.2 Multi-Gate Modes in a Barrier of Finite Length

We now explain how to calculate all the eigenmodes in an M-gate barrier spanning the full width L of an infinitely long channel, shown in Fig. 8.20. The width of each gate is then $B = L/M$. It is now convenient to choose the $x - z$ plane to coincide with one channel bank.

On the side $y \geq 0$, the unknown amplitudes of the M gates are denoted by

$$\theta(y) = (\theta_1, \theta_2, \ldots, \theta_j, \ldots \theta_N) \quad \text{for} \quad y \in Y_1 = \left(0, \frac{a}{M}\right),$$
$$Y_2 = \left(\frac{L}{M}, \frac{2L}{M}\right), \ldots Y_j = \left(\frac{(j-1)L}{M}, \frac{jL}{M}\right), \ldots, Y_M = \left(\frac{(M-1)L}{M}, a\right). \tag{8.10.14}$$

Let the gate rotation $\theta(y)$ be represented by a Fourier cosine series:

$$\theta(y) = \sum_{m=1}^{\infty} B_m \cos\left(\frac{m\pi y}{L}\right) \tag{8.10.15}$$

where B_m is the Fourier coefficient

$$B_m = \frac{2}{a}\int_0^a \theta(y)\cos\left(\frac{m\pi y}{a}\right)dy\,, \quad B_0 = 0\,. \tag{8.10.16}$$

If m=even (odd), the mode is symmetric (antisymmetric) with respect to the center line $y = L/2$. The Fourier coefficients can be calculated as

$$\begin{aligned} B_m = {} & \theta_1 \frac{2}{m\pi}\sin\left(\frac{m\pi}{M}\right) + \theta_2 \frac{2}{m\pi}\left[\sin\left(\frac{2m\pi}{M}\right) - \sin\left(\frac{m\pi}{M}\right)\right] + \cdots \\ & + \theta_j \frac{2}{m\pi}\left[\sin\left(\frac{jm\pi}{M}\right) - \sin\left(\frac{(j-1)m\pi}{M}\right)\right] + \cdots \\ & - \theta_M \frac{2}{m\pi}\sin\left(\frac{(M-1)m\pi}{M}\right). \end{aligned} \tag{8.10.17}$$

Similar to the analysis in the last subsection, the velocity potential on the right side of the vertical barrier $x = b$ is found to be

$$\Phi^+ = \sum_{j=1}^{M} \theta_j \phi_j(b, y, z, t) \tag{8.10.18}$$

where

$$\begin{aligned} \phi_j = {} & -i\omega \sum_{m=1}^{\infty} \frac{2}{m\pi}\left[\sin\left(\frac{jm\pi}{M}\right) - \sin\left(\frac{(j-1)m\pi}{M}\right)\right]\cos\left(\frac{m\pi y}{a}\right) \\ & \times \left\{ \frac{D_0}{\beta_{m0}C_0}\cosh[k(z+h)] + \sum_{n=1}^{\infty}\frac{D_n}{\beta_{mn}C_n}\cos[k_n(z+h)] \right\} \\ & \times e^{-i\omega t} + c.c.\,, \quad j = 1, 2, 3, \ldots M \end{aligned} \tag{8.10.19}$$

with

$$\beta_{m0} = \sqrt{(m\pi/a)^2 - k^2}\,, \quad \beta_{mn} = \sqrt{(m\pi/a)^2 + k_n^2} \tag{8.10.20}$$

To ensure a trapped mode we insist that β_{m0} must be real so that all terms decay exponentially with $|x|$. Specifically, if $k < \pi/L$, all terms in (8.10.19) are kept. If $\pi/L < k < 2\pi/L$, the terms associated with β_{10} is excluded. If $2\pi/L < k < 3\pi/L$, the term associated with β_{10} and β_{20} are excluded. If $M\pi/L < k < (M+1)\pi/L$, terms associated with $\beta_{10}, \beta_{20}, \beta_{30}, \ldots \beta_{M0}$ are excluded.

Invoking the equation of motion for gate j we again get the homogeneous matrix equation for $\{\theta_j\}$,

$$-\omega^2 I\theta_j + C\theta_j - F_{jp}\theta_p = 0\,, \quad j = 1, 2, 3, \ldots M\,; \tag{8.10.21}$$

where

$$F_{jp} = 2\rho\omega^2 L \sum_{m=1}^{\infty} \frac{2}{m^2\pi^2} \left[\sin\left(\frac{jm\pi}{M}\right) - \sin\left(\frac{(j-1)m\pi}{M}\right)\right]$$
$$\cdot \left[\sin\left(\frac{pm\pi}{M}\right) - \sin\left(\frac{(p-1)m\pi}{M}\right)\right] \sum_{n=0}^{\infty} \frac{D_n^2}{C_n\beta_{mn}}\,. \tag{8.10.22}$$

Again in the $m-$ series in (8.10.19) and (8.10.22), only terms with real β_{m0} are included.

The unknown frequency ω can be determined by the brute-force method of equating the determinant of (8.10.21) to zero and solving the simultaneous transcendental equations for all eigenfrequencies. Li and Mei (2003) have found, not suprisingly, that for the mode with wavelength L/K (or wavenumber $2\pi K/L$), the modal profile is the piece-wise constant substitute of the cosine curve $\cos(2K\pi y/L)$. In other words, the area between the discontinuous curve $\theta(y)$ and the y axis is the same as that under the smooth cosine curve. More explicitly, the rotation amplitude of gate j is

$$\theta_j = \theta_o \int_{Y_j} \cos\left(\frac{2K\pi y}{L}\right) dy$$
$$= \frac{L\theta_o}{2K\pi}\left(\sin\frac{2Kj\pi}{M} - \sin\frac{2K(j-1)\pi}{M}\right). \tag{8.10.23}$$

Being a homogeneous solution, the amplitude θ_o of an eigenmode is arbitrary. The relative amplitudes of all gates θ_j/θ_o are simply related to the relative amplitude of one gate, say θ_k/θ_o. Now one can calculate the eigenfrequency ω by requiring (8.10.21) on gate k only. This reduces the numerical tasks significantly. Indeed, if the number of gates per period is small, analytical confirmation can be made.

Numerical results are obtained for the following inputs which are close to the designed gates for Malamocco Inlet: number of gates = 20, height = 20 m, thickness $2b = 4.5$, water depth $h = 1$, gate width $B = 20$ m, gate inertia $I = 39.337 \times 10^6$ kg-m^2, weight = 2619 kN, $C = 60.246 \times 10^6$ kg m^2 s^{-2}. Ordered according to increasing periods, profiles of modes that are even $N_2, N_4, \ldots N_{18}$ with respect to the center of the barrier are

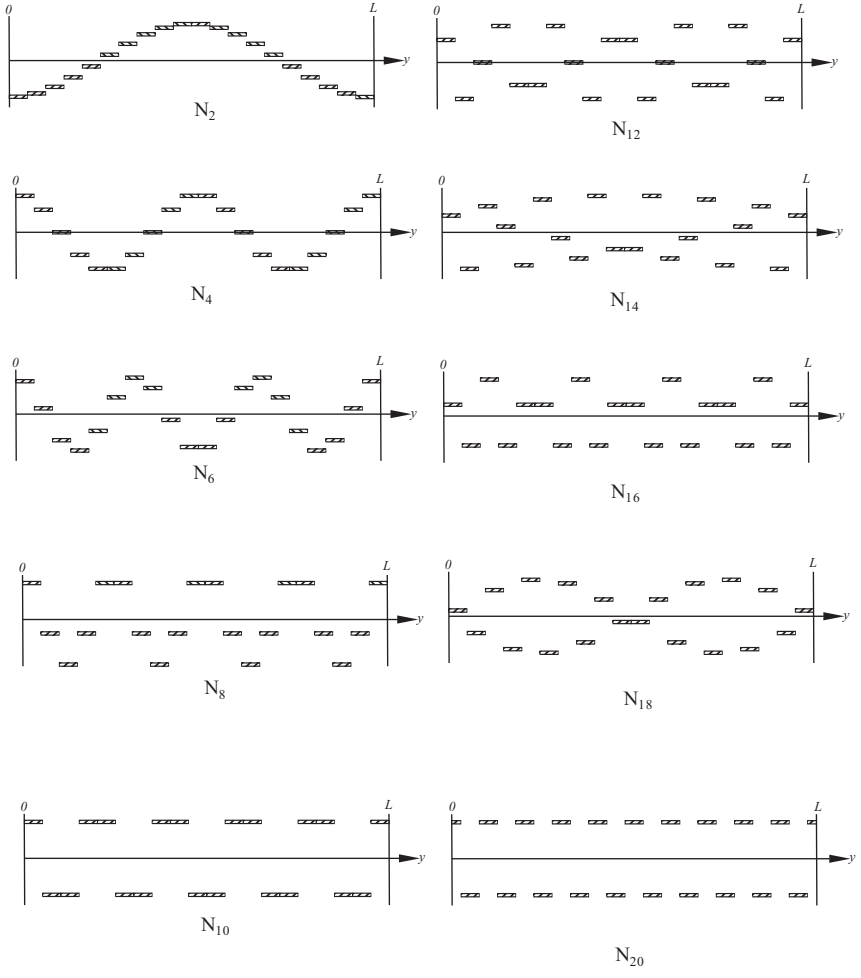

Figure 8.21: Profiles of symmetric modes of a 20-gate barrier in a channel. $N_2, \ldots N_{18}$ are the possible modes for 20 whole gates. Mode N_{20} is possible if there are two half gates at the ends.

shown in Fig. 8.21. Only these modes can be excited by long-crested, normally incident waves.

The dispersion relation between the eigenfrequency and the modal wave number is shown in Fig. 8.22. Modes with profiles both even and odd with repect to the center are included. From left to right, the first, second,... dot corresponds to mode $N_1, N_2, \ldots$, etc. The odd modes can only be excited by obliquely incident waves.

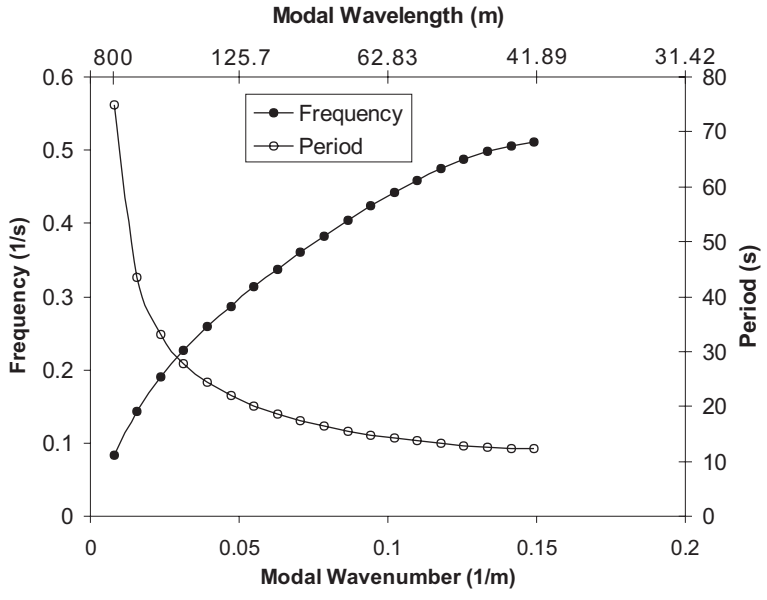

Figure 8.22: Dispersion relationship for a barrier of 20 gates (from Li and Mei, 2003, *Appl. Ocean Res.* Reprinted by permission of Elsevier Publishers).

8.11 Drift Forces

Consider the time-averaged momentum flux of a plane progressive wave across a vertical plane

$$\overline{M} = \rho \overline{\int_{-h}^{\zeta} u^2 \, dz} \, .$$

If the linearized result is used in the integrand, $\overline{M}$ may be calculated to second-order accuracy in wave slope,

$$\overline{M} = \frac{EC_g}{C} + O(kA)^3 \, , \tag{8.11.1}$$

where $E = \frac{1}{2}\rho g A^2$.

First, consider a two-dimensional obstacle in normally incident waves. If all the wave energy is absorbed by the body, as is the case of the wave-power devices discussed in Section 8.9, the mean momentum must also be totally absorbed by the body. Therefore, the body must experience a steady force EC_g/C. If the body reflects all the energy instead, then the reflected wave carries a momentum of EC_g/C in the opposite direction. The steady

force on the body must be equal to the total rate of momentum change $2EC_g/C$, which is similar to a steady jet impinging normally on a wall. More generally, a body oscillating in waves scatters waves by its presence and radiates waves by its motion. Let the amplitude of the left-going waves on the incidence side be $(R + \mathcal{A}_-)A$ and of the right-going waves on the transmission side be $(T + \mathcal{A}_+)A$. The net steady force on the body must be

$$\overline{F}_x = \frac{EC_g}{C}(1 + |R + \mathcal{A}_-|^2 - |T + \mathcal{A}_+|^2) \tag{8.11.2}$$

(Longuet–Higgins, 1977a), and can be calculated as soon as R, T, $\mathcal{A}_-$, and $\mathcal{A}_+$ are known from the linearized theory. This steady force is important in designing moorings or dynamic positioning devices to prevent the body from drifting, hence it is called the *drift force*. Because of energy conservation

$$|R + \mathcal{A}_-|^2 + |T + \mathcal{A}_+|^2 + E_{ff} = 1\,, \tag{8.11.3}$$

where E_{ff} is the efficiency of energy absorption, the drift force may also be expressed as

$$\overline{F}_x = \frac{EC_g}{C}(E_{ff} + 2|R + \mathcal{A}_-|^2)\,. \tag{8.11.4}$$

Thus, $\overline{F}_x$ is positive, that is, in the direction of the incident wave propagation, if $E_{ff} > 0$. However, if sufficient energy is supplied to the body so that

$$E_{ff} < -2|R + \mathcal{A}_-|^2\,, \tag{8.11.5}$$

then $\overline{F}_x$ becomes negative, that is, against the waves.

Figure 8.23 shows the horizontal drift force on a Salter duck under various conditions. Absorption of wave power is limited to the roll mode and is seen to reduce the drift force for a broad range of frequencies. In particular, at high ka, we expect $T \approx 0$ and the induced motion (hence $\mathcal{A}_-$) to be small, so that with no absorption, $\overline{F}_x \cong 2EC_g/C$, as is confirmed by the dotted and dashed curves. When absorption is complete, $R + A_- \cong 0$ and $E_{ff} \approx 1$ so that $\overline{F}_x = EC_g/C$ which implies a 50% reduction; this result also agrees with the solid and the dash–dot curves in Fig. 8.23.

General formulas for drift forces on three-dimensional bodies were first derived by Maruo (1960) and extended to include the drift moment about the vertical axis by Newman (1967). The derivation is also based on momentum balance and is described below in detail in the manner of Newman.

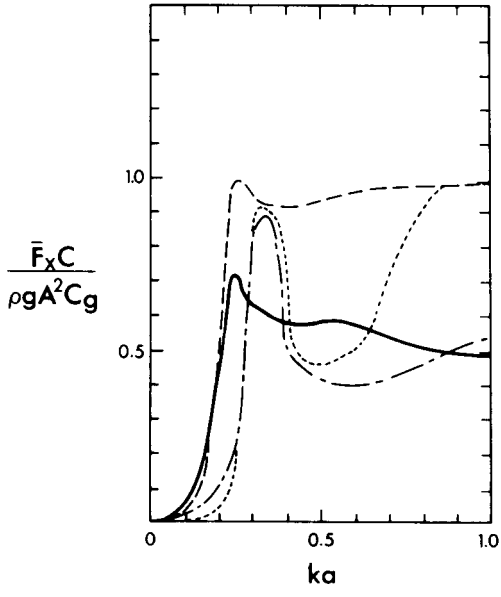

Figure 8.23: Horizontal drift force on a Salter cam with fixed axis: a = radius of circular stern. No energy absorption: solid curve, roll only; dash–dot curve, roll and sway. With energy absorption: dashed curve, roll only; dotted curve, roll and away (from Maeda, Tanaka, and Kinoshita, 1980, *Proc., 13th Symp. Naval Hydrody.* Reproduced by permission of U.S. Office of Naval Research).

For any vector quantity per unit volume inside the moving volume V bounded by S, the following kinematic transport theorem (see, e.g., Batchelor, 1967, p. 135) is true:

$$\frac{d}{dt}\iiint_V \mathbf{G}\,dV = \iiint_V \frac{\partial \mathbf{G}}{\partial t}\,dV + \iint_S \mathbf{G}U_n\,dS\,, \tag{8.11.6}$$

where U_n denotes the normal velocity of S. Now let $\mathbf{G} = \rho\mathbf{u}$ be the linear momentum per unit volume and $\mathbf{M}$ be the total linear momentum in V. In index form we have

$$\frac{dM_i}{dt} = \rho\iiint_V \frac{\partial u_i}{\partial t}\,dV + \rho\iint_S u_i U_n\,dS\,. \tag{8.11.7}$$

If we use the Euler equation in the form

$$\frac{\partial u_i}{\partial t} = -\frac{\partial}{\partial x_i}\left(\frac{P}{\rho} + gz\right) - \frac{\partial}{\partial x_j}(u_i u_j)\,,$$

the first integral on the right of Eq. (8.10.7) may be transformed to a surface integral via Gauss' theorem

$$\frac{dM_i}{dt} = -\iint_S (P + \rho g z \delta_{i3}) n_i \, dS - \iint_S \rho u_i (u_j n_j - U n) \, dS \,. \tag{8.11.8}$$

In particular, the horizontal components are

$$\frac{d}{dt}\begin{pmatrix} M_x \\ M_y \end{pmatrix} = -\rho \iint_S \left[\frac{P}{\rho} \begin{pmatrix} n_x \\ n_y \end{pmatrix} + \begin{pmatrix} u \\ v \end{pmatrix} (\mathbf{u}\cdot\mathbf{n} - U_n) \right] dS \,. \tag{8.11.9}$$

Now let S be the union of the wetted body surface S_B, the free surface S_F, the horizontal sea bottom B_0, and the fixed vertical cylinder S_∞ at "infinity." On the material surfaces S_B, S_F, and B_0, $\mathbf{u}\cdot\mathbf{n} - U_n = 0$. On the free surface, $P = 0$, while on S_∞, $U_n = 0$. On the flat bottom B_0, $n_x = n_y = 0$. Therefore, the total force needed to hold the body is

$$\begin{aligned} \begin{pmatrix} F_x \\ F_y \end{pmatrix} &\equiv \iint_{S_B} P \begin{pmatrix} n_x \\ n_y \end{pmatrix} dS \\ &= -\iint_{S_\infty} \left[P \begin{pmatrix} n_x \\ n_y \end{pmatrix} + \rho \begin{pmatrix} u \\ v \end{pmatrix} (\mathbf{u}\cdot\mathbf{n}) \right] dS - \frac{d}{dt}\begin{pmatrix} M_x \\ M_y \end{pmatrix} . \end{aligned} \tag{8.11.10}$$

When the time averages are taken and periodicity invoked, the last term on the right gives no contribution; the drift force components are

$$\begin{pmatrix} \overline{F}_x \\ \overline{F}_y \end{pmatrix} = -\overline{\iint_{S_\infty} \left[P \begin{pmatrix} n_x \\ n_y \end{pmatrix} + \rho \begin{pmatrix} u \\ v \end{pmatrix} (\mathbf{u}\cdot\mathbf{n}) \right] dS} \,. \tag{8.11.11}$$

If S_∞ is further taken to be a circular cylinder of large radius R, then we may employ polar coordinates to write

$$\begin{aligned} \overline{F}_x &= -\overline{\iint_{S_\infty} [P\cos\theta + \rho u_r (u_r \cos\theta - u_\theta \sin\theta) R \, d\theta \, dz]} \,, \\ \overline{F}_y &= -\overline{\iint_{S_\infty} [P\sin\theta + \rho u_r (u_r \sin\theta - u_\theta \cos\theta) R \, d\theta \, dz]} \,. \end{aligned} \tag{8.11.12}$$

So far, the results above are exact; from here on only second-order terms will be preserved. Using the Bernoulli equation, we get

$$-R\int_0^{2\pi} d\theta \begin{pmatrix}\cos\theta\\ \sin\theta\end{pmatrix} \overline{\int_{-h}^{\zeta} P\,dz}$$

$$\cong R\int_0^{2\pi} d\theta \begin{pmatrix}\cos\theta\\ \sin\theta\end{pmatrix} \left\{\rho\int_{-h}^{0} dz\,\overline{\left[\Phi_t + gz + \frac{1}{2}(\nabla\Phi)^2\right]}\right.$$

$$\left. + \rho\,\overline{\int_0^{\zeta} dz\left[\Phi_t + gz + \frac{1}{2}(\nabla\Phi)^2\right]}\right\}_{r=R}. \tag{8.11.13}$$

In the first integral on the right the time average can be performed directly on the integrand. The term $\overline{\Phi}_t$ is zero owing to periodicity, while the hydrostatic term $\rho g z$ does not contribute after integrating with respect to θ; the remaining term $\frac{1}{2}(\nabla\Phi)^2$ can be calculated with an error of $O(kA)^3$ by using the linearized Φ. In the second integral, the contribution from the term $\frac{1}{2}(\nabla\Phi)^2$ is $O(kA)^3$ and negligible; the remaining terms can be evaluated to $O(kA)^2$ as

$$\rho\,\overline{\int_0^{\zeta}(\Phi_t + gz)\,dz} = \rho\left(\overline{\Phi_t|_{z=0}\zeta + \frac{1}{2}g\zeta^2}\right) = -\frac{\rho}{2g}\,\overline{\Phi_t^2}\Big|_{z=0}$$

$$= -\frac{\rho}{2g}\,\overline{(\mathrm{Re}\, i\omega\phi e^{-i\omega t})^2_{z=0}} = -\frac{\rho\omega^2}{4g}|\phi|^2_{z=0}. \tag{8.11.14}$$

It follows that

$$\iint_{S_\infty} P\begin{pmatrix}\cos\theta\\ \sin\theta\end{pmatrix} R\,d\theta\,dz \cong \int_0^{2\pi} R\,d\theta\begin{pmatrix}\cos\theta\\ \sin\theta\end{pmatrix}$$

$$\times\left\{\left[-\int_{-h}^{0} dz\,\frac{1}{2}\,\overline{\rho(\nabla\Phi)^2}\right] + \frac{\rho\omega^2}{4g}|\phi|^2_{z=0}\right\}. \tag{8.11.15}$$

Substituting Eq. (8.11.15) into Eq. (8.11.12), we get

$$\overline{F}_x = -\int_0^{2\pi}\rho R\,d\theta\left\{\int_{-h}^{0} dz\left\{-\frac{1}{2}\left[\overline{\left(\frac{\partial\Phi}{\partial r}\right)^2} + \frac{1}{R^2}\,\overline{\left(\frac{\partial\Phi}{\partial\theta}\right)^2} + \overline{\left(\frac{\partial\Phi}{\partial z}\right)^2}\right]\cos\theta\right.\right.$$

$$\left.\left. + \overline{\left(\frac{\partial\Phi}{\partial r}\right)^2}\cos\theta - \frac{1}{R}\,\overline{\frac{\partial\Phi}{\partial r}\frac{\partial\Phi}{\partial\theta}}\sin\theta\right\} + \frac{\omega^2}{4g}|\phi|^2_{z=0}\cos\theta\right\}_{r=R}, \tag{8.11.16}$$

$$\overline{F}_y = -\int_0^{2\pi} \rho R\, d\theta \Bigg\{ \int_{-h}^{0} dz \Bigg\{ -\frac{1}{2}\left[\overline{\left(\frac{\partial \Phi}{\partial r}\right)^2} + \frac{1}{R^2}\overline{\left(\frac{\partial \Phi}{\partial \theta}\right)^2} + \overline{\left(\frac{\partial \Phi}{\partial z}\right)^2} \right] \sin\theta + \overline{\left(\frac{\partial \Phi}{\partial r}\right)^2} \sin\theta + \frac{\cos\theta}{R}\overline{\left(\frac{\partial \Phi}{\partial r}\frac{\partial \Phi}{\partial \theta}\right)} \Bigg\} + \frac{\omega^2}{4g}|\phi|^2_{z=0} \sin\theta \Bigg\}_{r=R} . \tag{8.11.17}$$

We now make use of the asymptotic formula for large r,

$$\Phi = \mathrm{Re}\,[(\phi^I + \tilde{\phi})e^{-i\omega t}] \tag{8.11.18a}$$

with

$$\phi^I = -\frac{igA}{\omega}\frac{\cosh k(z+h)}{\cosh kh} e^{ikr\cos\theta}, \tag{8.11.18b}$$

$$\tilde{\phi} = -\frac{igA}{\omega}\frac{\cosh k(z+h)}{\cosh kh}\mathcal{A}(\theta)\left(\frac{2}{\pi kr}\right)^{1/2} e^{ikr - i\pi/4} \tag{8.11.18c}$$

where $\tilde{\phi}$ represents the sum of the scattered and the radiated waves. It is useful to realize that in the quadratic terms in Eqs. (8.11.16) and (8.11.17), products involving only ϕ^I will not contribute, that is, there cannot be any drift force with incident waves alone. In the limit of $R \to \infty$, the terms multiplied by $1/R^2$ vanish. Also, since only cross products of ϕ^I and $\tilde{\phi}$ appear, the term

$$\frac{1}{R}\overline{\frac{\partial \Phi}{\partial r}\frac{\partial \Phi}{\partial \theta}} \sim R^{-3/2}$$

does not contribute to the integral. As a result, Eqs. (8.11.16) and (8.11.17) reduce to

$$\overline{F}_x = -\int_0^{2\pi} \rho R\, d\theta \cos\theta \Bigg\{ \int_{-h}^{0} dz \frac{1}{2}\left[\overline{\left(\frac{\partial \Phi}{\partial r}\right)^2} - \overline{\left(\frac{\partial \Phi}{\partial z}\right)^2} \right] + \frac{\omega^2}{4g}|\phi|^2_{z=0} \Bigg\}_{r=R} , \tag{8.11.19}$$

$$\overline{F}_y = -\int_0^{2\pi} \rho R\, d\theta \sin\theta \Bigg\{ \int_{-h}^{0} dz \frac{1}{2}\left[\overline{\left(\frac{\partial \Phi}{\partial r}\right)^2} - \overline{\left(\frac{\partial \Phi}{\partial z}\right)^2} \right] + \frac{\omega^2}{4g}|\phi|^2_{z=0} \Bigg\}_{r=R} . \tag{8.11.20}$$

The remaining task involves the familiar use of the stationary phase method; we only record the final results here:

$$\overline{F}_x = -\frac{\rho g A^2}{k}\frac{C_g}{C}\left\{\frac{1}{\pi}\int_0^{2\pi}\cos\theta|\mathcal{A}(\theta)|^2\,d\theta + 2\ \mathrm{Re}\mathcal{A}(0)\right\}, \quad (8.11.21)$$

$$\overline{F}_y = -\frac{\rho g A^2}{k}\frac{C_g}{C}\frac{1}{\pi}\int_0^{2\pi}\sin\theta|\mathcal{A}(\theta)|^2\,d\theta\,. \quad (8.11.22)$$

It should be emphasized that $\mathcal{A}$ combines scattering and radiation. Equation (8.11.21) can be rearranged by eliminating 2 Re$\mathcal{A}(0)$ with the help of the generalized optical theorem (8.9.15), yielding

$$\overline{F}_x = \frac{\rho g A^2 C_g}{kC}\left[\frac{\frac{1}{2}k\overline{\dot{E}}}{\frac{1}{2}\rho g A^2 C_g} + \frac{1}{\pi}\int_0^{2\pi}(1-\cos\theta)|\mathcal{A}|^2\,d\theta\right] \quad (8.11.23)$$

where $\overline{\dot{E}}$ is the rate of power absorption by the body, and the first term in the brackets is the efficiency of power absorption within a width λ/π of the wave front. The integral above is positive-definite, therefore, $\overline{F}_x$ is positive-definite if $\overline{\dot{E}} \geq 0$.

The moment about the z axis on a stationary body in waves is defined as

$$T_z = \iint_{S_B} P(\mathbf{r}\times\mathbf{n})\cdot\mathbf{e}_z\,dS\,. \quad (8.11.24)$$

We leave it as an exercise to show that the change of angular momentum about z is

$$-\iint_S [P(\mathbf{r}\times\mathbf{n})\cdot\mathbf{e}_z + \rho(\mathbf{r}\times\mathbf{u})\cdot\mathbf{e}_z(\mathbf{u}\cdot\mathbf{n} - U_n)]\,dS\,,$$

and that the mean drift moment is

$$\begin{aligned}\overline{T}_z &= -\rho\,\overline{\iint_{S_\infty}\frac{\partial\Phi}{\partial r}\frac{\partial\Phi}{\partial\theta}R\,d\theta\,dz} \\ &= \rho g A^2\frac{1}{k^2}\frac{C_g}{C}\,\mathrm{Im}\left[\left.\frac{d\mathcal{A}^*}{d\theta}\right|_{\theta=0} + \frac{1}{\pi}\int_0^{2\pi}\mathcal{A}(\theta)\frac{d\mathcal{A}^*(\theta)}{d\theta}\,d\theta\right]. \quad (8.11.25)\end{aligned}$$

In summary, the drift forces can be inferred from the far field of the first-order theory.

The subject is being developed further for the *slowly varying* drift force in irregular seas. If the incident waves consist of two slightly different frequencies $\omega \pm \Delta\omega/2$, the second-order response will contain terms such as $e^{\pm 2i\omega t}$ and $e^{\pm i\Delta\omega t}$. The latter has a much longer time scale than $2\pi/\omega$. The corresponding long-period forces can resonate the natural modes of the

mooring lines attached to a floating body, thereby causing severe strain. For further information see Newman (1974) and Faltinsen and Løken (1979).

Exercise 8.9

For two dimensions, show from Eq. (8.11.11) that

$$\overline{F}_x = \left[\frac{\rho}{2}\int_{-h}^{0}(\bar{v}^2 - \bar{u}^2)\,dz - \frac{\rho\omega^2}{4g}|\phi|^2_{z=0}\right]_{x\sim-\infty}^{x\sim\infty}$$

and then rederive Eq. (8.11.2).

Exercise 8.10

For a Hagen–Cockerall wave absorber in head seas, the scattering amplitude $A^S(\theta)$ is negligible if the raft is very slender. Use the approximate estimates of the radiated waves A^e and A^o [cf. Eqs. (8.9.52a) and (8.9.52b)] to calculate the drift force in the direction of the incident waves.

8.12 Principles of Calculating the Transient Motion of a Floating Body

In this section we shall endeavor to show how the transient response of a floating body can, in principle, be calculated from the sinusoidal response for which general numerical methods are available. The material here[4] is based on the work of Cummins (1962), Ogilvie (1964), and Wehausen (1967).

8.12.1 Radiated Waves Caused by Impulsive Motion of a Floating Body

Let a generalized displacement in the α direction be given impulsively to the body at the instant $t = \tau$, so that the generalized body velocity is

$$\Delta V_\alpha = V_\alpha(\tau)\delta(t-\tau)\,, \quad V_\alpha = \dot{X}_\alpha\,. \tag{8.12.1}$$

Let Φ^Δ be the velocity potential of the radiated waves caused by the impulse. Φ^Δ must satisfy the Laplace equation in the fluid, the free-surface condition (1.2.11), Section 1.2, with $P_a = 0$, and $\partial\Phi^\Delta/\partial n = 0$ on the horizontal bottom ($z = -h$). The boundary condition on the body surface is

[4] I have benefited from the survey by Serman (1978).

$$\frac{\partial \Phi^{\Delta}}{\partial n} = \Delta V_{\alpha} n_{\alpha} = V_{\alpha} n_{\alpha} \delta(t-\tau)\,. \tag{8.12.2}$$

In addition we require boundedness at infinity

$$|\nabla \Phi^{\Delta}| \to 0 \quad \text{as} \quad r \to \infty,\ t < \infty\,, \tag{8.12.3}$$

and that there be no disturbance before $t = \tau$:

$$\Phi^{\Delta} = 0\,, \quad t < \tau\,, \quad \text{all} \quad \mathbf{x}\,. \tag{8.12.4}$$

Cummins introduced the following decomposition:

$$\Phi^{\Delta}(\mathbf{x}, t) = V_{\alpha}(\tau)[\Omega_{\alpha}(\mathbf{x})\delta(t-\tau) + \Gamma_{\alpha}(\mathbf{x}, t-\tau)H(t-\tau)]\,, \tag{8.12.5}$$

where H is the Heaviside step function. Summation over the repeated index α is implied. We now require Ω_{α} and Γ_{α} to satisfy the following conditions on the body:

$$\frac{\partial \Omega_{\alpha}}{\partial n} = n_{\alpha} \tag{8.12.6a}$$

$$\text{on} \quad S_B\,.$$

$$\frac{\partial \Gamma_{\alpha}}{\partial n} = 0 \tag{8.12.6b}$$

Both Ω_{α} and Γ_{α} are further subjected to Laplace's equation and the bottom boundary condition. Care is needed in satisfying the remaining condition on the free surface. Substituting Eq. (8.12.5) into the free-surface condition (1.2.11), Section 1.2, and noting that $f(t)\delta(t) = f(0)\delta(t)$ for any smooth $f(t)$, we have

$$\frac{\partial^2 \Phi^{\Delta}}{\partial t^2} = \left\{ \ddot{\delta}\Omega_{\alpha} + \dot{\delta}\Gamma_{\alpha}(\mathbf{x}, 0) + \delta \frac{\partial}{\partial t}\Gamma_{\alpha}(\mathbf{x}, t-\tau) + H \frac{\partial^2}{\partial t^2}\Gamma_{\alpha}(\mathbf{x}, t-\tau) \right\} V_{\alpha}\,, \tag{8.12.7a}$$

$$g \frac{\partial \Phi^{\Delta}}{\partial z} = g \left[\delta \frac{\partial \Omega_{\alpha}}{\partial z} + H \frac{\partial \Gamma_{\alpha}}{\partial z} \right] V_{\alpha}\,, \tag{8.12.7b}$$

where the arguments of δ, $\dot{\delta}$, $\ddot{\delta}$, and H are all $t - \tau$. After inserting Eqs. (8.12.7a) and (8.12.7b) into Eq. (1.2.11), Section 1.2, we use the fact that H, δ, $\dot{\delta}$, and $\ddot{\delta}$ are singularities of different orders, and equate to zero their coefficients individually. In this manner four conditions are obtained on the free surface. The initial-boundary-value problems for Ω_{α} and Γ_{α} may be summarized:

$$\nabla^2\Omega_\alpha = 0 \qquad \text{in fluid}\,, \tag{8.12.8a}$$

$$\Omega_\alpha(\mathbf{x}) = 0\,, \quad z = 0\,, \tag{8.12.8b}$$

$$\frac{\partial\Omega_\alpha}{\partial z} = 0\,, \quad z = -h\,, \tag{8.12.8c}$$

$$\frac{\partial\Omega_\alpha}{\partial n} = n_\alpha \quad \text{on} \quad S_B\,, \tag{8.12.8d}$$

$$\Omega_\alpha \to 0 \qquad |\mathbf{x}| \to \infty\,. \tag{8.12.8e}$$

The above boundary-value problem for Ω_α may be regarded as a radiation problem in the limit of infinite frequency. For Γ_α we have

$$\nabla^2\Gamma_\alpha = 0 \qquad \text{in the fluid}\,, \tag{8.12.9a}$$

$$\Gamma_\alpha = 0\,, \quad z = 0,\ t = t_0\,, \tag{8.12.9b}$$

$$\frac{\partial\Gamma_\alpha}{\partial t} + g\frac{\partial\Omega_\alpha}{\partial z} = 0\,, \quad z = 0,\ t = t_0\,, \tag{8.12.9c}$$

$$\frac{\partial^2\Gamma_\alpha}{\partial t^2} + g\frac{\partial\Gamma_\alpha}{\partial z} = 0\,, \quad z = 0,\ t_0 < t < \infty\,, \tag{8.12.9d}$$

$$\frac{\partial\Gamma_\alpha}{\partial z} = 0\,, \quad z = -h\,, \tag{8.12.9e}$$

$$\frac{\partial\Gamma_\alpha}{\partial n} = 0\,, \quad \text{on} \quad S_B\,. \tag{8.12.9f}$$

Note that Γ_α is just a Cauchy–Poisson problem in the presence of a fixed body.

Let us try to obtain the response to a continuous $V(t)$ by integrating the effect of a succession of impulses over $-\infty < \tau < \infty$, that is, by integrating Eq. (8.12.5),

$$\Phi^R = \int_{-\infty}^{\infty} d\tau\, \Phi^\Delta = \Omega_\alpha(\mathbf{x})V_\alpha(t) + \int_{-\infty}^{t} \Gamma_\alpha(\mathbf{x}, t-\tau)V_\alpha(\tau)\, d\tau \tag{8.12.10a}$$

$$= \Omega_\alpha(\mathbf{x})V(t) + \int_0^{\infty} \Gamma_\alpha(\mathbf{x}, \tau)V_\alpha(t-\tau)\, d\tau\,. \tag{8.12.10b}$$

It is straightforward to verify that Φ^R satisfies the governing equation and all the boundary and initial conditions.

The hydrodynamic force on the body can be derived in terms of Ω_α and Γ_α by first taking the time derivatives of Φ^R

$$\frac{\partial \Phi^R}{\partial t} = \Omega_\alpha(\mathbf{x})\dot{V}_\alpha(t) - \Gamma_\alpha(\mathbf{x},0)V_\alpha(t) + \Gamma_\alpha(\mathbf{x},\infty)V_\alpha(-\infty) + \int_{-\infty}^{t} \Gamma_\alpha(\mathbf{x},t-\tau)\dot{V}_\alpha(\tau)\,d\tau\,. \tag{8.12.12}$$

Because of Eq. (8.12.9b) and $V_\alpha(-\infty) = 0$, we simply have

$$\frac{\partial \Phi^R}{\partial t} = \Omega_\alpha(\mathbf{x})\ddot{X}_\alpha(t) + \int_{-\infty}^{t} \Gamma_\alpha(\mathbf{x},t-\tau)\ddot{X}_\alpha(\tau)\,d\tau\,, \tag{8.12.13}$$

where use is made of $V_\alpha = \dot{X}_\alpha$. The β component of the generalized restoring force reacting on the body is

$$\mathscr{F}_\beta^R(t) = -\left[\rho \iint_{S_B} \Omega_\alpha(\mathbf{x}) n_\beta\,dS\right]\ddot{X}_\alpha + \int_{-\infty}^{t}\iint_{S_B} \rho\Gamma_\alpha(\mathbf{x},t-\tau)n_\beta\ddot{X}_\alpha(\tau)\,d\tau\,dS\,, \tag{8.12.14}$$

where n_β is the generalized normal. Following Wehausen, let us define

$$\mu_{\beta\alpha}(\infty) = \rho \iint_{S_B} \Omega_\alpha(\mathbf{x}) n_\beta\,dS\,, \tag{8.12.15}$$

$$L_{\beta\alpha}(t) = \rho \iint_{S_B} \Gamma_\alpha(\mathbf{x},t) n_\beta\,dS\,, \tag{8.12.16}$$

which are both real, then

$$\mathscr{F}_\beta^R(t) = -\mu_{\beta\alpha}(\infty)\ddot{X}_\alpha(t) - \int_{-\infty}^{t} L_{\beta\alpha}(t-\tau)\ddot{X}_\alpha(\tau)\,d\tau\,. \tag{8.12.17}$$

8.12.2 Relation to the Frequency Response

Let

$$V_\alpha(t) = \mathrm{Re}\,\overline{V}_\alpha e^{-i\omega t}\,, \tag{8.12.18}$$

and suppose the motion to have begun from $t \sim -\infty$. Substituting Eq. (8.12.18) into Eq. (8.12.10b), we get

$$\Phi^R(\mathbf{x},t) = \mathrm{Re}\left\{\left[\Omega_\alpha(\mathbf{x}) + \int_0^\infty \Gamma_\alpha(\mathbf{x},\tau)e^{i\omega\tau}\,d\tau\right]\overline{V}_\alpha e^{-i\omega t}\right\}. \tag{8.12.19}$$

Now the quantity in [ ] must be the normalized simple harmonic response due to forced radiation with $\partial\phi_\alpha/\partial n = n_\alpha$ on the body; therefore,

$$\begin{aligned}\phi_\alpha(\mathbf{x},\omega) &= \mathrm{Re}\,\phi_\alpha + i\ \mathrm{Im}\,\phi_\alpha \\ &= \Omega_\alpha(\mathbf{x}) + \int_0^\infty \Gamma_\alpha(\mathbf{x},\tau)e^{i\omega\tau}\,d\tau\,. \end{aligned} \tag{8.12.20}$$

Since $\Gamma_\alpha = 0$ for $\tau \le 0$, the integral above is just the Fourier transform of Γ_α. Once ϕ_α (and its special limit Ω_α) is solved for a broad range of frequencies by any of the modern numerical means, $\Gamma_\alpha(\mathbf{x},t)$ can be obtained by inverse Fourier transform for which the numerical technique of fast Fourier transform is available. The β component of the restoring force on the body is, from Eq. (8.12.14),

$$\begin{aligned}\mathscr{F}_\beta^R &= -\rho \iint_{S_B} \Phi_t^R n_\beta\,dS \\ &= \mathrm{Re}\left\{\left[-\rho\iint_{S_B}\Omega_\alpha n_\beta\,dS - \rho\int_0^\infty d\tau\,e^{i\omega\tau}\iint_{S_B}\Gamma_\alpha n_\beta\,dS\right]\overline{V}_\alpha e^{-i\omega t}\right\}. \end{aligned} \tag{8.12.21}$$

If Eqs. (8.12.15) and (8.12.16) are substituted into Eq. (8.12.21) and the result is compared with the definitions of apparent mass and damping coefficients in Section 8.3.2, we conclude that

$$\mu_{\alpha\beta}(\omega) + \frac{i}{\omega}\lambda_{\alpha\beta}(\omega) = \mu_{\alpha\beta}(\infty) + \int_0^\infty L_{\alpha\beta}(\tau)e^{i\omega\tau}\,d\tau\,. \tag{8.12.22}$$

Separating the real and imaginary parts, we finally get

$$\mu_{\alpha\beta}(\omega) - \mu_{\alpha\beta}(\infty) = \int_0^\infty L_{\alpha\beta}(\tau)\cos\omega\tau\,d\tau\,, \tag{8.12.23}$$

$$\lambda_{\alpha\beta}(\omega) = \omega\int_0^\infty L_{\alpha\beta}(\tau)\sin\omega\tau\,d\tau \tag{8.12.24}$$

(Wehausen, 1967). Conversely, if the added mass or damping coefficients are known for all frequencies $0 \le \omega < \infty$, $L_{\alpha\beta}(t)$ can be found by inverse cosine or sine transform. Also, since $L_{\alpha\beta}$ can be found from either Eq. (8.12.23) or (8.12.24), a relation should exist between the apparent mass and the damping coefficients. Such a relation is called the Kramers–Kronig relation (see Ogilvie, 1964) which also appears in other branches of physics.

8.12.3 Exciting Force Caused by Scattering of Transient Incident Waves

To complete the formulation of the dynamic problem of a body in transient incident waves it is necessary to know the exciting force on a stationary body caused by diffraction. Wehausen (1967) has shown that the exciting force can be obtained from the radiation problem through a generalized Haskind–Hanaoka relation, as described below.

Let us define

$$B_\alpha(\mathbf{x}, t-\tau) = \Omega_\alpha(\mathbf{x}) + \int_\tau^t \Gamma_\alpha(\mathbf{x}, t')\, dt' \,. \tag{8.12.25}$$

From the governing conditions of Ω_α and Γ_α it can be shown that B_α satisfies the following conditions:

$$\nabla^2 B_\alpha = 0 \,, \qquad \text{in the fluid} \,, \tag{8.12.25a}$$

$$\frac{\partial B_\alpha}{\partial n} = n_\alpha \qquad \text{on} \quad S_B \,, \tag{8.12.25b}$$

$$\frac{\partial B_\alpha}{\partial z} = 0 \,, \qquad z = -h \,, \tag{8.12.25c}$$

$$\frac{\partial^2 B_\alpha}{\partial t^2} + g\frac{\partial B_\alpha}{\partial z} = 0 \,, \qquad z = 0, \text{ all } t > 0 \,, \tag{8.12.25d}$$

$$\frac{\partial B_\alpha}{\partial t} = 0 \,, \qquad z = 0, \ t = 0 \,, \tag{8.12.25e}$$

$$B_\alpha(\mathbf{x}, t) = 0 \,, \qquad z = 0, \ t = 0 \,, \tag{8.12.25f}$$

$$B_\alpha(\mathbf{x}, t) = \Omega_\alpha(\mathbf{x}) \,, \qquad t = 0, \text{ in the fluid} \,, \tag{8.12.25g}$$

$$B_\alpha = O(R^{-2}) \,, \quad R \to \infty, \ t < \infty \,. \tag{8.12.25h}$$

The last condition on the behavior of B_α at infinity requires mathematical arguments too lengthy to enter here (Stoker, 1957).

Next we let $\Phi^I(\mathbf{x}, t)$ denote the potential of the transient incident wave and $\Phi^S(\mathbf{x}, t)$ the scattered wave potential. Φ^I is originated in a finite region before striking the body. Φ^S satisfies Eqs. (8.12.25a)–(8.12.25h) provided that n_α is replaced by $-\partial\Phi^I/\partial n$ in Eq. (8.12.25b) and Ω_α is replaced by 0 in Eq. (8.12.25g).

Let us apply Green's theorem to $\partial\Phi^S(\mathbf{x},\tau)/\partial\tau$ and $B_\alpha(\mathbf{x},t-\tau)$ for the usual control volume bounded by S_F, S_B, and B_0 and a circular vertical cylinder S_∞ of great radius R. After the familiar use of the governing equations, we get

$$\iint_{S_B}\left(\frac{\partial\Phi^S}{\partial\tau}n_\alpha-\frac{\partial^2\Phi^S}{\partial\tau\partial n}B_\alpha\right)dS + \iint_{S_F}\left(\frac{\partial\Phi^S}{\partial\tau}\frac{\partial B_\alpha}{\partial z}-\frac{\partial^2\Phi^S}{\partial\tau\partial z}B_\alpha\right)dS=0\,. \tag{8.12.26}$$

When the boundary conditions and $f_\tau(t-\tau)=-f_t(t-\tau)$ are used, the second integral may be expressed

$$-\frac{1}{g}\iint_{S_F}\left(\frac{\partial\Phi^S}{\partial\tau}\frac{\partial^2 B_\alpha}{\partial t^2}-\frac{\partial^3\Phi^S}{\partial\tau^3}B_\alpha\right)dS = \frac{1}{g}\iint_{S_F}\frac{\partial}{\partial\tau}\left(\frac{\partial\Phi^S}{\partial\tau}\frac{\partial B_\alpha}{\partial t}+\frac{\partial^2\Phi^S}{\partial\tau^2}B_\alpha\right)dS\,. \tag{8.12.27}$$

With this result Eq. (8.12.26) may be integrated with respect to τ from $-\infty$ to t, yielding

$$\int_{-\infty}^{t}dt\iint_{S_B}\left(\frac{\partial\Phi^S}{\partial\tau}n_\alpha-\frac{\partial^2\Phi^s}{\partial\tau\partial n}B_\alpha\right)dS=0\,, \tag{8.12.28}$$

where the integrated terms vanish by virtue of Eqs. (8.12.25e) and (8.12.25f) for B_α and the fact that $\partial\Phi^S/\partial t$, $\partial^2\Phi^S/\partial t^2\to 0$ as $t\to\infty$. Differentiating Eq. (8.12.28) with respect to t, and using

$$\frac{\partial\Phi^S}{\partial n}=-\frac{\partial\Phi^I}{\partial n}\quad\text{on}\quad S_B \tag{8.12.29}$$

along with Eqs. (8.12.25) and (8.12.25g), we find that

$$-\iint_{S_B}\frac{\partial\Phi^S}{\partial t}n_\alpha\,dS=\int_{-\infty}^{t}d\tau\iint_{S_B}\frac{\partial^2\Phi^I}{\partial\tau\partial n}\Gamma_\alpha(\mathbf{x},t-\tau)\,dS + \iint_{S_B}\frac{\partial^2\Phi^I}{\partial t\partial n}\Omega_\alpha(\mathbf{x})\,dS\,. \tag{8.12.30}$$

Finally, the exciting (diffraction) force is

$$\begin{aligned}\mathscr{F}_\alpha^D(t) &= -\rho \iint_{S_B} \left(\frac{\partial \Phi^I}{\partial t} + \frac{\partial \Phi^S}{\partial t} \right) n_\alpha \, dS \\ &= -\rho \iint_{S_B} \left(\frac{\partial \Phi^I}{\partial t} n_\alpha - \frac{\partial^2 \Phi^I}{\partial t \partial n} \Omega_\alpha \right) dS \\ &\quad + \rho \int_{-\infty}^{t} d\tau \iint_{S_B} \frac{\partial^2 \Phi^I}{\partial \tau \partial n}(\mathbf{x}, \tau) \Gamma_\alpha(\mathbf{x}, t-\tau) \, dS \end{aligned} \tag{8.12.31}$$

which is due to Wehausen (1967).

Since the right-hand side depends only on the incident wave and on Ω_α and Γ_α, which are defined for the radiation problem, Eq. (8.12.31) is an extended Haskind–Hanaoka relation and may be used to calculate the exciting force without solving the transient diffraction problem.

8.12.4 Linearized Equations of Transient Motion of a Floating Body

The governing equation (8.2.47) still holds, but the hydrodynamic restoring force is given by Eq. (8.12.17) and the exciting force by Eq. (8.12.31), with the result that

$$\begin{aligned}&[M_{\alpha\beta} + \mu_{\alpha\beta}(\infty)] \ddot{X}_\beta + \int_{-\infty}^{t} L_{\alpha\beta}(t-\tau) \ddot{X}_\beta(\tau) \, d\tau + C_{\alpha\beta} X_\beta \\ &\qquad = \mathscr{F}_\alpha^D + \mathbb{F}_\alpha \end{aligned} \tag{8.12.32}$$

which is a set of integro-differential equations to be solved for given initial position and velocity of the body.

From the above results it is evident that the transient response may be calculated, in principle, from sinusoidal responses numerically. On this basis an analytical theory has been worked out by Ursell (1964) and Maskell and Ursell (1970) for a two-dimensional circular cylinder freely floating on the free surface. At present all existing numerical methods are costly for high frequencies. However, this shortcoming is not fatal in practice since the most important responses usually occur in the range where the product of k and the body size is of order unity. Alternative numerical methods via transient Green's functions for initial-value problems are being developed for general bodies and may someday prove to be more effective.

(See *Proceedings of the 3rd International Conference on Numerical Ship Hydrodynamics*, 1981, Paris).

Appendix 8.A Derivation of Green's Function

For both two and three dimensions the Green functions have been deduced by John (1950) and by other authors. Only the details for two dimensions are explained here. Defining the Green function $G(\mathbf{x}|\mathbf{x}_0)$ by Eqs. (8.4.18)–(8.4.21), and taking the Fourier transform of Eqs. (8.4.18)–(8.4.20) with respect to x, we get

$$\frac{d^2\tilde{G}}{dz^2} - K^2\tilde{G} = \delta(z - z_0)e^{-iKx_0}\,, \tag{8.A.1}$$

$$\frac{d\tilde{G}}{dz} - \sigma\tilde{G} = 0\,, \quad z = 0\,, \tag{8.A.2}$$

$$\frac{d\tilde{G}}{dz} = 0\,, \quad z = -h\,, \tag{8.A.3}$$

where K is the Fourier transform variable. An equivalent boundary-value problem is defined by

$$\frac{d^2\tilde{G}}{dz^2} - K^2\tilde{G} = 0\,, \quad -h < z < z_0,\ z_0 < z < 0\,, \tag{8.A.4}$$

$$\tilde{G}|_{z=z_0^+} - \tilde{G}|_{z=z_0^-} = 0\,, \tag{8.A.5a}$$

$$\left.\frac{d\tilde{G}}{dz}\right|_{z=z_0^+} - \left.\frac{d\tilde{G}}{dz}\right|_{z=z_0^-} = e^{-iKx_0}\,, \tag{8.A.5b}$$

and by Eqs. (8.A.2) and (8.A.3). The second jump condition (8.A.5b) may be deduced by integrating Eq. (8.A.1) across z_0 and invoking Eq. (8.A.5a). In terms of

$$z_> = \max(z, z_0) \quad \text{and} \quad z_< = \min(z, z_0)\,, \tag{8.A.6}$$

the solution is easily expressed in a compact form

$$\tilde{G} = \frac{e^{-iKx_0}}{K}\,\frac{\sigma\sinh Kz_> + K\cosh Kz_>}{\sigma\cosh Kh - K\sinh Kh}\cosh K(z_< + h)\,. \tag{8.A.7}$$

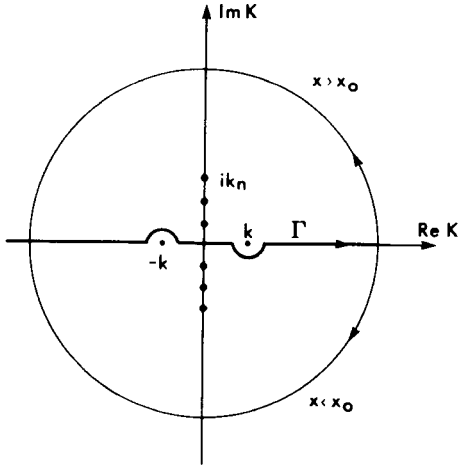

Figure A.1: Contours of integration.

In applying the Fourier inversion formula, an ambiguity arises along the real K axis where two poles exist at the real zeroes of

$$\sigma \cosh Kh - K \sinh Kh = 0 \quad \text{or} \quad K \tanh Kh = \sigma \,, \tag{8.A.8}$$

that is, $K = \pm k$. Now the radiation condition must be invoked to define the improper integral. To be checked for correctness, we now choose the path Γ which is indented above $-k$ and below $+k$ along two semicircles of small radii, as shown in Fig. A.1. Thus,

$$G(\mathbf{x}|\mathbf{x}_0) = \frac{1}{2\pi} \int_\Gamma dK\, e^{iK(x-x_0)} \times \left\{ \frac{1}{K} \frac{\sigma \sinh Kz_> + K \cosh Kz_>}{\sigma \cosh Kh - K \sinh Kh} \cosh K(z_< + h) \right\}. \tag{8.A.9}$$

The above representation can be manipulated into several different forms. One of them is an eigenfunction expansion which is deduced by recognizing that the integral has imaginary poles at the imaginary zeroes of Eq. (8.A.8), that is, at $K = \pm ik_n$, $n = 1, 2, 3, \ldots$, where k_n is a positive real root of

$$k_n \tan k_n h = -\sigma \,. \tag{8.A.10}$$

For $x > x_0$ we introduce a closed semicircular contour in the upper half complex plane of K, as shown in Fig. A.1, so that the integrand diminishes as Im $K \uparrow \infty$. By Jordan's lemma, the line integral along the semicircle

vanishes in the limit of infinite radius. Therefore, the original integral is equal to the sum of residues from the poles at k and ik_n, $n = 1, 2, 3 \ldots$. The residues may be calculated by repeated use of (8.A.8) and (8.A.10). Similarly, for $x < x_0$, we introduce a closed contour in the lower half plane, capturing the residues at $-k$ and $-ik_n$. The combined result is

$$G = -\frac{i}{k}\left(h + \frac{1}{\sigma}\sinh^2 kh\right)^{-1} e^{ik|x-x_0|}\cosh k(z+h)\cosh k(z_0+h) + \sum_{n=1}^{\infty}\frac{1}{k_n}\left(h - \frac{1}{\sigma}\sin^2 k_n h\right)^{-1} e^{-k_n|x-x_0|}\cos k_n(z+h)\cos k_n(z_0+h)\,. \tag{8.A.11}$$

Details are left as an exercise. Clearly, the first term represents the outgoing waves, while the series represents the evanescent modes. Thus, the radiation condition is satisfied. Indeed, any other indentation of the integral path would violate the radiation condition.

An alternative representation, which is important in the numerical method of integral equations, exhibits the singular part of the Green function explicitly. Near the source point (x_0, z_0) the Green function must be dominated by $(1/2\pi)\ln[(x-x_0)^2 + (z-z_0)^2]^{1/2}$. To extract this term we first use the symmetry of the bracket $\{\ \}$ in (8.A.9) and of the contour in order to use only one-half of the path, that is,

$$G(\mathbf{x}|\mathbf{x}_0) = \frac{1}{\pi}\int_0^{\infty}\frac{dK}{K}\cos K(x-x_0) \times \frac{\sigma\sinh Kz_> + K\cosh Kz_>}{\sigma\cosh Kh - K\sinh Kh}\cosh K(z_< + h)\,, \tag{8.A.12}$$

where the path of integration is the positive half of Γ in Fig. A.1. Let us define

$$\begin{aligned} r &= [(x-x_0)^2 + (z-z_0)^2]^{1/2}\,, \\ r' &= [(x-x_0)^2 + (z+z_0+2h)^2]^{1/2}\,, \end{aligned} \tag{8.A.13}$$

where r' is the distance between the field point and the image of the source below the sea bottom. From the following identities of Laplace transform:

$$\int_0^{\infty}\frac{dK}{K}e^{-Kb}(1-\cos Ka) = \ln\left[\frac{(a^2+b^2)^{1/2}}{b}\right], \tag{8.A.14}$$

$$\int_0^\infty \frac{dK}{K}(e^{-Kb} - e^{-Kh}) = \ln\left(\frac{h}{b}\right), \tag{8.A.15}$$

it follows that

$$\ln\frac{r}{h} = \int_0^\infty \frac{dK}{K}(e^{-Kh} - e^{-Kb}\cos Ka), \quad a = x - x_0, \; b = z_> - z_< \tag{8.A.16}$$

with a similar formula for $\ln(r'/h)$. Substituting (8.A.16) into (8.A.12), we obtain

$$\begin{aligned} 2\pi G = \ln\frac{r}{h} + \ln\frac{r'}{h} + \int_0^\infty \frac{dK}{K} \\ \times \left\{ \cos K(x - x_0)\left[2\frac{\sigma \sinh Kz_> + K\cosh Kz_>}{\sigma\cosh Kh - K\sinh Kh}\cosh K(z_< + h)\right.\right. \\ \left.\left. + e^{-K(z_< - z_>)} + e^{-K(z_> + z_< + 2h)}\right] - 2e^{-Kh}\right\}. \end{aligned}$$

After a little algebra and returning from $z_>$, $z_<$ to z and z_0, we get

$$\begin{aligned} G = \frac{1}{2\pi}\ln\frac{r}{h} + \frac{1}{2\pi}\ln\frac{r'}{h} + 2\int_0^\infty \frac{dK}{K}\left\{\frac{\cos K(x - x_0)}{\sigma\cosh Kh - K\sinh Kh}\right. \\ \left. \times \cosh K(z + h)\cosh K(z_0 + h) - e^{-Kh}\right\}, \end{aligned} \tag{8.A.17}$$

which is the form deduced by John (1950).

The first two logarithmic terms above represent two sources (one in the fluid and one beneath the sea bottom); their sum satisfies the boundary condition at $z = -h$. The contour integral therefore represents the effect of the free surface. It may be easily checked that the contribution from the small semicircle gives the outgoing wave, while the remaining principal-valued integral is of local importance only.

For infinite depth, the limit of (8.A.17) gives

$$G(\mathbf{x}|\mathbf{x}_0) = \frac{1}{2\pi}\ln r + \int_0^\infty \frac{dK}{K}\left[\frac{\sigma + K}{\sigma - K}e^{K(z + z_0)}\cos K(x - x_0) - e^{-K}\right]. \tag{8.A.18}$$

For a three-dimensional ocean of constant depth, the Hankel transform may be used instead of the Fourier transform. A formula similar to (8.A.9) is obtained. One must then use some integral identities of Bessel functions to deduce alternative representations. The explanations for two dimensions

should provide sufficient background for the reader to follow the details given in John (1950). Only certain key results are recorded here.

Corresponding to (8.A.12) the result can be expressed as

$$G = -\frac{1}{2\pi}\int_0^\infty dK K J_0(KR)\{\ \} \tag{8.A.19}$$

where the bracket { } is the same as that of (8.A.9). In series form G may be expressed as

$$G = -\frac{i}{2}\frac{k^2-\sigma^2}{h(k^2-\sigma^2)+\sigma}H_0^{(1)}(kR)\cosh k(z_0+h)\cosh k(z+h)$$
$$+\frac{1}{\pi}\sum_{n=1}^{\infty}\frac{k_n^2+\sigma^2}{-h(k_n^2+\sigma^2)+\sigma}K_0(k_nR)\cos k_n(z+h)\cos k_n(z_0+h)\,. \tag{8.A.20}$$

With the singular part exhibited, G may be written alternatively as

$$G = -\frac{1}{4\pi}\left(\frac{1}{r}+\frac{1}{r'}\right)+\frac{1}{4\pi}\int_0^\infty dK\, J_0(KR)\frac{2(\sigma+K)e^{-Kh}}{\sigma\cosh Kh - K\sinh Kh}$$
$$\times\cosh K(z+h)\cosh K(z_0+h)\,, \tag{8.A.21}$$

where

$$r = [(x-x_0)^2+(y-y_0)^2+(z-z_0)^2]^{1/2}\,,$$
$$r' = [(x-x_0)^2+(y-y_0)^2+(z+z_0+2h)^2]^{1/2}\,.$$

Finally, for infinite depth the three-dimensional Green's function is

$$G = -\frac{1}{4\pi r}+\frac{1}{4\pi}\int_0^\infty \frac{\sigma+K}{\sigma-K}e^{K(z+z_0)}J_0(KR)\,dK\,. \tag{8.A.22}$$

Viscous Damping in Small-Amplitude Waves

9

9.1 Introduction

Except in Chapter Six, we have so far disregarded the effect of viscosity because it is usually so weak and confined in such thin layers as to exert very little influence on the wave motion over a few periods or wavelengths. However, over a long time compared to a characteristic wave period, or a long distance compared to a characteristic wavelength, the cumulative effect of viscosity on wave attenuation can be of first-order importance. In this chapter, theories are developed for the damping of infinitesimal waves by molecular viscosity. Within this framework the mechanism of energy transfer is examined in detail. A formal method of perturbation is also demonstrated for calculating viscous effects on both the amplitude and phase of the wave. The possible importance of air, dismissed in the past by most authors but pointed out recently by Dore (1978), is briefly discussed. Finally, a semiempirical theory of turbulent boundary layer near the sea bottom is described with a simple example of its applications.

9.2 Linearized Equations of Viscous Flows and the Laminar Boundary Layer

The full Navier–Stokes equations are given in Eqs. (1.1.1) and (1.1.2), Chapter One. For convenience we quote them here in index form. Let the rectangular coordinates be denoted by x_i, $i = 1, 2, 3$, with $x_1 = x$, $x_2 = y$, $x_3 = z$ and the corresponding velocity components be denoted by u_i. The equation of continuity is

$$\frac{\partial u_j}{\partial x_j} = 0\,, \tag{9.2.1}$$

where summation over the repeated indices is implied. The equation of momentum conservation is

$$\frac{\partial u_i}{\partial t} + u_j \frac{\partial u_i}{\partial x_j} = -g\delta_{i3} - \frac{1}{\rho}\frac{\partial P}{\partial x_i} + \frac{1}{\rho}\frac{\partial \tau_{ij}}{\partial x_j}\,, \quad i = 1, 2, 3\,, \tag{9.2.2}$$

where τ_{ij} are the components of the viscous stress tensor

$$\tau_{ij} = 2\mu e_{ij}\,, \quad e_{ij} = \frac{1}{2}\left(\frac{\partial u_i}{\partial x_j} + \frac{\partial u_j}{\partial x_i}\right). \tag{9.2.3}$$

On a stationary solid the fluid velocity must vanish:

$$u_i = 0\,, \quad i = 1, 2, 3\,. \tag{9.2.4}$$

On a water surface $F = z - \zeta(x, y, t) = 0$ the kinematic condition still holds:

$$\frac{\partial \zeta}{\partial t} + u_1 \frac{\partial \zeta}{\partial x_1} + u_2 \frac{\partial \zeta}{\partial x_2} = u_3 \quad z = \zeta\,. \tag{9.2.5}$$

The dynamic boundary condition is the continuity of normal and tangential stresses:

$$\{-P\delta_{ij} + \tau_{ij}\} n_j = \{-P\delta_{ij} + \tau_{ij}\}_{\text{air}} n_j\,, \quad z = \zeta\,. \tag{9.2.6}$$

In this chapter the water surface will be assumed to be free of atmospheric pressure and stresses so that the right-hand side of Eq. (9.2.6) vanishes. In reality, surface contamination can complicate the above condition and affect wave damping considerably. It is also a common experience in the laboratory that fresh water gives a different damping rate from water that is visibly clean but has been in the tank for more than a day. This phenomenon is called *aging*. However, the physics of surface contamination and aging is not well understood and will not be pursued here.

To facilitate analysis, we assume infinitesimal amplitude and linearize Eq. (9.2.2),

$$\frac{\partial u_i}{\partial t} = -g\delta_{i3} - \frac{1}{\rho}\frac{\partial P}{\partial x_i} + \frac{1}{\rho}\frac{\partial \tau_{ij}}{\partial x_j}\,. \tag{9.2.7}$$

As is well known, any vector can be taken as the sum of an irrotational and a solenoidal vector (Morse and Feshbach, Vol. I, 1953, p. 53):

$$u_i = \frac{\partial \Phi}{\partial x_i} + U_i\,, \tag{9.2.8}$$

with $\mathbf{U}$ being solenoidal, that is,

$$\frac{\partial U_i}{\partial x_i} = 0\,, \tag{9.2.9}$$

and $\nabla\Phi$ being irrotational. It follows from the continuity equation (9.2.1) that

$$\nabla^2\Phi = 0\,. \tag{9.2.10}$$

We now let

$$P = -\rho g z + p = -\rho g z - \rho\Phi_t\,, \tag{9.2.11}$$

where p is the dynamic pressure. Substituting Eq. (9.2.8) into Eq. (9.2.7) and using Eq. (9.2.11), we obtain

$$\frac{\partial U_i}{\partial t} = \nu\nabla^2 U_i\,. \tag{9.2.12}$$

The unknowns Φ and $\mathbf{U}$ are coupled by the boundary conditions, though not by the governing equations. In particular, there must be no slip on the solid wall S,

$$\frac{\partial\Phi}{\partial x_i} + U_i = 0 \quad \text{on} \quad S\,. \tag{9.2.13}$$

On the free surface, we apply the linearized boundary conditions on the mean free surface $z = 0$. The kinematic condition reads

$$\frac{\partial\zeta}{\partial t} = \Phi_z + W\,. \tag{9.2.14}$$

Dynamically, we also require the vanishing of the normal stress

$$\frac{\partial\Phi}{\partial t} + g\zeta + \frac{2\mu}{\rho}\frac{\partial w}{\partial z} = 0\,, \tag{9.2.15a}$$

and of the tangential stresses

$$\mu\left(\frac{\partial u}{\partial z} + \frac{\partial w}{\partial x}\right) = \mu\left(\frac{\partial v}{\partial z} + \frac{\partial w}{\partial y}\right) = 0\,. \tag{9.2.15b}$$

Strictly speaking, one may question the legitimacy of applying the stress-free conditions on $z = 0$ unless the wave amplitude is much smaller than the boundary-layer thickness $\delta = O(\nu/\omega)^{1/2}$. However, since the stresses are related to the velocity gradient, viscosity has much less constraint on the free surface than near a solid wall where the velocity must vanish. In other words, the free-surface boundary layer is very weak. In fact, it will

be shown shortly that the damping rate from the free-surface boundary layer is of the order $O(\mu^{3/2})$ as compared to $O(\mu^{1/2})$ from near the solid walls and $O(\mu)$ in the main body of the fluid. Hence, the error incurred from misplacing the free surface is only of the order $O(\mu^{3/2}kA)$ which is too small to be of concern here.

By taking the scalar product of the momentum equation (9.2.2) with $\mathbf{u}$ and integrating over *any* material volume whose boundary is $S_0(t)$, we obtain an equation stating the balance of mechanical energy inside the volume $V(t)$:

$$\iiint_V \frac{\partial}{\partial t}\frac{1}{2}\rho u_i u_i \, dV + \iint_{S_0} \frac{1}{2}\rho u_i u_i u_j n_j \, dS$$
$$= \iint_{S_0} \{-P\delta_{ij} + \tau_{ij}\} n_j u_i \, dS - \iiint_V \rho g \delta_{i3} u_i \, dV - \frac{1}{2\mu}\iiint_V \tau_{ij}\tau_{ij} \, dV \,. \tag{9.2.16}$$

The left-hand side is the total rate of energy change in V; the second term is the flux of energy across the boundary. On the right-hand side, the first integral represents the rate of working by surface stresses (pressure and viscous stress) acting on the boundary; the second integral is the rate of work done by body force throughout the volume, and the third integral is the rate of viscous dissipation (rate of working by viscous stresses on strain) throughout the volume.

The above energy equation is exact. Consistent with linearization, the second integral on the left may be neglected, being of the order $O(kA)$ higher than the rest. The mean position of S_0 may be used to replace the instantaneous bounding surface of V.

For later convenience we review the well-known theory of Stokes for an oscillatory boundary layer near a smooth wall. Let the inviscid velocity just outside the boundary layer near a flat wall be $U_I(t)$. Within the boundary layer the tangential velocity u is governed by

$$\frac{\partial u}{\partial t} = \frac{\partial U_I}{\partial t} + \nu \frac{\partial^2 u}{\partial z^2} \,, \tag{9.2.17}$$

where z is normal to the wall. On the wall ($z = 0$), $u = 0$. For large z, $u \sim U_I$. Assume U_I to be simple harmonic in time,

$$U_I = \mathrm{Re}\, U_0 e^{-i\omega t} \,, \tag{9.2.18}$$

then the tangential velocity in the boundary layer is given by

$$u = \mathrm{Re}\,(U_0 F_1(\xi) e^{-i\omega t})\,, \tag{9.2.19}$$

where

$$F_1(\xi) = 1 - e^{-(1-i)\xi}\,, \tag{9.2.20}$$

with

$$\xi = \frac{z}{\delta}\,, \quad \delta = \left(\frac{2\nu}{\omega}\right)^{1/2}\,. \tag{9.2.21}$$

The corresponding shear stress at the wall is

$$\tau_{xz}^B = \mu \frac{\partial u}{\partial z}\bigg|_0 = \mu\ \mathrm{Re}\left[\frac{U_0}{\delta}\sqrt{2}\, e^{-i(\omega t + \pi/4)}\right], \tag{9.2.22}$$

which is out of phase with the inviscid velocity U_I by $\frac{1}{4}\pi$.

9.3 Damping Rate and the Process of Energy Transfer

To understand the physical mechanism of wave damping, it is illuminating to examine the detailed process of energy transfer in the fluid. First, let us estimate the order of magnitude of the rate of dissipation in various parts of the fluid. We decompose the fluid velocity as in Eq. (9.2.8) into the rotational part $\mathbf{U}$ which depends directly on viscosity, and the irrotational part $\nabla\Phi$.

Outside of all boundary layers, it is reasonable to expect that $|\mathbf{U}| \ll \nabla\Phi$. There the rate of strain is dominated by the irrotational part whose velocity scale is ωA and length scale is either the basin dimension L or the wavelength $2\pi/k$, whichever is smaller. The energy dissipation rate is then

$$O\left(\frac{1}{\mu}\iiint_{R_I} \tau_{ij}^2\, dV\right) \sim \frac{\mu^2}{\mu}\frac{\omega^2 A^2 L^3}{L^2} \sim \mu\omega^2 A^2 L \propto \mu\,. \tag{9.3.1}$$

Inside a wall boundary layer R_ε (see Fig. 9.1), the tangential components of $\mathbf{U}$ and $\nabla\Phi$, are comparable, but the normal gradient of the tangential component of $\mathbf{U}$ is much greater and dominates the strain rate, so that

$$O\left(\frac{1}{\mu}\iiint_{R_\varepsilon} \tau_{ij}^2\, dV\right) \sim \frac{\mu^2}{\mu}\frac{\omega^2 A^2}{\delta^2} L^2\delta \sim \mu\omega^2 A^2 L \cdot \frac{L}{\delta} \propto \mu^{1/2}\,. \tag{9.3.2}$$

Consider the neighborhood of the free surface. In principle, a boundary layer R_F also exists there; its importance depends on the free-surface

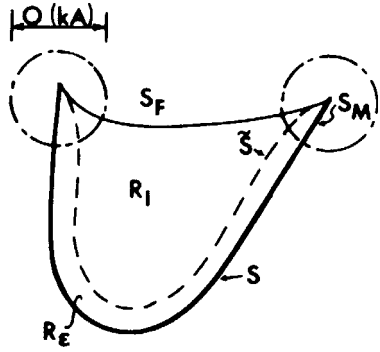

Figure 9.1: Division of fluid regions. The total fluid volume is defined by the instantaneous free surface S_F. Dashed lines designate the outer surface of the boundary layer.

condition. Consider first a clean surface. Since **U** is negligible beneath the boundary layer, it cannot grow to an appreciable magnitude within a short distance of $O(\delta)$. Thus, the stress is mainly controlled by the potential velocity field which varies according to the length scale L or $2\pi/k$ and is of the same order as the stress in the main body of the fluid exterior to the boundary layer. Because of the small volume $O(\delta L^2)$ the rate of dissipation in the free-surface boundary layer is only

$$O\left(\frac{1}{\mu}\iiint_{R_F}\tau_{ij}^2\,dV\right)\sim\mu\left(\frac{\omega A}{L}\right)^2L^2\delta\sim\mu\omega^2A^2L\frac{\delta}{L}\propto\mu^{3/2}\,. \qquad (9.3.3)$$

At the other extreme, if the free surface is heavily contaminated, for example, by oil slicks, the fluid particles are immobilized so that the free surface may resemble an inextensible, though flexible, sheet. The stress in the free-surface boundary layer can then be as great as in the boundary layer near a solid wall. As stated in Section 9.2, surface contamination is assumed to be absent. Therefore, the largest energy dissipation takes place inside the wall boundary layers; only in very deep and unbounded water or for very short waves ($kh \gg 1$) is the dissipation in the main body of the fluid important.

With the energy flux term neglected on the left-hand side, Eq. (9.2.16) will now be averaged over a period T. We define the average as follows:

$$\bar{f}(t)=\frac{1}{T}\int_t^{t+T}f(t')\,dt' \qquad (9.3.4)$$

which has the important property that $\overline{\partial f/\partial t} = \partial \bar{f}/\partial t$. For generality, we take V to contain part of R_ε, R_F, and R_I, where R_I is the inviscid core.

From the second term on the right-hand side of Eq. (9.2.16), the work done by the body force is negligible everywhere except on the free surface and is given by

$$\overline{\iiint_V \rho g_i u_i \, dV} = -\rho g \overline{\iint_{S_F} \frac{\partial \zeta}{\partial t} \, dA \left[\int_0^\zeta dz \right]}$$

$$= \rho g \iint_{S_F} \overline{\frac{\partial \zeta}{\partial t} \zeta} \, dS = -\frac{\partial}{\partial t} \iint_{S_F} \frac{1}{2} \rho g \overline{\zeta^2} \, dS$$

which is just the negative of the rate of change of the potential energy. Combining the preceding term with the change of the kinetic energy in R, we have from Eq. (9.2.16)

$$\frac{\partial}{\partial t} \left[\iiint_V \frac{1}{2} \rho \overline{u_i u_i} \, dV + \frac{1}{2} \iint_{S_F} \rho g \overline{\zeta^2} \, dS \right]$$

$$= \iint_{S_0} \overline{(-p\delta_{ij} + \tau_{ij}) n_j u_i \, dS} - \frac{1}{2\mu} \iiint_V \overline{\tau_{ij}^2} \, dV + O(A^3) \,. \qquad (9.3.5)$$

The left side represents the rate of change of the total kinetic and potential energy. On the right-hand side, the first integral gives the rates of working by the dynamic pressure p and by the viscous stresses, while the second integral gives the rate of dissipation.

From here on it is more convenient to employ dimensionless variables defined as follows:

$$\begin{aligned} (x', y', z') &= k(x, y, z) \,, \qquad t' = (gk)^{1/2} t \\ \mathbf{u}' &= \frac{\mathbf{u}}{A(gk)^{1/2}} \,, \qquad p' = \frac{p}{\rho g A} \\ \Phi' &= \frac{\Phi k}{A(gk)^{1/2}} \,, \qquad \zeta' = \frac{\zeta}{A} \end{aligned} \qquad (9.3.6)$$

where all variables without primes are dimensional. A and k are the typical wave amplitude and wavenumber, respectively. After substitution, the primes are dropped for brevity. Let

$$\varepsilon = k\nu^{1/2}(gk)^{1/4} \ll 1 \,. \qquad (9.3.7)$$

Equation (9.3.5) becomes

$$\underbrace{\left\{\iiint_V \frac{\partial}{\partial t}\frac{\overline{u_i u_i}}{2}\,dV + \iint_{S_F}\frac{\partial}{\partial t}\frac{\overline{\zeta^2}}{2}\,dS\right\}}_{I} = \underbrace{\iint_{S_0}\overline{-pu_i n_i}\,dS}_{II} + \underbrace{2\varepsilon^2\iint_{S_0}\overline{e_{ij}u_i n_j}\;dS}_{III} - \underbrace{2\varepsilon^2\iiint_V \overline{e_{ij}^2\,dV}}_{IV}\,. \qquad (9.3.8)$$

In this equation the free surface S_F may be excluded from the total S_0 which bounds V, due to the stress-free condition.

Referring to Figs. 9.1(b) and 9.2, we denote the meniscus boundary layer by R_M, whose dimensionless height is $O(kA)$. The solid boundaries of R_ε and R_M will be denoted by S and S_M, respectively, while the corresponding outer edges by $\tilde{S}$ and $\tilde{S}_M$, respectively. The precise physics in the neighborhood of the meniscus is a complex matter involving surface tension (Adams, 1941). In particular, the reversal of contact angles when the meniscus rises and falls is believed to contribute to damping by hysterisis (Miles, 1967), but the subject appears to be a poorly understood part of physical chemistry. We shall, therefore, not venture into hysterisis damping but postulate the following picture in the context of viscous fluid only. In the

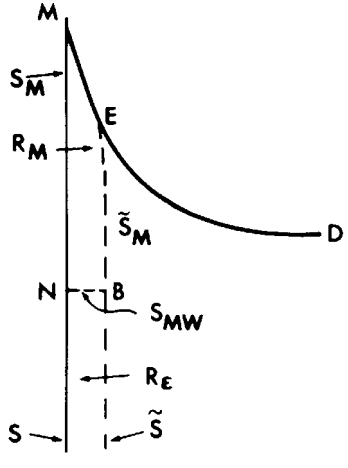

Figure 9.2: Enlarged view of the meniscus neighborhood. The line $NB(S_{MW})$ symbolizes the border between meniscus and wall boundary layers.

neighborhood of the meniscus the free surface attains its greatest height at the level M and the least height at the level N (Fig. 9.2). The wall below M is always wetted. The piece ME of the meniscus free surface changes from being nearly horizontal at the maximum rise to a thin film at the maximum fall. At any intermediate time during each period the meniscus consists of a thin viscous boundary layer $MNBE$ (of thickness $O(\varepsilon)$ and a height of $O(kA)$) near the wall, and a potential region whose boundary and volume change with time. The lower extreme of this boundary layer NB also forms the ceiling of the main wall boundary layer R_ε.

We now examine the leading terms in Eq. (9.3.8) for different control volumes (Mei and Liu, 1973).

9.3.1 The Entire Fluid

Let the volume V be the entire fluid volume R; hence the boundary surface consists of all wetted walls and the free surface:

$$V = R_I + R_\varepsilon + R_M\,, \quad S_0 = S + S_M + S_F\,.$$

In Eq. (9.3.8), term (I) is well approximated by

$$\frac{1}{2}\frac{\partial}{\partial t}\left\{\iiint_{R_I} \overline{u_i u_i}\, dV + \iint_{S_F} \overline{\zeta^2}\, dS\right\}$$

since $R_I = O(1) \gg R_\varepsilon + R_M = O(\varepsilon)$. The magnitude of $O(\partial/\partial t)$ is undetermined.

The sum of terms (II) and (III) vanishes on S_F because of the stress-free condition. Each term vanishes individually on S_W and S_M because $u_i = 0$.

Term (IV) $= O(\varepsilon)$ in the boundary layer since $e_{ij} = O(1/\varepsilon)$ and $R_\varepsilon + R_M = O(\varepsilon)$. The contribution from the essentially inviscid interior is $O(\varepsilon^2)$. Furthermore, the volume of the meniscus boundary layer is much smaller than that of the wall boundary layer ($R_M/R_\varepsilon = O(kA)$), while the straining rate is of the same order. Hence, we need only to account for the dissipation in the main wall boundary layer. In summary, we have, to $O(\varepsilon)$,

$$\frac{1}{2}\frac{\partial}{\partial t}\left\{\iiint_{R_t} \overline{u_i u_i}\, dV + \iint_{S_F} \overline{\zeta^2}\, dS\right\} = -2\varepsilon^2 \iiint_{R_t} \overline{e_{ij}^2}\, dV\,. \qquad (9.3.9)$$

This formula is the basis of many existing damping theories and implies that both the time derivative and the dimensionless damping rate are $O(\varepsilon)$.

9.3.2 Meniscus Boundary Layer

Now consider the meniscus boundary layer with volume $V = R_M$ and bounding surface $S_M + \tilde{S}_M + S_{MW}$, where S_M is the side wall, $\tilde{S}_M$ is the outer edge of the boundary layer, and S_{MW} is the borderline with the main wall layer (see Fig. 9.2). Referring to Eq. (9.3.8), we find the following:

Term (I): Since $u_i = O(1)$, $R_M = O(\varepsilon kA)$ and $\partial(^-)/\partial t = O(\varepsilon)$, term I is $O(\varepsilon^2 kA)$.

Term (II): S_M gives no contribution since $u_i = 0$. On S_{MW}, $u_i n_i = w = O(1)$, $p = O(1)$, and $S_{MW} = O(\varepsilon)$; hence the integral over S_{MW} is of $O(\varepsilon)$. Use is made of the fact that only the hydrodynamic pressure p does work. On the outer edge $\tilde{S}_M$ of the meniscus boundary layer the tangential velocity is $w = O(1)$. Note that the tangential (vertical) length scale is $O(kA)$; hence by continuity the normal (horizontal) velocity is $u_i n_i = O(\varepsilon/kA)$. Since $p = -\Phi_t = O(1)$ and the area of $\tilde{S}_M$ is of $O(kA)$, we have

$$\iint_{S_M} \overline{pu_i}\, n_i \, dS = O(\varepsilon)\,.$$

Term (III): On S_M, $u_i = 0$. On $\tilde{S}_M$, $e_{ij} = O(1)$. The integral on $S_M + \tilde{S}_M$ is $O(\varepsilon^2 kA)$. On S_{MW}, $e_{ij} = O(\varepsilon^{-1})$ and $u_i = O(1)$, and the area of $S_{MW} = O(\varepsilon)$; hence the integral is only of $O(\varepsilon^2)$.

Term (IV): As was estimated before, the dissipation rate in this volume is of $O(\varepsilon kA)$.

Thus, to $O(\varepsilon)$, Eq. (9.3.7) reduces to

$$\iint_{\tilde{S}_M} \overline{pu_i}\, n_i \, dS + \iint_{S_{MW}} \overline{pu_i}\, n_i \, dS = O(\varepsilon^2)\,, \tag{9.3.10}$$

which means that, by pressure working on S_M, power is fed into the meniscus boundary layer from the inviscid core, and then transmitted essentially undiminished to the main wall boundary layer, also through pressure working on S_{MW}. Thus, the meniscus boundary layer serves as a channel of energy flow from waves to the main side-wall boundary layer!

9.3.3 Wall Boundary Layer

Take the wall layer bounded by the solid surface S, the outer edge of the boundary layer $\tilde{S}$, and the narrow strip bordering the free-surface meniscus

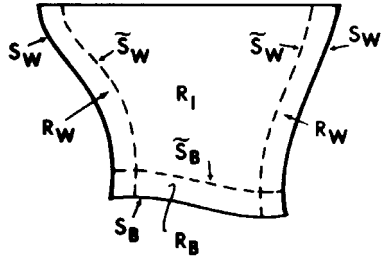

Figure 9.3: Basins with corners. The main boundary layer is separated into side-wall layer R_W and bottom layer R_B.

boundary layer S_{MW}. Similar estimates give that term (I) $= O(\varepsilon^2)$, term (II) $= O(\varepsilon)$, term (III) $= O(\varepsilon^2)$, and term (IV) $= O(\varepsilon)$. In particular, the pressure working term has contributions from both $\tilde{S}$ and S_{MW}. The resulting energy budget is, to $O(\varepsilon)$, given by

$$-\iint_{S_{MW}} \overline{pw}\, dS - \iint_{S} \overline{pu_i}\, n_i \, - dS 2\varepsilon^2 \iiint_{R_\varepsilon} \overline{e_{ij}^2}\, dV = -0\,. \qquad (9.3.11)$$

Physically, pressure working on the ceiling and on the side balances the dissipation within.

If the water basin has sharp convex corners below the free surface, it is convenient to separate the wall layer into a side-wall layer R_W, and a bottom layer R_B. Within the corner region whose volume is $O(\varepsilon^2)$ (see Fig. 9.3), the velocity field is essentially stagnant; all surface and volume integrals in Eq. (9.3.8) associated with the corner are at most of $O(\varepsilon^2)$ and can be ignored. Thus, the energy budget for the bottom boundary layer is

$$\iint_{\tilde{S}_B} \overline{pu_i}\, n_i \, dS - 2\varepsilon^2 \iiint_{R_B} \overline{e_{ij}^2}\, dV = O(\varepsilon^2)\,, \qquad (9.3.12)$$

that is, dissipation within R_B is balanced by pressure working on the side $\tilde{S}_B$.

9.3.4 Interior Core

It can be shown that term (I) $= O(\varepsilon)$, term (II) $= O(\varepsilon)$, term (III) $= O(\varepsilon^2)$ since e_{ij}, $u_j = O(1)$, and term (IV) $= O(\varepsilon^2)$. Furthermore, the free-surface integral can be transformed into one for potential energy as before. Hence,

$$\frac{\partial}{\partial t}\left\{\iiint_{R_t}\frac{1}{2}\overline{u_i u_i}\,dV+\iint_{S_F}\frac{1}{2}\overline{\zeta^2}\,dS\right\}=-\iint_{\tilde{S}+\tilde{S}_M}\overline{pu_i}\,n_i\,dS+O(\varepsilon^2)\,. \tag{9.3.13}$$

It may be verified that Eqs. (9.3.9)–(9.3.12) are totally consistent with Eq. (9.3.13). Upon using Eq. (9.3.10), we can also write Eq. (9.3.13) as

$$\frac{\partial}{\partial t}\left\{\iiint_{R}\frac{1}{2}\overline{u_i u_i}\,dV+\iint_{S_F}\frac{1}{2}\overline{\zeta^2}\,dS\right\}=-\iint_{\tilde{S}}\overline{pu_i}\,n_i\,dS-\iint_{\tilde{S}_{MW}}\overline{pw}\,dS\,, \tag{9.3.14}$$

where R is the average volume of the entire fluid.

9.3.5 The Damping Rate

A general formula for the damping rate can now be easily derived. As a slight modification of Eq. (1.5.10), Chapter One, we can show that

$$\begin{aligned} a_l a_m &= \frac{1}{2}\,\mathrm{Re}\,(A_l^* A_m)[\exp(2\omega^{(i)}t)](1+O(\varepsilon)) \\ &= \frac{1}{2}\,\mathrm{Im}\,(iA_l^* A_m)[\exp(2\omega^{(i)}t)](1+O(\varepsilon))\,, \end{aligned} \tag{9.3.15}$$

if

$$a_l(t)=\mathrm{Re}\,A_l\exp(-i(\omega^{(r)}+i\omega^{(i)})t)\,, \tag{9.3.16}$$

with $\omega^{(i)}=O(\varepsilon)\omega^{(r)}$. For the left-hand side of Eq. (9.3.14), the kinetic and potential energies may be calculated by the potential theory (Appendix 9.A) and are equal to each other. On the right-hand side the following formulas are true to the leading order:

$$\begin{aligned} [p]_{\tilde{S}} &= -\left[\frac{\partial\phi}{\partial t}\right]_{\tilde{S}} = i\omega_0[\phi_0]_S e^{-i\omega t}+O(\varepsilon)\,, \\ [p]_{\tilde{S}_{MW}} &= i\omega_0[\phi_0]_{\tilde{S},z=0}e^{-i\omega t}+O(\varepsilon)\,, \\ [\mathbf{u}_i n_i]_{\tilde{S}} &= -[\mathbf{n}\cdot\mathbf{U}]_S e^{-i\omega t}+O(\varepsilon^2)\,, \end{aligned} \tag{9.3.17}$$

where $(\phi)_0$ refers to the inviscid leading-order approximation, while $\{\mathbf{n}\cdot\mathbf{U}\}_S$ is the viscous correction of the normal velocity in the boundary layer, which will be explained more explicitly in Section 9.4. The term pw is of the order

$O(\varepsilon)$ and can be obtained from continuity after the tangential velocity is found.

Upon substituting Eq. (9.3.17) into Eq. (9.3.14), we obtain

$$2\omega^{(i)} \iiint_R |\nabla\phi_0|^2 \, dV$$
$$= \mathrm{Im}\left\{ i \left[\iint_S (i\omega_0\phi_0)^* (\mathbf{n}\cdot\mathbf{U})_S \, dS - \frac{1}{\varepsilon} \iint_{S_{MW}} (i\omega_0\phi_0)^*_S W \, dS \right] \right\},$$

which gives the dimensionless damping rate:

$$\frac{\omega^{(i)}}{\omega_0} = \frac{\mathrm{Im}\left\{ \iint_S \phi_0^* [\mathbf{n}\cdot\mathbf{U}]_S \, dS + \frac{1}{\varepsilon} \iint_{S_{MW}} \phi_0^* W \, dS \right\}}{2 \iiint_R |\nabla\phi_0|^2 \, dV} . \tag{9.3.18}$$

For a specific problem, the explicit value of the damping rate can be calculated from the potential solution and from the viscous correction in the boundary layers, both to the leading order.

Alternatively, one may start from Eq. (9.3.9) and obtain another formula for the damping rate. By the use of Eqs. (9.3.10), (9.3.11), and (9.3.12) the equivalence of the two formulas may be shown. It should be stressed that the meniscus term over S_{MW}, which is easily overlooked in intuitive reasoning, plays a crucial role.

9.4 Damping Rate by a Perturbation Analysis

In this section a more formal way of deducing Eq. (9.3.18) by a perturbation analysis is presented. The idea is to incorporate the slow rate of decay into a multiple-scale scheme and to make boundary-layer corrections iteratively (Johns, 1968; Dore, 1969; Greenspan, 1968; Mei and Liu, 1973). Let us first write the governing equations in Section 9.1 in terms of the dimensionless variables of Eq. (9.3.6):

$$\mathbf{u} = \nabla\Phi + \mathbf{U} , \tag{9.4.1}$$

$$\nabla^2\Phi = 0 , \tag{9.4.2}$$

$$\nabla\cdot\mathbf{U} = 0 , \tag{9.4.3}$$

$$\frac{\partial\mathbf{U}}{\partial t} = \varepsilon^2\nabla^2\mathbf{U} , \tag{9.4.4}$$

$$p = -\Phi_t . \tag{9.4.5}$$

The dimensionless boundary conditions are

$$\nabla\Phi + \mathbf{U} = 0\,, \quad \text{on} \quad S \equiv S_B + S_W \text{ (solid surface)}\,, \tag{9.4.6}$$

$$\frac{\partial\zeta}{\partial t} = W\frac{\partial\Phi}{\partial z}\,, \tag{9.4.7}$$

$$\left.\begin{aligned} &\Phi_t + \zeta + 2\varepsilon\frac{\partial w}{\partial z} = 0\,, && (9.4.8)\\ &\varepsilon^2\left(\frac{\partial u}{\partial z} + \frac{\partial w}{\partial x}\right) = \varepsilon^2\left(\frac{\partial v}{\partial z} + \frac{\partial z}{\partial y}\right) = 0\,, && (9.4.9)\end{aligned}\right\} \text{ on } \quad z = 0\,,$$

where the small parameter ε is defined by Eq. (9.3.7). Combining Eqs. (9.4.7)–(9.4.9), we have

$$\frac{\partial^2\Phi}{\partial t^2} + \frac{\partial\Phi}{\partial z} + W + 2\varepsilon^2\frac{\partial^2 w}{\partial t\partial z} = 0\,, \quad z = 0\,. \tag{9.4.10}$$

The tangential stress conditions are

$$\begin{aligned} &\varepsilon^2\left(2\frac{\partial^2\Phi}{\partial x\partial z} + \frac{\partial W}{\partial x}\right) + \varepsilon^2\frac{\partial U}{\partial z} = 0\,,\\ &\varepsilon^2\left(2\frac{\partial^2\Phi}{\partial y\partial z} + \frac{\partial W}{\partial y}\right) + \varepsilon^2\frac{\partial V}{\partial z} = 0\,. \end{aligned} \tag{9.4.11}$$

Equation (9.4.11) suggests that $\partial U/\partial z$, $\partial V/\partial z$ can be of the order $O(1)$. However, U and V vanish outside the boundary layer and they can grow at most to be $O(\varepsilon)$ inside. From continuity, we must have $\partial W/\partial z = O(\varepsilon)$. Thus, the last term in Eq. (9.4.10) is of the order $O(\varepsilon^2)$ and can be neglected. Consequently, we have

$$\frac{\partial^2\Phi}{\partial t^2} + \frac{\partial\Phi}{\partial z} + W = O(\varepsilon^2) \quad z = 0\,. \tag{9.4.12}$$

Since W is of the same order as the other terms only in a thin strip of the meniscus boundary layer and much less elsewhere, its global effect can only be felt at the order $O(\varepsilon)$.

Expecting that the rotational part $\mathbf{U}$ varies rapidly within the dimensionless distance $O(\varepsilon)$, we introduce a boundary-layer coordinate

$$\xi = \frac{x_N}{\varepsilon} \quad \text{so that} \quad \mathbf{U} = \mathbf{U}(\mathbf{x}_T, \xi)\,, \tag{9.4.13}$$

where $\mathbf{x}_T$, x_N form a locally rectangular coordinate system with x_N being in the normal direction pointing *into* the fluid from the wall, hence, opposite to $\mathbf{n}$, as shown in Fig. 9.4.

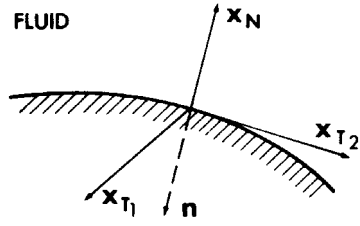

Figure 9.4: Local coordinate system.

If the dimensional radius of curvature of the wall is comparable to $1/k$, then $\partial/\partial x_T = O(\varepsilon\partial/\partial x_N)$. The continuity equation in terms of the local coordinate is

$$-\frac{\partial \mathbf{n}\cdot\mathbf{U}}{\partial x_N} + \frac{\partial U_{T_1}}{\partial x_{T_1}} + \frac{\partial U_{T_2}}{\partial x_{T_2}} = 0\,, \tag{9.4.14}$$

so,

$$-\frac{\partial \mathbf{n}\cdot\mathbf{U}}{\partial \xi} + \varepsilon\left(\frac{\partial U_{T_1}}{\partial x_{T_1}} + \frac{\partial U_{T_2}}{\partial x_{T_2}}\right) = 0\,. \tag{9.4.15}$$

We now introduce perturbation expansions. Since there is a damping time scale of the order $O(T/\varepsilon)$ in addition to the wave period T, it is natural to employ the multiple-scale expansions with t and εt as independent variables. Equivalently, we may expand the dimensionless ω in powers of ε. Thus,

$$\Phi = [\phi_0(\mathbf{x}) + \varepsilon\phi_1(\mathbf{x}) + O(\varepsilon^2)]e^{-i\omega t}\,, \tag{9.4.16a}$$

$$\mathbf{U} = [\mathbf{q}_0(\mathbf{x}_T,\xi) + \varepsilon\mathbf{q}_1(\mathbf{x}_T,\xi) + O(\varepsilon^2)]e^{-i\omega t}\,, \tag{9.4.16b}$$

$$\omega = \omega_0 + \varepsilon\omega_1 + O(\varepsilon^2)\,. \tag{9.4.16c}$$

When Eq. (9.4.16) is substituted into Eqs. (9.4.2)–(9.4.10) and the orders are separated, a sequence of problems is obtained.

(i) Inviscid solutioon at $O(\varepsilon^0)$:

$$\nabla^2\phi_0 = 0\,, \tag{9.4.17a}$$

$$\mathbf{n}\cdot\nabla\phi_0 = 0 \quad \text{on} \quad S\,, \tag{9.4.17b}$$

$$\frac{\partial\phi_0}{\partial z} - \omega_0^2\phi_0 = 0 \quad \text{on} \quad S_F\,, \quad z = 0\,. \tag{9.4.17c}$$

Note that W is not present at this order because of its small area of effectiveness. This solution gives rise to a nonzero tangential velocity on S.

(ii) Boundary-layer correction of $O(\varepsilon^0)$:

$$\frac{\partial^2 \mathbf{q}_0}{\partial \xi^2} = -i\omega_0 \mathbf{q}_0 \,, \tag{9.4.18a}$$

$$\mathbf{q}_0 = -\nabla \phi_0 \,, \quad \text{on} \quad S \,, \tag{9.4.18b}$$

$$\mathbf{q}_0 \to 0 \quad \xi \to \infty \,. \tag{9.4.18c}$$

Note that $\mathbf{q}_0$ is tangential to the wall S, that is, $\mathbf{n} \cdot \mathbf{q}_0 = 0$. The continuity equation gives

$$-\frac{\partial}{\partial \xi}(\mathbf{n} \cdot \mathbf{q}_1) + \left(\frac{\partial U_{T_1}}{\partial x_{T_1}} + \frac{\partial U_{T_2}}{\partial x_{T_2}} \right) = 0 \tag{9.4.19}$$

from which $\mathbf{n} \cdot \mathbf{q}_1$ may be integrated from $\xi \sim \infty$ (outside the boundary layer) inward to ξ, subject to the condition that $\mathbf{n} \cdot \mathbf{q}_1 = 0$ at $\xi \sim \infty$. In general, $(\mathbf{n} \cdot \mathbf{q}_1)$ is nonzero at the wall S ($\xi = 0$) and must be cancelled by $\partial \phi_1 / \partial x_N$ at the order $O(\varepsilon)$.

(iii) Inviscid correction of $O(\varepsilon)$:

$$\nabla^2 \phi_1 = 0 \,, \tag{9.4.20a}$$

$$\mathbf{n} \cdot \nabla \phi_1 = -[\mathbf{n} \cdot \mathbf{q}_1]_S \quad \text{on} \quad S \,, \tag{9.4.20b}$$

$$\frac{\partial \phi_1}{\partial z} - \omega_0^2 \phi_1 = 2\omega_0 \omega_1 \phi_0 - \frac{W_0}{\varepsilon} \quad \text{on} \quad S_F \,. \tag{9.4.20c}$$

Note that W_0/ε is effective only over an area of $O(\varepsilon)$.

Problem (i) is homogeneous and is an eigenvalue problem. The eigenfrequency ω_0 and the eigenfunction $\phi_0(x)$ can be found in principle.

Now Problem (ii) is the classical Stokes' problem of a plate oscillating in its own plane; the solution is similar to Eqs. (9.2.19)–(9.2.21). In the present dimensionless variables, the solution is

$$\mathbf{q}_0 = -[\nabla \phi_0]_S \Gamma(\xi) \,, \quad \Gamma(\xi) = \exp[1 - (1-i)(\omega_0/2)^{1/2} \xi] \tag{9.4.21}$$

which can be used to obtain $\mathbf{n} \cdot \mathbf{q}_1$ by integrating Eq. (9.4.19). Now Problem (iii) for ϕ_1 contains the unknown ω_1 which we are seeking. The homogeneous boundary-value problem is identical to that of ϕ_0 which has nontrivial solutions. By invoking the Fredholm alternative, that is, applying Green's formula to ϕ_0^* and ϕ_1

$$\iiint_R (\phi_0^* \nabla^2 \phi_1 - \phi_1 \nabla^2 \phi_0^*)\, dV = \iint_{S+S_F} \left(\phi_0^* \frac{\partial \phi_1}{\partial n} - \phi_1 \frac{\partial \phi_0^*}{\partial n} \right) dS\,,$$

and by using all boundary conditions on ϕ_0^* and ϕ_1, we obtain ω_1 immediately:

$$\omega_1 = \frac{\iint_S \phi_0^* [\mathbf{n} \cdot \mathbf{q}_1]_S \, dS + \iint_{S_F} \phi_0^* W_0 \, dS/\varepsilon}{2\omega_0 \iint_{S_F} |\phi_0|^2 \, dS}\,. \tag{9.4.22}$$

An alternative form of Eq. (9.4.22) may be derived by noting that

$$\nabla \cdot (\phi_0^* \nabla \phi_0) = |\nabla \phi|^2 + \phi_0^* \nabla^2 \phi_0 = |\nabla \phi_0|^2\,.$$

Integrating the preceding equation over the entire volume R and using Gauss' theorem, we obtain

$$\begin{aligned} \iiint_R |\nabla \phi_0|^2 \, dV &= \iint_{S+S_F} \phi_0^* \frac{\partial \phi_0}{\partial n} \, dS \\ &= \iint_{S_F} \phi_0^* \frac{\partial \phi_0}{\partial z} \, dS + \iint_S \phi_0^* \frac{\partial \phi_0}{\partial n} \, dS\,. \end{aligned}$$

From the boundary conditions on S_F and S, it follows that

$$\iiint_R |\nabla \phi_0|^2 \, dV = \omega_0^2 \iint_{S_F} |\phi_0|^2 \, dS\,. \tag{9.4.23}$$

Since $W_0 = 0$ except in S_{MW}, Eq. (9.4.22) becomes

$$\frac{\omega_1}{\omega_0} = \frac{1}{2} \frac{\iint_S \phi_0^* [\mathbf{n} \cdot \mathbf{q}_1]_S \, dS + \iint_{S_{MW}} (\phi_0^* W_0 \, dS/\varepsilon)}{\iiint_R |\nabla \phi_0|^2 \, dV}\,. \tag{9.4.24}$$

Finally we have, in *physical variables*, $\omega = \omega_0 + \omega_1$ and

$$\frac{\omega_1}{\omega_0} = \frac{\iint_S \phi_0^* [\mathbf{n} \cdot \mathbf{q}_1]_S \, dS + \iint_{S_{MW}} \phi_0^* W_0 \, dS}{2 \iiint_R |\nabla \phi_0|^2 \, dV}\,. \tag{9.4.25}$$

In particular, the imaginary part of Eq. (9.4.24) is precisely Eq. (9.3.18).

The perturbation analysis gives as a bonus the real part of ω_1 which represents a shift of the eigenfrequency due to viscosity.

The case of progressive waves in an infinitely long channel of uniform cross section (see Fig. 9.5) can be worked out in a manner similar to that for standing waves. If the progressive waves are strictly sinusoidal in time as in the case of a laboratory wave flume, we should expect them to attenuate in the direction of propagation. The spatial rate of attenuation can be derived

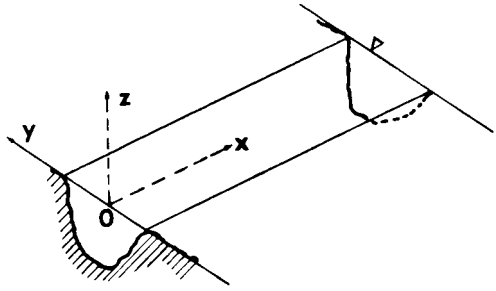

Figure 9.5

for arbitrary cross section by following the steps suggested in the next exercise.

Exercise 9.1: Boundary-Layer Effect on Progressive Waves in a Uniform Channel

Rewrite the linearized governing equations in terms of the following dimensionless variables

$$\begin{aligned}(x, y, z) &= \left(\frac{\omega^2}{g}\right)(x', y', z'), \quad t = \omega t', \\ u &= \frac{u'}{\omega A}, \quad \phi = \phi'\left(\frac{\omega}{gA}\right), \quad \zeta = \frac{\zeta'}{A}.\end{aligned} \tag{9.4.26}$$

Define the small parameter

$$\varepsilon = \frac{\omega^2}{g}\left(\frac{\nu}{\omega}\right)^{1/2}, \tag{9.4.27}$$

and assume the expansions

$$\Phi(x, y, z, t) = [\phi_0(y, z) + \varepsilon\phi_1(y, z) + \cdots]e^{i(kx-t)}, \tag{9.4.28a}$$

$$\mathbf{U} = [\mathbf{q}_0(\mathbf{x}_T, \xi) + \varepsilon\mathbf{q}_1(\mathbf{x}_T, \xi) + \cdots]e^{i(kx-t)}, \tag{9.4.28b}$$

$$k = k_0 + \varepsilon k_1 + \cdots, \tag{9.4.28c}$$

then show that

$$k_1 = \frac{-\iint_S \phi_0^*[\mathbf{n}\cdot\mathbf{q}_1]_S\, dS + \iint_{S_{MW}} \phi_0^* W_0\, dS/\varepsilon}{2k_0 \iiint_R |\phi_0|^2\, dV}, \tag{9.4.29}$$

where the numerator involves line integrals and the denominator is an area integral. Here S is the wetted wall contour, S_F is the contour of the free surface, and R is the total water area of a cross section of the channel.

9.5 Details for Standing Waves in a Circular Basin

Consider a circular basin of radius a' and depth h', and choose a polar-coordinate system with the origin at the center of the free surface. The first-order potential solution for a typical mode (m, n) with $m, n = 1, 2, 3, \ldots$, is, in physical variables,

$$\phi'(r', \theta, z') = \frac{-iA\omega_0'}{k'} \frac{\cosh k'(z' + h')}{\sinh k'h'} J_n(k'r') \sin n\theta \,, \tag{9.5.1}$$

where $k' = k'_{mn}$ is the mth root, $m = 1, 2, 3, \ldots$, of

$$J_n'(k'a') \equiv \frac{d}{dk'a'} J_n(k'a') = 0 \,, \tag{9.5.2}$$

and

$$\omega_0'^2 = gk' \tanh k'h' \,. \tag{9.5.3}$$

For nondimensionalization it is convenient to use $k' = k'_{mn}$ as the scaling wavenumber so that in dimensionless variables Eqs. (9.5.1)–(9.5.3) become

$$\phi_0 = -i\omega_0 \frac{\cosh(z + h)}{\sinh h} J_n(r) \sin n\theta \,, \tag{9.5.4}$$

$$J_n'(a) = 0 \,, \tag{9.5.5}$$

$$\omega_0 = \tanh h \,, \tag{9.5.6}$$

where

$$a = k'_{mn}a' \,, \quad h = k'_{mn}h' \,, \quad \text{and} \quad \omega_0 = \frac{\omega_0'}{(gk'_{mn})^{1/2}} \,. \tag{9.5.7}$$

Let U, V, and W denote the dimensionless components of the rotational velocity in the r, θ, and z directions, respectively. Divide the boundary layer into two parts, that is, the side wall and the bottom layer, designated by the subscripts W and B, and let the boundary-layer coordinates be

$$\xi_W = \frac{a - r}{\varepsilon} \quad \text{and} \quad \xi_B = \frac{z + h}{\varepsilon} \,. \tag{9.5.8}$$

The first-order boundary layer solutions are

$$U_{0W} = 0\,, \tag{9.5.9a}$$

$$V_{0W} = -\left(\frac{1}{r}\frac{\partial\phi_0}{\partial\theta}\right)_{r=a}\Gamma(\xi_W)$$

$$= i\omega_0\frac{n}{a}J_n(a)\frac{\cosh(z+h)}{\sinh h}\cosh n\theta\Gamma(\xi_W)\,, \tag{9.5.9b}$$

$$W_{0W} = -\left(\frac{\partial\phi_0}{\partial z}\right)_{r=a}\Gamma(\xi_W)$$

$$= i\omega_0 J_n(a)\frac{\sinh(z+h)}{\sinh h}\sin n\theta\Gamma(\xi_W) \tag{9.5.9c}$$

near the side wall, and

$$U_{0B} = -\left(\frac{\partial\phi_0}{\partial r}\right)_{z=-h}\Gamma(\xi_B)$$

$$= \frac{i\omega_0}{\sinh h}J_n'(r)\sin n\theta\Gamma(\xi_B)\,, \tag{9.5.10a}$$

$$V_{0B} = -\left(\frac{1}{r}\frac{\partial\phi_0}{\partial\theta}\right)_{z=-h}\Gamma(\xi_B)$$

$$= \frac{i\omega_0}{\sinh h}\frac{n}{r}J_n(r)\cos n\theta\Gamma(\xi_B)\,, \tag{9.5.10b}$$

$$W_{0B} = 0 \tag{9.5.10c}$$

near the bottom, with $\Gamma(\xi)$ being Stokes' solution as defined in Eq. (9.4.21). The induced velocity normal to the side-wall boundary layer is obtained by integrating the continuity equation (in polar coordinates)

$$[\mathbf{n}\cdot\mathbf{q}_1]_{S_W} = U_{1W} = \int_\infty^{\xi_W}\left(\frac{1}{a}\frac{\partial V_{0W}}{\partial\theta} + \frac{\partial W_{0W}}{\partial z}\right)d\xi_W$$

$$= -(1-i)\left(\frac{\omega_0}{2}\right)^{1/2}\left(\frac{n^2}{a^2}-1\right)\frac{\cosh(z+h)}{\sinh h}\sin n\theta J_n(a)\Gamma(\xi_W)\,, \tag{9.5.11}$$

where use is made of the fact that

$$-i\omega_0\int_\infty^\xi\Gamma(\xi)\,d\xi = -1(1-i)\left(\frac{\omega_0}{2}\right)^{1/2}\Gamma(\xi)\,.$$

Similarly, the normal velocity in the bottom boundary layer is

$$
\begin{aligned}
[\mathbf{n}\cdot\mathbf{q}_1]_{S_B} = W_{1B} &= \int_\infty^{\xi_B}\left(\frac{\partial U_{0B}}{\partial r}+\frac{U_{0B}}{r}+\frac{1}{r}\frac{\partial V_{0B}}{\partial\theta}\right)d\xi_B \\
&= \frac{i\omega_0}{\sinh h}\sin n\theta\left(J_n''+\frac{J_n'}{r}-\frac{n^2}{r^2}\right)\int_\infty^{\xi_B}\Gamma(\xi_B)\,d\xi_B \\
&= -(1-i)\left(\frac{\omega_0}{2}\right)^{1/2}\frac{\sinh n\theta}{\sinh h}J_n(r)\Gamma(\xi_B)\,. \qquad (9.5.12)
\end{aligned}
$$

Now the S integral in Eq. (9.4.22) or (9.4.23) is composed of two parts

$$
\begin{aligned}
&\iint_S \phi_0^*[\mathbf{n}\cdot\mathbf{q}_1]\,dS \\
&= \iint_{S_W}\phi_0^*[\mathbf{n}\cdot\mathbf{q}_1]\,dS+\iint_{S_B}\phi_0^*[\mathbf{n}\cdot\mathbf{q}_1]\,dS \\
&= \int_{-h}^0 dz\int_0^{2\pi}\left[i\omega_0\frac{\cosh(z+h)}{\sinh h}J_n(a)\sin n\theta\right] \\
&\quad\times\left[-(1-i)\left(\frac{\omega_0}{2}\right)^{1/2}\left(\frac{n^2}{a^2}-1\right)\frac{\cosh(z+h)}{\sinh h}J_n(a)\sin n\theta\right]a\,d\theta \\
&= \int_0^{2\pi}d\theta\int_0^a\left[i\omega_0 J_n(r)\frac{\sin n\theta}{\sinh h}\right]\left[-(1-i)\left(\frac{\omega_0}{2}\right)^{1/2}J_n(r)\frac{\sin n\theta}{\sinh h}\right]r\,d\theta\,. \qquad (9.5.13)
\end{aligned}
$$

If the orthogonality property

$$
\int_0^a rJ_n^2(r)\,dr=\frac{1}{2}(a^2-n^2)J_n^2(a)\quad\text{if}\quad J_n'(a)=0 \qquad (9.5.14)
$$

is used, Eq. (9.5.13) becomes

$$
\begin{aligned}
\iint_S\phi_0^*[\mathbf{n}\cdot\mathbf{q}]\,dS &= -(1+i)\omega_0\left(\frac{\omega_0}{2}\right)^{1/2}\left(\frac{n^2}{a^2}-1\right)\frac{aJ_n^2(a)}{\sinh^2 h}\frac{\pi}{4}(\sin 2h+2h) \\
&\quad-(1+i)\omega_0\left(\frac{\omega_0}{2}\right)^{1/2}\frac{a^2-n^2}{2}\frac{\pi J_n^2(a)}{\sinh^2 h} \\
&= -(1+i)\omega_0\left(\frac{\omega_0}{2}\right)^{1/2}\frac{\pi}{4}\frac{J_n^2(a)}{\sinh^2 h}(a^2-n^2) \\
&\quad\times\left[2-\frac{1}{a}(\sinh 2h+2h)\right]. \qquad (9.5.15)
\end{aligned}
$$

From Eqs. (9.5.4) and (9.5.9c) the second integral in Eq. (9.4.22) along the free surface is

$$\iint_{S_{MW}} \phi_0^* W_0 \frac{dS}{\varepsilon} = -\int_0^{2\pi} a\, d\theta \int_0^{\infty} d\xi_W \left[i\omega_0 \frac{\cosh h}{\sinh h} J_n(a) \sin n\theta \right] \cdot [-i\omega_0 J_n(a) \sin n\theta] \Gamma(\xi_W)$$

$$= \pi a J_n^2(a) \frac{1+i}{2(\frac{1}{2}\omega_0)^{1/2}}\,, \tag{9.5.16}$$

where the dispersion relation has been applied.

Finally, the denominator of Eq. (9.4.22) is

$$\iint_{S_F} |\phi_0|^2\, dS = \int_0^{2\pi} d\theta \int_0^a \omega_0^2 \frac{\cosh^2 h}{\sinh^2 h} \sin^2 n\theta r J_n^2(r)\, dr$$

$$= \frac{\pi}{\omega_0^2} \frac{1}{2} (a^2 - n^2) J_n^2(a)\,. \tag{9.5.17}$$

When Eqs. (9.5.15)–(9.5.17) are substituted into Eq. (9.4.22), the dimensionless frequency correction ω_1 is obtained:

$$\omega_1 = -(1+i) \left(\frac{\omega_0}{2} \right)^{1/2} \left[\frac{a^2 + n^2}{2a(a^2 - n^2)} + \left(1 - \frac{h}{a} \right) \frac{1}{\sinh\, 2h} \right] \tag{9.5.18}$$

where the dispersion relation is again applied.

Returning to dimensional variables, we now have

$$\omega = \omega_0 \left\{ 1 - k'\delta \frac{1+i}{2} \left[\frac{(k'a')^2 + n^2}{2k'a'((k'a')^2 - n^2)} + \left(1 - \frac{h'}{a'} \right) \frac{1}{\sinh 2kh'} \right] \right\} \tag{9.5.19}$$

where $\delta = (2\nu/\omega_0)^{1/2}$ is the boundary-layer thickness and ω_0 and k' are the eigenfrequency and the eigen wavenumber, respectively, of a specific mode (m, n). The imaginary part which gives the damping rate was first derived by Case and Parkinson (1957) by using Eq. (9.3.9). If $k'h'$ is large, the second term in Eq. (9.5.19) becomes insignificant. On the other hand, for a shallow basin where $k'h'$ and h'/a' are small, the bottom boundary layer becomes dominant.

It is interesting to examine the energy details for a side-wall boundary layer, using the explicit solution to check Eq. (9.3.11).

The average work done by the pressure on the strip of surface S_{MW} is, omitting the factor $\exp[-2\omega^{(i)}t]$,

$$\begin{aligned}
&\mathrm{Re}\int_0^{2\pi} a\,d\theta \int_0^{\infty} [p_0^*]_{z=0,r=a}[w_z]_{z=0}\,d\xi_W \\
&\quad = \mathrm{Re}\,a\int_0^{2\pi} d\theta[-\omega_0\phi_0^*]_{z=0,r=a}\int_0^{\infty}[W_{0W}]_{z=0}\,d\xi_W \\
&\quad = -\pi a\left(\frac{\omega_0}{2}\right)^{1/2} J_n^2(a)\,. \qquad (9.5.20)
\end{aligned}$$

The dynamic pressure and the potential part of the velocity are out of phase to the present order of approximation. The work done by the pressure on the interface between the inviscid interior and the side-wall layer is

$$\begin{aligned}
&\mathrm{Re}\int_h^0 dz\int_0^{2\pi} a\left[p_0^*\left(-\frac{\partial\phi_1}{\partial r}\right)\right]_{r=a} d\theta \\
&\quad = \mathrm{Re}\int_{-h}^0 dz\int_0^{2\pi} a[-i\omega_0\phi_0^* U_{1W}]_{r=a}\,d\theta \\
&\quad = -\frac{\pi a}{2}\left(\frac{\omega_0}{2}\right)^{1/2}\left(1+\frac{2h}{\sinh 2h}\right)\left(\frac{n^2}{a^2}-1\right)J_n^2(a)\,. \qquad (9.5.21)
\end{aligned}$$

Note that the outward normal points toward the z axis. Finally, the average rate of viscous dissipation in the side-wall layer is

$$\begin{aligned}
&\mathrm{Re}\int_{-h}^0 dz\int_0^{2\pi} a\,d\theta\int_0^{\infty}\left(\left|\frac{\partial V_{0W}}{\partial\zeta_W}\right|^2+\left|\frac{\partial W_{0W}}{\partial\zeta_W}\right|^2\right)d\xi_W \\
&\quad = \pi a\left(\frac{\omega_0}{2}\right)^{1/2} J_n^2(a)\left[\frac{1}{2}\left(\frac{n^2}{a^2}-1\right)\left(1+\frac{2h}{\sinh 2h}\right)+1\right]. \qquad (9.5.22)
\end{aligned}$$

The three energy terms in Eq. (9.3.11) add up precisely to zero, as estimated by Eq. (9.3.10).

Note from Eq. (9.5.14) that $n^2 < a^2 = (k'_{mn}a')^2$ for all modes. We conclude from Eq. (9.5.21) that the side-wall layer *receives* power from waves through the meniscus boundary layer above, spends only a part of it on internal dissipation, and gives up the rest to the inviscid interior!

A similar calculation for the bottom layer confirms Eq. (9.3.12) with no surprises.

Other interesting examples are left as exercises.

Exercise 9.2

Deduce for a progressive wave advancing down a uniform rectangular channel, that

$$k_1 = \frac{1+i}{2^{1/2}} \frac{k_0}{b} \left(\frac{2k_0 b + \sinh 2k_0 h}{2k_0 h + \sinh 2k_0 h} \right) \tag{9.5.23}$$

(Hunt, 1952) where $2b$ is the dimensionless width, h is the dimensionless depth, and $k_0 \tanh k_0 h = 1$. Discuss separately the energy balance in the boundary layers near the side wall and near the bottom.

Exercise 9.3

Get the frequency correction due to viscosity for the standing wave in a rectangular basin

$$\phi_0 = \frac{-i\omega_0}{\sinh h} \cosh(z+h) \cos \frac{n\pi x}{a} \cos \frac{m\pi y}{b} . \tag{9.5.24}$$

The physical wavenumber used for normalization is

$$k_{mn}^2 = \left(\frac{n\pi}{a'} \right)^2 + \left(\frac{m\pi}{b'} \right)^2 . \tag{9.5.25}$$

Show that

$$\omega_1 = -(1+i) \left(\frac{\omega_0}{2} \right)^{1/2} \left\{ \frac{1}{a} \left[2 - \left(\frac{n\pi}{a} \right)^2 \right] + \frac{1}{b} \left[2 - \left(\frac{m\pi}{b} \right)^2 \right] \right.$$
$$\left. + \frac{1}{\sinh 2h} \left[1 - 2\frac{h}{a} \left(\frac{n\pi}{a} \right)^2 - 2\frac{h}{b} \left(\frac{m\pi}{b} \right)^2 \right] \right\} \tag{9.5.26}$$

(Keulegan, 1959). Discuss separately the energy balance in the boundary layers near the side wall and near the bottom.

9.6 The Effect of Air on the Damping of Deep Water Waves

An additional factor, which has not received much attention until recently (Dore, 1978), is the presence of air above the water surface. Despite its relatively small density and viscosity, air, which must be moved by the waves, can contribute as much dissipation as water if the water depth is great and the side-wall effects are negligible.

The physical argument, due to Dore, is as follows. Let the physical properties of air be distinguished by primes. In deep water waves the rate of dissipation in water is of the order $O(\mu U^2/\lambda)$, where U is the typical orbital velocity in the waves. On the free surface, the tangential motion of the water particles induces a Stokes boundary layer in air. Because of the much smaller density of air, the motion of water particles near the free surface is hardly affected and the free-surface boundary layer in water remains ineffective. The rate of dissipation in the air boundary layer, whose thickness is $\delta' = (2\nu'/\omega)^{1/2}$, is of the order $O(\mu' U'^2/\delta')$. The ratio of the two dissipation rates is

$$O\left(\frac{\mu'\lambda}{\mu\delta'}\right). \tag{9.6.1a}$$

Although $\mu'/\mu \ll 1$, λ/δ' is much greater than unity for sufficiently long waves so that the ratio (9.6.1a) can be of order unity. Using definitions and the dispersion relation $\omega^2 = gk$, we may rewrite ratio (9.6.1a)

$$\frac{\mu'}{\mu}\left(\frac{\rho'}{\mu'}\right)^{1/2}\left(\frac{g}{\lambda}\right)^4 \lambda\,. \tag{9.6.1b}$$

Since the following values are representative

water	air
$\mu = 1.3 \times 10^{-2}$ g/cm − s	$\mu' = 1.76 \times 10^{-4}$ g/cm − s
$\rho = 1$ g/cm^3	$\rho' = 1.25 \times 10^{-3}$ g/cm^3

the ratio (9.6.1b) is small only if λ is much less than 10 cm. Thus, in a natural environment where the range of interest is $\lambda > 10$ cm, air cannot be ignored.

If one only wishes to find the damping rate, the simplest procedure is to start from the potential-theory result for water and calculate the boundary layer in the air to ensure that there is no slip between air and water. The rate of dissipation within this boundary layer may be added to that within the main body of water to give the total damping rate. This approach was used by Dore. However, we sketch below a perturbation analysis with a view to obtaining the damping rate as well as the real frequency shift. With two fluids the algebra is lengthy, but straightforward.

Defining $\varepsilon = k(\nu/\omega)^{1/2}$, $\varepsilon' = k(\nu'/\omega)^{1/2}$, we first note that $\mu'/\mu = 10^{-2} \ll 1$ and $\rho'/\rho = 10^{-3} \ll 1$, but that

$$\frac{\varepsilon'}{\varepsilon} = \left(\frac{\nu'}{\nu}\right)^{1/2} = \left(\frac{\mu'\rho}{\mu\rho'}\right)^{1/2} = O(1)\,.$$

Let us assume for the convenience of ordering that

$$\begin{gathered} O(\varepsilon) = O(\varepsilon') = O(\bar{\varepsilon})\,, \\ \alpha = \frac{\mu'}{\mu} = O(\bar{\varepsilon}) \quad \text{and} \quad \beta = \frac{\rho'}{\rho} = O(\bar{\varepsilon})\,. \end{gathered} \tag{9.6.2}$$

In terms of the normalized variables defined in Eq. (9.3.6), the linearized dimensionless equations are

$$\mathbf{u} = \nabla\Phi + \mathbf{U}\,, \quad \mathbf{u}' = \nabla\Phi' + \mathbf{U}'\,, \tag{9.6.3}$$

with

$$\nabla^2\Phi = 0\,, \qquad \nabla^2\Phi' = 0\,, \tag{9.6.4}$$

$$\frac{\partial\mathbf{U}}{\partial t} = \varepsilon\nabla^2\mathbf{U}\,, \qquad \frac{\partial\mathbf{U}'}{\partial t} = \varepsilon'^2\nabla^2\mathbf{U}\,, \tag{9.6.5}$$

$$\nabla\cdot\mathbf{U} = 0\,, \qquad \nabla\cdot\mathbf{U}' = 0\,. \tag{9.6.6}$$

The kinematic boundary conditions on the mean free surface $z = 0$ are

$$\frac{\partial\zeta}{\partial t} = W + \frac{\partial\Phi}{\partial z}\,, \tag{9.6.7a}$$

$$\frac{\partial\zeta}{\partial t} = W' + \frac{\partial\Phi'}{\partial z}\,, \tag{9.6.7b}$$

$$U = U'\,. \tag{9.6.8}$$

The dynamic stress conditions on the free surface are as follows:
normal:

$$\begin{aligned} &\frac{\partial\Phi}{\partial t} + \zeta + 2\varepsilon^2\left(\frac{\partial W}{\partial z} + \frac{\partial^2\Phi}{\partial z^2}\right) \\ &\qquad = \beta\left[\frac{\partial\Phi'}{\partial t} + \zeta + 2\varepsilon'^2\left(\frac{\partial W'}{\partial z} + \frac{\partial^2\Phi'}{\partial z^2}\right)\right], \end{aligned} \tag{9.6.9}$$

tangential:

$$2\frac{\partial^2\Phi}{\partial x\partial z} + \frac{\partial U}{\partial z} + \frac{\partial W}{\partial x} = \alpha\left(2\frac{\partial^2\Phi'}{\partial x\partial z} + \frac{\partial U'}{\partial z} + \frac{\partial W'}{\partial x}\right). \tag{9.6.10}$$

In addition, Φ, $\Phi' \to 0$ and $\mathbf{U}$, $\mathbf{U}' \to 0$, when $z \to -\infty$, ∞, respectively.

We now assume the following expansions:

$$\Phi = (\phi_0 + \bar{\varepsilon}\phi_1 + \bar{\varepsilon}^2\phi_2 + \cdots)e^{i\theta}\,, \tag{9.6.11}$$

$$U = (U_0 + \bar{\varepsilon}U_1 + \bar{\varepsilon}^2U_2 + \cdots)e^{i\theta}\,, \tag{9.6.12}$$

$$W = (\bar{\varepsilon}W_1 + \bar{\varepsilon}^2W_2 + \cdots)e^{i\theta}\,, \tag{9.6.13}$$

$$\zeta = (\zeta_0 + \bar{\varepsilon}\zeta_1 + \bar{\varepsilon}^2\zeta_2 + \cdots)e^{i\theta}\,, \tag{9.6.14}$$

and similar expansions for Φ', U', and W', with

$$\theta = x - \omega t\,, \tag{9.6.15}$$

$$\omega = \omega_0 + \bar{\varepsilon}\omega_1 + \bar{\varepsilon}^2\omega_2 + \cdots\,, \tag{9.6.16}$$

and

$$\phi_0 = \phi_n(x,z)\phi_n' = \phi_n'(x,z) \quad \text{and} \quad U_n = U_n\left(\frac{x,z}{\varepsilon}\right), \quad U_n' = U_n'\left(x, \frac{z}{\varepsilon'}\right). \tag{9.6.17}$$

The details of the perturbation analysis are very similar to those of Section 9.4. In the following chart we only indicate the procedure of obtaining ω_2:

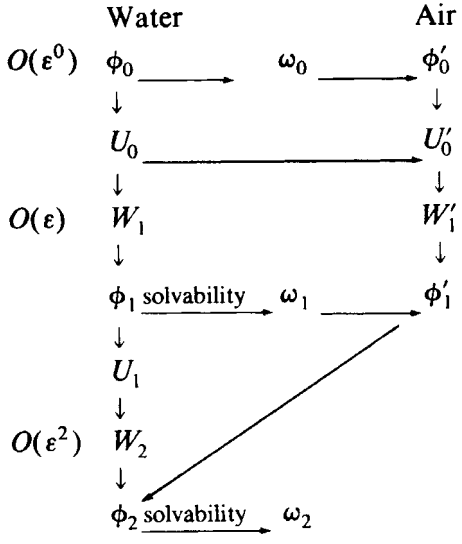

At each order, the potential parts ϕ_n and ϕ'_n are subject to the normal components of the kinematic and dynamic conditions, whereas the tangential components of the rotational velocity are subject to the tangential components of the same conditions. The vertical components W_n and W'_n follow from continuity. We leave it for the reader to verify that

$$\omega_0 = 1\,, \quad \bar{\varepsilon}\omega_1 = -\beta\,,$$

and

$$\begin{aligned}\bar{\varepsilon}^2\omega_2 &= \frac{1}{2}\left[\beta^2 - \frac{1}{\sqrt{2}}\left(\alpha\frac{\varepsilon^2}{\varepsilon'} + \beta\varepsilon'\right)\right] - i\left[2\varepsilon^2 + \frac{1}{\sqrt{2}}\left(\alpha\frac{\varepsilon^2}{\varepsilon'} + \beta\varepsilon'\right)\right] \\ &= \frac{1}{2}\left[\left(\frac{\rho'}{\rho}\right)^2 - \sqrt{2}\varepsilon\left(\frac{\mu'\rho'}{\mu\rho}\right)^{1/2}\right] - i\left[2\varepsilon^2 + \sqrt{2}\varepsilon\left(\frac{\mu'\rho'}{\mu\rho}\right)^{1/2}\right].\end{aligned} \tag{9.6.18}$$

The imaginary part of $\bar{\varepsilon}^2\omega_2$ gives the damping rate, as found by Dore. To have some numerical ideas, Dore has computed the time required for the wave amplitude to decrease by a factor of e^{-1}, for two examples:

Wavelength	Air–Water	Vacuum–Water
1 m	75.9 min	161.8 min
100 m	30.5 days	3.1 years .

The importance of air is evident. A more complete picture is seen in Fig. 9.6. The real part of the frequency change which shows the effect on the phase is

$$\mathrm{Re}\,(\bar{\varepsilon}\omega_1 + \bar{\varepsilon}^2\omega_2) = \frac{\rho'}{\rho} + \frac{1}{2}\left[\left(\frac{\rho'}{\rho}\right)^2 - \sqrt{2}\varepsilon\left(\frac{\mu'\rho'}{\mu\rho}\right)^{1/2}\right]. \tag{9.6.19}$$

In open seas, the coupling of air and water may involve a turbulent transfer of energy and momentum near the interface; this is an important part of the subject of wave generation by wind (Phillips, 1977). The intermittent breaking of large crests also contributes to the damping of random sea waves. However, these aspects are too complicated to be entered here.

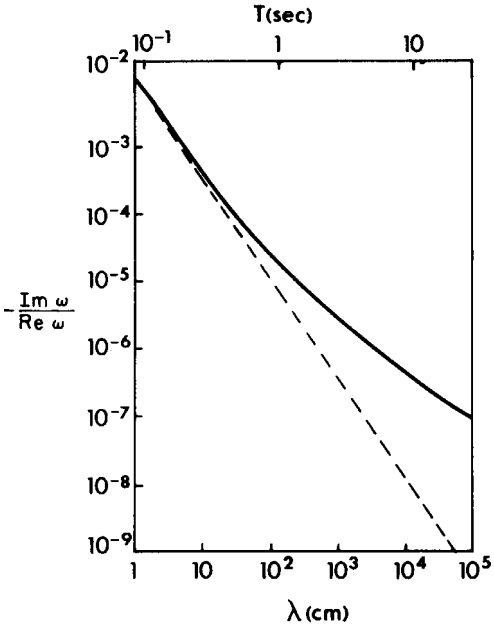

Figure 9.6: Viscous attenuation rates of surface waves in deep water with a clean surface. Solid curve: air–water interface; Dashed curve: vacuum–water interface (from Dore, 1978, *Geophys. Astrophys. Fluid Dyn.* Reproduced by permission of Gordon and Breach Scientific Publishers).

9.7 The Turbulent Boundary Layer Near a Rough Bottom

9.7.1 The Boundary-Layer Structure

When the wave amplitude becomes large, the laminar Stokes layer near a smooth wall can be unstable to infinitesimal disturbance and transition to turbulence is possible. According to Li (1954) who has conducted experiments with an oscillatory plate, the critical condition is $A_0/\delta = 280$, where A_0 is the orbital amplitude just outside the boundary layer. In nature the roughness at the sea bottom enhances turbulence. Jonsson (1966) has given the following empirical criteria for turbulence:

$$\mathsf{R_E} = \frac{\omega A_0^2}{\nu} > 1.26 \times 10^4 \quad \text{and} \quad \frac{A_0}{k_N} \geq \frac{4}{\pi}(2\mathsf{R_E})^{1/2}\,,$$

where $\mathsf{R_E}$ is the Reynolds number and k_N is the typical roughness height.[1] Assuming fully developed turbulence, Kajiura (1964) has proposed a semi-theoretical model. Specifically, an eddy viscosity ν_e is assumed to relate the stress to the velocity gradient within the bottom boundary layer, that is,

$$\frac{\tau_{xz}}{\rho} = \frac{\tau}{\rho} = \nu_e \frac{\partial u}{\partial z}\,, \tag{9.7.1}$$

where

$$\nu_e = \kappa |u_*| z\,. \tag{9.7.2}$$

The coefficient κ is the Kármán constant, which is approximately equal to 0.4 for steady boundary layers in clean water, while u_* is the friction velocity, which is formally related to the bottom stress τ^B by

$$\tau^B = \rho |u_*| u_*\,. \tag{9.7.3}$$

By definition, u_* depends on time also. When Eq. (9.7.1) is combined with the momentum equation

$$\frac{\partial u}{\partial t} = \frac{\partial U_I}{\partial t} + \frac{\partial}{\partial z}\left(\kappa |u_*| z \frac{\partial u}{\partial z}\right), \tag{9.7.4}$$

the mathematics of solving u becomes nonlinear. One simplification is to replace $|u_*|$ above by a representative constant. For example, Kajiura invokes the idea of equivalent linearization and introduces the constant $\tilde{u}_*$ such that

$$\tau^B = \rho \tilde{u}_* u_* \tag{9.7.5}$$

gives the same rate of dissipation as Eq. (9.7.3). Assuming u_* to be sinusoidal with amplitude $\hat{u}_*$, we can easily verify that

$$\tilde{u}_* = \frac{8}{3\pi} \hat{u}_*\,. \tag{9.7.6}$$

Alternatively, Grant (1977), and Grant and Madsen (1979) assume

$$\tau^B = \rho \bar{u}_* u_*\,, \tag{9.7.7}$$

where $\bar{u}_*$ is defined by the average bottom stress $\bar{\tau}^B$ according to

$$\bar{u}_* = \left(\frac{\bar{\tau}^B}{\rho}\right)^{1/2}. \tag{9.7.8}$$

[1] The subscript N is for Nikuradse whose experiments on roughness in steady turbulent flows are well known.

From Eq. (9.7.6) and the average of Eq. (9.7.3),

$$\bar{\tau}^B = \rho\overline{|u_*|u_*} = \frac{1}{2}\rho\hat{u}_*^2 = \frac{1}{2}\hat{\tau}^B\,, \tag{9.7.9}$$

where $\hat{\tau}^B$ denotes the amplitude of τ^B. It follows that

$$\sqrt{2}\bar{u}_* = \hat{u}_* = \frac{3\pi}{8}\tilde{u}_*\,. \tag{9.7.10}$$

We may now solve Eq. (9.7.4) for u subject to the boundary conditions

$$u \to U_I\,, \quad z \sim \infty\,, \tag{9.7.11}$$

$$u = 0\,, \qquad z = z_0\,, \tag{9.7.12}$$

where z_0 denotes the effective position of the bottom and is an empirical constant which depends on the roughness. The solution for a simple harmonic wave is

$$u = \mathrm{Re}\left[U_0 e^{-i\omega t}\left(1 - \frac{\ker 2\zeta^{1/2} - i\ \mathrm{kei}\,2\zeta^{1/2}}{\ker 2\zeta_0^{1/2} - i\ \ker 2\zeta_0^{1/2}}\right)\right], \tag{9.7.13}$$

where

$$\zeta = \frac{z}{l}\,, \quad \zeta_0 = \frac{z_0}{l}\,, \quad l = \frac{\kappa\bar{u}_*}{\omega}\,, \tag{9.7.14}$$

and $\ker(x)$ and $\mathrm{kei}(x)$ are the real and imaginary parts of $K_0(xe^{-i\pi/4})$, respectively. The above solution is essentially the same as Kajiura (1964) if $\bar{u}_*$ is replaced by $(3\pi/8(2)^{1/2})\tilde{u}_*$ (Grant, 1977; Grant and Madsen, 1979).

The friction velocity, so far unknown, may be found by combining Eqs. (9.7.1) and (9.7.2) and the original definition (9.7.3); the result is

$$u_* = \kappa z\frac{\partial u}{\partial z}\bigg|_{z=0}\,. \tag{9.7.15}$$

Using the approximation

$$\ker 2\zeta^{1/2} - i\ \mathrm{kei}\,2\zeta^{1/2} = -\frac{1}{2}\ln\zeta - 0.5772 + \frac{i}{4} + O(\zeta\ln\zeta) \tag{9.7.16}$$

for small ζ, we obtain

$$u_* = \mathrm{Re}\left[\frac{\kappa}{2}U_0 e^{-i\omega t}(\ker 2\zeta_0^{1/2} - i\ \mathrm{kei}\,2\zeta_0^{1/2})^{-1}\right], \tag{9.7.17}$$

which defines both the magnitude and the phase of u_*. In particular, the magnitude is

$$\hat{u}_* = \sqrt{2}\bar{u}_* = \frac{\kappa U_0}{[(\ker 2\zeta_0^{1/2})^2 + (\mathrm{kei}\, 2\zeta_0^{1/2})^2]^{1/2}}\,. \tag{9.7.18}$$

As soon as z_0 is prescribed, Eq. (9.7.18) gives $\bar{u}_*$, implicitly, after which u is completely known. For a natural sea bottom, however, it is not an easy matter to estimate z_0 because the bottom roughness depends not only on the sand grains but also on the ripples.

Extensive experiments on artificially roughened bottoms have been performed by Jonsson (1966) (see also Jonsson and Carlsen, 1976) and Horikawa and Watanabe (1968). These authors measured u as a function of x and t and calculated ν_e by

$$\nu_e = -\left[\int_\infty^z dz \frac{\partial}{\partial t}(u - U_I) \Big/ \frac{\partial u}{\partial z}\right]. \tag{9.7.19}$$

At any fixed instant of the wave period the eddy viscosity was found to increase from zero to a maximum value and then to decrease again with height. At some instants, however, negative eddy viscosity was found over part of the height. The magnitude of ν_e could be as much as 100 cm^2/s, and 20–40 cm^2/s was the typical range. At a fixed z, ν_e oscillated in time at twice the fundamental frequency. Horikawa and Watanabe also found that the measured velocity typically contained higher harmonics. The eddy viscosity, calculated from Eq. (9.7.19) by using the first harmonic only, varied widely over a wave period, the typical range being -15 cm^2/s to $+15$ cm^2/s. The temporal dependence of ν_e is not yet well understood and does not strictly conform with the theory given here.

Grant (1977) and Grant and Madsen (1979) have made a careful comparison of the theoretical (hence only first harmonic) velocity profile with the available experiments of Jonsson. With z_0 properly selected, they found Eq. (9.7.13) to give a fairly good prediction for the magnitude but not the phase of u. Furthermore, they have extended this type of theory to include currents (Grant and Madsen, 1979).

9.7.2 The Friction Coefficient

A practical motivation for studying bottom stresses is to find the friction coefficient f_w defined by

$$\tau^B = \frac{1}{2} f_w \rho |U_I| U_I\,, \tag{9.7.20}$$

which may be used to find the effect on the wave field outside the boundary layer.

Taking the maximum of both sides of Eq. (9.7.20) and using Eq. (9.7.10), we get

$$\hat{u}_* = \frac{1}{2} f_w^{1/2} U_0 \tag{9.7.21}$$

so that Eq. (9.7.18) is also an implicit equation for f_w in terms of U_0. Grant (1977) lets

$$U_0 = A_0 \omega \quad \text{and} \quad z_0 = \frac{k_N}{30}$$

for fully rough turbulent flows, where A_0 is the inviscid orbital amplitude just above the boundary layer and k_N is the characteristic bed roughness height.[2] Upon further using the approximation (9.7.16) for small ζ_0, he has shown that

$$\frac{1}{4.06 f_w^{1/2}} + \log_{10} \frac{1}{4 f_w^{1/2}} = \log_{10} \frac{A_0}{k_N} - 0.325\,, \tag{9.7.22}$$

which is of the form given by Jonsson (1966) except for the last constant being -0.08, and implied by Kajiura (1964). Figure 9.7 shows the variations of f_w versus A_0/k_N, according to Eq. (9.7.22) [Jonsson (1966) and Kajiura (1968) who used a more complex mode of ν_e]. The empirical curve of Kamphuis (1975) is also shown.

The length scale l is clearly a characteristic length of the boundary layer. Grant and Madsen found that at the height $2l$ the velocity u reached 90% of the inviscid value U_I. Thus, they defined the turbulent boundary-layer thickness δ_t to be $2l$ which implied from Eqs. (9.7.14) and (9.7.21) that

$$\frac{\delta_t}{A_0} = 0.4 f_w^{1/2}\,. \tag{9.7.23}$$

This ratio varied from $0.04 \sim 0.4$ for $A_0/k_N = 10^3 \sim 1$.

9.7.3 Bottom Friction on the Damping of Standing Shallow-Water Waves in a Basin

As an application of the foregoing results, we consider the effect of friction on standing waves in shallow water.

[2]It must be pointed out that in natural surroundings, k_N cannot be defined unequivocally.

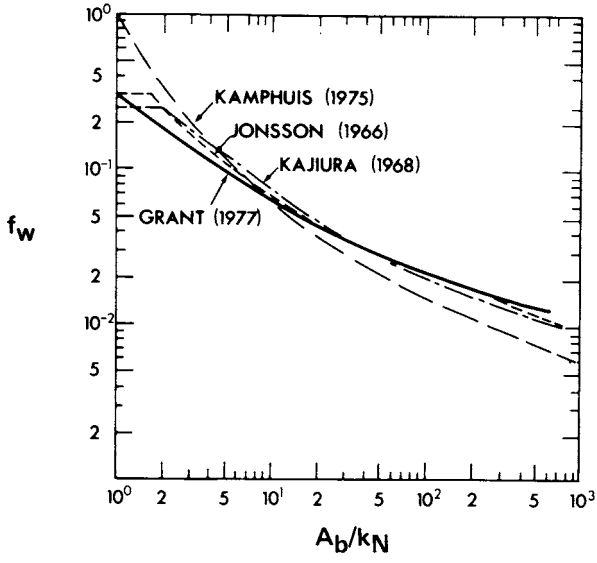

Figure 9.7: Comparison of wave friction factor formulas of Kamphuis (1975), Jonsson (1966), Kajiura (1968), and Grant (1977) (from Grant, 1977).

Let us recall the continuity equation

$$\frac{\partial \zeta}{\partial t} + \nabla \cdot (\mathbf{u}h) = 0\,, \tag{9.7.24}$$

and add the bottom stress to the momentum equation

$$\frac{\partial \mathbf{u}}{\partial t} = -g\nabla\zeta - \frac{\boldsymbol{\tau}^B}{\rho h}\,. \tag{9.7.25}$$

Multiplying Eq. (9.7.25) by $\mathbf{u}h$, we get

$$\begin{aligned}\frac{\partial}{\partial t}\left(\frac{1}{2}\mathbf{u}^2 h\right) &= -g\nabla\cdot(\mathbf{u}h\zeta) + g\zeta\nabla\cdot(\mathbf{u}h) - \frac{\boldsymbol{\tau}^B\cdot\mathbf{u}}{\rho} \\ &= -g\nabla\cdot(\mathbf{u}h\zeta) - \frac{\partial}{\partial t}\left(\frac{g\zeta^2}{2}\right) - \frac{\boldsymbol{\tau}^B\cdot\mathbf{u}}{\rho}\end{aligned}$$

after using Eq. (9.7.24). Integrating over the entire basin area S and invoking the no-flux boundary condition, we get

$$\frac{\partial}{\partial t}\iint_S \left(\frac{\rho}{2}\mathbf{u}^2 h + \frac{\rho}{2}g\zeta^2\right) dx\,dy = -\iint_S \boldsymbol{\tau}^B\cdot\mathbf{u}\,dx\,dy\,. \tag{9.7.26}$$

Since the integral on the left is the total energy E, Eq. (9.7.26) simply states that the energy decay rate is equal to the rate of work done at the bottom.

Using Eq. (9.7.20), invoking equivalent linearization and neglecting possible phase difference between $\boldsymbol{\tau}^B$ and $\mathbf{u}$, we get

$$\boldsymbol{\tau}^B = \frac{4\rho}{3\pi}\frac{f_w U_0}{h_0}\mathbf{u}h\,, \tag{9.7.27}$$

where $U_0 h/h_0$ is the amplitude of $\mathbf{u}$ which, in general, depends on $\mathbf{x}$. For estimation we shall simply redefine U_0 as a constant typical of $\mathbf{u}$. Substituting Eq. (9.7.27) into Eq. (9.7.26) and taking the time average over a wave period, we find

$$\frac{\partial \overline{E}}{\partial t} = \frac{4\rho}{3\pi}\frac{f_w U_0}{h_0}\iint_S \overline{\mathbf{u}^2}h\,dx\,dy = \frac{4}{3\pi}\frac{f_w U_0}{h_0}\overline{E}\,, \tag{9.7.28}$$

where we have assumed that the friction is small enough, so that the kinetic and potential energies are equal as in the inviscid limit (equipartition theorem, Appendix 9.A). Equation (9.7.28) implies that energy damps out according to

$$\overline{E}(t) = \overline{E}(0)e^{-\alpha t} \quad \text{with} \quad \alpha = \frac{4}{3\pi}\frac{f_w U_0}{h_0}\,. \tag{9.7.29}$$

To have a quantitative idea of the damping rate we take $h = 10$ m, $U_0 = (A/h)(gh)^{1/2} \cong 0.1$ m/s and $f = 0.025$. It follows that $\alpha \sim 10^{-4}$ s^{-1}.

It is now opportune to assess the possible importance of bottom friction in harbor resonance. For the open bay of Section 5.6, the radiation decay rate can be estimated from Eq. (5.6.22), Section 5.6, to be $\omega a/L$ where a is the half-width and L the length of the bay. If we take $a = 100$ m, $L = 5000$ m, and $h = 10$ m, the lowest resonant wavenumber is $k_0 = \pi/2L$ so that $\omega = (gh)^{1/2}k_0 = (\pi/2L)(gh)^{1/2} = \pi \times 10^{-3}$ s^{-1}. The corresponding radiation damping rate is about $\pi/5 \times 10^{-4}$ s^{-1} which is comparable to the bottom friction. Thus, in practical computations of harbor oscillations, bottom friction may be of importance.

In principle, U_0 represents the local velocity amplitude and is unknown *a priori*. Therefore, to include turbulent bottom friction in a general wave problem such as harbor oscillations would involve nonlinear mathematics and massive computations. In practice, one does not have sufficient information of the bottom roughness to warrant such an effort; the coefficient $f_w U_0/h_0$ in Eq. (9.7.27) is often taken to be a constant instead.

Over a natural sea bottom there are other physical factors which may contribute to the damping of waves. An important contribution to the bottom roughness is the sand ripples formed naturally by waves. According to an experimental study by Vitale (1979), ripples may amount to

25–34 percent of the total friction on a natural seabed. A theoretical model which accounts for energy losses from vortex shedding at the sharp fixed ripple crests has been advanced by Longuet–Higgins (1981). Smith and McLean (1977) and Grant and Madsen (1982) have developed semiempirical theories which include both the form drag and the movement of the sand ripples. Another factor is the scattering by topographical irregularities with dimensions as large as the typical wavelength, as discussed in the last Chapter. In addition, water percolates into the sea bottom and loses energy due to friction within the pores. This kind of loss is, however, difficult to estimate; various hypotheses regarding the solid skeleton (rigid, elastic, viscoelastic, porous or nonporous, etc.) have been proposed. Since the pertinence of the hypotheses must vary widely from one locale to another, we do not pursue it here.

Appendix 9.A An Equipartition Theorem

For simple harmonic infinitesimal waves

$$\mathbf{u} = \nabla\phi e^{-i\omega t}\,, \tag{9.A.1}$$

the time-averaged kinetic energy is

$$\frac{1}{2}\iiint_V \rho\,\overline{u_i u_i}\,dV = \frac{1}{4}\iiint_V \rho(\nabla\phi\cdot\nabla\phi^*)\,dV\,. \tag{9.A.2}$$

The potential energy is

$$\frac{1}{2}\iint_{S_F} \rho g\overline{\zeta^2}\,dS = \frac{\rho g}{4}\iint_{S_F}|\eta|^2\,dS = \frac{\rho}{4}\frac{\omega^2}{g}\iint_{S_F}|\phi|^2\,dS \tag{9.A.3}$$

after the kinematic boundary condition is invoked. By virtue of the identity (9.4.23), the right-hand-sides of Eqs. (9.A.2) and (9.A.3) are equal, implying that

$$\frac{1}{2}\rho\iiint_V \overline{u_i u_i}\,dV = \frac{1}{2}\iint_{S_F}\rho g\overline{\zeta^2}\,dS = \frac{1}{2}\overline{E}\,. \tag{9.A.4}$$

Thus, the total energy is equally divided between kinetic and potential energies. This is an example of the equipartition theorem which is valid in many other conservative physical systems.

The reader should try to check the equipartition theorem in standing waves by using the explicit formulas for u, ν, and ζ.

References

The numbers in square brackets refer to the page numbers where the references have been cited in the text.

Abramowitz, M. and I. A. Stegun (1972). *Handbook of Mathematical Functions*, Dover, New York. [172, 208, 249]

Adamo, A. and C. C. Mei, (2004). Linear resonance of Venice storm gates to incident sea waves. *Proc. Roy. Soc. Lond.*. In press. [427]

Adams, N. K. (1941). *The Physics and Chemistry of Surfaces*, Oxford University Press, London. [462]

Agnon, Y. and E. Pelinovsky (2001). Accurate refraction-diffraction equations for water waves on a variable-depth rough bottom. *J. Fluid Mech.* **449**: 301-311. [98]

Anderson, P. A. (1958). Absence of diffusion in certain random lattices. *Phys. Rev.* **109**: 1492–1505. [323]

Aranha, J. A., C. C. Mei, and D. K. P. Yue (1979). Some properties of a hybrid element method for water waves. *Int. J. Num. Methods Eng.* **14**: 1627–1641. [390, 394, 403]

Ardhuin, F. and T. Herbers (2000). Bragg scattering of random surface gravity waves by irregular sea bed topography. *J. Fluid Mech.*, **451:** 1–33. [307, 333]

Arthur, R. S. (1946). Refraction of water waves by islands and shoals with circular bottom contours. *Trans. Am. Geophys. Union* **27**: 168–177. [82]

Bai, K. J. and R. Yeung (1974). Numerical solutions of free-surface and flow problems. *Proc. 10th Symp. Naval Hydrodyn.* Office of Naval Research, 609–641. [188, 393]

Bartholomeuz, E. F. (1958). The reflection of long waves at a step. *Proc. Cambridge Philos. Soc.* **54**: 106–118. [135, 138]

Batchelor, G. K. (1967). *An Introduction to Fluid Dynamics*, Cambridge University Press, London. [5, 437]

Belzons, M., E. Guazzelli, and O. Parodi (1988). Gravity waves on a rough bottom: experimental evidence of one-dimensional localization. *J. Fluid Mech.* **186**: 539–558. [323, 331]

Berkhoff, J. C. W. (1972). Computation of combined refraction–diffraction. *Proc. 13th Conf. Coastal Eng. ASCE* **1**: 471–490. [96, 188]

Bessho, M. (1965). On the wave-free distribution in the oscillation problem of the ship. *J. Zosen Kiokai* **117**: 127–138. [377]

Bessho, M. (1967). On the two-dimensional theory of the rolling motion of ships. *Mem. Defense Acad. Yokoyuka* **7**: 105–125. [384]

Bigg, G. R. (1982). Diffraction and trapping of waves by cavities and slender bodies. Ph.D. thesis, Depart. of Applied Mathematics, University of Adelaide, Australia. [181, 185]

Bohm, D. (1951). *Quantum Theory*, Prentice-Hall, Englewood Cliffs, N. J. [146,157]

Booij, N. (1981). Gravity waves on water with non-uniform depth and current. *Communications on Hydraulics*, Dept. of Civil Engineering, Delft University of Technology, Report No. 81-1. [121, 185]

Bremmer, H. (1951). The WKB approximation as the first term of a geometric optical series. *Comm. Pure Appl. Math.* **4**: 105–115. [153]

Bretherton, F. P. and C. J. R. Garrett (1968). Wave trains in inhomogeneous moving media. *Proc. R. Soc. Lond. A* **302**: 529–554. [101, 109]

Brevik, I. and B. Aas (1980). Flume experiments on waves and currents, I. Rippled bed. *Coastal Eng.* **3**: 149–177. [119–121]

Buchwald, V. T. (1971). The diffraction of tides by a narrow channel. *J. Fluid Mech.* **46**: 501–511. [213]

Budal, K. (1977). Theory of absorption of wave power by a system of interacting bodies. *J. Ship Res.* **21**: 248–253. [412, 417, 418]

Budal, K. and J. Falnes (1975). A resonant point absorber of ocean wave power. *Nature* **256**: 478–479; **257**: 626–627. [405]

Budal, K., J. Falnes, A. Kyllingstad, and G. Oltedal (1979). Experiments with point absorbers. *Proc. 1st Symp. Wave Energy Utilization*, Chalmers Institute of Technology, Sweden, 253–282. [417]

Carrier, G. F. (1970). The dynamics of tsunamis. *Mathematical Problems in the Geophysical Sciences. I. Geophysical Fluid Dynamics*, American Mathematical Society, Providence, R.I., 157–181. [208, 260, 262, 267, 274]

Carrier, G. F., M. Krook, and C. E. Pearson (1966). *Functions of a Complex Variable — Theoy and Technique*, McGraw-Hill, New York. [29, 263]

Carrier, G. F. and R. P. Shaw (1969). *Tsunamis in the Pacific Ocean*, ed. W. M. Adams, East West Center Press, Honolulu, 377–398. [267–269]

Carrier, G. F., R. P. Shaw, and M. Miyata (1971). The response of narrow mouthed harbors in a straight coastline to periodic incident waves. *J. Appl. Mech.* **38 E-2**: 335–344. [239]

Case, K. M. and W. C. Parkinson (1957). Damping of surface waves in an incompressible liquid. *J. Fluid Mech.* **2**: 172–184. [476]

Chamberlain, P. G. and D. Porter (1995). The modified mild-slope equation. *J. Fluid Mech.* **291**: 393–407. [98]

Chao, Y. Y. (1971). An asymptotic evaluation of the wave field near a smooth caustic. *J. Geophys. Res.* **76**: 7401–7408. [82]

Chao, Y. Y. and W. J. Pierson, Jr. (1972). Experimental studies of the refraction of uniform wave trains and transient wave groups near a straight caustic. *J. Geophys. Res.* **77**: 4545–4554. [82]

Charkrabarti, S. K. and W. A. Tam (1975). Interaction of waves with a large vertical cylinder. *J. Ship Res.* **19**: 23–33. [373,374]

Chen, H. S. and C. C. Mei (1974a). Oscillations and wave forces in an offshore harbor. Parsons Lab., Massachusetts Institute of Technology, Report 190. [260]

Chen, H. S. and C. C. Mei (1974b). Oscillations and wave forces in a man-made harbor in the open sea. *Proc. 10th Symp. Naval Hydrodyn.*, Office of Naval Research, 573–594. [180, 260]

Cole, J. D. (1968). *Perturbation Methods in Applied Mathematics*, Blaisdell, Waltham, Mass. [56]

Collin, R. E. (1960). *Field Theory of Guided Waves*, McGraw-Hill, New York. [272, 306]

Consorzio Venezia Nuova (1988). Study on the influence of the inclination angle and the gate shape on gate response. Studio 2.2.10. Tech. Rep. by Delft Hydraulics. [426]

Crapper, G. D. (1972). Nonlinear gravity waves on steady non-uniform currents. *J. Fluid Mech.* **52**: 713–724. [120]

Cummins, W. E. (1962). The inpulse response functions and ship motion. *Schiffstechnik* **9**: 101–109. [442]

Dalrymple, R. A. and R. G. Dean (1972). The spiral wavemaker for littoral drift studies. *Proc. 13th Int. Conf. Coastal Eng.* [95]

Davey, N. (1944). The field between equal semi-infinite rectangular electrodes on magnetic pole-pieces. *Philos. Mag.* **35**: 819–844. [239]

Davies, A. G., (1982). The reflection of wave energy by undulations on the seabed. *Dyn. Atmos. Oceans.* **6**: 207–232. [309, 314]

Devillard, P., F. Dunlop, and J. Souillard (1988). Localization of gravity waves on a channel with a random bottom. *J. Fluid Mech.* **186**: 521–538. [324]

Dingemans, M. (1978). Refraction and diffraction of irregular waves, a literature survey. *Delft Hydraulics Laboratory Report*, W301, Part I. [109]

Dingemans, M. (1996). *Water Wave Propagation over Uneven Bottoms*. Vol. 1. World Scientific. 898pp. [109]

Dolan, T. J., (1983). *Wave mechanisms for the formation of longshore bars with emphasis on the Chesapeake Bay.* MCE thesis, University of Delaware, 208pp. [308]

Dolan, T. J., and R. G. Dean, (1985). Multiple longshore sand bars in the Upper Chesapeake Bay. *Estuarine, Coastal and Shelf Sciences*, **21**: 721-743. [308]

Donelan, M., M. S. Longuet-Higgins, and J. S. Turner (1972). Periodicity in whitecaps. *Nature* **239**: 449–451. [64]

Dore, B. D. (1969). The decay of oscillations of a non-homogeneous fluid within a container. *Proc. Cambridge Philos. Soc.* **65**: 301–307. [467]

Dore, B. D. (1978). Some effects of the air–water interface on gravity waves. *Geophys. Astrophys. Fluid Dynamics* **10**: 215–230. [455, 478, 483]

Eagleson, P. S. (1956). Properties of shoaling waves by theory and experiment. *Trans. Am. Geophys. Union* **31**: 565–572. [79]

Eckart, C. (1951). Surface waves in water of variable depth. Marine Physical Lab. of Scripps Inst. Ocean. Wave Report 100-99. [172]

Erdelyi, A. (ed.) (1954). *Tables of Integral Transform. I. Bateman Manuscript Project*, McGraw-Hill, New York. [49]

Evans, D. V. (1976). A theory for wave power absorption by oscillating bodies. *J. Fluid Mech.* **77**: 1–25. [409]

Evans, D. V. (1978). The oscillating water column wave-energy device. *J. Inst. Math. Appl.* **22**: 423–433. [405]

Evans, D. V. (1979). Some theoretical aspects of three-dimensional wave energy absorbers. *Proc. 1st. Symp. on Wave Energy Utilization*, Chalmers Institute of Technology, Sweden, 77–113. [419]

Evans, D. V. (1981). Power from water waves. *Ann. Rev. Fluid Mech.* **13**: 157–187. [425]

Evans, D. V., D. C. Jeffrey, S. H. Salter, and J. R. M. Taylor (1979). Submerged cylinder wave energy device: Theory and experiment. *Appl. Ocean Res.* **1**: 3–12. [405]

Evans, D. V., M. Levitin and D. Vasiliev, (1994). Existence theorems for trapped modes. *J. Fluid Mech.* **261**: 21–31. [427]

Falnes, J. (1980). Radiation impedance matrix and optimum power absorption for interacting oscillations in surface waves. *Appl. Ocean Res.* **2**: 75–80. [418, 419]

Falnes, J. (2002).*Ocdean Waves and Oscillating Systems– Linear Interactions including Wave-Energy Extraction*. Cambridge, 275pp. [406, 425]

Falnes, J. and K. Budal (1978). Wave power conversion by point absorbers. *Norwegian Maritime Res.* **6**: 211. [405, 417]

Faltinsen, O. M. and A. E. Løken (1979). Slow drift oscillations of a ship in irregular waves. *Appl. Ocean Res.* **1**: 21–31. [442]

Felsen, L. B. and N. Marcuvitz (1973). *Radiation and Scattering of Waves*, Prentice-Hall, Englewood Cliffs, N. J. [156]

Finkelslein, A. (1953). The initial value problem for transient water waves, Dissertation, New York University. [25]
ow the free surface of deep fluids. Naval Ship Research and Development Center Report 2375. [377]

Frank, W. (1967). The heaving damping coefficients of bulbous cylinders partially immersed in deep water. *J. Ship Res.* **11**: 151–153. [377]

French, M. J. (1979). The search for low cost wave energy and the flexible bag device. *Proc. 1st. Symp. Wave Energy Utilization*, Chalmers Institute of Technology, Sweden, 364–377. [406]

Friedrichs, K. O. (1948a). On the derivation of the shallowwater theory. *Comm. Pure Appl. Math.* **1**: 81–85. [125]

Garabedian, P. R. (1964). *Partial Differential Equations*, McGraw-Hill, New York. [57]

Garrett, C. J. C. (1970). Bottomless harbours. *J. Fluid Mech.* **43**: 432–449. [227, 234, 387]

Gerwick, B. C., Jr. and E. Hognestad (1973). Concrete oil storage tank placed on North Sea floor. *Civil Eng. ASCE* **43**: 81–85. [277]

Goldstein, H. (1950). *Classical Mechanics*, Addison-Wesley, Reading, Mass. [343]

Graham, J. M. R. (1980). The forces on sharp edged cylinders in oscillatory flow at low Keulegan–Carpenter numbers. *J. Fluid Mech.* **97**: 331–346. [278]

Grant, W. D. (1977). Bottom friction under waves in the presence of a weak current: Its relation to coastal sediment transport, Sc.D. Thesis, Dept. of Civil Engineering, Massachusetts Institute of Technology. [484-488]

Grant, W. D. and O. S. Madsen (1979a). Bottom friction under waves in the presence of a weak current. Tech. Mem. ERL-MESA, National Oceanic and Atmospheric Administration. [484-486]

Grant, W. D. and O. S. Madsen (1979b). Combined wave and current interaction with rough bottom. *J. Geophys. Res.* **84**: 1797–1808. [486]

Grant, W. D. and O. S. Madsen (1982). Movable bed roughness in unsteady oscillatory flow. *J. Geophys. Res.* **87**: 469–481. [490]

Greenspan, H. P. (1958). On the breaking of water waves of finite amplitude on a sloping beach. *J. Fluid Mech.* **4**: 330–334. [174, 467]

Guiney, D. C., B. J. Noye, and E. O. Tuck (1972). Transmission of waves through small apertures. *J. Fluid Mech.* **55**: 149–167. [239]

Guza, R. T. and A. J. Bowen (1976). Finite amplitude Stokes edge waves. *J. Marine Res.* **34**: 269–293. [174]

Hagen, G. E. (1975). Wave-driven generator. U.S. Pat. 4,077,213. [405]

Hammack, J. L. and H. Segur (1978). Modelling criteria for long water waves. *J. Fluid Mech.* **84**: 359–373. [691, 693]

Hanaoka, T. (1959). On the reverse flow theorem concerning wave-making theory. *Proc. 9th Japan Nat'l Congr. Appl. Mech.* 223–226. [383]

Hara, T., and C. C. Mei, (1987) Bragg scattering of surface waves by periodic bars. *J. Fluid Mech.* **178**: 221–241. [318]

Haren, P. and C. C. Mei (1980). Rafts for absorbing wave power. *Proc. 13th Symp. Naval Hydrodyn.* The Ship Building Research Institute, Japan, 877–886. [424]

Haren, P. and C. C. Mei (1981). Head-sea diffraction by a slender raft with application to wave-power absorption. *J. Fluid Mech.* **104**: 505–526. [181]

Haskind, M. D. (1944). The oscillation of a body immersed in a heavy fluid. *Prikl. Mat. Mekh.* **8**: 287–300. [356]

Haskind, M. D. (1957). The exciting forces and wetting of ships in waves (in Russian). *Izv. Akud. Nauk SSSR Otd. Tekh. Nauk* **7**: 65–79. English version available as David Taylor Model Basin Translation No. 307. [383]

Hasselman, K. (1966). Feyman diagrams an interaction rules of wave-wave scattering processes. *Review of Geophysics* **4**: 1–32. [307]

Hayashi, T., T. Kano, and M. Shirai (1966). Hydraulic research on the closely

spaced pile breakwater. *Proc. 10th Conf. Coastal Eng., Santa Barbara Specialty Conf. ASCE* 873–884. [277, 278, 283, 287–289]

Heathershaw, A. D., (1982). Seabed–wave resonance and sandbar growth. *Nature*, **296**: 343-345. [315, 318]

Hildebrand, F. B. (1962). *Advanced Calculus for Applications*, Prentice-Hall, Englewood Cliffs, N. J. [72]

Hill, M. N. (1962). *The Sea*, Vol. I, *Physical Oceanography*, Interscience, New York. [4]

Horikawa, K. and H. Nishimura (1970). On the function of tsunami breakwaters. *Coastal Eng. Jap.* **13**: 103–122. [293]

Horikawa, K. and A. Watanabe (1968). Laboratory study on oscillatory boundary layer flow. *Proc. 12th Conf. Coastal Eng.* **1**: 467–486. [486]

Houston, J. R. (1976). Long beach harbor: Numerical analysis of harbor oscillations. *U.S. Army Engineering Waterways Experiment Station, Vicksburg, MS*, Report **1**, Misc. Paper H-76-20. [199, 260]

Houston, J. R. (1978). Interaction of tsunamis with the Hawaiian Islands calculated by a finite element numerical model. *J. Phys. Ocean.* **8**: 93–102. [197, 198]

Houston, J. R. (1981). Combined refraction and diffraction of short waves using the finite element method. *Appl. Ocean Res.* **3**: 163–170. [98]

Hunt, J. N. (1952). Viscous damping of waves over an inclined bed in a channel of finite width. *Houille Blanche* **7**: 836–842. [478]

Hwang, L. S. and E. O. Tuck (1970). On the oscillation of harbours of arbitrary shape. *J. Fluid Mech.* **42**: 447–464. [255]

Ippen, A. T. and Y. Goda (1963). Wave induced oscillations in harbors. The solution for a rectangular harbor connected to the open-sea. Hydrodynamics Lab., Dept. of Civil Engineering, Massachusetts Institute of Technology Report 59. [258]

Ishimaru, A. (1997). *Wave Propagation and Scattering in Random Media*, IEEE Press. [322]

Issacs, J. D. (1948). Discussion of "Refraction of surface waves by current" J. W. Johnson. *Trans. Am. Geophys. Union* **29**: 739–742. [101]

Ito, Y. (1970). Head loss at tsunami breakwater opening. *Proc. 12th Conf. Coastal Eng. ASCE* 2123–2131. [293]

Jansson, K. G., J. K. Lunde, and T. Rindby (eds.) (1979). *Proc. 1st Symp. Wave Energy Utilization*, Chalmers Institute of Technology, Sweden. [403]

Jarlan, C. E. (1965). The application of acoustical theory to the reflective properties of coastal engineering structure. *Q. Bull. National Res. Council Canada* **1**: 23–63. [277]

Jawson, M. A. and G. T. Symm (1977). *Integral Equation Methods in Potential Theory and Elastostatics*, Academic, New York. [399]

bibitem Jeffreys, H. and B. S. Jeffreys (1953). *Methods of Mathematical Physics*, 3rd. ed., Cambridge University Press, London. [32]

John, F. (1949). On the motions of floating bodies I. *Comm. Pure Appl. Math.* **2**: 13–57. [340, 352]

John, F. (1950). On the motions of floating bodies II. *Comm. Pure Appl. Math.* **3**: 45–101. [352, 400, 450, 453, 454]

Johns, B. (1968). A boundary layer method for the determination of the viscous damping of small amplitude gravity waves. *Q. J. Mech. Appl. Math.* **21**: 93–103. [467]

Johnson, J. W. (1947). The refraction of surface waves by currents. *Trans. Am. Geophys. Union* **28**: 867–874. [101]

Jones, D. S., (1964). *The Theory of Electromagnetism*, Pergamon, London. [183]

Jonsson, I. G. (1966). Wave boundary layers and friction factors. *Proc. 10th Conf. Coastal Eng. ASCE* 127–148. [483, 486-488]

Jonsson, I. G. and O. Brink-Kjaer (1973). A comparison between two reduced wave equations for gradually varying depth. *Inst. Hydrodyn. Hydraul. Eng., Tech. Univ. Denmark Progr. Rep.* **31**: 13–18. [96]

Jonsson, I. G. and N. A. Carlsen (1976). Experimental and theoretical investigations in an oscillatory turbulent boundary layer. *J. Hydraul. Rec.* **14**: 45–60. [486]

Jonsson, I. G. and O. Skovgaard (1979). A mild slope equation and its application to tsunami calculations. *Marine Geodesy.* **2**: 41–58. [98]

Jonsson, I. G., O. Skovgaard, and O. Brink-Kjaer (1976). Diffraction and refraction calculations for waves incident on an island. *J. Marine Res.* **34**: 469–496.

Jonsson, I. G., O. Skovgaard, and J. O. Wang (1970). Interactions between waves and currents. *Proc. 12th Conf. Coastal Eng.* **1**: 486–501. [119, 121]

Kajiura, K. (1961). On the partial reflection of water waves passing over a bottom of variable depth. *Proc. Tsunami Meetings 10th Pacific Science Congress. IUGG Monograph* **24**: 206–234. [134, 151, 153]

Kajiura, K. (1963). The leading wave of a tsunami. *Bull. Earthquake Res. Inst. Univ. Tokyo* **41**: 525–571. [33, 39, 40, 50, 51]

Kajiura, K. (1964). On the bottom friction in an oscillatory current. *Bull. Earthquake Res. Inst. Univ. Tokyo* **42**: 147–174. [484, 485, 487]

Kajiura, K. (1968). A model of the bottom boundary layer in water waves. *Bull. Earthquake Res. Inst. Univ. Tokyo* **46**: 75–123. [487, 488]

Kamphuis, J. W. (1975). Friction factor under oscillatory waves. *J. Waterways Harhors Coastal Eng. ASCE* **101**: [135–144. 487, 488]

Kantorovich, L. V. and V. I. Krylov (1964). *Approximate Methocis in Higher Analysis*, Noordhoff, Groningen. [230]

Kehnemuyi, M. and R. C. Nichols (1973). The Atlantic generating station. *Nuclear Eng. Institute* **18**: 477. [260]

Keller, J. B. (1958). Surface waves on water on non-uniform depth. *J. Fluid Mech.* **4**: 607–614. [66]

Keller, J. B., (1964). Stochastic equations and wave prooationi in random media. *Proc. 16th Symp. Appl. Maths.* (ed. R.Bellman) Am. Math. Soc. 146–170. [323]

Keller, J. B. (1964), Stochastic equation and wave propagation in random media. *Proc. 16th Symp. Appl. Math.*, 145–170. Amer. Math. Soc. Rhode Island. [323]

Keulegan, G. H. (1948). Gradual damping of solitary waves. *J. Res. Natl. Bur. Stand.* **40**: 487–498. [681]

Keulegan, G. H. (1959). Energy dissipation in standing waves in rectangular basins. *J. Fluid Mech.* **6**: 33–50. [478]

Keulegan, G. H. and L. H. Carpenter (1956). Forces on cylinders and plates in an oscillating fluid. National Bureau of Standards Report 4821. [277, 339]

King, A. C. and D. J. Needham (1994). The initial development of a jet caused by fluid, body and free-surface interaction. Part 1. A uniformly accelerating plate. *J. Fluid Mech.* **268**: 89.

Kirby, J. T. (1986). A general wave equation for waves over rippled beds. *J. Fluid Mech.* **162**. 171–186. [98]

Kober, H. (1957). *Dictionary of Conformal Representations*, Dover, New York. [219]

Kreisel, G. (1949). Surface waves. *Q. Appl. Math.* **7**: 21–24. [362, 379, 380]

Kyozuka Y. and K. Yoshida (1981). On wave-free floating-body in heaving oscillations. *Appl. Ocean Res.* **3**: 183–194. [377]

Landau, L. D. and E. M. Lifshitz (1959). *Fluid Mechanics*, Pergamon, New York. [21]

Lautenbacher, C. C. (1970). Gravity wave refraction by islands. *J. Fluid Mech.* **41**: 655–672. [255]

LeBlond, P. H. and L. A. Mysak (1978). *Waves in the Ocean*, Elsevier, Amsterdam. [4]

Lee, J. J. (1971). Wave-induced oscillation in harbors of arbitrary geometry. *J. Fluid Mech.* **45**: 375–394. [238, 239, 258, 293, 300]

Lee, J. J. and F. Raichlen (1972). Oscillations in harbor with connection basins. *J. Waterways, Harbors Coastal Eng. Div. ASCE* **98**: 311–332. [252, 255]

Lenoir, M. and A. Jami (1978). A variational formulation for exterior problems in linear hydrodynamics. *Comp. Methods Appl. Mech.* **16**: 341–359. [393, 403]

Li, G., and C. C. Mei, (2003). Natural modes of mobile flood gates. *Appl. Ocean Res.* **25**: 115–126. [426, 433]

Li, H. (1954). Stability of oscillatory laminar flow along a wall. U.S. Army Beach Erosion Board. Tech. Memo. 47. [483]

Liao, C., and C. C. Mei, (2000). Numerical solution for trapped waves around inclined Venice gates. *J. Waterways, Port, Coastal adn Ocean Eng.* **126**: 236-244. [426]

Lighthill, M. J. (1979). Two-dimensional analysis related to wave energy extraction by submerged resonant ducts. *J. Fluid Mech.* **91**: 253–317. [405]

Liu, P. L. F. and C. C. Mei (1976a, b). Water motion on a beach in the presence of a breakwater 1. waves 2. mean currents. *J. Geophys. Res.-Oceans Atmos.* **81**: 3079–3084; 3085–3094. [185]

Long, R. B. (1973a). Scattering of surface waves by an irregular bottom. *J. Geophy. Res.* **78**: 987–1004. [307]

Long, R. B. (1973b). Scattering of surface waves by bottom irregularities. *J. Geophy. Res.* **78**: 7861–7870. [307]

Longuet-Higgins, M. S. (1967). On the trapping of wave energy round islands. *J. Fluid Mech.* **29**: 781–821. [157, 176, 179, 180]

Longuet-Higgins, M. S. (1974a). Breaking waves in deep or shallow water. *Proc. 10th Symp. Naval Hydrodyn.*, Office of Naval Research, 597–605. [63, 64]

Longuet-Higgins, M. S. (1977a). The mean forces exerted by waves on floating or submerged bodies, with applications to sand bars and wave power machines. *Proc. R. Soc. Lond. A* **352**: 463–480. [436]

Longuet-Higgins, M. S. (1981). Oscillating flow over sand ripples. *J. Fluid Mech.* **107**: 1–35. [490]

Lozano, C. J. and P. L. F. Liu (1980). Refraction–diffraction model for linear surface water waves. *J. Fluid Mech.* **101**: 705–720. [185]

Lozano, C. J. and R. E. Meyer (1976). Leakage and response of waves trapped round islands. *Phys. Fluids* **19**: 1075–1088. [96]

Ludwig, D. (1966). Uniform asymptotic expansions at a caustic. *Comm. Pure Appl. Math.* **19**: 215–250. [82, 94]

Luneberg, R. K. (1964). *Mathematical Theory of Optics*, University of California Press, Los Angeles. [69, 72, 82]

Mack, L. R. (1962). Periodic, finite-amplitude, axisymmetric gravity waves. *J. Geophysical Res.* **67** (2).

Madsen, O. S. (1978a). Mass transport in deep-water waves. *J. Phys. Ocean.* **8**: 1009–1015.

Madsen, O. S. (1978b). Wave induced pore pressures and effective stresses in a porous sea bed. *Geotechnique* **28**: 377–393.

Maeda, H., H. Tanaka, and T. Kinoshita (1980). Theoretical and experimental study of wave power absorption. *Proc. 14th Symp. Naval Hydrodyn.*, The Ship Building Res. Inst. Japan, 857–876. [437]

Mallory, J. K. (1974). Abnormal waves on the south east coast of South Africa. University of Capetown Libraries, Cape Town. [117]

Maruo, H. (1960). The drift of a body floating on waves. *J. Ship Res.* **4**: 1–10. [381, 436]

Maskell, S. J. and F. Ursell (1970). The transient motion of a floating body. *J. Fluid Mech.* **44**: 203–313. [449]

Massel, S. (1993). Extended refraction-diffraction equation for surface waves. *Coastal Eng.* **19**: 97-126. [100]

Masuda, M. (1979). Experimental full scale result of wave power machine KAIMEI. *Proc. 1st. Symp. Wave Energy Utilization*, Chalmers Institute of Technology, Sweden 349–363. [406]

Mattioli, F. (1978). Wave-induced oscillations in harbors of variable depth. *Computers and Fluids* **6**: 161–172. [255]

McCamy, R. C. and R. A. Fuchs (1954). Wave forces on a pile: A diffraction theory. *Tech. Memo.* No. **69**, U.S. Army Board, U.S. Army Corp. of Eng. [371]

McCormick, M. E. (1981). *Ocean Wave Energy Conversion*, Wiley-Interscience, New York, 233 pp. [404]

McKee, W. D. (1974). Waves on a shearing current: A uniformly valid asymptotic solution. *Proc. Cambridge Philos. Soc.* **75**: 295–301. [116]

Mehlum, E. and J. Stamnes (1979). Power production based on focusing of ocean swells. *Proc. 1st Wave Energy Utilization*, Chalmers Institute of Technology, Sweden, 29–35. [406]

Mei, C. C. (1966a). Radiation and scattering of transient gravity waves by vertical plates. *Q. J. Mech. Appl. Math.* **19**: 417–440. [61]

Mei, C. C. (1973). Shoaling of spiral waves in a circular basin. *J. Geophy. Res.* **78**: 977–980. [95]

Mei, C. C. (1976). Power extraction from water waves. *J. Ship Res.* **20**: 63–66. [409]

Mei, C. C. (1978). Numerical methods in water wave diffraction and radiation. *Ann. Rev. Fluid Mech.* **10**: 393–416. [387, 403]

Mei, C. C. (1985). Resonant reflection of surface waves by periodic sandbars. *J. Fluid Mech.* **152**: 315–335. [317, 318, 320]

Mei, C. C. and H. S. Chen (1975). Hybrid element method for water waves. *Symposium on Modeling Techniques*, 2nd Annual Symposium of the Waterways Harbors and Coastal Engineering Division American Society of Civil Engineers, Vol. 1, pp. 63–81. [257, 258]

Mei, C. C. and H. S. Chen (1976). A hybrid element method for steady linearized free surface flows. *Inst. J. Num. Math. Eng.* **10**: 1153–1175. [188]

Mei, C. C. and M. A. Foda (1979). An analytical theory of resonant scattering of SH waves by thin overground structures. *Earthquake Eng. Structure Dynamics* **7**: 335–353. [225]

Mei, C. C., M. A. Foda, and P. Tong (1979). Exact and hybrid-element solutions for the vibration of a thin elastic structure seated on the sea bottom. *Appl. Ocean Res.* **1**: 79–88. [188]

Mei, C. C. and M. H. Hancock, (2003). Weakly nonlinear surface waves over a random seabed. *J. Fluid Mech.* **475**: 247–268. [307, 324, 330–333]

Mei, C. C., T. Hara and M. Naciri, (1988). Note on Bragg scattering of water waves by parallel bars on the sea bed. *J. Fluid Mech.* **186**: 147–162. [320]

Mei, C. C. and P. L. F. Liu (1973). The damping of surface gravity waves in a bounded liquid. *J. Fluid Mech.* **59**: 239–256. [463, 467]

Mei, C. C. and P. L. F. Liu, (1977). Effects of topography on the circulation in and near the surf zone — Linear theory. *Estuary Coastal Marine Sci.* **5**: 25–37. [609]

Mei, C. C., P. L. F. Liu and T. G. Carter (1972). Mass transport in water waves. Parsons Lab., Massachusetts Institute of Technology Report 146: 287. [521, 535]

Mei, C. C., P. L. F. Liu, and A. T. Ippen (1974). Quadratic head loss and scattering of long waves. *J. Waterway Harbors Coastal Eng. Div. Proc. ASCE* **100**: 217–239. [278, 288, 301]

Mei, C. C., and M. Naciri, (1991). Note on ship oscillations ad wake solitons. *Proc. Roy. Soc. Lond.* **A, 432**, 535–546. [817, 825]

Mei, C. C. and R. P. Petroni (1973). Waves in a harbor with protruding breakwaters. *J. Waterways Harbors Coastal Eng. Proc. ASCE* **99**: 209–229. [241, 247–249]

Mei, C. C. P. Sammarco, E.S. Chan and C. Procacciini, (1994). Subharmonic

resonance of proposed storm gates for Venice Lagoon. *Proc. Roy. Soc. Lond.*, **444**: 257–265. [426, 430]

Mei, C. C. and E. O. Tuck (1980). Forward scattering by thin bodies. *SIAM J. Appl. Math.* **39**: 178–191. [181, 185]

Mei, C. C. and Ü. Ünlüata (1978). Resonant scattering by a harbor with two coupled basins. *J. Eng. Math.* **10**: 333–353. [240, 252, 254]

Meyer, R. (1955). Symétrie du coefficient (complexe) de transmission de houles á travers un obstacle quelconque. *Houille Blanche* **10**: 139–140. [379]

Meyer, R. E. (1970). Resonance of unbounded water bodies. *Mathematical Problems in Geophysical Sciences. I*, *Geophysical Fluid Dynamics*, American Mathematical Society, Providence, R.I., 189–227. [176]

Meyer, R. E. (1979a). Theory of water-wave refraction. *Adv. Appl. Mech.* **19**: 53–141. [65]

Meyer, R. E. (1979b). Surface-wave reflection by underwater ridges. *J. Phys. Ocean.* **9**: 150–157. [157]

Miles, J. W. (1962). Transient gravity wave response to an oscillating pressure. *J. Fluid Mech.* **13**: 145–150. [61, 63]

Miles, J. W. (1967). Surface-wave damping in closed basins. *Proc. Soc. Lond. A* **297**: 459–475. [462]

Miles, J. W. (1971). Resonant response of harbors: An equivalent circuit analysis. *J. Fluid Mech.* **41**: 241–265. [238, 239]

Miles, J. W. (1972). Wave propagation across the continental shelf. *J. Fluid Mech.* **54**: 63–80. [161]

Miles, J. W. and P. G. Chamberlain. (1998). Topographical scattering of gravity waves. *J. Fluid Mech.* **361**: 175–188. [98]

Miles, J. W. and Y. K. Lee (1975). Helmholtz resonance of harbors. *J. Fluid Mech.* **67**: 445–464. [294]

Miles, J. W. and W. Munk (1961). Harbor paradox. *J. Waterways Harbors Div. Proc. ASCE* **87**: 111–130. [202, 222, 224, 227, 245]

Minzoni, A. A. and G. B. Whitham (1977). On the excitation of edge wave on beaches. *J. Fluid Mech.* **79**: 273–287. [174]

Momoi, T. Tsunami in the vicinity of a wave origin (I–IV) *Bull. Earthquake Res. Inst. Univ. Tokyo* I: (1964a). **42**: 133–146; II: (1964b). **42**: 369–381; III: (1965). **43**: 53–93; IV: (1965b). **43**: 755–772. [39]

Morse, P. M. and H. Feshbach (1953). *Methods of Theoretical Physics I and II*, McGraw-Hill, New York. [242, 456]

Morse, P. M. and K. U. Ingard (1968). *Theoretical Acoustics*, McGraw-Hill, New York. [284]

Mynett, A. E., D. D. Serman, and C. C. Mei (1979). Characteristics of Salter's cam for extracting energy from ocean waves. *Appl. Ocean Res.* **1**: 13–20. [394, 395, 409–411]

Nachbin, A. and G. C. Papanicolaou (1992). Water waves in shallow channels of rapidly varying depth. *J. Fluid Mech.* **241**: 311–332. [324]

Nachbin, A. (1997). The localization length of randomly scattered water waves. *J. Fluid Mech.* **296**: 353–372. [324]

Nayfeh, A. H. (1973). *Perturbation Methods*, Wiley, New York. [56, 82]

Newman, J. N. (1960). The exciting forces on fixed bodies in waves. *J. Ship Res.* **6**: 10–17. [383]

Newman, J. N. (1965). Propagation of water waves past long two-dimensional obstacles. *J. Fluid Mech.* **23**: 23–29. [379]

Newman, J. N. (1967). The drift force and moment on ships in waves. *J. Ship Res.* **11**: 51–60. [436]

Newman, J. N. (1974). Second-order, slowly-varying forces on vessels in irregular waves. *Proc. Int. Symp. on the Dynamics of Marine Vehicles and Structures in Waves*, Univ. College, London. [442]

Newman, J. N. (1975). Interaction of waves with two dimensional obstacles: A relation between the radiation and scattering problems. *J. Fluid Mech.* **71**: 273–282. [385]

Newman, J. N. (1976). The interaction of stationary vessels with regular waves. *Proc. 11th Symp. Naval Hydrodyn.*, Office of Naval Research 491–502. [375, 384, 387, 409, 412,]

Newman, J. N. (1979). Absorption of wave energy by elongated bodies. *Appl. Ocean Res.* **1**: 189–196. [412, 419, 424]

Ogawa, K . and K. Yoshida (1959). A practical method for a determination of long gravitational waves. *Records Oceangraphic Works Jap.* **5**: 38–50. [153]

Ogilvie, T. F. (1960). *Propagation of Waves Over an Obstacle in Water of Finite Depth*, University of California–Berkeley, Inst. Eng. Res. Report 82-14. [135]

Ogilvie, T. F. (1963). First and second order forces on a cylinder submerged under the free surface. *J. Fluid Mech.* **16**: 451–472. [405]

Ogilvie, T. F. (1964). Recent progress toward the understanding and prediction of ship motions. *Proc. 5th Symp. Naval Hydrodyn.*, Office of Naval Research 3–97. [442, 446]

Onorato, M., A. R. Osborne, M.Serio and S Bertone, (2001). Freak waves in random oceanic sea states. *Phys. Rev. Lett.* **86** : 5831-5834. [117]

Özsoy, E. (1977). Dissipation and wave scattering by narrow openings. Coastal and Oceang. Engineering Lab. University of Florida UFL/COEL/TR-037. [288–290]

Papoulis, A. (1968). *Systems and Transforms with Applications in Optics*, McGraw-Hill, New York. [46]

Pelinofsky, E., A. Razin and E.V. Sasorova, (1988). Berkhoff approximation in a problem on surface gravity waves propagation in a basin with bottom irregularities. *Waves in Random Media*, **8**: 255-258. [334]

Peregrine, D. H. (1976). Interaction of water waves and currents. *Adv. Appl. Mech.* **16**: 10–117. [65, 120]

Peregrine, D. H. and R. Smith (1975). Stationary gravity waves on non-uniform free streams. *Math. Proc. Cambridge Philos. Soc.* **77**: 415–438. [116]

Phillips, O. M. (1977). *Dynamics of the Upper Ocean*, 2nd ed., Cambridge University Press, London. [101, 482]

Pihl, J. H., C. C. Mei and M. J. Hancock (2002). Surface gravity waves over a two-dimensional random seabed. *Phys. Rev. E.* **66**: 016611 1-11. [307, 324, 333]

Pleass, C. M. (1978). The use of wave powered system for desalinization — A

new opportunity. *Proc. Symp. Wave Tidal Energy. 1*, Paper D1-1, BHRA. [403]

Pocinki, L. S. (1950). The application of conformal transformations to ocean wave refraction problems. *Trans. Am. Geophys. Union* **31**: 856–860. [74, 92, 93]

Porter, D. and D. V. Evans, (1999). Reyleigh-Bloch surface waves along periodic gratings and their connection with trapped modes in wave guides. *J. Fluid Mech.* **386**: 233–258. [427]

Porter, D. and D. J. Staziger (1995). Extensions of the mild-slope equation. *J. Fluid Mech.* **300**: 367–382. [98, 100]

Radder, A. C. (1979). On the parabolic equation method for water wave propagation. *J. Fluid Mech.* **95**: 159–176. [185]

Richey, E. P. and C. K. Sollitt (1969). Attenuation of deep water waves by a porous-walled breakwater. Dept. of Civil Engineering, University of Washington, Seattle, Technical Report 25. [277]

Risser, J. F. (1976). Transient Response in Harbors, Master of Science Thesis, Dept. of Civil Engineering, Massachusetts Institute of Technology. [262, 269, 270, 274]

Roseau, M. (1952). Contribution a la theorie des ondes liquides de gravite en profondeur variable. *Pub. Sci. Tech. Due Ministére de l'Air*, 275. [166]

Salter, S. (1974). Wave power. *Nature* **249**: 720–724. [404]

Salter, S. H. (1979). Recent progress on ducks. *Proc. 1st Symp. Wave Energy Utilization*, Chalmers Institute of Technology, Sweden, 36–76.[410]

Sammarco, P., H. Tran and C. C. Mei (1997a) Subharmonic resonance of Venice storm gates in waves. I. Evolution equation and uniform incident waves. *J. Fluid Mech.* **349**: 295–325. [426]

Sammarco, P., H. Tran, O. Gottlieb and C. C. Mei (1997b). Subharmonic resonance of Venice storm gates in waves. II. Sinusoidally modulated incident waves. *J. Fluid Mech.* **349**: 327–359. [426]

Sarpkaya, T. and M. St. Q. Issacson (1981). *Mechanics of Wave Forces on Offshore Structures*, Van Nostrand Reinold, New York. [277, 338, 387]

Schlichting, H. (1968). *Boundary Layer Theory*, 6th ed., McGraw-Hill, New York. [338]

Schonfeld, J. C. (1972) Propagation of Two Dimensional Short Waves. *Delft University of Technology Manuscript* (in Dutch). [96]

Serman, D. D. (1978). Theory of Salter's wave energy device in random sea. Master of Science Thesis, Dept. of Civil Engineering, Massachusetts Institute of Technology. [352, 442]

Seto, H. and Y. Yamamoto (1975). Finite element analysis of surface wave problems by a method of superposition. *Proc. Inst. Int. Conf. Num. Ship Hydrod.* David Taylor Naval Ship Res. and Devel. Center, 49–70. [393]

Shepard, F. P. (1963). *Submarine Geology*, 2nd ed., Harper and Row, New York. [35]

Siew, P. F. and D. G. Hurley (1977). Long surface waves incident on a submerged horizontal plate. *J. Fluid Mech.* **83**: 141-151. [142]

Simon, M. J. (1981). Wave energy extractions by submerged cylindrical resonant duct. *J. Fluid Mech.* **104**: 159–181. [405, 412]

Sitenko, A. G. (1971). *Lectures in Scattering Theory*, Pergamon, New York. [166]
Skovgaard, O., I. G. Jonsson, and J. A. Bertelsen (1976). Computation of wave heights due to refraction and friction. *J. Waterways Harbors and Coastal Eng. Div. ASCE* **102**: 100–105. [94]
Sleath, J. F. A. (1970). Velocity measurements close to the bed in a wave tank. *J. Fluid Mech.* **42**: Part I, 111–123.
Smith, J. D. and S. R. McLean (1977). Spatially averaged flow over a wavy surface. *J. Geophys. Res.* **82**: 1732–1746. [490]
Smith, R. (1976). Giant waves. *J. Fluid Mech.* **77**: 417–431. [116]
Smith, R. and T. Sprinks (1975). Scattering of surface waves by a conical island. *J. Fluid Mech.* **72**: 373–384. [96]
Sneddon, I. N. (1951), *Fourier Transforms*, McGraw-Hill, New York. [42]
Snodgrass, F. E., W. H. Munk, and G. R. Miller (1962). Long period waves over California's continental borderland, part I. Background spectra. *J. Marine Res.* **20**: 3–30. [157]
Srokosz, M. A. (1979). Some theoretical aspects of wave power absorption. Ph.D. Thesis, Dept. of Appl. Math., University of Bristol. [419, 420]
Srokosz, M. A. (1980). Some relations for bodies in a canal, with an application for wave power absorption. *J. Fluid Mech.* **99**: 145–162. [387]
Stoker, J. J. (1948). The formation of breakers and bores. *Comm. Pure Appl. Math.* **1**: 1–87. [59]
Stoker, J. J. (1956). On radiation conditions. *Comm. Pure Appl. Math.* **9**: 577–595. [59]
Stoker, J. J. (1957). *Water Waves*, Interscience, New York. [29, 447]
Stokes, G. G. (1847). On the theory of oscillatory waves. *Trans. Cambridge Philos. Soc.* **8**: 441–455. Reprinted in *Math. Phys. Papers*, Cambridge University Press, London, Vol. 1, 314–326. [174]
Susbielles, G. and Ch. Bratu (1981). *Vagues et Quvrages Pétroliers en Mer* Editions Technip 27, Paris. [387]
Tappert, F. D., (1977). The parabolic approximation. *Wave Propagation and Underwater Acoustics*, 224–287, eds. J. B. Keller and J. S. Papadakis, Springer-Verlag, Berlin. [181]
Terrett, F. L., F. D. C. Osorio, and G. H. Lean (1968). Model studies of a perforated breakwater. *Proc. 11th Conf. Coastal Eng. ASCE* 1104–1109. [278, 283]
Thomas, J. R. (1981). The absorption of wave energy by a three-dimensional submerged duct. *J. Fluid Mech.* **104**: 189–215. [412]
Tong, P. P., T. H. H. Pian, and S. J. Lasry (1973). A hybrid-element approach to crack problems in plane elasticity. *Int. J. Num. Methods Eng.* **7**: 297–308. [188]
Tong, P. and J. N. Rossettos (1976). *Finite Element Method*, M.I.T. Presi, Cambridge, Mass. [186]
Trulsen, K. and K. B. Dysthe (1997). Freak waves – A three-diimensional wave simulation. *Proc. 21st Symp. Naval Hydrod.* Natioal Academy Press, 550-560. [117]

Tuck, E. O. (1975). Matching problems involving flow through small holes. *Adv. Appl. Mech.* **15**: 90–158. [135, 239]

Tuck, E. O. (1976). Some classical water-wave problems in variable depth. *Waves on Water of Variable Depth*, eds. D. G. Provis and R. Radak, Lecture Notes in Physics No. 64, Springer-Verlag, New York. [138, 142]

Ünlüata, Ü. and C. C. Mei (1973). Long wave excitation in harbors — An analytic study. Dept. of Civil Engineering, Massachusetts Institute of Technology Technical Report 171. [222, 227, 236, 239, 240]

Ünlüata, Ü. and C. C. Mei (1975). Effects of entrance loss on harbor oscillations. *J. Waterways Harbors and Coastal Eng. Div. ASCE* **101**: 161–180. [294, 303]

Ünlüata, Ü. and C. C. Mei (1976). Resonant scattering by a harbor with two coupled basins. *J. Eng. Math.* **10**: 333–353. [254]

Ursell, F. (1950). Surface waves on deep water in the presence of a submerged circular cylinder. *Proc. Camb. Philo. Soc.* **46**: I: 141-152, II, 153-158. [405]

Ursell, F. (1952). Edge waves on a sloping beach. *Proc. R. Soc. Lond. A* **214**: 79–97. [174]

Ursell, F. (1964). The decay of the free motion of a floating body. *J. Fluid Mech.* **19**: 305–319. [449]

Varisco, D., (1992). Interaction between flap gates and tidal current and waves. *Proc. 23rd Int. Conf. Coastal Eng.*, Am. Soc. Civil Engrs. [426]

Vitale, P. (1979). Sand bed friction factors for oscillatory flows. *J. Waterways, Port Coastal Ocean Div. ASCE* **105**: 229–245. [489]

Vittori, G., (1997) Free and forced oscillations of a gate system proposed for the protection of Venice Lagoon: the discrete and dissipative model. *coatal Eng.* **31**: 37–56. [427]

Vittori, G., (1998). Oscillating tidal barriers and random waves. *J. Hydraulic Eng.* **124**: 406-412. [427]

Vittori, G., G. Seminara and P. Blondeaux, (1996). Waves of finite amplitude trapped by oscillating gates. *Proc. Roy. Soc. Lond.* **452**: 791–811. [427]

Wait, J. (1962). *Electromagnetic Waves in Stratified Media*, Pergamon, New York. [153]

Wehausen, J. V. (1967). Initial value problem for the motion in an undulating sea for a body with a fixed equilibrium position. *J. Eng. Math.* **1**: 1–19. [442, 446, 447, 449]

Wehausen, J. V. (1971). The motion of floating bodies. *Ann. Rev. Fluid Mech.* **3**: 237–268. [375]

Whitham, G. B. (1962). Mass, momentum and energy flux in water waves. *J. Fluid Mech.* **12**: 135–147. [101]

Whitham, G. B. (1965). Nonlinear dispersive waves. *Proc. R. Soc. Lond. A* **283**: 238–261. [33]

Wirt, L. and T. Higgins (1979). DAM-ATOLL: Ocean Wave Energy Extraction, *Marine Technology Society Meeting*, New Orleans, La., Oct. 11–12. [406]

Wooley, M. and J. Platts (1975). Energy on the crest of a wave. *New Scientist* **66**: 241–243. [405]

Wu, T. Y. (1957). Water waves generated by the translatory and oscillatory sur-

face disturbance. California Institute of Technology, Engineering Division Report No. 85-3. [60]

Yeung, R. W. (1975). A hybrid integral equation method for time-harmonic free surface flow. *Proc. 1st Int. Conf. Num. Ship Hydrodyn.* David Taylor Naval Ship Research and Development Center 581–607. [403]

Yeung, R. W. (1982). Numerical methods in free-surface flows. *Ann. Rev. Fluid Mech.* **14**: 395–442. [387, 403]

Yu, J., and C. C. Mei, (2000a). Do longshore bars protect the shore? *J. Fluid Mech.* **404**: 251–268. [321]

Yu, J., and C. C. Mei, (2000b). Formation of sand bars under surface waves. *J. Fluid Mech.* **416**: 315–348. [526]

Yue, D. K. P., H. S. Chen, and C. C. Mei (1976). Water wave forces on three-dimensional bodies by a hybrid element method. Parsons Laboratory, Dept. of Civil Engineering, Massachusetts Institute of Technology Technical Report 215. [188, 393, 398]

Yue, D. K. P., H. S, Chen, and C. C. Mei (1978). A hybrid element method for diffraction of water waves by three-dimensional bodies. *Int. J. Num. Methods Engineering* **12**: 245–266. [188]

Yue, D. K. P. and C. C. Mei (1980). Forward diffraction of Stokes waves by a thin wedge. *J. Fluid Mech.* **99**: 33–52. [181]

Zienkiewicz, O. C. (1971). *Finite Element Method in Engineering Science*, McGraw-Hill, New York. [186]

Subject Index

Advanced Series on Ocean Engineering — Volume 23

THEORY AND APPLICATIONS OF OCEAN SURFACE WAVES

Part 2: Nonlinear Aspects

Chiang C. Mei, Michael Stiassnie
& Dick K.-P. Yue

World Scientific

THEORY AND APPLICATIONS OF OCEAN SURFACE WAVES

Part 2: Nonlinear Aspects

ADVANCED SERIES ON OCEAN ENGINEERING

Series Editor-in-Chief
Philip L- F Liu (*Cornell University*)

Vol. 9 Offshore Structure Modeling
by Subrata K. Chakrabarti (Chicago Bridge & Iron Technical Services Co., USA)

Vol. 10 Water Waves Generated by Underwater Explosion
by Bernard Le Méhauté and Shen Wang (Univ. Miami)

Vol. 11 Ocean Surface Waves; Their Physics and Prediction
by Stanislaw R Massel (Australian Inst. of Marine Sci)

Vol. 12 Hydrodynamics Around Cylindrical Structures
by B Mutlu Sumer and Jørgen Fredsøe (Tech. Univ. of Denmark)

Vol. 13 Water Wave Propagation Over Uneven Bottoms
Part I — Linear Wave Propagation
by Maarten W Dingemans (Delft Hydraulics)
Part II — Non-linear Wave Propagation
by Maarten W Dingemans (Delft Hydraulics)

Vol. 14 Coastal Stabilization
by Richard Silvester and John R C Hsu (The Univ. of Western Australia)

Vol. 15 Random Seas and Design of Maritime Structures (2nd Edition)
by Yoshimi Goda (Yokohama National University)

Vol. 16 Introduction to Coastal Engineering and Management
by J William Kamphuis (Queen's Univ.)

Vol. 17 The Mechanics of Scour in the Marine Environment
by B Mutlu Sumer and Jørgen Fredsøe (Tech. Univ. of Denmark)

Vol. 18 Beach Nourishment: Theory and Practice
by Robert G. Dean (Univ. Florida)

Vol. 19 Saving America's Beaches: The Causes of and Solutions to Beach Erosion
by Scott L. Douglass (Univ. South Alabama)

Vol. 20 The Theory and Practice of Hydrodynamics and Vibration
by Subrata K. Chakrabarti (Offshore Structure Analysis, Inc., Illinois, USA)

Vol. 21 Waves and Wave Forces on Coastal and Ocean Structures
by Robert T. Hudspeth (Oregon State Univ., USA)

Vol. 22 The Dynamics of Marine Craft: Maneuvering and Seakeeping
by Edward M. Lewandowski (Computer Sciences Corporation, USA)

Vol. 23 Theory and Applications of Ocean Surface Waves
Part 1: Linear Aspects
Part 2: Nonlinear Aspects
by Chiang C. Mei (Massachusetts Inst. of Technology, USA), *Michael Stiassnie* (Technion–Israel Inst. of Technology, Israel) and *Dick K. P. Yue* (Massachusetts Inst. of Technology, USA)

Vol. 24 Introduction to Nearshore Hydrodynamics
by Ib A. Svendsen (Univ. of Delaware, USA)

Advanced Series on Ocean Engineering — Volume 23

THEORY AND APPLICATIONS OF OCEAN SURFACE WAVES

Part 2: Nonlinear Aspects

Chiang C. Mei
Ford Professor of Engineering
Massachusetts Institute of Technology, USA

Michael Stiassnie
David Hacohen and Hillel Dan Professor of Civil Engineering
Technion-Israel Institute of Technology, Israel

Dick K.-P. Yue
Professor of Mechanical and Ocean Engineering
Massachusetts Institute of Technology, USA

World Scientific

NEW JERSEY • LONDON • SINGAPORE • BEIJING • SHANGHAI • HONG KONG • TAIPEI • CHENNAI

Published by

World Scientific Publishing Co. Pte. Ltd.

5 Toh Tuck Link, Singapore 596224

USA office: 27 Warren Street, Suite 401-402, Hackensack, NJ 07601

UK office: 57 Shelton Street, Covent Garden, London WC2H 9HE

British Library Cataloguing-in-Publication Data
A catalogue record for this book is available from the British Library.

THEORY AND APPLICATIONS OF OCEAN SURFACE WAVES
Part 2: Nonlinear Aspects

ISBN 981-238-893-1 — Set
ISBN 981-256-156-0 — Part 1
ISBN 981-256-158-7 — Part 2

ISBN 981-238-894-X (pbk) — Set
ISBN 981-256-157-9 (pbk) — Part 1
ISBN 981-256-159-5 (pbk) — Part 2

Printed in Singapore.

To: Caroline Mei, Hadassa Stiassnie and Eva Yue

This page intentionally left blank

Preface to Part 2

This is Part Two of the expanded edition of *The Applied Dynamics of Ocean Surface Waves* first published in 1982 by Wiley-InterScience. In this volume our focus is on the nonlinear aspects of water waves, leaving the linear theories in Part One.

During the last quarter century, the most important advances have been on the effects of nonlinearity, the perennial hallmark of water-wave dynamics. In comparison with the original edition, this volume now contains several new sections, two new chapters as well as new exercises. In Chapter 12 on nonlinear long waves in shallow water, we have now added a discussion on the radiation of upstream solitons when a slender-body moves in a shallow channel at a speed near the speed $\sqrt{gh}$ of the shallow-water waves. This phenomenon demonstrates that steady forcing can yield unsteady motion when nonlinearity is involved. Another new section treats the evolution of a soliton propagating over a randomly rough seabed, as a sequel to the linearlized problem for a sinusoidal wavetrain over a rough seabed of finite depth. The combined effects of localization and nonlinearity are analyzed as a first step toward the more complicated random scattering of a transient tsunami. This topic should be further developed for wave-forecasting models for coastal seas.

In Chapter 13 on weakly nonlinear narrow-banded waves in finite depth or deep water, we have added new material on the theory of infragravity waves which are long waves generated by short-wave groups. This topic is of interest to surf-beats and harbor resonance. As an application of the famed nonlinear Schrödinger equation for the wave envelope, we discuss a problem stimulated by the satellite sensing of long and narrow wakes, i.e., the presence of soliton envelopes in the wake of a ship. Finally the analytical theory of nonlinear diffraction by a large cylinder, a problem which was

not solved satisfactorily at the time of the first edition, is described at the end.

One of the two major additions is Chapter 14 (by M. Stiassnie) on the nonlinear dynamics of broad-banded surface waves, an important topic which is at the core of modern wave forecasting but was not dealt with in the original edition. Enormous advances have taken place in the last two or three decades in the nonlinear wave-wave interactions of broad spectra. In particular the celebrated mechanism of quartet resonance due to O. M. Phillips and the kinetic equation of Klaus Hasselmann are the foundations of current wave-forcasting models. Although originated from different angles, these ingredients can be unified by the powerful theory of weak turbulence due to V. E. Zakharov. The mathematics involved in Zakharov's theory is rather daunting. In view of its importance, we have presented a detailed discussion of its essentials in order to provide a gateway for newcomers to the field.

Despite the many theoretical developments, computational tools have become indispensable to comprehensive understanding and practical applications of nonlinear waves dynamics. In Chapter 15 (by D. K.-P. Yue), we present an extensive survey of two powerful methods for nonlinear wave-wave and wave-body interaction problems: the high-order spectral method and its variations, and the mixed-Eulerian-Lagrangian method. For each of the methods, the theoretical development and numerical implementation are described in detail, and the scope and efficacy in applications are illustrated in specific examples. The high-order spectral method is based on a Zakharov-equation mode-coupling perturbation idea but generalized in a direct computational framework to handle high nonlinear orders and very large numbers of (free) wave modes. Using (global) spectral basis functions and a pseudo-spectral approach exploiting fast transform techniques, the method obtains near linear computational effort and exponential convergence with perturbation order and number of wave modes. Applications of the method are presented for nonlinear evolutions of wave trains and groups and ship wakes, and nonlinear interactions of surface waves with currents, with bottom ripples, and with submerged bodies. For complex geometries, we present a versatile extension of the method, the high-order spectral element method, that require only element rather than global basis functions. As example, application of this method to the study of instability of nonlinear standing wave in a tank is given. The mixed-Eulerian-Lagrangian method is a useful method for steep and even overturning waves. The method obtains the nonlinear evolution of the free surface by following

surface Lagrangian point and solves the field equation using a boundary-integral equation formulation in the Eulerian flow variables. Development of the method and illustrative applications in two and three dimensions are presented. The latter include two- and three-dimensional plunging breaking waves, development of steep crescent waves, withdrawal from a submerged sink, plunging wave impact on a wall, and high-frequency nonlinear diffraction forces on a vertical cylinder in waves.

Among the major areas where significant progresses have been made but are not covered in this edition, we mention in particular the surf zone dynamics. A few key references are added at the end of Chapter 11. The topic of the wave-induced stresses in a poroelastic seabed, which was described in the last chapter of the old edition, has been deleted in the present edition.

Many challenges remain in the nonlinear physics and mathematics of water waves, and in the interactions of water waves with their surroundings. For example, we are still far from the full understanding and prediction of breaking waves. The complex interactions of surface waves with the atmosphere and with erodible seabeds await the combined efforts of researchers from several disciplines. The catastrophic Indian Ocean tsunami on December 26, 2004 highlights the urgent needs for reliable modelling of the nonlinear processes of wave runup and rundown along the coast. Improvements of tsunami warning systems and plans for evacuation can only come from better theories for forcasting or estimating disasters from the sea waves. It is the hope of the authors that this book can help stimulate greater efforts by fellow researchers and future students, not only to overcome old challenges, but also to open new vistas of both theory and applications.

Chiang C. Mei, Cambridge, Massachusetts, USA.
Michael Stiassnie, Haifa, Israel.
Dick K. P. Yue, Cambridge, Massachusetts, USA.

This page intentionally left blank

Contents

Part 2

This page intentionally left blank

Mass Transport Due to Viscosity

10

10.1 Introduction

In addition to pure fluctuations, waves can induce currents which do not change their directions during a time long in comparison with a wave period. Although the current velocity is often weak, its persistence can result in the transport of bottom sediments. In order to understand the changes of the sea bottom, it is necessary to acquire a good understanding of currents generated by waves.

Two different types of currents that owe their existence to wave fluctuations are of interest to us. In this chapter we examine the *mass transport* within the boundary layer near the sea bottom when the wave field above is essentially inviscid and irrotational. In the next chapter we shall examine the longshore current and its variations in and near the surf (breaking) zone of a gently sloping shore. In both cases the driving mechanism is the steady momentum flux due to the convective inertia of the waves, and dissipation plays a central role in maintaining the steady drift.

It was first discovered in acoustics that steady currents could be induced near a solid wall adjacent to an oscillating fluid. This phenomenon of *acoustic streaming* makes standing waves in tubes visible by the accumulation of dust particles at the nodes. Rayleigh (1883) first analyzed the phenomenon theoretically and determined Eulerian streaming in the boundary layer. Extension to water waves propagating in one direction was made by Longuet–Higgins (1953) who pointed out that Stokes drift had to be added to Eulerian streaming velocity in order to find the particle (Lagrangian) drift which is now known as the *mass transport velocity*. Hunt and Johns (1963) deduced formulas for the induced Eulerian streaming in

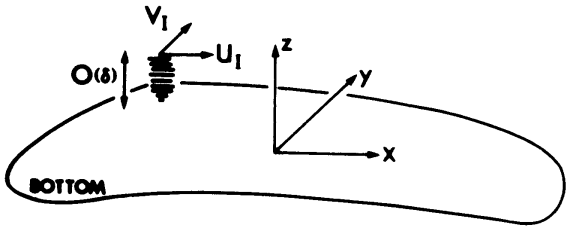

Figure 10.1: Local coordinates near the bottom.

two-dimensional waves and for Lagrangian drift at the outer edge of the boundary layer. Carter, Liu, and Mei (1973) gave Lagrangian drift throughout the boundary layer. While all of the theories above have been based on the assumption of constant viscosity, Longuet–Higgins (1958) and Johns (1970) have proposed theories of vertically varying eddy viscosity. Because of our incomplete knowledge of the turbulent boundary layer and because the variable eddy viscosity theory has not produced qualitatively different results, we shall only discuss the model of constant viscosity in this chapter.

10.2 Mass Transport Near the Sea Bottom — General Theory

It is convenient to adopt a local coordinate system (x, y, z) with x, y in the plane of the boundary layer and z pointing normally into the inviscid region as shown in Fig. 10.1. For small bottom slopes, z is nearly in the vertical direction. By continuity, the normal velocity component w is small so that w/u and $w/v = O(k\delta)$, where k is the typical wavenumber and δ is the boundary-layer thickness. Let A be the typical orbital amplitude near the bottom, then

$$\frac{\nu(\partial^2/\partial x^2 + \partial^2/\partial y^2)\begin{bmatrix} u \\ v \end{bmatrix}}{\frac{\partial}{\partial t}\begin{bmatrix} u \\ v \end{bmatrix}} \sim O(k\delta)^2\,, \quad \frac{(u\frac{\partial}{\partial x} + v\frac{\partial}{\partial y})\begin{bmatrix} u \\ v \end{bmatrix}}{\frac{\partial}{\partial t}\begin{bmatrix} u \\ v \end{bmatrix}} \sim O(kA)\,.$$

As long as $1 \gg kA \gg (k\delta)^2$, Navier–Stokes equations can be approximated by

$$\frac{\partial u}{\partial x} + \frac{\partial v}{\partial y} + \frac{\partial w}{\partial z} = 0\,, \tag{10.2.1a}$$

$$\frac{\partial u}{\partial t} + u\frac{\partial u}{\partial x} + v\frac{\partial u}{\partial y} + w\frac{\partial u}{\partial z} = -\frac{1}{\rho}\frac{\partial P}{\partial x} + \nu\frac{\partial^2 u}{\partial z^2}\,, \tag{10.2.1b}$$

$$\frac{\partial v}{\partial t} + u\frac{\partial v}{\partial x} + v\frac{\partial v}{\partial y} + w\frac{\partial v}{\partial z} = -\frac{1}{\rho}\frac{\partial P}{\partial x} + \nu\frac{\partial^2 v}{\partial z^2}\,, \tag{10.2.1c}$$

$$0 = -\frac{1}{\rho}\frac{\partial P}{\partial z} - g\,. \tag{10.2.1d}$$

In the last equation of vertical momentum, we have ignored terms of the order $O(k\delta)$. Thus, $p = P - \rho g z$ does not vary in the direction normal to the boundary layer and must be the same as its value in the inviscid flow field just outside. Consequently,

$$-\frac{1}{\rho}\frac{\partial p}{\partial x} = \frac{\partial U_I}{\partial t} + U_I\frac{\partial U_I}{\partial x} + V_I\frac{\partial U_I}{\partial y}\,, \tag{10.2.2a}$$

$$-\frac{1}{\rho}\frac{\partial p}{\partial y} = \frac{\partial V_I}{\partial t} + U_I\frac{\partial V_I}{\partial x} + V_I\frac{\partial V_I}{\partial y}\,, \tag{10.2.2b}$$

where U_I and V_I are the tangential components of the inviscid velocity field at the wall, with W_I being zero. In this section U_I and V_I are assumed to be prescribed. Let the total velocity components in the boundary layer u and v be expanded as a perturbation series with kA as the implied small parameter:

$$u = u_1 + u_2 + \cdots \tag{10.2.3a}$$

$$v = v_1 + v_2 + \cdots \tag{10.2.3b}$$

where $u_1 = O(\omega A)$ and $u_2 = O(\omega k A^2)$, and so on. At the first order, Eqs. (10.2.1b) and (10.2.1c) give

$$\frac{\partial u_1}{\partial t} = \frac{\partial U_I}{\partial t} + \nu\frac{\partial^2 u_1}{\partial z^2}\,, \tag{10.2.4a}$$

$$\frac{\partial v_1}{\partial t} = \frac{\partial V_I}{\partial t} + \nu\frac{\partial^2 v_1}{\partial z^2}\,. \tag{10.2.4b}$$

The boundary conditions are

$$(u_1, v_1) = 0 \qquad \text{on} \quad z = 0\,, \tag{10.2.5}$$

$$(u_1, v_1) \to U_I, V_I\,, \quad \frac{z}{\delta} \gg 1\,. \tag{10.2.6}$$

For simple harmonic motion, we write

$$U_I(x,y,t) = \mathrm{Re}[U_0(x,y)e^{-i\omega t}] \tag{10.2.7a}$$

$$V_I(x,y,t) = \mathrm{Re}[V_0(x,y)e^{-i\omega t}]\,. \tag{10.2.7b}$$

Since x and y are just parameters in the boundary-value problem, u_1 and v_1 are again given by the Stokes solution:

$$\begin{pmatrix} u_1 \\ v_1 \end{pmatrix} = \mathrm{Re}\left[\begin{pmatrix} U_0 \\ V_0 \end{pmatrix} F_1(\xi)e^{-i\omega t}\right], \tag{10.2.8}$$

where F_1 is given by $F_1 = 1 - e^{-(1-i)\xi}$, $\xi = z/\delta$. From the continuity equation, the normal component is found to be

$$\begin{aligned} w_1 &= -\delta \int_0^\xi d\xi \left(\frac{\partial u_1}{\partial x} + \frac{\partial v_1}{\partial y}\right) \\ &= -\delta\ \mathrm{Re}\left\{\left(\frac{\partial U_0}{\partial x} + \frac{\partial V_0}{\partial y}\right) e^{-i\omega t} \int_0^\xi F_1(\xi)\,d\xi\right\} \\ &= \mathrm{Re}\left\{\delta\left(\frac{\partial U_0}{\partial x} + \frac{\partial V_0}{\partial y}\right) e^{-i\omega t}\left[\frac{1+i}{2}[1 - e^{-(1-i)\xi}] - \xi\right]\right\}. \end{aligned} \tag{10.2.9}$$

Although w_1 is of the order $O(k\delta)$ times u_1 and v_1, which is insignificant by itself, its effects through the terms $w_1\partial u_1/\partial z$ and $w_1\partial v_1/\partial z$ are as important as the other convection terms and cannot be overlooked. Now at the next order, the equations are

$$\begin{aligned} \frac{\partial u_2}{\partial t} - \nu\frac{\partial^2 u_2}{\partial z^2} &= U_I\frac{\partial U_I}{\partial x} + V_I\frac{\partial U_I}{\partial y} \\ &\quad - \left(u_1\frac{\partial u_1}{\partial x} + v_1\frac{\partial u_1}{\partial y} + w_1\frac{\partial u_1}{\partial z}\right), \end{aligned} \tag{10.2.10a}$$

$$\begin{aligned} \frac{\partial v_2}{\partial t} - \nu\frac{\partial^2 v_2}{\partial z^2} &= U_I\frac{\partial V_I}{\partial x} + V_I\frac{\partial V_I}{\partial y} \\ &\quad - \left(u_1\frac{\partial v_1}{\partial x} + v_1\frac{\partial v_1}{\partial y} + w_1\frac{\partial v_1}{\partial z}\right). \end{aligned} \tag{10.2.10b}$$

Equations (10.2.10a) and (10.2.10b) can be used to obtain the complete second-order velocity field. Because the forcing terms on the right of Eqs. (10.2.10a) and (10.2.10b) contain zeroth and second harmonics, we

must expect that u_2 and v_2 contain the same harmonics in response, that is,

$$u_2 = \bar{u}_2 + \mathrm{Re}\,\tilde{u}_2 e^{-2i\omega t}\,, \quad v_2 = \bar{v}_2 + \mathrm{Re}\,\tilde{v}_2 e^{-2i\omega t}\,, \tag{10.2.11}$$

where $\bar{u}_2$ and $\bar{v}_2$ do not vary with time and are referred to as the *induced-streaming* velocities. In the terminology of electrical circuits, $\bar{u}_2$ and $\bar{v}_2$ are the DC (direct current) as opposed to the time-varying AC (alternating current) components. While the AC parts $\tilde{u}_2$ and $\tilde{v}_2$ modify the oscillatory velocity field, their influence is overshadowed by u_1 and v_1. The components $\bar{u}_2$ and $\bar{v}_2$ are new, however, and are the leading contribution to the steady motion. Although small, they are responsible for the steady drifting of fluid particles after many periods. Let us concentrate on these mean values by taking the averages of (10.2.10a) and (10.2.10b):

$$\begin{aligned} -\nu\frac{\partial^2 \bar{u}_2}{\partial z^2} &= \overline{U_I\frac{\partial U_I}{\partial x}} + \overline{V_I\frac{\partial U_I}{\partial y}} \\ &\quad - \left(\overline{u_1\frac{\partial u_1}{\partial x}} + \overline{v_1\frac{\partial u_1}{\partial y}} + \overline{w_1\frac{\partial u_1}{\partial z}}\right), \end{aligned} \tag{10.2.11a}$$

$$\begin{aligned} -\nu\frac{\partial^2 \bar{v}_2}{\partial z^2} &= \overline{U_I\frac{\partial V_I}{\partial x}} + \overline{V_I\frac{\partial V_I}{\partial y}} \\ &\quad - \left(\overline{u_1\frac{\partial v_1}{\partial x}} + \overline{v_1\frac{\partial v_1}{\partial y}} + \overline{w_1\frac{\partial v_1}{\partial z}}\right). \end{aligned} \tag{10.2.11b}$$

Before proceeding further let us use the continuity equation for $\mathbf{u}_1$ to rewrite

$$u_{1i}\frac{\partial}{\partial x_i}u_{1j} = \frac{\partial}{\partial x_i}(u_{1i}u_{1j})\,, \quad i = 1,2,3\,,$$

thus

$$\begin{aligned} -\nu\frac{\partial^2 \bar{u}_2}{\partial z^2} &= \overline{U_I\frac{\partial U_I}{\partial x}} + \overline{V_I\frac{\partial U_I}{\partial y}} \\ &\quad - \left(\frac{\partial}{\partial x}\overline{u_1u_1} + \frac{\partial}{\partial y}\overline{u_1v_1} + \frac{\partial}{\partial z}\overline{u_1w_1}\right), \end{aligned} \tag{10.2.12a}$$

$$\begin{aligned} -\nu\frac{\partial^2 \bar{v}_2}{\partial z^2} &= \overline{U_I\frac{\partial V_I}{\partial x}} + \overline{V_I\frac{\partial V_I}{\partial y}} \\ &\quad - \left(\frac{\partial}{\partial x}\overline{u_1v_1} + \frac{\partial}{\partial y}\overline{v_1v_1} + \frac{\partial}{\partial z}\overline{v_1w_1}\right). \end{aligned} \tag{10.2.12b}$$

The terms $\overline{u_1 u_1}$, $\overline{u_1 v_1}$, and so forth, are just the components of the Reynolds stress tensor representing momentum fluxes due to wave fluctuations. The physical picture is now clear, that is, the mean streaming current $(\bar{u}_2, \bar{v}_2)$ arises because a mean shear stress field must be present in order to balance the mean dynamic pressure field and the Reynolds stress field. Equations (10.2.12a) and (10.2.12b) may be integrated straightforwardly with the boundary conditions that there be no velocity at the wall and no stress at the outer edge of the boundary layer,

$$(\bar{u}_2,\, \bar{v}_2) \,=\, 0\,, \quad z = 0\,; \tag{10.2.13a}$$

$$\frac{\partial}{\partial z}(\bar{u}_2,\, \bar{v}_2) \to 0\,, \quad \frac{z}{\delta} \to \infty\,. \tag{10.2.13b}$$

After some algebra, the following results are obtained:

$$\bar{u} = \bar{u}_2 = -\frac{1}{\omega}\ \mathrm{Re}\left[F_2 U_0 \frac{\partial U_0^*}{\partial x} + F_3 V_0 \frac{\partial U_0^*}{\partial y} + F_4 U_0 \frac{\partial V_0^*}{\partial y}\right], \tag{10.2.14a}$$

$$\bar{v} = \bar{v}_2 = -\frac{1}{\omega}\ \mathrm{Re}\left[F_2 V_0 \frac{\partial V_0^*}{\partial y} + F_3 U_0 \frac{\partial U_0^*}{\partial x} + F_4 V_0 \frac{\partial U_0^*}{\partial x}\right], \tag{10.2.14b}$$

where U_0 and V_0 are the amplitudes of U_I and V_I as defined in Eq. (10.2.7), and

$$\begin{aligned} F_2 = {} & -\frac{1}{2}(1-3i)e^{(-1+i)\xi} - \frac{i}{2}e^{-(1+i)\xi} - \frac{1+i}{4}e^{-2\xi} \\ & + \frac{1}{2}(1+i)\xi e^{(-1+i)\xi} + \frac{3}{4}(1-i)\,, \end{aligned} \tag{10.2.15a}$$

$$F_3 = \frac{1}{2}ie^{(-1+i)\xi} - \frac{i}{2}e^{-(1+i)\xi} - \frac{1}{4}e^{-2\xi} + \frac{1}{4}\,, \tag{10.2.15b}$$

$$\begin{aligned} F_4 = {} & -\frac{1}{2}(1-2i)e^{(-1+i)\xi} + \frac{1+i}{2}\xi e^{-(1-i)\xi} \\ & - \frac{i}{4}e^{-2\xi} + \frac{1}{4}(2-3i)\,. \end{aligned} \tag{10.2.15c}$$

The present two-dimensional formulas were first derived by Hunt and Johns (1963).

The results just given are Eulerian streaming velocities. To infer the motion of a marked fluid particle, it is necessary to calculate Lagrangian velocity. Let $\mathbf{x}(\mathbf{x}_0, t)$ be the position of the particle which was at point $\mathbf{x}_0$ when $t = t_0$, namely,

$$\mathbf{x}(\mathbf{x}_0, t_0) = \mathbf{x}_0 \,.$$

At any subsequent time t, the position and velocity of the particle are related by

$$\frac{d\mathbf{x}}{dt} \equiv \mathbf{u}_L(\mathbf{u}_0, t) \tag{10.2.16}$$

where $\mathbf{u}_L$ denotes Lagrangian velocity of the particle. When a particle arrives at $\mathbf{x}$ at the time t, its Lagrangian velocity must be the same as its Eulerian velocity $\mathbf{u}(\mathbf{x}, t)$, that is,

$$\mathbf{x}_L(\mathbf{x}_0, t) = \mathbf{u}(\mathbf{x}, t) \,.$$

From Eq. (10.2.16), the particle position at time t is

$$\mathbf{x} = \mathbf{x}_0 + \int_{t_0}^{t} dt' \mathbf{u}_L(\mathbf{x}_0, t') \,,$$

so that

$$\mathbf{u}_L(\mathbf{x}_0, t) = \mathbf{u}\left[\mathbf{x}_0 + \int_{t_0}^{t} dt' \mathbf{u}_L(\mathbf{x}_0, t'), t\right] .$$

For sufficiently small $t - t_0$ (say within a few periods), the integral, being the particle displacement, is of the order $O(A)$ and is comparable to the orbital size. Hence, we may expand $\mathbf{u}$ as a Taylor series:

$$\begin{aligned} \mathbf{u}_L(\mathbf{x}_0, t) &\simeq \mathbf{u}(\mathbf{x}_0, t) + (\mathbf{x} - \mathbf{x}_0) \cdot \nabla_0 \mathbf{u}(\mathbf{x}_0, t) + \cdots \\ &\simeq \mathbf{u}(\mathbf{x}_0, t) + \left[\int_{t_0}^{t} dt' \mathbf{u}_L(\mathbf{x}_0, t')\right] \cdot \nabla_0 \mathbf{u}(\mathbf{x}_0, t) + \cdots \,, \end{aligned}$$

where $\nabla_0 = (\partial/\partial x_0, \partial/\partial y_0, \partial/\partial z_0)$. Clearly, to the first order $\mathbf{u}_L$ and $\mathbf{u}$ are the same so that we may replace $\mathbf{u}_L$ by $\mathbf{u}$ in the integral with second-order accuracy. The streaming velocity is

$$\bar{\mathbf{u}}_L(\mathbf{x}_0, t) = \bar{\mathbf{u}}(\mathbf{x}_0, t) + \overline{\left[\int_{t_0}^{t} dt' \mathbf{u}(\mathbf{x}_0, t')\right] \cdot \nabla_0 \mathbf{u}(\mathbf{x}_0, t)} + \cdots \,. \tag{10.2.17}$$

Thus, for sufficiently small time, the particle velocity is equal to its initial velocity plus a correction due to the fact that the particle moves in an environment where the velocity field varies. The correction is proportional to the distance traveled and to the spatial rate of change of the local velocity field. Now $\bar{\mathbf{u}} = \bar{\mathbf{u}}_2$ and the quadratic terms are both of second order; hence, in the second term $\mathbf{u}$ may be approximated by $\mathbf{u}_1$. Finally, since all spatial

variables are $\mathbf{x}_0$, the subscripts $(\ )_0$ may be dropped. The components of $\bar{\mathbf{u}}_L$ are then

$$\bar{u}_L = \bar{u}_2 + \overline{\left(\int^t u_1\,dt'\right)\frac{\partial u_1}{\partial x}} + \overline{\left(\int^t v_1\,dt'\right)\frac{\partial u_1}{\partial y}} + \overline{\left(\int^t w_1\,dt'\right)\frac{\partial u_1}{\partial z}}\,, \tag{10.2.18a}$$

$$\bar{v}_L = \bar{v}_2 + \overline{\left(\int^t u_1\,dt'\right)\frac{\partial v_1}{\partial x}} + \overline{\left(\int^t v_1\,dt'\right)\frac{\partial v_1}{\partial y}} + \overline{\left(\int^t w_1\,dt'\right)\frac{\partial v_1}{\partial z}}\,; \tag{10.2.18b}$$

the lower limits of integration are immaterial. Equations (10.2.18a) and (10.2.18b) give the components of the *mass transport velocity* of a marked fluid particle which is located at (x, y, z) at time t.

The difference between Lagrangian and Eulerian drifts is represented by the integral terms above, or in vector form, by

$$\overline{\left[\int^t \mathbf{u}_1(\mathbf{x}, t')\,dt'\right]\cdot\nabla\mathbf{u}_1(\mathbf{x}, t)}\,, \tag{10.2.19}$$

which is known as *Stokes' drift*.

With the known expressions of u_1, v_1, and w_1 in Eqs. (10.2.8) and (10.2.9), various terms in Stokes' drift can be evaluated

$$\overline{\left(\int^t u_1\,dt'\right)\frac{\partial u_1}{\partial x}} = \mathrm{Re}\,\frac{1}{2\omega}\left\{U_0\frac{\partial U_0^*}{\partial x}[1 - e^{-(1-i)\xi} - e^{-(1+i)\xi} + e^{-2\xi}]\right\},$$

$$\overline{\left(\int^t v_1\,dt'\right)\frac{\partial u_1}{\partial y}} = \mathrm{Re}\,\frac{1}{2\omega}\left\{V_0\frac{\partial U_0^*}{\partial y}[1 - e^{-(1-i)\xi} - e^{-(1+i)\xi} + e^{-2\xi}]\right\},$$

$$\overline{\left(\int^t w_1\,dt'\right)\frac{\partial u_1}{\partial z}} = \mathrm{Re}\,\frac{1}{2\omega}\left\{\left[U_0\frac{\partial U_0^*}{\partial x} + U_0\frac{\partial V_0^*}{\partial y}\right]\right.$$

$$\left.\times\,[e^{-2\xi} - e^{-(1-i)\xi} + (1+i)\xi e^{-(1-i)\xi}]\right\}.$$

The other terms may be obtained by interchanging u_1 and v_1. Combining Stokes' with Eulerian mean drift, we finally obtain Lagrangian mass transport velocities:

$$\bar{u}_L = \frac{1}{4\omega}\,\mathrm{Re}\left\{F_5 U_0 \frac{\partial U_0^*}{\partial x} + F_6 V_0 \frac{\partial U_0^*}{\partial y} + F_7 U_0 \frac{\partial V_0^*}{\partial y}\right\}, \tag{10.2.20a}$$

$$\bar{v}_L = \frac{1}{4\omega}\,\mathrm{Re}\left\{F_5 V_0 \frac{\partial V_0^*}{\partial y} + F_6 U_0 \frac{\partial V_0^*}{\partial x} + F_7 V_0 \frac{\partial U_0^*}{\partial x}\right\}, \tag{10.2.20b}$$

where

$$F_5 = -8ie^{-(1-i)\xi} + 3(1+i)e^{-2\xi} - 3 + 5i\,, \tag{10.2.21a}$$

$$F_6 = -4ie^{-(1-i)\xi} + (1+2i)e^{-2\xi} - 1 + 2i\,, \tag{10.2.21b}$$

$$F_7 = -4ie^{-(1-i)\xi} + (2+i)e^{-2\xi} - 2 + 3i\,. \tag{10.2.21c}$$

These formulas were derived by Carter, Liu, and Mei (1973) from Hunt and Johns (1963). In particular, at the outer edge of the boundary layer

$$F_5 \to -3 + 5i\,, \quad F_6 \to -1 + 2i\,, \quad F_7 \to -2 + 3i\,,$$

so that the mass transport velocity at $z \gg \delta$ is

$$\bar{u}_L = -\frac{1}{4\omega}\,\mathrm{Re}\left[3U_0\frac{\partial U_0^*}{\partial x} + V_0\frac{\partial V_0^*}{\partial y} + 2U_0\frac{\partial V_0^*}{\partial y} - i\left(5U_0\frac{\partial U_0^*}{\partial x} + 3U_0\frac{\partial V_0^*}{\partial y} + 2V_0\frac{\partial U_0^*}{\partial y}\right)\right], \tag{10.2.22a}$$

$$\bar{v}_L = -\frac{1}{4\omega}\,\mathrm{Re}\left[3V_0\frac{\partial V_0^*}{\partial y} + U_0\frac{\partial V_0^*}{\partial y} + 2V_0\frac{\partial U_0^*}{\partial x} - i\left(5V_0\frac{\partial U_0^*}{\partial y} + 3V_0\frac{\partial U_0^*}{\partial x} + 2U_0\frac{\partial V_0^*}{\partial x}\right)\right] \tag{10.2.22b}$$

(Hunt and Johns, 1963). The one-dimensional version for $u \neq 0$ and $v = 0$ was first given by Longuet–Higgins (1953). Thus far, Eqs. (10.2.20) and (10.2.21) are applicable to any oscillatory flows, water waves being a special case.

Although the mass transport velocities owe their existence to viscosity, their limits at the outer edge of the boundary layer do not depend on ν. Also, as soon as the inviscid wave field is known, it is, in principle,

a straightforward matter of numerical differentiation to obtain the mass transport in the boundary layer. We now study two special cases and their possible qualitative implications on sediment transport.

10.3 Bottom Mass Transport Under a Long Crested Wave

Consider a wave system described by

$$\zeta = \mathrm{Re}\, A[e^{-i(kx+\omega t)} + R\, e^{i(kx-\omega t)}]\,, \tag{10.3.1}$$

which represents the sum of an incident wave and a reflected wave, R being the reflection coefficient. Without loss of generality we may take A and R to be real since the phase of a complex R may be eliminated by redefining x. The corresponding velocity potential is

$$\Phi = \mathrm{Re}\left[-\frac{igA}{\omega}\frac{\cosh k(z+h)}{\cosh kh}(e^{-ikx} + Re^{ikx})e^{-i\omega t}\right]. \tag{10.3.2}$$

This potential includes the standing waves as a special case ($R = 1$) and may also be applied to shoaling waves on a mildly sloping beach if R is taken to be zero and kx is replaced by $\int k\, dx$. At the sea bottom $z = -h$, the inviscid tangential velocity is

$$\begin{aligned} U_I &= \mathrm{Re}\, U_0 e^{-i\omega t} = \Phi_x(x, -h, t)\,, \\ &= \mathrm{Re}\left[-\frac{-\omega A}{\sinh kh}(e^{-ikx} - Re^{ikx})e^{-i\omega t}\right], \quad V_I = 0 \end{aligned} \tag{10.3.3}$$

hence,

$$U_0 = \frac{-\omega A}{\sinh kh}(e^{-ikx} - Re^{ikx})\,, \quad V_0 = 0\,. \tag{10.3.4}$$

Lagrangian mass transport in the boundary layer follows from Eqs. (10.2.20a) and (10.2.21a)

$$\begin{aligned} \bar{u}_L &= \mathrm{Re}\left(\frac{1}{4\omega}F_5 U_0 \frac{\partial U_0^*}{\partial x}\right) \\ &= \frac{k\omega A^2}{4\sinh^2 kh}[(1-R^2)(8e^{-\xi}\cos\xi - 3e^{-2\xi} - 5) \\ &\quad + 2R\sin 2kx(8e^{-\xi}\sin\xi - 3e^{-2\xi} - 3)]\,, \end{aligned} \tag{10.3.5}$$

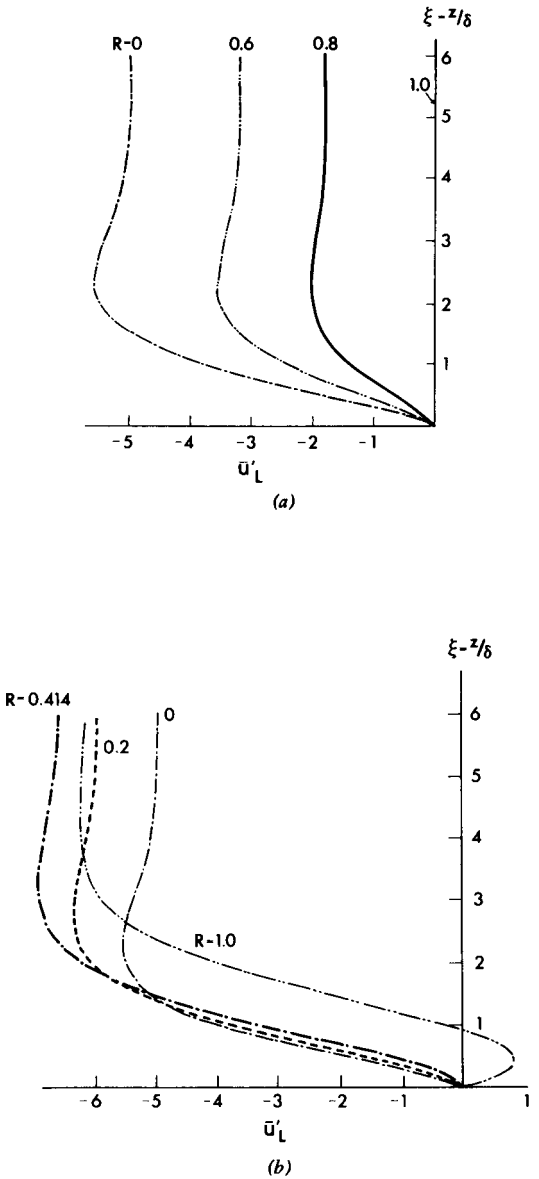

Figure 10.2: Mass transport profile within Stokes boundary layer near the bottom for various instants and reflection coefficients. Envelope maxima are at $2kx = 0$ and 2π and envelope minima at $2kx = \pi$. Dimensionless $\bar{u}'_L = \bar{u}_L(4\sinh^2 kh/\omega kA^2)$. (*a*) $2kx = 0$, (*b*) $2kx = \frac{\pi}{2}$; (*c*) $2kx = \frac{3}{2}\pi$ (from Carter et al., 1973, *J. Waterway, Port, Coastal and Ocean Div.* Reproduced by permission of American Society of Civil Engineers).

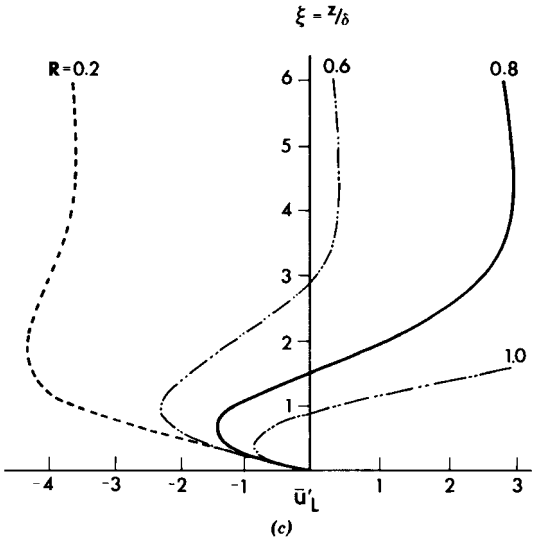

Figure 10.2: (*Continued*)

which is due to Longuet–Higgins (1953). For several values of R the profiles of $\bar{u}_L$ are shown in Figs. 10.2(a)–10.2(c).

The special case of a purely progressive wave corresponds to $R = 0$:

$$\bar{u}_L = \frac{k\omega A^2}{4\sinh^2 kh}(8e^{-\xi}\cos\xi - 3e^{-2\xi} - 5)\,, \tag{10.3.6}$$

which varies monotonically from zero at $\xi = 0$ to

$$\bar{u}_L(\infty) = -\frac{5k\omega A^2}{4\sinh^2 kh} \quad \text{as} \quad \xi \to \infty\,. \tag{10.3.7}$$

On the other hand, in front of a long and straight sea wall the reflection is nearly complete so that $R = 1$. In this case

$$\bar{u}_L = \frac{k\omega A^2}{4\sinh^2 kh} 2\,\sin 2kx(8e^{-\xi}\sin\xi + 3e^{-2\xi} - 3)\,, \tag{10.3.8}$$

where the vertical variation described by the parenthesis changes sign at $\xi \approx 1$, see Fig. 10.2(b). The sign of $\bar{u}_L$ now depends on kx and ξ. In Fig. 10.3 we sketch the free surface of a standing wave with nodes at $kx = \frac{1}{2}\pi, \frac{3}{2}\pi, \ldots$ and antinodes at $kx = 0, \pi, 2\pi, \ldots$. Above $\xi \simeq 1$, that is, in the top part of the boundary layer, the mass transport always converges toward the

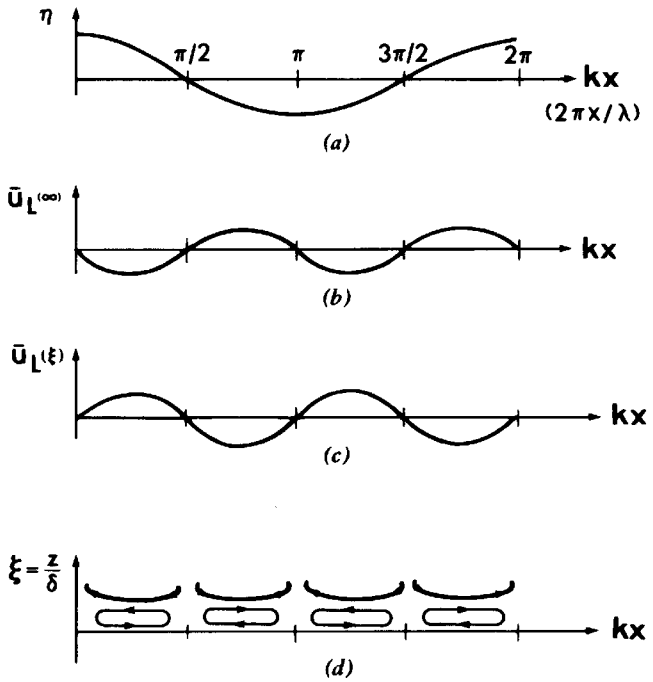

Figure 10.3: Schematic variation of mass transport velocity beneath a standing wave.

antinodes and diverges away from the nodes, while below $\xi \simeq 1$, that is, in the bottom part of the boundary layer, the reverse is true. From the curves for $R = 1$ in Fig. 10.2(b) the net mass flux above the level $\xi = 1$ certainly exceeds that below, implying that the streak lines must be as sketched in Fig. 10.3(d). Near the antinodes some fluid sinks below $\xi \simeq 1$ to form closed circulating cells within the boundary layer, while other fluid escapes upward. A more complete picture involves the introduction of a thicker boundary layer which is caused by the convective inertia of the streaming velocity but will not be discussed here (Mei, Liu, and Carter, 1972; Dore, 1976).

The mass transport velocity near the bottom ($\xi \approx 0$) is likely to be influential for the motion of heavy sediments which roll on the bottom. Near the bottom, $\bar{u}_L$ is in the direction of the incident wave for a purely progressive wave ($R = 0$) and is alternately along and opposite to the incident wave for a completely reflected wave ($R = 1$). It is therefore interesting to

examine the effect of intermediate R. Reversal of sign in $\bar{u}_L(x,\xi)$ near the bottom requires that the profile of $\bar{u}_L$ has a slope greater than zero, that is,

$$\frac{\partial \bar{u}_L}{\partial \xi}(x,0) > 0\,, \quad \xi = 0\,. \tag{10.3.9}$$

Because of Eq. (10.3.5), Eq. (10.3.9) implies

$$R^2 + 2R\sin 2kx - 1 > 0\,.$$

For a fixed x the critical value R_c is

$$R_c = -\sin 2kx + (1+\sin^2 2kx)^{1/2}\,. \tag{10.3.10}$$

If $R > R_c$, reversal of direction occurs. Since $0 < R < 1$, an acceptable solution of R_c can occur only when $\sin 2kx > 0$ or $0 < 2kx < \pi$. Accordingly, the variation of R_c versus $2kx$ is shown in Fig. 10.4. The lowest R_c is $2^{1/2} - 1 = 0.414$ which occurs at $2kx = \frac{1}{2}\pi$ or $x/\lambda = \frac{1}{4}$. For any $0.414 < R < 1$ reversal of $\bar{u}_L$ occurs in the range of $x_1 < x < x_2$ where $R = R_c$

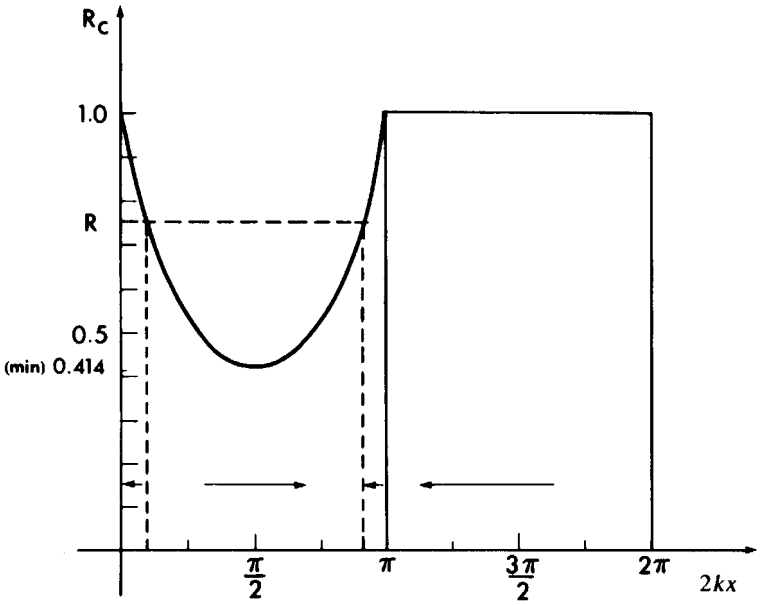

Figure 10.4: Critical reflection coefficient for reversal of bottom mass transport velocity (from Carter, Liu, and Mei, 1973, *J. Waterway, Port, Coastal and Ocean Div.* Reproduced by permission of American Society of Civil Engineers).

at $x = x_1$ and x_2. The corresponding vertical variations of $\bar{u}_L(x, \xi)$ can be seen in Figs. 10.2(a)–10.2(c).

In the case of partial reflection $0 < R < 1$, the total wave can be viewed as a progressive wave with a modulated envelope

$$\begin{aligned} \zeta &= \text{Re}\,\{[A(1 + Re^{-2ikx})]e^{-i(kx+\omega t)}\} \\ &= \text{Re}\,\mathcal{A}(x)e^{-i(kx+\omega t-\theta_{\mathcal{A}}(x))} \end{aligned} \tag{10.3.11}$$

where $\theta_{\mathcal{A}}$ is the phase of the square bracket above and

$$\mathcal{A} = [A(1 + R^2) + 2R\,\cos 2kx]^{1/2}\,. \tag{10.3.12}$$

The amplitude $\mathcal{A}$ of the envelope is the greatest [$= A(1 + R)$] at $2kx = 0, \pm 2\pi, \pm 4\pi, \ldots$ and the smallest [$= A(1 - R)$] at $2kx = \pm\pi, \pm 3\pi, \pm 5\pi, \ldots$. Thus, if $R > 0.414$, reversal of $\bar{u}_L$ occurs within the quarter-wavelength in front of every peak $\mathcal{A}_{\max}$ of the envelope.

The mass transport near the bottom of the boundary layer should be particularly relevant to heavy particles which roll on the bottom as *bed load*. On many beaches of the world the sand size distribution is commonly in the range from 0.05 mm to 10 mm (pebbles). As pointed out in Section 9.7 the eddy viscosity is typically 10–100 cm^2/s for a hydrodynamically rough bottom. The scale of the boundary-layer thickness $\delta = (2\nu/\omega)^{1/2}$ can be estimated to be roughly 6–18 cm for a wave of period 10s and is larger than most sand grains. Once the sand grains are mobilized by the first-order oscillatory velocity of the nearby fluid, the heavy ones will likely move, on the average, in the same general direction as the mass transport velocity near the bottom; the magnitude of the velocity of the sand particles themselves is so far too difficult to predict. For beaches of mild slope and for normally incident waves of short periods, reflection is small and the direction of net sand movement should be onshore. If reflection is large as in the vicinity of a sea wall, a cliff, near a beach of steep slope, or in the presence of a large offshore sand bar, $\bar{u}_L$ can be opposite in direction to the incident waves and can cause deposition on the sea bottom along parallel lines spaced at half-wavelengths apart. Dunes parallel to the coasts can, therefore, be formed at the same spacings. Such periodic dunes can be found on the coast of Florida (see Plate 10.1, from Lau and Travis, 1973).

In the case of large reflection ($R > 0.414$) the sign change of $\bar{u}_L$ should also have consequences on *sediment sorting*. Because fine particles are more likely to be transported in suspension, they should be influenced by the value of $\bar{u}_L$ near the top of the boundary layer. Therefore, they may drift

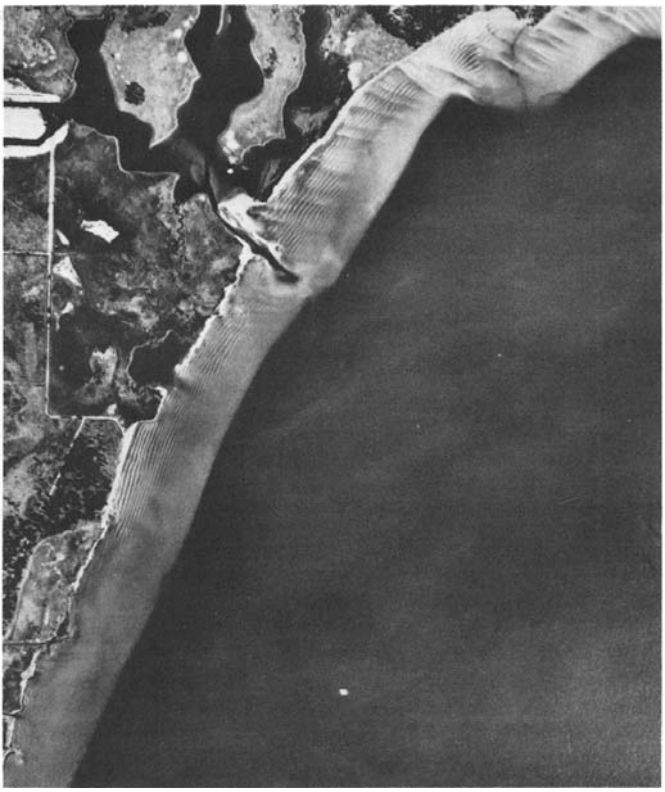

Plate 10.1: Aerial view of submarine longshore bars Escambia Bay, Florida (from Lau and Travis, 1973, *J. Geophys. Res.* Reproduced by permission of American Geophysical Union).

in opposite directions to the heavier particles rolling beneath. In a standing wave the light particles should be deposited around the antinodes and the heavy particles around the nodes no matter what the initial distribution of sediment size is. This *sorting* has been observed in the laboratory by Noda (1968) De Best and Bijker (1971), and Carter, Liu, and Mei (1973). In nature, finer sand is similarly found near dune troughs and coarser sand near dune crests (Inman, 1957). Bagnold (1946) and Herbich, Murphy, and Van Weele (1965) experimented with sand beds under a standing wave. Dunes were found to be present at precisely the intervals of half of the length of the surface waves. Carter et al. (1973) performed experiments for partially standing waves over a solid bottom sprinkled sparcely with sand;

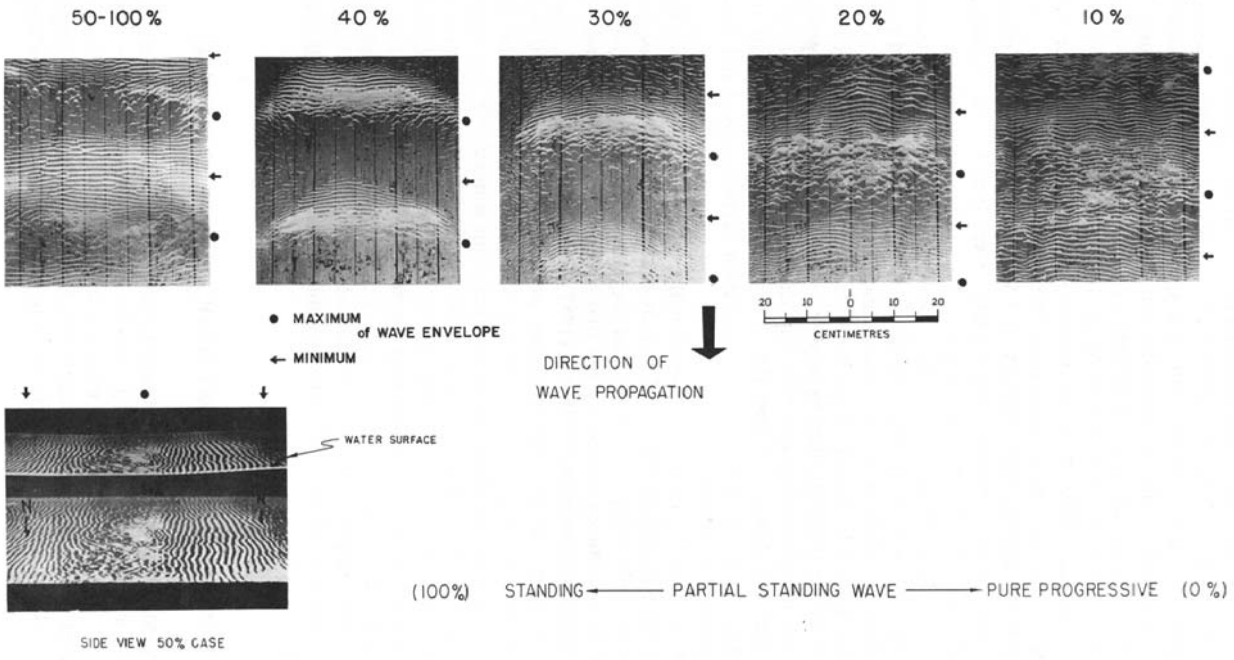

Plate 10.2: Sediment morphology for variable beach reflectivity (from Carter, Liu, and Mei, 1973, *J. Waterway, Port, Coastal and Ocean Div.* Reproduced by permission of American Society of Civil Engineers).

they found the same initial tendency of scour and deposition on a bottom covered with a thick layer of sand. For $R > 0.50$, the tendency toward large-scale depositions became visible near the peaks of the wave envelope (Plate 10.3), thereby supporting the relevance of the present theory to the initial development of a flat sandy bottom. Laboratory evidence of sediment sorting is shown in Plates 10.3 and 10.4.

Once grown to a sufficient size, the dunes will alter the wave field; the conclusions of this section are no longer appropriate. The interaction between waves and dunes has been studied by Yu and Mei (2000b).

As seen in Plate 10.2, ripples with wavelengths much less than the surface wavelength are a prominant feature of a sandy bottom. Formed when the oscillation amplitudes are slightly above the threshold of sand movement, these gentle (rolling-grain) ripples are the results of an instability mechanism (Blondeaux (1990), Vittori and Blondeaux (1990, 1993). See also the review by Blondeaux (2001)). If the oscillations are strong and far above the threshold, ripples can be steep and are accompanied by vortex shedding. Observations by Inman (1957), Zenkovich (1967), and

Plate 10.3: Side view of a sandy bed under a standing wave after four days. Initially the bed is a pink layer of sand mixture of two diameters: 0.2 mm (red) and 0.11 mm (light), in roughly equal parts. Eventually coarse (red) sand is accumulated beneath the node where ripples and a bar crest are formed. Beneath antinodes, the bed is flat and is covered by fine (light) sand. Experiments by Blake Landry and Matthew Hancock, Dept. Civil & Environ. Eng., MIT. Photograph by Felice Frankel, MIT, 2003.

Plate 10.4: Top view of a sandy bed under a standing wave after four days. Initially the bed is a pink layer of sand mixture of two diameters: 0.2 mm (red) and 0.11 mm (light), in roughly equal parts. Periodic bands of coarse (red) and fine (light) sands are eventually found beneath wave nodes and antinodes. Experiments and photograph by Blake Landry and Matthew Hancock, Dept. Civil & Environ. Eng., MIT, 2003.

others show that the ripple dimensions, amplitude, and wavelength depend strongly on the fluid orbital velocity (hence, the depth of water) and the grain size and size distribution. Theoretical modelling is a challenging task involving both turbulence of an oscillatory flow and sediment transport. The reader is referred to Hansen et al. (1994) and Anderssen et al. (2001) for recent progress.

Exercise 10.1: Induced Streaming Near a Lake Bottom

Consider an rectangular lake with vertical banks and constant depth h. Find the details of the mass transport field in the bottom boundary layer under the standing wave mode,

$$\Phi = \mathrm{Re}\left\{C \cos\frac{\pi x}{a} \cos\frac{\pi y}{b} \cosh k(z+h) e^{-i\omega t}\right\},$$

where

$$k = \sqrt{\left(\frac{\pi}{a}\right)^2 + \left(\frac{\pi}{b}\right)^2}, \quad \omega^2 = gk \tanh kh\,.$$

Discuss the streaming patterns next to the bottom and to the top of the boundary layer.

10.4 Bottom Mass Transport Near a Small Structure

Since the simple wave system in Section 10.3 already reveals many interesting features in the mass transport and its possible implications on the sand-bed configuration, it is now tempting to work out some cases that correspond to more complex wave systems. In principle, this is a straightforward but largely numerical problem; once the inviscid wave field (U_0, V_0) is known the mass transport is obtained from Eqs. (10.2.20a) and (10.2.20b) by differentiation. For illustration we shall study in this section only a three-dimensional problem where analytical information is possible (Lamoure and Mei, 1977).

There are many coastal structures, man-made or natural, whose governing horizontal dimension a, say, is much less than the prevailing wavelength ($\sim 1/k$). The head of a breakwater and the piles of an oil drilling rig are such instances. Near these bodies where the local curvature is large, eddy formation or flow separation can exist when the wave amplitudes are sufficiently large. The corresponding flow field is impossible to deduce purely theoretically. However, for low-amplitude swells that are present

most of the time, separation can be insignificant near the sea bottom and a potential theory may be applied to the waves. The assumption of small structure $ka \ll 1$ then simplifies the calculation of waves near the body, as demonstrated in Section 8.4 for a vertical pile of circular cross section. In addition, we shall assume for simplicity that all the solid lateral boundaries are vertical and the sea bottom is horizontal. The inviscid potential may be related to the free-surface displacement η by

$$\phi = -\frac{ig\eta(x,y)}{\omega}\frac{\cosh k(z+h)}{\cosh kh}e^{-i\omega t}\,, \tag{10.4.1}$$

where η is governed by the Helmholtz equation. In the near field of the structure, that is, in the neighborhood within the radius of $O(a)$, the proper horizontal length scale of motion is a, so that the horizontal Laplacian in the Helmholtz equation is much more important

$$\frac{k^2\eta}{\nabla^2 n} \sim O(ka)^2 \ll 1 \quad \text{where} \quad \nabla = \left(\frac{\partial}{\partial x}, \frac{\partial}{\partial y}\right).$$

It follows that

$$\nabla^2\eta \simeq 0\,. \tag{10.4.2}$$

Thus, the inviscid flow in the near field is harmonic in the horizontal plane, and many solutions in classical hydrodynamics that are solved by methods of conformal mapping can be employed here for analytical purposes.

The solution in the near field is indeterminate by a complex constant factor, which must be found by matching with the solution in the *far field* about a wavelength away from the structure. The details of the matching process are unimportant for present purposes. Since the complex constant factor is common to both U_0 and V_0, the phases of U_0 and V_0 cancel out in Eqs. (10.2.20a) and (10.2.20b).[1] Hence we can discuss the variation of mass transport by taking U_0 and V_0 to be real without any loss of generality, that is,

$$\bar{u}_L = \frac{1}{4\omega}\,\mathrm{Re}\left[U_0\frac{\partial U_0}{\partial x}(F_5 - F_7) + F_6 V_0\frac{\partial U_0}{\partial y}\right],$$

$$\bar{v}_L = \frac{1}{4\omega}\,\mathrm{Re}\left[F_6 U_0\frac{\partial V_0}{\partial x} + (F_5 - F_7)V_0\frac{\partial V_0}{\partial y}\right],$$

[1] These formulas do not hold within the distance of $O(\delta)$ from the vertical wall.

where

$$(U_0, V_0) = -\frac{ig\nabla\eta}{\omega}\operatorname{sech} kh\,. \tag{10.4.3}$$

Since $F_5 - F_7 = F_6$ from Eq. (10.2.21), we have

$$\bar{u}_L = \frac{1}{4\omega}\operatorname{Re}\left[F_6\left(U_0\frac{\partial U_0}{\partial x} + V_0\frac{\partial U_0}{\partial y}\right)\right], \tag{10.4.4a}$$

$$\bar{v}_L = \frac{1}{4\omega}\operatorname{Re}\left[F_6\left(U_0\frac{\partial V_0}{\partial x} + V_0\frac{\partial V_0}{\partial y}\right)\right], \tag{10.4.4b}$$

or, in vector form,

$$\begin{aligned}\bar{\mathbf{u}}_L &= \frac{1}{4\omega}\operatorname{Re} F_6\mathbf{U}_0\cdot\nabla\mathbf{U}_0\\ &= \frac{1}{4\omega}\nabla\frac{|\mathbf{U}_0|^2}{2}(4e^{-\xi}\sin\xi + e^{-2\xi} - 1)\,.\end{aligned} \tag{10.4.5}$$

Note that the strength of the mass transport velocity is proportional to the horizontal gradient of the inviscid velocity. Furthermore, the factor for vertical variation inside the boundary layer is

$$\begin{aligned}\operatorname{Re} F_6 &= 4e^{-\xi}\sin\xi + e^{-2\xi} - 1 \simeq 2\xi \quad \text{for} \quad \xi \ll 1\,,\\ &\simeq -1 \qquad\qquad\qquad\quad \text{for} \quad \xi \gg 1\,.\end{aligned}$$

Thus, there is a sign reversal within the boundary layer. Very close to the bottom

$$\bar{\mathbf{u}}_L \simeq \frac{\xi}{4\omega}\nabla|\mathbf{U}_0|^2\,, \quad \xi \ll 1\,, \tag{10.4.6}$$

so that the mass transport is in the direction of increasing $|\mathbf{U}_0|^2$. In particular, fluid must drift toward the convex corner of a vertical structure. On the other hand, near the top of the boundary layer

$$\bar{\mathbf{u}}_L \simeq \frac{-1}{8\omega}\nabla|\mathbf{U}_0|^2\,, \tag{10.4.7}$$

so that the mass transport points away from the convex corner. The variation of $\operatorname{Re} F_6$ for all ξ is plotted in Fig. 10.5.

The above simple conclusion suggests that heavy sediments, once mobilized to roll on the bottom, may be attracted toward the neighborhood of high oscillating velocity. More specifically, for a pile in the presence of

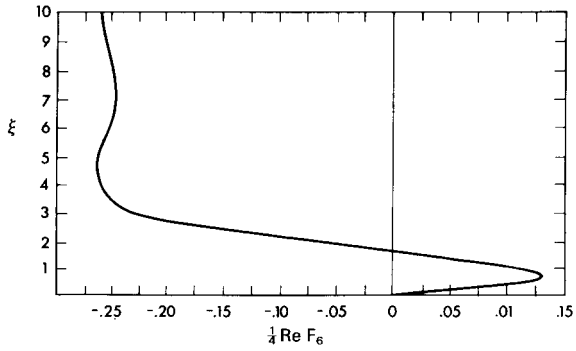

Figure 10.5: Vertical variation of Lagrangian mass transport in gravity waves near a small body; $\xi = z/\delta$ (from Lamoure and Mei, 1977, *J. Fluid Mech.* Reproduced by permission of Cambridge University Press).

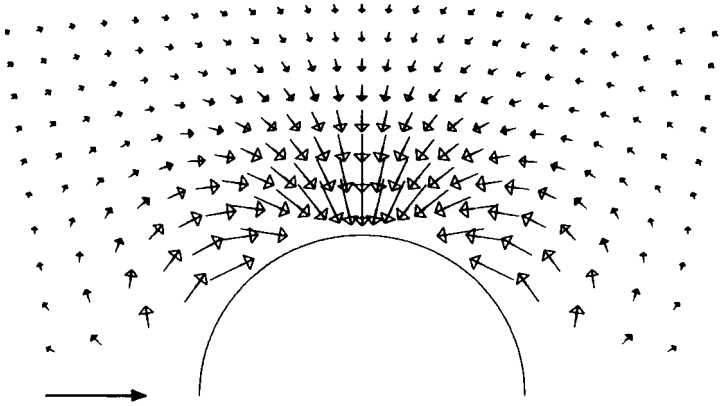

Figure 10.6: Mass transport velocity vectors in gravity waves near the solid bottom in the presence of a circular cylinder (from Lamoure and Mei, 1977, *J. Fluid Mech.* Reproduced by permission of Cambridge University Press).

waves from $x \sim -\infty$ ($\theta = \pi$) deposition is the largest near the two extremities on the two sides of the x axis, as shown in Fig. 10.6. By similar reasoning, heavy sediments would tend to deposit near the tip of a breakwater. Deposition would also tend to narrow the neck of a narrow harbor entrance.

Why is $\bar{\mathbf{u}}_L$ parallel to $\nabla^2|\mathbf{U}_0|^2$? Consider a vertical column of fluid of unit square cross section with its base somewhere inside the boundary layer and its top at the outer edge. The mean shear stress acting at the base is

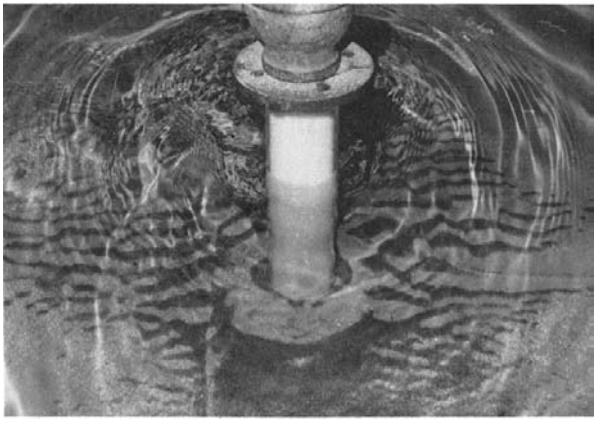

Plate 10.5: Sediment accumulation (see dark areas) near two sides of a circular pile. Wave crests are parallel to the ripple marks. Prior to wave motion, there were no sand particles in an annular area next to the cylinder (from Lamoure and Mei, 1977, *J. Fluid Mechs.* Reproduced by permission of Cambridge University Press).

$\mu\partial\bar{\mathbf{u}}/\partial z$. The net normal stresses acting on a unit area of the vertical sides are the mean pressure gradient $\frac{1}{2}\rho\nabla\overline{\mathbf{U}_I^2}$ and the gradient of the normal Reynolds stress $-(1/\rho)\rho\nabla\overline{\mathbf{u}^2}$. Because $w \cong 0$, the shear components of the Reynolds stress are negligible. Equating the forces, we have

$$\mu\frac{\partial\bar{\mathbf{u}}}{\partial\mathbf{z}} = \frac{\rho}{2}\int_z^\infty \overline{\nabla(\mathbf{U}_I^2 - \mathbf{u}^2)}\,dz\,.$$

From the boundary-layer solution, the integral on the right is coplanar with and proportional to $\nabla\mathbf{U}_0^2$; the same must be true for $\bar{\mathbf{u}}$ and $\bar{\mathbf{u}}_L$.

The qualitative prediction of Eq. (10.4.7) has been verified experimentally by Lamoure and Mei (1977); see Plate 10.5. We caution that, in nature, the presence of solid particles in fluid not only produces turbulence but affects the nature of turbulence by their own dynamics. Hence the mechanics of littoral drift by waves is far more complex than the mass transport of pure fluid.

Other beach topographies have been attributed to the mass transport under complex wave systems by Holman and Bowen (1982).

Exercise 10.2

A plane incident wave of amplitude A propagates in the positive x direction in a sea of constant depth. A small circular pile is located at the origin. Use the fact from Section 8.3 that

$$\zeta \simeq \operatorname{Re} A e^{-i\omega t}\left[1 + ik\cos\theta\left(r + \frac{a^2}{r}\right)\right], \quad \text{for} \quad r = O(a)$$

to deduce the following formulas for the mass transport velocity in the bottom boundary layer near the pile:

$$\bar{\mathbf{u}}_L = \frac{1}{a}\left(\frac{gkA}{\omega\cos kh}\right)^2\left(\frac{a}{r}\right)^3\left\{\begin{array}{c}\left(-\dfrac{a^2}{r^2} + \cos 2\theta\right)\mathbf{e}_r \\ \sin 2\theta\,\mathbf{e}_\theta\end{array}\right\}\frac{1}{2\omega}\operatorname{Re} F_6\,. \tag{10.4.8}$$

Make some computations to verify Fig. 10.6.

10.5 Remarks on Induced Streaming Outside the Stokes Boundary Layer

One of the main features of the preceding deductions is that Eulerian streaming velocity approaches a finite value at the outer edge of the Stokes boundary layer. It is interesting to ask what the effect of this current is on the essentially inviscid core. Does this current induce further current throughout the entire water depth by viscous diffusion?

In studying the boundary layers near oscillating bodies, Stuart (1966) suggested that if the amplitude of motion was sufficiently large, the convective inertia of the induced current became important in the average momentum balance and had to be counteracted by a new shear stress in a relatively thick boundary layer. Riley (1967) and Wang (1968) developed this subject further. In particular, Wang analyzed systematically the variety of possibilities outside the Stokes layer. The following is a synopsis of Wang's reasoning.

In terms of physical variables, denoted with primes, the equations of motion are

$$\nabla' \cdot \mathbf{u}' = 0\,, \tag{10.5.1}$$

$$\frac{\partial \boldsymbol{\Omega}'}{\partial t'} - \nabla' \times (\mathbf{u}' \times \boldsymbol{\Omega}') = -\nu\nabla' \times (\nabla \times \boldsymbol{\Omega}')\,, \tag{10.5.2}$$

where $\boldsymbol{\Omega}' = \nabla' \times \mathbf{u}'$ is the vorticity vector. Note that the Navier–Stokes equation has been replaced by the vorticity equation (10.5.2).

Let the unknowns be split into a mean (DC) and a fluctuating (AC) part as follows:

$$\mathbf{u}' = \bar{\mathbf{u}}' + \tilde{\mathbf{u}}'\,, \tag{10.5.3}$$

$$\boldsymbol{\Omega}' = \overline{\boldsymbol{\Omega}}' + \tilde{\boldsymbol{\Omega}}' , \tag{10.5.4}$$

with $(\bar{\ })$ representing the time mean over a period and $(\tilde{\ })$ representing the fluctuations. Substituting into Eqs. (10.5.1) and (10.5.2) and taking time averages, we obtain equations governing the mean motion:

$$\boldsymbol{\Omega}' \cdot \bar{\mathbf{u}}' = 0 , \tag{10.5.5}$$

$$\nabla' \times \overline{(\tilde{\mathbf{u}}' \times \tilde{\boldsymbol{\Omega}}')} + \nabla' \times (\bar{\mathbf{u}}' \times \overline{\Omega}') = \nu \nabla' \times (\nabla \times \overline{\boldsymbol{\Omega}}') . \tag{10.5.6}$$

In Eq. (10.5.6) the first term corresponds to the Reynolds stress contribution, which is the *steady part* of self-interaction of two oscillating components. This term is nonzero if $\tilde{\mathbf{u}}'$ and $\tilde{\boldsymbol{\Omega}}'$ are not always out of phase by $\frac{1}{2}\pi$.

Subtracting Eqs. (10.5.5) and (10.5.6) from Eqs. (10.5.1) and (10.5.2), we obtain the equations governing the fluctuations:

$$\nabla' \cdot \tilde{\mathbf{u}}' = 0 , \tag{10.5.7}$$

$$\frac{\partial \tilde{\boldsymbol{\Omega}}'}{\partial t'} - \nabla'(\bar{\mathbf{u}}' \times \tilde{\boldsymbol{\Omega}}') - \nabla' \times (\tilde{\mathbf{u}}' \times \overline{\boldsymbol{\Omega}}') - \nabla' \times \widetilde{(\tilde{\mathbf{u}}' \times \tilde{\boldsymbol{\Omega}}')}$$
$$= -\nu \nabla' \times (\nabla \times \tilde{\boldsymbol{\Omega}}') , \tag{10.5.8}$$

where the last term on the left of Eq. (10.5.8) is the *unsteady part* of self-interaction. We now normalize the variables as follows:

$$\begin{aligned} x &= kx' , \qquad t = \omega t' \\ \tilde{\mathbf{u}} &= \frac{\tilde{\mathbf{u}}'}{\omega A} , \qquad \bar{\mathbf{u}} = \frac{\bar{\mathbf{u}}'}{\omega k A^2} , \\ \tilde{\boldsymbol{\Omega}} &= \frac{\tilde{\boldsymbol{\Omega}}'}{\omega k A} , \quad \overline{\boldsymbol{\Omega}} = \frac{\overline{\boldsymbol{\Omega}}'}{\omega k^2 A^2} , \end{aligned} \tag{10.5.9}$$

where ω is the wave frequency, k is the wavenumber, and A is the wave amplitude. The scale of the fluctuation velocity is the fluid velocity in waves and the scale of the mean drift is that of the mass transport velocity [cf. Eq. (10.3.5)]. In dimensionless form Eqs. (10.5.5)–(10.5.8) become

$$\nabla \cdot \bar{\mathbf{u}} = 0 , \tag{10.5.10}$$

$$\underset{\text{(Reynolds stress)}}{(kA)^{-2} \nabla \times \overline{(\tilde{\mathbf{u}} \times \tilde{\boldsymbol{\Omega}})}} + \underset{\left(\begin{smallmatrix}\text{steady}\\ \text{convection}\end{smallmatrix}\right)}{\nabla \times (\bar{\mathbf{u}} \times \overline{\boldsymbol{\Omega}})} = \underset{\text{(diffusion)}}{\frac{\delta^2}{a^2} \nabla \times (\nabla \times \overline{\boldsymbol{\Omega}})} , \tag{10.5.11}$$

for the steady streaming, where

$$\delta = \left(\frac{2\nu}{\omega}\right)^{1/2} \tag{10.5.12}$$

and

$$\nabla \cdot \tilde{\mathbf{u}}' = 0\,, \tag{10.5.13}$$

$$\frac{\partial \tilde{\mathbf{\Omega}}'}{\partial t'} - (kA)^2[\nabla(\bar{\mathbf{u}} \times \tilde{\mathbf{\Omega}}) + \nabla \times (\tilde{\mathbf{u}} \times \overline{\mathbf{\Omega}})] - (kA)[\nabla \times \widetilde{(\tilde{\mathbf{u}} \times \tilde{\mathbf{\Omega}})}]$$
$$= -(k\delta)^2 \nabla \times \nabla \times \tilde{\mathbf{\Omega}} \tag{10.5.14}$$

for the fluctuations.

It is now easy to delineate various regions and their proper approximations. In most laboratory setups, the wave slope and the viscosity are small,

$$kA \ll 1\,, \quad k\delta \ll 1\,. \tag{10.5.15}$$

Therefore, for the fluctuations the convective term may be ignored from Eq. (10.5.14). Viscous diffusion can be ignored except near a solid wall within a layer of thickness $O(\delta)$. Within this layer the normal derivative dominates and Eq. (10.5.14) is approximately

$$\frac{\partial \tilde{\mathbf{\Omega}}}{\partial t} = (k\delta)^2 \frac{\partial^2 \tilde{\mathbf{\Omega}}}{\partial n^2}\,, \tag{10.5.16}$$

which governs the structure of the Stokes layer $O(\delta)$.

Now examine Eq. (10.5.11) for the steady streaming inside the Stokes layer. The Reynolds stress due to the mean motion is unimportant, and $\partial/\partial n \sim 1/k\delta$. Hence the Reynolds stress due to fluctuations must be balanced by a steady viscous stress:

$$\left(\frac{1}{kA}\right)^2 \cdot \nabla \times \overline{(\tilde{\mathbf{u}} \times \tilde{\mathbf{\Omega}})} = -\left(\frac{\delta}{A}\right)^2 \frac{\partial^2 \overline{\mathbf{\Omega}}}{\partial n^2}\,. \tag{10.5.17}$$

Outside the Stokes layer, since the cross product of the fluctuating parts $\tilde{\mathbf{u}}$, $\tilde{\mathbf{\Omega}}$ is known to be exponentially small, we have from Eq. (10.5.11)

$$\nabla \times (\bar{\mathbf{u}} \times \overline{\mathbf{\Omega}}) = -\left(\frac{\delta}{A}\right)^2 \nabla \times (\nabla \times \overline{\mathbf{\Omega}}) \tag{10.5.18}$$

which leads to several possibilities:

(i) $\delta/A \gg 1$: The amplitude is very much smaller than the Stokes-layer thickness. The approximation

$$\nabla \times (\nabla \times \overline{\mathbf{\Omega}}) \simeq 0 \tag{10.5.19}$$

can be made which corresponds to small-Reynolds-number (creeping) flows. While unrealistic in practical situations, this approximation is the easiest to analyze.

(ii) $\delta/A \ll 1$: The amplitude is much greater than the Stokes-layer thickness, which corresponds to high-Reynolds-number flows. Viscosity and inertia are both important within a layer of thickness

$$O(\delta_1) = o\left(\frac{\delta}{kA}\right). \tag{10.5.20}$$

Within this layer the normal derivative again dominates so that

$$\nabla \times (\bar{\mathbf{u}} \times \overline{\mathbf{\Omega}}) \cong -(k\delta_1)^2 \frac{\partial^2 \overline{\mathbf{\Omega}}}{\partial n^2}\,, \tag{10.5.21}$$

which corresponds to the Blasius equation in the classical laminar boundary-layer theory. Vorticity is expected to be confined within this second boundary layer and diminishes to zero outside it (Stuart, 1966).

(iii) $\delta/A = O(1)$: Equation (10.5.18) must be solved exactly.

The case of standing waves has been analyzed by Mei, Liu, and Carter (1972) and Dore (1976) for the double structure of boundary layers, corresponding to Case (ii) above.

One aspect of two-dimensional progressive waves in a channel of constant depth deserves special remark. In earlier theoretical papers (e.g., Longuet–Higgins, 1953), the amplitude attenuation along the channel (x direction) was totally ignored, and the induced streaming was strictly horizontal and independent of x,

$$\bar{u} = \bar{u}(z) \propto A^2 f(z)\,, \quad \bar{v} = 0\,.$$

Under these assumptions the induced streaming is governed by Eq. (10.5.19) even when $\delta/A \ll 1$ and there is no double-layer structure. However, the attenuation rate in the longitudinal direction is not exactly zero and is known to be

$$\frac{1}{kA}\frac{dA}{dx'} = O(k\delta)\,. \tag{10.5.22}$$

If the vertical length scale is taken to be $1/k$ for the time being, the order of magnitude of the terms in Eq. (10.5.18) is as follows:

$$\nabla \times (\bar{\mathbf{u}}' \times \overline{\boldsymbol{\Omega}}') = \nu \nabla \times (\nabla \times \bar{\mathbf{U}}'),$$

$$(k^2\delta)(\omega k A^2)(\omega k^2 A^2) \sim (\nu)(k^2)(\omega k^2 A^2) \tag{10.5.23}$$

or

$$O\left(\frac{\text{viscous diffusion}}{\text{inertia}}\right) = \frac{k\delta}{(kA)^2}. \tag{10.5.24}$$

For inertia terms to be negligible it is necessary that $k\delta \gg (kA)^2$ and not that $\delta/A \gg 1$. In many laboratory tanks with smooth bottoms, the ratio (10.5.24) is usually less than O(1); for example, take $\nu = 10^{-2}$ cm^2/s, $k = 2\pi/50$ (wavelength = 50 cm), $\omega = 2\pi/T = 4\pi$ ($T = \frac{1}{2}$ s), and $A = 1 \sim 5$ cm, then $\delta = (10^{-2}/4\pi)^{1/2} = 0.03$ cm and

$$\frac{k\delta}{(kA)^2} = 0.05 \sim 0.25.$$

For very small $k\delta/(kA)^2$, there can be secondary boundary layers near the free surface and the solid bottom, of the thickness

$$\delta_2 = O\left(\frac{1}{k}\frac{(k\delta)^{1/2}}{kA}\right),$$

which is rather thick and may eventually grow to be comparable to the water depth. Furthermore, over a rough or sediment-laden bottom the eddy viscosity which is many times larger than the laminar viscosity can increase the boundary-layer thickness δ_2 even further. Convective inertia of the induced streaming can then become as important as lateral diffusion throughout the entire depth.

The details of secondary boundary layers in water waves are complicated (Dore, 1977). In the following section we only investigate the classic case of creeping flow theory due to Longuet–Higgins (1953).

10.6 Creeping Flow Theory of Mass Transport in a Channel of Finite Depth

In his original analysis, Longuet–Higgins (1953) employed a curvilinear coordinate system embedding the free surface so that the boundary layer could be measured from the instantaneous free surface. An alternative is to employ the Lagrangian coordinate system in terms of which the free-surface condition can be conveniently stated (Ünlüata and Mei, 1970). Let a and c

be the initial horizontal and vertical coordinates of a fluid particle. In the a-c plane, the position of the free surface is simply $c = 0$ at all times and is no longer unknown. Use of the Lagrangian coordinate system has been made later by Piedra-Cueva (1995) and Ng (2004) for partially standing waves in gravity waves. In the latter Ng also revised a step in the reasoning of Ünlüata and Mei (1970) for progressive waves.

We refer the readers to Monin and Yaglom (1971) for a derivation of the Navier–Stokes equations in Lagrangian form and only quote the results for two dimensions.

Continuity:

$$\frac{\partial(x,z)}{\partial(a,c)} \equiv \begin{vmatrix} \dfrac{\partial x}{\partial a} & \dfrac{\partial x}{\partial c} \\ \dfrac{\partial z}{\partial a} & \dfrac{\partial z}{\partial c} \end{vmatrix} = 1\,, \tag{10.6.1}$$

x momentum:

$$x_{tt} = -\frac{1}{\rho}\frac{\partial(P,z)}{\partial(a,c)} + \nu\nabla^2 x_t\,, \tag{10.6.2}$$

z momentum:

$$z_{tt} + g = -\frac{1}{\rho}\frac{\partial(x,P)}{\partial(a,c)} + \nu\nabla^2 z_t\,, \tag{10.6.3}$$

where the Laplacian ∇^2, which is an Eulerian operator, can be transformed to

$$\nabla^2 x_t = \frac{\partial(\partial(x_t,z)/\partial(a,c),z)}{\partial(a,c)} + \frac{\partial(x,\partial(x,x_t)/\partial(a,c))}{\partial(a,c)}\,. \tag{10.6.4}$$

Vanishing of the normal and tangential stresses on the free surface can be stated exactly as

$$(-P + \tau_{zz})x_a + \tau_{xz}z_a = 0 \tag{10.6.5a}$$

$$\text{on} \quad c = 0\,,$$

$$\tau_{zx}x_a - (-P + \tau_{xx})z_a = 0 \tag{10.6.5b}$$

where

$$\tau_{zz} = 2\mu[x_a z_{tc} - z_{ta}x_c]\,, \tag{10.6.5c}$$

$$\tau_{xx} = 2\mu[x_{ta}z_c - x_{tc}z_a]\,, \tag{10.6.5d}$$

$$\tau_{xz} = \mu[x_a z_{tc} + z_{ta}x_c - z_{tc}z_a - x_c x_{ta}]\,. \tag{10.6.5e}$$

The usual kinematic condition is accounted for by the very fact that $c = 0$ always refers to the free surface.

Pierson (1962) first applied Eqs. (10.6.1)–(10.6.3) to small-amplitude waves by introducing the perturbation series

$$x = a + x_1 + x_2 + \cdots , \tag{10.6.6a}$$

$$z = c + z_1 + z_2 + \cdots , \tag{10.6.6b}$$

$$P = (p_0 - \rho g c) + p_1 + p_2 + \cdots , \tag{10.6.6c}$$

where

$$(x_1, z_1, p_1) \sim O(kA) , \quad (x_2, z_2, p_2) \sim O(kA)^2 .$$

Thus, these series are valid for a small time range in which the net displacement is small. The following equations are obtained at the order $O(kA)$:

$$x_{1ta} + z_{1tc} = 0 , \tag{10.6.7}$$

$$x_{1tt} + g z_{1a} + \frac{p_{1a}}{\rho} = \nu \nabla_L^2 x_{1t} , \tag{10.6.8a}$$

$$z_{1tt} + g z_{1c} + \frac{p_{1c}}{\rho} = \nu \nabla_L^2 z_{1t} , \tag{10.6.8b}$$

where ∇_L^2 denotes the Laplacian for Lagrangian coordinates

$$\nabla_L^2 = \frac{\partial^2}{\partial a^2} + \frac{\partial^2}{\partial c^2} .$$

On the free surface, the normal and tangential stresses vanish:

$$p_1 = 2\rho\nu z_{1tc} , \qquad c = 0 . \tag{10.6.9a}$$

$$x_{1tc} + z_{1ta} = 0 , \tag{10.6.9b}$$

On the bottom the no-slip condition is

$$x_{1t} = z_{1t} = 0 , \quad c = -h . \tag{10.6.10}$$

Formally, the first-order problem is identical to the linearized Navier–Stokes equations in Eulerian form if we identify

$$x_{1t} = u_1 , \quad z_{1t} = v_1 . \tag{10.6.11}$$

Let

$$x_1 = x_1^p + x_1^r\,, \quad z_1 = z_1^p + z_1^r\,, \tag{10.6.12}$$

where the potential (irrotational) part is governed by

$$(x_{1t}^p, z_{1t}^p) = \nabla_L \Phi\,, \tag{10.6.13}$$

$$\Phi_t = -\frac{p_1}{\rho} + g z_1\,, \tag{10.6.14}$$

$$\nabla_L^2 \Phi = 0\,, \tag{10.6.15}$$

and the rotational part is governed by

$$x_{1tt}^r = \nu \nabla_L^2 x_t^r\,, \tag{10.6.16a}$$

$$z_{1tt}^r = \nu \nabla_L^2 z_t^r\,, \tag{10.6.16b}$$

$$x_{1ta}^r + z_{1tc}^r = 0\,. \tag{10.6.17}$$

The results in Section 10.3 may now be used. In the core outside the Stokes layers the solution is

$$\begin{pmatrix} x_1^p \\ z_1^p \end{pmatrix} = \frac{A e^{i\theta}}{\sinh kh} \begin{pmatrix} i \cosh k(c+h) \\ \sinh k(c+h) \end{pmatrix}, \tag{10.6.18}$$

with

$$\theta = ka - \omega t\,. \tag{10.6.19}$$

In the bottom boundary layer we have

$$x_1 = \frac{iA}{\sinh kh} \left\{ 1 - \exp\left[-(1-i)\frac{c+h}{\delta} \right] \right\} e^{i\theta}\,, \tag{10.6.20}$$

$$z_1 = \frac{k\delta A}{(1-i)\sinh kh} \left\{ \exp\left[-(1-i)\frac{c+h}{\delta} \right] - 1 \right\} e^{i\theta}\,. \tag{10.6.21}$$

In the free-surface boundary layer, which was ignored previously, the potential part does not change significantly. Equation (10.6.16a) is approximately

$$\frac{\partial x_{1t}^r}{\partial t} = \nu \frac{\partial^2 x_{1t}^r}{\partial c^2}\,. \tag{10.6.22}$$

The shear stress condition (10.6.9) on $c = 0$ now implies

$$\frac{\partial x_{1t}^r}{\partial c} = -\left(\frac{\partial x_{1t}^p}{\partial c} + \frac{\partial z_{1t}^p}{\partial a} \right) = -2\omega k A e^{i\theta}\,. \tag{10.6.23}$$

With the further requirement that

$$x_{1t}^r \to 0\,, \quad \frac{c}{\delta} \to -\infty\,, \tag{10.6.24}$$

x_1^r is easily found to be

$$x_1^r = -\frac{2iAk\delta}{1-i} e^{i\theta} \exp\left[(1-i)\frac{c}{\delta}\right], \tag{10.6.25}$$

hence by continuity

$$z_1^r = O(k\delta \cdot x_1^r) = O(k\delta)^2\,. \tag{10.6.26}$$

The total solution in the free-surface layer is:

$$x_1 = iA\left\{\coth kh - \frac{2k\delta}{(1-i)} \exp\left[(1-i)\frac{c}{\delta}\right]\right\} e^{i\theta}\,, \tag{10.6.27}$$

$$\frac{\partial x_1}{\partial c} = ikA\left\{1 - 2\exp\left[(1-i)\frac{c}{\delta}\right]\right\} e^{i\theta}\,, \tag{10.6.28}$$

$$z_1 = A\{1 + O(k\delta)^2\} e^{i\theta}\,. \tag{10.6.29}$$

Note that x_1^r itself is insignificant but gives rise to $O(1)$ vorticity $(\partial x_1/\partial c)$.

The second-order equations have been worked out by Pierson. The horizontal momentum is governed by

$$x_{2tt} + g z_{2a} + \frac{p_{2a}}{\rho} - \nu \nabla_L^2 x_{2t} = G\,, \tag{10.6.30a}$$

where

$$\begin{aligned} G = &-x_{1tt}x_{1a} - z_{1tt}z_{1a} + \nu\{(x_{1taa} + 3x_{1tcc})x_{1a} + 2x_{1taa}z_{1c} \\ &+ x_{1ta}(z_{1ac} - x_{1cc}) - 2x_{1tac}(z_{1a} + x_{1c}) \\ &- x_{1tc}(z_{1aa} - x_{1ac}) - z_{1a}(z_{1taa} + z_{1tcc})\}\,. \end{aligned} \tag{10.6.30b}$$

The vertical momentum is governed by

$$z_{2tt} + g z_{2c} + \frac{p_{2c}}{\rho} - \nu \nabla_L^2 z_{2tt} = H\,, \tag{10.6.31a}$$

where

$$\begin{aligned} H = &-x_{1tt}x_{1c} - z_{1tt}z_{1c} + \nu\{(x_{1taa} + x_{1tcc})x_{1c} \\ &+ z_{1c}(3z_{1taa} - z_{1cc}) - 2z_{1tac}(z_{1a} + x_{1c}) \\ &- z_{1ta}(x_{1aa} + x_{1cc}) - z_{1tc}(z_{1aa} + z_{1cc})\}\,. \end{aligned} \tag{10.6.31b}$$

The normal stress boundary condition on the free surface is

$$-\frac{p_2}{\rho} + p_1 x_{1a} - \mu(z_{1c}^2)_t + \mu x_{1tc} z_{1a} + \mu(z_{1a})^2)_t = 0\,, \quad c = 0\,. \tag{10.6.32}$$

We now consider the time averages. After making use of the first-order results, we find

$$\bar{p}_2 = 0\,, \quad \text{on} \quad c = 0\,. \tag{10.6.33}$$

By integrating (10.6.31a) with respect to c from the core to the free surface and denoting the mean surface displacement by $\bar{\zeta}_{2a}(a) = \bar{z}_2(a, c = 0)$, we get

$$g\bar{\zeta}_{2a}(a) - g\bar{z}_2(a,c) - \frac{\bar{p}_2(a,c)}{\rho} = \int_c^0 \bar{H}\, dc\,.$$

On the right-hand side, $\bar{H}$ is dominated by the inviscid terms in the free surface boundary layer. Making use of the first-order solutions, and the fact that the time averages of the quadratic products are independent of a, we find

$$g\bar{\zeta}_{2a} = g\bar{z}_{2a}(a,c) + \frac{\bar{p}_{2a}(a,c)}{\rho}\,. \tag{10.6.34}$$

(Ng, 2004). It follows that

$$\nu\frac{d^2\bar{x}_{2t}}{dc^2} = g\bar{\zeta}_{2a} - \overline{G} \tag{10.6.35}$$

for all c. Denoting

$$x_1 = AX(c)e^{i\theta}\,, \quad z_1 = AZ(c)e^{i\theta} \tag{10.6.36}$$

where X and Z can be inferred for different regions, we obtain from Eq. (10.6.30b), after some algebra, that

$$\overline{G} = \frac{A^2}{2}\nu\omega k\ \mathrm{Re}\left\{k^2(|X|^2 + |Z|^2) - 4X^*\frac{d^2X}{dc^2} - ik\frac{d}{dc}(X^*Z)\right.$$
$$\left. - 3\left|\frac{dX}{dc}\right|^2 - Z^*\frac{d^2Z}{dc^2}\right\}. \tag{10.6.37}$$

Inside the free-surface boundary layer only the terms

$$4X^*\frac{d^2X}{dc^2} \quad \text{and} \quad 3\left|\frac{dX}{dc}\right|^2$$

dominate; Eq. (10.6.37) can be substantially simplified. On the free surface, the condition (10.6.5b) on the tangential stress gives

$$x_{2tc} + z_{2ta} = 3x_{1ta}z_{1a} - 2x_{1tc}x_{1a} + x_{1c}x_{1ta}\,, \quad c = 0\,. \tag{10.6.38}$$

After Eqs. (10.6.27) and (10.6.29) are used, the time average of Eq. (10.6.38) yields, happily,

$$\frac{d\bar{x}_{2t}}{dc} = O(k^2\delta^2\omega k^2A^2)\,, \quad c = 0\,. \tag{10.6.39}$$

With this boundary condition, Eq. (10.6.35) can be integrated. In particular, the result leads to

$$\frac{d\bar{x}_{2t}}{dc} \to 4\omega k^2A^2 \coth kh\,, \quad \frac{c}{\delta} \to -\infty \tag{10.6.40}$$

at the outer edge of the free-surface layer.

Either by a similar analysis, or by invoking the known result of Eq. (10.3.7), we have

$$\bar{x}_{2t} \to \frac{5\omega kA^2}{4}\sinh kh\,, \quad \frac{c+h}{\delta} \to \infty \tag{10.6.41}$$

at the outer edge of the bottom layer.

Now in the core region between the two boundary layers, Eq. (10.6.35) takes the simple form

$$\nu\frac{d^2\bar{x}_{2t}}{dc^2} = g\bar{\zeta}_{2a} + 2\nu\omega k^3A\frac{\cosh 2(c+h)}{\sinh^2 kh}\,, \tag{10.6.42}$$

since $\overline{G}$ can be calculated from the first-order potential solution. Equation (10.6.42) is readily solved, subject to Eqs. (10.6.40) and (10.6.41) at $c = 0$ and $c = -h$, respectively; the result is

$$\bar{x}_{2t} = \frac{g}{\nu}\bar{\zeta}_{2a}(c^2 - h^2) + \frac{\omega kA^2}{\sinh^2 kh} \times \left[\frac{3}{4} + k(c+h)\sinh 2kh + \frac{1}{2}\cosh 2k(c+h)\right] \tag{10.6.43}$$

which is Lagrangian mass transport outside the two boundary layers. The mean sea-level gradient $\partial\bar{\zeta}_2/\partial a$ can be determined by imposing one more condition. For example, in a tank of great but finite length, the total mass

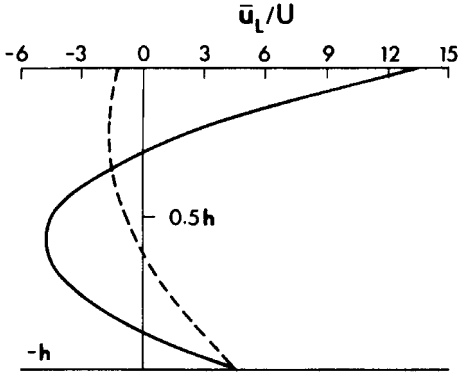

Figure 10.7: Comparison of mass transport velocity profiles for $kh = 0.5$, $T = 10$ s. Solid curve: Dore (1978, air–water); dashed curve: Longuet–Higgins (1953, vacuum–water). $U = A\omega^2 k(\sinh kh)^{-1}$ (from Dore, 1978, *Geophys. Astrophys. Fluid Dyn.* Reproduced by permission of Gordon and Breach Scientific Publishers).

flux across the depth is zero; $\partial\bar{\zeta}_2/\partial a = O(\nu\omega kA^2) = O(k\delta kA)^2$ is then readily found. The corresponding mass transport velocity is

$$\bar{x}_{2t} = \frac{A^2\omega k}{4\sinh^2 kh}\left[3 + 2\cosh 2k(c+h) + 3\left(\frac{\sinh 2kh}{2kh} + \frac{3}{2}\right)\left(\frac{c^2}{h^2} - 1\right)\right.$$

$$\left. + kh\sinh 2kh\left(1 + 4\frac{c}{h} + 3\frac{c^2}{h^2}\right)\right]. \qquad (10.6.44)$$

(Longuet–Higgins, 1953). A typical plot is shown in Fig. 10.7.

In a laboratory tank of length L, the state of zero net flow is reached when a return flow is established throughout the length of the tank; the time required is $T_1 \sim O(L/\omega^2 kA^2)$. Now the time required for viscous diffusion to reach the entire depth is $T_2 = O(h^2/\nu)$. The ratio

$$\frac{T_2}{T_1} = \frac{h^2\omega kA^2}{L\nu} = \frac{(kh)^2}{2kL}\left(\frac{A}{\delta}\right)^2$$

is of the order $O(1)$ in normal laboratory tanks. Thus, when vorticity is diffused throughout the depth, the return mass transport is just about established in most of the length. However, Eq. (10.6.44) has not been convincingly verified in experiments.

Note that the results for infinite depth cannot be obtained by taking the limit of Eq. (10.6.41) or (10.6.42). This is not surprising, since the theory is

constructed on the basis that the attenuating length scale in the direction of wave propagation is infinite (i.e., $\gg h$). One cannot take the limit of $h \to \infty$ without first accounting for the effects of attenuation and Stuart's double boundary layers. These remedies have been studied by Dore (1977), and Liu and Davis (1977).

Finally, the presence of air, which was shown in Section 9.6 to have a pronounced effect on wave damping, can also be important in the mass transport. By recalculating the boundary layers near the free surface, Dore (1978) found that Eq. (10.6.39) must be modified. As a result Eq. (10.6.44) had to be corrected by adding the following expression:

$$\frac{1}{4h}\left(\frac{\omega}{2}\right)^{3/2}\frac{1}{k}(1+\coth kh)^2\left(\frac{\rho' u'}{\rho\mu}\right)^{1/2}\frac{1}{\nu^{1/2}}(c+h)(3c+h) \qquad (10.6.45)$$

where ρ' and μ' refer to air. For a typical frequency and depth the resulting velocity profile is compared to Eq. (10.6.44), in Fig. 10.7.

Exercise 10.3: Peristaltic Pumping by Water Waves (Longuet–Higgins, 1983)

It has been suggested that wave energy can be used to transport water through a water channel that is bounded below by a rigid horizontal bottom and above by a flexible but inextensible membrane. The mean channel height is Δ. Passing waves cause the membrane to move so that

$$z = \Delta + b\cos(kx - \omega t)\,.$$

Assume $kA \ll 1$, $b/\Delta \ll 1$, $\delta/\Delta \ll 1$. Show first that the leading-order inviscid velocity in the channel is

$$u = \frac{\omega b}{k\Delta}\cos(kx-\omega t) \quad w = \frac{z}{\Delta}\omega b\sin(kx-\omega t)\,.$$

Next show that the horizontal velocity of the membrane is much less than u above. Use known results to show that the mass transport velocity at the outer edges of both top and bottom boundary layers is

$$\bar{u}_L = \frac{5}{4}\frac{q^2}{C} \quad z = 0, \Delta \quad \text{where} \quad q = \frac{bC}{\Delta}\,, \quad C = \frac{\omega}{k}\,.$$

Then derive the equation for the Eulerian streaming velocity in the core between the top and bottom Stokes layers,

$$\nu\frac{\partial^2 \bar{u}}{\partial z^2} = \frac{1}{\rho}\frac{\partial \bar{P}}{\partial x} + \overline{u\frac{\partial u}{\partial x}} + \overline{w\frac{\partial u}{\partial z}} \quad 0 < z < h\,,$$

where $\frac{1}{\rho}\frac{\partial \overline{P}}{\partial x}$ is the steady constant pressure gradient in the channel. Show finally that the Lagrangian mass transport in the core outside the boundary layers satisfies

$$\nu \frac{\partial^2 \bar{u}_L}{\partial z^2} = \frac{1}{\rho}\frac{\partial \bar{p}}{\partial x} \quad 0 < z < h\,.$$

With the derived boundary conditions find the mass transport throughout the core and the total mass flux rate with the pressure gradient as a parameter.

10.7 Further References

As pointed out earlier, Longuet–Higgins' theory for the mass transport in a sea of finite depth leads to an unbounded limit for infinite depth. As an alternative to Stuart's second boundary layer, it turns out that earth rotation can give a finite limit. While irrelevant in the laboratory, this new physical factor cannot be ruled out in an ocean where distances of hundreds of kilometers are involved. Madsen (1978) and Huang (1978) showed independently that the wind-induced current in the Ekman layer near the sea surface could interact and modify the wave-induced mass transport in a nontrivial way. In particular, the mass transport was found to be confined within the Ekman layer. Madsen assumed that the effect of wind (hence, of air) was only to provide a steady driving shear stress to maintain the wave motion. Possible direct effect of air on wave-induced Reynolds' stresses in water was, however, not taken into account. In view of Dore's conclusion cited in Section 10.6, further study, which may yield results useful in oil spills, is desirable.

The effect of earth rotation is of first-order influence to tidal waves whose frequencies are comparable to the angular velocity of the earth. To the coastal engineer, the tide-induced mass transport may be of interest in affecting the silting and scour in an estuary, near a barrier island, and so on. Pertinent theoretical studies have been made by Hunt and Johns (1963), Longuet–Higgins (1970c), Moore (1970), and Huthnance (1981). Lamoure and Mei (1977) examined the bottom mass transport near small bodies and found for the northern hemisphere that the mass transport near the sea bottom had a counterclockwise tilt and varied in a spiraling manner in the Ekman layer.

This page intentionally left blank

Radiation Stresses, Bound Long Waves and Longshore Current

11

11.1 Introduction

One of the most important reasons for studying nearshore currents is to help understand the interaction between the shoreline and the fluid motion in the sea. In the past, geographers and geomorphologists accumulated a good deal of descriptive knowledge on the formation and evolution of coastlines (Johnson, 1919; King, 1959; Zenkovich, 1967; Shepard and Wanless, 1973). Since the loss of sand and the recession of beaches can be undesirable to parks, residential areas, and coastal highways, and the accumulation of silt near a harbor entrance or a river inlet can be hazardous to navigation or flood control, it is the task of engineers to grapple with the mysteries of beach processes in order to plan proper defenses.

Most of the guidelines for coastal protection practices have been based on observational studies both in the field and in the laboratory (see, for example, *Shore Protection Manual*, U.S. Army Coastal Engineering Research Center, 1977, Vols. I–III). These studies have been and will undoubtedly remain indispensible in increasing our knowledge of shore processes. In recent years, much progress has also been made in the development of semiempirical theories on both the causative currents and the resultant sediment motion. The whole problem of shoreline dynamics is extremely complex, due in part to the turbulent interaction between sediments and fluid flow and in part to the large variety of currents that can be present (wind waves, tides, storm surges, river currents, and large-scale ocean circulation caused by wind, thermal or salinity gradients, etc.). Among these currents a prominent role is played by the *longshore current* induced by breaking waves in the surf zone.

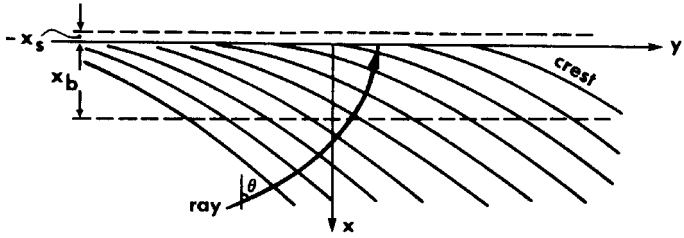

Figure 11.1: Waves incident on an infinitely long plane beach.

With reference to Fig. 11.1, let us first give a bird's-eye description of the physical processes on a straight beach. A train of periodic waves with frequency ω and amplitude A_∞ is incident from deep water $x \sim +\infty$ at the incidence angle θ_∞. When waves first feel the bottom, refraction causes the x component of the wavelength to decrease so that the wave rays tend to strike the shore normally; the wave amplitude varies such that energy is roughly conserved between two adjacent rays. In sufficiently shallow water the wave profile steepens and eventually breaks at a certain line $x = x_b$, where the depth is $h_b = h(x_b)$. This line of first breaking is called the *breaker line*, which divides the *shoaling zone* seaward of x_b and the *breaker zone* or the *surf zone* shoreward of x_b. Kinematically, the wave rays proceed in roughly the same direction as if there were no breaking. Once inside the surf zone, turbulence prevails so that the breaking wave is dissipated and diminishes in height. When the shore is reached, the wave crest finally exhausts itself in the form of a thin sheet rushing up the beach. After the highest climb, the sheet of fluid retreats seaward by gravity, encounters, and is swallowed by the next onrushing wave crest. Aside from this to-and-fro motion, however, there is also a less conspicuous drift along the shore in the direction of the longshore component of the incidence waves. This steady drift, called the *longshore current*, can be significant in magnitude, say $O(1$ m/s). Since the turbulent fluctuations in the surf zone dislodge many sand particles from their rest position and mix them with the fluid, the steady longshore drift becomes a powerful mechanism for sand transport, and, in turn, for the evolution of the beach.

In the earliest analytical theories on longshore currents, focus was centered on the total longshore flux in the entire surf zone. Putnam, Munk, and Traylor (1949) assumed that the crests of a periodic wavetrain were so well separated that they were practically independent of each other. The momentum flux of a solitary crest incident obliquely was averaged over the

actual period to give the mean momentum flux entering the surf zone. After breaking, the crest dissipated into a much slower current along the shore and carried away certain momentum flux. By equating the longshore component of the net momentum flux into a control volume to the bottom friction experienced by this volume, they obtained the total longshore discharge. Eagleson (1965) discarded the assumption of solitary crests and modified the above argument by taking time averages of a periodic wavetrain described by the small-amplitude theory. He also considered the growth of the longshore current from a headland or an infinitely long surf zone barrier where the longshore current was zero. In both cases, only the mean across the surf zone was derived. In arriving at explicit results, empirical assumptions on breaking waves and bottom friction were introduced.

The idea of the mean momentumn flux is the precursor of the theory of *radiation stresses* initiated by Longuet–Higgins and Stewart (1962). As will be explained in this Chapter, the radiation stresses are analogous to the Reynolds stresses in turbulence, being the consequence of convective inertia and obtained by averaging over wave fluctuations. The first application of radiation stresses was on the phenomena of set-down and surf beats outside the surf zone. The same tool was applied later to predict the longshore current along a straight beach, independently by Bowen (1969), Longuet–Higgins (1970a, b), and Thornton (1970). In the shoaling zone where the wave steepness is small, these stresses can be calculated from the leading-order theory of waves, without the usual headache of closure in turbulence. In the surf zone where breaking and turbulence prevail, empirical relations between the radiation stresses and mean-flow quantities are introduced in order to enable the prediction of a longshore current profile.

In this chapter we shall first develop the radiation stress theory by averaging the fundamental equations of hydodynamics. Applications to setdown and bound long waves will be briefly demonstrated. After a discussion of the empirical knowledge of breaking waves, semiempirical theories are presented for the uniform longshore current on a straight beach. Two examples of more complex wave fields are also discussed.

11.2 Depth and Time-Averaged Equations for the Mean Motion

The main objective of this section is to obtain conservation laws of mass and horizontal momentum for the mean current field by arguments similar

to those leading to the Reynolds equations for the mean turbulent flow (Longuet–Higgins and Stewart, 1962; Phillips, 1977).

For the convenience of vertical integration, the vertical and horizontal directions are distinguished. Specifically, we denote the vertical velocity by w and the vertical coordinate by z, the horizontal velocity components by u_i $(i = 1, 2;\ u_1 = u,\ u_2 = v)$, and the horizontal coordinates by x_i $(i = 1, 2;\ x_1 = x,\ x_2 = y)$. We define the mean velocity U_i $(i = 1, 2)$ by integrating u_i over the instantaneous water depth and then over the time period T, that is,

$$U_i(x, y, t) = \frac{1}{\bar{\zeta} + h} \overline{\int_{-h}^{\zeta} u_i \, dz}\,, \quad i = 1, 2\,, \tag{11.2.1}$$

where $\zeta(x, y, t)$ is the free-surface displacement, $\bar{\zeta}$ is its time mean, and $h(x, y)$ is the still water depth. Physically, $\rho U_i(\bar{\zeta} + h)$ is the mean rate of mass flux across a vertical plane of unit width along $x_i = \text{const}$. The vector (U_1, U_2) may, therefore, be called the *mass flux velocity*, which depends only on the horizontal coordinates and the long time scale. Denoting the deviation from the mean by $\tilde{u}_i$, we have

$$u_i = U_i + \tilde{u}_1(x, y, z, t)\,. \tag{11.2.2}$$[1]

It follows from the definition that

$$\overline{\int_{-h}^{\zeta} \tilde{u}_i \, dz} = 0\,. \tag{11.2.3}$$

11.2.1 Averaged Equation of Mass Conservation

Integrating the local continuity equation over the depth, we get

$$\int_{-h}^{\zeta} \frac{\partial u_i}{\partial x_i} \, dz + [w]_{\zeta} - [w]_{-h} = 0\,, \tag{11.2.4}$$

where $[w]_{\zeta}$ denotes the value of w at $z = \zeta$ and $[w]_{-h}$, denotes the value of w on the bottom. With Leibniz's rule, Eq. (11.2.4) can be written

$$\frac{\partial}{\partial x_i} \int_{-h}^{\zeta} u_i \, dz + \left[-u_i \frac{\partial \zeta}{\partial x_i} + w \right]_{\zeta} - \left[u_i \frac{\partial h}{\partial x_i} + w \right]_{-h} = 0\,. \tag{11.2.5}$$

[1] This definition differs slightly from that of Phillips (1977, p. 45).

On the free surface, the kinematic boundary condition

$$\frac{\partial \zeta}{\partial t} + u_i \frac{\partial \zeta}{\partial x_i} = w\,, \quad z = \zeta\,, \tag{11.2.6}$$

may be recalled. For simplicity, we assume a rigid sea bottom at $z = -h$, then

$$u_i = w = 0 \quad \text{for real fluid}\,, \tag{11.2.7}$$

or

$$\left[u_i \frac{\partial h}{\partial x_i} + w \right]_{-h} = 0 \quad \text{for inviscid fluid}\,. \tag{11.2.8}$$

Because of Eqs. (11.2.6) and (11.2.7) or Eq. (11.2.8), Eq. (11.2.5) becomes

$$\frac{\partial \zeta}{\partial t} + \frac{\partial}{\partial x_i} \int_{-h}^{\zeta} u_i \, dz = 0\,. \tag{11.2.9}$$

Upon taking the time average, we get

$$\frac{\partial \bar{\zeta}}{\partial t} + \frac{\partial}{\partial x_i}[U_i(\bar{\zeta} + h) = 0 \tag{11.2.10}$$

exactly; the same result was deduced before [see Eq. (2.5.12)] as an approximation for long waves in shallow water.

11.2.2 Averaged Equations of Momentum Conservation

In order to include the laboratory case of smooth and rigid bottoms, we allow both viscous and turbulent stresses to be present. For a rough and rigid bottom, the viscous stresses are unimportant almost everywhere and may be discarded from the following discussion.

Let us first rearrange the Navier–Stokes equations of motion as follows: horizontal momentum ($j = 1, 2$):

$$\frac{\partial u_j}{\partial t} + \frac{\partial u_i u_j}{\partial x_i} + \frac{\partial u_j w}{\partial z} = \frac{1}{\rho} \frac{\partial}{\partial x_i}(-P\delta_{ij} + \tau_{ij}) + \frac{1}{\rho} \frac{\partial \tau_{j3}}{\partial z}\,, \tag{11.2.11}$$

vertical momentum:

$$\frac{\partial w}{\partial t} + \frac{\partial u_i w}{\partial x_i} + \frac{\partial w^2}{\partial z} = -\frac{1}{\rho} \frac{\partial}{\partial z}(P + \rho g z) + \frac{1}{\rho} \frac{\partial \tau_{i3}}{\partial x_i} + \frac{1}{\rho} \frac{\partial \tau_{33}}{\partial z}\,, \tag{11.2.12}$$

where τ_{ij}, τ_{j3}, and τ_{33} are the components of the viscous stress tensor. When the horizontal momentum equation (11.2.11) is integrated vertically, terms on the left-hand side give

$$\int_{-h}^{\zeta} dz \frac{\partial \rho u_j}{\partial t} = \frac{\partial}{\partial t}\int_{-h}^{\zeta} \rho u_j \, dz - \rho[u_j]_{\zeta}\frac{\partial \zeta}{\partial t}\,,$$

$$\int_{-h}^{\zeta} dz \frac{\partial \rho u_i u_j}{\partial x_i} = \frac{\partial}{\partial x_i}\int_{-h}^{\zeta} \rho u_i u_j \, dz - \rho[u_i u_j]_{\zeta}\frac{\partial \zeta}{\partial x_i} - \rho[u_i u_j]_{-h}\frac{\partial h}{\partial x_i}\,,$$

$$\int_{-h}^{\zeta} dz \frac{\partial \rho u_i w}{\partial z} = \rho[u_i w]_{\zeta} - \rho[u_i w]_{-h}\,.$$

Summing up these terms and invoking the kinematic boundary conditions on the free surface and on the bottom, that is, Eqs. (11.2.6) and (11.2.7), we obtain for the left-hand side of Eq. (11.2.11)

$$\text{L.H.S.} = \frac{\partial}{\partial t}\int_{-h}^{\zeta} \rho u_j \, dz + \frac{\partial}{\partial x_i}\int_{-h}^{\zeta} (\rho u_i u_j)\, dz\,. \tag{11.2.13}$$

Similarly, the right-hand side of Eq. (11.2.11) gives

$$\begin{aligned}\text{R.H.S.} &= \int_{-h}^{\zeta} \frac{\partial}{\partial x_i}(-P\delta_{ij} + \tau_{ij})\, dz + \int_{-h}^{\zeta} \frac{\partial \tau_{j3}}{\partial z}\, dz \\ &= \frac{\partial}{\partial x_i}\int_{-h}^{\zeta} (-P\delta_{ij} + \tau_{ij})\, dz - [-P\delta_{ij} + \tau_{ij}]_{\zeta}\frac{\partial \zeta}{\partial x_i} \\ &\quad - [-P\delta_{ij} + \tau_{ij}]_{-h}\frac{\partial h}{\partial x_i} + [\tau_{j3}]_{\zeta} - [\tau_{j3}]_{-h}\,. \end{aligned} \tag{11.2.14}$$

On the free surface, the atmospheric force per unit area must balance the fluid stresses. This balance implies that in the jth direction

$$[-P\delta_{ij} + \tau_{ij}]n_i + \tau_{j3}n_3 = \tau_j^F\,, \quad z = \zeta,\ j = 1, 2\,, \tag{11.2.15}$$

where τ_j^F is the externally applied horizontal stress component which is defined to include both atmospheric pressure and shear stress given from meteorological data and $\mathbf{n} = (n_1, n_2, n_3)$ is the unit outward normal vector. On the free surface described by $F(x, y, z, t) = z - \zeta(x, y, t) = 0$, the unit outward normal is $\mathbf{n} = \nabla F/|\nabla F|$ where $\nabla F = (-\partial\zeta/\partial x, -\partial\zeta/\partial y, 1)$. Hence, Eq. (11.2.15) can be written

$$-[-P\delta_{ij} + \tau_{ij}]_{\zeta}\frac{\partial \zeta}{\partial x_i} + [\tau_{j3}]_{\zeta} = \tau_j^F|\nabla F|\,, \quad z = \zeta\,. \tag{11.2.16}$$

On the bottom $B(x,y,z) = z+h(x,y) = 0$ we denote the total horizontal shear stress by τ_j^B, that is,

$$\tau_{ij} n_i + \tau_{j3} n_3 = \tau_j^B \,, \quad z = -h(x,y), \; j = 1,2 \,. \tag{11.2.17}$$

Since the unit outward normal to the bottom is $\mathbf{n} = -\nabla B/|\nabla B|$ where $\nabla B = (\partial h/\partial x, \partial h/\partial y, 1)$, Eq. (11.2.17) may be expressed as

$$\tau_{ij} \frac{\partial h}{\partial x_i} + \tau_{j3} = -\tau_j^B |\nabla B| \,, \quad z = -h \,. \tag{11.2.18}$$

With Eqs. (11.2.16) and (11.2.18), Eq. (11.2.14) becomes

$$\text{R.H.S.} = \frac{\partial}{\partial x_i} \int_{-h}^{\zeta} [-P\delta_{ij} + \tau_{ij}] \, dz + [P]_{-h} \frac{\partial h}{\partial x_j} + [\tau_j^F |\nabla B| - \tau_j^B |\nabla B|] \,. \tag{11.2.19}$$

Equating Eqs. (11.2.13) and (11.2.19), we have

$$\frac{\partial}{\partial t} \int_{-h}^{\zeta} \rho u_j \, dz + \frac{\partial}{\partial x_i} \int_{-h}^{\zeta} \rho u_i u_j \, dz = [P]_{-h} \frac{\partial h}{\partial x_j} + \frac{\partial}{\partial x_i} \int_{-h}^{\zeta} [-P\delta_{ij} + \tau_{ij}] \, dz + [\tau_j^F |\nabla F| - \tau_j^B |\nabla B|] \,. \tag{11.2.20}$$

Physically, Eq. (11.2.20) represents the momentum balance in a vertical column of fluid of height $\zeta + h$ and unit cross section ($d_x = 1, d_y = 1$). On the left-hand side the terms are successively the acceleration and the net momentum flux through the vertical sides of the column. On the right, the terms represent, in the sequence shown, the pressure by the bottom to the fluid, the net surface stresses on the vertical sides, and the surface stress at the free surface and the sea bottom.

The time average of the left-hand side of Eq. (11.2.20) may be written

$$\rho(\bar{\zeta} + h) \left(\frac{\partial U_j}{\partial t} + U_i \frac{\partial U_j}{\partial x_i} \right) + \rho \frac{\partial}{\partial x_i} \overline{\left(\int_{-h}^{\zeta} \tilde{u}_i \tilde{u}_j \, dz \right)} \tag{11.2.21}$$

after using Eq. (11.2.10). On the right-hand side of Eq. (11.2.20) we define $\bar{p}$ as the mean dynamic pressure at the bottom, that is,

$$\bar{p} = [\overline{P}]_{-h} - \rho g(\bar{\zeta} + h) \,, \tag{11.2.22}$$

so that

$$[\overline{P}]_{-h} \frac{\partial h}{\partial x_j} = \bar{p} \frac{\partial h}{\partial x_j} + \frac{\partial}{\partial x_j} \left[\frac{1}{2} \rho g (\bar{\zeta} + h)^2 \right] - \rho g (\bar{\zeta} + h) \bar{p} \frac{\partial \bar{\zeta}}{\partial x_j} \,. \tag{11.2.23}$$

Substituting Eqs. (11.2.21) and (11.2.23) into the time average of Eq. (11.2.20), we obtain finally for $j = 1, 2$

$$\rho(\bar{\zeta} + h)\left[\frac{\partial U_j}{\partial t} + U_i\frac{\partial U_j}{\partial x_i}\right]$$
$$= \bar{p}\frac{\partial h}{\partial x_j} - \rho g(\bar{\zeta} + h)\frac{\partial \bar{\zeta}}{\partial x_j}$$
$$+ \frac{\partial}{\partial x_i}\left\{-S_{ij}\overline{\int_{-h}^{\zeta}\tau_{ij}\,dz}\right\} + \overline{\tau_j^F|\nabla F|} - \overline{\tau_j^B}|\nabla F|\,, \qquad (11.2.24)$$

where the following definition has been introduced

$$S_{ij} = \overline{\int_{-h}^{\zeta}[P\delta_{ij} + \rho\tilde{u}_i\tilde{u}_j]\,dz} - \frac{\rho g}{2}(\bar{\zeta} + h)^2\delta_{ij}\,. \qquad (11.2.25)$$

Physically, S_{ij} is the (i, j) component of the stress tensor representing the *excess momentum fluxes*.[2] Since

$$\frac{\rho g}{2}(\bar{\zeta} + h)^2 = \int_{-h}^{\bar{\zeta}}\rho g(\bar{\zeta} - z)\,dz$$

is just the total mean hydrostatic pressure over the mean depth, S_{ij} may be written

$$S_{ij} = \left[\overline{\int_{-h}^{\zeta}P\,dz} - \int_{-h}^{\bar{\zeta}}\rho g(\bar{\zeta} - z)\,dz\right]\delta_{ij} + \overline{\int_{-h}^{\zeta}\rho\tilde{u}_i\tilde{u}_j\,dz}\,. \qquad (11.2.26)$$

Thus, S_{ij} represents the sum of the ith component of the excess hydrodynamic pressure on, and the net momentum flux across, a surface normal to the jth direction. Also on the right-hand side of Eq. (11.2.24), the quantity $\overline{\int_{-h}^{\zeta}\tau_{ij}\,dz}$ corresponds to the mean momentum flux tensor caused by fluctuations of molecular scale. $\bar{p}\partial h/\partial x_j$ is the mean hydrodynamic reaction at the sea bottom and $\rho g\partial\bar{\zeta}/\partial x$ is the hydrostatic pressure gradient due to the mean sea level.

Thus far, Eqs. (11.2.10) and (11.2.24) are *exact*. In particular, the orders of magnitude of the mean current and the waves are yet arbitrary. Practical applications of these equations sometimes permit (or even demand) certain simplifications as will be shown later.

[2]The definition of S_{ij} is slightly different from Phillips [1977, Eq. (3.6.12)]. The difference is of the fourth order for infinitesimal waves.

11.2.3 Some Preliminary Simplifications

Let us introduce certain simplifying assumptions before proceeding further.

First, let all mean quantities be slowly varying in time, and let there be no atmospheric disturbance on the free surface

$$\bar{\tau}_j^F = 0\,. \tag{11.2.27}$$

This assumption precludes the study of the transient effects of wind which may have very direct influence on the short-term evolution of beaches. Little work has been done in this regard.

Let us now discuss further approximations for Eq. (11.2.26) when the following quantities are small: (i) viscosity, (ii) bottom slope, $|\nabla h| \leqq O(kA)$, and (iii) wave slope kA. In addition the averages are slowly varying in time so that

$$\frac{\partial \bar{f}}{\partial t} = \omega k A \bar{f}\,. \tag{11.2.28}$$

Viscous Stress Terms

The integrated viscous stress terms, being the product of molecular viscosity and the horizontal gradients of the horizontal velocity, are of the order

$$\overline{\int_{-h}^{\zeta} \tau_{ij}\, dz} \sim O(\mu k \omega A h)\,. \tag{11.2.29}$$

Since S_{ij} is of the order $O(\rho(\omega A)^2 h)$, we get

$$\frac{\overline{\int_{-h}^{\zeta} \tau_{ij}\, dz}}{S_{ij}} = O\left(\frac{k\nu}{\omega A}\right) = O(\mathsf{R}_\mathsf{E}^{-1}) \tag{11.2.30}$$

where

$$\mathsf{R}_\mathsf{E} = \frac{\omega A}{k\nu} = \frac{A}{k\delta^2}$$

is the Reynolds number based on the wave orbital velocity and the wavelength. Under practical circumstances the above ratio is very small and the integral of viscous stress τ_{ij} is negligible.

The bottom stress $\bar{\tau}_j^B$ is, however, not necessarily small. In the present chapter the bottom slope of the beach will always be regarded as small,

$$|\nabla B| = 1 + O(\nabla h)^2\,,$$

and we may approximate

$$\bar{\tau}_j^B|\nabla B| = \bar{\tau}_j^B[1 + O(\nabla h)^2] \tag{11.2.31}$$

in Eq. (11.2.24). Recall from Section 8.9 that the $\bar{\tau}_j^B$ can be related to the local orbital velocity if there is a turbulent boundary layer.

Dynamic Pressure $\bar{p}\partial h/\partial x_j$

To estimate the mean dynamic pressure, we integrate the vertical momentum equation (11.2.12) and employ Leibniz's rule as before,

$$\begin{aligned}
[P]_z &= \rho g(\zeta - z) + \rho\left[\frac{\partial}{\partial t}\int_z^\zeta w\,dz + \frac{\partial}{\partial x_i}\int_z^\zeta u_i w\,dz\right] \\
&= -\rho\left[w\left(\frac{\partial\zeta}{\partial t} + u_i\frac{\partial\zeta}{\partial x_i} - w\right)\right]_\zeta - \rho[w^2]_z - \frac{\partial}{\partial x_i}\int_z^\zeta \tau_{i3}\,dz \\
&\quad - \left[-P + \tau_{33} - \tau_{i3}\frac{\partial\zeta}{\partial x_i}\right]_\zeta + [\tau_{33}]_z\,,
\end{aligned} \tag{11.2.32}$$

where $[P]_z$ means P evaluated at an arbitrary height z. The free-surface boundary terms vanish by Eqs. (11.2.6) and (11.2.16) if the atmospheric pressure is zero. The time average of the mean water pressure at any z is, therefore,

$$[\overline{P}]_z = \rho g(\bar{\zeta} - z) + \frac{\partial}{\partial x_i}\overline{\int_{-h}^\zeta \rho u_i w\,dz} - \rho[\overline{w^2}]_z - \frac{\partial}{\partial x_i}\overline{\int_z^\zeta \tau_{i3}\,dz} + [\bar{\tau}_{33}]_z\,. \tag{11.2.33}$$

The integrated molecular viscous term is of the order $O(\mathsf{R}_\mathsf{E}^{-1})$ relative to the others. From continuity, the term $[\bar{\tau}_{33}]_z$ may be estimated by

$$[\bar{\tau}_{33}]_z = \mu\frac{\partial\bar{w}}{\partial z} \sim \left(\mu\frac{\partial\bar{u}_i}{\partial x_i}\right)$$

and is also negligible. Thus, to a good approximation, we have

$$[\overline{P}]_z \simeq \left\{\rho g(\bar{\zeta} - z) + \frac{\partial}{\partial x_i}\overline{\int_{-h}^\zeta \rho u_i w\,dz} - \rho[\overline{w^2}]_z\right\}\{1 + O(\mathsf{R}_\mathsf{E}^{-1})\}\,, \tag{11.2.34}$$

implying that viscosity does not have any direct influence on $[\overline{P}]_z$. The same is true for $[\overline{P}]_{-h}$

$$[\overline{P}]_{-h} \cong \rho g(\bar{\zeta}+h)\frac{\partial}{\partial x_i}\overline{\int_{-h}^{\zeta}\rho u_i w\,dz}\,. \tag{11.2.35}$$

Combining Eqs. (11.2.35) and (11.2.22), we have simply

$$\bar{p}\frac{\partial h}{\partial x_j} = \left\{\frac{\partial h}{\partial x_j}\frac{\partial}{\partial x_i}\overline{\int_{-h}^{\zeta}\rho u_i w\,dz}\right\}[1+O(\mathsf{R}_{\mathsf{E}}^{-1}|\nabla h|)]\,. \tag{11.2.36}$$

Finally, let us compare the preceding term with other terms in Eq. (11.2.24). For short-crested waves we should expect the length scale of variations of U_i, $\bar{\zeta}$, S_{ij}, and so on, to be k^{-1} so that the largest terms among

$$\rho(\bar{\zeta}+h)U_i\frac{\partial U_j}{\partial x_i}\,,\quad \rho g(\bar{\zeta}+h)U_i\frac{\partial\bar{\zeta}}{\partial x_j}\,,\quad \frac{\partial S_{ij}}{\partial x_i}$$

are of the order $O(kh\rho\omega^2A^2)$. Now because of the factor ∇h,

$$\bar{p}\frac{\partial h}{\partial x_i} = O(|\nabla h|\rho(\omega A)^2 kh) \tag{11.2.37}$$

is unimportant and can be ignored.

For long-crested waves refracted by the sea bottom, all mean quantities are expected to vary slowly in horizontal directions as the depth h itself; hence $\bar{p}\partial h/\partial x_i$ is again $O(|\nabla h|)$ times smaller than the largest remaining terms and may be ignored.

The Excess Momentum Flux Tensor — The Radiation Stresses for Small Fluctuations

In the exact definition for S_{ij}, Eq. (11.2.25), let $\tilde{u}_i$ and $\tilde{\zeta} \equiv \zeta - \bar{\zeta}$ be further decomposed into wave and turbulent fluctuations, which will be distinguished by single and double primes, respectively; thus

$$\tilde{u}_i = u_i' + u_i''\,,\quad \tilde{\zeta} = \zeta - \bar{\zeta} = \zeta' + \zeta''\,. \tag{11.2.38}$$

Clearly, $\tilde{\zeta} = O(A)$. If we assume that the characteristic time scales of the two fluctuations are vastly different, then u_i' and u_j'' are uncorrelated

$$\overline{u_i'u_j''} = 0\,,\quad \overline{\zeta'\zeta''} = 0\,. \tag{11.2.39}$$

The second term in Eq. (11.2.25) may now be approximated as

$$\overline{\rho\int_{-h}^{\zeta}\tilde{u}_i\tilde{u}_j\,dz} = \rho\int_{-h}^{\bar{\zeta}}\overline{\tilde{u}_i\tilde{u}_j}dz + O(\rho\omega^2A^3)$$

$$\cong \rho\int_{-h}^{\bar{\zeta}}\overline{u_i'u_j'}\,dz + \rho\int_{-h}^{\bar{\zeta}}\overline{u_i''u_j''}\,dz\,. \qquad (11.2.40)$$

The leading term is of the order $O(\rho h\omega^2A^2) = O(\rho gA^2)$.

To obtain a more explicit formula for the remaining terms in Eq. (11.2.25), we integrate Eq. (11.2.32) vertically and then average the result with respect to time:

$$\overline{\int_{-h}^{\zeta}P\,dz} = \rho g\overline{\frac{(\zeta+h)^2}{2}} + \rho\overline{\int_{-h}^{\zeta}dz\frac{\partial}{\partial t}\int_{z}^{\zeta}w\,dz}$$

$$+\rho\overline{\int_{-h}^{\zeta}dz\frac{\partial}{\partial x_i}\int_{z}^{\zeta}u_iw\,dz} - \rho\overline{\int_{-h}^{\zeta}w^2\,dz}\,. \qquad (11.2.41)$$

Again, the integrated viscous stresses have been ignored. The first term on the right of Eq. (11.2.41) may be rewritten

$$\frac{\rho g}{2}\overline{(\zeta+h)^2} = \frac{\rho g}{2}[(\bar{\zeta}+h)^2 + \overline{\zeta'^2} + \overline{\zeta''^2}]\,. \qquad (11.2.42)$$

The second term in Eq. (11.2.41) becomes, upon partial integration,

$$\overline{\rho\int_{-h}^{\zeta}dz\frac{\partial}{\partial t}\int_{z}^{\zeta}w\,dz'} = \overline{\rho\frac{\partial}{\partial t}\int_{-h}^{\zeta}dz\int_{z}^{\zeta}w\,dz'} = \rho h^2\frac{\partial W}{\partial t} \qquad (11.2.43)$$

where W denotes the averaged vertical velocity which is, by definition,

$$W = \frac{1}{\bar{\zeta}+h}\overline{\int_{-h}^{\zeta}w\,dz} = \frac{1}{\bar{\zeta}+h}\left(\int_{-h}^{\bar{\zeta}}\bar{w}\,dz + \overline{\int_{\bar{\zeta}}^{\zeta}w\,dz}\right).$$

Assume that the horizontal scales of depth and U_i are comparable. Then either for a strong current $[O(U_i) = (gh)^{1/2}]$ with $\nabla h/kh = O(k^2A^2)$ or for a weak current $[O(U_i) = \omega A]$ with $\nabla h/kh = O(kA)$, the mean vertical current W is much smaller than w' or w'' by a factor $O(\nabla h)$ or $O(kA)$. In view of (11.2.28), the time-derivative term in (11.2.43) is of the order $\rho(kh)^2\omega^2A^3$ which is negligible. It also follows that

$$\overline{\rho\int_{-h}^{\zeta}dz\frac{\partial}{\partial x_i}\int_{z}^{\zeta}u_iw\,dz} \cong \rho\int_{-h}^{\bar{\zeta}}dz\frac{\partial}{\partial x_i}\int_{z}^{\bar{\zeta}}[\overline{u_i'w'} + \overline{u_i''w''}]\,dz\,, \qquad (11.2.44)$$

and

$$-\rho\overline{\int_{-h}^{\zeta} w^2\,dz} \cong -\rho\int_{-h}^{\bar{\zeta}} (\overline{w'^2} + \overline{w''^2})\,dz\,, \tag{11.2.45}$$

with a relative error of $O(|\nabla h|, kA)$. When Eqs. (11.2.42)–(11.2.45) are substituted into Eq. (11.2.41) and then into Eq. (11.2.25), the result is

$$S_{ij} = S'_{ij} + S''_{ij}\,, \tag{11.2.46}$$

where

$$S'_{ij} = \rho\int_{-h}^{\bar{\zeta}} \overline{u'_i u'_j}\,dz + \delta_{ij}\left\{\rho\frac{\overline{g\zeta'^2}}{2} + \rho\int_{-h}^{\bar{\zeta}} dz\frac{\partial}{\partial x_i}\int_z^{\bar{\zeta}} \overline{u'_i w'}\,dz'\right.$$

$$\left. -\rho\int_{-h}^{\bar{\zeta}} \overline{w'^2}\,dz\right\}. \tag{11.2.47}$$

Similarly, S''_{ij} is defined with all $(\,)'$ being replaced by $(\,)''$

$$S''_{ij} = \rho\int_{-h}^{\bar{\zeta}} \overline{u''_i u''_j}\,dz + \delta_{ij}\left\{\rho\frac{\overline{g\zeta''^2}}{2} + \int_{-h}^{\bar{\zeta}} dz\frac{\partial}{\partial x_i}\int_z^{\bar{\zeta}} \overline{u''_i w''}\,dz'\right.$$

$$\left. -\int_{-h}^{\bar{\zeta}} \overline{w''^2}\,dz\right\}. \tag{11.2.48}$$

S'_{ij} and S''_{ij} are, respectively, the excess momentum flux tensors due to wave and turbulent fluctuations. S'_{ij} is called the *radiation stress* tensor by Longuet–Higgins and Stewart (1962, 1964). Since the last term in S''_{ij}

$$\rho\int_{-h}^{\bar{\zeta}} \overline{u''_i u''_j}\,dz$$

is the negative of the integrated Reynolds stress due to horizontal turbulent fluctuations, S''_{ij} is an extension of the Reynolds stress, with additional contributions from vertical fluctuations.

Away from the surf zone, turbulence is usually unimportant so that $S''_{ij} \ll S'_{ij}$; the wave radiation stress S'_{ij} can be evaluated by using the first-order wave theory, as will be shown shortly. Inside the surf zone, waves and turbulence can be equally strong; nonlinearity becomes important and u'_i may even be comparable to the phase velocity. While Eq. (11.2.25) still holds, definitions (11.2.47) and (11.2.48), which are approximate for small

kA, should be modified. More important, neither stress can be deduced theoretically, and empirical closure conditions are needed.

In contrast to Eq. (11.2.48), Phillips (1977) did not include the diagonal terms in the curly brackets. This formal difference is, however, only of academic significance in view of the uncertainties in the closure hypothesis to be introduced for S''_{ij}.

11.2.4 Summary of Approximate Averaged Equations

The approximate equations for the mean motion may now be collected below:

$$\frac{\partial \bar{\zeta}}{\partial t} + \frac{\partial}{\partial x_i}[U_i(\bar{\zeta} + h)] = 0 \tag{11.2.50}$$

and

$$\frac{\partial U_j}{\partial t} + U_i \frac{\partial U_j}{\partial x_i} = -g\frac{\partial \bar{\zeta}}{\partial x_j} - \frac{1}{\rho(\bar{\zeta}+h)}\frac{\partial}{\partial x_i}(S'_{ij} + S''_{ij}) - \frac{\bar{\tau}^B_j}{\rho(\bar{\zeta}+h)}\,, \tag{11.2.51}$$

where S'_{ij} and S''_{ij} are given by Eqs. (11.2.47) and (11.2.48).

In the shoaling zone and away from lateral boundaries, such as breakwaters and jetties, turbulence is negligible so that S''_{ij} may be further neglected. For small-amplitude waves the radiation stresses are second-oreder in wave steepness, so are the mean current velocity annd the mean sea-level. The quadratic products of the mean quantities in Eq. (11.2.50) and(11.2.51) are of the fourth order and may also be ignored, so that

$$\frac{\partial \bar{\zeta}}{\partial t} + \frac{\partial (U_j h)}{\partial x_j} = 0 \tag{11.2.52}$$

and

$$\frac{\partial U_i}{\partial t} = -g\frac{\partial \bar{\zeta}}{\partial x_i} + \frac{1}{\rho h}\frac{\partial S'_{ij}}{\partial x_j}\,. \tag{11.2.53}$$

For monochromatic waves, the mean quantities are independent of time. Eq. (11.2.53) is then simplified to

$$0 \cong -g\frac{\partial \bar{\zeta}}{\partial x_j} - \frac{1}{\rho h}\frac{\partial S'_{ij}}{\partial x_i}\,. \tag{11.2.54}$$

If the bathymetry is one-dimensional and waves are normal to the shore, then there is no shoreward current anywhere. The mean sea-level is in static balance with the radiation stress field.

11.3 Radiation Stresses in the Shoaling Zone — Small-Amplitude Waves on Constant or Nearly Constant Depth

In this section we derive some explicit formulas for the wave-induced radiation stresses S'_{ij} in the shoaling zone. Consider first the more practical case of weak current where U_i is comparable to the wave velocity field (u'_i, w'). Due to the absence of breaking, turbulence must be rather insignificant except near the bottom. Consequently, the wave and the current fields should not affect each other at the first order in wave slope, and the linearized theory for waves is still applicable to the leading order. In particular, in a region of nearly constant depth and several wavelengths away from local scatterers, the wave potential can be expressed by Eq. (10.4.1), Chapter 10, while wave-induced free-surface displacement ζ' is

$$\zeta'(x, y, t) = \mathrm{Re}\left\{\eta(x, y)e^{-i\omega t}\right\}$$

with η governed by the Helmholtz equation. Keeping only terms of the second order in wave slope, the upper limits of integration in Eq. (11.2.47) may be replaced by 0. The various terms involved are evaluated individually as follows:

$$\mathrm{I} = \rho \int_{-h}^{0} \overline{u'_i u'_j}\, dz = \frac{\rho g}{4}\, \mathrm{Re}\left(\frac{\partial \eta}{\partial x_i}\frac{\partial \eta^*}{\partial x_j}\right)\frac{1}{k^2}\left[1 + \frac{2kh}{\sinh 2kh}\right], \qquad (11.3.1)$$

$$\mathrm{II} = \frac{1}{2}\rho g\overline{\zeta'^2} = \frac{1}{4}\rho g|\eta|^2\,, \qquad (11.3.2)$$

$$\mathrm{III} = \rho \int_{-h}^{0} dz \frac{\partial}{\partial x_i}\int_{z}^{0} \overline{u'_i w'}\, dz$$

$$= \frac{\rho g}{4}\, \mathrm{Re}\frac{\partial}{\partial x_i}\left(\eta^*\frac{\partial \eta}{\partial x_i}\right)\frac{1}{2k^2}[2kh\coth 2kh - 1]\,, \quad i = 1, 2\,; \qquad (11.3.3)$$

$$\mathrm{IV} = -\rho \int_{-h}^{0} \overline{w'^2}\, dz = \frac{\rho g}{4}|\eta|^2\left(\frac{2kh}{\sinh 2kh} - 1\right). \qquad (11.3.4)$$

Summing up the four integrals and using the Helmholtz equation, we obtain

$$\begin{aligned} S_{ij} &= \mathrm{I} + \mathrm{II} + \mathrm{III} + \mathrm{IV} \\ &= \frac{\rho g}{4}\left\{ \mathrm{Re}\left[\frac{\partial \eta}{\partial x_i}\frac{\partial \eta^*}{\partial x_j}\right]\frac{1}{k^2}\left(1+\frac{2kh}{\sinh 2kh}\right)\right. \\ &\quad \left. + \delta_{ij}\left[|\eta|^2\frac{2kh}{\sinh 2kh} + \frac{2kh\coth 2kh - 1}{2k^2}\left(\left|\frac{\partial \eta}{\partial x}\right|^2 + \left|\frac{\partial \eta}{\partial y}\right|^2 - k^2|\eta|^2\right)\right]\right\} \end{aligned} \tag{11.3.5}$$

(Mei, 1973), where primes for the radiation stresses are omitted from here on until Section 11.6.

The following two limits are easily found

1 Deep water $kh \gg 1$, $\omega^2 = gk$.

$$\frac{S_{xx}}{h} = \frac{S_{yy}}{h}\frac{\rho g}{4}\frac{1}{k}(|\nabla\eta|^2 - k^2|\eta|^2)\,, \tag{11.3.6a}$$

$$\frac{S_{xy}}{h} = \frac{S_{yx}}{h} = 0\,. \tag{11.3.6b}$$

2 Shallow water $kh \ll 1$, $\omega = (gh)^{1/2}k$.

$$S_{xx} = \frac{\rho g}{2}\left(\frac{1}{k^2}\left|\frac{\partial \eta}{\partial x}\right|^2 + 2|\eta|^2\right), \tag{11.3.7a}$$

$$S_{yy} = \frac{\rho g}{2}\left(\frac{1}{k^2}\left|\frac{\partial \eta}{\partial y}\right|^2 + 2|\eta|^2\right), \tag{11.3.7b}$$

$$S_{xy} = S_{yx} = \frac{\rho g}{2}\frac{1}{k^2}\,\mathrm{Re}\frac{\partial \eta}{\partial x}\frac{\partial \eta^*}{\partial y}\,. \tag{11.3.7c}$$

For the special example of a progressive wave in the direction θ with respect to the x axis,

$$\eta = Ae^{i\psi}\,, \quad A \text{ real}\,, \tag{11.3.8}$$

where

$$\psi = k_1 x_1 + k_2 x_2\,, \tag{11.3.9}$$

$$k_1 = k\cos\theta\,, \quad k_2 = k\sin\theta\,, \quad x_1 = x\,, \quad x_2 = y\,.$$

It is straightforward to show that the radiation stresses are

$$S_{ij} = \frac{\rho g A^2}{4}\left\{\frac{k_i k_j}{k^2}\left(1+\frac{2kh}{\sinh 2kh}\right)+\delta_{ij}\frac{2kh}{\sinh 2kh}\right\}$$
$$= \frac{E}{2}\left\{\frac{k_i k_j}{k^2}\frac{2C_g}{C}+\delta_{ij}\left(\frac{2C_g}{C}-1\right)\right\} \tag{11.3.10}$$

(Longuet–Higgins and Stewart, 1962, 1964). More explicitly, the components of the radiation stresses may be written

$$S_{xx} = S_{11} = \frac{E}{2}\left[\frac{2C_g}{C}\cos^2\theta+\left(\frac{2C_g}{C}-1\right)\right], \tag{11.3.11a}$$

$$S_{yy} = S_{22} = \frac{E}{2}\left[\frac{2C_g}{C}\sin^2\theta+\left(\frac{2C_g}{C}-1\right)\right], \tag{11.3.11b}$$

$$S_{xy} = S_{yx} = S'_{12} = S'_{21} = E\frac{C_g}{C}\sin\theta\cos\theta\,. \tag{11.3.11c}$$

In very deep water $C_g/C \to \frac{1}{2}$ so that

$$S_{xx} \cong \frac{E}{2}\cos^2\theta\,, \tag{11.3.12a}$$

$$S_{yy} \cong \frac{E}{2}\sin^2\theta\,, \tag{11.3.12b}$$

$$S_{xy} = S_{yx} \cong \frac{E}{2}\sin\theta\cos\theta\,, \tag{11.3.12c}$$

while on very shallow water, $C_g/C \to 1$, so that

$$S_{xx} \cong \frac{E}{2}[2\cos^2\theta+1]\,, \tag{11.3.13a}$$

$$S_{yy} \cong \frac{E}{2}(2\sin^2\theta+1)\,, \tag{11.3.13b}$$

$$S_{xy} = S_{yx} \cong E\sin\theta\cos\theta\,. \tag{11.3.13c}$$

Applications of Eqs. (11.3.10)–(11.3.13) will be found in the next section.

Although Eqs. (11.3.11)–(11.3.13) are derived for strictly constant depth, they are a good first approximation for slowly varying depth if A and k are interpreted as the local values corresponding to the local h.

For a strong current on a nearly constant depth, the linearized equations governing the leading order wave field can be inferred from Eqs. (3.6.17), (3.6.19), (3.6.20), and (3.6.23), Chapter Three, by ignoring nonlinearity and spatial variations of U_i and h. It can be shown that formulas (11.3.5) and (11.3.10) still hold if h is replaced by $h + \bar{\zeta}$, where $\bar{\zeta}$ is the mean sea level induced by the strong current according to (3.6.13), and ω and k must satisfy Eqs. (3.6.29)–(3.6.33), all of Chapter Three.

Exercise 11.1: Radiation Stresses in a Partially Standing Wave

Let the first-order waves be composed of incident and reflected waves,

$$\eta = Ae^{ikx} + Be^{-ikx}\,. \tag{11.3.14}$$

Use Eq. (11.3.5) to show that the radiation stress components are

$$\begin{aligned} S_{ij} = \frac{\rho g}{4}\Bigg\{ &(|A|^2 + |B|^2 - 2\ \mathrm{Re}\,[AB^* e^{2ikx}])\left(1 + \frac{2kh}{\sinh 2kh}\right) \\ &+ \delta_{ij}\Bigg[(|A|^2 + |B|^2 + 2\ \mathrm{Re}\,[AB^* e^{2ikx}])\frac{2kh}{\sinh 2kh} \\ &- 2(2kh\coth 2kh - 1)\ \mathrm{Re}\,[AB^* e^{2ikx}]\Bigg]\Bigg\} \end{aligned} \tag{11.3.15}$$

and

$$\begin{aligned} S_{11} = &\frac{\rho g}{4}(|A|^2 + |B|^2) \\ &\times \left(1 + \frac{4kh}{\sinh 2kh} + \frac{\rho g}{2}\ \mathrm{Re}\,[AB^* e^{2ikx}](1 - 4kh\coth 2kh)\right) \end{aligned} \tag{11.3.16}$$

in particular.

Derive a general formula for the mean-free surface displacement

$$\bar{\zeta} = -\frac{1}{2g}(\overline{u_1^2} - \overline{w_1^2}) = -\frac{g}{4\omega^2}\left(|\eta_x|^2 - \frac{\omega^4}{g^2}|\eta|^2\right) \tag{11.3.17}$$

and then show for the partially standing wave that

$$\bar{\zeta} = -\frac{k(|A|^2 + |B|^2)}{2\sinh 2kh} - \frac{k(1 + \tanh^2 kh)}{2\tanh kh}\ \mathrm{Re}\,(AB^* e^{2ikx})\,. \tag{11.3.18}$$

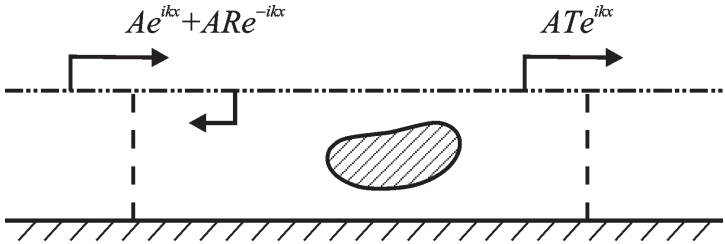

Figure 11.2: Drift force on a floating body.

Exercise 11.2: Drift Force on a Two-Dimensional Body

Consider a very long vessel moored in transverse waves (beam sea). The free-surface displacement in the far fields are, at the leading order,

$$\eta = A(e^{ikx} + R\,e^{-ikx})\,, \quad kx \sim -\infty\,; \quad \eta = AT\,e^{ikx}\,, \quad kx \sim \infty \tag{11.3.19}$$

where R and T are the reflection and transmission coefficients, respectively. Use the spatial averages of S_{11} and $\bar{\zeta}$ to calculate the net horizontal force at a station in the far field at $kx \sim -\infty$ by adding the radiation stress and the hydrostatic pressure force. Do the same for $kx \sim \infty$ and take the difference of the two results to show that the drift force on the body is

$$\begin{aligned} \text{Drift force} &= \langle S_{11} + \rho g \bar{\zeta} h \rangle_{kx\sim-\infty} - \langle S_{11} + \rho g \bar{\zeta} h \rangle_{kx\sim\infty} \\ &= \rho g |A|^2 (1 + |R|^2 - |T|^2) \frac{C_g}{C} \\ &= 2\rho g |A|^2 |R|^2 \frac{C_g}{C}\,. \end{aligned} \tag{11.3.20}$$

(Longuet–Higgins, 1977a).

11.4 Long Waves Forced by Radiation Stress of Short Waves

Consider progressive short waves with frequency bandwidth of the order $O(\epsilon\omega)$ where $\epsilon = kA$, the temporal and spatial variations of the period-averages must have the time scale $O(1/\omega\epsilon)$ and the spatial scale, $O(1/\epsilon k)$ so that $\bar{\zeta}$, U_i, S_{ij} in (11.2.52) and (11.2.53) are functions of $t_1 = \epsilon t$

and $x_{1i} = \epsilon x_i$. These two equations may be combined to give the forced long-wave equation

$$\frac{\partial}{\partial x_{1i}}\left(gh\frac{\partial \bar{\zeta}}{\partial x_{1i}}\right) - \frac{\partial^2 \bar{\zeta}}{\partial t_1^2} = -\frac{1}{\rho}\frac{\partial^2 S_{ij}}{\partial x_{1i}\partial x_{1j}}\,. \tag{11.4.1}$$

Thus, long waves are forced by the divergence of the radiation stress of the short waves. This result resembles the equation governing sound generation by turbulent fluctuations (Lighthill, 1952, 1954). We now discuss two simple applications.

11.4.1 Set-Down or Bound Long Wave

Let us consider a narrow-banded progressive wavetrain propagating in the x direction over a horizontal seabed. The amplitude is $A = A(x_1 - C_g t_1)$. Recall that

$$S_{11} = E\left(\frac{2C_g}{C} - \frac{1}{2}\right), \quad E = \frac{1}{2}\rho g|A|^2\,. \tag{11.4.2}$$

From the one-dimensional long-wave equation,

$$\frac{\partial^2 \bar{\zeta}}{\partial t_1^2} - gh\frac{\partial^2 \bar{\zeta}^2}{\partial x_1^2} = \frac{1}{\rho}\frac{\partial^2 S_{11}}{\partial x_1^2}\,. \tag{11.4.3}$$

it is evident that S_{11} and $\bar{\zeta}$ must depend only on the moving coordinate $\xi \equiv x_1 - C_g t_1$. Changing to the moving coordinate, we find

$$\frac{\partial}{\partial x_1} = \frac{\partial}{\partial \xi}\,, \quad \frac{\partial}{\partial t_1} = -C_g\frac{\partial}{\partial \xi}$$

so that (11.4.3) becomes a second-order ordinary differential equation, which can be readily integrated to give

$$\bar{\zeta} = -\frac{S_{11}/\rho}{gh - C_g^2} = -\frac{g|A|^2}{2(gh - C_g^2)}\left(\frac{2C_g}{C} - \frac{1}{2}\right). \tag{11.4.4}$$

This result represents an infragravity wave bound to the envelope and propagating at the group velocity of the short waves. Furthermore, since $gh > C_g$ and $2C_g/C > 1$ for all k, $\bar{\zeta}$ is negative (see Fig. 11.3). For these reasons this long wave is also known as the bound wave or the set-down wave (Longuet–Higgins and Stewart, 1964).

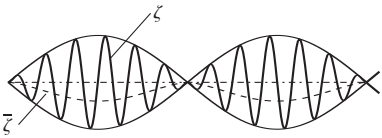

Figure 11.3: Set-down long waves bound to the envelope of the short wave groups.

11.4.2 Parasitic Long Seiches in a Wave Flume

In many laboratory experiments monochromatic short waves are generated by an oscillating piston at one end of a long tank. A gentle beach at the opposite end induces breaking so that little energy is reflected. Frequently, unintended seiches (standing waves) of a long period are observed and contaminate the experiment. What causes these seiches and how can they be avoided?

Due to mechanical imperfections, the piston may generate waves within a narrow frequency band. As a result a long set-down wave is forced by the radiation stress, with the frequency comparable to the frequency band-width. In addition, free long waves, to be explained shortly, are also generated due to the finite length of the flume. Unlike the short waves that generate them, these long waves tend not to break on the sloping beach, and can be resonated to significant amplitude if their wavelength is close to that of a standing wave mode in the flume.

Quantitative analysis can be facilitated by the theory here. Let the piston displacement be prescribed by

$$X(t, t_1) = X_{10}(t_1) + X_{11}(t_1)e^{-i\omega t} + * \tag{11.4.5}$$

where $t_1 = \epsilon t$, with $\epsilon = O(kA)$. The first term represents the slow drift while the second term the fast oscillations with a slowly modulated amplitude, both are of the order of A. By solving a linearized radiation problem as in Chapter 8, the radiated wave amplitude A can be found from the piston amplitude X_{11}. We leave it as an exercise to show that

$$A(t_1, x_1 = 0) = -\frac{2iC}{C_g} \tanh kh \, X_{11}(t_1) \, . \tag{11.4.6}$$

For $x_1 > 0$ we invoke wave-action conservation so that $A = A(t_1 - x_1/C_g)$, or,

$$A = -\frac{2iC}{C_g} \tanh kh \, X_{11}(t_1 - x_1/C_g) \, . \tag{11.4.7}$$

The mean sea-level of the long wave $\bar{\zeta}$ is governed by (11.4.3), and is related to $U(x_1, t_1)$ by

$$\frac{\partial \bar{\zeta}}{\partial t_1} + h\frac{\partial U}{\partial x_1} = 0\,, \quad \frac{\partial U}{\partial t_1} + g\frac{\partial \bar{\zeta}}{\partial x_1} = -\frac{1}{\rho h}\frac{\partial^2 S_{11}}{\partial x_1^2}\,.$$

The kinematic boundary condition at the piston gives, approximately,

$$U(x_1 = 0, t_1) = \frac{\partial X_{10}}{\partial t_1} \tag{11.4.8}$$

which also implies that

$$\frac{\partial \bar{\zeta}}{\partial x_1} = -\frac{1}{\rho g h}\frac{\partial S_{11}}{\partial x_1} - \frac{1}{g}\frac{\partial^2 X_{10}}{\partial t_1^2}\,, \quad x_1 = 0\,. \tag{11.4.9}$$

Note that since $S_{11} = S_{11}(t_1 - x/C_g)$, we can also write

$$\frac{\partial S_{11}}{\partial x_1} = -\frac{1}{C_g}\frac{\partial S_{11}}{\partial t_1}\,. \tag{11.4.10}$$

The solution for the long wave can be split into two parts

$$\bar{\zeta} = \bar{\zeta}_B + \bar{\zeta}_F\,. \tag{11.4.11}$$

The forced or *bound* long wave $\bar{\zeta}_B$ satisfies only the inhomogeneous equation (11.4.3). The solution is just (11.4.4).

The *free* long wave $\bar{\zeta}_F$ must now satisfy the homogeneous wave equation, i.e., (11.4.3) with zero on the right, and the inhomogeneous boundary condition on the piston at $x_1 = 0$,

$$\begin{aligned}\frac{\partial \bar{\zeta}_F}{\partial x_1} &= -\frac{1}{g}\frac{\partial^2 X_0}{\partial t_1^2} - \frac{\partial \bar{\zeta}_B}{\partial x_1} + \frac{1}{\rho g h C_g}\frac{\partial S_{11}}{\partial t_1} \\ &= -\frac{1}{g}\frac{\partial^2 X_0}{\partial t_1^2} - \frac{1}{\rho g h}\frac{\partial S_{11}}{\partial t_1}\frac{C_g}{gh - C_g^2}\,.\end{aligned} \tag{11.4.12}$$

The solution is easily found to be

$$\begin{aligned}\bar{\zeta}_F(t_1 - x_1/\sqrt{gh}) = &\frac{1}{\rho}\frac{C_g}{\sqrt{gh}}\frac{S_{11}(t - x_1/\sqrt{gh})}{gh - C_g^2} \\ &+ \frac{h}{\sqrt{gh}}\frac{\partial}{\partial t_1}X_{10}(t_1 - x_1/\sqrt{gh})\end{aligned} \tag{11.4.13}$$

which travels at the fast speed $\sqrt{gh}$. Note that the first term is positive, hence is a set-up. Note also that the height of the set-up is smaller by the

factor $C_g/\sqrt{gh}$ than the set-down, but the length is greater by the factor $\sqrt{gh}/C_g$. Therefore their volume displacements are equal and opposite, ensuring mass conservation.

In the special case of a wave packet, A and hence S_{11} are of finite duration and length. The free long wave will eventually be separated from and outrun both the wave packet and the bound long wave.

In wave flume experiments, short progressive waves are mostly destroyed on a sloping beach by breaking, so are the bound long waves. If the free long-wave frequency $2\epsilon\Omega$ matches that of a standing wave mode in the flume of length L,

$$2\epsilon\Omega/\sqrt{gh} \approx n\pi/L\,,$$

resonance can occur. To eliminate this resonance one can program the piston to perform the slow-drift oscillations such that

$$\frac{\partial X_{10}}{\partial t_1} = -\frac{C_g S_{11}}{\rho h(gh - C_g^2)}\,, \tag{11.4.14}$$

then the sum of terms on the right-hand side of (11.4.13) vanishes. Without any forcing by the wavemaker the free long waves should not appear.

In Chapter 13 more will be discussed about long waves forced nonlinearly by short waves.

Exercise 11.3: Short Waves Generated by an Oscillating Piston

Use the usual governing equations and the following piston condition,

$$\phi_{11_x} = -i\omega X_{11}\,, \quad x = 0$$

to show that the radiation potential is formally

$$\phi_{11} = a_0(x_1, t_1) f_0(z) e^{ikx} + \sum_{n=1}^{\infty} a_n(t_1) f_n(z) e^{-k_n x}\,,$$

where k and ik_n are, respectively, the real and imaginary roots of the dispersion relation, and $f_0(z), f_n(z)$ are the orthonormal eigenfunctions defined in Chapter 7. Apply the piston boundary condition and orthogonality to get

$$a_0(x_1 = 0, t_1) = -\left(\frac{\omega}{k}\int_{-h}^{0} f_0(z)\,dz\right) X_{11} = -\frac{\omega \sinh kh}{k^2}\frac{\sqrt{2}X_{11}(t_1)}{\sqrt{h + \frac{g}{\omega^2}\sinh^2 kh}}\,.$$

From the first harmonic part of the dynamic condition on the free surface show that

$$A = \frac{2i\omega}{g} \frac{\sqrt{2} a_0 \cosh kh}{\sqrt{h + \frac{g}{\omega^2} \sinh^2 kh}}, \quad \forall\, x_1,\ t_1 > 0\,.$$

Finally, verify that

$$A = -\frac{2iC}{C_g} X_{11} \tanh kh\,.$$

Exercise 11.4: Free Long Waves Generated by a Sinusoidally Modulated Piston

Show that, if the piston motion is free of slow drift and the envelope of the piston oscillation is sinusoidal,

$$X_{10} = 0\,, \quad X_{11}(t_1) = \bar{X} \sin \Omega t_1$$

then the free long wave is

$$\bar{\zeta}_F = -\frac{\bar{X}^2 (\frac{2C_g}{C} - \frac{1}{2})}{h(\frac{\sqrt{gh}}{C_g} - \frac{C_g}{\sqrt{gh}})} \left(\frac{C}{C_g} \tanh kh \right)^2 \cos 2\Omega \left(t_1 - \frac{x_1}{\sqrt{gh}} \right).$$

A more general discussion of short-wave induced long waves will be given in Chapter 13, without the use of radiation stresses.

We now turn to the longshore current in the surf zone.

11.5 Empirical Knowledge of Breaking Waves

At present, theoretical information on breaking waves on a sloping beach is still inadequate, especially with regard to breaking-induced turbulence. A succinct summary of the empirical knowledge of sinusoidal waves normally incident on a plane beach is given in Battjes (1974a, b), from which much of the present section is extracted. The film entitled *Breaking Waves* made by Kjeldsen and Olsen (1971) is also very informative.

11.5.1 Breaking of Standing Waves on a Slope

On a smooth plane beach, the parameters which govern wave breaking are the wave slope and the beach slope $s = \tan \alpha$. For sufficiently large s or sufficiently low amplitudes, an incident wave does not break and is

completely reflected. When s decreases and/or kA increases, a threshold is reached where breaking begins. Irribarren and Nogales (1949) and others have found empirically that the single dimensionless parameter

$$\xi = \frac{s}{(H/\lambda_\infty)^{1/2}} = s\left(\frac{\pi}{k_\infty A}\right)^{1/2} \tag{11.5.1}$$

plays an important role, where H is the total height of the breaking wave and λ_∞ is the wavelength in deep water. The critical value is roughly

$$\xi_c \simeq \frac{4}{\pi^{1/2}} \simeq 2.3 \quad \text{or} \quad k_\infty A = \left(\frac{\pi}{4}\right)^2 s^2 . \tag{11.5.2}$$

If $\xi < 2.3$, waves break and the reflection coefficient reduces to below unity. A heuristic explanation for the parameter ξ has been proposed by Munk and Wimbush (1969). Their reasoning is that the fluid acceleration downward along the slope cannot exceed the acceleration of a free-falling particle, that is, $g\sin\alpha$, without causing breaking. For a standing wave of local amplitude A, the maximum vertical fluid acceleration may be estimated as $\omega^2 A$; the maximum acceleration along the slope is roughly $\omega^2 A/\sin\alpha$. Hence, the critical value for breaking is

$$\frac{\omega^2 A}{\sin\alpha} = g\sin\alpha \quad \text{or} \quad k_\infty A = \sin^2\alpha .$$

For small slope $s = \tan\alpha \simeq \sin\alpha$,

$$\xi_c \simeq \frac{s}{(H/\lambda_\infty)^{1/2}} = \frac{s\pi^{1/2}}{(k_\infty A)^{1/2}} = \pi^{1/2} = 1.772 \tag{11.5.3}$$

which is essentially the same as Eq. (11.5.2) for small slope except for the factor $(4/\pi)^2 = 1.62$. As will be shown in Chapter 12, Eq. (11.5.3) is the same as the theoretical deduction of Carrier and Greenspan (1957) based on Airy's nonlinear approximation and the criterion that the free surface is vertical at the breaking point. While the quantitative agreement may be accidental, it is reassuring that the role of ξ as the governing parameter has theoretical support.

As ξ decreases beyond the critical value, reflection from the slope decreases. Moraes (1970) has performed extensive experiments for wave reflection for various incoming waves and beach slopes. From these data Battjes (1974a) found that the reflection coefficient could be expressed as the function of ξ alone as shown in Fig. 11.4. This, of course, gives further significance to the quantity ξ which has been called the *surf parameter* by Battjes.

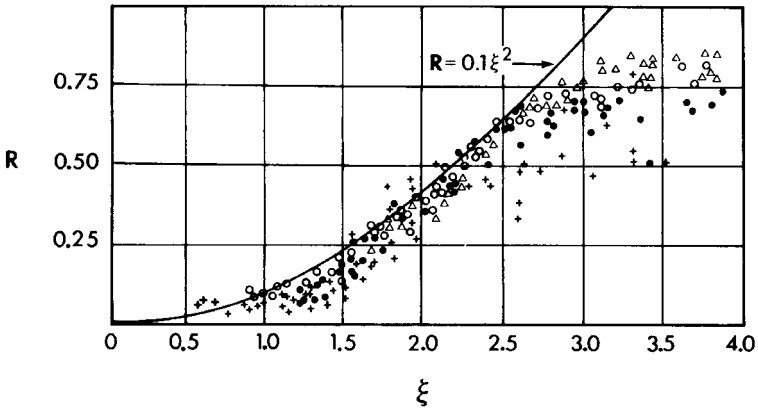

Figure 11.4: Reflection coefficient of a beach as a function of surf parameter $\xi = s(k_\infty A/\pi)^{-1/2}$ where A is the local amplitude. +: $s = 0.1$; ●: $s = 0.15$; ◯: $s = 0.20$; and △: $s = 0.30$ (from Battjes, 1974a, based on Moraes' data).

11.5.2 Types of Breakers on Mild Beaches

Three types of breakers may be crudely distinguished when ξ is below ξ_c (Galvin, 1968).[3] The *collapsing breaker* is associated with a large beach slope and flat incident waves. A small amount of breaking occurs only at the instantaneous shoreline. Dissipation of wave energy is quite small and reflection is nearly complete. When the beach slope decreases and/or the incident wave slope increases, a crest becomes forward-leaning as it advances toward the shore; its amplitude grows so that the profile is quite asymmetric. The crest ultimately curls forward and forms a jet plunging into the trough ahead; this type of breaker is called a *plunging breaker*, or a *plunger*. Because of the air tunnel formed by the splashing crest, the front of the breaking wave is accompanied by much noise and turbulence. Shortly after the collapse of the tunnel, a traveling bore is formed which marches shoreward with continued dissipation. If the beach slope is further decreased and/or the incident wave slope increased, the onset of breaking occurs at a greater distance offshore when the wave crest is still symmetric. Breaking is signalled by the presence of foam draping the forward side of the crest; the trough in front is not visibly disturbed. This is called a *spilling breaker* in which dissipation takes place with a less violent appearance. Galvin classifies the breaker type on a quantitative scale:

[3]Galvin further calls an essentially nonbreaking wave on a beach a *surging breaker*.

$$\begin{aligned} \xi_b &< 0.4 && \text{spilling} \\ 0.4 < \xi_b &< 2.4 && \text{plunging} \\ \xi_b &> 2.0 && \text{collapsing} \end{aligned}$$

where ξ_b is the value of ξ at the breaker line. It must be emphasized that transition from one type to another is always gradual so that the numerical values marking the border lines cannot be precise. Theoretically, all three types may be regarded as plunging with the collapsing breakers having the narrowest surf zone and the spilling breakers having a negligible overhanging crest.

11.5.3 Maximum Wave Height

The maximum wave height corresponds to the limiting amplitude of a crest before breaking. There is as yet no simple theory for predicting the maximum wave height on a sloping beach. For a strictly horizontal bottom, there are perturbation theories of the Stokes type for periodic progressive waves (see Chapter Thirteen). By taking the Stokes wave solution and assuming that at the threshold of breaking the fluid velocity at the crest equals the phase speed, Miche (1951) calculated the maximum wave height

$$\left(\frac{H}{\lambda}\right)_{\max} = \left(\frac{2H}{2\pi}\right)_{\max} = 0.14 \tanh kh \,. \tag{11.5.4}$$

For very shallow water $kh \ll 1$, Eq. (11.5.4) gives

$$\frac{H_{\max}}{h} = 0.88 \,, \tag{11.5.5}$$

which turns out to be in good agreement with experiments. Because the Stokes theory implies a symmetrical wave profile, the above result is more relevant to spilling breakers. Now breaking is a manifestation of extreme nonlinearity; a perturbation theory of a few orders is hardly satisfactory. An exact numerical theory of Schwartz (1974) for maximum wave height indicates, nevertheless, that Miche's estimate is quite good.

Experimental results for maximum wave height on a sloping bottom obtained by Iversen, Goda, Bowen et al., and Battjes have been collected by Battjes (1974a) as shown in Fig. 11.5. The ratio of height to depth at breaking is denoted by γ. The empirical range

$$\gamma = \frac{H_b}{h_b} = 0.7 - 1.2 \tag{11.5.6}$$

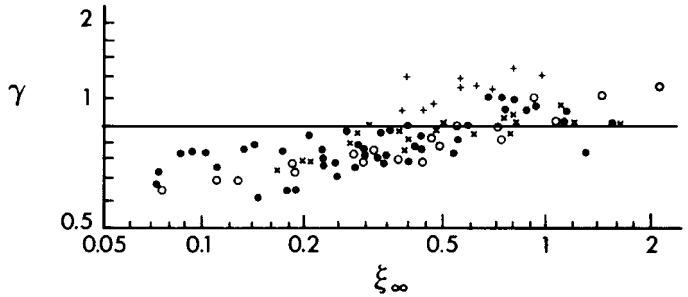

Figure 11.5: Breaker height to depth ratio as a function of $\xi_\infty = s(k_\infty A_\infty/\pi)^{-1/2}$ (from Battjes (1974a)). Sources of data are: ●: Iversen; ◯: Goda; + : Bowen *et al.*; and ×: Battjes (1974a).

is roughly comparable to Eq. (11.4.5) and shows a weak dependence on the parameter ξ. In the absence of a satisfactory theory for wave breaking, these empirical results have been used for predicting the breaker line on a gently sloping beach in conjunction with a convenient theory for shoaling waves. From the theoretical relation between H and h before breaking, Eq. (11.5.6) may be invoked to calculate the breaking depth h_b which, in turn, gives the position of the breaker line. As a crude estimate we take the linearized shoaling theory, Eq. (3.3.9), Chapter Three, to relate the wave amplitude and the depth for the entire shoaling zone. Near the breaker line, $kh \ll 1$; Eq. (3.3.10), Chapter Three, applies, namely,

$$\frac{A}{A_\infty} = (2|\cos\theta_\infty|)^{-1/2} \left(\frac{\omega^2 h}{g}\right)^{-1/4} \tag{11.5.7}$$

where A_0 and θ_0 have been replaced by A_∞ and θ_∞, respectively, and $k_\infty h_\infty \gg 1$ is assumed. Invoking $(A/h)_b = \frac{1}{2}(H/h)_b = \frac{1}{2}\gamma$, we get

$$\frac{\omega^2 h_b}{g} = \left(\frac{1}{\gamma}\frac{\omega^2 A_\infty}{g}\right)^{4/5} (2|\cos\theta_\infty|)^{-1/2}\,. \tag{11.5.8}$$

From the observed data of H, Komar and Gaughan (1972) found that the best value for γ was 1.42 which was larger than that of Eq. (11.5.6). This discrepancy is likely due to the inadequacy of the linearized theory at the breaker line.

The ratio of breaker height to depth at the breaking line $\gamma = 0.7$–1.2 has been used also to approximate the ratio of height to depth of a breaking wave as it travels across the surf zone (Munk, 1949a). This simple

statement describes empirically the diminishing of wave amplitude and has been adopted as a basic assumption in all longshore current theories.

11.6 The Structure of a Uniform Longshore Current on a Plane Beach

Assume for simplicity that the beach has a plane bottom, that is, $h = sx$. Uniformity in the longshore direction of y implies that $\partial/\partial y = 0$. Hence the continuity equation is

$$\frac{\partial}{\partial x}[U(\bar{\zeta} + h)] = 0\,,$$

which leads to

$$U \equiv 0 \quad \text{for all} \quad x\,. \tag{11.6.1}$$

The mean velocity can only be alongshore, that is, $V = V(x)$.

In the offshore–onshore (x) direction, the bottom friction can be omitted from the momentum equation since $U = 0$; thus,

$$0 = -g\frac{\partial \bar{\zeta}}{\partial x} - \frac{1}{\rho(\bar{\zeta} + h)}\frac{\partial}{\partial x}(S'_{xx} + S''_{xx})\,. \tag{11.6.2}$$

In the alongshore (y) direction, the momentum equation reads

$$0 = -\frac{1}{\rho(\bar{\zeta} + h)}\left[\frac{\partial}{\partial x}(S'_{xy} + S''_{xy}) + \bar{\tau}_y^B\right]. \tag{11.6.3}$$

These formal equations are valid for both shoaling and surf zones. As in uniform pipe flows in ordinary fluid mechanics, the convective inertia terms are absent identically.

11.6.1 Shoaling Zone: $x > x_b$

In most of the shoaling zone the turbulence intensity is weak so that $S''_{xx} \ll S'_{xx}$. Furthermore, $\bar{\zeta}$ is of the second order in wave slope $O(kA^2)$ and is negligible compared to the still water depth. Hence, Eq. (11.6.2) can be written

$$0 \simeq -g\frac{\partial \bar{\zeta}}{\partial x} - \frac{1}{\rho h}\frac{\partial S'_{xx}}{\partial x}\,, \tag{11.6.4}$$

where S'_{xx} can be given approximately by Eq. (11.3.11a):

$$S'_{xx} = \frac{\rho g A^2}{4}\left[\frac{2C_g}{C}\cos^2\theta + \frac{2C_g}{C} - 1\right], \tag{11.6.5}$$

while C_g, C, θ, and A refer to the refracting waves implied by Eqs. (11.5.7) and (11.5.8). Qualitatively, S'_{xx} decreases as h increases, that is, $\partial S'_{xx}/\partial x < 0$. It follows from Eq. (11.6.4) that $\partial\bar{\zeta}/\partial x > 0$, and ζ steadily increases with x. Since it vanishes in very deep water, $\bar{\zeta}$ must be below the still water level; this variation is called the *set-down*. After some algebra, Eq. (11.6.4) may be integrated with respect to x to give $\bar{\zeta}$ (see Longuet–Higgins and Stewart, 1962, for normal incidence). The same result can also be derived simply by using the dynamic condition on the free surface. Approximating to the second order only, we have

$$g\zeta + \frac{\partial\Phi}{\partial t} + \zeta\frac{\partial^2\Phi}{\partial t\partial z} + \frac{1}{2}(u'^2 + v'^2 + w'^2) \simeq 0\,, \quad z = 0\,,$$

whose time average is

$$g\bar{\zeta} + \overline{\zeta\frac{\partial w'}{\partial t}} + \frac{1}{2}(\overline{u'^2} + \overline{v'^2} + \overline{w'^2}) = 0\,.$$

Using the kinematic condition on the free surface $\partial\zeta/\partial x = w'$, we get

$$g\bar{\zeta} = -\frac{1}{2}(\overline{u'^2} + \overline{v'^2} - \overline{w'^2})\,.$$

The linearized wave field may be recalled as

$$\Phi = \mathrm{Re}\,\frac{-igA}{\omega}\frac{\cosh k(z+h)}{\cosh kh}\exp\left[i\left(\int \alpha\,dx + \beta y - \omega t\right)\right].$$

Calculating the mean squares of the velocity components from this potential, we obtain

$$\bar{\zeta} = -\frac{kA^2}{2\sinh 2kh} \tag{11.6.6}$$

where derivatives of h have been ignored. Equation (11.6.6) is formally the same as if $h = \text{const}$. Very near the breaker line $kh \ll 1$, Eq. (11.6.6) may be approximated by

$$\bar{\zeta} \simeq -\frac{A^2}{4h}\,. \tag{11.6.7}$$

For normal incidence, experiments by Bowen, Inman, and Simmons (1968) have confirmed Eq. (11.6.6) very well for nearly all points in the

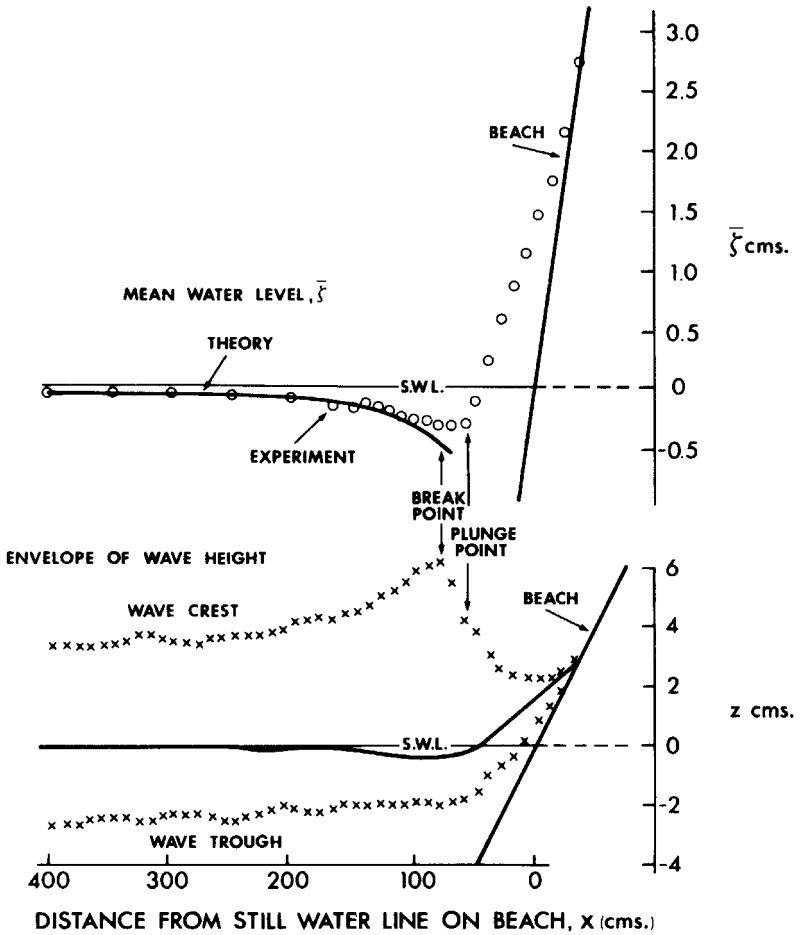

Figure 11.6: Comparison of experiments with theory for set-down and set-up on a plane beach. Data: wave period = 1.14 s; deep water wave height $H_\infty = 6.45$ cm; breaker height $H_b = 8.55$ m; beach slope = 0.082 (from Bowen et al., 1968, *J. Geophys. Res.*).

shoaling zone except very near the breaker line (see Fig. 11.6) where discrepancies are likely caused by nonlinearity and turbulence through S''_{xx}.

Now let us consider the alongshore (y) momentum. In the shoaling zone and far away from the breaker line, turbulence is negligible and there is no current; therefore,

$$\frac{\partial S'_{xy}}{\partial x} = 0 \quad \text{or} \quad S'_{xy} = \text{const.} \tag{11.6.8}$$

This result is a special case of the more general conclusion (11.2.52). As a check note that $EC_g \cos\theta$ is the constant rate of energy flux into a unit distance of y, and $(\sin\theta)/C$ is constant by Snell's law; therefore S'_{xy} is constant by Eq. (11.3.11c).

Near the breaker line there is a lateral transfer of turbulent momentum through the integrated Reynolds stress:

$$S''_{xy} = \rho \int_{-h}^{\bar{\zeta}} \overline{u''v''}\, dz\,. \tag{11.6.9}$$

If the modification of waves by turbulence diffused out of the surf zone is ignored, it follows from Eq. (11.6.3) that

$$0 = -\frac{\partial S''_{xy}}{\partial x} - \bar{\tau}_y^B\,. \tag{11.6.10}$$

This equation must be supplemented with further hypotheses on S''_{xy} and $\bar{\tau}_y^B$ as will be discussed later.

11.6.2 Surf Zone: $x < x_b$

Although formal equations are available (see Eqs. (11.2.47) and (11.2.48)), the stresses S'_{ij} and S''_{ij} are both unknown in the surf zone due to breaking-induced turbulence. This is a familiar situation in usual turbulent flows and closure hypotheses are needed in order to render the problem determinate. For the radiation stresses S'_{xx} and S'_{xy}, Bowen (1969), Longuet–Higgins (1970a, b), and Thornton (1970) introduced the important hypothesis that the relations (11.3.11)–(11.3.13) between S'_{ij} and $E = \frac{1}{2}\rho g A^2$ be formally valid even though they are derived for small-amplitude nonbreaking waves. In addition, the breaking-wave amplitude is assumed to be related to the local depth $(\bar{\zeta} + h)$ by

$$A = \frac{\gamma}{2}(\bar{\zeta} + h) \tag{11.6.11}$$

where γ is the same empirical constant given in Eq. (11.5.6).

We now apply this new hypothesis to the x-momentum equation in the surf zone. Using the shallow water approximation, we get

$$S'_{xx} = \frac{3}{16}\gamma^2 \rho g (\bar{\zeta} + h)^2\,. \tag{11.6.12}$$

The cited authors did not include the turbulent stress S''_{xx} defined by Eq. (11.2.48); this omission is not easy to assess since S'_{xx} and S''_{xx} have

not been measured separately.[4] Combining Eq. (11.6.12) with Eq. (11.6.4), we get the following differential equation:

$$0 = -\frac{\partial \bar{\zeta}}{\partial x} - \frac{3}{8}\gamma^2 \frac{\partial}{\partial x}(\bar{\zeta} + h)\,,$$

which immediately leads to

$$\frac{\partial \bar{\zeta}}{\partial x} = \frac{-\frac{3}{8}\gamma^2 \partial h/\partial x}{1 + \frac{3}{8}\gamma^2}\,. \tag{11.6.13}$$

Integrating with respect to x and matching $\bar{\zeta}$ with the mean sea level $\bar{\zeta}_b$ at the breaker line, we get

$$\bar{\zeta} - \bar{\zeta}_b = \frac{\frac{3}{8}\gamma^2 (h_b - h)}{1 + \frac{3}{8}\gamma^2}\,. \tag{11.6.14}$$

A crude estimate of $\bar{\zeta}_b$ can be obtained by using Eq. (11.5.8) and $(A/h)_b = \frac{1}{2}\gamma$ in Eq. (11.6.7). With this result the total mean depth may be written

$$\bar{\zeta} + h = \frac{h - h_s}{1 + \frac{3}{8}\gamma^2}\,, \tag{11.6.15}$$

where

$$h_s = -\left[\left(1 + \frac{3}{8}\gamma^2\right)\bar{\zeta}_b + \frac{3}{8}\gamma^2 h_b\right] \tag{11.6.16}$$

is the still water depth of the mean shoreline at which $(\bar{\zeta} + h)_s = 0$.

As the incident wave amplitude A_∞ increases, h_b increases. While the change in $\bar{\zeta}_b$ is small, the right-hand side of Eq. (11.6.14) increases. Hence, the set-up $\bar{\zeta}$ increases. Equation (11.6.13) has been verified experimentally for a plane beach by Bowen, Inman, and Simmons (1968); see Fig. 11.6. It may now be concluded that the momentum balance in the x direction results in a static set-down in the shoaling zone and a set-up in the surf zone.

With the mean sea-level known, the radiation shear stress in the shallow surf zone is

$$S'_{xy} \simeq \frac{1}{16}\rho g \gamma^2 (\bar{\zeta} + h)^2 \sin 2\theta \tag{11.6.17}$$

when Eq. (11.6.11) is combined with Eq. (11.3.13c). From Eq. (11.2.51), S'_{xy} now acts as the forcing term in the longshore direction which must

[4] Recall that in a turbulent pipe flow, terms analogous to S''_{xx} are present which alter the mean pressure corresponding to $\bar{\zeta}$ here.

be balanced by bottom friction and the turbulent Reynolds stress. At this stage empirical relations must be added to express $\bar{\tau}_y^B$ and S''_{xy} in terms of the mean current $V(x)$. We follow Longuet–Higgins (1970a) in this regard.

In open-channel hydraulics *bottom friction* is usually related to the total mean velocity excluding u_i'':

$$\bar{\tau}^B = \frac{f}{2}\rho\overline{|\mathbf{U}+\mathbf{u}'|(\mathbf{U}+\mathbf{u}')}\,, \quad f = \text{friction coefficient}\,, \tag{11.6.18}$$

where $\mathbf{u}'$ is the wave velocity field evaluated at $z = -h$. Thus, in the y direction the mean bottom friction is

$$\bar{\tau}_y^B = \frac{f}{2}\rho\overline{|\mathbf{U}+\mathbf{u}'|(V+v')}\,. \tag{11.6.19}$$

For reasonably small incidence angle the wave vector in shallow water is essentially in the x direction, namely, $v' \ll u'$, while the shear current is in the y direction so that the total velocity is approximately

$$\mathbf{U}+\mathbf{u}' \cong u'\mathbf{e}_x + V\mathbf{e}_y\,,$$

and

$$\overline{\tau_y^B} \cong \frac{f}{2}\rho\overline{(u'^2+V^2)^{1/2}}V\,.$$

Now $u' = U_0\cos\omega(t+t_0)$ where U_0 is the amplitude of the orbital (oscillatory) velocity at the bottom. In the surf zone the magnitudes of V and U_0 are usually comparable and the average

$$\begin{aligned}\overline{(U_0\cos^2\omega t + V^2)^{1/2}} &= \frac{1}{T}\int_0^T (V^2 + U_0\cos^2\omega t)^{1/2}\,dt \\ &= \frac{1}{T}\int_0^T ((V^2+U_0^2) - U_0^2\sin^2\omega t)^{1/2}\,dt \end{aligned} \tag{11.6.20}$$

may be evaluated in terms of the complete elliptic integral of the second kind (Jonsson, Skovgaard, and Jacobsen, 1974). Longuet–Higgins assumes, however, that $V \ll U_0$ so that

$$\overline{(u^2+V^2)^{1/2}} \simeq \overline{|u'|} = U_0\overline{|\cos\omega t|} = \frac{2}{\pi}U_0\,.$$

Consequently, the bottom friction becomes

$$\bar{\tau}_y^B \simeq -\frac{1}{\pi}f\rho U_0 V\,. \tag{11.6.21}$$

The orbital velocity amplitude in the shoaling zone near the breaker line may be estimated according to the linear shallow water theory,

$$U_0 = \frac{A}{h}(gh)^{1/2}\,.$$

In the surf zone, no wave theory is available, but an order-of-magnitude estimate can be made by replacing h with $\bar{\zeta}+h$, and by using Eq. (11.6.11):

$$U_0 = \frac{A}{\bar{\zeta}+h}(g(\bar{\zeta}+h))^{1/2} \simeq \frac{1}{2}\gamma[g(\bar{\zeta}+h)]^{1/2}\,. \tag{11.6.22}$$

The mean depth for a plane beach may be inferred from Eq. (11.6.15):

$$\bar{\zeta}+h = s'x'\,, \tag{11.6.23}$$

where

$$s' = \frac{s}{1+\frac{3}{8}\gamma^2}\,, \tag{11.6.24}$$

and

$$x' = x - x_s = x - \frac{h_s}{s} \tag{11.6.25}$$

is the offshore distance measured from the mean shoreline. Thus, from Eq. (11.6.21)

$$\bar{\tau}_y^B = \frac{1}{\pi}\frac{f}{2}\rho\gamma(gs'x')^{1/2}V\,. \tag{11.6.26}$$

Moreover, Longuet–Higgins assumes the same formula for the shoaling zone.

The integrated Reynolds stress or the turbulent radiation stress S''_{xy} is assumed to be of the following form:

$$-S''_{xy} = (\bar{\zeta}+h)\rho\nu_e\frac{\partial V}{\partial x}\,, \tag{11.6.27}$$

where ν_e is the eddy viscosity which has the dimension

$$[\nu_e] = [U][L]\,.$$

Longuet–Higgins takes the velocity scale $[U]$ to be proportional to $(g(\bar{\zeta}+h))^{1/2}$ which is of the same order as the orbital velocity U_0. Analogous to the mixing length of a turbulent flow near a wall, $[L]$ may be taken to be proportional to the distance x' from the shore. Thus,

$$-S''_{xy} = N\rho g^{1/2}s'^{3/2}x'^{5/2}\frac{dV}{dx'} \tag{11.6.28}$$

after the use of Eq. (11.6.23); N is an empirical coefficient. Again the same expression is assumed for the shoaling zone, which is likely an overestimate because of the expected reduction of turbulence.

In summary, the momentum equation is

$$\begin{aligned} & N\rho g^{1/2}s'^{3/2}\frac{dV}{dx'}\left(x'^{5/2}\frac{dV}{dx'}\right) - \frac{1}{\pi}\frac{f}{2}\rho\gamma g^{1/2}s'^{1/2}x'^{1/2}V \\ & \quad = -\frac{5}{16}g^{3/2}s'^{5/2}\gamma^2\left(\frac{\sin\theta}{C}\right)_\infty (x')^{3/2}\,, \quad 0 < x' < x'_b\,, \\ & \quad = 0\,, \qquad\qquad x' > x'_b\,, \end{aligned} \tag{11.6.29}$$

which may be solved by requiring that V be bounded for all $0 < x' < \infty$.

The solution for the longshore current profile $V(x')$ can be simply obtained. The analytical details are straightforward and we shall only present the numerical results in Fig. 11.7. The results depend on the parameter

$$P = 2\pi\frac{s'N}{\gamma f} \tag{11.6.30}$$

which signifies the relative importance of lateral turbulent diffusion to bottom friction. Qualitatively, the longshore velocity decays outside the surf zone. The experimental results of Galvin and Eagleson (1965) scatter within the range $0.05 < P < 1.0$ in Fig. 11.7.

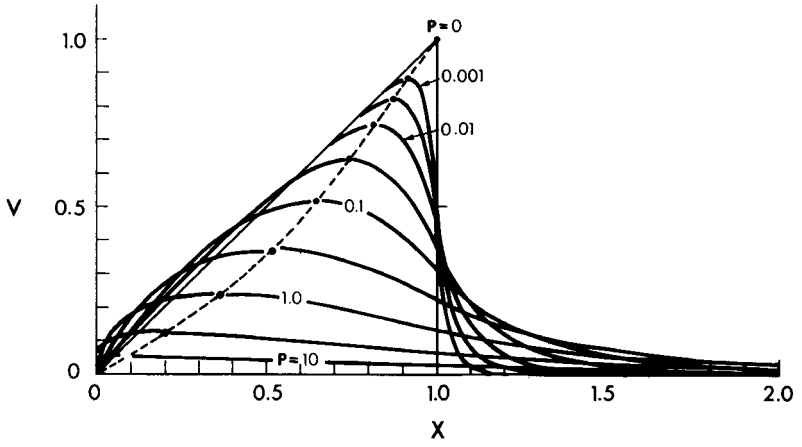

Figure 11.7: Theoretical form of the longshore current V/V_b as a function of $X = x/x_b$ and the lateral mixing parameter $P = 2\pi(s'N/\gamma f)$ (from Longuet–Higgins, 1970b, *J. Geophys. Res.*).

The profile for zero turbulent diffusion gives a useful guide for the order of magnitude of the longshore current, although the discontinuity at the breaker line is physically unrealistic. Taking $N = 0$, we have

$$\begin{aligned} V &= 0\,, && x > x_b\,, \\ V &= \frac{5\pi}{8}\frac{\gamma s'}{\rho f} g s' x' \left(\frac{\sin\theta}{C}\right)_b\,, && x < x_b\,, \end{aligned} \tag{11.6.31}$$

which is a discontinuous distribution with the following maximum at the breaker line:

$$V_m = \frac{5\pi}{8}\frac{\gamma s'}{\rho f}(g(\bar{\zeta} + h)_b)^{1/2} \sin\theta_b\,. \tag{11.6.32}$$

Thus, V_m increases with increasing incidence angle, bottom slope, or incident wave amplitude through $(\bar{\zeta}+h)_b$. By using empirical data in open-channel flows and assuming a sand grain diameter of 1 mm for bed roughness, Longuet–Higgins (1970a) estimated $f = 0.02$. Equation (11.6.32) then crudely agrees with both field and laboratory data if the breaker line depth h_b is reasonably estimated.

11.7 Other Empirical Hypotheses or Improvements

From the simple example of a longshore current it is evident that one must resort to a number of empirical approximations that are based on limited observations. For example, that S'_{ij} has the same expression in both surf and shoaling zones can only be regarded as a physically plausible assumption. The hypothesis of Eq. (11.6.11) has some experimental support only for normally incident waves on a plane beach, but little is known for more complicated waves. Unfortunately, there appears to be no better replacements yet for these major assumptions. A few other questions, and attempted answers, are discussed below in order to reflect ideas on this subject.

11.7.1 Bottom Friction

The Friction Factor in the Joint Presence of Waves and Currents

Abundant experimental information exists for the friction coefficient f_c when the flow is unidirectional and steady. On the other hand, there are data for pure oscillatory flows without breaking waves, and semiempirical

formulas for f_w are available [see Eq. (9.7.22), Chapter Nine]. These data are only appropriate for the shoaling zone. Jonsson, Skovgaard, and Jacobsen (1974) have proposed an interpolation formula for the combined case where both waves and current are present. They define the instantaneous f by

$$\tau^B = \frac{1}{2}\rho f|\mathscr{U}|\mathscr{U}\,, \tag{11.7.1}$$

where $\mathscr{U}$ is the vector sum of the current and the inviscid orbital velocity at the sea bottom. The instantaneous f is assumed to be

$$f = f_w + (f_c - f_w)\sin\mu\,, \tag{11.7.2}$$

$\mu(t)$ being the angle between $\mathscr{U}$ and the instantaneous wave orbital velocity.

In the special case where the current and the wave orbits are orthogonals, we have

$$\tan\mu = \frac{V}{U_0\cos\omega t}\,. \tag{11.7.3}$$

The time average of Eq. (11.7.1) leads to the integral in Eq. (11.6.20) which, in turn, gives

$$\bar{\tau}_y^B = \frac{1}{2}f_e\rho V^2\,, \tag{11.7.4}$$

where the effective f_e is

$$f_e = f_c + \left\{\frac{2}{\pi}\left[1+\left(\frac{V_0}{V}\right)^2\right]^{1/2} E(m) - 1\right\} f_w\,, \tag{11.7.5}$$

with $E(m)$ being the complete elliptic integral of the first kind and m its modulus.

$$E(m) = \int_0^{\pi/2}(1 - m\sin^2\tau)^{1/2}\,d\tau \quad m = U_0^2(V^2+U_0^2)^{-1}\,. \tag{11.7.6}$$

For weak current $V/Uo \ll 1$, it may be shown again that

$$\bar{\tau}_y^B = \frac{1}{\pi}f_w\rho U_0 V\,. \tag{11.7.7}$$

No direct experimental verification of the general formula (11.7.2) is yet available. Moreover, adequate information on f_w is still missing for the surf zone. The situation is much better in the shoaling zone where

a more rational theory has been proposed by Grant and Madsen (1979) which extends the turbulent boundary-layer picture to waves with currents for any angle between them.

Large Angle of Incidence and Strong Current

Most existing laboratory experiments are performed with a fairly large incidence angle at the breaker line (10°–50°), and the measured longshore currents are often comparable to the local orbital velocity. Both these facts are not in accord with the assumptions made in Section 11.6. More specifically, if we use Eq. (11.6.31) for the longshore current velocity V and $\frac{1}{2}\gamma(g(\bar{\zeta}+h))^{1/2}$ for the local orbital velocity U, then the assumption $V/u \ll 1$ implies a severe limitation on the incidence angle throughout the surf zone:

$$\sin\theta \ll \frac{4f(1+3\gamma^2/8)}{5\pi s} \cong \frac{0.315f}{s}$$

(Liu and Dalrymple, 1977). If we take $f = 0.01$, $s = 0.1$ for laboratory experiments and $s = 0.01$ for natural beaches, then the theory (11.6.31) is limited to $\theta \ll 1.8°$ in the laboratory and $\theta \ll 18°$ in the field. Liu and Dalrymple (1978) reconsidered the problem by allowing large incidence angle and relatively strong longshore current, but ignoring lateral turbulence for simplicity. We shall first discuss their theory of weak current but large angle of incidence.

Let the total velocity be

$$\mathscr{U} = (\overline{U}\cos\alpha + u'\cos\theta)\mathbf{e}_x + (\overline{U}\sin\alpha + u'\sin\theta)\mathbf{e}_y\,, \tag{11.7.8}$$

where $\overline{U}$ and u' are the mean current and the oscillatory velocity, respectively, and α and θ are their inclinations with respect to the x axis. Let U_0 denote the magnitude of u', that is, $u' = U_0\cos\omega t$, and assume the current to be weak, that is, $\overline{U}/U_0 \ll 1$, then

$$|\mathscr{U}| \cong |u'| + \overline{U}\frac{|u'|}{u'}\cos(\theta-\alpha)\,.$$

Putting this result into Eq. (11.7.1), taking averages, and using the fact that

$$\overline{|u'|} = \frac{2U_0}{\pi}\,, \quad \overline{|u'|u'} = 0\,,$$

we obtain

$$\bar{\tau}^B = \rho f \left(\frac{U_0}{\pi}\right) \{[U(1+\cos^2\theta) + V\sin\theta\cos\theta]\mathbf{e}_x + [V(1+\sin^2\theta) + U\sin\theta\cos\theta]\mathbf{e}_y\} \tag{11.7.9}$$

where

$$U = \overline{U}\cos\alpha\,, \quad V = \overline{U}\sin\alpha\,.$$

When the mean current and the orbital velocity are colinear, $\theta = \alpha = 0$, $V = 0$, and $\overline{U} = U$ so that

$$\bar{\tau}_B = 2f\left(\frac{U_0}{\pi}\right) U\mathbf{e}_x\,. \tag{11.7.10a}$$

On the other hand, if the two velocities are perpendicular, $\theta = 0$, $\alpha = \frac{1}{2}\pi$, then $U = 0$ and $\bar{u} = V$, so that

$$\bar{\tau}^B = \rho f\left(\frac{U_0}{\pi}\right) V\mathbf{e}_y \tag{11.7.10b}$$

which is the same as Eq. (11.7.7). The preceding formulas differ by a factor of 2, as first pointed out by Jonsson (1966).

For a longshore current, $U = 0$ and $\alpha = \frac{1}{2}\pi$. Let θ be arbitrary so that

$$\bar{\tau}^B = \rho\frac{f}{2}\left(\frac{U_0}{\pi}\right)\{(V\sin 2\theta)\mathbf{e}_x + 2V(1+\sin^2\theta)\mathbf{e}_y\}\,. \tag{11.7.11}$$

Using this result and proceeding as in Section 11.6, one obtains

$$0 = -g\frac{d\bar{\zeta}}{dx} - \frac{g\gamma^2}{8(\bar{\zeta}+h)}\frac{d}{dx} \times \left[(\bar{\zeta}+h)^2 + \left(\frac{3}{2} - \sin^2\theta\right)\right] - \frac{f}{2}\frac{\gamma}{\pi}g^{1/2}(\bar{\zeta}+h)^{-1/2}V\sin\theta\cos\theta \tag{11.7.12}$$

in the x direction (offshore), and

$$0 = -\frac{g\gamma^2}{8(\bar{\zeta}+h)}\frac{d}{dx}[(\bar{\zeta}+h)^2\sin\theta\cos\theta] - \frac{f}{2}\frac{\gamma}{\pi}g^{1/2}(\bar{\zeta}+h)^{-1/2}V(1+\sin\theta) \tag{11.7.13}$$

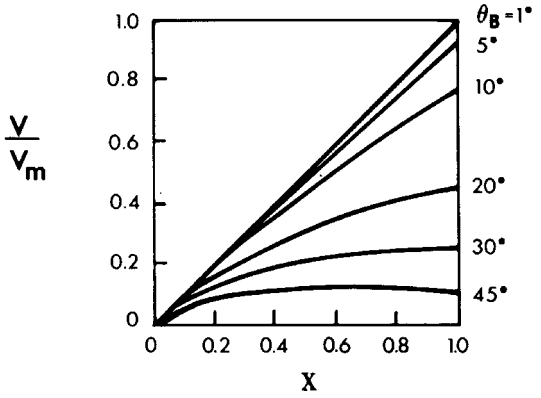

Figure 11.8: Nondimensional longshore current profiles by assuming weak current in bottom friction. Lateral diffusion is ignored. V_m is given by Eq. (11.6.32) and $X = (x - x_s)/(x_b - x_s)$ (from Liu and Dalrymple, 1978, *J. Marine Res.*).

in the y direction (alongshore). Note that the mean sea level $\bar{\zeta}$ is no longer independent of the longshore current. If Snell's law, $(\sin\theta)/C = ((\sin\theta)/C)_b$, and $C = [g(\bar{\zeta}+h)]^{1/2}$ are assumed, Eqs. (11.7.12) and (11.7.13) may be combined to give a single ordinary differential equation for $(\bar{\zeta}+h)$. The boundary condition is:

$$(\bar{\zeta} + h) = (\bar{\zeta} + h)_b \,. \tag{11.7.14}$$

From the solution the mean shoreline position x_s can be immediately inferred, and the longshore current distribution V can be computed. The resulting formulas are omitted and only the current profiles are shown in Fig. 11.8. For a larger angle of incidence, the current velocity falls below the prediction [Eq. (11.6.32)] by Longuet–Higgins.

Liu and Dalrymple further considered the effect of a strong current $|u'/U| \geq 1$. In general, the total velocity magnitude is

$$|\mathscr{U}| = [(u')^2 + \overline{U}^2 + 2u'\overline{U}\cos(\theta - \alpha)]^{1/2} \,.$$

It turns out that the following three-term expansion for small $u'/\bar{U}$

$$|\mathscr{U}| \cong \overline{U}\left\{1 + \left(\frac{u'}{U}\right)\cos(\theta-\alpha) + \frac{1}{2}\left(\frac{u'}{U}\right)\sin^2(\theta-\alpha)\right\}^{1/2}$$

gives a fairly good numerical approximation for $|u'/U| < 1$ as long as $\theta - \alpha > 45°$, which is normally the case. The error term is $\frac{1}{2}(u'/U)^3\cos(\theta-\alpha)$ which

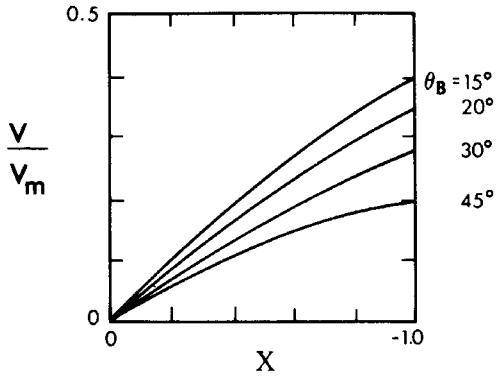

Figure 11.9: Nondimensional longshore current profiles by assuming strong current in bottom friction. Lateral diffusion is ignored; bottom slope $s = 0.05$; $f = 0.025$ (from Liu and Dalrymple, 1978, *J. Marine Res.*).

further diminishes as $|\theta - \alpha| \to \frac{1}{2}\pi$. With this approximation the averaged bottom stress becomes, in general,

$$\bar{\tau}^B = \frac{\rho f}{4}\left\{\left[\frac{U_0^2}{2}\left(\frac{1}{2}\sin^2(\theta-\alpha)\cos\alpha + \cos(\theta-\alpha)\cos\theta\right) + \overline{U}U\right]\mathbf{e}_x \right.$$
$$\left. + \left[\frac{U_0^2}{2}\left(\frac{1}{2}\sin^2(\theta-\alpha)\sin\alpha + \cos(\theta-\alpha)\sin\theta\right) + \overline{U}V\right]\mathbf{e}_y\right\}. \tag{11.7.15}$$

For a longshore current $\alpha = \frac{1}{2}\pi$, we have

$$\bar{\tau}^B = \frac{\rho f}{2}\left\{\left[\frac{U_0^2}{2}\sin^2\theta\right]\mathbf{e}_x + \left[V^2 + \frac{U_0^2}{4}(1+\sin^2\theta)\right]\mathbf{e}_y\right\} \tag{11.7.16}$$

which may be inserted in the mean momentum equations for numerical solution. Sample results in Fig. 11.9 show a considerable reduction from the weak-current theory of Longuet–Higgins [see Eq. (11.6.32)].

11.7.2 Lateral Turbulent Diffusion S''_{xy}

In the theory of Bowen (1969), the simplest assumption is made that the eddy viscosity is constant in and outside the surf zone.

In the mixing length argument, Longuet–Higgins (1970b) estimates the velocity scale to be less than $O.1U_0 = 0.1\{\frac{1}{2}[g(\bar{\zeta}+h)]^{1/2}\}$, and the mixing length scale to be $\kappa x'$ where $\kappa = 0.40$ is the Karman constant; thus

$$N \leqq (0.1)\left(\frac{\gamma}{2}\right)\kappa \leqq 0.016\,. \tag{11.7.17}$$

Thornton (1970) and Jonsson, Skovgaard, and Jacobsen (1974) suggest that

$$-S''_{xy} = \rho\left(\frac{\gamma^2}{2\pi}s'\right) g^{1/2} s'^{3/2} x'^{5/2} \frac{dV}{dx}\,, \tag{11.7.18}$$

which implies an equivalent N of

$$N = \frac{\gamma^2}{2\pi}s' \simeq 0.1 s'\,. \tag{11.7.19}$$

For $s' \sim 0.1$, Eq. (11.7.19) is not much different from Eq. (11.6.28) except that the former depends on the beach slope.

Battjes (1975) argues that turbulence in the surf zone is derived primarily from wave breaking and not from the horizontal shear in the mean longshore current. The rate of dissipation (into heat) of turbulent energy should be equal to the rate of loss of wave energy by breaking. The latter is approximately

$$\begin{aligned}\frac{d}{dx}(EC_g) &= \frac{d}{dx}\left(\frac{1}{2}\rho g A^2 C_g\right)\\ &\simeq \frac{\gamma^2}{8}\rho g \frac{d}{dx}[h^2(gh)^{1/2}]\\ &= \frac{5\gamma^2}{16}\rho g^{3/2} h^{3/2}\frac{dh}{dx}\,.\end{aligned}$$

Now the rate of turbulent energy dissipation ε can be estimated by the fluctuating velocity q'' and the eddy size which must be limited by the depth h. By dimensional reasoning, we have $\varepsilon = q''^3/h$ per unit mass. Equating ε and dEC_g/dx in order of magnitude, we get an estimate of the turbulent velocity:

$$q'' \sim \left(\frac{5\gamma^2}{16}\frac{dh}{dx}\right)^{1/3}(gh)^{1/2}\,. \tag{11.7.20}$$

Battjes further assumes that the integrated Reynolds stress is related to the mean shear by

$$-S''_{xy} = -\rho\int_{-h}^{\bar{\zeta}} \overline{u''v''}\,dz \sim \rho h(q''h)\frac{dV}{dx}\,.$$

Substituting Eq. (11.7.20) for q'', he finds an expression for the eddy viscosity,

$$\nu_e \sim q'' h = K \left(\frac{5}{16} \rho g^{3/2} h^{3/2} \frac{dh}{dx} \right)^{1/3} h \tag{11.7.21}$$

where K is a constant of order unity. In order to compare Eq. (11.7.21) with Longuet–Higgins' assumption we express ν_e as

$$\nu_e = Nx(gh)^{1/2} .$$

The corresponding N for a plane beach with slope s is

$$N = \left(\frac{5}{16} \gamma^2 \right)^{1/3} s^{4/3} K . \tag{11.7.22}$$

This result differs slightly from that of Thornton and Jonsson et al. in the dependence of N on beach slope s. Available experiments are not yet sufficiently extensive to enable a choice among these alternative models.

Finally, observations by dye injection have shown that turbulence outside the surf zone is weak (Inman, Tait, and Nordstrom, 1971); therefore they do not support the assumption made in most theories that the eddy viscosities in and outside the surf zone are the same. Although this weakness is widely recognized, no satisfactory substitute is yet known.

11.8 Currents Behind an Offshore Breakwater

The uniform longshore current along a straight beach is one dimensional with variations in the offshore–onshore direction only; the associated mathematics is especially simple since the convective acceleration of the mean current vanishes identically. We shall now discuss briefly two examples where the wave system, hence also the current, are two dimensional. Certain approximations will be made for the sake of mathematical expedience. Specifically, we shall omit convective inertia and turbulent diffusion. Further, we shall use very simple models for the bottom friction by ignoring the variation of the angle between the local mean current and the wave velocities. Also omitted is the possible modification of the waves by the mean current. Intuitively, waves are modified the most where there is a strong rip current (a narrow current in the offshore direction), and our omission is likely to give quantitatively poor results. Owing to the lack of

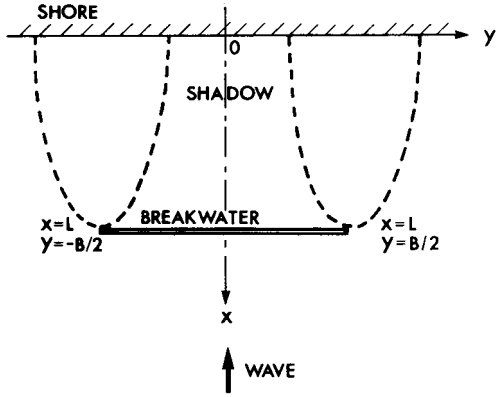

Figure 11.10: An offshore breakwater.

definitive empirical information, an elaborate model will not be attempted here so that the results are of qualitative and order-of-magnitude significance only. The purpose of our examples in this section and the next is to illustrate how much a simple model can tell us about the current patterns, the difference in forcing mechanisms, and the possible inferences on littoral transport, in two interesting situations.

For the prevention of a given stretch of beach from excessive erosion, an offshore breakwater is sometimes built at a certain distance parallel to the shore to reduce the influence of the incident waves, as shown in Fig. 11.10. A well-known consequence is that, after a long time, the sandy beach may develop a cusp at the center of the wave shadow. If the breakwater is close enough to the shore, the cusp head may eventually reach the back of the breakwater. This process is known in coastal geography to be partly responsible for the linking of an offshore island with the mainland and is called the tombolo effect. More on the offshore island will be discussed later. For the offshore breakwater, laboratory studies on a plane beach have been conducted by Sauvage de Saint Marc and Vincent (1955). On the bottom of a rigid beach, two opposing currents were observed to flow toward the center line of the shadow, and then to combine into a rip current toward the breakwater. When the bottom of the beach was covered with sand, the sand particles drifted towards and were deposited near the stagnation point along the initial shore. The deposition eventually grew to be a cusp. It is, therefore, of engineering and scientific interest to predict the current pattern behind the breakwater.

11.8.1 The Wave Field

Assume the bottom contours of the beach to be straight and parallel so that $h = h(x)$. Let the breakwater be of length B and be located outside the breaker line at $x = L$ from the still water shoreline ($x = 0$), where $L > x_b$. A normally incident wavetrain arrives from $x \sim \infty$. The waves in the shoaling zone must be first calculated by accounting for both diffraction and refraction; generally this is a numerical task. For this special case we follow the analytical approach of Liu and Mei (1974, 1976a) who extended the *parabolic approximation* to the case of varying depth.

According to the geometrical optics approximation, the lines $y = \pm B/2$ and the breakwater divide the whole region into three zones. In the illuminated zone $|y| > B/2$, a plane progressive wave is dominant. In the reflection zone $|y| < B/2$, $x > L$, there is a standing wave due to the superposition of the incident and the reflected waves. All these waves are slowly refracted by the changing depth. In the shadow zone $|y| < B/2$, $0 < x < L$, no waves are present. This approximation is, of course, discontinuous near the boundaries of these zones. Boundary layers are needed to describe the transition smoothly by accounting for diffraction.

The exact linearized formulation of the diffraction problem calls for the solution of the boundary-value problem for the velocity potential $\mathbf{\Phi}(x, y, z) = \phi(x, y, z)e^{-i\omega t}$, where ϕ satisfies Eqs. (3.5.4a)–(3.5.4b), Section 3.5, with $h = h(x)$. We assume that the depth varies slowly within a wavelength and define a small parameter μ such that

$$\mu = O\left(\frac{1}{kh}\frac{dh}{dx}\right) \ll 1\,. \tag{11.8.1}$$

Intuitively, the slow depth variation produces slow variations in the amplitude and phase of the propagating wave. Let us concentrate on the vicinity of the shadow boundary along $y = B/2$, $0 < x < L$ and introduce $\tilde{y} = y - B/2$. Far outside the shadow, the waves simply experience shoaling effects; the potential should approach

$$\phi \sim \psi(\mu x, z) \exp\left[-i \int k(\mu x)\, dx\right] \tag{11.8.2}$$

where $k(x)$ is the local wavenumber. If the breakwater is long enough so that the transition regions of the two shadow boundaries do not intersect, we expect that

$$\phi \sim 0 \tag{11.8.3}$$

far inside the shadow. Now we assume

$$\phi = \psi(\mu x, z) D \exp\left(-i \int k\, dx\right) \tag{11.8.4}$$

where the factor D accounts for diffraction and takes the following limits:

$$D \to 1 \quad \text{as} \quad \tilde{y} \to \infty \tag{11.8.5a}$$

and

$$D \to 0 \quad \text{as} \quad \tilde{y} \to -\infty\,. \tag{11.8.5b}$$

In the classical problem of tip diffraction in a uniform medium (corresponding to $h = \text{const}$), it is known that the neighborhood of the shadow boundary is like a boundary layer. In particular, the variations in the transverse ($\tilde{y}$) direction are much more rapid than those in the longitudinal (x) direction, and that variations in both directions are slow sufficiently far away from the tip. Accepting this for the time being, we now let the diffraction factor D depend on x, $\tilde{y}$ slowly so that

$$D = D(\alpha x, \beta \tilde{y}) \quad \text{with} \quad \alpha \ll \beta \ll 1\,.$$

The precise nature of α and β will be determined later. Substituting Eq. (11.8.4) into Laplace's equation, we obtain

$$\left\{\frac{\partial^2 \psi}{\partial z^2} - k^2 \psi + \mu\left[2ik\frac{\partial \psi}{\partial(\mu x)} + i\frac{\partial k}{\partial(\mu x)}\psi\right]\right\} D$$
$$+ \left[\beta^2 \frac{\partial^2 D}{\partial(\beta \tilde{y})^2} - \alpha i k \frac{\partial D}{\partial(\alpha x)}\right]\psi = O(\alpha\mu, \alpha^2, \mu^2)\,, \tag{11.8.6}$$

where the exponential factor has been omitted. The boundary conditions are

$$\frac{\partial \psi}{\partial z} - \frac{\omega^2}{g}\psi = 0\,, \quad z = 0 \tag{11.8.7}$$

and

$$\frac{\partial \psi}{\partial z} = \mu i k \frac{dh}{d(\mu x)}\psi + O(\mu^2)\,, \quad z = -h(x)\,. \tag{11.8.8}$$

Note that the boundary conditions do not depend on $\tilde{y}$. For $\tilde{y} \to \infty$, $D \to 1$, Eq. (11.8.6) reduces to

$$\frac{\partial^2 \psi}{\partial z^2} - k^2 \psi = -\mu\left[2ik\frac{\partial \psi}{\partial(\mu x)} + i\frac{\partial k}{\partial(\mu x)}\psi\right] + O(\mu^2) \tag{11.8.9}$$

subject to the boundary conditions (11.8.7) and (11.8.8). This problem is a special case of the refraction theory, Chapter Three; the leading-order solution is

$$\psi = \frac{igA}{\omega}\frac{\cosh k(z+h)}{\cosh kh}[1+O(\mu)] \tag{11.8.10}$$

where ω, k and A must satisfy Eqs. (3.1.15) and (3.3.9), Chapter Three, with $\theta = \theta_0 = 0$. Because of Eq. (11.8.9), it follows from Eq. (11.8.6) that

$$\beta^2\frac{\partial^2 D}{\partial(\beta\tilde{y})^2} - 2\alpha ik\frac{\partial D}{\partial(\alpha x)} \simeq 0\,. \tag{11.8.11}$$

Since the task of deducing the approximate equation is at last achieved, the small parameters μ, α, and β may now be dropped and the original variables x and y restored. Thus, Eq. (11.8.11) is simply

$$\frac{\partial^2 D}{\partial\tilde{y}^2} - ik\frac{\partial D}{\partial x} \simeq 0\,, \tag{11.8.12}$$

subject to the boundary conditions (11.8.5a) and (11.8.5b). The variable coefficient in Eq. (11.8.12) may be eliminated by introducing

$$\xi = k_0\int_x^L \frac{dx}{k}\,, \tag{11.8.13}$$

where k_0 is the wavenumber at the breakwater $x = L$. Then,

$$\frac{\partial^2 D}{\partial\tilde{y}^2} + 2ik_0\frac{\partial D}{\partial\xi} = 0\,, \tag{11.8.14}$$

which is just the Schrödinger equation. Indeed, the present boundary-value problem has been solved in Section 2.4.2 in a totally different context. For convenience the salient results are quoted here. Let

$$\sigma = \frac{k_0\tilde{y}}{(\pi k_0\xi)^{1/2}}\,, \tag{11.8.15}$$

then the diffraction factor D may be expressed

$$D = \frac{1}{2^{1/2}}e^{-i\pi/4}\left\{\left[\frac{1}{2}+C(\sigma)\right]+i\left[\frac{1}{2}+S(\sigma)\right]\right\}. \tag{11.8.16}$$

The magnitude of D is

$$|D| = \frac{1}{2^{1/2}}\left\{\left[\frac{1}{2}+C(\sigma)\right]^2+\left[\frac{1}{2}+S(\sigma)\right]^2\right\}^{1/2}. \tag{11.8.17}$$

The diffraction factor is constant for $\sigma = \text{const}$. Therefore, one may define the boundary of the transition zone by

$$(k_0\tilde{y})^2 = (\text{const})\pi k_0\xi = (\text{const})\pi k_0 \int_x^L \frac{dx}{k} \tag{11.8.18}$$

which is a sort of parabola.

From the solution for D, Eq. (11.8.18), it is clear that

$$\frac{1}{k_0 D}\frac{\partial D}{\partial x} = O\left(\frac{\partial \sigma}{\partial x}\right) = O(k_0\xi)^{-1}\,,$$

$$\frac{1}{k_0 D}\frac{\partial D}{\partial \tilde{y}} = O\left(\frac{\partial \sigma}{\partial \tilde{y}}\right) = O(k_0\xi)^{-1/2}\,. \tag{11.8.19}$$

Thus, variations in x and y directions are small only when $k_0\xi$ is large. In view of Eq. (11.8.13) the distance from the tip must be large. Because of these restrictions, the present approximate theory may be applied to the offshore breakwater of finite length only if $k_0 L$ and $k_0 B$ are both large so that the two shadow boundary layers do not intersect.

In summary, the potential in the shadow boundaries near $y = \pm\frac{1}{2}B$, $x < L$ is given approximately by

$$\mathbf{\Phi} = \text{Re}\left(-\frac{ig\tilde{A}}{\omega}\frac{\cosh k(z+h)}{\cosh kh}\exp\left[-i\left(\int k\,dx + \omega t + \Theta\right)\right]\right), \tag{11.8.20a}$$

where

$$\tilde{A} = A\left\{\frac{1}{2}\left[\frac{1}{2} + C(\sigma)\right]^2 + \frac{1}{2}\left[\frac{1}{2} + S(\sigma)\right]^2\right\}^{1/2}, \tag{11.8.20b}$$

$$\Theta = \frac{\pi}{4} - \tan^{-1}\frac{\frac{1}{2} + S(\sigma)}{\frac{1}{2} + C(\sigma)}\,, \tag{11.8.20c}$$

and

$$\sigma = \frac{k_0(y \pm \frac{1}{2}B)}{(\pi k_0\xi)^{1/2}}\,. \tag{11.8.20d}$$

The diffraction factor $|D|$ is shown in Fig. 11.11 for the side $y > 0$.

Again we use the linearized theory to estimate the position of the breaker line $x = x_b(y)$. By invoking the hypothesis

$$\tilde{A} = (x_b; y) = \frac{\gamma}{2}h(x_b)\,,$$

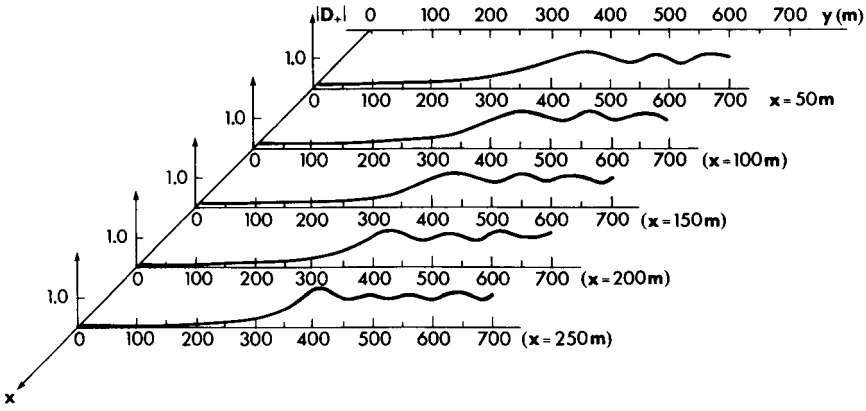

Figure 11.11: Variation of diffraction factor $|D_+|$ on the side of $x > 0$ for normal incidence on an offshore breakwater. The breakwater is at $x = 350$ m and has a length of 700 m (from Liu and Mei, 1976a, *J. Geophys. Res.* Reproduced by permission of American Geophysical Union).

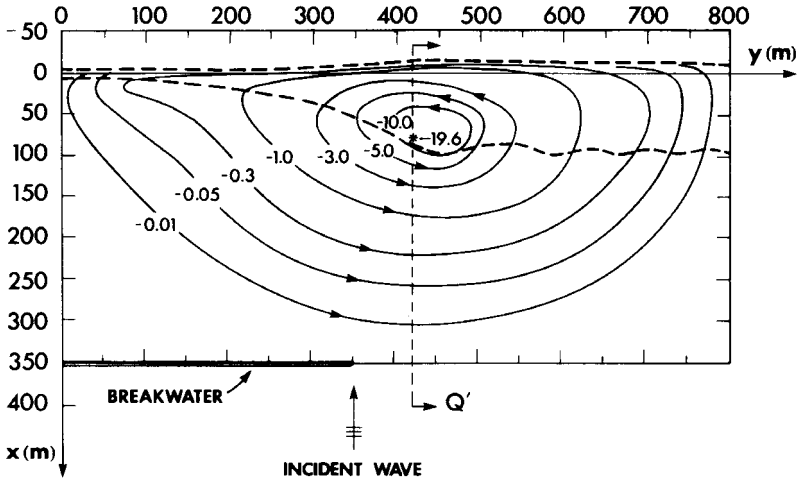

Figure 11.12: Streamline of mean current behind an offshore breakwater of normal incidence (breaker line is shown in dashes) (from Liu and Mei, 1976b, *J. Geophys. Res.* Reproduced by permission of American Geophysical Union).

which is an extrapolation of the empirical result established for strictly plane waves, and by using Eq. (11.8.20b) for $\tilde{A}$, we can determine a crude breaker line. A further simplification may be made by taking $x = 0$ in the expression for ξ, that is,

$$\xi \to \xi_0 = k_0 \int_0^L \frac{dx}{k} .$$

The estimated breaker line is shown by dashes in Fig. 11.12, the important feature being the increase of the surf zone width from zero in the shadow to the finite limit far outside.

We emphasize that the quantitative prediction of wave transformation in the shoaling zone can certainly be improved. Indeed, a uniformly valid theory is now available (Liu, Lozano, and Pantazarus, 1979) which supports the present theory quite favorably.

11.8.2 The Mean Motion

With the convective inertia and turbulent diffusion S''_{ij} ignored for mathematical simplicity, the equations of motion are

$$\frac{\partial}{\partial x_i}[U_i(\bar{\zeta} + h)] = 0 , \tag{11.8.21}$$

$$0 = \rho g(\bar{\zeta} + h)\frac{\partial \bar{\zeta}}{\partial x_j} - \frac{\partial S'_{ij}}{\partial x_i} - \bar{\tau}_j^B . \tag{11.8.22}$$

In the shoaling zone we approximate $\bar{\zeta} + h$ by h so that

$$\frac{\partial}{\partial x_i}(U_i h) = 0 , \tag{11.8.23}$$

$$0 = -\rho g h\frac{\partial \bar{\zeta}}{\partial x_j} - \frac{\partial S'_{ij}}{\partial x_i} - \bar{\tau}_j^B . \tag{11.8.24}$$

As shown in Section 11.2.4 the current is expected to be significant in the surf zone but not in most of the shoaling zone. Thus, the mean sea level and the radiation stress should be in static equilibrium. Let us denote the corresponding mean sea level by $\bar{\zeta}_w$ so that

$$0 = -\rho g h\frac{\partial \bar{\zeta}_w}{\partial x_j} - \frac{\partial S'_{ij}}{\partial x_i} , \quad x > x_b .$$

More specifically, since the wave in the shoaling zone is approximately a slowly modulated progressive wave normally incident toward the beach, the part $\bar{\zeta}_w$ is

$$\bar{\zeta}_w = -\frac{k\tilde{A}^2}{2\sinh 2kh}\,. \tag{11.8.25}$$

Very near the breaker line there must be some current in the shoaling zone due to continuity. As a consequence, a new adjustment of mean sea level $\bar{\zeta}_c$ is induced. Let the total mean sea level be expressed by

$$\bar{\zeta} = \bar{\zeta}_c + \bar{\zeta}_w\,, \tag{11.8.26}$$

where $\bar{\zeta}_c$ is related to the current through the bottom stress by

$$0 = -\rho g h\frac{\partial \bar{\zeta}_c}{\partial x_i} - \bar{\tau}_j^B\,. \tag{11.8.27}$$

In the surf zone it is no longer reasonable to ignore $\bar{\zeta}$ with respect to h; hence the problem is still nonlinear despite the omission of convective inertia. Now the radiation stresses are again assumed to be of the same form as in the shoaling zone. Since the waves are slowly modulated and normally incident progressive waves in shallow water, these stresses are given by

$$S'_{xx} \simeq \frac{3}{4}\rho g\tilde{A}^2\,, \tag{11.8.28a}$$

$$S'_{yy} = \frac{1}{4}\rho g\tilde{A}^2\,, \tag{11.8.28b}$$

$$S'_{zz} = S'_{yx} \simeq 0\,, \tag{11.8.28c}$$

[see Eq. (11.3.3)]. Note that while S'_{xy} is the only driving force in the longshore current, it disappears in normally incident waves. Again the assumption $\tilde{A} = \frac{1}{2}\gamma(\bar{\zeta} + h)$ is made so that the radiation stresses become

$$S'_{xx} = \frac{1}{16}\rho g\gamma^2(\bar{\zeta} + h)^2\,,$$

$$S'_{yy} = \frac{1}{16}\rho g\gamma^2(\bar{\zeta} + h)^2\,. \tag{11.8.29}$$

To complete the formulation, the following simple model for the bottom friction is introduced:

$$\bar{\tau}_i^B = \frac{f}{2}\rho U_0 U_i \,, \tag{11.8.30}$$

where U_0 is taken to be a constant typical of the orbital velocity in the shoaling zone

$$U_0 = \left(\frac{gkA}{\omega \cosh kh}\right)_{x_b}, \quad x > x_b \,, \tag{11.8.31}$$

and the following orbital velocity in the surf zone

$$\begin{aligned} U_0 &= \frac{\tilde{A}}{\bar{\zeta}+h}(g(\bar{\zeta}+h))^{1/2} \\ &= \frac{\gamma}{2}(g(\bar{\zeta}+h))^{1/2}, \quad x < x_b \,. \end{aligned} \tag{11.8.32}$$

With these assumptions the equations are closed. We add the boundary conditions that the mean flow is tangential to the mean shoreline ($\bar{\zeta}+h=0$), to the line of symmetry ($y=0$), and to the breakwater and vanishes at infinity. The mathematical problem is now determinate.

The above nonlinear boundary-value problem can only be solved numerically, as reported in Liu and Mei (1976b, see (1974) for further details). Only the calculated results are described here. Figure 11.12 presents the stream function ψ defined by

$$U(\bar{\zeta}+h) = -\frac{\partial \psi}{\partial y}, \quad V(\bar{\zeta}+h) = \frac{\partial \psi}{\partial x} \,. \tag{11.8.33}$$

The geometrical dimensions chosen for this sample case are $B = 700$ m, $L = 350$ m, and $dh/dx = 1/50$. The incident wave is assumed to be a swell of period $T = 10$ s and amplitude $A_\infty = 0.5$ m. For reference, the incident wavelength is 79 m and the amplitude is 0.52 m at the depth of the breakwater ($h = 7$ m). The empirical coefficients used are $f = 0.02$ and $\gamma = 0.8$.

The streamlines for the side $y > 0$ show a counterclockwise circulation. On the side $y < 0$ there is a symmetric cell in the clockwise direction. This result is certainly in agreement with known observations of currents and is consistent with the cusp or tombolo formation.

Figure 11.13 shows the corresponding mean sea level on the side of $y > 0$. Deep inside the shadow the mean sea level is zero; far outside the shadow the mean sea level has a set-up in the surf zone and a set-down in the shoaling zone, as expected.

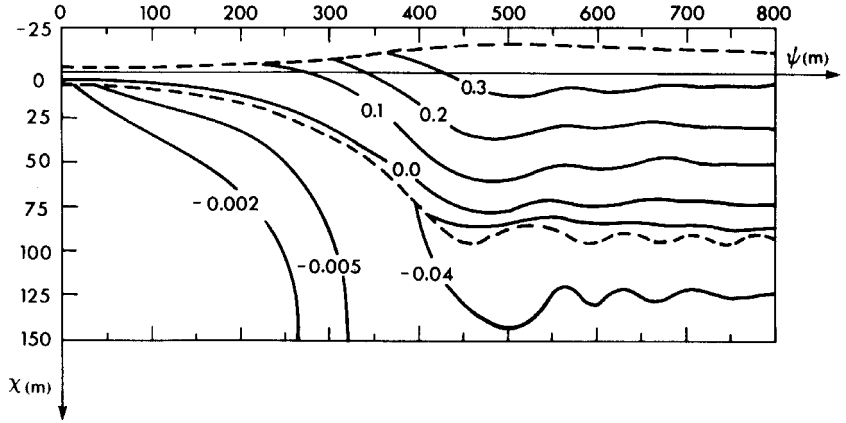

Figure 11.13: Contours of mean sea level displacement $\bar{\zeta}$ behind an offshore breakwater at normal incidence. Mean shore line and mean breaker line are shown in dashes (from Liu and Mei, 1976b, *J . Geophys. Res.* Reproduced by permission of American Geophysical Union).

For a better understanding of the physical mechanism of the circulation, we substitute assumptions (11.8.29), (11.8.30), and (11.8.32) into the momentum equation (11.8.22), and then take the curl, yielding,

$$\frac{\partial}{\partial x}\left(\frac{V}{\bar{\zeta}+h}\right)-\frac{\partial}{\partial y}\left(\frac{U}{\bar{\zeta}+h}\right)$$

$$=\frac{2g}{f}\left\{\frac{h\bar{\zeta}_y-\frac{1}{4}\gamma^2(\bar{\zeta}+h)_x\bar{\zeta}_y}{\gamma g^{1/2}(\bar{\zeta}+h)^{3/2}}+\frac{\gamma\bar{\zeta}_{xy}}{2[g(\bar{\zeta}+h)^{1/2}}\right\}. \qquad (11.8.34)$$

The left-hand side of Eq. (11.8.34) is the potential vorticity in the mean flow; the right-hand side may be viewed as the forcing vorticity. Now the behavior of $\bar{\zeta}$ is easy to speculate, although it is a part of the solution. Because of the small numerical value of the factor $\frac{1}{4}\gamma^2 \simeq 0.16$ which is associated with S'_{xx} and S'_{yy}, the most important term is $h\bar{\zeta}_y$ in the first fraction on the right of Eq. (11.8.34). For $y > 0$, $\bar{\zeta}_y$ is certainly positive; the driving vorticity is positive and the responding current must be counterclockwise. Therefore, the gradient of mean sea level is the driving force; the radiation stresses act in an indirect way to produce the mean sea level.

If convective inertia were included, the streamlines would be more crowded around the x axis, resulting in a stronger rip current. Inclusion of the turbulent term S''_{xy} would push the center of the cell seaward

where the speed is maximum. These effects have not yet been investigated quantitatively.

Although only the results for an offshore breakwater with normally incident waves are presented here, the following variations have also been studied by Liu and Mei (1976b): (i) oblique incidence: the added feature is that a uniform longshore current must be superposed, and (ii) oblique incidence on a long breakwater intersecting the shore normally. A cell is found around the shadow boundary, and flow is directed toward the breakwater near the shore and seaward along the shadow face of the breakwater. Laboratory evidence relevant to the second example has been reported by Shimano, Hom-ma, and Horikawa (1958) who performed experiments in a wave tank with a jetty intersecting the beach at an angle different from 90°. When the incident wave crests were parallel to the beach, flow was indeed found to be outward along the shadow side of the jetty. This tendency is qualitatively consistent with the results of the present section.

The formation of tombolos behind an offshore island is a common geographical phenomenon as discussed by Zenkovich (1967) whose sketches are reproduced here as Figs. 11.14(a) and 11.14(b). For an island long in the direction parallel to the mainland coast, it is further possible to have two spits emanating from the mainland behind the island. The spits either form a lagoon first and then a single tombolo to link with the

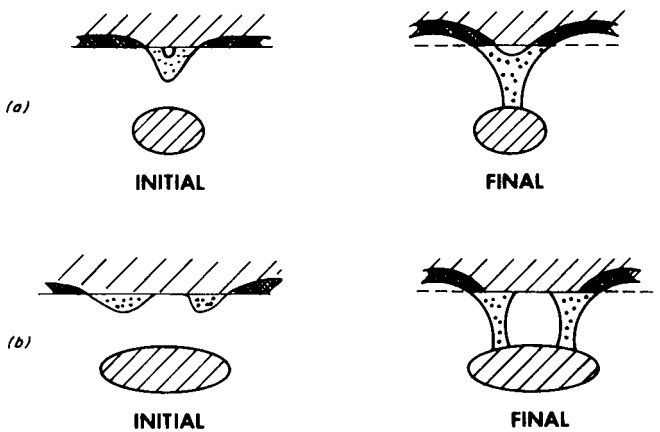

Figure 11.14: Formation of tombolos from the mainland toward the island when only the mainland beach is erodible (after Zenkovich, 1967, *Processes of Coastal Development*, Oliver and Boyd Publishers). (a) Small island and single tombolo; (b) long island and twin tombolos. Dots: area of deposition; double hatches: area of erosion; single hatches: undisturbed land.

island [Fig. 11.14(a)] or extend to the island directly as twin tombolos [Fig. 11.14(b)]. These varieties may be explained by the fact that breaking-induced currents are sufficiently strong to move heavy sediments only slightly outside, hence accumulation should occur slightly inside of the shadow boundaries. For a long island the shadows do not overlap, so that there must be two initial spits which form new natural barriers for further deposition. If the initial spits are close, a lagoon forms first before reaching the island. For a still longer island twin tombolos result. So far we have tacitly assumed that only the shore of the mainland is erodible; the possible impact on an erodible island shore is the motivation of the next section.

11.9 Currents Around a Conical Island

Having discussed some effects of an offshore island on the mainland beach, we now turn to the effects of the beach on the island itself (Mei and Angelides, 1976). For simplicity in wave computation we select a conical island whose depth contours are concentric circles. From the shore ($r = b$) to the toe ($r = a$), the depth is a function of r only. Beyond the toe the sea depth is assumed to be constant (see Fig. 11.15). A plane wave is incident from the left $x \sim -\infty$ where $\theta = -\pi$. As in the last section, we first calculate the

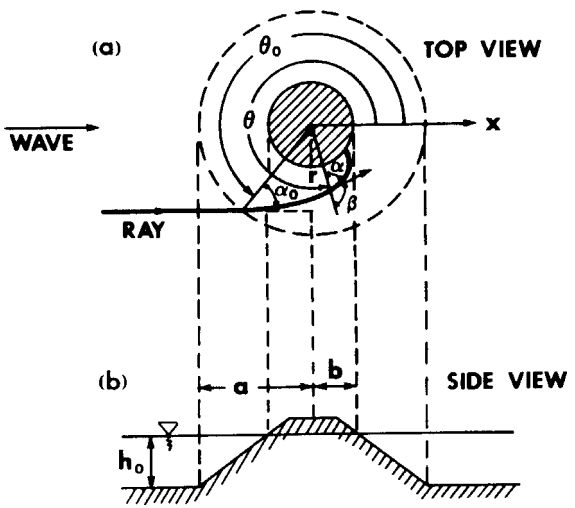

Figure 11.15: Definitions for a conical island.

waves in the shoaling zone, then the breaker line, by invoking an empirical rule. Radiation stresses, calculated for the shoaling zone, are applied to the surf zone with the assumed closure relation between the breaking wave amplitude and the local mean depth. By neglecting convection and lateral turbulent diffusion, the mean circulation is obtained numerically from the average conservation equations of mass and momentum.

11.9.1 The Wave Field

The island slope dh/dr is assumed to be so gentle that the ray (geometrical-optics) theory of refraction applies outside the surf zone. Because of symmetry, only the half to the right of the island, $\pi < \theta < 2\pi$, will be discussed. With reference to Fig. 11.15 the equation of the ray $r = r(\theta)$ is given by Eq. (3.4.4), Chapter Three. To illustrate the effect of the island size, we shall fix the wave frequency, the beach length $a - b$, the deep water depth h_0, and the slope dh/dr. Only the island radius b is left as a free parameter. Specifically, we take $T = 2\pi/\omega = 10$ s, $h_0 = 100$ ft, $dh/dr = 1/20$, $a - b = 2000$ ft. and take $b = 10,000$, 7370, and 5831 ft. for Cases I, II, and III, respectively.

After calculating the ray paths by numerical integration, the refracted wave amplitude A may be computed by invoking energy conservation in a ray tube. Assuming the linear refraction theory to be valid up to the breaker line, we introduce the familiar hypothesis that $(A/h)_b = \frac{1}{2}\gamma$, which determines the breaker line $r = r_b(\theta)$.

Figures 11.16(a), (b), and (c) show the geometry of the rays. Upon comparing these curves, it is evident that as the island size increases, the extent of the lee shore where no rays can enter increases. Case III is the threshold where the lee shore is just zero. In reality modifications due to diffraction must be present so that the wave intensity does not drop to zero without some further penetration. The existence of the lee shore for a large island is physically obvious, and suggests immediately that for a very large island there is no current caused by breaking in a portion of the lee.

11.9.2 The Mean Motion

The approximate mean equations of motion can be conveniently expressed in polar coordinates:

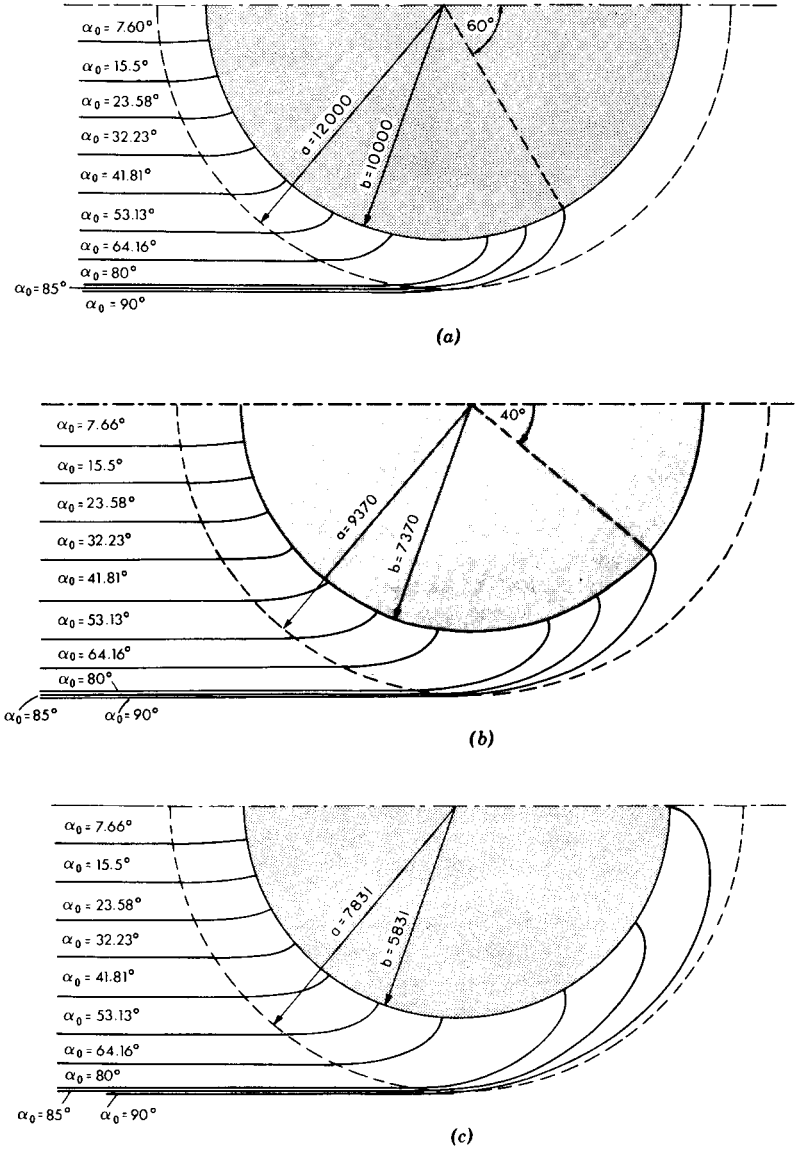

Figure 11.16: Geometry of rays near a conical island (from Mei and Angelides, 1976, *Coastal Eng.* Reproduced by permission of Elsevier Scientific Publishing Co.). (*a*) Large island with a long lee shore; (*b*) intermediate island with a reduced lee shore; (*c*) small island with no lee shore.

Continuity:

$$\frac{\partial}{\partial r}[(\bar{\zeta}+h)U_r]+\frac{1}{r}\frac{\partial}{\partial\theta}[(\bar{\zeta}+h)U_\theta]+\frac{1}{r}U_r(\bar{\zeta}+h)=0\,, \tag{11.9.1}$$

r Momentum:

$$0\simeq-\rho g(\bar{\zeta}+h)\frac{\partial\bar{\zeta}}{\partial r}-\frac{\partial S_{rr}}{\partial r}-\frac{f}{2}\rho U_0U_r\,, \tag{11.9.2}$$

θ Momentum:

$$0\simeq-\rho g(\bar{\zeta}+h)\frac{1}{r}\frac{\partial\bar{\zeta}}{\partial\theta}-\frac{\partial S_{r\theta}}{\partial r}-\frac{f}{2}\rho U_0U_\theta\,, \tag{11.9.3}$$

where U_r and U_θ are the components of the mean current in the r and θ directions, respectively. Formal derivation of these equations is left as an exercise. Suffice it to say that the continuity equation is exact, and the momentum equations are approximately valid when

$$\frac{\partial}{\partial r}\gg\frac{1}{r}\quad\text{or}\quad\frac{1}{r}\frac{\partial}{\partial\theta}\,, \tag{11.9.4}$$

which applies in the present example since the island is large and the radial range of the current is anticipated to be in and near the narrow surf zone. It is further reasonable to approximate the refracted waves locally by a plane progressive wave with incidence angle β. In shallow water, the important components of the radiation stress are

$$S'_{rr}\simeq\frac{1}{4}\rho gA^2(3-2\sin^2\beta)\,, \tag{11.9.4a}$$

$$S'_{r\theta}=S'_{\theta r}=\frac{1}{4}\rho gA^2\sin^2\beta\,, \tag{11.9.4b}$$

where β is the local incidence angle which differs for different rays and is a function of r and θ.

The closure condition $A=\gamma(\bar{\zeta}+h)/2$ and assumptions of U_0 similar to that of Section 11.8 are again introduced. The current velocities are replaced by the stream function ψ defined by

$$U_r=\frac{-1}{\bar{\zeta}+h}\frac{1}{r}\frac{\partial\psi}{\partial\theta}\,, \tag{11.9.5a}$$

$$U_\theta=\frac{1}{\bar{\zeta}+h}\frac{\partial\psi}{\partial r}\,. \tag{11.9.5b}$$

ψ must vanish on $\theta = \pi$, 2π, along the mean shoreline, and at $r \to \infty$. The mean motion is solved numerically as before. The streamlines calculated for an incident wave amplitude of $A_0 = 3$ ft are shown for three islands, Cases I, II, and III in Figs. 11.17(a), 11.17(b), and 11.17(c), respectively.

The general picture is that there are two symmetric cells hugging the shores on each side of the island axis. Near the shoreline the flow is directed from the upwave side to the lee. Without significantly penetrating the lee shore, the current returns at low velocities via the shoaling zone. The primary function of S'_{rr} is to establish the set-up in the surf zone, while the shear component $S'_{r\theta}$ provides the forcing of the longshore current. Thus, the driving mechanism here is roughly analogous to that of the uniform longshore current. The main difference is that the driving force varies in the longshore direction. One reason for such a difference is that $\partial S'_{r\theta}/\partial r$ depends on the local incidence angle β which increases with θ. The dominant term here is

$$\frac{g\gamma^2}{8}(\bar{\zeta} + h)\frac{\partial(\bar{\zeta} + h)}{\partial r}\sin 2\beta\,.$$

For a ray with a larger α_0, the value of β at the breaker line is also larger, that is, the incidence is more oblique. Numerically, it is found that $\partial S'_{r\theta}/\partial r$ always increases with θ from $\theta = \pi$ to the edge of the lee shore. Another reason is that the breaker zone width decreases from $\theta = \pi$ to the edge of the lee shore. Thus, the total driving force across the surf zone, which can be measured by the product of $\partial S'_{r\theta}/\partial r$ and the surf zone width, is zero at $\theta = \pi$, maximum at some intermediate θ, and zero again at the edge of the lee shore. Consequently, the center of the circulating cell is somewhere between the upwave point and the edge of the lee shore, as shown in Figs. 11.17(a)–11.17(c)

As the island radius decreases from Cases I to III, ray convergence is more pronounced so that the current velocity is increased. The extent of the lee shore is also reduced, until in Case III the two longshore currents converge at the center of the lee and form a rip current leaving the island.

From these current patterns, one may venture to explain certain observations near an offshore island. On the upwave side, erosion prevails; sand is transported toward the island lee by longshore currents. Because of the large weight, sediments are deposited somewhere before reaching the edges of the lee shore. Therefore, if the island is large enough to have a finite lee shore, two sand spits may form, which may converge to form a lagoon if

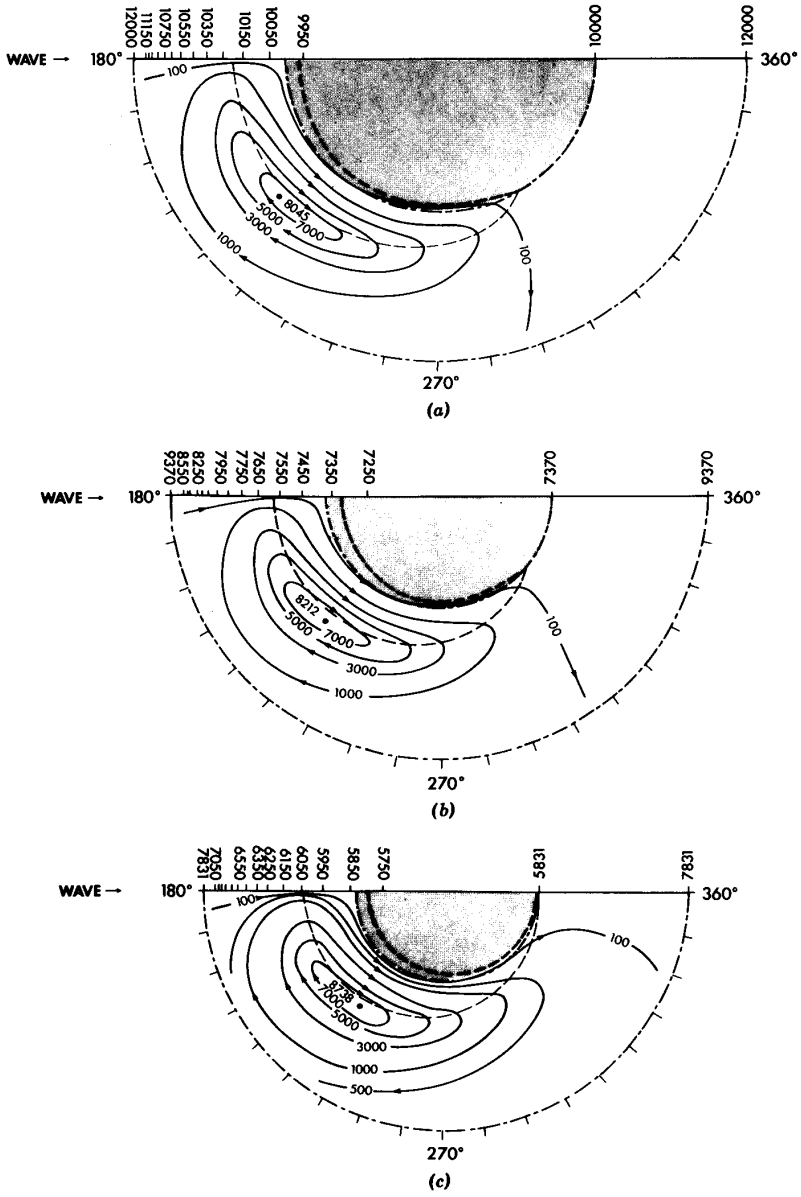

Figure 11.17: Streamlines of breaking-induced currents (from Mei and Angelides, 1976, *Coastal Eng.* Reproduced by permission of Elsevier Scientific Publishing Co.). (*a*) A large island; (*b*) an intermediate island; (*c*) a small island.

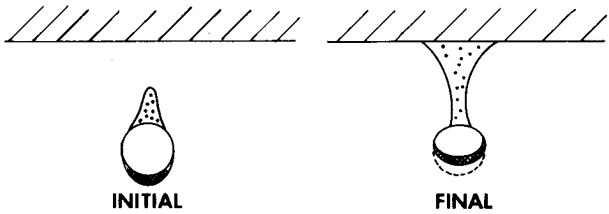

Figure 11.18: Tombolo from a small island toward the mainland when only the island beach is erodible (from Zenkovich, 1960, *Processes of Coastal Development*, Oliver and Boyd).

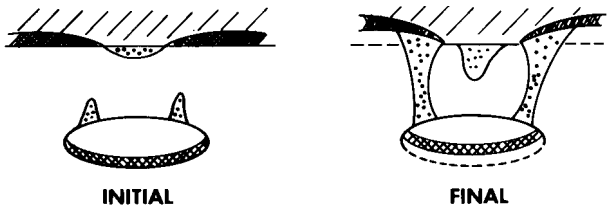

Figure 11.19: Polygenetic formation of tombolos (from Zenkovich, 1967, *Processes of Coastal Development*, Oliver and Boyd).

the mainland is very far, or may reach the mainland directly to form twin tombolos. If the island is so small that there is no lee shore, as in Case III, deposition occurs at the center of the lee and a single spit is formed. These features are known to happen when the mainland has a rocky coast (see Fig. 11.18) as was discussed by Zenkovich (1967).

In general the shores of both the island and the mainland are sandy. Spits can emanate from both of them; the tendency is shown in Fig. 11.19 and is called *polygenetic* by Zenkovich.

11.10 Related Works on Nearshore Currents

Since the introduction of radiation stresses, the literature on nearshore currents due to breaking waves has grown considerably. For uniform longshore currents, James (1974a, b) applied the theory of cnoidal waves and its approximation, the so-called *hyperbolic waves*, to allow for large amplitudes. Battjes (1972) developed a stochastic theory for longshore currents due to random waves; lateral turbulence was ignored.

On two-dimensional rip currents which are relevant for the formation of beach cusps, Arthur (1962) demonstrated the effect of nonlinear convective inertia of the current on the intensification of rips. Bowen (1969) and Bowen and Inman (1969) suggested that the presence of long-period edge waves might be a cause of longshore variation of the mean sea-level, which, in turn, would induce periodic circulation cells. Sonu (1972) gave field evidence that rip currents could also be generated as a consequence of the periodic variation of beach contours. Noda (1974) developed a numerical model accounting for refraction and wave-current interaction for Sonu's problem. In the presence of periodic shoreline variation (shoals and embayments), rip currents can emanate from the shoals or from the embayments (Komar, 1971). Mei and Liu (1977) found that the ratio of the surf zone width to the longshore wavelength of the beach topography influenced the direction of the circulation cells. In nearly all of these theories, lateral turbulence was ignored. Extending Arthur's work, Tam (1973) used a boundary-layer approximation and treated the rip as a turbulent jet within which convective inertia was strong. The presence of the *rip head*, that is, the sudden expansion and dissipation into a big stagnant patch, was attributed to the sudden change of bottom slope. LeBlond and Tang (1974) studied the wave-current interaction for rips. Dalrymple (1975) gave experimental evidence of rip currents near a straight beach when two wavetrains were incident symmetrically from opposite sides of the shore-normal. Liu and Lennon (1978) applied the finite-element method for numerical modelling of nearshore currents.

From the discussions in this chapter, it is evident that the idea of radiation stress has enabled us to study increasingly complex nearshore current problems with at least qualitative reliability. Formidable obstacles remain for a scientifically satisfactory understanding and quantitative modelling of the breaking waves. For progresses in surf-zone dynamics since the early days of the radiation stresses concept, the readers are referred to the expert surveys by Battjes (1988), and Svensen and Putrevu (1996).

This page intentionally left blank

Nonlinear Long Waves in Shallow Water

12

12.1 Derivation and Classification of Approximate Equations

As pointed out in Chapter One, the linearized shallow-water approximation is useful only if the following two length ratios are small:

$$\mu \equiv kh \ll 1 \quad \text{and} \quad \varepsilon \equiv \frac{A}{h} \ll 1\,. \tag{12.1.1}$$

The second restriction is a severe one for many coastal problems; therefore, a nonlinear theory of shallow water waves is needed. The presence of two small parameters (three length scales) introduces new subtleties into the procedure of approximation since the magnitude of one ratio relative to the other is now important. Historically, two different theories, one by Airy and the other by Boussinesq (1877), and Korteweg and de Vries (1895), were separately developed which led to opposite conclusions regarding wave breaking on constant depth. The confusion was resolved in a fundamental paper by Ursell (1953) and further clarified by Lin and Clark (1959). In particular, Ursell has shown that the ratio

$$U_r = \frac{A}{h}\frac{1}{(kh)^2} = \frac{kA}{(kh)^3} = \frac{A\lambda^2}{h^3(2\pi)^2} \tag{12.1.2}$$

plays a central role in deciding the choice of approximations which correspond to very different physics. This ratio has since been widely referred to as the Ursell parameter and will be denoted by U_r in this book, although it also appeared in the earlier theory of Stokes.

For simplicity we shall illustrate the approximation procedure for constant depth, using the formalism of Benney (1966) and Peregrine (1967). The extension to variable depth is left as an exercise.

Since there are now two small parameters, it is advantageous to use dimensionless variables for the sake of clarity. The scales of the variables are suggested by the linearized theory:

$$(x', y') = k(x, y)\,, \quad z' = \frac{z}{h}\,, \quad t' = k(gh)^{1/2}t$$

$$\zeta' = \tfrac{\zeta}{A}\,, \quad \Phi' = \Phi\left[\frac{A}{kh}(gh)^{1/2}\right]^{-1}. \tag{12.1.3}$$

Note that the implied normalizations on velocity components are

$$(u, v) = \left(\frac{\partial}{\partial x}, \frac{\partial}{\partial y}\right)\Phi = \frac{A}{h}(gh)^{1/2}\left(\frac{\partial}{\partial x'}, \frac{\partial}{\partial y'}\right)\Phi' = \frac{A}{h}(gh)^{1/2}(u', v')$$

$$w = \frac{\partial\Phi}{\partial z} = \frac{1}{kh}\frac{A}{h}(gh)^{1/2}\frac{\partial\Phi'}{\partial z'} = \frac{1}{kh}\frac{A}{h}(gh)^{1/2}(w')\,. \tag{12.1.4}$$

The difference in scaling for horizontal and vertical components is required by continuity. The normalized equations are

$$\mu^2(\Phi'_{x'x'} + \Phi'_{y'y'}) + \Phi'_{z'z'} = 0\,, \qquad -1 < z' < \varepsilon\zeta' \tag{12.1.5}$$

$$\mu^2[\zeta'_{t'} + \varepsilon\Phi'_{x'}\zeta'_{x'} + \varepsilon\Phi'_{y'}\zeta'_{y'}] = \Phi'_{z'}\,, \quad z' = \varepsilon\zeta' \tag{12.1.6}$$

$$\mu^2[\Phi'_{t'} + \zeta'] + \frac{1}{2}\varepsilon[\mu^2(\Phi'^2_{x'} + \Phi'^2_{y'}) + \Phi'^2_{z'}] = 0\,, \qquad z' = \varepsilon\zeta' \tag{12.1.7}$$

$$\Phi'_{z'} = 0\,, \qquad z = -1\,. \tag{12.1.8}$$

For convenience the primes will be dropped from here on. First, we only assume $\mu = kh$ to be small, leaving ε to be arbitrary for the time being. Since Φ is analytic, we may expand it as a power series in the vertical coordinate,

$$\Phi(x, y, z, t) = \sum_{n=0}^{\infty}(z+1)^n\Phi_n \tag{12.1.9}$$

where $\Phi_n = \Phi_n(x, y, t)$, $n = 0, 1, 2, 3, \ldots$, whose orders of magnitude are yet unknown. Using ∇ to denote the horizontal gradient $(\partial/\partial x, \partial/\partial y)$, we first evaluate the derivatives

$$\nabla\Phi = \sum_0^\infty (z+1)^n \nabla\Phi_n \,, \tag{12.1.10a}$$

$$\nabla^2\Phi = \sum_0^\infty (z+1)^n \nabla^2\Phi_n \,, \tag{12.1.10b}$$

$$\frac{\partial\Phi}{\partial z} = \sum_0^\infty (z+1)^{n-1}\Phi_n = \sum_0^\infty (z+1)^n (n+1)\Phi_{n+1} \,, \tag{12.1.10c}$$

$$\frac{\partial^2\Phi}{\partial z^2} = \sum_0^\infty (z+1)^{n-1}(n+1)n\Phi_{n+1} = \sum_0^\infty (z+1)^n (n+2)(n+1)\Phi_{n+2} \,. \tag{12.1.10d}$$

Substituting Eqs. (12.1.10b) and (12.1.10d) into the Laplace equation, we obtain

$$\mu^2\nabla^2\Phi + \frac{\partial^2}{\partial z^2}\Phi = \sum_{n=0}^\infty (z+1)^n [\mu^2\nabla^2\Phi_n + (n+2)(n+1)\Phi_{n+2}] = 0 \,. \tag{12.1.11}$$

Since z is arbitrary within $(-1, \varepsilon\zeta)$, the coefficient of each power of $(z+1)$ must vanish, which yields a recursive relation

$$\Phi_{n+2} = \frac{-\mu^2\nabla^2\Phi_n}{(n+2)(n+1)} \,, \quad n = 0, 1, 2, \ldots \,. \tag{12.1.12}$$

On the horizontal bottom Eq. (12.1.8) leads to

$$\Phi_1 \equiv 0$$

which implies from Eq. (12.1.12) that all Φ_n's with odd n vanish

$$\Phi_1 = \Phi_3 = \Phi_5 = \cdots 0 \,. \tag{12.1.13}$$

For even n, we have, specifically,

$$\begin{aligned} \Phi_2 &= \frac{-\mu^2}{2\cdot 1}\nabla^2\Phi_0 = \frac{-\mu^2}{2!}\nabla^2\Phi_0 \,, \\ \Phi_4 &= \frac{-\mu^2}{4\cdot 3}\nabla^2\Phi_2 = \frac{\mu^4}{4!}\nabla^2\nabla^2\Phi_0 \,, \\ \Phi_6 &= \frac{-\mu^2}{6\cdot 5}\nabla^2\Phi_4 = \frac{-\mu^6}{6!}\nabla^2\nabla^2\nabla^2\Phi_0 \,. \end{aligned} \tag{12.1.14}$$

Since $\Phi_0 = O(\phi) = O(1)$, it may be concluded that $\Phi_2 = O(\mu^2)$, $\Phi_4 = O(\mu^4)$, and so on. Thus, with an error of $O(\mu^6)$ the potential is

$$\Phi = \Phi_0 - \frac{\mu^2}{2}(z+1)^2\nabla^2\Phi_0 + \frac{\mu^4}{24}(z+1)^4\nabla^2\nabla^2\Phi_0 + O(\mu^6)\,. \qquad (12.1.15)$$

We must now make use of the boundary conditions on the free surface. Because of the multiplier μ^2 it is sufficient to keep $O(\mu^4)$ terms in Φ_t, Φ_x, and Φ_y.

$$\mu^2\left[\frac{H_t}{\varepsilon} + \nabla H\cdot\left(\nabla\Phi_0 - \frac{\mu^2}{2}H^2\nabla^2\nabla\Phi_0\right)\right]$$

$$= -\mu^2 H\nabla^2\Phi_0 + \frac{\mu^4}{6}H^3\nabla^2\nabla^2\Phi_0 + O(\mu^6)\,, \qquad (12.1.16)$$

$$\mu^2\left[\Phi_{0_t} - \frac{\mu^2}{2}H^2\nabla^2\Phi_{0_t} + \zeta\right] + \frac{1}{2}\varepsilon\mu^2[(\nabla\Phi_0)^2 - \mu^2H^2\nabla\Phi_0\cdot\nabla^2(\nabla\Phi_0)]$$

$$+ \frac{1}{2}\varepsilon\mu^4H^2(\nabla^2\Phi_0)^2 = O(\mu^6)\,, \qquad (12.1.17)$$

where

$$H = 1 + \varepsilon\zeta \qquad (12.1.18)$$

denotes the total depth. By defining

$$\mathbf{u}_0 = \nabla\Phi_0 \qquad (12.1.19)$$

as the horizontal velocity at the bottom, Eq. (12.1.16) may be written

$$\frac{1}{\varepsilon}H_t + \nabla H\cdot\left(\mathbf{u}_0 - \frac{\mu^2}{2}H^2\nabla^2\mathbf{u}_0\right)$$

$$+ H\nabla\cdot\mathbf{u}_0 - \frac{\mu^2}{6}H^3\nabla^2(\nabla\cdot\mathbf{u}_0) = O(\mu^4)\,. \qquad (12.1.20)$$

Taking the gradient of Eq. (12.1.17), we have

$$\mathbf{u}_{0_t} + \varepsilon\mathbf{u}_0\cdot\nabla\mathbf{u}_0 + \frac{\nabla H}{\varepsilon} + \mu^2\nabla$$

$$\times\left[-\frac{\varepsilon}{2}H^2\mathbf{u}_0\cdot\nabla^2\mathbf{u}_0 + \frac{\varepsilon}{2}H^2(\nabla\cdot\mathbf{u}_0)^2 - \frac{1}{2}H^2\nabla\cdot\mathbf{u}_{0_t}\right] = O(\mu^4)\,. \qquad (12.1.21)$$

Once ζ and $\mathbf{u}_0$ are solved, the actual velocity components are given by

$$(u, v) = \nabla\Phi = \mathbf{u}_0 - \frac{\mu^2}{2}(z+1)^2\nabla\nabla\cdot\mathbf{u}_0 + O(\mu^4)\,, \tag{12.1.22}$$

$$w = \frac{\partial\Phi}{\partial z} = -\mu^2(z+1)\nabla^2\Phi_0 = \mu^2(z+1)\nabla\cdot\mathbf{u}_0 + O(\mu^4)\,. \tag{12.1.23}$$

The pressure field may be obtained from Bernoulli's equation whose dimensionless form is, exactly,

$$-P = z + \varepsilon\left\{\Phi_t + \frac{\varepsilon}{2}\left[(\nabla\Phi)^2 + \frac{1}{\mu^2}\Phi_z^2\right]\right\}, \tag{12.1.24}$$

where P has been normalized by $\rho g h$. The approximate pressure field follows by substituting Eqs. (12.1.22) and (12.1.23) into Eq. (12.1.24):

$$\begin{aligned}-P = z + \varepsilon\Bigg\{&\left[\Phi_{0_t} - \frac{\mu^2}{2}(z+1)^2\nabla\cdot\mathbf{u}_{0_t}\right]\\ &+ \frac{\varepsilon}{2}[\mathbf{u}_0^2 - \mu^2(z+1)^2\mathbf{u}_0\cdot\nabla^2\mathbf{u}_0 + \mu^2(z+1)^2(\nabla\cdot\mathbf{u}_0)^2]\Bigg\} + O(\mu^4)\,.\end{aligned}$$

Equation (12.1.17) can be used to eliminate Φ_{0_t}, so that

$$\begin{aligned}P = (\varepsilon\zeta - z) &- \frac{\varepsilon\mu^2}{2}[H^2 - (z+1)^2]\\ &\times\{\nabla\cdot\mathbf{u}_{0_t} + \varepsilon[\mathbf{u}_0\cdot\nabla^2\mathbf{u}_0 - (\nabla\cdot\mathbf{u}_0)^2]\} + O(\mu^4)\,.\end{aligned} \tag{12.1.25}$$

Instead of $\mathbf{u}_0$ we may introduce the depth-averaged horizontal velocity $\bar{\mathbf{u}}$ defined by

$$\begin{aligned}\bar{\mathbf{u}} &= \frac{1}{H}\int_{-1}^{\varepsilon\zeta} dz\nabla\Phi\\ &= \frac{1}{H}\int_{-1}^{\varepsilon\zeta} dz\left(\mathbf{u}_0 - \frac{\mu^2}{2}(z+1)^2\nabla\nabla\cdot\mathbf{u}_0 + \cdots\right)\\ &= \mathbf{u}_0 - \frac{\mu^2}{6}H^2\nabla^2\mathbf{u}_0 + O(\mu^4)\,,\end{aligned} \tag{12.1.26}$$

which can be inverted to give

$$\mathbf{u}_0 = \bar{\mathbf{u}} + \frac{\mu^2}{6}H^2\nabla^2\bar{\mathbf{u}} + O(\mu^4)\,. \tag{12.1.27}$$

After Eq. (12.1.27) is substituted into Eq. (12.1.20), it follows at once that

$$H_t + \varepsilon \nabla \cdot (H\bar{\mathbf{u}}) = 0\,, \tag{12.1.28}$$

which is just the depth-averaged law of continuity and is, in fact, exact to all orders of (μ^2) [cf. Eq. (11.2.10), Chapter Eleven]. Expressing $\mathbf{u}_0$ in terms of $\bar{\mathbf{u}}$ to the stated accuracy, we have

$$\bar{\mathbf{u}}_t + \varepsilon \bar{\mathbf{u}} \cdot \nabla \bar{\mathbf{u}} + \frac{\nabla H}{\varepsilon} + \frac{\mu^2}{6}(H^2 \nabla^2 \bar{\mathbf{u}})_t + \mu^2 \nabla \left\{ -\frac{\varepsilon}{3} H^2 \bar{\mathbf{u}} \cdot \nabla^2 \bar{\mathbf{u}} + \frac{\varepsilon}{2} H^2 (\nabla \cdot \bar{\mathbf{u}})^2 - \frac{H^2}{2} \nabla \cdot \bar{\mathbf{u}}_t \right\} = O(\mu^4)\,. \tag{12.1.29}$$

It deserves emphasis that all the equations thus far are valid for arbitrary ε. Extension to higher orders in μ^2 is straightforward, although tedious.

Let us express Eqs. (12.1.28), (12.1.29), and (12.1.25) in physical variables

$$H_t + \nabla \cdot (H\bar{\mathbf{u}}) = 0\,, \tag{12.1.30}$$

$$\bar{\mathbf{u}}_t + \bar{\mathbf{u}} \cdot \nabla \bar{\mathbf{u}} + g \nabla H + \frac{1}{6}(H^2 \nabla^2 \bar{\mathbf{u}})_t + \nabla \left\{ -\frac{1}{3} H^2 \bar{\mathbf{u}} \cdot \nabla^2 \bar{\mathbf{u}} + \frac{H^2}{2} (\nabla \cdot \bar{\mathbf{u}})^2 - \frac{H^2}{2} \nabla \cdot \bar{\mathbf{u}}_t \right\} = 0\,, \tag{12.1.31}$$

and

$$P = \rho g(\zeta - z) - \frac{1}{2}[H^2 - (z+h)^2]\{\nabla \cdot \mathbf{u}_t + [\mathbf{u} \cdot \nabla^2 \mathbf{u} - (\nabla \cdot \mathbf{u})^2]\}\,. \tag{12.1.32}$$

We now turn to limiting cases.

Airy's Theory for Very Long Waves: $\boldsymbol{\rho \to 0, \varepsilon = O(1)}$

Airy's theory is the leading-order approximation for very long waves of finite amplitude. By omitting terms proportional to μ^2 from Eqs. (12.1.25) and (12.1.29), we get, in physical variables,

$$\zeta_t + \nabla \cdot [(\zeta + h)\bar{\mathbf{u}}] = 0\,, \tag{12.1.33}$$

$$\bar{\mathbf{u}}_t + \bar{\mathbf{u}} \cdot \nabla \bar{\mathbf{u}} + g \nabla \zeta = 0\,, \tag{12.1.34}$$

$$P = \rho g(\zeta - z)\,. \tag{12.1.35}$$

The preceding equations are actually valid for variable $h(x, y)$. A distinguishing feature of Airy's approximation is that the pressure is hydrostatic.

Boussinesq Theory: $O(\varepsilon) = O(\mu^2) < 1$

For weakly nonlinear and moderately long waves in shallow water, we approximate Eqs. (12.1.28), (12.1.29), and (12.1.25) to include terms of order $O(\varepsilon)$ and $O(\mu^2)$ only, obtaining

$$\zeta_t + \nabla \cdot [(\varepsilon\zeta + 1)\bar{\mathbf{u}}] = 0\,, \tag{12.1.36}$$

$$\bar{\mathbf{u}}_t + \varepsilon\bar{\mathbf{u}} \cdot \nabla\bar{\mathbf{u}} + \nabla\zeta - \frac{\mu^2}{3}\nabla\nabla \cdot \bar{\mathbf{u}}_t = 0\,, \tag{12.1.37}$$

$$P = \varepsilon\zeta - z + \frac{\varepsilon\mu^2}{2}(z^2 + 2z)\nabla \cdot \bar{\mathbf{u}}_t\,. \tag{12.1.38}$$

In physical variables, they are

$$\zeta_t + \nabla \cdot [(\zeta + h)\bar{\mathbf{u}}] = 0\,, \tag{12.1.39}$$

$$\bar{\mathbf{u}}_t + \bar{\mathbf{u}} \cdot \nabla\bar{\mathbf{u}} + g\nabla\zeta - \frac{h^2}{3}\nabla\nabla \cdot \bar{\mathbf{u}}_t = 0\,, \tag{12.1.40}$$

$$P = \rho g(\zeta - z) + \frac{\rho}{2}(2zh + z^2)\nabla \cdot \bar{\mathbf{u}}_t\,. \tag{12.1.41}$$

Equations (12.1.36) and (12.1.37), or, equivalently, Eqs. (12.1.39) and (12.1.40), are called the Boussinesq equations. Note that the pressure field is no longer hydrostatic. Formally, Airy's and Boussinesq's theories differ by the linear term multiplied by μ^2 in Eq. (12.1.37). To see the physical significance of this term, let us examine the linearized versions of Eqs. (12.1.39) and (12.1.40) for one-dimensional infinitesimal waves

$$\zeta = Ae^{i(kx-\omega t)}\,, \quad \bar{\mathbf{u}} = Ue^{i(kx-\omega t)}\,.$$

When the exponential factors are cancelled, we get

$$-i\omega A + ikhU = 0\,,$$

$$i\omega U + ikgA - \frac{h^2}{3} - (ik)^2(-i\omega)U = 0\,,$$

which is a homogeneous set of equations for A and U. For a nontrivial solution the discriminant must vanish, that is,

$$\begin{vmatrix} -i\omega & ikh \\ igk & -i\omega\left(1+\dfrac{k^2h^2}{3}\right) \end{vmatrix} = 0\,,$$

or

$$\omega^2 = \frac{ghk^2}{1+\frac{1}{3}k^2h^2} = ghk^2\left(1-\frac{k^2h^2}{3}+\cdots\right), \tag{12.1.42}$$

or

$$\text{phase velocity } C \cong (gh)^{1/2}\left(1-\frac{k^2h^2}{3}\right)^{-1/2}$$

$$\cong (gh)^{1/2}\left(1-\frac{k^2h^2}{3}\right)^{1/2}. \tag{12.1.43}$$

The term $\frac{1}{3}(kh)^2 = \frac{1}{3}\mu^2$ above arises from the term $(\frac{1}{3}h^2)u_{xxt}$ and represents frequency dispersion. Indeed, Eq. (12.1.42) is precisely the two-term expansion of the familiar dispersion relation for arbitrary depth, $\omega^2 = gk\tanh kh$.

In summary, Boussinesq equations account for the effects of nonlinearity ε and dispersion μ^2 to the leading order. When $\varepsilon \gg \mu^2$, they reduce to Airy equations which are valid for all ε; when $\varepsilon \ll \mu^2$, they reduce to the linearized approximation with weak dispersion. When $\varepsilon \to 0$ and $\mu^2 \to 0$, the classical linearized wave equation is obtained.

Variable Depth

If the horizontal scale of depth variation is no greater than the typical wavelength, the procedure beginning from Eq. (12.1.9) may be extended. Now the bottom boundary condition is, in physical variables,

$$\Phi_z = -h_x\Phi_x - h_y\Phi_y\,, \quad z = -h(x,y)\,, \tag{12.1.44}$$

or in dimensionless variables,

$$\Phi_z = -\mu^2(h_x\Phi_x + h_y\Phi_y)\,, \quad z = -h(x,y)\,, \tag{12.1.45}$$

where the variable depth is normalized by the typical depth h_0, which is also used in defining the dimensionless variables of Eqs. (12.1.3) and (12.1.4). Instead of Eq. (12.1.9), one may assume

$$\Phi = \sum_{n=0}^{\infty}[z+h(x,y)]^n\Phi_n(x,y)\,. \tag{12.1.46}$$

By substituting Eq. (12.1.46) into Laplace's equation and applying Eq. (12.1.45), we obtain a set of recursive relations among Φ_n. In particular, Φ_n's for odd n no longer vanish. Following arguments similar to those given here, Mei and LeMèhautè (1966, with corrections by Madsen (see Madsen and Mei, 1969)) obtained the Boussinesq equations for one-dimensional waves. For two dimensions the following equations were deduced by Peregrine (1967) in terms of $\bar{u}$ and ζ:

$$\zeta_t + \nabla \cdot [(h+\zeta)\bar{\mathbf{u}}] = 0\,, \tag{12.1.47}$$

$$\frac{\partial \bar{\mathbf{u}}}{\partial t} + \bar{\mathbf{u}} \cdot \nabla \bar{\mathbf{u}} + g\nabla\zeta = \frac{h}{2}\nabla[\nabla \cdot (h\bar{\mathbf{u}}_t)] - \frac{h^2}{6}\nabla[\nabla \cdot \bar{\mathbf{u}}_t]\,. \tag{12.1.48}$$

The algebra involved is straightforward but lengthy and may be left to the reader.

In recent years there have been many extensions of Boussinesq approximtions to higher orders in order to account for steeper waves and greater depth, i.e., larger ϵ and μ^2. water. In this book, we shall restrict our discussions to analytical aspects within the accuracy presented in the preceding sections. For advances on the higher-order theories and the associated computational schemes, readers may wish to consult Madsen an Schäffer (1998), Madsen, Bingham and Liu (2002), Madsen and Agnon (2003), Masden Bingham, and Schäffer (2003), and Fuhrman, Madsen and Bingham (2004).

Exercise 12.1

Derive from Eqs. (12.1.5)–(12.1.7) and (12.1.45) the following alternative approximate equation for varying depth by keeping terms up to $O(\varepsilon^2)$ and $O(\mu^2)$ for $\varepsilon = O(\mu)$:

$$g\nabla \cdot (h\nabla\phi_0) - \phi_{0_{tt}} = \frac{1}{2}(\nabla\phi_0)_t^2 + \nabla \cdot (\phi_{0_t}\nabla\phi_0) + \frac{1}{2}\nabla \cdot \left[\nabla\phi_0(\nabla\phi_0)^2\right] + g\nabla \cdot \left(\frac{h^3}{6}\nabla\nabla^2\phi_0 - \frac{h^2}{2g}\nabla\phi_{0_{tt}}\right), \tag{12.1.49}$$

where $\phi_0(x, y, t)$ is the velocity potential at $z = 0$. In dimensionless form, the error is of the order $O(\varepsilon\mu^2, \mu^4)$ relative to the leading terms kept in Eq. (12.1.40). Begin by letting

$$\Phi = \sum_{n=0} \frac{z^n}{n!}\phi_0(x, y, t)\,.$$

12.2 Nondispersive Waves in Water of Constant Depth

12.2.1 Analogy to Gas Dynamics

When $(A/h)(kh)^{-2} \gg 1$, the approximate equations given by Eqs. (12.1.33) and (12.1.34) are analogous to those governing two-dimensional gas dynamics in an isentropic flow (Riabouchinsky, 1932). Let

$$\hat{\rho} = (\zeta + h) \tag{12.2.1}$$

denote the density of a fictitious compressible fluid. The continuity equation becomes

$$\frac{\partial \hat{\rho}}{\partial t} + \nabla \cdot (\hat{\rho}\bar{\mathbf{u}}) = 0\,. \tag{12.2.2}$$

Defining a fictitious pressure by

$$\hat{p} = \frac{g}{2}(\zeta + h)^2 = \frac{g}{2}\hat{\rho}^2\,, \tag{12.2.3}$$

and using Eq. (12.2.1), we may rewrite the momentum equation in the form

$$\hat{\rho}\left[\frac{\partial \bar{\mathbf{u}}}{\partial t} + \bar{\mathbf{u}} \cdot \nabla \bar{\mathbf{u}}\right] = -\nabla \hat{p}\,. \tag{12.2.4}$$

Equations (12.2.2) and (12.2.4) are just the continuity and momentum equations for a compressible fluid, while Eq. (12.2.3) is the equation of state for an isentropic flow of a perfect gas. In general, the equation of state for a calorically perfect gas is

$$\frac{p}{p_0} = \left(\frac{\rho}{\rho_0}\right)^{C_p/C_v} \exp\left[\frac{C_p(s - s_0)}{C_v(C_p - C_v)}\right], \tag{12.2.5}$$

where s is the entropy and p_0, ρ_0, and s_0 are the reference values of p, ρ, and s, respectively. C_p and C_v are specific heats under constant pressure and constant volume, respectively. Thus, Eq. (12.2.3) corresponds to a gas with $C_p/C_v = 2$, which does not exist in reality.

Because of this analogy, knowledge and methods established in gas dynamics can be transferred directly to long water waves. This aspect is most thoroughly exploited in Stoker (1957) on which much of the present section is based. It must be emphasized that while Eqs. (12.2.2) and (12.2.4) are exact in gas dynamics, they are only approximate in water waves when the horizontal scale of motion is much larger than the vertical

scale. In particular, while the gas-dynamic theory succeeds in predicting shock formation, Airy's theory is basically unsuitable for predicting bore formation, a problem of enormous importance for which the full solution is not yet forthcoming. Therefore, care must be exercised in interpreting the results of Airy's theory.

12.2.2 Method of Characteristics for One-Dimensional Problems

As in one-dimensional gas dynamics, the *method of characteristics* is a very useful tool in Airy's shallow-water wave theory. The salient features of this method will be outlined only to the extent needed. A full account of the general method is available in Courant and Friedrichs (1949), Courant and Hilbert (1962), and Stoker (1957), among others.

With the overbars omitted for brevity, Eqs. (12.1.33) and (12.1.34) become

$$\frac{\partial \zeta}{\partial t} + \frac{\partial}{\partial x}[(h+\zeta)u] = 0\,, \tag{12.2.6}$$

$$\frac{\partial \zeta}{\partial t} + u\frac{\partial u}{\partial x} + g\frac{\partial \zeta}{\partial x} = 0\,. \tag{12.2.7}$$

Let us rearrange the governing equations by introducing

$$C^2 = g(\zeta + h)\,. \tag{12.2.8}$$

The continuity and momentum equations may be written

$$2C_t + 2uC_x + Cu_x = 0\,, \tag{12.2.9}$$

$$u_t + 2CC_x + uu_x = 0\,. \tag{12.2.10}$$

By adding and subtracting the two equations above, we get

$$\left[\frac{\partial}{\partial t} + (u+C)\frac{\partial}{\partial x}\right][u+2C] = 0\,. \tag{12.2.11}$$

$$\left[\frac{\partial}{\partial t} + (u-C)\frac{\partial}{\partial x}\right][u-2C] = 0\,. \tag{12.2.12}$$

Equations (12.2.11) and (12.2.12) describe the total rate of change of $u \pm 2C$ along the curves which are governed by

$$\frac{dx}{dt} = u \pm C\,. \tag{12.2.13}$$

These curves are called the *characteristics*. The solutions to $dx/dt = u + C$ are a one-parameter family of curves which we shall call C_+ characteristics, the parameter being the initial position of a curve at a given time t_0. Similarly, the solutions to $dx/dt = u - C$ are also a one-parameter family of curves, to be called C_- characteristics. A set of partial differential equations possessing real characteristics are said to be *hyperbolic*. Because the right-hand sides are zero, Eqs. (12.2.11) and (12.2.12) may be integrated to give

$$\begin{aligned} &u + 2C = \text{const} \quad \text{along } C_+\,, \\ &u - 2C = \text{const} \quad \text{along } C_-\,. \end{aligned} \tag{12.2.14}$$

The quantities $u \pm 2C$ are called the *Riemann invariants*.

Let us explain how a typical initial-value problem can be solved in principle. Consider the example where $u(x,0) = F(x)$ and $C(x,0) = G(x)$ are given for $t = 0$, all x. The Riemann invariants are

$$\begin{aligned} &\text{along } C_+ : \quad \frac{dx}{dt} = u + C\,, \quad u + 2C = F(x) + 2G(x) = R_+(x)\,; \\ &\text{along } C_- : \quad \frac{dx}{dt} = u - C\,, \quad u - 2C = F(x) - 2G(x) = R_-(x)\,. \end{aligned} \tag{12.2.15}$$

Consider the x-t diagram (Fig. 12.1). Divide the x axis into small intervals by grid points $x = x_1^0, \ldots, x_i^0, \ldots$; from the initial values $u(x_i^0, 0)$ and $C(x_i^0, 0)$ we calculate the initial stretch of the characteristics

$$\begin{aligned} C_+ : &\quad x = x_i^0 + [u(x_i^0,0) + C(x_i^0,0)]t\,, \\ C_- : &\quad x = x_i^0 + [u(x_i^0,0) - C(x_i^0,0)]t\,. \end{aligned} \tag{12.2.16}$$

Consider a C_+ curve starting from x_i^0 and a C_- curve starting from a neighboring grid point x_{i+1}^0. Their intersecting point x_i^1, t_i^1 is found by solving the simultaneous equations

$$\begin{aligned} x_i^1 &= x_i^0 + [u(x_i^0,0) + C(x_i^0,0)]t_i^1\,, && C_+\,, \\ x_i^1 &= x_{i+1}^0 + [u(x_{i+1}^0,0) + C(x_{i+1}^0,0)]t_i^1\,, && C_-\,. \end{aligned} \tag{12.2.17}$$

Let us denote the intersecting point by $P_i^1 = (x_i^1, t_i^1)$. From all such neighboring points a row of new points $P_i^1(x_i^1, t_i^1)$, $i = 1, 2, \ldots$, is obtained. Now

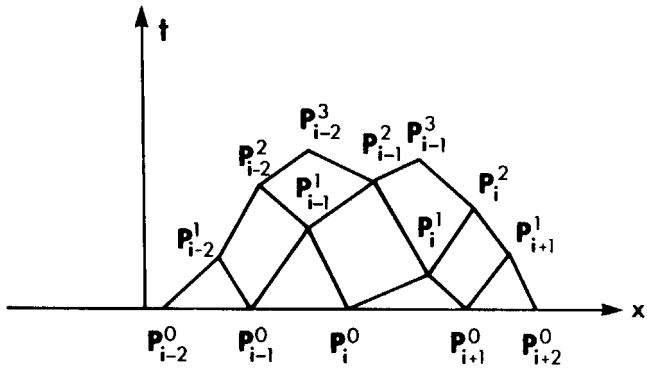

Figure 12.1: x-t diagram.

because P_i^1 is on the C_+ characteristic which is originated at $P_i^0(x_i^0, 0)$, we have

$$u(P_i^1) + 2C(P_i^1) = u(P_i^0) + 2C(P_i^0)\,. \tag{12.2.18}$$

Because P_i^1 is also on the C_- characteristic originated at $P_{i+1}^0(x_{i+1}^0, 0)$, we have

$$u(P_i^1) - 2C(P_i^1) = u(P_{i+1}^0) - 2C(P_{i+1}^0)\,. \tag{12.2.19}$$

Equations (12.2.18) and (12.2.19) can now be solved for $u(P_i^1)$ and $C(P_i^1)$. After obtaining the solution for all $i = 1, 2, 3, \ldots$ we have marched forward in time, although t_i^1 are in general not equal for all i. The points P_i^1 then form a new initial line from which the characteristics C_+ and C_- can be extended, and the solution procedure for u and C repeated, and so on. In this way a network of characteristic curves and the solution at each grid point are found.

Through each point P passes a pair of characteristics C_+ and C_-. From the procedure just described it is clear that the solution at P depends only on the initial data between these two characteristics. As shown in Fig. 12.2, the triangular region, bounded by the initial curve and the two passing characteristics $C_\pm$, is called the *domain of dependence*. On the other hand, the initial data at point P_i^0 are felt by every later point in the sector bounded by the two characteristics $C_\pm$ initiated from P_i^0. This sector is called the *range of influence*.

Instead of an initial-value problem, consider an initial-boundary-value problem for the quadrant $x > 0$, $t > 0$; Fig. 12.3. Let the two characteristics

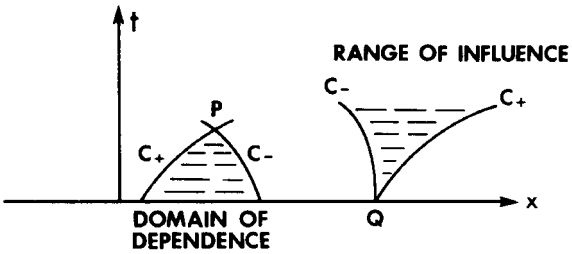

Figure 12.2

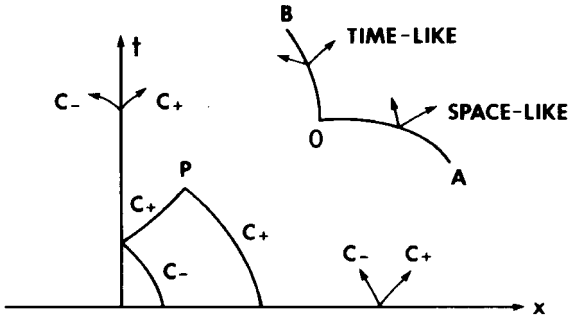

Figure 2.3

$C_\pm$ emanating from the t axis point to the opposite sides of the t axis. Then only one boundary condition is needed on the t axis because the two unknowns u and C at any interior point P are uniquely determined by the two equations (Riemann invariants) along the two intersecting characteristics. For example, one may prescribe $u(0,t)$, while $C(0,t)$ must be compatible to the value determinable from the Riemann invariant along C_- going back to the x axis. In general, the initial curve can be anything in the x-t plane. If a section of the initial curve, say AO, is such that at every point both C_+ and C_- point into the region of interest as t increases, the curve AO is called *space-like*, and two initial conditions are needed. If a section OB is such that at every point only one (C_+ or C_-) points into the region of interest, then this section is called *time-like* and one boundary condition is required.

In principle, integration of the characteristics equations may be carried out graphically or numerically; the unknowns as well as the characteristics are found in the course of solution. In more general hyperbolic problems the characteristics equations corresponding to Eqs. (12.2.11) and (12.2.12)

are inhomogeneous with the right-hand side depending on x, t, u, and C. There are no Riemann invariants and integration must be carried out numerically. Nevertheless, the partial differential equations are reduced to ordinary differential equations by means of characteristics.

In practice, the method of finite differences is a more convenient alternative. The basic aspects are amply described in Stoker (1957), while further extensions and improvements are a well-developed part of computational hydraulics. Interested readers should consult Abbott (1979) and current literature in hydraulics for further details. In the following subsections only analytic examples will be treated to explore the physical implications of nonlinearity.

12.2.3 Simple Waves and Constant States

As in gas dynamics, some useful concepts may be built on the basis of the following important theorem (Courant and Friedrichs, 1949):

> *If one of the C_+ (or C_-) characteristics is straight, then all other C_+ (or C_-) characteristics in the neighborhood must also be straight.*

Consider two points A and B along the known straight characteristic C_+. From the Riemann invariant along C_+ it follows that

$$u(A) + 2C(A) = u(B) + 2C(B)\,. \tag{12.2.20}$$

Since C_+ is straight, the following is true:

$$u(A) + C(A) = u(B) + C(B)\,. \tag{12.2.21}$$

After subtracting Eq. (12.2.21) from Eq. (12.2.20), we see that

$$C(A) = C(B)\,, \tag{12.2.22}$$

which implies

$$u(A) = u(B)\,. \tag{12.2.23}$$

Thus, along a straight characteristic C_+, u and C are constants. Conversely, if u and C are constants along C_+, then C_+ is straight. Now let C'_+ be a neighboring characteristic of the C_+ family and C_- and C'_- be two characteristics of the C_- family. The intersecting points A, B, C, and D

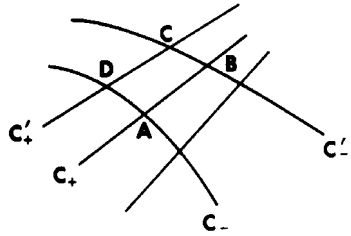

Figure 12.4

are shown in Fig. 12.4. Using the Riemann invariants along C'_+, C_-, and C'_-, respectively, we have

$$u(C) + 2C(C) = u(D) + 2C(D)\,, \tag{12.2.24}$$

$$u(D) + 2C(D) = u(A) + 2C(A)\,, \tag{12.2.25}$$

$$u(C) + 2C(C) = u(B) + 2C(B)\,. \tag{12.2.26}$$

Because of Eqs. (12.2.22) and (12.2.23) the last two equations give

$$u(C) - 2C(C) = u(D) - 2C(D)\,. \tag{12.2.27}$$

It is evident from Eqs. (12.2.24) and (12.2.27) that

$$u(C) = u(D)\,, \quad C(C) = C(D)\,. \tag{12.2.28}$$

Thus, C'_+ is also straight, and the theorem is proved.

A region R in the x, t diagram is called a *simple wave* zone if all characteristics of one family are straight. Note that the straight characteristics are not necessarily parallel; the constant values of u and C are different along different characteristics. A special case of the simple wave is called the *constant state* where u and C are the same constants throughout. Both families of C_+ and C_- are then straight and parallel. It is clear that adjacent to a constant state there must be a simple wave.

Let us use these notions to study an initial-boundary-value problem.

12.2.4 Expansion and Compression Waves — Tendency of Breaking

In a linearized theory, the disturbances due to an initial depression on the free surface and to an initial elevation of the same shape are essentially the

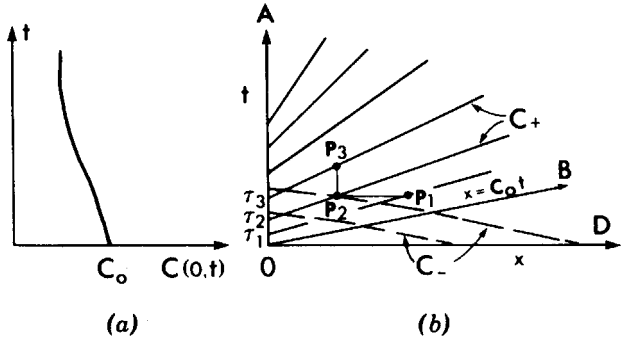

Figure 12.5: Expansion waves.

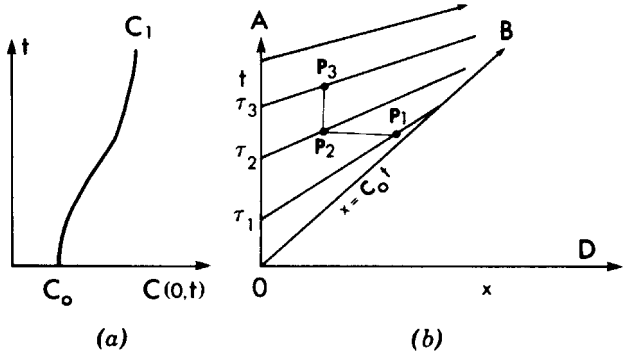

Figure 12.6: Compression waves.

same except for a change of sign. The situation is quite different in a nonlinear problem. As an illustration, consider $\zeta(0,t)$ and hence $C(0,t)$ to be prescribed at the end ($x = 0$) of a long channel ($x > 0$). Figures 12.5(a) and 12.6(a) show $C(0,t)$ as a decreasing and increasing function of t, respectively. As shown in Figs. 12.5(b) and 12.6(b), there is always an undisturbed zone DOB where

$$u = 0\,, \quad C = C_0 = (gh)^{1/2} \tag{12.2.29}$$

which is a constant state.

Being next to a constant state, the sector BOA must be a simple wave where C_+ characteristics are straight. By using the Riemann invariant along a C_- which crosses the t axis at a given instant t, we get

$$u(0,t) - 2C(0,t) = 0 - 2C_0\,. \tag{12.2.30}$$

Therefore, the velocity at the channel estuary is not arbitrary but is given by

$$u(0,t) = 2C(0,t) - 2C_0\,. \tag{12.2.31}$$

Alternatively, one may prescribe $u(0,t)$; $C(0,t)$ is then implied by Eq. (12.2.31). Moreover, any C_+ intersecting the t axis at $t = \tau$ has the slope

$$\frac{dx}{dt} = u(0,\tau) = C(0,\tau) = 3C(0,\tau) - 2C_0\,. \tag{12.2.32}$$

From the Riemann invariant along a C_+ characteristic,

$$u + 2C = u(0,\tau) + 2C(0,\tau) = 4C(0,\tau) - 2C_0\,,$$

whereas from the Riemann invariant along a C_- characteristic,

$$u - 2C = -2C_0\,.$$

At the intersection point $P(x,t)$ of these two curves, we must have

$$C(x,t) = C(0,\tau) \tag{12.2.33a}$$

and

$$u(x,t) = 2[C(0,\tau) - C_0]\,. \tag{12.2.33b}$$

If $C(0,\tau)$ is a decreasing function of time, then the C_+ characteristics in zone AOB spread out as a fan. Referring to Fig. 12.5(b), we compare $P_2(x,t_2)$ with two other points $P_1(x_1,t_2)$ and $P_3(x,t_3)$ with $x_1 > x$ and $t_3 > t_2$. It follows from Eq. (12.2.33a) that

$$C(P_3) - C(P_2) = C(0,\tau_3) - C(0,\tau_2) < 0\,,$$

$$C(P_2) - C(P_1) = C(0,\tau_2) - C(0,\tau_1) < 0\,.$$

Hence, the free-surface height increases with x for a fixed time. This physical situation is called an expansion wave.

Next, if $C(0,t)$ is an increasing function of time, then the neighboring C_+ characteristics in zone AOB tend to intersect. Referring to Fig. 12.6(b), we compare $P_2(x,t_2)$ with two other points $P_1(x_1,t_2)$ and $P_3(x,t_3)$, with $x_1 > x$ and $t_3 > t_2$ before the intersection occurs. From Eq. (12.2.33a) we have

$$C(P_3) > C(P_2) > C(P_1)$$

instead. Thus, the free-surface height increases with time at a fixed x and decreases with x at a given t. As the two neighboring C_+ curves approach the intersection, the free-surface height becomes steeper. At the first moment of such an intersection, the free surface becomes locally vertical, and the wave profile *breaks*.

The preceding deduction on breaking requires that the free-surface slope be so large as to be incompatible with the basic assumption of Airy's theory, that is, $kA \sim \partial A/\partial x \ll 1$. Therefore, the implications near and after initial breaking cannot be reliable quantitatively. There are also cases where even the qualitative predictions are of doubtful validity. Consider, for example, the disturbance generated in a long wave tank by first pushing the wavemaker for a finite distance and then stopping it. The velocity $u(0,t)$ must increase from zero to a maximum and decrease to zero after a finite duration. From Eq. (12.2.31), $C(0,t)$ first increases from and then decreases to C_0. The C_+ characteristics emanating from the t axis must first lean toward and then away from their neighbors. After the wavemaker stops, a hump of finite length propagates on the free surface toward $x \sim \infty$. The front of the hump is a compression wave tending to steepen, while the lee is an expansion wave tending to flatten. According to Airy's approximation, an initial hump of finite amplitude would always break at the front. By a similar reasoning, waves generated by an oscillating flap started from rest would break near the front of every wave crest. These conclusions are, however, not always observed in experiments. Indeed, there is a considerable range of ε and μ where an initial hump or periodically driven waves does not break at all. Theoretically, the increase of free-surface slope implies that higher horizontal gradients, corresponding to frequency dispersion which is neglected in Airy's theory, become more and more important. Because of the large gradient near a breaking crest, a valid theory must be able to account for derivatives of all orders and full nonlinearity, which implies that the full equation must be solved exactly, at least locally. More research is needed in this difficult area.

While inadequate for the prediction of initial breaking, Airy's theory has relevance, however, to the events after breaking. Specifically, the propagation of a bore can be treated as a discontinuous (shock) solution within the framework of Airy's theory. A good example is the classical theory of hydraulic jumps in open channels. For a horizontal bottom, theories on bore propagation are thoroughly discussed in Stoker (1948).

12.3 Nonbreaking Waves on a Slope

For tsunamis with very long periods, the wave slope is so small that wave breaking is not important, that is, the shore is highly reflective. Of engineering interest is the quantity called *run-up*, that is, the maximum landward excursion of the shoreline. Since the water depth at the shoreline is zero, a nonlinear theory is needed. Airy's approximation, being valid for arbitrary A/h, is clearly the proper one to use.

Let us begin with Eqs. (12.1.47) and (12.1.48) without the dispersion terms and the overhead symbol ($\bar{}$):

$$\frac{\partial \zeta}{\partial t} + \frac{\partial}{\partial x}[u(h(x) + \zeta)] = 0\,, \tag{12.3.1}$$

$$\frac{\partial u}{\partial t} + u\frac{\partial u}{\partial x} + g\frac{\partial \zeta}{\partial x} = 0\,, \tag{12.3.2}$$

which may be rewritten

$$(\zeta + h)_t + [u(\zeta + h)]_x = 0\,, \tag{12.3.3}$$

$$u_t + uu_x + g(\zeta + h)_x = gh_x\,. \tag{12.3.4}$$

With the definition

$$C^2 = g(\zeta + h)\,, \tag{12.3.5}$$

Eqs. (12.3.3) and (12.3.4) may be further written

$$2C_t + 2uC_x + Cu_x = 0\,, \tag{12.3.6}$$

$$u_t + uu_x + 2CC_x = gh_x\,. \tag{12.3.7}$$

By adding and subtracting Eqs. (12.3.6) and (12.3.7), we arrive at a pair of characteristics equations:

$$\left[\frac{\partial}{\partial t} + (u \pm C)\frac{\partial}{\partial x}\right][u \pm 2C] = gh_x\,. \tag{12.3.8}$$

In general, Eq. (12.3.8) cannot be integrated to give Riemann invariants unless h_x is constant. For simplicity it is assumed from here on that

$$h = sx\,, \tag{12.3.9}$$

and that the sea is to the right of the slope. The Riemann invariants are

$$u + 2C - mt = \alpha \quad \text{along} \quad C_+ : \quad \frac{dx}{dt} = u + C\,, \tag{12.3.10}$$

and

$$u - 2C - mt = \beta \quad \text{along} \quad C_- : \quad \frac{dx}{dt} = u - C\,, \tag{12.3.11}$$

where $m = sg$. Since the values of α or β are different along different C_+ or C_- characteristics, the x, t plane may be covered with a new set of coordinate curves $\alpha = \text{const}$ and $\beta = \text{const}$. This suggests transforming the independent coordinates from x, t to α, β. Along a particular C_+ characteristic, only β is varying; hence the differential equation for C_+ may be written

$$x_\beta - (u + C)t_\beta = 0\,. \tag{12.3.12}$$

Likewise, the differential equation for C_- is

$$x_\alpha - (u - C)t_\alpha = 0\,. \tag{12.3.13}$$

Now Eqs. (12.3.12) and (12.3.13) are a set of partial differential equations for the dependent variables x and t as functions α and β. Since u and C are linearly related to the new independent variables α and β, these new equations are linear. Let us further introduce (λ, σ) as independent variables:

$$\frac{\lambda}{2} = \frac{\alpha + \beta}{2} = u - mt\,, \tag{12.3.14}$$

$$\frac{\sigma}{4} = \frac{\alpha - \beta}{4} = C\,, \tag{12.3.15}$$

so that

$$\frac{\partial}{\partial \alpha} = \frac{\partial \lambda}{\partial \alpha}\frac{\partial}{\partial \lambda} + \frac{\partial \sigma}{\partial \alpha}\frac{\partial}{\partial \sigma} = \frac{\partial}{\partial \lambda} + \frac{\partial}{\partial \sigma}\,,$$

$$\frac{\partial}{\partial \beta} = \frac{\partial \lambda}{\partial \beta}\frac{\partial}{\partial \lambda} + \frac{\partial \sigma}{\partial \beta}\frac{\partial}{\partial \sigma} = \frac{\partial}{\partial \lambda} + \frac{\partial}{\partial \sigma}\,.$$

The equations for the characteristic curves become

$$-x_\lambda + x_\sigma - u(-t_\lambda + t_\sigma) - C(-t_\lambda + t_\sigma) = 0\,,$$

$$x_\lambda + x_\sigma - u(t_\lambda + t_\sigma) + C(t_\lambda + t_\sigma) = 0\,,$$

which may be added and subtracted to give

$$x_\sigma - ut_\sigma + Ct_\lambda = 0\,, \tag{12.3.16}$$

$$x_\lambda - ut_\lambda + Ct_\sigma = 0\,. \tag{12.3.17}$$

By cross-differentiation a single linear partial differential equation is obtained,

$$\sigma(t_{\lambda\lambda} - t_{\sigma\sigma}) - 3t_\sigma = 0 \tag{12.3.18}$$

(Stoker, 1948).

Carrier and Greenspan (1957) chose to use an auxiliary dependent variable ψ, as follows: With the help of Eqs. (12.3.14) and (12.3.15), t and C may be eliminated from Eq. (12.3.16) to yield

$$x_\sigma + \frac{u}{m}\left(\frac{\lambda}{2} - u\right)_\sigma - \frac{\sigma}{4m}\left(\frac{\lambda}{2} - u\right)_\lambda = 0\,,$$

which may be written

$$\left(x - \frac{u^2}{2m} - \frac{\sigma^2}{16m}\right)_\sigma + \frac{\sigma}{4m}u_\lambda = 0\,. \tag{12.3.19}$$

Similarly, Eq. (12.3.17) may be written

$$\left(x - \frac{u^2}{2m}\right)_\lambda + \frac{u}{2m} + \frac{\sigma u_\sigma}{4m} = 0\,. \tag{12.3.20}$$

Equation (12.3.19) suggests the introduction of a "stream function" ψ such that

$$\frac{-u}{m} = \frac{\psi_\sigma}{\sigma}\,, \tag{12.3.21}$$

$$x - \frac{u^2}{2m} - \frac{\sigma^2}{16m} = \frac{\psi_\lambda}{4}\,. \tag{12.3.22}$$

When the above substitutions are made into Eq. (12.3.20), a single equation for ψ is obtained

$$(\sigma\psi_\sigma)_\sigma - \sigma\psi_{\lambda\lambda} = 0\,, \tag{12.3.23}$$

which is equivalent to Eq. (12.3.18). Once ψ is found, u, C, x, and t are found, respectively, from Eqs. (12.3.21), (12.3.15), (12.3.22), and (12.3.14) in terms of the parameters λ and σ, which may be eliminated to give $u(x,t)$

and $C(x,t)$. The free-surface displacement is found from Eqs. (12.3.5), (12.3.19) and (12.3.15) to be:

$$\zeta = -s\left(x - \frac{\sigma^2}{16m}\right) = -s\left(\frac{u^2}{2m} + \frac{\psi_\lambda}{4}\right) \tag{12.3.24}$$

after Eq. (12.3.22) is taken into account.

It is useful to attach some physical significance to the new variables σ and λ. By definition, $\frac{1}{16}\sigma^2 = C^2 = g(\zeta + h)$ is proportional to the total depth, the instantaneous shoreline being at $\sigma = 0$. In the limit of deep water u becomes much less than C; it follows from Eq. (12.3.14) that $t \sim -\lambda/2m$ so that λ is closely related to time.

Because of the simplicity of Eq. (12.3.23), analytical solutions may be sought for some convenient initial and/or boundary conditions on ψ. The corresponding physical problem and solution are then found by inverse transformation. A simple example is discussed below.

12.3.1 Standing Waves of Finite Amplitude

Let us study a simple solution of the type

$$\psi = f(\sigma)\cos\left(\frac{\omega\lambda}{2m}\right). \tag{12.3.25}$$

The coefficient has been chosen so that ω represents frequency. Substituting Eq. (12.3.25) into Eq. (12.3.23), we get

$$\sigma^2 f'' + \sigma f' + \left(\frac{\omega}{2m}\right)\sigma^2 f = 0\,. \tag{12.3.26}$$

A solution which is finite at $\sigma = 0$ is $J_0((\omega/2m)\sigma)$; thus,

$$\psi = \frac{8g}{\omega} A J_0\left(\frac{\omega}{2m}\sigma\right)\cos\left(\frac{\omega}{2m}\lambda\right). \tag{12.3.27}$$

At large distances

$$\sigma = 4X \cong 4(gh)^{1/2} = 4(gsx)^{1/2}\,, \quad x > 0\,,$$

$$\lambda \sim -2mt\,,$$

so that

$$\psi \simeq \frac{8g}{\omega} A J_0\left(2\omega\left(\frac{x}{sg}\right)^{1/2}\right)\cos\omega t\,. \tag{12.3.28}$$

It is easily shown that Eq. (12.3.28) is just the standing-wave solution to the linearized equations

$$\frac{\partial \zeta}{\partial t} + \frac{\partial}{\partial x}(sxu) = 0\,,$$

$$\frac{\partial u}{\partial t} + g\frac{\partial \zeta}{\partial x} = 0\,. \tag{12.3.29}$$

The corresponding free surface is

$$\zeta_{\text{linear}} = -AJ_0\left(2\omega\left(\frac{x}{sg}\right)^{1/2}\right)\sin\omega t\,. \tag{12.3.30}$$

In Eq. (12.3.27), ψ is clearly a single-valued function of λ and σ. Is it also a single-valued function of x and t? In the theory of implicit functions it is well known that the mapping between (x,t) and (λ,σ) is not one-to-one only when the Jacobian

$$J = \frac{\partial(x,t)}{\partial(\sigma,\lambda)} = \begin{vmatrix} x_\sigma & t_\sigma \\ x_\lambda & t_\lambda \end{vmatrix} \tag{12.3.31}$$

vanishes at some λ and σ. Since $\partial C/\partial x$, which is proportional to the surface slope, is also given by

$$\frac{\partial C}{\partial x} = \frac{\begin{vmatrix} C_\sigma & t_\sigma \\ C_\lambda & t_\lambda \end{vmatrix}}{J}\,,$$

the vanishing of J implies a vertical free surface, hence breaking. To gain some qualitative insight on the inception of breaking, we calculate J from Eq. (12.3.17),

$$\begin{aligned} J &= (ut_\sigma - Ct_\lambda)t_\lambda - (ut_\lambda - Ct_\sigma)t_\sigma\,, \\ &= C(t_\sigma^2 - t_\lambda^2)\,. \end{aligned}$$

Since

$$t_\sigma = \frac{1}{m}u_\sigma = -\left(\frac{\psi_\sigma}{\sigma}\right)_\sigma\,,$$

$$t_\lambda = \frac{u_\lambda}{m} - \frac{1}{2m} = -\frac{\psi_{\sigma\lambda}}{\sigma} - \frac{1}{2m}\,,$$

from Eq. (12.3.14), the vanishing of J implies

$$\pm\left(\frac{\psi_\sigma}{\sigma}\right)_\sigma + \left(\frac{\psi_{\sigma\lambda}}{\sigma} + \frac{1}{2m}\right) = 0\,. \tag{12.3.32}$$

The derivatives involved above can be found from Eq. (12.3.27). With the abbreviations $(\omega/2s)\sigma = \sigma'$ and $\omega\lambda/2s = \lambda'$, condition (12.3.32) becomes, after some algebra,

$$-\frac{8gA}{\omega}\left(\frac{\omega}{2m}\right)^3 m\{\pm[-(\sigma' J_0(\sigma) - 2J_1(\sigma'))\cos\lambda'] + \sigma' J_1(\sigma')\sin\lambda'\} = \frac{1}{2}\sigma'^2\,. \tag{12.3.33}$$

For a fixed λ, the curly bracket on the left first increases with σ', then oscillates with diminishing amplitude about a mean which grows as $(\sigma')^{1/2}$, while the right-hand side increases as σ'^2. If the left-hand side is less than the right for small σ', then it remains so for all σ'. Since for small σ'

$$[-\sigma' J_0(\sigma') - 2J_1(\sigma')] \cong \frac{\sigma'^3}{8} + O(\sigma'^5)\,,$$

$$\sigma' J_1(\sigma') = \frac{\sigma'^2}{2} + O(\sigma'^4)\,,$$

the left-hand side of Eq. (12.3.33) is approximately

$$4gA\left(\frac{\omega}{2m}\right)^2\left[\pm\frac{\sigma'^3}{8}\cos\lambda' + \frac{\sigma'^2}{2}\sin\lambda'\right] + \cdots$$

which is always less than the right-hand side if

$$4gA\left(\frac{\omega}{2m}\right)^2 < 1\,. \tag{12.3.34a}$$

Thus, if

$$A < \frac{gs^2}{\omega} = \frac{1}{4\pi^2} gT^2 s^2\,, \tag{12.3.34b}$$

no breaking will occur. Note that the limiting amplitudes increase with the squares of the period and of the bottom slope. This breaking criterion is meaningful only as a qualitative rather than quantitative guide. In fact, A should not be too close to this limiting value for the solution to be valid. It is nevertheless interesting that Eq. (12.3.34) is of the same form as the empirical law Eq. (11.5.2), Chapter Eleven, in terms of the surf parameter.

Let us assume that Eq. (12.3.34) is satisfied and study the run-up of the shoreline. By taking $\sigma = 0$ in Eq. (12.3.22), we locate the instantaneous shoreline

$$x(0,\lambda) = \frac{u^2(0,\lambda)}{2m} + \frac{\psi_\lambda(0,\lambda)}{4}\,. \tag{12.3.35}$$

From Eqs. (12.3.21) and (12.3.27), we get

$$u(0,\lambda) = \frac{gA\omega}{m}\cos\frac{\omega\lambda}{2m}\,, \tag{12.3.36a}$$

$$\psi_\lambda(0,\lambda) = \frac{-4gA}{m}\sin\frac{\omega\lambda}{2m}\,, \tag{12.3.36b}$$

$$x(0,\lambda) = \frac{A}{s}\left[-\sin\frac{\omega\lambda}{2m} + \frac{gA}{2}\left(\frac{\omega}{m}\right)^2\cos^2\frac{\omega\lambda}{2m}\right]. \tag{12.3.36c}$$

At the shoreline, t and λ are related by

$$t = -\frac{1}{m}\left(\frac{\lambda}{2} - u(0,\lambda)\right) = \frac{-1}{2m}\left[\lambda - \frac{2gA\omega}{m}\cos\frac{\omega\lambda}{2m}\right]. \tag{12.3.37}$$

Equations (12.3.36c) and (12.3.37) give the shoreline in terms of the parameter λ. Using condition (12.3.34a) in Eqs. (12.3.36), we find the run-up for waves just beginning to break at the shore,

$$-x \le \frac{A}{s}\left(\sin\frac{\omega\lambda}{2m} - \frac{1}{2}\cos^2\frac{\omega\lambda}{2m}\right). \tag{12.3.38}$$

The maximum run-up occurs when $\omega\lambda/2m = \frac{1}{2}\pi$, so that $x = -A/s$. This result can also be obtained from the linearized theory which is presumably invalid at the shore (Keller, 1961). From Eq. (12.3.30), the linear theory gives A as the maximum wave height at $x = 0$. Thus, by assuming the free surface to be horizontal near the shore, the maximum run-up is again $-A/s$. This coincidence gives us some hope that the linearized approximation may give a reasonable estimate for the run-up of nonbreaking waves on beaches of more general profile, for which a nonlinear analysis is too difficult.

The instantaneous free-surface profile and the flow field predicted by the present nonlinear theory are quite different from the linear theory; some computed results by Carrier and Greenspan (1957) are shown in Fig. 12.7.

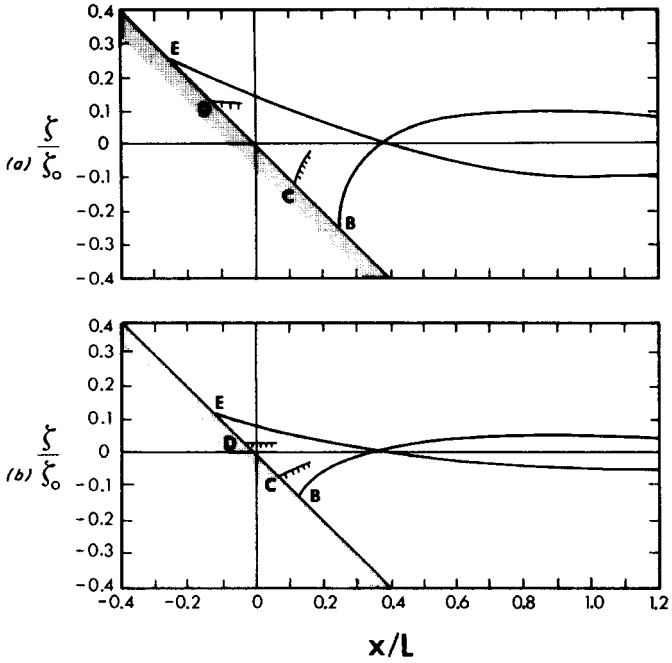

Figure 12.7: Standing wave profiles on a beach according to Eq. (12.3.27) at E, point of maximum run-up $\omega\lambda/2m = (\frac{1}{2})\pi$; B, $\omega\lambda/2m = \frac{3}{2}\pi$; C, D, intermediate times. (a) $A/\zeta_0 = 1$; (b) $A/\zeta_0 = \frac{1}{2}$ where $L = 4gs/\omega^2$, $\zeta_0 = 4gs^2/\omega^2$ (from Carrier and Greenspan, 1957, *J. Fluid Mech.* Reproduced by permission of Cambridge University Press).

12.3.2 Matching with Deep Water

In the sense of matched asymptotics, the results of Section 12.3.1 may be further used as the inner solution to be matched with a linear standing-wave solution in the deep sea. This is possible because the outer limit of the nonlinear Airy equations is linear and is the same as the inner limit ($kh \to 0$) of the linear WKB theory in gradually varying depth (Carrier, 1966; and Mei, 1966b).

Far from the beach the linearized theory should suffice. By adding two progressive waves propagating in opposite directions on a slowly varying bottom (Chapter Three), a standing wave is obtained,

$$\Phi = \frac{2gA^0}{\omega}\frac{\cos k(z+h)}{\cosh kh}\cos\omega t\cos\left(\int^x k\,dx\right), \qquad (12.3.39)$$

$$\zeta = -2A^0 \sin\omega t \cos\left(\int^x k\,dx\right), \tag{12.3.40}$$

where the lower limit of integration is, so far, arbitrary. The amplitude A^0 is given by A of Eq. (3.3.9), Chapter Three, with $\alpha = \alpha_0 = 0$. Let the reference point be far offshore ($x \sim \infty$) where the depth is great. Then in very shallow water

$$A^0 = A_\infty (k_\infty h)^{-1/4} 2^{-1/2}, \tag{12.3.41}$$

and

$$\int^x k\,dx = \frac{k_\infty^{1/2}}{s}\int^{sx} \frac{dh}{h^{1/2}} = \frac{2\omega x^{1/2}}{(gs)^{1/2}} + \delta, \tag{12.3.42}$$

where $(\,)_\infty$ denotes quantities far offshore and δ is an integration constant. Hence, the inner approximation of Eq. (12.3.40) is

$$\zeta \cong -A_\infty 2^{1/2}\left(\frac{g}{\omega^2}\right)^{1/4} s^{-1/4} x^{-1/4} \sin\omega t \cos\left(\frac{2\omega x^{1/2}}{(gs)^{1/2}} + \delta\right). \tag{12.3.43}$$

On the other hand, the nonlinear solution valid near the shore becomes linear far offshore. Specifically, when $2\omega(x/sg)^{1/2} \gg 1$, the outer approximation is, from Eq. (12.3.30),

$$\begin{aligned}\zeta &\cong -AJ_0\left(2\omega\left(\frac{x}{sh}\right)^{1/2}\right)\sin\omega t \\ &= -A\pi^{-1/2}\left(\frac{g}{\omega^2}\right)^{1/4} s^{1/4} x^{-1/4} \cos\left(2\omega\left(\frac{x}{sg}\right)^{1/2} - \frac{\pi}{4}\right)\sin\omega t\,.\end{aligned} \tag{12.3.44}$$

Matching Eq. (12.3.43) with Eq. (12.3.44), we find

$$\delta = -\frac{\pi}{4} \tag{12.3.45a}$$

and

$$A = A_\infty \left(\frac{2\pi}{s}\right)^{1/2}. \tag{12.3.45b}$$

Together Eqs. (12.3.27) and (12.3.40) give a uniformly valid theory for all depths.

Equations (12.3.45b) and (12.3.34b) can be combined to give the breaking criterion

$$k_\infty A = s^2 \quad \text{or} \quad k_\infty A_\infty = \frac{1}{(2\pi)^{1/2}} s^{5/2} . \tag{12.3.46}$$

With Eq. (12.3.45b) the empirical criterion (11.5.2), Chapter Eleven, may be written

$$k_\infty A = \left(\frac{\pi}{4}\right)^2 s^2 \quad \text{or} \quad k_\infty A_\infty = \frac{1}{(2\pi)^{1/2}} \left(\frac{\pi}{4}\right)^2 s^{5/2} . \tag{12.3.47}$$

Based on a linearized theory of standing waves on a slope, Miche (1944) assumed breaking to begin when the free surface at the water edge was tangential to the sloping bottom. His criterion for the critical moment was derived in terms of $k_\infty A_\infty$ and may be expressed as

$$k_\infty A = 2s^2 , \quad k_\infty A_\infty = \left(\frac{1}{\pi}\right)^{1/2} s^{5/2} \tag{12.3.48}$$

because of Eq. (12.3.45b). Recall from Eq. (11.5.1), Section 11.5, that $\xi = s(\pi/k_\infty A)^{1/2}$ is the surf parameter. Thus, the critical value of ξ is the largest in the experiments, intermediate by the nonlinear theory of Airy, and the smallest by the linearized theory of Miche. We hasten to emphasize that neither theory should be expected to be quantitatively correct, but both confirm the basic significance of the surf parameter. To bring the theory closer to experiments, it is likely that the boundary conditions must be exactly met near the breaking crest.

Despite the difficulties in predicting the incipient breaking, Airy's equations provide a useful framework for bore propagation. Assuming that the bore is already present, one may treat the motion away from the bore by Airy's equations and connect both sides of the bore by proper shock conditions. Early studies of this kind may be found in Stoker (1957) for horizontal bottom and in Keller, Levine, and Whitham (1960) for a beach. Further analytical studies of a single bore and its run-up on a beach have been given by Ho and Meyer (1962), Shen and Meyer (1963a, b), and summarized by Meyer and Taylor (1972). Using finite differences, Hibberd and Peregrine (1979) have investigated a bore incident from a horizontal bottom toward a sloping beach. While these situations may be simulated in the laboratory, periodicity and breaking inception are two other aspects that are ever-present in nature and should be included in a more complete picture of bores climbing a beach.

12.3.3 Transient Responses to Initial Inputs

Another advantage of the linear equations (12.3.23) is that several interesting initial-value problems can be treated conveniently in an inverse way. A typical example is to let $\psi(\sigma,0)=0$ and $\psi_\lambda(\sigma,0)$ be prescribed for $\lambda=0$, $\sigma>0$. The initial-value problem with finite ψ at $\sigma=0$ may be obtained straightforwardly by Laplace transform. In view of Eqs. (12.3.14), (12.3.21) and (12.3.22), the initial conditions $\psi(\sigma,0)=0$ and $\psi_\lambda(\sigma,0)\neq 0$ imply the physical conditions $u(x,0)=0$ and $\zeta(x,0)$ at $t=0$. Carrier and Greenspan studied a number of initial humps in this way.

Another interesting transformation which renders the nonlinear equations linear has been found by Tuck and Hwang (1972). Let

$$x^*=x+\frac{\zeta}{s}\,,\quad t^*=t-\frac{u}{gs}\,,$$

$$u^*(x^*,t^*)=u(x,t)\,,\quad \zeta^*(x^*,t^*)=\zeta+\frac{u^2}{2g}\,. \tag{12.3.49}$$

Then it can be shown straightforwardly that $u(x^*,t^*)$ and $\zeta(x^*,t^*)$ satisfy the linearized equations

$$\frac{\partial\zeta^*}{\partial t^*}+s\frac{\partial}{\partial x^*}(x^*u^*)=0\,, \tag{12.3.50}$$

$$\frac{\partial u^*}{\partial t^*}+g\frac{\partial\zeta^*}{\partial x^*}=0\,. \tag{12.3.51}$$

Note that $sx^*=sx+\zeta$. Thus, one can also seek solutions in terms of the transformed variables, then find the physical problem later. A sample problem is to prescribe

$$\zeta^*(x^*,0)=ae^{-x^*/b} \tag{12.3.52}$$

and

$$u^*(x^*,0)=0\,. \tag{12.3.53}$$

The initial free surface is then given by

$$x=x^*-\frac{a}{s}e^{-x^*/b} \tag{12.3.54}$$

or

$$x=-b\ln\frac{\zeta}{a}-\frac{\zeta}{s}\,. \tag{12.3.55}$$

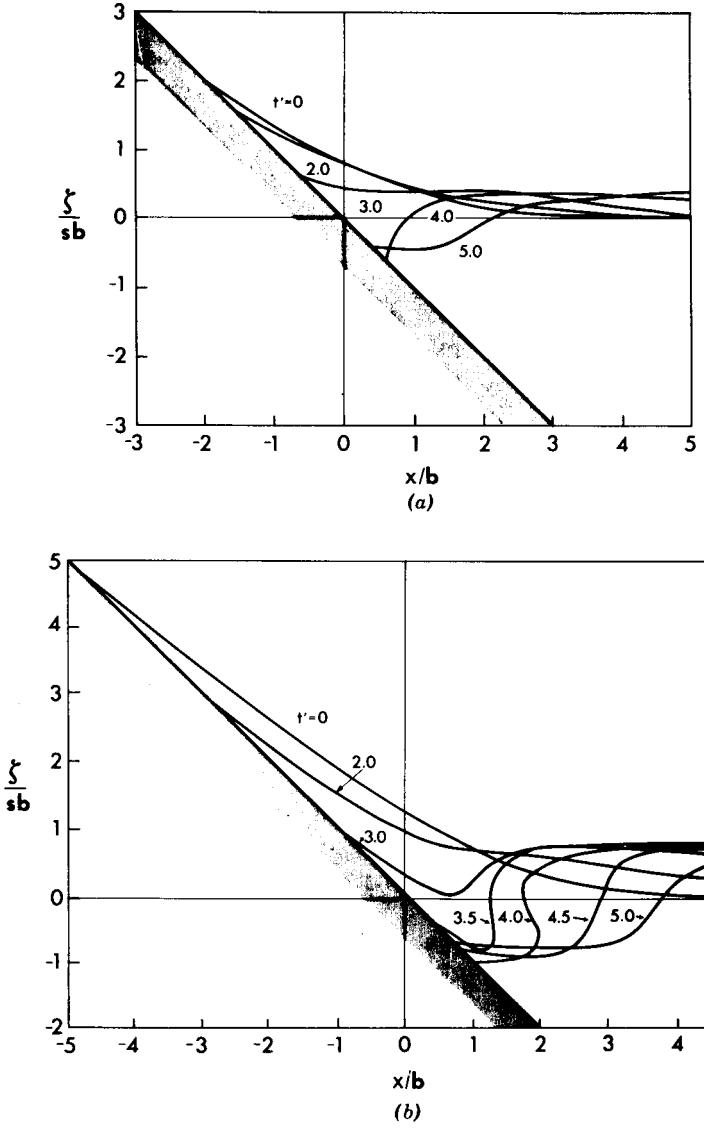

Figure 12.8: Transient waves on a beach where $t' = t(gs/b)^{1/2}$. (a) $a/sb = 2.0$; (b) $a/sb = 5.0$ (from Tuck and Hwang, 1972, *J. Fluid Mech.* Reproduced by permission of Cambridge University Press).

The history of free-surface motion is shown in Figs. 12.8(a) and 12.8(b).

12.4 Subharmonic Resonance of Edge Waves

In Section 4.8 linearized edge waves are found to be free modes trapped on a sloping beach. It was mentioned there that progressive edge waves may be generated directly by a storm traveling along the coast at a speed close to the phase velocity of an edge wave mode. The typical period of this kind of edge wave is related to the spatial extent of the storm area and is of the order of several hours. On the other hand, shorter edge waves of periods less than a few minutes are also of practical interest because they can induce either harbor seiches or rip currents which are responsible for *beach cusps*.

Can edge waves be excited by the ever-present incident swell?

If the coastline has an indentation, a linear resonance mechanism similar to harbor resonance is possible. Imagine a rectangular cove of length L with width B on an otherwise straight coast. Let the bottom of the cove be a beach of constant slope s. If the incident waves have the frequency w which nearly satisfies the eigenvalue condition

$$\omega^2 = gks(2n+1) \quad \text{with} \quad k = \frac{2m\pi}{B}, \quad n, m = \text{integers},$$

and if the cove length L is $O(2\pi/k)$, then a trapped edge wave can certainly be excited in the cove. The finiteness of L makes it possible to have some radiation damping and enables the incident wave to supply energy to the edge wave.

In their studies of nearshore circulation, Bowen and Inman (1969) found field evidence of standing edge waves of periods comparable in order of magnitude to the period of the incoming swell. The amplified edge waves cause longshore modulation of the incident swell which may be sufficiently short to break near the shore. The periodic modulation affects the breaking wave height and the radiation stresses, leading to periodic cells of currents, which, in turn, lead to beach cusps. Motivated by these interests, Guza and Davis (1974) and Guza and Bowen (1976) made a systematic examination of the nonlinear mechanism of *subharmonic resonance* in which a standing edge wave of frequency ω was resonated by a normally incoming and reflected wave of frequency 2ω. Guza and Bowen employed Airy's shallow-water approximation as the basis of their theory. In addition to the initial

instability of edge waves, the incident and reflected waves were found to leak energy by radiation due to quadratic nonlinearity. Consideration of cubic nonlinearity and of radiation damping enabled them to predict both the initial resonant growth and the final equilibrium amplitude. Their own experiments also strongly supported these findings.

Minzoni and Whitham (1977) further extended the theory of Guza et al. In particular, they began with the more complete but complicated theory of Friedrichs (1949) for normally incident and reflected waves on a beach of finite slope. Since most beach slopes are small, we shall follow Guza and Bowen in using the shallow-water equations

$$\zeta_t + [(sx+\zeta)\Phi_x]_x + [(sx+\zeta)\Phi_y]_y = 0\,, \tag{12.4.1}$$

$$\Phi_t + \frac{1}{2}(\Phi_x^2 + \Phi_y^2) + g\zeta = 0\,. \tag{12.4.2}$$

However, the more systematic perturbation arguments of Minzoni and Whitham will be applied, as in Rockliff (1978).

Eliminating ζ from Eqs. (12.4.1) and (12.4.2), we acquire a single nonlinear equation for Φ:

$$\begin{aligned}\mathcal{L}\Phi \equiv & -\Phi_{tt} + sg[(x\Phi_x)_x + x\Phi_{yy}] \\ = & \, 2(\Phi_x\Phi_{xt} + \Phi_y\Phi_{yt}) + \Phi_t(\Phi_{xx}\Phi_{yy}) \\ & + \frac{1}{2}(\Phi_x^2 + \Phi_y^2)(\Phi_{xx} + \Phi_{yy}) \\ & + \Phi_x^2\Phi_{xx} + \Phi_y^2\Phi_{yy} + 2\Phi_x\Phi_y\Phi_{xy}\,. \end{aligned} \tag{12.4.3}$$

12.4.1 Perfect Tuning

We first discuss the simple case of perfect tuning. The linearized approximation of Eq. (12.4.3) admits two solutions. The first solution is the normally incident and reflected waves with frequency 2ω

$$\Phi_0 = -\frac{igA}{2\omega} J_0\left(4\omega\left(\frac{x}{gs}\right)^{1/2}\right) e^{-2i\omega t} + * \tag{12.4.4}^{1}$$

which is finite at the shore $x = 0$; ω can be arbitrary. The second solution is an edge wave mode of frequency ω (see Section 4.8). For simplicity, we shall only take the lowest mode (mode 0) which is described by

[1] ( ) + * is the abbreviation for ( ) + the complex conjugate of ( ).

$$\Phi_e = -\frac{igB}{\omega} e^{-kx} \cos ky \, e^{-2i\omega t} + * , \tag{12.4.5}$$

subject to the dispersion relation (eigenvalue condition)

$$\omega = (gks)^{1/2} . \tag{12.4.6}$$

If both Φ_0 and Φ_e are initially present, the quadratic term involving the pair (Φ_0, Φ_e) will, at the second order, give rise to a simple harmonic forcing term proportional to $G(x) \cos ky \, e^{-i\omega t}$ where $G(x)$ is a certain function of x. Unless $G(x)$ is in some sense orthogonal to the homogeneous solution e^{-kx}, the edge wave will be further resonated to great amplitude. The two waves are said to be perfectly tuned since the frequency ratio is exactly 1 to 2.

Let the linear terms on the left of Eq. (12.4.3) be denoted by $\mathcal{L}\Phi$ and the quadratic and cubic terms on the right be denoted symbolically by their possible combinations

$$\begin{aligned} \mathcal{L}\Phi_e + \mathcal{L}\Phi_0 = {} & (\Phi_e, \Phi_e) + (\Phi_0, \Phi_0) + (\Phi_e, \Phi_0) \\ & + (\Phi_e, \Phi_e, \Phi_e) + (\Phi_0, \Phi_0, \Phi_0) \\ & + (\Phi_e, \Phi_0, \Phi_0) + (\Phi, \Phi_e, \Phi_e) . \end{aligned} \tag{12.4.7}$$

The harmonics of the terms of the right are, respectively,

$$\begin{aligned} & (0, \pm 2) \quad (0, \pm 4) \quad (\pm 1, \pm 3) \quad (\pm 1, \pm 3) \\ & (\pm 2, \pm 6) \quad (\pm 1, \pm 3, \pm 5) \quad (0, \pm 2, \pm 4) . \end{aligned} \tag{12.4.8}$$

Let a and b denote the order of magnitude of A and B, respectively; the order of the terms on the right of Eq. (12.4.7) are, respectively,

$$(b^2) , \quad (a^2) , \quad (ab) , \quad (b^3) , \quad (a^3) , \quad (a^2 b) , \quad (ab^2) . \tag{12.4.9}$$

Terms containing first harmonics are potentially resonance-forcing. Since $b \ll a$ at the initial stage of resonant growth, the third term on the right of Eq. (12.4.7) is of the order $O(ab)$ and is the most important term for resonating Φ_e. In response to this forcing, the amplitude B of the edge wave is no longer constant in time. From $-\partial^2 \Phi_e / \partial t^2$, a term proportional to $\partial B / \partial t$, which represents the initial growth of B, is expected. Since $\partial B / \partial t$, must be comparable to the leading-force term of $O(ab)$, the time scale of resonant growth must be $O(1/a)$. Consequently, two time scales are inherent in this problem: ω^{-1} and $(\omega k a)^{-1}$.

As resonance develops further, the edge wave is no longer small in comparison with the standing wave. Let us postulate the existence of a final equilibrium state where some cubic terms become as important as the quadratic terms. From Eqs. (12.4.8) and (12.4.9), we see that (Φ_e, Φ_0) can only be balanced by (Φ_e, Φ_e, Φ_e) which implies that $O(ab) = O(b^3)$ or $b = O(a^{1/2})$ at equilibrium. To account for this eventuality we allow Φ_e to be $O(a^{1/2})$, introduce the slow time $T = at$, and assume a multiple-scale expansion as follows:

$$\begin{aligned}\Phi = {} & [a^{1/2}\psi_1(x,y,T) + a^{3/2}\psi_2(x,y,T) + \cdots]e^{-i\omega t} + * \\ & + [a\phi_1(x,T) + a^2\phi_2(x,y,T) + \cdots]e^{-2i\omega t} + * + \cdots . \end{aligned} \tag{12.4.10}$$

The left-hand side of Eq. (12.4.3) becomes

$$\begin{aligned} & a^{1/2}\{\omega^2\psi_1 + gs[(x\psi_{1x})_x + x\psi_{1yy}]\}e^{-i\omega t} + * \\ & \quad + a\{4\omega^2\phi_1 + gs[(x\phi_{1x})_x\}e^{-2i\omega t} + * \\ & \quad + a^{3/2}\left\{\omega^2\psi_2 + gs[(x\psi_{2x})_x + x\psi_{2yy}] + 2i\omega\frac{\partial\psi_1}{\partial T}\right\}e^{-i\omega t} + * + \cdots . \end{aligned} \tag{12.4.11}$$

The right-hand side of Eq. (12.4.3) may be symbolically rewritten

$$\begin{aligned} & a(\psi_1,\psi_1)e^{-2i\omega t} + * + a^{3/2}(\psi_1^*,\phi_1)e^{-i\omega t} + * \\ & \quad + a^{3/2}(\psi_1^*,\psi_1,\psi_1)e^{-i\omega t} + * + \cdots . \end{aligned} \tag{12.4.12}$$

We now examine the perturbation equations sequentially and explicitly.

At $O(a^{1/2})$, the governing equation is

$$\omega^2\psi_1 + gs[(x\psi_{1x})_x + x\psi_{1yy}] = 0\,, \tag{12.4.13}$$

which has a homogeneous solution

$$\psi_1 = -\frac{igB}{\omega}e^{-kx}\cos ky \tag{12.4.14a}$$

with

$$\omega^2 = gks\,, \tag{12.4.14b}$$

that is, the lowest edge wave mode. For later purposes note that the factor $F = e^{-kx}$ which describes the x dependence satisfies

$$\begin{aligned} \omega^2 F + gs[(xF_x)_x - xk^2 F]\cdot = 0\,; \\ xF' = 0 \quad \text{at} \quad x = 0\,; \quad F \to 0\,, \quad x \sim \infty\,. \end{aligned} \tag{12.4.15}$$

At $O(a)$, the governing equation is

$$4\omega^2\phi_1 + gs(x\phi_{1x})_x = (\psi_1, \psi_1)\,, \tag{12.4.16a}$$

where the quadratic forcing term is, after some algebra,

$$(\psi_1, \psi_1) = 2i\frac{(gk)^2}{\omega}B^2 e^{-2kx}\,. \tag{12.4.16b}$$

The solution to Eq. (12.4.16) has both homogeneous and particular parts. The homogeneous solution is just the standing wave

$$\phi_1^h = -\frac{igA}{2\omega}J_0(4(kx)^{1/2})\,, \tag{12.4.17}$$

where A is the amplitude at the shore. The particular solution should be finite at $x = 0$ and outgoing at infinity. We leave it as an exercise to show that

$$\phi_1^p = i\frac{2\pi gk}{\omega s}B^2 G(\xi)\,, \tag{12.4.18a}$$

where $\xi = kx$ and

$$\begin{aligned} G(\xi) = &-E_2(\xi)J_0(4\xi^{1/2}) + E_1(\xi)Y_0(4\xi^{1/2}) \\ &+ (E_2(\infty) - iE_1(\infty)J_0(4\xi^{1/2})\,, \end{aligned} \tag{12.4.18b}$$

with

$$\begin{aligned} E_1(\xi) &= \int_0^\xi e^{-2\xi}J_0(4\xi^{1/2})\,d\xi\,, \\ E_2(\zeta) &= \int_0^\xi e^{-2\xi}Y_0(4\xi^{1/2})\,d\xi\,. \end{aligned} \tag{12.4.18c}$$

It is easy to check that ϕ_1^p satisfies the radiation condition.

Now we examine the $O(a^{3/2})$ problem. It is straightforward to calculate the cubic terms

$$(\psi_1^*, \psi_1, \psi_1) = -3i\left(\frac{g}{\omega}\right)^3 k^4 B^2 B^* e^{-3kx}\cos ky\,. \tag{12.4.19}$$

The quadratic terms are lengthier and can be written in the following form:

$$(\psi_1^*, \phi_1) = e^{-kx}\cos ky \left\{ iAB^* \frac{g^2}{2\omega}\left(2k\frac{dJ_0}{dx} + \frac{d^2J_0}{dx^2}\right) - i\frac{2\pi g^2 k}{\omega s}B^*B^2\left(2k\frac{dG}{dx} + \frac{d^2G}{dx^2}\right)\right\}. \tag{12.4.20}$$

Without the factor $\cos ky$, the $O(a^{3/2})$ equation may be summarized as follows:

$$\begin{aligned}\omega^2 H + gs[(xH_x)_x - k^2 xH] &= \left[-2g\frac{\partial B}{\partial T} + iAB^*\frac{g^2}{2\omega}\left(2k\frac{dJ_0}{dx} + \frac{d^2J_0}{dx^2}\right)\right. \\ &\quad \left. - i\frac{2\pi g^2 k}{\omega s}B^*B^2\left(2k\frac{dG}{dx} + \frac{d^2G}{dx^2}\right)\right]e^{-kx} \\ &\quad - 3i\left(\frac{g}{\omega}\right)^3 k^4 B^2 B^* e^{-3kx}\,,\end{aligned} \tag{12.4.21}$$

where H is defined by

$$\psi_2 \equiv H(x)\cos ky\,. \tag{12.4.22}$$

Since the homogeneous problem (12.4.15) has the nontrivial solution $F = e^{-kx}$, there must be a solvability condition for H (Fredholm alternative). This condition is derived as usual by multiplying Eq. (12.4.21) by F and Eq. (12.4.15) by H, and integrating the difference from 0 to ∞. After partial integration we obtain

$$\int_0^\infty dx e^{-kx}\{\text{RHS of Eq. (12.4.21)}\} = 0\,. \tag{12.4.23}$$

This orthogonality condition gives a differential equation for B. With the change of variable $\xi = kx$, Eq. (12.4.23) becomes

$$\frac{\partial B}{\partial T} = \frac{iAB^*gk^2}{2\omega}\alpha - i\frac{2\pi g k^3}{\omega s}B^*B^2\beta - i\frac{3}{4}\frac{g^2}{\omega^3}k^4 B^*B^2\,, \tag{12.4.24}$$

where α and β are a pair of definite integrals

$$\begin{aligned}\alpha &= \int_0^\infty d\xi e^{-2\xi}\left(2\frac{dJ_0}{d\xi} + \frac{d^2J_0}{d\xi^2}\right) = 8E_1(\infty) \\ &= 8/2e^2 = 0.0541314\,,\end{aligned} \tag{12.4.25a}$$

and

$$\beta = \int_0^\infty d\xi e^{-2\xi} \left(2\frac{dG}{d\xi} + \frac{d^2G}{d\xi^2} \right) = -\frac{1}{\pi} + 8E_G \,, \tag{12.4.25b}$$

where

$$\begin{aligned} E_G &= \int_0^\infty d\xi e^{-2\xi} G(\xi) \\ &= -i(E_1(\infty))^2 + 2\int_0^\infty d\xi e^{-2\xi} Y_0(4\xi^{1/2}) \int_0^\xi d\tau e^{-2\tau} J_0(4\xi^{1/2}) \\ &= 0.02862 - 0.0045782i \,. \end{aligned}$$

The evaluation of the preceding integrals is detailed in Appendix 12.A.

Equation (12.4.24) describes the nonlinear evolution of the edge wave amplitude B and may be integrated numerically for a given A and an initial value $B(0)$. Its physical significance can be better seen by multiplying with B^* and adding the result to its complex conjugate, yielding

$$\frac{\partial |B|^2}{\partial T} = \frac{-gk^2\alpha A}{\omega} \operatorname{Im} B^{*2} + \frac{4\pi g k^3}{\omega^3} |B|^4 \operatorname{Im} \beta \,. \tag{12.4.26}$$

This is an energy equation stating that the change of the edge wave is due to its interaction with the standing wave (the first term on the right) and the radiation of the second harmonic (the second term). Indeed, $\operatorname{Im}\beta$ is negative so that radiation causes damping, as expected.

During the initial state when B is still much less than A, the last two terms (proportional to B^*B^2) may be omitted from Eq. (12.4.24), leaving

$$\frac{\partial B}{\partial T} = \frac{4igk^2}{\omega} E_1(\infty) A B^* \,. \tag{12.4.27}$$

Differentiating Eq. (12.4.27), we get

$$\frac{\partial^2 B}{\partial T^2} = |A|^2 \left[\frac{4gk^2}{\omega} E_1(\infty) \right]^2 B \,, \tag{12.4.28}$$

which can be solved to give

$$B(T) = B(0) \exp\left(\pm \frac{4gk^2}{\omega} |A| E_1(\infty) T \right) . \tag{12.4.29}$$

Hence the growth rate is proportional to $|A|$. Since $gk^2/\omega = \omega^3/gs^2$, the growth rate increases with higher frequency and smaller beach slope. This

result agrees with the limit of the full theory at $s \to 0$ by Minzoni and Whitham.[2]

Consider now the nonlinear equilibrium state, when $\partial B/\partial T = 0$. From Eqs. (12.4.24) and (12.4.25) the equilibrium amplitude of the edge wave is found to be

$$|B| = \left[\frac{4E_1(\infty)s|A|}{k|16\pi E_G - \frac{5}{4}|}\right]^{1/2}. \tag{12.4.30}$$

The corresponding run-up, defined as the maximum excursion of the shoreline, is

$$X_R = \frac{4|B|}{s} = 8\left(\frac{E_1(\infty)}{|16\pi E_G - \frac{5}{4}|}\right)^{1/2}\left(\frac{|A|}{ks}\right)^{1/2}$$

$$= 3.815\left(\frac{|A|}{ks}\right)^{1/2} = 3.815\left(\frac{|A|g}{\omega^2}\right)^{1/2}, \tag{12.4.31a}$$

which is equivalent to the limiting result ($s \to 0$) of Minzoni and Whitham (1977, Eq. (76)):

$$X_R = 5.4\left(\frac{ga_0}{\sigma^2}\right)^{1/2} \tag{12.4.31b}$$

where $a_0 = 2A$ and $\omega = 2\sigma$. This result also agrees with the theory of Guza and Bowen (1976). Model experiments were performed by the latter authors for a beach angle of $s = 6^\circ$ and an incident wave period of $2\pi/2\omega = 2.7s$. For $2A$ ranging from 2 to 4 cm, the measured coefficient in Eq. (12.4.31b) was on the average 4.5 instead of 5.4, but in the experiments the standing waves ϕ_1 were very steep. In addition, the radiated second harmonic was also confirmed experimentally.

In view of Eq. (12.3.47), Section 12.3.2, the edge wave run-up can be expressed in terms of the deep-water amplitude A_∞ instead of A.

Guza and Bowen, and Minzoni and Whitham also discussed imperfect tuning and showed that a higher equilibrium amplitude could be achieved

[2]It may be remarked that while they give the same growth criterion for the leading-order edge wave as the small-slope limit of the full theory, Airy's equations for a plane beach can lead to difficulties at the third order. Despite the solvability condition, Whitham (1976) found for a progressive edge wave of permanent form that the third-order solution became logarithmically unbounded with y as compared to the linear (first-order) solution. This nonuniformity has to be avoided either by using the full theory of arbitrary slope or by letting the sea depth approach a constant far offshore (Minzoni, 1976).

when phase matching was imperfect. For other issues their papers and Rockliff (1978) should be consulted.

12.4.2 Effects of Detuning

If there is a slight frequency mismatch between the edge wave and the incident/reflected wave system, we can replace (12.4.4) by

$$\Phi_0 = \frac{-igA}{2\omega} J_0(4\sqrt{kx}) e^{-2i(\omega+\epsilon\Omega)t} + * \tag{12.4.32}$$

where $\Omega = O(\omega)$ and ϵ is the small dimensionless parameter characterizing the incident wave amplitude a. This amounts to replacing A in Section 12.4.1 by

$$A_0 e^{-2i\epsilon\Omega t} = A_0 e^{-2i\Omega T}\,.$$

Therefore (12.4.24) is replaced by

$$-i\frac{\partial B}{\partial T} = \frac{2}{e^2}\frac{gk^2}{\omega^2} A_0 e^{-2i\Omega T} B^* - \frac{g^2k^4}{\omega^3}\left(16\pi E_G - \frac{5}{4}\right)|B|^2 B \tag{12.4.33}$$

which includes the effects of small detuning. The complex evolution equation (12.4.38) for $\mathcal{B}$ is of Landau–Stuart type appearing often in stability problems, and can be analyzed by the theory of dynamical systems (Rockliff, 1978).[3] As an alternative, let $B = \bar{B}e^{-i\Omega T}$, then

$$\frac{\partial B}{\partial T} = \left(\frac{\partial \bar{B}}{\partial T} - i\Omega\bar{B}\right) e^{-i\Omega T}$$

and (12.4.33) becomes

$$-i\frac{\partial \bar{B}}{\partial T} = \Omega\bar{B} + \frac{2}{e^2}\frac{gk^2}{\omega^2} A_0 \bar{B}^* - \frac{g^2k^4}{\omega^3}\left(16\pi E_G - \frac{5}{4}\right)|\bar{B}|^2\bar{B}\,. \tag{12.4.34}$$

Let us denote

$$\delta = \frac{2}{e^2} = 0.27\,, \quad \sigma - i\gamma = 16\pi E_G - \frac{5}{4} = 0.189 - 0.23i\,, \tag{12.4.35}$$

and introduce the normalization,

$$T = T_0\tau\,, \quad \bar{B} = B_0\mathcal{B}\,, \tag{12.4.36}$$

[3]The details here are a part of an unpublished work by Prof. Oded Gottlieb, Technion, Israel (private communication).

with

$$T_0 = \frac{\omega}{\delta k A_0 g k}\,, \quad (kB_0)^2 = \frac{\omega^2}{gk}\delta k A_0\,. \tag{12.4.37}$$

We then get the dimensionless evolution equation with detuning,

$$-i\frac{\partial \mathcal{B}}{\partial \tau} = \widehat{\Omega}\mathcal{B} + \mathcal{B}^* - (\sigma - i\gamma)|\mathcal{B}|^2\mathcal{B}\,, \tag{12.4.38}$$

where

$$\widehat{\Omega} = \frac{\Omega\omega}{\delta A_0 k^2}\,. \tag{12.4.39}$$

The preceding complex equation can be converted to two equations for two real variables, if we express $\mathcal{B}$ in the polar form

$$\mathcal{B} = \sqrt{I}e^{i\theta}\,, \tag{12.4.40}$$

where $I = |\mathcal{B}|^2$ is called the *action variable* and θ the *angle variable*. Equation (12.4.38) becomes

$$-i\left(\frac{dI}{d\tau} + 2iI\frac{d\theta}{d\tau}\right) = 2\widehat{\Omega}I - 2(\sigma - i\gamma)I^2 + 2Ie^{-2i\theta}\,. \tag{12.4.41}$$

Separating the imaginary and real parts, we get

$$\frac{dI}{d\tau} = -2\gamma I^2 + 2I\sin 2\theta \tag{12.4.42}$$

and

$$\frac{d\theta}{d\tau} = \widehat{\Omega} - \sigma I + \cos 2\theta\,. \tag{12.4.43}$$

These two real equations form a dynamical system of two-degrees of freedom, and were first analyzed by Rockliff (1978) using the tools of nonlinear dynamics.

The final states of equilibrium,[4] if they exist, are found by taking $d/d\tau = 0$. We then get from (12.4.42) and (12.4.43)

$$I(-\gamma I + \sin 2\theta) = 0 \tag{12.4.44}$$

and

$$\widehat{\Omega} - 2\sigma I + \cos 2\theta = 0\,. \tag{12.4.45}$$

[4]An equilibrium state is also called a fixed point in the phase space (I, θ).

The first equilibrium state is trivial with zero amplitude, i.e., $I = 0$ for all $\widehat{\Omega}$. The edge wave is not excited. The angle variable which will be needed later is

$$\cos 2\theta = -\widehat{\Omega}\,. \tag{12.4.46}$$

The second equilibrium state corresponds to the solution of

$$\sin 2\theta = \gamma I \tag{12.4.47}$$

and

$$\cos 2\theta = -\widehat{\Omega} + \sigma I\,. \tag{12.4.48}$$

Eliminating θ we get

$$(\widehat{\Omega} - \sigma I)^2 + \gamma^2 I^2 = 1\,, \tag{12.4.49}$$

which is a quadratic equation for I, having the solutions

$$\begin{aligned} I_0^{\pm} &= \frac{\widehat{\Omega}\sigma}{\sigma^2+\gamma^2} \pm \sqrt{\frac{\widehat{\Omega}\sigma}{\sigma^2+\gamma^2} - \frac{\widehat{\Omega}^2 - 1}{\sigma^2+\gamma^2}} \\ &= \frac{\sigma}{\sigma^2+\gamma^2}\left(\widehat{\Omega} \pm \sqrt{1 + \frac{\gamma^2}{\sigma^2}(1-\widehat{\Omega}^2)}\right). \end{aligned} \tag{12.4.50}$$

The corresponding angle variables are

$$\cos 2\theta_0^{\pm} = 2\sigma I_0^{\pm} - \widehat{\Omega}\,. \tag{12.4.51}$$

Referring to the bifurcation diagram Fig. 12.9 which relates the equilibrium action and the detuning frequency, the first equilibrium state of no motion coincides with the entire $\widehat{\Omega}$ axis. For the second equilibrium state

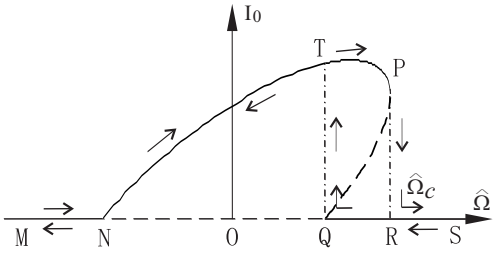

Figure 12.9: Bifurcation diagram relating the action I_0 of equilibrium state and detuning frequency $\widehat{\Omega}$. Solid line: stable branch. Dashed line: unstable branch.

of finite motion, I_0 must be real and positive. Both I_0^+ and I_0^- are possible roots if

$$1 < \widehat{\Omega} < \widehat{\Omega}_c \equiv \sqrt{1 + \frac{\sigma^2}{\gamma^2}}\,, \tag{12.4.52}$$

as marked by QR in Fig. 12.9. Only I_0^+ is possible if

$$-1 < \widehat{\Omega} < 1\,, \tag{12.4.53}$$

i.e., segment NQ in Fig. 12.9.

To see if the equilibrium states can be realized physically, one must study their stability.

Consider first the finite amplitude state. Let us add some infinitesimal disturbances to both I_0 and θ_0 by substituting

$$I = I_0 + I'\,, \quad \theta = \theta_0 + \theta' \tag{12.4.54}$$

into (12.4.42) and (12.4.43). After linearizing we get

$$\frac{dI'}{d\tau} = (2\sin 2\theta_0 - 4\gamma I_0)I' + 4I_0\cos 2\theta_0)\theta' \tag{12.4.55}$$

and

$$\frac{d\theta'}{d\tau} = -\sigma I' - 2\sin 2\theta_0 I'\,. \tag{12.4.56}$$

Making use of (12.4.47) and (12.4.48), we get

$$\frac{d}{d\tau}\begin{pmatrix} I' \\ \theta' \end{pmatrix} = \begin{bmatrix} -2\gamma I_0 & -4I_0(\Omega - \sigma I_0) \\ -\sigma & -2\gamma I_0 \end{bmatrix}\begin{pmatrix} I' \\ \theta' \end{pmatrix}. \tag{12.4.57}$$

Substituting

$$\begin{pmatrix} I' \\ \theta' \end{pmatrix} = \begin{pmatrix} \tilde{I}' \\ \tilde{\theta}' \end{pmatrix} e^{-\lambda t} \tag{12.4.58}$$

into (12.4.57), we get the eigenvalue condition

$$\begin{vmatrix} \lambda - 2\gamma I_0 & -4I_0(\Omega - \sigma I_0) \\ -\sigma & \lambda - 2\gamma I_0 \end{vmatrix} = 0$$

or

$$(\lambda - 2\gamma I_0)^2 - \sigma 4I_0(\Omega - \sigma I_0) = 0\,. \tag{12.4.59}$$

The two eigenvalues are

$$\lambda_{\pm} = 2\gamma I_0 \pm \sqrt{4\sigma I_0(\widehat{\Omega} - \sigma I_0)}\,. \tag{12.4.60}$$

For stability, λ must have a positive real part. If $\widehat{\Omega} > \sigma I_0$, both eigenvalues are real. The larger eigenvalue λ_1 is always positive, while the smaller root λ_2 is positive only if

$$\sqrt{4\sigma I_0(\widehat{\Omega} - \sigma I_0)} < 2\gamma I_0$$

or

$$I_0 > \frac{\sigma\widehat{\Omega}}{\sigma^2 + \gamma^2}\,. \tag{12.4.61}$$

Recall that if $\widehat{\Omega}^2 < 1$, I_0^+ is the the only root which satisfies the preceding inequality in view of (12.4.50), hence stable in the range QR.

If

$$1 < \Omega < \sqrt{\frac{\sigma^2 + \gamma^2}{\sigma^2}} = \widehat{\Omega}_c \tag{12.4.62}$$

there are two equilibrium states with finite amplitudes. The smaller root satisfies

$$I_0^- < \frac{\sigma\Omega}{\sigma^2 + \gamma^2} \tag{12.4.63}$$

hence is unstable (see dashed branch QP in Fig. 12.9). The larger root is

$$I_0^+ > \frac{\sigma\Omega}{\sigma^2 + \gamma^2} \tag{12.4.64}$$

and stable (see solid branch TP).

Now we turn to the stability of the trivial state where the edge wave is not excited, $I_0 = 0$. Then $\cos 2\theta_0 = -\widehat{\Omega}$. Linearizing (12.4.42) and (12.4.43) we get

$$\frac{dI'}{d\tau} = 2I'\sqrt{1 - \Omega^2} \tag{12.4.65}$$

hence

$$I' = I'(0)e^{2\tau\sqrt{1-\widehat{\Omega}^2}}\,. \tag{12.4.66}$$

Hence the zero state is unstable for $\widehat{\Omega}^2 < 1$ (NQ in Fig. 12.9) and stable for $\widehat{\Omega}^2 > 1$ (MN and NS).

What will happen if the detuning frequency of the incident/reflected waves is increased from M along the $\widehat{\Omega}$ axis? Starting from the left of N, i.e., $\widehat{\Omega} < -1$, the first equilibrium state of zero amplitude is stable, amounting to no resonance of edge waves. When N is crossed, i.e., $-1\widehat{\Omega} < -1$, the first equilibrium state is unstable but the second state is stable. Edge waves of initially infinitesimal amplitude must grow to reach an amplitude corresponding to a point on the stable branch NT. Note that the amplitude at perfect tuning is not the largest. With greater detuning beyond $\widehat{\Omega} = 1$, the stable amplitude continues to become larger, and then falls to the final value corresponding to point P at $\widehat{\Omega} = \widehat{\Omega}_c$. Afterwards only the first state exists and is stable; the edge wave disappears.

If we reverse the direction and lower the detuning frequency from above towards $\widehat{\Omega} > \widehat{\Omega}_c$, i.e., from S to R, no edge wave is excited from infinitesimal amplitude until point Q (where $\widehat{\Omega} = 1$) is crossed. Then the zero state is no longer stable; an edge wave of finite amplitude is resonated with amplitude given by a point on the branch TN. When $\widehat{\Omega}$ drop below -1, edge waves are again no longer excitable.

As described in Section 7.11, the mobile storm barrier for Venice Lagoon admits trapped modes similar to edge waves here. These modes can also be excited nonlinearly by subharmonic resonance; the gate dynamics is also governed by Landau-Stuart equation. Many theoretical deductions common to both edge waves and gate oscillations have been confirmed experimentally by Sammarco et al. (1997a, b).

12.5 Dispersive Long Waves of Permanent Form and the Korteweg–De Vries (KdV) Equation

In linear wave theories, solutions of the type $e^{ik(x-Ct)}$ are the most elementary; it is natural to inquire whether in nonlinear theories solutions which depend on x, t in the combination $(x - Ct)$ exist. Since these solutions represent waves propagating at constant speed without change of form, they are called the *permanent* or *stationary waves*. From earlier discussions, nonlinearity is known to steepen a crest, while dispersion tends to counteract this trend by "dispersing" into waves of different lengths. Permanent waves, if any, must therefore correspond to a dynamical equilibrium in which the two effects are in perfect balance.

The normalized equations of Boussinesq, Eqs. (12.1.36) and (12.1.37), can be written for one-dimensional waves as follows:

$$\zeta_t + \varepsilon(\zeta\Phi_x)_x + \Phi_{xx} = 0\,, \tag{12.5.1}$$

$$\Phi_t + \zeta + \frac{\varepsilon}{2}\Phi_x^2 = \frac{\mu^2}{3}\Phi_{xxt}\,, \tag{12.5.2}$$

upon substituting Φ_x for u. For brevity the symbols $(\ )'$ and $(^-)$ have been omitted. The spatial and times scales for normalization are k^{-1} and $(k\sqrt{gh})^{-1}$, respectively. Eliminating ζ from Eqs. (12.5.1) and (12.5.2), we obtain a single equation for Φ

$$\Phi_{tt} - \Phi_{xx} = \frac{\mu^2}{3}\Phi_{xxtt} - \varepsilon\left(\Phi_x^2 + \frac{1}{2}\Phi_t^2\right)_t\,, \tag{12.5.3}$$

where terms smaller than $O(\varepsilon, \mu^2)$ have been ignored. Equation (12.5.3) may also be called the Boussinesq equation. We now seek a solution of the following form:

$$\Phi = \Phi(\xi) \quad \text{with} \quad \xi = x - Ct\,. \tag{12.5.4}$$

Since

$$\frac{\partial}{\partial x} = \frac{d}{d\xi} \equiv (\ )' \quad \text{and} \quad \frac{\partial}{\partial t} = -C\frac{d}{d\xi} \equiv -C(\ )'\,,$$

Eq. (12.5.3) becomes

$$(C^2 - 1)\Phi'' = \frac{\mu^2}{3}C^2\Phi'''' + \varepsilon C\left(1 + \frac{C^2}{2}\right)(\Phi'^2)'\,.$$

Now the preceding equation implies that $C = 1 + O(\varepsilon, \mu^2)$; hence, in all terms on the right-hand side C may be approximated by unity without affecting the accuracy. Integrating once with respect to ξ, we get

$$(C^2 - 1)\Phi' + A_1 = \frac{\mu^2}{3}\Phi''' + \frac{3\varepsilon}{2}(\Phi')^2\,.$$

To the leading order, $\zeta = -\Phi_t = \Phi'$; thus,

$$(C^2 - 1)\zeta + A_1 = \frac{\mu^2}{3}\zeta'' + \frac{3\varepsilon}{2}\zeta^2\,.$$

Finally, we multiply the above equation by ζ' and integrate once more to get

$$-\frac{\varepsilon}{2}\zeta^3 + (C^2 - 1)\frac{\zeta^2}{2} + A_1\zeta + A_2 = \frac{\mu^2}{6}\zeta'^2 \tag{12.5.5}$$

where the integration constants A_1 and A_2 are both of the order $O(\varepsilon, \mu^2)$.

Two cases will now be discussed.

12.5.1 Solitary Waves

A solitary wave[5] has a single crest whose amplitude diminishes to zero as $|\xi| \to \infty$. Since ζ, ζ', and ζ'' vanish at infinity, so should the constants A_1 and A_2. Equation (12.5.5) becomes simply

$$(\zeta')^2 = 3\zeta^2 \left(\frac{C^2 - 1}{\varepsilon} - \zeta \right) \left(\frac{\varepsilon}{\mu^2} \right). \tag{12.5.6}$$

For the right-hand side to be positive we must have

$$C > 1 \quad \text{or} \quad C > (gh)^{1/2}$$

in physical variables; this wave speed is called *supercritical*. Furthermore, we must insist that $\zeta \leq (C^2 - 1)/\varepsilon$. Hence $(C^2 - 1)/\varepsilon$ is just the maximum amplitude of the crest which is unity because of the normalization, that is,

$$C^2 = 1 + \varepsilon \,. \tag{12.5.7}$$

In dimensional form Eq. (12.5.7) reads

$$C = (gh)^{1/2} \left(1 + \frac{A}{h} \right)^{1/2} = [g(h + A)]^{1/2} \tag{12.5.8}$$

which was first found by Rayleigh. Thus, the wave speed increases with amplitude.

With Eq. (12.5.7), Eq. (12.5.6) can be written

$$\frac{d\zeta}{d\xi} = \frac{(3\varepsilon)^{1/2}}{\mu} \zeta (1 - \zeta)^{1/2}$$

which can be integrated to give

$$\frac{\varepsilon^{1/2}}{\mu} 3^{1/2} (\xi - \xi_0) = -2 \tanh^{-1} (1 - \zeta)^{1/2}$$

or

$$\zeta = \operatorname{sech}^2 \frac{(3\varepsilon)^{1/2}}{2\mu} (\xi - \xi_0) \,. \tag{12.5.9}$$

[5]Discovered by John Scott Russell in 1834.

The corresponding profile is a solitary hill with the crest at $\xi = \xi_0$. The integration constant ξ_0 may be taken to be zero. In dimensional form the surface profile is

$$\zeta = A \operatorname{sech}^2 \frac{3^{1/2}}{2} \left(\frac{A}{h^3}\right)^{1/2} (x - Ct)\,. \tag{12.5.10}$$

Thus, the higher the peak, the narrower the profile.

Solitary waves can be easily generated in a long tank by almost any kind of impulse. For experimental proof of this theory see Dailey and Stephan (1952).

Major advances in numerical theory have been made in the past decade so that it is now possible to compute strongly nonlinear solitary waves. From the exact boundary conditions on the free surface, Byatt-Smith (1970) obtained an integral-differential equation which was then solved numerically. Fenton (1972) extended an expansion procedure due to Benjamin and Lighthill (1954) to the ninth order and made calculations comparable in accuracy to Byatt-Smith's as long as the amplitude was less than $\frac{3}{4}$ of the still-water depth. In a series of remarkable papers, Longuet–Higgins and associates made a most thorough investigation. By first deducing a number of exact relations on mass, momentum, energy, and circulation (Longuet–Higgins, 1974b), then carrying out numerical computations with the aid of either Padé approximants (Longuet–Higgins and Fenton, 1974) or an integral-differential equation (Byatt-Smith and Longuet–Higgins, 1976), they uncovered a great deal of accurate information. Perhaps the most striking discovery is that the highest wave is not the most energetic. For fascinating details of both the approaches and the results, the reader is referred to these papers.

12.5.2 Cnoidal Waves

Besides the solitary wave just discussed, periodic permanent waves are possible. Let us first rewrite Eq. (12.5.5) as follows:

$$\begin{aligned} \frac{1}{3}\frac{\mu^2}{\varepsilon}(\zeta')^2 &= -\zeta^3 + \frac{C^2+1}{\varepsilon}\zeta^2 + B_1\zeta + B_2 \\ &= (\zeta_3 - \zeta)(\zeta - \zeta_2)(\zeta - \zeta_1) = P_3\,, \end{aligned} \tag{12.5.11}$$

where $\zeta_1 < \zeta_2 < \zeta_3$ are the three zeroes of the third-order polynomial P_3. Since the left-hand side of Eq. (12.5.11) is positive, the right-hand side

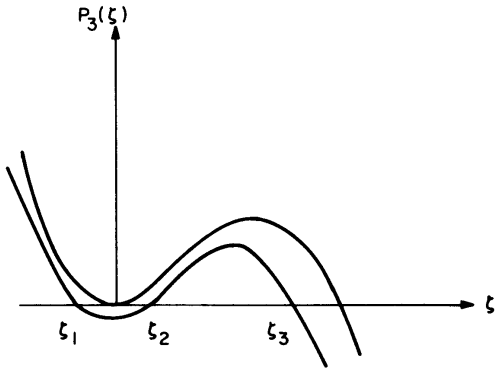

Figure 12.10: Polynomial P_3.

must be positive also for a real solution. As shown in Fig. 12.10, ζ must lie between the two zeroes ζ_3 and ζ_2 which correspond to the heights of the crest and the trough, respectively. Their difference is the total dimensionless wave height

$$(\zeta_3 - \zeta_2) = H\,. \tag{12.5.12}$$

Equation (12.5.11) can be integrated in terms of an elliptic integral by introducing

$$\zeta = \zeta_3 \cos^2\phi + \zeta_2 \sin^2\phi \quad \text{with} \quad \phi = \phi(\xi)\,, \tag{12.5.13}$$

and differentiating,

$$\zeta' = (\zeta_3 - \zeta_2)\phi'(-2\sin\phi\cos\phi)\,. \tag{12.5.14}$$

Equations (12.5.13) and (12.5.14) may be inserted into both sides of Eq. (12.5.11), yielding

$$\begin{aligned} 4\phi'^2(\zeta_3 - \zeta_2)^2 \sin^2\phi\cos^2\phi \\ &= \frac{3\varepsilon}{\mu^2}[\zeta_3(1-\cos^2\phi) - \zeta_2\sin^2\phi] \\ &\quad \cdot [-\zeta_3\cos^2\phi + \zeta_2(1-\sin^2\phi)][\zeta_1 - \zeta_3(1-\sin^2\phi) - \zeta_2\sin^2\phi] \\ &= \frac{3\varepsilon}{\mu^2}(\zeta_3-\zeta_2)^2\sin^2\phi\cos^2\phi[(\zeta_3-\zeta_1) - (\zeta_3-\zeta_2)\sin^2\phi)]\,, \end{aligned} \tag{12.5.15}$$

or, after cancellation of common factors,

$$(\phi')^2 = \frac{3}{4}\frac{\varepsilon}{\mu^2}(\zeta_3 - \zeta_1)[1 - m\sin^2\phi]\,, \tag{12.5.16}$$

with

$$m = \frac{\zeta_3 - \zeta_2}{\zeta_3 - \zeta_1}\,, \tag{12.5.17}$$

where $1 > m > 0$. Finally, we get

$$\int_0^\phi \frac{d\phi}{(1 - m\sin^2\phi)^{1/2}} \equiv F(\phi, m) = \pm\frac{(3\varepsilon)^{1/2}}{2\mu}(\zeta_3 - \zeta_1)^{1/2}(\xi - \xi_0)\,.$$

The integral is the standard form for the incomplete elliptic integral of the first kind with modulus m. The above relation can be regarded as an implicit equation for ϕ as a function of ξ. More explicitly, we denote

$$\cos\phi = \mathrm{Cn}\left[\frac{(3\varepsilon)^{1/2}}{2\mu}(\zeta_3 - \zeta_1)^{1/2}(\xi - \xi_0)\right],$$

$$\sin\phi = \mathrm{Sn}\left[\frac{(3\varepsilon)^{1/2}}{2\mu}(\zeta_3 - \zeta_1)^{1/2}(\xi - \xi_0)\right],$$

where Cn and Sn are called the cosine-elliptic and the sine-elliptic functions. From Eq. (12.5.13) the surface height is then

$$\zeta = \zeta_2 + (\zeta_3 - \zeta_2)\ \mathrm{Cn}^2\left[\frac{(3\varepsilon)^{1/2}}{2\mu}(\zeta_3 - \zeta_1)^{1/2}(\xi - \xi_0)\right], \tag{12.5.18}$$

where ζ_2 is the level of the trough measured from the mean and is negative. In physical terms the surface height is

$$\zeta = \zeta_2 + (\zeta_3 - \zeta_2)\ \mathrm{Cn}^2\left[\frac{3^{1/2}}{2}\frac{(\zeta_3 - \zeta_2)^{1/2}}{h^{3/2}}(x - Ct - x_0)\right]. \tag{12.5.19}$$

Korteweg and de Vries (1895) coined the word cnoidal for the function Cn; thus Eq. (12.5.18) or (12.5.19) is now called the *cnoidal* wave.

Since $\cos\phi$ is periodic with period 2π, $\mathrm{Cn}(z)$ is, by definition, periodic with z with the period $4K$, where

$$K = F\left(\frac{\pi}{2}, m\right) = \int_0^{\pi/2} \frac{d\phi}{(1 - m\sin^2\phi)^{1/2}} \tag{12.5.20}$$

is the standard symbol for the complete elliptic integral of the first kind. Since Cn^2 must have the period $2K(m)$, the dimensionless wavelength λ of a cnoidal wave is given by

$$\frac{(3\varepsilon)^{1/2}}{2\mu}(\zeta_3-\zeta_1)^{1/2}\lambda = 2k(m)$$

or

$$\lambda = \frac{4K(m)\mu}{[3(\zeta_3-\zeta_1)\varepsilon]^{1/2}}\,. \tag{12.5.21}$$

The wavelength depends on the amplitude through m. Equation (12.5.18) may be rewritten

$$\zeta = \zeta_2 + (\zeta_3-\zeta_2)\ \mathrm{Cn}^2\left[\frac{2K}{\lambda}(x-Ct)\right]. \tag{12.5.22}$$

The wave speed is found from Eq. (12.5.11) in terms of ζ_1, ζ_2, and ζ_3

$$\frac{C^2-1}{\varepsilon} = \zeta_1+\zeta_2+\zeta_3\,,$$

or

$$C^2 = 1+\varepsilon(\zeta_1+\zeta_2+\zeta_3)\,. \tag{12.5.23}$$

In principle, the cnoidal wave is specified by three parameters ζ_1, ζ_2, and ζ_3, or equivalently by ζ_2, ζ_3, and the wavelength λ. For engineering usage, it is more convenient to replace ζ_1, ζ_2, and ζ_3, by the wavelength λ, the mean depth and the wave height H measured vertically from trough to crest. Let us define the mean depth so that the net area occupied by fluid within a wavelength is zero:

$$\int_0^\lambda \zeta\, d\xi = 0\,,$$

which implies

$$\int_0^\pi (\zeta_3\cos^2\phi+\zeta_2\sin^2\phi)\frac{d\xi}{d\phi}\,d\phi = 0$$

because of Eq. (12.5.13). From Eq. (12.5.17) and the square root of Eq. (12.5.16), the left-hand side of the preceding integral may be rewritten

$$\int_0^{\pi/2} d\phi\frac{\zeta_1+(\zeta_3-\zeta_1)(1-m\sin^2\phi)}{(1-m\sin^2\phi)^{1/2}} = 0\,,$$

where a constant multiplier has been dropped and the symmetry of $\sin^2\phi$ about $\phi = \frac{1}{2}\pi$ is used. Using Eq. (12.5.20) and the definition

$$E(m) = \int_0^{\pi/2} (1 - m\sin^2\phi)^{1/2}\, d\phi \tag{12.5.24}$$

for the elliptic integral of the second kind, we have

$$\zeta_1 K(m) + (\zeta_3 - \zeta_1)E(m) = 0 \tag{12.5.25}$$

or

$$\zeta_1 = -\frac{E}{K}(\zeta_3 - \zeta_1) = \frac{\zeta_3 - \zeta_2}{m}\frac{E}{K} = -\frac{H}{m}\frac{E}{K}\,. \tag{12.5.26}$$

It follows from Eq. (12.5.25) that

$$\zeta_3 = -\zeta_1\left(\frac{K}{E} - 1\right) = \frac{H}{E}\left(1 - \frac{E}{K}\right), \tag{12.5.27}$$

and, finally,

$$\zeta_2 = \zeta_3 - H = \frac{H}{m}\left(1 - m - \frac{E}{K}\right). \tag{12.5.28}$$

Thus, all three parameters ζ_1, ζ_2, and ζ_3 are expressed in terms of H and m, the mean depth of h being fixed. These expressions may be inserted into Eq. (12.5.23) for the dimensionless wave speed

$$C^2 = 1 + \varepsilon\frac{H}{m}\left[-m + 2 - \frac{3E}{K}\right], \tag{12.5.29}$$

and into Eq. (12.5.21) for the dimensionless wavelength

$$\lambda = \frac{4K\mu}{(3\varepsilon)^{1/2}}\left(\frac{m}{H}\right)^{1/2}. \tag{12.5.30}$$

Now the dimensionless wave period is

$$T = \frac{\lambda}{C} = \frac{(4\mu/(3\varepsilon)^{1/2}(m/H)^{1/2}K}{[1+\varepsilon)(H/m)(-m+2-3E/K)]^{1/2}}\,. \tag{12.5.31}$$

To return to physical variables the following transformation is necessary:

$$x \to kx\,, \quad t \to k(gh)^{1/2}t\,, \quad C \to (gh)^{1/2}C\,,$$

$$\lambda \to k\lambda\,, \quad H \to \frac{H}{A}\,.$$

By using the definitions $\mu = kh$ and $\varepsilon = A/h$, it is easy to obtain that, in physical variables,

$$C^2 = gh\left[1 + \frac{H}{h}\frac{1}{m}\left(-m + 2 - 3\frac{E}{K}\right)\right], \tag{12.5.32}$$

$$\lambda = 4Kh\left(\frac{m}{3H/h}\right)^{1/2}, \tag{12.5.33}$$

$$T \cong \left(\frac{h}{g}\right)^{1/2} \frac{4K(m/3H/h^{-1})^{1/2}}{[1 + (H/h)(1/m)(-m + 2 - 3E/K)]^{1/2}}, \tag{12.5.34}$$

$$\zeta = \zeta_2 + H\ \mathrm{Cn}^2\left[\frac{2K}{\lambda}(x - Ct)\right]. \tag{12.5.35}$$

The parameter m can, in principle, be eliminated from any pair among Eqs. (12.5.32)–(12.5.34) so as to obtain relations of the type $C = C(T, H)$, $\lambda = \lambda(T, H)$, and so on. However, it is simpler to leave m as a parameter. Wiegel (l960) has plotted the wave profile ζ for various values of m ranging from 0 to almost 1; sample results are reproduced in Figs. 12.11 and 12.12.

For a better understanding of these curves it is helpful to check the following two limiting cases:

(i) $m \to 1$. In this limit $\zeta_2 \to \zeta_1$, $E(1) = 1$, and $K(1) \to \infty$; consequently, $\lambda \to \infty$ and $\mathrm{Cn}^2 u + \mathrm{sech}^2 u$. However, from Eq. (12.5.30) the ratio K/λ approaches a finite limit so that

$$\zeta = H\ \mathrm{sech}^2\frac{3^{1/2}}{2}\left(\frac{H}{h^3}\right)^{1/2}(x - Ct)$$

which is just Eq. (12.5.10). Thus, the solitary wave is the limit of the cnoidal wave with infinite wavelength. If the wavelength is kept fixed, the wave profile becomes isolated peaks, as is represented by the curve with $m \approx 1$ in Fig. 12.11. The wave speed becomes

$$C^2 = gh\left(1 + \frac{H}{h}\right).$$

This equation corresponds to the horizontal asymptotes in Fig. 12.12.

(ii) $m \to 0$. In this limit $\zeta_3 - \zeta_2 = H \to 0$, that is, the waves are infinitesimal. It can be easily shown that

$$C^2 \to gh, \quad Cn(u|m) \to Cn(u|0) \to \cos u, \quad K \to \frac{\pi}{2},$$

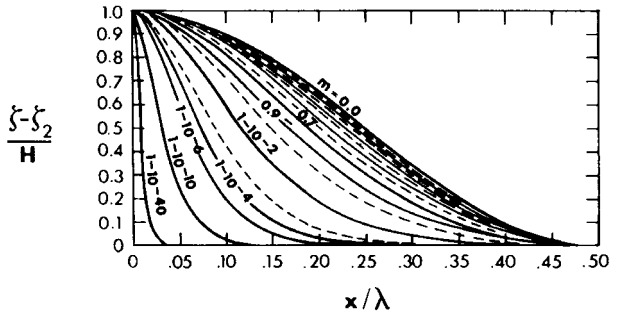

Figure 12.11: Surface profiles of cnoidal waves (from Wiegel, 1960, *J. Fluid Mech.* Reproduced by permission of Cambridge University Press).

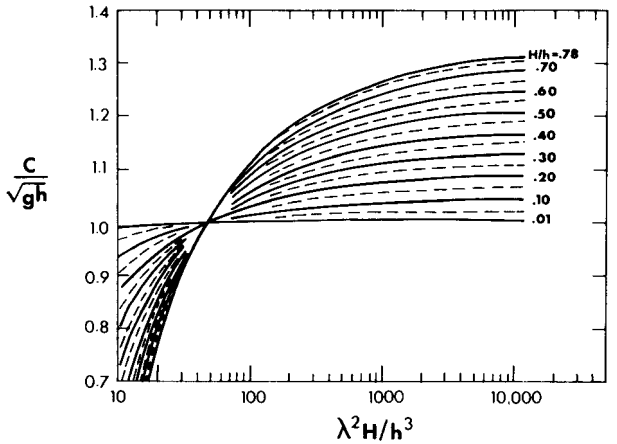

Figure 12.12: Dispersion relation of cnoidal waves (from Wiegel, 1960, *J. Fluid Mech.* Reproduced by permission of Cambridge University Press).

and

$$\zeta = \zeta_2 + H\cos^2\frac{\pi}{\lambda}(x - Ct)\,.$$

Now $\zeta_2 = -a = -\frac{1}{2}H$ so that

$$\zeta = \frac{H}{2}\cos\frac{2\pi}{\lambda}(x - Ct)$$

which is the linearized sinusoidal wave, as is evident in Fig. 12.11. In Fig. 12.12 the wave speed is represented by the horizontal line $C/(gh)^{1/2} = 1$.

A fifth-order theory has also been worked out by Fenton (1979).

12.5.3 The Korteweg–de Vries (KdV) Equation

The permanent waves studied so far depend on the following variable:

$$\xi = x - Ct = x - t + O(\varepsilon)t$$

because of Eq. (12.5.7). Thus, an observer traveling at the linearized long-wave speed, which is unity in dimensionless variables, witnesses a slow variation in time. The dimensionless scale of the slow-time variation is $1/\varepsilon$, which suggests the following variables for the more general transient evolution of nonlinear and dispersive long waves propagating in positive x direction:

$$\sigma = x - t\,, \quad \tau = \varepsilon t\,. \tag{12.5.36}$$

In terms of these variables, the derivatives become

$$\frac{\partial}{\partial x} \to \frac{\partial}{\partial \sigma}\,, \quad \frac{\partial}{\partial t} \to -\frac{\partial}{\partial \sigma} + \varepsilon \frac{\partial}{\partial \tau}\,.$$

By substituting these derivatives into the alternate Boussinesq equation (12.5.3), we get immediately

$$(\phi_\sigma)_\tau + \frac{3}{4}(\phi_\sigma^2)_\sigma + \frac{\mu^2}{6\varepsilon}\phi_{\sigma\sigma\sigma} = O(\varepsilon, \mu^2)\,.$$

To the leading order ϕ_σ may be replaced by ζ or u, that is,

$$\zeta_\tau + \frac{3}{2}\zeta\zeta_\sigma + \frac{\mu^2}{6\varepsilon}\phi_{\sigma\sigma\sigma} \cong 0\,. \tag{12.5.37}$$

This is commonly called the Korteweg–de Vies (or KdV) equation. In physical variables and stationary coordinates, Eq. (12.5.37) takes the form

$$\frac{\partial \zeta}{\partial t} + (gh)^{1/2}\left(1 + \frac{3}{2}\frac{\zeta}{h}\right)\frac{\partial \zeta}{\partial x} + \frac{h^2}{6}(gh)^{1/2}\frac{\partial^3 \zeta}{\partial x^3} = 0\,. \tag{12.5.38}$$

In the stationary frame of reference the nonlinear and the dispersion terms are small quantities of order ε and μ^2, respectively, hence one may replace $(gh)^{1/2}\zeta_x$ by $-\zeta_t$ without affecting the accuracy. Possible alternative forms for Eq. (12.5.38) are:

$$\zeta_t + (gh)^{1/2}\zeta_x + \frac{3}{2}(gh)^{1/2}\frac{\zeta}{h}\begin{pmatrix} \zeta_x \\ -\dfrac{1}{(gh)^{1/2}}\zeta_t \end{pmatrix}$$

$$+ \frac{h^2}{6}(gh)^{1/2}\begin{bmatrix} \zeta_{xxx} & \text{(12.5.39a)} \\ -\dfrac{1}{(gh)^{1/2}}\zeta_{xxt} & \text{(12.5.39b)} \\ \dfrac{1}{(gh)}\zeta_{xtt} & \text{(12.5.39c)} \\ -\dfrac{1}{(gh)^{3/2}}\zeta_{ttt} & \text{(12.5.39d)} \end{bmatrix} = 0\,.$$

It is easy to check that none of these forms will alter the linearized dispersion relation to the accuracy $O(\varepsilon, \mu^2)$. The permanent solitary and cnoidal waves can also be deduced from Eq. (12.5.37) by assuming $\zeta = \zeta(\sigma - C\tau)$; the details are left as an exercise.

12.6 Nonlinear Dispersive Standing Waves on a Horizontal Bottom

In studying the interaction between two trains of permanent waves propagating in two different directions, Benney and Luke (1964) found that the interaction effect remained $O(\varepsilon)$ times smaller than the primary waves, as long as $\tau = \varepsilon t = O(1)$ and the angle of intersection was greater than $O(\mu)$. This conclusion implies that two permanent nonlinear waves that do not travel in the same direction may be superimposed to give another leading-order solution to the Boussinesq equations. In particular, standing waves can be constructed by adding two opposite-going cnoidal waves. To show this result, it is convenient and sufficient to begin with Eq. (12.5.3).

We introduce the multiple-scale expansion

$$\Phi = \phi^{(0)}(x, t; \tau) + \varepsilon\phi^{(1)}(x, t; \tau) + \cdots \tag{12.6.1}$$

into Eq. (12.5.3) and get

$$\phi^{(0)}_{tt} - \phi^{(0)}_{xx} = 0\,, \tag{12.6.2}$$

$$\phi^{(1)}_{tt} - \phi^{(1)}_{xx} = \frac{1}{3}\frac{\mu^2}{\varepsilon}\phi^{(0)}_{xxtt} - \left[(\phi^{(0)}_x)^2 + \frac{1}{2}(\phi^{(0)}_t)^2\right]_t - 2\phi^{(0)}_{t\tau}\,. \tag{12.6.3}$$

The general solution to Eq. (12.6.2) is

$$\phi^{(0)} = \phi^+(\sigma_+;\tau) + \phi^-(\sigma_-;\tau)\,, \tag{12.6.4}$$

where

$$\sigma_\pm = x \mp t\,. \tag{12.6.5}$$

Thus, ϕ^+ and ϕ^- travel to the right and left, respectively. Equation (12.6.3) may be written

$$\begin{aligned}-4\frac{\partial^2\phi^{(1)}}{\partial\sigma_+\partial\sigma_-} &= 2\frac{\partial}{\partial\tau}\frac{\partial\phi^+}{\partial\sigma_+} + 3\frac{\partial\sigma^+}{\partial\sigma_+}\frac{\partial^2\phi^+}{\partial\sigma_+^2} + \frac{1}{3}\frac{\mu^2}{\varepsilon}\frac{\partial^4\phi^+}{\partial\sigma_+^4} - 2\frac{\partial}{\partial\tau}\frac{\partial\phi^-}{\partial\sigma_-}\\ &\quad - 3\frac{\partial\sigma^-}{\partial\sigma_-}\frac{\partial^2\phi^-}{\partial\sigma_-^2} + \frac{1}{3}\frac{\mu^2}{\varepsilon}\frac{\partial^4\phi^-}{\partial\sigma_-^4} + \frac{\partial^2\phi^+}{\partial\sigma_+^2}\frac{\partial\phi^-}{\partial\sigma_-} - \frac{\partial\phi^+}{\partial\sigma_+}\frac{\partial^2\phi^-}{\partial\sigma_-^2}\,.\end{aligned} \tag{12.6.6}$$

For $\phi^{(1)}$ not to grow linearly with σ_+ or σ_-, the first and second lines on the right-hand side of Eq. (12.6.6) must vanish separately. Writing

$$\zeta^+ = -\phi_t^+ = \phi_{\sigma_+}^+\,, \quad \text{and} \quad \zeta^- = -\phi_t^- = -\phi_{\sigma_-}^-\,, \tag{12.6.7}$$

we obtain

$$\frac{\partial\zeta^+}{\partial\tau} + \frac{3}{2}\zeta^+\frac{\partial\zeta^+}{\partial\sigma_+} + \frac{\mu^2}{6\varepsilon}\frac{\partial^3\zeta^+}{\partial\sigma_+^3} = 0 \tag{12.6.8}$$

and

$$-\frac{\partial\zeta^-}{\partial\tau} + \frac{3}{2}\zeta^-\frac{\partial\zeta^-}{\partial\sigma_-} + \frac{\mu^2}{6\varepsilon}\frac{\partial^3\zeta^-}{\partial\sigma_-^3} = 0\,. \tag{12.6.9}$$

Thus, the right- and left-going waves are decoupled and satisfy their own Korteweg–de Vries (KdV) equations separately. To the leading order, $\zeta^{(0)}$, which corresponds to $\phi^{(0)}$, may be constructed by superposition:

$$\zeta^{(0)} = \zeta^+(\sigma_+;\tau) + \zeta^-(\sigma_-;\tau)\,. \tag{12.6.10}$$

Consider a one-dimensional tank in the spatial domain $0 \le x \le \pi$. If

$$\zeta^+ = F(-\sigma_+;\tau) \quad \text{and} \quad \zeta^- = F(\sigma_-;\tau)\,, \tag{12.6.11}$$

then the corresponding velocity field

$$u^{(0)} = -F(-\sigma_+;\tau) + F(\sigma_-;\tau) \tag{12.6.12}$$

vanishes at the left wall $x = 0$ for all t. In order for $u^{(0)}$ to vanish also at $x = \pi$ we require

$$-F(t-\pi;\tau) + F(t+\pi;\tau) = 0\,,$$

which implies that $F(\sigma;\tau)$ is periodic in σ with the period 2π. A cnoidal wave of unit amplitude meets all these conditions:

$$F(\sigma;\tau) = f_2 + (f_3 - f_2)\,\mathrm{Cn}^2\left[\left(\frac{3\varepsilon}{2\mu^2}(f_3 - f_1)\right)^{1/2}(\sigma + \gamma\tau); m\right], \tag{12.6.13}$$

$$\frac{\varepsilon}{\mu^2} = \frac{4mK^2}{3\pi^2}\,, \tag{12.6.14a}$$

$$\gamma = \frac{1}{m}\left(1 - \frac{3}{2}\frac{E}{K}\right) - \frac{1}{2}\,, \tag{12.6.14b}$$

$$f_1 = -\frac{E}{mK}\,, \tag{12.6.14c}$$

$$f_3 = f_2 + 1 = \frac{1}{m}\left(1 - \frac{E}{K}\right). \tag{12.6.14d}$$

The standing wave is given by

$$\zeta^{(0)} = F((1+\gamma\varepsilon)t - x) + F((1+\gamma\varepsilon)t + x) \tag{12.6.15}$$

with the dimensionless period of

$$T = 2\pi(1+\gamma\varepsilon)^{-1}\,. \tag{12.6.16}$$

The dimensionless crest-to-trough amplitude of the standing wave is 2. Given the following physical data: amplitude A_0, tank depth h, tank length L, and modal index n, the Ursell parameter

$$U_r = \frac{\varepsilon}{\mu^2} = \frac{A_0}{h}\left(\frac{L}{h}\right)^2\left(\frac{1}{n\pi}\right)^2$$

is known, and m and γ can be calculated from Eqs. (12.6.14a) and (12.6.14b), respectively. The remaining parameters f_1, f_2, and f_3 follow from Eqs. (12.6.14c) and (12.6.14d).

Figure 12.13 shows the sample history of a standing wave within half of the tank for $n = 1$ and $U_r = 1.825$. Unlike the sloshing mode of a linear standing wave, the free surface is never horizontal and fixed nodes do not

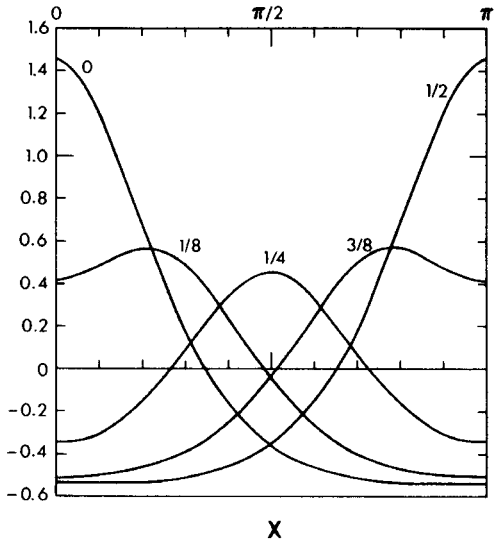

Figure 12.13: Instantaneous free surfaces of nonlinear standing waves within half of a wavelength. Numbers near each profile indicate t/T for half a period (S. R. Rogers and C. C. Mei, 1978, in an unpublished manuscript).

exist. Furthermore, a crest bounces back and forth between two end walls. As the Ursell number becomes very large, the bouncing crest approaches a solitary wave except very near the ends. These features are also present in the theory of nonlinear standing waves when kh is not small (Wehausen and Laitone, 1960, p. 665).

Lepelletier (1980) performed experiments by oscillating a shallow-water tank sinusoidally and horizontally at very low amplitudes, until steady resonance was reached. In the case where $kh = 0.314$, $A_0/h = 0.055$–0.2 (i.e., $U_r = 0.5$–2) the measurements agreed with the present theory very well. For two other cases with larger U_r (case (i) $kh = 0.157$, $A_0/h = 0.043$–0.23, $U_r = 1.72$–9.32; case (ii) $kh = 0.107$, $A_0/h = 0.04$–0.075, $U_r = 3.5$–7.0), appreciable quantitative discrepancies existed which were attributed to the strictly sinusoidal excitation.

Returning to Eq. (12.6.6), the next order correction is

$$\varepsilon\phi^{(1)} = \varepsilon\left[\phi_+^{(1)} + \phi_-^{(1)}\frac{1}{4}\left(\phi^-\frac{\partial\phi^+}{\partial\sigma_+} - \phi^+\frac{\partial\phi^-}{\partial\sigma_-}\right)\right], \tag{12.6.17}$$

where $\phi_+^{(1)})(\sigma_+)$ and $\phi_-^{(1)})(\sigma_-)$ are the homogeneous solutions to the KdV equations (12.6.8) and (12.6.9) and are indeterminate until cubic terms of

the order $O(\varepsilon^2, \varepsilon\mu^2, \mu^4)$ are examined. The remaining terms in Eq. (12.6.17) represent the weak effect of interaction and can be straightforwardly calculated (Benney and Luke, 1964).

12.7 Evolution of an Initial Pulse

Since mid-1960's, the KdV equation has been the object of intensive research, as it describes a wide range of nonlinear dispersive waves in different branches of physics. Extensive numerical studies of the KdV equation by Zabusky and Kruskal (1965) for periodic boundary conditions have shown that an initial hump goes through recurring stages of disintegration into, and recombination of, pulses, each of which has the properties of a solitary wave. These solitary waves travel at different speeds and may pass through one another. After the encounter, the solitary waves leave each other with the original features preserved; the only effect of the interaction is a change of phase. Because these features are common in the physics of particles such as electrons, protons, and so on, Zabusky and Kruskal coined the word *soliton* for a solitary wave.

In a landmark paper, Gardner, Greene, Kruskal, and Miura (1967) reported an analytical solution to the initial-value problem due to a disturbance of finite length in an infinite domain, $|x| < \infty$. Subsequent development stimulated by this work has had a profound impact on the study of nonlinear waves not only in fluids but also in numerous branches of physics and engineering. This section is intended as an introduction to this expanding literature. More extensive expositions may be found in Ablowitz and Segur (1981), Karpman (1975), Gardner et al. (1974), Lamb (1980), Scott et al. (1973), Miura (1974, 1976), and Whitham (1974).

The procedure of Gardner et al. may be regarded as an extension to the classical method of Fourier transform for linear partial differential equations (Ablowitz et al., 1974). Let $u(x,t)$ be governed by $u_t = \mathcal{L}u$ where $\mathcal{L}$ is a linear differential operator in x with constant coefficients, and let the initial data $u(x,0)$ be prescribed for $|x| < \infty$. To find $u(x,t)$ for $t > 0$ we may take the exponential Fourier transform with respect to x and solve the initial-value problem for $\hat{u}(k,t)$ where k is the transform variable. Afterward the inverse Fourier transform is performed for $u(x,t)$. In the nonlinear problem here, the Fourier transform is replaced by the mapping into a linear eigenvalue problem (or direct scattering problem, step I). We then look for some information regarding the transient evolution of the eigenvalue

problem from the given initial data (step II). Finally, an inverse mapping is performed to determine the transient solution (step III). The inverse mapping involves the so-called inverse scattering theory which is a linear problem. Therefore, by this indirect procedure the nonlinear problem is replaced by a series of linear problems.

In the following discussions, the original arguments of Gardner et al. are followed.

First we switch to their convention and write the KdV equation in the form

$$\eta_t - 6\eta\eta_x + \eta_{xxx} = 0 \tag{12.7.1}$$

which can be achieved by making the transformation

$$\zeta \to -4\eta\,, \quad \sigma \to \frac{\mu}{(6\varepsilon)^{1/2}}x\,, \quad \tau \to \frac{\mu}{(6\varepsilon)^{1/2}}t$$

to Eq. (12.5.37). The initial data $\eta(x,0)$ is prescribed for $|x| < \infty$. For later use we express the solitary wave of amplitude $\frac{1}{2}f^2$ by

$$\eta = -\frac{f_2}{2}\,\mathrm{sech}^2\frac{f}{2}(x - f^2 t)\,. \tag{12.7.2}$$

For step I, the transformed problem turns out to center around the Schrödinger equation

$$\psi_{xx} + (\lambda - \eta)\psi = 0 \tag{12.7.3}$$

where $\eta = \eta(x,t)$ with t being a parameter. In a typical quantum-mechanical problem, the *potential* η is prescribed, and the task is to find the eigenvalues λ and the eigenfunctions. Consider the case where $\eta < 0$ in a finite region, but vanishes sufficiently fast for $|x| \to \infty$. It is known that there are then two kinds of eigenvalue problems. On one hand the negative eigenvalues form a discrete spectrum, $\lambda = \lambda_n = -k_n^2$, $n = 1, 2, 3, \ldots$; the associated eigenfunctions ψ_n vanish at infinity, hence are called *bound states*. Their asymptotic behavior at infinity is

$$\begin{aligned} \psi_n &\sim c_n e^{-k_n x}\,, \; x \sim \infty\,, \\ &\sim d_n e^{k_n x}\,, \quad x \sim -\infty\,, \end{aligned} \tag{12.7.4}$$

where c_n and d_n are the normalization constants chosen so that

$$\int_{-\infty}^{\infty} \psi_n^2\, dx = 1 \quad \text{all} \quad n\,. \tag{12.7.5}$$

In general, k_n, c_n, and d_n, depend on the parameter t. On the other hand, the positive eigenvalues $\lambda = k^2 > 0$ form a continuous spectrum and the eigenfunction for each k has the following asymptotic behavior:

$$\psi \sim a(k,t)e^{-ikx}\,, \quad x \sim -\infty\,, \tag{12.7.6a}$$

$$\psi \sim e^{-ikx} + b(k,t)e^{ikx}\,, \quad x \sim \infty\,. \tag{12.7.6b}$$

Clearly, for each of these k's, ψ describes a direct scattering problem where a is the transmission coefficient and b is the reflection coefficient; both coefficients depend on t.

For step II, a surprising discovery of Gardner et al. is that the eigenvalues of Eq. (12.7.3) do not vary with time if $\eta(x,t)$ in Eq. (12.7.3) satisfies the KdV equation (12.7.1) and vanishes sufficiently fast as $|x| \to \infty$. This result can be verified by solving η from Eq. (12.7.3) and substituting into Eq. (12.7.1) to get

$$\lambda_t \psi^2 + (\psi R_x - \psi_x R)_x = 0\,, \tag{12.7.7a}$$

where

$$R = \psi_t + \psi_{xxx} - 3(\eta + \lambda)\psi_x\,. \tag{12.7.7b}$$

Taking $\lambda = \lambda_n$ to be the nth discrete eigenvalue and integrating Eq. (12.7.7a) from $x \sim -\infty$ to $x \sim +\infty$, we obtain $\lambda_n = \text{const}$ by using Eq. (12.7.5). Consequently, λ_n may be determined from the initial data of η, that is, $\eta(x,0)$. Afterward, the bound-state eigenfunctions $\psi_n(x,0)$ and the normalization constants $c_n(0)$ can be calculated for $t = 0$. The continuous eigenvalue $\lambda = k^2$ ranges from 0 to ∞; this fact does not change with time, so λ may be taken as constant. The corresponding scattering problem for $\eta(x,0)$ may be solved for the initial values $a(k,0)$ and $b(k,0)$.

We shall now show that $c_n(t)$ and $b(k,t)$ may be determined from their initial values $c_n(0)$ and $b(k,0)$ without having to know $\psi(x,t)$ for all x. Equation (12.7.7a), which is valid for both discrete and continuous spectra, may be integrated twice to give

$$\psi_t + \psi_{xxx} - 3(\eta + \lambda)\psi_x = c\psi + D\psi \int^x \frac{dx}{\psi^2}\,. \tag{12.7.8}$$

If ψ is the eigenfunction of the discrete spectrum, ψ^{-2} is exponentially large and we must insist that $D = 0$. Multiplying Eq. (12.7.8) by ψ and integrating from $x \sim -\infty$ to $x \sim +\infty$, we get

$$\frac{\partial}{\partial t}\int_{-\infty}^{\infty} \frac{1}{2}\psi^2\,dx + \int_{-\infty}^{\infty} (\psi\psi_{xx} - 2\psi_x^2 - 3\lambda\psi^2)_x\,dx = C\int_{-\infty}^{\infty} \psi^2\,dx\,.$$

Clearly, the second integral vanishes for bound states and the first integral vanishes because of Eq. (12.7.5). Hence $C = 0$ and

$$\psi_t + \psi_{xxx} - 3(\eta + \lambda)\psi_x = 0\,. \tag{12.7.9}$$

For $x \sim +\infty$, $\eta \sim 0$ and ψ is given asymptotically by Eq. (12.7.4a); the above equation now implies that

$$\dot{c}_n - 4k_n^3 c_n = 0\,,$$

hence

$$c_n(t) = c_n(0)e^{4k_n^3 t}\,. \tag{12.7.10}$$

For the continuous spectrum we consider $x \sim -\infty$ and substitute Eq. (12.7.6a) (the transmission side) into Eq. (12.7.8) to get

$$a_t + 4ik^3 a = Ca + \frac{D}{a}\int^x e^{2ikx}\,dx\,. \tag{12.7.11}$$

Since a is independent of x, D must vanish so that

$$a_t + (4ik^3 - C)a = 0\,. \tag{12.7.12}$$

Consider next $x \sim +\infty$. By substituting Eq. (12.7.6b) (the incidence side) into Eq. (12.7.8) and separating the coefficients of $e^{\pm ikx}$, we find

$$C = 4ik^3 \tag{12.7.13a}$$

and

$$\dot{b} - 8ik^3 b = 0\,. \tag{12.7.13b}$$

From Eqs. (12.7.12), (12.7.13a) and (12.7.13b), the evolution of a and b are found:

$$a(k,t) = a(k,0) \quad b(k,t) = b(k,0)e^{8ik^3 t}\,. \tag{12.7.14}$$

Step III involves the inverse scattering problem for Eq. (12.7.3). According to Gelfand and Levitan (1955), $\eta(x,t)$ can be uniquely determined if the *scattering data* $c_n(t)$ and $b(k,t)$ are known. Specifically, we must first construct the kernel

$$B(x,t) = \frac{1}{2\pi}\int_{-\infty}^{\infty} b(k,t)e^{ikx}\,dk + \sum_{n=1}^{N} c_n^2(t)e^{-k_n x}\,, \tag{12.7.15}$$

and solve the Gelfand–Levitan integral equation[6] for K,

$$K(x,y,t) + B(x+y,t) + \int_x^\infty B(y+z,t)K(x,z,t)\,dz = 0\,. \qquad (12.7.16)$$

Afterward $\eta(x,t)$ is given by

$$\eta(x,t) = -2\frac{d}{dx}K(x,x,t)\,. \qquad (12.7.17)$$

The basis of Eqs. (12.7.15)–(12.7.17) is a well-developed subject in mathematical physics but is too lengthy to be discussed here; interested readers may consult Lamb (1980) or Ablowitz and Segur (1981) for a thorough discussion.

If the initial potential leads to no reflection ($b(k,t) = 0$), so that only the discrete eigenvalues enter the kernel B, the linear Gelfand–Levitan integral equation can be solved explicitly (Gardner et al., 1967; Segur, 1973). Otherwise much information can still be deduced analytically.

Let us examine the asymptotic behavior for large x and t. Since our interest is only in $K(x,x,t)$ we need only consider

$$B(x+z,t) = \frac{1}{2\pi}\int_{-\infty}^{\infty} b(k,0)e^{ik(x+z)-8ik^3t}\,dk + \sum_{n=1}^{N} c_n^2(0)e^{[8k_n^3t-k_n(x+z)]}\,. \qquad (12.7.18)$$

For large t and $x \sim 4k_N^2 t$, where k_N is the largest of the discrete eigenvalues ($k_N > k_{N-1} > \cdots > k_2 > k_1$), the Nth term dominates among the series terms and the major contribution to the integral of Eq. (12.7.16) comes from the neighborhood of the lower limit, that is, $z = x \sim 4k_N^2 t$. Furthermore, the integral in Eq. (12.7.18) may be shown by the method of stationary phase to diminish with t as $t^{-1/3}$ (Segur, 1973). Let B be approximated by the dominant term

$$B(x+z,t) = c_n^2(0)e^{-k_N(x+z)+8k_N^3t}\,. \qquad (12.7.19)$$

The Gelfand–Levitan equation becomes

$$K(x,x,t) + c_N^2(0)e^{8k_N^3t-2k_Nx} + c_N^2(0)e^{8k_N^3t-2k_Nx} \times \int_{-\infty}^{\infty} e^{-k_Nz}K(x,z,t)\,dz \cong 0\,. \qquad (12.7.20)$$

[6] Also called the Marchenko equation (see Lamb, 1980).

Only the second variable in K pertains to the integral equation which can be solved by assuming

$$K(x,z,t) = L(x,t)e^{-k_N z}$$

so that

$$L + c_N^2(0)e^{8k_N^3 t}e^{-k_N x} + c_N^2(0)e^{8k_N^3 t}L\int_x^\infty e^{-2k_N z}\,dz = 0\,.$$

It follows that

$$K(x,x,t) = -\frac{c_N^2(0)e^{8k_N^3 t - 2k_N x}}{1 + (c_N^2(0)/2k_N)e^{8k_N^3 t - 2k_N x}}\,. \tag{12.7.21}$$

Finally, Eq. (12.7.17) gives

$$\eta = -2k_N^2\ \mathrm{sech}^2(k_N(x - x_0) - 4k_N^3 t)\,, \tag{12.7.22}$$

with

$$\frac{2k_N}{c_N^2(0)} \equiv e^{-2k_N x_0}\,.$$

In view of Eq. (12.7.2), Eq. (12.7.22) is a soliton of amplitude $2k_N^2$ and speed $4k_N^2$!

If we focus instead on large t but $x \sim 4k_n^2 t$ for any other n, the dominant term in B is the nth term in the series of Eq. (12.7.18). Evidently, a soliton of amplitude $2k_n^2$ should then travel at the speed $4k_n^2$. In summary, the initial hump eventually disintegrates into N solitons, each of which corresponds to a discrete eigenvalue of the initial "potential well." By a more elaborate analysis of the integral in Eq. (12.7.18), an oscillatory tail can be shown to follow the train of solitons. However, the lag increases with time so that the solitons are eventually alone at the front. This disintegration of an initial pulse to a train of solitons is also called *fission*.

The following results which follow the known properties of the Schrödinger equation are quoted below without proof:

1 If $\int \eta(x,0)\,dx < 0$, which corresponds to a net hump, there is at least one bound state, hence one soliton.

2 Let η_0 and l be the characteristic height and length of the initial hump, then the number of bound states N is proportional to $\eta_0^{1/2} l$.

Rather than deducing these results in general terms, let us cite an exactly solvable example which is well known in quantum mechanics (Landau

and Lifshitz, 1958, p. 70) and was first used in the present context by Zabusky (1968). If the initial profile can be expressed by

$$\eta(x,0) = -p(p+1)\,\mathrm{sech}^2 x\,, \quad p > 0\,, \tag{12.7.23}$$

the Schrödinger equation can be reduced to a hypergeometric equation. The bound-state eigenvalues are:

$$-\lambda_{N-1-n} = k_{N-1-n}^2 = (p-n)^2 = (c+N-1-n)^2 \tag{12.7.24}$$

for $n = 0, 1, 2, \ldots, N-1$ where c is the noninteger difference between $p+1$ and N. The number N of bound states is the largest integer satisfying

$$N \le p+1\,. \tag{12.7.25}$$

The success of Gardner et al. hinges, in part, on finding the proper linear eigenvalue problem [cf. (12.7.3)] which leads to constant eigenvalues. Their ingenuity has inspired further generalizations by Lax (1968), Zakharov and Shabat (1972), Ablowitz et al. (1974), and others for other equations governing nonlinear dispersive waves, all for pure initial-value problems on an infinite line. Apparently, similar treatments have not been successful for many other types of initial-boundary-value problems, for which numerical methods are now available for quantitative information (see, e.g., Zabusky (1968) and Fornberg and Whitham (1978)).

12.8 Fission of Solitons by Decreasing Depth

In general, the effects of varying depth on long waves of finite amplitudes may be studied by solving numerically the partial differential equations (12.1.47) and (12.1.48) with appropriate initial and boundary conditions. For normal incidence on one-dimensional topography, Madsen and Mei (1969) and Madsen, Mei, and Savage (1970) expressed an equivalent set of equations in quasi-hyperbolic form and solved them by the method of characteristics. It was found numerically and confirmed experimentally that a soliton traveling from one constant depth to another constant but smaller depth, disintegrates into several solitons of varying sizes, trailed by an oscillatory tail. This *fission* is clearly related to the result of the last section. Analytical confirmation and extension were provided later by Tappert and Zabusky (1971), Johnson (1973), and Ono (1972).

The analytical theory is based on a KdV equation with variable coefficients under the assumption that the scale of depth variation $\mathscr{L}$ is

$L\varepsilon^{-1}$, that is, much longer than wavelength L inherent in Eqs. (12.1.47) and (12.1.48). Let us, therefore, approximate Boussinesq equations further. After normalization and noting $h_x = O(\varepsilon)$, $h_{xx} = O(\varepsilon^2)$, and so on, we get

$$\zeta_t + (\varepsilon\zeta + h)u]_x = 0\,, \tag{12.8.1}$$

$$u_t + \varepsilon u u_x + \zeta_x - \frac{\mu^2}{3} h^2 u_{xxt} = 0\,. \tag{12.8.2}$$

Let the following new variables be introduced:

$$X = \varepsilon x\,, \quad \xi = \frac{1}{\varepsilon}\int^X h^{1/2}\,dX - t \tag{12.8.3}$$

so that $h = h(X)$ with $h = 1$, $X \le X_0$, and ξ is the coordinate moving at the local linear wave speed. With the following changes

$$\frac{\partial}{\partial t} \to \frac{\partial}{\partial \xi}\,, \quad \frac{\partial}{\partial x} \to \varepsilon\frac{\partial}{\partial X} + h^{-1/2}\frac{\partial}{\partial \xi}\,, \tag{12.8.4}$$

Equations (12.8.1) and (12.8.2) become

$$-\zeta_\xi + \varepsilon h_X u + \varepsilon h u_X + \varepsilon\zeta_\xi h^{-1/2}u + \varepsilon\zeta h^{-1/2}u_\xi + h^{1/2}u_\xi = 0\,,$$

$$-h^{-1/2}u_\xi + \varepsilon u u_\xi + \varepsilon h^{1/2}\zeta_X + \zeta_\xi + \frac{\mu^2}{3}h^{3/2}u_{\xi\xi\xi} = 0\,.$$

Adding the two equations above and using the leading-order approximation $u \cong h^{-1/2}\zeta$, we get, to the leading order,

$$2h^{1/2}\zeta_X + \frac{1}{2}\frac{h_X}{h^{1/2}}\zeta + \frac{3}{h}\zeta\zeta_\xi + \frac{\mu^2}{3\varepsilon}h\zeta_{\xi\xi\xi} = 0\,. \tag{12.8.5}$$

This extended KdV equation was deduced by Kakutani (1971) and Johnson (1973) and may be expressed in several forms. For example, let us apply the following transformation (Ono, 1972):

$$\zeta = -4h^2\psi\,, \quad \tau = \frac{\mu^2}{6\varepsilon}\int_{X_0}^X h^{1/2}\,dX\,, \quad \xi = \frac{\mu^2}{6\varepsilon}\sigma\,, \tag{12.8.6}$$

where the exponents of h are chosen so as to remove most of the variable coefficients. Equation (12.8.5) reduces to

$$\psi_r - 6\psi\psi_\sigma + \psi_{\sigma\sigma\sigma} + \nu(\tau)\psi = 0\,, \tag{12.8.7}$$

where

$$\nu = \frac{9}{4}\frac{h_X}{h^{3/2}}\left(\frac{6\varepsilon}{\mu^2}\right) \tag{12.8.8}$$

represents the effect of variable depth. Any finite-difference scheme devised for the KdV equation works for Eq. (12.8.7) as well (see Johnson, 1972).

To apply Eq. (12.8.7) to soliton fission by a shelf, Johnson and Ono proceeded along the following intuitive line inherent in the WKB approximation. A pair of integral laws are first derived which relate the initial and the end states of the transition. With the assumption that the soliton preserves its qualitative shape while climbing the transition, the two integral laws give the size and width of the pulse at the end of the transition, thereby specifying the initial data for the shallower shelf. The solution of the previous section can then be employed to find the eventual number of solitons.

Integrating Eq. (12.8.7) with respect to σ from $-\infty$ to ∞, we get

$$\frac{\partial}{\partial\tau}\int_{-\infty}^{\infty}\psi\,d\sigma+(-3\psi^2+\psi_{\sigma\sigma})_{-\infty}^{\infty}+\nu(\tau)\int_{-\infty}^{\infty}\psi\,d\sigma=0\,.$$

If ψ and its derivatives are assumed to vanish at infinities, then

$$\left(\exp\int_0^{\tau}\nu\,d\tau\right)\int_{-\infty}^{\infty}\psi\,d\sigma=\text{const}\equiv\mathscr{I}\,. \tag{12.8.9}$$

Multiplying Eq. (12.8.7) by ψ and integrating with respect to σ, we get

$$\frac{\partial}{\partial\tau}\int_{-\infty}^{\infty}\frac{\psi^2}{2}\,d\sigma+\left[-2\psi^3+\psi\psi_{\sigma\sigma}-\frac{1}{2}\psi_\sigma^2\right]_{-\infty}^{\infty}+2\nu\int_{-\infty}^{\infty}\frac{\psi^2}{2}\,d\sigma=0\,,$$

which may be integrated with respect to τ to give

$$\left(\exp 2\int_0^{\tau}\nu\,d\tau\right)\int_{-\infty}^{\infty}\psi^2\,d\sigma=\text{const}=\mathscr{E}\,. \tag{12.8.10}$$

Equations (12.8.9) and (12.8.10) are two invariants of the approximate equation (12.8.7). From Eq. (12.8.8), it may be shown that

$$\exp\int_0^{\tau}\nu\,d\tau=h^{9/4}\,,$$

hence $\mathscr{I}$ and $\mathscr{E}$ may be written

$$\mathscr{I}=h^{9/4}\int_{-\infty}^{\infty}\psi\,d\sigma \tag{12.8.11a}$$

and

$$\mathscr{E}=h^{9/2}\int_{-\infty}^{\infty}\psi^2\,d\sigma\,. \tag{12.8.11b}$$

Let us apply these invariants to a soliton climbing from a sea of unit depth on the left, over a smooth transition, to a horizontal shelf of smaller depth $h < 1$. We choose two stations X_0 and X_1 such that X_0 is at least half a wavelength before the transition, and X_1 is equally far after the transition; the corresponding τ values are $\tau = 0$ and $\tau = \tau_1$. For $L/\mathscr{L} = O(\varepsilon)$, it is reasonable to expect that the incident soliton retains roughly its pulse shape; hence

$$\psi = -\frac{\alpha^2}{2}\,\mathrm{sech}^2\beta(\sigma - C_\tau) \tag{12.8.12}$$

gives a good description. The parameters α and β are local height and length measures, being equal to α_0 and β_0 at $\tau = 0$, and to α_1 and β_1 at $\tau = \tau_1$. With these values, two algebraic equations are obtained from Eqs. (12.8.11a, b) for α_1 and β_1 which can be solved in terms of α_0 and β_0:

$$\alpha_1^2 = \alpha_0^2 h^{-9/4}\,, \quad \beta_1 = \beta_0\,.$$

Now assume that the initial pulse is a soliton so that $\alpha_0 = 2$ and $\beta_0 = 1$. At the beginning of the shelf the pulse parameters must be $\alpha_1^2 = 4h^{-9/4}$ and $\beta_1 = 1$, or,

$$\psi = -2h^{-9/4}\,\mathrm{sech}^2(\sigma - \text{phase}) \tag{12.8.13}$$

which is no longer a soliton. Note from Eq. (12.8.6) that the peak amplitude changes according to

$$\frac{\zeta_1}{\zeta_0} \sim h^{-1/4} \tag{12.8.14}$$

(Ostrovsky and Pelinovskiy, 1970) which is the same as Green's law governing linear sinusoidal waves.

The known shape of the pulse at the beginning of the shelf, that is, Eq. (12.8.13), can be used as the initial data of the initial-value problem of Section 11.7. Using the results (12.7.23)–(12.7.25), we may conclude that N solitons will emerge ultimately if N is a positive integer and

$$N(N+1) > 2h^{-9/4} > (N-1)N \tag{12.8.15a}$$

or

$$\left(\frac{N(N+1)}{2}\right)^{-4/9} > h > \left(\frac{(N-1)N}{2}\right)^{-4/9}\,. \tag{12.8.15b}$$

This simple result was found by Tappert and Zabusky (1971), Johnson (1973), and Ono (1972) and is in accord with the numerical solution of the Boussinesq equations by Madsen and Mei (1969) and the numerical solution of Eq. (12.8.5) by Johnson (1972).

It should be remarked that for still longer transition $L/\mathscr{L} = O(\varepsilon^2)$, say, an incident soliton no longer emerges as a single pulse upon reaching the shelf. Since the coefficient ν in Eq. (12.8.7) is slowly varying in τ (e.g., $\nu(\varepsilon\tau)$), the WKB perturbation analysis may be applied. In this way Ko and Kuehl (1978) found a low shelf trailing behind the primary pulse (see also Kaup and Newell, 1978).

The approximation (12.8.5), valid for wave propagation to the right, cannot account for reflection by the transition which, however, can be predicted by the more complete equations of Boussinesq (Peregrine, 1967; Madsen and Mei, 1969). In particular, Peregrine notes that weak reflection should be describable by the linearized Airy equations for variable depth, which can be handled analytically by the method of characteristics. The result is approximately a flat plateau having twice the length of the transition. If the slope of the transition is s, then the physical height of the plateau is $\frac{1}{2}s(\frac{1}{3}A/h)^{1/2}h$ where A is the amplitude of the incident soliton.

Miles (1979) points out that the invariant $\mathscr{E}$ implies energy conservation since $d\sigma \propto h^{-1/2}\,dx$ and $u \cong \zeta h^{-1/2}$ to the first order,

$$\mathscr{E} \propto h^{1/2}\int_{-\infty}^{\infty}\zeta^2\,d\sigma \sim \int_{-\infty}^{\infty}\zeta^2\,dx\,;$$

the last integral above is twice the total potential energy and is equal to the total energy by equipartition. The invariant $\mathscr{I}$ may be recast as

$$\mathscr{I} \propto h^{3/4}\int_{-\infty}^{\infty}\zeta\,dx$$

which has no direct physical meaning. Miles further notes that Eq. (12.8.5) does not conserve mass, that is

$$\mathfrak{M} = \int_{-\infty}^{\infty}\zeta\,dx \neq \text{const}\,,$$

and that $\mathscr{I}$ and $\mathfrak{M}$ are both conserved only by accounting for reflection and the secondary shelf of Ko and Kuehl. This observation is consistent with the fuller solution of Peregrine (1967).

Extensions of the preceding considerations for slowly varying width and depth may be found in Miles (1979, 1980 and the references therein).

12.9 Viscous Damping of Solitary Waves

In his experiments with solitary waves, Russell (1838) also studied the effects of viscous damping. A proper theory, however, did not appear until a century later (Keulegan, 1948). Because of nonlinearity and aperiodicity of the wave, the necessary damping analysis is different in detail from that for periodic waves. Apparently unaware of Keulegan's work, Ott and Sudan (1970) studied the same problem in a more general physical context and applied a perturbation analysis similar to that in Chapter Nine. Damping of cnoidal waves has been examined more recently by Issacson (1976) and Miles (1976).

In this section we shall rederive Keulegan's results by the perturbation method[7] of Ott and Sudan.

If the length scale of the solitary wave is λ, the time scale is $\lambda(gh)^{-1/2} = \lambda/C$ with $C = (gh)^{1/2}$. The laminar boundary-layer thickness is of the order δ where $\delta = (\nu\lambda/C)^{1/2}$. Since the length scale λ for solitary waves may be defined by $\lambda/h = \varepsilon^{-1/2}$ where $\varepsilon = A_0/h$, the ratio of δ to the water depth is

$$\alpha = \frac{\delta}{h} = \left(\frac{\nu}{Ch}\right)^{1/2} \varepsilon^{-1/4} . \tag{12.9.1}$$

In typical experiments, $O(\varepsilon) = 0.1$, $\nu = 10^{-2}$ cm s^2, $h = O(20$ cm$)$, the value of α is ~ 0.0033 which is very small. Even if ν is taken to be 1 cm s^2 in order to approximate a turbulent boundary layer, α is still just 0.033. Therefore, the inviscid approximation is expected to remain valid in most of the fluid.

Let us recall the integrated equation of mass conservation

$$\frac{\partial\zeta}{\partial t} + h\frac{\partial\bar{u}}{\partial x} + \frac{\partial(\bar{u}\zeta)}{\partial x} = 0 . \tag{12.9.2}$$

The integrated equation of momentum conservation must now include the effect of shear stress acting at the bottom

$$\frac{\partial\bar{u}}{\partial x} + \bar{u}\frac{\partial\bar{u}}{\partial x} + g\frac{\partial\zeta}{\partial x} + \frac{gh^2}{3}\frac{\partial^3\zeta}{\partial x^3} = \frac{\tau_n}{h} . \tag{12.9.3}$$

For a laminar boundary layer the bottom shear stress is given by

$$\tau_b = -\nu\left.\frac{\partial u}{\partial z}\right|_{z=-h} . \tag{12.9.4}$$

[7] Details presented here were worked out by Dr. Philip L. F. Liu in 1974, at the suggestion of C. C. Mei. Some errors exist in Ott and Sudan.

Note that u, being the local velocity, depends on z, but $\bar{u}$ does not. To help recognize the relative magnitude of each term, the following normalized variables are used:

$$\zeta' = \frac{\zeta}{A_0}, \quad x' = \frac{x}{\lambda}, \quad t' = \frac{tC}{\lambda}, \quad \bar{u}' = \bar{u}\left(\frac{A_0}{h}C\right)^{-1}$$

$$u' = u\left(\frac{A_0}{h}C\right)^{-1}, \quad z' = \frac{z+h}{\delta}. \tag{12.9.5}$$

The dimensionless equations are, after primes are omitted,

$$\frac{\partial \zeta}{\partial t} + \frac{\partial \bar{u}}{\partial x} + \varepsilon \frac{\partial \bar{u}\zeta}{\partial x} = 0, \tag{12.9.6}$$

$$\frac{\partial \bar{u}}{\partial t} + \frac{\partial \zeta}{\partial x} + \varepsilon \bar{u}\frac{\partial \bar{u}}{\partial x} + \frac{\varepsilon}{3}\frac{\partial^3 \zeta}{\partial x^3} = -\alpha \frac{\partial u}{\partial z}\bigg|_0. \tag{12.9.7}$$

Since $\alpha \ll \varepsilon$, we expect that viscosity may be ignored to the order $O(\varepsilon)$. The resulting equations lead to the solitary wave. Suppose that the coordinate transformation (12.5.36) is used, then Eqs. (12.9.6) and (12.9.7) become

$$\varepsilon \frac{\partial \zeta}{\partial \tau} - \frac{\partial \zeta}{\partial \sigma} + \frac{\partial \bar{u}}{\partial \sigma} + \varepsilon \frac{\partial}{\partial \sigma}(\bar{u}\zeta) = 0,$$

$$\varepsilon \frac{\partial \bar{u}}{\partial \tau} - \frac{\partial \bar{u}}{\partial \sigma} + \frac{\partial \bar{\zeta}}{\partial \sigma} + \varepsilon \zeta \frac{\partial \zeta}{\partial \sigma} + \frac{\varepsilon}{3}\frac{\partial^3 \zeta}{\partial \sigma^3} = -\alpha \frac{\partial u}{\partial z}\bigg|_0.$$

The sum of the two equations above gives

$$\frac{\partial}{\partial \tau}(\bar{u}+\zeta) + \frac{\partial}{\partial \sigma}(\bar{u}\zeta) + \zeta \frac{\partial \zeta}{\partial \sigma} + \frac{1}{3}\frac{\partial^3 \zeta}{\partial \sigma^3} = -\frac{\alpha}{\varepsilon}\frac{\partial u}{\partial z}\bigg|_0. \tag{12.9.8}$$

Let us assume that $\varepsilon^2 \ll \alpha \ll \varepsilon$; we may substitute $\bar{u} = \zeta$ into the preceding equation and obtain, with an error of $O(\varepsilon^2)$,

$$\frac{\partial \zeta}{\partial \tau} + \frac{3}{2}\zeta \frac{\partial \zeta}{\partial \sigma} + \frac{1}{6}\frac{\partial^3 \zeta}{\partial \sigma^3} = -\frac{\alpha}{2\varepsilon}\frac{\partial u}{\partial z}\bigg|_0, \tag{12.9.9}$$

where $\alpha/\varepsilon \ll 1$.

Without terms of $O(\alpha/\varepsilon)$, the inviscid solitary wave is, in dimensionless variables,

$$\zeta = a\ \mathrm{sech}^2\left[\frac{(3a)^{1/2}}{2}\left(\sigma - \frac{a}{2}\tau\right)\right]. \tag{12.9.10}$$

Since the bottom stress is expected to induce a slow decay, a new slow variable is introduced,

$$\tilde{\tau} = \alpha\tau \tag{12.9.11}$$

which characterizes the attenuation, that is, $a = a(\tilde{\tau})$. Moreover, the phase speed must also vary slowly through a, hence we introduce

$$\rho = \sigma - \frac{1}{2\alpha}\int^{\tilde{\tau}} a(\tilde{\tau}')\,d\tilde{\tau}' = \sigma - \frac{1}{2}\int^{\tau} a(\tau')\,d\tau' \tag{12.9.12}$$

in accordance with our earlier experience with slowly varying media. Assuming the perturbation series

$$\begin{aligned}
\zeta &= \zeta_0(\rho,\tilde{\tau}) + \alpha\zeta_1(\rho,\tilde{\tau}) + \cdots,\\
\bar{u}(x,t) &= \bar{u}_0(\rho,\tilde{\tau}) + \alpha\bar{u}_1(\rho,\tilde{\tau}) + \cdots,\\
u(x,z,t) &= u_0(\rho,z,\tilde{\tau}) + \alpha u_1(\rho,z,\tilde{\tau}) + \cdots,
\end{aligned} \tag{12.9.13}$$

and noting that

$$\frac{\partial}{\partial\sigma} = \frac{\partial}{\partial\rho}, \quad \frac{\partial}{\partial\tau} = -\frac{a}{2}\frac{\partial}{\partial\rho} + \alpha\frac{\partial}{\partial\tilde{\tau}},$$

we obtain from Eq. (12.9.9) that

$$-\frac{a}{2}\frac{\partial\zeta_0}{\partial\rho} + \frac{3}{2}\zeta_0\frac{\partial\zeta_0}{\partial\rho} + \frac{1}{6}\frac{\partial^3\zeta_0}{\partial\rho^3} = 0 \tag{12.9.14a}$$

and

$$-\frac{a}{2}\frac{\partial\zeta_1}{\partial\rho} + \frac{3}{2}\frac{\partial}{\partial\rho}(\zeta_0\zeta_1) + \frac{1}{6}\frac{\partial^3\zeta_1}{\partial\rho^3} = -\frac{1}{2}\frac{\partial u_0}{\partial z}\bigg|_0 - \frac{\partial\bar{u}_0}{\partial\tilde{\tau}}. \tag{12.9.14b}$$

The solution to Eq. (12.9.14a) is simply

$$\zeta_0 = a\,\operatorname{sech}^2\frac{(3a)^{1/2}}{2}\rho. \tag{12.9.15}$$

Following Ott and Sudan (1970), we introduce the operators $\mathscr{L}_0$ and $\mathscr{L}_1$ and rewrite Eqs. (12.9.14a) and (12.9.14b) as

$$\mathscr{L}_0\,\zeta_0 \equiv \frac{\partial}{\partial\rho}\left[\frac{1}{6}\frac{\partial^2}{\partial\rho^2} + \frac{3}{4}\zeta_0 - \frac{a}{2}\right]\zeta_0 = 0 \tag{12.9.16a}$$

and

$$\mathcal{L}_1\,\zeta_1 = \frac{\partial}{\partial\rho}\left[\frac{1}{6}\frac{\partial^2}{\partial\rho^2} + \frac{3}{2}\zeta_0 - \frac{a}{2}\right]\zeta_1 = -\frac{1}{2}\frac{\partial u_0}{\partial z}\bigg|_0 - \frac{\partial\bar{u}_0}{\partial\tilde{\tau}}\,. \qquad (12.9.16b)$$

By straightforward partial integration, it can be shown that $\mathcal{L}_0$ and $\mathcal{L}_1$ are adjoint operators of each other, namely,

$$\int_{-\infty}^{\infty} d\rho(\zeta_0\,\mathcal{L}_1\,\zeta_1 - \zeta_1\,\mathcal{L}_0\,\zeta_0) = 0\,. \qquad (12.9.17)$$

Because of Eqs. (12.9.16a) and (12.9.16b), Eq. (12.9.17), implies a solvability condition for ζ_1

$$\int_{-\infty}^{\infty}\zeta_0\left(-\frac{1}{2}\frac{\partial u_0}{\partial z}\bigg|_0 - \frac{\partial\bar{u}_0}{\partial\tilde{\tau}}\right)d\rho = 0 \qquad (12.9.18)$$

which gives a constraining equation for a. Note that up to this point the discussion is easily modified if the damping mechanism is a turbulent boundary layer.

It is now necessary to calculate the bottom stress to the leading order in terms of α. In the stationary reference frame the velocity in the boundary layer can be approximated by

$$u_0 = \bar{u}_0 + u_b\,,$$

where $\bar{u}_0$ is the inviscid approximation and u_b is the boundary-layer correction. In terms of the dimensionless variables of Eq. (12.9.5), u_b satisfies

$$\frac{\partial u_b}{\partial t} = \frac{\partial^2 u_b}{\partial z^2} \qquad (12.9.19)$$

to the required accuracy. In the moving reference frame of ρ, $\tilde{\tau}$, and z, the preceding equation may be written

$$-\frac{\partial u_b}{\partial\rho} = \frac{\partial^2 u_b}{\partial z^2}\,, \qquad (12.9.20)$$

since $\partial/\partial t \cong -\partial/\partial\sigma \cong -\partial/\partial\rho$. The boundary conditions are

$$\begin{aligned} u_b(\rho, z, \tilde{\tau}) = -\bar{u}(\rho, \tilde{\tau}) = -\zeta_0\,, \quad z = 0 \\ u_b \to 0\,, \quad z \to \infty\,. \end{aligned} \qquad (12.9.21)$$

Since $-\rho$ plays the role of time, the "initial" condition is

$$u_b = 0\,, \quad \rho \to +\infty\,.$$

It should be stressed that the velocities $\bar{u}_0$ and u_b are measured in the rest frame, although the space coordinate ρ refers to a moving frame. Because the disturbance $-\bar{u}_b(\rho, \tilde{\tau})$ is effectively bounded in the range $|\rho| = O(1)$, u_b is expected to vanish for $\rho \to -\infty$ also. Thus, we can take the exponential Fourier transform with respect to ρ:

$$\tilde{u}_b(k) = \int_{-\infty}^{\infty} u_b e^{-ik\rho}\, d\rho\,.$$

From Eq. (12.9.20) it follows that

$$\frac{\partial^2 \tilde{u}_b}{\partial z^2} = -ik\tilde{u}_b\,.$$

The solution which is bounded for $k \to \pm\infty$ is

$$u_b = -\frac{1}{2\pi}\int_{-\infty}^{\infty} dk\, e^{ik\rho}\tilde{\zeta}_0 \exp\left[\sqrt{\frac{|k|}{2}}z(-1 + i\ \mathrm{sgn}\, k)\right].$$

Substituting the inverse transform of $\tilde{\zeta}_0$ into the preceding formula, we obtain

$$\begin{aligned} u_b(\rho, z, \tilde{\tau}) &- \frac{1}{2\pi}\int_{-\infty}^{\infty} d\rho'\zeta_0(\rho')\int_{-\infty}^{\infty} dk\, e^{ik(\rho-\rho')}e^{-\sqrt{|k|/2}z} \\ &\times\left[\cos\left(\mathrm{sgn}\, k\sqrt{\frac{|k|}{2}}z\right) + i\sin\left(\mathrm{sgn}\, k\sqrt{\frac{|k|}{2}}z\right)\right] \\ &-\frac{1}{\pi}\int_{-\infty}^{\infty} d\rho'\zeta_0(\rho')\int_0^{\infty} dk\, e^{-\sqrt{k/2}z} \\ &\times\left[\cos k(\rho-\rho')\cos\sqrt{\frac{k}{2}}z - \sin k(\rho-\rho')\sin\sqrt{\frac{k}{2}}z\right] \\ &= -\frac{1}{\pi}\int_{-\infty}^{\infty} d\rho'\zeta_0(\rho')\int_0^{\infty} dk\, e^{-\sqrt{k/2}z}\cos\left[k(\rho-\rho') + \sqrt{\frac{k}{2}}z\right]. \end{aligned} \tag{12.9.22}$$

Keulegan further transformed Eq. (12.9.22) to the following single integral:

$$u_b = -\frac{2}{\sqrt{\pi}}\int_0^{\infty} ds\, e^{-s^2}\zeta_0(\theta) \quad \text{where} \quad \theta = \frac{z^2}{4s^2} + \rho\,. \tag{12.9.23}$$

Details are left in Appendix 12.B. After some manipulation, the shear stress on the bottom can be calculated,

$$-\frac{1}{2}\frac{\partial u_0}{\partial z}\bigg|_0 = -\frac{1}{2}\frac{\partial u_b}{\partial z}\bigg|_0 = -\sqrt{\frac{3}{\pi}}a^{3/2}\int_0^\infty ds$$

$$\times \operatorname{sech}^2\left[\frac{\sqrt{3a}}{2}(\rho+s^2)\right]\tanh\left[\frac{\sqrt{3a}}{2}(\rho+s^2)\right]. \qquad (12.9.24)$$

Since $\bar{u}_0 \cong \zeta_0$, we may differentiate Eq. (12.9.15) to obtain

$$-\frac{\partial \bar{u}_0}{\partial \tilde{\tau}} = -\frac{da}{d\tilde{\tau}}\operatorname{sech}^2\left(\frac{\sqrt{3a}}{2}\rho\right)\left\{1-\frac{\sqrt{3a}}{2}\rho\tanh\left(\frac{\sqrt{3a}}{2}\rho\right)\right\}. \qquad (12.9.25)$$

Equations (12.9.24) and (12.9.25) may be substituted into Eq. (12.9.18), yielding

$$\int_{-\infty}^{\infty} d\rho\, a\operatorname{sech}^2\frac{\sqrt{3a}}{2}\rho\left\{\sqrt{\frac{3}{\pi}}a^{3/2}\int_0^\infty ds\operatorname{sech}^2\left[\frac{\sqrt{3a}}{2}(\rho+s^2)\right]\right.$$

$$\left.\times\tanh\left[\frac{\sqrt{3a}}{2}(\rho+s^2)\right]+\left(\operatorname{sech}^2\frac{\sqrt{3a}}{2}\rho\right)\left[1-\frac{\sqrt{3a}}{2}\rho\tanh\frac{\sqrt{3a}}{2}\rho\right]\frac{da}{d\tilde{\tau}}\right\}=0. \qquad (12.9.26)$$

With the change of variables

$$r=\frac{\sqrt{3a}}{2}\rho, \quad S=(3a)^{1/4}2^{-1/2}s,$$

Eq. (12.9.26) may be transformed to

$$\frac{da}{d\tilde{\tau}}\int_0^\infty dr(\operatorname{sech}^4 r)(1-r\tanh r)+a^{5/4}\int_{-\infty}^{\infty}dr\left(\frac{2}{\pi}3^{1/2}\right)^{1/2}$$

$$\times\operatorname{sech}^2 r\int_0^\infty dS[\operatorname{sech}^2(r+S^2)][\tanh(r+S^2)]=0. \qquad (12.9.27)$$

We leave it as an exercise to show that the first single integral above is unity; the second double integral has been evaluated numerically by Keulegan and is approximately π^{-1}. Hence, from Eq. (12.9.27),

$$\frac{da^{-1/4}}{d\tilde{\tau}} \cong -\frac{1}{4}\left(\frac{2\cdot 3^{1/2}}{\pi^3}\right)^{1/2} = -0.08356$$

which gives the law of attenuation:

$$1 - a^{-1/4} = -0.0836\tilde{\tau} \tag{12.9.28a}$$

or, in physical variables,

$$\left(\frac{A_0}{A}\right)^{1/4} = 1 + 0.08356 \left(\frac{\nu\lambda}{C}\right)^{1/2} \frac{1}{\lambda}\frac{Ct}{h}\,. \tag{12.9.28b}$$

Using the fact that $\lambda = h(h/A_0)^{1/2}$, we have, at last,

$$A^{-1/4} = A_0^{-1/4} + 0.08356 \left(\frac{\nu}{(gh)^{1/2}h^{3/2}}\right)^{1/2} \frac{Ct}{h}\,, \tag{12.9.29}$$

where Ct is essentially the distance traveled by the solitary wave. This formula has been verified against the measurements of Russell.

Experiments with a rough bottom have been performed by Ippen and Kulin (1957), Ippen and Mitchell (1957), Özhan and Shi-igai (1977), and Naheer (1978). Theories based on an empirical formula for the bottom stress have been proposed, but they are not yet completely satisfactory when compared to experiments.

Finally, it is worth remarking that Eq. (12.9.18), which is the mathematical result of the Fredholm alternative, also has the physical meaning of energy conservation. Returning to physical variables, letting $x' = x - Ct$ and using $\bar{u}_0 \cong \zeta$, we may rewrite Eq. (12.9.18)

$$\frac{\partial}{\partial t}\rho h \int_{-\infty}^{\infty} dx' \bar{u}_0^2 = -\mu \int_{-\infty}^{\infty} dx' \bar{u}_0 \frac{\partial u_0}{\partial z}\bigg|_0\,. \tag{12.9.30}$$

The left-hand side is the rate of change of the total wave energy per unit length of crest. Consider the viscous dissipation in the boundary layer

$$-\int_{-\infty}^{\infty} dx' \int_{-\infty}^{\infty} \mu \left(\frac{\partial u_0}{\partial z}\right)^2 dx = -\int_{-\infty}^{\infty} dx' \int_{-\infty}^{\infty} \mu \left(\frac{\partial u_b}{\partial z}\right)^2 dz\,.$$

The integrand may be written

$$\mu \left(\frac{\partial u_b}{\partial z}\right)^2 = \mu \frac{\partial}{\partial z}\left(u_b \frac{\partial u_b}{\partial z}\right) - \mu\mu_b \frac{\partial^2 u_b}{\partial z^2}\,. \tag{12.9.31}$$

Using the physical form of Eq. (12.9.20)

$$-\rho C \frac{\partial u_b}{\partial x'} = \mu \frac{\partial^2 u_b}{\partial z^2}\,,$$

we get, by integrating Eq. (12.9.31),

$$\int_0^\infty \mu \left(\frac{\partial u_b}{\partial z}\right)^2 dz = -\mu\mu_b \frac{\partial u_b}{\partial z}\bigg|_0 + \rho C \int_0^\infty dz \int_{-\infty}^\infty dx' u_b \frac{\partial u_b}{\partial x'} .$$

The last term may be integrated with respect to x' and the result is zero. Using the boundary condition at the bottom, $u_b = -\bar{u}_0$, we obtain

$$-\int_{-\infty}^\infty dx \int_0^\infty \mu \left(\frac{\partial u_b}{\partial z}\right)^2 dz = -\mu \int_0^\infty dz \int_{-\infty}^\infty dx \bar{u}_0 \frac{\partial u_b}{\partial z}\bigg|_0 .$$

Therefore, Eq. (12.9.30), or its dimensionless form (12.9.18), simply states that the rate of change of wave energy is due to dissipation. Equation (12.9.30) was first derived by Boussinesq (1878) and can be modified for other types of dissipation.

12.10 Remarks on Modeling Large-Scale Tsunamis

Most of the large-scale tsunamis are caused by ruptures at the edges of great tectonic plates covering the earth. The extent of the fault of these ruptures is usually very large. For example, the Alaskan earthquake of 1964 has an approximate fault area of 100 km × 700 km, while the Chilean earthquake of 1960 has 200 km × 1000 km. While the maximum vertical displacement of the ground is only 10 m or less, the rise time at any cross section is short (< 5 s) so that a great deal of energy is suddenly imparted to the fluid.

Despite its usually low amplitude (1 m or less) in the deep ocean, tsunamis can reach large amplitudes near the coast as a result of refraction and local topography. Enormous losses of life and property have been recorded in historical accounts of tsunamis (Murty, 1977; Bolt, 1978). Clearly, efficient ways of calculating tsunami responses along the coast is of practical importance. The reliability of a forecast depends on our knowledge of the location of the epicenter, the magnitude of the earthquake, the extent of the fault area, and the type of rupture. Once estimated from seismological recordings, these data can, in principle, be used in a hydrodynamic theory to predict the propagation of water waves across the ocean and to forecast the run-up along the coast of particular concern.

Assuming that some crude estimates on the ground motion are available, one must then choose the appropriate (simple, yet accurate) equations to calculate the wave propagation. From several existing works and exchanges

at a recent tsunami meeting (Hwang and Lee, 1980), a fairly clear picture has emerged for tsunamis generated at epicenters in the deep ocean. For simplicity the one-dimensional propagation will be discussed here.

For earthquakes of the Alaskan or Chilean magnitude, the sea surface displacement above the epicenter is probably no more than 1 m. For the typical values: $L = 100$ km and $h = 4$ km, the measure of nonlinearity and dispersion are

$$\varepsilon = \frac{A}{h} = 2.5 \times 10^{-4}\,, \quad \mu^2 = \left(\frac{h}{L}\right)^2 = 1.6 \times 10^{-3}\,.$$

Thus, the long-wave approximation is suitable here. Although Boussinesq equations are the most uniformly valid, solving a simpler equation is more preferable, if appropriate. In particular, let us first focus our attention to the propagation across the ocean and assess the range of distance or time over which the simplest linear nondispersive theory is adequate.

As a rough guidance for regions not too close to shore, it is sufficient to examine the special case of constant depth and unidirectional propagation. We start with the KdV equation which includes both nonlinearity and dispersion to the leading order

$$\zeta_t + (gh)^{1/2}\left(1 + \frac{3}{2}\frac{\zeta}{h}\right)\zeta_x + \frac{h^2}{6}(gh)^{1/2}\zeta_{xxx} = 0 \tag{12.10.1}$$

in physical variables, or

$$\zeta'_{t'} + \zeta'_{x'} + \frac{3}{2}\varepsilon\zeta'\zeta'_{x'} + \frac{\mu^2}{6}\zeta'_{x'x'x'} = 0 \tag{12.10.2}$$

in the following dimensionless variables:

$$t = \frac{L}{(gh)^{1/2}}t'\,, \quad x = Lx'\,, \quad \zeta = A\zeta'\,, \tag{12.10.3}$$

where x and x' refer to the stationary frame. Assuming that ε and μ^2 are both small, we expand

$$\zeta' = \zeta_0 + \varepsilon\zeta_1 + \cdots\,.$$

The linear nondispersive equation gives the first approximation

$$\zeta_{0t'} + \zeta_{0x'} = 0\,. \tag{12.10.4}$$

In terms of $\sigma = x' - t'$ and $\xi = x' + t'$, the solution is

$$\zeta_0 = F(\sigma)\,, \tag{12.10.5}$$

where $F = \zeta'(x', 0)$ is the initial form of ζ'. The next approximation must be

$$\left(\frac{\partial}{\partial t'} + \frac{\partial}{\partial x'}\right)\zeta_1 = \frac{\partial \zeta_1}{\partial \xi} = -\frac{3}{2}FF_\sigma - \frac{1}{6}\frac{\mu^2}{\varepsilon}F_{\sigma\sigma\sigma}$$

or

$$\varepsilon\zeta_1 = \frac{1}{2}\varepsilon\xi\left(-\frac{3}{2}FF_\sigma - \frac{1}{6}\frac{\mu^2}{\varepsilon}F_{\sigma\sigma\sigma}\right). \tag{12.10.6}$$

Certainly, after a sufficiently long time or distance the perturbation expansion breaks down so that either nonlinearity or dispersion, or both, becomes important (Cole, 1968, p. 253). If the Ursell number $U_r = \varepsilon/\mu^2$ is large, nonlinearity is more important than dispersion; thus the linear and nondispersive approximation (12.10.4) can be used for fixed x' if $\varepsilon t' \ll 1$, that is,

$$\frac{A}{h}\frac{(gh)^{1/2}}{L}t \ll 1 \quad \text{or} \quad \left(\frac{g}{h}\right)^{1/2} t \ll \frac{L}{A}. \tag{12.10.7}$$

When $\varepsilon\xi$ increases to $O(1)$, Airy's nonlinear nondispersive approximation is needed. If, however, $U_r \ll 1$, then Eq. (12.10.4) is valid as long as $\mu^2\xi \ll 1$ or

$$\left(\frac{g}{h}\right)^{1/2} t \ll \left(\frac{L}{h}\right)^3 \tag{12.10.8}$$

for fixed x'. When $\mu^2\xi = O(1)$, dispersive effects must be added, but not nonlinearity. If $U_r = O(1)$, both inequalities (12.10.7) and (12.10.8) apply. When $\varepsilon t' \sim \mu^2 t' = O(1)$, the full KdV equation must be used.

To have some quantitative idea, let us take a wide fault in a deep ocean, $h = 4 \times 10^3$ m, $L = 2 \times 10^5$ m, and the maximum vertical surface displacement $A = 1$ m. Then $U_r = \varepsilon/\mu^2 = 0.625 = O(1)$ and the time for the linear nondispersive theory to break down is $t \sim (h/g)^{1/2}(L/h)^3 = 2.5 \times 10^6$ s. During this time the fastest wave has propagated the distance $x = (gh)^{1/2}t \sim 5 \times 10^5$ km, which is far greater than the typical dimension of the world oceans. Hence the linear nondispersive theory is quite adequate throughout the deep ocean, which justifies its use for transoceanic propagation as mentioned in Section 4.11.

For a fault of much smaller width, or at a short distance away from the edge of a continental shelf, the length scale L can be less. Take $h = 4$ km, $L = 2 \times 10^4$ m, and $A = 1$ m as an illustration. The time for a linear nondispersive theory to break down is $t \sim 2500$ s over which the leading

wave has only propagated $x \sim 500$ km. Since $\varepsilon/\mu^2 = 0.00125$, the linear dispersive equation must be used if the distance from the fault is comparable to or greater than 500 km.

As we have discussed in Chapter Two, dispersion is important for leading waves of a transient disturbance. Let us examine how far the linear but *dispersive* theory can be applied. In a penetrating paper, Hammack and Segur (1978) showed that for the *leading wave* a more precise measure for nonlinearity involved the volume of the initial disturbance, not just A/h. We shall present their reasoning by first normalizing Eq. (12.10.1) with

$$\alpha = \frac{x - (gh)^{1/2}t}{h}, \quad \tau = \frac{1}{6}\left(\frac{g}{h}\right)^{1/2} t, \quad f = \frac{3}{2}\frac{\zeta}{h}. \tag{12.10.9}$$

The KdV equation then becomes

$$f_\tau + 6ff_\alpha + f_{\alpha\alpha\alpha} = 0, \tag{12.10.10}$$

whose linear dispersive approximation is

$$f_\tau + f_{\alpha\alpha\alpha} = 0. \tag{12.10.11}$$

The initial condition is assumed to be

$$f(\alpha, 0) = \phi(\alpha) \left(= \frac{\frac{3}{2}\zeta(x,0)}{h}\right). \tag{12.10.12}$$

Now the dimensionless total volume for a unit length along the fault is

$$\delta = \int_{-\infty}^{\infty} \phi(\alpha)\, d\alpha = \frac{3}{2}\frac{1}{h^2}\int_{-\infty}^{\infty} \zeta(x,0)\, dx = O\left(\frac{AL}{h^2}\right). \tag{12.10.13}$$

Clearly, δ is an important parameter characterizing the magnitude of the initial disturbance. Note that the Ursell number may be written

$$U_r = \frac{L\delta}{h} = \frac{AL^2}{h^3}. \tag{12.10.14}$$

For small δ, a perturbation solution $f = \delta f_1 + \delta^2 f_2 + \cdots$ may be sought so that

$$f_{1\tau} + f_{1\alpha\alpha\alpha} = 0 \qquad \text{with} \quad \delta f_1(\alpha, 0) = \phi(\alpha) \tag{12.10.15a}$$

$$f_{2\tau} + f_{2\alpha\alpha\alpha} = -6f_1 f_{1\alpha} \quad \text{with} \quad f_2(\alpha, 0) = 0. \tag{12.10.15b}$$

The objective now is to examine when the perturbation expansion breaks down and the KdV equation is needed. The solution to Eq. (12.10.15a) can be found by Fourier transform

$$\delta f_1 = \frac{1}{2\pi}\int_{-\infty}^{\infty} \bar{\phi}(k) e^{i(k\alpha + k^3\tau)}\, dk\,, \tag{12.10.16}$$

where $\bar{\phi}$ is the exponential Fourier transform of $\phi(\xi)$. For large τ and fixed α, the method of stationary phase may be applied to yield

$$\delta f_1(\alpha,\tau) = \delta(3\tau)^{-1/3}\left[Ai(\chi) + C_1\frac{U_r}{\delta}(3\tau)^{-1/3}Ai'(\chi)\right.$$
$$\left. + C_2\left(\frac{U_r}{\delta}\right)^2(3\tau)^{-2/3}Ai''(\chi) + O\left(\frac{U_r}{\delta}\right)^3\frac{1}{3\tau}\right], \tag{12.10.17}$$

where $Ai(\chi)$ is the Airy integral with the argument

$$\chi = \frac{\alpha}{(3\tau)^{1/3}}\,. \tag{12.10.18}$$

The constants C_1 and C_2 are of order unity and depend only on the precise profile of $\phi(\alpha)$. The approximate Eq. (12.10.17) is valid if

$$\frac{U_r}{\delta}(3\tau)^{-1/3} \ll 1 \quad \text{or} \quad \left(\frac{g}{h}\right)^{1/2} t \gg \left(\frac{L}{h}\right)^3. \tag{12.10.19}$$

The second-order solution is lengthy and only the result is cited here:

$$f_2 = f_{2p} + f_{2h}\,, \tag{12.10.20}$$

where

$$f_{2p} = -\left[\int_{-\infty}^{\alpha} f_1(z,\tau)\, dz\right]^2, \tag{12.10.21}$$

$$f_{2h} = \left\{\int_{-\infty}^{\chi} Ai(z)\, dz + \frac{1}{2\pi}\int_{-\infty}^{\infty}\left[\tilde{\Theta}(k) - \frac{1}{ik}\right] e^{i(k\alpha + k^3\tau)}\, dk\right\}, \tag{12.10.22}$$

with

$$\Theta(\alpha) = \frac{1}{\delta^2}\left[\int_{-\infty}^{\alpha}\phi(\alpha)\, d\alpha\right]^2,$$

and $\tilde{\Theta}(k)$ being the Fourier transform of $\Theta(\alpha)$. f_{2p} is a particular solution satisfying the inhomogeneous governing equation, and f_{2h} is the homogeneous solution which helps satisfy the zero initial condition. For

large time, we use the first terms of Eqs. (12.10.17) and (12.10.22) to approximate the perturbation series:

$$f = \delta f_1 + \delta^2 f_2 \cong \delta(3\tau)^{-1/3} Ai(\chi) + \delta^2 \int_{-\infty}^{\chi} Ai(z)\, dz + \delta^2 \left[\int_{-\infty}^{\chi} Ai(z)\, dz\right]^2 . \qquad (12.10.23)$$

The second-order terms do not involve powers of τ.

Evidently, for nonlinearity to remain small we must have

$$(3\tau)^{-1/3} \gg \delta \quad \text{or} \quad \left(\frac{g}{h}\right)^{1/2} t \ll \left(\frac{h^2}{AL}\right)^3 \qquad (12.10.24)$$

otherwise the perturbation expansion breaks down and the full KdV equation is needed.

We can summarize the time range of validity for each approximation in Table 12.1. Hammack and Segur (1978) further studied theoretically and experimentally the oscillatory tails behind solitons and found them to be accurately described by the KdV equation (12.10.10), but not by Eq. (12.10.11). In reality, the finite length of the fault, and hence the two-dimensional spreading, must reduce the importance of nonlinearity in KdV or Boussinesq equations. More precise criteria should be sought by examining the two-dimensional KdV equation, as the problem warrants.

Table 12.1: Choice of approximate equations.

$U_r = \frac{AL^2}{h^3}$	$\tau = \left(\frac{g}{h}\right)^{1/2} \frac{t}{6}$	Approximate Equation
$\gg 1$	$\ll \frac{L}{A}$	Linear nondispersive
	$O\left(\frac{L}{A}\right)$	Nonlinear nondispersive
$\ll 1$	$\ll \left(\frac{L}{h}\right)^3$	Linear nondispersive
	$O\left(\frac{L}{h}\right)^3$	Linear dispersive
$\gtrless 0(1)$	$\left(\frac{h^2}{AL}\right)^3 \gg \tau \gg \left(\frac{L}{h}\right)^3$	Linear dispersive for leading waves
	$O\left(\frac{h^2}{AL}\right)^3$	Nonlinear dispersive for leading waves

Finally, when the leading waves of a deep ocean tsunami reach a continental shelf, the depth is drastically reduced ($h \sim 100$ m, say), then for $L = 100$ km, $A = 1$ m

$$\varepsilon = \frac{A}{h} = 10^{-2}\,, \quad \mu^2 = \left(\frac{h}{L}\right)^2 = 10^{-6}\,, \quad \text{and} \quad U_r = 10^4\,.$$

A linear nondispersive theory is valid unless

$$O(\tau) = \frac{L}{A} = 10^5 \quad \text{or} \quad O(t) = 2 \times 10^6 \text{ s}\,.$$

The corresponding travel distance is $x = (gh)^{1/2}t = O(60,000)$ km which far exceeds the width of all continental shelves. On the other hand, if a fault of width $L = 1$ km[8] occurs near the edge of the shelf, we get for the same A, $(h/L)^2 = 10^{-2}$ and $U_r = 1$. The linear nondispersive theory remains applicable if $\tau \ll L/A = 10^3$ or $t \ll 2 \times 10^4$ s. The corresponding distance traveled by the leading wave is $\ll 600$ km. Since the typical width of continental shelves is of the order of 200 km, KdV or Boussinesq equations may be needed as the basis of calculation.

12.11 Evolution of Periodic Waves Over Constant Depth–Harmonic Generation

It has long been known experimentally (Goda, 1967) that it is extremely difficult to generate long, simple harmonic progressive waves of finite amplitude in a shallow tank. Even when the wavemaker oscillates sinusoidally, the recorded waves at different stations along the tank differ from a sinusoidal wave markedly. In particular, within a period defined by the linearized theory, there are smaller secondary crests whose phase and size vary for different recording stations. A typical series of records are shown in Fig. 12.14 (Boczar-Karakiewicz, 1972) where the numbers in circles correspond to successive gauges spaced at equal intervals. A harmonic analysis of the wave records at various stations indicates that all the harmonics of the period ω vary periodically with respect to the distance from the wavemaker. This phenomenon suggests that nonlinearity

[8] This is the typical crater size of a nuclear explosion. Waves generated by such explosions near the shelf edge is of interest to the deployment of submarine weapons (see the article by G. C. Wilson, *Washington Post*, p.A.3. 1980 (3/26).

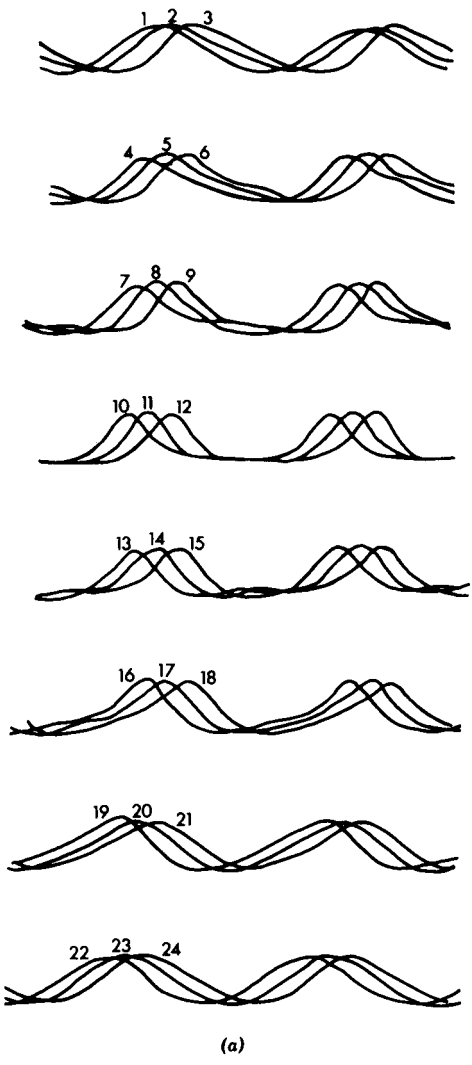

Figure 12.14: Free-surface records at various stations from the wavemaker. Numbers identify the recording stations. The distance between two adjacent stations is 30 cm. Station (I) is 80 cm from the wavemaker. (*a*) $A = 5$ cm: $H = 30$ cm, $T = 1.90$ s, $\lambda = 3.23$ m ($U_r = 0.45$); (*b*) $A = 5$ cm: $H = 20$ cm, $T = 2.75$ s, $\lambda = 3.86$ m ($U_r = 2.35$) (from Boczar-Karakiewicz, 1972 *Arch. Hydrorechniki*).

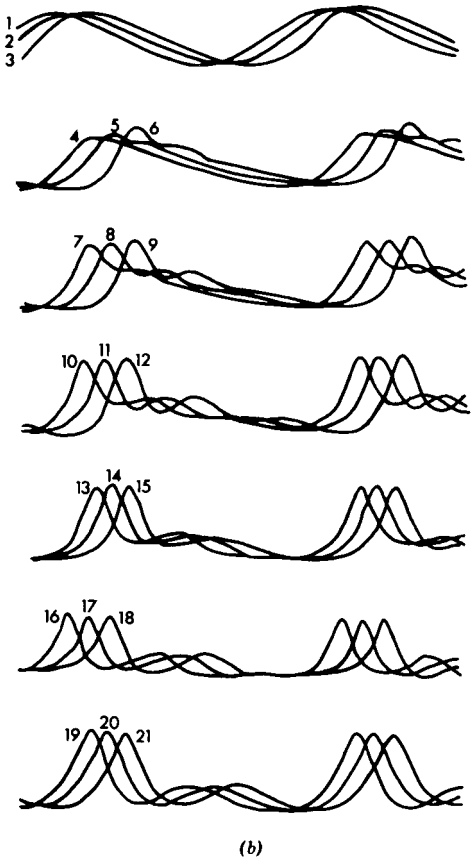

Figure 12.14: (*Continued*)

alone can render the wave spectrum nonuniform in space or unsteady in time.

In experiments with a submerged shelf of rectangular cross section, Jolas (1960) reported that a simple harmonic incident wave sometimes produced waves of higher harmonics on the transmission side. A similar phenomenon is known in the vastly different subject of *nonlinear optics*. If a monochromatic laser beam of frequency ω and high intensity shines through a slab of quartz crystal, the transmitted waves contain frequencies ω and 2ω, that is, first and second harmonics. In the most dramatic case only second harmonics are found on the transmission side; this phenomenon is now called

second harmonic generation (SHG). Thus, light of one color can emerge in a different color after passing through the quartz crystal. A theoretical explanation of this optical phenomenon was given in the celebrated paper by the physicists Armstrong, Bloembergen, Ducuing and Pershan (1962) who showed the decisive role played by the mechanism of *nonlinear resonant interaction*. At the same time, very similar theories for deep-water waves were developed independently by Phillips (1960), Benney (1962), and Bretherton (1964). Since then, these ideas have brought about fundamental advances in the dynamics of surface and internal waves.

In this section we examine the effects of nonlinear interaction in shallow water with a view to understanding the observed phenomena (Mei and Ünlüata, 1972; Bryant, 1973).

12.11.1 The Initial Development of Near-Resonant Interaction in Water of Constant Depth

Let long sinusoidal waves be generated at one end of a uniform channel of infinite length and constant depth. How do they evolve as they propagate downstream?

The KdV equation is appropriate here. For reasons explained later we choose the following form,

$$\zeta_t + \zeta_x - \frac{3}{2}\varepsilon\zeta\zeta_t - \frac{\mu^2}{6}\zeta_{ttt} = 0\,, \tag{12.11.1}$$

which corresponds to Eq. (12.5.39d). Let the characteristic time scale be $2\pi/\omega$ where ω is the frequency of the fundamental harmonic, and let the characteristic horizontal length be $(gh)^{1/2}/\omega$ so that

$$\mu = \omega\left(\frac{h}{g}\right)^{1/2}.$$

At $x = 0$, the free-surface displacement is prescribed

$$\zeta(0,t) = \frac{1}{2}a(e^{-it} + e^{it})\,. \tag{12.11.2}$$

Let us treat ε to be small and μ^2 to be arbitrary, and first try a naive expansion in powers of ε,

$$\zeta = \zeta_0 + \varepsilon\zeta_1 + \cdots\,. \tag{12.11.3}$$

At the leading order, ζ_0 satisfies the linear dispersive equation

$$\zeta_{0t} + \zeta_{0x} - \frac{\mu^2}{6}\zeta_{0ttt} = 0\,. \tag{12.11.4}$$

The following solutions

$$e^{\pm i(Kx-\Omega t)}$$

are admissible if Ω and K are related by

$$\Omega + \frac{\mu^2}{6}\Omega^3 = K\,, \tag{12.11.5}$$

or, in dimensional form, by

$$\Omega'\left(1 + \frac{1}{6}\frac{\Omega'^2 h}{g}\right) = K'(gh)^{1/2} \quad \text{where} \quad \Omega' = \omega\Omega\,, \quad K' = \frac{\omega}{(gh)^{1/2}} = K\,. \tag{12.11.6}$$

In particular, if $\Omega = n$ ($\Omega' = n\omega$ in physical variables), the corresponding wavenumber is

$$K_n = n + \frac{\mu^2}{6}n^3\,. \tag{12.11.7}$$

Among the four alternative forms of the KdV equation, Eq. (12.5.39d) [or, Eq. (12.11.1)] is chosen because its implied dispersion relation (12.11.5) is the closest to the exact linear dispersion relation

$$\Omega = \frac{K}{\mu}\tanh K\mu\,, \tag{12.11.8}$$

even for very high Ω and K. The comparison is shown in Fig. 12.15 for $\mu = (0.05)^{1/2}$. To satisfy condition (12.11.2) we take

$$\zeta_0 = \frac{1}{2}a\{\exp[i(K_1x - t) + *\} = \frac{1}{2}a\{\exp(i\phi_1) + *]\,, \tag{12.11.9}$$

where

$$\phi_1 = K_1x - t \tag{12.11.10}$$

and

$$K_1 = 1 + \frac{\mu^2}{6}\,. \tag{12.11.11}$$

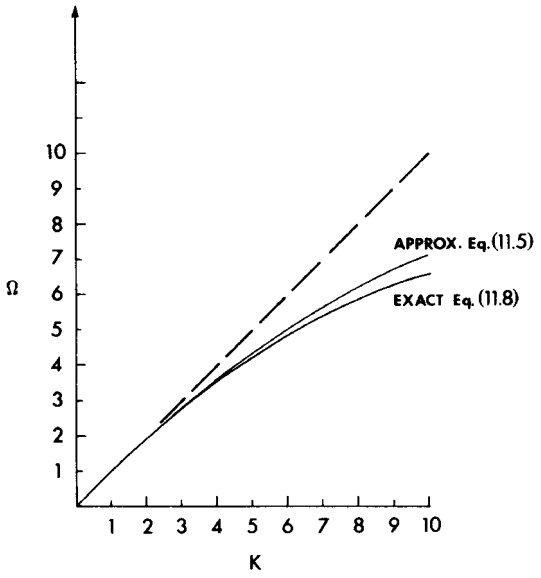

Figure 12.15: Comparison of dispersion curves for $\mu = \omega(h/g)^{1/2} = 0.05$. The straight line refers to the nondispersive limit. Ω has been normalized by the first harmonic frequency ω and K by $\omega(gh)^{-1/2}$.

At the next order, ζ_1 satisfies

$$\zeta_{1t} + \zeta_{1x} - \frac{\mu^2}{6}\zeta_{1ttt} = \frac{3}{2}\zeta_0\zeta_{0t}\,. \tag{12.11.12}$$

The nonlinear forcing term is

$$-\frac{3}{8}a^2[ie^{2i(K_1x-t)} + *] = -\frac{3}{8}a^2[ie^{2i\phi_1} + *]\,.$$

Because the *phase mismatch*

$$K_2 - 2K_1 = 2 + \frac{\mu^2}{6}2^3 - 2\left[1 + \frac{\mu^2}{6}\right] = \mu^2 \tag{12.11.13}$$

is small, the forcing term $\exp(2i\phi_1)$ is very close to the second harmonic $\exp[i(K_2x - 2t)]$ which is a homogeneous solution of Eq. (12.11.12). We therefore expect the second harmonic $e^{\pm i\phi_2}$ to be nearly resonated. The explicit solution to (12.11.12) is

$$\zeta_1 = \frac{3a^2}{8\mu^2}(e^{2iK_1x} - e^{iK_2x})e^{-2it} + * \tag{12.11.14}$$

where a homogeneous solution has been added to satisfy the boundary condition that $\zeta_1(0) = 0$. Now $\varepsilon\zeta_1$ may be regarded as a second harmonic with a slowly and periodically varying amplitude

$$\begin{aligned}\varepsilon\zeta_1 &= \frac{3}{8}\frac{\varepsilon}{\mu^2}a^2[(e^{-i\mu^2 x}-1)e^{i\phi_2}+*] \\ &= \frac{3}{8}\frac{\varepsilon}{\mu^2}a^2(-2ie^{-i\mu^2 x/2}e^{i\phi_2})\sin\frac{\mu^2}{2}x\,. \end{aligned} \tag{12.11.15}$$

In general $\varepsilon\zeta_1$ is of the order $O(\varepsilon/\mu^2)$ and is small only if $\varepsilon \ll \mu^2$. As μ diminishes to zero, $\varepsilon\zeta_1$ becomes unbounded. By expanding Eq. (12.11.15) for small εx, we find

$$\varepsilon\zeta_1 = -\frac{3}{8}a^2\varepsilon x(ie^{i\phi_2}+*) \tag{12.11.16}$$

so that the second harmonic is resonated to grow linearly as εx.

If both first and second harmonics are comparable, then their product can resonate the third harmonic $e^{\pm i\phi_3}$ also. The reason lies with the dispersion curve (Ω versus K) which is nearly straight for small μ so that $K_3 - (K_1 + K_2)$ is also small. In fact, if any two among $e^{\pm i\phi_1}$, $e^{\pm i\phi_2}$, and $e^{\pm i\phi_3}$ are present at the first order, the third can be resonated to the first order. Thus, the first three harmonics interact resonantly also. However, the corresponding phase mismatch

$$K_3 - (K_1 + K_2) \cong 3 + \frac{\mu^2}{6}3^3 - \left(1 - \frac{\mu^2}{6} + 2 + \frac{\mu^2}{6}2^3\right) = 3\mu^2 \tag{12.11.17}$$

is greater than $K_2 - 2K_1$. The maximum amplitude attainable by the third harmonic can be estimated to be only one-third of the second harmonic. By an extension of the argument, still higher harmonics can be resonated by a similar nonlinear mechanism. In particular, the nth harmonic can be resonated by any of the pairs $(1, n-1)$, $(2, n-2)$, or $(3, n-3)$. Since the smallest phase mismatch is

$$\begin{aligned} K_n - (K_1 + K_{n-1}) &= \frac{\mu^2}{6}\{n^3 - [1^3 + (n-1)^3]\} \\ &= \frac{\mu^2}{6}n(n-1)\,, \end{aligned}$$

the amplitude of the nth harmonic is roughly

$$\frac{\varepsilon}{\mu^2}\frac{2}{n(n-1)}$$

times as big as the first harmonic. The accuracy of this estimate deteriorates for large n because of the limited validity of Eq. (12.11.7).

The naive perturbation method as just described is clearly inadequate for $\varepsilon x = O(1)$. If the nonlinearity is so weak that only the first few harmonics are important, it is possible to use the method of multiple scales (Mei and Ünlüata, 1972). A more accurate method by Bryant (1973) is to assume a Fourier series which involves a large number of harmonics, as follows.

12.11.2 Governing Equations for Coupled Harmonics

The result of Eq. (12.11.16) suggests that amplitudes of the various harmonics vary in x. We therefore assume the solution

$$\zeta = \frac{1}{2}\sum_{1}^{\infty}[A_n(x)e^{in(x-t)} + A_n^*(x)e^{-in(x-t)}]\,, \tag{12.11.18}$$

where the simplest nondispersive phase function

$$\psi = x - t \tag{12.11.19}$$

is used for convenience. The following alternative is also possible:

$$\zeta = \frac{1}{2}\sum_{1}^{\infty}[B_n(x)e^{i\phi_n} + B_n^*(x)e^{-i\phi_n}]\,, \tag{12.11.20}$$

with

$$\phi_n = K_n x - nt\,. \tag{12.11.21}$$

The coefficients A_n and B_n are related by

$$A_n = B_n e^{ix(K_n - n)} = B_n e^{i(\mu^2/6)n^3 x}\,, \quad n = 1, 2, 3, \ldots\,. \tag{12.11.22}$$

Substituting Eq. (12.11.18) into the KdV equation (12.11.1), we obtain, from the linear terms,

$$\zeta_1 + \zeta_x - \frac{\mu^2}{6}\zeta_{ttt} = \frac{1}{2}\sum_{n=1}^{\infty}\left[\left(\frac{dA_n}{dx} - i\frac{\mu^2}{6}n^3 A_n\right)e^{in\psi} + *\right]$$

$$= \frac{1}{2}\sum_{n=1}^{\infty}\left[\left(\frac{dB_n}{dx}\right)e^{i\phi_n} + *\right]. \tag{12.11.23}$$

The nonlinear term in Eq. (12.11.1) can be manipulated to give

$$\begin{aligned}
&\frac{3}{4}\varepsilon(\zeta^2)_t \\
&\quad=\frac{3}{16}\varepsilon\frac{\partial}{\partial t}\left\{\left[\sum_{l=1}^{\infty}(A_l e^{il\psi}+A_l^* e^{-il\psi})\right]\left[\sum_{m=1}^{\infty}(A_m e^{im\psi}+A_m^* e^{-im\psi})\right]\right\} \\
&\quad=\frac{3}{16}\varepsilon\frac{\partial}{\partial t}\left\{\sum_{l=1}^{\infty}A_l^*A_l+\sum_{n=1}^{\infty}\left\{e^{in\psi}\left[\sum_{l=1}^{\prime}\alpha_l A_l A_{n-l}+2\sum_{l=1}^{\infty}A_l^*A_{n+l}\right]+*\right\}\right\} \\
&\quad=\frac{3}{16}\varepsilon\sum_{n=1}^{\infty}\left\{e^{in\psi}\left[\sum_{l=1}^{\prime}(-in\alpha_l)A_l A_{n-l}+(-2in)\sum_{l=1}^{\infty}A_l^*A_{n+l}\right]+*\right\}.
\end{aligned} \tag{12.11.24}$$

The inner series $\sum'$ terminates at $\frac{1}{2}n$ for even n and $\frac{1}{2}(n-1)$ for odd n. The coefficient α_l is 2 if $l=1,2,3,\ldots,\frac{1}{2}(n-1)$ and $\alpha_l=1$ if $l=\frac{1}{2}n$. Details are given in Appendix 12.C. Substituting Eqs. (12.11.23) and (12.11.24) into Eq. (12.11.1), we obtain from the coefficients of $e^{in\psi}$ that

$$\begin{aligned}
&\left(\frac{dA_n}{dx}-i\frac{\mu^2}{6}n^3A_n\right) \\
&\qquad=-i\varepsilon\frac{3}{8}\left\{\sum_{l=1}^{\prime}(n\alpha_1)A_l A_{n-1}+\sum_{l=1}^{\infty}2nA_l^*A_{n+1}\right\},\quad n=1,2,3,\ldots.
\end{aligned} \tag{12.11.25}$$

From the coefficients of $e^{-in\psi}$, conjugate equations are obtained. Equation (12.11.25) is an infinite set of coupled nonlinear ordinary differential equations for all harmonics. If nonlinearity is not too severe, the importance of higher harmonics should diminish with n. We can, therefore, truncate the Fourier series after a finite number of terms (say N) and solve N equations for N unknown coefficients A_n with given initial values at $x=0$.

If the Fourier series is truncated at $n=1$, then

$$\frac{dA_1}{dx}-i\frac{\mu^2}{6}A_1=0\,. \tag{12.11.26}$$

which is possible only when nonlinearity is very weak. A correction for the second harmonic is obtained by assuming that $A_2 \ll A_1$

$$\frac{dA_2}{dx}-i\mu^2\frac{4}{3}A_2=-i\varepsilon\frac{3}{4}A_1^2 \tag{12.11.27}$$

which may be written

$$e^{i4\mu^2 x/3}\frac{d}{dx}(e^{-i4\mu^2 x/3}A_2) = -i\varepsilon\frac{3}{4}A_1^2\,. \tag{12.11.28}$$

Subject to the initial conditions $A_1 = a_0$ and $A_2 = 0$ at $x = 0$, the solutions to Eqs. (12.11.27) and (12.11.28) are easily found to be

$$A_1 = a_0 e^{i(\mu^2/6)x}\,, \tag{12.11.29}$$

$$A_2 = \frac{3}{4}\frac{\varepsilon}{\mu^2}A_0^2(e^{i\mu^2 x/3} - e^{i4\mu^2 x/3})\,, \tag{12.11.30}$$

which may be shown to correspond to $\varepsilon\zeta_1$ in Eq. (12.11.15).

If we truncate the Fourier series after two terms, that is, disregard $A_3 = A_4 = \cdots = 0$ in the first two equations of Eq. (12.11.25) (Mei and Ünlüata, 1972; Bryant, 1973), we then have

$$\frac{dA_1}{dx} - i\frac{\mu^2}{6}A_1 = -i\varepsilon\frac{3}{4}A_1^* A_2\,, \tag{12.11.31}$$

$$\frac{dA_2}{dx} - i\mu^2\frac{4}{3}A_2 = -i\varepsilon\frac{3}{4}A_1^2\,, \tag{12.11.32}$$

or, by using Eq. (12.11.22),

$$\frac{dB_1}{dx} = -i\varepsilon\frac{3}{4}B_1^* B_2 e^{i\mu^2 x} \tag{12.11.33}$$

and

$$\frac{dB_2}{dx} = -i\varepsilon\frac{3}{4}B_1^2 e^{-i\mu^2 x}\,. \tag{12.11.34}$$

The last two equations are identical to those governing two coupled harmonics in nonlinear optics and were solved by Armstrong, Bloembergen, Ducuing, and Pershan (1962) in the following manner.

12.11.3 Exact Solution of the Two-Harmonics Problem

Let

$$B_1(x) = \rho_1 e^{i\beta_1(x)} \quad \text{and} \quad B_2(x) = \rho_2 e^{i\beta_2(x)} \tag{12.11.35}$$

so that ρ_1 and ρ_2 are the amplitudes and β_1 and β_2 are the phases. Substituting Eq. (12.11.35) into the conjugate of (12.11.33) and (12.11.34), we get

$$\rho_1' e^{-i\beta_1} - i\beta_1' \rho_1 e^{-i\beta_1} = iS\rho_1\rho_2 e^{i(\beta_1-\beta_2-\Delta x)}\,, \tag{12.11.36}$$

$$\rho_2' e^{i\beta_2} - i\beta_2' \rho_2 e^{i\beta_2} = -iS\rho_1^2 e^{i(2\beta_1-\Delta x)}\,, \tag{12.11.37}$$

where $S = \frac{3}{4}\varepsilon$, $\Delta = \mu^2$ and primes denote derivatives with respect to x. Let us introduce

$$\theta = 2\beta_1 - \beta_2 - \Delta x\,. \tag{12.11.38}$$

Equations (12.11.36) and (12.11.37) become

$$\rho_1' - i\beta_1'\rho_1 = iS\rho_1\rho_2 e^{i\theta}\,, \tag{12.11.39}$$

$$\rho_2' + i\beta_2'\rho_2 = -iS\rho_1^2 e^{i\theta}\,. \tag{12.11.40}$$

From the real parts of the two preceding equations we get

$$\rho_1' = -S\rho_1\rho^2 \sin\theta\,, \tag{12.11.41}$$

$$\rho_2' = S\rho_1^2 \sin\theta\,, \tag{12.11.42}$$

which may be combined and integrated to give

$$\rho_1^1 + \rho_1^2 = \rho_0^2 = \rho_1^2(0) + \rho_2^2(0)\,. \tag{12.11.43}$$

This relation, called the Manley–Rowe relation in electronics, asserts that a loss of energy in one harmonic must result in a gain in the other. The imaginary parts of Eqs. (12.11.39) and (12.11.40) yield

$$\beta_1' = -S\rho_2\cos\theta\,, \quad \beta_2' = -\frac{1}{\rho^2}S\rho_1^2\cos\theta\,.$$

From Eq. (12.11.38) it follows that

$$\theta' = 2\beta_1' - \beta_2' - \Delta = -\Delta - \left(2\rho_2 S - \frac{\rho_1^2}{\rho_2}S\right)\cos\theta \tag{12.11.44}$$

which, after we eliminate S from Eq. (12.11.42), and use the Manley–Rowe relation (12.11.43), may be rewritten

$$\theta' = -\Delta + \left(-\frac{2\rho_2\rho_1'}{\rho_1^2} + \frac{\rho_2'}{\rho_2} \right) \cot\theta$$

$$= -\Delta + \left(\frac{2\rho_1'}{\rho_1} + \frac{\rho_2'}{\rho_2} \right) \cot\theta \,. \tag{12.11.45}$$

In terms of the normalized variables

$$u = \frac{\rho_1}{\rho_0} \quad \text{and} \quad v = \frac{\rho_2}{\rho_0} \,, \quad \zeta = S\rho_0 x \,, \tag{12.11.46}$$

Eqs. (12.11.41), (12.11.42), (12.11.43), and (12.11.45) become

$$\frac{du}{d\zeta} = -uv\sin\theta \,, \tag{12.11.47}$$

$$\frac{dv}{d\zeta} = u^2 \sin\theta \,, \tag{12.11.48}$$

$$u^2 + v^2 = 1 \,, \tag{12.11.49}$$

$$\frac{d\theta}{d\zeta} = -\delta + \left(2\frac{du/d\zeta}{u} + \frac{dv/d\zeta}{v} \right) \cot\theta \,. \tag{12.11.50}$$

Thus, there are three unknowns u, v, and θ governed by three differential equations (12.11.47), (12.11.48), and (12.11.50). The dimensionless parameter for phase mismatch between the two harmonics is

$$\delta = \frac{\Delta}{S\rho_0} = \frac{\mu^2}{\frac{3}{4}\epsilon} = \frac{4}{3}\frac{h}{a_0}(k_1 h)^2 \tag{12.11.51}$$

which is essentially the inverse of the Ursell parameter.

A little manipulation of Eq. (12.11.50) leads to

$$\frac{d}{d\zeta}(u^2 v\cos\theta) = \delta u^2 v\sin\theta \,.$$

Upon combining the above result with an alternate form of Eq. (12.11.48)

$$\frac{\delta}{2}\frac{dv^2}{d\zeta} = \delta u^2 v\sin\theta \,, \tag{12.11.52}$$

we get

$$\frac{d}{d\zeta}(u^2 v\cos\theta) = \frac{\delta}{2}\frac{dv^2}{d\zeta}$$

which gives another integral

$$-\frac{\delta v^2}{2} + u^2 v \cos\theta = \text{const} = \Gamma_\delta \,. \tag{12.11.53}$$

The constant Γ_δ can be related to the initial data

$$\Gamma_\delta = -\frac{\delta}{2} v^2(0) + u^2(0) v(0) \cos[2\beta_1(0) - \beta_2(0)] \tag{12.11.54a}$$

$$= \Gamma_0 - \frac{\delta}{2} v^2(0) \,, \tag{12.11.54b}$$

with

$$\Gamma_0 = u^2(0) v(0) \cos[2\beta_1(0) - \beta_2(0)] \tag{12.11.54c}$$

in terms of which Eq. (12.11.53) may be written

$$u^2 v \cos\theta = \Gamma_0 + \frac{\delta}{2}[v^2 - v^2(0)] \,. \tag{12.11.55}$$

There are now two integrals for the three unknowns u, v, and θ. Only one differential equation remains to be integrated. If we eliminate u from Eq. (12.11.48) by using Eq. (12.11.49), then

$$\frac{1}{2}\frac{dv^2}{d\zeta} = v(1 - v^2)\sin\theta \,.$$

Squaring Eq. (12.11.52), we get

$$\left(\frac{1}{2}\frac{dv^2}{d\zeta}\right)^2 = u^4 v^2 \sin^2\theta = u^4 v^2 (1 - \cos^2\theta)$$

$$= v^2(1 - v^2)^2 - \left\{\Gamma_0 + \frac{\delta}{2}[v^2 - v^2(0)]\right\}^2 \equiv Q(v^2) \tag{12.11.56}$$

after using Eqs. (12.11.49) and (12.11.55). The quantity $Q(v^2)$ is a cubic polynomial for v^2. Bounded solutions exist only if $Q(r^2)$ has three real zeros $v_a^2 < v_b^2 < v_c^2$. Letting

$$Q = (v_c^2 - v^2)(v_b^2 - v^2)(v^2 - v_a^2) \,, \tag{12.11.57}$$

we get

$$\zeta = \pm \int_{v^2(0)}^{v^2(\zeta)} \frac{dv^2}{2[Q(v^2)]^{1/2}} \,, \tag{12.11.58}$$

which can be expressed in terms of elliptic integrals, as in the case of cnoidal waves. The result is

$$v^2 = v_a^2 + (v_b^2 - v_c^2)\ \mathrm{Sn}^2[(v_c^2 - v_a^2)^{1/2}(\zeta - \zeta_0), m]\,, \tag{12.11.59}$$

with

$$m = \left(\frac{v_b^2 - v_a^2}{v_c^2 - v_a^2}\right)^{1/2} < 1\,. \tag{12.11.60}$$

The period of Sn is $4K$ with

$$K = \int_0^{\pi/2} \frac{d\theta}{(1 - m^2 \sin^2\theta)^{1/2}} \tag{12.11.61}$$

so that the period of Sn^2 is $2K$. In terms of the normalized, coordinate ζ the dimensionless wavelength is

$$\lambda = \frac{2K}{(v_c^2 - v_a^2)^{1/2}}\,. \tag{12.11.62}$$

For the general case where both harmonics have nonzero initial values $u(0) \neq 0$ and $v(0) \neq 0$, numerical results can be found in Armstrong et al. (1962).

Let us examine the special case where $v(0) = 0$, $u(0) = 1$, then $\Gamma_0 = 0$ and

$$\begin{aligned} Q(v^2) &= v^2 \left\{ v^4 - \left[2 + \left(\frac{\delta}{2}\right)^2\right] v^2 + 1 \right\} \\ &= v^2 (v^2 - v_b^2)(v^2 - v_c^2)\,, \end{aligned} \tag{12.11.63}$$

where

$$v_b^2 = \frac{1}{v_c^2} = \left[\left(1 + \frac{\delta^2}{16}\right)^{1/2} + \frac{\delta}{4}\right]^{-2}\,. \tag{12.11.64}$$

The maximum modulation amplitude of v is v_b. From Eq. (12.11.60), we have

$$m = \frac{v_b}{v_c} = \frac{1}{v_c^2} = \left[\left(1 + \frac{\delta^2}{16}\right)^{1/2} + \frac{\delta}{4}\right]^{-2}\,. \tag{12.11.65}$$

As the initial amplitude a_0 increases and/or the first harmonic wavelength decreases, the Ursell parameter increases, hence δ decreases. From

Eqs. (12.11.64) and (12.11.65), v_b^2 increases while m and K both increase. Thus, the maximum second harmonic amplitude increases. Since $m \cong 1 - \frac{1}{2}\delta$ and $K \cong \frac{1}{2}\ln(32/\delta)$ for small δ (Abramowitz and Stegun, 1972, p. 591), the spatial period of modulation, which may be called the *beat* or *recurrence distance*, is, on the dimensionless scale of x [cf. Eq. (12.11.46c)]:

$$\lambda \cong \frac{2K}{2S\rho_0} \cong \frac{2}{3}\frac{\delta}{\mu^2}\ln\frac{32}{\delta}$$

which decreases with δ. Thus, for smaller δ, more energy exchange between first and second harmonics takes place within a shorter distance. Recall, however, that for sufficiently small δ the third or higher harmonics may no longer be negligible.

For very small amplitudes, $\delta \gg 1$, $m \cong (2/\delta)^2 \ll 1$ and $K \cong \pi/2$. The recurrence distance is $\lambda \cong 2\pi/\delta$ in normalized terms and $2\pi h(kh)^{-3}$ in physical terms, as is also implied by Eq. (12.11.15). Longuet–Higgins (1977b) has deduced this result more physically by considering two linearized free waves of frequencies ω and 2ω. Because of dispersion, a first-harmonic crest gains in phase relative to a second-harmonic crest. The recurrence distance is simply the distance over which the net gain is exactly one wavelength of the second harmonic.

The theory based on two interacting harmonics agrees reasonably well in both amplitude variation and recurrence distance, with the measurements of Boczar-Karakiewicz (1972), see Fig. 12.16, and of Goda (1967); comparison of recurrence distance is given in Mei and Ünlüata, (1972, Fig. 1). By extending the idea of phase gain to two cnoidal wavetrains of periods $2\pi/\omega$ and $4\pi/\omega$, and ignoring their interactions, Longuet–Higgins (1977) has also calculated the recurrence length which conforms with the experiments of Boczar-Karakiewicz. Bryant (1973) has made more accurate computations by including 11 harmonics and integrating numerically the coupled equations which are deduced from both the KdV equation and the Laplace equation with the free-surface conditions approximated only to the second order in wave slope. A sample of his results is shown in Fig. 12.17; note in particular the third harmonic and its short beat length. Thus, as a periodic small-amplitude swell propagated toward a beach, second harmonics are first generated, then third and fourth..., until the depth is so small that many harmonics are present and the wave breaks, causing further small-scale fluctuations.

Qualitatively, the present results are already relevant to a submerged shelf of length L. Let a small-amplitude simple harmonic wave of frequency

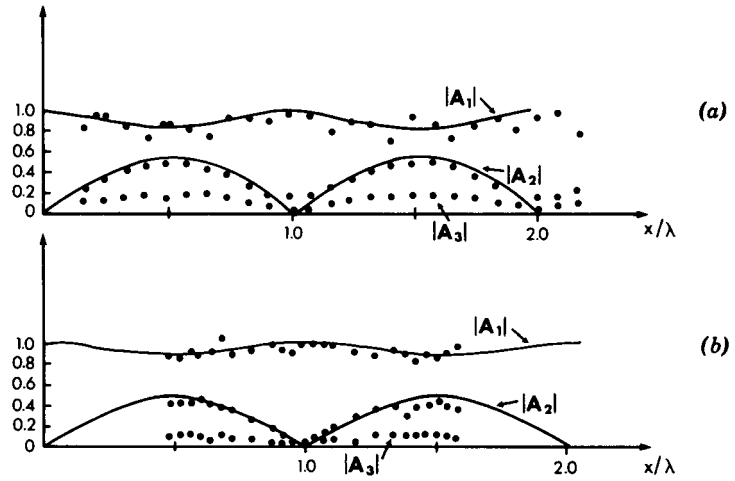

Figure 12.16: Comparison of two-harmonics theory with experiments by Boczar-Karakiewicz (1972) (comparison is due to Ü. Ünlüata, private communication). All harmonic amplitudes A_j are normalized by $|A_1(0)|$. (*a*) $\delta = 2.61$; (*b*) $\delta = 3.12$.

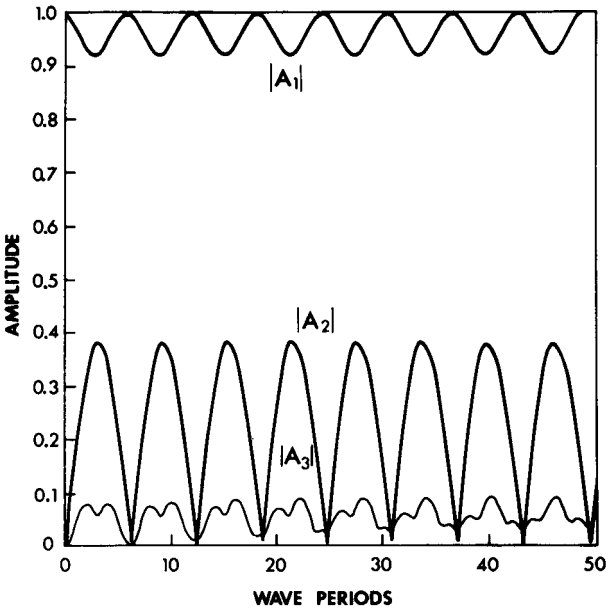

Figure 12.17: The first three harmonics using 11 coupled equations from μ-exact formulation. $\varepsilon = 0.05$; $\mu = (0.2)^{1/2}$ (from Bryant, 1973, *J. Fluid Mech.* Reproduced by permission of Cambridge University Press).

ω arrive from the left. Upon striking the shelf, the transmitted wave undergoes harmonic generation if the Ursell parameter on the shelf is not small. When L is half of the beat or recurrence distance, a large amount of second harmonic will enter the deep water on the transmission side of the shelf. On the other hand, when L is nearly equal to the beat length, very little second harmonic will be seen on the transmission side. This explanation is supported by the observations of Jolas (1960) for a submerged bar.

For variable depth involving a sandbar, an approximate theory has been given by Lau and Barcilon (1972). Otherwise, the numerical solution of Eq. (12.8.5) for slowly varying depth is straightforward. If the depth variation has the same length scale as the waves, reflection is no longer negligible and a numerical solution of Boussinesq equations is necessary (Peregrine, 1967; Madsen, Mei and Savage, 1970).

12.12 Nonlinear Resonance in a Narrow Bay

In Chapter Five the phenomenon of harbor resonance was studied on the basis of an inviscid linearized theory. For a sufficiently narrow mouth and steady forcing, the amplification was typically tenfold or larger. With some uncertainties in the friction coefficient, the effect of entrance loss was found in Chapter Six to reduce the peak amplitude. However, friction is not the only mechanism for reducing resonant amplification. Indeed, results in the preceding section suggest that nonlinearity provides an alternative mechanism in converting energy from first to higher harmonics. A quantitative assessment of nonlinear effects should be interesting and is given below for the simplest configuration of a narrow rectangular bay (Rogers and Mei, 1977).

The bay has the length L and width $2a$. The coastline is designated by the y axis and the axis of the bay coincides with the x axis. The sea depth is constant h everywhere. An incident wave arrives normally from $x \sim +\infty$.

Rogers and Mei adopted the Boussinesq equations and the following dimensionless variables:

$$t' = \omega t\,, \quad (x', y') = \frac{(x, y)\omega}{(gh)^{1/2}}\,, \quad z' = \frac{z}{h}$$

$$\zeta' = \frac{\zeta}{h}\,, \quad \mathbf{u}' = \frac{\mathbf{u}}{(gh)^{1/2}}\,. \tag{12.12.1}$$

After primes are omitted, Eqs. (12.1.36) and (12.1.37) become

$$\zeta_1 + \nabla \cdot \mathbf{u} + \nabla \cdot (\zeta \mathbf{u}) = 0\,, \tag{12.12.2}$$

$$\mathbf{u}_t + \nabla\zeta + \frac{1}{2}\nabla \cdot \mathbf{u}^2 + \frac{1}{3}\mu^2 \nabla\zeta_{tt} = 0\,, \tag{12.12.3}$$

where $\mu^2 = \omega^2 h/g \ll 1$. The normalized quantities $\mathbf{u}$ and ζ are of the order $O(\varepsilon)$. The error includes terms of the order $O(\varepsilon)^2$, $O(\varepsilon\mu^2)$, and $O(\mu^4)$.

Because of nonlinearity, the response contains higher harmonics

$$\left.\begin{matrix}\zeta(x,y,t)\\ \mathbf{u}(x,y,t)\end{matrix}\right\} = \frac{1}{2}\sum_n \begin{bmatrix}\zeta_n(x,y)\\ \mathbf{u}_n(x,y)\end{bmatrix} e^{-int}\,, \quad n = 0, \pm 1, \pm 2, \ldots \tag{12.12.4}$$

where ζ_{-n} and $\mathbf{u}_{-n}$ are the complex conjugates of ζ_n and $\mathbf{u}_n$, respectively. Substituting Eq. (12.12.4) into Eqs. (12.12.2) and (12.12.3) and separating the harmonics, we get

$$-in\zeta_n + \nabla \cdot \mathbf{u}_n + \frac{1}{2}\sum_s \nabla \cdot (\zeta_s \mathbf{u}_{n-s}) = 0\,, \tag{12.12.5}$$

$$-inu_n + \left(1 + \frac{1}{3}\mu^2 n^2\right)\nabla\zeta_n + \frac{1}{4}\sum_s \nabla \cdot (\mathbf{u}_s \cdot \mathbf{u}_{n-s}) = 0\,, \tag{12.12.6}$$

which may be combined to give

$$(\nabla^2 + k_n^2)\zeta_n = \sum_n \left[\frac{-i}{2} n\nabla \cdot (\zeta_n \mathbf{u}_{n-s}) - \frac{1}{4}\nabla^2(\mathbf{u}_s \cdot \mathbf{u}_{n-s})\right], \tag{12.12.7}$$

where

$$k_n^2 = \frac{n^2}{(1 - \frac{1}{3}\mu^2 n^2)}\,. \tag{12.12.8}$$

Although there is an infinite number of terms in the Fourier series (hence an infinite set of coupled equations (12.12.7)), in practice, truncation after a finite number of terms is necessary. In general, the task of solving the two-dimensional coupled equations is still formidable, and the mathematical statement for the radiation condition does not appear simple. If, however, the harbor mouth is sufficiently narrow, $\delta \equiv \omega a/(gh)^{1/2} \ll 1$, the radiated waves due to the piston action at the mouth must be weak. Thus, if the nonlinear effect is unimportant in the incoming waves, it remains unimportant in the ocean. A more precise reasoning is as follows. For order estimates it suffices to consider the first harmonic which is expected to

be the largest. From the linearized theory of Section 5.6.2b, it is known that the amplification factor in the harbor is proportional to $O(\delta^{-1})$, so that in the harbor $\zeta = O(A_1/\delta)$ where A_1 is the amplitude of the incident wave. By assumption $A_1/\delta = O(\varepsilon)$. From Eqs. (5.6.3) and (5.6.19) or Eq. (5.7.38), Chapter 5, the radiated wave ζ^R outside the harbor is of the order $\sim A_1 H_0^{(1)}(k_1 r)$ at resonance. Since the Hankel function is large for small r, we take the wave near the harbor entrance $r = O(\delta)$

$$O(\zeta^R) = A_1 \ln \delta = \varepsilon\delta \ln \delta$$

and

$$\zeta^I + \zeta^R = O(\varepsilon\delta)\,.$$

Hence the quadratic terms in the ocean are of the order $O(\varepsilon\delta \ln \delta)^2$ at most and are negligible compared to the nonlinear terms $O(\varepsilon^2)$ in the harbor. Thus, in the harbor we keep terms of $O(A_1/\delta) = O(\varepsilon)$ and $O(\varepsilon^2)$, while in the ocean we only keep the linear terms $O(\varepsilon\delta \ln \delta)$ and drop the nonlinear terms which are at most of $O(\varepsilon\delta \ln \delta)^2$.

In the ocean, the linear solution for each harmonic may be expressed by

$$\zeta_n = A_n \cos k_n x + \zeta_n^R\,, \tag{12.12.9a}$$

with

$$\zeta_n^R = \frac{k_n^2}{2n} \int_{-\delta}^{\delta} dy' U_n(y') H_0^{(1)}(k_n[x^2 + (y - y')^2]^{1/2})\,. \tag{12.12.9b}$$

The functions U_n are just the piston velocities corresponding to the nth harmonic and are related to the surface gradient by

$$\frac{\partial \zeta_n}{\partial x} = \frac{ik_n^2}{n} U_n\,, \quad |y| < \delta\,, \quad x = 0\,. \tag{12.12.10}$$

In the far field at a distance $O(k_1 r)$ from the entrance, the Hankel function in Eq. (12.12.9b) may be approximated to give

$$\zeta_n^R = \frac{k_n^2}{2n} \overline{U}_n k_n \delta H_0^{(1)}(k_n r)[1 + O(n\delta)]\,, \quad r = (x^2 + y^2)^{1/2} \tag{12.12.11}$$

where $\overline{U}_n$ is the average of U_n. Across the entrance, hence in the near field, the approximation of Eq. (12.12.9b) for small k_n is

$$\zeta_n^R(0,y) = \frac{k_n^2}{n}\left\{\delta\overline{U}_n + \frac{1}{\pi}\int_{-\delta}^{\delta} dy' U_n(y') \ln\frac{\gamma k_n}{2}|y-y'| + O(k_n\delta)^2 \ln k_n\delta\right\}. \tag{12.12.12}$$

If the average of Eq. (12.12.12) is taken across the entrance, then

$$\bar{\zeta}_n^R|_{x=0} = Z_n\overline{U}_n \equiv \overline{U}_n\frac{k_n^2\delta}{n} \times\left\{1 + \frac{2i}{\pi}\left(\ln k_n\delta + \ln\frac{\gamma}{2}\right) + \frac{1}{4}\iint_{-1}^{1}\ln|\alpha-\alpha'|\frac{U_n(\alpha')}{\overline{U}_n}\,d\alpha\,d\alpha'\right\}. \tag{12.12.13}$$

Taking the average of Eq. (12.12.10) and eliminating $\overline{U}_n$ with the help of Eq. (12.12.13), we get for the average of ζ_n [cf. Eq. (12.12.9a)]

$$-\frac{in}{k_n^2}Z_n\frac{\partial\bar{\zeta}_n}{\partial x} + A_n = \bar{\zeta}_n\,, \quad x=0\,, \quad |y|<\delta\,. \tag{12.12.14}$$

The quantity Z_n will be called the *entrance impedance* which depends on the profile of $U_n(y)$. Equation (12.12.14) will be viewed as a boundary condition which must be satisfied by the solution within the harbor. Assuming that $k_n\delta$ is small enough so that U_n may be approximated quasi-statically as in Section 2, we find the impedance explicitly:

$$Z_n = \frac{k_n}{n}k_n\delta\left(1 + \frac{2i}{\pi}\ln\frac{2\gamma k_n\delta}{\pi e}\right). \tag{12.12.15}$$

This approximation is good only if the higher harmonics are unimportant. That an analytical expression for Z_n is possible is due to the assumption of a straight coast and horizontal ocean bottom. For a more general coastline and ocean depth the impedance must be found numerically.

The narrowness of a harbor entrance enables us to decouple the harbor and the ocean and to study the harbor as a separate but interior boundary-value problem with $\partial\zeta_n/\partial n = 0$ on the solid boundary and Eq. (12.12.14) at the entrance. If the harbor shape and depth are not simple, direct numerical methods such as finite elements may be applied. For a narrow rectangular bay, the numerical work is less demanding since the problem is essentially one dimensional ($\partial\zeta/\partial y \sim \partial u/\partial y = O(\delta^2)$) everywhere except in the $O(\delta)$ neighborhood of the entrance. The justification follows from Section 4.1.1.

The one-dimensional version of Eq. (12.12.7) is

$$\zeta_n'' + k_n\zeta_n = -\frac{in}{2}\sum_s(\zeta_s u_{n-s})' - \frac{1}{4}\sum_s(u_s u_{n-s})'' \tag{12.12.16}$$

where $(\ )' = d(\ )/dx$. From Eqs. (12.12.5) and (12.12.6), $u_n' = in\zeta_n(1 + O(\varepsilon))$ and $u_n = -(i/n)\zeta_n'(1 + O(\varepsilon\mu)^2)$ for $n \neq 0$. Within the Boussinesq approximation we have

$$\begin{aligned}\sum_s(\zeta_s u_{n-s})' &= \sum_s(\zeta_n u_{n-s}' + \zeta_{n-s}') \\ &= \sum_{s\neq n}\left(i(n-s)\zeta_n\zeta_{n-s} - \frac{i}{n-s}\zeta_s'\zeta_{n-s}'\right),\end{aligned}$$

and

$$\begin{aligned}\frac{1}{2}\sum_s(u_s u_{n-s})'' &= \sum_s(u_{n-s}u_s'' + u_s'u_{n-s}') \\ &= \sum_{s\neq n}\frac{i}{n-s}\zeta_s'\zeta_{n-s}' - \sum_s(n-s)\zeta_s\zeta_{n-s}\,.\end{aligned}$$

Substituting these two equations into Eq. (12.12.16), we obtain

$$\zeta_n'' + k_n^2\zeta_n = \frac{1}{2}\sum_s(n^2 - s^2)\zeta_s\zeta_{n-s} - \frac{1}{2}\sum_{s\neq n}\frac{n+s}{n-s}\zeta_s'\zeta_{n-s}'\,. \tag{12.12.17}$$

Since ζ_n is independent of y, it is equal to its own average. We now impose the no-flux condition at the end $x = -L$ and Eq. (12.12.14) at the entrance, that is,

$$\frac{\partial\zeta_n}{\partial x} = 0\,, \qquad x = -L\,, \tag{12.12.18}$$

$$-\frac{in}{k_n^2}Z_n\frac{\partial\zeta_n}{\partial x} + A_n = \zeta_n\,, \quad x = 0\,. \tag{12.12.19}$$

The nonlinear truncated system of the boundary-value problems (12.12.17)–(12.12.19) can be solved numerically.

The zeroth harmonic corresponds to mean-sea-level changes ζ_0 or mean current u_0, which can be obtained by integrating the one-dimensional version of Eqs. (12.12.5) and (12.12.6)

$$u_0(x) = -\frac{1}{2}\sum_s \zeta_s u_{-s}\,, \tag{12.12.20}$$

$$\zeta_0(x) = -\frac{1}{4}\sum_s |u_s|^2 + \text{const}\,. \tag{12.12.21}$$

Note that Eq. (12.12.20) already satisfies $u_s = 0$ at $x = -l$ for all s. By properly defining the mean sea level of the ocean, $A_0 = 0$. Since $Z_0 = 0$, we have $\zeta_0(0) = 0$ by the impedance condition (12.12.19), implying that

$$\zeta_0(x) = \frac{1}{4}\sum_s |u_s(0)|^2 - |u_x(x)|^2\,. \tag{12.12.22}$$

From Eqs. (12.12.20) and (12.12.22), ζ_0 and $u_0 = O(\varepsilon^2)$, and may be omitted in the nonlinear equations for other harmonics. Spatially, the mean-sea-level change is the greatest at $x = -l$. As a function of frequency ζ_0 is resonated along with the first harmonic ζ_1.

The two-point nonlinear boundary-value problem for N harmonics can be solved by an iterative method. If the solution of the last iteration is used to linearize the nonlinear terms, then at each iterative step the resulting problem is linear and can be solved by the method of complementary functions. For details Rogers and Mei (1978) may be consulted.

Let us show some of the computed and experimental results for two bays of the same width and depth, but of different lengths, which correspond to the first and third resonant modes for the same fundamental frequency. Now it can be inferred from the linearized theory [Eq. (5.6.20), Chapter Five] that the first and third resonant modes are at $L = \frac{1}{2}\pi$, and $\frac{5}{2}\pi$ for fixed k but varying L, while all peaks are of equal height. The actual resonant values of L were found experimentally to be $L = 1.227$ and 7.23. For each bay, three different incident wave amplitudes were examined by Rogers and Mei (1978), but only two will be presented here. The dimensionless inputs are

$$L = \frac{L'\omega}{(gh)^{1/2}} = 1.227, 7.23\,, \quad \delta = \frac{a\omega}{(gh)^{1/2}} = 0.169\,,$$

$$\mu^2 = \frac{\omega^2 h}{g} = 0.257\,, \quad \varepsilon = |A_1| = 0.015, 0.04\,.$$

From the measurements, the magnitude and phase of the second and third harmonics A_2, A_3 were also obtained and used as inputs for computation. In

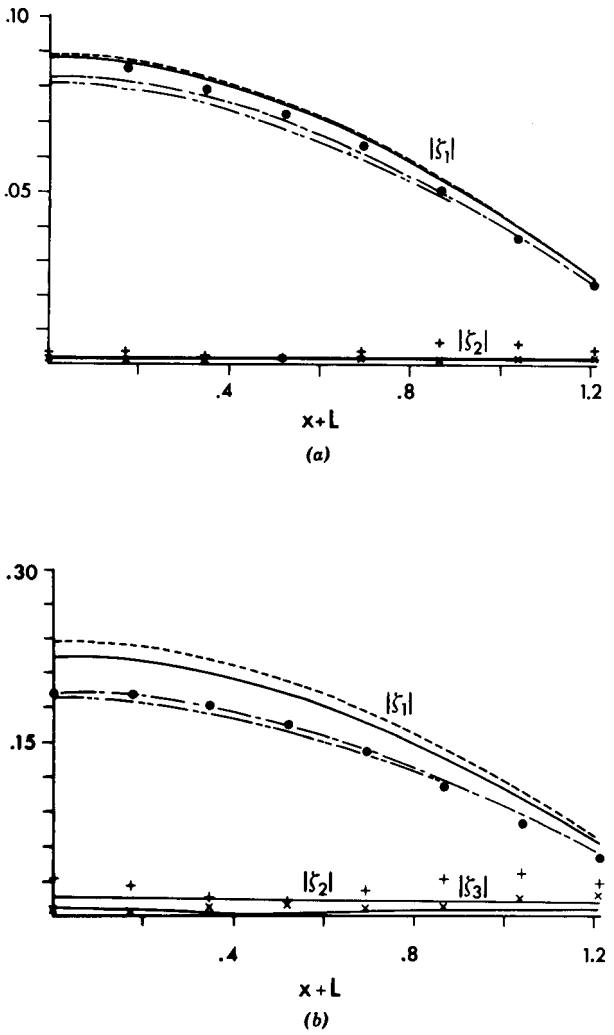

Figure 12.18: Resonance in a narrow bay. ◯, +, ×: measured amplitudes of $|\zeta_1|$, $|\zeta_2|$, and $|\zeta_3|$. Calculated first harmonic: - - - -: linear theory; _____: inviscid nonlinear theory; — · — ·: nonlinear theory with entrance loss; — - — -: nonlinear theory with entrance and boundary-layer losses. (*a*) $L' = 1.211$ ft, $A_1 = 0.015$; (*b*) $L' = 1.211$ ft, $A_1 = 0.04$ (from Rogers and Mei, 1978, *J. Fluid Mech.* Reproduced by permission of Cambridge University Press).

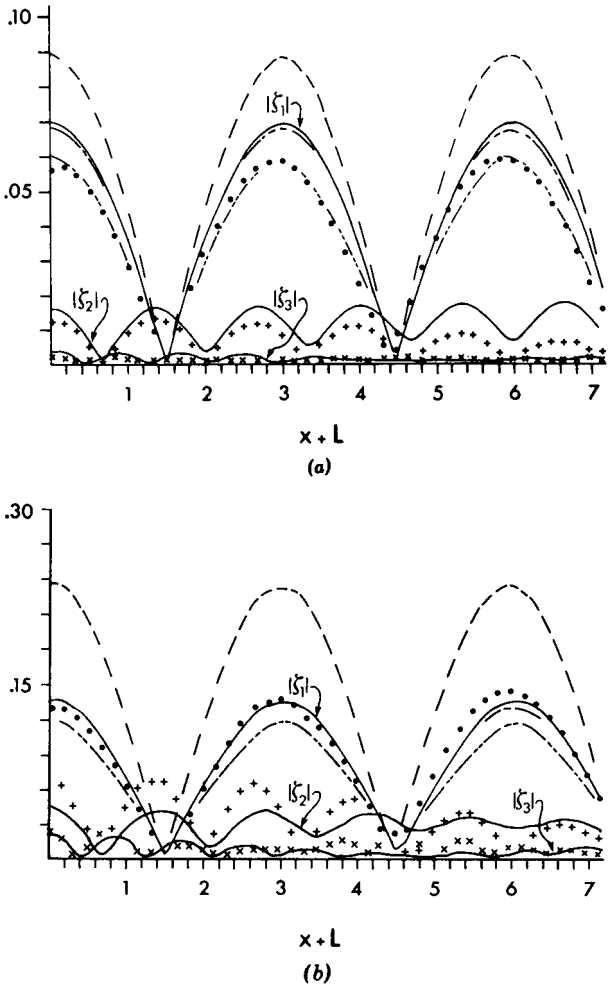

Figure 12.19: See Fig. 12.18 for caption. Calculated second and third harmonics by inviscid nonlinear theory are also shown by solid curves. (*a*) $L' = 7.136$ ft, $A_1 = 0.015$; (*b*) $L' = 7.136$ ft, $A_1 = 0.040$ (from Rogers and Mei, 1978, *J. Fluid Mech.* Reproduced by permission of Cambridge University Press).

Figs. 12.18 and 12.19 the numerical results are compared with the measured harmonics along the center line of the bay. Although minor discrepancies can be seen, they can be corrected after accounting for the entrance loss and for the laminar friction in the wall boundary layers of the bay. Several conclusions are apparent for the present problem:

1 For the shortest bay at quarter wavelength mode, a linear theory is sufficient if the entrance friction is accounted for.

2 As the bay becomes longer nonlinearity is more influential in generating higher harmonics; entrance and boundary-layer losses become less important. For a sufficiently long bay nonlinearity can overwhelm frictional effects.

A numerical study of the nonlinear response in an arbitrarily shaped harbor to transient inputs has been reported by Lepelletier (1980).

12.13 Solitons Ahead of a Ship Advancing in a River

If a slender ship travels steadily on the surface of water, waves are expected in the wake. In deep water, Kelvin's linearized theory reveals two systems of waves, the divergent and the transverse, in a wedge-like wake of half-angle equal to 19.28° (see Lamb, 1932; Stoker, 1953; Newman, 1977; or Wehausen and Laitone, 1960). For finite depth, the linearized theory shows that the half-angle rises sharply to 90° as the ship speed U increases to the phase speed $\sqrt{gh}$ of the fastest long wave. Higher than this critical speed, the transverse waves disappear while the half-angle decreases from 90° (Wehausen and Laitone 1960). Towing-tank experiments for a ship cruising steadily near the critical speed have revealed a much more complex phenomenon. In particular, in addition to the conventional waves in the wake, transient waves are radiated upstream of a steadily advancing ship (Thiews and Landweber, 1935; Izubuchi and Nagasawa, 1937). More recent experiments by Huang et al. (1983), Ertekin (1984) and Ertekin et al. (1986) have further identified these upstream waves to be solitons. The experimental setup of Ertekin is shown in Fig. 12.20, and sample records in Figs. 12.21 and 12.22. These records have stimulated much theoretical studies by Wu and Wu (1982); Cole (1985); Akylas (1984); Mei (1986); Mei and Choi (1987); Chen and Sharma (1995); and others. Studies of

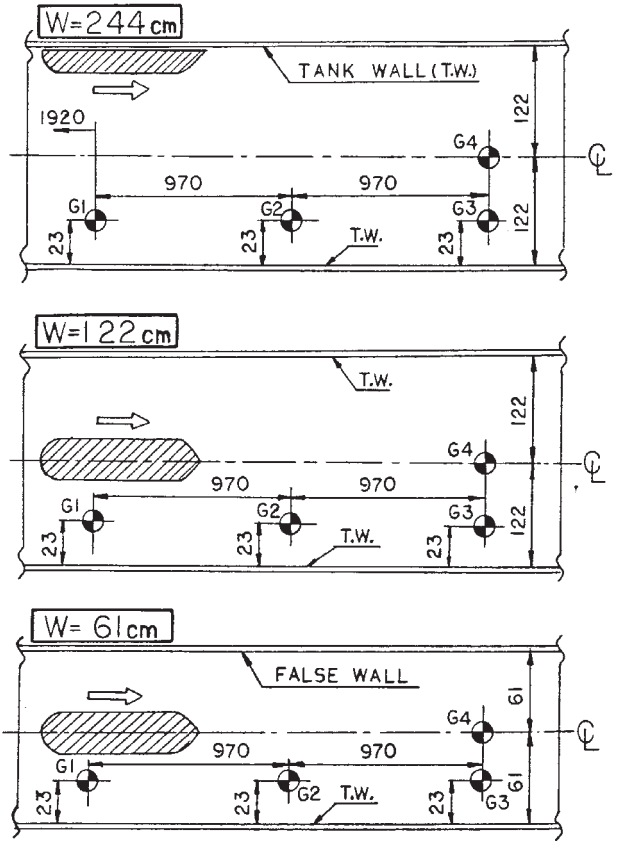

Figure 12.20: Towing-tank setup of Ertekin (1984). Stations for wave recording are marked as G1–G4. Distances are in centimeters. Three ship models were tested in the same tank.

upstream solitons have also been advanced in oceanography for tidal flows through a narrow strait Melville and Helfrich (1987).

In the theory of compressible fluids, transonic aerodynamics is known to require a nonlinear treatment involving shocks. Nevertheless, the flow around an aircraft at constant transonic speed is still steady, describable by the celebrated theory of Tricomi equation. Our water-wave problem is more intricate as it is further affected by dispersion, and provides an example that in nonlinear dynamics, a steady forcing does not necessarily lead to a steady response.

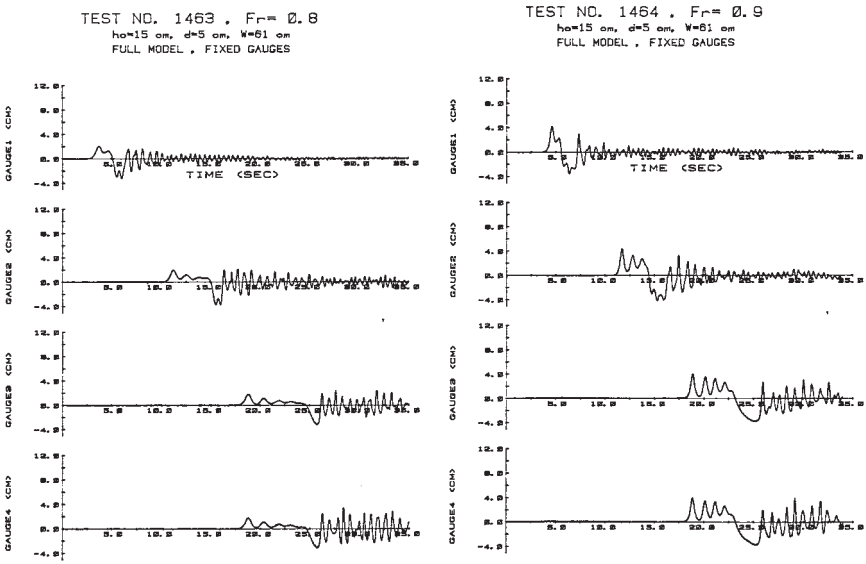

Figure 12.21: Sample time series of wave recorded at stations G-1 to G-4 for subcritical ship speeds, Ertekin (1984).

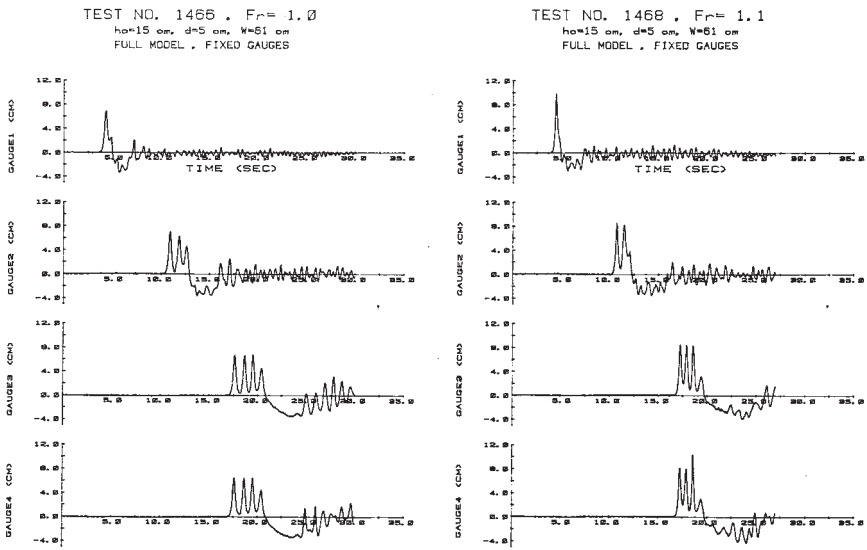

Figure 12.22: Sample time series of wave recorded at stations G-1 to G-4 for critical and superciritcal ship speeds, Ertekin (1984).

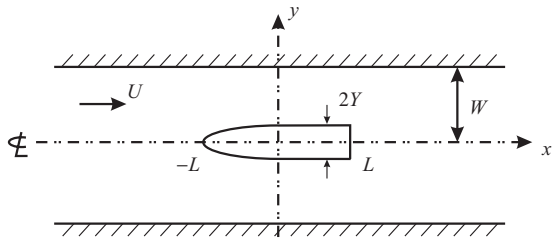

Figure 12.23: A ship cruising in a shallow channel of finite width. The coordinate system is fixed on the ship.

Let us examine the surface waves generated by the moving ship in a channel of constant depth h and width $2W$. It is convenient to choose the coordinate system fixed on the ship so that there is a steady current of equal speed flowing in the opposite direction. For simplicity we shall further treat a ship which has vertical side walls extending the full depth of the channel, as shown in Fig. 12.23. Modification for a ship with draft less than the channel depth is treated in Mei and Choi (1987).

Referring to Fig. 12.23, let the centerline of the channel be the x axis, the ship hull be

$$y = \pm Y(x)\,, \quad -L < x < L \tag{12.13.1}$$

and the channel bank be at $y = \pm W$. By symmetry we need only treat one half of the channel and the ship. Thus the fluid region is defined by

$$-\infty < x < \infty\,, \quad W > y > \begin{cases} Y(x)\,, & |x| < L \\ 0\,, & |x| > L \end{cases}\,, \quad -h < z < \zeta\,. \tag{12.13.2}$$

We shall focus our attention on slender ships ($W/L \ll 1$), so that nonlinearity is weak, i.e., $\epsilon \equiv A/h \ll 1$ where A will be related to the ship cross section later. We also assume that the ship is very long compared to the water depth, i.e., $\mu^2 = (h/L)^2 \ll 1$. The Boussinesq approximation in Section 12.1.3 is therefore appropriate, except that the horizontal length scale $1/k$ is here replaced by the ship length L. Let the total depth-averaged horizontal velocity be $(U+u, v)$, where (u, v) denote the components of the perturbation velocity. We get from the Boussinesq equations (12.1.36) and (12.1.37) the following dimensionless equations

$$\mathcal{D}\zeta + \nabla \cdot [(1 + \epsilon\zeta)\mathbf{u}] = 0 \tag{12.13.3}$$

$$\mathcal{D}\mathbf{u} + \epsilon\mathbf{u}\cdot\nabla\mathbf{u} + \nabla\zeta - \frac{\mu^2}{3}\nabla\nabla\cdot(\mathcal{D}\mathbf{u}) = 0 \tag{12.13.4}$$

where

$$\mathcal{D} \equiv \frac{\partial}{\partial t} + U\frac{\partial}{\partial x}\,. \tag{12.13.5}$$

Introducing the depth-averaged velocity potential, $\mathbf{u} = \nabla\bar{\phi}$, we rewrite the last equation as

$$\nabla\left(\mathcal{D}\bar{\phi} + \frac{\epsilon}{2}(\nabla\bar{\phi})^2 + \zeta - \frac{\mu^2}{3}\nabla\cdot\nabla(\mathcal{D}\bar{\phi})\right) = 0 \tag{12.13.6}$$

which can be integrated to give

$$\mathcal{D}\bar{\phi} + \frac{\epsilon}{2}(\nabla\bar{\phi})^2 + \zeta - \frac{\mu^2}{3}\nabla\cdot\nabla(\mathcal{D}\bar{\phi}) = 0\,. \tag{12.13.7}$$

Eliminating ζ from (12.13.3) and (12.13.7), we get

$$\nabla^2\bar{\phi} - \mathcal{D}^2\bar{\phi} - \frac{\epsilon}{2}\mathcal{D}(\nabla\bar{\phi})^2\epsilon - \nabla\cdot(\mathcal{D}\bar{\phi}\nabla\bar{\phi}) + -\frac{\mu^2}{3}\nabla^2(\mathcal{D}^2\bar{\phi}) = 0\,. \tag{12.13.8}$$

As a historical digression, Tuck (1966) studied the problem of a uniform flow past a slender ship in shallow and unbounded sea, based on the steady, linearized and nondispersive limit of (12.13.8), i.e., in physical coordinates,

$$U^2\frac{\partial^2\Phi}{\partial x^2} = gh\left(\frac{\partial^2\Phi}{\partial x^2} + \frac{\partial^2\Phi}{\partial y^2}\right). \tag{12.13.9}$$

On the ship hull, vanishing of the normal flux requires

$$\frac{\partial\Phi}{\partial y} = 0\,, \quad y = W \tag{12.13.10}$$

and

$$\frac{\partial\Phi}{\partial y} = \begin{cases} U\dfrac{\partial Y}{\partial x}\,, & |x| < L,\ y = 0\,; \\ 0\,, & |x| > L\,,\ y = 0\,. \end{cases} \tag{12.13.11}$$

In addition, waves are expected only far downstream at $x \sim \infty$. Interesting results on hydrodynamic forces (lift and drag) on the ship can be found by slender-body approximation for both subcritical ($U < \sqrt{gh}$) and supercritical ($U > \sqrt{gh}$) speeds. However, when U is close to the linearized long-wave

speed $\sqrt{gh}$, i.e., the transcritical speed, the linearized approximation gives unbounded results and fails. Keeping the nonlinear terms is not enough, as shocks must result and would require additional account of dispersion represented by terms of higher derivatives.

Normalizing Y by the maximum beam B, i.e., $Y = BY'$, the dimensionless boundary condition on the sides are, to the leading order,

$$\frac{\partial\bar{\phi}}{\partial y} = \begin{cases} \left(\frac{B}{L}\frac{F}{\epsilon}\right)\frac{dY(x)}{dx}\,, & |x|<1\,; \\ 0\,, & |x|>1\,, \end{cases} \tag{12.13.12}$$

where $F = U/\sqrt{gh}$ is the Froude number, and

$$\frac{\partial\bar{\phi}}{\partial y} = 0\,, \quad -\infty < x < \infty,\ y = W/L\,. \tag{12.13.13}$$

We now focus attention to the neighborhood of the critical speed by assuming

$$F^2 = 1 - 2\alpha\mu^2 \tag{12.13.14}$$

where $\alpha = O(1)$. Note that $\alpha < 0$ for supercritical flows $F > 1$ and $\alpha > 0$ for subcritical flows ($F < 1$). In order to account for the transients observed in the reported experiments, we need to estimate the time scale, say, μ^{-m} in dimensionless terms. Let a new time $\tau = \mu^m t$ be introduced. The linear terms can be expanded to

$$\begin{aligned} \nabla^2\bar{\phi} - \mathcal{D}^2\bar{\phi} &= (1-F^2)\frac{\partial^2\bar{\phi}}{\partial x^2} + \frac{\partial^2\bar{\phi}}{\partial y^2} - \frac{\partial^2\bar{\phi}}{\partial t^2} - 2F\frac{\partial\bar{\phi}}{\partial t} \\ &= 2\alpha\mu^2\frac{\partial^2\bar{\phi}}{\partial x^2} + \frac{\partial^2\bar{\phi}}{\partial y^2} - \mu^{2m}\frac{\partial^2\bar{\phi}}{\partial\tau^2} - 2\mu^m(1-2\alpha\mu^2)\frac{\partial^2\bar{\phi}}{\partial\tau\partial x}\,. \end{aligned} \tag{12.13.15}$$

Clearly near the critical speed, nonlinearity $O(\epsilon)$ and dispersion $O(\mu^2)$ are important to the transient evolution if $m = 2$. With this choice the leading transient term is the last, which is approximately,

$$-2\mu^2\frac{\partial^2\bar{\phi}}{\partial\tau\partial x}\,.$$

Keeping the terms up to $O(\epsilon, \mu^2)$, we get from (12.13.8)

$$2\alpha\mu^2\frac{\partial^2\bar{\phi}}{\partial x^2}+\frac{\partial^2\bar{\phi}}{\partial y^2}-2\mu^2\frac{\partial^2\bar{\phi}}{\partial\tau\partial x}$$
$$=\frac{\epsilon}{2}\frac{\partial}{\partial x}(\nabla\bar{\phi})^2+\epsilon\nabla\cdot\left(\frac{\partial\bar{\phi}}{\partial x}\nabla\bar{\phi}\right)+\frac{\mu^2}{3}\nabla^2\left(\frac{\partial^2\bar{\phi}}{\partial x^2}\right).$$

Next we consider a wide channel with $W/L\gg 1$. It is physically more natural to normalize the y coordinate by W instead of L. Introducing a new dimensionless coordinate $\eta=Ly/W$, the above equation becomes

$$\frac{\partial^2\bar{\phi}}{\partial\eta^2}=\frac{\mu^2W^2}{L^2}\left\{-2\alpha\frac{\partial^2\bar{\phi}}{\partial x^2}+2\frac{\partial^2\bar{\phi}}{\partial\tau\partial x}+\frac{\epsilon}{2\mu^2}\frac{\partial}{\partial x}\left[\left(\frac{\partial\bar{\phi}}{\partial x}\right)^2+\frac{L^2}{W^2}\left(\frac{\partial\bar{\phi}}{\partial y}\right)^2\right]\right.$$
$$\left.+\frac{\epsilon}{\mu^2}\left[\frac{\partial}{\partial x}\left(\frac{\partial\bar{\phi}}{\partial x}\right)^2+\frac{L^2}{W^2}\frac{\partial}{\partial\eta}\left(\frac{\partial\bar{\phi}}{\partial x}\frac{\partial\bar{\phi}}{\partial\eta}\right)\right]+\frac{1}{3}\left[\frac{\partial^2}{\partial x^2}+\frac{L^2}{W^2}\frac{\partial^2}{\partial\eta^2}\right]\frac{\partial^2\bar{\phi}}{\partial x^2}\right\}. \tag{12.13.16}$$

For $L/W\ll 1$, this equation further reduces to

$$\frac{\partial^2\bar{\phi}}{\partial\eta^2}=\mu^2\frac{W^2}{L^2}\left\{-2\alpha\frac{\partial^2\bar{\phi}}{\partial x^2}+2\frac{\partial^2\bar{\phi}}{\partial\tau\partial x}+\frac{3\epsilon}{2\mu^2}\frac{\partial}{\partial x}\left(\frac{\partial\bar{\phi}}{\partial x}\right)^2+\frac{1}{3}\frac{\partial^4\bar{\phi}}{\partial x^4}\right\}. \tag{12.13.17}$$

The boundary conditions on the sides are

$$\frac{\partial\bar{\phi}}{\partial\eta}=\frac{BW}{\epsilon L^2}\frac{dY}{dx}=\frac{BW}{h^2}\frac{\mu^2}{\epsilon}\frac{dY}{dx}\,,\quad \eta=0 \tag{12.13.18}$$

$$\frac{\partial\bar{\phi}}{\partial\eta}=0\,,\quad \eta=1\,. \tag{12.13.19}$$

We define A such that $\epsilon=\mu^2$ and get

$$\frac{\partial\bar{\phi}}{\partial\eta}=\frac{BW}{h^2}\frac{dY}{dx}\,,\quad \eta=0\,. \tag{12.13.20}$$

In terms of the velocity components defined by

$$\bar{u}=\frac{\partial\bar{\phi}}{\partial x}=u\,,\quad \bar{v}=\frac{\partial\bar{\phi}}{\partial\eta}=\frac{L}{W}v\,, \tag{12.13.21}$$

we have from (12.13.17):

$$\frac{\partial\bar{v}}{\partial\eta}=\mu^2\frac{W^2}{L^2}\left\{-2\alpha\frac{\partial\bar{u}}{\partial x}+2\frac{\partial\bar{u}}{\partial\tau}+\frac{3\epsilon}{2\mu^2}\frac{\partial\bar{u}^2}{\partial x}-\frac{1}{3}\frac{\partial\bar{u}}{\partial x^3}\right\}. \tag{12.13.22}$$

The boundary condition on the sides are

$$\bar{v} = \frac{BW}{h^2}\frac{dY}{dx}, \quad \eta = 0; \quad \bar{v} = 0, \quad \eta = 1. \tag{12.13.23}$$

Let us consider two cases:

Case (i): *Moderately wide channel* : $W^2/L^2 = c_1/\mu$ with $c_1 = O(1)$. Now

$$\mu^2 \frac{W^2}{L^2} = c_1 \mu. \tag{12.13.24}$$

We must let

$$\frac{BW}{h^2} = b_1\mu = O(\mu), \quad \text{implying} \quad \frac{B}{W} = O(\mu^4) \tag{12.13.25}$$

so that

$$\bar{v} = b_1 \mu \frac{dY}{dx}, \quad \eta = 0. \tag{12.13.26}$$

In the ship literature, the ratio B/W is called the blockage coefficient. At the leading order $\bar{v} = \partial\bar{\phi}/\partial\eta = 0$, implying that $\bar{\phi}$ is independent of η and $\bar{u} = \bar{u}(x,\tau)$ for all $0 < \eta < 1$. Thus the motion is approximately one dimensional. Going to the next order we integrate (12.13.22) from $\eta = 0$ to $\eta = 1$ and get

$$\frac{\partial\bar{u}}{\partial\tau} - \alpha\frac{\partial\bar{u}}{\partial x} + \frac{3}{2}\bar{u}\frac{\partial\bar{u}}{\partial x} + \frac{1}{6}\frac{\partial\bar{u}}{\partial x^3} = \frac{b_1}{2c_1}\frac{dY}{dx} = \frac{B}{2W\mu^4}\frac{dY}{dx} \tag{12.13.27}$$

which is an inhomogeneous KdV equation with forcing.

Away from the ship $dY/dx = 0$; (12.13.27) becomes homogeneous and has the soliton solution:

$$\zeta = \zeta_0 \operatorname{sech}^2\left[\frac{1}{4}(3\zeta_0)^{1/2}(x + C\tau)\right] \tag{12.13.28}$$

where the phase speed relative to the ship is

$$C = \frac{\zeta_0}{2} + \alpha. \tag{12.13.29}$$

As smaller α corresponds to larger F, for the same amplitude a soliton is slower if the ship moves faster.

Equation (12.13.27) must be solved numerically. For a parabolic hull $Y = 1 - x^2$ Mei (1985) has reported computations for various blockage coefficients corresponding to the experiments of Ertekin et al. (1982). Typical evolution of upstream solitons are shown in Figs. 12.24 and 12.25 for one case with $B/W\mu^4 = 10.4$ for a range of speeds. It is seen that as α

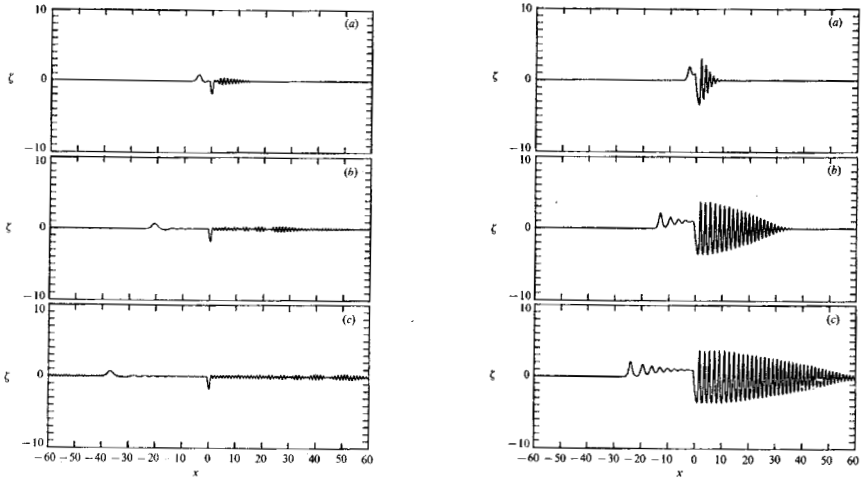

Figure 12.24: Free-surface evolution for slender ship advancing at a subcritical speed in a shallow channel (Mei, 1986).

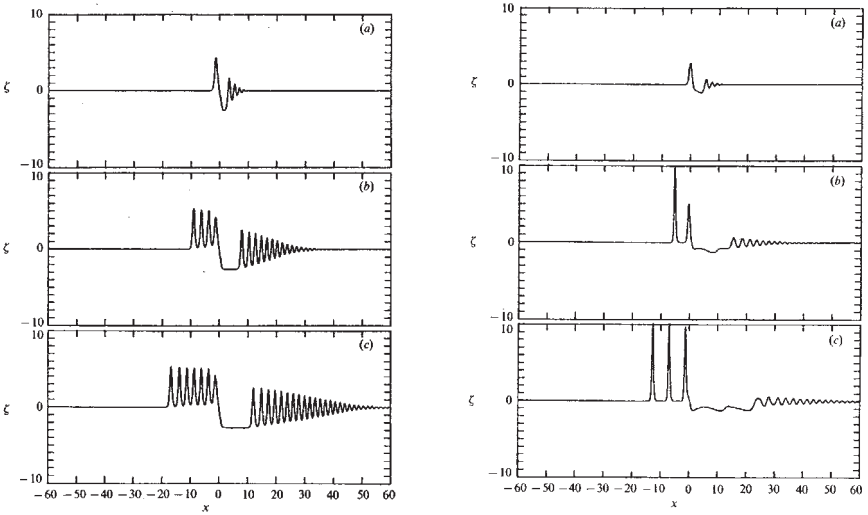

Figure 12.25: Free-surface evolution for a slender ship advancing at critical and supercritical speed in a shallow channel (from Mei, 1986, *J. Fluid Mech.* Reproduced by permission of Cambridge University Press).

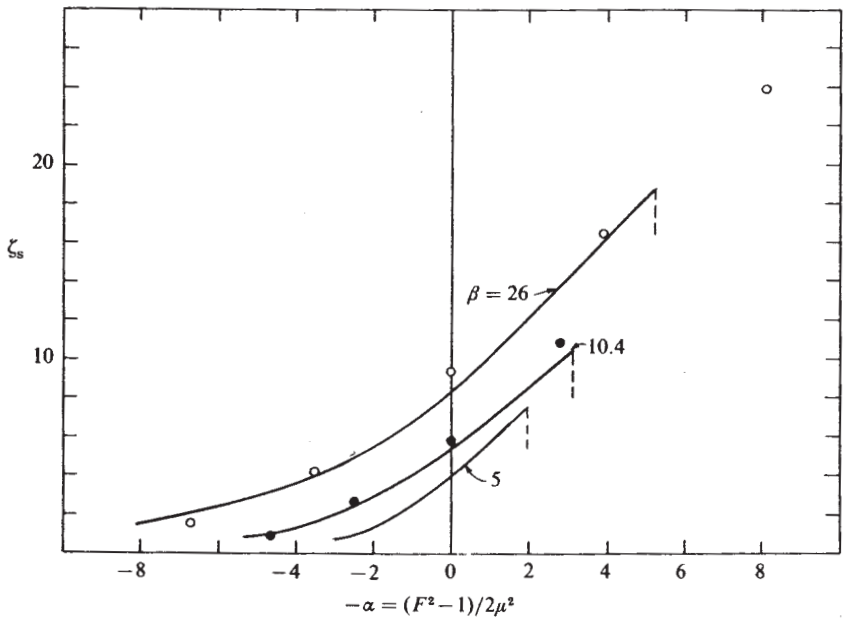

Figure 12.26: Comparison of theory with experiments of leading soliton amplitude (from Mei, 1986, *J. Fluid Mech.* Reproduced by permission of Cambridge University Press).

decreases from positive values (the ship speed increases from subcritical range), upstream solitons are born and grow with time. At supercritical speeds their amplitudes and wavelengths become uniform. At sufficiently high supercritical speed, no solitons are radiated upstream. Figure 12.26 shows a comparison of the amplitudes of the leading soliton for a range of speeds. Despite the large blockage coefficients (10.4 and 26), and the more complex wake surface in the experiments, the agreement for the main feature upstream is surprisingly good.

Case (*ii*): *Very wide channel* : $W/L = c_2/\mu$ with $c_2 = O(1)$. Thus

$$\mu^2 \frac{W^2}{L^2} = c_2\mu = O(\mu)\,. \tag{12.13.30}$$

We must assume

$$\frac{BW}{h^2} = b_2 = O(1) \quad \text{implying} \quad \frac{B}{W} = O(\mu^3)\,, \tag{12.13.31}$$

so that

$$\frac{\partial \bar{v}}{\partial \eta} = 2c_2 \left\{ \frac{\partial \bar{u}}{\partial \tau} - \alpha \frac{\partial \bar{u}}{\partial x} + \frac{3}{2}\bar{u}\frac{\partial \bar{u}}{\partial x} + \frac{1}{6}\frac{\partial^3 \bar{u}}{\partial x^3} \right\}. \tag{12.13.32}$$

Consistent with the existence of the depth-averaged potential, the mean flow is irrotational in the horizontal plane

$$\frac{\partial \bar{v}}{\partial x} = \frac{\partial \bar{u}}{\partial \eta}. \tag{12.13.33}$$

The last two equations constitute the two dimensional extension of the KdV theory and are called Kademtsev–Petrashivilli (K–P) equations. They can also be combined to give a single equation

$$\frac{\partial^2 \bar{u}}{\partial \eta^2} = 2c_2 \frac{\partial}{\partial x} \left\{ \frac{\partial \bar{u}}{\partial \tau} - \alpha \frac{\partial \bar{u}}{\partial x} + \frac{3}{2}\bar{u}\frac{\partial \bar{u}}{\partial x} + \frac{1}{6}\frac{\partial^3 \bar{u}}{\partial x^3} \right\}. \tag{12.13.34}$$

Because of the orders of the highest derivatives in x and η are in the 2:1 ratio, (12.13.34) is the parabolic extension of KdV equation. Together with the boundary conditions on the sides

$$\bar{v} = b_2 \frac{dY}{dx}, \quad \eta = 0 \tag{12.13.35}$$

$$\bar{v} = 0, \qquad \eta = 1 \tag{12.13.36}$$

and the initial conditions, the problem must be solved numerically. The K–P equations have been used Chen and Sharma (1995) for predicting forces on a ship with finite draft. Typical forms of the free surfaces are shown in Fig. 12.27.

Li and Scalvounos (2002) has exxtended the above theories to hiorizontally unbounded shallw water, for a slender ship moving at near-critical speed. By solving thje Boussinesq equations numerically they found upstream soliton-like waves with parabolic axes. Thus one-dimensional solitons are the results of finite channel width.

Exercise 12.2: Upstream Soliton Due to a Moving Surface Pressure (Akylas, 1984)

Consider the effect of a moving one-dimensional atmospheric pressure distribution $P(x - Ut)$ over a layer of water of constant depth h. $P(\xi)$ is a prescribed function of ξ with its characteristic length scale L being quite large compared to the depth h, i.e., $\mu = h/L \gg 1$. Water is incompressible

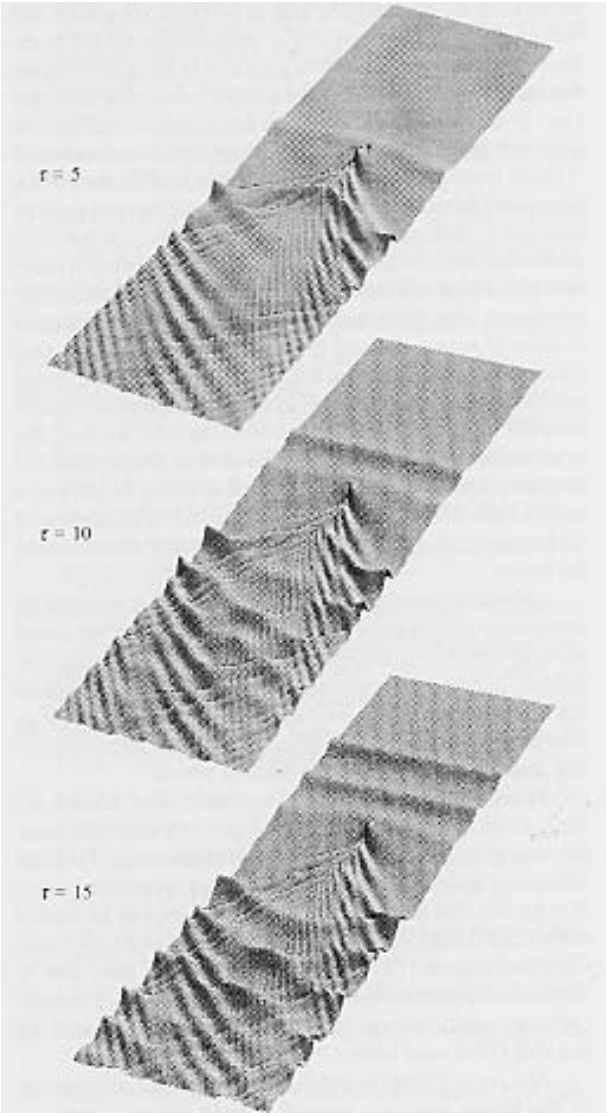

Figure 12.27: Snap-shots of free-surface at dimensionless instants $\tau = 5, 10, 15$ for a slender ship advancing at critical speed in a wide shallow channel (from Chen and Sharma, 1995, *J. Fluid Mech.* Reproduced by permission of Cambridge University Press).

and of constant density. If U is close to $\sqrt{gh}$, find the nonlinear equation governing the free-surface displacement $\zeta(x,t)$.

Show that if the order of magnitude of the pressure intensity is $p = O(\rho g A(kh)^2)$, the equation governing the free-surface displacement is a one-dimensional forced KdV equation.

Exercise 12.3: Near-Critical Flow Over a Bump (Cole, 1985)

Consider the two-dimensional problem of a steady uniform flow of speed U passing over a bump on an otherwise horizontal bottom, $z = -h + D(x)$. The length of the bump L is very large compared to the mean depth h, i.e., $\mu = h/L \ll 1$. Show that when $D/L = O(\mu^5)$ and U is close to the critical speed $\sqrt{gh}$, $F^2 = U/\sqrt{gh} = 1+\alpha\mu^2$ where $\alpha = O(1)$, the free-surface height is governed by the dimensionless forced KdV equation

$$\zeta_t + \frac{\alpha}{2}\zeta_x - \frac{3}{2}\zeta\zeta_x - \frac{1}{6}\zeta_{xxx} = \frac{1}{2}D_x\,.$$

12.14 Localization of Solitons Over a Randomly Rough Seabed

In Chapter 8 we studied infinitesimal and monochromatic waves over randomly irregular seabed of intermediate depth. For long periodic waves in shallow water, the mutual influence of harmonic generation and localization over a very large domain of disorder has been studied by Grataloup and Mei (2003). It is found that the amplitudes of the fundamental and higher harmonics are governed by coupled nonlinear equations similar to those in optics, but with additional terms whose complex coefficients are deterministic and related to certain correlation functions of disorder.

In this section we examine the propagation of a soliton over a shallow water with a weakly random bathymetry. The basic equation was first derived by Kawahara (1976) who did not exmamine the implied physics in detail. Following Mei and Li (2004), we first show how the asymptotic equation governing the coherent motion is derived. Analytical and numerical results will be discussed. For earlier works, see Howe (1971) and Rosales and Papanicolau (1983).

12.14.1 Asymptotic Equation for Uni-Directional Waves

We consider a simple case where the still water depth $h(x) = H(1-\mu b(x))$ differs slightly from the constant H where $\mu b(x)$ is a random function of x

with zero mean. The height of the irregularities is of the order $\mu = KH \ll 1$ and K is a constant characteristic wavenumber. For $\epsilon = A/H \ll 1$ and $KH \ll 1$ but $\epsilon = O(\mu^2)$, it is easy to show that the normalized Boussinesq approximation (12.1.47) and (12.1.48) hold so that the normalized equations read

$$\frac{\partial \zeta}{\partial t} + \frac{\partial}{\partial x}[(1 - \mu b + \epsilon\zeta)u] = 0 \tag{12.14.1}$$

and

$$\frac{\partial u}{\partial t} + \epsilon u \frac{\partial u}{\partial x} + \frac{\partial \zeta}{\partial x} = \frac{\mu^2}{3} \frac{\partial^3 u}{\partial x^2 \partial t} \,. \tag{12.14.2}$$

Within the stated accuracy, the preceding two equations can be combined to give the stochastic differential equation,

$$\frac{\partial^2 \zeta}{\partial t^2} - \frac{\partial^2 \zeta}{\partial x^2} = -\mu \frac{\partial}{\partial x}\left(b(x)\frac{\partial \zeta}{\partial x}\right) + \epsilon \frac{\partial^2}{\partial x^2}\left(u^2 + \frac{\zeta^2}{2}\right) + \frac{\mu^2}{3}\frac{\partial^4 \zeta}{\partial x^4} \,. \tag{12.14.3}$$

Let the seabed be rought only in $x > 0$. In the smooth region $x < 0$ where $b = 0$, the incident soliton is described, in dimensional foarm, by

$$\zeta^*(x^*, t^*) = A \operatorname{sech}^2 \frac{\sqrt{3}}{2}\left(\frac{A}{H^3}\right)^{1/2} (x^* - Ct^*) \,, \quad \text{with}$$

$$C = \sqrt{gH}\left(1 + \frac{A}{H}\right) . \tag{12.14.4}$$

It is convenient to choose the length of the incident soliton of amplitude A, $1/K$, as the horizontal scale, i.e.,

$$K = \left(\frac{A}{H^3}\right)^{1/2} \tag{12.14.5}$$

so that $\epsilon = \mu^2$.

Let us derive the statistical average of (12.14.3). Anticipating that the small disorder affects the leading order after a long distance inversely proportional to the mean square of the disorder, we introduce two space variables x and $X = \mu^2 x$ and expand u and ζ as power series of μ:

$$\begin{aligned} \zeta(x, X; t) &= \zeta_0 + \mu\zeta_1 + \mu^2\zeta_2 + O(\mu^3) \,, \\ u(x, X; t) &= u_0 + \mu u_1 + \mu^2 u_2 + O(\mu^3) \,. \end{aligned} \tag{12.14.6}$$

The perturbation equations are simply

$$\frac{\partial^2\zeta_0}{\partial t^2} - \frac{\partial^2\zeta_0}{\partial x^2} = 0 \tag{12.14.7}$$

$$\frac{\partial^2\zeta_1}{\partial t^2} - \frac{\partial^2\zeta_1}{\partial x^2} = -\frac{\partial}{\partial x}\left(b(x)\frac{\partial\zeta_0}{\partial x}\right) \tag{12.14.8}$$

$$\frac{\partial^2\zeta_2}{\partial t^2} - \frac{\partial^2\zeta_2}{\partial x^2} = -\frac{\partial}{\partial x}\left(b(x)\frac{\partial\zeta_1}{\partial x}\right) + 2\frac{\partial^2\zeta_0}{\partial x\partial X} + \frac{\partial}{\partial x}\left(u_0^2 + \frac{\zeta_0^2}{2}\right) + \frac{1}{3}\frac{\partial^4\zeta_0}{\partial x^4}\,. \tag{12.14.9}$$

At the leading order, $O(1)$, the governing wave equation (12.14.7) is homogeneous and deterministic. We consider only a right-going wave with vanishing amplitude at $x - t \sim -\infty$,

$$\zeta_0(x, X; t) = u_0(x, X; t) = \bar{\zeta}(X; \sigma)\,, \tag{12.14.10}$$

where $\sigma = x - t$. The explicit dependence of $\bar{\zeta}$ on X and σ is yet undetermined.

At the first order $O(\mu)$, the inhomogeneous equation (12.14.8) has random forcing, hence the response ζ_1 is random, and can be solved by means of Green's function defined by

$$G_{tt} - G_{xx} = \delta(x - x')\delta(t - t') \tag{12.14.11}$$

subject to

$$G = G_t = 0\,, \quad -\infty < x < \infty\,, \quad t < t'\,. \tag{12.14.12}$$

The formal solution is

$$\zeta_1(x, X; t) = -\int_{-\infty}^{t} dt' \int_{-\infty}^{\infty} dx' G(x, t; x', t')\frac{\partial}{\partial x'}\left(b(x')\frac{\partial\bar{\zeta}(x' - t', X')}{\partial x}\right). \tag{12.14.13}$$

We leave it as an exercise to show that the Green function is

$$G(x, t; x', t') = \frac{1}{2}H((t - t') - |x - x'|) \tag{12.14.14}$$

where $H(z)$ is the Heaviside step function. Clearly ζ_1 represents the incoherently scattered wave and has zero mean.

Denoting the ensemble average by $\langle\cdot\rangle$, we obtain from (12.14.9),

$$\frac{\partial^2\langle\zeta_2\rangle}{\partial t^2}-\frac{\partial^2\langle\zeta_2\rangle}{\partial x^2}=-\frac{\partial}{\partial x}\left\langle b(x)\frac{\partial\zeta_1}{\partial x}\right\rangle+2\frac{\partial^2\bar{\zeta}}{\partial x\partial X}+\frac{3}{2}\frac{\partial\bar{\zeta}^2}{\partial x}+\frac{1}{3}\frac{\partial^4\bar{\zeta}}{\partial x^4}\,. \tag{12.14.15}$$

By virtue of (12.14.10), the last three terms are all functions of $\sigma=x-t$, hence are homogeneous solutions of the averaged wave equation. Together they can be transformed to

$$2\frac{\partial^2\bar{\zeta}}{\partial\sigma\partial X}+\frac{3}{2}\frac{\partial^2\bar{\zeta}^2}{\partial\sigma^2}+\frac{1}{3}\frac{\partial^4\bar{\zeta}}{\partial\sigma^4}\,. \tag{12.14.16}$$

Let us rewrite the first forcing term in (12.14.15) by using (12.14.13),

$$\left\langle -b(x)\frac{\partial\zeta_1}{\partial x}\right\rangle=\int_{-\infty}^{\infty}dt'\int_{-\infty}^{\infty}dx'\left[\frac{\partial}{\partial x'}\left(\langle b(x)b(x')\rangle\frac{\partial\zeta}{\partial x'}\right)\right]\frac{\partial G(x,x',t,t')}{\partial x}\,. \tag{12.14.17}$$

We now add the assumption that the disorder is statistically homogeneous on the short scale, i.e.,

$$\langle b(x)b(x')\rangle\equiv\Gamma(\xi,X)=\Gamma(x'-x,X) \tag{12.14.18}$$

where $\Gamma(\xi,X)$ is a positive and even function of $\xi=x'-x$. It is shown in Appendix 12.A that

$$\left\langle -b(x)\frac{\partial\zeta_1}{\partial x}\right\rangle=\frac{1}{\pi}\int_{-\infty}^{\infty}\beta(\kappa,X)\hat{\bar{\zeta}}(X;\kappa)e^{i\kappa(x-t)}\,d\kappa \tag{12.14.19}$$

where $\hat{\bar{\zeta}}$ is the Fourier transform of ζ,

$$\hat{\bar{\zeta}}(\kappa,X)=\int_{-\infty}^{\infty}\bar{\zeta}(x'-t';X)e^{-i\kappa(x'-t')}\,d(x'-t')\,,$$

and $\beta(\kappa,X)$ is the complex coefficient defined by

$$\beta=\frac{ik}{4}\int_{-\infty}^{\infty}\frac{\partial}{\partial\xi}(\Gamma(\xi,X)e^{i\kappa\xi})\,\mathrm{sgn}\,(\xi)e^{i\kappa|\xi|}\,d\xi\,. \tag{12.14.20}$$

In view of (12.14.19), we get

$$-\frac{\partial}{\partial x}\left\langle b(x)\frac{\partial\zeta_1}{\partial x}\right\rangle=\frac{1}{\pi}\frac{\partial}{\partial\sigma}\int_{-\infty}^{\infty}e^{i\kappa\sigma}\beta(\kappa,X)\hat{\bar{\zeta}}(\kappa,X)\,d\kappa\,. \tag{12.14.21}$$

Thus all forcing terms on the right of (12.14.15) are function of $\sigma = x-t$. To avoid unbounded resonance for $\langle\zeta_2\rangle$, their sum must vanish. After integrating this solvability condition with respect to σ, we obtain the asymptotic equation for the leading-order displacement, as seen by an observer traveling at the linear phase speed[9] during a very long course of propagation,

$$\frac{\partial\bar{\zeta}}{\partial X} + \frac{3}{2}\bar{\zeta}\frac{\partial\bar{\zeta}}{\partial\sigma} + \frac{1}{6}\frac{\partial^2\bar{\zeta}}{\partial\sigma^3} = -\frac{1}{2\pi}\int_{-\infty}^{\infty}\beta(\kappa,X)\widehat{\bar{\zeta}}(\kappa,X)e^{i\kappa\sigma}\,d\kappa\,. \qquad (12.14.22)$$

This is just a KdV equation modified by the additional term on the right representing the scattering effect of disorder. The time-like coordinate X represents the distance traveled by the wave.

In Appendix 12.E the coefficient β is shown to be

$$\beta = i\kappa\frac{\Gamma(0)}{2} + \kappa^2\left\{\frac{1}{2}\hat{\Gamma}(0) + \frac{1}{2}\hat{\Gamma}(2\kappa) + i\kappa\hat{P}(2\kappa)\right\}. \qquad (12.14.23)$$

where $\hat{\Gamma}(\kappa)$ is the exponential Fourier Transform of $\Gamma(\xi)$ and P is the integral

$$P(\xi) = \int_{|\xi|}^{\infty}\Gamma(u)du\,.$$

Substituting (12.14.23) into (12.14.22), we get, after using the convolution theorem,

$$\begin{aligned}\frac{\partial\bar{\zeta}}{\partial X} + \frac{3}{2}\bar{\zeta}\frac{\partial\bar{\zeta}}{\partial\sigma} + \frac{1}{6}\frac{\partial^3\bar{\zeta}}{\partial\sigma^3}&\\ = \frac{\Gamma(0)}{2}\frac{\partial\bar{\zeta}}{\partial\sigma} + \frac{\widehat{\Gamma}(0)}{8}\frac{\partial^2\bar{\zeta}}{\partial\sigma^2} + \frac{1}{16}\int_{-\infty}^{\infty}\Gamma\left(\frac{\sigma-\sigma'}{2}\right)\frac{\partial^2\bar{\zeta}}{\partial\sigma'^2}\,d\sigma'&\\ + \frac{1}{8}\int_{-\infty}^{\infty}P\left(\frac{\sigma-\sigma'}{2}\right)\frac{\partial^3\bar{\zeta}}{\partial\sigma'^3}\,d\sigma'\,. \qquad (12.14.24)\end{aligned}$$

Incoherent (random) scattering affects the leading-order part of the wave (which is coherent) only on the average, through new terms on the right-hand side of the extended KdV equation. First, all these new terms are of the order of the root-mean-square of the disorder. The first and fourth terms represent, respectively, the effects of disorder on the phase velocity and dispersion, hence on the wave phase. Because $\Gamma(\xi)$ is positive-definite, disorder tends to reduce both the wave speed and dispersion. On the other hand, the second and third terms signify diffusion, making (12.14.31) a

[9]The linear phase speed is unity in dimensionless form and $\sqrt{gH}$ in physical scale.

hybrid of KdV and Burgers, hence would lead to spatial attenuation, i.e., localization.

Spatial attenuation can be seen alternately from the energy of the coherent wave. Multiplying both sides of (12.14.22) and integrating the result with respect to σ, we get

$$\frac{d}{dX}\int_{-\infty}^{\infty}\frac{\bar{\zeta}^2}{2}\,d\sigma = -\frac{1}{2\pi}\int_{-\infty}^{\infty}\beta(\kappa)|\widehat{\bar{\zeta}}(\kappa)|^2\,d\kappa\,.$$

Since $\bar{\zeta}(\sigma)$ is real in all σ, its Fourier transform $\widehat{\bar{\zeta}}(\kappa)$ and its complex conjugate must satisfy $\widehat{\bar{\zeta}}(-\kappa) = \widehat{\bar{\zeta}}^{*}(\kappa)$. From (12.14.23), it is seen that $\mathrm{Re}\,(\beta(\kappa))$ is even and $\mathrm{Im}\,(\beta(\kappa))$ is odd in κ. It follows that

$$\frac{d}{dX}\int_{-\infty}^{\infty}\frac{\bar{\zeta}^2}{2}\,d\sigma = -\frac{1}{\pi}\int_{0}^{\infty}\mathrm{Re}\,(\beta(\kappa))|\widehat{\bar{\zeta}}(\kappa)|^2\,d\kappa\,. \tag{12.14.25}$$

Since $\mathrm{Re}\,(\beta(\kappa)) > 0$ for all positive κ (cf. (12.14.23), the right-hand side of (12.14.25) is negative. Physically, energy is drained from the coherent wave for the radiation of the much smaller, randomly scattered incoherent waves, leading to spatial attenuation of $\bar{\zeta}$.

12.14.2 Gaussian Correlation Function

For better insight we choose the correlation function to be Gaussian, with the correlation length taken to be l^*. The dimensional correlation function is,

$$\langle b^*(x^*)b^*(x^{*\prime})\rangle = D^{*2}\exp\left(\frac{(x^{*\prime}-x^*)^2}{2l^{*2}}\right) \tag{12.14.26}$$

where D^* is the root-mean-square amplitude of the random roughness. The normalized correlation function is

$$\Gamma(\xi) = D^2\exp\left(-\frac{\xi^2}{2l^2}\right) \tag{12.14.27}$$

where

$$l = Kl^*\,,\quad D^2 = \frac{D^{*2}}{H^2}\frac{1}{\mu^2} = \frac{D^{*2}}{AH} = O(1)\,. \tag{12.14.28}$$

It follows that

$$\widehat{\Gamma}(\kappa) = \sqrt{2\pi}D^2 l\exp\left(-\frac{\kappa^2 l^2}{2}\right) \tag{12.14.29}$$

and

$$P(\xi) = \int_{|\xi|}^{\infty} \Gamma(u)\, du = \sqrt{\frac{\pi}{2}} D^2 l \ \mathrm{erfc}\left(\frac{|\xi|}{\sqrt{2}\, l}\right) \tag{12.14.30}$$

where $\mathrm{erfc}\,(z)$ is the complementary error function.

The Fourier transform of $P(\xi)$ is

$$\widehat{P}(\kappa) = \frac{\sqrt{2\pi} D^2 l^2}{\kappa l} \exp\left(-\frac{\kappa^2 l^2}{2}\right) \mathrm{erfi}\left(\frac{\kappa l}{\sqrt{2}}\right) \tag{12.14.31}$$

where $\mathrm{erfi}\,(z)$ is the imaginary error function defined by

$$\mathrm{erfi}\,(z) = \frac{2}{\sqrt{\pi}} \int_0^z e^{t^2}\, dt\,. \tag{12.14.32}$$

Consequently (12.14.24) becomes

$$\begin{aligned} &\frac{\partial \bar{\zeta}}{\partial X} + \frac{3}{2}\bar{\zeta}\frac{\partial \bar{\zeta}}{\partial \sigma} + \frac{1}{6}\frac{\partial^3 \bar{\zeta}}{\partial \sigma^3} \\ &\quad = D^2 \left\{ \frac{1}{2}\frac{\partial \bar{\zeta}}{\partial \sigma} + \frac{\sqrt{2\pi}\, l}{8}\frac{\partial^2 \bar{\zeta}}{\partial \sigma^2} + \frac{1}{16}\int_{-\infty}^{\infty} \exp\left(-\frac{|\sigma - \sigma'|^2}{8\, l^2}\right) \frac{\partial^2 \bar{\zeta}}{\partial \sigma'^2}\, d\sigma' \right. \\ &\qquad \left. + \frac{\sqrt{2\pi}\, l}{16}\int_{-\infty}^{\infty} \mathrm{erfc}\left(\frac{|\sigma - \sigma'|}{2\sqrt{2}\, l}\right) \frac{\partial^3 \bar{\zeta}}{\partial \sigma'^3}\, d\sigma' \right\}. \end{aligned} \tag{12.14.33}$$

Asymptotic analysis has been carried out by Mei and Li (2004) for weak disorder (small D) and for long travel distance (large X). Specifically, if a soliton enters a semi-infinite zone of disorder $X > 0$ where D is small, the amplitude decays with X algebraically as

$$A(X) \cong \frac{5}{\sqrt{2\pi}} \frac{1}{D^2 X} \tag{12.14.34}$$

which differs from the exponential decay of small-amplitude and periodic waves. For any finite D, dispersion becomes less important than diffusion after a long travel distance, so that (12.14.33) is reduced to Burger's equation

$$\frac{\partial \bar{\zeta}}{\partial X} + \frac{3\bar{\zeta}}{2}\frac{\partial \bar{\zeta}}{\partial \sigma} = \frac{D^2}{2}\frac{\partial \bar{\zeta}}{\partial \sigma} + \frac{\sqrt{2\pi} D^2 l}{4}\frac{\partial^2 \bar{\zeta}}{\partial \sigma^2}\,. \tag{12.14.35}$$

By making use of the analytical solution due to Cole and Hopf (see Whitham, 1974), it can be shown that a soliton crest attenuates in height as $1/\sqrt{X}$ while spreads in width as $\sqrt{X}$.

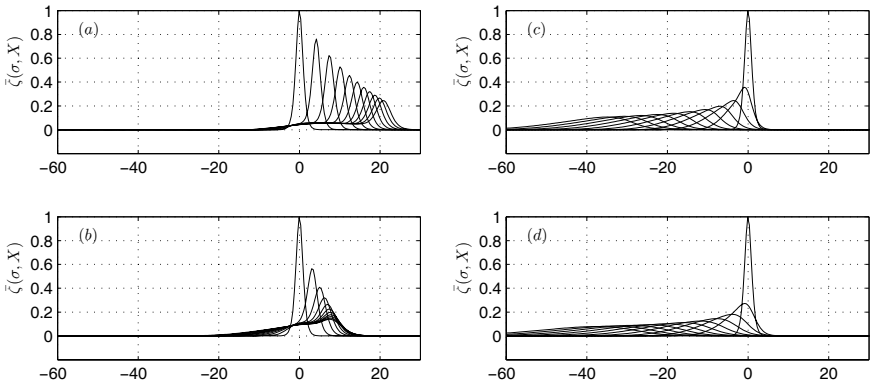

Figure 12.28: Effects of roughness amplitude on soliton evolution over a random seabed of the same correlation length $l = 1$. The total travel distance is 100 ($0 \leq X \leq 100$). Wave profiles are shown at every $\Delta X = 10$. (a) $D^2 = 0.10$; (b) $D^2 = 0.25$; (c) $D^2 = 0.50$; (d) $D^2 = 1.0$ (from Mei and Li, 2004, *Phys. Rev. E*. Reproduced by permission of Amer. Phy. Soc.).

12.14.3 Computed Results of Soliton Evolution Over a Long Rough Seabed

We now discuss numerical solutions of initial-value problems to the nonlinear integro-differential equation (12.14.33). Details of the numerical method can be found in Mei and Li (2004). Two seabeds with low-amplitude roughness are first chosen for the same correlation length of $l = 1$. The numerical solutions are shown in Figs. 12.28(a) and 12.28(b). As the propagation distance X increases, the wave profile flattens gradually. For the lower roughness, the wave crest first travels forward in the moving coordinate, therefore faster than the linear phase speed over a smooth bed (1 in dimensionless form or $\sqrt{gH}$ in physical dimensions, in the stationary frame of reference). As the crest loses its height with X, it also slows down to below the linear phase speed. By comparing Figs. 12.28(a) and 12.28(b), the soliton is slowed down sooner by the bed with higher roughness.

With still higher roughness, solitons are further slowed, as shown in Figs. 12.28(c) and 12.28(d). For $D^2 = 0.5$, the forward push by inertia loses more ground to retardation by roughness, see Fig. 12.28(c). For the highest roughness with $D^2 = 1.0$ (see Fig. 12.28(d)). Inertia is overpowered by roughness and nonlinearity is no longer effective. The wave crest travels always at a speed lower than the linear wave speed for a smooth bed.

A larger l corresponds also to a stronger disorder. Enhanced slowing down, stronger dissipation and faster attenuation are expected; these

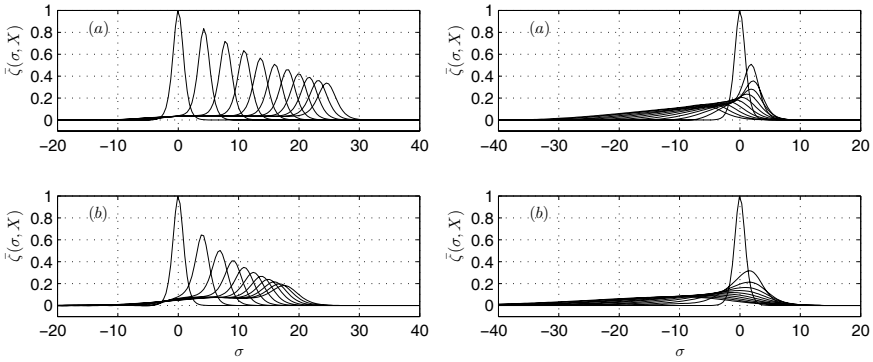

Figure 12.29: Effects of correlation length on soliton evolution over a random seabed. The total distance of travel is 100 ($0 \le X \le 100$). Wave profiles are shown at every $\Delta X = 10$. *Left*: $D^2 = 0.10$, (*a*) $l = 0.5$; (*b*) $l = 2.0$. *Right*: $D^2 = 0.50$, (*a*) $l = 0.5$; (*b*) $l = 2.0$ (from Mei and Li, 2004, *Phys. Rev. E.* Reproduced by permission of Amer. Phys. Soc.).

features are confirmed by Figs. 12.29(*a*) and 12.29(*b*) for $D^2 = 0.1$. If the seabed roughness is higher with $D = 0.5$, these effects are further augmented, as seen in Figs. 12.28(*c*) and 12.29(*b*).

Mei and Li have also examined soliton passage of over a finite stretch of random seabed. They found that, after being flattened, the wave pulse undergoes fission and disintegrates into several small solitons according to the analytical theory of Section 12.7.

Appendix 12.A Evaluation of Certain Integrals in Section 12.4

The typical integral is

$$I(f) = \int_0^\infty d\zeta\, e^{-2\zeta}(2f_\zeta + f_{\zeta\zeta})\,. \tag{12.A.1}$$

By partial integration

$$I(f) = -4f(0) - f_\zeta(0) + 8\int_{-\infty}^{\infty} d\zeta\, e^{-2\zeta} f\,. \tag{12.A.2}$$

Let $f = J_0(4\zeta^{1/2})$, then $J_0(0) = 1$, but

$$\lim_{\zeta\to 0} J_{0\zeta} = \lim_{\zeta\to 0} J_0' \frac{2}{\zeta^{1/2}} = \frac{2}{\zeta^{1/2}}\left(-\frac{4\zeta^{1/2}}{2}\right) = -4\,.$$

Hence,

$$I(J_0) = 8\int_0^\infty d\zeta\, e^{-2\zeta} J_0(4\zeta^{1/2}) = \frac{8}{2e^2} = 0.0541314 \tag{12.A.3}$$

which can be found from Abramowitz and Stegun (1972).

Let $f = G(\zeta)$. From the defining equation (12.4.18b) we find

$$G(0) = E_2(\infty) - iE_1(\infty)\,, \tag{12.A.4}$$

and

$$G_\zeta(0) = \frac{1}{\pi} - 4(E_2(\infty) - iE_1(\infty))\,, \tag{12.A.5}$$

therefore

$$-4G(0) - G_\zeta(0) = -\frac{1}{\pi}\,. \tag{12.A.6}$$

Now

$$\begin{aligned} E_G \equiv \int_0^\infty d\zeta\, e^{-2\zeta} G &= -\int_0^\infty d\zeta\, e^{-2\zeta} J_0(4\zeta^{1/2}) \int_0^\zeta d\xi\, e^{-2\xi} Y_0(4\xi^{1/2}) \\ &\quad + \int_0^\infty d\zeta\, e^{-2\zeta} Y_0(4\zeta^{1/2}) \int_0^\zeta d\xi\, e^{-2\zeta} J_0(4\xi^{1/2}) \\ &\quad + (E_2(\infty) - iE_1(\infty))E_1(\infty) \\ &= -i(E_1(\infty))^2 + 2\int_0^\infty d\zeta\, e^{-2\zeta} Y_0(4\zeta^{1/2}) \int_0^\zeta d\xi\, e^{-2\xi} J_0(4\xi^{1/2})\,. \end{aligned} \tag{12.A.7}$$

The last double integral above can be numerically evaluated to be 0.01431331. Upon using Eq. (12.A.3), we obtain

$$E_G = 0.02862 - 0.0045992i\,. \tag{12.A.8}$$

Appendix 12.B Reduction of an Integral in Section 12.9

Keulegan's manipulations are as follows: Equation (12.9.22) is first broken into two parts

$$u_b = -\frac{1}{\pi}\left\{\int_{-\infty}^{\rho} d\rho' + \int_{\rho}^{\infty} d\rho'\right\}\int_0^\infty dk\,[\ ] \tag{12.B.1}$$

with the same integrand. In the first integral, to be denoted by I_1, we let

$$k(\rho - \rho') = 2a^2 \quad \text{and} \quad \left(\frac{k}{2z}\right)^{1/2} = qa\,,$$

so that

$$I_1 = -\frac{4}{\pi}\int_{-\infty}^{\rho} \frac{d\rho'}{\rho - \rho'}\zeta_0(\rho') \int_0^{\infty} ae^{-qa}\cos(2a^2 + qa)\,da\,.$$

The a integral above vanishes identically [see Gradshteyn and Ryzhik, 1965, p. 499, formula 3.966(1)]. In the second integral of (12.B.1), we let

$$k(\rho' - \rho) = 2a^2 \quad \text{and} \quad \left(\frac{k}{2z}\right)^{1/2} = qa\,,$$

and use a and q to replace k and ρ' as new variables; then

$$u_b = I_2 = -\frac{4}{\pi}\int_0^{\infty} \frac{dq}{q} 2\zeta_0 \int_0^{\infty} ae^{-qa}\cos(2a^2 - qa)\,da\,.$$

The a integral here can again be found from Gradshteyn and Ryzhik [1965, 3.966(2)] as

$$\frac{\pi}{8}^{1/2} qe^{-q^2/4}\,.$$

With a further change from q to $2s$, Eq. (12.9.23) follows at once.

Appendix 12.C The Square of a Fourier Series

We wish to rearrange the following product:

$$\left(\sum\right)^2 = \left(\sum_{l=-\infty}^{\infty} A_l e^{il\theta}\right)\left(\sum_{m=-\infty}^{\infty} A_m e^{im\theta}\right)$$

$$= \sum_{-\infty}^{\infty}\sum_{-\infty}^{\infty} A_l A_m e^{i(l+m)\theta}\,, \quad A_0 = 0\,. \tag{12.C.1}$$

Let $n = l + m$, then

$$\left(\sum\right)^2 = \sum_{n=-\infty}^{\infty} e^{in\theta} \sum_{l=-\infty}^{\infty} A_l A_{n-l}\,. \tag{12.C.2}$$

Consider the l series. Using the fact that $A_0 = 0$, we break up the series as follows:

$$\sum_l \equiv \sum_{l=-\infty}^{\infty} A_l A_{n-l}$$

$$= \sum_{l=-\infty}^{-1} A_l A_{n-l} + \sum_{l=1}^{n-1} A_l A_{n-l} + \sum_{l=n}^{\infty} A_l A_{n-l} \,. \qquad (12.C.3)$$

In the first series we change l to $-l'$; in the last series we change $n - l$ to $-l'$. The two series can be added to give

$$2\sum_{l=1}^{\infty} A_{-l} A_{n+l} \,. \qquad (12.C.4)$$

The second series on the right-hand side of Eq. (12.C.3) can be rewritten depending on the parity of n, that is, whether n is odd or even. If $n =$ even $= 2p$, then

$$\sum_{l=1}^{2p-1} A_l A_{2p-l} = A_1 A_{2p-1} + A_2 A_{2p-2} + \cdots A_p A_p + \cdots A_{2p-2} A_2 + A_{2p-1} A_1 \,.$$

Except for $A_p A_p$, the above terms may be added in pairs (e.g., the first and the last, etc.) to give

$$\sum_{l=1}^{p} \alpha_l A_l A_{2p-l} = \sum_{l=1}^{n/2} \alpha_l A_l A_{n-l} \,, \qquad (12.C.5)$$

where α_1 is defined by

$$\alpha_l = 2 \quad \text{if} \quad l = 1, 2, \ldots, \frac{n}{2} - 1 \,,$$

$$\alpha_l = 1 \quad \text{if} \quad l = \frac{n}{2} \,. \qquad (12.C.6)$$

If $n =$ odd $= 2p + 1$, $p = 0, 1, 2, \ldots$, then

$$\sum_{l=1}^{2p} A_l A_{2p+1-l} = A_1 A_{2p} + A_2 A_{2p-1} + \cdots A_p A_{p+1} + A_{p+1} A_p + \cdots A_{2p} A_1$$

$$= \sum_{l=1}^{p} 2 A_l A_{2p+1-l} = \sum_{l=1}^{(n-1)/2} \alpha_l A_l A_{n-l} \,. \qquad (12.C.7)$$

The two alternatives (12.C.5) and (12.C.7) can be written as a single series, so that the second series on the right of Eq. (12.C.3) becomes

$$\sum_{l=1}^{'} \alpha_l A_l A_{n-l} \tag{12.C.8}$$

where the upper limit of $\sum'$ is $\frac{1}{2}n$ if n is even and $\frac{1}{2}(n-1)$ if n is odd.

Finally, by combining Eqs. (12.C.4) and (12.C.8) into Eq. (12.C.2), we obtain

$$\left(\sum\right)^2 = \sum_{n=1}^{\infty} e^{in\theta} \left\{ \sum_{l=1}^{'} \alpha_l A_l A_{n-l} + \sum_{l=1}^{\infty} 2A_l^* A_{n+l} \right\} + \sum_{l=1}^{\infty} 2A_l A_{-l} + * \,. \tag{12.C.9}$$

Appendix 12.D Details of Random Forcing

In terms of the Fourier transform, we can write

$$\begin{aligned} \frac{\partial \bar{\zeta}}{\partial x'} &= \frac{1}{2\pi} \int_{-\infty}^{\infty} i\kappa e^{i\kappa(x'-x-(t'-t))} \widehat{\bar{\zeta}}(\kappa, X) e^{i\kappa(x-t)} \, d\kappa \\ &= \frac{1}{2\pi} \int_{-\infty}^{\infty} i\kappa e^{i\kappa\xi} e^{-i\kappa\tau} \widehat{\bar{\zeta}}(\kappa, X) e^{i\kappa(x-t)} \, d\kappa \end{aligned} \tag{12.D.1}$$

where

$$\xi = x' - x \,, \quad \tau = t' - t \,.$$

Note that

$$\frac{\partial G}{\partial x} = \frac{\partial G}{\partial |\xi|} \operatorname{sgn}(\xi) = -\frac{1}{2} \delta(\tau - |\xi|) \operatorname{sgn}(\xi) \,. \tag{12.D.2}$$

Using these results in (12.14.17), we get, after simple variable transformations, that

$$\begin{aligned} -\left\langle b(x) \frac{\partial \zeta_1}{\partial x} \right\rangle = \frac{1}{4\pi} \iiint_{-\infty}^{\infty} d\tau \, d\xi \, d\kappa \, e^{i\kappa(x-t)} i\kappa \\ \times \frac{\partial}{\partial \xi} [\Gamma(\xi) \widehat{\zeta}(\kappa) e^{-i\kappa\xi}] e^{i\kappa\tau} \delta(\tau - |\xi|) \operatorname{sgn}(\xi) \,. \end{aligned}$$

Since

$$\int_{-\infty}^{\infty} d\tau e^{i\kappa\tau} \delta(\tau - |\xi|) = e^{i\kappa|\xi|}$$

the triple integral above becomes

$$-\left\langle b(x)\frac{\partial\zeta_1}{\partial x}\right\rangle = \frac{1}{2\pi}\iint_{-\infty}^{\infty} d\xi\, d\kappa\, e^{i\kappa(x-t)}\widehat{\zeta}(\kappa) \times \frac{i\kappa}{2}\frac{\partial}{\partial\xi}[\Gamma(\xi,X)e^{-i\kappa\xi}]e^{i\kappa|\xi|}\ \mathrm{sgn}\,(\xi)$$

which gives (12.14.19) after using the definition (12.14.20).

Appendix 12.E Details of β

Let us perform partial integration of (12.14.20)

$$\begin{aligned}\beta &= \frac{i\kappa}{4}\{\Gamma(\xi)e^{i\kappa\xi}\ \mathrm{sgn}\,(\xi)e^{i\kappa|\xi|}\}_{\xi=-\infty}^{\xi=\infty} \\ &\quad - \frac{i\kappa}{4}\int_{-\infty}^{\infty}(\Gamma(\xi)e^{i\kappa\xi})i\kappa e^{i\kappa|\xi|}\,d\xi \\ &= -i\kappa\frac{\Gamma(0)}{2} + \frac{\kappa^2}{4}\int_{-\infty}^{\infty}\Gamma(\xi)e^{i\kappa\xi}e^{i\kappa|\xi|}\,d\xi \qquad (12.E.1)\end{aligned}$$

where

$$\frac{d}{d\xi}(\mathrm{sgn}\,(\xi)e^{i\kappa|\xi|}) = ike^{i\kappa|\xi|} \qquad (12.E.2)$$

is used. Since the integrand in the last integral is even in ξ, we find

$$\int_{-\infty}^{\infty}\Gamma(\xi)e^{i\kappa\xi}e^{i\kappa|\xi|}\,d\xi = \frac{1}{2}\int_{-\infty}^{\infty}\Gamma(\xi)\,d\xi + \int_0^{\infty}\Gamma(\xi)\cos 2\kappa\xi\,d\xi + i\int_0^{\infty}\Gamma(\xi)\sin\kappa\xi\,d\xi\,. \qquad (12.E.3)$$

Note that

$$\begin{aligned}\frac{1}{2}\int_{-\infty}^{\infty}\Gamma(\xi)\,d\xi &= \frac{1}{2}\widehat{\Gamma}(0)\,, \\ \int_0^{\infty}\Gamma(\xi)\cos 2\kappa\xi\,d\xi &= \frac{1}{2}\widehat{\Gamma}(2\kappa)\,, \qquad (12.E.4)\end{aligned}$$

and the third term in (12.E.3) can be manipulated by partial integration

$$
\begin{aligned}
i\int_0^\infty \Gamma(\xi)\sin 2\kappa\xi\, d\xi &= -i\int_0^\infty \sin 2\kappa\xi\, d\int_\xi^\infty \Gamma(u)\, du \\
&= 2i\kappa\int_0^\infty du\int_\xi^\infty \Gamma(u)\cos 2\kappa\xi\, d\xi \\
&= 2i\kappa\int_0^\infty P(\xi)\cos 2\kappa\xi\, d\xi \\
&= ik\widehat{P}(2\kappa) \qquad (12.E.5)
\end{aligned}
$$

where $P(\xi)$ is

$$
P(\xi) = \int_{|\xi|}^\infty \Gamma(u)\, du\,. \qquad (12.E.6)
$$

With (12.E.4) and (12.E.5), β in (12.E.1) can be rewritten as

$$
\beta = -i\kappa\frac{\Gamma(0)}{2} + \kappa^2\left\{\frac{1}{2}\widehat{\Gamma}(0) + \frac{1}{2}\widehat{\Gamma}(2\kappa) + i\kappa\widehat{P}(2\kappa)\right\}. \qquad (12.E.7)
$$

Narrow-Banded Nonlinear Waves in Water of Intermediate or Great Depth

13

13.1 Introduction

For arbitrary depth, $O(kh) \geq 1$, the effects of finite amplitude have been of long-standing interest. In older literature considerable attention was paid to the calculation of periodic progressive or standing waves. In particular, Stokes' contribution (1847) on higher-order waves of uniform amplitude set the tone of research for nearly 100 years. Much of the subsequent effort has been devoted to the maximum wave height when the depth is either constant or infinite. These classical contributions have been thoroughly summarized in Wehausen and Laitone (1960).

More recent interest in nonlinear deep-water waves owes its impetus to our need for a better understanding of the sea spectrum development. Shortly after the birth of two complementary theories of wave generation by wind, due separately to Miles (1957) and Phillips (1957), a cornerstone was laid by Phillips (1960) who introduced the mechanism of nonlinear resonant interaction in which four wavetrains slowly exchanged energy among one another if their phases were suitably matched; an era of examining nonlinear waves for their transient evolution was then launched. This resonance mechanism is now regarded as one of the most important factors in the sea spectrum formation. For an authoritative account of this vital area of oceanography the reader is referred to Phillips (1977).

Also of great interest is a special kind of resonant interaction pertaining to a wavetrain with a narrow band of frequencies and wavelengths. We are indebted to Benjamin and Feir (1967) for their decisive demonstration that Stokes' waves are unstable to slowly modulated periodic (side-band) disturbances. The same instability mechanism was confirmed and extended by

the elegant theory of Whitham (1967) and further extended by Benney and Roskes (1969). The early stage of the nonlinear evolution of a wave packet subsequent to the initial stability was pursued by Lighthill (1967), who used a pair of nonlinear equations of conservation type due to Whitham. With additional accounts for higher-order dispersive effects, Chu and Mei (1971) modified Whitham's equations and traced the evolution of a wave packet for a longer time. An alternative line of development is based on the cubic Schrödinger equation (Zakharov, 1968; Benney and Roskes, 1969), which was shown by Davey (1972) to be equivalent to the conservation equations used by Chu and Mei. Further theoretical advances received a strong boost by Zakharov and Shabat (1972) for their exact analytical solution of the cubic Schrödinger equation. Extensive efforts, including both numerical and experimental, by Yuen, Lake, and associates (see Yuen and Lake, 1980) have now unveiled many new physical secrets of Stokes' waves on deep water.

Of greater complexity are sea waves with a broad distribution of frequencies and directions. A deterministic theory accurate to third order in wave steepness will be the subject of Chapter Fourteen, with emaphsis on Phillips' quartet resonance and Zakharov's theory of the Fourier spectrum. Theories for strongly nonlinear waves have also taken giant strides with the help of new computing techniques. Employing Pade's approximant, Schwartz (1974) was able to solve accurately for progressive waves of arbitrary steepness (up to the limiting height) on water of constant depth. The mathematically awesome problem of breaking has been the subject of determined attacks by Longuet–Higgins and associates. By ingeneous approximations, incisive local, global, and stability analyses, and direct numerical integration, these pioneering contributions have not only led to many remarkable results (see, Longuet–Higgins, 1975, 1978a, b; Longuet–Higgins and Cokelet 1976, 1978; Longuet–Higgins and Fox, 1977, 1978, Vinje and Brevig, 1981), but also inspired futher breakthroughs with the aid of ever-faster computer. A relatively new and powerful numerical technique for highly nonlinear waves is described in Chapter Fifteen.

The scope of the present chapter is limited to the slow evolution of nearly periodic waves, i.e., narrow-banded waves. First, general evolution equations are deduced for nearly uniform Stokes' waves over a horiaontal seabed. The initial instability due to periodic side-band disturbances is discussed next. Typical features of the nonlinear evolution of unidirectional waves are shown through numerical examples. Attention is then shifted to long (infragravity) waves forced by short waves advancing over a variable

depth of parallel contours. As engineering applications we also examine the encounter of nonlinear waves with horizontally two-dimensional bodies. In the first example we treat the diffraction of uniform Stokes waves by a thin wedge. In the second the far field of a slender ship advancing and oscillating in head seas is studied as an application of the two-dimensional wave-modulation theory. Finally the diffraction of second-order Stokes waves by a blunt body is solved analytically.

A more realistic analysis of sea surface requires the consideration of nonlinear interaction of waves within a broad frequency or wave-number band. This difficult topic is the focus of Chapter Fourteen. Recent advances in computational wave hydrodynamics will be surveyed in Chapter Fifteen.

13.2 Evolution Equations for Slowly Modulated Weakly Nonlinear Waves Over Horizontal Seabed

The objective of this section is to deduce a general set of conditions governing a slowly varying train of surface waves which are essentially sinusoidal and propagating in one direction. To this end we shall apply the method of multiple scales.[1] The following account is a mixture of Benney and Roskes (1969), Chu and Mei (1970), and Davey and Stewartson (1974).

13.2.1 Intermediate Depth

For simplicity, the sea bottom is taken to be horizontal at a finite depth h,

$$\frac{\partial \Phi}{\partial z} = 0\,, \quad z = -h\,. \tag{13.2.1}$$

Now any analytic function $[f(x,y,z,t)]_{z=\zeta}$ may be expanded into a Taylor series about $z=0$,

$$f(x,y,\zeta,t) = [f]_0 + \zeta\left[\frac{\partial f}{\partial z}\right]_0 + \frac{\zeta^2}{2}\left[\frac{\partial^2 f}{\partial z^2}\right]_0 + \cdots\,,$$

where

$$[f]_0 = f(x,y,0,t)\cdots\,.$$

[1] Another formalism which is applicable to this class of problems is Whitham's method of averaged Lagrangian. For a full exposition, see Whitham (1974).

Let it be assumed that $\partial f/\partial z = O(kf)$ where k is the characteristic wavenumber. For small $\zeta = O(A)$ the successive terms in the expansion are progressively smaller, essentially in increasing powers of kA. The expansions for the free-surface boundary conditions [Eqs. (1.1.16) and (1.1.14), Chapter 1] are

$$\left[\frac{\partial^2\Phi}{\partial t^2} + g\frac{\partial\Phi}{\partial z}\right]_0 + \zeta\left[\frac{\partial}{\partial z}\left(\frac{\partial^2\Phi}{\partial t^2} + g\frac{\partial\Phi}{\partial z}\right)\right]_0 + \left[\frac{\partial}{\partial t}\mathbf{u}^2\right]_0 + \frac{\zeta^2}{2}\left[\frac{\partial^2}{\partial z^2}\left(\frac{\partial^2\Phi}{\partial t^2} + g\frac{\partial\Phi}{\partial z}\right)\right]_0 + \zeta\left[\frac{\partial^2}{\partial t\partial z}\mathbf{u}^2\right]_0 + \frac{1}{2}[\mathbf{u}\cdot\nabla\mathbf{u}^2]_0 + \cdots = 0 \tag{13.2.2}$$

and

$$-g\zeta = \left[\frac{\partial\Phi}{\partial t}\right]_0 + \zeta\left[\frac{\partial^2\Phi}{\partial t\,\partial z}\right]_0 + \left[\frac{\mathbf{u}^2}{2}\right]_0 + \frac{\zeta^2}{2}\left[\frac{\partial}{\partial t}\frac{\partial^2\Phi}{\partial z^2}\right]_0 + \zeta\left[\frac{\partial}{\partial z}\frac{\mathbf{u}^2}{2}\right]_0 + \cdots \tag{13.2.3}$$

up to the third order $0(kA)^3$.

Let x be the direction of the carrier wave. To allow for slow modulation, we introduce the following cascade of variables:

$$\begin{aligned} x\,, \quad & x_1 = \varepsilon x\,, \quad x_2 = \varepsilon^2 x \ldots\,, \\ & y_1 = \varepsilon y\,, \quad y_2 = \varepsilon^2 y \ldots\,, \\ t\,, \quad & t_1 = \varepsilon t\,, \quad t_2 = \varepsilon^2 t \ldots\,, \end{aligned} \tag{13.2.4}$$

where $\varepsilon = kA \ll 1$, and assume the following perturbation expansions for the unknowns:

$$\Phi = \sum_{n=1} \varepsilon^n \phi_n\,, \quad \zeta = \sum_{n=1} \varepsilon^n \zeta_n\,, \tag{13.2.5}$$

where

$$\begin{aligned} \phi_n &= \phi_n(x, x_1, x_2, \ldots; y_1, y_2, \ldots; z\,; t, t_1, t_2, \ldots)\,, \\ \zeta_n &= \zeta_n(x, x_1, x_2, \ldots; y_1, y_2, \ldots; t, t_1, t_2, \ldots)\,. \end{aligned} \tag{13.2.6}$$

The original derivatives are first changed according to Eq. (2.4.3), Chapter Two, and then substituted into Laplace's equation, the perturbed

free-surface conditions (13.2.2) and (13.2.3), and the bottom condition (13.2.1). The first three orders are collected below.

Laplace equation:

$$\left(\frac{\partial^2}{\partial x^2}+\frac{\partial^2}{\partial z^2}\right)\phi_n = F_n\,, \quad n=1,2,3\,, \tag{13.2.7a}$$

where

$$F_1 = 0\,, \tag{13.2.7b}$$

$$F_2 = -2\phi_{1_{xx_1}}\,, \tag{13.2.7c}$$

$$F_3 = -\left[\left(\frac{\partial^2}{\partial x_1^2}+\frac{\partial^2}{\partial y_1^2}\right)\phi_1 + 2\phi_{1_{xx_2}} + 2\phi_{2_{xx_1}}\right]. \tag{13.2.7d}$$

Free-surface condition (13.2.2):

$$\Gamma\phi_n = G_n \quad \text{on} \quad z=0\,, \tag{13.2.8a}$$

where

$$\Gamma = g\frac{\partial}{\partial z}+\frac{\partial^2}{\partial t^2}\,, \tag{13.2.8b}$$

$$G_1 = 0\,, \tag{13.2.8c}$$

$$G_2 = -[\zeta_1\Gamma_z\phi_1 + (\phi_{1_x}^2+\phi_{1_z}^2)_t + 2\phi_{1_{tt_1}}]\,, \tag{13.2.8d}$$

$$\begin{aligned} G_3 = -\Bigg[&\zeta_2\Gamma_z\phi_1 + \zeta_1\Gamma_z\phi_2 + \frac{1}{2}\zeta_1^2\Gamma_{zz}\phi_1 + 2(\phi_{1_x}\phi_{2_x}+\phi_{1_z}\phi_{2_z})_t \\ &+ \zeta_1(\phi_{1_x}^2+\phi_{1_z}^2)_{tz} + \frac{1}{2}\left(\phi_{1_x}\frac{\partial}{\partial x}+\phi_{1_z}\frac{\partial}{\partial z}\right)(\phi_{1_x}^2+\phi_{1_z}^2) \\ &+ 2\phi_{2_{tt_1}} + 2\phi_{1_z}\phi_{1_{zt_1}} + 2\phi_{1_{x_1}}\phi_{1_{xt}} + 2\phi_{1_x}\phi_{1_{xt_1}} \\ &+ 2\phi_{1_x}\phi_{1_{tx_1}} + 2\zeta_1\phi_{1_{ztt_1}} + 2\phi_{1_{tt_2}} + \phi_{1_{t_1t_1}}\Bigg]. \end{aligned} \tag{13.2.8e}$$

Bernoulli equation on the free surface:

$$-g\zeta_n = H_n\,, \quad \text{on} \quad z=0\,, \tag{13.2.9a}$$

where

$$H_1 = \phi_{1_t}\,, \tag{13.2.9b}$$

$$H_2 = \phi_{2_t} + \frac{1}{2}(\phi_{1_x}^2 + \phi_{1_z}^2) + \phi_{1_{t_1}} + \zeta_1\phi_{1_{zt}}\,, \tag{13.2.9c}$$

$$\begin{aligned} H_3 = {} & \phi_{3_t} + \phi_{1_x}\phi_{2_x} + \phi_{1_z}\phi_{2_z} + \zeta_1\phi_{2_{zt}} + \zeta_2\phi_{1_{zt}} \\ & + \frac{1}{2}\zeta_1^2\phi_{1_{zzt}} + \frac{1}{2}\zeta_1(\phi_{1_x}^2 + \phi_{1_z}^2)_z + \phi_{2_{t_1}} \\ & + \phi_{1_x}\phi_{1_{x_1}} + \phi_{1_{t_1}} + \zeta_1\phi_{1_{zt_1}}\,. \end{aligned} \tag{13.2.9d}$$

Condition on the bottom:

$$\frac{\partial\phi_n}{\partial z} = 0\,, \quad z = -h\,. \tag{13.2.10}$$

The first-order solution is the usual linearized propagating wave. At the higher orders the nonlinear forcing terms on the free surface imply that higher harmonics must be present in the higher-order solutions. We therefore expand

$$\{\phi_n, F_n, G_n\} = \sum_{m=-n}^{n} e^{im\psi}\{\phi_{nm}, F_{nm}, G_{nm}\}\,, \tag{13.2.11a}$$

where

$$\psi = kx - \omega t \tag{13.2.11b}$$

is the phase of the fundamental harmonic at the leading order. For the resulting ϕ to be real, we require that

$$\phi_{n,-m} = (\phi_{nm})^*\,. \tag{13.2.12}$$

Furthermore, the amplitudes depend on the slow variables and z

$$\begin{aligned} (\phi_{nm}, F_{nm}) &= \text{functions of } (x_1, x_2, \ldots, y_1, y_2, \ldots, z, t_1, t_2, \ldots)\,, \\ G_{nm} &= G_{nm}(x_1, x_2, \ldots, y_1, y_2, \ldots, t_1, t_2, \ldots)\,. \end{aligned} \tag{13.2.13}$$

Substituting Eq. (13.2.11a) into the perturbation equations (13.2.7a), (13.2.8), and (13.2.10), we obtain at each order (n) and harmonic (m) a boundary-value problem in z:

$$\left(\frac{\partial^2}{\partial z^2} - m^2k^2\right)\phi_{nm} = F_{nm}\,, \quad -h < z < 0\,, \tag{13.2.14}$$

$$\left(g\frac{\partial}{\partial z} - m^2\omega^2\right)\phi_{nm} = G_{nm}\,, \quad z = 0\,, \tag{13.2.15}$$

$$\frac{\partial}{\partial z}\phi_{nm} = 0\,, \qquad z = -h\,. \tag{13.2.16}$$

The above boundary-value problems will be solved sequentially. For convenience the following abbreviations will be employed:

$$\begin{gathered} Q = k(z+h)\,, \quad q = kh\,, \\ \operatorname{ch} q = \cosh q\,, \quad \operatorname{sh} q = \sinh q\,, \quad \operatorname{th} q = \tanh q\,. \end{gathered} \tag{13.2.17}$$

$n = 1$: The forcing terms are

$$F_{10} = G_{10} = 0, \quad F_{11} = G_{11} = 0\,. \tag{13.2.18}$$

The solutions, which are homogeneous, are

$$m = 0: \quad \phi_{10} = \phi_{10}(x_1, x_2, y_1, y_2, t_1, t_2, \ldots) = \phi_{10}^*\,, \tag{13.2.19}$$

$$m = 1: \quad \phi_{11} = -\frac{g\operatorname{ch} Q}{2\omega \operatorname{ch} q} iA\,, \tag{13.2.20a}$$

with

$$\omega^2 = gk \operatorname{th} kh\,, \tag{13.2.20b}$$

and $A = A(x_1, x_2, y_1, y_2, t_1, t_2, \ldots)$. The total first-order solution is

$$\phi_1 = \phi_{10} - \frac{g\operatorname{ch} Q}{2\omega \operatorname{ch} q}(iAe^{i\psi} + *)\,, \tag{13.2.21}$$

$$\zeta_1 = \frac{1}{2}(Ae^{i\psi} + *)\,. \tag{13.2.22}$$

Both ϕ_{10} and A are, so far, arbitrary functions of the slow variables.

$n = 2$: For $n \geqq 2$, special care regarding solvability must be given to $m = 0$ (the zeroth harmonic, or the mean), and to $m = 1$ (the first harmonic), as the homogeneous problems have nontrivial solutions. For $m = 0$, the homogeneous solution is constant in z; the solvability condition for ϕ_{n0} is simply

$$\frac{1}{g}G_{n0} - \int_{-h}^{0} dz\, F_{n0}\,. \tag{13.2.23}$$

For $m = 1$, the homogeneous solution is proportional to $\cosh k(z+h)$, and the solvability condition for ϕ_{n1} follows from Green's formula

$$\frac{1}{g}G_{n1} = \int_{-h}^{0} dz\, F_{n1} \frac{\cosh k(z+h)}{\cosh kh}\,. \tag{13.2.24}$$

Equations (13.2.23) and (13.2.24) will lead to the so-called *evolution equations*.

For higher harmonics $|m| \geq 2$, the boundary-value problems admit no homogeneous solution. Indeed, if there were one, it would be of the form (13.2.20a) with (k, ω) replaced by $(mk, m\omega)$. However, mk and $m\omega$ would then be subjected to the dispersion relation (13.2.20b), which is not possible. Consequently, the inhomogeneous problems for $|m| \geq 2$ are always solvable.

The forcing terms for the second-order problems are

$$F_{20} = G_{20} = 0\,, \tag{13.2.25}$$

$$F_{21} = -\frac{\omega \operatorname{ch} Q}{\operatorname{sh} q}\frac{\partial A}{\partial x_1}\,, \quad F_{22} = 0\,, \tag{13.2.26}$$

$$G_{21} = \frac{\omega^2 \operatorname{ch} q}{k \operatorname{sh} q}\frac{\partial A}{\partial t_1}\,, \quad G_{22} = \frac{3i\omega^3 A^2}{4 \operatorname{sh}^2 q}\,. \tag{13.2.27}$$

The solution for the zeroth harmonic is

$$\phi_{20} = \phi_{20}(x_1, x_2, y_1, y_2, t_1, t_2, \ldots) = \phi_{20}^*\,. \tag{13.2.28}$$

For $m = 1$, we invoke the solvability condition by substituting Eqs. (13.2.26) and (13.2.27) into Eq. (13.2.24), and obtain

$$\frac{\partial A}{\partial t_1} + C_g \frac{\partial A}{\partial x_1} = 0 \quad \text{with} \quad C_g = \frac{\partial \omega}{\partial k}\,, \tag{13.2.29}$$

which has been found before in Section 2.4. The solution is

$$\phi_{21} = -\frac{\omega}{2k^2 \operatorname{sh} q}(Q \operatorname{sh} Q)\frac{\partial A}{\partial x_1}\,. \tag{13.2.30}$$

We note immediately that ϕ_{21} blows up as $kh \uparrow \infty$, which is not surprising, because the limiting process violates the original premise that $O(x_1), O(x_2), \ldots > O(h)$. Therefore, we restrict the present solution to $kh = O(1)$ and deal later with the infinite depth separately.

For $m = 2$, the inhomogeneous solution is straightforward:

$$\phi_{22} = -\frac{3}{16}\frac{\omega \operatorname{ch} 2Q}{\operatorname{sh}^4 q} iA^2 \,. \tag{13.2.31}$$

The total second-order solution is

$$\phi_2 = \phi_{20} - \frac{\omega}{2k^2 \operatorname{sh} q}(Q \operatorname{sh} Q)\left(\frac{\partial A}{\partial x_1} e^{i\psi} + *\right) - \frac{3}{16}\frac{\omega \operatorname{ch} 2Q}{\operatorname{sh}^4 q}(iA^2 e^{2i\psi} + *)\,, \tag{13.2.32}$$

and

$$\zeta_2 = \left\{-\frac{1}{g}\phi_{10t_1} - \frac{k}{2 \operatorname{sh} 2q}|A|^2\right\} + \frac{1}{2\omega}\left(i\frac{\partial A}{\partial_{t_1}} e^{i\psi} + *\right) - \frac{q \operatorname{sh} q}{2k \operatorname{ch} q}\left(i\frac{\partial A}{\partial x_1} e^{i\psi} + *\right) + \frac{k \operatorname{ch} q(2 \operatorname{ch}^2 q + 1)}{8 \operatorname{sh}^3 q}(A^2 e^{2i\psi} + *)\,. \tag{13.2.33}$$

$n = 3$: For $m = 0$, the forcing terms are

$$F_{30} = -\left(\frac{\partial^2}{\partial x_1^2} + \frac{\partial^2}{\partial y_1^2}\right)\phi_{10}\,, \tag{13.2.34}$$

$$G_{30} = \frac{\omega^3 \operatorname{ch}^2 q}{2k \operatorname{sh}^2 q}(AA^*)_{x_1} - \frac{\omega^2}{4 \operatorname{sh}^2 q}(AA^*)_{t_1} - \frac{\partial^2 \phi_{10}}{\partial t_1^2}\,, \tag{13.2.35}$$

where Eq. (13.2.29) has been used. Condition (13.2.23) requires that $G_{30} = ghF_{30}$ so that

$$\frac{\partial^2 \phi_{10}}{\partial t_1^2} - gh\left(\frac{\partial^2}{\partial x_1^2} + \frac{\partial^2}{\partial y_1^2}\right)\phi_{10} = \frac{\omega^3 \operatorname{ch}^2 q}{2k \operatorname{sh}^2 q}(AA^*)_{x_1} - \frac{\omega^2}{4 \operatorname{sh}^2 q}(AA^*)_{t_1}\,. \tag{13.2.36}$$

Physically, Eq. (13.2.36) describes a long wave generated by short-wave modulation. For $m = 1$, the forcing terms are

$$F_{31} = \frac{\omega}{k \operatorname{sh} q}\left[Q \operatorname{sh} Q + \frac{1}{2} \operatorname{ch} Q\right] i\frac{\partial^2 A}{\partial x_1^2} - \frac{\omega \operatorname{ch} Q}{\operatorname{sh} q}\left(\frac{\partial A}{\partial x_2} - \frac{i}{2k}\frac{\partial^2 A}{\partial y_1^2}\right) \tag{13.2.37}$$

and

$$G_{31} = \frac{1}{16\,\mathrm{sh}^5 q}\omega^3 k\,\mathrm{ch}\,q(\mathrm{ch}\,4q + 8 - 2\,\mathrm{th}^2 q)i|A|^2 A$$
$$- \frac{\omega k}{\mathrm{sh}\,2q}\left(\frac{\partial\phi_{10}}{\partial t_1} - \frac{2\omega\,\mathrm{ch}^2 q}{k}\frac{\partial\phi_{10}}{\partial x_1}\right) iA$$
$$+ \frac{\omega\,\mathrm{ch}\,q}{2k\,\mathrm{sh}\,q} i\frac{\partial^2 A}{\partial t_1^2} - \frac{\omega^2 q}{k^2} i\frac{\partial^2 A}{\partial x_1\,\partial t_1} + \frac{\omega^2\,\mathrm{ch}\,q}{k\,\mathrm{sh}\,q}\frac{\partial A}{\partial t_2}\,. \qquad (13.2.38)$$

Invoking the solvability condition (13.2.24), we have

$$\frac{\partial A}{\partial t_2} + C_g\frac{\partial A}{\partial x_2} - \frac{iC_g}{2k}\frac{\partial^2 A}{\partial y_1^2} - \frac{i\omega q}{k^2\,\mathrm{sh}\,2q}\,\mathrm{ch}^2 q\frac{\partial^2 A}{\partial x_1^2}$$
$$+ \frac{i}{2\omega}\frac{\partial^2 A}{\partial t_1^2} - \frac{ik^2 A}{2\omega\,\mathrm{ch}^2 q}\left(\frac{\partial\phi_{10}}{\partial t_1} - \frac{2\omega\,\mathrm{ch}^2 q}{k}\frac{\partial\phi_{10}}{\partial x_1}\right) - \frac{iq\,\mathrm{sh}\,q}{k\,\mathrm{ch}\,q}\frac{\partial^2 A}{\partial x_1\,\partial t_1}$$
$$+ \frac{i\omega k^2(\mathrm{ch}\,4q + 8 - 2\,\mathrm{th}^2 q)}{16\,\mathrm{sh}^4 q}|A|^2 A = 0\,. \qquad (13.2.39)$$

With the help of Eq. (13.2.29) we write

$$\frac{\partial^2 A}{\partial t_1^2} = C_g^2\frac{\partial^2 A}{\partial x_1^2}\,, \quad \frac{\partial^2 A}{\partial t\,\partial x_1} = C_g\frac{\partial^2 A}{\partial x_1^2}$$

in Eq. (13.2.39). Finally, we add Eqs. (13.2.29) and (13.2.39), and consider ϕ_{10} and A as functions of x_1, y_1, and t_1 only, that is,

$$\frac{\partial}{\partial t_1} + \varepsilon\frac{\partial}{\partial t_2} \to \frac{\partial}{\partial t_1}\,, \quad \frac{\partial}{\partial x_1} + \varepsilon\frac{\partial}{\partial x_2} \to \frac{\partial}{\partial x_1}\,,$$

yielding

$$\left(\frac{\partial}{\partial t_1} + C_g\frac{\partial}{\partial x_1}\right) A + i\varepsilon\Bigg\{ - \frac{1}{2}\left(\frac{\partial^2\omega}{\partial k^2}\right)\frac{\partial^2 A}{\partial x_1^2} - \frac{C_g}{2k}\frac{\partial^2 A}{\partial y_1^2}$$
$$+ \frac{\omega k^2(\mathrm{ch}\,4q + 8 - 2\,\mathrm{th}^2 q)}{16\,\mathrm{sh}^4 q}|A|^2 A - \left(\frac{k^2}{2\omega\,\mathrm{ch}^2 q}\frac{\partial\phi_{10}}{\partial t_1} - k\frac{\partial\phi_{10}}{\partial x_1}\right) A\Bigg\} = 0\,, \qquad (13.2.40)$$

where

$$-\frac{1}{2}\frac{\partial^2\omega}{\partial k^2} = \frac{C_g^2}{2\omega} - \frac{\omega q\,\mathrm{ch}^2 q}{k^2\,\mathrm{sh}\,2q} + \frac{q\,\mathrm{sh}\,q}{k\,\mathrm{ch}\,q}C_g > 0\,. \qquad (13.2.41)$$

Equations (13.2.36) and (13.2.40) were first obtained by Benney and Roskes. Together, they govern the coupled slow evolution of first-order amplitude A and the mean flow potential ϕ_{10}. It is significant that third-order nonlinearity affects first-order amplitude if the time and distance are ε^{-2} times greater than the wave period and length, respectively.

For two-dimensional problems ($\partial/\partial y_1 = 0$), further simplifications are possible. If we let

$$\xi = x_1 - C_g t_1\,, \quad \tau = \varepsilon t_1\,, \tag{13.2.42}$$

then

$$\frac{\partial}{\partial t_1} = \varepsilon\frac{\partial}{\partial \tau} - C_g\frac{\partial}{\partial \xi} \quad \text{and} \quad \frac{\partial}{\partial x_1} = \frac{\partial}{\partial \xi}\,,$$

and Eq. (13.2.36) may be integrated once with respect to ξ, yielding

$$\frac{\partial \phi_{10}}{\partial \xi} = S(\tau) - \frac{\omega^2(2\omega\,\mathrm{ch}^2 q + kC_g)}{4k\,\mathrm{sh}^2 q(gh - C_g^2)}|A|^2 + O(\varepsilon)\,,$$

where $S(\tau)$ is an arbitrary function of τ. Substituting this result into Eq. (13.2.40), we get

$$-i\frac{\partial A}{\partial \tau} + \alpha\frac{\partial^2 A}{\partial \xi^2} + \beta|A|^2 A + \gamma A = 0\,, \tag{13.2.43a}$$

where

$$\alpha = -\frac{1}{2}\omega''(k) \tag{13.2.43b}$$

$$\beta = \frac{\omega k^2}{16\,\mathrm{sh}^4 q}(\mathrm{ch}\,4q + 8 - 2\,\mathrm{th}^2 q) - \frac{\omega}{2\,\mathrm{sh}^2 2q}\frac{(2\omega\,\mathrm{ch}^2 q + kC_g)^2}{(gh - C_g^2)}\,, \tag{13.2.43c}$$

and

$$\gamma(\tau) = \frac{S(\tau)k}{2\omega\,\mathrm{ch}^2 q}(2\omega\,\mathrm{ch}^2 q + kC_g)\,. \tag{13.2.43d}$$

The function $S(\tau)$ vanishes for a wavetrain beginning from rest where A and $\partial\phi_{10}/\partial\xi$ tend to zero as $\xi \to \infty$. Otherwise, the term γA may be eliminated from Eq. (13.2.43a) by introducing

$$A = B\exp\left(-i\int \gamma\, d\tau\right), \tag{13.2.44}$$

resulting in the cubic Schrödinger equation

$$-iB_\tau + \alpha B_{\xi\xi} + \beta|B|^2 B = 0 \tag{13.2.45}$$

which was derived for finite depth by Hashimoto and Ono (1972). A similar equation was deduced earlier for infinite depth by Zakharov (1968).

Equation (13.2.43) or (13.2.45) may be expressed in real functions by letting

$$A = a \exp\left[i\left(\int W\, d\xi - \int \gamma\, d\tau\right)\right] \tag{13.2.46a}$$

in Eq. (13.2.43), or, equivalently, by letting

$$B = a \exp\left(i \int W\, d\xi\right) \tag{13.2.46b}$$

in Eq. (13.2.45), where $W = W(\xi, \tau)$. Separating the real and imaginary parts, we get

$$\frac{\partial a^2}{\partial \tau} - 2\alpha \frac{\partial}{\partial \xi}(W a^2) = 0\,, \tag{13.2.47a}$$

$$\frac{\partial W}{\partial \tau} + \frac{\partial}{\partial \xi}\left[\alpha\left(\frac{1}{a}\frac{\partial^2 a}{\partial \xi^2} - W^2\right) + \beta a^2\right] = 0\,. \tag{13.2.47b}$$

These equations are in the form of conservation laws $\partial P/\partial \tau + \partial Q/\partial \xi = 0$; they were derived for deep-water waves by Chu and Mei (1970), and by Whitham (1967) without the term $(1/a)\partial^2 a/\partial \xi^2$. The connection between Eqs. (13.2.45) and (13.2.47) was pointed out by Davey (1972).

13.2.2 Deep Water Limit

The formal limits of Eqs. (13.2.36) and (13.2.40) for $kh \to \infty$ are

$$\left(\frac{\partial^2}{\partial x_1^2} + \frac{\partial^2}{\partial y_1^2}\right)\phi_{10} = 0\,, \tag{13.2.48}$$

$$\left(\frac{\partial}{\partial t_1} + C_g \frac{\partial}{\partial x_1}\right)A + i\varepsilon\left\{\frac{\omega}{4k^2}\left(\frac{1}{2}A_{x_1 x_1} - A_{y_1 y_1}\right) + \frac{1}{2}\omega k^2 |A|^2 A + k\phi_{10_{x_1}} A\right\} = 0\,, \tag{13.2.49}$$

which appear to be quite reasonable results. The kinematic or total boundary condition on the free surface requires that

$$\frac{\partial \phi_{10}}{\partial z} = 0\,, \quad z = 0\,. \tag{13.2.50}$$

A possible solution for ϕ_{10} is a time-varying current

$$\frac{\partial \phi_{10}}{\partial t_1} = f(t_1)\,, \tag{13.2.51}$$

where f is prescribed from upstream conditions. Equation (13.2.49) then governs A only. Nevertheless, the solution for ϕ_{21}, is no longer meaningful as pointed out after Eq. (13.2.30). Inconsistency also arises at the third-order free-surface condition, (13.2.8a), which gives for $h \to \infty$

$$\frac{\partial^2 \phi_{10}}{\partial t_1^2} = \frac{\omega^3}{2k}(AA^*)_{x_1} \tag{13.2.52}$$

and renders the problem for A and ϕ_{10} overdetermined. To remedy this difficulty, Roskes (1969) reasoned that by assuming $kh \gg 1$ at the start one should allow slow modulation in the vertical direction as well. Thus, he introduced

$$z_1 = \varepsilon z\,, \quad z_2 = \varepsilon^2 z \cdots\,. \tag{13.2.53}$$

However, these coordinates should only enter the long-scale quantities $\phi_{10}, \phi_{20}, \ldots$, and so on; the short-wave potential is nonzero only within a wavelength from the free surface (hence in the region $z_1, z_2, \ldots \ll 1$). Carrying out the perturbation analysis, one finds, instead of Eq. (13.2.36),

$$\left(\frac{\partial^2}{\partial x_1^2} + \frac{\partial^2}{\partial y_1^2} + \frac{\partial^2}{\partial z_1^2}\right)\phi_{10} = 0\,, \tag{13.2.54}$$

and instead of Eq. (13.2.39),

$$(A_{t_2} + C_g A_{x_2}) + i\left\{\frac{\omega}{8k^2}(A_{x_1x_1} - 2A_{y_1y_1}) + \frac{1}{2}\omega k^2 |A|^2 A\right\}$$
$$+ k\left(\frac{\partial \phi_{10}}{\partial z_1} + i\frac{\partial \phi_{10}}{\partial x_1}\right)A = 0\,. \tag{13.2.55}$$

If $h = O(\varepsilon k)^{-1}$, the bottom condition can be generalized slightly so that

$$\frac{\partial \phi_{10}}{\partial n_1} = 0\,, \quad z_1 = 0 \quad \text{and} \quad -h_1(x_1, y_1) \quad \text{with} \quad h_1 = O(1)\,. \tag{13.2.56}$$

Thus, the potential ϕ_{10} of the large-scale current is deflected by bottom variations, which then affect the short-wave amplitude indirectly through Eq. (13.2.55). Furthermore, Eq. (13.2.52) is replaced by

$$g\frac{\partial\phi_{20}}{\partial z_1} = -\frac{\partial^2\phi_{10}}{\partial t_1^2} + \frac{\omega^3}{2k}(AA^*)_{x_1} \tag{13.2.57}$$

which provides a boundary condition for ϕ_{20} and removes the overdeterminancy on ϕ_{10} and A.

In the simplest case of constant h_1 we can take

$$\frac{\partial\phi_{10}}{\partial x_1} = \mathscr{U}(\tau) \tag{13.2.58}$$

which is a spatially constant current determined by the condition far upstream. Note that the magnitude of the current is $\varepsilon\partial\phi_{10}/\partial x = \varepsilon^2\partial\phi_{10}/\partial x_1 = \varepsilon^2\mathscr{U} = O(\varepsilon^2)$. Equation (13.2.55) can be further simplified by the coordinate transformation (13.2.42); the result is

$$\frac{\partial A}{\partial\tau} + i\left\{\frac{\omega}{4k^2}\left(\frac{1}{2}A_{\xi\xi} - A_{y_1y_1}\right) + k\mathscr{U}A + \frac{\omega k^2}{2}|A|^2A\right\} = 0\,. \tag{13.2.59}$$

The current term may be removed by $A = B\exp(-ik\int\mathscr{U}\,dr)$, yielding,

$$\frac{\partial B}{\partial\tau} + i\left\{\frac{\omega}{8k^2}(B_{\xi\xi} - 2B_{y_1y_1}) + \frac{\omega k^2}{2}|B|^2B\right\} = 0\,, \tag{13.2.60}$$

which was first derived by Zakharov (1968). In the limit of $\partial/\partial y_1 = 0$, Eq. (13.2.60) reduces to Eq. (13.2.45) with

$$\alpha = \frac{\omega}{8k^2} \quad \text{and} \quad \beta = \frac{\omega k^2}{2}\,. \tag{13.2.61}$$

13.3 Uniform Stokes' Waves

We seek a solution which has no slow modulation in x and y, that is, A, $\partial\phi_{10}/\partial x_1, \partial\phi_{10}/\partial t_1, \ldots$ do not depend on $x_1, x_2, \ldots$ and $y_1, y_2, \ldots$. Equation (13.2.29) requires that A be independent of t_1; thus, $A = A(t_2)$. From Eq. (13.2.36) we get

$$\phi_{10} = \mathscr{U}x_1 - gbt_1 \tag{13.3.1}$$

where $\mathscr{U}$ and b are arbitrary constants. With Eq. (13.3.1), Eq. (13.2.39) is reduced to

$$\frac{\partial A}{\partial t_2} + i\omega_2 |A|^2 A = 0\,, \tag{13.3.2}$$

where

$$\omega_2 = \frac{\omega k^2}{16\,\mathrm{sh}^4 q}(8 + \mathrm{ch}\,4q - 2\,\mathrm{th}^2 q) - \frac{1}{|A|^2}\left(k\mathscr{U} + \frac{gk^2 b}{2\omega\,\mathrm{ch}^2 q}\right). \tag{13.3.3}$$

The solution is readily found to be

$$A = a_0 \exp(-i\omega_2 a_0^2 t_2)\,, \tag{13.3.4}$$

with a_0 real and an arbitrary phase ignored. Thus, up to $O(\varepsilon^2)$ nonlinearity changes the wave phase only. The wave profile is, to the leading order,

$$\zeta_1 = \frac{1}{2}(a_0 e^{i\tilde{\psi}} + *)\,, \tag{13.3.5a}$$

where

$$\tilde{\psi} = (kx - \tilde{\omega}t) \tag{13.3.5b}$$

is the new phase, and

$$\tilde{\omega} = \omega + \varepsilon^2 \omega_2 a_0^2 \tag{13.3.6}$$

is the nonlinear dispersion relation. The phase speed also depends on amplitude

$$\tilde{C} = \frac{\omega}{k} + \varepsilon^2 \frac{\omega_2}{k} a_0^2\,. \tag{13.3.7}$$

The ordering parameter ε has served its purpose and may be removed.

The second-order solution is

$$\phi_2 = \phi_{20} - \frac{3}{16}\frac{\omega\,\mathrm{ch}\,2Q}{\mathrm{sh}^4 q}(ia_0^2 e^{2i\tilde{\psi}} + *)\,, \tag{13.3.8}$$

$$\zeta_2 = b - \frac{k}{2\,\mathrm{sh}\,2q} a_0^2 + \frac{k\,\mathrm{ch}\,q(2\,\mathrm{ch}^2 q + 1)}{8\,\mathrm{sh}^3 q}(a_0^2 e^{2i\tilde{\psi}} + *)\,. \tag{13.3.9}$$

From the solvability of ϕ_{40} it may be shown that $\partial\phi_{20}/\partial z = 0$, implying that $\phi_{20} = \phi_{20}(x_1, x_2, \ldots, y_1, y_2, \ldots)$ which does not affect the velocity field at the second order. The second harmonic in ζ_2 is always positive for $\tilde{\psi} = 0, \pi, 2\pi, \ldots$ and elevates the crests and the troughs; therefore, the total free surface is more peaked at the crests and flatter at the troughs. The second term in Eq. (13.3.9) represents the mean sea-level set-down which

corresponds to Eq. (13.3.5), and has been deduced before in Section 11.6 [cf. Eq. (11.6.6)].

The ratio of ζ_2 to ζ_1 is of the order $ka_0/(kh)^3$ when $kh \ll 1$. Thus, Stokes' theory is valid in shallow water only if

$$\frac{ka_0}{(kh)^3} \ll 1\,. \tag{13.3.10}$$

The above ratio is precisely the Ursell parameter mentioned in the preceding chapter and is a measure of frequency dispersion versus nonlinearity.

Because of the arbitrariness of $\mathscr{U}$ and b, various expressions for the Stokes wave have been used in the literature. For example, by letting A be indcpendent of ξ and S be a constant, we may integrate Eq. (13.2.43a) to obtain Eq. (13.3.4) with

$$\omega_2^2 a_0^2 = \beta a_0^2 + \gamma\,. \tag{13.3.11}$$

This dispersion relation can be reconciled with Eq. (13.3.3) if

$$\mathscr{U} = S - \frac{\omega(2\omega\,\mathrm{ch}^2 q + kC_g)}{4k\,\mathrm{sh}^2 q(gh - C_g^2)}a_0^2 \tag{13.3.12a}$$

and

$$b = \frac{1}{g}\mathscr{U} C_g\,. \tag{13.3.12b}$$

The preceding expressions are equivalent to those given by Davey and Stewartson (1974).

13.4 Side-Band Instability of Stokes' Waves

The uniform Stokes waves have been applied for many years in engineering literature as a basis of computing wave forces. Massive work has been devoted to higher-order corrections in order to gain a fuller account of nonlinearity. Nevertheless, it is a common experience in the laboratory that a uniform train of relatively steep waves is difficult to maintain in a long-wave tank (see, e.g., Russell and Osorio, 1957). This difficulty was first explained theoretically by the penetrating work of Benjamin and Feir (1967) who found that Stokes' waves were unstable to *side-band* disturbances, that is, disturbances whose frequencies deviated slightly from the fundamental frequency of the carrier waves.

Let us start from the nonlinear Schrödinger equation [NLS, (13.2.45)]. The basic Stokes wave

$$B_0 = a_0 e^{-i\beta a_0^2 \tau} \tag{13.4.1}$$

is the solution to

$$-i\frac{\partial B_0}{\partial \tau} + \beta |B_0|^2 B_0 = -i\frac{\partial B_0}{\partial \tau} + \beta a_0^2 B_0 = 0\,. \tag{13.4.2}$$

Let the following small disturbance

$$B = B_0(1+\delta)\,, \quad \delta \ll 1 \tag{13.4.3}$$

be introduced into (13.2.45) so that

$$-i\frac{\partial B_0}{\partial \tau}(1+\delta) - iB_0\frac{\partial \delta}{\partial \tau} + \alpha B_0 \frac{\partial^2 \delta}{\partial \xi^2} + \beta a_0^2 B_0 (1+\delta)^2 (1+\delta^*) = 0\,.$$

Keeping only first-order terms in δ, we get

$$B_0 \left\{ -i\frac{\partial B_0}{\partial \tau}\frac{\delta}{B_0} - i\frac{\partial \delta}{\partial \tau} + \alpha \frac{\partial^2 \delta}{\partial \xi^2} + \beta a_0^2 (2\delta + \delta^*) \right\} = 0$$

which can be simplified to

$$-i\frac{\partial \delta}{\partial \tau} + \alpha \frac{\partial^2 \delta}{\partial \xi^2} + \beta a_0^2 (\delta + \delta^*) = 0 \tag{13.4.4}$$

after using (13.4.2). Putting $\delta = c + id$ in the preceding equation and separating the real and imaginary parts, we obtain

$$\frac{\partial c}{\partial \tau} + \alpha \frac{\partial^2 d}{\partial \xi^2} = 0\,,$$

$$-\frac{\partial d}{\partial \tau} + \alpha \frac{\partial^2 c}{\partial \xi^2} + 2\beta a_0^2 c = 0\,.$$

Either c or d can be eliminated by cross differentiation to give

$$\alpha^2 \frac{\partial^4 (c,d)}{\partial \xi^4} + 2\alpha\beta a_0^2 \frac{\partial^2 (c,d)}{\partial \xi^2} - \frac{\partial^2 (c,d)}{\partial \tau^2} = 0\,. \tag{13.4.5}$$

Consider the following traveling wave disturbance

$$c = \mathrm{Re}\left\{ C e^{i(K\xi - \Omega\tau)} \right\}, \quad d = \mathrm{Re}\left\{ D e^{i4(K\xi - \Omega\tau)} \right\} \tag{13.4.6}$$

where C and D are complex constants. As will be explained later, this disturbance represents physically the side-bands. For a nontrivial solution to (13.4.5), the following dispersion relation must hold,

$$\Omega = \pm\sqrt{\alpha^2 K^2 - 2\alpha\beta a_0^2}\,. \tag{13.4.7}$$

If $\alpha\beta < 0$, the square root is always real and the side-band disturbance is purely sinusoidal, hence is neutrally stable. If, however, $\alpha\beta > 0$, Ω can be imaginary and the side-band disturbance can increase exponentially with time, hence is unstable; this occurs when

$$K^2 < \frac{2\beta a_0^2}{\alpha}\,. \tag{13.4.8}$$

Because of Eq. (13.2.61), Stokes' waves on *deep water* are unstable if

$$\left|\frac{K}{k}\right| < 8^{1/2} k a_0\,. \tag{13.4.9}$$

The steeper the waves, the broader the unstable side band. The dispersion relation corresponding to Eq. (13.4.7) is

$$\Omega = \pm\omega\left[\frac{K^2}{8k^2}\left(\frac{K^2}{8k^2} - k^2 a_0^2\right)\right]^{1/2}\,. \tag{13.4.10}$$

The unstable growth rate is zero at both $K = 0$ and $8^{1/2}k^2 a_0$. The maximum growth rate occurs when

$$\left|\frac{K}{k}\right| = 2ka_0\,, \tag{13.4.11}$$

at which

$$\operatorname{Max}\Omega = \pm i\frac{1}{2}\omega(k^2 a_0^2)\,. \tag{13.4.12}$$

The corresponding $\bar{a}'$ and $\overline{W}'$ are out of phase by $\frac{1}{2}\pi$. Generally, the growth rate $\operatorname{Im}\Omega$ varies with the wavelength of the side-band disturbance as shown in Fig. 13.1.

To see the physical meaning of the disturbance represented by (13.4.6), we return to the free-surface displacement

$$\zeta = \operatorname{Re}\{Ae^{ikx-i\omega t}\} = \operatorname{Re}\left\{B\exp\left(ikx - i\omega t - i\int\gamma\,d\tau\right)\right\}$$

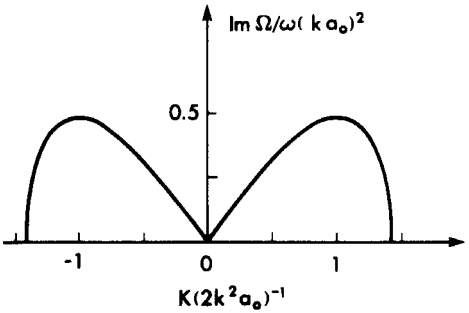

Figure 13.1: The asymptotic growth rate of the side-band amplitudes as à function of a modulational wavenumber (from Benjamin and Feir, 1967, *J. Fluid Mech.* Reproduced by permission of Cambridge University Press).

and substitute (13.4.3) and then (13.4.6) to get

$$\zeta = \mathrm{Re}\left\{ a_0 \left[\exp\left(ikx - i\omega t - i\beta a_0^2 \epsilon^2 t - i \int \gamma \, d\tau \right) \right] \right.$$
$$\cdot \left[1 + \frac{1}{2}(C + iD) \exp(iK(x_1 - C_g t_1) - i\Omega t_2) \right.$$
$$\left. \left. + \frac{1}{2}(C^* - iD^*) \exp(-iK(x_1 - C_g t_1) + i\Omega t_2) \right] \right\}.$$

The first term in the curley brackets is the carrier (Stokes) waves. The next two are small disturbances with the frequency shifts $\pm\epsilon\Omega = \epsilon K C_g$ from the carrier wave, hence they are called side-bands.

A physical explanation of this side-band instability has been given by Lighthill (1978, p. 462). Consider a Stokes wavetrain with a slowly modulated envelope. The crests near a peak of the envelope are faster than those on either side of the peak and, therefore, tend to shorten the waves ahead and lengthen the waves behind. Now the group velocity in deep water is larger for longer waves. The rate of energy transport is lower in front and higher behind, hence accumulation occurs near the envelope peak, whose height must increase. Similarly, the trough of the envelope will tend to decrease, resulting in instability.

Controlled experiments by Feir as reported in Benjamin (1967) and by Lake and Yuen (1977) support the theory fairly well as shown in Fig. 13.2. The discrepancy decreases for smaller wave slope or slower rate of modulation (smaller K/k).

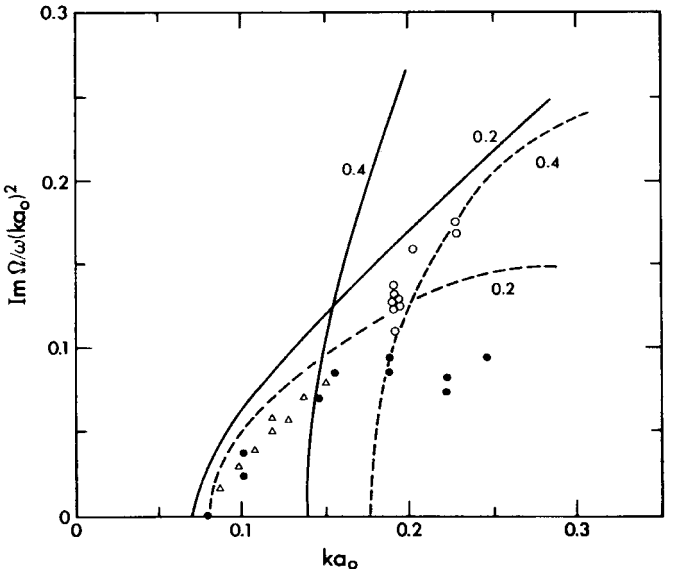

Figure 13.2: Comparison of calculated amplification rate with experimental results as a function of wave slope. Theoretical results: solid curve, by Eq. (13.4.10); dashed curve, Crawford et al. (1981). For $K/k = 0.2$, the Longuet–Higgins (1978b) results by exact theory cannot be distinguished from the dashed line. Experimental results: ◯, $K/k = 0.4$ and ●, $K/k = 0.2$, by Lake et al. (1977); △, $K/k = 0.2$ by Benjamin (1967) (from Crawford et al., 1981, *J. Fluid Mech.* Reproduced by permission of Cambridge University Press).

From the expressions of α and β in Eqs. (13.2.43b) and (13.2.43c), it can be shown that the Stokes waves on finite depth are unstable to colinear side-band disturbances if $kh > 1.36$.

Benney and Roskes (1969) further studied side-band disturbances which propagated obliquely to the primary Stokes waves [cf. Eqs. (13.3.1) and (13.3.4)]. Starting from Eqs. (13.2.36) and (13.2.40) directly and letting

$$A = (a_0 + A') \exp(-i\omega_2 a_0^2 \tau)\,,$$

$$\phi_{10} = \mathscr{U} x_1 - gbt_1 + \phi'_{10}\,,$$

with

$$\begin{pmatrix} A' \\ \phi'_{10} \end{pmatrix} \propto \exp(i(K_1 x_1 + K_2 y_1 - \Omega t_1))\,,$$

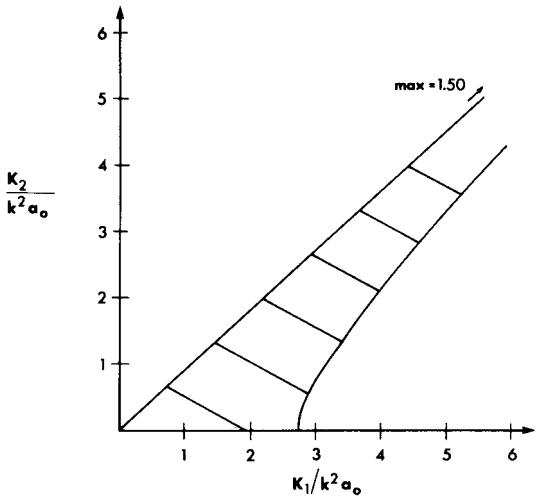

(*a*)

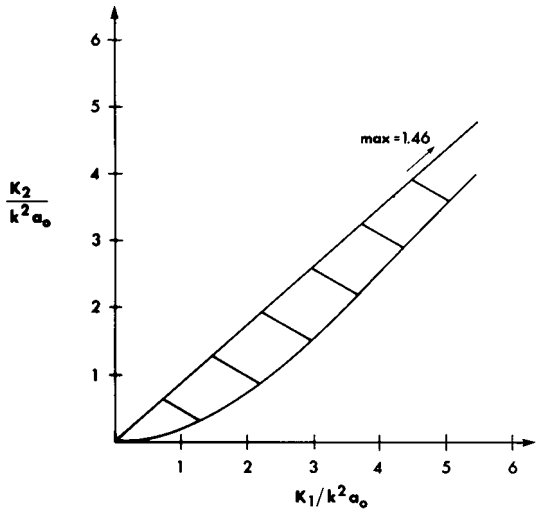

(*b*)

Figure 13.3: Instability of side-band waves which are inclined to the primary Stokes waves for various values of kh. Unstable regions are shaded. The maximum growth rate $\mathrm{Im}\,\Omega/\omega k^2 a_0^2$ is also marked (from Benney and Roskes, 1969, *Studies Appl. Math.* Reproduced by permission of the Editor). (*a*) $kh = 2.00$; (*b*) $kh = 1.36$; (*c*) $kh = 0.7$; (*d*) $kh = 0.30$. At $kh = 0.38$ the instability region reduces to a straight line.

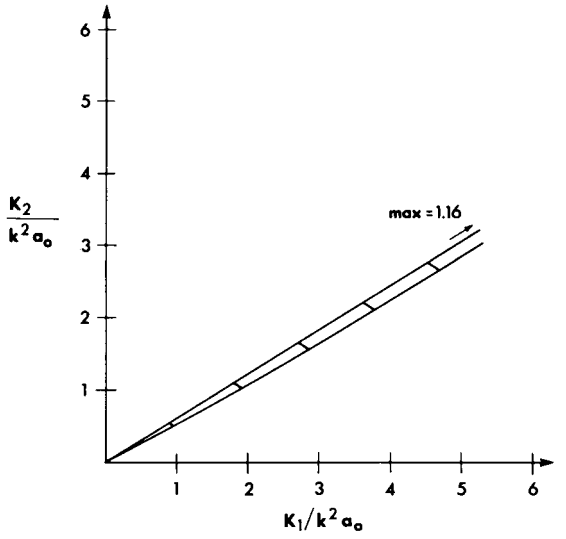

(*c*)

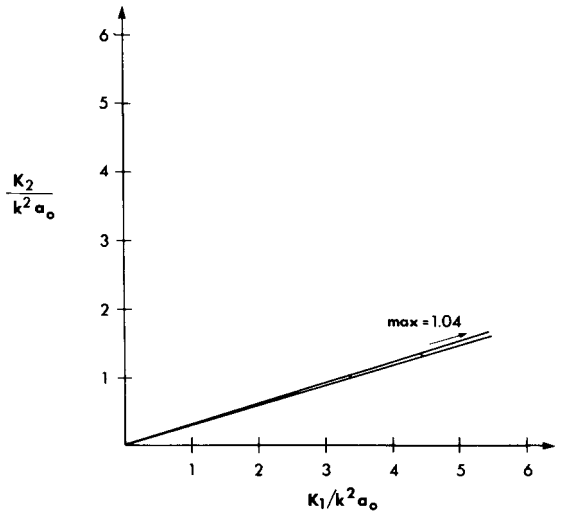

(*d*)

Figure 13.3: (*Continued*)

they showed that in the K_1, K_2 plane there were always regions in which the Stokes waves were unstable, except for $kh = 0.38$. Sample regions of instability are plotted in Fig. 13.3. Because of the difference in the shaded area, the likelihood of instability is greater for greater water depth. In nature, modulation in any direction is possible; therefore, Stokes' waves are always susceptible to instability.

The subject of wave instability in infinitely deep water has been studied in several ways in the ensuing years. For disturbances colinear with the primary waves, Longuet–Higgins (1978a, b) started from the numerically exact solution for a steady progressive wave and superimposed perturbations both shorter (superharmonics) and longer (subharmonics) than the primary wave. In particular, the subharmonic disturbance is an extension of the Benjamin-Feir wave. In the first quadrant of the plane $K/2k$ (ordinate) versus ka_0 (abscissa), the zone of instability in the first quadrant was found to be a crest-like region, instead of the whole region to the right of the straight line $K/2k = 2^{1/2}ka_0$ according to Eq. (13.4.9) (see Fig. 13.4). Thus for sufficiently high ka_0 the waves are restabilized. In addition Longuet–Higgins (1978b) found that infinitely long perturbations

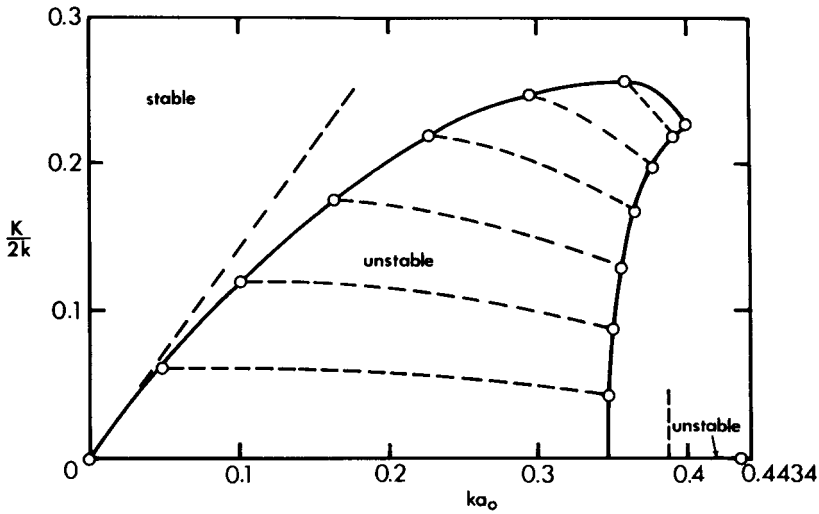

Figure 13.4: Stability diagram for numerically exact periodic nonlinear waves in deep water. The tangent at the origin corresponds to $K/2k = \sqrt{2}ka_0$ [cf. Eq. (13.4.9)] (from Longuet–Higgins, 1978b, *Proc. R. Soc. Lond.* Reproduced by permission of the Royal Society of London).

could induce very rapid instability at $ka_0 \cong 0.41$. (The maximum possible steepness is $ka_0 = 0.4434$.)

There are now two approximate theories which improve the results of the cubic Schrödinger equation. One is due to Dysthe (1979) who retained the slow modulation assumption ($\Omega/\omega, K/k \ll 1$) but included nonlinear terms of the fourth order. His instability region was bounded only on the left by a curve which roughly coincided with the left boundary of the crest shown in Fig. 13.4. The predicted wavenumber of the most unstable side-band mode was, however, below Eq. (13.4.11), the exact numerical theory and the experimental values. The second approximate theory is due to Crawford et al. (1981) who applied an integro-differential equation of Zakharov (1968) which is valid to third order in wave slope but not restricted to side-band disturbances adjacent to the main waves (namely, K/k need not be small). Their instability region was also a finite crest whose left side agreed with Longuet–Higgins remarkably well, and the predicted growth rates were also closer to the measured values, as shown in Fig. 13.2. More details of the broad-band approximation will be discussed in Chapter Fourteen.

The subsequent evolution of initial instability must, of course, be treated as a nonlinear problem, to which we turn within the framework of the cubic Schrödinger equation (namely, small ka_0).

Exercise 13.1

Consider a progressive edge wave of the lowest mode on a plane beach of slope ε:

$$\phi = -\frac{igD}{2\Omega}\exp(-Kx_1)\exp i(Ky_1 - \Omega t_1) + * + \text{higher-order terms}$$

for $x_1 > 0$, where $x_1 = \varepsilon x, y_1 = \varepsilon y, t_1 = \varepsilon t$, and $\Omega^2 = gK$. Show by using Eq. (12.1.49), and assuming $D = D(y_2, y_3, \ldots, t_2, t_3, \ldots)$, that the envelope evolves according to the following equations:

$$\left(\frac{\partial}{\partial t_2} + C_g\frac{\partial}{\partial y_2}\right)D = 0$$

and

$$i\left(\frac{\partial}{\partial t_3} + C_g\frac{\partial}{\partial y_3}\right)D - \frac{1}{2}\frac{\partial^2\Omega}{\partial K^2}\frac{\partial^2 D}{\partial y_2^2} - \frac{\Omega K^4}{4}|D|^2 D + \frac{\Omega}{4}D = 0$$

where $C_g = g/2\Omega$ is the group velocity of the edge wave along the shore and $-a^2\Omega/\partial K^2 = g^2/4\Omega^3$. Note that the envelope is unstable to side-band disturbances.

Exercise 13.2

Derive the instability criterion for obliquely incident side-band disturbances and confirm Fig. 13.3.

Exercise 13.3: Short-Crested Waves in a Long Tank[2]

Consider a long wave tank of rectangular cross section of width $2a$. Choose the coordinate system so that the tank axis is $x > 0$ and the side walls are $y = \pm a$. At the end $x = 0$ a wavemaker is a rigid plate performing angular oscillations about a vertical hinge coinciding with the z axis. Assume that the wavelength and the tank width are comparable in order of magnitude to the mean depth h.

Show first by a linearized theory for monochromatic waves, that there are special forcing frequencies ω_m across which a propagating mode turns to an evanescent mode, and that at $\omega = \omega_m$ unbounded resonance occurs. Now examine how the linearized theory breaks down near resonance. Let $\omega = \omega_m + \mu^2\Omega,\ \mu \ll 1$. Examine the next-order approximation to decide the appropriate slow time and space coordinates that describe the resonant growth in space and in time, i.e., find the powers a and b in $x_a = \mu^a x,\ t_b = \mu^b t$. Finally by including weak nonlinearity show that the amplitude of the resonant mode is governed by a nonlinear Schrödinger equation. Deduce the coefficients of the asymptotic equation.

Excercise 13.4: Snake Wavemaker in a Large Basin

Let there be a programmable wave-generator consisting of many narrow pistons along one side ($y = 0$) of a wide test basin ($-\infty < x < \infty, y > 0$). Let the transverse displacement of the pistons be approximated by a continuous function

$$Y(x, z, t) = \frac{\epsilon^2 a}{2} f(z) e^{i(\alpha x - \omega t)} + *$$

where a, ω, α can be controlled by computer programing, and

$$f(z) \equiv \frac{\cosh k(z + h)}{\cosh kh}\,.$$

(i) Show by a linearized theory that the free-surface displacement in an infinitely large basin is an obliquely progressive wave

$$\zeta = -i\frac{\epsilon^2 a\omega^2}{2g\beta} e^{i(\alpha x + \beta y - \omega t)} + *$$

[2]For a related problem in an acoustic duct, see Aranha, Mei and Yue, 1982.

where $\alpha^2 + \beta^2 = k^2$, with $\omega^2 = gk \tanh kh$.

(ii) If $\beta \to 0$, the crests become perpendicular to the x-axis (the line of wavemakers) and spatial resonance occurs. Give reasons that you should introduce $y_1 = \epsilon y$, and possibly t_1, t_2.

(iii) Consider a nonlinear theory in which the wave amplitude can be much larger than the forcing, i.e., $\zeta \propto \epsilon$ while $Y \propto \epsilon^2$. Assume uniformity in x, i.e., infinitely wide tank, i.e., $\partial/\partial x_1, \partial/\partial x_2 = 0$. What limiting form of (13.2.36) and (13.2.39) can be used to describe the slow and nonlinear evolution of A?

(iv) From the fully nonlinear boundary condition on the wavemaker deduce the boundary condition $\partial A/\partial y_1 = 2\omega^2 a/g$.

(v) By first showing that A has constant phase if a is real, show that the steady-state limit of A is

$$|A(y_1)| = \frac{(2ka)^{1/2}/(\frac{2kK}{C_g})^{1/4}}{1 + \frac{y_1}{2}(\frac{2kK}{C_g})^{1/4}(2Ka)^{1/2}}$$

where

$$K = \frac{\omega^2 k^2(\cosh 4kh + 8 - 2\tanh^2 kh)}{16 \sinh^4 kh}\,.$$

Exercise 13.5: Uniform Flow Over a Wavy Bed (Sammarco, Mei and Trulsen, 1994)

A steady uniform flow of velocity U passes over a series of periodic sandbars on the seabed:

$$z = -h + b \sin Kx\,, \quad \text{where} \quad Kh = O(1)\,.$$

If the number of bars is infinite find the steady waves on the free surface caused by the bars for any general U. Observe that there is a special $U = U_c$ at which the linearized result fails. To avert unbounded growth near resonance $U = U_c(1 + \epsilon U_1)$, derive a nonlinear theory by allowing the free-surface amplitude to be much larger than the bar amplitude, i.e., $kA = O(\epsilon)$, but $Kb = O(\epsilon^2)$.

13.5 Permanent Envelopes in Deep Water: Nonlinear Solutions of the Evolution Equation

Benney and Newell (1967) first showed that Eq. (13.2.45) admits permanent wave envelopes as solutions which are functions of $(x - Ut)$ (also see Chu and

Mei, 1970; Hashimoto and Ono, 1972; Zakharov and Shabat, 1972; Scott, Chu, and McLaughlin, 1973, etc.). For illustration we consider the deep water solution by Scott, et al. Let us first nondimensionalize Eq. (13.2.60), with $\mathscr{U} = \partial/\partial y_1 = 0$, by letting

$$A' = \frac{A}{a_0}\,, \quad \xi' = k^2 a_0 \xi\,, \quad \tau' = \omega(ka_0)^2\tau\,. \tag{13.5.1}$$

With the primes omitted for brevity, the cubic Schrödinger equation becomes

$$-i\frac{\partial A}{\partial \tau} + \frac{1}{8}\frac{\partial^2 A}{\partial \xi^2} + \frac{1}{2}|A|^2 A = 0\,. \tag{13.5.2}$$

We seek a solution of the form

$$A = ae^{ir(\xi - V_\tau - \delta)} \quad \text{where } a = a(\xi - U\tau)\,, \quad r, \delta = \text{const}\,, \tag{13.5.3}$$

that is, a carrier wave with envelope a. The phase angle δ specifies the initial position. Substituting Eqs. (13.5.3) into (13.5.2) and denoting derivatives with respect to the argument by primes, we have

$$\frac{1}{8}a'' - r\left(\frac{1}{8}r + V\right)a + \frac{1}{2}a^3 + i\left(U + \frac{r}{4}\right)a' = 0\,. \tag{13.5.4}$$

The imaginary part implies

$$r = -4U \tag{13.5.5}$$

which may be used in the real part to yield

$$\frac{1}{8}a'' + 4U\left(V - \frac{U}{2}\right)a + \frac{1}{2}a^3 = 0\,. \tag{13.5.6}$$

Multipling Eq. (13.5.6) by a' and integrating, we get

$$(a')^2 + 32U\left(V - \frac{U}{2}\right)a^2 + 2a^4 = C \tag{13.5.7}$$

where C is a constant. Multiplying Eq. (13.5.7) by a^2 and defining

$$E = a^2\,, \tag{13.5.8}$$

we further get

$$(E')^2 + 64U(2V - U)E^2 + 8E^3 = 4CE\,,$$

which may be rewritten

$$(E')^2 = 8(E_{\max} - E)(E - E_{\min})E \equiv P(E)\,. \tag{13.5.9}$$

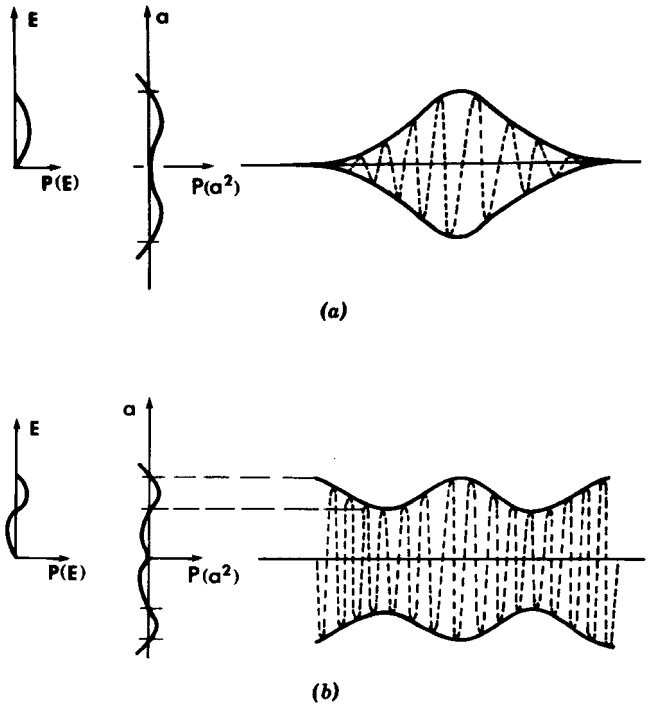

Figure 13.5: Cnoidal and solitary envelopes.

Note that

$$8(E_{\max} + E_{\min}) = -64U(2V - U)\,, \tag{13.5.10}$$

and, by definition (13.5.8), $E_{\min} > 0$; hence, we must insist that $U(2V - U) < 0$. The cubic polynomial $P(E)$ is sketched in Fig. 13.5, and the corresponding $P(a^2)$ which is a sixth-degree polynomial is also sketched. A solution exists only if P is positive.

When $C = 0$, $E_{\min}$ vanishes, and Eq. (13.5.9) becomes

$$(E')^2 = 8E^2(E_{\max} - E)\,. \tag{13.5.11}$$

$P(E)$ has two zeroes as shown in Fig. 13.5(a). Upon integration we obtain

$$E = E_{\max}\ \mathrm{sech}^2[(2E_{\max})^{1/2}(\xi - U\tau)] \tag{13.5.12}$$

or

$$a = a_{\max}\ \mathrm{sech}\,[2^{1/2}a_{\max}(\xi - U\tau)] \tag{13.5.13a}$$

which describes a solitary wave packet or an *envelope soliton.* Note that $a_{\max} = E_{\max}^{1/2}$, while U and V are related by Eq. (13.5.10) with $E_{\min} = 0$. In particular, one may take $U = 0$, $VU = -1/16$ and $a_{\max} = 1$ so that

$$a = \operatorname{sech} 2^{1/2}\xi\,, \quad A = (\operatorname{sech} 2^{1/2}\xi)e^{-i(\tau/4+\delta)}\,. \tag{13.5.13b}$$

More generally, $C \neq 0$ and $E_{\min} > 0$ [as shown in Fig. 13.5(b)]. The solution to Eq. (13.5.9) can be expressed in a cosine-elliptic function which has been discussed more fully in the shallow water theory,

$$E = E_{\min} + \Delta E \operatorname{Cn}^2\{(2\Delta E)^{1/2}\gamma^{-1}(\xi - U\tau)\}\,, \tag{13.5.14}$$

with

$$\Delta E = E_{\max} - E_{\min} = \text{energy amplitude}\,,$$

$$\gamma = \left(\frac{\Delta E}{E_{\max}}\right)^{1/2}\,.$$

The wavelength of the envelope is

$$\lambda = \frac{2^{1/2}}{(\Delta E)^{1/2}} \int_0^{\pi/2} \frac{du}{(1 - \gamma^2 \sin^2 u)^{1/2}} \tag{13.5.15}$$

(see, e.g., Chu and Mei, 1970). Again ∇E, U, and V can be specified, subject to Eq. (13.5.10).

For finite depth, Eq. (13.2.45) may be rescaled by

$$\xi = \alpha\bar{\xi} \quad \text{and} \quad \tau = \alpha\bar{\tau}$$

to give the following canonical equation:

$$-i\frac{\partial B}{\partial \bar{\tau}} + \frac{\partial^2 B}{\partial \bar{\xi}^2} + \kappa|B|^2 B = 0\,, \tag{13.5.16}$$

where $\kappa = \alpha\beta$. For $\kappa > 0$ (i.e., $kh > 1.36$) the extension to Eq. (13.5.13a) is easily verified to be

$$B = a \exp\left[-i\frac{U}{2}(\bar{\xi} - V\tau - \bar{\xi}_1)\right], \tag{13.5.17}$$

where

$$a = a_{\max} \operatorname{sech}\left[\left(\frac{\kappa}{2}\right)^{1/2} a_{\max}(\bar{\xi} - \bar{\xi}_0 - U\bar{\tau})\right], \tag{13.5.18}$$

with

$$a_{\max} = \frac{2}{\kappa} U \left(\frac{U}{8} - V \right). \tag{13.5.19}$$

The soliton is characterized by the free parameters $a_{\max}$ and U and by the phases $\bar{\xi}_0$ and $\bar{\xi}_1$.

For $\alpha\beta < 0$, a soliton exists which is a depression at the center and approaches a finite constant at $|\xi| \sim \infty$. The expression is

$$B = \left(\frac{2}{|\kappa|} \right)^{1/2} \frac{(\lambda - i\nu)^2 + e^{2\nu(\bar{\xi} - \bar{\xi}_0 - 2\lambda\bar{\tau})}}{1 + e^{2\nu(\bar{\xi} - \bar{\xi}_0 - 2\lambda\bar{\tau})}}, \tag{13.5.20}$$

where

$$v = (1 - \lambda^2)^{1/2} \tag{13.5.21}$$

(Zakharov and Shabat, 1973). A little manipulation shows that

$$|B| = \left(\frac{2}{|\kappa|} \right)^{1/2} [1 - \nu \operatorname{sech}^2 \nu(\bar{\xi} - \bar{\xi}_0 - 2\lambda\bar{\tau})]^{1/2}. \tag{13.5.22}$$

Thus, the soliton is characterized by ξ_0 and the amplitude ν. A slightly more general solution was deduced independently by Hesegawa and Tappert (1973). These solutions are known either as the *dark soliton* or the *envelope-hole soliton*. Note that as ν increases toward 1, λ decreases so that a deeper hole travels more slowly. In the limit of $\nu \to 1$, $\lambda \to 0$ and

$$B \to \left(\frac{2}{|\kappa|} \right)^{1/2} \tanh(\bar{\xi} - \bar{\xi}_0) \tag{13.5.23}$$

which is called the *phase jump* because of the sign change from -1 at $\bar{\xi} \sim -\infty$ to $+1$ at $\bar{\xi} \sim \infty$.

Periodic permanent envelopes for both $\alpha\beta \gtrless 0$ have been given by Hashimoto and Ono (1972).

13.6 Transient Evolution of One-Dimensional Wave Envelope on Deep Water

As the linearized instability theory must fail beyond the initial stage of exponential growth, the fuller nonlinear theory must be employed for the evolution over long periods of time. Early experiments by Feir (1967) showed that the envelope of a wave packet tended to break up into several groups strung together. Numerical solution of Eq. (13.2.47) by Chu and

Mei (1971) confirmed this trend. Both these attempts, however, did not cover a long enough time interval to reveal the entire physical picture. A theoretical breakthrough was scored by Zakharov and Shabat (1972) who extended the technique of Gardner et al. (1967) and solved Eq. (13.5.16) exactly for both $\kappa\ (=\alpha\beta) \gtrless 0$ when the initial data $B(\xi, 0)$ vanished sufficiently fast as $|\bar{\xi}| \uparrow \infty$. Their success is based on an important observation by Lax (1968): To solve any nonlinear evolution equation

$$\frac{\partial B}{\partial \bar{\tau}} = NB \tag{13.6.1}$$

where N is a nonlinear operator, one must first seek two linear operators L and M, both involving only derivatives with respect to $\bar{\xi}$ and containing $B(\bar{\xi}, \bar{\tau})$ in the coefficients, such that

$$L_{\bar{\tau}} = LM - ML \tag{13.6.2}$$

and

$$i\psi_{\bar{\tau}} = M\psi\,. \tag{13.6.3}$$

If the operators are found, the eigenvalues σ of the problem

$$L\psi = \sigma\psi \tag{13.6.4}$$

will remain constant for all time $(\bar{\tau})$. This statement can be verified by differentiating Eq. (13.6.4) with respect to $\bar{\tau}$,

$$\begin{aligned}
\sigma_{\bar{\tau}}\psi &= L_{\bar{\tau}}\psi + (L - \sigma)\psi_{\bar{\tau}} \\
&= LM\psi - ML\psi + (L - \sigma)\psi_{\bar{\tau}} \\
&= (L - \sigma)(i\psi_{\bar{\tau}} - M\psi) = 0
\end{aligned}$$

where Eqs. (13.6.2)–(13.6.4) have been used. Thanks to this invariance, the initial data $B(\bar{\xi}, 0)$ alone enables one to solve Eq. (13.6.4) for the spectrum of σ and also $\psi(x, 0)$. For localized initial data, we expect $B(\bar{\xi}, \bar{\tau})$ to be localized in $\bar{\xi}$ too; the operator M can be simplified so that Eq. (13.6.3) may be easily solved for $\psi(\pm\infty, \bar{\tau})$, based on the knowledge of $\psi(\pm\infty, 0)$. Now the eigenvalues σ and the far field $\psi(\pm\infty, \bar{\tau})$ are known for all $\bar{\tau}$; the *inverse scattering theory* may be called upon to solve $B(\bar{\xi}, \bar{\tau})$ for all $\bar{\xi}$, with $\bar{\tau}$ being a parameter. The mathematical background of the last step is unfortunately very complicated, leaning heavily on the complex function theory. For a thorough treatise of the inverse scattering theory, see Ablowitz and Segur (1981).

For the cubic Schrödinger equation (13.5.16), Zakharov and Shabat found that the eigenfunction ψ is a two-component vector $\psi = (\psi_1, \psi_2)$ and that L and M are 2×2 matrices:

$$L = i \begin{bmatrix} 1+p & 0 \\ 0 & 1-p \end{bmatrix} \frac{\partial}{\partial \bar{\xi}} + \begin{bmatrix} 0 & B \\ B^* & 0 \end{bmatrix} \quad \text{with} \quad \kappa = \frac{2}{1-p^2} \tag{13.6.5a}$$

$$M = -p \begin{bmatrix} 1 & 0 \\ 0 & 1 \end{bmatrix} \frac{\partial^2}{\partial \bar{\xi}^2} + \begin{bmatrix} \dfrac{|B|^2}{1+p} & iB_{\bar{\xi}} \\ -iB^*_{\bar{\xi}} & \dfrac{-|B|^2}{1-p} \end{bmatrix}. \tag{13.6.5b}$$

In general, the search for these operators is no trivial task, but a systematic approach for a certain class of problems has now been found by Ablowitz et al. (1974).

The theory of Zakharov and Shabat has since been elaborated for detailed implications by Satsuma and Yajima (1974)[3] and confirmed numerically and experimentally by Yuen and Lake (1975). The main physical features of these works for $\kappa > 0$ are summarized below.

1 An arbitrarily shaped envelope will eventually evolve into a finite number of solitons, plus minor oscillations which decay as $t^{-1/2}$.

2 The jth soliton is given by

$$B_j(\bar{\xi}, \bar{\tau}) = 2 \left(\frac{2}{\kappa} \right)^{1/2} b_j \{ \operatorname{sech} 2b_j (\bar{\xi} - \bar{\xi}_j - 4a_j \bar{\tau}) \} \times \{ \exp[4i(a_j^2 - b_j^2)\bar{\tau} - 2ia_j \bar{\xi} + i\phi_j] \}, \tag{13.6.6}$$

where a_j and b_j are the real and imaginary parts of the discrete eigenvalue σ_j of Eq. (13.6.4). The soliton has the amplitude $2(2/\kappa)^{1/2} b_j$, phase speed $4a_j$, and phases $\bar{\xi}_j$ and ϕ_j which are related to the reflection coefficient of the scattering problem (the continuous eigenvalue spectrum). In general, these complex eigenvalues σ_j may have distinct real parts; thus, the solitons may drift apart with time. A special case is the so-called N-soliton solution which corresponds to N distinct eigenvalues $\sigma_j, j = 1, \ldots, N$. If there are N solitons at $t = 0$ with the slowest one in front, then the faster solitons will overtake the slower ones at sufficiently large $\bar{\tau}$. The only effect of collision between a pair of solitons is a shift of phases $\bar{\xi}_i$ and ϕ_i.

[3] I thank Professor Harvey Segur for this reference.

3 When the initial data $B(\bar{\xi},0)$ is real and not antisymmetric in $\bar{\xi}$, the discrete eigenvalues are purely imaginary. In this case all solitons stay together and form *bound solitons*. As a slight extension, if the initial

$$B(\bar{\xi},0)=\overline{B}(\bar{\xi})e^{iV\xi}$$

where V is a real constant and $\overline{B}(\bar{\xi})$ is real and nonantisymmetric in $\bar{\xi}$, then all solitons have the same speed $-2V$ (relative to the group velocity in the rest frame). Because each soliton oscillates at the period $4b_j^2$, the composite envelope exhibits recurrence with frequencies $4(b_i^2-b_j^2)$. The number of recurrence frequencies is equal to the number of distinct differences between b_i^2 and b_j^2. For example, if N is the number of solitons, then for $N=2$ there is only one recurrence frequency; for $N=3$, there are two recurrence frequencies, . . . , and so on.

For the special case of

$$B(\bar{\xi},0)=B_0\ \mathrm{sech}\,\frac{\bar{\xi}}{\bar{\lambda}}\,,\quad B_0\ \text{real}\,, \tag{13.6.7}$$

Eq. (13.6.4) with Eq. (13.6.5a) can be reduced to a hypergeometric equation for ψ; the discrete eigenvalues and the scattering coefficients for the continuous eigenvalues can be obtained explicitly (Satsuma and Yajima, 1974; Kuehl, 1976). In particular, the discrete eigenvalues are

$$\sigma_j=i\left(\left(\frac{\kappa}{2}\right)^{1/2}B_0\bar{\lambda}-j+\frac{1}{2}\right),\quad j=1,2,3,\ldots\,. \tag{13.6.8}$$

Thus, for N solitons to emerge, the initial size $B_0\bar{\lambda}$ must be such that

$$\left(\frac{\kappa}{2}\right)^{1/2}B_0\bar{\lambda}-N+\frac{1}{2}>0\,. \tag{13.6.9}$$

Moreover, when

$$\left(\frac{\kappa}{2}\right)^{1/2}B_0\bar{\lambda}=N\,,\quad N=\text{positive integer}\,, \tag{13.6.10}$$

the inverse scattering problem can be solved for $B(\bar{\xi},\bar{\tau})$ explicitly; the result only involves N bound solitons.

To apply the above criteria to Eq. (13.5.2) with the initial data $A(\xi,0)=A_0\ \mathrm{sech}\,\xi/\lambda$, the following changes are necessary:

$$B_0\to A_0\,,\quad \bar{\lambda}\to\frac{\lambda}{\alpha}\,,\quad \kappa\to\alpha\beta\,.$$

Criteria (13.6.9) and (13.6.10) then become

$$\left(\frac{\beta}{2\alpha}\right)^{1/2} A_0\lambda > N - \frac{1}{2} \quad \text{for } N \text{ solitons with tail} \tag{13.6.11}$$

and

$$\left(\frac{\beta}{2\alpha}\right)^{1/2} A_0\lambda = N \quad \text{for } N \text{ solitons only}. \tag{13.6.12}$$

For deep water $\alpha = \frac{1}{8}$, $\beta = \frac{1}{2}$, the left side of Eqs. (13.6.11) and (13.6.12) becomes $2^{1/2}A_0\lambda$.

To confirm their analytical results, Satsuma and Yajima (1974) also computed numerically, from Eq. (13.5.2), a number of cases including solitons either in a bounded state or emerging with different speeds. There are now several numerical techniques (Lake, Yuan, Rungaldier, and Ferguson, 1977; Fornberg and Whitham, 1978) which are relatively straightforward to execute. They can be readily applied to, or modified for, cases yet unsolvable by the inverse scattering theory, such as semi-infinite domains, periodic boundary conditions, two space dimensions, variable coefficients for inhomogenous media, and so on. We cite below a simple implicit scheme of the Crank–Nicolsen type, which was applied by Yue (1980) to two of the three cases to be discussed. Referring to Eq. (13.5.2), let $\Delta\xi$ and $\Delta\tau$ be the discrete intervals on the ξ and τ axes and denote

$$A_j^n = A(j\Delta\xi,\ n\Delta\tau)\,.$$

Equation (13.5.2) is approximated by

$$\begin{aligned} A_j^{n+1} = A_j^n - \frac{\Delta\tau}{2}\Bigg\{ &\frac{i}{8(\Delta\xi)^2}(A_{j+1}^{n+1} - 2A_j^{n+1} + A_{j-1}^{n+1}) + \frac{i}{2}|\tilde{A}_j^{n+1}|^2 A_j^{n+1} \\ &+ \frac{i}{8(\Delta\xi)^2}(A_{j+1}^{n} - 2A_j^{n} + A_{j-1}^{n}) + \frac{i}{2}|\tilde{A}_j^{n}|^2 A_j^{n}\Bigg\} + O(\Delta\tau^3, \Delta\xi^2)\,. \end{aligned} \tag{13.6.13}$$

In the nonlinear terms, $\tilde{A}_j^{n+1}$ is estimated by the results at the nth time step according to an Euler scheme:

$$\begin{aligned} \tilde{A}_j^{n+1} = A_j^n - \Delta\tau\left\{\frac{i}{8(\Delta\xi)^2}(A_{j+1}^n - 2A_j^n + A_{j-1}^n) + \frac{i}{2}|A_j^n|^2 A_j^n\right\} \\ + O(\Delta\tau^2, \Delta\xi^2)\,. \end{aligned} \tag{13.6.14}$$

As examples, numerical solutions for the following types of initial data will be discussed for physical pictures:

1 A single pulse.
2 A step envelope.
3 Periodic modulation of a uniform wavetrain.

In cases 1 and 2, the initial data are not localized, and analytical solutions are not yet possible.

13.6.1 Evolution of a Single Pulse

For convenience, we express the initial data by

$$A(\xi, 0) = \operatorname{sech}\left(\frac{2^{1/2}\xi}{\lambda}\right). \tag{13.6.15}$$

Recall from Eq. (13.5.13b) that $A(\xi, 0)$ coincides with a soliton of unit height if $\lambda = 1$.

First, we take $\lambda = 2$, corresponding to an initial pulse twice as long as a soliton of equal height. It follows from Eq. (13.6.12) that $N = 2$ so that two and only two solitons should emerge. For this case, the explicit solution has been given by Satsuma and Yajima (1975, p. 300 after the transformation $u \to NA$, $x \to 2^{1/2}\xi/N$, and $t \to \tau/2N^2$)

$$A(\xi, \tau) = \frac{2[\operatorname{ch}(3\xi/2^{1/2}) + 3e^{-i\tau/2}\operatorname{ch}(\xi/2^{1/2})]}{\operatorname{ch} 2(2)^{1/2}\xi + 4\operatorname{ch} 2^{1/2}\xi + 3\cos\frac{1}{2}\tau} \exp\left(-\frac{i\tau}{16}\right). \tag{13.6.16}$$

Numerical confirmation is shown in Fig. 13.6(a). From the time history of the pulse center $|A(0, \tau)|$, shown in Fig. 13.6(b), the recurrence period is seen to be $\tau_0 = 12.6$, while the theoretical value is $2\pi/\frac{1}{2} = 12.566$. Typical snapshots $|A(\xi, \tau_i)|$ are given in Fig. 13.6(c) at quarter-period intervals to show the stages of evolution. Figure 13.6(d) shows the phase p defined by $A(\xi, \tau) = |A|e^{ip\pi}$ at these same instants. Note first that the phase curves for two instants separated by a recurrence period differ only by a constant. Thus, the phase variation, that is, the wavenumber, is unchanged. Also note that at the instant c_0 (or $c_1, \ldots$) when the envelope has a node, the phase changes sharply, implying that the frequency distribution has a sharp trough in the front half of the group. By symmetry, there is a peak in the frequency distribution in the rear half of the group. These predictions (Chu and Mei, 1971) are in qualitative agreement with Feir's experiments. Due

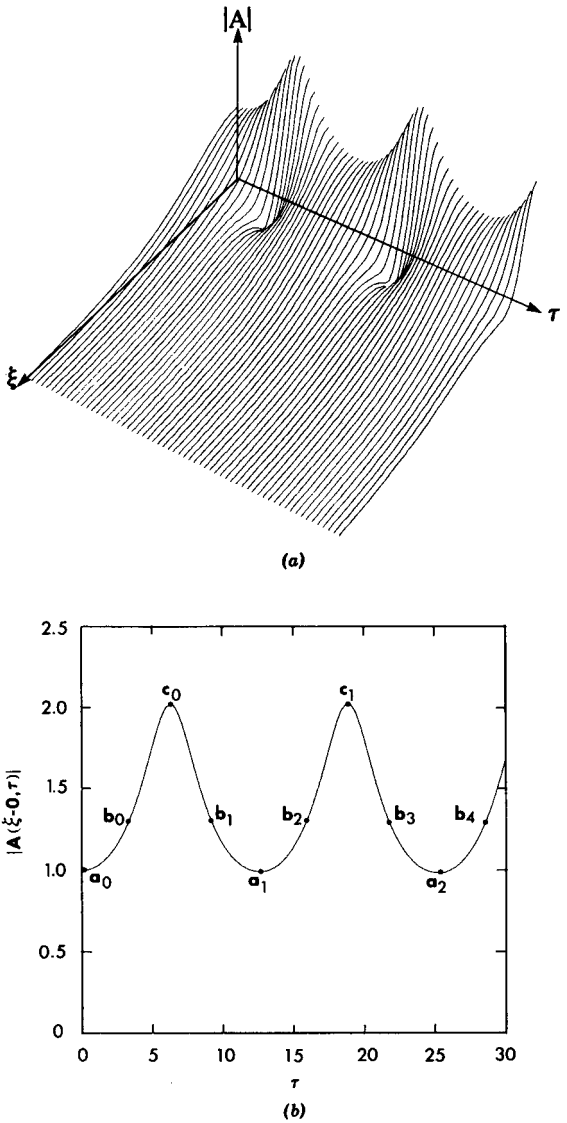

Figure 13.6: Evolution of an initial pulse envelope twice the length of the soliton of equal height $A(\xi, 0) = \text{sech}\,(\xi/2^{1/2})$ (from Yue, 1980). (a) The overall view for $0 < \tau < 30$, $0 < \xi < 6$. (b) Centerline amplitude $|A(\xi = 0, \tau)|$ as a function of slow time τ. The recurrence period is $\tau_0 = 12.6$. The marked points a_js and c_i's are at τ_0 apart, while b_i's are at $\frac{1}{2}\tau_0$ apart. (c) Snapshots of $|A(\xi, \tau)|$ at instants marked on (a). (d) Snapshots of the phase factor p. ($p\pi$ = phase of A) at the instants marked on (a).

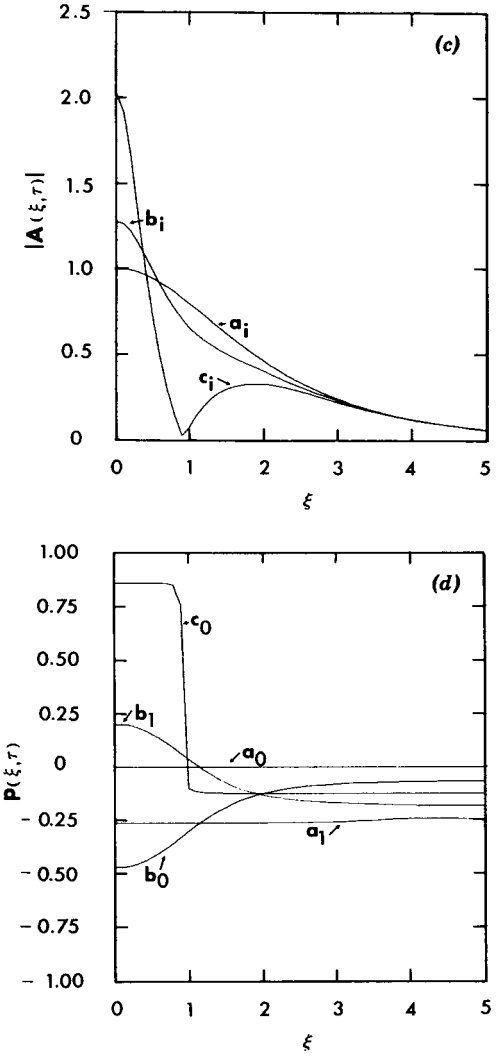

Figure 13.6: (*Continued*)

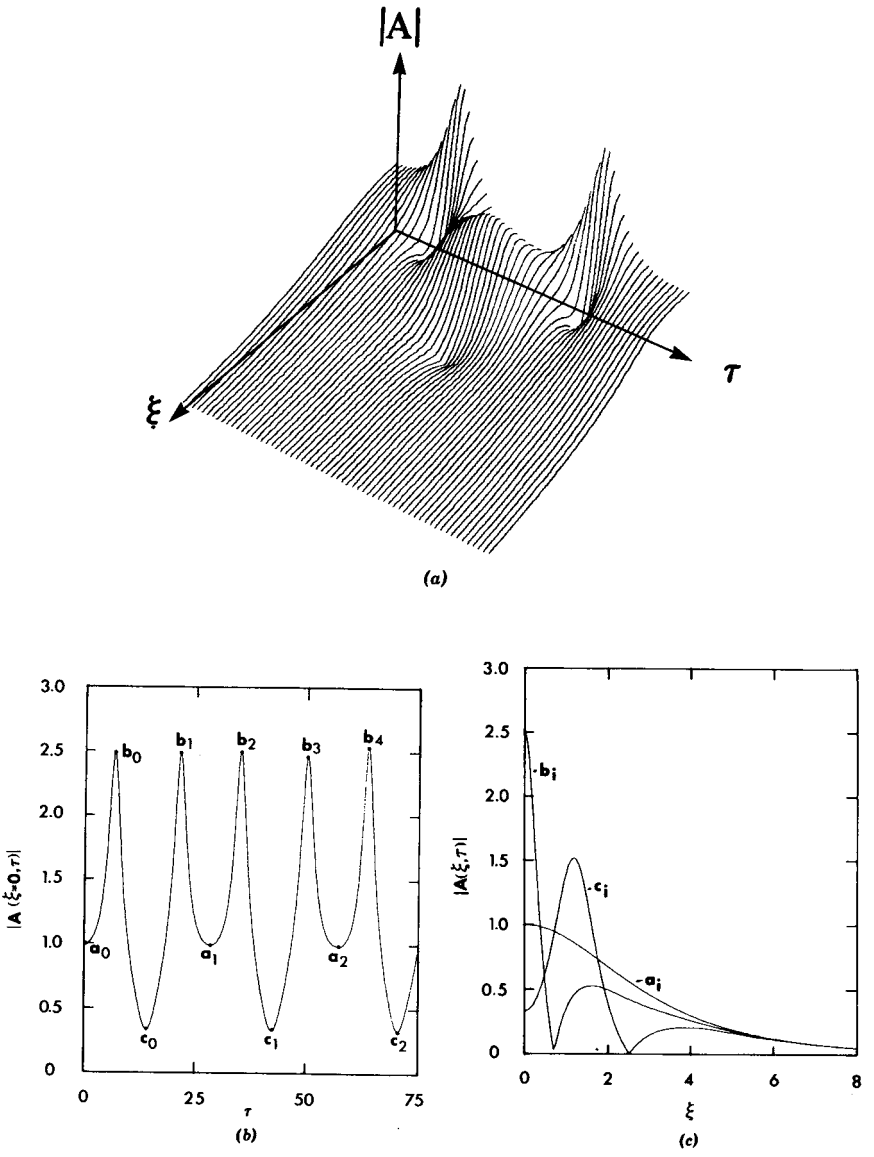

Figure 13.7: Evolution of an initial pulse envelope thrice as long as a soliton of equal height $A(\xi, 0) = \text{sech}\,(2^{1/2}\xi/3)$ (from Yue, 1980). (a) Overall view for $0 < \xi < 6$, $0 < \tau < 30$. (b) Centerline amplitude $|A(\xi = 0, \tau)|$. (c) Snapshots of the envelope amplitude at sample instants of a recurrence period as marked in (b). (d) Snapshots of envelope phase at sample instants of a recurrence period.

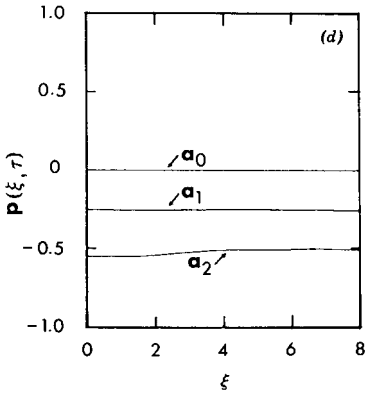

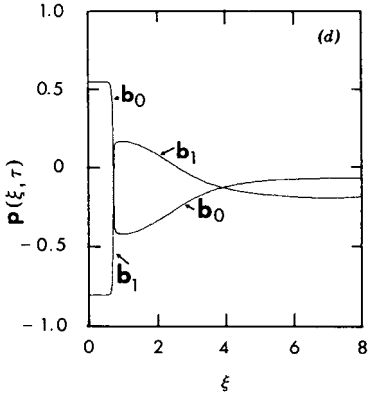

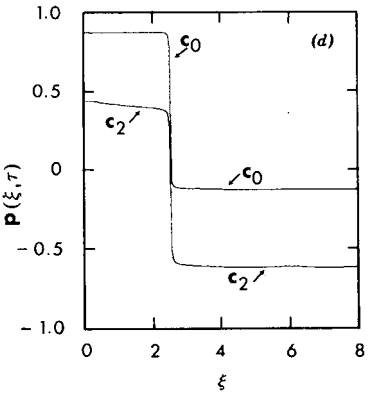

Figure 13.7: (*Continued*)

to the long time scales, it is difficult to check recurrence quantitatively in a laboratory unless damping is taken into account.

Let us take $\lambda = 3$ next. The corresponding N is 3 according to Eq. (13.6.12). The overall view is given by Fig. 13.7(a). In Fig. 13.7(b) the history of the pulse center shows distinctly the existence of more than one recurrence period. Figure 13.7(c) shows the typical profile at various stages. Again the nodes of the envelope are accompanied by rapid changes of phases which are not shown here.

Yue (1980) also computed for two initial pulses with the same carrier frequency and the same shape, but which were well separated,

$$A(\xi, 0) = \operatorname{sech}\left[2\sqrt{2}(\xi - \xi_0)\right] + \operatorname{sech}\left[2\sqrt{2}(\xi + \xi_0)\right].$$

In particular, each pulse was half as wide as a soliton of unit height but the combined profile had the same area as a single soliton of unit height. His results showed that after a complex evolution the two pulses coalesced into a single soliton of height 0.4.

More generally, two initial pulses with complex amplitudes may lead to solitons traveling at different speeds (see Satsuma and Yajima for a variety of numerical examples).

13.6.2 Evolution of the Front of a Uniform Wavetrain

In Section 2.4 the front of a suddenly started sinusoidal wavetrain was found to be governed by a linear Schrödinger equation. As the envelope advanced, undulations developed behind the front in a way describable by Fresnel integrals. We now reexamine the problem by including nonlinearity. The task is to solve Eq. (13.5.2) with the following initial data:

$$A(\xi) = \frac{1}{2}\left(1 + \tanh\frac{\xi}{\lambda}\right). \tag{13.6.17}$$

Far ahead of the front there is no disturbance,

$$A \to 0\,, \quad \xi \to \infty\,. \tag{13.6.18}$$

Far behind the front, a uniform Stokes wave should be approached,

$$A \to e^{-i\tau/2}\,, \quad \xi \to \infty\,. \tag{13.6.19}$$

Note from the definitions of ξ and τ by Eq. (13.5.1), with primes omitted but implied, that a smaller $\varepsilon = ka_0$ corresponds to greater physical distance and longer time.

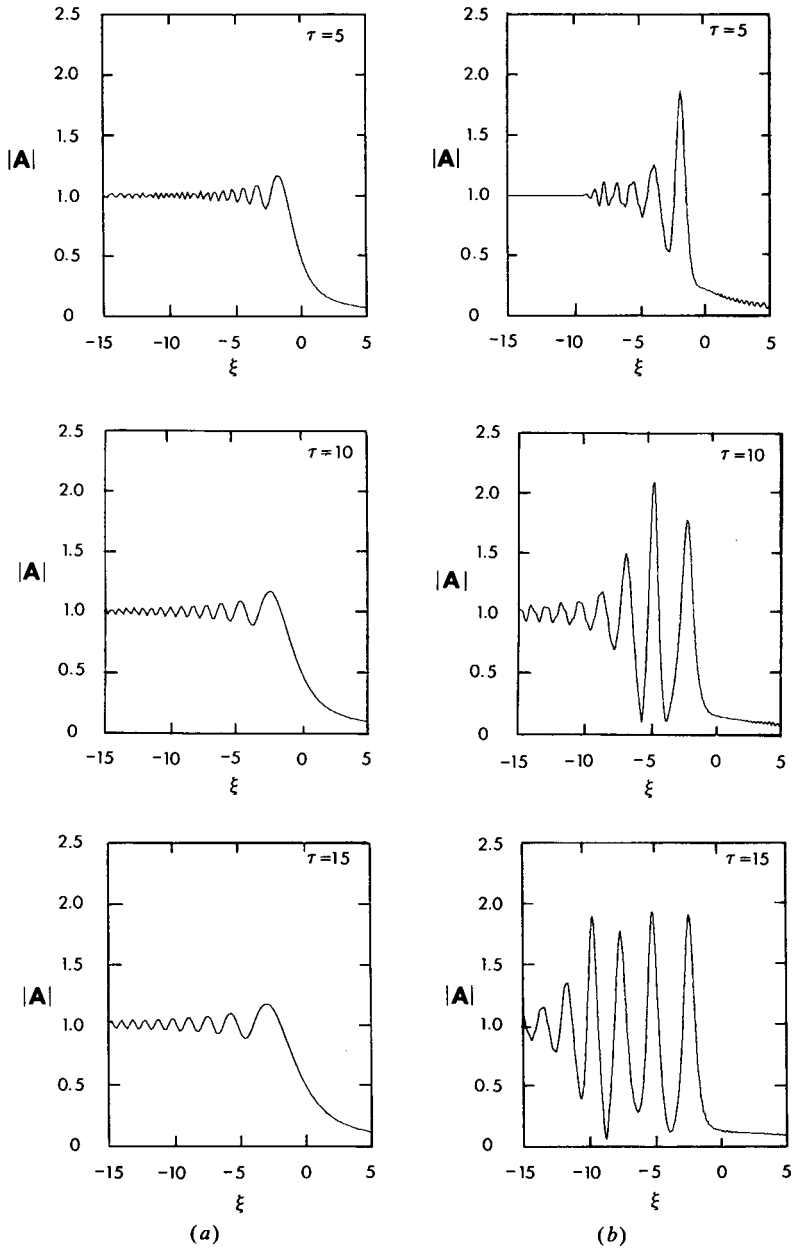

Figure 13.8: Evolution of the front of a periodic wavetrain (from Yue, 1980). (*a*) Linear theory; (*b*) nonlinear theory.

Figure 13.8 shows the contrast between linear and nonlinear theories for an abrupt transition $\lambda \approx 0$. The effect of finite amplitudes dramatically changes the front of the envelope, creating much stronger undulations. There are yet no appropriate experiments with which the nonlinear inviscid theory can be compared. Yue (1980) examined other values of λ but found no qualitatively new features.

13.6.3 Periodic Modulation of a Uniform Wavetrain — Evolution Beyond the Initial Stage of Instability

After the initial period of instability, the side-band disturbance grows so large that the full nonlinear effect of Eq. (13.5.2) becomes important. Chu and Mei (1971) calculated the nonlinear evolution for the most unstable case $K/k = 2ka_0$ by using Eqs. (13.2.47a) and (13.2.47b), but could not

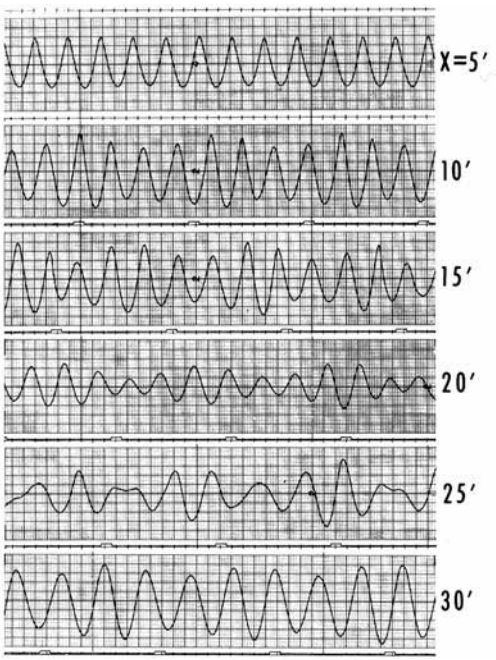

Figure 13.9: Sample records of the free-surface displacement of an initially uniform wavetrain. Initial wave frequency is 3.6 Hz (from Lake et al., 1977, *J. Fluid Mech.* Reproduced by permission of Cambridge University Press).

carry the computations beyond the first occurrence of an envelope node ($a \approx 0$). Based on Eq. (13.5.2) with the requirement of periodicity over one modulational period, more extensive calculations have been accomplished by Yuen and Ferguson (1978a, b). They found recurrence to be the dominant feature so that the envelope with a modulational wavelength evolved periodically from one crest to several and back to one again. A sample of experimental evidence is shown in Fig. 13.9. Correspondingly, energy in the lower harmonics spread to higher harmonics and then returned to the lower harmonics, and so on. The intermediate stage became progressively more complex in appearance if K/k was reduced. By varying K/k, Yuen and Ferguson found a systematic pattern for this complex variation. For $2ka_0 < K/k < 2(2)^{1/2}ka_0$, only the first harmonic in the Stokes wavetrain was unstable to the disturbance, and the evolution was the simplest. However, when K/k fell slightly below $2ka_0$, both the first and second harmonics were unstable; the evolution became more involved. Figure 13.10(a) shows the wavelengths and growth rates of several initial modulational disturbances, all of the form $a = a_0(1 - 0.1\cos K\xi)$ with the appropriate phase in accordance with Eqs. (13.4.5) and (13.4.6); corresponding evolutions are depicted in Fig. 13.10(b).

An approximate analytical theory has been worked out also by Stiassnie and Kroszynski (1982) by ignoring the higher harmonics of the disturbance, that is, by assuming

$$B = C_0 + C_{-1}e^{-2i\pi\bar{\xi}} + C_1 e^{2i\pi\bar{\xi}}\,. \tag{13.6.20}$$

where $C_0(\bar{\tau})$ corresponds to the carrier wave and $C_{\pm 1}(\bar{\tau})$ correspond to the side-band disturbances. As in the case of harmonic generation in shallow-water waves (cf. Section 12.11), we can substitute Eq. (13.6.20) into Eq. (13.5.16) to obtain two coupled nonlinear ordinary differential equations for C_0 and C_1 subject to the initial conditions $C_0(0) = 1$ and $C_{\pm 1}(0) = \delta e^{i\theta}$, C_{-1} being equal to C_1. These two equations may be solved explicitly in terms of elliptic integrals. When the coefficient $\kappa = \alpha\beta$ in Eq. (13.5.16) is such as to render the first harmonic unstable, $C_{\pm 1}$ oscillate at an amplitude comparable to C_0. The period of modulational recurrence so obtained agrees well with the numerically computed result by adding a large number of higher harmonics to Eq. (13.6.20). The approximate amplitude is, however, less satisfactory.

The regularity in the long-time evolution of Stokes wave suggests that for waves that are not too steep, nonlinearity tends to bring coherence rather than chaos. This fact may have important ramifications on the

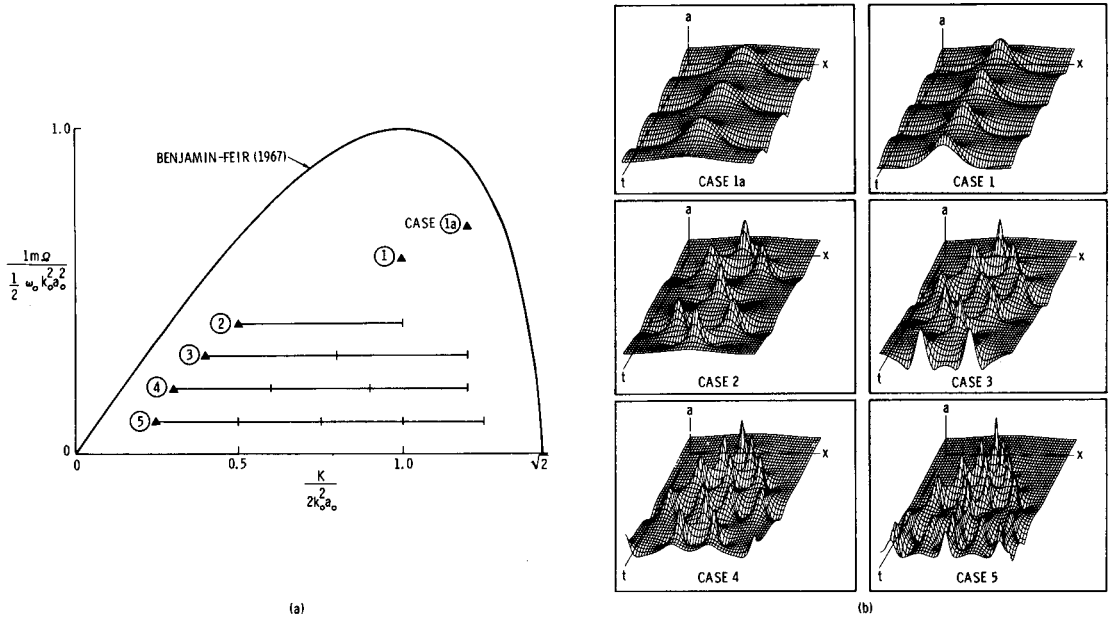

Figure 13.10: Relationship between initial conditions and long-time evolution of solutions of the nonlinear Schrödinger equation. (a) The perturbation wavenumber K of the various cases, and (b) their corresponding time evolution. The initial conditions consist of a uniform wavetrain with wavenumber k_0 and amplitude a_0 subject to a 10% perturbation. The numerals circled in (a) identify the cases in (b), and also correspond to the number of harmonics of the perturbation (including the primary) that lie within the unstable regime according to the stability analysis. Note that the number of unstable harmonics corresponds exactly to the number of modes that dominate the evolution. For example, Case 4 shows an evolution in which the lst, 2nd, 3rd, 4th, lst, and 2nd harmonics, in that order, took turns dominating the evolution as indicated by the number of peaks at various stages of evolution in the amplitude plot (from Yuen and Ferguson 1978. *Physics of Fluids*. Reprinted by permission of American Institute of Physics).

development of the wind-wave spectrum (Lake and Yuen, 1978; Mollo-Christensen and Ramamonjiarisoa, 1978). For still steeper waves, Lake et al. (1977) observed experimentally that the carrier frequency tended to reduce with propagation distance (compare the records at 5 ft. and 30 ft. in Fig. 13.9), and that the reduction was associated with the faster growth of the lower sideband [C_{-1} in Eq. (13.6.20)]. By experimenting with a wide range of ka, Melville (1982) found for $ka_0 < 0.29$ and for spontaneous disturbances, that the lower sideband also grew faster than the upper sideband [C_1 in Eq. (13.6.20)]. In addition, breaking was prevalent for $0.21 < ka_0 < 0.29$ which partially eroded the phenomenon of recurrence. Further down the wave channel both sidebands fell to local minima while breaking ceased, and then rose again. He also found breaking to be accompanied by an amplitude reduction of the upper sideband relative to the lower sideband, thereby enhancing the frequency downshift. Beyond $ka_0 > 0.3$ three-dimensional instability dominated. It is well known that the peak of a typical wind-wave spectrum shifts to lower frequencies with increasing fetch (see Hasselman et al., 1973, Fig. 2.5). Therefore, the cited experiments suggest that this downward shift may be contributed partly by nonlinearity and not by wind alone. This feature is not present in the solutions of the cubic Schrödinger equation, which predicts that opposite sidebands with equal initial amplitudes remain equal throughout cycles of rise and fall (Yuen and Ferguson, 1978a). Numerical solution of Dysthe's extended nonlinear Schrödinger equation with higher order dispersive terms has indeed shown higher growth of the lower side-band at the periodically recurring maxima of both side-bands (Lo and Mei, 1985). With an empirical model of breaking, Trulsen and Dysthe (1990) have found the downshift to be sustained. Theoretical efforts for frequency downshift of broad-banded sea specturm are still in progress.

We now turn to nonlinear effects in waves over variable depth.

13.7 Infragravity Waves Over Slowly Varying Depth

From swell records along beaches, Munk (1949) and Tucker (1950) observed long waves of period between 1 to 5 minutes, and found strong correlation between the long wave and the swell envelope. For storms of 1–2 days duration, the long-wave height is roughly one-tenth of the swell amplitude. Munk attributed this correlation to the nonlinear interaction

between waves and coined the term *surf beats* for these long waves. He suggested that they may be of relevance to harbor or bay oscillations. Since the natural frequencies of moored ships and floating platforms for oil-drilling platforms are in the similar range, the presence of infragravity waves has the potential to induce either straining of the mooring lines or excessive oscillations. The nonlinear mechanism of surf beats was first explained theoretically by Longuet–Higgins and Stewart (1962) through the idea of the *radiation stresses*. Interests on this topic was further advanced by the field observations of Herbers, Elgar and Guza (1994, 1995a, b). These authors introduced the term *infragravity waves* which is now widely used in the literature on coastal engineering and oceanography.

In Section 13.2, it was shown by a perturbation analysis that slowly modulated short waves over horizontal seabed forces long waves. A similiar result (11.10.5) was derived earlier by a different reasoning in terms of radiation stresses. In this section we follow Mei and Benmoussa (1984) and first extend these results for one train of refracted waves over bathymetries with horizontal length scales much greater than a typical wavelength, then discuss the physics of infragravity waves.

13.7.1 Equation for Long Waves Forced by One Train of Short Waves

We extend the ray approximation in Chapter 3 and begin as in Section 13.2.1 by requiring the following boundary condition on the seabed

$$\phi_z + h_x\phi_x + h_y\phi_y = 0\,, \quad z = -h(x,y)\,. \tag{13.7.1}$$

For slowly varying bathymetry we again let, without loss of generality, the same small parameter ϵ characterize both the wave steepness kA and the slow modulation in space and time, i.e., $h = h(\mathbf{x}_1)$.

The nonlinear boundary conditions on the free surface are approximated by Taylor expansion for small ζ. Multiple-scale expansions (13.2.5) are again assumed, so that (13.2.6) to (13.2.9) still hold. Instead of (13.2.11), the following WKB expansions are introduced,

$$\phi(\mathbf{x},z,t) = \sum_{n=1}^{\infty}\epsilon^n\phi_n = \sum_{n=1}^{\infty}\epsilon^n\sum_{m=-n}^{m=n}\phi_{nm}(\mathbf{x}_1,z,t_1)e^{imS/\epsilon} \tag{13.7.2}$$

$$\zeta(\mathbf{x},t) = \sum_{n=1}^{\infty}\epsilon^n\zeta_n = \sum_{n=1}^{\infty}\epsilon^n\sum_{m=-n}^{m=n}\zeta_{nm}(\mathbf{x}_1,t_1)e^{imS/\epsilon} \tag{13.7.3}$$

where $S(\mathbf{x}_1, t_1)/\epsilon$ is the phase function of the fundamental harmonic, related to the wave frequency and wavenumber by

$$\omega = -\frac{\partial S}{\partial t_1}, \quad \mathbf{k} = \nabla_1 S \tag{13.7.4}$$

with $\nabla_1 = (\partial/\partial x_1, \partial/\partial y_1)$ being the horizontal gradient with respect to the slow coordinates. After separating different orders and harmonics, the perturbation equations are deduced for nth order and mth harmonic as before. Only the seabed boundary condition must now be changed to:

$$\frac{\partial \psi_{nm}}{\partial z} = B_{nm}, \quad z = -h \tag{13.7.5}$$

where

$$\begin{aligned} B_{10} &= B_{11} = B_{20} = 0, \\ B_{21} &= -\nabla_1 h \cdot (i\mathbf{k}\phi_{11}), \\ B_{30} &= -\nabla_1 h \cdot \nabla_1 \phi_{10}. \\ &\cdots \end{aligned} \tag{13.7.6}$$

The vertical boundary-value problems for ϕ_{10}, ϕ_{11} and ϕ_{20} are homogeneous and that for ϕ_{21} has been treated in the lineaized theory of Chapter 3. In particular, we still have $\phi_{10} = \phi(\mathbf{x}_1, t_1)$, and ϕ_{11} is the same as that given by the ray approximation. From Bernoulli equation on the free surface, we still get

$$\zeta_{20} = -\frac{A}{4}\frac{\omega^2}{g \sinh^2 kh} - \frac{1}{g}\frac{\partial \phi_{10}}{\partial t_1}. \tag{13.7.7}$$

As for the long wave, changes come at the third order, where the problem for ϕ_{30} is now inhomogeneous. By applying Green's formula to ϕ_{10} and ϕ_{30}, we get the solvability condition

$$\frac{G_{30}}{g} = \int_{-h}^{0} F_{30}\, dz + B_{30} \tag{13.7.8}$$

which gives

$$\frac{\partial \zeta_{20}}{\partial t_1} + \nabla_1 \cdot \left(h \nabla_1 \phi_{10} + \frac{g\mathbf{k}}{2\omega}|A|^2 \right) = 0. \tag{13.7.9}$$

Taking the time derivative of this result and making use of (13.7.7), we get

$$\nabla_1 \cdot (gh\nabla_1\zeta_{20}) - \frac{\partial^2\zeta_{20}}{\partial t_1^2}$$
$$= \nabla_1 \cdot \left(\frac{g\mathbf{k}}{2\omega}\frac{\partial|A|^2}{\partial t_1}\right) - \nabla_1 \cdot \left(h\nabla_1\left(\frac{\omega|A|^2}{4\sinh^2 kh}\right)\right). \tag{13.7.10}$$

We leave it as an exercise to show the equivalence of (13.7.10) and (13.2.36) for constant h.

By using

$$\nabla_1 k = -\frac{\omega k\nabla_1 h}{C_g \sinh 2kh} \tag{13.7.11}$$

and

$$\frac{\partial|A|^2}{\partial t_1} + \nabla_1 \cdot (\mathbf{C}_g|A|^2) = 0\,, \tag{13.7.12}$$

the right-hand-side of (13.7.10) can be written in a different form

$$-\nabla_1 \cdot \left\{\nabla_1\left(\frac{gkh|A|^2}{2\sinh 2kh}\right) + \frac{g}{2\omega}[\mathbf{k}\cdot\nabla_1(\mathbf{C}_g|A|^2) + |A|^2 C_g\nabla_1 k]\right\}. \tag{13.7.13}$$

Now the first term above can be rewritten as

$$-\frac{\partial^2}{\partial x_{1i}\partial x_{1j}}\left[\frac{g|A|^2}{2}\left(\frac{C_g}{C} - \frac{1}{2}\right)\delta_{ij}\right],$$

the second term as

$$-\frac{g}{2\omega}\frac{\partial}{\partial x_{1i}}\left[k_i\frac{\partial}{\partial x_{1j}}\left(C_g|A|^2\frac{k_j}{k}\right)\right]$$
$$= -\frac{g}{2\omega}\frac{\partial^2}{\partial x_{1i}\partial x_{1j}}\left(C_g|A|^2\frac{k_i k_j}{k}\right) + \frac{g}{2\omega}\frac{\partial}{\partial x_{1i}}\left[\left(C_g|A|^2\frac{k_j}{k}\right)\frac{\partial k_i}{\partial x_{1j}}\right],$$

and the third term as

$$-\frac{g}{2\omega}\frac{\partial}{\partial x_{1i}}\left[\frac{C_g|A|^2}{2k}\frac{\partial(k_j k_j)}{\partial x_{1i}}\right] = -\frac{g}{2\omega}\frac{\partial}{\partial x_{1i}}\left[\frac{C_g|A|^2 k_j}{k}\frac{\partial k_j}{\partial x_{1i}}\right]$$
$$= -\frac{g}{2\omega}\frac{\partial}{\partial x_{1i}}\left[\frac{C_g|A|^2 k_j}{k}\frac{\partial k_i}{\partial x_{1j}}\right],$$

where the irrotationality of $\mathbf{k}$ has been used. Therefore (13.7.10) can be reduced to the following form,

$$\nabla_1 \cdot (gh\nabla_1 \zeta_{20}) - \frac{\partial^2 \zeta_{20}}{\partial t_1^2} = -\frac{1}{\rho} \frac{\partial^2 S_{ij}}{\partial x_{1_i} \partial x_{1_j}}\,, \tag{13.7.14}$$

where S_{ij} with $i, j = 1, 2$ are the components of the radiation stress tensor for a progressive wave

$$S_{ij} = \frac{\rho g |A|^2}{2} \left[\left(\frac{C_g}{C} - \frac{1}{2} \right) \delta_{ij} + \frac{C_g}{C} \frac{k_i k_j}{k^2} \right]. \tag{13.7.15}$$

If ζ_{20} is identifed with $\bar{\zeta}$, Eqs. (13.7.14) and (12.10.5) are the same.

From the form of (13.7.14), two kinds of long waves can be foreseen. One corresponds to the homogeneous solution, propagating at the characteristic speed $\sqrt{gh}$. The other is forced by the inhomogeneous terms on the right, which are associated with the slowly mudulated short waves. Since the short-wave envelope propagates at the (slower) group velocity C_g, the forced long wave must do likewise, hence is bound to the short-wave envelope. It is known in Chapter Four that a submarine ridge may refract, reflect or trap long waves. When there is forcing by the radiation stress in the short waves, what can we expect of the long waves? This matter is of interest to the dependence of the sea spectrum on local bathymetry.

Let us introduce the normalization

$$\mathbf{x}_1 = \frac{\mathbf{X}}{k_\infty} \quad t_1 = \frac{T}{\omega} \quad h \to \frac{h}{k_\infty} \quad h_0 \to \frac{h_0}{k_\infty} \quad k \to k_\infty k$$

$$A \to a_0 A \quad \bar{\zeta} \to (k_\infty a_0^2)\xi \quad C_g \to \frac{\omega}{k_\infty} C_g\,, \tag{13.7.16}$$

where $k_\infty = \omega^2/g$. The dispersion relation becomes

$$1 = k \tanh kh \tag{13.7.17}$$

while (13.7.12) and (13.7.10) become

$$\frac{\partial |A|^2}{\partial T} + \nabla \cdot \mathbf{C}_g |A|^2 = 0 \quad \nabla = \left(\frac{\partial}{\partial X}, \frac{\partial}{\partial Y} \right) \tag{13.7.18}$$

$$\nabla \cdot (h\nabla \xi) - \frac{\partial^2 \xi}{\partial T^2} = \frac{\partial}{\partial T} \nabla \cdot \left(\frac{\mathbf{k}|A^2|}{2} \right) - \nabla \cdot \left[h\nabla \left(\frac{|A|^2}{4 \sinh^2 kh} \right) \right]. \tag{13.7.19}$$

In the sequel we only consider a one-dimensional bathymetry where the seabed is not horizontal only in a finite strip,

$$h = \begin{cases} h_0\,, & X < X_0\,; \\ h(X)\,, & X_0 < X < X_1\,. \\ h = h_1\,, & X > X_1\,; \end{cases} \tag{13.7.20}$$

13.7.2 Short-Wave Envelope

Refraction of the short waves is analyzed by the ray theory in Chapter 3.

Let the obliquely incident wave from $x \sim -\infty$ be long-crested and sinusoidally modulated, and that the envelope is in the form of a progressive wave colinear with the short waves. If the central frequency of the carrier wave is ω, the corresponding central wavenumber vector in the three regions are

$$\mathbf{k} = (k_x, k_y) = \begin{cases} (k_0 \cos\alpha_0,\ k_0 \sin\alpha_0)\,, & X < X_0\,; \\ (k_x = k\cos\alpha,\ k_0 \sin\alpha_0)\,, & X_0 < X < X_1\,. \\ (k_1 \cos\alpha_1,\ k_1 \sin\alpha_1)\,, & X > X_1\,; \end{cases} \tag{13.7.21}$$

In the region of variable depth, the local wavenumber $k(X)$ and the angle of incidence $\alpha(X)$ vary slowly in X according to the local dispersion relation and Snell's law. A simple model of slowly modulated incident short waves is the superposition of two colinear sinusoidal wavetrains of slightly different wavenumbers $\mathbf{k}_\pm = \mathbf{k}_0(1 \pm \epsilon)$, and the same normalized amplitude (unity). Let $\omega_\pm = \omega_0 \pm \epsilon\Omega$ denote the frequency corresponding to $\mathbf{k}_\pm$, respectively. Then according to the dispersion relation $\omega_0 = \omega(k_0)$ and $\omega_\pm = \omega(k_0(1\pm\epsilon))$, we must have

$$\omega \pm \epsilon\Omega = \omega(k_0(1 \pm \epsilon)) = \omega(k_0) \pm \epsilon k_0 \left[\frac{d\omega}{dk}\right]_0 + O(\epsilon^2),$$

hence,

$$\Omega = k_0 \left[\frac{d\omega}{dk}\right]_0 = C_{g_0} k_0\,. \tag{13.7.22}$$

The incident-wave displacement can be written at the leading order as

$$\zeta = \frac{A}{2} \exp(ik_0 \cos\alpha_0 x + ik_0 \sin\alpha_0 y - i\omega t) + * \tag{13.7.23}$$

where the incident wave amplitude is

$$A(X,Y,T) = \frac{1}{2}\exp[i(k_{x_0}X + k_{y_0}Y - \Omega T)] + *$$
$$= \cos((k_{x_0}X + k_{y_0}Y - \Omega T)) \tag{13.7.24}$$

which is sinusoidally modulated.

In the region of varying depth, (13.7.18) can be written as

$$\frac{\partial|A|^2}{\partial T} + \frac{\partial}{\partial X}(C_{g_x}|A|^2) + \frac{\partial}{\partial Y}(C_{g_y}|A|^2) = 0\,. \tag{13.7.25}$$

Since C_{g_x} and C_{g_y} are both functions of X, we assume the solution to be of the following form

$$A = \frac{1}{2}\hat{A}e^{i\psi} + * \tag{13.7.26}$$

where

$$\psi \equiv \int_{X_0}^{X} K_x dX + k_y Y - \Omega T \tag{13.7.27}$$

and $\hat{A}$ is a real function of X. Note that

$$|A|^2 = \frac{1}{2}\hat{A}^2 + \frac{1}{4}\hat{A}^2(e^{2i\psi} + *)\,. \tag{13.7.28}$$

By substituting (13.7.28) into (13.7.25) and extracting from the coefficient of the zeroth harmonic, we get

$$\hat{A}(X) = \sqrt{(C_{g_x})_0/C_{g_x}}\,, \tag{13.7.29}$$

which is the well-known result for a shoaling wavetrain. From the coefficients of the second harmonic, we get,

$$\Omega = K_x C_{g_x} + k_y C_{g_y} = (K_x k_x + k_y^2)\frac{C_g}{k}\,, \tag{13.7.30}$$

which describes the phase hence the propagation of the envelope. Dividing the preceding equation by $\Omega = C_{g_0}k_0$, we get

$$1 = \frac{C_g}{C_{g_0}}\left(\frac{K_x k_x}{k_0 k} + \frac{k_0^2}{k_0 k}\right)$$

or

$$K_x = \frac{C_{g_0} k_0 k}{C_g k_x} - \frac{k_y^2}{k_x} = \frac{C_{g_0} k_0}{C_g k} \frac{k^2}{k_x} - \frac{k_x^2 + k_y^2}{k_x} + k_x$$

$$= k_x + \left(\frac{C_{g_0}}{C_0} \frac{C}{C_g} - 1 \right) \frac{k^2}{k_x}, \tag{13.7.31}$$

where

$$\frac{C C_{g_0}}{C_0 C_g} = \frac{(1 + \frac{2k_0 h_0}{\sinh 2k_0 h_0})}{(1 + \frac{2kh}{\sinh 2kh})}.$$

In very deep water, $kh \uparrow \infty$, the above ratio is greater than unity, hence $K_x > k_x$. On the other hand in very shallow water, $kh \downarrow 0$, this ratio can be less than unity, hence K_x can be less than k_x.

Let h increase with X. For sufficiently large angle of incidence, a caustic may exist such that $k_x \downarrow 0$; the short waves are reflected. Then $K_x \uparrow \infty$

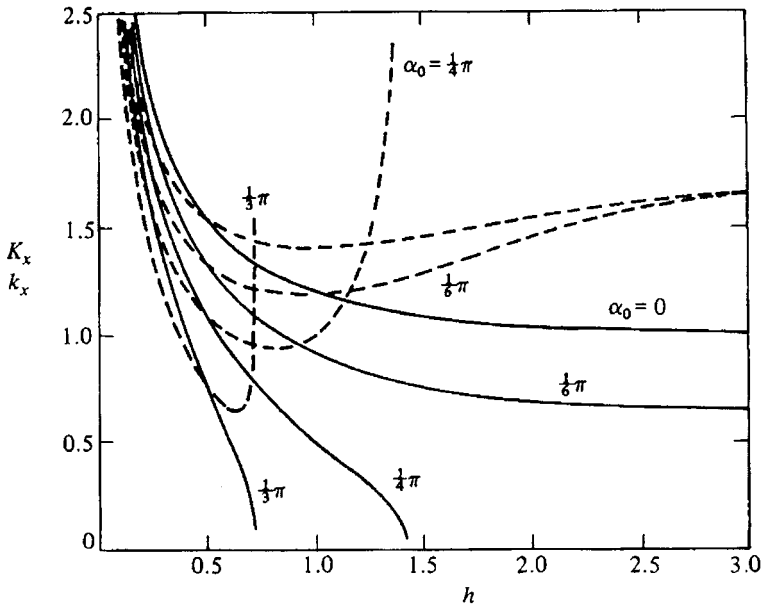

Figure 13.11: Effects of depth and incidence angle on the dimensionless wavenumber components k_x (solid curves) and K_x (dashed curves) of short and long waves (from Mei and Benmoussa, 1984, *J. Fluid Mech.* Reprinted by permission of Cambridge University Press).

and the envelope is in the X-direction hence is orthogonal to the short-wave crests. Thus short waves and their envelope propagate in different directions! If on the other hand $h(X)$ decreases with X, K_x is smaller than k_x, and the difference diminishes as $h \downarrow 0$. Sample variations of k_x and K_x for different incidence angles and depths are shown in Fig. 13.11 for $h_0 = 0.5$. Very near the caustic, the ray theory breaks down, hence the result above loses validity locally.

The direction of the short-wave envelope is $\tan\beta = k_y/K_x$. If through the strip $X_0 < X < X_1$ the depth increases with X from h_0 to $h_1 > h_0$, then on the transmission side

$$K_{x_1} > K_{x_0} = k_{x_0}$$

so that

$$\tan\beta_1 < \tan\beta_0 (= \tan\alpha)\,.$$

If h decreases in X, the inequality signs are reversed.

13.7.3 Mean Sea-Level

Now let us turn to the long-scale response. The forcing term on the right of (13.7.19) consists of a steady part ξ_0 and a sinusoidal part. Therefore, we assume the long-scale displacement to be

$$\xi = \xi_0(X) + \frac{1}{2}[\tilde{\xi}(X)\exp 2i(k_y Y - \Omega T) + *]\,. \tag{13.7.32}$$

The steady part is the mean sea level which satisfies

$$\frac{\partial}{\partial X}\left(h\frac{\partial \xi_0}{\partial X}\right) = -\frac{\partial}{\partial X}\left[h\frac{\partial}{\partial X}\left(\frac{\overline{|A|^2}}{4\sinh^2 kh}\right)\right].$$

It follows easily that

$$\xi_0 = -\frac{\hat{A}^2}{8\sinh^2 kh}\,. \tag{13.7.33}$$

The integration constants are chosen so that ξ_0 is zero in deep water. The result is a depression, i.e., set-down. Sample variations of the mean set-down ξ_0 with depth are shown in Fig. 13.12. Again, the prediction near the caustic is not reliable and needs refinement.

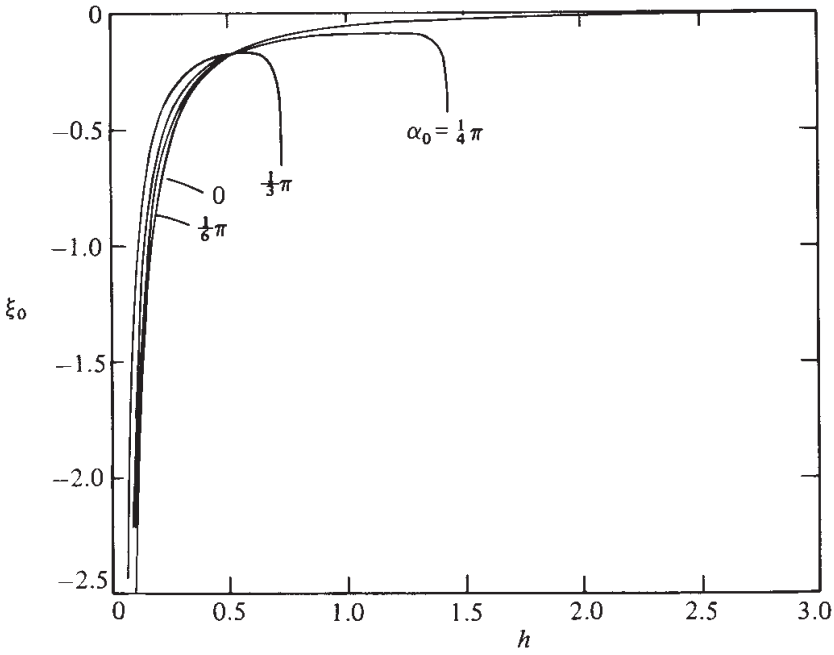

Figure 13.12: Effects of depth and incidence angle on mean sea level set-down xi_0. Depth on the incidence side is $h_0 = 0.5$ (from Mei and Benmoussa, 1984, *J. Fluid Mech.* Reprinted by permission of Cambridge University Press).

13.7.4 Free and Bound Infragravity Waves

The second harmonic part of (13.7.32) represents long (infragravity) waves and must satisfy

$$\frac{d}{dX}h\frac{d\tilde{\xi}}{dX} + 4(\Omega^2 - k_y^2 h)\tilde{\xi} = \left\{ \left[\frac{kh(K_x^2 + k_y^2)}{\sinh 2kh} + \frac{\Omega^2 k}{C_g} \right] \frac{(C_{g_x})_0}{C_{g_x}} \right.$$
$$+ \left[\frac{d}{dX}h\frac{d\xi_0}{dX} + i\left(4K_x h\frac{d\xi_0}{dX} + 2\xi_0 \frac{d}{dX}(K_x h) \right) \right]$$
$$\left. - \frac{i}{2}\Omega C_{g_{x_0}} \frac{d}{dX}\left(\frac{k}{C_g} \right) \right\} \exp\left(2i \int_{X_0}^{X} K_x \, dX \right). \tag{13.7.34}$$

This is an inhomogeneous differential equation with variable coefficients. Let us examine the solutions in regions of constant and variable depths separately.

In regions of constant depth, the last two lines on the right-hand side of (13.7.34) vanish. The particular solution can be written as

$$\xi_L = (\overline{\xi}_L)_j \exp\left(2i\int_{X_0}^{X_1} K_x dX\right), \quad \begin{matrix} j=0\,, & \text{if } X < X_0\,, \\ j=1\,, & \text{if } X > X_1\,. \end{matrix} \tag{13.7.35}$$

where

$$(\overline{\xi}_L)_0 = -\left\{\frac{[\frac{kh(K_x^2+k_y^2)}{\sinh 2kh} + \frac{\Omega^2 k}{C_g}]}{4[(K_x^2+k_y^2)h - \Omega^2]}\right\}_0, \tag{13.7.36}$$

$$(\overline{\xi}_L)_1 = -\left\{\frac{\frac{(C_{gx})_0}{C_{gx}}[\frac{kh(K_x^2+k_y^2)}{\sinh 2kh} + \frac{\Omega^2 k}{C_g}]}{4[(K_x^2+k_y^2)h - \Omega^2]}\right\}_1. \tag{13.7.37}$$

Quantities inside brackets $\{.\}_0$ and $\{.\}_1$ are defined by evaluating $h = h_0$ and $h = h_1$, respectively.

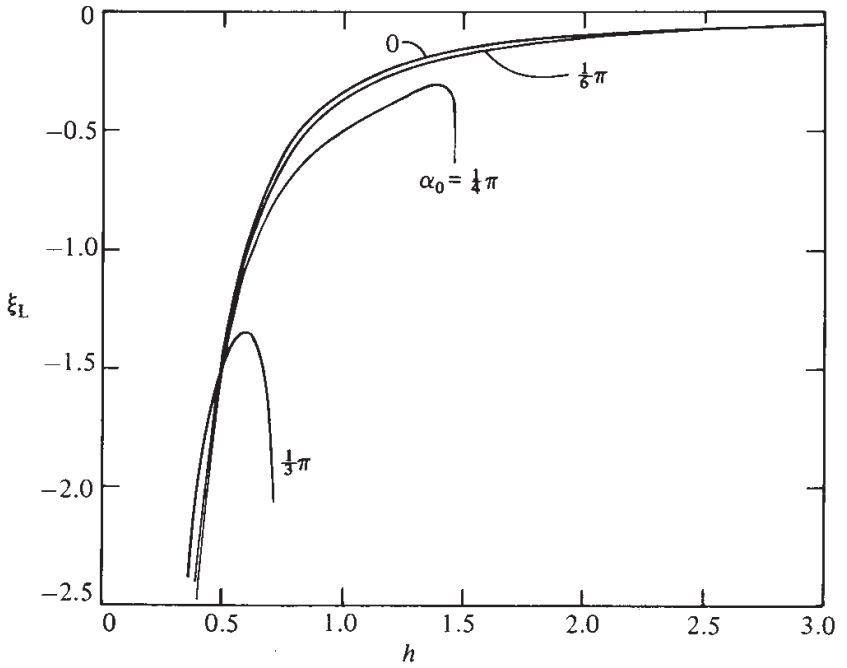

Figure 13.13: Effects of depth and incidence angle on the amplitude ξ_L of the bound long wave (from Mei and Benmoussa, 1984, *J. Fluid Mech.* Reprinted by permission of Cambridge University Press).

From (13.7.32) and (13.7.35), ξ_L travels with the envelope of the short waves, hence they are the *bound* (*or locked*) *long waves*. The amplitude $(\xi_L)_0$ on the incidence side is plotted in Fig. 13.13 as a function of h for several angles of incidence.

We now define the *free long waves* in the two regions of constant depth $X < X_0, X > X_1$ by

$$\tilde{\xi} = (\xi_F)_j + (\overline{\xi}_L)_j \exp\left(2i \int_{X_0}^{X_1} K_x dX\right), \quad \begin{matrix} j = 0\,, & \text{if } X < X_0\,, \\ j = 1\,, & \text{if } X > X_1\,. \end{matrix} \tag{13.7.38}$$

The free long waves satisfy the homogeneous differential equation with constant coefficients:

$$\frac{d}{dX}\left(h_j \frac{d(\xi_F)_j}{dX}\right) + 4(\Omega^2 - k_y^2 h_j)(\xi_F)_j = 0 \quad j = 0, 1\,. \tag{13.7.39}$$

The nature of the free long wave in each region depends on the sign of

$$\lambda_j^2 = \frac{1}{h_j}(\Omega^2 - k_y^2 h_j) = k^2 \left[\frac{{C_{g_0}}^2}{h_j} - \sin^2 \alpha_0\right]. \tag{13.7.40}$$

If h_j is small enough so that $\lambda_j^2 > 0, (\xi_F)_j$ must be outgoing waves

$$(\xi_F)_j = (\overline{\xi}_F)_j \exp(2i|\lambda_j|\,|X|) \tag{13.7.41}$$

which propagate in the direction

$$\tan\theta_j = \pm \frac{k_y}{|\lambda_j|} \tag{13.7.42}$$

The propagation speed is $C_j = \sqrt{h_j}$. On the other hand, if h_j is sufficiently large so that $\lambda_j^2 < 0$, then $(\xi_F)_j$ must attenuate exponentially with distance

$$(\xi_F)_j = (\overline{\xi}_F)_j \exp(-2|\lambda_j||X|)\,. \tag{13.7.43}$$

Thus, the free long wave is trapped in the shallow zone only, despite the fact the short waves pass over the strip. The critical depth h_* at which $\lambda_j = 0$ is plotted as a function of h_0 and α_0 in Fig. 13.14.

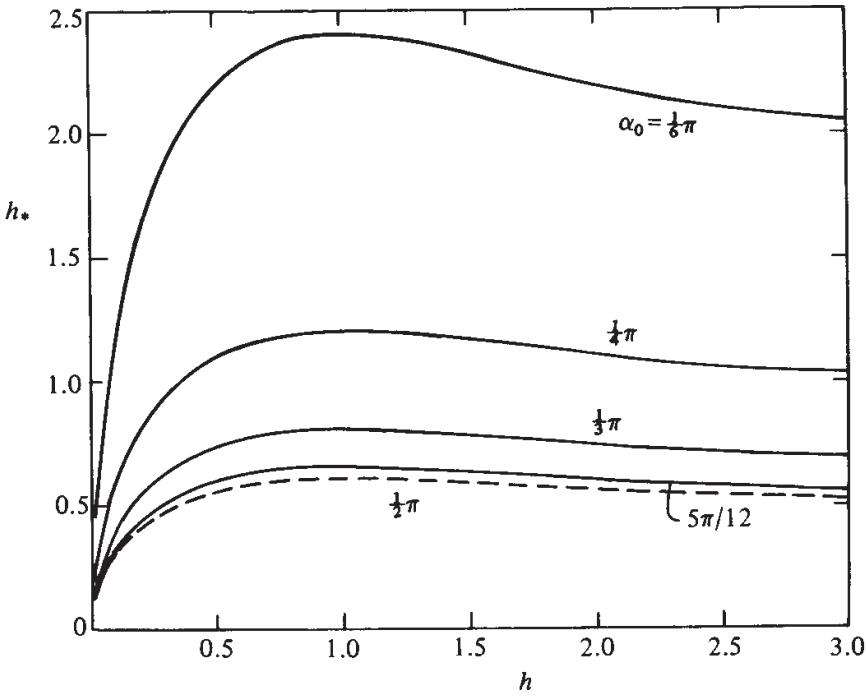

Figure 13.14: The critical depth h_* vs. h_0 for several angles of incidence α_0. For $\alpha_0 = \pi/2$ (dashed curve), the critical depth is at $h_* = C_{g0}^2$ (from Mei and Benmoussa, 1984, *J. Fluid Mech.* Reprinted by permission of Cambridge University Press).

In the zone of variable depth $X_0 < X < X_1$, we introduce the locked and free long waves by

$$\tilde{\xi} = \overline{\xi}_L(X) \exp\left(2i \int_{X_0}^{X} K_x dX\right) + \xi_F(X) \tag{13.7.44}$$

where $\overline{\xi}_L$ is formally defined to be

$$\overline{\xi}_L = -\frac{\frac{(C_{gx})_0}{C_{gx}}\left[\frac{kh(K_x^2+k_y^2)}{\sinh 2kh} + \frac{\Omega^2 k}{C_g}\right]}{4[(K_x^2+k_y^2)h - \Omega^2]} \tag{13.7.45}$$

with k, h, K_x, C_g, etc., being functions of X depending on the local bathymetry. The dimensionless equation governing ξ_F is

$$\frac{d}{dX}\left(h\frac{d\xi_F}{dX}\right)+[4(\Omega^2-k_y^2h)]\xi_F$$

$$=\left\{h\frac{d^2Z}{dX^2}+\frac{dh}{dX}\frac{dZ}{dX}+i\left(4hK_x\frac{dZ}{dX}+2Z\frac{d}{dX}[K_xh]\right)\right.$$

$$\left.-\frac{1}{2}{C_{g_0}}^2k_0^2\cos\alpha_0\frac{d}{dX}\left(\frac{k}{C_g}\right)\right\}\exp\left(2i\int_{X_0}^{X}dX\,k_x\right) \qquad (13.7.46)$$

where $Z=\xi_0-\xi_L$.

At X_0 and X_1, continuity of the surface displacement is required

$$\xi_F=(\xi_F)_j \quad \text{at} \quad x=X_j\,. \qquad (13.7.47)$$

Assume that the slope of the seabed dh/dX is also continuous,[4] then $d\xi_0/dX$ and $d\xi_L/dX$ must also be continuous, implying the continuity of the free wave slope

$$\left[\frac{d\xi_F}{dX}\right]_{X_0-}^{X_0+}=0\,,\quad \left[\frac{d\xi_F}{dX}\right]_{X_1-}^{X_1+}=0\,. \qquad (13.7.49)$$

The resulting boundary-value problem for ξ_F in the region $X_0<X<X_1$ is then solved numerically.

Sample results of ξ_F are shown in Fig. 13.15 for a submarine ridge connecting two regions of equal and constant depth:

$$h=\begin{cases}h_0+\dfrac{\Delta h}{2}\left(1-\cos\dfrac{2X}{L}\right), & 0<X<L\,;\\ h_0\,, & X<0,\ X<L\,.\end{cases} \qquad (13.7.50)$$

Over the narrower ridge with $L=2$, incoming waves with all three incidence angles produce only outgoing free long waves. This result is because these waves are much longer than L. For a wider ridge, free long waves are relatively strong on the transmission side, if the incidence is nearly normal.

[4]It was pointed out by Liu(1989) that if dh/dX is discontinuous, then $d\xi_0/dX$ and $d\xi_B/dX$ must also be discontinuous. Integration of Eq. (13.7.46) across the line X_j we get instead

$$\left[h\frac{d\xi}{dX}\right]_{X_j-\delta}^{X_j+\delta}=\left[h\frac{d\xi_0}{dX}\right]_{X_j-\delta}^{X_j+\delta}\exp\left\{2i\int_{X_0}^{X_j}K_x dX\right\}\quad j=0,1\,. \qquad (13.7.48)$$

implying that $d\xi_F/dX$ is not continuous.

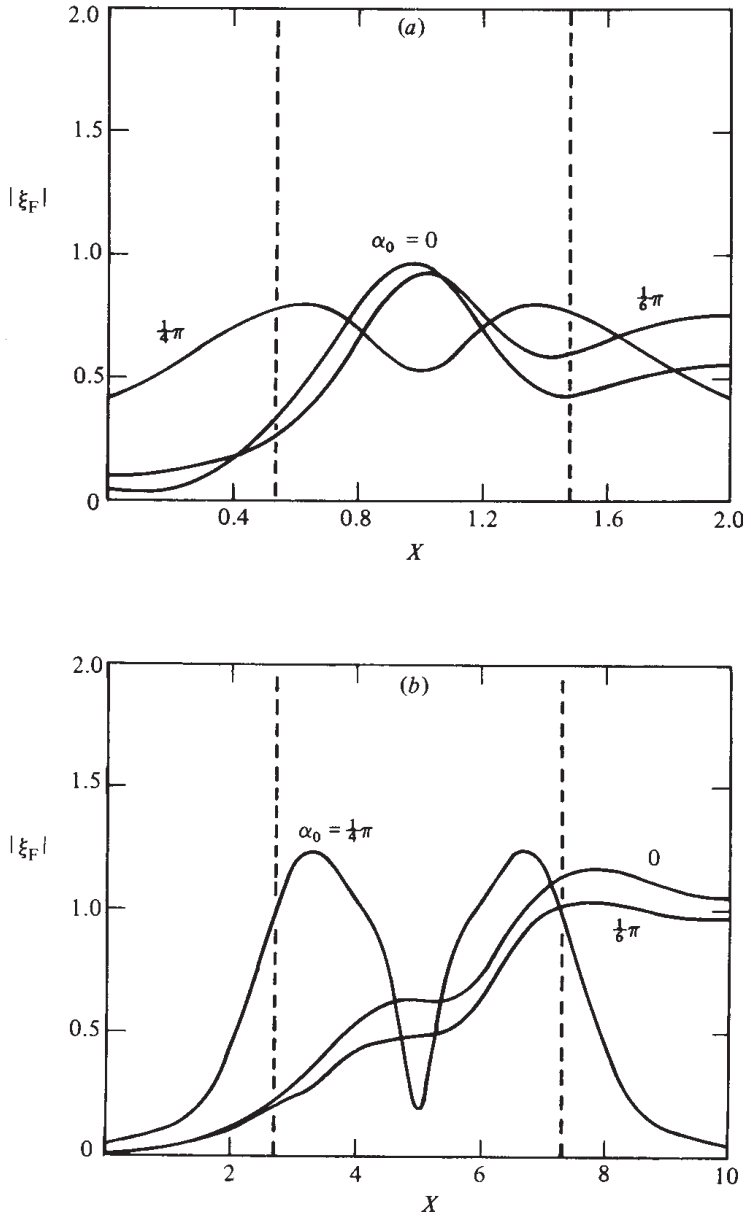

Figure 13.15: Amplitude of trapped free long waves over a ridge with $h_0 = 1, \Delta h = -0.5$. for various incidence angles (from Mei and Benmoussa, 1984, *J. Fluid Mech.* Reprinted by permission of Cambridge Univeristy Press).

However, the free long waves are trapped over the ridge, if the incidence is sufficiently oblique. (See Fig. 13.15 for $\alpha_0 = \pi/4$).

Thus, the physics of infragravity waves is very much affected directly, as well as indirectly through the short waves, by bathymetry.

Other results over a submarine canyon can be found in Mei and Benmoussa (1984). Corrections for a bathymetry with discontinuous slope has been reported by Liu (1989).

13.8 Infragravity Waves Over Periodic Bars

In Section 7.2 we studied by linearized approximation the Bragg scattering of infinitesimal waves by periodic bars. Let us examine here the second-order long waves.

By assuming that ϵ characterizes both the wave steepness and the rate of resonant growth, the perturbation analysis of Section 7.2 can be extended to periodic bars over a slowly varying depth, and to the second order. In particular, let the bars be described by

$$\delta = \frac{D}{2}\left(\exp\frac{2i}{\epsilon}\int^{x_1}\alpha(x_1)\,dx_1 + *\right). \tag{13.8.1}$$

At the first order the first harmonic solution $(\phi_{11}, \zeta_{11})\exp(-i\omega t)$ is still given by the linearized theory of Section 8.2, i.e.,

$$\begin{aligned}\phi_{11} &= -\frac{ig}{2\omega}(Ae^{iS_+} + Be^{iS_-})\frac{\cosh k(z+h)}{\cosh kh}\,,\\ \zeta_{11} &= \frac{1}{2}(Ae^{iS_+} + Be^{iS_-})\end{aligned} \tag{13.8.2}$$

where

$$S_\pm = \pm\frac{1}{\epsilon}\int^{x_1}\alpha(x_1)\,dx_1 + \beta y\,, \tag{13.8.3}$$

with θ being the local angle of incidence and

$$\alpha = k\cos\theta\,, \quad \beta = k\sin\theta\,. \tag{13.8.4}$$

The amplitudes of the incident and reflected waves are coupled by

$$\frac{\partial A}{\partial t_1} + \mathbf{C}_g^+\cdot\nabla_1 A + \frac{1}{2}A\nabla_1\cdot\mathbf{C}_g^+ = -i\Omega_0 B\cos 2\theta \tag{13.8.5}$$

$$\frac{\partial B}{\partial t_1} + \mathbf{C}_g^- \cdot \nabla_1 B + \frac{1}{2} B \nabla_1 \cdot \mathbf{C}_g^- = -i\Omega_0 A \cos 2\theta \tag{13.8.6}$$

where

$$\Omega_0 = \frac{\omega k D}{2 \sinh 2kh} \,. \tag{13.8.7}$$

Solvability of ϕ_{30} gives the governing equation for the long-wave displacment

$$\begin{aligned} &\frac{\partial^2 \zeta_{20}}{\partial t_1^2} - g\nabla_1(h\nabla_1 \zeta_{20}) \\ &\quad = g\nabla_1 \cdot \left\{ h\nabla_1 \left[\frac{k(|A|^2 + |B|^2)}{2 \sinh 2kh} \right] \right\} \\ &\qquad - \frac{g}{2\omega} \frac{\partial}{\partial t_1} \left\{ \alpha \frac{\partial}{\partial x_1} (|A|^2 - |B|^2) + \beta \frac{\partial}{\partial y_1} (|A|^2 + |B|^2) \right\} . \end{aligned} \tag{13.8.8}$$

The corresponding long-wave potential is related by the averaged Bernoulli equation:

$$\zeta_{20} = -\frac{\partial \phi_{10}}{\partial t_1} - \frac{k(|A|^2 + |B|^2)}{2 \sinh 2kh} \,. \tag{13.8.9}$$

Let the bars be confined in a finite domain $0 < x_1 < L$. Continuity of pressure and normal velocity requires

$$[A]_-^+ = 0 \,, \quad [B]_-^+ = 0 \tag{13.8.10}$$

at $O(\epsilon)$, and

$$\begin{aligned} \left[\frac{\partial \phi_{10}}{\partial t_1} + |\nabla \phi_{11}|^2 + \left| \frac{\partial \phi_{11}}{\partial z} \right|^2 \right]_-^+ &= 0 \,, \\ \left[\frac{\partial \phi_{10}}{\partial x_1} + \frac{\partial \phi_{20}}{\partial x} \right]_-^+ &= 0 \end{aligned} \tag{13.8.11}$$

at $O(\epsilon^2)$. After using (13.8.10) and (13.8.9), the matching conditions (13.8.11) become

$$\begin{aligned} [\zeta_{20}]_-^+ &= 0 \,, \\ \left[\frac{\partial \zeta_{20}}{\partial x_1} \right]_-^+ &= -\frac{k}{2 \sinh 2kh} \frac{\partial}{\partial x_1} (|A|^2 + |B|^2) \end{aligned} \tag{13.8.12}$$

at $x_1 = 0, L$.

Restricting further to normal incidence, the amplitude equations reduce to

$$\begin{aligned} \frac{\partial A}{\partial t_1} + C_g \frac{\partial A}{\partial x_1} &= -i\Omega_0 B\,, \\ \frac{\partial B}{\partial t_1} - C_g \frac{\partial B}{\partial x_1} &= -i\Omega_0 A\,, \end{aligned} \tag{13.8.13}$$

and the long-wave equation becomes

$$\begin{aligned} \frac{\partial^2 \zeta_{20}}{\partial t_1^2} - gh\frac{\partial^2 \zeta_{20}}{\partial x_1^2} &= \frac{g}{2}\left(\frac{2C_g}{C} - \frac{1}{2}\right)\frac{\partial}{\partial x_1^2}(|A|^2 + |B|^2) \\ &\quad + \frac{g\Omega_0}{C}\frac{\partial}{\partial x_1}(iA^*B + *)\,. \end{aligned} \tag{13.8.14}$$

The system (13.8.13) and (13.8.14) are hyperbolic partial differential equations and can be solved numerically by standard methods for any initial data. Computational details can be found in Hara and Mei (1987).

As a numerical example we show in Fig. 13.16 some computed results for the scattering of a packet of short waves incident from the left of a bar patch. In terms of the dimensionless coordinates where x is normalized by L, t by L/C_g, and (A, B) by the maximum of the incident wave packet, the profiles of $|A|, |B|$ and ζ_{20} are shown for three instants: $t = 0, 3\pi$, and 6π. The bars are located within $0 < x < \sigma$ where $\sigma = \Omega_0 L/C_g$ is the normalized patch width. At $t = 0$ the front of the incident-wave group is just touching the first bar. There is no reflection, and the long wave consists only of the set-down. At $t = 3\pi$, considerable reflection has taken place. Both the incident and the reflected packets have split into several groups, exhibiting the dispersive property of the envelope. On the transmission side the leading trough advances at the high speed $\sqrt{gh}$, and is followed by a slower crest, then by a bound (set-down) trough moving at the group velocity of the short waves. On the reflection side, a crest is moving ahead of the bound long wave toward the left. At a later time $t = 6\pi$, dispersion of the short-wave envelopes is fully developed. The leading long waves on both sides are far outrunning the short-wave envelopes and the bound set-downs.

If the patch is sufficiently wide, all the short waves can be reflected. While there are no short waves on the transmission side, free long waves can still be radiated to both sides. Thus, shelter cannot be found behind

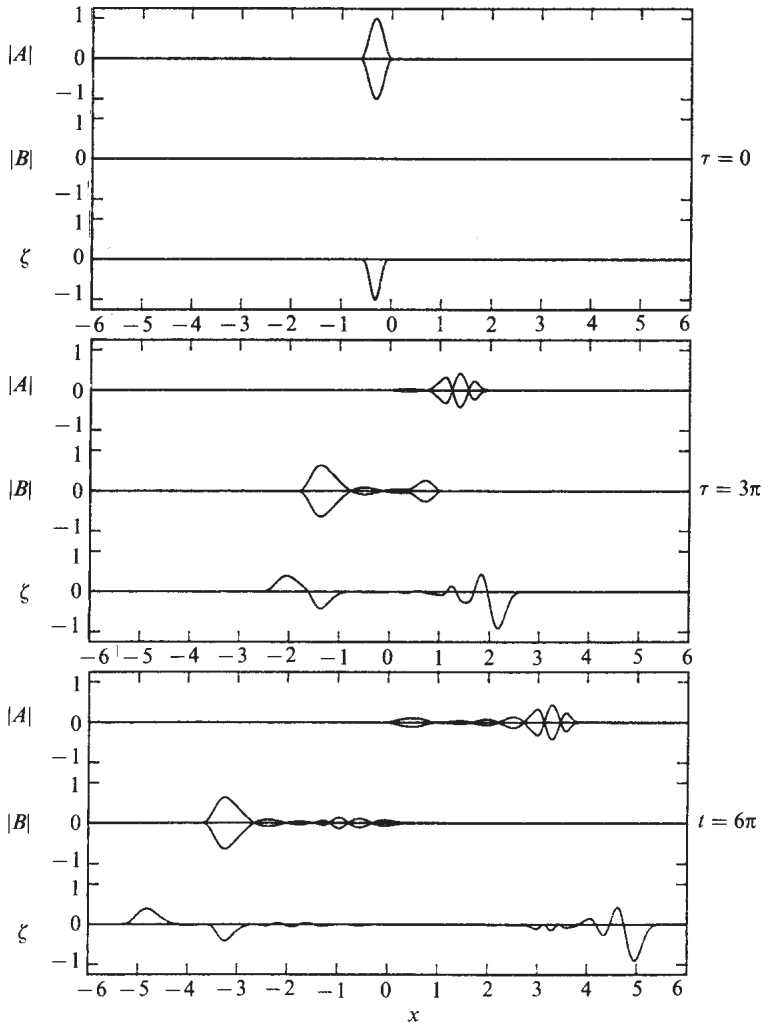

Figure 13.16: Scattering of a wave packet by a patch of periodic bars. The bars are confined within $o < x < \sigma = 5$. A: amplitude of incident short waves. B: amplitude of reflected short waves. ζ (same as ζ_{20} in the text): long-wave displacement (from Hara and Mei, 1987, *J. Fluid Mech.* Reprinted by permission of Cambridge University Press).

the bar patch, which becomes a magic wall transforming the pitch of a tune. On one side the violin is played; on the other side the cello is heard.

13.9 Remarks on Third-Order Effects of Short Waves Over Slowing Varying Depth

For coastal interest the evolution of short waves (swell) on variable depth is of obvious importance. To avoid analytical difficulties in the general case, existing theories on the effect of cubic nonlinearity are all limited to slowly varying one-dimensional topography [$h = h(x)$]. As suggested by Eq. (13.2.39) where x_2 and t_2 appear, bottom variation becomes as important as nonlinearity if its horizontal length scale is no greater than $O(\varepsilon^{-2})$ times the swell length, that is, $h = h(x_2)$. This class of bottom has been studied by Djordjevic and Redekopp (1978) who extended the work of Ono (1974) for slowly modulated periodic waves on very shallow water (describable by the KdV equation).

Djordjevic and Redekopp (1978) used the perturbation method described in Section 13.2 with the new boundary condition on the bottom:

$$\frac{\partial \Phi}{\partial z} = \varepsilon^2 \frac{dh}{dx_2} \frac{\partial \Phi}{\partial x} \,. \tag{13.9.1}$$

Instead of Eq. (13.2.42) they introduced

$$\xi = \frac{1}{\varepsilon} \int^X \frac{dX}{C_g(X)} - \varepsilon t \,, \quad X = \varepsilon^2 x \tag{13.9.2}$$

[cf. Eq. (12.8.3), Section 12.8], and obtained for the envelope

$$-i\mu A - iA_x + \alpha' A_{\xi\xi} + \beta' |A|^2 A + \gamma' A = 0 \,, \tag{13.9.3}$$

which is similar to Eq. (13.2.43a), where

$$\alpha' = \frac{\alpha}{C_g^3} \,, \quad \beta' = \frac{\beta}{C_g} \,, \quad \gamma' = \frac{\gamma}{C_g} \,, \quad \gamma = \gamma(X) \tag{13.9.4}$$

with α, β, and γ given by Eqs. (13.2.43b)–(13.2.43d), γ being a function of X through the integration constant $S(X)$ in Eq. (13.2.43d). The first term in Eq. (13.9.3) is new and depends on the local slope

$$\mu = \frac{dq}{dX} \frac{(1 - \mathrm{th}^2 q)(1 - q\,\mathrm{th}\, q)}{\mathrm{th}\, q + q(1 - \mathrm{th}^2 q)} \,, \quad q = kh \,. \tag{13.9.5}$$

Since $X = O(\varepsilon)$ for $\xi = O(1)$ according to definition (13.9.2), Eq. (13.9.3) is a suitable basis for a numerical solution of the initial-value problem for a given $A(\xi, X = 0)$. Introducing further approximations to Eq. (13.9.3), Djordjevic and Redekopp examined analytically the evolution of a soliton for both $\alpha'\beta' < 0$ and > 0. In the former case, it was necessary to limit the bottom slope still further to $O(\delta^{3/2}\varepsilon^2)$ so that the new coordinates

$$\tilde{X} = \delta^{3/2} X\,, \quad \tilde{\xi} = \delta^{-1} \int^{\tilde{X}} \frac{d\tilde{X}}{C(\tilde{X})} - \delta^{1/2}\xi$$

could be introduced. A perturbation analysis was then pursued. For very shallow water $kh \ll 1$, a KdV equation with variable coefficients similar to Eq. (12.8.5) was obtained. Following the heuristic argument of Section 12.8, they studied the evolution of an envelope-hole soliton climbing a shelf. If the depths on two sides of the sloping regions were h_0 and h_1 with $h_0 > h_1$ fission into n envelope-hole solitons was found to occur when

$$\frac{h_1}{h_0} > \left[\frac{n(n+1)}{2}\right]^{-8/27}, \quad h = 1, 2, 3\,.$$

For the case $\alpha'\beta' > 0$ everywhere, Djordjevic and Redekopp applied the method of Section 12.8 to Eq. (13.9.3) directly. One of their conclusions was that fission of convex solitons was possible only if the propagation was from shallower to deeper water. Numerical and experimental confirmations of these results are desirable.

The additional effects of a nonuniform current in the x direction has been studied by Turpin, Benmoussa and Mei (1983).

We now leave the topic of unidirectional propagation and one-dimensional bathymetry and discuss some two-dimensional examples of nonlinear waves encountering solid bodies. In the first two the body is slender, while in the third, the body is blunt.

13.10 Diffraction of Steady Stokes' Waves by a Thin Wedge or a Slightly Slanted Breakwater

For solitary waves incident obliquely on a straight wall in shallow water, experiments have been performed by Perroud (1957) and Chen (1961) and reported by Wiegel (l964). For an angle of incidence $\theta_i > 45°$, the incident and reflected wave crests intersected at the wall with equal angles, that is, *specular reflection*. However, when the incidence angle was reduced

($20° < \theta_i < 45°$), there was a third wave crest (called the *stem*) which intersected the wall normally; the incident crest, the reflected crest, and the stem met at a point some distance away from the wall. For incidence angles less than 20°, the reflected crest disappeared, leaving only the incident crest and the stem. Because of its geometrical resemblance to the reflection of shock waves in gas dynamics (see Lighthill, 1949; Whitham, 1974), the phenomenon in shallow-water waves has also been called the *Mach stem effect* by Wiegel.

Similar experiments of oblique incidence of periodic waves in finite water depth have been performed by Nielsen (1962) and by Berger and Kohlhase (1976). The kinematics of the wave crests resembled that of the solitary waves. The wave amplitude along the barrier, that is, the stem height, increased downwave for a finite distance and then leveled off gradually. At any station this amplitude increased with the angle of incidence. The width of the stem region, which generally increased with distance along the wall, was larger with smaller incidence angle and water depth. The stem width appeared to be greater for longer incident waves. Data scatter was substantial in all these experiments.

For shallow waters a theory for the Mach stems and Mach reflection of solitary waves has been proposed by Miles (1977), whose deductions have been compared with experiments by Melville (1980). Noting that the evolution equation of the present chapter is the nonlinear extension of the parabolic approximation of Section 4.10, Yue and Mei (1980) carried out a nonlinear study of grazing incidence on a thin wedge; their main findings are summarized in this section.

Recall from Section 4.10 that the parabolic approximation applies when

$$\frac{L_y}{L_x} = \varepsilon \ll 1 \quad \text{and} \quad kL_x \gg 1\,, \tag{13.10.1}$$

where L_x and L_y denote the characteristic lengths of modulation along x and y, respectively. Now for Stokes' waves the wave slope kA_0 affects the phase over the length scale $O(k^3A_0^2)^{-1}$, as Eq. (13.3.4) implies. Therefore, nonlinearity must be taken into account if the body length scale is such that

$$kL_x = O(kA_0)^{-2}\,. \tag{13.10.2a}$$

The parabolic approximation implies a lateral length scale such that

$$kL_y = O(kA_0) = O(\varepsilon)\,. \tag{13.10.2b}$$

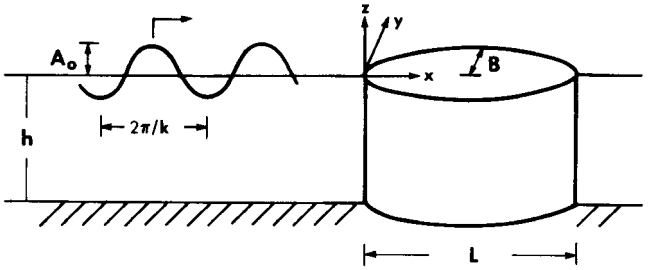

Figure 13.17: Head-sea incidence on a long and slender obstacle.

Equations (13.10.2a) and (13.10.2b) suggest that only

$$x_2 = \varepsilon^2 x \equiv X \quad \text{and} \quad y_1 = \varepsilon y \equiv Y \tag{13.10.3}$$

are the pertinent slow coordinates. If steady state is assumed, then there is no time dependence. Therefore, we can put

$$\frac{\partial}{\partial t_1} = \frac{\partial}{\partial t_2} = \frac{\partial}{\partial x_1} = 0 \tag{13.10.4}$$

into Eq. (13.2.39) and obtain again a cubic Schrödinger equation

$$2\frac{\partial A}{\partial X} - \frac{i}{k}\frac{\partial^2 A}{\partial Y^2} + iK'|A|^2 A = 0\,, \tag{13.10.5}$$

where

$$K' = k^3\Theta \equiv k^3 \frac{C}{C_g}\frac{\operatorname{ch} 4q + 8 - 2\operatorname{th}^2 q}{8\operatorname{sh}^4 q} \tag{13.10.6}$$

is always positive. ϕ_{10} is taken to be zero.

Assume that the body is bounded by vertical walls which are symmetric about the x axis (see Fig. 13.17) and is described by

$$y = \pm y_B(x) \quad \text{or } Y = \pm\varepsilon y_B \tag{13.10.7}$$

in normalized coordinates. Vanishing of the normal velocity on the body requires that

$$\Phi_y = \Phi_x \frac{dy_B}{dx} \quad \text{on} \quad y = y_B$$

or

$$\varepsilon\Phi_Y = \left[\left(\frac{\partial}{\partial x} + \varepsilon^2\frac{\partial}{\partial X}\right)\Phi\right]\frac{dy_B}{dx} \quad \text{on} \quad Y = \varepsilon y_B\,. \tag{13.10.8}$$

A similar condition holds on $y = -y_B$. Substituting the first-order potential (13.2.21) (without ϕ_{10}) into Eq. (13.10.8), we find, to the leading order,

$$\frac{\partial A}{\partial Y} = ikA\frac{1}{\varepsilon}\frac{dy_B}{dx} \quad \text{on} \quad Y = \varepsilon y_B\,. \tag{13.10.9}$$

With considerable generality one may assume $dy_B/dx = O(\varepsilon)$ so that

$$kB = O(\varepsilon^{-1})\,. \tag{13.10.10}$$

For a wedge, $y_B = \varepsilon x$, Eq. (13.10.9) becomes simply

$$\frac{\partial A}{\partial Y} = ikA \quad \text{on} \quad Y = X\,. \tag{13.10.11}$$

The remaining boundary conditions are

$$A \to A_0 e^{-iK'A_0^2X/2}\,, \quad Y \to +\infty \tag{13.10.12}$$

and

$$A = A_0\,, \quad X = 0\,. \tag{13.10.13}$$

The reduced problem for A is of the initial-boundary-value type and can be solved numerically. In terms of the normalized variables

$$\overline{A} = \frac{A}{A_0}\,, \quad \overline{X} = kX = \varepsilon^2 kx\,, \quad \overline{Y} = kY = \varepsilon ky\,, \tag{13.10.14}$$

Eq. (13.10.5) becomes

$$2i\frac{\partial \overline{A}}{\partial \overline{X}} + \frac{\partial^2 \overline{A}}{\partial \overline{Y}^2} - K|\overline{A}|^2\overline{A} = 0\,. \tag{13.10.15}$$

The only parameter is

$$K = \left(\frac{kA_0}{\varepsilon}\right)^2 \Theta(kh)\,, \tag{13.10.16}$$

where Θ is defined in Eq. (13.10.6) and plotted in Fig. 13.18. For fixed kh, K is a measure of nonlinearity versus the wedge angle ε.

Figure 13.19 shows the square of the envelope height (proportional to the mean setup) along the wall. The linear result ($K = 0$) oscillates in X and gradually attenuates toward 4. With increasing nonlinearity ($K = 4$), the envelope height decreases and rapidly approaches a constant. Three-dimensional views of the free surface are given in Fig. 13.20 showing that for nonlinear waves, stems are evident within a wedge next to the wall;

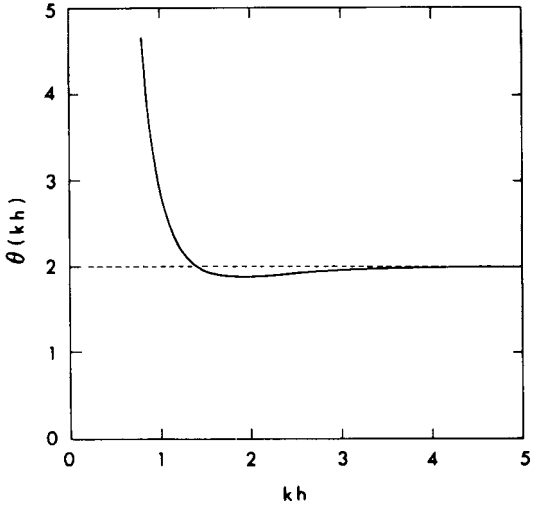

Figure 13.18: The function $\Theta(kh)$ defined by Eq. (13.10.6).

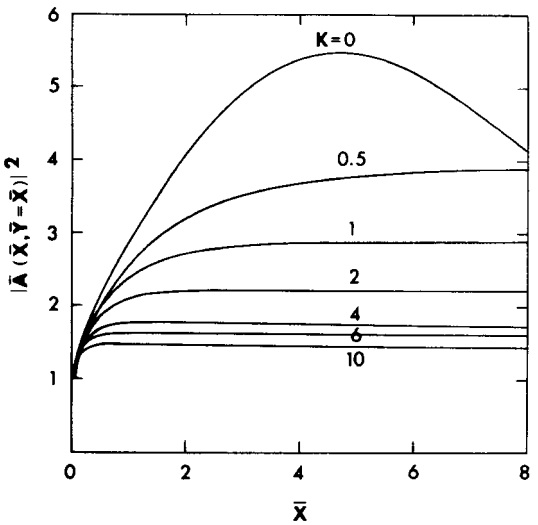

Figure 13.19: Squared-amplitude along the wall of a wedge for different values of nonlinearity K (from Yue and Mei, 1980, *J. Fluid Mech.* Reproduced by permission of Cambridge University Press).

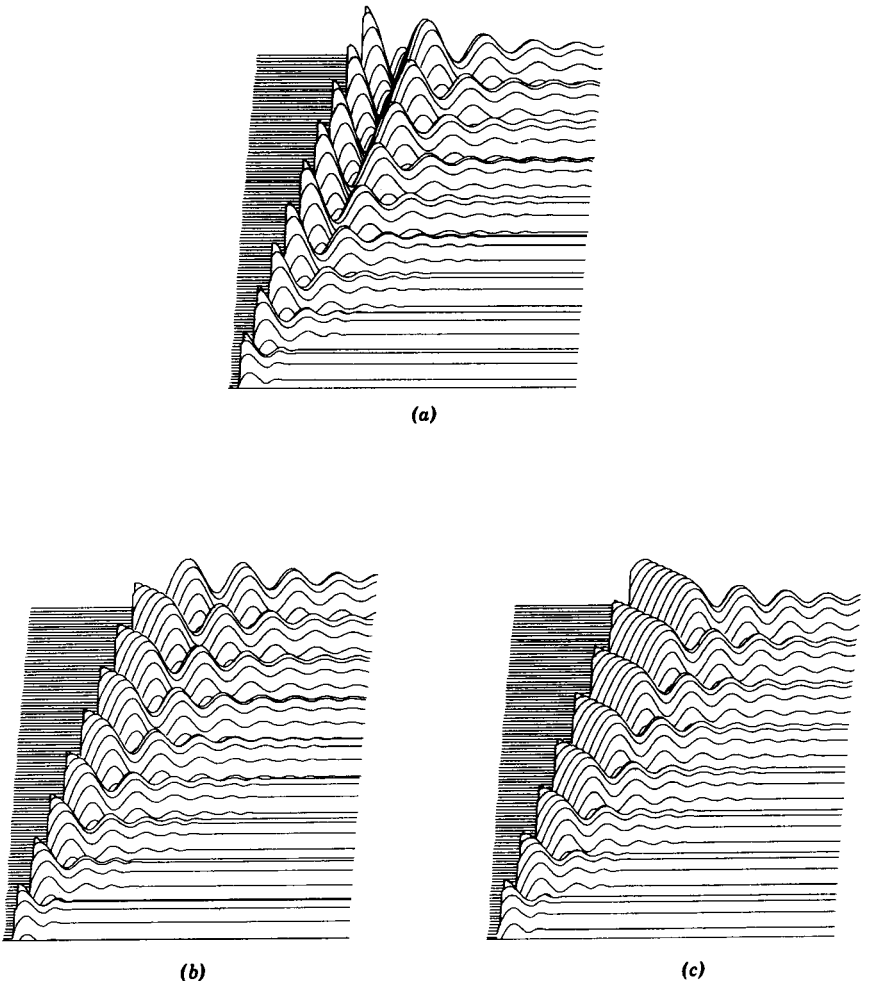

Figure 13.20: Snapshot of free surface near a wedge of half angle $\alpha = 17.55°$ ($\varepsilon^2 = 0.1$) shown in undistorted horizontal coordinates. (a) $K = 0$ (linear); (b) $K = 1$; (c) $K = 2$. Note the forward bending of crests near the wedge (shaded) for $K = 1, 2$ (from Yue and Mei, 1980, *J. Fluid Mech.* Reproduced by permission of Cambridge University Press).

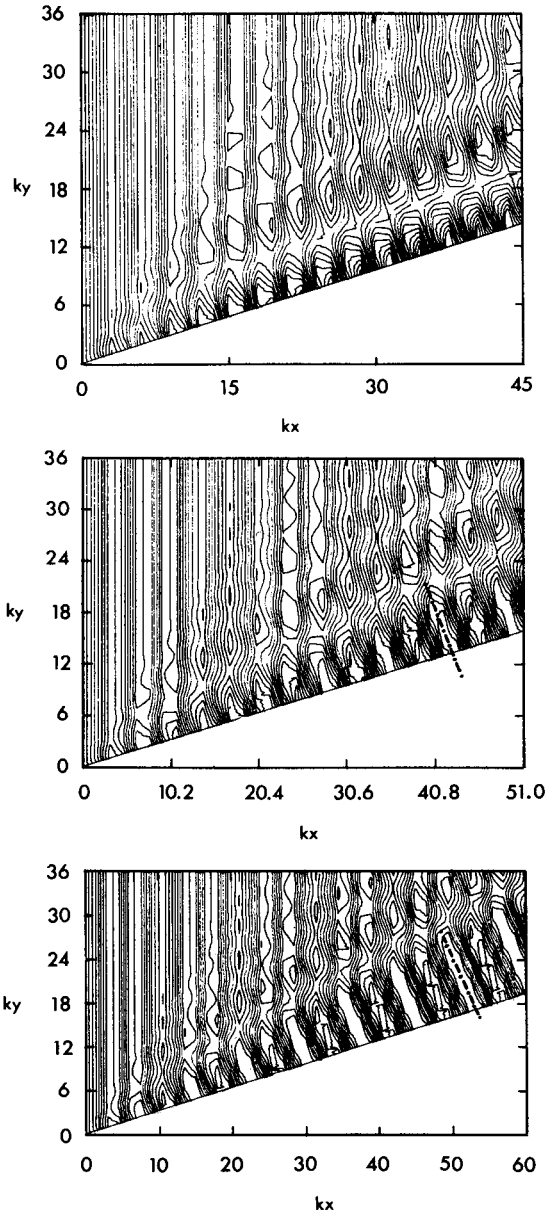

Figure 13.21: Snapshot of free-surface contours for the same three cases of Fig. 13.20. The slope of the dash–dot line is drawn according to Eq. (13.10.17) (from Yue and Mei, 1980, *J. Fluid Mech.* Reproduced by permission of Cambridge University Press).

the wedge angle increases with nonlinearity K. Finally, in Fig. 13.21 the contour plots of the free-surface displacement show distinctly the sudden bending of wave crests within the plateau.

Outside the plateau, A^2 undulates in a way expected of diffraction. By ignoring these undulations, Yue and Mei found that a discontinuous shock approximation gave a crude estimate of the envelope height of the plateau region $E_- = A_-^2$ and of the apex angle β of the plateau. The results are

$$E_- = \frac{1}{2K}[2K + 1 + (8K + 1)^{1/2}], \tag{13.10.17}$$

and

$$\beta = \frac{3 + (8K + 1)^{1/2}}{4}, \tag{13.10.18}$$

which compare well with the numerical results. The corresponding theoretical prediction on the bending angle of the stems is given by

$$\tan\delta \cong \varepsilon^3 \left[\frac{K}{2} + \frac{3 + (8K + 1)^{1/2}}{4}\right]. \tag{13.10.19}$$

The smallness of δ implies that the stems are nearly perpendicular to the wall, Fig. 13.21. Despite its closeness to the numerical theory, the shock approximation is a poor representation of the diffraction phenomenon outside the wedge, and hence is not elaborated here.

The present example combines the parabolic approximation and the cubic nonlinearity. Similar numerical analysis can be readily made for the nonlinear diffraction near the shadow boundary of a thin breakwater or for other problems where the direction of the incident wave is not changed significantly by diffraction (see Yue, 1980). Extension of the nonlinear parabolic approximation to include refraction by slowly varying depth has been reviewed by Liu (1989).

13.11 Soliton Envelopes in the Wake of a Ship

One of the puzzles revealed by satellite images of the ocean surface is the very long and narrow wake extending many kilometers (Fu and Holt, 1982). This wake is in sharp contrast to the Kelvin ship wake which is a wedge of half angle of $\theta = 19.8^\circ$ ($\tan\theta = 1/\sqrt{8}$) enclosing divergent and transverse waves (Lamb, 1932; Wehausen and Laitone, 1960).

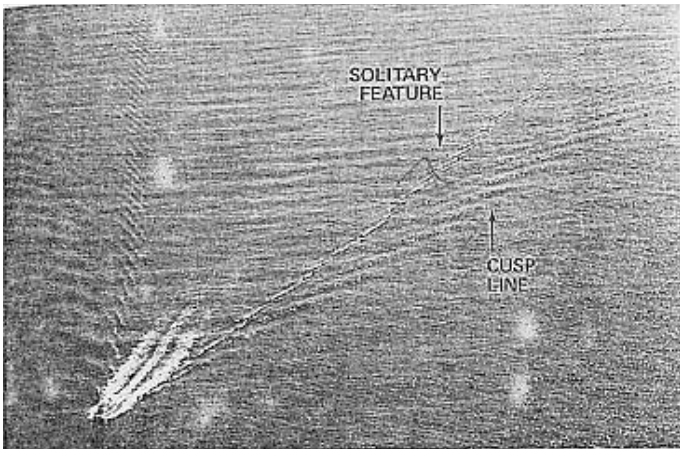

Figure 13.22: Aerial photograph of the wake of the Coast Guard cutter *Point Brower* traveling at 7.7 m/s. The solitary feature is visible inside the 19.5° Kelvin cusp line. The experimentally determined wake's half-angle of the feature is 10.9°. The lengths of the starboard and port rays in the photo are about 1.1 and 0.7 km, respectively. The width of each feature is increasing for the first 0.5 km while the change in the width is reduced thereafter (from Brown et al., 1987, *J. Fluid Mech.* Reprinted by permission of Cambridge University Press).

Various hypotheses have been offered so far to explain the narrow V-wakes; numerous physical factors such as bubbles and vortices generated by ship propellers are thought to be important. Motivated by these satellite images, Brown et al. (1987) measured at several fixed stations free-surface displacements due to a passing ship in a wavy sea. One of the distinctive features observed by them is the appearance of a pair of steady wave envelopes, one on each side of the ship's path. Beginning from the bow, the envelope is a straight line inclined at 11° from the ship path. Each envelope is close in shape to a steady two-dimensional soliton, see Fig. 13.22.

It is not clear that the observations by Brown et al. are central to the V-wake i the satellite images. Nevertheless, soliton envelopes in the wake of a ship are interesting by themselves and have prompted a theory by Mei and Naciri (1991) summarized below. By Doppler's effect, an incident wave of frequency ω_0 propagating parallel to the ship's path appears to a ship-bound observer as oscillations at the encounter frequency

$$\omega = \omega_0 - V\omega_0^2/g \tag{13.11.1}$$

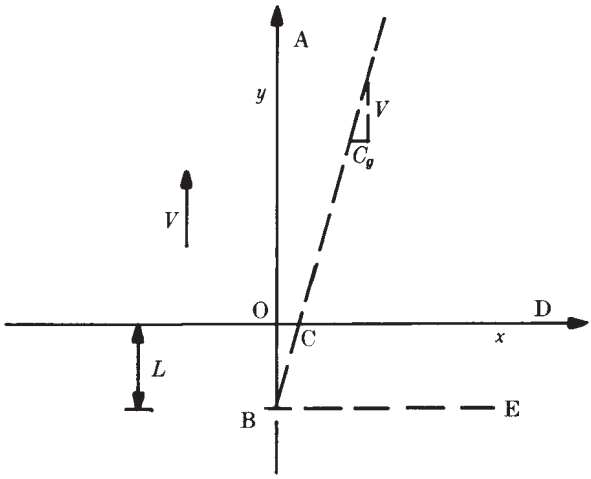

Figure 13.23: Plan view of ship-bound coordinates. Segment BO represents the centerline of the ship (from Mei and Naciri, 1991, *Proc. Roy. Soc. London*. Reprinted by permission of The Royal Society).

where V is the ship speed. According to the linearized theory, the ship must be induced to oscillate at the same encounter frequency ω. For a head sea, $V < 0$, hence $\omega > \omega_0$. For a following sea, $V > 0$ and $\omega < \omega_0$. The oscillating and advancing ship acts as a plane piston, radiating sideways relatively short, nearly plane waves away from its course, resulting in wave packets trailing in the wake.

In principle steady Kelvin waves due to the finite ship volume must coexist with the oscillating waves radiated by the ship (Stoker, 1957; Wehausen and Laitone, 1969; Newman, 1977). Since the two waves appear quite separate in the observed records, let us consider only a ship of negligible volume, and focus attention to the evolution of the radiated waves in the far wake. Specifically, we choose a ship-bound coordinate system with the y axis coinciding with the ship axis and the positive x axis pointing to the port side of the ship. A uniform ambient current V along the y axis is then present, see Fig. 13.23. To a far-wake observer, the amplitude of the radiated waves near the ship can be considered as given along the centerline of the ship from separate calculations based on existing linearized theories in ship hydrodynamics (e.g., Sclavounos and Nakos, 1990).

We assume the ship length L to be long compared to the length of the waves induced by ship oscillation ($2\pi/k = 2\pi g/\omega^2$), so that

$$kL = O(\epsilon^{-1}), \quad \epsilon = k\bar{A}, \tag{13.11.2}$$

where $\bar{A}$ is the characteristic amplitude of the radiated waves. Since

$$kL = \frac{\omega^2 L}{g} = \frac{\omega_0^2 L}{g}\left(1 + \frac{V\omega_0}{g}\right)^2, \tag{13.11.3}$$

this assumption is reasonable as long as ω_0 is sufficiently high. Let us define the near wake to be kx, $ky = O(\epsilon^{-1})$ and the far wake to be kx, $ky = O(\epsilon^{-2})$. Let the multiple-scale coordinates be introduced $t, t_1 = \epsilon t$, $t_2 = \epsilon^2 t$; $x, x_1 = \epsilon x$, $x_2 = \epsilon^2 x$; $y, y_1 = \epsilon y$, $y_2 = \epsilon^2 y$. To the leading order the ship appears as a line segment ($x_1 = 0$, $0 < y_1 < \ell = \epsilon L$). In either a head sea or a following sea, only heave and pitch motions are dominant; mirror symmetry with respect to the y allows one to treat only the side of $x > 0$. An observer in the far-wake sees the free-surface displacement near the ship as

$$\zeta = \frac{\epsilon A}{2} e^{ikx - i\omega t} + *, \quad \text{as } kx_1 \to 0. \tag{13.11.4}$$

Let us assume that the form of A near the ship is already calculated from a linearized theory. Along the ship's path, the boundary conditions for the wave envelope are

$$A = A_0(y_1, t_1), \quad x_1 = x_2 = 0, \quad -\ell < y_1 < 0, \tag{13.11.5}$$

where A_0 is known, and

$$\frac{\partial A}{\partial x_1} = 0, \quad x_1 = x_2 = 0, \quad y_1 > 0 \tag{13.11.6}$$

by symmetry.

If the ship speed is zero, the envelope equation for A is given by (13.2.59) with $\mathcal{U} = 0$,

$$\frac{\partial A}{\partial t_1} + C_g \frac{\partial A}{\partial x_1} + i\epsilon\left[\frac{\omega}{8k^2}\left(\frac{\partial^2 A}{\partial x_1^2} - 2\frac{\partial^2 A}{\partial y_1^2}\right) + \frac{\omega k^2}{2}|A|^2 A\right] = 0 \quad x_1 > 0. \tag{13.11.7}$$

With a steady current V along the y axis, (13.11.7) must be modified by Galilean transformation so that

$$\frac{\partial A}{\partial t_1} + C_g \frac{\partial A}{\partial x_1} + V\frac{\partial A}{\partial y_1} + i\epsilon\left[\frac{\omega}{8k^2}\left(\frac{\partial^2 A}{\partial x_1^2} - 2\frac{\partial^2 A}{\partial y_1^2}\right) + \frac{\omega k^2}{2}|A|^2 A\right] = 0. \tag{13.11.8}$$

This equations holds in both near and far wakes $O \leq (kx_1, ky_1) \leq O(1/\epsilon)$. In addition to the boundary conditions (13.11.5) and (13.11.6) we impose also

$$A(x_1, -\ell, \epsilon t_1) = 0 \quad x_1 > 0 \tag{13.11.9}$$

and

$$A(\infty, y_1, \epsilon t_1) = 0 \quad y_1 > 0\,. \tag{13.11.10}$$

Using the following dimensionless variables,

$$\begin{aligned} a = kA \quad \xi = kx_1 - \frac{C_g}{V} ky_1\,, \\ \eta = \epsilon \frac{C_g}{V} ky_1\,, \quad \tau = \epsilon k(y_1 - Vt_1) \end{aligned} \tag{13.11.11}$$

then

$$\begin{aligned} \frac{\partial}{\partial t_1} = -\epsilon kV \frac{\partial}{\partial \tau}\,, \quad \frac{\partial}{\partial x_1} = k \frac{\partial}{\partial \xi}\,, \\ \frac{\partial}{\partial y_1} = k \frac{C_g}{V} \left(-\frac{\partial}{\partial \xi} + \epsilon \frac{\partial}{\partial \eta} \right) + \epsilon \frac{\partial}{\partial \tau}\,. \end{aligned} \tag{13.11.12}$$

Omitting terms of order $O(\epsilon)$, we get from (13.11.8) for $a(\xi, \eta, \tau)$

$$-ia_\eta + \frac{1}{4} \left[1 - 2 \left(\frac{C_g}{V} \right)^2 \right] a_{\xi\xi} + |a|^2 a = 0\,. \tag{13.11.13}$$

Note that the variable τ does not appear explicitly. In the new coordinate system η is time-like and ξ is space-like. From here on we further assume A_0 to be independent of t_1 so that $\partial A/\partial t_1 = 0$.

Referring to Fig. 13.23 the boundary data on the segment $BO : (x_1 = 0, -\ell < y_1 < 0)$, where $\ell = \epsilon(C_g/V)kL$ is the normalized length of the ship, can be transferred to the segment OC on the stern line as follows. Since both lines are in the near-wake region, the leading-order part of (13.11.8) suffices, i.e.,

$$C_g \frac{\partial A}{\partial x_1} + V \frac{\partial A}{\partial y_1} = 0\,.$$

The simple hyperbolic equation can be solved to give

$$A = A \left(kx_1 - \frac{C_g}{V} ky_1 \right) + O(\epsilon)\,.$$

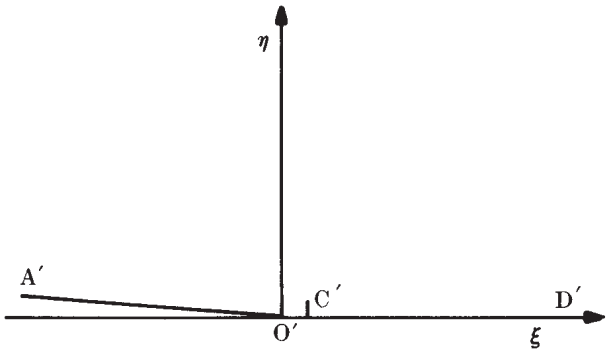

Figure 13.24: The transformed plane.

To satisfy the boundary condition (13.11.5) (without t_1), we require

$$A\left(-ky_1\frac{C_g}{V}\right) = A_0\left(\frac{y_1}{\ell}\right), \quad x_1 = 0\,. \tag{13.11.14}$$

In the ξ, η plane (see Fig. 13.24), the corresponding condition is

$$a = a_0\left(-\frac{\xi}{\xi_0}\right)e^{i\beta V\xi/C_g} \quad 0 < \xi < \xi_0\,, \quad \eta = 0 \tag{13.11.15}$$

with

$$a_0 = kA_0\,, \quad \xi_0 = \frac{C_g}{V}k\ell\,. \tag{13.11.16}$$

Equation (13.11.15) is now an initial condition on the segment $O'C'$ along the ξ axis in Fig. 13.24. The condition (13.11.9) on BE in Fig. 13.23 becomes an initial data and can be transfered to CD and then to $C'D'$ on the ξ axis (initial line) of Fig. 13.24, i.e.,

$$a(\xi, 0) = 0 \quad \xi > \xi_0\,. \tag{13.11.17}$$

From (13.11.11) and (13.11.12) the boundary condition (13.11.6) is transformed to

$$\frac{\partial a}{\partial \xi} = 0 \quad \text{on} \quad \epsilon\xi + \eta = 0 \tag{13.11.18}$$

in the (ξ, η) plane which implies, to leading order,

$$a = 0 \quad \eta = 0\,, \quad -\infty < \xi < 0\,. \tag{13.11.19}$$

Thus the original boundary-value problem for A in the first quadrant of the (x_1, y_1) plane becomes the standard initial-value problem governed by (13.11.13) in the upper half (ξ, η) plane, subject to the initial constraints (13.11.15), (13.11.17), and (13.11.19) along the entire line $\eta = 0$.

The theoretical results summarized in Sections 13.5 and 13.6 may now be applied. Firstly, a is linearly unstable in η if

$$\frac{C_g}{V} < \frac{1}{\sqrt{2}}\,, \tag{13.11.20}$$

i.e., if the speed or the frequency is high enough. Equation (13.11.13) can be futher tranformed into canonical form by the following change of variable

$$\sigma = \left(\xi - \frac{\xi_0}{2}\right) \Bigg/ \sqrt{1 - 2\left(\frac{C_g}{V}\right)^2}\,.$$

The initial-value problem now becomes

$$-ia_\eta + \frac{1}{4}a_{\sigma\sigma} + |a|^2 a = 0 \quad |\sigma| < \infty,\ \eta > 0 \tag{13.11.21}$$

$$a(\sigma, 0) = \begin{cases} 0\,, & |\sigma| > \dfrac{\sigma_0}{2}\,, \\ a_0\left(-\dfrac{\sigma}{\sigma_0}\right) e^{i\lambda\sigma}\,, & |\sigma| < \dfrac{\sigma_0}{2}\,, \end{cases} \tag{13.11.22}$$

where

$$\sigma_0 = \frac{\xi_0}{\sqrt{1 - 2(\frac{C_g}{V})^2}} = \frac{\frac{C_g}{V} k^2 L \bar{A}}{\sqrt{1 - 2(\frac{C_g}{V})^2}}\,. \tag{13.11.23}$$

For a ship heaving while advancing in waves,

$$a(\sigma, 0) = \operatorname{sech}(\sigma/\sigma_0) \tag{13.11.24}$$

is qualitatively representative of the initial data. The controlling parameter here is σ_0, which increases with the chracteristic wave steepness $\epsilon = k\bar{A}$, the ship length L, and also with the ratio C_g/V which is smaller for short radiated waves or higher V.

Let us recall from Section 13.6 some known analytical properties of the time-dependent soliton theory and discuss their implications. Under the condition (13.11.20) the simplest solution to (13.11.21) is a soliton envelope

$$a = \operatorname{sech}\sqrt{2}(\sigma - W\eta) \tag{13.11.25}$$

where W is arbitrary. The area under the envelope is $\pi/\sqrt{2} \approx 2.22$. With the initial data given by (13.11.24), $a(\xi, \eta)$ will flatten for large η if the area under the initial profile is less than the soliton area, i.e., $\sigma_0 < 1\sqrt{2}$, otherwise a will evolve into N bound solitons with N being the integer part of the area ratio $\sqrt{2}\sigma_0$.

From the definition of σ, the axis of the bound soliton(s) is $\sigma = 0$ which is the line $y = Vx/C_g$ in the physical plane; it is inclined with respect to the y axis at the angle

$$\theta = \tan^{-1}\frac{C_g}{V}\,. \tag{13.11.26}$$

Since the apex angle of the Kelvin wake is $\tan\theta = 1/\sqrt{8}$ (Stoker, 1953; Wehausen and Laitone, 1960), the soliton axis lies within the Kelvin wake if

$$\frac{C_g}{V} < \frac{1}{\sqrt{8}}\,. \tag{13.11.27}$$

If the ship speed V increases in a head sea, the encounter frequency (the frequency of ship oscillations) and k increase while C_g decreases; hence the angle θ decreases. In a following sea the encounter frequency is less than the incident sea-wave frequency ω_0. The group velocity C_g of the radiated waves can be rather large. For low enough ship speed such that

$$\frac{1}{\sqrt{8}} < \frac{C_g}{V} < \frac{1}{\sqrt{2}} \quad \text{or} \quad 19.5^\circ < \theta < 35.23^\circ \tag{13.11.28}$$

the envelope solitons are then outside the Kelvin wake.

By using an Adams-Bashforth method, Mei and Naciri have performed numerical calculations for the initial envelope

$$a(\xi, 0) = \frac{1}{2}\tanh\frac{1}{p}\left(\frac{\sigma}{\sigma_0} + \frac{1}{2}\right) - \frac{1}{2}\tanh\frac{1}{p}\left(\frac{\sigma}{\sigma_0} - \frac{1}{2}\right). \tag{13.11.29}$$

This near-field profile, symmetric about $\sigma = 0$, has unit height and an area equal to σ_0. The parameter p characterizes the taper with a small p corresponding to a nearly rectangular envelope. Figs. 13.25(a), (b) and (c) show the envelope evolution for $\sigma_0 = 1.6, 3$ and 5, and for $p = 0.3$. For smaller σ_0, the envelope flattens out with distance η behind the stern. Case (a) with $\sigma_0 = 1.6$ corresponds to an initial envelope with an area

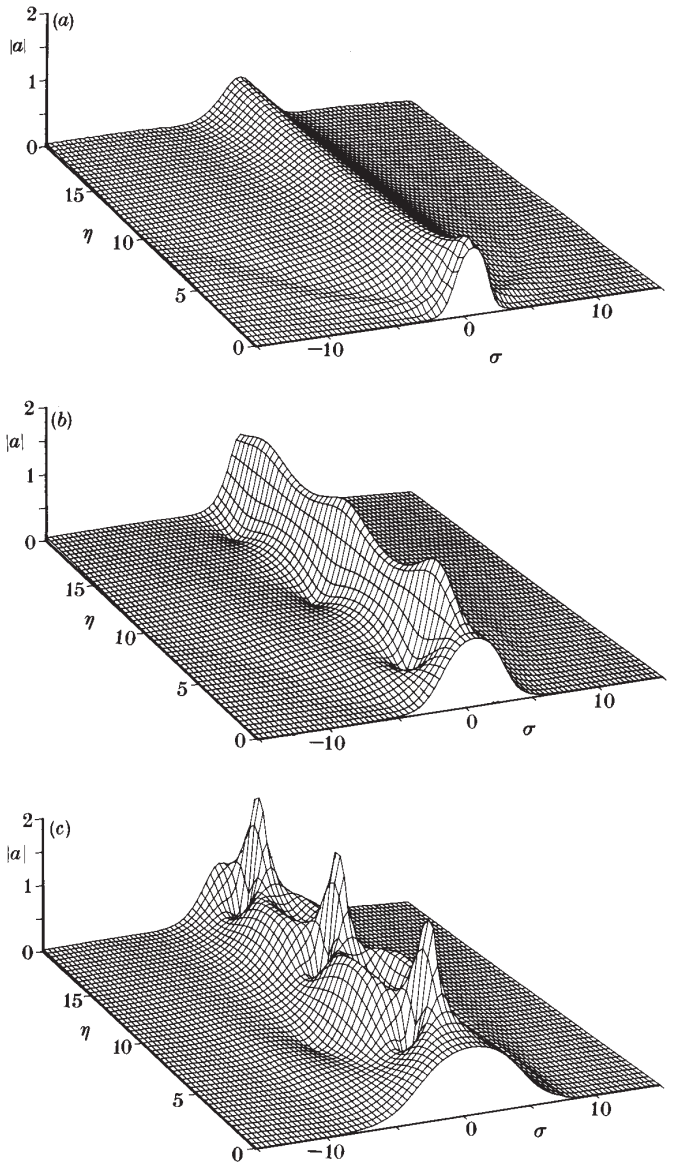

Figure 13.25: Heave-induced wake envelope in the distorted plane of (σ, η) for different σ_0. (a): $\sigma_0 = 1.6$, (b): $\sigma_0 = 3$, and (c): $\sigma_0 = 5$ (from Mei and Naciri, 1991, *Proc. Roy. Soc. London.* Reprinted by permission of The Royal Society).

less than that of a soliton. The envelope first flattens in η, then gradually sharpens, and approaches a bound soliton. For $\sigma_0 = 3$, Case (b), the initial area is nearly twice that of a soliton. Two bound solitons are present, as is evidenced by one modulational period along η. The largest envelope ($\sigma_0 = 5$) is less than 3 times as large as the soliton, yet three bound solitons are apparent.

On the other hand, if $a(\sigma, 0)$ is real and odd in σ, then two solitons may emerge with axes inclined in opposite directions away from the η axis. This case corresponds qualitatively to an advancing ship perfoming pitch oscillations about the midship line. Detailed discussion of this case can be found in Mei ad Naciri (1991).

Based on the time series recorded by Brown et al. for 24 runs at a fixed measuring station, and for the same ship speed of 7.7 m/sec, the averaged carrier frequency at the distance 0.5 km aft is about $\omega = 3.28$ rad/sec. With these values, the inclination of the soliton axis can be calculated from (13.11.26) to be $\theta = 10.96°$, which is close to the reported value of 11°. Periodic depressions in the envelope are also observed.

Since the data of the sea state and on-board records of ship motion have not been reported by Brown et al., detailed checks of the present theory cannot be made. For further discussions on the order-of-magnitude relevance, the reader is refered to Mei and Naciri. A more complete theory for ships in waves must of course include the effects of the finite ship volume, and possible interactions between Kelvin wake and the soliton envelopes.

13.12 Second-Order Diffraction by a Vertical Cylinder

Second-order forces on a large body due to waves of finite amplitude are of vital interest in offshore engineering. Due to quadratic interactions of two first-order incident waves of nearly equal frequencies, second-order drift force oscillating at the difference frequency may induce significant slow oscillations inside a harbor or around a floating platform for oil-drilling. These drift forces can cause severe strains in the mooring or anchoring systems, and must be accoiunted for in the design of the dynamic-positioning system. Forcing at the sum frequency can also lead to undesirable ringing around an offshore structure.

Even for a vertical circular cylinder, the second-order diffraction problem has challenged many authors (Charkrabarti, 1972; Yamaguchi and Tsuchiya, 1974; Raman and Venkatanarasalah, 1976; Issacson, 1977; Charkrabarti, 1978; Molin, 1979; Miloh, 1980; Wehausen, 1980; Hunt and Baddour, 1981). It was not until (1989) that the numerical method of boundary integral equations was applied successfully by Kim and Yue (1989) for a body axially symmetric with respect to the vertical axis. Later the special case of a vertical circular cylinder was solved analytically by Chau and Eatok Taylor (1992), by means of eigenfunction expansions and three-dimensional Green's functions.

In real seas, the varying bathymetry around a scatterer requires the treatment of both refraction and diffraction. By extending the mild-slope approximation to the second order in wave steepness, Chen (2005) has developed a theory for both monochromatic and random incident waves of broad bandwidth and for quite general boundaries and bathymetry. In this section we shall demonstrate her method by deriving the analytical solution for the special case of a circular cylinder standing vertically in a sea of constant depth.

13.12.1 First-Order Solution

After the usual Taylor expansion about $z = 0$, and the introduction of pertubation series in powers of $\epsilon = kA$, we get the perturbation equations for the first- and second-order problems. Let

$$\Phi_1 = -\frac{ig\eta}{\omega}\frac{\cosh k(z+h)}{\cosh kh}e^{-i\omega t} + *\,, \quad \zeta_1 = \eta e^{-i\omega t} + * \tag{13.12.1}$$

be the first-order potential and free surface displacement respectively. We recall the familiar result

$$\eta = \eta^I + \eta^S$$

where

$$\eta^I = \frac{A}{2}e^{ikr\cos\theta} = \frac{A}{2}\sum_{n=0}^{\infty}\epsilon_n i^n J_n(kr)\cos\theta\,, \tag{13.12.2}$$

$$\eta^S = -\frac{A}{2}\sum_{n=0}^{\infty}\epsilon_n i^n \frac{J_n'(ka)}{H_n'(ka)}H_n(kr)\cos n\theta \tag{13.12.3}$$

are the incident and the scattered waves respectively.

13.12.2 The Second-Order Problem

At the second order, $O(\epsilon^2)$, the velocity potential Φ_2 satisfies

$$\nabla^2\Phi_2 + \frac{\partial^2\Phi_2}{\partial z^2} = 0\,, \quad -h < z < 0\,, \tag{13.12.4}$$

in water, where ∇ denotes the horizontal gradient operator,

$$\frac{\partial\Phi_2}{\partial z} = 0\,, \quad z = -h\,, \tag{13.12.5}$$

on the seabed,

$$\frac{\partial\Phi_2}{\partial r} = 0\,, \quad r = a\,, \tag{13.12.6}$$

on the cylinder, and

$$\frac{\partial\Phi_2}{\partial z} + \frac{1}{g}\frac{\partial^2\Phi_2}{\partial t^2} = \frac{1}{g^2}\frac{\partial\Phi_1}{\partial t}\frac{\partial}{\partial z}\left[g\left(\frac{\partial\Phi_1}{\partial z}\right) + \frac{\partial^2\Phi_1}{\partial t^2}\right] - \frac{1}{g}\frac{\partial}{\partial t}(\nabla_3\Phi_1)^2\,, \quad z = 0\,, \tag{13.12.7}$$

on the mean sea surface, where ∇_3 denotes the three-dimensional gradient operator. After using the first-order potential in the inhomogeneous terms on the right, (13.12.7) can be rewritten as follows

$$\frac{\partial\Phi_2}{\partial z} + \frac{1}{g}\frac{\partial^2\Phi_2}{\partial t^2} = \frac{A^2}{4}\mathcal{F}e^{-2i\omega t} + *\,, \tag{13.12.8}$$

where the forcing function is found after some alegbra to be

$$\mathcal{F} = \widehat{\beta}\eta\eta + \bar{\beta}\nabla\eta\cdot\nabla\eta\,, \tag{13.12.9}$$

with

$$\widehat{\beta} = \frac{igk^2}{\omega} - \frac{3i\omega^3}{g}\,, \quad \bar{\beta} = -\frac{2ig}{\omega}\,. \tag{13.12.10}$$

Bernoulli's equation on the free surface gives the second-order free-surface dispacement,

$$\zeta_2 = \left[-\frac{1}{g}\frac{\partial\Phi_2}{\partial t} + \frac{1}{g^2}\frac{\partial\Phi_1}{\partial t}\frac{\partial^2\Phi_1}{\partial t\partial z} - \frac{1}{2g}(\nabla_3\Phi_1)^2\right]_{z=0}\,, \quad z = 0\,. \tag{13.12.11}$$

which can be decomposed as follows,

$$\zeta_2 = \zeta_2^{(1)} + \zeta_2^{(2)} \tag{13.12.12}$$

where

$$\begin{aligned}\zeta_2^{(1)} &= \left[\frac{1}{g^2}\frac{\partial\Phi_1}{\partial t}\frac{\partial^2\Phi_1}{\partial t\partial z} - \frac{1}{2g}(\nabla_3\Phi_1)^2\right]_{z=0}, \\ \zeta_2^{(2)} &= \left[-\frac{1}{g}\frac{\partial\Phi_2}{\partial t}\right]_{z=0}.\end{aligned} \tag{13.12.13}$$

The first part $\zeta_2^{(1)}$ can be calculated immediately from the first-order potential. The second part $\zeta_2^{(2)}$ is associated with the unknown second-order potential Φ_2, which is the main object of mathematical task. Note that the first part consists of zeroth and second harmonics,

$$\zeta_2^{(1)} = \eta_{2,0}^{(1)} + \eta_{2,2}^{(1)} e^{-2i\omega t} + *\,. \tag{13.12.14}$$

The zeroth harmonic corresponds to the mean setup/setdown

$$\eta_{2,0}^{(1)} = \frac{\omega^2}{g}|\eta|^2 - \frac{g}{\omega^2}|\nabla\eta|^2\,. \tag{13.12.15}$$

while the second-harmonic has the amplitude

$$\eta_{2,2}^{(1)} = \frac{3\omega^2}{2g}\eta^2 + \frac{g}{2\omega^2}(\nabla\eta)^2\,. \tag{13.12.16}$$

13.12.3 Second-Order Forcing

The forcing term F can be split into two parts,

$$\mathcal{F} = \mathcal{I} + \mathcal{S} \tag{13.12.17}$$

where

$$\mathcal{I} = \widehat{\beta}\eta^I\eta^I + \bar{\beta}\nabla\eta^I\cdot\nabla\eta^I\,, \tag{13.12.18}$$

represents the self-interaction of the progressive incident wave, and

$$\mathcal{S} \equiv \mathcal{S}_{IS} + \mathcal{S}_{SS} \tag{13.12.19}$$

with

$$\mathcal{S}_{IS} = 2[\widehat{\beta}\eta^I\eta^S + \bar{\beta}\nabla\eta^I\cdot\nabla\eta^S] \tag{13.12.20}$$

being the cross-interaction between incident and scattered waves, and

$$\mathcal{S}_{SS} = [\widehat{\beta}\eta^S\eta^S + \bar{\beta}\nabla\eta^S\cdot\nabla\eta^S]\,, \tag{13.12.21}$$

the self-interaction of the scattered wave.

By straightforward calculation, we obtain, explicitly

$$\begin{aligned}\mathcal{I} &= \frac{A^2}{4}(\widehat{\beta} - \bar{\beta}k^2)e^{i2kr\cos\theta} \\ &= \frac{A^2}{4}\frac{3i\omega k}{\sinh kh \cosh kh}\, e^{i2kr\cos\theta}\,. \end{aligned} \tag{13.12.22}$$

To calculate the forcing function $\mathcal{S}$, we first abreviate the first-order incident wave as

$$\eta^I = \sum_{m=-\infty}^{\infty} T_m e^{im\theta}\,, \quad \text{with} \quad T_n(r) = \frac{A}{2} i^m J_m(kr)\,, \tag{13.12.23}$$

and the first-order scattered waves as

$$\eta^{(S)} = \sum_{m=-\infty}^{\infty} \widehat{S}_m e^{im\theta}\,, \quad \text{where} \quad \widehat{S}_m(r) = \frac{A}{2} i^m \alpha_m H_m(kr) \tag{13.12.24}$$

with $\alpha_m = \alpha_{-m} = -J'_m(ka)/H'_m(ka)$. Note that both the T_m and $\widehat{S}_m$ are even with respect to m, i.e., $T_m = T_{-m}$ and $\widehat{S}_m = \widehat{S}_{-m}$.

Typical quadratic products of the first-order incident wave and the first-order scattered wave are of the form

$$\begin{aligned}\eta^{(I))}\eta^{(S)} &= \sum_{m=-\infty}^{\infty} T_m e^{im\theta} \sum_{n=-\infty}^{\infty} \widehat{S}_n e^{in\theta} \\ &= \sum_{m=-\infty}^{\infty} \sum_{n=-\infty}^{\infty} T_{m-n}\widehat{S}_n e^{im\theta}\,. \end{aligned} \tag{13.12.25}$$

Therefore, $\mathcal{S}$ can be expressed as a Fourier series

$$\mathcal{S} = \sum_{m=-\infty}^{\infty} \mathcal{S}_m e^{im\theta} = \sum_{m=0}^{\infty} \epsilon_m \mathcal{S}_m(r)\cos m\theta\,, \tag{13.12.26}$$

with

$$\begin{aligned}\mathcal{S}_m = \sum_{n=-\infty}^{\infty} \Bigg\{ &\left[\widehat{\beta} - \frac{n(m-n)}{r^2}\bar{\beta}\right] \widehat{S}_n (2T_{m-n} + \widehat{S}_{m-n}) \\ &+ \bar{\beta}\frac{\partial \widehat{S}_n}{\partial r}\left(2\frac{\partial T_{m-n}}{\partial r} + \frac{\partial \widehat{S}_{m-n}}{\partial r}\right)\Bigg\}\,. \end{aligned} \tag{13.12.27}$$

13.12.4 Second-Order Boundary-Value Problems

In view of (13.12.8), we seek the second-order potential of the following form

$$\Phi_2 = (\Xi + \Psi)e^{-2i\omega t} + *\,, \tag{13.12.28}$$

where Ξ and Ψ represent respectively the responses to $\mathcal{I}$ and $\mathcal{S}$. Specifically, (Ξ, Ψ) satisfy the following boundary-value problem

$$\nabla^2(\Xi, \Psi) + \frac{\partial^2(\Xi, \Psi)}{\partial z^2} = 0\,, \quad -h < z < 0\,, \tag{13.12.29}$$

$$\frac{\partial(\Xi, \Psi)}{\partial z} = 0\,, \quad z = -h\,, \tag{13.12.30}$$

$$\frac{\partial(\Xi, \Psi)}{\partial z} - \frac{4\omega^2}{g}(\Xi, \Psi) = (\mathcal{I}, \mathcal{S})\,, \quad z = 0\,, \tag{13.12.31}$$

$$\frac{\partial(\Xi, \Psi)}{\partial r} = 0\,, \quad r = a\,. \tag{13.12.32}$$

Due to the different asymptotic behaviours of $\mathcal{I}$ and $\mathcal{S}$, Ξ and Ψ must satisfy different boundary conditions at large r, to be specified later.

To solve the three-dimensional boundary-value problems for Ξ and Ψ, we shall apply the method in Section 3.5 to derive two-dimensional depth-averaged equations and the solutions.

13.12.5 Response to $\mathcal{I}$

The response to $\mathcal{I}$ can be sought as the sum of two parts:

$$\Xi = \Xi^I + \Xi^F \tag{13.12.33}$$

Both parts satisfy (13.12.29) and (13.12.30). In addition Ξ^I only satisfies the inhomogeneous condition (13.12.31) on $z = 0$. The solution is just the second-order correction of Stokes' wave,

$$\Xi^I = -\frac{3i\omega A^2}{16}\frac{\cosh 2k(z+h)}{\sinh^4 kh}e^{2ikr\cos\theta}\,. \tag{13.12.34}$$

The part Ξ^F satisfies the homogeneous free-surface condition but the inhomogeneous condition on the cylinder

$$\frac{\partial \Xi^F}{\partial r} = -\frac{\partial \Xi^I}{\partial r}\,, \quad r = a\,, \tag{13.12.35}$$

hence can be regarded as a free wave radiating energy to infinity.

To solve for Ξ^F we first rewrite the boundary condition by using partial wave expansion

$$e^{2ikr\cos\theta} = \sum_{m=0}^{\infty} \epsilon_m i^m J_m(2kr)\cos m\theta \tag{13.12.36}$$

and also expand

$$\cosh 2k(z+h) = \sum_{\ell=0}^{\infty} a_l \frac{\cos\kappa_l(z+h)}{\cos\kappa_l h} \tag{13.12.37}$$

where $\cos\kappa_l(z+h)$ is a vertical eigen-function corresponding to frequency 2ω. For any non-zero integer $l = 1, 2, 3, \ldots, \kappa_l$ is the l-th positve real root of

$$-4\omega^2 = g\kappa_l \tan\kappa_l h\,, \quad l = 1, 2, 3, \ldots \tag{13.12.38}$$

and $\kappa_0 = i\kappa$ is imaginary where κ is the positive real root of

$$4\omega^2 = g\kappa \tanh\kappa h\,. \tag{13.12.39}$$

We leave it as an exercise to show by orthogonality of the eigenfunctions that

$$a_l = -\frac{g}{A_l}\frac{4k\sinh^3 kh}{\cosh kh}\frac{1}{4k^2+\kappa_l^2} \tag{13.12.40}$$

where

$$A_l = \frac{gh}{2\cos^2\kappa_l h}\left(1 + \frac{\sin 2\kappa_l h}{2\kappa_l h}\right). \tag{13.12.41}$$

Condition (13.12.35) becomes

$$\frac{\partial\Xi^F}{\partial r} = \frac{3i\omega A^2}{16\sinh^4 kh}\sum_{l=0}^{\infty} a_l \frac{\cos\kappa_l(z+h)}{\cos\kappa_l h}\sum_{m=0}^{\infty}\epsilon_m i^m J'_m(2ka)\cos m\theta\,, \quad r = a\,. \tag{13.12.42}$$

We now solve for Ξ^F by assuming

$$\Xi^F = -\frac{ig}{2\omega}\sum \sigma_l(r,\theta)\frac{\cos\kappa_l(z+h)}{\cos\kappa_l h}\,. \tag{13.12.43}$$

From the Laplace equation we find

$$\nabla^2\sigma_l - \kappa_l^2\sigma_l = 0\,, \quad l = 0, 1, 2, 3, \ldots, \quad r > a\,. \tag{13.12.44}$$

The solution is a Bessel-Fourier series,

$$\sigma_l = \sum_{m=0}^{\infty} \epsilon_m i^m \cos m\theta \alpha_{lm} K_m(\kappa_l r) \tag{13.12.45}$$

where for $l = 0$, $K_m(\kappa_0 r) = K_m(-i\kappa r) = \frac{\pi}{2} i^{m+1} H_m^{(1)}(\kappa r)$ is the Hankel function of the first kind representing outgoing wave, and

$$\alpha_{lm} = \frac{3\omega^2 A^2}{4g \sinh^4 kh} \frac{a_l J'_m(2ka)}{\kappa_l K'_m(\kappa_l a)} \,. \tag{13.12.46}$$

13.12.6 Response to $\mathcal{S}$

We also express Ψ as a series of depth-eigenfuntions[5] for frequency 2ω,

$$\Psi = -\frac{ig}{2\omega} \sum_{l=0}^{\infty} \xi_l(r,\theta) \frac{\cosh \kappa_l(z+h)}{\cos \kappa_l h} \,. \tag{13.12.47}$$

By applying Green's formula to Ψ_l and $\cosh \kappa_l(z+h)$ in the vertical direction as in Section 3.5, and using orthogonality, we obtain

$$\nabla^2 \xi_l - \kappa_l^2 \xi_l = -i \frac{2\omega}{A_l} \mathcal{S} \,, \quad l = 0, 1, 2, 3, \ldots \,. \tag{13.12.48}$$

To solve these inhomogeneous equations, we employ the method of Green's function, defined here by the following equations

$$\nabla^2 G_l - \kappa_l^2 G_l = \frac{1}{r} \delta(r - r_0)(\delta(\theta - \theta_0) \,. \quad r, r_0 > a \,, \tag{13.12.49}$$

$$\frac{\partial G_l}{\partial r} = 0 \,, \quad r = a \,, \tag{13.12.50}$$

and

$$\sqrt{r} \left(\frac{\partial G_0}{\partial r} - i\kappa_0 G_0 \right) \to 0 \,, \quad r \to \infty \,, \tag{13.12.51}$$

but

$$G_l \to 0 \,, \quad r \to \infty \,, \quad l = 1, 2, 3, \ldots \,. \tag{13.12.52}$$

[5] A similar procedure has been used by Massel (1993) and Porter and Staziger (1995) to extend the realm of the mild-slope equation in the linearized theory. See review in Dingemans (1996).

By the standard method of eigenfunction expansions, one can derive the following result,

$$G_l = \frac{1}{2\pi} \sum_{m=0}^{\infty} \epsilon_m g_{lm} \cos m(\theta - \theta_0) \tag{13.12.53}$$

where

$$g_{lm}(r, r_0) = \left[\frac{I'_m(\kappa_l a)}{K'_m(\kappa_l a)} K_m(\kappa_l r_0) - I_m(\kappa_l r_0) \right] K_m(\kappa_l r) \,, \quad r > r_0 \,; \tag{13.12.54}$$

and

$$g_{lm}(r, r_0) = \left[\frac{I'_m(\kappa_l a)}{K'_m(\kappa_l a)} K_m(\kappa_l r) - I_m(\kappa_l r) \right] K_m(\kappa_l r_0) \,, \quad r < r_0 \,. \tag{13.12.55}$$

Clearly this Green function is symmetric: $G_l(r, \theta; r_0, \theta_0) = G_l(r_0, \theta_0; r, \theta)$. Defining

$$r_> = \mathrm{Max}(r, r_0) \,, \quad r_< = \mathrm{Min}(r, r_0) \tag{13.12.56}$$

the Green function can be expressed more compactly as,

$$G_l = \sum_{m=0}^{\infty} \frac{\epsilon_m}{2\pi} \left[\frac{I'_m(\kappa_l a)}{K'_m(\kappa_l a)} K_m(\kappa_l r_<) - I_m(\kappa_l r_<) \right] K_m(\kappa_l r_>) \cos m(\theta - \theta_0) \,. \tag{13.12.57}$$

Let us apply Green's theorem for the entire fluid area Ω bounded within by the cylinder and by a circle of infinite radius on the outside,

$$\int_0^{2\pi} \int_a^{\infty} (\xi_l \nabla^2 G_l - G_l \nabla^2 \xi_l) r \, d\theta \, dr = \oint_{\partial\Omega} \left(\xi_l \frac{\partial G_l}{\partial n} - G_l \frac{\partial \xi_l}{\partial n} \right) dS \,. \tag{13.12.58}$$

The left-hand side is $2\pi \xi_l(r_0, \theta_0)$. On the right-hand side, the line integral vanishes on the cylinder and on the sea bottom. The line integral along the infinitely large circle vanishes for all evanescent modes $l = 1.2.3, \ldots$. For $l = 0$ it can also be shown to vanish in the limit,

$$\int_{\partial\Omega_\infty} \left(\xi_0 \frac{\partial G_0}{\partial n} - G_0 \frac{\partial \xi_0}{\partial n} \right) dS = O\left(\frac{1}{\sqrt{r}} \right) \to 0 \,, \quad r \to \infty \,. \tag{13.12.59}$$

After invoking the symmetry of G_l, we find at any field point (r, θ),

$$\xi_l(r,\theta) = \int_0^{2\pi} \int_a^{\infty} -i\frac{2\omega\mathcal{S}}{A_l} G_l(r,\theta;r_0,\theta_0)\, r_0\, dr_0\, d\theta_0\,. \tag{13.12.60}$$

Because the quadratic forcing term attenuate slowly with r, ξ_0 does not satisfy the standard radiation condition (13.12.51) at every point along the infinite circle. Instead it is the entire *integral* but not the *integrand* in (13.12.59) that vanishes. This result is called the *weak radiation condition* the proof of which requires the asymptotic behavior of ξ_0 at large r (Appendix 13.A) and the use of the method of stationary phase (see Appendix 13.B).

Substituting the Green function (13.12.57) into (13.12.60), we obtain

$$\xi_l(r,\theta) = \int_a^{\infty} r_0\, dr_0 \int_0^{2\pi} d\theta_0 \left[-i\frac{2\omega\mathcal{S}(r_0,\theta_0)}{A_l}\right] \sum_{m=0}^{\infty} \frac{\epsilon_m}{2\pi} \cos m(\theta-\theta_0)$$

$$\times \left[\frac{I_m'(\kappa_l a)}{K_m'(\kappa_l a)} K_m(\kappa_l r_<) - I_m(\kappa_l r_<)\right] K_m(\kappa_l r_>)\,. \tag{13.12.61}$$

In particular, the value on the cylinder $r = a$ can be obtained after using the Fourier expansion (13.12.26) for $\mathcal{S}(r,\theta)$, the orthgonality of cosines, and the Wronakian identity of Bessel functions,

$$\xi_l(a,\theta) = \sum_{m=0}^{\infty} \frac{\epsilon_m}{\kappa_l a} \cos m\theta \int_a^{\infty} r_0\, dr_0 \left[-i\frac{2\omega\mathcal{S}_m(r)}{A_l}\right] \frac{K_m(\kappa_l r)}{K_m'(\kappa_l a)}\,. \tag{13.12.62}$$

The infinite integrals above must be computed numerically. Again for $l = 0$ the asympotic behavior of the integrand can be utilized to facilitate the numerical integration as in Chau and Eatok Taylor, who obtained an equivalent analytical solution by a three-dimensional Green function.

Equation (13.12.61) can be subtituted into (13.12.44) to get Ψ, and then be combined with Ξ to get Φ_2. The result is an exact solution requiring merely numerical quadrature.

Finally the second-order displacement $\zeta_2^{(2)}(r,\theta,t)$ is

$$\zeta_2^{(2)} = \eta_{2,2}^{(2)} e^{-2i\omega t} + *\tag{13.12.63}$$

where

$$\eta_{2,2}^{(2)}(r,\theta) = L\sum_{m=0}^{\infty}\epsilon_m i^m \cos m\theta\left[J_m(2kr) - \frac{2k}{p}\frac{J'_m(2ka)}{H'_m(pa)}H_m(pr)\right]$$
$$+\sum_{l=0}^{\infty}\sum_{m=0}^{\infty}\left\{\epsilon_m\cos(m\theta)\int_a^{\infty} r\,dr\left[-i\frac{\omega_n\mathcal{S}_m(r)}{A_{l,l}}\right]K_m(\kappa_l r_>)\right.$$
$$\left.\times\left[\frac{I'_m(\kappa_l a)}{K'_m(\kappa_l a)}K_m(\kappa_l r_<) - I_m(\kappa_l r_<)\right]\right\}. \qquad (13.12.64)$$

Combined with (13.12.14), the second-order free surface height is completely detemined.

13.12.7 Sample Numerical Results

Sample variation of the amplitude of the zeroth and second harmonic, $\eta_{2,2}^{(0)}, \eta_{2,2}^{(2)}$, due to the first-order motion, as well as $\eta_{2,2}^{(2)}$ due to Φ_2, are shown

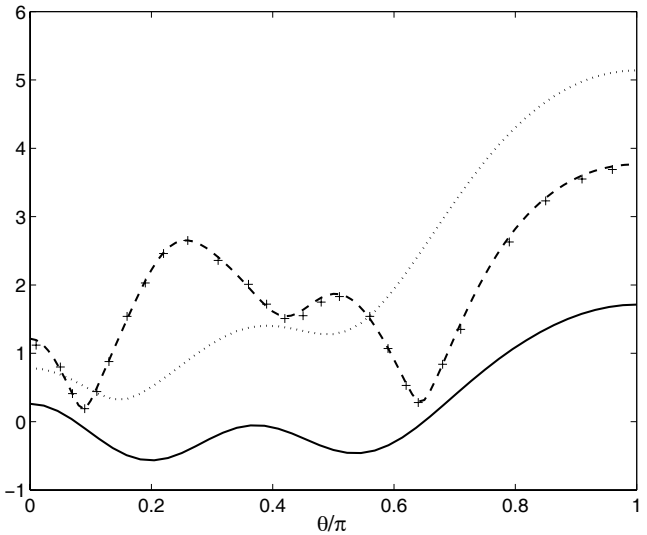

Figure 13.26: Dimensionless amplitudes of the second-order free surface elevations on a vertical cylinder. Solid line : mean setup $\eta_{2,0}^{(1)}a/A^2$ (zeroth harmonic component due to Φ_1. Dashed line: second-harmonic component due to Φ_1, $\eta_{2,2}^{(1)}a/A^2$. Dotted line: second-harmonic component due to Φ_2, $\eta_{2,2}^{(1)}a/A^2$. Crosses are the numerical results of Kim and Yue and of Chau and Eatok Taylor. The input parameters are $r/a = 1$, $h/a = 1$ and $\omega^2 a/g = 2$ (from Chen, 2005).

in Fig. 13.26. These numerical results agree with the theories of Kim and Yue (1989) and of Chau and Eatok-Taylor (1992).

In conclusion, it may be pointed out that the present method not only reduces the three dimensional problem to two dimensions but can also be extended to mildly sloping seabed and for random incident waves of a broad freequency band (Chen, 2005).

Appendix 13.A Asymptotic Behavior ξ_0 in the Far-Field

We seek the asymptotic solution of

$$\nabla^2\xi_0 + \kappa^2\xi_0 = -i\frac{\omega\mathcal{S}}{A_0}\,. \tag{13.A.1}$$

Let us first examine the the forcing terms $\mathcal{S}_{IS}$ and $\mathcal{S}_{IS}$ defined in (13.12.19) and (13.12.20). For large r, we can approximate the first-order scattered wave as

$$\eta^S \approx Q(\theta)\frac{e^{ikr}}{\sqrt{kr}} \tag{13.A.2}$$

where $Q(\theta)$ is the angular intensity factor

$$Q(\theta) = \sum_{m=0}^{\infty}\sqrt{\frac{2}{\pi}}\left[-\epsilon_m i^m\frac{J'_m(ka)}{H'_m(kr)}\cos m\theta\right]e^{-i\pi(\frac{m}{2}+\frac{1}{4})}\,. \tag{13.A.3}$$

In order to estimate the forcing term $\mathcal{S}_{IS}$, we need only estimate $\eta^S\eta^I$

$$\eta^S\eta^I \approx AQ\frac{e^{ikr(\cos\theta+1)}}{\sqrt{kr}}\,, \tag{13.A.4}$$

and

$$\nabla\eta^S\cdot\nabla\eta^I \approx AQk^2\cos\theta\frac{e^{ikr(\cos\theta+1)}}{\sqrt{kr}}\,. \tag{13.A.5}$$

Therefore, we obtain

$$\mathcal{S}_{IS} \approx [\widehat{\beta} - \bar{\beta}k^2\cos\theta]\frac{A}{2}Q(\theta)\frac{e^{ikr(\cos\theta+1)}}{\sqrt{kr}} + O(r^{-3/2})\,. \tag{13.A.6}$$

It is easy to see that

$$\mathcal{S}_{SS} = O\left(\frac{e^{i2kr}}{kr}\right) \tag{13.A.7}$$

which is negligible compared to $\mathcal{S}_{IS}$. Hence $\mathcal{S}$ is dominated by $\mathcal{S}_{IS}$ at large kr. From Eq. (13.A.1), it can be seen that

$$\xi_0 \approx F(\theta)\frac{e^{ikr(\cos\theta+1)}}{\sqrt{kr}} \tag{13.A.8}$$

where $F(\theta)$ is a known function of θ.

Appendix 13.B Weak Radiation Condition

We show here that the following line integral vanishes

$$I = \int_{\partial\Omega_\infty}\left(\xi_0\frac{\partial G_0}{\partial r} - G_0\frac{\partial \xi_0}{\partial r}\right)dS \to 0\,. \tag{13.B.1}$$

Since G_0 satisfies the strong radiation condition,

$$G_0 \approx \frac{H(\theta)}{\sqrt{kr}}e^{i\kappa r}\,. \tag{13.B.2}$$

Putting the asymptotic expressions of ξ_0 and G_0 into Eq. (13.B.1), we obtain for large r,

$$\begin{aligned} I &= \int_0^{2\pi} r\,d\theta\,H(\theta)F(\theta)\frac{e^{i\kappa r}}{\sqrt{\kappa r}}\frac{e^{ikr(\cos\theta+1)}}{\sqrt{kr}}[-ik(\cos\theta+1)+i\kappa] \\ &= i\int_0^{2\pi} d\theta\frac{H(\theta)}{\sqrt{\kappa}}\frac{L(\theta)}{\sqrt{k}}e^{ir[\kappa+k(\cos\theta+1)]}[-k(\cos\theta+1)+\kappa]\,. \end{aligned} \tag{13.B.3}$$

For large r, we use the method of stationary phase, and let

$$\varphi(\theta) = k\cos\theta + k + \kappa \tag{13.B.4}$$

be the phase function. Since

$$\frac{d\varphi}{d\theta} = -k\sin\theta$$

the stationary phase points are at $\theta = (0,\pi)$, where

$$\frac{d^2\varphi}{d\theta^2} = -k\cos\theta = (-k,k)\,.$$

It follows from (2.1.28) that

$$I \approx \left\{ i\frac{F(0)}{\sqrt{\kappa}}\frac{H(0)}{\sqrt{k}} e^{ir(\kappa+2k)}(\kappa-2k)e^{-i\pi/4} + i\frac{F(\pi)}{\sqrt{\kappa}}\frac{H(\pi)}{\sqrt{k}} e^{ir\kappa}\kappa e^{i\pi/4} \right\} \sqrt{\frac{2\pi}{kr}}\,. \tag{13.B.5}$$

Clearly

$$I = O\left(\frac{1}{\sqrt{kr}}\right) \to 0\,, \quad kr \to \infty\,,$$

hence the weak radiation condition is satisfied.

Broad-Banded Nonlinear Surface Waves in the Open Sea

14

Wind-generated waves on the open ocean surface are usually too complex to be described by one regular slowly varying wavetrain, and require more elaborate spectral representations to acount for sea states with a broad band of wavelengths and directions. For infinitesimal waves, there are spectral theories to describe the random sea surface based on linear superposition of many simple wavetrains. The amplitude-spectrum (which contains the amplitudes and phases), or sometimes only the energy spectrum, can be used to convey the information about the complicated geometry and kinematics of the ocean surface. Statistical stationarity is often assumed. A detailed description of such classical treatments can be found in Ochi (1998).

The evolution of gravity-wave spectra is, however, a very dynamical process governed in general by three physical processes: (a) energy input by the wind, (b) energy transfer between the different spectral modes due to nonlinear interaction, and (c) energy dissipation by wave breaking and/or complex interactions with the seabed. Wind input and dissipation are pronounced in windy conditions and in shallow water, whereas nonlinear interaction is always present even outside the storm area and in deep water. Since the early 1960's much fundamental progress has been made on the nonlinear processes in ocean waves, pioneered in particular by Owen M. Phillips, Klaus Hasselmann, and Vladimir E. Zakharov. In recent years the so-called weak-turbulence theory initiated by Zakharov has made a strong impact on the advances of ocean-wave physics. This chapter is intended as an introduction to the weak-turbulence theory with a view to preparing the reader for studying the expanding literature. For the derivation of Zakharov's equation we follow a procedure described by Yuen and Lake (1982). The mathematical details are however dauntingly lengthy. In

order that the reader does not lose sight of the main line of reasoning, we leave many steps of derivation to the Appendices. After deriving Zakharov's equation we shall show a few of its applications. In addition to simple solutions of one or two wavetrains, we shall derive the exact solution of four waves in resonant interactions. We shall also show how the cubic Schrödinger equation can be obtained as the limit of narrow frequency band. Benjamin–Feir instability is then revisited with a view to demonstrate several predictions beyond the usual narrow-band approximation. Hasselmann's kinetic equation, which is the basis of forecasting models of random waves, is derived here from Zakharov's equation. Thus, various theories developed for specific conditions are unified by the work of Zakharov. Finally references to more general theories are given in the concluding section.

14.1 Background

We first recall the Laplace equation

$$\nabla^2\phi = 0\,, \quad -h < z < \zeta \tag{14.1.1}$$

for the velocity potential $\phi(\mathbf{x}, z, t)$, where $\mathbf{x} = (x, y)$ denotes the horizontal position vector and z the vertical coordinate measured upward from the still-water level. Recall also the kinematic and dynamic boundary conditions on the free surface $z = \zeta$:

$$\zeta_t + (\nabla_{\mathbf{x}}\phi)\cdot(\nabla_{\mathbf{x}}\zeta) - \phi_z = 0\,, \tag{14.1.2}$$

where $\nabla_{\mathbf{x}}$ denotes the horizontal gradient operator, and

$$\phi_t + \frac{1}{2}(\nabla\phi)^2 + g\zeta = 0\,. \tag{14.1.3}$$

In this chapter we shall only consider a horizontal bottom $z = -h$ on which no flux is permitted

$$\phi_z = 0\,. \tag{14.1.4}$$

Laplace equation (14.1.1) has a unique solution when the free-surface displacement $\zeta(\mathbf{x}, t)$, and the velocity potential on the free surface

$$\phi^s = \phi(\mathbf{x}, \zeta(\mathbf{x}, t), t) \tag{14.1.5}$$

are specified. To show in principle that ζ and ϕ^s can be obtained for all subsequent time from their values at an earlier instant, let us begin with the chain rule:

$$\nabla_{\mathbf{x}}\phi^s = (\nabla_{\mathbf{x}}\phi)_\zeta + \left(\frac{\partial\phi}{\partial z}\right)_\zeta \nabla_{\mathbf{x}}\zeta\,.$$

Denoting the vertical velocity on the free surface by w^s, i.e.,

$$w^s = \left(\frac{\partial\phi}{\partial z}\right)_\zeta$$

the free surface conditions (14.1.2) and (14.1.3) can be rewritten as

$$\zeta_t + (\nabla_{\mathbf{x}}\phi^s)\cdot(\nabla_{\mathbf{x}}\zeta) - w^s[1+(\nabla_{\mathbf{x}}\zeta)^2] = 0\,, \tag{14.1.6}$$

$$\phi^s_t + g\zeta + \frac{1}{2}(\nabla_{\mathbf{x}}\phi^s)^2 - \frac{1}{2}(w^s)^2[1+(\nabla_{\mathbf{x}}\zeta)^2] = 0\,. \tag{14.1.7}$$

Now, at any time step when ζ and ϕ^s are known for all $\mathbf{x}$, one can in principle solve the boundary value problem for ϕ governed by (14.1.1), subject to the no-flux boundary condition on the seabed. From the result one can calculate w^s. Equations (14.1.6) and (14.1.7) then provide ζ_t and ϕ^s_t which can be integrated to obtain ζ and ϕ^s at the next time step, and so on. This is indeed the basis of a numerical theory for highly nonlinear waves by Liu, Dommermuth and Yue (1992), to be discussed in Chapter 15.

To motivate later nonlinear analysis, we recall from the linearized theory discussed in Section 1.1.4, that for a progressive wave the free-surface height and the potential on the surface can be written as:

$$\zeta = \frac{1}{2\pi}\left(\frac{\omega}{2g}\right)^{1/2}(B\,e^{i(\mathbf{k}\cdot\mathbf{x}-wt)} + B^*\,e^{-i(\mathbf{k}\cdot\mathbf{x}-wt)}) \tag{14.1.8}$$

and

$$\phi^s = \frac{-i}{2\pi}\left(\frac{g}{2\omega}\right)^{1/2}(B\,e^{i(\mathbf{k}\cdot\mathbf{x}-wt)} - B^*\,e^{-i(\mathbf{k}\cdot\mathbf{x}-wt)})\,, \tag{14.1.9}$$

where the wave frequency ω is related to the wavenumber vector $\mathbf{k}$ by the dispersion relation

$$\omega = [g|\mathbf{k}|\tan(|\mathbf{k}|h)]^{1/2}\,. \tag{14.1.10}$$

B is a complex amplitude of constant magnitude, and the asterisk denotes its complex conjugate.

For weakly nonlinear waves, we shall first derive two conditions for the Fourier transforms of the surface quantities ϕ^s and ζ, and then combine them to get a single relation for the amplitude spectrum B. The relation will be an integro-differential equation, as we shall derive next.

14.2 Fourier Formulation

Let us define the two-dimensional Fourier transform[1] of a function $f(\boldsymbol{x})$ by

$$\hat{f}(\mathbf{k}) = \frac{1}{2\pi} \int_{-\infty}^{\infty} f(\mathbf{x}) \exp[-i\mathbf{k} \cdot \mathbf{x}] \, d\mathbf{x} \, .$$

By repeated use of the following properties of the delta function:

$$\int_{-\infty}^{\infty} \delta(\mathbf{k}) \, e^{-i\mathbf{k}\cdot\mathbf{x}} d\mathbf{k} = 1 \tag{14.2.1}$$

and

$$\begin{aligned} \delta(\mathbf{k}) &= \frac{1}{(2\pi)^2} \int_{-\infty}^{\infty} e^{i\mathbf{k}\cdot\mathbf{x}} \, d\mathbf{x} \\ &= \frac{1}{(2\pi)^2} \int_{-\infty}^{\infty} e^{-i\mathbf{k}\cdot\mathbf{x}} \, d\mathbf{x} \, , \end{aligned} \tag{14.2.2}$$

it is shown in Appendix 14.A.1 that the horizontal Fourier tranforms of (14.1.6) and (14.1.7) yield

$$\begin{aligned} &\hat{\zeta}_t(\mathbf{k}, t) - \frac{1}{(2\pi)} \iint_{-\infty}^{\infty} (\mathbf{k}_1 \cdot \mathbf{k}_2) \hat{\phi}^s(\mathbf{k}_1, t) \hat{\zeta}(\mathbf{k}_2, t) \\ &\quad \cdot \delta(\mathbf{k} - \mathbf{k}_1 - \mathbf{k}_2) \, d\mathbf{k}_1 \, d\mathbf{k}_2 - \hat{w}^s \\ &\quad + \frac{1}{(2\pi)^2} \iiint_{-\infty}^{\infty} (\mathbf{k}_2 \cdot \mathbf{k}_3) \hat{w}^s(\mathbf{k}_1, t) \hat{\zeta}(\mathbf{k}_2, t) \hat{\zeta}(\mathbf{k}_3, t) \\ &\quad \cdot \delta(\mathbf{k} - \mathbf{k}_1 - \mathbf{k}_2 - \mathbf{k}_3) \, d\mathbf{k}_1 \, d\mathbf{k}_2 \, d\mathbf{k}_3 = 0 \, , \end{aligned} \tag{14.2.3}$$

[1] The definition of Fourier transform here is different from that in Chapter Two only by the numerical factor $1/2\pi$.

and

$$\hat{\phi}^s_t(\mathbf{k},t) + g\hat{\zeta}(\mathbf{k},t) - \frac{1}{4\pi}\iint_{-\infty}^{\infty}(\mathbf{k}_1\cdot\mathbf{k}_2)\hat{\phi}^s(\mathbf{k}_1,t)$$
$$\cdot\,\hat{\phi}^s(\mathbf{k}_2,t)\delta(\mathbf{k}-\mathbf{k}_1-\mathbf{k}_2)\,d\mathbf{k}_1\,d\mathbf{k}_2$$
$$-\frac{1}{4\pi}\iint_{-\infty}^{\infty}\hat{w}^s(\mathbf{k}_1,t)\hat{w}^s(\mathbf{k}_2,t)$$
$$\cdot\,\delta(\mathbf{k}-\mathbf{k}_1-\mathbf{k}_2)\,d\mathbf{k}_1\,d\mathbf{k}_2 = 0\,. \tag{14.2.4}$$

Let us eliminate the surface vertical velocity $\hat{w}^s$ so that the two conditions above involve two unknowns $\hat{\phi}^s(\mathbf{k},t)$ and $\hat{\zeta}(\mathbf{k},t)$ only. The results will then be combined to give a single relation for $B(\mathbf{k},t)$. For this purpose we must first derive w^s from the interior velocity potential $\hat{\phi}(\mathbf{k},z,t)$. This procedure is lengthy and is outlined below.

The Fourier transform of the Laplace equation (14.1.1) gives

$$\frac{\partial^2\hat{\phi}(\mathbf{k},z,t)}{\partial z^2} + |\mathbf{k}|^2\hat{\phi}(\mathbf{k},z,t) = 0\,.$$

Its solution, which satisfies the seabed boundary condition Eq. (14.1.4), is

$$\hat{\phi}(\mathbf{k},z,t) = \hat{\Phi}(\mathbf{k},t)\cosh(|\mathbf{k}|(z+h))\,. \tag{14.2.5}$$

By opening the brackets in (14.2.5), substituting $z=\zeta(\mathbf{x},t)$ and taking the inverse Fourier transform, we get for the velocity potential on the free surface

$$\phi^s(\mathbf{x},t) = \frac{1}{2\pi}\int_{-\infty}^{\infty}\hat{\Phi}(\mathbf{k},t)[\cosh(|\mathbf{k}|h)\cosh(|\mathbf{k}|\zeta(\mathbf{x},t))$$
$$+\sinh(|\mathbf{k}|h)\sinh(|\mathbf{k}|\zeta(\mathbf{x},t))]\exp[i\mathbf{k}\cdot\mathbf{x}]\,d\mathbf{k}\,. \tag{14.2.6}$$

On the other hand, by differentiating (14.2.5) with respect to z and taking the inverse transform, we obtain an integral expression for the vertical velocity on the free surface

$$w^s(\mathbf{x},t) = \frac{1}{2\pi}\int_{-\infty}^{\infty}|\mathbf{k}|\hat{\Phi}(\mathbf{k},t)[\cosh(|\mathbf{k}|h)\sinh(|\mathbf{k}|\zeta(\mathbf{x},t))$$
$$+\sinh(|\mathbf{k}|h)\cosh(|\mathbf{k}|\zeta(\mathbf{x},t))]\exp[i\mathbf{k}\cdot\mathbf{x}]\,d\mathbf{k}\,. \tag{14.2.7}$$

So far no approximations have been made.

We shall now make an additional assumption that the wave steepness is small, i.e., $|\mathbf{k}|\zeta = O(\epsilon) \ll 1$. This assumption allows us to expand all functions of $|\mathbf{k}|\zeta$ in (14.2.6) and (14.2.7) in Taylor series up to the order $(|\mathbf{k}|\zeta)^2$. Thus,

$$\phi^s(\mathbf{x},t) = \frac{1}{2\pi}\int_{-\infty}^{\infty}\hat{\phi}(\mathbf{k}_1,t)\left[\cosh(\mathbf{k}_1 h)\left(1+\frac{|\mathbf{k}_1|^2}{2}\zeta^2\right)+|\mathbf{k}_1|\sinh(|\mathbf{k}_1|h)\zeta\right] \cdot e^{i\mathbf{k}_1\cdot\mathbf{x}}\,d\mathbf{k}_1\,. \tag{14.2.8}$$

Taking the Fourier transform of (14.2.8), and expressing ζ as a Fourier integral

$$\zeta(\mathbf{x},t) = \frac{1}{2\pi}\int_{-\infty}^{\infty}\hat{\zeta}(\mathbf{k},t)\exp[i\mathbf{k}\cdot\mathbf{x}]\,d\mathbf{k}\,,$$

we get

$$\begin{aligned}\hat{\phi}^s(\mathbf{k},t) = {}& \hat{\Phi}(\mathbf{k},t)\cosh(|\mathbf{k}|h) + \frac{1}{2\pi}\iint_{-\infty}^{\infty}|\mathbf{k}_1|\sinh(|\mathbf{k}_1|h)\\ & \cdot\hat{\Phi}(\mathbf{k}_1,t)\hat{\zeta}(\mathbf{k}_2,t)\delta(\mathbf{k}-\mathbf{k}_1-\mathbf{k}_2)\,d\mathbf{k}_1\,d\mathbf{k}_2\\ & + \frac{1}{(2\pi)^2}\iiint_{-\infty}^{\infty}\frac{1}{2}|\mathbf{k}_1|^2\cosh(|\mathbf{k}_1|h)\hat{\Phi}(\mathbf{k}_1,t)\\ & \cdot\hat{\zeta}(\mathbf{k}_2,t)\hat{\zeta}(\mathbf{k}_3,t)\delta(\mathbf{k}-\mathbf{k}_1-\mathbf{k}_2-\mathbf{k}_3)\,d\mathbf{k}_1\,d\mathbf{k}_2\,d\mathbf{k}_3\,.\end{aligned} \tag{14.2.9}$$

Details are given in Appendix 14.A.2. Similarly (14.2.7) can be transformed to

$$\begin{aligned}\hat{w}^s(\mathbf{k},t) = {}& |\mathbf{k}|\hat{\Phi}(\mathbf{k},t)\sinh(|\mathbf{k}|h) + \frac{1}{2\pi}\iint_{-\infty}^{\infty}|\mathbf{k}_1|^2\cosh(|\mathbf{k}_1|h)\\ & \cdot\hat{\Phi}(\mathbf{k}_1,t)\hat{\zeta}(\mathbf{k}_2,t)\delta(\mathbf{k}-\mathbf{k}_1-\mathbf{k}_2)\,d\mathbf{k}_1\,d\mathbf{k}_2\\ & + \frac{1}{(2\pi)^2}\iiint_{-\infty}^{\infty}\frac{1}{2}|\mathbf{k}_1|^3\sinh(|\mathbf{k}_1|h)\hat{\Phi}(\mathbf{k}_1,t)\\ & \cdot\hat{\zeta}(\mathbf{k}_2,t)\hat{\zeta}(\mathbf{k}_3,t)\delta(\mathbf{k}-\mathbf{k}_1-\mathbf{k}_2-\mathbf{k}_3)\,d\mathbf{k}_1\,d\mathbf{k}_2\,d\mathbf{k}_3\,.\end{aligned} \tag{14.2.10}$$

We now invert (14.2.9) iteratively so as to express $\hat{\Phi}(\mathbf{k},t)$ in terms of the surface unknowns $\hat{\phi}^s$ and $\hat{\zeta}$. Leaving the details in Appendix 15.A.3, we only cite the result:

$$\hat{\Phi}(\mathbf{k}) = \frac{\hat{\phi}^s(\mathbf{k},t)}{\cosh(|\mathbf{k}|h)} - \frac{1}{\cosh(|\mathbf{k}|h)} \cdot \frac{1}{2\pi} \iint_{-\infty}^{\infty} |\mathbf{k}_1| \hat{\phi}^s(\mathbf{k}_1,t)\hat{\zeta}(\mathbf{k}_2,t)$$
$$\cdot \tanh(|\mathbf{k}_1|h)\delta(\mathbf{k}-\mathbf{k}_1-\mathbf{k}_2)\, d\mathbf{k}_1\, d\mathbf{k}_2$$
$$- \frac{1}{\cosh(|\mathbf{k}|h)} \frac{1}{(2\pi)^2} \iiint_{-\infty}^{\infty} \frac{|\mathbf{k}_1|}{4}$$
$$\cdot \{2|\mathbf{k}_1| - \tanh(|\mathbf{k}_1|h) \cdot [|\mathbf{k}-\mathbf{k}_2| \cdot \tanh(|\mathbf{k}-\mathbf{k}_2|h)$$
$$+ |\mathbf{k}-\mathbf{k}_3| \cdot \tanh(|\mathbf{k}-\mathbf{k}_3|h) + |\mathbf{k}_1+\mathbf{k}_2| \cdot \tanh(|\mathbf{k}_1+\mathbf{k}_2|h)$$
$$+ |\mathbf{k}_1+\mathbf{k}_3| \cdot \tanh(|\mathbf{k}_1+\mathbf{k}_3|h)]\}\hat{\phi}^s(\mathbf{k}_1,t)\hat{\zeta}(\mathbf{k}_2,t)\hat{\zeta}(\mathbf{k}_3,t)$$
$$\cdot \delta(\mathbf{k}-\mathbf{k}_1-\mathbf{k}_2-\mathbf{k}_3)\, d\mathbf{k}_1\, d\mathbf{k}_2\, d\mathbf{k}_3\,. \tag{14.2.11}$$

Substituting this result into (14.2.10) yields

$$\hat{w}^s(\mathbf{k},t) = |\mathbf{k}| \tanh(|\mathbf{k}|h)\hat{\phi}^s(\mathbf{k},t)$$
$$- \frac{1}{2\pi} \iint_{-\infty}^{\infty} |\mathbf{k}_1| [|\mathbf{k}| \tanh(|\mathbf{k}|h) \tanh(|\mathbf{k}_1|h) - |\mathbf{k}_1|]$$
$$\cdot \hat{\phi}^s(\mathbf{k}_1,t)\hat{\zeta}(\mathbf{k}_2,t)\delta(\mathbf{k}-\mathbf{k}_1-\mathbf{k}_2)\, d\mathbf{k}_1\, d\mathbf{k}_2$$
$$- \frac{1}{(2\pi)^2} \iiint_{-\infty}^{\infty} S^{(1)}(\mathbf{k},\mathbf{k}_1,\mathbf{k}_2,\mathbf{k}_3)\hat{\phi}^s(\mathbf{k}_1,t)\hat{\zeta}(\mathbf{k}_2,t)\hat{\zeta}(\mathbf{k}_3,t)$$
$$\cdot \delta(\mathbf{k}-\mathbf{k}_1-\mathbf{k}_2-\mathbf{k}_3)\, d\mathbf{k}_1\, d\mathbf{k}_2\, d\mathbf{k}_3\,. \tag{14.2.12}$$

The lengthy expression of the kernel $S^{(1)}$ is given in Apppendix 14.B along with other kernels to be introduced later.

The transformed vertical velocity at the free surface $\hat{w}^s$, given by (14.2.12), is now substituted into the two free surface conditions (14.2.3) and (14.2.4) so that the terms up to the third order of wave steepness are retained.

Finally, we multiply (14.2.3) by $[g/2\omega(\mathbf{k})]^{1/2}$, and (14.2.4) by $i[\omega(\mathbf{k})/2g]^{1/2}$, then take their sum and define the new complex amplitude,

$$b(\mathbf{k},t) = \left(\frac{g}{2\omega(\mathbf{k})}\right)^{1/2} \hat{\zeta}(\mathbf{k},t) + i\left(\frac{\omega(\mathbf{k})}{2g}\right)^{1/2} \hat{\phi}^s(\mathbf{k},t)\,, \tag{14.2.13}$$

where the wave frequency ω is related to the wavenumber by the dispersion relation (14.1.10). The following integral-differential equation is obtained for the evolution of b,

$$
\begin{aligned}
&\frac{db(\mathbf{k},t)}{dt} + i\omega(\mathbf{k})b(\mathbf{k},t) \\
&\quad + i\iint_{-\infty}^{\infty} V^{(1)}(\mathbf{k},\mathbf{k}_1,\mathbf{k}_2)b(\mathbf{k}_1,t)b(\mathbf{k}_2,t)\cdot\delta(\mathbf{k}-\mathbf{k}_1-\mathbf{k}_2)\,d\mathbf{k}_1\,d\mathbf{k}_2 \\
&\quad + i\iint_{-\infty}^{\infty} V^{(2)}(\mathbf{k},\mathbf{k}_1,\mathbf{k}_2)b^*(\mathbf{k}_1,t)b(\mathbf{k}_2,t)\delta(\mathbf{k}+\mathbf{k}_1-\mathbf{k}_2)\,d\mathbf{k}_1\,d\mathbf{k}_2 \\
&\quad + i\iint_{-\infty}^{\infty} V^{(3)}(\mathbf{k},\mathbf{k}_1,\mathbf{k}_2)b^*(\mathbf{k}_1,t)b^*(\mathbf{k}_2,t)\delta(\mathbf{k}+\mathbf{k}_1+\mathbf{k}_2)\,d\mathbf{k}_1\,d\mathbf{k}_2 \\
&\quad + i\iiint_{-\infty}^{\infty} W^{(1)}(\mathbf{k},\mathbf{k}_1,\mathbf{k}_2,\mathbf{k}_3)b(\mathbf{k}_1,t)b(\mathbf{k}_2,t)b(\mathbf{k}_3,t) \\
&\quad \cdot\delta(\mathbf{k}-\mathbf{k}_1-\mathbf{k}_2-\mathbf{k}_3)\,d\mathbf{k}_1\,d\mathbf{k}_2\,d\mathbf{k}_3 \\
&\quad + i\iiint_{-\infty}^{\infty} W^{(2)}(\mathbf{k},\mathbf{k}_1,\mathbf{k}_2,\mathbf{k}_3)b^*(\mathbf{k}_1,t)b(\mathbf{k}_2,t)b(\mathbf{k}_3,t) \\
&\quad \cdot\delta(\mathbf{k}+\mathbf{k}_1-\mathbf{k}_2-\mathbf{k}_3)\,d\mathbf{k}_1\,d\mathbf{k}_2\,d\mathbf{k}_3 \\
&\quad + i\iiint_{-\infty}^{\infty} W^{(3)}(\mathbf{k},\mathbf{k}_1,\mathbf{k}_2,\mathbf{k}_3)b^*(\mathbf{k}_1,t)b^*(\mathbf{k}_2,t)b(\mathbf{k}_3,t) \\
&\quad \cdot\delta(\mathbf{k}+\mathbf{k}_1+\mathbf{k}_2-\mathbf{k}_3)\,d\mathbf{k}_1\,d\mathbf{k}_2\,d\mathbf{k}_3 \\
&\quad + i\iiint_{-\infty}^{\infty} W^{(4)}(\mathbf{k},\mathbf{k}_1,\mathbf{k}_2,\mathbf{k}_3)b^*(\mathbf{k}_1,t)b^*(\mathbf{k}_2,t)b^*(\mathbf{k}_3,t) \\
&\quad \cdot\delta(\mathbf{k}+\mathbf{k}_1+\mathbf{k}_2+\mathbf{k}_3)\,d\mathbf{k}_1\,d\mathbf{k}_2\,d\mathbf{k}_3 = 0\,. \qquad (14.2.14)
\end{aligned}
$$

The explicit expressions of all kernals $V^{(n)}$ and $W^{(n)}$ are given in Appendix 14.B.

After b is solved, the transforms $\hat{\zeta}$ and $\hat{\phi}^s$ are obtained from

$$\hat{\zeta}(\mathbf{k},t) = \sqrt{\frac{\omega(\mathbf{k})}{2g}}[b(\mathbf{k},t) + b^*(-\mathbf{k},t)]\,, \qquad (14.2.15)$$

$$\hat{\phi}^s(\mathbf{k},t) = -i\sqrt{\frac{g}{2\omega(\mathbf{k})}}[b(\mathbf{k},t) - b^*(-\mathbf{k},t)]\,. \qquad (14.2.16)$$

14.3 Multiple Time Scales

Equation (14.2.14) is accurate to the third order in the small parameter of the problem, $|\mathbf{k}|\zeta$. Its complexity, however, prevents one from using it in practice in most cases. Let us distill the most important effect of resonant

interactions from the less important parts of bound waves. It was first discovered by Phillips (1960) that for gravity waves without surface tension, resonance is possible with four interacting wavetrains. Anticipating that weakly nonlinear resonance evolves over a much longer time scale, we apply the method of multiple-scale expansions and introduce two time variables[2] $(t, t_2 = \epsilon^2 t)$. In particular let us follow Zakharov (1968) and assume that the wave field can be divided into several parts with the leading part $\tilde{B}$, varying slowly in time, and other smaller parts B', B'' varying rapidly in time, thus,

$$b(\mathbf{k},t) = [\varepsilon\tilde{B}(\mathbf{k},t_2) + \varepsilon^2 B'(\mathbf{k},t,t_2) + \varepsilon^3 B''(\mathbf{k},t,t_2) + \cdots] \cdot \exp[-i\omega(\mathbf{k})t]\,. \tag{14.3.1}$$

Substituting (14.3.1) into (14.2.14) and noting that

$$\frac{\partial b(\mathbf{k},t)}{\partial t} \to -i\omega(\mathbf{k})[\varepsilon\tilde{B} + \varepsilon^2 B' + \varepsilon^3 B'' + \cdots]e^{-i\omega(\mathbf{k})t} + \left(\varepsilon^2\frac{\partial B'}{\partial t} + \varepsilon^3\frac{\partial B''}{\partial t} + \varepsilon^3\frac{\partial\tilde{B}}{\partial t_2} + \cdots\right)e^{-i\omega(\mathbf{k})t},$$

we obtain after separating terms according to their order in ε the following perturbation equations:

Order ε is satisfied identically;

Order ε^2 gives the following equation for B':

$$i\frac{\partial B'}{\partial t} = \iint_{-\infty}^{\infty}\Big[V^{(1)}_{0,1,2}\tilde{B}_1\tilde{B}_2\delta_{0-1-2}\exp[i(\omega-\omega_1-\omega_2)t] + V^{(2)}_{0,1,2}\tilde{B}_1^*\tilde{B}_2\delta_{0+1-2}\exp[i(\omega+\omega_1-\omega_2)t] + V^{(3)}_{0,1,2}\tilde{B}_1^*\tilde{B}_2^*\delta_{0+1+2}\exp[i(\omega+\omega_1+\omega_2)t]\Big]\,d\mathbf{k}_1\,d\mathbf{k}_2\,, \tag{14.3.2}$$

where a compact notation is introduced, in which the arguments $\mathbf{k}_i$ of all functions are replaced by subscripts i, with the subscript zero assigned to $\mathbf{k}$, e.g.,

$$\omega_1 = \omega(|\mathbf{k}_1|)\,, \quad \tilde{B}_1 = \tilde{B}(\mathbf{k}_1,t_2)\,,$$
$$V^{(3)}_{0,1,2} = V^{(3)}(\mathbf{k},\mathbf{k}_1,\mathbf{k}_2)\,, \quad \delta_{0+1-2} = \delta(\mathbf{k}+\mathbf{k}_1-\mathbf{k}_2)\,,$$

[2]It can be shown that there is no need for $t_1 = \epsilon t$ because no resonance is possible with just three waves.

etc. The explicit forms of all kernels $V^{(3)}_{\ell,m,n}$ are given in Appendix 14.B. Integrating (14.3.2) with respect to t, while keeping t_2 constant, we get

$$B' = -\iint_{-\infty}^{\infty} \Bigg[V^{(1)}_{0,1,2} \tilde{B}_1 \tilde{B}_2 \delta_{0-1-2} \frac{\exp[i(\omega-\omega_1-\omega_2)t]}{\omega-\omega_1-\omega_2} + V^{(2)}_{0,1,2} \tilde{B}^*_1 \tilde{B}_2 \delta_{0+1-2} \frac{\exp[i(\omega+\omega_1-\omega_2)t]}{\omega+\omega_1-\omega_2} + V^{(3)}_{0,1,2} \tilde{B}^*_1 \tilde{B}^*_2 \delta_{0+1+2} \frac{\exp[i(\omega+\omega_1+\omega_2)t]}{\omega+\omega_1+\omega_2} \Bigg] d\mathbf{k}_1 \, d\mathbf{k}_2 \,. \tag{14.3.3}$$

It can be shown (Hasselmann, 1962) by using the convexity of the dispersion curve (14.1.10) that the two equalities

$$\mathbf{k} \pm \mathbf{k}_1 \pm \mathbf{k}_2 = 0 \,, \quad \text{and} \quad \omega \pm \omega_1 \pm \omega_2 = 0 \tag{14.3.4}$$

cannot be simultaneously satisfied for any gravity wavetrains, i.e., three sinusoidal gravity waves cannot resonate one another.[3] All the denominators in (14.3.3) differ from zero under the constraints of the corresponding δ-functions. The constant of integration in (14.3.3) has been set to zero without loss of generality.

At order $O(\varepsilon^3)$ of (14.2.14) the following equation is obtained:

$$i\frac{\partial \tilde{B}}{\partial t_2} + i\frac{\partial B''}{\partial t} = \iiint_{-\infty}^{\infty} \Big\{ \tilde{T}^{(1)}_{0,1,2,3} \tilde{B}_1 \tilde{B}_2 \tilde{B}_3 \delta_{0-1-2-3} \exp[i(\omega-\omega_1-\omega_2-\omega_3)t] + \tilde{T}^{(2)}_{0,1,2,3} \tilde{B}^*_1 \tilde{B}_2 \tilde{B}_3 \delta_{0+1-2-3} \exp[i(\omega+\omega_1-\omega_2-\omega_3)t] + \tilde{T}^{(3)}_{0,1,2,3} \tilde{B}^*_1 \tilde{B}^*_2 \tilde{B}_3 \delta_{0+1+2-3} \exp[i(\omega+\omega_1+\omega_2-\omega_3)t] + \tilde{T}^{(4)}_{0,1,2,3} \tilde{B}^*_1 \tilde{B}^*_2 \tilde{B}^*_3 \delta_{0+1+2+3} \exp[i(\omega+\omega_1+\omega_2+\omega_3)t] \Big\} \cdot d\mathbf{k}_1 \, d\mathbf{k}_2 \, d\mathbf{k}_3 \,, \tag{14.3.5}$$

[3] Triplet resonance can happen in capillary-gravity waves for which the dispersion relation (14.1.10) must be replaced by $\omega^2 = (g|\mathbf{k}| + \sigma|\mathbf{k}|^3)\tanh(|\mathbf{k}|h)$ where σ is the coefficient of surface tension (see McGoldrick, 1965). In this case, resonant interactions of three waves are possible and an appropriate modification of (14.3.1) and (14.3.2) is required. These extremely short waves are not considered here.

where the kernels $\tilde{T}^{(n)}_{0,1,2,3}$ are given in Appendix 14.B.

Note first that the structure of the integrals in (14.3.5) allows some freedom in the choice of the kernels. In particular, $\tilde{T}^{(2)}(\mathbf{k},\mathbf{k}_1,\mathbf{k}_3,\mathbf{k}_2)$ can be replaced by $\alpha\tilde{T}^{(2)}(\mathbf{k},\mathbf{k}_1,\mathbf{k}_2,\mathbf{k}_3)+(1-\alpha)\tilde{T}^{(2)}(\mathbf{k},\mathbf{k}_1,\mathbf{k}_3,\mathbf{k}_2)$ with arbitrary α, without altering the value of the second integral. Any $\tilde{T}^{(2)}$ properly derived can be made symmetric in $\mathbf{k}_2,\mathbf{k}_3$ by choosing $\alpha = 0.5$. This symmetrized $\tilde{T}^{(2)}$ is denoted by $T^{(2)}$ in the sequel, i.e.,

$$T^{(2)}_{0,1,2,3} = \frac{1}{2}\Big(\tilde{T}^{(2)}_{0,1,2,3} + \tilde{T}^{(2)}_{0,1,3,2}\Big)\,. \tag{14.3.6}$$

Second, the term associated with $\tilde{T}^{(2)}$ requires special treatment, since the argument of its exponent may become close to zero under the constraints imposed by the δ-function. This happens under the conditions

$$\mathbf{k}+\mathbf{k}_1-\mathbf{k}_2-\mathbf{k}_3 = 0\,, \quad |\omega+\omega_1-\omega_2-\omega_3| \le O(\varepsilon^2)\,. \tag{14.3.7}$$

Physically, (14.3.7) gives the conditions for resonance, first discovered by Phillips (1960). Let us, therefore, separate the nearly resonating quartet and non-resonating quartets. It can now be seen that (14.3.5) consists of terms of two types: those depending on the fast time t and those depending only on the slow time. This enables us to split (14.3.5) into two separate equations, one representing the slow variation of the leading order and the other representing fast variations of higher order. This splitting is achieved by introducing a new kernel T defined as follows:

$$T_{0,1,2,3} = \begin{cases} T^{(2)}_{0,1,2,3} = \dfrac{1}{2}\Big(\tilde{T}^{(2)}_{0,1,2,3} + \tilde{T}^{(2)}_{0,1,3,2}\Big) & \text{for nearly resonating quartets}\,, \\ 0\,, & \text{otherwise}\,. \end{cases} \tag{14.3.8}$$

Thus, the slowly varying part is governed by

$$\boxed{\begin{aligned} i\frac{\partial\tilde{B}}{\partial t_2} = \iiint_{-\infty}^{\infty} & T_{0,1,2,3}\tilde{B}_1^*\tilde{B}_2\tilde{B}_3\delta_{0+1-2-3} \\ & \cdot \exp[i(\omega+\omega_1-\omega_2-\omega_3)t]\,d\mathbf{k}_1\,d\mathbf{k}_2\,d\mathbf{k}_3\,, \end{aligned}} \tag{14.3.9}$$

and the fast varying part is concerned with the higher order:

$$
\begin{aligned}
i\frac{\partial B''}{\partial t} = \iiint_{-\infty}^{\infty} \Big\{ & \tilde{T}^{(1)}_{0,1,2,3} \tilde{B}_1 \tilde{B}_2 \tilde{B}_3 \delta_{0-1-2-3} \exp[i(\omega - \omega_1 - \omega_2 - \omega_3)t] \\
& + \Big(\tilde{T}^{(2)}_{0,1,2,3} - T_{0,1,2,3} \Big) \tilde{B}^*_1 \tilde{B}_2 \tilde{B}_3 \delta_{0+1-2-3} \exp[i(\omega + \omega_1 - \omega_2 - \omega_3)t] \\
& + \tilde{T}^{(3)}_{0,1,2,3} \tilde{B}^*_1 \tilde{B}^*_2 \tilde{B}_3 \delta_{0+1+2-3} \exp[i(\omega + \omega_1 + \omega_2 - \omega_3)t] \\
& + \tilde{T}^{(4)}_{0,1,2,3} \tilde{B}^*_1 \tilde{B}^*_2 \tilde{B}^*_3 \delta_{0+1+2+3} \exp[i(\omega + \omega_1 + \omega_2 + \omega_3)t] \Big\} \\
& \cdot d\mathbf{k}_1 \, d\mathbf{k}_2 \, d\mathbf{k}_3 \, . \qquad (14.3.10)
\end{aligned}
$$

Note that with this splitting (14.3.10) can be integrated with respect to t without difficulty.

Also, we can add to $T_{0,1,2,3}$ in (14.3.9) a term of the form

$$(\omega + \omega_1 - \omega_2 - \omega_3) B_{0,1,2,3}$$

where $B_{0,1,2,3}$ is given in Appendix 14.B, without loss of generality. We remark further that, under exact resonance conditions, i.e., when the right-hand side of the second equation in (14.3.7) equals zero, $T_{0,1,2,3}$ satisfies additional symmetries

$$T_{0,1,2,3} = T_{1,0,2,3} = T_{2,3,0,1} \, . \qquad (14.3.11)$$

For near resonance, we can define a new kernel which possesses the above symmetries,

$$\hat{T}_{0,1,2,3} = \frac{1}{4} (T_{0,1,2,3} + T_{1,0,2,3} + T_{2,3,0,1} + T_{3,2,0,1}) \, . \qquad (14.3.12)$$

It can be shown that

$$\hat{T}_{0,1,2,3} = T_{0,1,2,3} + (\omega + \omega_1 - \omega_2 - \omega_3) B_{0,1,2,3} \, . \qquad (14.3.13)$$

Equation (14.3.9), either with T or with the symmetric $\hat{T}$, is called *Zakharov's equation*. Since only the slow time is involved, we shall write t instead of t_2 from here on for the sake of brevity.

With the symmetric kernel $\hat{T}_{0,1,2,3}$ (14.3.12) in Zakharov's equation (14.3.9), one can derive the following three integrals of motion, related to the conservation of energy, momentum, and wave-action, respectively,

$$
\begin{aligned}
H = & \int_{-\infty}^{\infty} \omega |\tilde{B}|^2 \, d\mathbf{k} + \frac{1}{2} \iiiint_{-\infty}^{\infty} \hat{T}_{0,1,2,3} \tilde{B}^* \tilde{B}^*_1 \tilde{B}_2 \tilde{B}_3 \delta_{0+1-2-3} \\
& \cdot \exp[i(\omega + \omega_1 - \omega_2 - \omega_3)t] \, d\mathbf{k} \, d\mathbf{k}_1 \, d\mathbf{k}_2 \, d\mathbf{k}_3 \qquad (14.3.14)
\end{aligned}
$$

$$\mathbf{M} = \int_{-\infty}^{\infty} \mathbf{k}|\tilde{B}|^2 \, d\mathbf{k} \tag{14.3.15}$$

$$\mathcal{A} = \int_{-\infty}^{\infty} |\tilde{B}|^2 \, d\mathbf{k} \, . \tag{14.3.16}$$

Krasitski (1994), who used a Hamiltonian approach to derive (14.3.9) and these integrals, maintains that the very existence of the above conservation laws indicates the superiority of $\hat{T}_{0,1,2,3}$ over $T_{0,1,2,3}$. In the balance of this chapter we will use $\hat{T}_{0,1,2,3}$, but drop the "hat" for the sake of brevity.

14.4 Conditions for Quartet Resonance

The importance of four-wave resonance in Zakharov's equation can be clearly seen from (14.3.9) and (14.3.8). In this section we demonstrate how to calculate the Phillips' quartet. Mathematically, for given $\mathbf{k}_0, \mathbf{k}_1$, we need to find $\mathbf{k}_2, \mathbf{k}_3$ which satisfy

$$\mathbf{k}_0 + \mathbf{k}_1 = \mathbf{k}_2 + \mathbf{k}_3 \tag{14.4.1}$$

and

$$\omega_0 + \omega_1 = \omega_2 + \omega_3 \, . \tag{14.4.2}$$

For simplicity we restrict the discussion to deep-water waves, for which the dispersion relation is

$$\omega^2 = g|\mathbf{k}| \, . \tag{14.4.3}$$

Note that besides $\mathbf{k}_0$ and $\mathbf{k}_1$, we have an *additional free parameter*, since (14.4.1) and (14.4.2) provide three scalar equations for the four scalar components of $\mathbf{k}_2$ and $\mathbf{k}_3$; i.e., for $k_{2,x}$, $k_{2,y}$, $k_{3,x}$, $k_{3,y}$.

For the sake of clarity, we switch from the original coordinate system (x, y) to an auxiliary system $(\tilde{x}, \tilde{y})$, for which the coordinate $\tilde{x}$ is chosen in the direction of the vector $\mathbf{k}_0 + \mathbf{k}_1$, as shown in Fig. 14.1($a$), where the length $\overline{AC} = k_{0,\tilde{x}} + k_{1,\tilde{x}}$. We have chosen to write the wavenumbers $\mathbf{k}_2$ and $\mathbf{k}_3$ in the auxiliary system in terms of the dimensionless variables (p, q):

$$\mathbf{k}_2 = \frac{1}{2}(k_{0,\tilde{x}} + k_{1,\tilde{x}})\{1+p, q\} = \frac{\overline{AC}}{2}\{1+p, q\} = \frac{\omega_{0+1}^2}{2g}\{1+p, q\} \, , \tag{14.4.4}$$

$$\mathbf{k}_3 = \frac{1}{2}(k_{0,\tilde{x}} + k_{1,\tilde{x}})\{1-p, -q\} = \frac{\overline{AC}}{2}\{1-p, -q\} = \frac{\omega_{0+1}^2}{2g}\{1-p, -q\} \, . \tag{14.4.5}$$

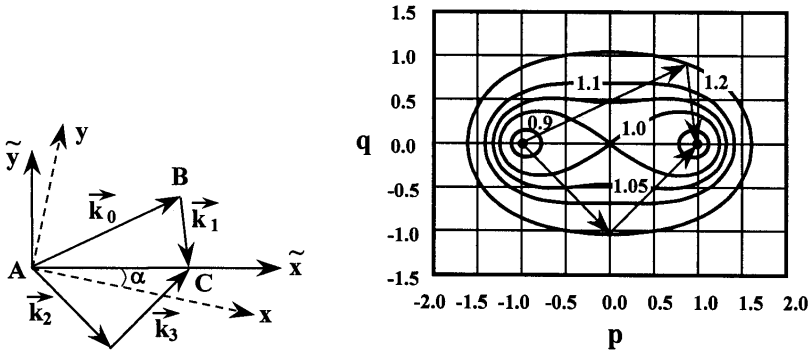

(*a*) (*b*)

Figure 14.1: Quartet resonance. (*a*) The original wavenumber vectors and definition of two coordinate systems (the original system x, y is arbitrary and the orientation of $\tilde{x}, \tilde{y}$ is dictated by the direction of $\mathbf{k}_0 + \mathbf{k}_1$); (*b*) Resonance curves for deep water waves (wavenumber vectors are normalized by $\frac{1}{2}|\mathbf{k}_0 + \mathbf{k}_1|$).

Equations (14.4.4) and (14.4.5) guarantee the fulfillment of (14.4.1). Similarly we write ω_2, ω_3 in terms of the dimensionless Ω:

$$\omega_2 = \frac{1}{2}(\omega_0 + \omega_1) + \frac{\omega_{0+1}}{\sqrt{2}}\Omega = \frac{\omega_{0+1}}{\sqrt{2}}(I + \Omega)\,, \tag{14.4.6}$$

$$\omega_3 = \frac{1}{2}(\omega_0 + \omega_1) - \frac{\omega_{0+1}}{\sqrt{2}}\Omega = \frac{\omega_{0+1}}{\sqrt{2}}(I - \Omega)\,, \tag{14.4.7}$$

where the value of

$$I = (\omega_0 + \omega_1)/\sqrt{2}\omega_{0+1} \tag{14.4.8}$$

is defined by $\mathbf{k}_0$ and $\mathbf{k}_1$.

We express ω_2, ω_3 in (14.4.6) and (14.4.7) in a way so that (14.4.2) is satisfied. From (14.4.8) and (14.4.3) it is clear that $I \in (1/\sqrt{2}, \infty)$. We choose

$$\Omega = |\omega_2 - \omega_3|/\sqrt{2}\omega_{0+1} \tag{14.4.9}$$

as the *additional free parameter*.

From Fig. 14.1(*a*), one can see that $k_{2,\tilde{y}}^2 = k_{3,\tilde{y}}^2$, which can be written as

$$\frac{\omega_2^4}{g^2} - k_{2,\tilde{x}}^2 = \frac{\omega_3^4}{g^2} - k_{3,\tilde{x}}^2\,. \tag{14.4.10}$$

Equations (14.4.4)–(14.4.7) are now substituted into (14.4.10) to yield

$$p = \pm 2I\Omega(I^2 + \Omega^2)\,. \tag{14.4.11}$$

In the relation

$$k_{2,\tilde{y}} = \frac{\omega_2^4}{g^2} - k_{2,\tilde{x}}^2 \tag{14.4.12}$$

(14.4.4) and (14.4.6) can be used to give

$$q = \pm\sqrt{(I+\Omega)^4 - [1 + 2I\Omega\,(I^2+\Omega^2)]^2}\,. \tag{14.4.13}$$

Note that (14.4.11) and (14.4.13) fix (p, q) in terms of I and Ω. From (14.4.13) it can be seen that the range of the free parameter Ω is restricted by

$$\Omega \in \begin{cases} (\sqrt{1-I^2}, 1/2I)\,, & \text{for} \quad I \le 1 \\ (0, 1/2I)\,, & \text{for} \quad I > 1\,. \end{cases} \tag{14.4.14}$$

From Fig. 14.1(a), one can also see that

$$\sin\alpha = (k_{0,y} + k_{1,y})/\overline{AC}\,, \quad \cos\alpha = (k_{0,x} + k_{1,x})/\overline{AC}\,. \tag{14.4.15}$$

The coordinate rotation gives, for any vector $\mathbf{k}$, the relations:

$$k_x = k_{\tilde{x}}\cos\alpha - k_{\tilde{y}}\sin\alpha \tag{14.4.16}$$

$$k_y = k_{\tilde{x}}\sin\alpha + k_{\tilde{y}}\cos\alpha\,. \tag{14.4.17}$$

Applying (14.4.16) and (14.4.17) for $\mathbf{k}_2$ and $\mathbf{k}_3$ and substituting from (14.4.4)–(14.4.5) and (14.4.15), we finally obtain

$$\mathbf{k}_2 = \frac{1}{2}\{(1+p)(k_{0,x}+k_{1,x}) - q(k_{0,y}+k_{1,y}); (1+p)(k_{0,y}+k_{1,y}) + q(k_{0,x}+k_{1,x})\}\,, \tag{14.4.18}$$

$$\mathbf{k}_3 = \frac{1}{2}\{(1-p)(k_{0,x}+k_{1,x}) + q(k_{0,y}+k_{1,y}); (1-p)(k_{0,y}+k_{1,y}) - q(k_{0,x}+k_{1,x})\}\,, \tag{14.4.19}$$

in the original coordinate system (x, y) in the terms of the vectors $\mathbf{k}_0, \mathbf{k}_1$ and (p, q).

In Fig. 14.1(b) we plot the curves of constant I in the (p, q) plane; the parameter Ω varies along each curve. Beginning from the two focal points $(p = \pm 1, q = 0)$, any pair of vectors $\mathbf{k}_0, \mathbf{k}_1$ which meet at a point on a curve

of constant I are in resonance with another pair $\mathbf{k}_2, \mathbf{k}_3$, meeting at any point on the same curve. The figure-of-eight curve (for $\mathbf{k}_0 = \mathbf{k}_1$, i.e., $I = 1$) is of particular interest, due to its relevance to the sideband stability of Stokes waves. It also separates the two domains indicated in (14.4.14).

14.5 Simple Solutions

The simplest solution of Zakharov's equation (14.3.9) is that for a Stokes wave in deep water with the wavenumber $\mathbf{k}_0 = (k_0, 0)$. Let the solution be of the form

$$\tilde{B}(\mathbf{k}, t) = b(t)\delta(\mathbf{k} - \mathbf{k}_0)\,. \tag{14.5.1}$$

It follows from Zakharov's equation that

$$i\frac{\partial b}{\partial t} = T_{0,0,0,0}|b|^2 b\,.$$

The solution is

$$b = B_0 \exp(-iT_{0,0,0,0}|B_0|^2 t)\,.$$

It can be shown that

$$T_{0,0,0,0} = T(\mathbf{k}_0, \mathbf{k}_0, \mathbf{k}_0, \mathbf{k}_0) = |\mathbf{k}_0|^3/4\pi^2 = k_0^3/4\pi^2\,. \tag{14.5.2}$$

Recall that the free-surface displacement ζ at the leading order is

$$\zeta = \frac{1}{2\pi}\int_{-\infty}^{\infty}\left(\frac{\omega(\mathbf{k})}{2g}\right)^{1/2}\{\tilde{B}(\mathbf{k}, t)\, e^{i[\mathbf{k}\cdot\mathbf{x} - \omega(\mathbf{k})t]} + *\}d\mathbf{k}\,, \tag{14.5.3}$$

hence

$$\zeta = \frac{1}{2\pi}\sqrt{\frac{\omega_0}{2g}}\{B_0 \exp[i(k_0 x - \omega_0 t - k_0^3|B_0|^2 t/4\pi^2)] + *\}\,. \tag{14.5.4}$$

Defining

$$\frac{1}{2\pi}\sqrt{\frac{\omega_0}{2g}}B_0 = \frac{a_0}{2} \tag{14.5.5}$$

so that a_0 is the surface-wave amplitude, we get

$$\tilde{B}(\mathbf{k}, t) = 2\pi a_0\sqrt{\frac{\omega_0}{2k_0}}e^{-i\omega_0(a_0 k_0)^2 t/2}\delta(\mathbf{k} - \mathbf{k}_0) \tag{14.5.6}$$

and

$$\zeta = a_0 \cos\left(k_0 x - \omega_0 t - \frac{1}{2}\omega_0 a_0^2 k_0^2 t\right) \tag{14.5.7}$$

where $\omega_0 = (gk_0)^{1/2}$ is used.

The surface potential is given to the leading order by

$$\phi^s = \frac{-i}{2\pi}\int_{-\infty}^{\infty}\left(\frac{g}{2\omega(\mathbf{k})}\right)^{1/2}\{\tilde{B}(\mathbf{k},t)\, e^{i[\mathbf{k}\cdot\mathbf{x}-\omega(\mathbf{k})t]} - *\}\, d\mathbf{k}\,, \tag{14.5.8}$$

or,

$$\phi^s = a_0\frac{\omega_0}{k_0}\sin\left(k_0 x - \omega_0 t - \frac{1}{2}\omega_0 a_0^2 k_0^2 t\right). \tag{14.5.9}$$

The Stokes-wave frequency now depends on the amplitude

$$\omega = \omega_0\left(1 + \frac{1}{2}a_0^2 k_0^2\right), \tag{14.5.10}$$

as found in Chapter 13.

Another simple solution is that for the standing wave with amplitude a_0:

$$\tilde{B}(\mathbf{k},t) = \pi a_0\sqrt{\frac{\omega_0}{2k_0}}e^{+i\omega_0(a_0k_0)^2 t/8}\{\delta(\mathbf{k}-\mathbf{k}_0) + \delta(\mathbf{k}+\mathbf{k}_0)\}\,. \tag{14.5.11}$$

It can be verified that

$$\begin{aligned} T(\mathbf{k}_0,\mathbf{k}_0,\mathbf{k}_0,\mathbf{k}_0) &= T(-\mathbf{k}_0,-\mathbf{k}_0,-\mathbf{k}_0,-\mathbf{k}_0) \\ &= -T(\mathbf{k}_0,-\mathbf{k}_0,\mathbf{k}_0,-\mathbf{k}_0) \\ &= k_0^3/4\pi^2\,. \end{aligned} \tag{14.5.12}$$

The free-surface elevation is obtained by substituting (14.5.11) into (14.5.3).

$$\zeta = a\cos(k_0 x)\cos(\omega_0 t - \omega_0 k_0^2 a_0^2 t/8) \tag{14.5.13}$$

so that Stokes' corrected frequency for a standing wave is

$$\omega = \omega_0\left(1 - \frac{1}{8}a_0^2 k_0^2\right). \tag{14.5.14}$$

Second-order terms for the progressive and standing waves can be obtained by substituting (14.5.6) and (14.5.11) into (14.3.3), respectively.

14.6 Interaction of Two Waves

We consider the interaction of two weakly nonlinear wavetrains in any two directions, denoted by subscripts a and b. By taking

$$\tilde{B}(\mathbf{k},t) = B_a(t)\delta(\mathbf{k}-\mathbf{k}_a) + B_b(t)\delta(\mathbf{k}-\mathbf{k}_b) \tag{14.6.1}$$

and substituting (14.6.1) into (14.3.9), we find

$$i\frac{dB_a}{dt} = T_{a,a,a,a}|B_a|^2B_a + \{T_{a,b,a,b} + T_{a,b,b,a}\}|B_b|^2B_a \tag{14.6.2}$$

$$i\frac{dB_b}{dt} = T_{b,b,b,b}|B_b|^2B_b + \{T_{b,a,b,a} + T_{b,a,a,b}\}|B_a|^2B_b\,. \tag{14.6.3}$$

In what follows, we denote $T_{a.a.a.a}$ by T_a and $T_{b,b,b,b}$ by T_b for brevity. The symmetry properties of $T_{0,1,2,3}$, (14.3.11), allows us to write both expressions in the curly brackets of (14.6.2) and (14.6.3) as $2T_{a,b,a,b}$, which will be denoted by $2T_{a,b}$. The solution of the pair of ordinary differential equations (14.6.2) and (14.6.3) is given by

$$B_a(t) = A_a \exp\{-i(T_aA_a^2 + 2T_{a,b}A_b^2)t\} \tag{14.6.4}$$

$$B_b(t) = A_b \exp\{-i(T_bA_b^2 + 2T_{a,b}A_a^2)t\}\,. \tag{14.6.5}$$

We now substitute (14.6.1), (14.6.4) and (14.6.5) in (14.5.3) and write the result in the form

$$\zeta(\mathbf{x},t) = a_a\cos(\mathbf{k_a}\cdot\mathbf{x} - \Omega_a t) + a_b\cos(\mathbf{k_b}\cdot\mathbf{x} - \Omega_b t) \tag{14.6.6}$$

where a_a and a_b represent the amplitudes of the two wavetrains, and are related to the constants A_a and A_b by

$$\begin{aligned} A_0 &= 2\pi\left(\frac{\omega_a}{2k_a}\right)^{1/2} a_a\,, \\ A_b &= 2\pi\left(\frac{\omega_b}{2k_b}\right)^{1/2} a_b\,. \end{aligned} \tag{14.6.7}$$

The frequencies of the wavetrains are given by

$$\Omega_a = \omega_a + T_aA_a^2 + 2T_{a,b}A_b^2 \tag{14.6.8}$$

$$\Omega_b = \omega_b + T_bA_b^2 + 2T_{a,b}A_a^2\,. \tag{14.6.9}$$

Clearly this result is just an extension of Stokes waves theory. The primary effect of nonlinearity is to change the frequencies. The change is composed

of two parts. Take wavetrain b for example. In (14.6.9), the first correction to ω_b is

$$T_b A_b^2 = \frac{k_b^3}{4\pi^2} \cdot 4\pi^2 \frac{\omega_b}{2k_b} a_b^2$$
$$= \frac{1}{2}\omega_b (k_b a_b)^2 , \tag{14.6.10}$$

which is the Stokes correction [cf. (14.5.10)] due to the nonlinearity of the wavetrain itself and is present even if the other wavetrain is absent. The second correction in (14.6.9) is given by $2T_{a,b}A_a^2$ and is entirely due to the presence of the other wavetrain. It is of the same order as the usual Stokes correction. For more details, see Hogan et al. (1988).

14.7 Interaction of Four Waves (Quartet Interaction)

In this section we study the evolution of wave fields which consist of a resonating quartet of free waves, all in deep water, so that

$$\tilde{B}(\mathbf{k}, t) = B_a(t)\delta(\mathbf{k} - \mathbf{k}_a) + B_b(t)\delta(\mathbf{k} - \mathbf{k}_b)$$
$$+ B_c(t)\delta(\mathbf{k} - \mathbf{k}_c) + B_d(t)\delta(\mathbf{k} - \mathbf{k}_d) \tag{14.7.1}$$

where

$$\mathbf{k}_a + \mathbf{k}_b - \mathbf{k}_c - \mathbf{k}_d = 0 \tag{14.7.2}$$

$$\omega_a + \omega_b - \omega_c - \omega_d = \Delta_{a,b,c,d}\,; \quad \omega_j = (g|\mathbf{k}_j|)^{1/2} . \tag{14.7.3}$$

Substitution of (14.7.1) into (14.3.9) under the constraint (14.7.2) gives a system of four first-order nonlinear ordinary differential equations:

$$i\frac{dB_a}{dt} = (\Omega_a - \omega_a)B_a + 2T_{abcd}\, e^{i\Delta_{a,b,c,d}t} B_b^* B_c B_d \tag{14.7.4}$$

$$i\frac{dB_b}{dt} = (\Omega_b - \omega_b)B_b + 2T_{abcd}\, e^{i\Delta_{a,b,c,d}t} B_a^* B_c B_d \tag{14.7.5}$$

$$i\frac{dB_c}{dt} = (\Omega_c - \omega_c)B_c + 2T_{abcd}\, e^{-i\Delta_{a,b,c,d}t} B_d^* B_a B_b \tag{14.7.6}$$

$$i\frac{dB_d}{dt} = (\Omega_d - \omega_c)B_d + 2T_{abcd}\, e^{-i\Delta_{a,b,c,d}t} B_c^* B_a B_b \tag{14.7.7}$$

where the Stokes-corrected frequencies are:

$$\Omega_a = \omega_a + T_{aaaa}|B_a|^2 + 2T_{abab}|B_b|^2 + 2T_{acac}|B_c|^2 + 2T_{adad}|B_d|^2 \tag{14.7.8}$$

$$\Omega_b = \omega_b + 2T_{babc}|B_a|^2 + T_{bbbb}|B_b|^2 + 2T_{bcbc}|B_c|^2 + 2T_{bdbd}|B_d|^2 \tag{14.7.9}$$

$$\Omega_c = \omega_c + 2T_{caca}|B_a|^2 + 2T_{cbcb}|B_c|^2 + T_{cccc}|B_c|^2 + 2T_{cdcd}|B_d|^2 \tag{14.7.10}$$

$$\Omega_d = \omega_d + 2T_{dada}|B_a|^2 + 2T_{dbdb}|B_d|^2 + 2T_{cdcd}|B_c|^2 + T_{dddd}|B_d|^2 \,. \tag{14.7.11}$$

These equations have been derived by the multiple-scales method by Benney (1962). The solution to be described below for periodic envelopes follows Bretherton (1964).

14.7.1 Reduction to One Unknown

Multiplying (14.7.4), (14.7.5), (14.7.6) and (14.7.7) by B_a^*, B_b^*, B_c^* and B_d^*, respectively, and substracting their complex conjugates, we obtain

$$\frac{d}{dt}|B_a|^2 = \frac{d}{dt}|B_b|^2 = -\frac{d}{dt}|B_c|^2 = -\frac{d}{dt}|B_d|^2 = 4T_{abcd}\,\mathrm{Im}\{B_a^* B_b^* B_c B_d\, e^{i\Delta_{a,b,c,d}t}\}\,. \tag{14.7.12}$$

An auxiliary real function $Z(t)$ is defined by

$$\frac{dZ}{dt} = \mathrm{Im}\{B_a^* B_b^* B_c B_d\, e^{i\Delta_{a,b,c,d}t}\}\,, \quad Z(0) = 0\,. \tag{14.7.13}$$

Substituting (14.7.13) into (14.7.12) and integrating, we get

$$|B_a|^2 - |\beta_a|^2 = |B_b|^2 - |\beta_b|^2 = -|B_c|^2 + |\beta_c|^2 = -|B_d|^2 + |\beta_d|^2 = 4T_{abcd}Z \tag{14.7.14}$$

where $\beta_j = B_j(0)$.

Using the rule for the derivative of a product and Eqs. (14.7.4) to (14.7.7), we obtain

$$\begin{aligned}
&\frac{d}{dt}\{B_a^* B_b^* B_c B_d\, e^{i\Delta_{a,b,c,d}t}\} \\
&\quad = i\{\Omega_a - \omega_a + \Omega_b - \omega_b - \Omega_c + \omega_c - \Omega_d - \omega_d\} B_a^* B_b^* B_c B_d\, e^{i\Delta_{a,b,c,d}t} \\
&\qquad + 2iT_{abcd}\{|B_a|^2|B_c|^2|B_d|^2 + |B_b|^2|B_c|^2|B_d|^2 - |B_a|^2|B_b|^2|B_c|^2 \\
&\qquad - |B_a|^2|B_b|^2|B_d|^2\} + i\Delta_{a,b,c,d} B_a^* B_b^* B_c B_d\, e^{i\Delta_{a,b,c,d}t}\,. \qquad (14.7.15)
\end{aligned}$$

We can now substitute (14.7.3) into (14.7.15) and denote

$$\Omega = \Omega_a + \Omega_b - \Omega_c - \Omega_d \qquad (14.7.16)$$

so that

$$\begin{aligned}
&\frac{d}{dt}\{B_a^* B_b^* B_c B_d\, e^{i\Delta_{a,b,c,d}t}\} \\
&\quad = i\Omega\{B_a^* B_b^* B_c B_d\, e^{i\Delta_{a,b,c,d}t}\} \\
&\qquad + 2iT_{abcd}\{|B_a|^2|B_c|^2|B_d|^2 + |B_b|^2|B_c|^2|B_d|^2 \\
&\qquad - |B_a|^2|B_b|^2|B_c|^2 - |B_a|^2|B_b|^2|B_d|^2\}\,. \qquad (14.7.17)
\end{aligned}$$

In view of the definition (14.7.13), the real part of both sides of (14.7.17) gives

$$\frac{d}{dt}\,\mathrm{Re}\,\{B_a^* B_b^* B_c B_d\, e^{i\Delta_{a,b,c,d}t}\} = -\Omega\frac{dZ}{dt}\,. \qquad (14.7.18)$$

Equation (14.7.14) enables us to write (14.7.16) as

$$\Omega = \Omega_0 + \Omega_1 Z \qquad (14.7.19)$$

where

$$\begin{aligned}
\Omega_0 = {}& \Delta_{a,b,c,d} + (T_{aaaa} + 2T_{abab} - T_{acac} - 2T_{adad})|\beta_a|^2 \\
&+ (2T_{abab} + T_{bbbb} - 2T_{bcbc} - 2T_{bdbd})|\beta_b|^2 \\
&+ (2T_{caca} + 2T_{cbcb} - T_{cccc} - 2T_{cdcd})|\beta_c|^2 \\
&+ (2T_{dada} + 2T_{dbdb} - 2T_{dcdc} - T_{dddd})|\beta_d|^2 \qquad (14.7.20)
\end{aligned}$$

and

$$\Omega_1 = 4T_{abcd}\{T_{aaaa} + T_{bbbb} + T_{cccc} + T_{dddd} + 4T_{abab} - 4T_{acac} - 4T_{adad} - 4T_{bcbc} - 4T_{bdbd} + 4T_{cdcd}\}\,. \tag{14.7.21}$$

Let us integrate (14.7.18) from $t = 0$ to give

$$\mathrm{Re}\,\{B_a^* B_b^* B_c B_d\, e^{i\Delta_{a,b,c,d}t}\} = \mathrm{Re}\,\{\beta_a^*\beta_b^*\beta_c\beta_d\, e^{i\Delta_{a,b,c,d}t}\} - \int_0^z \Omega\, dZ\,. \tag{14.7.22}$$

From (14.7.13) and (14.7.22) we get

$$\left\{\frac{dZ}{dt}\right\}^2 = |B_a|^2|B_b|^2|B_c|^2|B_d|^2 - \left[\mathrm{Re}\,\{\beta_a^*\beta_b^*\beta_c\beta_d\} - \Omega_0 Z - \frac{\Omega_1}{2}Z^2\right]^2 \tag{14.7.23}$$

which can be rewritten as

$$\left(\frac{dZ}{dt}\right)^2 = P_4(Z) = \sum_{\ell=0}^{4} a_\ell Z^{4-\ell} \tag{14.7.24}$$

where the coefficients of the fourth-order polynomial are

$$a_0 = -\frac{1}{4}\Omega_1^2 + 256T_{abcd}^4 \tag{14.7.25}$$

$$a_1 = -\Omega_0\Omega_1 + 64T_{abcd}^4(|\beta_a|^2 + |\beta_b|^2 - |\beta_c|^2 - |\beta_d|^2) \tag{14.7.26}$$

$$a_2 = -\Omega_0^2 + \Omega_1|\beta_a\beta_b\beta_c\beta_d|\cos(\arg\beta_a + \arg\beta_b - \arg\beta_c - \arg\beta_d) + 16T_{abcd}^2(|\beta_a\beta_b|^2 - |\beta_a\beta_c|^2 - |\beta_a\beta_d|^2 - |\beta_b\beta_c|^2 - |\beta_b\beta_d|^2 + |\beta_c\beta_d|^2) \tag{14.7.27}$$

$$a_3 = 2\Omega_0(|\beta_a\beta_b\beta_c\beta_d|\cos(\arg\beta_a + \arg\beta_b - \arg\beta_c - \arg\beta_d) - 4T_{abcd}(|\beta_a\beta_b\beta_c|^2 + |\beta_a\beta_b\beta_d|^2 - |\beta_a\beta_c\beta_d|^2 - |\beta_b\beta_c\beta_d|^2) \tag{14.7.28}$$

$$a_4 = |\beta_a\beta_b\beta_c\beta_d|^2\sin^2(\arg\beta_a + \arg\beta_b - \arg\beta_c - \arg\beta_d)\,. \tag{14.7.29}$$

14.7.2 Solution for Periodic Envelopes

The formal solution of (14.7.24) is

$$t = \int_0^Z \frac{dZ}{\sqrt{P_4(Z)}}\,. \tag{14.7.30}$$

The details depend on the number and values of the real roots of the polynomial. In principle, various scenarios may exist. However, for the example at hand, the polynomial P_4 has four real roots, $z_4 > z_3 > 0 > z_2 > z_1$, and $a_0 > 0$. The solution can be expressed in terms of elliptic functions. Applying a known property of elliptic functions [see formula (255.00) in Byrd and Friedman (1971)] to Eq. (14.7.30), we obtain

$$a_0^{1/2} t = \gamma \left\{ \mathrm{sn}^{-1}\left(\sqrt{\frac{(z_4 - z_2)(z_3 - z)}{(z_3 - z_2)(z_4 - z)}},\ \kappa \right) + \mathrm{sn}^{-1}(\delta, \kappa) \right\} \tag{14.7.31}$$

where sn is the Jacobian elliptic function with modolus

$$\kappa = \sqrt{\frac{(z_3 - z_2)(z_4 - z_1)}{(z_4 - z_2)(z_3 - z_1)}} \tag{14.7.32}$$

and

$$\gamma = \sqrt{\frac{2}{(z_4 - z_2)(z_3 - z_1)}}\,, \quad \delta = \sqrt{\frac{z_3(z_4 - z_2)}{z_4(z_3 - z_2)}}\,. \tag{14.7.33}$$

It follows by inverting (14.7.31) that

$$\begin{aligned} Z &= \frac{z_4(z_3 - z_2)\ \mathrm{sn}^2 u - z_3(z_4 - z_2)}{(z_3 - z_2)\ \mathrm{sn}^2 u - (z_4 - z_2)}\,; \\ u &= \mathrm{sn}^{-1}(\delta, \kappa) - a_0^{1/2} t/\gamma\,. \end{aligned} \tag{14.7.34}$$

Utilizing known formulas [(123.01) and (131.01) in Byrd and Friedman (1971)], we obtain

$$\mathrm{sn}(u, \kappa) = \frac{\delta \mathrm{cn}(a_0^{1/2} t/\gamma)\mathrm{dn}(a_0^{1/2} t/\gamma) + s[(1 - \delta^2)(1 - \kappa^2\delta^2)]^{1/2}\mathrm{sn}(a_0^{1/2} t/\gamma)}{1 - (\kappa\delta)^2 \mathrm{sn}^2(a_0^{1/2} t/\gamma)}, \tag{14.7.35}$$

where

$$s = \mathrm{sgn}(\sin\theta) \tag{14.7.36}$$

and

$$\theta = -\arg\beta_a - \arg\beta_b + \arg\beta_c + \arg\beta_d\,. \tag{14.7.37}$$

Note that the amplitudes $|B_j|,\ j = a, b, c, d$ in (14.7.14) depend on Z and are periodic, with the period

$$T = 2\int_{z_2}^{z_3} dZ/\sqrt{P_4} = \frac{2\gamma}{a_0^{1/2}}\mathrm{sn}^{-1}(1,\kappa) = \frac{2\gamma}{a_0^{1/2}}K(\kappa) \tag{14.7.38}$$

where K is the complete elliptic integral of first kind.

In Fig. 14.2 we show the computed evolution of the nondimensional wave amplitudes $k_a a_a,\ k_a a_b,\ k_a a_c$, and $k_a a_d$ as a function of time t/T_a, where T_a is the period of wave a. The amplitudes a_j are related to the variable B_j through

$$a_j = \frac{1}{\pi}\left(\frac{\omega_j}{2g}\right)^{1/2}|B_j|\,. \tag{14.7.39}$$

For illustration, we fix the wavenumbers $\mathbf{k}_a = (0.9806, -0.1961)$ and $\mathbf{k_b} = (0.9806, 0.1961)$ in all three cases, and the initial steepness and phases of all four waves. The chosen initial conditions are

$$\begin{aligned} k_a a_a &= 0.2\,, \quad k_b a_b = 0.15\,, \\ k_c a_c &= 0.08\,, \quad k_d a_d = 0.03 \end{aligned} \tag{14.7.40}$$

and

$$\begin{aligned} \arg\beta_a &= \pi/6\,, \quad \arg\beta_b = 0\,, \\ \arg\beta_c &= -\pi/6\,, \quad \arg\beta_d = 0\,. \end{aligned} \tag{14.7.41}$$

The wavenumbers in Fig. 14.2(a) have been chosen to give exact resonance with $\mathbf{k_c} = (1.2902,\ 0.2747)$ and $\mathbf{k}_d = (0.6709,\ -0.2747)$. The conditions in Figs. 14.2(b) correspond to near-resonance and weak-resonance, respectively. Specifically, in Fig. 14.2(b), $\mathbf{k}_c = (1.1767,\ 0.1961)$, $\mathbf{k}_d = (0.7845,\ -0.1961)$, and the detuning $[\omega_a + \omega_b - \omega_c - \omega_d]/\omega_a = 0.0086$; whereas in Fig. 14.2($c$), $\mathbf{k}_c = (1.3728,\ 0.4903)$, $\mathbf{k}_d = (0.5883,\ -0.4903)$,

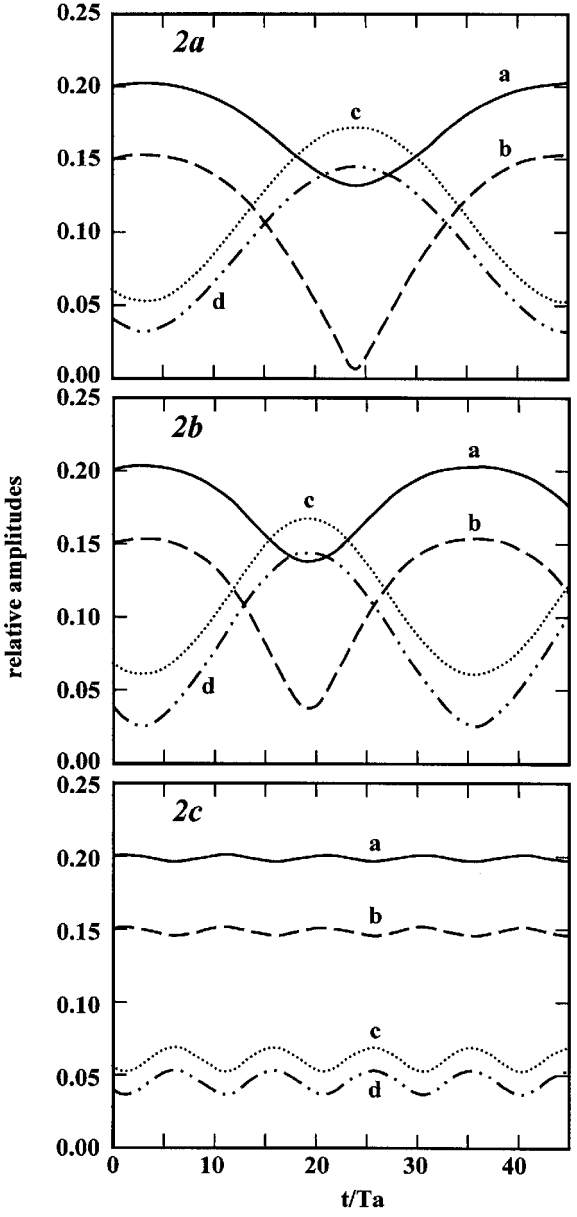

Figure 14.2: Slow evolution of wave amplitudes for four waves in resonant interaction: (a) exact resonance; (b) near-resonance; (c) far from resonance.

and the detuning is -0.083. The periodic nature of the evolution is evident. The evolution periods and the intensity of nonlinear interaction are seen to diminish when the system moves away from resonance.

14.8 The Cubic Schrödinger Equation

As shown by Zakharov (1968), the cubic Schrödinger equation discussed in Chapter 13 for narrow-banded seas is a special case of (14.3.9) with energy concentrated around $\mathbf{k} = \mathbf{k}_0 = (k_0, 0)$. Let all wavenumbers be rewritten as

$$\mathbf{k} = \mathbf{k}_0 + \mathbf{m} \tag{14.8.1}$$

with

$$\mathbf{m} = (m, \lambda)\,, \quad |\mathbf{m}|/k_0 \ll 1\,. \tag{14.8.2}$$

We now introduce a new spectral amplitude

$$A(\mathbf{m}, t) = \tilde{B}(\mathbf{k}, t) \exp\{-i[\omega(\mathbf{k}) - \omega(\mathbf{k}_0)]t\} \tag{14.8.3}$$

first in (14.3.9)

$$\begin{aligned} i\frac{\partial A(\mathbf{m}, t)}{\partial t} &- [\omega(\mathbf{k}) - \omega(\mathbf{k}_0)]A(\mathbf{m}, t) \\ &= \iiint_{-\infty}^{\infty} T(\mathbf{k}_0 + \mathbf{m}, \mathbf{k}_0 + \mathbf{m}_1, \mathbf{k}_0 + \mathbf{m}_2, \mathbf{k}_0 + \mathbf{m}_3) \\ &\quad \cdot A^*(\mathbf{m}_1)A(\mathbf{m}_2)A(\mathbf{m}_3)\delta(\mathbf{m} + \mathbf{m}_1 - \mathbf{m}_2 - \mathbf{m}_3)\, d\mathbf{m}_1\, d\mathbf{m}_2\, d\mathbf{m}_3\,, \end{aligned} \tag{14.8.4}$$

and next in (14.5.3)

$$\begin{aligned} \zeta(x, t) = \frac{1}{2\pi}&\left(\frac{\omega(\mathbf{k}_0)}{2g}\right)^{1/2} \\ &\cdot \left\{ e^{i[k_0 x - \omega(k_0)t]} \int_{-\infty}^{\infty} \left(1 + \frac{m}{4k_0}\right) A(\mathbf{m}, t) e^{i\mathbf{m}\cdot x}\, d\mathbf{m} + * \right\}. \end{aligned} \tag{14.8.5}$$

The last equation is rewritten as

$$\zeta(x, t) = \mathrm{Re}\,\{a(x, t)e^{i[k_0 x - \omega(\mathbf{k}_0)t]}\} \tag{14.8.6}$$

where $a(x,t)$ is given by the following Fourier transform

$$a(x,t) = \left(\frac{2\omega(\mathbf{k}_0)}{g}\right)^{1/2} \frac{1}{2\pi} \int_{-\infty}^{\infty} \left(1 + \frac{m}{4k_0}\right) A(\mathbf{m},t) e^{i\mathbf{m}\cdot x}\, d\mathbf{m}\,. \qquad (14.8.7)$$

Let us approximate, for deep water only, the frequency difference $\omega(\mathbf{k}) - \omega(\mathbf{k}_0)$ on the left of (14.8.4) by Taylor expansion in powers of the spectral width

$$\omega(\mathbf{k}) - \omega(\mathbf{k}_0) = \frac{1}{2}\left(\frac{g}{k_0}\right)^{1/2} \left[m - \frac{m^2}{4k_0} + \frac{\lambda^2}{2k_0} + O\left(\frac{|\mathbf{m}|^3}{k_0^3}\right)\right], \qquad (14.8.8)$$

see (14.8.2).

It follows by mulitplying (14.8.4) by $[2\omega(\mathbf{k}_0)/g]^{1/2}(1+m/4k_0)$ and taking its inverse Fourier transform that

$$\begin{aligned} &i\frac{\partial a}{\partial t} + \frac{1}{2}\left(\frac{g}{k_0}\right)^{1/2} \left[i\frac{\partial a}{\partial x} - \frac{1}{4k_0}\frac{\partial^2 a}{\partial x^2} + \frac{1}{2k_0}\frac{\partial^2 a}{\partial y^2}\right] \\ &\quad \cdot \left(\frac{2\omega(\mathbf{k}_0)}{g}\right)^{1/2} \frac{1}{2\pi} \iiint_{-\infty}^{\infty} \left(1 + \frac{m_2 + m_3 - m_1}{4k_0}\right) \\ &\quad \cdot T(\mathbf{k}_0 + \mathbf{m}_2 + \mathbf{m}_3 - \mathbf{m}_1, \mathbf{k}_0 + \mathbf{m}_1, \mathbf{k}_0 + \mathbf{m}_2, \mathbf{k}_0 + \mathbf{m}_3) \\ &\quad \cdot A^*(\mathbf{m}_1) A(\mathbf{m}_2) A(\mathbf{m}_3)\, e^{i(\mathbf{m}_2 + \mathbf{m}_3 - \mathbf{m}_1)\cdot \mathbf{x}}\, d\mathbf{m}_1\, d\mathbf{m}_2\, d\mathbf{m}_3\,. \end{aligned} \qquad (14.8.9)$$

Next, one can show by Taylor expansion of T, that

$$T(\mathbf{k}_0 + \mathbf{m}_2 + \mathbf{m}_3 - \mathbf{m}_1, \mathbf{k}_0 + \mathbf{m}_1, \mathbf{k}_0 + \mathbf{m}_2, \mathbf{k}_0 + \mathbf{m}_3) = \frac{k_0^3}{4\pi^2} \qquad (14.8.10)$$

to zero order in the spectral width. Substituting (14.8.10) on the right-hand side of (14.8.9) and evaluating the Fourier integrals, we get the two-dimensional Schrödinger equation,

$$i\left(a_{,x} + \frac{2k_0}{\omega_0} a_{,t}\right) - \frac{1}{4k_0} a_{,xx} + \frac{1}{2k_0} a_{,yy} = k_0^3 |a|^2 a\,. \qquad (14.8.11)$$

By including higher order approximations, Dysthe's (1979) modification of the Schrödinger equation can also be derived, see Stiassnie (1984).

The Schrödinger equation is best known for its exact envelope soliton solution

$$a = a_0\, e^{-i\omega_0 k_0^2 a_0^2 t/4} \operatorname{sech}\left[\sqrt{2} a_0 k_0^2 \left(x - \frac{\omega_0}{2k_0} t\right)\right] \qquad (14.8.12)$$

where $\omega_0^2 = g k_0$.

From (14.8.6) one can see that

$$\zeta = a_0 \operatorname{sech}\left[\sqrt{2}a_0 k_0^2\left(x - \frac{\omega_0}{2k_0}t\right)\right]\cos\left[k_0 x - \omega_0\left(1 + \frac{1}{4}k_0^2 a_0^2\right)t\right]. \tag{14.8.13}$$

Envelope solitons, which go through mutual interactions with only minor changes, have attracted wide interest, see Sections 13.5 and 13.6 in this book and Ablowitz and Segur (1981).

14.9 Benjamin–Feir Instability of Stokes Waves

The special quartet for which $\mathbf{k}_b = \mathbf{k}_a$ and $2\mathbf{k}_a = \mathbf{k}_c + \mathbf{k}_d$, is important for studying the stability of the $\mathbf{k}_a$ wave when exposed to two disturbances at $\mathbf{k}_c = \mathbf{k}_a + \mathbf{K}$ and $\mathbf{k}_d = \mathbf{k}_a - \mathbf{K}$. For this case (14.7.4)–(14.7.7) and (14.7.8)–(14.7.11) are reduced to

$$i\frac{dB_a}{dt} = (\Omega_a - \omega_a)B_a + 2T_{aacd}\,e^{i\Delta_{aacd}t}B_a^* B_c B_d \tag{14.9.1}$$

$$i\frac{dB_c}{dt} = (\Omega_c - \omega_c)B_c + T_{aacd}\,e^{i\Delta_{aacd}t}B_a^2 B_d^* \tag{14.9.2}$$

$$i\frac{dB_d}{dt} = (\Omega_d - \omega_d)B_d + T_{aacd}\,e^{i\Delta_{aacd}t}B_a^2 B_c^* \tag{14.9.3}$$

and

$$\Omega_a = \omega_a + T_{aaaa}|B_a|^2 + 2T_{acac}|B_c|^2 + 2T_{adad}|B_d|^2 \tag{14.9.4}$$

$$\Omega_c = \omega_c + 2T_{acac}|B_a|^2 + T_{cccc}|B_c|^2 + 2T_{cdcd}|B_d|^2 \tag{14.9.5}$$

$$\Omega_d = \omega_d + 2T_{adad}|B_a|^2 + 2T_{cdcd}|B_c|^2 + T_{dddd}|B_d|^2\,. \tag{14.9.6}$$

Nonlinear periodic solutions very similar to (14.7.34) have been obtained, see Shemer and Stiassnie (1985).

Crawford et al. (1981) have used Zakharov's equation to examine the problem that Benjamin–Feir examined earlier by the cubic Schrödinger equation, and found a number of improved results. To this end, we assume $B_c, B_d \ll B_a$ and linearize (14.9.1)–(14.9.3).

At the zeroth order

$$i\frac{dB_a}{dt} = T_{aaaa}|B_a|^2 B_a\,, \tag{14.9.7}$$

and at the first order

$$i\frac{dB_c}{dt} = 2T_{acac}|B_a|^2 B_c + T_{aacd}\,e^{-i\Delta_{aacd}t} B_a^2 B_d^*\,, \tag{14.9.8}$$

$$i\frac{dB_d}{dt} = 2T_{adad}|B_a|^2 B_d + T_{aacd}\,e^{-i\Delta_{aacd}t} B_a^2 B_c^*\,, \tag{14.9.9}$$

where $\Delta_{aacd} = 2\omega_a - \omega_c - \omega_d$.

The solution of (14.9.7) is just the Stokes wave

$$B_a = \beta_a e^{-iT_{aaaa}|\beta_a|^2 t} \tag{14.9.10}$$

where $\beta_a = B_a(0)$ is assumed to be real and positive.

Substituting (14.9.10) into (14.9.8) and (14.9.9), we get

$$i\frac{dB_c}{dt} = 2T_{acac}\beta_a^2 B_c + T_{aacd}\,e^{-i(\Delta_{aacd}+2T_{aaaa}\beta_a^2)t}\,\beta_a^2 B_d^* \tag{14.9.11}$$

and

$$i\frac{dB_d}{dt} = 2T_{adad}\beta_a^2 B_d + T_{aacd}\,e^{-i(\Delta_{aacd}+2T_{aaaa}\beta_a^2)t}\beta_a^2 B_c^*\,. \tag{14.9.12}$$

Assuming a solution of the form

$$B_c = \beta_c e^{-i[\frac{1}{2}\Delta_{aacd}+T_{aaaa}\beta_a^2+\sigma]t}\,, \quad \beta_c = B_c(0)\,, \tag{14.9.13}$$

and

$$B_d = \beta_d e^{-i[\frac{1}{2}\Delta_{aacd}+T_{aaaa}\beta_a^2-\sigma^*]t}\,, \quad \beta_d = B_d(0)\,, \tag{14.9.14}$$

one can show that the eigenvalue σ must be given by

$$\sigma = (T_{acac} - T_{adad})\beta_a^2 \pm D^{1/2} \tag{14.9.15}$$

where

$$D = \left[\frac{1}{2}\Delta_{aacd} + (T_{aaaa} - T_{acac} - T_{adad})\beta_a^2\right]^2 - T_{aacd}^2\beta_a^4 \tag{14.9.16}$$

is the discriminant of a quadratic eigenvalue condition.

Positive values of D correspond to stability. When D is negative, the imaginary part of σ, i.e., $\operatorname{Im}\sigma = \operatorname{Im}[(-D)^{1/2}]$ is the growth rate of instability (Crawford et al., 1981).

For the simplest two-dimensional case where the Stokes wave is in deep water and the sidebands are in the same direction, $\mathbf{k}_a = (k_o, 0)$, $\mathbf{K} = (\kappa, 0)$. If we further assume narrow sidebands $\kappa/k_0 \ll 1$, then the following relations hold:

$$\begin{pmatrix} \omega_c \\ \omega_d \end{pmatrix} = \omega(k_0 \pm \kappa) = \omega(k_0) \left(1 \pm \frac{\kappa}{2k_0} - \frac{\kappa^2}{8k_0^2} + \cdot\right) \tag{14.9.17}$$

$$\beta_a = \left(\frac{2g}{\omega_0}\right)^{1/2} \pi\, a_0\,, \tag{14.9.18}$$

where a_0 is the first-order amplitude of $\mathbf{k}_a$.

Due to the narrowness of the spectrum

$$T_{acac} \approx T_{adad} \approx T_{aacd} \approx T_{aaaa} = k_0^3/4\pi^2\,, \tag{14.9.19}$$

and

$$\Delta_{aacd} = 2\omega(k_0) - \omega(k_0 + \kappa) - \omega(k_0 - \kappa) \approx \frac{1}{4}\omega_0 \kappa^2/k_0^2\,,$$

$$\omega_0 = \omega(k_0) = \sqrt{g\, k_0}\,. \tag{14.9.20}$$

From (14.9.16) it is clear that instability prevails as long as

$$\kappa/k_0 < 2\sqrt{2}(a_0 k_0)\,. \tag{14.9.21}$$

The growth rate is given by

$$(-D)^{1/2} = \frac{\omega_0}{2\sqrt{2}} \left(\frac{\kappa}{k_0}\right) \left[(k_0 a_0)^2 - \frac{1}{8}\left(\frac{\kappa}{k_0}\right)^2\right]^{1/2} \tag{14.9.22}$$

which attains its maximum at $\kappa_{\max} = 2k_0^2 a_0$, and where its value is $\omega_0 k_0^2 a_0^2/2$. These are just the results predicted in Section 13.4 by the cubic Schrödinger equation.

Crawford et al. (1981) have used (14.9.15) to compute the growth rate for a wider range of wave steepness despite the theoretical limitation of Zakharov's equation. The numerical growth rate for different values of $k_0 a_0$ are shown in Fig. 14.3 as a function of the dimensionless modulation wavenumber

$$\Delta \equiv \frac{\kappa}{2k_0^2 a_0}\,. \tag{14.9.23}$$

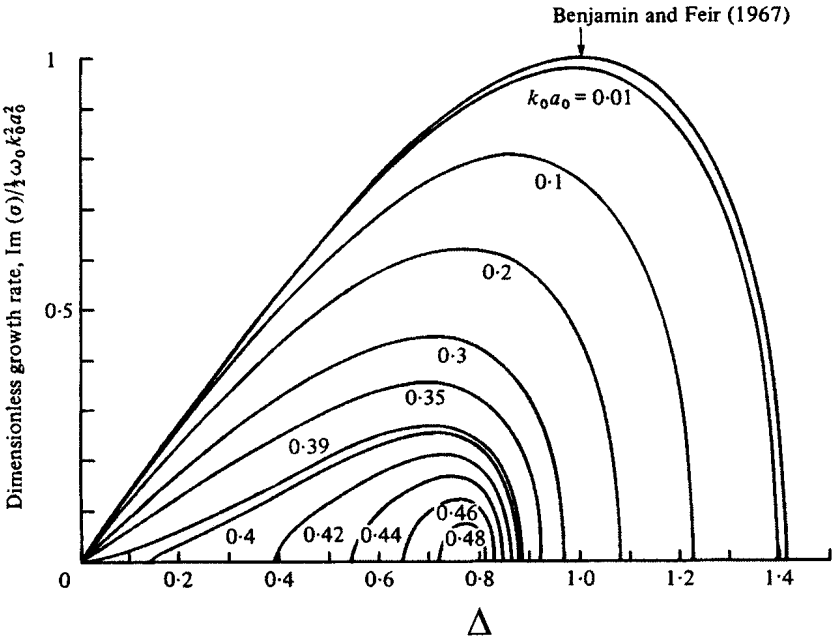

Figure 14.3: Instability growth rate as a function of perturbation wavenumber for various values of wave steepness (from Crawford et al. (1981), *J. Fluid Mech.* Reprinted by permission of Cambridge University Press).

These results show that as k_0a_0 increases, the growth rate decreases. When $k_0a_0 > 0.39$, sideband disturbances with long modulational wavelength are stable! Although such high steepness should lie beyond the realm of validity of Zakharov's theory, comparison with the numerical theory for steep waves by Longuet–Higgins (1978) shows remarkable agreement, as seen in Fig. 14.4. When numerical predictions from (14.9.15) are compared with experiments, the agreement up to moderate k_0a_0 is much better than that from cubic Schrödinger equation, see Fig. 13.2.

In the three-dimensional case where the sidebands are in different directions from the carrier wave, $\mathbf{k}_0 = (k_0, 0)$ and $\mathbf{K} = (K_x, K_y)$, the stability boundary is defined by the vanishing of D defined by (14.9.16) where $|\mathbf{K}|/k_0$ is not necessarily small. Figure 14.5 gives a sample result from (14.9.15), which shows that in the first quadrant of the $\mathbf{K}$ plane, the region of instability is limited to the interior of the horn-like domain. In contrast, the instability region is unbounded according to the cubic

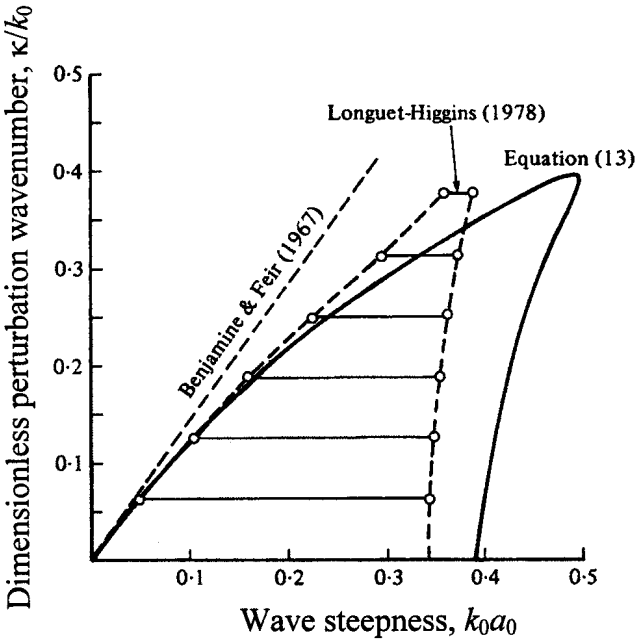

Figure 14.4: Stability boundary for growth of unstable disturbances for uni-directional wavetrains, and comparison with results by Longuet–Higgins (1978). Note that Eq. (13), noted in the figure, is the same as (14.9.15) (from Crawford et al. (1981), *J. Fluid Mech.* Reprinted by permission of Cambridge University Press).

Schrödinger equation (Benney and Roskes, 1969) and bounded in a horn with a straight side according to Dysthe (1979), both of which are limited to small $|\mathbf{K}|/k_0$.

Beyond the initial stage of unstable growth, the long-time evolution is obtained from an analytical solution of (14.9.1)–(14.9.3), which is very similar to (14.7.34), see Shemer and Stiassnie (1985). The notable feature is the periodic recurrence. Initially, the sidebands $\mathbf{k}_c, \mathbf{k}_d$ grow at the expense of the carrier wave $\mathbf{k}_a$, but after reaching their peaks their energy is returned to the carrier wave. This exchange recurs periodically, in accordance with (14.7.38). A sample of this behaviour is shown in Fig. 14.6 for which initially $k_a a_a = k_0 a_0 = 0.13$, $a_c = a_d = 0.1\, a_a$, $\arg\beta_c + \arg\beta_d = -\pi/4$ and $\kappa = 0.22$. The recurrence period T for this case is about 190 carrier periods.

Note that the lower sideband grows to a slightly higher peak than the upper sideband. This unequal growth of sidebands is not predictable

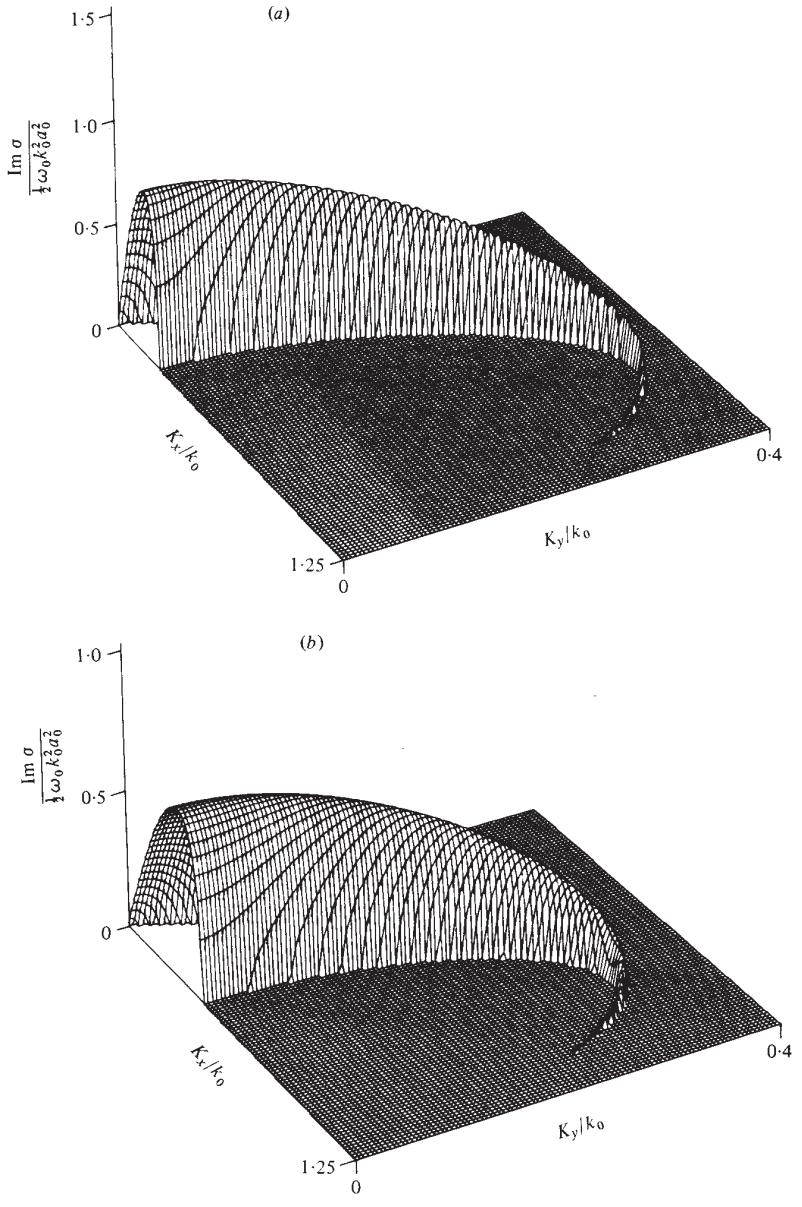

Figure 14.5: Instability growth rate for two values of wave steepness according to (14.9.15). (*a*) $k_0 a_0 = 0.1$, (*b*) $k_0 a_0 = 0.2$, as $k_0 a_0$ increases, the horn is lower in height and has a larger curvature (from Crawford et al. (1981), *J. Fluid Mech.* Reprinted by permission of Cambridge University Press).

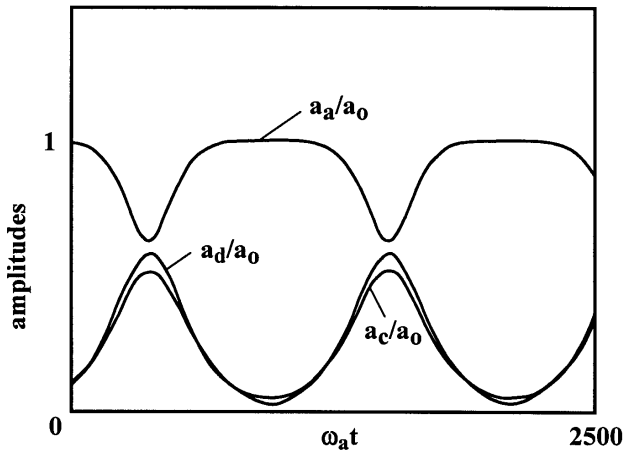

Figure 14.6: Long-time evolution initiated by the Benjamin–Feir instability of a Stokes wave.

by solving the cubic Schrödinger equation which can only reproduce the periodic recurrence. This of course implies that Zakharov's equation is more accurate than the cubic Schrödinger equation and contains Dysthe's extension.

It is well known that the peak frequency of a wind-wave spectrum decreases with the propagation distance, while the peak amplitude increases. This phenomenon is known as the *frequency downshift*. Lake et al. (1977) have suggested that the faster growth of the lower sideband can contribute to the downshift of the spectral peak. Their reasoning is as follows. Inevitable nonlinear effects cause sidebands around the peak frequency to grow with fetch. When the faster growth of the lower sideband overtakes both the upper sideband and the carrier wave, downward shift of the spectral peak occurs. If the waves are steep enough, breaking may intervene so that the downshift is not reversible. Experiments by Melville (1982, 1983) confirms this suggestion. Further discussions of frequency downshift by using theories of narrow frequency band have been examined by Lo and Mei (1985) and Trulsen and Dysthe (1992).

14.10 Kinetic Equation of Hasselmann

Surface waves in an open ocean are so complex that they must be considered as a random process for practical predictions. In past decades numerical

models have been developed on the basis of the so-called *kinetic equation* for the action spectrum $C(\mathbf{k}, t)$ (to be defined later)

$$\frac{dC}{dt} = S_{in} + S_{nl} + S_{ds} + S_{bot} \tag{14.10.1}$$

where the right-hand side consists of source terms representing the physical mechanisms of wind-input, nonlinear wave-wave interactions, dissipation due to breaking and bottom friction. Of the four mechanisms, our theoretical understanding of S_{nl} is the most advanced. All others must be modeled by including considerble empirical data. A comprehensive survey of all source terms and the numerical implementation can be found in Komen et al. (1994). We shall derive the nonlinear source term as an application of Zakharov's theory.

Treating the free surface displacement as random, we first discretize the amplitude spectrum defined by (14.1.8) as follows

$$\tilde{B}(\mathbf{k}, t) = \sum_n B_n(t)\delta(\mathbf{k} - \mathbf{k}_n) \tag{14.10.2}$$

where the phases of all B_n are assumed to be random variables uncorrelated and uniformly distributed in $[-\pi, \pi]$ at the lowest order. In (14.10.2) and elsewhere n is a large number, so that in the limit the discretized terms are densely distributed over the wavenumber plane. The Zakharov equation (14.3.9) is then replaced by

$$i\frac{dB_n}{dt} = \sum_{p,q,r} \hat{T}_{npqr}\delta_{npqr}e^{i\Delta_{npqr}t}B_p^*B_qB_r \tag{14.10.3}$$

where δ_{npqr} is the generlized Kronecker delta defined by

$$\delta_{npqr} = \begin{cases} 1\,, \ \mathbf{k}_n + \mathbf{k}_p = \mathbf{k}_q + \mathbf{k}_r\,, \\ 0\,, \qquad \text{otherwise} \end{cases},$$

and

$$\Delta_{npqr} = \omega_n + \omega_p - \omega_q + \omega_r\,.$$

Multiplying (14.10.3) by $-iB_n^*$ and adding the complex conjugate to the result give

$$\frac{d|B_n|^2}{dt} = 2\,\mathrm{Im}\sum_{p,q,r} \hat{T}_{npqr}\delta_{npqr}e^{i\Delta_{npqr}t}B_n^*B_p^*B_qB_r\,. \tag{14.10.4}$$

We now take the ensemble average of (14.10.4). Note that the assumed statistical independence and uniform probability of the phases of B_n, B_p, B_q, B_r implies that to the leading order

$$\langle B_n^* B_p^* B_q B_r \rangle = \frac{|B_n||B_p||B_q||B_r|}{(2\pi)^4} \iiint_{-\pi}^{\pi} \cdot e^{-i(\theta_n+\theta_p-\theta_q-\theta_r)}\, d\theta_n\, d\theta_p\, d\theta_q\, d\theta_r$$

which vanishes unless $p = q, n = r$ or $n = q, p = r$. Thus the ensemble average of the sum on the right is, to the leading order,

$$2\,\mathrm{Im}\left\{ \langle |B_n|^2 \rangle \sum_r \hat{T}_{nrnr} \langle |B_n|^2 \rangle \right\}$$

which is zero. To calculate the same term to higher order accuracy, the product $B_n^* B_p^* B_q B_r$ is differentiated with respect to t and (14.10.3) is substituted for the derivatives

$$\begin{aligned} i\frac{d}{dt}(B_n^* B_p^* B_q B_r) = &-B_p^* B_q B_r \sum_{u,v,w} \hat{T}_{nuvw}\delta_{nuvw} e^{-i\Delta_{nuvw}t} B_u B_v^* B_w^* \\ &- B_n^* B_q B_r \sum_{u,v,w} \hat{T}_{puvw}\delta_{puvw} e^{-i\Delta_{puvw}t} B_u B_v^* B_w^* \\ &+ B_n^* B_p^* B_r \sum_{u,v,w} \hat{T}_{quvw}\delta_{quvw} e^{i\Delta_{quvw}t} B_u^* B_v B_w \\ &+ B_n^* B_p^* B_q \sum_{u,v,w} \hat{T}_{ruvw}\delta_{ruvw} e^{i\Delta_{ruvw}t} B_u^* B_v B_w \end{aligned} \tag{14.10.5}$$

where the symmetry of the kernel, $\hat{T}_{npqr} = \hat{T}_{nprq} = \hat{T}_{pnqr} = \hat{T}_{qrnp}$ has been used. Upon taking the ensemble average, contributions of most of the terms on the right-hand-side of (14.10.5) cancel out, leaving,

$$\begin{aligned} i\frac{d}{dt}\langle B_n^* B_p^* B_q B_r \rangle = &-2\hat{T}_{npqr}\delta_{npqr} e^{-i\Delta_{npqr}t} \\ &\cdot [C_q C_r (C_p + C_n) - C_n C_p (C_q + C_r)] \end{aligned} \tag{14.10.6}$$

where

$$C_n = \langle |B_n|^2 \rangle \tag{14.10.7}$$

which is the discrete representation of the action spectrum, in view of the definition, (14.1.7).

We now integrate (14.10.6) with respect to t by assuming the initial condition,

$$\langle B_n^* B_p^* B_q B \rangle = 0 \quad t = t_0 \,, \tag{14.10.8}$$

where t_0 is negative and very large. Antipating that C_n varies slowly in time and noting that the largest contribution of the integral

$$\mathrm{Re} \int_{t_0}^{t} e^{-i\Delta_{pqnr}(t-\tau)}\, d\tau = \frac{\sin(\Delta_{npqr}(t-t_0))}{\Delta_{npqr}} \tag{14.10.9}$$

comes from the viscinity of $\Delta_{npqr} = 0$ if $t_o \to -\infty$, we make the approximation

$$\langle B_n^* B_p^* B_q B_r \rangle \approx 2i\hat{T}_{npqr}\delta_{npqr} \cdot [C_q C_r (C_p + C_n) - C_n C_p (C_q + C_r)]$$
$$\cdot \int_{t_0}^{t} e^{-i\Delta_{npqr}\tau}\, d\tau \tag{14.10.10}$$

so that the ensemble average of Eq.(14.10.4) becomes

$$\frac{dC_n}{dt} = 4 \sum_{p,q,r} \hat{T}^2_{npqr}\delta_{npqr} \frac{\sin(\Delta_{npqr}(t-t_0))}{\Delta_{npqr}}$$
$$\cdot [C_q C_r (C_p + C_n) - C_n C_p (C_q + C_r)] \,. \tag{14.10.11}$$

Taking the limit $t_0 \to -\infty$ and using the fact that

$$\lim_{t_0 \to -\infty} \frac{\sin(-\Delta_{npqr} t_0)}{\pi \Delta_{npqr}} = \delta(\Delta_{npqr})$$
$$= \delta(\omega_n + \omega_p - \omega_q - \omega_r) \,, \tag{14.10.12}$$

we obtain

$$\frac{dC_n}{dt} = 4\pi \sum_{p,q,r} \hat{T}^2_{npqr}\delta_{npqr}\delta(\omega_n + \omega_p - \omega_q - \omega_r)$$
$$\cdot [C_q C_r (C_p + C_n) - C_n C_p (C_q + C_r)] \,. \tag{14.10.13}$$

Note that this limit signifies the dominance of the Phillips' four-wave resonance.

Returning to the continuous form, the action spectrum is governed by

$$\frac{dC(\mathbf{k},t)}{dt} = 4\pi \iiint \int_{-\infty}^{\infty} d\mathbf{k}_1\, d\mathbf{k}_2\, d\mathbf{k}_3 \cdot \hat{T}^2(\mathbf{k},\mathbf{k}_1,\mathbf{k}_2,\mathbf{k}_3)\delta(\mathbf{k}_1+\mathbf{k}_2-\mathbf{k}_3-\mathbf{k}_4)\delta(\omega+\omega_1-\omega_2-\omega_3) \cdot \{C(\mathbf{k}_2)C(\mathbf{k}_3)[C(\mathbf{k})+C(\mathbf{k}_1)] - C(\mathbf{k})C(\mathbf{k}_1)[(C(\mathbf{k}_2)+C(\mathbf{k}_3)]\}\,. \tag{14.10.14}$$

This is Hasselmann's kinetic equation for energy transfer among waves of different wavenumbers. With additional terms representing energy input from wind, and outputs through dissipation at the free surface and the sea bed, the action spectrum at any time can be numerically integrated from a known initial state. Information on full wave forecasting models and the numerical integration schemes can be found in Komen et al. (1994).

It may be pointed out that the derivation here hinges on the choice of $t_0 = -\infty$ in the assumption (14.10.8). Other choices are possible. For example Janssen (2003) chooses $t_0 = 0$ so that the delta function in frequency in (14.10.14) is replaced by a smeared function

$$\delta(\omega+\omega_1-\omega_2-\omega_3) \to \frac{\sin \Delta_{npqr} t}{\pi \Delta_{nprq}}\,.$$

This has the physical effect of giving more weight to waves that are slightly phase-mismatched according to Phillips' quartet resonance condition. For sufficiently large time, Janssen's choice would approach Hasselmann's asymptotically. Further theoretical study is warranted.

14.11 Extensions

In this chapter Zakharov's equation (14.3.9) has been developed by taking into account third-order nonlinear interactions among a quartet of waves; this order is the lowest that causes a significant change of the leading-order gravity-wave amplitudes, albeit on the slow time-scale t_2.

Resonant interactions among five wavetrains (quintet resonance) can occur if fourth-order nonlinearity is taken into account, and will affect the leading-order amplitudes on the time-scale t_3. This topic has been studied by Stiassnie and Shemer (1984, 1987), Krasitskii (1994), Annenkov and Shrira (2001). By this extension the so-called class-II instabilities, first

found numerically by McLean (1982), was also predicted analytically. So far experimental verifications are scarce, and available mainly for quartet resonance [see McGoldrick et al. (1966); Shemer et al. (2001)].

One drawback of Zakharov's equation is the fact that it treats the whole (x, y) plane, i.e., the whole ocean surface, as one unit. To overcome this limitation, Rasmussen (1998) allows for spatial variations, and derives the equation:

$$\begin{aligned} i\frac{\partial B}{\partial t} + i\mathbf{c}_g \cdot \nabla_{\mathbf{x}} B - \frac{g}{8\omega k} \\ \cdot \left\{ \frac{k_x^2 - 2k_y^2}{k^2}\frac{\partial^2 B}{\partial x^2} + \frac{6k_x k_y}{k^2}\frac{\partial^2 B}{\partial x dy} + \frac{k_y^2 - 2k_x^2}{k^2}\frac{\partial^2 B}{\partial y^2} \right\} \\ = \iiint_{-\infty}^{\infty} T_{0,1,2,3} B_1^* B_2 B_3 \delta_{0+1-2-3} e^{i(\omega_0+\omega_1-\omega_2-\omega_3)t}\, d\mathbf{k}_1\, d\mathbf{k}_2\, d\mathbf{k}_3\,. \end{aligned} \tag{14.11.1}$$

The left-hand side of (14.11.1) is similar to the linear part of the cubic Schrödinger equation (14.8.11), and the right-hand side to that of the original Zakharov equation (14.3.9). Note, that (14.11.1) depends on the spatial variable x_1, and on the time variables t_1 and t_2. If the actual spatial coordinate is x_2 the second-order derivatives on the left-hand side can be omitted. A relatively easy derivation of (14.11.1) and its relation to the physical variables ζ, ϕ^s are given in Rasmussen and Stiassnie (1999). It is fair to mention that difficulties related to the question of scale-separation still shed some doubt on the applicability of (14.11.1), and await further research.

From (14.10.14) one can see that the energy transfer occurs on the rather long time-scale t_4, since the rate of change of the action density C is proportional to C^3. A much faster energy transfer, with time-scale t_2, is possible in the presence of spatial inhomogeneities. This was clearly demonstrated by Alber (1978) who derived an equation describing the evolution of a random narrowband wavetrain. Recently, Stiassnie (2001) has derived a mathematical model for nonlinear interactions of an inhomogeneous random and broadbanded water-wave field, using two-point spectral correlation functions as dependent variables. In Stiassnie (2001) the author conjectures that almost any homogeneous wave-field is unstable to inhomogeneous disturbances; but this has to await future proof.

For a recent review about evolution models of nonlinear gravity waves over uneven topography, the reader is referred to Agnon and Sheremet (2000).

Appendix 14.A Details of Derivation

Appendix 14.A.1 Fourier Transforms of the Free Surface Conditions

We shall only illustrate the transform of a typical quadratic term $\nabla_{\mathbf{x}}\phi^s\cdot\nabla_{\mathbf{x}}\zeta$, see (14.1.6),

$$\begin{aligned}
&\widehat{\nabla_{\mathbf{x}}\phi^s\cdot\nabla_{\mathbf{x}}\zeta}\\
&\quad=\frac{1}{2\pi}\int_{-\infty}^{\infty}\nabla_{\mathbf{x}}\phi^s\cdot\nabla_{\mathbf{x}}\zeta e^{-i\mathbf{k}\cdot\mathbf{x}}\,d\mathbf{x}\\
&\quad=\frac{1}{(2\pi)^3}\int_{-\infty}^{\infty}e^{-i\mathbf{k}\cdot\mathbf{x}}\,d\mathbf{x}\int_{-\infty}^{\infty}(\widehat{\nabla_{\mathbf{x}}\phi^s})_1e^{+i\mathbf{k}_1\cdot\mathbf{x}}\,d\mathbf{k}_1\int_{-\infty}^{\infty}(\widehat{\nabla_{\mathbf{x}}\zeta})_2e^{+i\mathbf{k}_2\cdot\mathbf{x}}\,d\mathbf{k}_2\\
&\quad=\frac{1}{(2\pi)^3}\iiint_{-\infty}^{\infty}(\widehat{\nabla_{\mathbf{x}}\phi^s})_1(\widehat{\nabla_{\mathbf{x}}\zeta})_2e^{+i(\mathbf{k}_1+\mathbf{k}_2-\mathbf{k})\cdot\mathbf{x})}\,d\mathbf{k}_1\,d\mathbf{k}_2\,d\mathbf{x}\,. \qquad (14.A.1)
\end{aligned}$$

Since

$$(\widehat{\nabla_{\mathbf{x}}\phi^s})_1\equiv\frac{1}{2\pi}\int_{-\infty}^{\infty}\nabla\phi^s e^{-ik_1\cdot\mathbf{x}}\,d\mathbf{x}=i\mathbf{k}_1\hat{\phi}^s(k_1,t)$$

$$(\widehat{\nabla_{\mathbf{x}}\zeta})_2\equiv\frac{1}{2\pi}\int_{-\infty}^{\infty}\nabla\zeta\, e^{-ik_2\cdot\mathbf{x}}\,d\mathbf{x}=i\mathbf{k}_2\hat{\zeta}(k_2,t)$$

and

$$\frac{1}{(2\pi)^2}\int_{-\infty}^{\infty}e^{i(\mathbf{k}_1+\mathbf{k}_2-\mathbf{k})\cdot\mathbf{x}}\,d\mathbf{x}=\delta(\mathbf{k}-\mathbf{k}_1-\mathbf{k}_2), \qquad (14.A.2)$$

it follows that

$$\begin{aligned}
\widehat{\nabla_{\mathbf{x}}\phi^s\cdot\nabla_{\mathbf{x}}\zeta}=-\frac{1}{2\pi}\int_{-\infty}^{\infty}&\mathbf{k}_1\cdot\mathbf{k}_2\hat{\phi}^s(\mathbf{k}_1,t)\hat{\zeta}(\mathbf{k}_2,t)\\
&\cdot\delta(\mathbf{k}-\mathbf{k}_1-\mathbf{k}_2)\,d\mathbf{k}_1\,d\mathbf{k}_2\,. \qquad (14.A.3)
\end{aligned}$$

Conditions (14.2.3) and (14.2.4) follow easily.

Appendix 14.A.2 Surface Properties for Waves of Small Steepness

After Taylor expansion of (14.2.6) up to $O(\epsilon^3)$ we get (14.2.8)

$$\phi^s(\mathbf{x},t) = \frac{1}{2\pi}\int_{-\infty}^{\infty} \hat{\phi}(\mathbf{k}_1,t) \cdot \left[\cosh(\mathbf{k}_1 h)\left(1+\frac{|\mathbf{k}_1|^2}{2}\zeta^2\right) + |\mathbf{k}_1|\sinh(|\mathbf{k}_1|h)\,\zeta\right] e^{i\mathbf{k}_1\cdot\mathbf{x}}\,d\mathbf{k}_1\,. \tag{14.A.4}$$

Expressing ζ as a Fourier integral

$$\zeta(\mathbf{x},t) = \frac{1}{2\pi}\int_{-\infty}^{\infty} \hat{\zeta}(\mathbf{k},t)\exp[i\mathbf{k}\cdot\mathbf{x}]\,d\mathbf{k}\,.$$

Substituting it into (14.A.4) and taking the Fourier transform of the result, we get,

$$\begin{aligned}\hat{\phi}^s(\mathbf{k},t) &= \hat{\Phi}(\mathbf{k},t)\cosh(|\mathbf{k}|h) + \frac{1}{(2\pi)^3}\iiint_{-\infty}^{\infty} |\mathbf{k}_1|\sinh(|\mathbf{k}_1|h) \\ &\quad\cdot \hat{\Phi}(\mathbf{k}_1,t)\hat{\zeta}(\mathbf{k}_2,t)e^{i(\mathbf{k}-\mathbf{k}_1-\mathbf{k}_2)\cdot\mathbf{x}}\,d\mathbf{x}\,d\mathbf{k}_1\,d\mathbf{k}_2 \\ &\quad+\frac{1}{(2\pi)^4}\iiiint_{-\infty}^{\infty}\frac{1}{2}|\mathbf{k}_1|^2\cosh(|\mathbf{k}_1|h)\hat{\Phi}(\mathbf{k}_1,t)\hat{\zeta}(\mathbf{k}_2,t)\hat{\zeta}(\mathbf{k}_3,t) \\ &\quad\cdot e^{i(\mathbf{k}-\mathbf{k}_1-\mathbf{k}_2-\mathbf{k}_3)\cdot\mathbf{x}}\,d\mathbf{x}\,d\mathbf{k}_1\,d\mathbf{k}_2\,d\mathbf{k}_3\,.\end{aligned}$$

Making use of (14.A.2), we obtain

$$\begin{aligned}\hat{\phi}^s(\mathbf{k},t) &= \hat{\Phi}(\mathbf{k},t)\cosh(|\mathbf{k}|h) + \frac{1}{(2\pi)}\iint_{-\infty}^{\infty} |\mathbf{k}_1|\sinh(|\mathbf{k}_1|h) \\ &\quad\cdot \hat{\Phi}(\mathbf{k}_1,t)\hat{\zeta}(\mathbf{k}_2,t)\delta(\mathbf{k}-\mathbf{k}_1-\mathbf{k}_2)\,d\mathbf{k}_1\,d\mathbf{k}_2 \\ &\quad+\frac{1}{(2\pi)^2}\iiint_{-\infty}^{\infty}\frac{1}{2}|\mathbf{k}_1|^2\cosh(|\mathbf{k}_1|h)\hat{\Phi}(\mathbf{k}_1,t)\hat{\zeta}(\mathbf{k}_2,t)\hat{\zeta}(\mathbf{k}_3,t) \\ &\quad\cdot \delta(\mathbf{k}-\mathbf{k}_1-\mathbf{k}_2-\mathbf{k}_3)\,d\mathbf{k}_1\,d\mathbf{k}_2\,d\mathbf{k}_3\end{aligned}$$

which is (14.2.9). Equation (14.2.10) is derived similarly.

Appendix 14.A.3 Inverting (14.2.9) by Iteration

To start with, we subsitute the crudest approximation (zeroth iterate)

$$\hat{\Phi}^{(0)}(\mathbf{k},t) = \frac{\hat{\phi}^s(\mathbf{k},t)}{\cosh(|\mathbf{k}|h)}$$

into the right-hand side of (14.2.9), and get the first iterate

$$\begin{aligned}\hat{\Phi}^{(1)}(\mathbf{k},t) = \frac{\hat{\phi}^s(\mathbf{k},t)}{\cosh(|\mathbf{k}|h)} &- \frac{1}{\cosh(|\mathbf{k}|h)}\frac{1}{2\pi}\iint_{-\infty}^{\infty}|\mathbf{k}_1|\tanh(|\mathbf{k}_1|h)\\ &\cdot\hat{\phi}^s(\mathbf{k}_1,t)\hat{\zeta}(\mathbf{k}_2,t)\delta(\mathbf{k}-\mathbf{k}_1-\mathbf{k}_2)\,d\mathbf{k}_1\,d\mathbf{k}_2\\ &- \frac{1}{\cosh(|\mathbf{k}|h)}\frac{1}{(2\pi)^2}\iiint_{-\infty}^{\infty}\frac{|\mathbf{k}_1|^2}{2}\hat{\phi}^s(\mathbf{k}_1,t)\hat{\zeta}(\mathbf{k}_2,t)\hat{\zeta}(\mathbf{k}_3,t)\\ &\cdot\delta(\mathbf{k}-\mathbf{k}_1-\mathbf{k}_2-\mathbf{k}_3)\,d\mathbf{k}_1\,d\mathbf{k}_2\,d\mathbf{k}_3\,.\end{aligned}$$

For the second iterate, we substitute $\hat{\Phi}^{(1)}$ into the right of (14.2.9),

$$\begin{aligned}\hat{\Phi}^{(2)}(\mathbf{k},t) = \frac{\hat{\phi}^2(\mathbf{k},t)}{\cosh(|\mathbf{k}|h)} &- \frac{1}{\cosh(|\mathbf{k}|h)}\frac{1}{2\pi}\iint_{-\infty}^{\infty}|\mathbf{k}_1|\tanh(|\mathbf{k}_1|h)\\ &\cdot\hat{\phi}^s(\mathbf{k}_1,t)\hat{\zeta}(\mathbf{k}_2,t)\delta(\mathbf{k}-\mathbf{k}_1-\mathbf{k}_2)\,d\mathbf{k}_1\,d\mathbf{k}_2\\ &- \frac{1}{\cosh(|\mathbf{k}|h)}\frac{1}{(2\pi)^2}\iiint_{-\infty}^{\infty}\frac{|\mathbf{k}_1|^2}{2}\hat{\phi}^s(\mathbf{k}_1,t)\hat{\zeta}(\mathbf{k}_2,t)\hat{\zeta}(\mathbf{k}_3,t)\\ &\cdot\delta(\mathbf{k}-\mathbf{k}_1-\mathbf{k}_2-\mathbf{k}_3)\,d\mathbf{k}_1\,d\mathbf{k}_2\,d\mathbf{k}_3\\ &+ \frac{1}{\cosh(|\mathbf{k}|h)}\frac{1}{(2\pi)^2}\iiint_{-\infty}^{\infty}|\mathbf{k}_1|\tanh(|\mathbf{k}_1|h)|\mathbf{k}_m|\tanh(|\mathbf{k}_m|h)\\ &\cdot\hat{\phi}^s(\mathbf{k}_m,t)\hat{\zeta}(\mathbf{k}_n,t)\hat{\zeta}(\mathbf{k}_2,t)\\ &\cdot\delta(\mathbf{k}_m+\mathbf{k}_n-\mathbf{k}_1)\delta(\mathbf{k}_1+\mathbf{k}_2-\mathbf{k})\,d\mathbf{k}_m\,d\mathbf{k}_n\,d\mathbf{k}_1\,d\mathbf{k}_2\,. \qquad (14.A.5)\end{aligned}$$

Now the four-fold integral can be integrated with respect to $\mathbf{k}_1$ in two ways. One is to get rid of the first delta function,

$$\begin{aligned}&\iiint_{-\infty}^{\infty}|\mathbf{k}_m+\mathbf{k}_n|\tanh(|\mathbf{k}_m+\mathbf{k}_n|h)|\mathbf{k}_m|\tanh(|\mathbf{k}_m|h)\\ &\quad\cdot\hat{\phi}^s(\mathbf{k}_m,t)\hat{\zeta}(\mathbf{k}_n,t)\hat{\zeta}(\mathbf{k}_2,t)\\ &\quad\cdot\delta(\mathbf{k}_m+\mathbf{k}_n+\mathbf{k}_2-\mathbf{k})\,d\mathbf{k}_m\,d\mathbf{k}_n\,d\mathbf{k}_2 \qquad (14.A.6)\end{aligned}$$

which can in turn be rewritten in two ways. In the first we change the dummy variables from $\mathbf{k}_m \to \mathbf{k}_1$ and $\mathbf{k}_n \to \mathbf{k}_3$ to get

$$\begin{aligned}\iiint_{-\infty}^{\infty} &|\mathbf{k}_1 + \mathbf{k}_3| \tanh(|\mathbf{k}_1 + \mathbf{k}_3|h)|\mathbf{k}_1| \tanh(|\mathbf{k}_1|h) \\ &\cdot \hat{\phi}^s(\mathbf{k}_1, t)\hat{\zeta}(\mathbf{k}_3, t)\hat{\zeta}(\mathbf{k}_2, t) \\ &\cdot \delta(\mathbf{k}_1 + \mathbf{k}_3 + \mathbf{k}_2 - \mathbf{k})\, d\mathbf{k}_1\, d\mathbf{k}_3\, d\mathbf{k}_2\,. \end{aligned} \tag{14.A.7}$$

In the second we change the notations from $\mathbf{k}_m \to \mathbf{k}_1$, $\mathbf{k}_n \to \mathbf{k}_2$, and $\mathbf{k}_2 \to \mathbf{k}_3$, to get

$$\begin{aligned}\iiint_{-\infty}^{\infty} &|\mathbf{k}_1 + \mathbf{k}_2| \tanh(|\mathbf{k}_1 + \mathbf{k}_2|h)|\mathbf{k}_1| \tanh(|\mathbf{k}_1|h) \\ &\cdot \hat{\phi}^s(\mathbf{k}_1, t)\hat{\zeta}(\mathbf{k}_2, t)\hat{\zeta}(\mathbf{k}_3, t) \\ &\cdot \delta(\mathbf{k}_3 + \mathbf{k}_1 + \mathbf{k}_2 - \mathbf{k})\, d\mathbf{k}_3\, d\mathbf{k}_1\, d\mathbf{k}_2\,. \end{aligned} \tag{14.A.8}$$

The other way is to get rid of the second delta function,

$$\begin{aligned}\iiint_{-\infty}^{\infty} &|\mathbf{k} - \mathbf{k}_2| \tanh(|\mathbf{k} - \mathbf{k}_2|h)|\mathbf{k}_m| \tanh(|\mathbf{k}_m|h) \\ &\cdot \hat{\phi}^s(\mathbf{k}_m, t)\hat{\zeta}(\mathbf{k}_n, t)\hat{\zeta}(\mathbf{k}_2, t) \\ &\cdot \delta(\mathbf{k}_m + \mathbf{k}_n + \mathbf{k}_2 - \mathbf{k})\, d\mathbf{k}_m\, d\mathbf{k}_n\, d\mathbf{k}_2\,. \end{aligned}$$

Making the same two replacements of dummy variables, we get two equivalent expressions,

$$\begin{aligned}\iiint_{-\infty}^{\infty} &|\mathbf{k} - \mathbf{k}_2| \tanh(|\mathbf{k} - \mathbf{k}_2|h)|\mathbf{k}_1| \tanh(|\mathbf{k}_1|h) \\ &\cdot \hat{\phi}^s(\mathbf{k}_1, t)\hat{\zeta}(\mathbf{k}_2, t)\hat{\zeta}(\mathbf{k}_3, t) \\ &\cdot \delta(\mathbf{k}_1 + \mathbf{k}_2 + \mathbf{k}_3 - \mathbf{k})\, d\mathbf{k}_1\, d\mathbf{k}_2\, d\mathbf{k}_3 \end{aligned} \tag{14.A.9}$$

and

$$\begin{aligned}\iiint_{-\infty}^{\infty} &|\mathbf{k} - \mathbf{k}_3| \tanh(|\mathbf{k} - \mathbf{k}_3|h)|\mathbf{k}_1| \tanh(|\mathbf{k}_1|h) \\ &\cdot \hat{\phi}^s(\mathbf{k}_1, t)\hat{\zeta}(\mathbf{k}_2, t)\hat{\zeta}(\mathbf{k}_3, t) \\ &\cdot \delta(\mathbf{k}_1 + \mathbf{k}_2 + \mathbf{k}_3 - \mathbf{k})\, d\mathbf{k}_1\, d\mathbf{k}_2\, d\mathbf{k}_3\,. \end{aligned} \tag{14.A.10}$$

We now replace the 4-fold integral in (14.A.5) by the average of (14.A.7)–(14.A.10). The result is (14.2.11).

Appendix 14.B Kernels

The kernel in (14.2.12) is

$$S^{(1)}_{0,1,2,3} = \frac{\omega_0^2}{g}\frac{|\mathbf{k}_1|}{4}\left\{2|\mathbf{k}_1| - \frac{\tanh(|\mathbf{k}_1|h)}{g}(\omega^2_{0-2}+\omega^2_{0-3}+\omega^2_{1+2}+\omega^2_{1+3})\right\}$$
$$-\frac{\omega_1^2}{2g}\left\{|\mathbf{k}_1|^2 - \frac{1}{2}(|\mathbf{k}-\mathbf{k}_2|^2+|\mathbf{k}-\mathbf{k}_3|^2+|\mathbf{k}_1+\mathbf{k}_2|^2+|\mathbf{k}_1+\mathbf{k}_3|^2)\right\}. \tag{14.B.1}$$

The interaction coefficients in (14.2.14) are as follows:
Second order:

$$V^{(1)}_{0,1,2} = -2V_{-0,1,2} + V_{1,2,0} \tag{14.B.2}$$

$$V^{(2)}_{0,1,2} = 2(V_{0,1,2} - V_{-0,2,1} - V_{-1,2,0}) \tag{14.B.3}$$

$$V^{(3)}_{0,1,2} = 2V_{0,1,2} + V_{1,2,0}\,, \tag{14.B.4}$$

where

$$V_{0,1,2} = \frac{1}{8\pi}\left(\frac{g\omega_2}{2\omega_0\omega_1}\right)^{1/2}\left[\mathbf{k}\cdot\mathbf{k}_1 + \left(\frac{\omega_0\omega_1}{g}\right)^2\right]. \tag{14.B.5}$$

Third order:

$$W^{(1)}_{0,1,2,3} = W_{1,2,-0,3} - W_{-0,1,2,3} \tag{14.B.6}$$

$$W^{(2)}_{0,1,2,3} = W_{-0,-1,2,3} + W_{2,3,-0,-1} - W_{2,-1,-0,3}$$
$$- W_{-0,2,-1,3} - W_{-0,3,2,-1} - W_{3,-1,2,-0}\,, \tag{14.B.7}$$

$$W^{(3)}_{0,1,2,3} = 2W_{-0,-1,-2,3} - W_{-0,3,-1,-2}$$
$$+ W_{-1,-2,-0,3} - 2W_{-1,3,-0,-2}\,, \tag{14.B.8}$$

$$W^{(4)}_{0,1,2,3} = W_{0,1,2,3} + W_{1,2,0,3}\,, \tag{14.B.9}$$

where

$$W_{0,1,2,3} = \frac{1}{64\pi^2}\left(\frac{\omega_2\omega_3}{\omega_0\omega_1}\right)^{1/2} |\mathbf{k}||\mathbf{k}_1|$$
$$\cdot\Bigg\{2|\mathbf{k}|\tanh(|\mathbf{k}_1|h) + 2||\mathbf{k}_1|\tanh(|\mathbf{k}|h)$$
$$-\frac{1}{g}\tanh(|\mathbf{k}|h)\tanh(|\mathbf{k}_1|h)[\omega^{(2)}_{0+2} + \omega^{(2)}_{0+3} + \omega^{(2)}_{1+2} + \omega^{(2)}_{1+3}]\Bigg\}. \tag{14.B.10}$$

The kernels of (14.3.5) are

$$\tilde{T}^{(1)}_{0,1,2,3} = W^{(1)}_{0,1,2,3} - \frac{V^{(1)}_{0,1,2+3}V^{(1)}_{2+3,3,2}}{\omega_{2+3} - \omega_2 - \omega_3} - \frac{V^{(1)}_{0,1+3,2}V^{(1)}_{1+3,3,1}}{\omega_{1+3} - \omega_1 - \omega_3}$$
$$- \frac{V^{(2)}_{0,-1-3,2}V^{(3)}_{-1-3,3,1}}{\omega_{1+3} + \omega_1 + \omega_3}, \tag{14.B.11}$$

$$\tilde{T}^{(2)}_{0,1,2,3} = W^{(2)}_{0,1,2,3} - \frac{V^{(1)}_{0,2,3-1}V^{(2)}_{3-1,1,3}}{\omega_{3-1} + \omega_1 - \omega_3} - \frac{V^{(1)}_{0,3-1,2}V^{(2)}_{3-1,1,3}}{\omega_{3-1} + \omega_1 - \omega_3}$$
$$- \frac{V^{(2)}_{0,2-0,2}V^{(2)}_{1-3,3,1}}{\omega_{1-3} + \omega_3 - \omega_1} - \frac{V^{(3)}_{0,-0-1,1}V^{(3)}_{-2-3,3,2}}{\omega_{2+3} + \omega_2 + \omega_3}$$
$$- \frac{V^{(3)}_{0,1,-0-1}V^{(3)}_{-2-3,3,2}}{\omega_{2+3} + \omega_2 + \omega_3} - \frac{V^{(1)}_{2+3,2,3}V^{(2)}_{0,1,0+1}}{\omega_{2+3} - \omega_2 - \omega_3} \tag{14.B.12}$$

$$T^{(2)}_{0,1,2,3} = \frac{1}{2}(\tilde{T}^{(2)}_{0,1,2,3} + \tilde{T}^{(2)}_{0,1,3,2}) \tag{14.B.13}$$

$$\tilde{T}^{(3)}_{0,1,2,3} = W^{(3)}_{0,1,2,3} - \frac{V^{(2)}_{0,1+2,3}V^{(1)}_{1+2,2,1}}{\omega_{1+2} - \omega_1 - \omega_2} - \frac{V^{(2)}_{0,1-2+3}V^{(2)}_{-2+3,2,3}}{\omega_{2-3} + \omega_2 - \omega_3}$$
$$- \frac{V^{(3)}_{0,1,2-3}V^{(2)}_{2-3,3,2}}{\omega_{2-3} + \omega_3 - \omega_2} - \frac{V^{(3)}_{0,1-3,2}V^{(2)}_{1-3,3,1}}{\omega_{1-3} + \omega_3 - \omega_1}$$
$$- \frac{V^{(1)}_{0,3,-1-2}V^{(3)}_{-1-2,1,2}}{\omega_{1+2} + \omega_1 + \omega_2} - \frac{V^{(1)}_{0,-1-2,3}V^{(3)}_{-1-2,2,1}}{\omega_{1+2} + \omega_1 + \omega_2} \tag{14.B.14}$$

$$\tilde{T}^{(4)}_{0,1,2,3} = W^{(4)}_{0,1,2,3} - \frac{V^{(3)}_{0,1,2+3}V^{(1)}_{2+3,3,2}}{\omega_{2+3}-\omega_2-\omega_3} - \frac{V^{(3)}_{0,1+3,2}V^{(1)}_{1+3,3,1}}{\omega_{1+3}-\omega_1-\omega_3}$$
$$- \frac{V^{(2)}_{0,1,-2-3}V^{(3)}_{-2-3,3,2}}{\omega_{2+3}+\omega_2+\omega_3}\,. \tag{14.B.15}$$

The kernel in (14.3.13) is

$$B_{0,1,2,3} = \frac{(V^{(3)}_{0,1,-0-1} + V^{(3)}_{0,-0-1,1})(V^{(3)}_{2,3,-2-3} + V^{(3)}_{2,-2-3,3})}{4(\omega_0+\omega_1+\omega_{0+1})(\omega_2+\omega_3+\omega_{2+3})}$$
$$+ \frac{(V^{(1)}_{1,2,1-2} + V^{(1)}_{1,1-2,2})(V^{(1)}_{3,0,3-0} + V^{(1)}_{3,3-0,0})}{4(\omega_1-\omega_2-\omega_{1-2})(\omega_3-\omega_0-\omega_{3-0})}$$
$$+ \frac{(V^{(1)}_{1,3,1-3} + V^{(1)}_{1,1-3,3})(V^{(1)}_{2,0,2-0} + V^{(1)}_{2,2-0,0})}{4(\omega_1-\omega_3-\omega_{1-3})(\omega_2-\omega_0-\omega_{2-0})}$$
$$- \frac{(V^{(1)}_{0+1,0,1} + V^{(1)}_{0+1,1,0})(V^{(1)}_{2+3,2,3} + V^{(1)}_{2+3,3,2})}{4(\omega_{0+1}-\omega_0-\omega_1)(\omega_{2+3}-\omega_2-\omega_3)}$$
$$- \frac{(V^{(1)}_{0,2,0-2} + V^{(1)}_{0,0-2,2})(V^{(1)}_{3,1,3-1} + V^{(1)}_{3,3-1,1})}{4(\omega_0-\omega_2-\omega_{0-2})(\omega_3-\omega_1-\omega_{3-1})}$$
$$- \frac{(V^{(1)}_{0,3,0-3} + V^{(1)}_{0,0-3,3})(V^{(1)}_{2,1,2-1} + V^{(1)}_{2,2-1,1})}{4(\omega_0-\omega_3-\omega_{0-3})(\omega_2-\omega_1-\omega_{2-1})}\,. \tag{14.B.16}$$

Numerical Simulation of Nonlinear Wave Dynamics

15

15.1 Introduction

For time-dependent and nonlinear free-surface motions, analytical solutions are rarely available, and theoretical studies and practical applications rely very much on numerical simulations. Numerical methods are developed according to the specific applications of interest, based on assumptions regarding the dominant physical processes involved.

For instance, for marine structures and ships with characteristic dimensions larger than those of the surface waves, viscous effects and surface tension can often be neglected. On the other hand, nonlinear free-surface effects become important under conditions of large motions and extreme loads, for which high performance, safety and ultimate survivability are of concern.

Significant advances in the simulation of nonlinear wave dynamics have been made in the past 30 years. A number of articles give comprehensive reviews of this progress. These include the excellent reviews by Mei (1978) for ideal, linear free-surface flows using integral-equation and finite-element methods; Schwartz and Fenton (1982) for ideal, nonlinear flows with emphasis on theoretical methods; Yeung (1982) for both linear and nonlinear ideal flows; Floryan and Rasmussen (1989) for viscous flows with moving interfaces; Tsai and Yue (1996) for incompressible, nonlinear free-surface flow; and Scardovelli and Zaleski (1999) for viscous free-surface and interfacial flows focusing on fixed-grid volume-of-fluid methods.

Numerical methods in nonlinear free-surface flow computations can be generally categorized into volume-discretization and boundary-discretization approaches. Volume-discretization methods are applicable to

both inviscid and viscous flows, while boundary-discretization approaches are mainly used when the flow is inviscid and irrotational.

Volume discretization methods can be broadly classified in terms of their use of structured versus unstructured grids. The former includes approaches such as finite difference (e.g. Rogers and Kwak, 1991; Colagrossi et al., 2003) and finite volume (e.g. Kothe, 1998; Tryggvason et al., 2001); the latter is characterized by methods such as finite-elements (e.g. Ma et al., 2001a, b; Tezduyar, 2003; Idelsohn et al., 2003) and its variations. A key distinction when nonlinear waves are involved is the way the interface is tracked or captured. Recent reviews of these include Tryggvason et al. (2003) and Sethian and Smereka (2003). Volume-discretization methods are in general more versatile but also more computationally expensive because of the extra spatial dimension involved.

In many wave hydrodynamics applications in ocean and coastal engineering, the assumption of inviscid irrotational flow is valid, while the demands for high resolution and large spatial-temporal domains are high. In this context, boundary-discretization methods (and their variations) are the favored choice and these methods and their applications to nonlinear wave dynamics is the focus of this chapter.

We describe in detail two relatively modern developments: (a) the high-order spectral method; (b) the high-order spectral element method; and (c) the mixed Euler-Lagrangian method. The spectral methods in (a) and (b) are powerful methods that account for high-order wave interactions and are extremely efficient computationally; while method (c) is useful for fully nonlinear (e.g. overturning wave) simulations but is relatively more computationally expensive. For (a), we present detailed formulation and numerical implementation, and example applications to two- and three-dimensional nonlinear wave interactions and to cases involving variable current, bottom topography and submerged bodies. The method can be extended to more complex situations involving surface-piercing bodies and/or walls. Details of the formulation and implementation of this extension (b) are provided, and illustrated by an application of the method to study the classical problem of instability of steep standing waves in a tank. For (c), both Cauchy and Green integral formulations are given. For the latter, a development of a high-order boundary-element method is presented. As illustration, applications to two- and three-dimensional breaking waves, steep crescent waves, plunging wave impact, and nonlinear wave diffraction by surface-piercing structures are discussed.

15.2 General Initial Boundary-Value Problem

For convenience, we recall the equations for the initial-boundary-value problem governing the general problem of steep interacting waves, with or without the presence of a floating or submerged body. We define a Cartesian coordinate system $\mathbf{r} \equiv (x, y, z)$, and let $(x, y) \equiv \mathbf{x}$ be the horizontal coordinates, z the vertical coordinate, positive upward, and $z = 0$ the mean free surface.

The fluid is assumed homogeneous, incompressible, inviscid, and its motion irrotational. The flow is described by a velocity potential $\Phi(\mathbf{r}, t)$, which satisfies the Laplace equation,

$$\nabla^2 \Phi(\mathbf{r}, t) = 0\,, \quad \mathbf{r} \in \mathcal{V}(t)\,, \tag{15.2.1}$$

where $\mathcal{V}(t)$ represents the fluid domain. On a prescribed impervious boundary, $\mathcal{B}(t)$, the normal velocity of the flow equals that of the boundary:

$$\frac{\partial \Phi}{\partial n} \equiv \Phi_n = \mathbf{U}(\mathbf{r}, t) \cdot \mathbf{n}\,, \quad \mathbf{r} \in \mathcal{B}(t)\,, \tag{15.2.2}$$

where $\mathbf{n}$ is the unit normal out of $\mathcal{B}(t)$ and $\mathbf{U}$ the prescribed velocity of $\mathcal{B}(t)$. On the free surface, $\mathcal{F}(t)$, the dynamic boundary condition can be written in Lagrangian form:

$$\frac{\mathrm{D}\Phi}{\mathrm{D}t} = \frac{1}{2}|\nabla\Phi|^2 - gz - \frac{P_{\mathcal{F}}}{\rho}\,, \quad \mathbf{r} \in \mathcal{F}(t)\,, \tag{15.2.3}$$

where $\mathrm{D}/\mathrm{D}t \equiv \partial/\partial t + \nabla\Phi \cdot \nabla$ denotes material derivative and $P_{\mathcal{F}}$ the given pressure on $\mathcal{F}(t)$. The kinematic boundary condition on $\mathcal{F}(t)$ in Lagrangian form is:

$$\frac{\mathrm{D}\mathbf{r}}{\mathrm{D}t} = \nabla\Phi\,, \quad \mathbf{r} \in \mathcal{F}(t)\,. \tag{15.2.4}$$

For deep water, the appropriate far-field condition is

$$\nabla\Phi(\mathbf{r}, t) \to 0\,, \quad \text{as} \quad z \to -\infty\,. \tag{15.2.5}$$

At the initial time, $t = 0$, the free surface position $\mathcal{F}(0)$ and the velocity potential on the free surface $\Phi(\mathbf{r} \in \mathcal{F}(0))$ are given, while $\mathcal{B}(t)$ and $\mathbf{U}(\mathbf{r} \in \mathcal{B}(t), t)$ are presumed given (or can be solved for) for all t. The initial boundary-value problem is complete with the imposition of appropriate radiation conditions in the far field.

In the case of non-overturning waves, the free surface ($\mathcal{F}(t)$) can be represented by $z = \zeta(\mathbf{x}, t)$ where ζ is continuous and a single-valued function of $\mathbf{x}$. The kinematic and dynamic boundary conditions ((15.2.4), (15.2.3)) can be written in Eulerian form in terms of ζ:

$$\left.\begin{aligned} \zeta_t + \nabla_{\mathbf{x}}\zeta \cdot \nabla_{\mathbf{x}}\Phi - \Phi_z = 0\,, \\ \Phi_t + g\zeta + \frac{1}{2}(\nabla\Phi \cdot \nabla\Phi) + \frac{P_{\mathcal{F}}}{\rho} = 0\,, \end{aligned}\right\} \quad z = \zeta(\mathbf{x}, t) \tag{15.2.6}$$

where $\nabla_{\mathbf{x}} \equiv (\partial/\partial x, \partial/\partial y)$ denotes the horizontal gradient.

The pressure in the fluid or on the body is determined in terms of Φ according to Bernoulli's equation:

$$\frac{P(\mathbf{r}, t)}{\rho} = -\Phi_t - \frac{1}{2}\nabla\Phi \cdot \nabla\Phi - gz\,. \tag{15.2.7}$$

The instantaneous hydrodynamic force on the body is obtained by direct integration of (15.2.7) over the instantaneous body wetted surface.

15.3 High-Order Spectral (HOS) Method

Obtaining useful solutions to the general nonlinear wave hydrodynamic problem stated above is a challenging task. Although linearized theory is often sufficient for routine design and analysis in ocean engineering applications, it is precisely the conditions of extreme loads and motions essential to the critical performance, safety, and even survival, for which nonlinear effects must be considered. Despite this, fully-nonlinear results are so far still relatively limited due to both theoretical and computational difficulties (e.g. see Tsai and Yue, 1996 for a review). Much of the attention in the past has been devoted to the understanding of weakly-nonlinear waves using a variety of perturbation techniques.

As described in Chapter Thirteen, a powerful approach for studying weakly-nonlinear slowly-modulated waves is the nonlinear Schrödinger equation (NLS) first derived for water waves by Zakharov (1968). By including the leading nonlinearity at third order (in wave slope), NLS predicts salient phenomena such as envelope solitons (Zakharov and Shabat, 1972) and recurrence (Yuen and Ferguson, 1978). Dysthe (1979) extended NLS to fourth order which is able to model nonsymmetric features such as the unequal growth of side-band perturbations of a Stokes wave train,

and the forward steepening and fission of wave packets (Lo and Mei, 1985). The main shortcomings of NLS are the requirements of narrow-bandedness and slow modulation which limits its usefulness in many applications. In three dimensions, the limitations of NLS are much more severe in that perturbations which are initially confined in a narrow band do not necessarily remain so (Martin and Yuen, 1980).

Somewhat more general alternatives to NLS are the so-called Zakharov equations (Zakharov, 1968; Crawford et al., 1981) and the closely related mode-coupling approaches (e.g. Phillips, 1960; Benney, 1962; West et al., 1974; Cohen et al., 1976). These weakly nonlinear theories do not rely on the narrow-banded assumption, and obtain useful results in two and three dimensions such as linear instability, restablization at large amplitudes, and bifurcation (e.g. Yuen and Lake, 1982). These matters have been summarized in Chapter Fourteen. For computations, the Zakharov equation is discretized in terms of a fixed number of free waves whose amplitudes are governed by coupled nonlinear evolution equations. These differential equations resemble the so-called mode-coupling equations which are obtained by directly substituting a series of Fourier modes into the governing equations and expanding to a given order. In both theories, all the nonlinear interactions among the wave modes are accounted for up to the desired perturbation order. Generalizing to include more free wave modes and to higher order is straightforward in theory. In practice, however, this is severely limited by the intractable complexity of the algebra involved with increasing mode number and order. Thus, only a small number, say $O(10)$, of free wave modes and low perturbation orders are typically used in practice. Examples include Stiassnie and Shemer (1984)'s extension of the Zakharov equation to include quintet (fourth-order) interactions, and extensive studies of the mode-coupling equations (mainly at third order).

By extending the Zakharov/mode-coupling idea into a direct computational approach, Dommermuth and Yue (1987a) and West et al. (1987) independently developed a powerful numerical method: the high-order spectral (HOS) method. This method computationally accounts for nonlinear interactions up to an arbitrary specified order M in wave steepness; and a large number of free wave modes, say $N = O(1000)$ per horizontal dimension, are typically used in nonlinear simulations. Each of the latter wave components is free in that it is subject to its own evolution equation. HOS accounts for nonlinear interactions among all these modes, up to the desired perturbation order M, according to the nonlinear free-surface

boundary conditions, which are treated in a pseudo-spectral manner (Fornberg and Whitham, 1978). By using fast transform techniques, the computational effort is only linearly proportional the total number of modes N and the order M. The convergence with N and M is shown to be exponentially fast for waves up to approximately 80% of Stokes limiting steepness ($\epsilon \sim 0.35$). Such high efficiency and accuracy makes the HOS an ideal approach for mechanism studies in nonlinear wave dynamics. The HOS method has been tested extensively and compared to experiments and other weakly and fully nonlinear predictions for wave-wave interactions in two and three dimensions (Dommermuth and Yue, 1987a; Dommermuth and Yue, 1987c). The method has been generalized to include the presence of atmospheric forcing (Dommermuth and Yue, 1988a), long-short waves (Zhang et al., 1993), finite depth and depth variations (Liu and Yue, 1998), variable current (Wu, 2004), and fixed and moving submerged bodies (Liu et al., 1992; Zhu et al., 1999). Recently, HOS has been applied and further developed for the prediction of nonlinear ocean wave-field evolution over large spatial-temporal domains.

The basic mathematic formulation and implementation issues of HOS are described in this section. Representative applications of the HOS method for nonlinear wave-wave, wave-current, and wave-bottom interactions are presented in Section 15.4. The extension of the method to nonlinear wave-body interactions is discussed in Section 15.5.

15.3.1 Mathematical Formulation

For clarity, we first consider the relatively simple case of interaction of nonlinear waves in deep water. Extensions to include the presence of finite depth and variable bottom, variable current, and submerged bodies are described subsequently. As in Zakharov (1968), we define the potential on the free surface

$$\Phi^s(\mathbf{x}, t) \equiv \Phi(\mathbf{x}, \zeta(\mathbf{x}, t), t)\,. \tag{15.3.1}$$

Upon using chain rules

$$\Phi_t(\mathbf{x}, \zeta, t) = \Phi^s_t(\mathbf{x}, t) - \Phi_z(\mathbf{x}, \zeta, t)\zeta_t\,, \quad \text{and} \tag{15.3.2}$$

$$\nabla_{\mathbf{x}}\Phi(\mathbf{x}, \zeta, t) = \nabla_{\mathbf{x}}\Phi^s(\mathbf{x}, t) - \Phi_z(\mathbf{x}, \zeta, t)\nabla_{\mathbf{x}}\zeta\,, \tag{15.3.3}$$

we can rewrite the free surface boundary conditions (15.2.6) as:

$$\left.\begin{aligned} \zeta_t + \nabla_{\mathbf{x}}\zeta \cdot \nabla_{\mathbf{x}}\Phi^s - (1 + \nabla_{\mathbf{x}}\zeta \cdot \nabla_{\mathbf{x}}\zeta)\Phi_z(\mathbf{x}, \zeta, t) = 0\,, \\ \Phi^s_t + g\zeta + \frac{1}{2}\nabla_{\mathbf{x}}\Phi^s \cdot \nabla_{\mathbf{x}}\Phi^s - \frac{1}{2}(1 + \nabla_{\mathbf{x}}\zeta \cdot \nabla_{\mathbf{x}}\zeta)\Phi_z^2(\mathbf{x}, \zeta, t) = -\frac{P_{\mathcal{F}}}{\rho}\,. \end{aligned}\right\} \tag{15.3.4}$$

An apparent advantage of using (15.3.4) instead of (15.2.6) as free-surface boundary conditions is that given the initial values of ζ and Φ^s, (15.3.4) can be directly integrated in time for the new values of ζ and Φ^s in terms of the surface vertical velocity $\Phi_z(\mathbf{x}, \zeta, t)$ (only) to be obtained from the boundary-value problem. A more subtle but important advantage of the Zakharov representation (15.3.4) is that it leads naturally and effectively to the high-order perturbation expansion in wave steepness below.

High-order expansions

We assume that Φ and ζ are $O(\epsilon)$ quantities, where ϵ, a small parameter, is a measure of the wave steepness. We consider a consistent approximation up to a given order M in ϵ, and write Φ in a perturbation series in ϵ:

$$\Phi(\mathbf{x}, z, t) = \sum_{m=1}^{M} \Phi^{(m)}(\mathbf{x}, z, t)\,, \tag{15.3.5}$$

where $\Phi^{(m)} = O(\epsilon^m)$ are the perturbation potentials and $()^{(m)}$ denotes a quantity of $O(\epsilon^m)$.

We then further expand each $\Phi^{(m)}$ evaluated on the instantaneous free surface $z = \zeta$ in Taylor series about the mean free surface $z = 0$, so that

$$\Phi^s(\mathbf{x}, t) = \sum_{m=1}^{M} \sum_{\ell=0}^{M-m} \frac{\zeta^\ell}{\ell!} \left.\frac{\partial^\ell \Phi^{(m)}}{\partial z^\ell}\right|_{z=0}\,. \tag{15.3.6}$$

The method in principle is capable of accounting for nonlinearities up to an arbitrary order M in ϵ. In practice, however, (15.3.6) places a limit on the maximum steepness of the free surface we can consider. In particular, the validity and convergence of (15.3.6) is limited by the radius of convergence (from $z = 0$) of Φ, which cannot extend beyond the first singularity in the analytic continuation of Φ above $z = \zeta$.

At a given time instant, ζ and Φ^s are obtained by the nonlinear evolution equations (15.3.4). Thus, we can treat (15.3.6) as a Dirichlet boundary condition for the unknown Φ. Expanding (15.3.6) and collecting terms at

each order, we obtain a sequence of Dirichlet boundary conditions for the unknown $\Phi^{(m)}$ on $z = 0$:

$$\Phi^{(m)}(\mathbf{x}, 0, t) = f^{(m)}\,, \quad m = 1, 2, \ldots, M\,, \tag{15.3.7}$$

where

$$\begin{cases} f^{(1)} = \Phi^s \\ f^{(m)} = -\displaystyle\sum_{\ell=1}^{m-1} \frac{\zeta^\ell}{\ell!} \left.\frac{\partial^\ell \Phi^{(m-\ell)}}{\partial z^\ell}\right|_{z=0}\,, \quad m = 2, 3, \ldots, M\,. \end{cases} \tag{15.3.8}$$

These boundary conditions, in addition to Laplace's equation and the deep water condition

$$\nabla\Phi^{(m)} \to 0\,, \quad \text{as} \quad z \to -\infty\,, \quad m = 1, 2, \ldots, M\,, \tag{15.3.9}$$

define a sequence of boundary-value problems for $\Phi^{(m)}$, $m = 1, 2, \ldots, M$, in the domain $z \le 0$. These problems can be solved successively at increasing orders for any prescribed Φ^s and ζ.

Spectral approach for the boundary-value problem solution

As in a typical mode-coupling approach, we represent each $\Phi^{(m)}$ as an eigenfunction expansion of free modes which satisfy all but the Dirichlet free-surface condition (15.3.7). Thus we write

$$\Phi^{(m)}(\mathbf{x}, z, t) = \sum_{n=1}^{\infty} \Phi_n^{(m)}(t)\Psi_n(\mathbf{x}, z)\,, \quad z \le 0\,, \tag{15.3.10}$$

where, in practice, the number of eigenmodes in (15.3.10) is truncated at some suitable number N. Substitution of (15.3.10) into (15.3.7) determines the modal amplitudes $\Phi_n^{(m)}(t)$ in terms of the modal components of Φ^s and ζ. After the boundary-value problems for $\Phi^{(m)}$ are solved up to the desired order M, the vertical velocity on the free surface is given by

$$\Phi_z(\mathbf{x}, \zeta, t) = \sum_{m=1}^{M} \sum_{\ell=0}^{M-m} \frac{\zeta^\ell}{\ell!} \sum_{n=1}^{N} \Phi_n^{(m)}(t) \left.\frac{\partial^{\ell+1}}{\partial z^{\ell+1}} \Psi_n(\mathbf{x}, z)\right|_{z=0}\,. \tag{15.3.11}$$

Substitution of (15.3.11) into (15.3.4) yields the final result:

$$\zeta_t + \nabla_{\mathbf{x}}\zeta \cdot \nabla_{\mathbf{x}}\Phi^s - (1 + \nabla_{\mathbf{x}}\zeta \cdot \nabla_{\mathbf{x}}\zeta) \times \left[\sum_{m=1}^{M} \sum_{\ell=0}^{M-m} \frac{\zeta^\ell}{\ell!} \sum_{n=1}^{N} \Phi_n^{(m)}(t) \left.\frac{\partial^{\ell+1}}{\partial z^{\ell+1}} \Psi_n(\mathbf{x}, z)\right|_{z=0}\right] = 0\,, \tag{15.3.12}$$

and

$$\Phi_t^s + g\zeta + \frac{1}{2}\nabla_{\mathbf{x}}\Phi^s \cdot \nabla_{\mathbf{x}}\Phi^s - \frac{1}{2}(1 + \nabla_{\mathbf{x}}\zeta \cdot \nabla_{\mathbf{x}}\zeta)$$
$$\times \left[\sum_{m=1}^{M}\sum_{\ell=0}^{M-m}\frac{\zeta^\ell}{\ell!}\sum_{n=1}^{N}\Phi_n^{(m)}(t)\,\frac{\partial^{\ell+1}}{\partial z^{\ell+1}}\Psi_n(\mathbf{x},z)\bigg|_{z=0}\right]^2 = -\frac{P_{\mathcal{F}}}{\rho}\,. \qquad (15.3.13)$$

Equations (15.3.12) and 15.3.13) are the evolution equations for ζ and Φ^s in terms of the modal amplitudes $\Phi_n^{(m)}$. These evolution equations can then be integrated for the new values of Φ^s and ζ. The process is repeated starting from initial conditions.

Comparison to direct collocation method

In a variation that does not involve the expansions (15.3.5) and (15.3.6), the eigenfunctions are continued above $z = 0$, and (15.3.1) is written directly as

$$\Phi(\mathbf{x},\zeta,t) = \sum_{n=1}^{N}\Phi_n(t)\exp[|\mathbf{K}_n|\zeta + \mathrm{i}\mathbf{K}_n\cdot\mathbf{x}] = \Phi^s(\mathbf{x},t)\,. \qquad (15.3.14)$$

By collocating (15.3.14) at discrete points $\mathbf{x}_j$ on the exact free surface, the modal amplitudes are obtained as solution of a system of algebraic equations. Examples of this method include Rienecker and Fenton (1981) who performed the collocation in physical space, and Bryant (1983) who collocated in Fourier Space. For maximum and minimum surface elevation $\zeta_{\max}$ and $\zeta_{\min}$ respectively, the ratio $\exp|\mathbf{K}_n|\zeta_{\max}/\exp|\mathbf{K}_n|\zeta_{\min}$ increases rapidly with n for finite ϵ. As N increases, the conditioning of the equation system deteriorates severely, independent of convergence of (15.3.6). Moreover, the operation count is typically $O(N^3)$ per time step. The present scheme using (15.3.7) has an operation count linearly proportional to N (see Section 15.3.2) and may be viewed as a more effective and efficient perturbation solution of the system (15.3.14).

Basis function in deep water

In deep water, the eigenfunctions in (15.3.10) can be obtained in simple closed form. Assuming a rectangular domain, $-L/2 \le x \le L/2$ and $-W/2 \le y \le W/2$, and periodic boundary conditions in both horizontal dimensions, we write

$$\Psi_n(\mathbf{x},z) = \exp(|\mathbf{K}_n|z + \mathrm{i}\mathbf{K}_n\cdot\mathbf{x})\,. \qquad (15.3.15)$$

Here the wavenumber vector $\mathbf{K}_n \equiv (K_{xn}, K_{yn}) = (2\pi p/L, 2\pi q/W)$, $p = 0, \pm 1, \ldots, \pm(N_x - 1)$, $q = 0, \pm 1, \ldots, \pm(N_y - 1)$, where N_x and N_y are the maximum numbers of Fourier modes considered in the x- and y-directions, respectively. Clearly, Ψ_n in (15.3.15) is harmonic and satisfies the deep water condition. With (15.3.15), the perturbation potential (15.3.10) and the surface vertical velocity (15.3.11) can be written as:

$$\Phi^{(m)}(\mathbf{x}, z, t) = \sum_{n=1}^{N} \Phi_n^{(m)}(t) \exp(|\mathbf{K}_n| z + \mathrm{i}\mathbf{K}_n \cdot \mathbf{x}), \quad z \le 0, \tag{15.3.16}$$

and

$$\Phi_z(\mathbf{x}, \zeta, t) = \sum_{m=1}^{M} \sum_{\ell=0}^{M-m} \frac{\zeta^\ell}{\ell!} \sum_{n=1}^{N} \Phi_n^{(m)}(t) |\mathbf{K}_n|^{\ell+1} \exp(\mathrm{i}\mathbf{K}_n \cdot \mathbf{x}). \tag{15.3.17}$$

Basis function in constant finite depth

In the case of constant finite depth h, the eigenfunction Ψ_n can be expressed as:

$$\Psi_n(\mathbf{x}, z) = \frac{\cosh[|\mathbf{K}_n|(z+h)]}{\cosh|\mathbf{K}_n| h} \exp(\mathrm{i}\mathbf{K}_n \cdot \mathbf{x}). \tag{15.3.18}$$

which reduces to (15.3.15) as $h \to \infty$. In this case, (15.3.10) and (15.3.11) can be expressed as:

$$\Phi^{(m)}(\mathbf{x}, z, t) = \sum_{n=1}^{N} \Phi_n^{(m)}(t) \frac{\cosh[|\mathbf{K}_n|(z+h)]}{\cosh|\mathbf{K}_n| h} \exp(\mathrm{i}\mathbf{K}_n \cdot \mathbf{x}), \quad z \le 0, \tag{15.3.19}$$

and

$$\Phi_z(\mathbf{x}, \zeta, t) = \sum_{m=1}^{M} \sum_{\ell=0}^{M-m} \frac{\zeta^\ell}{\ell!} \sum_{n=1}^{N} \Phi_n^{(m)}(t) \frac{\exp(\mathrm{i}\mathbf{K}_n \cdot \mathbf{x})}{\cosh(|\mathbf{K}_n| h)} \times \frac{\partial^{\ell+1}}{\partial z^{\ell+1}} \{\cosh[|\mathbf{K}_n|(z+h)]\} \Big|_{z=0}. \tag{15.3.20}$$

Basis function in the presence of a varying bottom

The analysis is slightly more complicated for a mildly varying bottom given by $z = -h + b(\mathbf{x})$. The kinematic condition on the bottom is

$$\Phi_z - \nabla_{\mathbf{x}} b \cdot \nabla_{\mathbf{x}} \Phi = 0, \quad z = -h + b(\mathbf{x}). \tag{15.3.21}$$

In the spirit of (15.3.5) and (15.3.6), we expand the bottom condition (15.3.21) in a Taylor series with respect to the mean bottom $z = -h$. For simplicity, we assume the bottom variation $b(\mathbf{x}) = O(\epsilon)$. After substituting the perturbation expansion of the potential (15.3.5) and collecting terms at the respective orders, we obtain for successive orders a sequence of Neumann conditions on $z = -h$:

$$\Phi_z^{(m)}(\mathbf{x}, -h, t) = B^{(m)}\,, \quad m = 1, 2, \ldots, M\,, \tag{15.3.22}$$

where $B^{(1)} = 0$, and

$$B^{(m)} = \sum_{\ell=1}^{m-1} \left\{ \frac{\partial}{\partial x} \left[\frac{b^\ell}{\ell!} \frac{\partial^{(\ell-1)}}{\partial z^{(\ell-1)}} \Phi_x^{(m-\ell)} \bigg|_{z=-h} \right] + \frac{\partial}{\partial y} \left[\frac{b^\ell}{\ell!} \frac{\partial^{(\ell-1)}}{\partial z^{(\ell-1)}} \Phi_y^{(m-\ell)} \bigg|_{z=-h} \right] \right\}, \quad m = 2, 3, \ldots, M\,. \tag{15.3.23}$$

At each order m, we express the perturbation potential as:

$$\Phi^{(m)} = \alpha^{(m)} + \beta^{(m)} \tag{15.3.24}$$

where

$$\alpha^{(m)}(\mathbf{x}, z, t) = \sum_{n=1}^{N} \alpha_n^{(m)}(t) \frac{\cosh[|\mathbf{K}_n|(z+h)]}{\cosh(|\mathbf{K}_n|h)} \mathrm{e}^{\mathrm{i}\mathbf{K}_n \cdot \mathbf{x}} \tag{15.3.25}$$

and

$$\beta^{(m)}(\mathbf{x}, z, t) = \beta_0^{(m)} z + \sum_{n=1}^{N} \beta_n^{(m)}(t) \frac{\sinh(|\mathbf{K}_n|z)}{|\mathbf{K}_n| \cosh(|\mathbf{K}_n|h)} \mathrm{e}^{\mathrm{i}\mathbf{K}_n \cdot \mathbf{x}}\,. \tag{15.3.26}$$

Note that $\alpha^{(m)}$ and $\beta^{(m)}$ respectively satisfy zero Neumann condition on $z = -h$ and zero Dirichlet condition on $z = 0$. In general, the number of free-surface and bottom wavenumbers, say N_f and N_b, can be chosen independently in the HOS method. For simplicity and without loss of generality, we use $N_f = N_b = N$, where applicable, in subsequent discussions.

In the presence of submerged bodies, the present HOS method can be extended using different basis functions. The details are described in Section 15.5. In the case of surface-piercing bodies/boundaries, the free-surface becomes discontinuous, Fourier spectral basis functions can no longer be applied without losing the spectral convergence, due to Gibb's phenomenon. In this case, expansions using basis functions (such as Chebyshev polynomial) whose convergence does not depend on the end conditions

must be employed. When large N is involved, however, the conditioning of the resulting system of algebraic equations deteriorates rapidly with increasing N. In this case, a special approach, the high-order spectral element (HOSE) method, has been developed and used with efficacy. The HOSE method is presented in Section 15.6.

15.3.2 Numerical Implementation

The time simulation of the nonlinear wave problem using N wave modes and retaining nonlinearities up to a specified order M consists of three main steps. Beginning from initial values for ζ and Φ^s, at each successive time step: (i) solve the boundary-value problem for the perturbation velocity potentials $\Phi^{(m)}(\mathbf{x}, z, t)$, $m = 1, \ldots, M$; (ii) evaluate the vertical velocity at the free surface $\Phi_z(\mathbf{x}, \zeta, t)$; and (iii) integrate the evolution equations (15.3.12) and (15.3.13) forward in time for $\zeta(\mathbf{x}, t + \Delta t)$ and $\Phi^s(\mathbf{x}, t + \Delta t)$; and the process (i)–(iii) is repeated.

In the HOS method, the modal amplitudes of the perturbation potential $\Phi_n^{(m)}(t)$ subject to the Dirichlet condition (15.3.7) are solved using a pseudo-spectral method. Specifically, all spatial derivatives of $\Phi^{(m)}$, Φ^s and ζ are evaluated in wavenumber space while nonlinear products (such as those in (15.3.8) and (15.3.11)) are calculated in physical space at a discrete set of points $\mathbf{x}_j$. For periodic boundary conditions using the Fourier expansions ((15.3.16) in deep water and (15.3.19) in finite depth), $\mathbf{x}_j$ are equally spaced and fast-Fourier transforms are used to project between the wavenumber and physical domains. At each order, (15.3.7) is solved in wavenumber space by equating Fourier modes, and the number of operations required is $O(N \ln N)$. For perturbations up to order M, the operation count is then $O(MN \ln N)$ per time step.[1] The (near) linear computational effort with mode number N and perturbation order M, and the exponential convergence with both M and N (see Section 15.3.3) are notable characteristics of the computational efficacy of HOS methods.

After the surface vertical velocity is obtained from (15.3.11), the nonlinear evolution equations (15.3.12) and (15.3.13) are integrated as a coupled

[1] At first glance, the effort for computing the summation in (15.3.11) appears to be proportional to M^2. After the summation is rewritten as

$$\sum_{\ell=0}^{M} \frac{\zeta^\ell}{\ell!} \sum_{n=1}^{N} \left[\sum_{m=1}^{M-\ell} \Phi_n^{(m)}(t) \right] \frac{\partial^{\ell+1}}{\partial z^{\ell+1}} \Psi_n(\mathbf{x}, z) \Big|_{z=0} ,$$

however, it becomes clear that the effort in fact is linearly proportional to M.

set of nonlinear ordinary differential equations. We typically employ the fourth-order Runge-Kutta (RK4) scheme which requires twice as many evaluations as the commonly used multi-step predictor-corrector (e.g. the Adams-Bashforth-Moulton, ABM) methods of the same order but has a somewhat lower global truncation error and a larger stability region (see, e.g. Dommermuth et al., 1988).

15.3.3 Error Considerations

The main sources of computational error for the high-order nonlinear simulations are: (i) errors due to truncation in the number of spectral modes N, and the perturbation order M; (ii) error due to the finite (periodic) computational domain for a given simulation time, T_S; (iii) amplification of round-off and truncation errors; (iv) aliasing errors of the pseudo-spectral method; (v) errors due to numerical time integration; and (vi) for estimates of steady-state quantities (e.g. mean and harmonic force coefficients) from limit cycle results, errors due to the finite simulation time, T_S, of the initial-value problem.

Errors due to truncation in the number of modes N and order M

For sufficiently smooth ζ and Φ^s, the numerical error in the spectral representations of $\Phi^{(m)}$, $m = 1, \ldots, M$, vanishes exponentially as $N \to \infty$. Similarly, for mild nonlinearities, the truncation errors after order M is $O(\epsilon^{M+1})$, and the convergence is exponential with increasing M. As pointed out after (15.3.6), such convergence ceases beyond a certain wave steepness owing to singularities in the analytic continuation of the velocity potential. For regular Stokes waves, the maximum wave steepness for exponential convergence of the method is found to be $\epsilon = kA \sim 0.35$ (see Table 15.1 in Section 15.4.1). The corresponding maximum local slope is $\epsilon_L \equiv (\partial\zeta/\partial x)_{\max} \sim 0.38$. One notes that the incident Stokes wave steepness ϵ is neither the limiting nor most useful parameter for the general diffraction problem due to local wave steepening/transformation as they self interact or are diffracted/refracted by current, bottom or body. The maximum local steepness, ϵ_L, is thus a more general and useful measure. The limiting value of $\epsilon_L \sim 0.38$ for exponential convergence has been confirmed in a variety of HOS simulations. For local wave steepness beyond this limit, exponentially fast convergence is generally lost. It is very important to point out that even in this situation, (algebraically) converged HOS results may still obtain; for example, converged HOS results with $\epsilon_L \sim 1.5$

are reported in Liu et al. (1992) for steep waves over a horizontal submerged cylinder.

Error due to the finite computational domain

For a computational domain fixed relative to wavelength and dimension of the body (or variable current or bottom topography), the solution in the near field of the body will eventually be distorted due to "reflections" from the periodic boundaries as the simulation time, T_S, is increased. This error is avoided by successively increasing the size of the periodic domain until the quantities of interest no longer vary. Alternatively, or in addition, a spatial tapering filter can be effectively applied (as, for example in Section 15.4.5). With the $O(N)$ efficiency of the HOS method, the computation cost increases only linearly with the area of the computational domain, and this source of error has not been a critical factor in practice for even very large applications.

Amplification of round-off and truncation errors

The integrity of the numerical results can be severely limited by the amplification of computational errors. Consider, for instance, a small random error δ_{mn} in the modal amplitude $\Phi_n^{(m)}$, i.e. $\Phi_n^{(m)} = \tilde{\Phi}_n^{(m)}(1+\delta_{mn})$, where the tilde denotes "exact" values. The error in $f^{(m)}$, (15.3.8), after using (15.3.10) is then given by

$$f^{(m)} - \tilde{f}^{(m)} = -\sum_{\ell=1}^{m-1} \frac{\zeta^\ell}{\ell!} \sum_{n=1}^{N} \tilde{\Phi}_n^{(m)} \delta_{(m-\ell),n} \frac{\partial^\ell \Psi_n}{\partial z^\ell} \,. \tag{15.3.27}$$

In general, $|\partial^\ell \Psi_n / \partial z^\ell| \approx |\mathbf{K}_n|^\ell$, while $|\mathbf{K}_n| \sim n$, so that at any order the error in the highest wavenumber modes is the most amplified. On the other hand, in any computational model without dissipation, nonlinear interactions cause energy in the lower modes to cascade to higher modes which eventually accumulates at the highest wavenumbers retained in the model. The combined effect is probably a root cause of large wavenumber instabilities encountered in many nonlinear free-surface simulations where large wavenumbers (or fine spatial resolutions) are used. To eliminate such high-wavenumber instabilities, we follow Longuet–Higgins and Cokelet (1976) and apply a smoothing function to ζ and Φ^s. Their five-point smoothing function can be effectively applied in wavenumber space, which is equivalent to the low-pass filter

$$\Lambda(\mathbf{K}_n) = \frac{1}{8}\left[5 + 4\cos\left(\frac{\pi|\mathbf{K}_n|}{|\mathbf{K}_N|}\right) - \cos\left(\frac{2\pi|\mathbf{K}_n|}{|\mathbf{K}_N|}\right)\right]. \tag{15.3.28}$$

Alternatively, we may simply use an ideal low-pass filter:

$$\Lambda_I(\mathbf{K}_n,\nu)=\left\{\begin{array}{lll} 1 & \text{for} & \dfrac{|\mathbf{K}_n|}{|\mathbf{K}_N|}\le\nu \\ \\ 0 & \text{for} & \dfrac{|\mathbf{K}_n|}{|\mathbf{K}_N|}>\nu \end{array}\right\} \quad 0<\nu\le 1\,. \tag{15.3.29}$$

Since the ideal filter does not affect the lower wavenumbers, (15.3.29) is often preferred. In many simulations no smoothing or filtering is necessary. For very steep waves (involving possibility of wave breaking in the underlying physical problem) a useful alternative or additional treatment is to introduce wavenumber-dependent damping terms explicitly in the spectral equations.

Aliasing errors

In a pseudo-spectral approach, the product $h(x)=f(x)\cdot g(x)$, represented respectively by Fourier modes h_n, f_n, g_n, $n\le N$, is performed in physical space at equally-spaced points. This results in aliasing errors due to the finite Fourier representations. It is well known that in this case the best approximation (in the mean square sense) to the product is the so-called alias-free sum (e.g. Orszag, 1971). To obtain this, we double the number of Fourier modes and the number of collocation points to $2N$, calculate the product $H=FG$, as before in physical space, where $(F_n,G_n)=(f_n,g_n)$ for $|n|\le N$, and $(F_n,G_n)=(0,0)$ for $N<|n|\le 2N$, and define the alias-free product, h, by $h_n=H_n$ for $|n|\le N$. For products involving two or more terms, the multiplication is done successively where each factor is made alias-free before multiplying by the next term.

Errors due to numerical time integration

Provided that the boundary-value solution is obtained with the desired accuracy, the specific formula used for time integration of the evolution equations (15.3.12) and (15.3.13) is not critical, provided the criteria for stability and accuracy are obtained. For the linearized free-surface problem it is straightforward to carry out the linear stability analysis (e.g. Yeung, 1982) obtaining, for example, that Runge-Kutta and leap-frog methods can be conditionally stable, and implicit or semi-implicit (Crank-Nicolson) methods are generally (unconditionally) stable. Implicit methods involve additional computational effort and the preferred choices are stable multi-step explicit methods. We typically use the fourth-order Runge-Kutta (RK4) scheme which is explicit, and has a larger stability region and

a smaller truncation error than the leap-frog method. For stability, the Courant condition for RK4 is (Dommermuth and Yue, 1988)

$$\Delta t^2 \leq \frac{8\Delta x}{\pi g} \tag{15.3.30}$$

where Δt is the time step and Δx the local grid spacing. The local truncation error of RK4 is (Δt^5). The global truncation error for $t = O(1)$ is fourth order in Δt.

Errors in the estimation of mean and limit-cycle force coefficients

In many engineering applications, the quantities of practical interest are often steady-state values such as the mean and harmonic coefficients (under periodic input). In HOS simulations, a time history of the quantity of interest is obtained, and, after steady state (limit-cycle) is reached, the harmonics of the quantity are extracted. To obtain such harmonic coefficients from the initial-value simulation we define for definiteness

$$F_n(\tau_0) = \frac{1}{T}\int_{\tau_0}^{\tau_0+T} F(t)\mathrm{e}^{-\mathrm{i}n\omega t}\,\mathrm{d}t\,, \quad n = 0, 1, \ldots\,, \tag{15.3.31}$$

where $F(t)$ is the time-dependent force on the body obtained from the simulation, T the fundamental period (of the incident wave), $\omega = 2\pi/T$, and τ_0 a time beyond which limit-cycle values are obtained (or assumed). In practice, $F_n(\tau_0)$ is evaluated for successively increasing τ_0 until convergence is obtained. As in most simulation methods, the computational effort of HOS is linearly proportional to simulation time. In many applications, involving bodies for example, substantial care goes into the numerical implementation of HOS to minimize per time step effort to obtain efficient long-time simulations (see Section 15.5.2).

15.3.4 Relation to Frequency-Domain Perturbation Results

As pointed out above, steady and harmonic amplitudes are obtained via harmonic analysis of the limit-cycle time histories of HOS time-domain (initial-value problem) simulations. These results can be related in a direct way to the coefficients of frequency domain perturbation methods (e.g. linear and second-order wave forces and runup on a fixed cylinder analyzed in Section 13.11). In a typical frequency-domain approach the time dependence is factored out explicitly and the velocity potential, for instance, is written as:

$$\Phi = \sum_{n=0}^{\infty} \Re(\tilde{\phi}_n \mathrm{e}^{-\mathrm{i}n\omega t}) \,, \tag{15.3.32}$$

where $\omega = 2\pi/T$. Each $\tilde{\phi}_n$ is then expanded in a perturbation series in the wave steepness, ϵ:

$$\tilde{\phi}_n = \sum_{m=1}^{\infty} \epsilon^m \tilde{\phi}_n^{(m)} \,, \tag{15.3.33}$$

and the boundary-value problems for $\tilde{\phi}_n^{(m)}$ are solved.

In HOS simulation, the initial-boundary-value problem for $\Phi(\mathbf{x}, z, t)$ is integrated to the specified order M in ϵ up to the requisite time. Despite the truncation at M (see (15.3.5) and (15.3.6)), the presence of the nonlinear terms in (15.3.4) eventually causes all time harmonics to be present in Φ, in fact in each $\Phi^{(m)}$. Assuming a limit cycle is reached, the (complex) amplitudes of these harmonics are extracted via Fourier decomposition:

$$\phi_n^{(m)} = \frac{1}{T} \int_{\tau_0}^{\tau_0+T} \Phi^{(m)}(t) \mathrm{e}^{-\mathrm{i}n\omega t} \, \mathrm{d}t \,, \quad n = 1, 2, \ldots \,; \quad m = 1, 2, \ldots, M \,. \tag{15.3.34}$$

It should be pointed out that, in general, $\phi_n^{(m)}$, $n > m$ (and $\phi_0^{(1)}$), are small, as expected, but do not vanish. In the high-order time-domain approach, there is no *direct* relationship between m-th order terms in (15.3.34) and those in (15.3.33). For direct comparisons, it is useful to define the amplitude:

$$\phi_n^{\langle M \rangle} = \sum_{m=1}^{M} \phi_n^{(m)} \,, \quad n = 1, 2, \ldots \,. \tag{15.3.35}$$

Note that the magnitude of $\phi_n^{\langle M \rangle}$ is $O(\epsilon^n)$, except for $\phi_0^{\langle M \rangle}$, which is of second order. With this notation, then, the amplitudes in (15.3.33) and (15.3.35) are related by:

$$\left.\begin{aligned} \tilde{\phi}_0^{(2)} &= \phi_0^{\langle 2 \rangle} + O(\epsilon^3) \\ \tilde{\phi}_n^{(n)} &= \phi_n^{\langle M \rangle} + O(\epsilon^{n+1}) \,, \quad n > 0 \,, \quad \text{and} \quad M \geq n \,; \end{aligned}\right\} \tag{15.3.36}$$

while such simple relationships cannot, in general, be written for the amplitudes in (15.3.34). Similar formulae and results apply also to other quantities such as forces, wave amplitudes, etc. The relationships in (15.3.36) have been verified in the direct studies of nonlinear wave diffractions by a submerged circular cylinder (Section 15.5) and a surface-piercing vertical

cylinder (Section 15.7.8). We remark that, in some sense, the present time-domain results are more 'physical' in that they correspond directly to what one would actually measure in a laboratory.

15.4 Applications of HOS to Nonlinear Wave-Wave, Wave-Current, and Wave-Bottom Interactions

We apply HOS simulations to a number of gravity surface wave problems involving nonlinear wave-wave, wave-current, and wave-bottom interactions in this section to illustrate the usefulness and efficacy of the method. To assess the essential convergence property of HOS simulations with the number of spectral modes N and interaction order M, we first compute finite-amplitude Stokes waves and compare the results with the exact ("infinite-order") Stokes solution (Schwartz, 1974) (Section 15.4.1). To evaluate HOS accuracy and performance in simulating steep waves and long-time nonlinear evolution, we compare the HOS results to experiments and other existing theories for three different applications: an overturning wave created by an asymmetrically applied surface pressure computed using a fully-nonlinear mixed-Eulerian-Lagrangian scheme (MEL) (Longuet–Higgins and Cokelet, 1976; Vinje and Brevig, 1981; see Section 15.4.2); the long-time evolution of a two-dimensional wave train calculated using the modified (fourth-order) Zakharov equation (Stiassnie and Shemer, 1987) (Section 15.4.3); and experimental measurements of the evolution of a wave packet (Su, 1982) (Section 15.4.4). After its convergence and accuracy are verified, as illustrations, we generalize and apply HOS simulations to several more advanced studies: the nonlinear steady ship waves created by a moving pressure disturbance (Section 15.4.5); the nonlinear wave blocking by a variable current (Section 15.4.6); and the mechanisms of generalized high-order Bragg resonant interactions of surface waves with periodic bottom undulations (Section 15.4.7).

15.4.1 Stokes Waves

We test the accuracy and convergence with respect to the number of spectral modes N, order M, and time step Δt of the HOS method using exact progressive Stokes waves as a benchmark. For the solution of the latter, we follow Schwartz (1974), but solve the nonlinear equations associated with the mapping function (Schwartz' Eqs. 2.6) directly using Newton

iteration rather than high-order perturbation. The final results are exact to 14 significant figures. For simplicity, we consider deep water and use a computational domain of length $L = \lambda = 2\pi$, where λ is the fundamental wavelength of the Stokes wave. The eigenfunctions are given by (15.3.16) with integer wavenumbers $\mathbf{K}_n = (n, 0)$, $n = 0, \pm 1, \pm 2, \ldots, \pm N$. The numerical tests consist of two parts:

(*a*) *Convergence of the boundary-value problem solution*

This corresponds to steps (i) and (ii) in Section 15.3.2. We prescribe here ζ and Φ^s from exact Stokes waves and solve (15.3.7) for the velocity potential. In particular we compare the surface vertical velocity $\Phi_z|_{z=\zeta}$ against the exact value.

Table 15.1 shows the maximum absolute error in $\Phi_z|_{z=\zeta}$ as a function of the order M and the maximum alias-free wavenumber N for a range of steepness ϵ, defined here for the Stokes wave as $\epsilon \equiv k(\zeta_{\max} - \zeta_{\min})/2$ where $k = 1$ is the fundamental wavenumber. From Table 15.1, it is clear that for the $\epsilon \lesssim 0.35$ (approximately 80% of the Stokes limiting steepness), the error decreases exponentially fast with both N and M as they increase. For any given M, the results converge to a limit exponentially rapidly as N is increased. For sufficiently large N, exponential convergence with M also takes place. At $\epsilon = 0.40$, which is approximately 90% of Stokes limiting steepness, the expected convergence rate with respect to M is not realized.

(*b*) *Convergence of the numerical time integration*

We again use Stokes waves to evaluate the time integration truncation error of the HOS method. The initial conditions for Φ^s and ζ are prescribed from the exact Stokes solution for a specified ϵ, and the wave is allowed to propagate across the computational domain. We consider the maximum absolute error in the surface elevation after time $t/T = 1$ and 10 for fundamental wave period T. No smoothing or filtering is used. Table 15.2 gives a summary of this error for a range of time-step sizes $\Delta t/T$ for $\epsilon = 0.1$ ($N = 16, M = 6$) and $\epsilon = 0.2$ ($N = 16, M = 8$). By examining the ratios of the errors as Δt is decreased, it is seen that the expected $O(\Delta t^4)$ global error is attained (provided that the solution to the boundary-value problem is sufficiently accurate).

For practical computations, the parameters M, N, and Δt are chosen to give a desired accuracy (say $\delta \approx 10^{-5}$) using the simple procedure: (i) select the order of the perturbation M so that $\delta \approx \epsilon^M$; (ii) choose the minimum number of Fourier modes N based on Table 15.1 to realize the

Table 15.1: Maximum absolute error in the free-surface velocity $(\partial\Phi/\partial z)_{z=\zeta}$ of a Stokes wave of steepness ϵ for different values of mode number N and order of approximation M.[a]

		M						
ϵ	N	2	4	6	8	10	12	14
0.1	8	0.75×10^{-3}	0.68×10^{-5}	0.72×10^{-7}	0.22×10^{-8}	0.10×10^{-8}		
	16	0.75×10^{-3}	0.68×10^{-5}	0.65×10^{-7}	0.64×10^{-9}	0.49×10^{-10}		
0.2	8	0.59×10^{-2}	0.22×10^{-3}	0.15×10^{-4}	0.18×10^{-5}	0.13×10^{-5}		
	16	0.60×10^{-2}	0.22×10^{-3}	0.87×10^{-5}	0.37×10^{-6}	0.38×10^{-7}		
	32	0.60×10^{-2}	0.22×10^{-3}	0.88×10^{-5}	0.35×10^{-6}	0.14×10^{-7}	0.75×10^{-9}	
0.3	8	0.19×10^{-1}	0.22×10^{-2}	0.47×10^{-3}	0.14×10^{-3}	0.16×10^{-3}		
	16	0.20×10^{-1}	0.18×10^{-2}	0.19×10^{-3}	0.59×10^{-4}	0.24×10^{-4}		
	32	0.20×10^{-1}	0.18×10^{-2}	0.17×10^{-3}	0.16×10^{-4}	0.17×10^{-5}		
	64	0.20×10^{-1}	0.18×10^{-2}	0.17×10^{-3}	0.16×10^{-4}	0.16×10^{-5}	0.21×10^{-6}	0.33×10^{-7}
0.35	8	0.31×10^{-1}	0.64×10^{-2}	0.22×10^{-3}	0.13×10^{-2}	0.13×10^{-2}		
	16	0.31×10^{-1}	0.41×10^{-2}	0.99×10^{-3}	0.71×10^{-3}	0.22×10^{-3}		
	32	0.31×10^{-1}	0.40×10^{-2}	0.53×10^{-3}	0.94×10^{-4}	0.95×10^{-4}	0.16×10^{-3}	
	64	0.31×10^{-1}	0.40×10^{-2}	0.53×10^{-3}	0.73×10^{-4}	0.11×10^{-4}	0.38×10^{-5}	0.68×10^{-3}
0.40	32	0.45×10^{-1}	0.79×10^{-2}	0.28×10^{-2}	0.81×10^{-2}			
	64	0.45×10^{-1}	0.79×10^{-2}	0.15×10^{-2}	0.35×10^{-3}	0.91×10^{-3}		
	128	0.45×10^{-1}	0.79×10^{-2}	0.15×10^{-2}	0.30×10^{-3}	0.89×10^{-3}		

[a] From Dommermuth and Yue (1987a).

Table 15.2: Maximum absolute error in the free-surface elevation ζ of a progressive Stokes wave of steepness ϵ and period T after integration time t for different values of time step Δt.[a]

		$T/\Delta t$				
ϵ	t/T	20	30	40	50	60
0.1	1	0.79×10^{-4}	0.16×10^{-4}	0.49×10^{-5}	0.19×10^{-5}	0.88×10^{-6}
	10	0.63×10^{-3}	0.12×10^{-3}	0.38×10^{-4}	0.15×10^{-4}	0.66×10^{-5}
0.2	1	0.30×10^{-3}	0.63×10^{-4}	0.21×10^{-4}	0.88×10^{-5}	
	10	0.28×10^{-2}	0.51×10^{-3}	0.16×10^{-3}	0.66×10^{-4}	

[a] From Dommermuth and Yue (1987a).

required accuracy; and (iii) choose Δt according to Table 15.2 subject to the linear Courant stability condition (15.3.30).

15.4.2 Wave Steepening

The HOS method is developed based on the assumption that the free surface is single-valued, and, because of expansions of the potential about the mean free surface in (15.3.6), limited to waves that are not too steep (see Table 15.1). We consider here a wave which gradually steepens (and eventually overturns) and make quantitative comparisons between the predictions of HOS and fully-nonlinear mixed Euler-Lagrangian (MEL) calculations. The primary objective is to see how far the HOS simulation can be continued before it fails, and to elucidate on the overall behavior of the HOS simulation (for example, deviation from energy conservation) near that limit.

We consider the same problem for HOS and MEL simulations: we start with an initial exact deep-water Stokes wave with $[\epsilon, k] = [0.15, 1]$ and apply (temporarily) a surface pressure moving with the wave:

$$P_{\mathcal{F}}(x,t) = \left\{ \begin{array}{ll} P_0 \sin\left(\dfrac{2\pi t}{T}\right) \cos(x - ct)\,, & 0 \le t \le \dfrac{T}{2}\,, \\ 0\,, & t > \dfrac{T}{2}\,, \end{array} \right\} \tag{15.4.1}$$

where T and c are, respectively, the fundamental period and phase speed of the Stokes wave, and $P_0 = .35$ for this simulation. (For simplicity, the time and mass units are chosen so that the fluid density $\rho = 1$ and the

Table 15.3: Convergence in the maximum total energy ratio $E(T/2)/E(0)$ of a Stokes wave with an applied asymmetric surface pressure. RK4 with $T/\Delta t = 100$ is used for all the calculations. For the case with smoothing, a five-point smoothing filter (15.3.28) is applied at every time step.[a]

MEL		HOS			
				No smoothing	With smoothing
$N_m = 32$	7.04	$N = 16$	$M = 4$	7.03	6.98
$N_m = 64$	7.11	$N = 16$	$M = 5$	7.15	7.10
$N_m = 128$	7.13	$N = 16$	$M = 6$	7.16	7.11
$N_m = 256$	7.14				

[a] From Dommermuth and Yue (1987a).

gravitational acceleration $g = 1$.) The wave increases in energy until it reaches its maximum at $t = T/2$ at which point the pressure is turned off. Table 15.3 shows the convergence of results for the ratio of the maximum total energy to the initial energy of the wave $E(T/2)/E(0)$. The MEL formulation used here is similar to that of Vinje and Brevig (1981) (see Section 15.7.1). Cauchy's integral theorem is applied for this periodic deep water case and the free surface is discretized into N_m linear segments with piecewise linear variation of the complex potential on each segment. For definiteness, no smoothing is used in the MEL calculation. For the HOS method, we consider both the case when there is no smoothing and when five-point smoothing (15.3.28) is applied at every time step. At $t = T/2$, the wave has acquired a total energy over seven times its initial value. Even for this steep wave, the HOS method appears to converge rapidly as M increases ($N = 16$ already gives more than sufficient accuracy at $M = 6$). Hereafter, all the results are obtained using $N_m = 64$ for MEL calculations; $N = 16$ and $M = 6$ for HOS simulations; and RK4 with $T/\Delta t = 100$ for both time integrations.

One objective of these simulations is to compare how well the numerical methods conserve energy as the wave evolves with time. The results show that, up to the point when the HOS without smoothing fails, it conserves total energy better than the other two methods. The failure occurs at $t \approx .9T$ which is shortly after the kinetic energy of the wave has reached its maximum. The wave itself begins to turn over after the next maxima of the kinetic energy, and both the HOS with smoothing as well as MEL (without smoothing) break down soon after at $\approx 1.5T$. In the HOS simulations, the amplitudes of the high-wavenumber modes increase as the wave steepens, and the final failure is marked by a change in the total energy due to a rapid

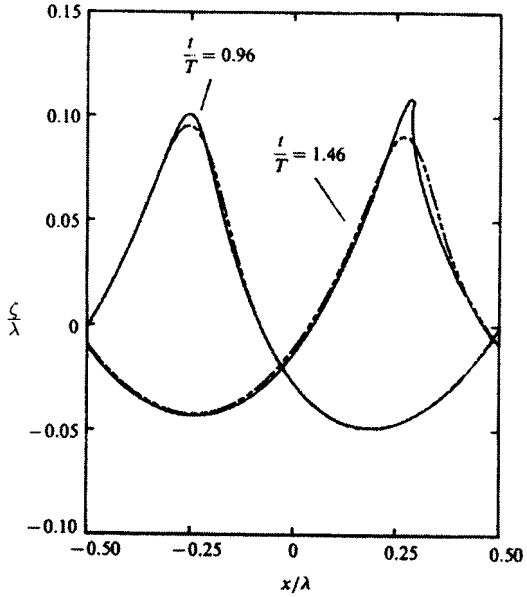

Figure 15.1: Free-surface profiles ζ of a steepening wave, fundamental period T and wavelength λ, under an asymmetric pressure calculated using MEL (——) and spectral method with smoothing (– - - –) at times $t/T = 0.96$ and 1.46. The vertical scale is exagerated (from Dommermuth and Yue, 1987a, *J. Fluid Mech.* Reproduced by permission of Cambridge University Press).

growth of energy of the modes near the truncated end. An unrelated source of error is the saw-tooth instability (see Section 15.7.3) which also affects the highest wavenumbers. Thus, smoothing filters (15.3.28) and (15.3.29) help to alleviate both problems.

Figure 15.1 plots the free-surface profiles obtained using MEL and HOS (with smoothing) for two relatively late times $t/T = .96$ and 1.46. Note that for earlier times the comparisons are substantially better and the profiles cannot be distinguished graphically. For the later phase, the comparisons are satisfactory over most of the wave profile with the main discrepancies occurring on the forward face (where the slope predicted by HOS is not as steep as that by MEL), and at the crest as the wave steepens (and eventually overturns). For the HOS computation, the maximum local wave slope reached is $(\partial\zeta/\partial x)_{\max} \approx 0.9$ (six times the initial steepness) at $t \approx 1.05T$, at which point the total wave height is over three times its initial value. These results provide important answers regarding how high-order

simulations using the HOS method behave when the wave becomes steep or breaking: (a) away from the breaking (spatially and temporally), the prediction remains quantitatively good; and (b) near the breaking, the HOS prediction deviates from the correct solution but significantly remains qualitatively close and well-behaved.

This comparison study allows us to make a passing remark on relative computational efforts. For this relatively small problem, the MEL simulation with $N_m = 64$ takes $O(20)$ times longer computationally than the HOS simulation with $N = 16$ and $M = 6$ using the same processor. Importantly, the computational effort for HOS increases only linearly with N and M, while the computation time for MEL, which has only a second-order accuracy, increases quadratically with the number of segments N_m.

15.4.3 Modulation of a Stokes Wave Train Due to Type I Instabilities

Stiassnie and Shemer (1984) extended Zakarov's equation to fourth order which they used in a later work (Stiassnie and Shemer, 1987, hereafter denoted as S&S) to simulate the coupled evolution of class I and class II instabilities of surface gravity waves on deep water. We here compare HOS calculations to their simulation for type I instability of a Stokes wave train. For their Airy wave steepness of $\epsilon_0 = (\kappa a)_0 = .13$, the wavenumbers of the most unstable class I modes are $k \pm \Delta k$ with $\Delta k/k \approx 22\%$, where k is the wavenumber of the fundamental wave. In order to make a comparison, we use as initial condition a Stokes wave, $[\epsilon, k] = [.13, 9]$, modulated by two Airy sideband waves ($k = 9$ is chosen so that integral numbers of the sideband modes can be fitted into the computational domain):

$$\left.\begin{aligned} \zeta(x,0) &= \zeta_0[0.13,9] + 0.1a_0\cos\left(7x - \frac{\pi}{4}\right) \\ &\quad + 0.1a_0\cos\left(11x - \frac{\pi}{4}\right), \\ \Phi^s(x,0) &= \Phi_0^s[0.13,9] + 0.1\frac{a_0}{\sqrt{7}}\mathrm{e}^{7\zeta}\cos\left(7x - \frac{\pi}{4}\right) \\ &\quad + 0.1\frac{a_0}{\sqrt{11}}\mathrm{e}^{11\zeta}\cos\left(11x - \frac{\pi}{4}\right), \end{aligned}\right\} \tag{15.4.2}$$

which to leading order is the same as that used by S&S. Here $\zeta(\epsilon, k)$ and $\Phi^s(\epsilon, k)$ are respectively the free-surface elevation and potential of a

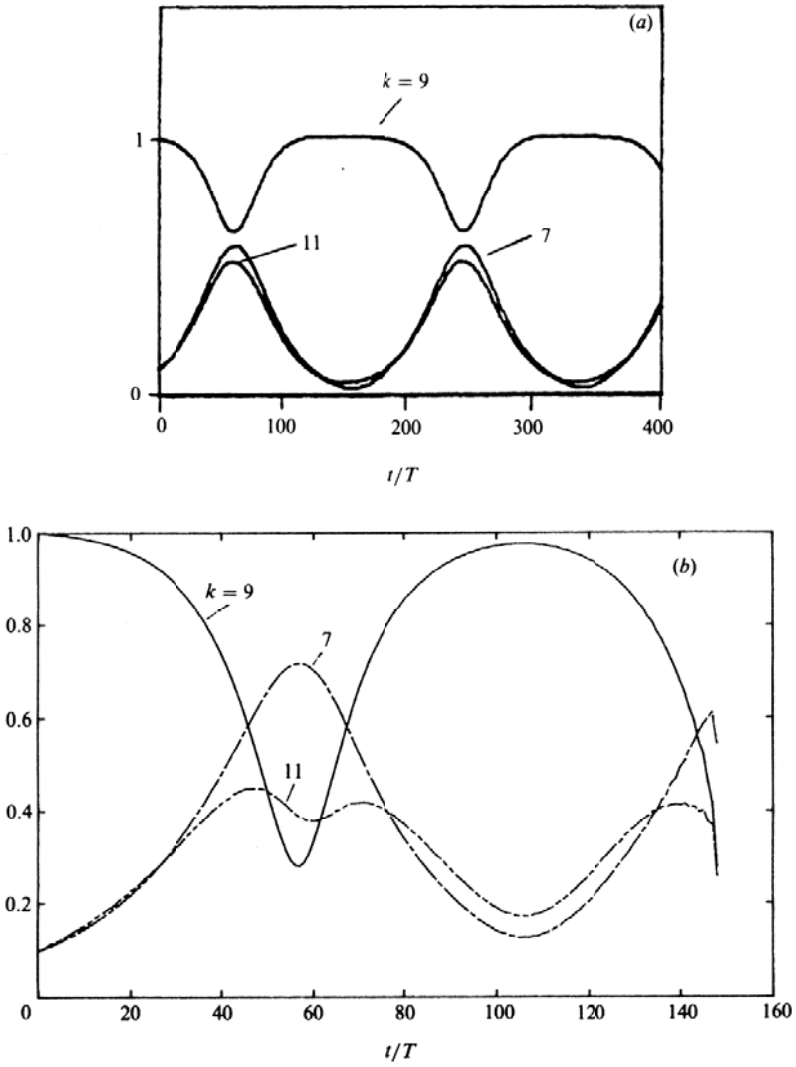

Figure 15.2: Time histories of the amplitudes of the fundamental ($k = 9$), subharmonic ($k = 7$) and superharmonic ($k = 11$) modes relative to the initial amplitude of the fundamental for an evolving Stokes wavetrain. (a) From Stiassnie and Shemer (1987); (b) the HOS result. T is the period of the fundamental (from Dommermuth and Yue, 1987a, *J. Fluid Mech.* Reproduced by permission of Cambridge University Press).

right-going Stokes wave of steepness ϵ and wavelength $\lambda = 2\pi/k$ whose phase is such that there is a crest at $x = -\pi$ at time $t = 0$. In S&S's fourth-order simulation, only a limited approximation with 5 free waves were used. To compare with S&S, we set $M = 4$ but consider a total of $N = 64$ free wave modes. The time step is $\Delta t = T/50$, and no smoothing filter is used.

The time histories of the fundamental ($k = 9$), subharmonic ($k = 7$), and superharmonic ($k = 11$) are plotted in Fig. 15.2 and compared to S&S's results (their Fig. 1). Both computations predict a first minimum of the fundamental near $t \approx 60T$ which closely corresponds to the time scale for type I interactions, T/ϵ_0^2. The amplitudes of each harmonic relative to the initial amplitude of the fundamental do not agree as well, but the overall qualitative behavior (for example the relative amplitudes of the two side harmonics at their maximum and minimum) is preserved.

Unlike S&S, the HOS simulation breaks down after $t \approx 140$, at which time the wave steepens and possible local breaking cannot be ruled out. This is further indicated by the conservation of total energy for the HOS computation. The total energy is conserved to within 0.01% for $t < 40T$, to within 0.1% for $t < 50T$, and to within 2% for the duration of the simulation. (For comparison, S&S reported total energy conserved to within 1%). Near $t \approx 60T$, which corresponds to the minimum of the fundamental amplitude and maxima of the sideband amplitudes, there is an abrupt change (of the order of 0.5%) in the total energy, after which the numerical result recovers but eventually breaks down at $t \approx 140$, which again corresponds to maxima in the sideband perturbations.

Figure 15.3 shows the actual free-surface elevations at times $t/T = 0$, 57, and 104. At $t/T = 0$ and 104, the fundamental dominates, while at $t/T = 57$ the sidebands do. The maximum local wave slope reaches almost four times ($(\partial\zeta/\partial x)_{\max} \approx 0.6$) that of the initial wave at $t = 57T$, which also indicates why the computed total energy is not as well conserved near that time.

To study the effect of modulation bandwidth ($\Delta k/k$), we perform large HOS simulations with $N = 2048$ and $M = 4$. To avoid wave breaking, we choose the fundamental wave with smaller wave steepness $\epsilon_0 = (ka)_0 = 0.05$. Two modulation bandwidths are considered: $\Delta k/k = 0.1$ and 0.05. For both cases, the initial amplitudes of the subharmonic (a_{+1}) and superharmonic (a_{-1}) sidebands are set to be $a_{\pm 1}/a_0 = 0.1$. Figure 15.4 shows the long-time evolution of the amplitudes of the fundamental and two sidebands. Qualitatively different evolution features are observed with different

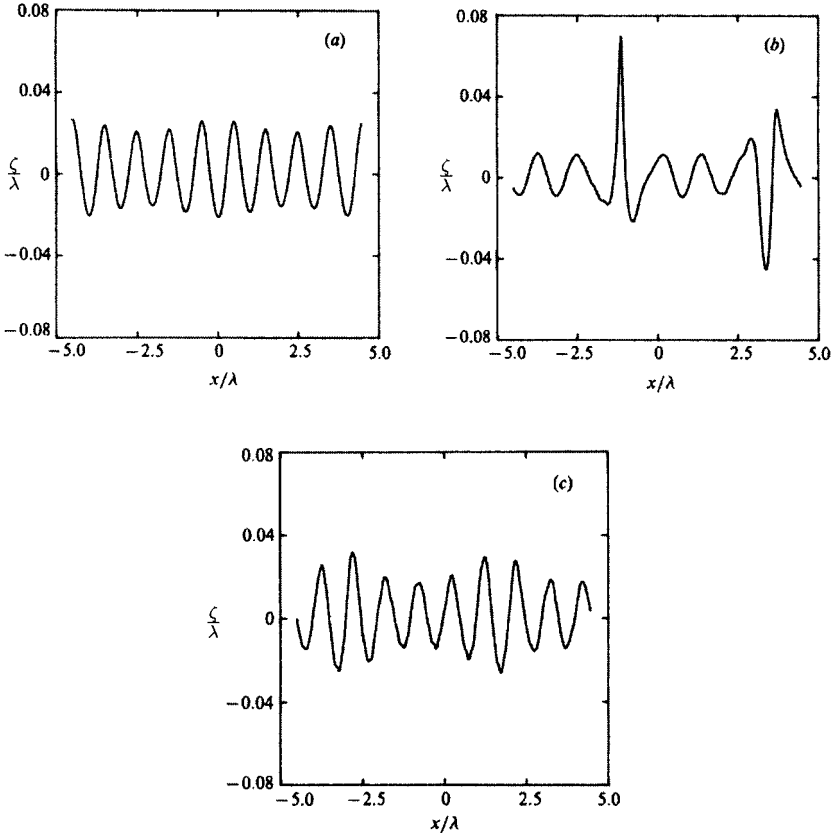

Figure 15.3: Instantaneous free-surface elevation of an evolving Stokes wavetrain (fundamental period T and wavelength λ) at times: (a) $t/T = 0$; (b) 57; and (c) 104. The vertical scales are exaggerated (from Dommermuth and Yue, 1987a, *J. Fluid Mech.* Reproduced by permission of Cambridge University Press).

modulation bandwidths. For large modulation bandwidth ($\Delta k/k = 0.1$, Fig. 15.4(a)), simple recurrence obtains as predicted by S&S. For small modulation bandwidth ($\Delta k/k = 0.05$, Fig. 15.4(b)), complex evolution patterns for both fundamental and sidebands are observed, and no recurrence is seen for the simulation up to $t/T = 1600$. Based on a spectral analysis of the wavefield, it is found that in this case, in addition to the initial sidebands, additional unstable sidebands (resulted from nonlinear

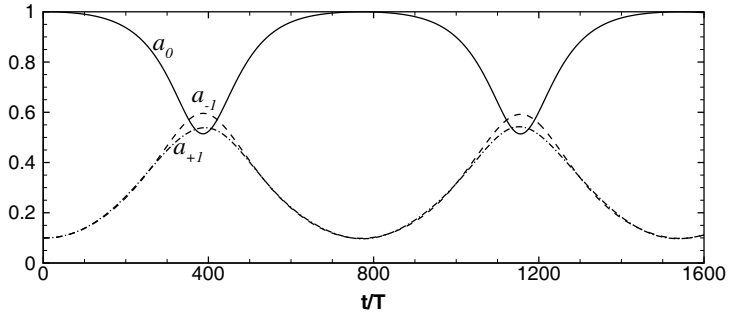

(*a*)

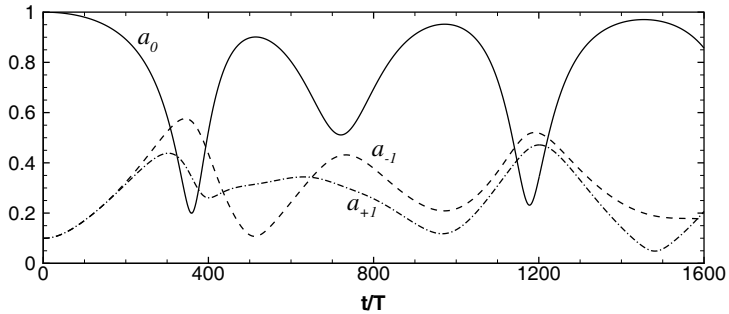

(*b*)

Figure 15.4: Time histories of the amplitudes of the fundamental (a_0), subharmonic (a_{-1}) and superharmonic (a_{+1}) modes relative to the initial amplitude of the fundamental for an evolving Stokes wavetrain with modulation bandwidth $\Delta k/k = 0.1$ (*a*) and 0.05 (*b*). T is the period of the fundamental.

interactions of the fundamental and the initial sidebands) are also significantly developed during the evolution.

15.4.4 Evolution of a Wave Packet

Su (1982) studied experimentally the evolution of wave groups that had initially square envelopes. For (Airy) wave steepnesses ranging from $\epsilon_0 = 0.09$ to 0.28, he measured the free-surface elevation at eight stations down the tank. For wave steepnesses $\epsilon_0 \geq 0.14$, he observed intense two- dimensional breaking at distances between ten and twenty carrier wavelengths from the wavemaker. Fifteen to twenty-five wavelengths from the wavemaker, crescent-shaped breaking waves often developed, and from twenty

to forty-five wavelengths away, two-dimensional spilling breaking was common. We here compare the HOS simulation to one of Su's experiments which initially had an steepness of $\epsilon_0 = 0.15$ and a packet which contained approximately five fundamental waves at the beginning. To simulate this experiment, we begin with a Stokes wavetrain which has 15 waves in the computational domain, i.e. $[\epsilon, k] = [.15, 15]$, and modulate it with a tapering function of the form:

$$F(x; \sigma, x_b, x_e) = 0.5\{\tanh[\sigma(x - x_b)] - \tanh[\sigma(x - x_e)]\}\,. \tag{15.4.3}$$

The parameter σ measures the steepness of the taper at the beginning and end positions, x_b and x_e, respectively, of the resulting envelope. To avoid Gibb's phenomenon at the boundaries, (15.4.3) is periodically extended. The initial condition which approximately gives the desired five waves in the packet is then

$$\left.\begin{aligned} \zeta(x,0) &= F\left(x; \frac{30}{\pi}, -\frac{\pi}{3}, \frac{\pi}{3}\right) \zeta_0[0.15, 15]\,, \\ \Phi^s(x,0) &= F\left(x; \frac{30}{\pi}, -\frac{\pi}{3}, \frac{\pi}{3}\right) \Phi_0^s[0.15, 15]\,. \end{aligned}\right\} \tag{15.4.4}$$

The parameters for the HOS simulation are $N = 256$, $M = 6$, and $T/\Delta t = 40$. To allow the computations to continue after the waves may have become locally too steep, and possibly also to model some loss of wave energy due to breaking, we apply the ideal filter Λ_I with $\nu = .5$ whenever the total energy of the wave packet changes by more than 1%. This smoothing operation eliminates all Fourier modes whose wavenumbers are greater than eight times the fundamental.

Figure 15.5 shows the comparisons between Su's wave probe measurements and the HOS simulation results. The experimental traces are reproduced directly from Su (1982) and do not have a vertical scale. The horizontal scales are, however, the same. Overall, the agreement is qualitatively good and appears to improve as the wave group travels down the tank. At about fifty wavelengths from the wavemaker, we confirm the experimental observation that the wave group fissions into two packets. Our results are comparable to the computations for the same experiment by Lo and Mei (1985), who used Dysthe's fourth-order (nonlinear) Schrödinger equation.

Figure 15.6 displays the total energy time-history of the simulation. The energy is conserved well except at approximately $t/T \approx 40$–50. In

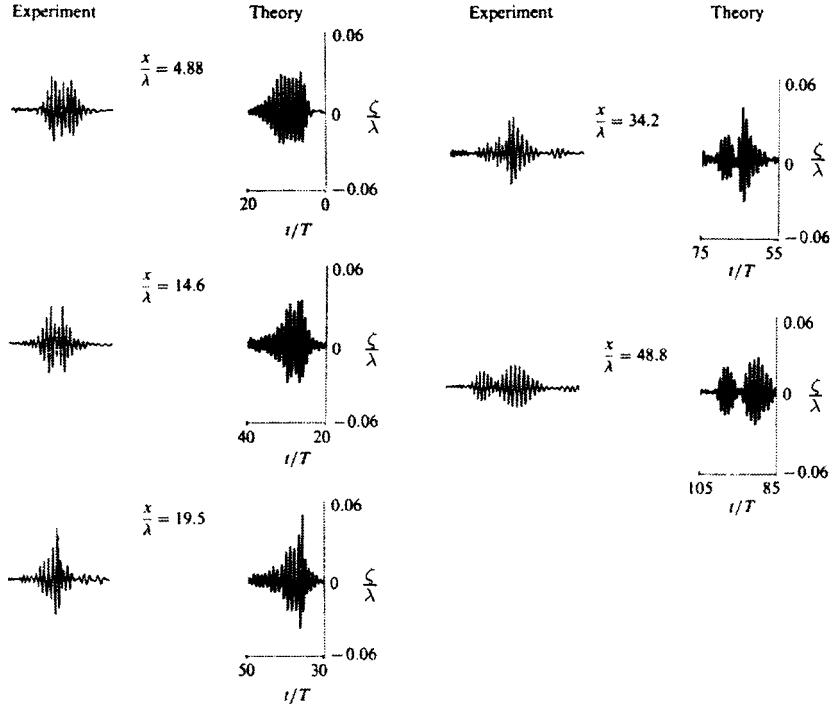

Figure 15.5: Comparison between experiments (Su, 1982) and theory (i.e. the HOS simulation) for the free-surface elevation of an evolving wave packet (fundamental period T and wavelength λ) at positions from the wavemaker $x/\lambda = 4.88$, 14.6, 19.5, 34.2 and 48.4 (from Dommermuth and Yue, 1987a, *J. Fluid Mech.* Reproduced by permission of Cambridge University Press).

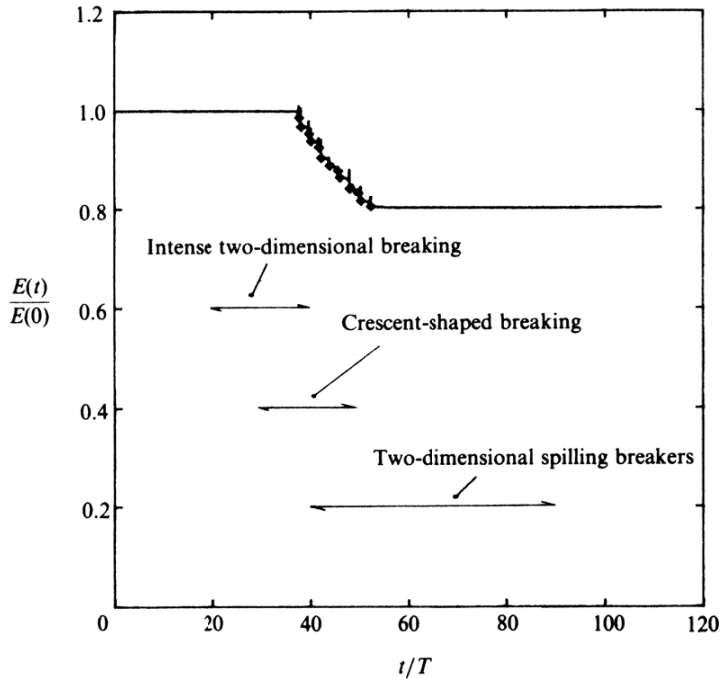

Figure 15.6: Computed total energy of an evolving wave packet, fundamental period T and wavelength λ. Diamond symbols indicate the use of ideal filter $\Lambda_I(\nu = 0.5)$ which is applied whenever the total energy changes by more than 1% (from Dommermuth and Yue, 1987a, *J. Fluid Mech.* Reproduced by permission of Cambridge University Press).

this region, the filter $\Lambda_I(k, 0.5)$ (triggered by a 1% change in energy) is repeatedly applied which eventually removed almost 20% of the energy from the system. It is found that filtering (singly or in close succession) is often required at intervals of approximately two fundamental periods which may be related to the relative motion between the waves and their envelope as suggested by Longuet–Higgins (1974). It is interesting to note that the time range over which smoothing is used roughly corresponds to times at which wave breaking was observed in the experiments. By monitoring the total energy and suitably removing energy in the higher wavenumber modes, the HOS computations can be continued beyond the stages of apparent local breaking, and, significantly, produce (qualitatively) good results compared to experiments. More recently, Wu (2004) generalized the smoothing technique here to the physical space and obtained good agreement between HOS

simulation and the experiment of Tulin and Waseda (1999) for waves that have undergone plunging breaking. Ironically, and not insignificant from a practical perspective, this type of robust behavior of HOS simulations in the presence of wave breaking, renders HOS more useful for many general steep-wave applications than even fully-nonlinear methods such as MEL (Section 15.7), which break down as soon as the wave begins to spill or plunge into itself.

15.4.5 Nonlinear Three-Dimensional Waves Due to a Moving Surface Disturbance

In this section, high-resolution HOS simulations are used to study the three-dimensional nonlinear wave pattern associated with a surface pressure distribution moving in deep water. This is treated as an initial-boundary-value problem starting from rest in the context of potential flow. A novel tapering function procedure is employed to model the outflow boundaries for long-time simulations in a finite computational domain. The focus here is the understanding of free-surface nonlinear effects on three-dimensional ship wakes.

For linearized free-surface conditions, the resulting Neumann-Kelvin problem has been studied since Kelvin (1886). Considering the waves created by a localized pressure distribution moving with constant speed U, Kelvin developed the method of stationary phase to show that the far-field steady wave pattern consists of a superposition of diverging and transverse wave systems which are confined within two rays forming angles of $\pm\theta_0$ with the track. The angle of the rays, or cusp lines, is given by $\theta_0 = \sin^{-1}(1/3) \cong 19.5^o$. This far-field result can be derived by simple geometric arguments (e.g. Havelock, 1908; Lamb, 1932; Lighthill, 1956). Details of the wave pattern are quite complicated and mathematically may be expressed as the sum of a double and a single integral with the far-field waves given predominantly by the latter (e.g. Peters, 1949). Ursell (1960) analyzed the far-field behavior in the cusp region and near the track, and found that the wave amplitudes are respectively $O(r^{-1/2})$ and $O(r^{-3})$ inside and outside the cusp lines and that in a finite region of width $O(r^{1/3})$ across $\theta = \theta_0$ there is a transition from oscillatory to exponentially decaying behavior in an Airy-function-like manner where the amplitude is $O(r^{-1/3})$ where r is distance from the source normalized by g/U^2.

Despite the analytical developments, the accurate numerical calculation of even linear ship waves is still not without challenge, in part due to the inherent inconsistency of the Neumann-Kelvin approximation, and the substantive computational effort required for realistic three-dimensional geometries (e.g. Doctors and Beck, 1987; Guevel et al., 1977). The difficulty is more severe when one is primarily interested in the short-wave field, for instance, as observed by back-scattered synthetic-aperture radar signals (e.g. Vesecky and Stewart, 1982; Fu and Holt, 1982), where the calculations based on discrete distributions of singularities may not be able to provide the necessary resolution (Milgram, 1987).

Interest in nonlinear ship wave effects has been motivated by the lack of agreement between linearized theory and observations (see, e.g. the survey by Tulin, 1978). A deficiency known since Hovgaard (1909) is the fact that bow wave crests tend to lie outside the theoretical cusp lines and by an amount which varies with speed. To account for this, Gadd (1969) included second-order corrections to both the singularity distributions on the ship centerplane and the condition at the free surface, but with limited success. In a discussion of Gadd's paper, Lighthill (in Gadd, 1969) suggested a more useful approach to account for the nonlinear effects on wave propagation speed, using Whitham's theory for slowly-varying dispersive waves (Lighthill, 1967; Whitham, 1974). This approach was in fact followed by Howe (1967, 1968) (for a simpler problem involving a wavetrain resulting from open-channel flow past a slowly-modulated wavy wall) where he predicted phase jumps or "shocks", a result which violates the original assumption of slow variations and appears to be nonphysical (Newman, 1970).

Subsequently, a number of attempts to account for some free-surface nonlinearities were made (e.g. Newman, 1970; Hogben, 1972; Dagan, 1972a; Kitazawa and Takagi, 1976). Much of the work is analytic in nature and involves perturbations to higher order in one or more of the small parameters of the problem. Such approaches are not without difficulties, and the uniformity of the expansion, for example, around the zero-speed limit (Ogilvie, 1968; Dagan, 1972b, 1975) is still problematic (Miloh and Dagan, 1985). This has prompted the introduction of a number of quasi-linear techniques (Dawson, 1977; Inui and Kajitani, 1977), which have found useful numerical applications (e.g. Xia and Larsson, 1986). The related problem of nonlinearity specifically in the Kelvin cusp region has received somewhat less attention (Newman, 1971; Akylas, 1987), but we now know that

resonant quartet interactions along the cusp lines may not be as strong as first conjectured by Newman (1971). These studies typically utilize perturbation techniques in a far-field local analysis and, therefore, cannot be readily extended to an examination of the total wave pattern.

We apply the HOS method to the nonlinear ship waves problem (Dommermuth and Yue, 1988a). For simplicity, we consider the steady three-dimensional nonlinear waves generated by a moving surface pressure disturbance. The disturbance moves forward at a constant speed U. We define a Cartesian coordinates system fixed with the moving pressure disturbance. Referring to this coordinate system, the pressure disturbance is stationary, and a uniform current moves towards the pressure disturbance (with a speed $-U$). We set the origin at the mean water level, the x-axis pointing into the uniform current (of speed $-U$), and the z-axis positive upward. The gravity waves created by a surface pressure distribution, $P_{\mathcal{F}}(\mathbf{x})$, turned on at $t = 0$, can be described by a total velocity potential, $-Ux + \Phi(\mathbf{x}, z, t)$, where $\Phi(\mathbf{x}, z, t)$ satisfies Laplace's equation within the fluid. In terms of Φ^s and ζ, the kinematic and dynamic free-surface boundary conditions in the Zakharonv form in the presence of a uniform current of speed $-U$ are:

$$\left.\begin{aligned} &\zeta_t - U\zeta_x + \nabla_{\mathbf{x}}\zeta \cdot \nabla_{\mathbf{x}}\Phi^s \\ &\qquad -(1 + \nabla_{\mathbf{x}}\zeta \cdot \nabla_{\mathbf{x}}\zeta)\Phi_z(\mathbf{x}, \zeta, t) = 0\,, \\ &\Phi^s_t - U\Phi^s_x + g\zeta + \frac{1}{2}\nabla_{\mathbf{x}}\Phi^s \cdot \nabla_{\mathbf{x}}\Phi^s \\ &\qquad -\frac{1}{2}(1 + \nabla_{\mathbf{x}}\zeta \cdot \nabla_{\mathbf{x}}\zeta)\Phi^2_z(\mathbf{x}, \zeta, t) = -\frac{P_{\mathcal{F}}(\mathbf{x})}{\rho}\,. \end{aligned}\right\} \tag{15.4.5}$$

The initial conditions are $\Phi^s(\mathbf{x}, 0) = 0$ and $\zeta(\mathbf{x}, 0) = 0$ at $t = 0$, at which time the pressure distribution, $P_{\mathcal{F}}(\mathbf{x})$, is applied instantaneously. With the exception of the terms proportional to U, the initial-boundary-value problem is identical to Section 15.3.1, and the modification of the HOS method for the present problem is straightforward.

As before, we choose periodic boundary conditions in both horizontal dimensions, and consider the rectangular domain, $-L/2 < x < L/2$ and $-W/2 < y < W/2$. As an example, we consider an axisymmetric pressure distribution, $P_{\mathcal{F}}(\mathbf{x}) = P_{\mathcal{F}}(r)$, centered at $(x, y) = (x_c, 0)$ with radial extents $R < L/2$, $W/2$. The radial distance from the center of the pressure r is given by $r^2 = (x - x_c)^2 + y^2$. To retain spectral convergence and accuracy, the pressure distribution must be chosen to be smooth enough to avoid

Gibb's phenomena. To do this, we specify the surface pressure in terms of a Hermitian polynomial:

$$P_{\mathcal{F}}(r) = \begin{cases} P_{\max}\Pi\left(\dfrac{r}{R}\right), & 0 \le r \le R \\ 0, & r > R \end{cases} \tag{15.4.6}$$

where $P_{\max}$ is the maximum pressure at the center $r = 0$; and the Hermitian polynomial, $\Pi(s)$, $0 \le s \le 1$,

$$\Pi(s) = 1 - 462s^6 + 1980s^7 - 3465s^8 + 3080s^9 - 1386s^{10} + 252s^{11} \tag{15.4.7}$$

has the property

$$\Pi(0) = 1\,, \quad \Pi(1) = 0\,, \quad \text{and}$$

$$\left(\frac{\mathrm{d}^k}{\mathrm{d}s^k}\right)\Pi(0) = \left(\frac{\mathrm{d}^k}{\mathrm{d}s^k}\right)\Pi(1) = 0 \quad \text{for} \quad k = 1, 2, 3, 4, 5\,.$$

To allow for long-time simulations, we develop a procedure wherein the free-surface elevation and potential are truncated smoothly (tapered) at the longitudinal ends of the computational domain after each time step. Specifically, we multiply ζ and Φ^s by a tapering function $\Omega(x, \Delta)$ which is equal to one in the middle and smoothly approaches zero at the ends:

$$\Omega(x, \Delta) = \begin{cases} 1\,, & |x| < \dfrac{L}{2} - \Delta \\ \Pi\left(\dfrac{(|x| - \frac{L}{2} + \Delta)}{\Delta}\right), & \dfrac{L}{2} - \Delta \le |x| \le \dfrac{L}{2} \end{cases} \tag{15.4.8}$$

where Δ measures the width of the tapering region and is a parameter to be chosen. In Dommermuth and Yue (1988a), systematic numerical tests indicate that this simple tapering procedure is remarkably effective and allows us to carry out long simulations to obtain the steady-state wake.

For convenience, the mass, time, and length units are chosen such that the density $\rho = 1$, the gravitational acceleration $g = 1$, and the diameter of the pressure distribution $2R = 1$. For this computation, we fix $U = 0.4$ and $P_{\max} = 0.015$. The pressure distribution is placed at $x_c = 5$ in a computational domain with $L = 16$ and $W = 8\sqrt{2}$. This allows us to simulate up to approximately 12 transverse waves behind the pressure. The numbers of unaliased Fourier modes we use are $N_x = N_y = 128$. Nonlinear interactions up to third order ($M = 3$) are included. A tapering function

$\Omega(x, 0.5\lambda_0)$ and an ideal smoothing filter $\Lambda(\mathbf{K}_n, 0.9)$ are applied to ζ and Φ^S after each time step. We use a constant time step $\Delta t = T/50 = 2\pi U/50$ and carry out the simulation up to $t/T = 20$. Here $T \equiv 2\pi U$ is the time it takes to travel one fundamental wavelength $\lambda_0 \equiv 2\pi U^2$ at speed U. Note that for this problem, the linear transient solution in a periodic domain and the linear steady-state solution in an unbounded domain can be obtain in closed form (see Dommermuth and Yue, 1988a for details).

Figure 15.7 plots the free-surface elevation along the linear cusp line $(x - x_c) = y\sqrt{8}$ at $t/T = 20$. In this case, the linear time-domain theory does not agree as well with the linear far-field asymptotes. The surprising result is the substantial forward shift of the nonlinear wave phase which increases progressively with distance along the cusp line. This phase shift is almost half a wavelength at a distance of $r \sim 14$. The amplitudes on the cusp line also show large differences, with the nonlinear wave amplitudes typically greater by as much as 25%, say, at $r \sim 10$. The present results

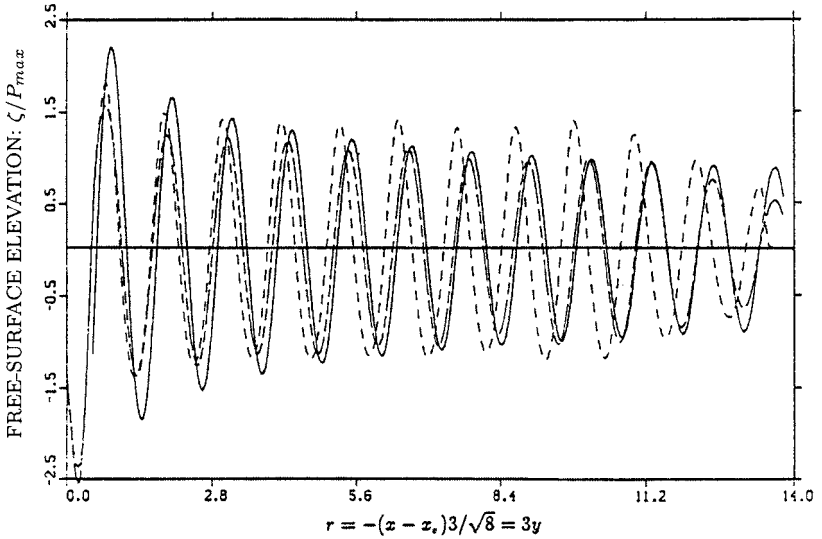

Figure 15.7: Cusp-line profiles (on $x - x_c = y\sqrt{8}$) of the free-surface elevation at $t/T = 20$. The curves are for the nonlinear computation (– – –), the linear transient result (— - - - —), and the linear steady-state far-field asymptotic result (——) (from Dommermuth and Yue, 1988a, *17th Symp. on Naval Hydrodynamics*. Reproduced by permission of National Academy Press).

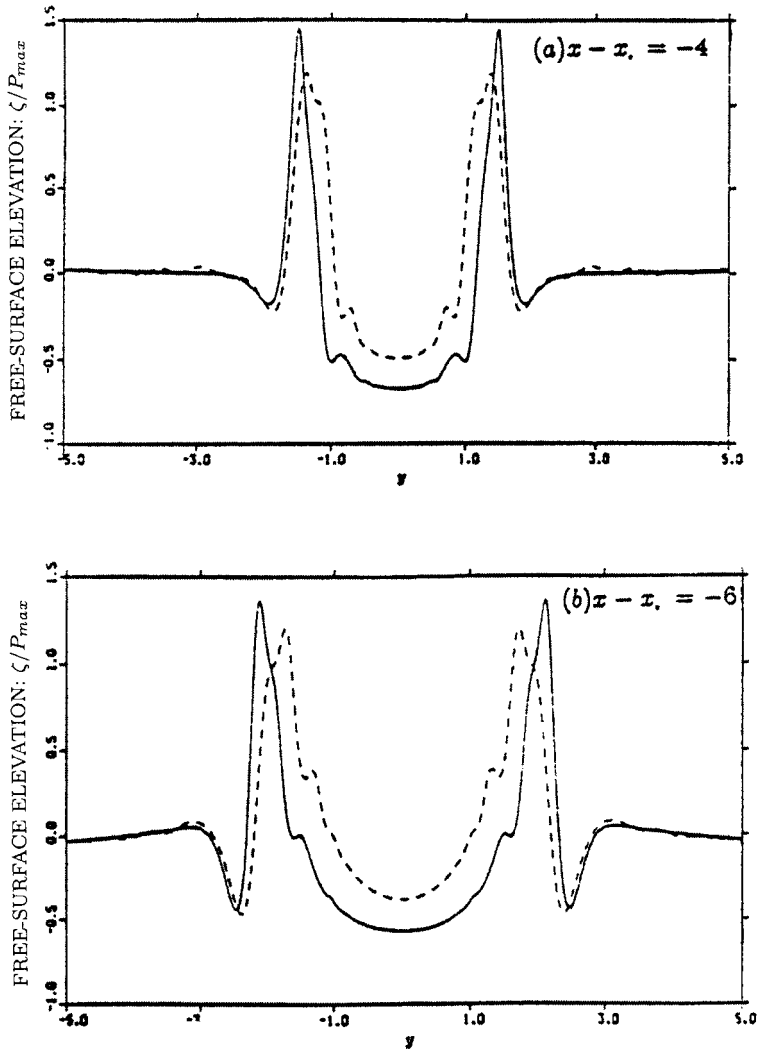

Figure 15.8: Transverse profiles of the free-surface elevation across the track at $t/T = 20$ at downstream distances $x - x_c =$ (a) -4; (b) -6; (c) -8; and (d) -10. The curves are for the nonlinear computation (——) and the linear transient result (– – –) (from Dommermuth and Yue, 1988a, *17th Symp. on Naval Hydrodynamics*. Reproduced by permission of National Academy Press).

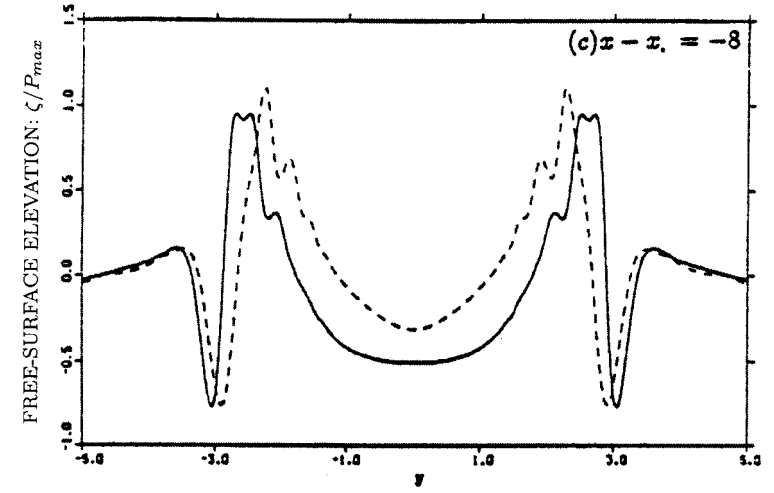

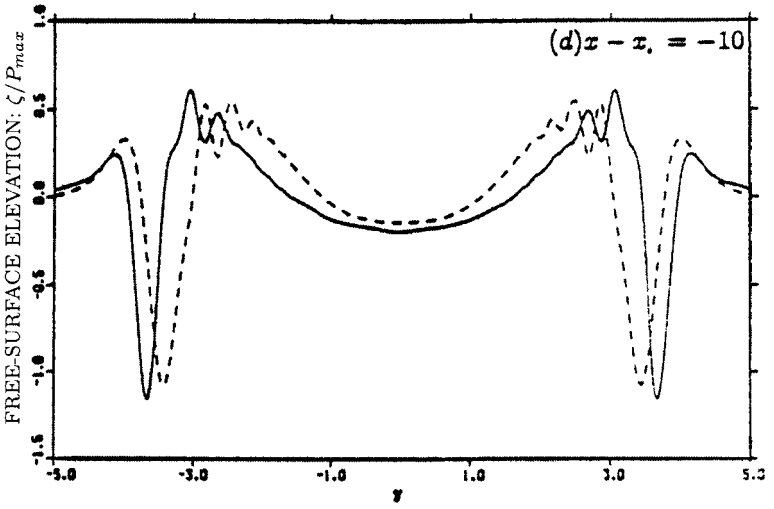

Figure 15.8 (*Continued*)

differ qualitatively from the far-field perturbation analysis of Akylas (1987), who found only a small change in phase and almost no change in amplitude along the cusp lines. This indicates the importance of a nonlinear model which includes the interactions in the near and intermediate fields.

The overall difference between the linear and nonlinear wave patterns is further clarified by the transverse wave elevation cuts in Figs. 15.8 at a number of downstream stations all at $t/T = 20$. The deviation of the nonlinear profiles from the linearized results are appreciable, with typically lower troughs on the track, higher crests towards the cusp lines, and an outward phase shift at the outer edge of the cusp lines which appears to increase with distance downstream. Taken together, Figs. 15.7 and 15.8 indicate a forward shift and a somewhat wider wake angle for the nonlinear wave pattern in the near and intermediate field. This is in general agreement with physical observations.

Details of the three-dimensional wave pattern in a rectangular domain over the cusp region are show in Fig. 15.9 in the form of contour plots of the free-surface elevation (at $t/T = 20$). For clarity, the vertical coordinate is magnified by a factor of $\sqrt{8}$ so that the Kelvin cusp line has a slope of one on the plot. For the nonlinear case, the highest crests and the lowest troughs move outside of the linear cusp angle as the distance downstream increases. The peaks and troughs of the linear free surface are inside of the cusp lines, which agrees with Ursell's (1960) calculations. In the patch of the free surface shown, the highest nonlinear elevation is 30% greater than the highest linear elevation, and the lowest nonlinear wave trough is 10% deeper than the lowest linear wave.

Finally, one notes that the present nonlinear simulations also confirm the existence of a nonlinear steady-state of waves on the cusp line. (Detailed results are shown in Dommermuth and Yue, 1988a.) This contradicts the conclusion of Newman (1971), but is in agreement with the result of Akylas (1987).

15.4.6 Nonlinear Wave Interaction with Ambient Current

Wave-current interactions play a role in ocean wave evolution, hydrodynamic loads on offshore structures, and in the interpretation of remote sensing surface data. For this problem, Longuet–Higgins and Stewart

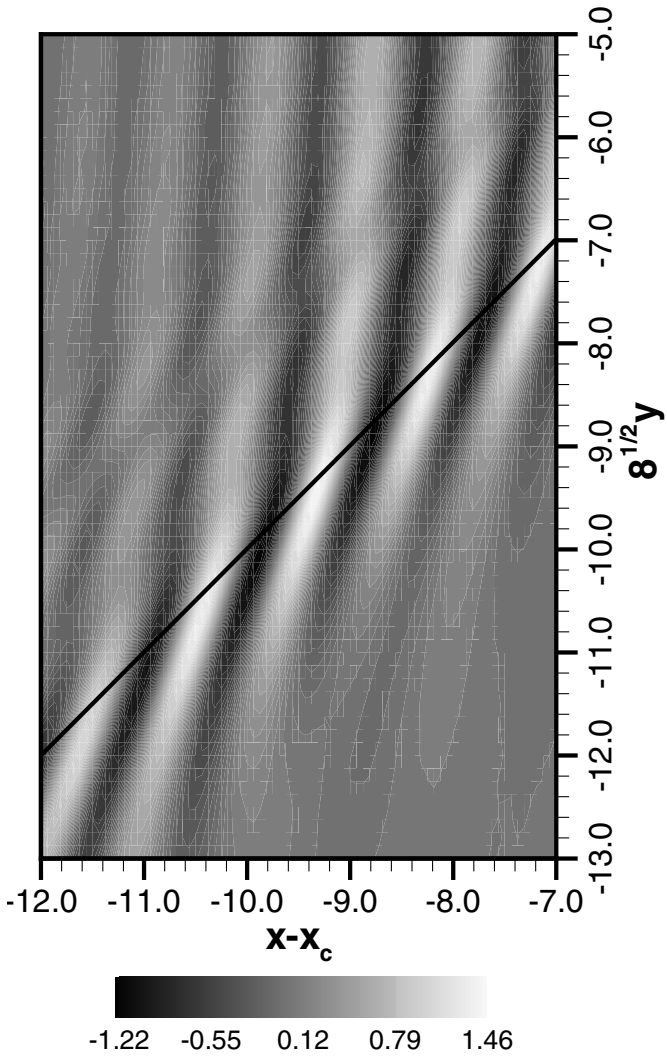

(*a*)

Figure 15.9: Contour plots of the free-surface elevation, $\zeta/P_{\max}$, at $t/T = 20$, in a rectangular region on the Kelvin cusp line for (*a*) the nonlinear computations; and (*b*) linear transient result. For clarity, the height of the plots is magnified by a factor of $\sqrt{8}$, so that the cusp lines (——) now have a slope of one. Note that the gray scales under the plots are different for the linear and nonlinear cases (from Dommermuth and Yue, 1988a, *17th Symp. on Naval Hydrodynamics*. Reproduced by permission of National Academy Press).

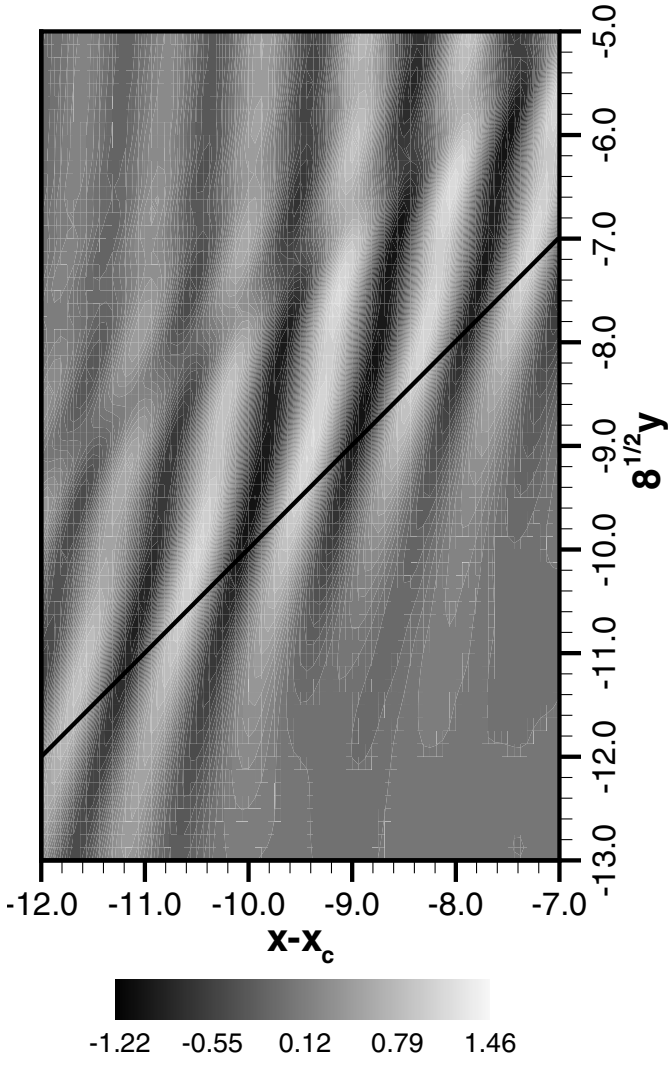

(*b*)

Figure 15.9 (*Continued*)

(1960, 1961) introduced the concept of radiation stress and derived the correct energy equation. They showed that for waves on steady nonuniform currents, the total wave energy is not conserved due to energy exchange between wave and current. Later, Bretherton and Garrett (1968) showed that instead of total wave energy, the wave action is conserved for waves travelling on a slowly varying current. Since then, much progress has been made in this problem area (for a review, see Peregrine, 1976 and Jonsson, 1990).

Wave blocking and wave focusing are two important phenomena associated with wave-current interactions which have attracted special attention. When a propagating wave encounters an opposing current of increasing magnitude, wave blocking phenomenon occurs at a place where the current speed matches the group velocity of the wave (e.g. Jonsson and Arneborg, 1995). In the blocking region, the wave becomes shorter and steeper, and eventually breaks as it is reflected and travels back (Smith, 1975; Shyu and Phillips, 1990; Shyu and Tung, 1999). The large wave steepness that occurs here make it important to consider the effects of nonlinearity. Steep waves may also be generated due to focusing of waves refracted by a curved shearing current. This is believed to be the mechanism for the generation of giant waves in the Agulhas Currents (e.g. Gerber, 1993). These phenomena also occur for irregular waves and thus are important to the understanding of ocean wave evolution (e.g. Huang et al., 1972; Tayfun et al., 1976; Lai et al., 1989; Tung, 1992). A linearized account of these effects is given in Section 3.7, Part 1, of this book.

Although it is clear that nonlinear effects associated with wave-current interactions could be important (e.g. Thomas, 1981, 1990), theoretical studies have been limited. Peregrine and Thomas (1978) applied the finite-amplitude wave theory of Whitham (1974) and showed that the basic characteristics of a wave travelling on a slowly varying current differ significantly from the linear-theory prediction. This theory, however, does not include the effect of wave reflection and fails in the blocking region where the assumption of slowly-varying waves breaks down.

We here extend and apply the HOS method of Section 15.3 to study the problem of nonlinear wave interactions with variable current. We assume that the spatial scale of the current is much larger than that of waves and focus on the effect of the current upon the wave motion. For simplicity, we assume that the current field is steady and prescribed, and ignore the feedback effect of waves on the current. We assume that the total flow velocity $\mathbf{V}$ can be decomposed into two parts:

$$\mathbf{V}(\mathbf{x}, z, t) = \nabla\Phi(\mathbf{x}, z, t) + \mathbf{U}(\mathbf{x}, z) \tag{15.4.9}$$

where $\nabla\Phi$ is the velocity due to wave motion, and $\mathbf{U}$ the velocity of the current. The potential flow assumption in (15.4.9) has been supported by experiments of wave interactions with collinear currents, Thomas (1981, 1990), for a current that is essentially irrotational with vorticity restricted to thin layers. We further assume that the current is slowly varying with $|\nabla \times \mathbf{U}| = O(\epsilon^{M+1})$, where ϵ is the wave steepness and M is the order of nonlinearity considered in the wave interactions.

Based on (15.4.9), we rewrite the nonlinear kinematic and dynamic boundary conditions (15.3.4) for the wave motion in the presence of a slowly varying current as:

$$\left.\begin{aligned} &\zeta_t + \nabla_{\mathbf{x}}\zeta \cdot (\nabla_{\mathbf{x}}\Phi^s + \mathbf{U}) \\ &\qquad -(1 + \nabla_{\mathbf{x}}\zeta \cdot \nabla_{\mathbf{x}}\zeta)\Phi_z(\mathbf{x}, \zeta, t) = 0\,, \\ &\Phi^s_t + g\zeta + \nabla_{\mathbf{x}}\Phi^s \cdot \mathbf{U} + \frac{1}{2}\nabla_{\mathbf{x}}\Phi^s \cdot \nabla_{\mathbf{x}}\Phi^s \\ &\qquad -\frac{1}{2}(1 + \nabla_{\mathbf{x}}\zeta \cdot \nabla_{\mathbf{x}}\zeta)\Phi_z^2(\mathbf{x}, \zeta, t) = -\frac{P_{\mathcal{F}}}{\rho}\,. \end{aligned}\right\} \tag{15.4.10}$$

In the above, $\Phi^s \equiv \Phi(\mathbf{x}, \zeta(\mathbf{x}, t), t)$, and ζ is the free-surface elevation due to wave motion. The condition (15.4.10) is applied on the instantaneous free surface $z = \zeta(\mathbf{x}, t)$. Using (15.4.10) in place of (15.3.4) as the evolution equation, the HOS procedure in Section 15.3 is directly applied here. This method has been recently employed by Wu (2004) in a study of the nonlinear wave-current blocking problem.

As an illustration, we consider a two-dimensional problem where the waves and current can be co- or counter-propagating. Figure 15.10 shows a sketch of the variation of the current speed in a periodic computational domain. The interest is in the left half of the computational domain, and

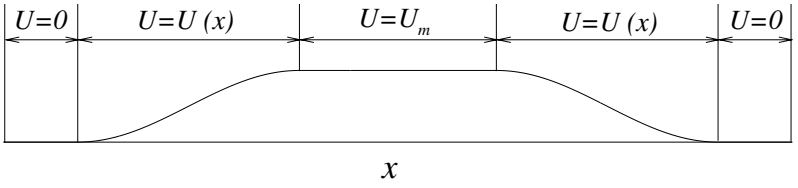

Figure 15.10: Sketch of the variation of current speed in a periodic computational domain for HOS computations of nonlinear wave-current interactions.

the right half is included in order to create periodic boundaries in x for HOS computations. The actual length of the computational domain depends on the $U(x)$ considered. The incident wave propagates from left to right with wavelength λ_0, wavenumber $k_0 = 2\pi/\lambda_0$, amplitude a_0, period T_0, and phase speed c_0 in the absence of current. For the HOS simulation, the initial free-surface elevation and velocity potential of the incident wave are obtained using the exact Stokes wave solution (Schwartz, 1974). To enable long-time simulations for obtaining the steady-state prediction, we apply a simple tapering function procedure (see (15.4.8)) in a small region at the periodic boundaries.

Figure 15.11 plots the nonlinear ($M = 3$) HOS results for the variation of the amplitude, wavenumber, and steepness of the wave as it travels in a following current. For comparison, the linear solution (e.g. Longuett–Higgins and Stewart, 1961; or Section 3.7.3, Part 1, of this book) is also shown. For the computations, we use the incident wave steepness $(ka)_0 = 0.2$, a computational domain of length $256\lambda_0$, the number of wave modes $N = 4096$, and the time step $T_0/\Delta t = 64$. The steady state of the wavefield of interest is reached after a simulation time of $\sim 160T_0$. As Fig. 15.11 shows, the nonlinear solution differs only slightly from the linear prediction.

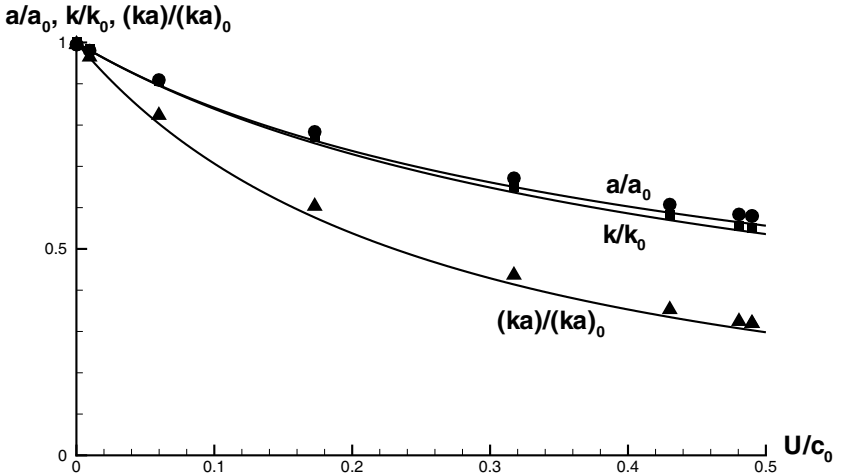

Figure 15.11: Variation of the wave amplitude a, wavenumber k, and steepness ka as a function of current speed U for an incident wave (amplitude a_0, wavenumber k_0, and steepness $(ka)_0 = 0.2$) travelling in a variable following current. The plotted are from the linear theory (——) and HOS simulations with $M = 3$ (• for a, ■ for k, and ▲ for ka).

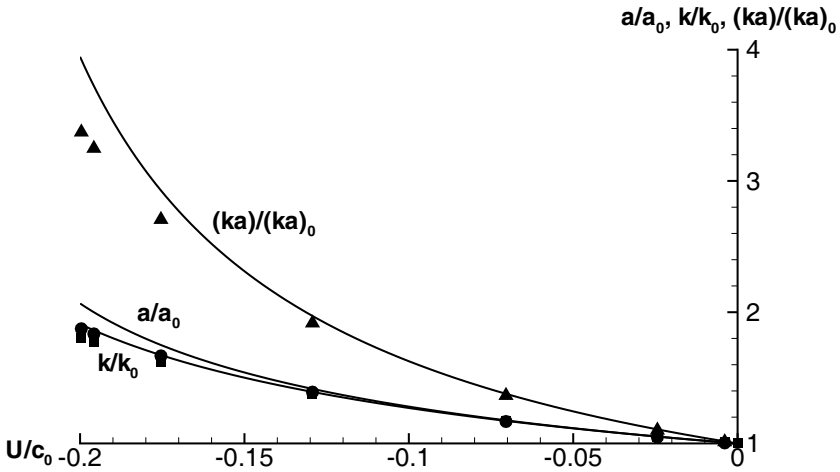

Figure 15.12: Variation of the wave amplitude a, wavenumber k, and steepness ka as a function of current speed U for an incident wave (amplitude a_0, wavenumber k_0, and steepness $(ka)_0 = 0.05$) travelling in a variable opposing current. The plotted are from the linear theory (——) and HOS simulations with $M = 3$ (• for a, ■ for k, and ▲ for ka).

This is not surprising since the wave steepness becomes smaller with U in the following current.

Figure 15.12 plots the comparisons for the case of an opposing current. In this case, the incident wave steepness $(ka)_0 = 0.05$, and the steady state of the wave-field is reached after $\sim 250T_0$. The linear theory in general over-predicts the amplitude, wave number, and steepness of the wave. The over-estimation increases with the current speed. As $|U|/c_0$ approaches 0.25 (the stopping point), the wave steepens rapidly and nonlinear effects are critical.

To elucidate the nonlinear effects in wave blocking, we consider a strong opposing current and focus on the wave-field in the blocking region. In this case, we use a computational domain of length $16\lambda_0$ and $N = 4096$ wave modes. The incident wave steepness is $(ka)_0 = 0.015$ (in the presence of $U/c_0 = -0.2$). Figure 15.13 plots the total wave profile of the wave-field at $t = 256T_0$, obtained using HOS simulations with $M = 1$ and 3. In both linear ($M = 1$) and nonlinear ($M = 3$) results, the wave steepens significantly as it travels toward the stopping point and is largely reflected there. Both the amplitude and phase of the wave differ significantly between the linear and nonlinear solutions in this vicinity of wave blocking. As the

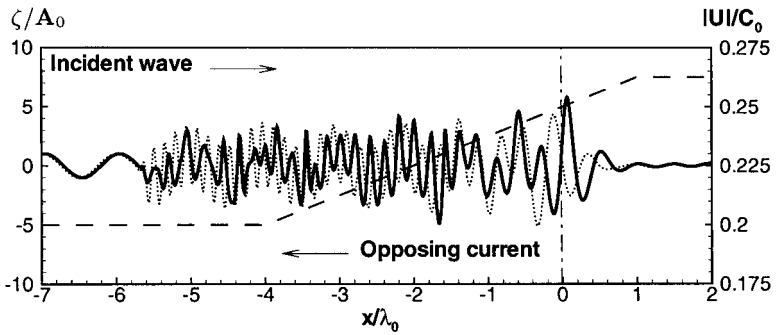

Figure 15.13: Free-surface profile of the total wave-field in the blocking region for an incident wave of steepness $(ka)_0 = 0.015$ travelling in a strong opposing current. The plotted are: HOS computations of the wave profile with $M = 3$ (——) and $M = 1$ ($\cdot\ \cdot\ \cdot$), and current profile ($-\ -\ -$). $x = 0$ corresponds to the stopping point predicted by the linear theory.

reflected wave moves away from the stopping point, it becomes shorter and steeper, and eventually breaks. In the nonlinear computations, wave breaking is "modelled" by filtering and is the reason that the nonlinear wave amplitude is much smaller than the linear solution in the region far away from the stopping point ($x/\lambda < -3.5$).

15.4.7 Generalized Bragg Scattering of Surface Waves by Bottom Ripples

A natural and important application of HOS simulations in surface wave dynamics is the nonlinear wave interaction with variable bottom topography. When an incident wave travels over and interacts with nonuniform bottom depth, the wave is modified and may be partially reflected. For mild bottom variations the reflection is in general weak. When the bottom contains periodic undulations and the incident wave and bottom ripple wavenumbers satisfy so-called Bragg conditions, however, the Bragg scattered wave becomes resonant and can be greatly amplified. For larger wave and/or bottom steepnesses, higher-order Bragg resonances resulting from nonlinear interactions among the surface and bottom wave components can be expected. Such resonant wave interactions with bottom ripples play a significant role in the evolution of nearshore surface waves and in the development of shore-parallel bars (e.g. Heathershaw and Davies, 1985; Mei, 1985; Hara and Mei, 1987; Yu and Mei, 2000). The leading second-order

triad (class I) Bragg resonance is thoroughly considered using the linearized theory in Part 1, Chapter 7, where the effect of randomness of the bottom variation is also addressed. We here focus on the study of third-order quartet (class II and class III) wave-bottom interactions (Liu and Yue, 1988) using direct HOS simulations.

Class I Bragg resonance

The mechanism for Bragg resonances can be viewed in a way that is analogous to that for nonlinear surface wave-wave resonant interactions in the absence of bottom undulations. Thus, general Bragg conditions can be deduced from the well-known resonance condition for nonlinear wave-wave interactions (e.g. Phillips, 1960). For a wave field over uniform depth h, interactions among different wave components become resonant at order m in wave steepness if the wave numbers $\mathbf{k}_j$ and the corresponding frequencies ω_j satisfy:

$$\left.\begin{aligned} \mathbf{k}_1 \pm \mathbf{k}_2 \pm \cdots \pm \mathbf{k}_{m+1} = 0 \\ \omega_1 \pm \omega_2 \pm \cdots \pm \omega_{m+1} = 0 \end{aligned}\right\} \quad (m \geq 2)\,, \tag{15.4.11}$$

where the same combination of signs is to be taken in both equations, and $\mathbf{k}_j$ and ω_j satisfy the linear dispersion relation

$$\omega_j^2 = g|\mathbf{k}_j| \tanh |\mathbf{k}_j| h\,. \tag{15.4.12}$$

Generalized Bragg resonance conditions in the presence of bottom ripples are obtained by replacing one or more of the free-surface wave components in (15.4.11) by periodic bottom ripple components of corresponding wavenumbers $\mathbf{k}_{bj}$ but with zero frequencies (since the ripples are fixed). Thus, by combining wavenumbers and frequencies of surface waves and bottom ripples, we obtain general conditions for Bragg resonances at each order, $m = 2, 3, \ldots$.

Consider two surface wave components, wavenumbers $\mathbf{k}_1$ and $\mathbf{k}_2$, propagating over a rippled horizontal bottom containing a single wavenumber $\mathbf{k}_b$ (analogous to surface waves, this refers to a fixed sinusoidally varying bottom with crest lines normal to $\mathbf{k}_b$ and with wavelength $\lambda_b = 2\pi/|\mathbf{k}_b|$). From (15.4.11) with $m = 2$, we obtain the condition for class I Bragg resonance

$$\left.\begin{aligned} \mathbf{k}_1 - \mathbf{k}_2 - \mathbf{k}_b = 0 \\ \omega_1 - \omega_2 = 0 \end{aligned}\right\}. \tag{15.4.13}$$

This is the classical Bragg resonance involving the triad interaction of the bottom ($\mathbf{k}_b$), the incident ($\mathbf{k}_1$ say) and the Bragg reflected wave ($\mathbf{k}_2$) components. This condition has been studied experimentally by Davies and Heathershaw (1984). For small incident wave and bottom slopes, reflection at or near the class I Bragg resonance is predicted well by multiple-scales perturbation theory under the assumption of linearized surface waves (Mei, 1985; Part 1, Chapter 7). Here we obtain direct computational demonstration of class I Bragg resonance using the HOS method which also allows us to investigate higher-order nonlinear effects of the free surface and bottom on this class of resonant reflection.

To compare with experiments, we choose a case of Davies and Heathershaw (1984) with the length of the bottom patch $L_0/\lambda_b = 10$ and the slope of the bottom undulations $k_b d = 0.31$. In addition to the normal incidence they consider, we study also the more general case of oblique incidence. We perform direct HOS simulations to obtain the steady-state (limit-cycle)

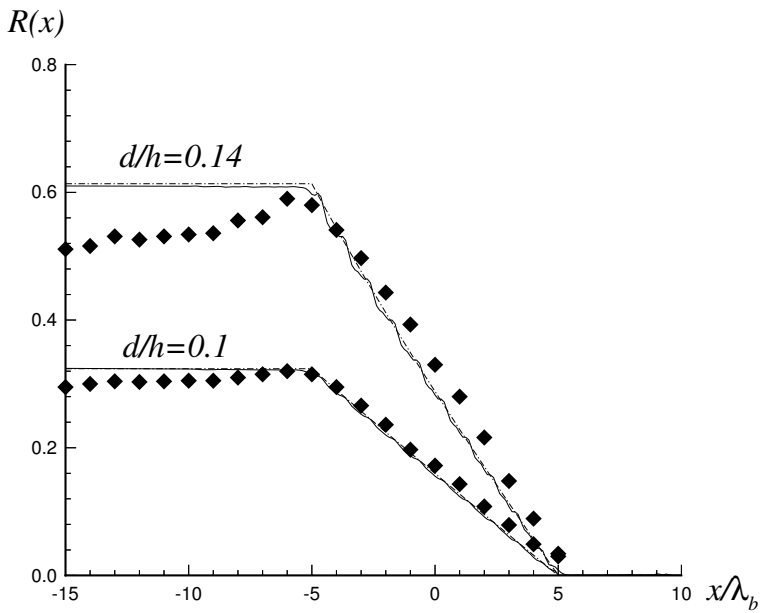

Figure 15.14: Spatial variation of the class I Bragg reflection coefficient over a bottom ripple patch $-5\lambda_b < x < 5\lambda_b$, for $kA = 0.05$, $k_b d = 0.31$. Results plotted are: experiments (Davies and Heathershaw, 1984) (♦); perturbation theory (Mei, 1985) (— · —); and HOS computations for $M = 3$ (——) (from Liu and Yue, 1998, *J. Fluid Mech.* Reproduced by permission of Cambridge University Press).

free-surface elevation $\zeta(\mathbf{x}, t)$ from which the reflection and transmission wave amplitudes are extracted (see Liu and Yue, 1998 for details).

In the case of normal incidence, $\mathbf{k}_1$ and $\mathbf{k}_b$, and consequently $\mathbf{k}_2$, are in the same direction and the problem is two dimensional. Figure 15.14 shows the HOS solution, $M = 3$ for the spatial variation of the Bragg reflection coefficient $R(x)$ at the (linearized) Bragg resonance value, $k \equiv k_1 = k_2 = k_b/2$, for two different mean water depths corresponding to $d/h = 0.1$ and 0.14. For this computation, the other physical and computational parameters used are: the incident wave steepness $kA = 0.05$, the computational domain length $L = 32\lambda$, the number of wave modes $N = 2048$, and the time step $\Delta t = T/64$, where λ, T, and A are the wavelength, period, and amplitude of the incident wave, respectively. Note that the result for $M = 2$ hardly differs from that for $M = 3$ for this case, and thus is not shown in the figure. The small oscillations in the HOS results are due to the use of Goda and Suzuki (1976)'s simple formula to extract steady-state

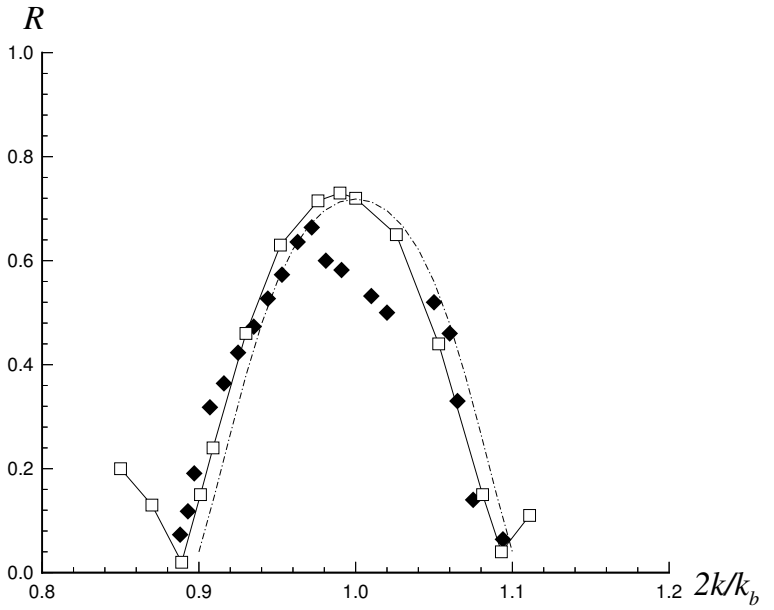

Figure 15.15: Class I Bragg reflection coefficient near the class I condition, $2k/k_b = 1$, for $kA = 0.05$, $k_b d = 0.31$, $d/h = 0.16$. Results plotted are: experiments (Davies and Heathershaw, 1984) (♦); perturbation theory (Mei, 1985) (— · —); and HOS computations for $M = 3$ (□) (from Liu and Yue, 1998, *J. Fluid Mech.* Reproduced by permission of Cambridge University Press).

coefficient from time history. For comparison, we show also results from the experiments of Davies and Heathershaw (1984), and the multiple-scale perturbation theory of Mei (1985). The agreement is satisfactory, with all three results showing the linear variations and slopes of $R(x)$ over the bottom patch ($x/\lambda_b \in [-5, 5]$).

Figure 15.15 shows the variation of the Bragg reflection coefficient in the neighborhood of the class I Bragg resonance for the case $d/h = 0.16$. The HOS results (with $M = 3$) are compared with the measured values of Davies and Heathershaw (1984) and the perturbation solution of Mei (1985) (described in detail in Part 1, Chapter 7). The agreement among them is overall satisfactory. One effect seen in the experimental data is the down shift in wavenumber of the peak Bragg reflected wave relative to the linearized Bragg point, $2k/k_b = 1$. This is predicted by the high-order HOS computation but is not present in Mei's perturbation theory.

The resonant wavenumber down-shift is attributed to nonlinear effects associated with the problem. In the present case, free-surface nonlinearity is manifest primarily in the Stokesian decrease in surface wavenumber with increasing steepness which should result in an increase of the resonant (linearized) value of k relative to k_b. On the other hand, nonlinear effects associated with the bottom variations would in general lead to a downshift of the resonant wavenumber. To obtain an estimate of this effect, we assume small-amplitude surface waves and slowly-varying bottom variations, and write the dispersion relation as:

$$\omega^2 = gk \tanh k[h + b(x)] \,. \tag{15.4.14}$$

For $kb \ll kh = O(1)$, we expand the wavenumber $k(x)$ in a perturbation series:

$$k(x) = k_0 + k_1(x) + k_2(x) + \cdots \,, \tag{15.4.15}$$

where k_0 is independent of x and given by $\omega^2 = gk_0 \tanh k_0 h$. Substituting (15.4.15) into (15.4.14) and solving for the perturbation wavenumbers, we obtain:

$$\frac{k_1(x)}{k_0} = -\frac{2k_0}{2k_0 h + \sinh 2k_0 h} \,, \tag{15.4.16}$$

and

$$\frac{k_2(x)}{k_0} = \frac{2(k_0 b)^2}{(2k_0 h + \sinh 2k_0 h)^3} \times [4k_0 h + (3 + \cosh 2k_0 h) \sinh 2k_0 h] \,. \tag{15.4.17}$$

After taking the spatial average $\overline{(\ )}$ of $k(x)$, it follows that

$$\bar{k} = k_0 + \frac{(k_0|b|)^2}{(2k_0h + \sinh 2k_0h)^3} \times [4k_0h + (3 + \cosh 2k_0h)\sinh 2k_0h] + \cdots . \qquad (15.4.18)$$

The second term in (15.4.18) is always positive, so that bottom nonlinearity in general increases the average free-surface wavenumber and thus shifts the peak Bragg reflection to a lower wavenumber relative to the linearized Bragg point. Note that non-constant $k(x)$ also leads to evanescent wave modes which have been attributed as a cause of the resonant frequency down-shift (Guazzelli et al., 1992).

Nonlinear free-surface and bottom effects on class I Bragg reflection can be obtained systematically by repeating the simulations varying the free-surface and bottom wave steepnesses. This has been performed by Liu (1994). The results indicate that nonlinearities of the free-surface and bottom boundaries are second order in the associated steepness and are generally small as far as the Bragg reflected wave amplitude is concerned. This has also been found by Kirby (1986) based on the extended-mild-slope equation.

As indicated by (15.4.13), class I Bragg resonance also occurs when the incident wave ($\mathbf{k}_1$) is oblique to the bottom ripples ($\mathbf{k}_b$). We consider the same bottom geometry ($d/h = 0.16$) but vary the angle θ between $\mathbf{k}_b$ and $\mathbf{k}_1$ (measured counter-clockwise from $\mathbf{k}_b$ which we set parallel to the x axis). The problem is now three-dimensional, and for the numerical simulation, we employ a (doubly-periodic) computational domain of dimensions $N_{wx}\lambda_x$ by $N_{wy}\lambda_y$, where the incident wavelength is $\lambda = 2\pi/|\mathbf{k}_1| = \lambda_x \cos\theta = \lambda_y \sin\theta$ and $(N_{wy}/N_{wx})^{1/2} = \tan\theta$. The simulations are carried out until steady-state free-surface elevation is obtained, from which the reflection and transmission coefficients are determined.

Figure 15.16 plots the class I Bragg reflection coefficient at class I Bragg resonance (15.4.13) as a function of the oblique incidence angle θ. Comparison is made to the perturbation theory of Mei et al. (1988), and the agreement is excellent. For both the numerical solution and the perturbation theory, Fig. 15.16 shows that at the critical incidence angle of $\theta = \pi/4$, wave propagation is unaffected by the presence of the bottom ripples. For oblique incidence, the magnitude of the incident wavenumber kh increases (in order to still satisfy Bragg condition) and the relative effect of the bottom variations diminishes. Thus the downshift observed in Fig. 15.16 as well as the Bragg resonance effect itself become weak as θ increases.

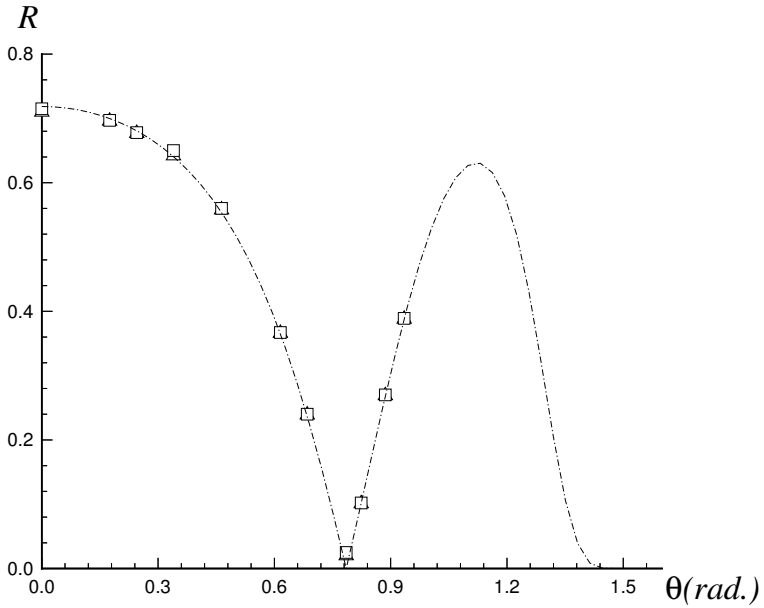

Figure 15.16: Class I Bragg reflection coefficient as a function of incidence wave angle θ relative to the bottom ripples, for $kA = 0.05$, $k_b d = 0.31$, $d/h = 0.16$. Results plotted are: perturbation theory (Mei et al., 1988)(— · —); and HOS computations for $M = 2$ ($\triangle$), and $M = 3$ ($\square$) (from Liu and Yue, 1998, *J. Fluid Mech.* Reproduced by permission of Cambridge University Press).

Class II Bragg resonance

At third order ($m = 3$), quartet Bragg resonance conditions satisfying (15.4.11) obtain involving either two/two or three/one surface/bottom wave components. We denote these, respectively, as class II and class III Bragg resonances. For the former, consider a doubly-sinusoidal bottom containing ripples with wavenumbers $\mathbf{k}_{b1}$ and $\mathbf{k}_{b2}$. The class II Bragg resonance condition is obtained simply by replacing $\mathbf{k}_b$ in (15.4.13) by the sum or difference of $\mathbf{k}_{b1}$ and $\mathbf{k}_{b2}$:

$$\left.\begin{aligned} \mathbf{k}_1 - \mathbf{k}_2 - (\mathbf{k}_{b1} \pm \mathbf{k}_{b2}) = 0\,, \\ \omega_1 - \omega_2 = 0\,. \end{aligned}\right\} \tag{15.4.19}$$

The $-/+$ sign above refers to sub-/super-harmonic resonances, respectively.

Although class II Bragg resonance involves quartet interactions (two bottom components) and is in theory one order higher than class I Bragg reflection, for realistic bottom conditions the resonant wave can in fact have

amplitudes which are comparable in magnitude to class I reflection (and occurs at distinct frequencies). This has been observed, for example, in the experiments of Guazzelli et al. (1992) who consider the two-dimensional problem of normal incidence of a wave over a bottom containing doubly-sinusoidal ripples.

To illustrate the effect of class II Bragg resonance, we study the case of Guazzelli et al. (1992) involving normal incidence over bottom undulations containing unidirectional doubly-sinusoidal (two different wavelengths) ripples. The bottom topography they consider is: ripple patch length $L_0 = 48$ cm, ripple amplitudes $d_1 = d_2 = 1$ cm, ripple wavenumbers $k_{b1} = \pi/3$ cm^{-1} and $k_{b2} = \pi/2$ cm^{-1}, and mean water depth $h = 4$ cm.

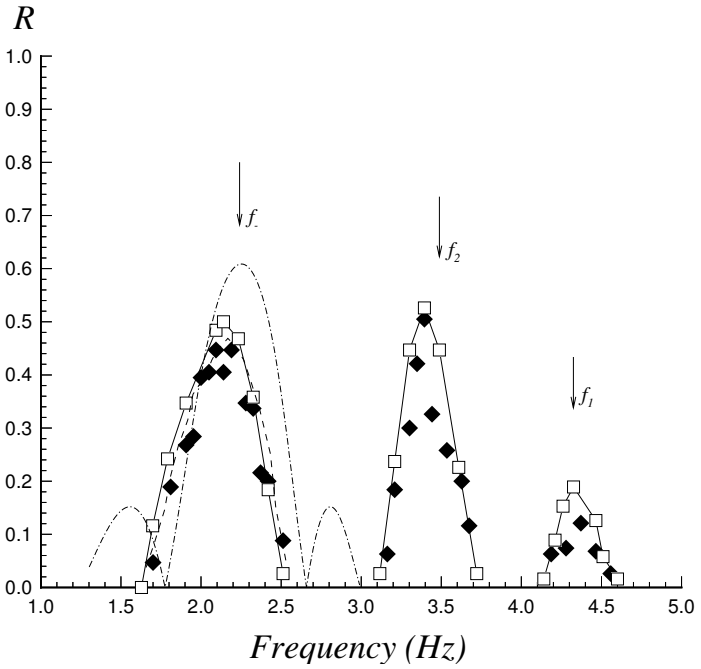

Figure 15.17: Bragg reflection coefficient for a wave incident normally upon a doubly periodic ripple bottom in the neighborhood of frequencies satisfying class I Bragg resonances: f_1 at $k = k_{b1}/2$; f_2 at $k = k_{b2}/2$; and sub-harmonic class II Bragg resonance: f_- at $k = (k_{b1} - k_{b2})/2$. Results plotted are: experiments (Guazzelli et al., 1992) (♦), HOS computations for $M = 3$ (□); and, near f_-, SAMM numerical results (Guazzelli et al., 1992) (- - -), and perturbation theory (Rey et al., 1996) (— · —) (from Liu and Yue, 1998, *J. Fluid Mech.* Reproduced by permission of Cambridge University Press).

For these conditions, we perform HOS ($M = 3$) simulations for a range of incident wavenumber k.

Figure 15.17 shows the Bragg reflection coefficient in the neighborhood of the two class I and the sub-harmonic class II Bragg resonances. The HOS results are compared with the experimental data and the successive-application-matrix model (SAMM) prediction of Guazzelli et al. (1992), and the multiple-scale perturbation solution of Rey et al. (1996). The HOS computations agree well with measurements at all three resonances for both the peak frequencies and amplitudes. As in the case of class I Bragg resonance (see Fig. 15.15), perturbation theory does not predict the down-shift of the peak frequency, and in this case also overestimates the peak reflection amplitude for the class II Bragg resonance. As pointed out by Guazzelli et al. (1992), the downshift at f_- is predicted by SAMM, which accounts for bottom nonlinearities. Note that, for the conditions chosen, the sub-harmonic class II reflected wave is comparable in magnitude to the lower-order class I Bragg reflection, and is appreciable relative to the incident wave.

We remark that, in theory, a super-harmonic class II Bragg resonance also exists in this case and is observed in HOS simulations. In this case, however, the amplitude of this high wavenumber super-harmonic class II reflected wave is very small relative to those associated with class I and sub-harmonic class II resonances shown in Fig. 15.17.

As indicated by the condition (15.4.19), class II resonance also occurs when the bottom contains bidirectional ripples. In this case, the problem becomes three-dimensional and is of more practical interest. In Liu and Yue (1998), it is shown that a super-harmonic Bragg reflected wave, which propagates in the direction perpendicular to the incident wave, is resonantly excited with a proper wavenumber combination of the incident wave and bottom ripples.

Class III Bragg resonance

The other wave-bottom resonance at third-order involves the quartet interaction of three surface and one bottom wave components. Consider the propagation of three surface waves, wavenumbers $\mathbf{k}_1$, $\mathbf{k}_2$, $\mathbf{k}_3$, over a horizontal bottom containing uniformly-sinusoidal ripples, wavenumber $\mathbf{k}_b$. From (15.4.11), it follows that Bragg resonance obtains at $m = 3$ if

$$\left.\begin{aligned} \mathbf{k}_1 \pm \mathbf{k}_2 - \mathbf{k}_3 \pm \mathbf{k}_b = 0\,, \\ \omega_1 \pm \omega_2 - \omega_3 = 0\,. \end{aligned}\right\} \tag{15.4.20}$$

(Without loss of generality, $\omega_1 \geq \omega_2$ is assumed here.) We denote this resonance, which is quadratic in the surface wave slope and linear in the bottom slope, class III Bragg resonance. Unlike class I and class II Bragg reflections, the class III resonant wave may be reflected or transmitted (relative to the incident waves) depending on the wave-bottom geometry (see Section 3.3 of Liu and Yue, 1998).

To illustrate the mechanism of this class of Bragg resonance, we consider the simplest possible case involving a single incident wave, wavenumber $\mathbf{k}$, frequency ω, incident normally upon uniformly sinusoidal ripples of a single wavenumber $\mathbf{k}_b$. For this case, the class III Bragg resonance condition (15.4.20) can be satisfied by accounting for the incident wave twice (i.e. $\mathbf{k}_2 = \mathbf{k}_1 \equiv \mathbf{k}$), and a reflected sub-harmonic ($\mathbf{k}_3 \equiv \mathbf{k}_r = 2\mathbf{k} - \mathbf{k}_b$) or transmitted super-harmonic ($\mathbf{k}_3 \equiv \mathbf{k}_t = 2\mathbf{k} + \mathbf{k}_b$) wave is generated at double-frequency

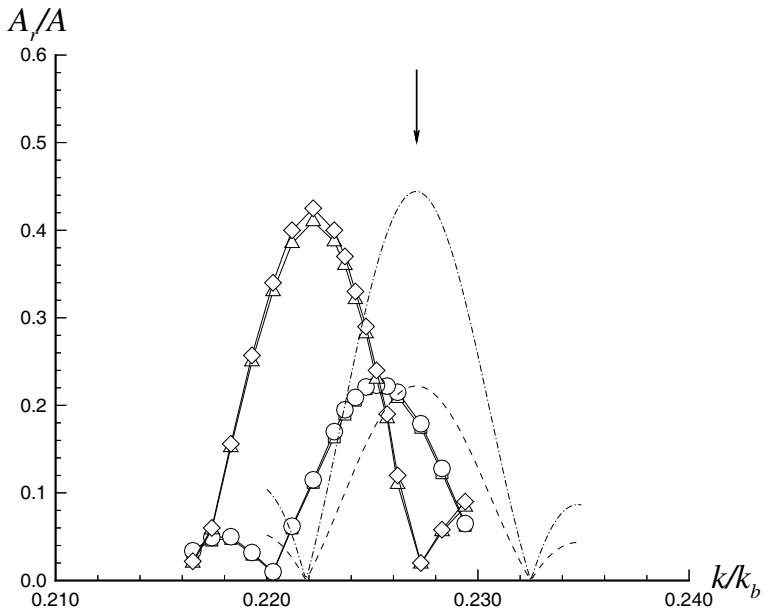

Figure 15.18: Class III sub-harmonic Bragg reflection coefficient near the linearized Bragg resonance condition, $k/k_b = 0.227$ (indicated by $\downarrow$) for $k_b h = 2.642$, $k_b d = 0.25$ and $L_0 = 36\lambda_b$. Results for two incident steepnesses are given for: (i) $kA = 0.03$ for HOS simulations with $M = 3$ (—□—), $M = 4$ (—◯—); and regular perturbation theory (- - -) of Liu and Yue (1998); and (ii) $kA = 0.06$ for HOS simulations with $M = 3$ (—△—), $M = 4$ (—◇—), and regular perturbation theory of Liu and Yue (1998) (— ·—) (from Liu and Yue, 1998, *J. Fluid Mech.* Reproduced by permission of Cambridge University Press).

(2ω) as a result of quartet interactions among the surface waves and the bottom ripple.

For numerical illustration, we choose a patch of bottom ripples with the patch width $L_0 = 36\lambda_b$ and the bottom steepness $k_b d = 0.25$ in a mean depth of $k_b h = 2.642$. For such a bottom topography, according to (15.4.20), class III Bragg resonance occurs when the incident wavenumber is $k \approx 0.227 k_b$ resulting in the generation of a sub-harmonic wave, wavenumber $k_r \approx 0.546 k_b$, which is reflected (i.e. propagates in a direction opposite to the incident wave).

Figure 15.18 shows the variation of the sub-harmonic reflection coefficient in the neighborhood of the class III resonance wavenumber ($k = 0.227 k_b$). The numerical results are obtained from HOS using orders $M = 3$ and $M = 4$. For both incident wave steepnesses $kA = 0.03$ and 0.06, it is clear that the class III Bragg phenomenon is captured well by accounting for interactions up to third order, $M = 3$. For comparison, the prediction by the regular perturbation theory of Liu and Yue (1998) is also plotted in Fig. 15.18. For both incident wave steepnesses $kA = 0.03$ and 0.06, it is seen that the comparisons are excellent except that the location of peak reflection is down-shifted in wavenumber relative to the linearized Bragg point. Unlike the earlier class I and II resonances, nonlinear surface wave interactions enter the picture, and the downshift is greater for larger surface wave steepness in this case.

Figure 15.19 shows the comparison between the simulation results and the regular perturbation solution of Liu and Yue (1998) for the spatial variation of the sub-harmonic class III Bragg reflection coefficient over the bottom ripple patch. For the present bottom geometry, the perturbation solution of the reflected sub-harmonic wave amplitude (A_r) over the bottom ripple is obtained to be

$$A_r(x) \approx 0.0058(kA)^2(k_b d)\left(\frac{L_0}{2-x}\right), \quad -\frac{L_0}{2} < x < \frac{L_0}{2}. \qquad (15.4.21)$$

The comparison is excellent for the smaller incident wave steepness case of $kA = 0.03$, and, as expected, is less so but still satisfactory for the larger steepness case of $kA = 0.06$, where the perturbation theory somewhat overestimates A_r.

For class III super-harmonic wave transmission, analogous results are obtained. For illustration, we consider a case where $L_0 = 5\lambda_b$, $k_b d = 0.025$, and $k_b h = 0.325$. According to (15.4.20), for class III Bragg resonance, we set incident wavenumber $k = 2.031 k_b$, and anticipate the resonant

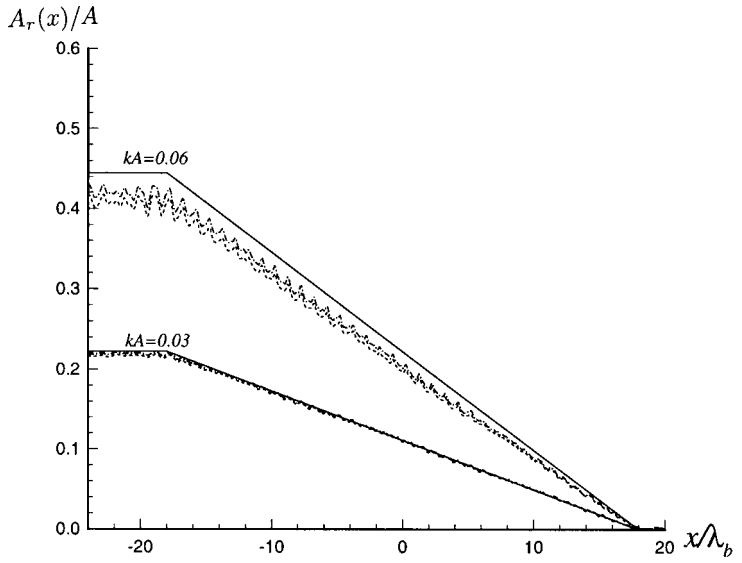

Figure 15.19: Spatial variation of the class III sub-harmonic Bragg reflected wave amplitude over a bottom patch ($|x|/\lambda_b \leq 18$) of sinusoidal ripples, $k_b d = 0.25$ and $k_b h = 2.642$. The perturbation solution of Liu and Yue (1998)(——) is obtained at the exact linearized class III condition, $k/k_b = 0.227$; while the HOS simulations with $M = 3$ (- - -) and $M = 4$ (— · —) are obtained at $k/k_b = 0.225$ for $kA = 0.03$ and $k/k_b = 0.222$ for $kA = 0.06$, corresponding respectively to peak amplitudes in the reflected wave (see Fig. 15.18) (from Liu and Yue, 1998, *J. Fluid Mech.* Reproduced by permission of Cambridge University Press).

generation of a super-harmonic transmitted wave (traveling in the same direction as the incident wave) of wavenumber $k_t \approx 5.062 k_b$.

Figure 15.20 shows the spatial variation of the class III super-harmonic transmitted wave amplitude $A_t(x)$ obtained using HOS with $M = 3$ and $M = 4$ compared with the perturbation solution of Liu and Yue (1998) which is obtained to be

$$A_t(x) \approx 6.3862(kA)^2(k_b d)\left(x + \frac{L_0}{2}\right), \quad -\frac{L_0}{2} < x < \frac{L_0}{2}. \qquad (15.4.22)$$

The agreement is again excellent for the smaller incident wave steepness $kA = 0.03$, and is acceptable for $kA = 0.06$ for which the perturbation solution still somewhat overestimates A_t.

Class III Bragg resonance can also occur when the incident wave ($\mathbf{k}$) is oblique to the bottom ripples ($\mathbf{k}_b$). For this case, a main interest is

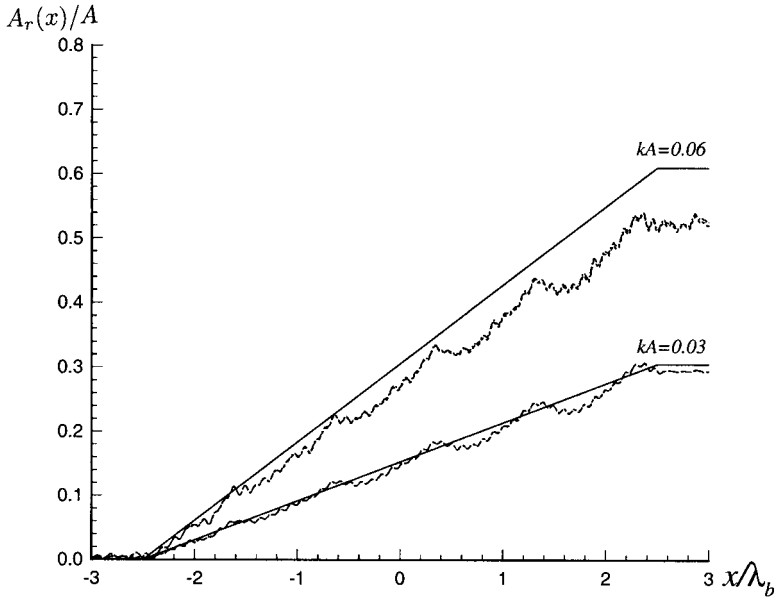

Figure 15.20: Spatial variation of the class III super-harmonic Bragg transmitted wave amplitude over a bottom patch ($|x|/\lambda_b \leq 2.5$) of sinusoidal ripples, $k_b d = 0.025$ and $k_b h = 0.325$. The perturbation solution of Liu and Yue (1998) (——) is obtained at the exact linearized class III condition, $k/k_b = 2.031$; while the HOS simulations with $M = 3$ (- - -) and $M = 4$ (— · —) are obtained at $k/k_b = 2.021$ for $kA = 0.03$ and $k/k_b = 2.025$ for $kA = 0.06$, corresponding respectively to peak amplitudes in the transmitted wave (from Liu and Yue, 1998, *J. Fluid Mech.* Reproduced by permission of Cambridge University Press).

the effect of the incident angle θ between $\mathbf{k}$ and $\mathbf{k}_b$ upon the development and amplitudes of the class III resonant reflected/transmitted double-frequency waves. This is investigated in Liu and Yue (1998) using direct HOS simulations.

Analytical understanding aside, the general class of problems involving irregular three-dimensional waves travelling over complex bottom variations and undergoing (possibly) multiple linear and nonlinear wave-wave and wave-bottom resonances over different domains is intriguing and of potential practical importance. In most cases, explicit enumeration of the (possible) resonant interactions is infeasible and of limited value. On the other hand, the HOS method provides a direct and remarkably effective computational tool for such problems and is a subject of ongoing research.

15.5 HOS Method for Nonlinear Wave Interaction with Submerged Bodies

The HOS method developed in the preceding two sections for simulating nonlinear wave-wave, wave-current, and wave-bottom interactions can be extended to include the presence of submerged (fixed or moving) bodies. This has been achieved in two dimensions by Liu et al. (1992) and in three dimensions by Liu (1994) and Zhu et al. (1999). Using separate singularity distributions on the free surface and body surface, and employing global spectral representations for each of these, the method retains exponential convergence with the numbers of body (N_B) and free-surface (N_F) modes and with perturbation order M. With the use of fast transform techniques, the computational burden remains effectively linear functions of the number of unknown modes $N_F + N_B$ and of M. To illustrate the method, we follow Liu et al. (1992) and consider the two-dimensional problem. The specific problem considered is the nonlinear wave diffraction by a fixed submerged circular cylinder (with axis parallel to the mean free surface).

15.5.1 Mathematical Formulation

For convenience, a local cylindrical coordinate system (r, θ) is placed at the center of the cylinder, which is at a depth H below the mean water level. Thus, $r^2 = x^2 + (z+H)^2$ and θ is measured counter-clockwise from positive x. On the cylinder boundary, a no-flux condition

$$\Phi_r(R, \theta, t) = 0\,, \quad \text{for} \quad 0 \le \theta < 2\pi\,, \tag{15.5.1}$$

is specified, where R is the radius of the cylinder. One notes that the initial boundary-value problem for the nonlinear wave-body interaction is basically that for nonlinear wave-wave interaction except for the additional body boundary condition (15.5.1). The whole formulation of the HOS method for the nonlinear wave problem in Section 15.3.1 thus applies here with the exception of the boundary-value solution for the perturbation potential $\Phi^{(m)}$. For computation, periodic conditions far upstream and downstream, say at $x = \pm L/2$ are also assumed.

To solve for $\Phi^{(m)}$, we distribute dipoles $\mu^{(m)}(x, t)$ over the mean position of the free surface, and sources $\sigma^{(m)}(\theta, t)$ over the surface of the cylinder. Noting that $\mu^{(m)}$ and $\sigma^{(m)}$ are L- and 2π-periodic in x and θ respectively, we expand them as Fourier series:

$$\mu^{(m)}(x,t)=\sum_{n=0}^{\infty}\mu_n^{(m)}(t)\mathrm{e}^{\mathrm{i}2n\pi x/L}\,,\quad \sigma^{(m)}(\theta,t)=\sum_{n=0}^{\infty}\sigma_n^{(m)}(t)\mathrm{e}^{\mathrm{i}n\theta}\,,\qquad(15.5.2)$$

where real parts of the complex quantities are implied. The unknown perturbation potential $\Phi^{(m)}$ is then given in terms of the modal amplitudes $\mu_n^{(m)}(t)$ and $\sigma_n^{(m)}(t)$:

$$\Phi^{(m)}(x,z,t)=\sum_{n=0}^{\infty}\mu_n^{(m)}(t)\Psi_{Fn}(x,z)+\sum_{n=0}^{\infty}\sigma_n^{(m)}(t)\Psi_{Bn}(x,z)\,,\qquad(15.5.3)$$

where Ψ_{Fn} and Ψ_{Bn} are influence functions of the n-th mode dipole and source distributions on the free surface and body, respectively. These influence functions are given in terms of the Fourier integrals:

$$\Psi_{Fn}(x,z)=\int_{-L/2}^{L/2}\mathrm{e}^{\mathrm{i}2n\pi x'/L}G_{z'}(x,z;x',0)\,\mathrm{d}x'\,,\qquad(15.5.4)$$

$$\Psi_{Bn}(x,z)=\int_{0}^{2\pi}\mathrm{e}^{\mathrm{i}n\theta'}G(r,\theta;R,\theta')R\,\mathrm{d}\theta'\,,\qquad(15.5.5)$$

where $G(x,z;x',z')$ is the L-periodic source potential in two dimensions:

$$G(x,z;x',z')=\frac{1}{2}\log\left[\sin^2\left(\frac{x-x'}{\frac{L}{\pi}}\right)+\sinh^2\left(\frac{z-z'}{\frac{L}{\pi}}\right)\right].\qquad(15.5.6)$$

With this construction, (15.5.3) satisfies Laplace's equation and all the boundary conditions with the exception of those on the mean free surface and the body. Substituting (15.5.3) into (15.3.7) and (15.5.1) for each order, the modal amplitudes $\mu_n^{(m)}(t)$ and $\sigma_n^{(m)}(t)$ are determined successively for $m=1,\ldots,M$, in terms of $\Phi^{(m)}(x,0,t)$, which ultimately is given by the known $\Phi^s(x,t)$ and $\zeta(x,t)$ according to (15.3.8).

After the boundary-value problems for $\Phi^{(m)}$ are solved up to the desired order M, the vertical velocity on the free surface is given by

$$\Phi_z(x,\zeta,t)=\sum_{m=1}^{M}\sum_{\ell=0}^{M-\ell}\frac{\zeta^\ell}{\ell!}\frac{\partial^{\ell+1}}{\partial z^{\ell+1}}\Phi^{(m)}(x,z,t)\bigg|_{z=0}\,.\qquad(15.5.7)$$

The vertical derivatives here (and in (15.3.8)) are obtained in terms of the modal amplitudes:

$$\Phi_z^{(m)}(x,0,t) = \sum_{n=0}^{\infty} \mu_n^{(m)}(t) \frac{\partial}{\partial z} \Psi_{Fn}(x,0) + \sum_{n=0}^{\infty} \sigma_n^{(m)}(t) \frac{\partial}{\partial z} \Psi_{Bn}(x,0)\,. \tag{15.5.8}$$

Thereafter, higher derivatives are found by using Laplace's equation (e.g. $\Phi_{zz}^{(m)} = -\Phi_{xx}^{(m)}$, $\Phi_{zzz}^{(m)} = -(\Phi_z^{(m)})_{xx}, \ldots$), and the x-derivatives are easily evaluated in the Fourier space. The potential on the body is available from (15.5.3), and the pressure on the cylinder can be evaluated according to Bernoulli's equation:

$$\frac{P(\theta,t)}{\rho} = -\frac{\partial}{\partial t} \sum_{m=1}^{M} \Phi^{(m)}(R,\theta,t) - \frac{1}{2R^2} \left[\frac{\partial}{\partial \theta} \sum_{m=1}^{M} \Phi^{(m)}(R,\theta,t) \right]^2 . \tag{15.5.9}$$

15.5.2 Numerical Implementation

In implementation, the numbers of Fourier modes for the dipole and source distributions are truncated at some suitable number, say, N_F for $\mu^{(m)}$ and N_B for $\sigma^{(m)}$. Note that since $\mu^{(m)}$ and $\sigma^{(m)}$ are in general smooth periodic functions of x and θ respectively, the convergence of (15.5.2) with N_F and N_B is exponentially rapid. At each time, the modal amplitudes $\mu_n^{(m)}(t)$, $n = 0, \ldots, N_F$, and $\sigma_n^{(m)}(t)$, $n = 0, \ldots, N_B$, are determined by satisfying the Dirichlet and Neumann conditions at N_F and N_B equally-spaced control points on the mean free surface and body, respectively. The resulting $N_F + N_B$ linear equations can be formally represented as:

$$\left.\begin{aligned} [C_{\mu\mu}]\{\mu^{(m)}\} + [C_{\mu\sigma}]\{\sigma^{(m)}\} &= \{f^{(m)}\}\,, \\ [C_{\sigma\mu}]\{\mu^{(m)}\} + [C_{\sigma\sigma}]\{\sigma^{(m)}\} &= 0\,, \end{aligned}\right\} \tag{15.5.10}$$

where $[C_{\mu\mu}]$, $[C_{\mu\sigma}]$, $[C_{\sigma\mu}]$, and $[C_{\sigma\sigma}]$ are, respectively, the $N_F \times N_F$, $N_F \times N_B$, $N_B \times N_F$, and $N_B \times N_B$ modal influence matrices given in terms of the basis functions; and $\{\mu^{(m)}\}$, $\{\sigma^{(m)}\}$, the vectors of the unknown modal amplitudes $\mu_n^{(m)}$, $n = 0, \ldots, N_F$, and $\sigma_n^{(m)}$, $n = 0, \ldots, N_B$. Solving these equations, we obtain:

$$\left.\begin{aligned} \{\sigma^{(m)}\} &= [T_{\sigma f}]\{f^{(m)}\}\,, \\ \{\mu^{(m)}\} &= [T_{\mu f}]\{f^{(m)}\} + [T_{\mu\sigma}]\{\sigma^{(m)}\}\,, \end{aligned}\right\} \tag{15.5.11}$$

where $[T_{\sigma f}]$ $(N_B \times N_F)$, $[T_{\mu f}]$ $(N_F \times N_F)$, and $[T_{\mu\sigma}]$ $(N_F \times N_B)$, are related to the inverses of the influence matrices in (15.5.10). Once $\{\mu^{(m)}\}$ and $\{\sigma^{(m)}\}$ are obtained, the perturbation vertical velocities at the control points on the free surface follow from (15.5.8), which take the form:

$$\{\Phi_z^{(m)}\} = [W_\mu]\{\mu^{(m)}\} + [W_\sigma]\{\sigma^{(m)}\}\,, \tag{15.5.12}$$

where $[W_\mu]$ $(N_F \times N_F)$, and $[W_\sigma]$ $(N_F \times N_B)$ are known matrices given by (15.5.8) in terms of the basis functions.

It is very important to note that in the HOS method, the $[T]$ and $[W]$ matrices in (15.5.11) and (15.5.12) are functions of the (mean) geometry only. For the diffraction problem, then, they are independent of time and need to be evaluated only once for the entire simulation. More significantly, since for typical applications (especially for three-dimensional problems), $N_F \gg N_B$, in the spectral approach, the $N_F \times N_F$ matrices $[T_{\mu f}]$ and $[W_\mu]$ need not be explicitly realized as the contributions $[T_{\mu f}]\{f^{(m)}\}$ and $[W_\mu]\{\mu^{(m)}\}$ can be evaluated in $O(N_F \ln N_F)$ operations via fast transforms. Consequently, the net computational effort is approximately proportional to N_F and not N_F^2. Specifically, the total operational count of the method is $[O(MN_F \ln N_F) + O(MN_F N_B)]$ per time step, with an initial set-up effort of $[O(N_B^2 N_F) + O(N_B N_F \ln N_F)]$.

If the body is not fixed, the boundary condition (15.5.1) becomes:

$$\Phi_n(r, \theta, t) = \mathbf{U}(t) \cdot \mathbf{n}\,, \quad (r, \theta) \in \mathcal{B}(t) \tag{15.5.13}$$

where $\mathbf{U}(t)$ represents the instantaneous velocity of the body, and $\mathcal{B}(t)$ the position of the body. For small body motions, we can apply the perturbation expansion (15.3.5) to the boundary condition (15.5.13) and expand each term in (15.5.13) in Taylor series about the mean position of the body $\bar{\mathcal{B}}$. Upon doing this, we derive a sequence of Neumann body boundary conditions for the perturbation potential $\Phi^{(m)}$ applied on $\bar{\mathcal{B}}$, with which the above procedure of the generalized HOS method can be directly applied (Liu et al., 1999). For large body motions this approach is ineffective as Taylor series expansion of (15.5.13) about $\bar{\mathcal{B}}$ converges slowly. In this case, the condition (15.5.13) needs to be imposed at the instantaneous position $\mathcal{B}(t)$. To reduce the effort in computing the influence matrices $[T_{\sigma f}]$, $[T_{\mu f}]$, $[T_{\mu\sigma}]$, $[W_\mu]$, and $[W_\sigma]$ in (15.5.11) and (15.5.12) at each time, we expand

each element of these matrices in a rapidly convergent series (e.g. Chebyshev polynomials) in space with the coefficients pre-calculated. This technique has been implemented and found to be effective by Zhu et al. (1999) who studied the nonlinear response of a near-surface buoy tethered to the ocean bottom by a cable subject to the action of surface waves.

15.5.3 Application to Nonlinear Wave Diffraction by a Submerged Circular Cylinder

We apply the generalized HOS to study the diffraction of Stokes waves by a fixed, two-dimensional submerged circular cylinder with horizontal axis. This is a classical problem for which a number of established theoretical, computational and experimental results are available. Using conformal mapping, Dean (1948) found, to leading order in wave steepness, that a fixed circular cylinder under waves does not reflect waves, and the transmitted waves merely experience a change in phase but not amplitude. Ursell (1950), using a multipole expansion, found the complete linear solution and showed that it is unique. Following Ursell's approach, Ogilvie (1963) showed that the linear potential leads to a mean (second-order) vertical force but that the horizontal mean force at second order vanishes identically.

This last result is in contrast to experimental observations (e.g. Salter et al., 1976) that a free cylinder just awash experiences a negative drift force which causes it to move towards the wavemaker. Longuet–Higgins (1977a) argued that this negative drift force can be attributed mostly to wave breaking, and, to a lesser degree, to the second-harmonic component of the transmitted wave. This is not supported by measurements of Miyata et al. (1988) and Inoue and Kyozuka (1984) who found that as the cylinder was moved closer to the free surface, which led to more intense breaking, the negative horizontal drift force was actually reduced and ultimately reversed sign. Using a Stokes expansion, Vada (1987) solved the second-order (frequency-domain) diffraction problem but was unable to calculate all the terms (at fourth order) of the non-vanishing mean horizontal force, since third-order potentials are involved. For the second-order oscillatory forces, however, Vada's results were in good agreement with the measurements of Chaplin (1984), thereby confirming Chaplin's suggestion that inviscid flow models would be good for Keulegan-Carpenter numbers less than about two for second-order forces. As pointed out by Chaplin, however, this is not necessarily true for first-order forces.

A number of fully-nonlinear time-domain computations of this problem were also attempted. Vinje and Brevig (1981) used the mixed Eulerian-Lagrangian method of Longuet–Higgins and Cokelet (1976) to study the forces acting on a cylinder under a breaking wave, but their results were only qualitative. Using a similar method, Cointe (1989) obtained higher-order harmonic forces and transmission coefficients but did not focus on the question of the horizontal drift force. Stansby and Slaouti (1983) used the method of Zaroodny and Greenberg (1973) to study the forces on cylinders under waves and found that steady-state was rapidly approached. No conclusions were made, however, regarding the steady forces.

For the reflected and transmitted waves, the theoretical prediction of Dean (1948) and Ursell (1950) of no leading-order reflected waves was confirmed by the measurements of Chaplin (1984) to even higher order for mild waves. Grue (1991) performed a careful set of experiments which showed that the transmitted waves are, however, significantly affected by nonlinear wave interactions over the submerged body. Motivated by these results, there are a number of recent theoretical demonstrations (Friis, 1990; McIver and McIver, 1990; Wu, 1991) of the fact that the reflection coefficient is identically zero to second order. The most general result to date is the work of Palm (1991), who proved that the leading order component of any harmonic of the reflected wave also vanishes.

We apply the general HOS method to this problem and used the analytical results and experimental observations to validate and assess the accuracy and performance of method. In the computation, we choose as initial conditions exact deep-water Stokes waves of steepness $\epsilon = kA$ ($2A \equiv \zeta_{\max} - \zeta_{\min}$), wavelength $\lambda = L/N_w$, i.e. N_w complete waves in the periodic domain $[-L/2, L/2]$, and period T. The numerical parameters used are: $N_w = 16$, $N_F = 64N_w$, $N_B = 256$, and $\Delta t = T/64$. Convergence tests show that the maximum error in the (fourth-order) mean horizontal wave force on the cylinder $\bar{F}_x$ obtained using these parameters is less than 1% (Liu et al., 1992).

Diffracted waves

In the HOS simulations, we record the time series of the free-surface elevation at a location far upstream (at $x = -8R$), and another far downstream ($x = 8R$), the latter corresponding to the measurement position of Grue (1991). At these positions, the limit cycle for the surface elevation up to third harmonics is approached after simulation time of $T_S/T \sim 7$–8. The

harmonic amplitudes of the transmitted and reflected waves are then obtained via Fourier analysis of the limit-cycle time histories at these two locations. The reflection and transmission coefficients for the n-th harmonic are defined respectively to be $R_n = a'_n/a_1$ and $T_n = b_n/a_1$, where a_1 is the incident wave amplitude of the first harmonic, and a'_n and b_n are respectively the reflected and transmitted wave amplitudes of the n-th harmonic.

To study the effect of nonlinearity on wave reflection and transmission, we first fix $kR = 0.4$ and $kH = 0.6$, and consider the dependence of R_n and T_n on the incident wave slope $\epsilon = kA$. The HOS simulation results show that R_n, $n = 1, 2, 3$, is at most of $O(\epsilon^n)$ and is at least one order smaller than the transmission coefficients. These results provide a direct numerical confirmation of the analytical predictions of Palm (1991).

The dependence of the first-harmonic transmission coefficient, T_1, on incident wave steepness $\epsilon = kA$ is shown in Fig. 15.21(a). For linear theory, $T_1 \equiv 1$ and is not a function of ϵ. However, the measurements of Grue (1991) show that T_1 in fact decreases appreciably from 1 as ϵ increases. The converged numerical results confirm this nonlinear dependence quantitatively up to $\epsilon \sim 0.08$. (Beyond $\epsilon \sim 0.08$, extensive wave breaking over the cylinder is reported by Grue (1991)). From Fig. 15.21(a), we also conclude that it is necessary to include third-order ($M = 3$) contributions to correctly account for the behavior of T_1.

Figure 15.21(b) shows the comparisons for the second-harmonic transmission coefficient T_2 among the HOS simulation results, Vada (1987)'s second-order frequency-domain computations, and Grue (1991)'s experimental data. The strong nonlinear interactions over the cylinder result in a significant reduction of T_2 from the second-order perturbation result (which predicts a linear dependence on ϵ). Although our numerical results show some indication of convergence at $M = 4$, comparison to the measured data indicates that still higher order effects are present in T_2 for near-breaking conditions.

The dependence of T_n on the body submergence H/R is studied by fixing $kR = 0.4$, $kA = 0.08$ and varying kH. The numerical results for T_1 and T_2 are shown in Fig. 15.22. For this case, two experimental points at $H/R = 1.5$ and 2 are available from Grue (1991). For large H/R, T_1 approaches 1 rapidly, while T_2 decreases monotonically. The coefficients are overpredicted by these asymptotes, however, as the cylinder approaches the surface and nonlinear effects evidently become important. This is seen from

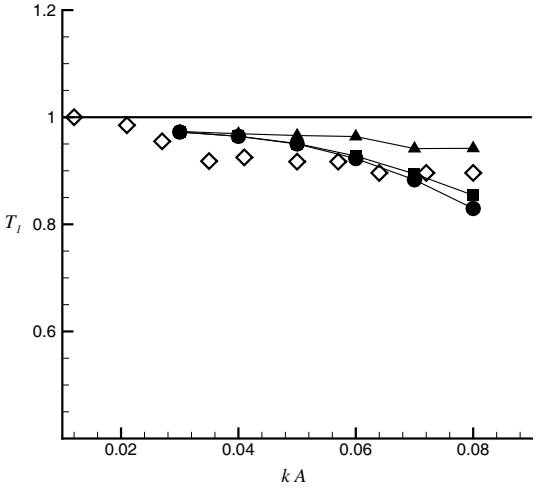

(a)

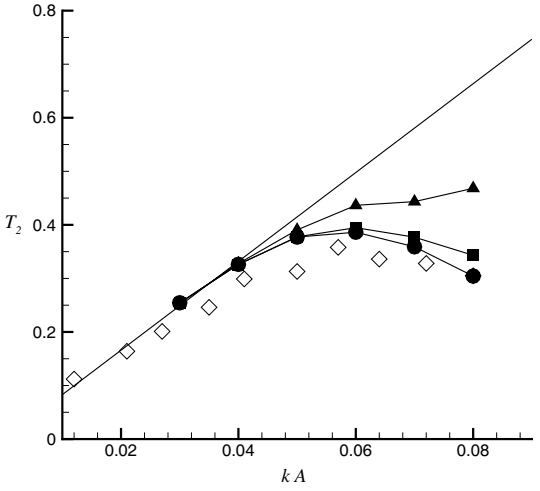

(b)

Figure 15.21: Dependence of (a) the first-harmonic (T_1) and (b) second-harmonic (T_2) wave transmission coefficients on the incident wave slope kA. Experiments (Grue, 1991) ($\Diamond$) and HOS simulation results for $M = 2$ ($\blacktriangle$), $M = 3$ ($\blacksquare$), and $M = 4$ ($\bullet$). (——): linear solution in (a), and second-order computation (Vada, 1987) in (b). ($kR = 0.4$, $H/R = 1.5$) (from Liu et al., 1992, *J. Fluid Mech.* Reproduced by permission of Cambridge University Press).

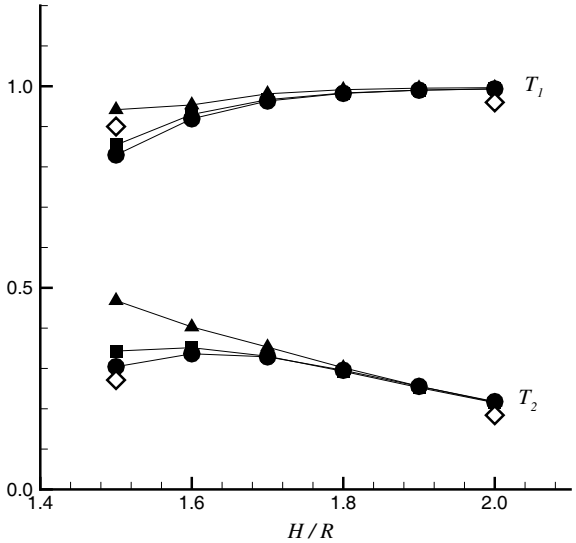

Figure 15.22: Dependence of the first- and second-harmonic wave transmission coefficients on the body submergence H/R. Experiments (Grue, 1991) (◇); and HOS simulation results for $M = 2$ (▲), $M = 3$ (■), and $M = 4$ (●). ($kR = 0.4, kA = 0.08$) (from Liu et al., 1992, *J. Fluid Mech.* Reproduced by permission of Cambridge University Press).

the differences among the results for $M = 2$, 3, and 4. Indeed, comparison with experimental data suggests again that even higher-order interactions play a role.

Oscillating forces

Figure 15.23(a) shows the comparisons for the first-harmonic horizontal force amplitude F_{x1} among the HOS ($M = 4$) simulation results, linear (potential flow) analytic solution (Ogilvie, 1963), and experimental measurements of Chaplin (1984). Following Chaplin, F_{x1} is plotted here as a function of the Keulegan-Carpenter number defined as $K_C = \pi \mathrm{e}^{-kH} A/R$, based on linear deep water waves. Comparing just the theoretical and computed results, it is remarkable that the first-harmonic amplitude is affected very little by nonlinear effects at least up to $K_C \sim 1$. On the other hand, as suggested by Chaplin, effects of (clockwise) circulation around the cylinder result in a sharp decrease of F_{x1} for $K_C >\sim 0.5$ (possible effects of flow separation and wave breaking also cannot be ruled out). The HOS simulation results also show a reduction due to nonlinear diffraction but

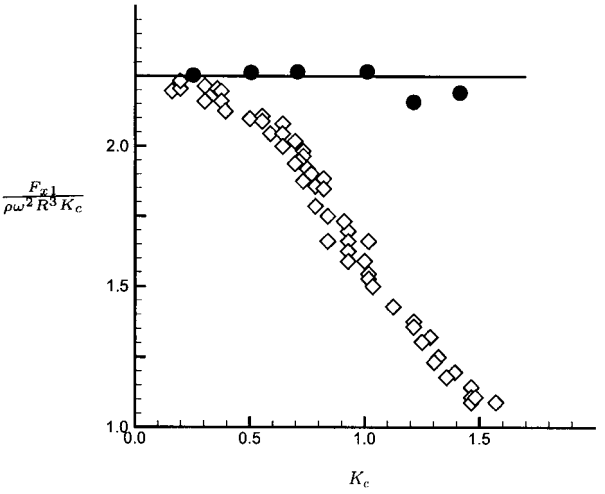

(*a*)

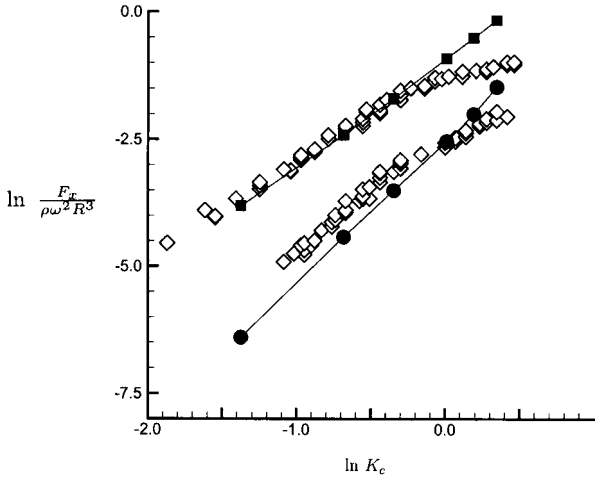

(*b*)

Figure 15.23: (*a*) The first-harmonic (F_{x1}) and (*b*) The second- and third-harmonic (F_{x2}, F_{x3}) horizontal forces as a function of Keulegen-Carpenter number K_c. Experiments (Chaplin, 1984) (◇); In (*a*), linear result (Ogilvie, 1963) (——); and HOS simulation results for $M = 4$ (●). In (b), HOS simulation results with $M = 4$ for F_{x2} (■) and F_{x3} (●). ($kR = 0.21$, $H/R = 2.0$) (from Liu et al., 1992, *J. Fluid Mech.* Reproduced by permission of Cambridge University Press).

the magnitude is small compared to that due to circulation or real fluid effects.

In direct contrast to the first-harmonic force, circulation does not appear to affect the higher-harmonic forces as shown in Fig. 15.23(b) for F_{x2} and F_{x3}. The higher-order (potential flow) results are in excellent agreement with Chaplin's data up to $K_C \sim 1$, beyond which the effects of wave breaking evidently are important. The computed data also readily confirm the expected quadratic and cubic dependencies respectively of F_{x2} and F_{x3} on the Keulegan-Carpenter number.

Mean forces

First, we show the dependence of mean forces on body submergence by varying kH with fixed $kR = 0.4$ and $kA = 0.12$. This is shown in Figs. 15.24 where HOS calculations using $M = 2, 3, 4$ are compared with the measurements of Miyata et al. (1988). The horizontal drift force $\bar{F}_x$, Fig. 15.24(a), is negative (against the direction of wave propagation) with a magnitude which increases, as expected, with decreasing submergence. Except for relatively shallow submergence, $H/R <\sim 1.75$, the numerical predictions agree well with measurements. Since our computations do not account for wave breaking, it is evident that nonlinear diffraction effects rather than wave breaking is the dominant cause of the negative drift force. For $H/R <\sim 1.75$, extensive wave breaking is observed in the experiments, and the magnitude of the negative drift force is smaller compared to the diffraction results. This provides indirect evidence that the presence of wave breaking lead to positive mean horizontal forces on the cylinder.

For the mean uplift force $\bar{F}_z$, Fig. 15.24(b), the HOS simulation results compare well with both the second-order analytic solution (Ogilvie, 1963) and the measurements of Miyata et al. (1988). Higher (then second) order interactions and wave breaking effects are less important for the vertical mean force.

Since $\bar{F}_x = 0$ up to second order in wave steepness (Ogilvie, 1963), the next available contribution is at most fourth order. Likewise, one may expect a fourth-order correction to the second-order $\bar{F}_z$. These expectations are confirmed by HOS computations of the mean forces for varying incident wave slopes kA while fixing kR and kH. Further investigation of the negative horizontal drift force using HOS computations reveals that the dominant contribution of this force is primarily due to the quadratic interaction of the first- and third-order first-harmonic waves rather than

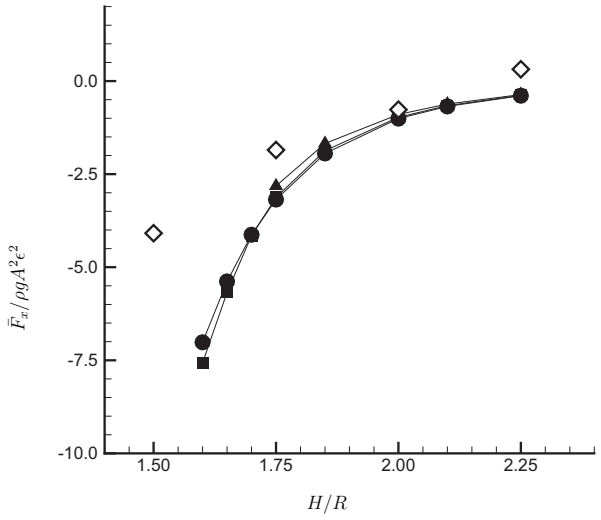

(*a*)

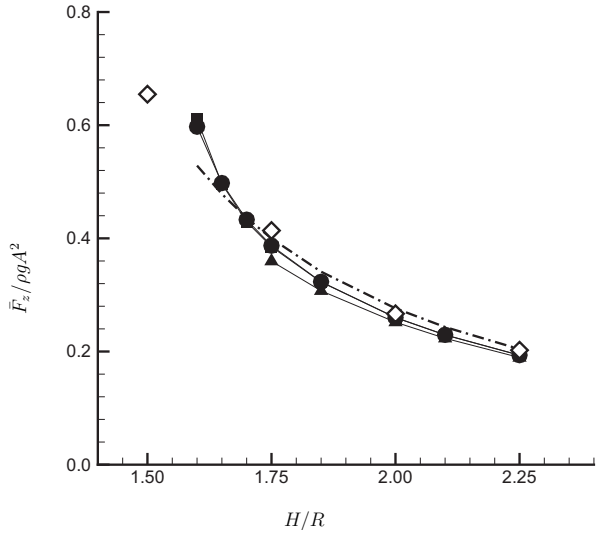

(*b*)

Figure 15.24: (*a*) Horizontal and (*b*) vertical drift force as functions of body submergence. Experiments (Miyata et al., 1988) (◇); linear potential solution (Ogilvie, 1963) (— · —); and HOS simulation results for $M = 2$ (▲), $M = 3$ (■), and $M = 4$ (●). ($kR = 0.4$, $\epsilon = kA = 0.12$) (from Liu et al., 1992, *J. Fluid Mech.* Reproduced by permission of Cambridge University Press).

the self-interaction of the second-order second-harmonic waves, which, in fact, reduces the magnitude of the negative drift force (for details, see Liu et al., 1992).

The generalized HOS method for nonlinear wave-body interactions has been extended to the case of three-dimensional submerged bodies (Liu, 1994) and body motions (Liu et al., 1999; Zhu et al., 1999). Liu (1994) considered the high-order nonlinear wave diffraction effects upon a near-surface (three-dimensional) submarine-shaped body. Of special interest for this problem are the mean forces and moments on the body. For this problem, the mean vertical force is second order and always positive (upwards) and is predicted from linear theory. The behavior of the important mean pitch moment has been less clear. For a spheroid in head seas, linear slender-body theory predicts zero mean pitch moment while linearized full three-dimensional computations (Lee and Newman, 1991) obtain a mean pitch moment that is bow-down. The question arises as to what the sign and magnitude of the nonlinear contribution to the mean pitch moment might be and whether, for small slenderness, it might be comparable to the (linearized theory) three-dimensional effect. Liu (1994) found using three-dimensional HOS calculations that the nonlinear theory contributions to the mean pitch moment is of opposite sign (bow-up in head seas) of that due to three-dimensionality. In fact, for a given slenderness, the mean pitch moment changes sign as the incident wave steepens, or when the body is moved closer to the free surface.

Zhu et al. (1999) studied the response of a tethered near-surface spherical buoy under the action of ambient incident waves. The generalized HOS method is coupled to a nonlinear cable dynamics program which is capable of modelling the complete slack and snapping of the cable. For a range of realistic parameters, they found that beyond a threshold value of the incident wave amplitude the buoy performs chaotic motion characterized by the snapping of the cable and the generation of high-frequency short surface waves. This is a heretofore unexpected and highly efficient mechanism for transfer of incident wave energy to (very) high wavenumbers.

15.6 High-Order Spectral Element (HOSE) Method

Due to the use of global basis functions, the HOS methods in Sections 15.4 and 15.5 are limited to problems with relatively simple boundaries. For

problems involving complex boundaries, direct extension of the HOS method requires global basis functions which are difficult to obtain. In the presence of a surface-piercing body, for example, Fourier basis functions should not be used for the free surface because of Gibb's phenomenon and poor convergence. Basis functions such as Chebyshev polynomials whose convergence does not depend on smooth boundary conditions can be used in these cases (see e.g. Gottlieb and Orszag, 1977), but the resulting equation system using such basis functions is known to be ill-conditioned as the mode number increases (Canuto et al., 1988). To date, realistic direct HOS simulations for these problems have not been achieved.

To overcome these difficulties and to retain the merits of HOS, Zhu, Liu and Yue (2003) developed a high-order spectral element (HOSE) method which is based on the idea of HOS but is now applicable to general wave-body problems involving complex boundaries. Instead of global spectral expansions, in HOSE the boundary domain is divided into elements and spectral expansions using local basis functions are applied over each element. Since global fast transform techniques can no longer be used, the computational effort is increased but the exponential convergence with respect to the total number of spectral modes/unknowns (for fixed number of elements) and the interaction order is retained. Significantly, HOSE is shown to be efficacious for problems with surface-piercing bodies. In this section, the detailed formulation and implementation of HOSE is given, and as an illustrative application, we use HOSE simulations and the transition matrix (TM) approach to investigate the stability of finite-amplitude standing surface waves in a circular tank under the influence of gravity (Zhu et al., 2003).

15.6.1 Mathematical Formulation

To illustrate the formulation of the HOSE method, we consider as a canonical example the (standing) wave motion in a tank (or basin) in the context of potential flow. We define a Cartesian coordinate system $\mathbf{r} \equiv (x, y, z)$ with the vertical axis z positive upwards and $z = 0$ on the mean free surface. For later convenience, we also define a polar coordinate system (r, θ) in the horizontal plane with $x = r\cos\theta$ and $y = r\sin\theta$. The initial boundary-value problem for the velocity potential $\Phi(\mathbf{r}, t)$ consists of the Laplace equation (15.2.1) inside the fluid, the nonlinear kinematic and dynamic boundary conditions (15.3.4) on the instantaneous free surface $z = \zeta(\mathbf{x}, t)$, and the no-flux condition on the side and bottom of the tank,

$$\frac{\partial \Phi}{\partial n} \equiv \Phi_n = 0\,. \tag{15.6.1}$$

As initial conditions, both the free-surface elevation and velocity potential at the initial time $t = 0$ are specified. For *standing* waves of period T, we impose an additional condition (in lieu of an initial condition), say:

$$\Phi^s(\mathbf{x}, 0) = \Phi^s\left(\mathbf{x}, \frac{T}{2}\right) = 0\,, \tag{15.6.2}$$

corresponding to stationary conditions at $t/T = 0, 0.5, \ldots$.

The procedures of the HOSE method differ to those of the HOS method in Sections 15.3 and 15.4 primarily in the construction of the boundary-value solutions for the perturbation potentials. In HOSE, a spectral-element approach is used for the boundary-value solution while in HOS, global basis functions representation is used.

Spectral-element approach for the boundary-value solution

In HOSE, as in HOS, we decompose (with the perturbation expansions) the original nonlinear boundary-value problem for Φ into a sequence of linear boundary-value problems for $\Phi^{(m)}$, $m = 1, \ldots, M$, consisting of the Laplace equation ($\nabla^2\Phi^{(m)} = 0$) inside the mean fluid domain, Dirichlet boundary condition (15.3.7) on the mean free surface $\bar{S}_F$, and Neumann boundary condition on the mean body/wall/bottom surface $\bar{S}_B$ ($\Phi_n^{(m)} = 0$). The sequence of linear problems for $\Phi^{(m)}$, $m = 1, 2, \ldots, M$ are solved in order starting from $m = 1$.

To solve the boundary-value problem for $\Phi^{(m)}$, $m = 1, 2, \ldots, M$, we divide the boundary $\bar{S}_F$ and $\bar{S}_B$ respectively into N_{FE} and N_{BE} piece-wise smooth elements. On each element, we expand the potential $\Phi^{(m)}$ and normal velocity $\Phi_n^{(m)}$ in spectral series:

$$\Phi^{(m)}(\mathbf{r}, t) = \sum_{\ell=1}^{\infty} \alpha_{j\ell}^F(t)\Psi_{j\ell}^F(\mathbf{r})\,, \quad \Phi_n^{(m)}(\mathbf{r}, t) = \sum_{\ell=1}^{\infty} \beta_{j\ell}^F(t)\Theta_{j\ell}^F(\mathbf{r}) \tag{15.6.3}$$

for $\mathbf{r} \in \bar{S}_{F_j}$, $j = 1, \ldots, N_{FE}$ and

$$\Phi^{(m)}(\mathbf{r}, t) = \sum_{\ell=1}^{\infty} \alpha_{j\ell}^B(t)\Psi_{j\ell}^B(\mathbf{r})\,, \quad \Phi_n^{(m)}(\mathbf{r}, t) = \sum_{\ell=1}^{\infty} \beta_{j\ell}^B(t)\Theta_{j\ell}^B(\mathbf{r}) \tag{15.6.4}$$

for $\mathbf{r} \in \bar{S}_{B_j}$, $j = 1, \ldots, N_{BE}$. In the above, $\Psi_{j\ell}^F$ ($\Theta_{j\ell}^F$) and $\Psi_{j\ell}^B$ ($\Theta_{j\ell}^B$) are the ℓ-th spectral basis functions for $\Phi^{(m)}$ ($\Phi_n^{(m)}$) on the j-th free-surface

and body elements, respectively; and $\alpha^F_{j\ell}$ ($\beta^F_{j\ell}$) and $\alpha^B_{j\ell}$ ($\beta^B_{j\ell}$) are the corresponding modal amplitudes.

We now apply Green's theorem to $\Phi^{(m)}$ and the appropriate free-space (Rankine) Green function, and upon truncating the expansions (15.6.3) and (15.6.4) to finite numbers of free-surface (N_{FM}) and body (N_{BM}) spectral modes (per element), we obtain the following linear system of equations:

$$\sum_{j=1}^{N_{BE}} \sum_{\ell=1}^{N_{BM}} \alpha^B_{j\ell}(t) C^{BF}_{j\ell}(\mathbf{r}) - \sum_{j=1}^{N_{FE}} \sum_{\ell=1}^{N_{FM}} \beta^F_{j\ell}(t) D^{FF}_{j\ell}(\mathbf{r}) = R_F(\mathbf{r}, t)\,, \qquad (15.6.5)$$

for $\mathbf{r} \in \bar{S}_{F_j}$ and

$$\sum_{j=1}^{N_{BE}} \sum_{\ell=1}^{N_{BM}} \alpha^B_{j\ell}(t) C^{BB}_{j\ell}(\mathbf{r}) - \sum_{j=1}^{N_{FE}} \sum_{\ell=1}^{N_{FM}} \beta^F_{j\ell}(t) D^{FB}_{j\ell}(\mathbf{r}) = R_B(\mathbf{r}, t)\,, \qquad (15.6.6)$$

for $\mathbf{r} \in \bar{S}_{B_j}$. The forcing terms R_F and R_B are known:

$$R_F(\mathbf{r}, t) = -\sum_{j=1}^{N_{FE}} \sum_{\ell=1}^{N_{FM}} \alpha^F_{j\ell}(t) C^{FF}_{j\ell}(\mathbf{r}) + \sum_{j=1}^{N_{BE}} \sum_{\ell=1}^{N_{BM}} \beta^B_{j\ell}(t) D^{BF}_{j\ell}(\mathbf{r}) \qquad (15.6.7)$$

and

$$R_B(\mathbf{r}, t) = -\sum_{j=1}^{N_{FE}} \sum_{\ell=1}^{N_{FM}} \alpha^F_{j\ell}(t) C^{FB}_{j\ell}(\mathbf{r}) + \sum_{j=1}^{N_{BE}} \sum_{\ell=1}^{N_{BM}} \beta^B_{j\ell}(t) D^{BB}_{j\ell}(\mathbf{r})\,. \qquad (15.6.8)$$

In the above, the influence coefficients are known and given by integrals over the boundary elements in terms of the free-surface and body basis functions and the Green function. From (15.6.5) and (15.6.6), the unknown modal amplitudes $\alpha^B_{j\ell}$ and $\beta^F_{j\ell}$ are solved.

Choice of spectral basis functions

Unlike in HOS, the HOSE local basis functions (Ψ and Θ) in (15.6.3) and (15.6.4) are not required to satisfy specific essential boundary conditions. While there is significant flexibility in the choice of these functions, a desirable requirement is the exponential convergence of the expansions for the element.

For standing waves in a circular tank with vertical side wall and a horizontal bottom (say of radius R and depth h), we divide $\bar{S}_F$ into N_{FE} concentric (circular) annular elements S_{F_j}, $j = 1, \ldots, N_{FE}$, with $(j-1)\Delta R \le r \le j\Delta R$, $\Delta R \equiv R/N_{FE}$ (and $0 \le \theta \le 2\pi$). The side wall ($r = R$, $-h \le z \le 0$) and bottom ($z = -h$, $0 \le r \le R$) of the

tank are each treated as single element, tagged as $\bar{S}_w$ and $\bar{S}_b$, respectively (i.e. $\bar{S}_B = \bar{S}_w + \bar{S}_b$). For these spectral elements, an appropriate choice for the basis functions for both the free-surface and wall/bottom elements is Fourier-Chebyshev in the azimuthal-radial directions. For S_{F_j}, $j = 1, \ldots, N_{FE}$, we employ a double expansion with $N_{F\theta}$ and N_{Fr} Fourier and Chebyshev modes:

$$\Psi^F_{jpq}(\mathbf{r}) \equiv \Psi^F_{pq} = T_q(r)\mathrm{e}^{\mathrm{i}p\theta}\,, \quad |p| = 0, 1, \ldots, \frac{N_{F\theta}}{2}\,; \quad q = 0, 1, \ldots, N_{Fr}\,; \tag{15.6.9}$$

where T_q represents the q-th order Chebyshev polynomial of the first kind. For $\bar{S}_w$ and $\bar{S}_b$, we use, respectively, the basis functions:

$$\Psi^w_{pq}(\mathbf{r}) = T_q(z)\mathrm{e}^{\mathrm{i}p\theta}\,, \quad |p| = 0, 1, \ldots, \frac{N_{w\theta}}{2}\,; \quad q = 0, 1, \ldots, N_{wz}\,; \tag{15.6.10}$$

$$\Psi^b_{pq}(\mathbf{r}) = T_q(r)\mathrm{e}^{\mathrm{i}p\theta}\,, \quad |p| = 0, 1, \ldots, \frac{N_{b\theta}}{2}\,; \quad q = 0, 1, \ldots, N_{br}\,. \tag{15.6.11}$$

The same sets of basis functions are used for Θ^F and Θ^B, $B = w, b$.

Note that, for this geometry, in theory $N_{FE} = 1$ (with sufficiently large Chebyshev modes) suffices. In practice, for given machine accuracy, the maximum number of Chebyshev modes, say N_C, we can use in an element is strongly limited by the condition number of the resulting equation system (e.g. Canuto et al., 1988). Thus, as a practical matter, we place an upper limit on N_C (typically $N_C \lesssim 32$ for double precision) and increase the number of elements, in this case N_{FE}, to achieve the necessary accuracy. For this problem, a single element for each $\bar{S}_b$ and $\bar{S}_w$ is found to be sufficient for the value of N_C we use.

Evaluation of high z-derivatives of $\Phi^{(m)}$

To evaluate the Dirichlet boundary condition for $\Phi^{(m)}$ (cf. (15.3.8)) and the free-surface vertical velocity (15.3.11) or (15.5.7), we need to determine, to high orders, the z-derivatives of $\Phi^{(m)}$ (i.e. $\Phi^{(m)}_{zz}, \Phi^{(m)}_{zzz}, \ldots$) on the mean free surface $\bar{S}_F$. To do that, we employ an approach wherein the high-order z-derivatives of $\Phi^{(m)}$ are solved directly via the associated boundary-value problems. For example, to evaluate $\Phi^{(m)}_{zz}$, the boundary-value problem is the same as that for $\Phi^{(m)}$ but with $\Phi^{(m)}$ replaced by $\Phi^{(m)}_z$. The additional computational effort is not significant since the equation system for the boundary-value problem is the same and needs to be inverted only once (for a given mean geometry, independent of order or time). Note that to obtain

high accuracy in the evaluation, it is important to ensure the requisite continuity across inter-element boundaries, at least C^1, for example, for $\Phi_z^{(m)}$ on $\bar{S}_F$. To do that, we replace the Dirichlet boundary condition at the edges of boundary elements by the continuity condition.

15.6.2 Numerical Implementation

Implementation

In a pseudo-spectral approach, we employ a collocation method to solve (15.6.5) and (15.6.6) for the unknown modal amplitudes $\alpha_{j\ell}^B$ and $\beta_{j\ell}^F$. To ensure exponential convergence, the collocation points are distributed uniformly for the Fourier expansion and placed at the maxima of $T_{N_C}(r)$ for the Chebyshev spectral representation containing N_C terms. The resulting system contains $N_F + N_B$ equations ($N_F = N_{FM}N_{FE}$, $N_B = N_{BM}N_{BE}$) which are written formally as:

$$\begin{bmatrix} C^{BF} & D^{FF} \\ C^{BB} & D^{FB} \end{bmatrix} \begin{Bmatrix} \alpha^B \\ \beta^F \end{Bmatrix} = \begin{Bmatrix} R^F \\ R^B \end{Bmatrix}. \tag{15.6.12}$$

Here C^{BF}, D^{FF}, C^{BB} and D^{FB} are, respectively, the $N_B \times N_F$, $N_F \times N_F$, $N_B \times N_B$ and $N_F \times N_B$ modal influence matrices given in terms of the basis functions; R^F and R^B are vectors given, respectively, by R_F and R_B; and α^B and β^F are the vectors of unknown modal amplitudes.

Note that the matrix inversion in (15.6.12) is required only once for a given problem geometry, and is independent of the time, order or base flow. In practice, the computational effort of HOSE is dominated by the operation account at each time step. For the general wave-body interaction problem, an operation of $O((N_F + N_B)^2)$ is required. For the problem of standing wave motion in a circular basin, the computational effort is reduced by a factor $N_{F\theta}$ by using fast Fourier transforms in the azimuthal direction, where $N_{F\theta}$ is the total number of Fourier modes. The total operation count for the simulation of finite-amplitude waves in a circular tank including wave-wave and wave-wall interactions up to order M is $O(M(N_F + N_B)^2/N_{F\theta})$ per time step.

Determination of the base flow for a nonlinear standing wave

To determine the frequency and configuration of a nonlinear standing wave (satisfying (15.6.2)), we seek an initial free-surface profile $\zeta(\mathbf{x}, t = 0)$ for an initial free-surface velocity potential $\Phi^s(\mathbf{x}, t = 0) = 0$ such that Φ^s, through

the nonlinear evolution, returns to zero again after some time (corresponding to $T/2$). To do this, we follow the Newtonian iteration method of Mercer and Roberts (1992) but use HOSE computations for the nonlinear wave simulation.

The procedure to obtain a standing wave of a specified amplitude A is as follows: (i) given an initial (estimate of) $\zeta(\mathbf{x},0)$ and T (and $\Phi^s(\mathbf{x},0)=0$), use HOSE to obtain $\zeta(\mathbf{x},T/2)$ and $\Phi^s(\mathbf{x},T/2)$; (ii) compute the error vector $\boldsymbol{\mathcal{E}}=\{E_j\}$:

$$E_j=\begin{cases}\Phi^s\left(\mathbf{x}_j,\dfrac{T}{2}\right), & j=1,\ldots,N_F\\[2ex] \zeta(\mathbf{x},0)_{\max}-\zeta\left(\mathbf{x},\dfrac{T}{2}\right)_{\min}-2A, & j=N_F+1\end{cases}\tag{15.6.13}$$

where $\mathbf{x}_j$, $j=1,\ldots,N_F$ are the HOSE collocation points on $\bar{S}_F$; (iii) compute the Jacobian matrix $\boldsymbol{\mathcal{J}}=[J_{j\ell}]$:

$$J_{j\ell}=\begin{cases}\dfrac{\partial E_j}{\partial\zeta(\mathbf{x}_\ell,0)}, & \ell=1,\ldots,N_F\\[2ex] \dfrac{\partial E_j}{\partial T}, & \ell=N_F+1\end{cases}\tag{15.6.14}$$

for $j=1,\ldots,N_F+1$; (iv) update $\zeta(\mathbf{x},t=0)$ and T using $\boldsymbol{\mathcal{J}}$. The Newtonian iteration process (i)-(iv) is repeated until $\|\boldsymbol{\mathcal{E}}\|$ becomes smaller than a preset tolerance (set to be 10^{-12} in this study).

Generally, we use the linearized $\zeta(\mathbf{x},0)$ and T as initial guess. To accelerate the convergence for steeper waves, a useful alternative is to obtain the initial guess using (Richardson) extrapolation of the (converged) nonlinear solutions for smaller amplitudes.

Convergence test

The accuracy and performance of the HOSE method are verified through extensive and systematic convergence tests (Zhu, 2000; Zhu et al., 2003). We present here two representative results for the case of nonlinear standing waves in a circular tank.

We first show the convergence of the HOSE boundary-value solver itself. The analytic solution of linear standing waves in a circular tank is used as the benchmark solution:

$$\Phi(r,\theta,z,t)=\frac{A}{\omega_{\ell,\nu}}J_\nu(k_{\ell,\nu}r)\frac{\cosh k_{\ell,\nu}(z+h)}{\cosh k_{\ell,\nu}h}\cos(\ell\theta)\cos(\omega_{\ell,\nu}t)\tag{15.6.15}$$

Table 15.4: Convergence of the normalized maximum error of the vertical velocity on the mean free surface of a standing wave (with wavenumber $k_{3,4}$ and amplitude $A/R = 0.05$) in a circular tank ($h/R = 0.5$) with respect to the number of free-surface elements N_{FE} and the number of free-surface Chebyshev modes N_{Fr}. The symbol $*$ indicates the error to be smaller than 10^{-6} and affected by machine precision limitations ($N_{F\theta} = N_{w\theta} = N_{b\theta} = 16$, $N_{wz} = N_{br} = 16$).[a]

$N_{FE}\backslash N_{Fr}$	4	8	16
1	7.60×10^{-1}	1.01×10^{-1}	1.10×10^{-4}
2	1.04×10^{-1}	5.93×10^{-4}	3.28×10^{-6}
3	4.04×10^{-2}	3.83×10^{-5}	$*$
4	1.27×10^{-2}	3.65×10^{-6}	$*$
8	5.09×10^{-4}	$*$	$*$

[a]From Zhu et al. (2003).

where A denotes the wave amplitude, ℓ and ν are non-negative integers representing the wavenumbers in the azimuthal and radial directions respectively, and J_ν is the ν-th order Bessel function of the first kind. In (15.6.15), the (linear) frequency $\omega_{\ell,\nu}$ is related to the wavenumber $k_{\ell,\nu}$ by the linear dispersion relation: $\omega^2_{\ell,\nu} = g k_{\ell,\nu} \tanh(k_{\ell,\nu} h)$, where $k_{\ell,\nu}$ is the root of the equation

$$J'_\nu(k_{\ell,\nu} R) = 0\,, \quad \ell = 0, 1, \ldots\,, \quad \text{and} \quad \nu = 1, 2, \ldots\,. \tag{15.6.16}$$

With the velocity potential on the mean free surface $\bar{S}_F$ specified using (15.6.15) (say at $t = 0$), HOSE is used to solve for the vertical velocity Φ_z on $\bar{S}_F$. Table 15.4 shows the maximum error of Φ_z on $\bar{S}_F$ of standing wave $k_{3,4}$ with amplitude $A/R = 0.05$ in a tank with $h/R = 0.5$. It is computed with fixed numbers of Fourier modes (in the azimuthal direction) on the free surface ($N_{F\theta} = 16$) and the side wall and bottom of the tank ($N_{w\theta} = N_{b\theta} = 16$), and numbers of Chebyshev modes on the side wall and bottom of the tank ($N_{wz} = N_{br} = 16$), but with varying the number of free surface elements N_{FE} and the number of free-surface Chebyshev modes N_{Fr}. As expected, for fixed (and sufficient) N_{FE}, exponential convergence with N_{Fr} is observed; while for fixed N_{Fr}, rapid convergence with N_{FE} is obtained. Similar fast convergence features are also obtained by varying N_{wz} and N_{br} with fixed $N_{FE} = N_{Fr} = 8$ and $N_{F\theta} = N_{w\theta} = N_{b\theta} = 16$ (see Zhu et al., 2003 for details).

To show the convergence of HOSE with the interaction order M, we consider the problem of determining the finite-amplitude standing waves

Table 15.5: Nonlinear frequency $\Omega_{0,6}$ (normalized by its linearized value $\omega_{0,6}$) of nonlinear axisymmetric standing wave with wavenumber $k_{0,6}$ in a circular tank, obtained using varying numbers of free-surface elements N_{FE} and order M ($N_{Fr} = 8$, $N_{F\theta} = N_{w\theta} = N_{b\theta} = 16$, $N_{wz} = N_{br} = 16$, $T/\Delta t = 128$, $h/R = 0.5$).[a]

$M \backslash N_{FE}$	1	2	4	8
1	1.00000	1.00000	1.00000	1.00000
2	1.04388	0.99953	0.99938	0.99938
3	1.04387	0.99897	0.99881	0.99881
4	1.04387	0.99896	0.99880	0.99880

[a] From Zhu et al. (2003).

in a circular tank. For the time integration of the evolution equations in HOSE, a fourth-order Runge-Kutta scheme is employed. For reference, we denote the nonlinear frequency of a nonlinear standing wave in a circular tank with wavenumber $k_{\ell,\nu}$ by $\Omega_{\ell,\nu}$. Since $\Omega_{\ell,\nu}$ has a direct dependence on the wave amplitude (see e.g. Tsai and Yue, 1987), we here fix the amplitude of the standing wave: $A \equiv (\zeta_{\max} - \zeta_{\min})/2 = 0.016R$, and consider the convergence of $\Omega_{\ell,\nu}$ with respect to M. Table 15.5 shows the case for $\Omega_{0,6}$ with $N_{Fr} = 8$, $N_{F\theta} = N_{w\theta} = N_{b\theta} = 16$, $N_{wz} = N_{br} = 16$, and $T/\Delta t = 128$. When nonlinear effects are included ($M > 1$), the value of of $\Omega_{0,6}$ becomes smaller than that for the linear standing wave ($M = 1$) : $\omega_{0,6} = [gk_{0,6} \tanh(k_{0,6}h)]^{1/2}$. For fixed N_{FE}, exponential convergence for $\Omega_{0,6}$ with respect to M is obtained; while for a fixed M, comparably rapid convergence with N_{FE} is achieved.

15.6.3 Application of HOSE to the Study of Stability of Standing Waves in a Circular Tank

Transition Matrix Method

To investigate the instability of standing waves, the base flow of which cannot be rendered steady in any reference frame, the transition matrix approach (e.g. von Kerczek and Davis, 1975) based on Floquet theory is adopted. For completeness, we outline this standard approach below.

We write the evolution equations (15.3.4) symbolically in terms of a nonlinear operator $\mathcal{N}$:

$$\frac{\partial \mathbf{u}}{\partial t} = \mathcal{N}(\mathbf{u}) \,, \tag{15.6.17}$$

where $\mathbf{u} = (\zeta(\mathbf{x}, t), \Phi^s(\mathbf{x}, t))$. In a linear stability analysis, we write $\mathbf{u}$ as the sum of a base standing wave $\mathbf{u}_0$, satisfying (15.2.1), (15.3.4) (15.6.1) and (15.6.2); and a small perturbation $\mathbf{u}'$, which satisfies (15.2.1) and (15.6.1) only:

$$\mathbf{u}(\mathbf{x}, t) = \mathbf{u}_0(\mathbf{x}, t) + \mathbf{u}'(\mathbf{x}, t)\,. \tag{15.6.18}$$

Substituting (15.6.18) into (15.6.17) then gives:

$$\frac{\partial \mathbf{u}'}{\partial t} = \mathcal{L}(\mathbf{u}') \tag{15.6.19}$$

where $\mathcal{L}$ is a time-periodic linearized (variable-coefficient) operator given by the Jacobian of $\mathcal{N}$ with respect to $\mathbf{u}$ (evaluated at $\mathbf{u}_0$).

For a disturbance with N degrees of freedom, we express the solution of (15.6.19) as a combination of N linearly independent solutions $\mathbf{u}'_i$, $i = 1, \ldots, N$:

$$\mathbf{u}' = \sum_{i=1}^{N} \gamma_i \mathbf{u}'_i \tag{15.6.20}$$

where the coefficients γ_i, $i = 1, \ldots, N$, are obtained from the initial condition for $\mathbf{u}'$. Using separation of variables, we write:

$$\mathbf{u}'_i(\mathbf{x}, t) = \sum_{j=1}^{N} \mu_{ij}(t)\psi_j(\mathbf{x}) \tag{15.6.21}$$

where $\psi_j(\mathbf{x})$, $j = 1, \ldots, N$, are spatial basis functions and μ_{ij}, i, $j = 1, \ldots, N$, are the time-dependent modal amplitudes.

Substituting(15.6.20) and (15.6.21) into (15.6.19), we obtain an equation involving the $N \times N$ coefficient matrix $\mathcal{U} = [\mu_{ij}]$. Following standard Floquet theory (Coddington and Levinson, 1955), we write:

$$\mathcal{U}(t) = \mathcal{P}(t) \exp(\mathcal{C}t) \tag{15.6.22}$$

where the $N \times N$ matrices $\mathcal{P}$ and $\mathcal{C}$ are respectively time-periodic and time-independent. The instability of the flow depends on the eigenvalues λ_j ($j = 1, \ldots, N$) of $\mathcal{C}$: the flow is stable if $\mathrm{Re}(\lambda_j) \leq 0$, for all $j = 1, \ldots, N$; and unstable if $\mathrm{Re}(\lambda_j) > 0$, for any $j = 1, \ldots, N$ (the unstable mode is the eigenvector corresponding to λ_j with frequency $\mathrm{Im}(\lambda_j)$).

It is difficult to obtain $\mathcal{C}$ analytically, and one generally resorts to a numerical determination from (15.6.19) of the so-called transition matrix

$\mathcal{Q} \equiv \exp(\mathcal{C}T)$. In terms of the eigenvalues σ_j, $j = 1, \ldots, N$ of $\mathcal{Q}$, the eigenvalues of $\mathcal{C}$ are:

$$\lambda_j = \frac{\log \sigma_j}{T}\,, \quad j = 1, \ldots, N\,. \tag{15.6.23}$$

In practice, given a base flow $\mathbf{u}_0$, we obtain the $N \times N$ transition matrix $\mathcal{Q} \equiv [q_{ij}]$ by numerically integrating (15.6.17) with the initial condition:

$$\mathbf{u}_i(\mathbf{x}, 0) = \mathbf{u}_0(\mathbf{x}, 0) + \mathbf{u}_i'(\mathbf{x}, 0) = \mathbf{u}_0(\mathbf{x}, 0) + \delta\psi_i(\mathbf{x})\,, \quad \delta \ll 1\,, \tag{15.6.24}$$

for $i = 1, \ldots, N$, to obtain $\mathbf{u}_i(\mathbf{x}, T)$ and hence $\mathbf{u}_i'(\mathbf{x}, T)$ (from (15.6.18) with $\mathbf{u}_0(\mathbf{x}, T) = \mathbf{u}_0(\mathbf{x}, 0)$). Upon using (15.6.21), we obtain the modal amplitudes μ_{ij} of $\mathbf{u}_i'(\mathbf{x}, T)$. The process is repeated for each $i = 1, \ldots, N$. The elements of $\mathcal{Q}$ are:

$$q_{ij} = \frac{\mu_{ij}(T)}{\delta}\,, \quad i, j = 1, \ldots, N\,. \tag{15.6.25}$$

The key to the instability analysis above is the accurate (numerical) evaluation of $\mathbf{u}'(\mathbf{x}, T) = \mathbf{u}(\mathbf{x}, T) - \mathbf{u}_0$. Hence, two high-accuracy computational capabilities are required: (a) the determination of nonlinear base standing waves $\mathbf{u}_0$ satisfying (15.2.1), (15.3.4) (15.6.1) and (15.6.2); and (b) the integration in time of the nonlinear initial-boundary-value problem, (15.2.1), (15.3.4), and (15.6.1), to obtain $\mathbf{u}(\mathbf{x}, T)$ given $\mathbf{u}(\mathbf{x}, 0)$. An efficient and highly accurate approach based on the HOSE method is applied to accomplish both (a) and (b).

Instability of Standing Waves in a Circular Tank

Consider the three-dimensional instability of finite-amplitude standing waves in a circular tank, radius R and mean water depth h. For a base (large-amplitude) standing wave with wavenumber $k_{\ell,\nu}$ (azimuthal wavenumber ℓ and radial wavenumber ν), we investigate its stability to three-dimensional perturbations given by a Fourier-Bessel series with components:

$$J_\nu(\kappa_{\ell,\nu} r)\mathrm{e}^{\mathrm{i}\ell\theta}\,, \quad \ell = 0, 1, \ldots\,; \quad \nu = 1, 2, \ldots\,, \tag{15.6.26}$$

where J_ν is the νth-order Bessel function of the first kind, and $k_{\ell,\nu}$ is the root of the equation $J'\nu(k_{\ell,\nu}R) = 0$, $\ell = 0, 1, \ldots$, $\nu = 1, 2, \ldots$. Hereafter, to avoid possible confusion, we use k for the wavenumber of the base standing wave and κ for the wavenumber of each component of a perturbation, although numerically $k_{\ell,\nu} = \kappa_{\ell,\nu}$.

In the following, we consider separately the case of axisymmetric ($\ell = 0$) and non-axisymmetric ($\ell > 0$) base standing waves. For specificity, we set $h/R = 0.5$, and in the HOSE computations, use: $M = 3$, $N_{FE} = 16$, $N_{F\theta} = N_{w\theta} = N_{b\theta} = 64$, $N_{Fr} = 8$, $N_{wz} = N_{br} = 32$, and $T/\Delta t = 128$.

(a) Axisymmetric standing waves

Based on systematic computations for $\ell = 0$ and $\nu = 1, 2, \ldots$ for a range of base wave steepness ϵ, the stability analysis results are summed up as follows: the axisymmetric standing wave is unstable to three-dimensional disturbances for all ν (which is computed to beyond $\nu = 7$) when ϵ exceeds some threshold value ϵ_c (function of ν for a given h/R). The (most) unstable mode contains a pair of dominant components: $(\kappa_{1,\nu},\ \kappa_{1,\nu-1})$. The wave steepness ϵ is defined as $\epsilon \equiv |\nabla\zeta|_{\max}$ (at $t = 0$).

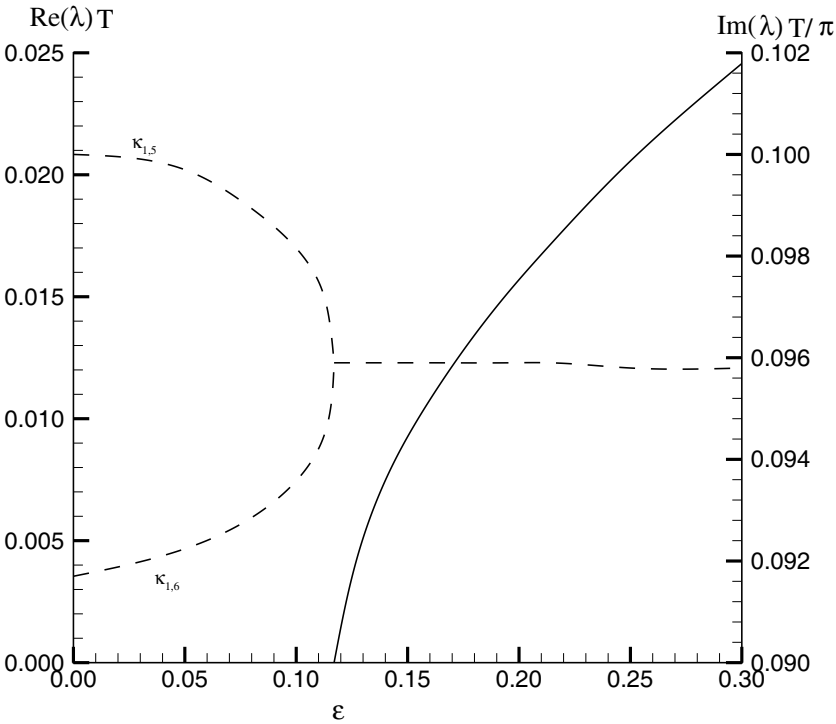

Figure 15.25: Growth rate Re(λ) (——) and eigen-frequency Im(λ) (- - -) of the perturbation containing $(\kappa_{1,5}, \kappa_{1,6})$ for the axisymmetric standing wave $k_{0,6}$ in a circular tank ($h/R = 0.5$) as a function of the fundamental wave steepness ϵ (from Zhu et al., 2003, *J. Fluid Mech.* Reproduced by permission of Cambridge University Press).

The instability here resembles that of plane standing waves (Mercer and Roberts, 1992). Figure 15.25 shows a typical result for the variation of the eigen-frequency and growth rate as ϵ increases from zero to beyond ϵ_c. The result is obtained for the axisymmetric wave $k_{0,6}$. When $\epsilon < \epsilon_c$, the eigen-frequencies of two perturbations, with (dominant) components $\kappa_{1,5}$ and $\kappa_{1,6}$ respectively, differ and the fundamental wave is stable. When $\epsilon > \epsilon_c$ ($\simeq 0.12$ in this case), the eigen-frequencies of these two modes coalesce, and the base wave becomes unstable (indicated by a positive growth rate in Fig. 15.25) to the perturbation containing these as dominant components.

Similar results are obtained for other values of ν (from 1 to 7). The salient features are similar to those for $\nu = 6$, shown in Fig. 15.25. Figure 15.26 plots the region of instability in the ϵ-ν plane for axisymmetric base standing waves. ϵ_c decreases as the radial wavenumber ν increases resulting in a upward concave stability boundary. This feature bears a resemblance to a different but related problem in which axisymmetric waves propagating radially from a heaving hemisphere develop an instability resulting in a distinct three-dimensional wave pattern (Tatsuno et al., 1969).

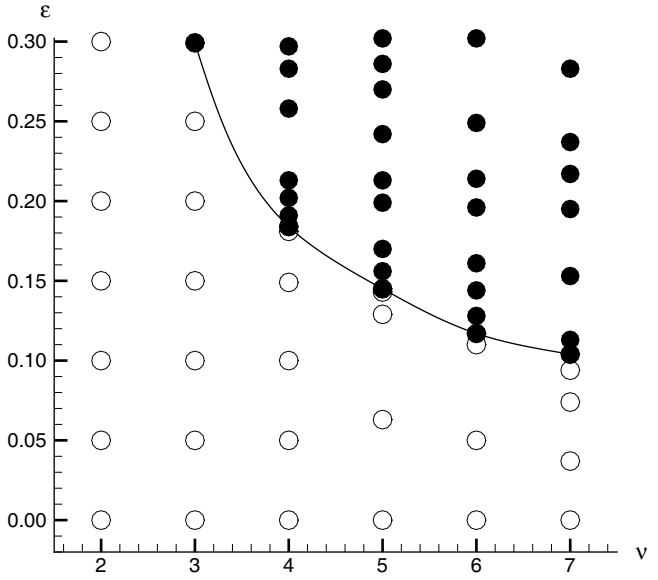

Figure 15.26: Region of (in)stability for axisymmetric standing waves $k_{0,\nu}$ as a function of ν and fundamental wave steepness ϵ. The plotted are: ○, stable and ●, unstable standing waves (from Zhu et al., 2003, *J. Fluid Mech.* Reproduced by permission of Cambridge University Press).

(b) Non-axisymmetric waves

Extensive computations and stability analyses are performed also for non-axisymmetric base standing waves for varying ℓ, ν and ϵ. Similar to axisymmetric standing waves, non-axisymmetric standing waves with azimuthal mode number $\ell \geq 1$ (calculated to beyond $\ell = 3$) are found to be unstable to three-dimensional perturbations beyond a certain critical base wave steepness $\epsilon > \epsilon_c$, where ϵ_c depends on ℓ and ν (for given h/R). For $\ell = 1$, the unstable perturbation is a single mode containing a pair of dominant Fourier-Bessel components: $\kappa_{0,\nu}$ and $\kappa_{0,\nu+1}$. For $\ell > 1$, the situation is more complex and involves two unstable modes with pairs of dominant Fourier-Bessel components: $(\kappa_{\ell-1,\nu+1}, \kappa_{\ell+1,\nu-1})$ and $(\kappa_{\ell-1,\nu}, \kappa_{\ell+1,\nu})$. Depending on the base wave ℓ and ν, the values of the critical steepness ϵ_c for these modes are generally close but not identical.

Figure 15.27(a) shows a typical $\ell = 1$ result for the case of a base standing wave with wavenumber $k_{1,5}$. The results are qualitatively similar to the axisymmetric case: beyond a certain ϵ_c, the eigen-frequencies of two separate (stable) modes with dominant components $\kappa_{0,5}$ and $\kappa_{0,6}$ coalesce forming a single unstable mode containing these dominant components. The growth rate of this unstable mode depends on increasing $\epsilon > \epsilon_c$ in a non-monotonic fashion in contrast to the axisymmetric cases (cf. Fig. 15.26). Analyzing the components of the unstable mode, it is found that, for $\epsilon >\sim 0.17$, two additional components, $\kappa_{2,4}$ and $\kappa_{2,5}$ (corresponding to $\kappa_{\ell+1,\nu-1}$ and $\kappa_{\ell+1,\nu}$), begin to grow in amplitude, and eventually become co-dominant (with $\kappa_{0,5}$ and $\kappa_{0,6}$) for $\epsilon \geq 0.20$.

For $\ell > 1$, the results differ qualitatively. In this case, two unstable perturbations are found, each containing a pair of dominant components, $(\kappa_{\ell-1,\nu+1}, \kappa_{\ell+1,\nu-1})$ and $(\kappa_{\ell-1,\nu}, \kappa_{\ell+1,\nu})$. Figure 15.27($b$) shows a sample result for the non-axisymmetric base standing wave with wavenumber $k_{3,5}$. The two unstable modes are plotted. For each of the modes, as ϵ approaches ϵ_c, instability is initiated by the merging of the eigen-frequencies of two separate modes (with different dominant components) to form a single unstable mode containing both the dominant components. The critical steepnesses of the unstable modes are close and the growth rate behaviors are qualitatively similar.

To assist in visualizing the features of the instabilities, Fig. 15.28 displays the instantaneous free-surface patterns for three sample cases. The figure shows, for example, how an initially axisymmetric base standing

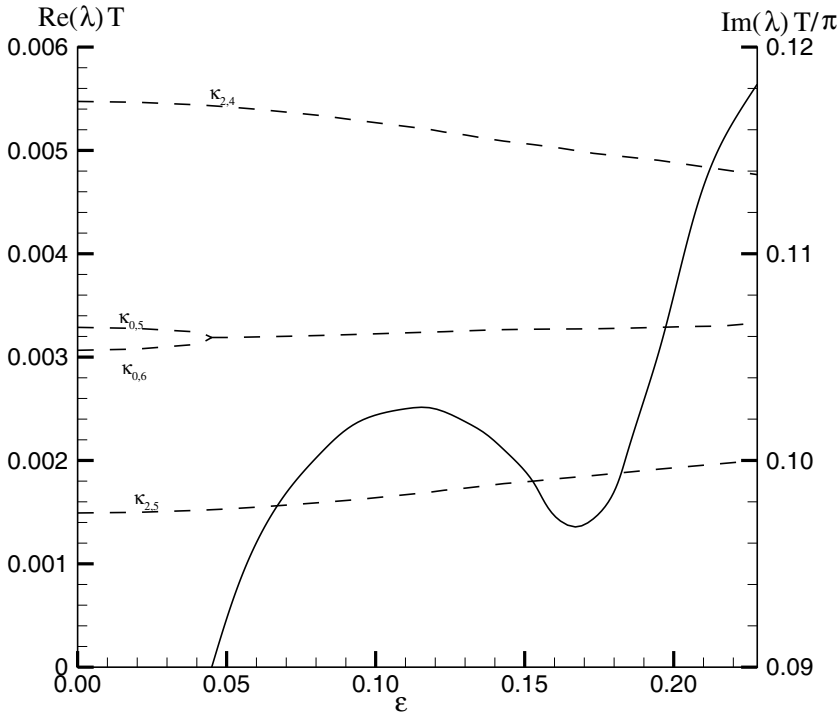

(*a*)

Figure 15.27: Growth rate Re(λ) (——) and eigen-frequency Im(λ) (- - -) of three-dimensional perturbations (labeled by their dominant components) for non-axisymmetric base standing waves with wavenumber $k_{1,5}$ (*a*) and $k_{3,5}$ (*b*) in a circular tank as a function of the fundamental wave steepness ϵ (from Zhu et al., 2003, *J. Fluid Mech.* Reproduced by permission of Cambridge University Press).

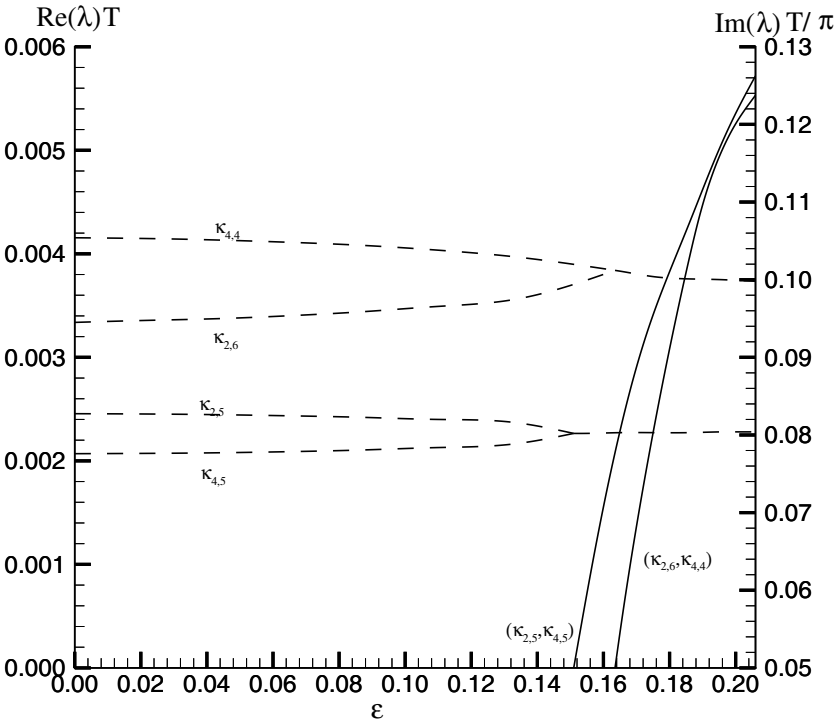

(*b*)

Figure 15.27 (*Continued*)

wave (wavenumber $k_{0,4}$) loses its axisymmetry as the dominant unstable mode (with wavenumber components $\kappa_{1,3}, \kappa_{1,4}$) develops, case (I). Similarly, a non-axisymmetric base standing wave (wavenumber $k_{1,5}$) will, depending on its initial steepness, develop into an axisymmetric standing wave (with dominant components $\kappa_{0,5}, \kappa_{0,6}$), case (II); or a non-axisymmetric standing wave with higher azimuthal wavenumber (with dominant components $\kappa_{2,4}, \kappa_{2,5}$), case (III).

Based on a frequency component analysis of the nonlinear wave interaction mechanisms, it is shown that, like propagating waves (McLean, 1982), the instabilities are associated with nonlinear (third-order quartet and higher) resonant interactions between the base flow and the unstable mode (for details, see Zhu et al., 2003). The mechanism of such nonlinear resonance of standing waves, in fact, closely resembles the internal

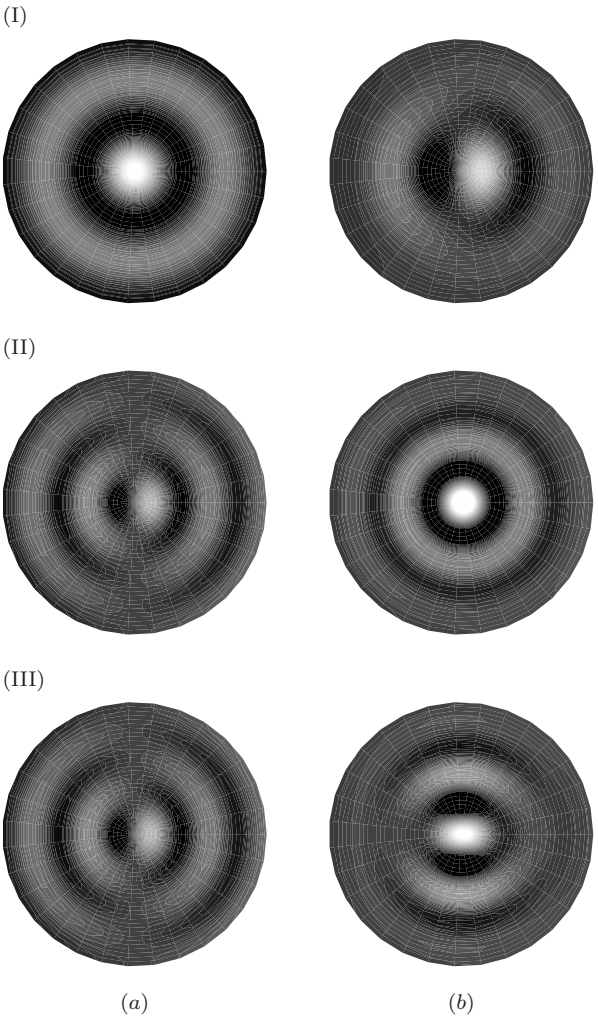

Figure 15.28: (*a*) Instantaneous free surface elevation of the base standing waves, and (*b*) the corresponding result, after significant development of the (dominant) unstable perturbations. The base flow (k) and perturbation (κ) wavenumbers for the sample cases are respectively: (I) $k_{0,4}$, and $\kappa_{1,3}$, $\kappa_{1,4}$; (II) $k_{1,5}$, and $\kappa_{0,5}$, $\kappa_{0,6}$; (III) $k_{1,5}$, and $\kappa_{2,4}$, $\kappa_{2,5}$ (from Zhu et al., 2003, *J. Fluid Mech.* Reproduced by permission of Cambridge University Press).

combination resonance observed, for example, in beams and plates (e.g. Nayfeh and Mook, 1979).

We have seen that the HOS method and generalizations represent powerful computational tools for the direct simulation and study of nonlinear wave and wave-body dynamics. The key characteristics are (arbitrary) high order M; large numbers of (body and wave) modes N; exponential convergence of the solution with respect to M and N; and computational effort approximately linearly proportional to M and (wave modes) N. The versatility of the HOS approach is demonstrated in the high-resolution results one can obtain for nonlinear wave evolution and interaction problems involving currents, bottom and bodies in direct physics-based simulations.

With modern high-performance parallel computing capabilities and continuous refinements in the method and algorithms, the efficiency and accuracy of HOS have recently been exploited to obtain direct phase-resolved predictions of large-scale nonlinear wavefields. For instance, Wu (2004) obtained a direct simulation of nonlinear ocean wave-field evolution in a domain of 30 km $\times$ 30 km for an evolution time of 30 minutes. The simulation used interaction order $M = 3$, number of wave modes $N = 4096 \times 4096$, and time step $\Delta t = T_p/64$. The peak period of the irregular wave field is $T_p = 12$ seconds. The computation was performed on an IBM SP3 high-performance parallel platform using 256 processors, and took ~ 100 hours. Such large-scale computations open new possibilities for modelling and predicting wavefield evolutions in the ocean, and in obtaining basic mechanistic (and simulation-based statistical) understanding of important phenomena such as wave groups, freak wave generation, and breaking wave distribution.

Novel engineering applications involving large-scale HOS wave simulations are also under development. An exciting recent attempt (Wu, 2004) is to use direct wave sensing data and HOS simulation to deterministically reconstruct a space-time wavefield, and to combine this prediction with large-amplitude ship motion calculations and ship control and path-planning optimizations for improved operations in severe seas.

15.7 Mixed Euler-Lagrangian Method

When waves are very steep or overturning/breaking, the HOS and HOSE methods, which are based on perturbation expansions (albeit high order), become ineffective or invalid. In this case, it is necessary to adopt an approach capable of handling fully nonlinear waves.

The simulation of fully-nonlinear unsteady wave-wave and wave-body problems in the context of potential flow began in earnest with the development of the mixed-Eulerian-Lagrangian (MEL) boundary-integral-equation (BIE) approach in the late 1970's. Almost all of the early efforts were in two dimensions, including the seminal work of Longuet–Higgins and Cokelet (1976) for steep over-turning waves, and Faltinsen (1977) who considered the presence of a floating body. With advances in computer capabilities and algorithm innovations and development, it became realistic only very recently to perform fully-nonlinear computations of three-dimensional problems (e.g. Xue et al., 2001; Liu et al., 2001).

The MEL approach shares a strategy common to many simulations of nonlinear initial-boundary-value problems, namely an effective decoupling of the (nonlinear) time evolution and the spatial compatibility (boundary-value problem) part of the problem. MEL takes special advantage of the potential flow free-surface problem (Section 15.2): the time evolution involves only boundary values and can be efficaciously followed using (free-surface) Lagrangian points; while the spatial problem is a linear Cauchy problem that can be effectively solved and coupled with the former using a boundary-integral equation (BIE) formulation (in the Eulerian variables). To be specific, consider that at any time t, we are given the position of the impervious boundary $\mathcal{B}(t)$, its velocity $\mathbf{U}(\mathbf{r} \in \mathcal{B}(t), t)$, the free-surface position $\mathcal{F}(t)$, and the free-surface potential $\Phi(\mathbf{r} \in \mathcal{F}(t), t)$. The boundary-value problem for Φ satisfying (15.2.1) is a generalized Cauchy problem whose solution is determined in terms of values on the boundary only. The numerical solution to the fully-nonlinear initial-boundary-value problem using a MEL approach then consists of a repeated two-step procedure starting from initial conditions:

I. Given $\mathcal{B}(t)$, $\Phi_n(\mathbf{r} \in \mathcal{B})$, $\mathcal{F}(t)$ and $\Phi(\mathbf{r} \in \mathcal{F})$, solve the boundary-value problem (BVP) for $\Phi_n(\mathbf{r} \in \mathcal{F})$, and in particular obtain thg velocity $\nabla\Phi(\mathbf{r} \in \mathcal{F})$.

II. Integrate in time the dynamic and kinematic free-surface boundary conditions (15.2.3) and (15.2.4) for $\Phi(\mathbf{r} \in \mathcal{F}(t+\Delta t))$ and $\mathcal{F}(t+\Delta t)$. Repeat the process.

This approach has three important characteristics: (i) the linear BVP is solved in step I with the actual (time exact) boundary at that time step; (ii) the integration of the nonlinear boundary conditions in time in step II is explicit; and (iii) only boundary values of the unknown (Φ and Φ_n) are involved on account of the elliptic field equation (15.2.1). As can be

expected, computation time and storage are generally dominated by step I; while computational complexities, associated for example with stability of the nonlinear free-surface boundary conditions, are mainly confined to step II. The key to the success of the MEL method has tended to be in the robust, efficient and accurate solution of step I.

15.7.1 Cauchy's Integral Formulation

For two-dimensional flows, an integral equation can be obtained, upon applying Cauchy's integral theorem, for the complex potential $\beta(\xi, t) = \Phi(x, z, t) + \mathrm{i}\Psi(x, z, t)$, where $\xi \equiv x + \mathrm{i}z$ and Ψ is the stream function. Taking the imaginary and real parts of the complex integral equation for $\xi \in \mathcal{F}$ and $\mathcal{B}$ respectively, one obtains second-kind Fredholm integral equations for Ψ on $\mathcal{F}$ and Φ on $\mathcal{B}$. Such a formulation for the BVP solution was proposed and implemented by Vinje and Brevig (1981).

Since that time, there have been numerous applications of this Cauchy's integral formulation of the MEL method. Some representative examples include: Greenhow et al. (1982) who studied the large-amplitude motions of a floating wave-energy device; Grosenbaugh and Yeung (1989) who investigated the unsteady bow wave of a two-dimensional body in forward motion; and Tsai and Yue (1993) who combined the free-surface simulation with vortex-sheet tracing to study the interactions between a vortex sheet shed in the wake of a surface-piercing body and the free surface.

For simplicity, we consider the case of deep water with periodic conditions in the horizontal (x) direction. Consider the region (in physical space ξ) bounded by the closed contour C which consists of the free surface $\mathcal{F}$, impervious (body) boundary $\mathcal{B}$, and the (vertical) periodic boundaries C_+ and C_- (up- and down-stream). Using the conformal mapping $\chi = \exp(\mathrm{i}\xi)$, $\mathcal{F}$ is mapped into a circle and the periodic boundaries are eliminated. In the mapped space (χ), the contour C contains $\mathcal{F}$ and $\mathcal{B}$ only. Since the complex potential $\beta(\chi, t)$ is analytic within C, Cauchy's theorem applies

$$\frac{1}{2\pi\mathrm{i}} \oint_C \frac{\Phi(\chi, t) + \mathrm{i}\Psi(\chi, t)}{\chi - \chi_0} \, \mathrm{d}\chi = 0 \,, \tag{15.7.1}$$

where χ_0 lies outside C. Let χ_0 approach a point on the boundary C. Introducing a small semicircular arc of radius ε and computing the integral along this small arc, (15.7.1) becomes

$$\frac{1}{2}\{\Phi(x_0,z_0,t)+\mathrm{i}\Psi(x_0,z_0,t)\}$$
$$-\frac{1}{2\pi\mathrm{i}}\fint_C \frac{\mathrm{d}\chi}{\chi-\chi_0}\{\Phi(x,z,t)+\mathrm{i}\Psi(x,z,t)\}=0\,, \qquad (15.7.2)^2$$

where $\fint$ denotes the Cauchy principal value.

Separating the real and imaginary parts, we get

$$\left\{\begin{array}{c}\pi\Psi(x_0,z_0,t)\\ -\pi\Phi(x_0,z_0,t)\end{array}\right\}+\left\{\begin{array}{c}\mathrm{Re}\\ \mathrm{Im}\end{array}\right\}\fint_C \frac{\mathrm{d}\chi}{\chi-\chi_0}\{\Phi+\mathrm{i}\Psi\}=0\,, \qquad (15.7.3)$$

which is a pair of coupled Fredholm integral equations of the second kind for Φ and Ψ along $C(=\mathcal{F}\cup\mathcal{B})$ for any instant t. In the MEL approach, at any t, the position of the impervious boundary $\mathcal{B}(\chi,t)$ and the stream function $\Psi(\chi,t)$ on $\mathcal{B}$ are prescribed based on the specified boundary condition (15.2.2), and the free-surface elevation $\mathcal{F}(\chi,t)$ and the velocity potential $\Phi(\chi,t)$ on it are given from integration of the evolution equations (15.2.3) and (15.2.4). Equation (15.7.3) is used to solve for the unknown $\Phi(\chi,t)$ on $\mathcal{B}$ and $\Psi(\chi,t)$ on $\mathcal{F}$.

The integral equation (15.7.3) is solved numerically by discretizing the boundary $C=\mathcal{F}\cup\mathcal{B}$ into, say, piecewise-linear segments: (i) subdivide $\mathcal{F}$ and $\mathcal{B}$ into N_F and N_B linear segments, respectively, (ii) represent Φ and Ψ by linear basis functions over each segment, and (iii) collocate at selected points on $\mathcal{F}$ and $\mathcal{B}$ corresponding to the end points of the segments. The resulting influence coefficients and their asymptotic approximations are given in Vinje and Brevig (1981). The resulting system of N $(=N_F+N_B)$ linear algebraic equations can be solved by iteration method (e.g. Baker et al., 1982) or direct Gaussian elimination. Once Φ and Ψ are known everywhere on C, a second-order difference formula can be used to find the velocities on the boundary, and the complex potential within C can then be obtained by the Cauchy formula

$$\beta(\chi,t)=\frac{1}{2\pi i}\oint_C \frac{\beta(\chi_0,t)}{\chi_0-\chi}\,\mathrm{d}\chi_0\,, \quad \chi \quad \text{within} \quad C\,. \qquad (15.7.4)$$

After the velocities on C are obtained, we can integrate the evolution equations (15.2.3) and (15.2.4) for the new Lagrangian value of $\Phi(\chi,t+\Delta t)$ on the free surface and its position $\mathcal{F}(\chi,t+\Delta t)$. As in HOS and HOSE, RK4 scheme can be used in time integration.

[2]If z_0 coincides with a sharp corner of interior angle $\alpha\pi$, the first curly brackets should be multiplied by α.

A useful extension of Cauchy's integral formulation (Dold, 1992) is obtained by applying the integral theorem to the complex velocity $q^* = \Phi_x + \mathrm{i}\Phi_z = R_s(\Phi_s + \mathrm{i}\Phi_n)$, where R_s is the complex unit tangent, and Φ_s and Φ_n are tangential and normal gradients of Φ on the boundary. Upon taking the real part of the complex integral equation, one obtains and solves, given Φ on $\mathcal{F}$, a second-kind integral equation for Φ_n on $\mathcal{F}$, and thereby obtains q on $\mathcal{F}$ directly. The free-surface evolution equations (15.2.3) and (15.2.4) can then be updated directly using q without the need for numerical differentiation. Representative examples using this approach include: Tanaka et al. (1987) who studied the instability and breaking of a solitary wave; and Cooker et al. (1990) who studied the interaction between a solitary wave and a submerged semicircular cylinder.

When (horizontally) periodic conditions do not apply, the method here can be generalized by proper incorporation of the boundary conditions on far up- and downstream side boundaries (C_+ and C_-). For example, Dommermuth et al. (1988) employed this method to study plunging breaking waves generated by a wavemaker at one end of a tank (see Section 15.7.4).

Cauchy's integral formulation is confined to two dimensions. For three-dimensional problems, MEL BIE solution can be obtained using Green's integral formulation.

15.7.2 Green's Integral Formulation

To formulate the BVP for the velocity potential Φ into a boundary integral equation (BIE), we introduce the Rankine (free-space) Green function

$$G(\mathbf{r}, \mathbf{r}') = \frac{1}{|\mathbf{r} - \mathbf{r}'|} \tag{15.7.5}$$

where $\mathbf{r} \equiv (x, y, z)$ is the field point while $\mathbf{r}' \equiv (x', y', z')$ is the source point. Applying Green's second identity to Φ and G and taking the limit $\mathbf{r} \to \partial\mathcal{V}$, where $\partial\mathcal{V}$ is the boundary of the fluid domain $\mathcal{V}$, we obtain a BIE:

$$\alpha(\mathbf{r})\Phi(\mathbf{r}) + \iint_{\partial\mathcal{V}} [\Phi(\mathbf{r}')G_n(\mathbf{r}, \mathbf{r}') - \Phi_n(\mathbf{r}')G(\mathbf{r}, \mathbf{r}')]\, \mathrm{d}S(\mathbf{r}') = 0\,, \tag{15.7.6}$$

for $\mathbf{r} \in \partial\mathcal{V}$, where the Cauchy principal part of the singular integral is assumed here and hereafter. Here n is the normal at $\mathbf{r}'$. In (15.7.6), the interior solid angle $\alpha(\mathbf{r})$ can be evaluated by

$$\alpha(\mathbf{r}) = -\iint_{\partial\mathcal{V}} G_n(\mathbf{r}, \mathbf{r}')\, \mathrm{d}S(\mathbf{r}')\,, \tag{15.7.7}$$

which obtains from (15.7.6) with a constant Φ. The boundary $\partial\mathcal{V}$ of the domain consists of the free surface $\mathcal{F}$, impervious boundary $\mathcal{B}$, and the boundary at far field. The far-field closure can generally be realized by imposing periodic boundary conditions or implementing an artificial damping layer on the free surface in the far field (as discussed in next Section 15.6.3). In either case, the contribution from the far-field boundary is eliminated. In the following, we consider $\partial\mathcal{V}$ to be a sum of $\mathcal{F}$ and $\mathcal{B}$ only.

At any time t, the free-surface elevation $\mathcal{F}$ and the velocity potential Φ on it are given from integration of the evolution equations (15.2.3) and (15.2.4). Thus, for $\mathbf{r} \in \mathcal{F}$, Dirichlet boundary condition is applied, and (15.7.6) is a Fredholm integral equation of the first kind for the unknown $\Phi_n(\mathbf{r} \in \mathcal{F}, t)$. For $\mathbf{r} \in \mathcal{B}$, on the other hand, Neumann boundary condition (15.2.2) is applied, and (15.7.6) becomes a Fredholm integral equation of the second kind for the unknown $\Phi(\mathbf{r} \in \mathcal{B}, t)$. From integral equation (15.7.6), we solve for unknown Φ_n on $\mathcal{F}$ and Φ on $\mathcal{B}$.

After obtaining the solution on the boundary from (15.7.6), the solution in the whole flow field can be evaluated using

$$\Phi(\mathbf{r}) = \frac{1}{4\pi} \iint_{\partial\mathcal{V}} [\Phi_n(\mathbf{r}')G(\mathbf{r}, \mathbf{r}') - \Phi(\mathbf{r}')G_n(\mathbf{r}, \mathbf{r}')] \, \mathrm{d}S(\mathbf{r}') \,, \tag{15.7.8}$$

for $\mathbf{r} \in \mathcal{V}$ for the velocity potential, and

$$\nabla\Phi(\mathbf{r}) = \frac{1}{4\pi} \iint_{\partial\mathcal{V}} [\Phi_n(\mathbf{r}')\nabla_{\mathbf{r}}G(\mathbf{r}, \mathbf{r}') - \Phi(\mathbf{r}')\nabla_{\mathbf{r}}G_n(\mathbf{r}, \mathbf{r}')] \, \mathrm{d}S(\mathbf{r}') \,, \tag{15.7.9}$$

for $\mathbf{r} \in \mathcal{V}$ for the velocity, where $\nabla_{\mathbf{r}} \equiv (\partial/\partial x, \partial/\partial y, \partial/\partial z)$. Once the velocity on $\mathcal{F}$ is obtained, we integrate the evolution equations (15.2.3) and (15.2.4) for the new Lagrangian value of $\Phi(\mathbf{r}, t + \Delta t)$ on the free surface and its position $\mathcal{F}(\mathbf{r}, t + \Delta t)$.

The integral equation (15.7.6) is solved numerically by discretizing the boundary. We first subdivide the boundaries $\mathcal{F}$ and $\mathcal{B}$ into two sets of piecewise smooth elements

$$S_{\mathcal{F}} = \bigcup_{j=1}^{N_{\mathcal{F}}} E_j \,, \quad S_{\mathcal{B}} = \bigcup_{j=1}^{N_{\mathcal{B}}} E_j \tag{15.7.10}$$

where E_j represents a generic element of the boundary, and $N_{\mathcal{F}}$ and $N_{\mathcal{B}}$ are the total numbers of elements of $\mathcal{F}$ and $\mathcal{B}$, respectively. Let $N_E = N_{\mathcal{F}} + N_{\mathcal{B}}$ denote the total number of boundary elements of the problem. The discretized form of (15.7.6) can be written as

$$\sum_{j=1}^{N_{\mathcal{B}}} I_d(\mathbf{r}) - \sum_{j=1}^{N_{\mathcal{F}}} I_s(\mathbf{r})$$

$$= -\alpha(\mathbf{r})\Phi(\mathbf{r}) - \sum_{j=1}^{N_{\mathcal{F}}} I_d(\mathbf{r}) + \sum_{j=1}^{N_{\mathcal{B}}} I_s(\mathbf{r}), \quad \mathbf{r} \in \mathcal{F}\,, \tag{15.7.11}$$

and

$$\alpha(\mathbf{r})\Phi(\mathbf{r}) + \sum_{j=1}^{N_{\mathcal{B}}} I_d(\mathbf{r}) - \sum_{j=1}^{N_{\mathcal{F}}} I_s(\mathbf{r})$$

$$= \sum_{j=1}^{N_{\mathcal{B}}} I_s(\mathbf{r}) - \sum_{j=1}^{N_{\mathcal{F}}} I_d(\mathbf{r})\,, \quad \mathbf{r} \in \mathcal{B}\,. \tag{15.7.12}$$

Here the elemental integrals I_s and I_d are defined by

$$I_s(\mathbf{r}) = \iint_{E_j} \Phi_n(\mathbf{r}')G(\mathbf{r},\mathbf{r}')\,\mathrm{d}S(\mathbf{r}') \tag{15.7.13}$$

and

$$I_d(\mathbf{r}) = \iint_{E_j} \Phi(\mathbf{r}')G_n(\mathbf{r},\mathbf{r}')\,\mathrm{d}S(\mathbf{r}') \tag{15.7.14}$$

where the Cauchy principal part of the singular integral is assumed if $\mathbf{r} \in E_j$. The terms on the left-hand side of (15.7.11) and (15.7.12) involve unknowns $\Phi(\mathbf{r} \in \mathcal{B}, t)$ and $\Phi_n(\mathbf{r} \in \mathcal{F}, t)$, while all the terms on the right-hand side of (15.7.11) and (15.7.12) are known. To solve (15.7.11) and (15.7.12), three inter-related approximations are required: (a) approximation of the boundaries $\mathcal{F}$ and $\mathcal{B}$ in terms of boundary elements E_j; (b) approximation of the functions Φ and Φ_n on E_j; and (c) using (15.7.11) and (15.7.12) to obtain discrete equations, say, by deploying point collocations or general weighted-residual approaches. We consider below two examples of these approximation schemes.

Constant panel method (CPM)

The simplest scheme is the so-called constant panel method (see e.g. Hess and Smith, 1964), which employs piecewise linear approximation of the geometry, piecewise constant approximations for the functions, and point collocations at element ("panel") centroids. Specifically, in CPM, E_j is approximated by a quadrilateral boundary element E_j^c, and over each boundary element E_j^c,

$$\Phi(\mathbf{r},t) = \Phi_j(\mathbf{r}_0,t)\,, \quad \Phi_n(\mathbf{r},t) = \Phi_{nj}(\mathbf{r}_0,t) \tag{15.7.15}$$

where $\mathbf{r} \in E_j^c$ and $\mathbf{r}_0$ is the centroid of E_j^c. With these approximation, I_s and I_d in (15.7.13) and (15.7.14) become:

$$I_s(\mathbf{r}) = \Phi_{nj} P_j(\mathbf{r}) \,, \quad I_d(\mathbf{r}) = \Phi_j Q_j(\mathbf{r}) \tag{15.7.16}$$

where

$$P_j(\mathbf{r}) = \iint_{E_j^c} G(\mathbf{r}, \mathbf{r}') \, \mathrm{d}S(\mathbf{r}') \,, \tag{15.7.17}$$

$$Q_j(\mathbf{r}) = \iint_{E_j^c} G_n(\mathbf{r}, \mathbf{r}') \, \mathrm{d}S(\mathbf{r}') \,. \tag{15.7.18}$$

For $\mathbf{r} \notin E_j^c$, the influence coefficients P_j and Q_j can be evaluated by direct quadrature. For $\mathbf{r} \in E_j^c$, the kernels in (15.7.17) and (15.7.18) are singular, but amenable to integration analytically (e.g. Newman, 1986).

Substituting (15.7.16) into (15.7.11) and (15.7.12), we obtain

$$\begin{aligned} &\sum_{j=1}^{N_\mathcal{B}} \Phi_j Q_j(\mathbf{r}) - \sum_{j=1}^{N_\mathcal{F}} \Phi_{nj} P_j(\mathbf{r}) \\ &\qquad = -\alpha(\mathbf{r})\Phi(\mathbf{r}) - \sum_{j=1}^{N_\mathcal{F}} \Phi_j Q_j(\mathbf{r}) + \sum_{j=1}^{N_\mathcal{B}} \Phi_{nj} P_j(\mathbf{r}) \,, \quad \mathbf{r} \in \mathcal{F} \,, \end{aligned} \tag{15.7.19}$$

and

$$\begin{aligned} &\alpha(\mathbf{r})\Phi(\mathbf{r}) + \sum_{j=1}^{N_\mathcal{B}} \Phi_j Q_j(\mathbf{r}) - \sum_{j=1}^{N_\mathcal{F}} \Phi_{nj} P_j(\mathbf{r}) \\ &\qquad = \sum_{j=1}^{N_\mathcal{B}} \Phi_{nj} P_j(\mathbf{r}) - \sum_{j=1}^{N_\mathcal{F}} \Phi_j Q_j(\mathbf{r}), \quad \mathbf{r} \in \mathcal{B} \,. \end{aligned} \tag{15.7.20}$$

Upon collocating (15.7.19) at $N_\mathcal{F}$ element centroids on $\mathcal{F}$ and (15.7.20) at $N_\mathcal{B}$ element centroids on $\mathcal{B}$, we obtain a system of N_E ($= N_\mathcal{F} + N_\mathcal{B}$) linear algebraic equations for N_E unknowns, from which we solve for the $N_\mathcal{F}$ unknown centroid values of Φ_n on $\mathcal{F}$ and $N_\mathcal{B}$ unknown centroid values of Φ on $\mathcal{B}$. Finally, (tangential) velocities on the boundaries can be calculated using a finite-difference scheme.

CPM is highly popular because of its relative simplicity. In the context of the MEL approach, CPM has a number of basic shortcomings. In MEL, free-surface Lagrangian points are updated using BIE solution on the boundary (using (15.2.3) and (15.2.4) which in particular require the

evaluation of tangential velocities). Inaccuracies in the latter results in distortions in subsequent BIE surface panelizations and values and the errors are compounded and amplified. A direct and critical consequence is that the overall accuracy and robustness of the MEL method is in general governed by the maximum (rather than the average) error of the BIE solution. In most applications, the linear convergence of CPM with panel size is too slow/expensive for accurate three-dimensional nonlinear simulations. In addition, at intersections of the free surface ("$\mathcal{F}$" or Dirichlet) and body ("$\mathcal{B}$" or Neumann) boundaries with discontinuous slopes, the local maximum error of CPM in general fails to converge with decreasing panel size (see e.g. Xü and Yue, 1992). Finally, in problems with non-wall-sided or moving body boundaries $\mathcal{B}$ that intersect the free surface $\mathcal{F}$, robust treatment of the weak singularity that arise at the $\mathcal{F} \cap \mathcal{B}$ intersection line generally requires collocation at the intersection itself (see e.g. Lin, Newman and Yue, 1984; Dommermuth et al., 1988). This requirement is, however, fundamentally incompatible with CPM.

Quadratic boundary element method (QBEM)

To circumvent the shortcomings of CPM, higher-order panel (or BIE) methods must be sought. Based on a systematic study of higher-order panels including super- and sub-parametric elements (order of the geometry representation respectively higher and lower than that for the boundary unknowns), Xü and Yue (1992) found that an iso-parametric quadratic boundary-element method (QBEM) is effective and economical.

In QBEM, we employ piecewise bi-quadratic representation of both boundary $\mathcal{F} \cup \mathcal{B}$ and the unknowns Φ and Φ_n on $\mathcal{F} \cup \mathcal{B}$. The boundary panels are now curvilinear quadrilaterals or (degenerate) curvilinear triangles with nine and seven nodes respectively where boundary positions, and Φ and Φ_n values are specified/collocated. Specifically, we use bi-quadratic

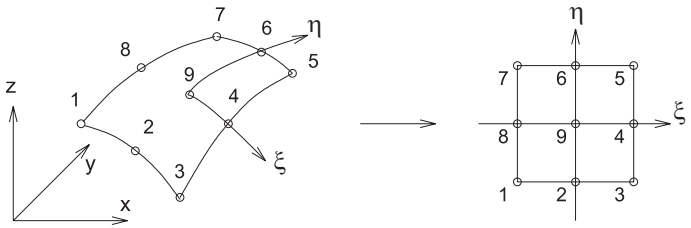

Figure 15.29: A generic nine-node curvilinear element $E_j^q(x, y, z)$ and its image in parametric space $E_j^q(\xi, \eta) : \xi \in [-1, 1], \eta \in [-1, 1]$.

isoparametric interpolation to represent the boundary and unknowns on the boundary. In doing that, a curvilinear quadrilateral with nine nodes or degenerate curvilinear triangle with seven nodes $E_j^q(x,y,z)$ is mapped into a square $E_j^q(\xi,\eta)$, $\xi \in [-1,1]$, $\eta \in [-1,1]$ in the parametric space, as illustrated in Fig. 15.29; and then all variables of interest (x,y,z,Φ,Φ_n) on $E_j^q(x,y,z)$ are represented by a two-dimensional Lagrangian polynomial in ξ, η for interpolations.

Let Υ signify a variable from the set of (x,y,z,Φ,Φ_n). The value of Υ at a point on the element surface is defined in terms of its nine nodal values and Lagrangian interpolation functions, viz.

$$\Upsilon(\xi,\eta) = \sum_{m=1}^{9} N_m(\xi,\eta)\Upsilon_m \tag{15.7.21}$$

where Υ_m denotes the m-th nodal value of Υ. Let the m-th nodal location in the parametric space be (ξ_m,η_m). The nine interpolation functions can be written explicitly as

$$\begin{cases} N_m(\xi,\eta) = \dfrac{1}{4}\xi(\xi+\xi_m)\eta(\eta+\eta_m) & m = 1,3,5,7\,, \\ N_m(\xi,\eta) = \dfrac{1}{2}(1-\xi_m^2\xi^2-\xi_m^2\eta^2) \\ \qquad\qquad \times[\eta_m\eta(1+\eta_m\eta)+\xi_m\xi(1+\xi_m\xi)] & m = 2,4,6,8\,, \\ N_9(\xi,\eta) = (1-\xi^2)(1-\eta^2) \end{cases} \tag{15.7.22}$$

Substituting (15.7.21) into (15.7.13) and (15.7.14), we have

$$I_s(\mathbf{r}) = \sum_{m=1}^{9} (\Phi_n)_{jm} P_{jm}(\mathbf{r})\,, \quad I_d(\mathbf{r}) = \sum_{m=1}^{9} \Phi_{jm} Q_{jm}(\mathbf{r}) \tag{15.7.23}$$

where the influence coefficients P_{jm} and Q_{jm} are defined by

$$P_{jm}(\mathbf{r}) = \iint_{E_j^q(\xi,\eta)} N_m(\xi,\eta) G(\mathbf{r},\xi,\eta) J(\xi,\eta)\,\mathrm{d}\xi\,\mathrm{d}\eta\,, \tag{15.7.24}$$

$$Q_{jm}(\mathbf{r}) = \iint_{E_j^q(\xi,\eta)} N_m(\xi,\eta) G_n(\mathbf{r},\xi,\eta) J(\xi,\eta)\,\mathrm{d}\xi\,\mathrm{d}\eta\,. \tag{15.7.25}$$

In (15.7.24) and (15.7.25), $J(\xi,\eta)$ is the Jacobian associated with the change of integration variable from $\mathrm{d}S(\mathbf{r})$ to $\mathrm{d}\xi\,\mathrm{d}\eta$. When $\mathbf{r} \notin E_j^q(\xi,\eta)$, the integrals in P_{jm} and Q_{jm} are regular and can be evaluated by numerical

integration. When $\mathbf{r} \in E_j(\xi, \eta)$, the kernels of P_{jm} and Q_{jm} become singular. Unlike in CPM, they cannot be integrated analytically for quadratic panels. In this case, they can be evaluated, for example, by direct quadrature after regularizing the kernels using polar coordinate transformations (for details, see Liu and Lu, 1988 and Xü, 1992).

Substituting (15.7.23) into (15.7.11) and (15.7.12), we obtain

$$\begin{aligned}\sum_{j=1}^{N_{\mathcal{B}}}\sum_{m=1}^{9}\Phi_{jm}Q_{jm}(\mathbf{r}) - \sum_{j=1}^{N_{\mathcal{F}}}\sum_{m=1}^{9}(\Phi_n)_{jm}P_{jm}(\mathbf{r}) \\ = -\alpha(\mathbf{r})\Phi(\mathbf{r}) - \sum_{j=1}^{N_{\mathcal{F}}}\sum_{m=1}^{9}\Phi_{jm}Q_{jm}(\mathbf{r}) \\ + \sum_{j=1}^{N_{\mathcal{B}}}\sum_{m=1}^{9}(\Phi_n)_{jm}P_{jm}(\mathbf{r}), \quad \mathbf{r} \in \mathcal{F}, \end{aligned} \tag{15.7.26}$$

and

$$\begin{aligned}\alpha(\mathbf{r})\Phi(\mathbf{r}) + \sum_{j=1}^{N_{\mathcal{B}}}\sum_{m=1}^{9}\Phi_{jm}Q_{jm}(\mathbf{r}) - \sum_{j=1}^{N_{\mathcal{F}}}\sum_{m=1}^{9}(\Phi_n)_{jm}P_{jm}(\mathbf{r}) \\ = \sum_{j=1}^{N_{\mathcal{B}}}\sum_{m=1}^{9}(\Phi_n)_{jm}P_{jm}(\mathbf{r}) - \sum_{j=1}^{N_{\mathcal{F}}}\sum_{m=1}^{9}\Phi_{jm}Q_{jm}(\mathbf{r}), \quad \mathbf{r} \in \mathcal{B}. \end{aligned} \tag{15.7.27}$$

Equations (15.7.26) and (15.7.27) are the discretized forms of the BIE in QBEM.

For a total of N_E $(= N_{\mathcal{F}} + N_{\mathcal{B}})$ quadratic boundary elements (among which $N_{\mathcal{F}}$ elements are on $\mathcal{F}$, and $N_{\mathcal{B}}$ elements on $\mathcal{B}$ respectively), say, there are a total of N nodal points. Note that the exact relation between N and N_E depends on the specific configuration and discretization of the boundary surface. Among N unknowns, the type of unknown (Φ or Φ_n) at each node depends on whether the node is located on $\mathcal{F}$ or $\mathcal{B}$. In order to determine these N unknowns, we collocate (15.7.26) or (15.7.27) at N nodes to obtain a system of N linear algebraic equations. The resulting linear algebraic system is in general dense, non-symmetric and, because of the first-kind equations on $\mathcal{F}$, not diagonally dominant. This algebraic system can be effectively solved using a generalized minimum residual (GMRES) algorithm (Saad and Schultz, 1986) with symmetric successive

over-relaxation (SSOR) pre-conditioning. Xü and Yue (1992) found that the required computational effort of this algorithm for the QBEM equations is less than $\sim O(N^{2.3})$.

Once Φ and Φ_n at each node are obtained, the velocity of the boundary is evaluated using (15.7.21). Upon using chain rule differentiation and the definition of normal velocity, we have the following relations:

$$\left.\begin{aligned} \Phi_\xi &= \Phi_x x_\xi + \Phi_y y_\xi + \Phi_z z_\xi \,, \\ \Phi_\eta &= \Phi_x x_\eta + \Phi_y y_\eta + \Phi_z z_\eta \,, \\ \Phi_n &= \Phi_x n_x + \Phi_y n_y + \Phi_z n_z \,, \end{aligned}\right\} \tag{15.7.28}$$

where $\mathbf{n} \equiv (n_x, n_y, n_z)$ is the unit normal of the boundary. On each element, ξ- and η-derivatives of Φ, x, y, and z as well as unit normal $\mathbf{n}$ are uniquely determined by (15.7.21). If the node is at the center of an element, we obtain a unique solution of $\nabla\Phi$ using (15.7.28). If the node is at the edge or corner of an element, the solutions of $\nabla\Phi$ obtained from neighboring elements may (slightly) differ. In practice, we may take the average of these different values as the solution of the velocity $\nabla\Phi$ for the edge/corner nodes. An alternate is to form a virtual element with the node under consideration at the center of the element. (This element is formed only for the purpose of calculating the velocity of the center node.) With this element, we solve for the velocity of the central node using (15.7.28). Xü (1992) compared these two approaches and found that they give a similar accuracy for the evaluation of the boundary velocity.

In general, QBEM obtains quadratic to cubic convergence with element size $\Delta\ell$ even in the presence of $\mathcal{F} \cap \mathcal{B}$ intersections with discontinuous boundary slopes. Furthermore, boundary nodes at panel edges provide robust treatment of boundary intersections. Significantly, for a given minimax (relative) error, say $O(10^{-3})$, QBEM is some two orders of magnitude more efficient than CPM for general applications. The efficiency and accuracy of the present MEL/BIE implementation is to a large extent a result of the efficacy of QBEM. Details of the QBEM implementation and performance can be found in Xü (1992), Xü and Yue (1992).

15.7.3 Numerical Implementation

A number of issues associated with the numerical implementation of the MEL/BIE method require special attention.

Far-field closure

As pointed out earlier, the proper formulation of the IBVP requires some specification of boundary conditions in the far field. In problems where periodic boundary conditions obtain or can be applied, the BIE domain is simplified by introducing the periodic Green function. In two dimensions, a periodic Green function in closed form is given by (15.5.6). In three dimensions, a doubly-periodic Green function G^p, for a periodic domain of dimensions L by W, can be written as a double sum of Rankine sources:

$$G^p(\mathbf{r},\mathbf{r}') = \sum_{m=-\infty}^{\infty}\sum_{n=-\infty}^{\infty}\{[(x+mL-x')^2+(y+nW-y')^2 + (z-z')^2]^{-\frac{1}{2}} - [(mL)^2+(nW)^2]^{-\frac{1}{2}}\} + \frac{2\pi z}{LW}\,, \qquad (15.7.29)$$

where, m and n are integers, and the last term is included to ensure $\nabla G^p \to 0$ as $z \to -\infty$. Efficient summation formulas are available for rapid evaluation of (15.7.29) (Breit, 1991; Newman, 1992).

In practice, periodic boundary conditions offers a useful closure even when the problem is non-periodic. In this case, the periodic boundaries are placed sufficiently far away (relative to the duration of the simulation) and the calculations are stopped before scattered waves from fictitious "periodic" images of the body arrive at the body itself.

A simple far-field closure scheme which avoids the added computational effort associated with the evaluation of the (doubly-)periodic Green function is the use of numerical damping ("sponge") layer (see e.g. Nakos, Kring and Sclavounos, 1993; Clément, 1996). In practice, a sponge layer is placed in a strip around the perimeter of the computational domain centered at the body. Within the sponge layer, we introduce artificial linear damping terms into the kinematic and dynamic boundary conditions on the free surface $\mathcal{F}$, for example:

$$\frac{\mathrm{D}\mathbf{r}}{\mathrm{D}t} = \nabla\Phi - \nu(x,y)(\mathbf{r}-\mathbf{r}_I)\,, \quad \mathbf{r}\in\mathcal{F}\,, \qquad (15.7.30)$$

$$\frac{\mathrm{D}\Phi}{\mathrm{D}t} = \frac{1}{2}|\nabla\Phi|^2 - z - \nu(x,y)(\Phi-\Phi_I)\,, \quad \mathbf{r}\in\mathcal{F} \qquad (15.7.31)$$

where $\mathrm{D}/\mathrm{D}t$ is the Lagrangian (material) time derivative; $\mathbf{r}_I$ and Φ_I are the free-surface position and velocity potential of the incident/ambient flow; and ν is an empirical damping coefficient which is, in general, a function of space.

In three-dimensional problems, where the energy density of the scattered wave must decrease with radial distance, a far-field matching technique can be applied. In this approach, the nonlinear computational solution is matched to a general linear solution of transient outgoing radiated waves. The determination of the linear wavefield as well as specification of the boundary condition for the nonlinear interior problem are obtained through a matching of the two on a boundary some distance away. Such a scheme is, in principle, untenable in two-dimensional flows since the nonlinearity of the radiated waves persists into the far field, and a matching to linear outer solutions is problematic (e.g. Vinje, Maogang and Brevig, 1982). This approach of far-field matching to a linear solution has been found to be effective in three dimensions. A special case is vertically axisymmetric flow problems where far-field matching closure is used by Dommermuth and Yue (1987b) and Xue and Yue (1998).

Time integration

Once the BVP at each time step is solved and the velocity $\nabla\Phi$ on $\mathcal{F}$ obtained from Φ and Φ_n on $\mathcal{F}$, the free-surface boundary conditions (15.2.3) and (15.2.4) can be integrated in time in a straightforward manner. A typical scheme is a fourth-order Adams-Bashforth-Moulton (ABM4) integrator coupled with a fourth-order Runge-Kutta (RK4) scheme for (re)starting (whenever there is a change in time step size). ABM4 and RK4 require two and four solutions of the BVP per time step, respectively.

In the simulations, we adopt dynamic time stepping (because of the changing Lagrangian grid), with the time step size determined by:

$$\Delta t \leq \frac{C_n(\Delta l)_{\min}}{|(\nabla\Phi)_{\mathcal{F}}|_{\max}}\,, \tag{15.7.32}$$

where $(\Delta l)_{\min}$ is the minimum distance between two neighboring nodes on $\mathcal{F}$ and $|(\nabla\Phi)_{\mathcal{F}}|_{\max}$ is the magnitude of the maximum (nodal) velocity on $\mathcal{F}$. Equation (15.7.32) can be derived directly from (15.2.3), with C_n, the Courant number, a computational parameter to be selected for stability (typically C_n <1). In practice, it is useful also to impose minimum and maximum time-step limits: $\Delta t_{\min} \leq \Delta t \leq \Delta t_{\max}$.

Sawtooth instability

A numerical problem encountered by most MEL simulations, and first reported by Longuet–Higgins and Cokelet (1976), is the appearance of "sawtooth" (wavelength twice the grid size) instabilities on the free surface as the waves become steep. Such instabilities appear to be intrinsic to

the discretized equations and are not strictly instability of the time integration itself (Roberts, 1983). The precise cause of such shortwave instabilities is still not completely understood. Moore (1983) suggested, through examining a nonlinear modal differential equation, that the instability is due to a resonant interaction between the numerically induced discrete waves and the (physical) continuous wave motions. That high-wavenumber instabilities should arise in an inviscid model can in some sense be expected from first principles in that strong nonlinear interactions should cause energy to transfer to and ultimately accumulate at the highest wavenumber modes represented in the discretization. Such instabilities can generally be removed by introducing some degree of numerical filtering (or damping) of the highest wavenumber modes. Some of the successful schemes include applying: smoothing formulae (e.g. Longuet–Higgins and Cokelet, 1976; Dold, 1992); regriding (e.g. Fink and Soh, 1978; Dommermuth et al., 1988); and smoothing surface fitting (e.g. Tsai and Yue, 1993).

Free-surface and body grid (re)generation

In the MEL approach, nodes on the free surface are Lagrangian particles which are advected and distorted with the underlying flow. One feature, for example, is the tendency for surface Lagrangian particles to concentrate in regions of high flow gradients. While this may be desirable from a physical point of view, the clustering of nodal points may be a root cause of instabilities in the time integration (see (15.7.32)) and subsequent development of "sawtooth" errors. In addition, such clustering may lead to unacceptable distortions of the boundary elements especially in the three-dimensional problem. An effective way to overcome these difficulties is found to be continuous or periodic regridding of free-surface and body boundary elements (Dommermuth and Yue, 1987b). In a typical regridding, cubic splines in both parametric directions are employed to create new sets of optimally spaced (in arclength) grid points on the free surface and on the body. Alternatively, we may employ elliptical grid generators with controlling factors on the free surface and transfinite interpolations on the body. Such grid regeneration in conjunction with updating of the free-surface body intersection line is an essential requirement of successful fully-nonlinear simulations involving changing wetted body surfaces (Liu, Xue and Yue, 2001).

Double-node technique for intersections of two surfaces

As pointed out earlier, the overall accuracy of the MEL solution is governed by the minimax error of the BIE problem. In a BIE solution of the BVP, non-uniform convergence may occur at boundary edges. In the MEL

approach, Dirichlet (D) and Neumann (N) boundary conditions (for the velocity potential) are specified on the free surface ($\mathcal{F}$) and body surfaces ($\mathcal{B}$) respectively. At $\mathcal{F}$-$\mathcal{B}$ intersections, which may have surface slope discontinuities, we have a confluence of boundary conditions of a D-N type. At such a confluence, the general solution to the BVP exhibits a weak singularity (Lewy, 1950) which results in a loss of local convergence of the numerical solution in the absence of special treatment. For example, numerical tests confirm that the maximum CPM error does not converge with increasing number of panels at such $\mathcal{F}$-$\mathcal{B}$ intersections (Xü and Yue, 1992). Similar poor convergence for CPM (but for a somewhat different reason) occurs even when there is no confluence of boundary conditions, say at $\mathcal{B}$-$\mathcal{B}$ boundary intersections with discontinuous slopes. A remarkably effective and robust treatment that overcomes these difficulties is the so-called "double-node" technique (e.g. Lin, Newman and Yue, 1984; Dommermuth and Yue, 1987b) whereby both the D and N conditions are specified at $\mathcal{F} \cap \mathcal{B}$ edged; N-N double nodes where two Neumann boundary conditions are specified at discontinuous slope $\mathcal{B}$-$\mathcal{B}$ edges; N-N-D triple nodes at $\mathcal{B}$-$\mathcal{B}$-$\mathcal{F}$ corners; etc.

In the double-node technique, the coincident nodes belonging to different surfaces are retained as separate nodes and treated distinctly, with different boundary conditions and/or different surface normals corresponding to the surface to which they belong applied. The trick is to apply both sets of boundary conditions (for the respective intersection surfaces) and solve for both sets of unknowns on these points. At a $\mathcal{F} \cap \mathcal{B}$ point, for example, three variables are in general involved: Φ and $\nabla\Phi \cdot \mathbf{n}$ with respect to the normals ($\mathbf{n}$) to $\mathcal{F}$ and $\mathcal{B}$ respectively. A D-N double node there specifies the D and N boundary conditions for Φ and its derivative with respect to the $\mathcal{B}$-normal at that point. Collocation at that point provides a single equation for the unknown $\mathcal{F}$-normal derivative of the potential. Similar multiple-node treatments of the N-N, D-N-N, N-N-N, ..., types can be worked out for intersections involving $\mathcal{F}$ and (discontinuous slope) $\mathcal{B}$ surfaces. In all cases, at each node point, there remains a single unknown involving the potential or its derivative with respect to a specified normal, which can be solved for by a collocation of the integral equation (15.7.6) at that point.

Intersection updating

Proper updating of the free-surface intersection line has proven to be of much importance to MEL simulations involving surface-piercing bodies (see

Liu, Xue and Yue, 2001). Kinematic boundary condition specifies that points on the $\mathcal{F}$-$\mathcal{B}$ intersection line must remain on both $\mathcal{F}$ and $\mathcal{B}$. In MEL, where the new positions P of these points are obtained from direct integration of the Lagrangian equations, neither (a) $P \in \mathcal{F}$ nor (b) $P \in \mathcal{B}$ is guaranteed, even for very small time steps. This often leads (eventually) to a break down of the overall simulation. To overcome this, a general scheme for updating the free-surface intersection points (applicable in three dimensions) is developed.

To satisfy condition (a), we impose the velocity of an intersection point P, $\mathbf{V}_p$, to be always along the tangential direction, $\mathbf{e}_\tau$, of the body surface. Here $\mathbf{e}_\tau$ denotes a unit tangential vector on the body surface at P. For three-dimensional problems, $\mathbf{e}_\tau$ is non-unique although either choice of the unit tangential vector will assure (a). In practice, we choose $\mathbf{e}_\tau$ to be that which is closest to the Lagrangian velocity at that point.

To satisfy condition (b), we now choose the magnitude of $\mathbf{V}_p$ to be given by

$$V_p = \frac{\nabla\Phi \cdot \mathbf{n}_\mathcal{F}}{\mathbf{e}_\tau \cdot \mathbf{n}_\mathcal{F}} \tag{15.7.33}$$

where $\mathbf{n}_\mathcal{F}$ is the unit normal vector to the free surface at P. Note that the classical Eulerian and Lagrangian forms of the intersection point velocities can be recovered from (15.7.33) if we set $\mathbf{e}_\tau = (0, 0, 1)$ and $\nabla\Phi/|\nabla\Phi|$, respectively.

The potential at the new position of the intersection point can be obtained by direct time integration:

$$\frac{\mathrm{D}\Phi}{\mathrm{D}t} = \frac{\partial\Phi}{\partial t} + \mathbf{V}_p \cdot \nabla\Phi \tag{15.7.34}$$

where $\mathrm{D}/\mathrm{D}t$ is substantial time derivative. For a moving body, the velocity of the intersection point can be written in the form:

$$\mathbf{V}_p = \frac{(\nabla\Phi - \mathbf{U}) \cdot \mathbf{n}_\mathcal{F}}{\mathbf{e}_\tau \cdot \mathbf{n}_\mathcal{F}}\mathbf{e}_\tau + \mathbf{U} \tag{15.7.35}$$

where $\mathbf{U}$ is the velocity of the body at P.

15.7.4 Application to Two- and Three-Dimensional Breaking Waves

Steep overturning waves are ubiquitous in the ocean environment. The dynamics of such waves is of importance in the consideration of extreme

slamming loads and wave over-topping on ships and marine structures, energy and momentum transfer from surface waves to currents, and turbulence mixing of the upper marine layer. The understanding and modelling of breaking waves is thus of fundamental and practical interests in ocean science and engineering.

For wave breaking, controlled experiments and numerical computations have generally assumed that the waves are two dimensional (see Rapp and Melville, 1990 for a review of experiments; and Banner and Peregrine, 1993, and Tsai and Yue, 1996 for reviews of numerical simulations). For simulation of steep two-dimensional waves, a seminal work was Longuet–Higgins and Cokelet (1976), who developed the MEL approach using a BIE formulation. Since then, a number of improvements/extensions were made, notably Vinje and Brevig (1981)'s development of Cauchy-integral formulation and Dold (1992)'s treatment of time evolution terms. The understanding of two-dimensional breaking waves was improved by New, McIver and Peregrine (1985) who performed detailed computations; Dommermuth et al. (1988) who obtained quantitative comparisons to breaking wave tank measurements; Yao, Wang and Tulin (1994) who considered wave-group dynamics; and Longuet–Higgins and Dommermuth (1997) who examined the role of crest instabilities.

Reliable results for truly three-dimensional problems are still relatively rare (e.g. Isaacson, 1982; Romate, 1989) because of limitations on accuracy/resolution which also affect stability, and computational efficiency and power. Recently, Xue et al. (2001) extended MEL/BIE to three dimensions using a high-order quadratic boundary-element method (QBEM). They applied this efficient approach for fully nonlinear computation of the dynamics of three-dimensional overturning waves. As in Longuet–Higgins and Cokelet (1976), they started with plane progressive Stokes waves (fundamental wavelength L) but applied briefly a three-dimensional surface pressure (of transverse wavelength W). Varying the ratio $\gamma \equiv W/L$ over a broad range, they performed high-resolution simulations of plunging waves with different degrees of three dimensionality. From these simulations, detailed wave kinematics and the three-dimensional effects on the kinematics were quantified.

In this section, we first describe a fully-nonlinear simulation of a two-dimensional plunging waves and its direct quantitative comparison to tank experiment (Dommermuth et al., 1988). The simulation of the two-dimensional problem is based on the MEL approach with Cauchy's integral formulation (Section 15.6.1). We then present sample computational results

of three-dimensional overturning waves (Xue et al., 2001), obtained using the MEL approach using QBEM for the BIE solution (Section 15.7.2).

Two-dimensional overturning waves — direct comparison to experiments

Ever since the work of Ursell, Dean and Yu (1959), who compared the waves created by a piston wavemaker to theoretical predictions based on linearized equations, the validity and limitations of classical small-amplitude wave theory have been well established. In particular, they found that for small wave steepness, $H/\lambda < 0.03$, (wave height H, wavelength λ), the error in the wave height in front of the wavemaker is of the order of 3%, although for steeper waves ($0.045 < H/\lambda < 0.048$) the deviations, presumably primarily due to nonlinearity, can be as much as 10%

Dommermuth et al. (1988) verified against carefully controlled experiments in a wave tank the validity of fully-nonlinear potential flow theory for steep gravity waves up to and including overturning. Surface tension is ignored. Specifically, the problem of a single plunging breaker created downstream of a piston wavemaker is considered. The breaking wave is produced by generating a spectrum of waves whose phases are adjusted so that their superposition gives rise to a rapid increase in wave amplitude a prescribed distance away from the wavemaker (Longuet–Higgins, 1974; Greenhow et al., 1982).

The experiments are conducted at the Ralph M. Parsons Laboratory of M.I.T. in a glass-walled channel 25 m long, 0.7 m wide, filled to a depth of 0.6 m with fresh water. A wooden beach of slope 0.1 covered with 5 cm thick fibrous mats dissipates the waves at the far end of the tank so that less than 4% of the incident wave amplitude is reflected. The beach toe is 19.5 m from the rest position of the paddle and extends to 25 m at the waterline. In the experiments, the wavemaker is programmed to give a single plunging wave. The wave plunges, that is the forward face touches the forward trough, at approximately 7.25 m from the wavemaker paddel at a time approximately 12.9 seconds from the paddle start. The wave gauges are positioned at $x = 1.9$, 3.0, 4.0, 5.0, 5.5, 6.0, 6.5, 7.1, and 7.3 meters (see Fig. 15.31(a)). The velocities are measured at $x = 3.0$ and 5.0 meters from near the bottom of the tank to above the still-water level. Measurements are obtained from repeated runs of the experiment which is repeatable to within 0.01 seconds over the duration, and to within ± 2 cm horizontally over the distance to breaking. Complete details of the experimental setup and procedure can be found in Chan (1986) and Rapp (1986).

High resolution fully nonlinear computations are carried out using the MEL solution scheme with the Cauchy's integral formulation for the BVP solution as described in Section 15.6.1. For normalization, the units of length, time, and mass are chosen so that the initial depth of the water, the gravitational acceleration, and the fluid density are all unity. For comparison with the single plunging wave experiment, we use a numerical tank of length 20 (corresponding to a length of 12 m for a physical tank depth of 0.6 m) with 500 linear segments on the free surface and 25 segments on the wavemaker and the far wall for a total of $N \approx 550$ unknowns. Altogether, about 4000 time steps are used to complete the simulation to the point where the plunger reenters the free surface. Of these, we use regriding every 15 time steps for the first 3000 steps, and employ smoothing every 5 steps for the final 1000 steps. In the dynamic time stepping procedure, the largest time step used is .08 at the beginning of the simulation and the smallest is .0004 near the end to capture the overturning wave. Consequently, more than half of the computational effort is used in the final 20% of the simulation time.

The velocity of the piston wavemaker is calculated by taking centered finite-differences of the wavemaker displacement which is measured in the experiment. This velocity is the only input to the numerical simulation. The measured time-history of the wavemaker velocity $U(t)$ is given as a Fourier-cosine series:

$$U(t) = \sum_{n=1}^{72} U_n \cos(\omega_n t - \theta_n) \tag{15.7.36}$$

where, to achieve about 3 significant figures of accuracy, 72 components are required. The amplitudes U_n, frequencies ω_n, and phases θ_n from the experiments are used directly in the MEL simulation. (The actual values of these quantities are tabulated in Appendix B of Dommermuth et al. 1988).

In Fig. 15.30(a), the free-surface elevations according to linearized theory are compared to wave probe measurements at $x = 3.17$, 5.00, 6.67, 8.33, 10.00, and 12.17. The agreement becomes less satisfactory as the wave group steepens and travels down the tank. Near the plunging point the predicted linear wave amplitudes are in error by as much as 100% although the phases appear to agree somewhat better.

Figure 15.30(b) shows the comparisons between the surface elevations predicted by the nonlinear potential theory and those measured by wave probes at $x = 3.17$, 5.00, 6.67, 9.17, 10.83, and 11.83. The computed and

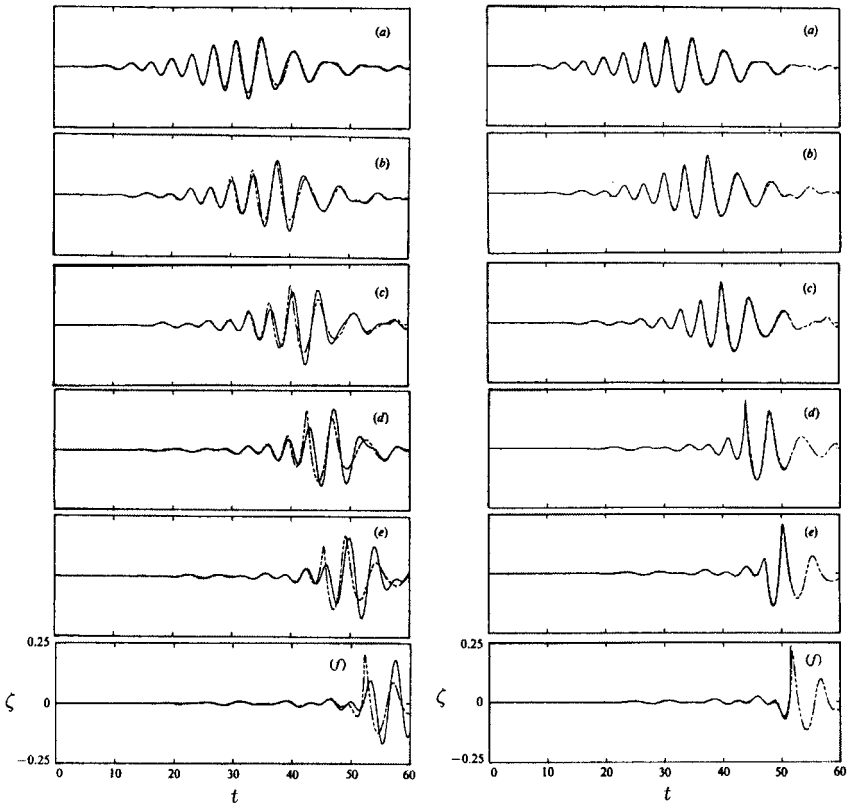

Figure 15.30: Comparison of free-surface elevation ζ among linear theory (——) (left column), nonlinear computations (——)(right column), and wave-probe measurements (– - - –) as a function of time. For the linear solution, the comparisons are made at distances from the wavemaker (normalized by mean water depth) of $x = 3.17$ (a), 5.00 (b), 6.67 (c), 8.33 (d), 10.00 (e), and 12.17 (f). For the nonlinear solution, the comparisons are made at $x = 3.17$ (a), 5.00 (b), 6.67 (c), 9.17 (d), 10.83 (e), and 11.83 (f) (from Dommermuth et al., 1988, *J. Fluid Mech.* Reproduced by permission of Cambridge University Press).

measured profiles can be barely distinguished up to the plunging location. Note that the nonlinear numerical simulation stops near $t = 52$ which is the time when the cusp of the plunging wave meets the wave trough in front (see Fig. 15.31).

Figure 15.31 plots the computed instantaneous free-surface profiles near the plunging location at times $t = 51.11$, 51.24, 51.34, 51.45, and 51.55 which are compared to the wave probe measurements at $x = 11.83$ taken

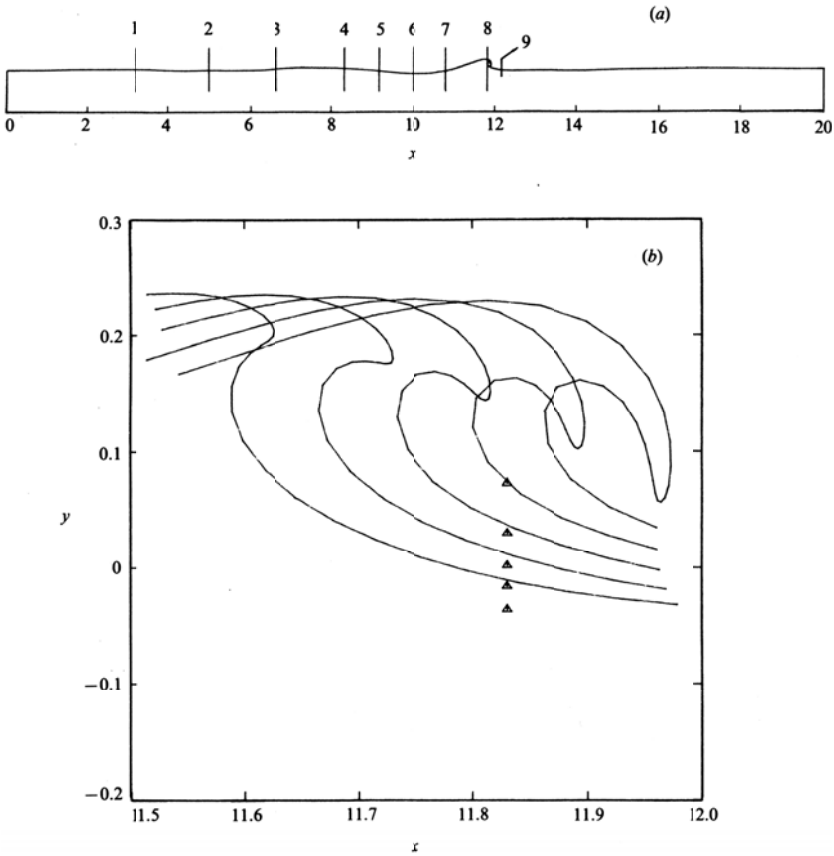

Figure 15.31: (*a*) Instantaneous free-surface profile of the simulated plunging wave at $t = 51.55$ showing the actual (undistorted) computational tank as well as the positions of the 9 wave probes in experiments. (*b*) Details of the computed overturning wave (to scale) at times $t = 51.11$, 51.24, 51.34, 51.45, and 51.55 from left to right respectively. Symbols ($\triangle$) represent wave probe measurements at $x = 11.83$ (probe 8) at the same time instants from bottom to top respectively (from Dommermuth et al., 1988, *J. Fluid Mech.* Reproduced by permission of Cambridge University Press).

at the same time instants. (Note that the wave has not yet become multi-valued at the probe.) The nonlinear computations predict a slightly earlier plunging breaking in both time and distance from the wavemaker. The deviations in the estimated plunging position and time are respectively $\Delta x \approx 0.15$ and $\Delta t \approx 0.25$. From the figure, the wave trough immediately in front of the breaker appears to rise faster and higher in the numerical simulation suggesting that the some of the errors can be attributed

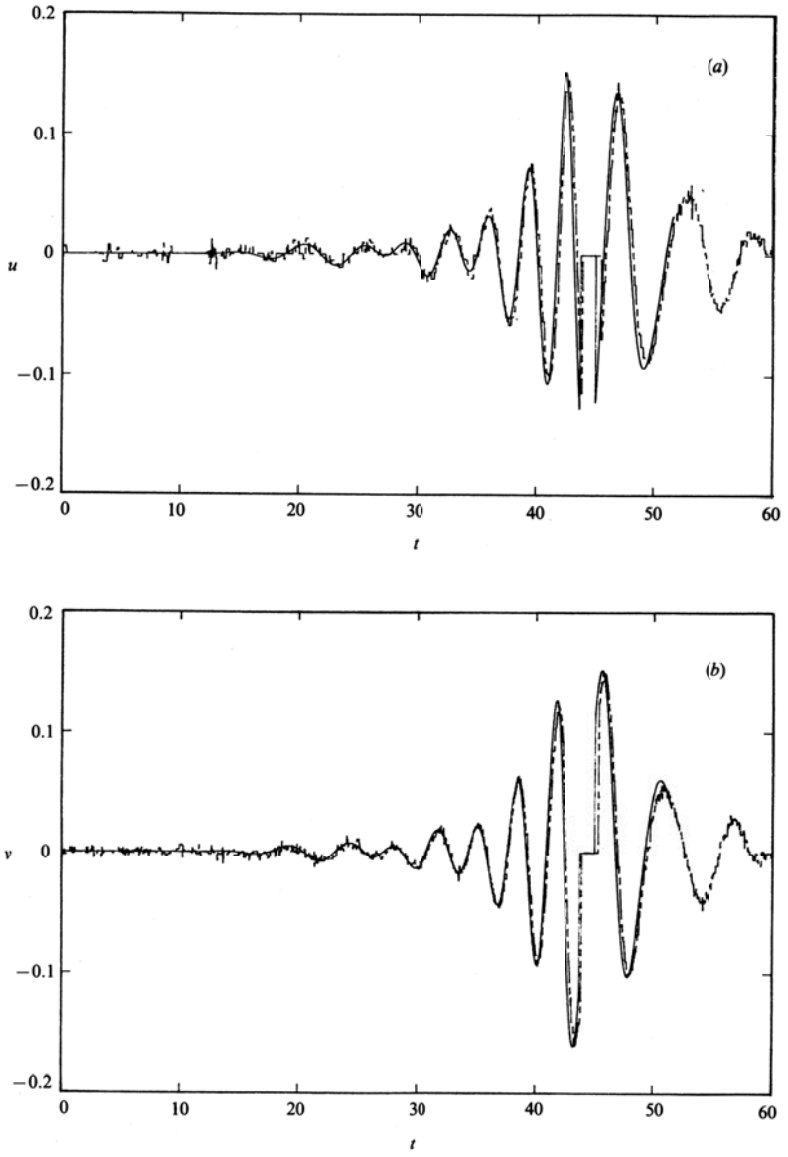

Figure 15.32: Water-particle velocities from nonlinear theory (——) compared to measurements using a laser-doppler anemometer (– - - –) as a function of time. (*a*) $u(8.33, -0.10, t)$, (*b*) $v(8.33, -0.10, t)$, (*c*) $u(8.33, 0.10, t)$, and (*d*) $v(8.33, 0.10, t)$ (from Dommermuth et al., 1988, *J. Fluid Mech.* Reproduced by permission of Cambridge University Press).

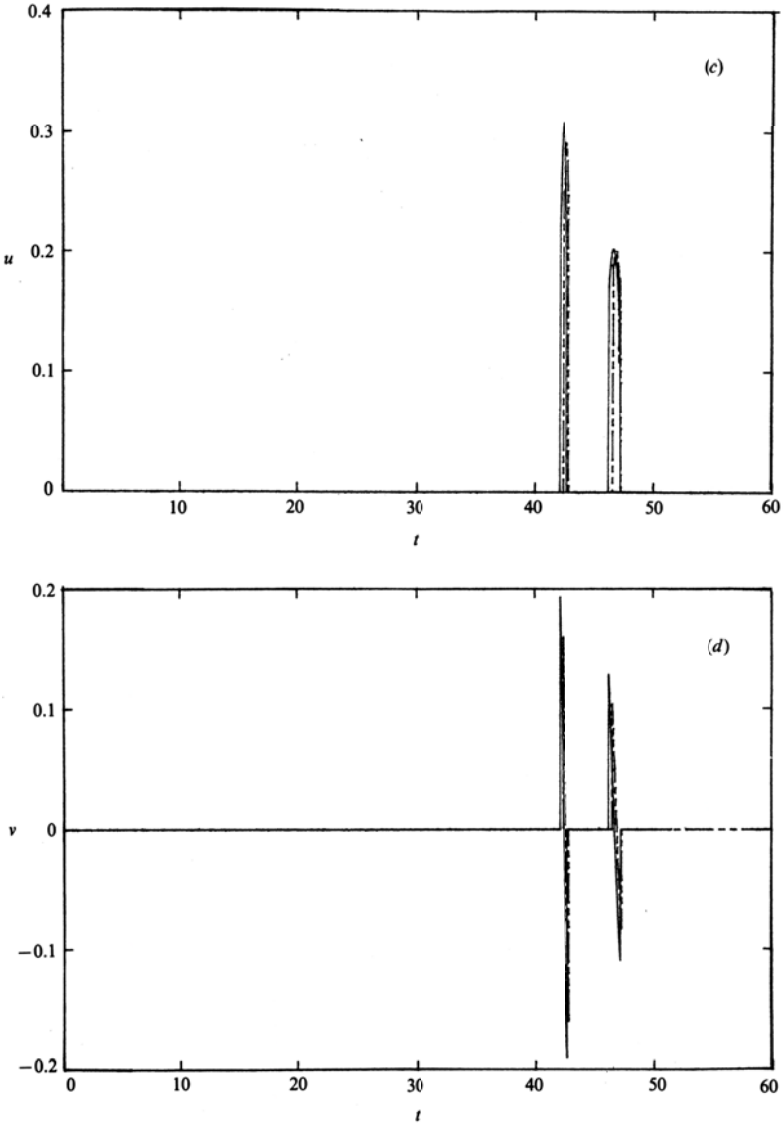

Figure 15.32 (*Continued*)

to reflection from the far wall. Another possible effect is the presence of some (albeit small) dissipation in the physical experiment which tends to delay the breaking event. Given the large local velocities and accelerations of the plunging wave (see Figs. 15.32) the observed discrepancies are, however, within the expected accuracies of the computation and experiment.

As a final comparison, we examine the fluid particle velocities measured using a laser-doppler anemometer and the velocities computed using Cauchy's integral formulation. Figure 15.32 shows these comparisons for the horizontal and vertical velocities $u(x_0, y_0, t)$ and $v(x_0, y_0, t)$ for $x_0 = 8.33$ and $y_0 = 0.1$ and -0.1. As before, the agreement is excellent. For points above the still-water level the velocity traces show intermittent pulses (positive for u and changing sign for v) which correspond to the passage of individual wave crests. When y_0 is below but close to the still-water level, the velocity curves may appear cut off at zero (truncated peaks for u and at upward zero-crossings for v) as the sampling point exits the water at the troughs.

New et al. (1985) examined the velocities and accelerations of particles in the free surface of periodic overturning waves on finite (shallow) depth and observed maximum horizontal velocities almost twice the linear phase speed and maximum accelerations up to six times that of gravity. It is of interest to examine these quantities in the present case of deep-water breaking waves created by the superposition of a spectrum of waves whose phases have been judiciously chosen. The vector velocities and accelerations of surface particles at time $t = 51.5$ just before reentry are shown in Fig. 15.33. The maximum velocity amplitude occurs in the cusp of the wave and is roughly twice as large as the linear phase speed based on a central frequency of $\omega_c \approx 1.4$. The maximum Lagrangian accelerations, which occur inside the loop, are of the order of $6g$ and are directed radially inward. In the cusp of the wave the maximum acceleration is approximately one g and is directed downward so that the tip of this overhanging wave is essentially in free fall. The resemblance of the kinematics of the deep-water plunging wave in the present case and that of the periodic shallow-water overturning wave computed by New et al. (1985) as well as that created by an asymmetrically applied surface pressure (Longuet–Higgins and Cokelet, 1976) is quite remarkable. This further confirms New et al.'s conjecture that the evolution of an overturning wave must be relatively independent of the interior dynamics, so that a local solution for the jet

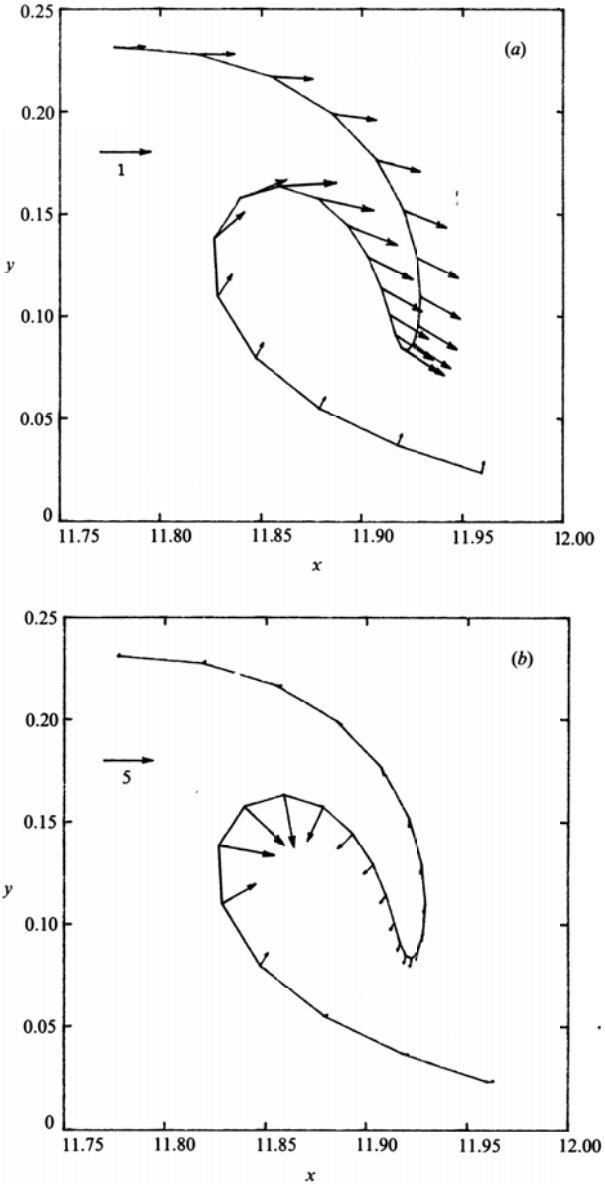

Figure 15.33: (*a*) Vector velocities and (*b*) Lagrangian accelerations of fluid surface particles of the deep-water plunging breaker at time $t = 51.5$ just before reentry occurs (from Dommermuth et al., 1988, *J. Fluid Mech.* Reproduced by permission of Cambridge University Press).

(Longuet–Higgins, 1982; New, 1983; Greenhow, 1983) may be surprisingly useful.

These simulations and detailed direct comparisons to experimental measurements for steep overturning waves illustrate the efficacy of the MEL method. They also confirm the validity and usefulness of potential-flow calculations for such waves and that physical mechanisms not accounted for by potential theory must play a very minor role up to the point of wave reentry.

Three-dimensional overturning waves

We turn to study the dynamics of three-dimensional overturning waves using a MEL approach deploying the quadratic boundary element method (QBEM) developed in Section 15.7.2. The problem we consider is the three-dimensional extension of the two-dimensional overturning wave considered by Longuet–Higgins and Cokelet (1976). Following Longuet–Higgins and Cokelet, we start with a plane Stokes wave but now apply, for a short time, a *three-dimensional* surface pressure to raise the energy density beyond the maximum for a steady Stokes wave.

As initial conditions, we choose the Stokes wave parameters: wavelength $L = 2\pi$, steepness $\epsilon = 0.4$, period $T \cong 5.806$ and phase speed $c \cong 1.082$. The imposed surface pressure has the same temporal (t) and longitudinal (x) dependencies as in the fourth case studied by Longuet–Higgins and Cokelet (1976), but is now further modulated by a periodic transverse variation of wavelength W:

$$P_{\mathcal{F}} = \begin{cases} p_0 \cos^2\left(\dfrac{\pi y}{W}\right) \sin t \sin(x - ct) & 0 \le t \le \pi \\ 0 & t > \pi \end{cases}, \tag{15.7.37}$$

where $p_0 = 0.146$. The co-propagating surface pressure increases from 0 at $t = 0$ to its maximum amplitude at $t = \pi/2$ ($t/T \cong 0.271$) and decreases to zero for $t \ge \pi$. Note that (15.7.37) is symmetric with respect to $y = 0$ and $\pm W/2$, so that the unknowns in the double-periodic domain of L by W can be halved by further taking advantage of symmetry. Physically, the problem can be thought of as one in a wave tank with side walls at any two values of $mW/2$, $m = 0, \pm 1, \pm 2, \ldots$. For definiteness, we refer hereafter to $y = 0$ where $P_{\mathcal{F}} = p_0$ is maximum as the "center", and $y = \pm W/2$ where $P_{\mathcal{F}} = 0$ is minimum as the "sides".

The geometric aspect ratio $\gamma \equiv W/L$ provides a measure of the three-dimensionality of the wave. To illustrate the importance of the three-dimensional effect and the difference from two-dimensional results, we

perform systematic simulations for a range of $\gamma = 0.5,\ 0.75,\ 1.0,\ 1.25,$ and 1.5. Based on convergence tests, we employ 65×25 free-surface grids (384 9-node quadratic elements) corresponding to $N = 1600$ unknowns for half of the computational domain, $[0, L] \times [-W/2, 0]$. The Courant number is set to be $C_n = 0.6$ for $t \leq \pi$ and $C_n = 0.4$ for $t > \pi$. Thirteen-point Savitzky-Golay type smoothing is applied every 3 time steps. The initial free-surface Lagrangian points are distributed non-uniformly according to the curvature of the Stokes waves and are followed throughout the simulation without regridding. The energy loss due to smoothing is less than 0.01% for the entire simulation.

(a) Basic features

Figure 15.34 shows the free-surface profiles and particle velocity components u, v, w, near the final stages of the three-dimensional overturning waves, for $\gamma = 1.5$, 1.0, 0.75 and 0.5. The free-surface profile, u and w are symmetric while v is antisymmetric about the centerline $y = 0$. The results for different values of γ can be qualitatively quite different. In particular, the three-dimensional wave plunging occurs near the center (where the pressure forcing was maximum) for $\gamma = 1.5$ and 1.0; while for $\gamma = 0.5$, the plunging wave develops near the side (where the forcing was minimum). For $\gamma = 0.75$, the plunging tip is located between the center and the side of the tank. Since the breaking location depends in general on the balance between the transverse dynamics and the nonlinear development of the plunging wave, three-dimensional breakers need not develop directly behind the region of maximum (surface or bottom) forcing.

The sequence of development in time of the plunging wave profiles and surface velocity components u, v, w is shown in Fig. 15.35 for $\gamma = 1.5$. When the surface forcing is turned off at $t = \pi$, the deviation from the two-dimensional Stokes wave is relatively small, although three-dimensional features of this "initial" condition are evident. As the wave steepens and the free surface eventually plunges forward and overturns, the horizontal velocity u on the centerline increases to almost three times its initial value. In contrast, changes in the magnitudes of the maximum and minimum vertical velocity w as the plunging wave develops are insignificant. Overall, the ratio of maximum u to maximum w, $(u/w)_m$, increases from an initial value of 1.4 to 3.5 as the wave overturns. Thus, wave overturning is primarily a result of the longitudinal motion.

From Fig. 15.35 for the surface v, it is seen that by virtue of symmetry, v vanishes at $y = 0, \pm W/2$, and is only nonzero in between. This transverse

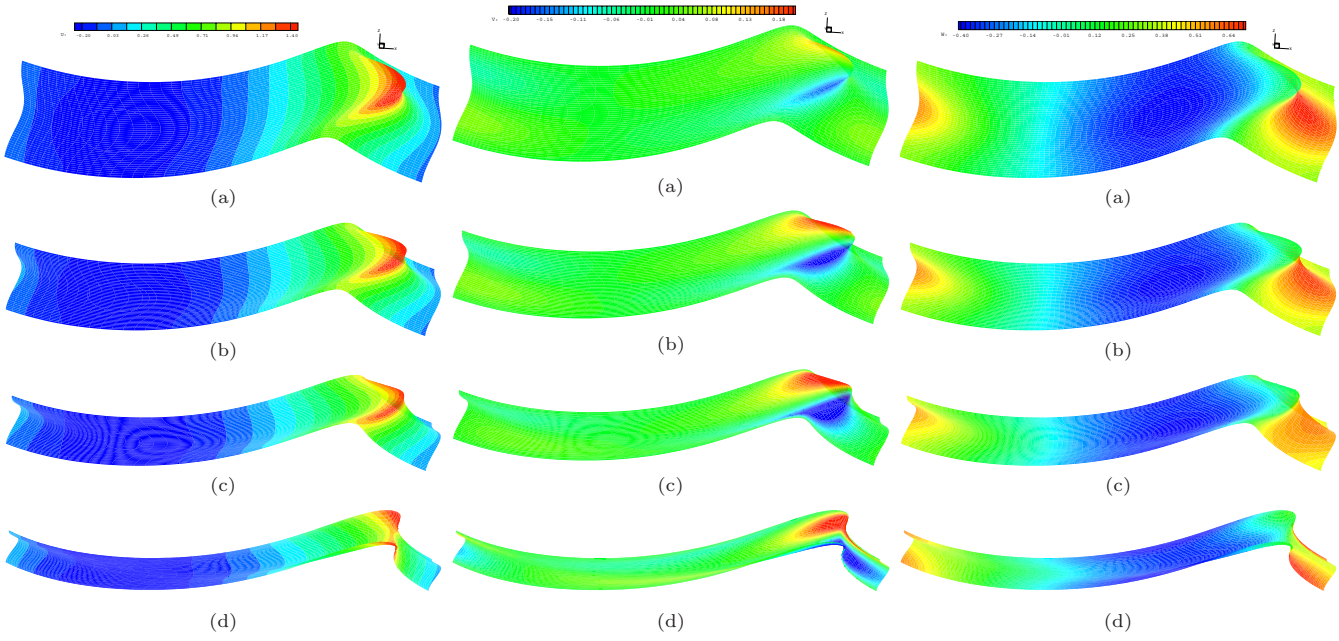

Figure 15.34: Distributions of the surface longitudinal velocity u (left column), transverse velocity v (middle column), and vertical velocity w (right column) at the late stage of three-dimensional overturning waves for different values of $\gamma = (a)$ 1.5 (at $t/T = 0.840$); (b) 1.0 ($t/T = 0.850$); (c) 0.75 ($t/T = 0.861$); and (d) 0.5 ($t/T = 0.880$). (The phase speed of the initial Stokes wave $c = 1.082$) (from Xue et al., 2001, *J. Fluid Mech.* Reproduced by permission of Cambridge University Press).

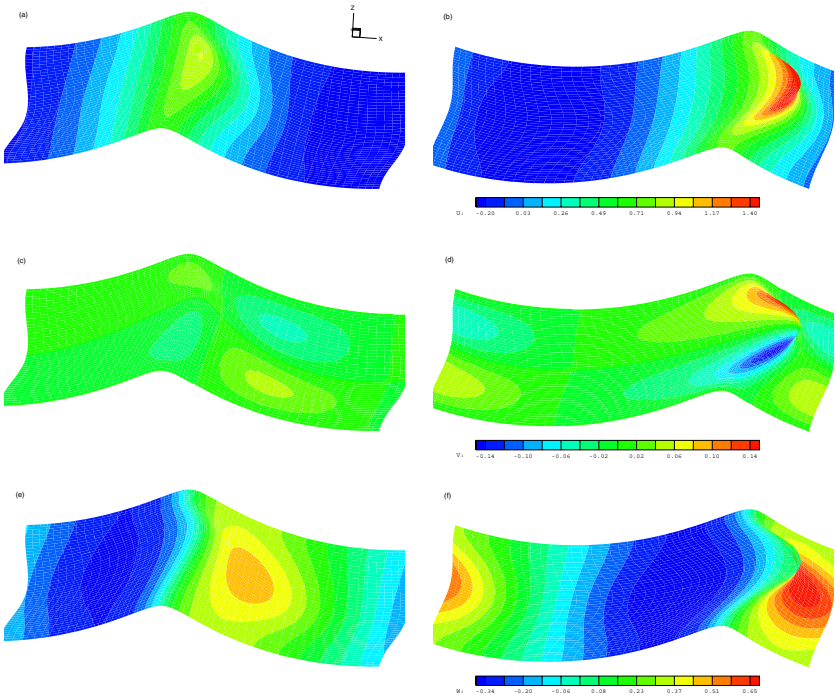

Figure 15.35: Distributions of the surface velocity components u, v and w for $\gamma = 1.5$. The results plotted are for u at $t/T =$ (a) 0.541 and (b) 0.840; for v at $t/T =$ (c) 0.541 and (d) 0.840; and for w at $t/T =$ (e) 0.541 and (f) 0.840. (The phase speed of the initial Stokes wave $c = 1.082$) (from Xue et al., 2001, *J. Fluid Mech.* Reproduced by permission of Cambridge University Press).

velocity is positive (towards the plunger at the centerline) on the front face, and negative near and behind the wave crest. At the final time instant shown, the ratio of maximum u to v for this value of $\gamma = 1.5$ is $(u/v)_m = 20.1$ and the overall effect of the transverse velocity is small.

(b) Effect of three-dimensionality

To address the effect of three-dimensionality, we make direct comparisons of wave characteristics such as profiles, velocities and accelerations, and kinetic and potential energies, for plunging waves with different three-dimensionality parameter γ. To do this, it is useful to define a reference time t^* at which such comparisons can be made. One choice is $t^* = t_v$, the instant at which the free surface first becomes vertical. In these simulations,

Table 15.6: Time t^* (normalized by the fundamental period of the initial Stokes wave $T = 5.806$), and the tip position ($X_{\rm tip}$, $Y_{\rm tip}$, $Z_{\rm tip}$), amplitude of the tip velocity $V_{\rm tip}$ and its three components ($u_{\rm tip}$, $v_{\rm tip}$, $w_{\rm tip}$), at $t = t^*$, of overturning waves for a wide range of γ values.[a]

γ	0.50	0.75	1.00	1.25	1.50	∞
$\frac{t^*}{T}$	0.879	0.861	0.849	0.842	0.839	0.813
$X_{\rm tip}$	6.234	6.313	6.328	6.316	6.313	6.080
$Y_{\rm tip}$	−1.312	0.000	0.000	0.000	0.000	0.000
$Z_{\rm tip}$	0.695	0.755	0.749	0.725	0.707	0.660
$\lvert V_{\rm tip}\rvert$	1.665	1.487	1.618	1.708	1.751	1.771
$u_{\rm tip}$	1.633	1.474	1.613	1.706	1.751	1.771
$v_{\rm tip}$	−0.304	0.000	0.000	0.000	0.000	0.000
$w_{\rm tip}$	0.112	0.180	0.115	0.060	0.005	−0.035

[a] From Xue et al. (2001).

however, t_v occurs at a relatively early stage of the plunging wave development. For $t > t_v$, the plunging wave kinematics continues to change rapidly. A more useful choice is to define t^* to be the instant at which the condition of free fall ($A_n \approx 0$) at the plunging tip first obtains. Here A_n represents the component of the free-surface particle acceleration in the normal direction of the free surface. (For definiteness, we define t^* to be given by $(A_n)_{\min}(t^*) = 0.02$, say, where $(A_n)_{\min}$ is the minimum value of A_n on the entire free surface.) At the tip region for $t \approx t^*$, the longitudinal velocity has effectively reached its maximum value, while the (subsequent) vertical velocity is predictable given essentially by the condition of free fall. While this choice of t^* is by no means unique, it is a pragmatic one since it is a late time we can (quantitatively) identify beyond which the good fidelity of numerical simulations cannot be guaranteed.

Table 15.6 gives the time t^*, and the plunging tip position and velocity at that instant for three-dimensional overturning waves with a range of the three-dimensionality parameter γ. Here the tip is defined to be the point where $A_n = (A_n)_{\min} = 0.02$ at $t = t^*$. For comparison, the corresponding values for a two-dimensional overturning wave (corresponding to $\gamma = \infty$) are also given. It is observed that t^* for the three-dimensional wave is always larger than that for the two-dimensional wave, and that t^* decreases uniformly as γ increases. This confirms the general expectation that breaking of a three-dimensional wave would take longer to develop.

As a result of the larger t^*, X_{tip} and Z_{tip} are generally greater for the three-dimensional overturning wave than in the two-dimensional case. For small γ (< 0.75), X_{tip} and Z_{tip} increase with γ while Y_{tip} is negative as a result of shift of wave breaking from the center to the side. Beyond this value of γ, X_{tip}, Z_{tip} approach the two-dimensional values monotonically as γ increases, while $Y_{\text{tip}} = 0$ (wave breaking at the center).

The tip velocity amplitude $|V_{\text{tip}}|$ is generally smaller than the two-dimensional value. $|V_{\text{tip}}|$ generally increases with γ except for very small γ where the transverse sloshing can significantly increase the magnitude of the tip velocity. The behavior of V_{tip} is dominated by its longitudinal component u_{tip} which is an order of magnitude larger than the transverse and vertical velocities v_{tip} and w_{tip}. For three-dimensional plunging waves, w_{tip} is positive and decreases monotonically with increasing γ for $\gamma > 0.75$. On the other hand, w_{tip} is negative for the two-dimensional case. This is consistent with the larger value of Z_{tip} for the three-dimensional case. The transverse tip velocity v_{tip} for the three-dimensional wave is generally negligible except for the case of small γ where it is negative as a result of the shift of the plunging tip from the center to the side.

Table 15.7 displays the maximum and minimum values of the velocity and acceleration amplitudes and components on the free surface at the time t^*. Note that the plunging wave $V_{\max}$ is substantially greater than the phase speed of the initial Stokes wave ($c \cong 1.082$). $V_{\max}$ usually obtains at a point near but not at the tip. Compared to V_{tip}, $V_{\max}$ is about 10% larger. From the simulations, $V_{\max}$ is achieved at the center for $\gamma \geq 1.0$ and on the side for $\gamma = 0.5$. For $\gamma = 0.75$, which is a transitional case, $V_{\max}$ obtains between the center and the side. Unlike V_{tip}, $V_{\max}$ of the three-dimensional wave can be greater than that of the two-dimensional wave. Similar to u_{tip}, $(V_x)_{\max}$ is much larger than $(V_y)_{\max}$ and $(V_z)_{\max}$ and behaves similarly to $V_{\max}$. Due to the effect of transverse sloshing, $(V_z)_{\max}$ varies inversely with $|(V_y)_{\min}|$. Thus there is a strong energy and momentum transfer from the vertical to transverse motion in the development of the three-dimensional overturning waves.

The variation of the maximum free-surface acceleration magnitude $A_{\max}$ with γ is similar to that of $V_{\max}$. $A_{\max}$ usually occurs under the tip at the front face of the overturning wave and reaches values of $O(5g)$. $A_{\max}$ of the three-dimensional overturning wave can be larger or smaller than the two-dimensional result depending on γ. Specifically, for $\gamma >/< 1.25$, $A_{\max}$ is greater/smaller than that of the two-dimensional value. This behavior of $A_{\max}$ is seen to be strongly correlated with the magnitude of $(A_z)_{\min}$.

Table 15.7: Maximum ($(\ )_{\max}$) and minimum ($(\ )_{\min}$) values on the free surface of the velocity amplitude, V, and velocity components, V_x, V_y, V_z; acceleration amplitude, A, and acceleration components, A_x, A_y, A_z; and wave elevation, ζ, at $t = t^*$, of overturning waves for a wide range of γ values.[a]

γ	0.50	0.75	1.00	1.25	1.50	∞
$V_{\max}$	1.885	1.536	1.748	1.859	1.921	1.846
$(V_x)_{\max}$	1.875	1.500	1.742	1.859	1.920	1.831
$(V_y)_{\max}$	0.056	0.043	0.056	0.059	0.056	0.000
$(V_z)_{\max}$	0.748	0.591	0.678	0.710	0.721	0.692
$V_{\min}$	0.260	0.268	0.255	0.249	0.246	0.327
$(V_x)_{\min}$	−0.295	−0.305	−0.321	−0.328	−0.331	−0.336
$(V_y)_{\min}$	−0.321	−0.371	−0.268	−0.199	−0.160	0.000
$(V_z)_{\min}$	−0.453	−0.398	−0.410	−0.413	−0.413	−0.428
$A_{\max}$	3.587	2.552	3.210	4.102	5.073	3.988
$(A_x)_{\max}$	3.224	2.201	2.720	3.119	3.368	3.682
$(A_y)_{\max}$	0.383	0.128	0.079	0.060	0.049	0.000
$(A_z)_{\max}$	0.511	0.386	0.406	0.427	0.442	0.494
$A_{\min}$	0.089	0.063	0.085	0.057	0.044	0.247
$(A_x)_{\min}$	−0.425	−0.402	−0.388	−0.388	−0.392	−0.365
$(A_y)_{\min}$	−0.252	−0.750	−0.667	−0.573	−0.506	0.000
$(A_z)_{\min}$	−2.224	−1.873	−2.571	−3.861	−4.934	−2.941
$\zeta_{\max}$	0.811	0.761	0.758	0.746	0.735	0.696
$\zeta_{\min}$	−0.266	−0.259	−0.263	−0.266	−0.269	−0.286
$\zeta_{\max} - \zeta_{\min}$	1.077	1.020	1.021	1.011	1.004	0.983

[a] From Xue et al. (2001).

For longitudinal free-surface acceleration, $(A_x)_{\max}$ is generally smaller in the presence of three-dimensionality. In the transverse direction, there is appreciable A_y primarily associated with the sloshing motion towards the side (as reflected in larger $|(A_y)_{\min}|$ values).

The dependence on γ of the maximum and minimum wave elevations $\zeta_{\max}$, $\zeta_{\min}$ and wave height $h \equiv \zeta_{\max} - \zeta_{\min}$ at t^* is also shown in Table 15.7. In general, h and $\zeta_{\max}$ of the three-dimensional overturning wave exceed those of the two-dimensional case. Both h and $\zeta_{\max}$ are seen to decrease uniformly as γ increases. For small γ, the three-dimensional h can be about 15% larger than the two-dimensional value. As for $\zeta_{\min}$, there is no significant difference between the two-dimensional and three-dimensional cases.

The free-surface profiles of the overturning wave on the center- and side-planes at the time t^* are shown in Fig. 15.36 for different γ's. Except for

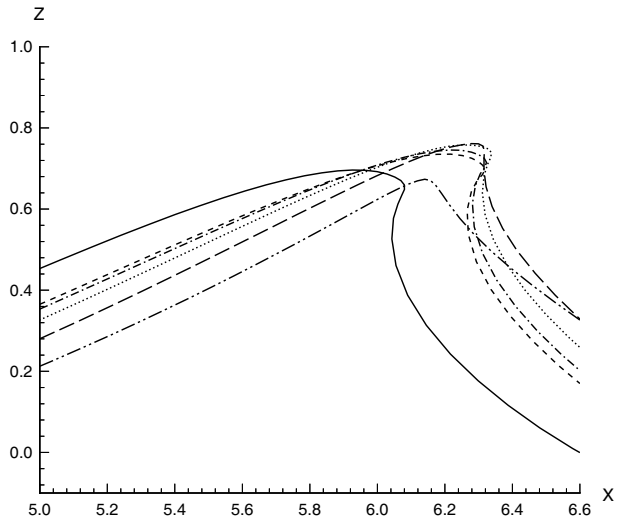

(*a*)

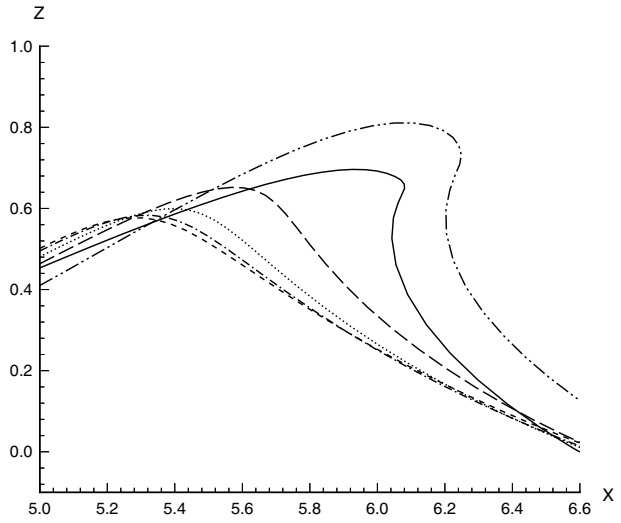

(*b*)

Figure 15.36: Free-surface profiles of two- and three-dimensional overturning waves at the time t^* on (*a*) the center-plane; and (*b*) the side for: $\gamma = \infty$, ——; $\gamma = 1.5$, - - -; $\gamma = 1.25$, — · —; $\gamma = 1.0$, · · · · ; $\gamma = 0.75$, – – –; and $\gamma = 0.5$, — · · — (from Xue et al., 2001, *J. Fluid Mech.* Reproduced by permission of Cambridge University Press).

$\gamma = 0.5$ where wave breaking occurs near the side, three-dimensional waves break with higher tip/crest at the center-plane than the two-dimensional wave. Careful examination of the center-plane profiles reveals that the $\gamma = 1.25$ case has a profile shape most similar to the two-dimensional plunging wave. For $\gamma < / > 1.25$, the overturning waves have less/more arced (concaved) front faces than that of the two-dimensional case.

Two main factors affect the development of the overturning profile. One is the nonlinear free-surface focusing from both the longitudinal and transverse directions. The latter explains why the three-dimensional wave can be more energetic on the center-plane. The other is transverse sloshing which spreads the energy from the center-plane to the side. For $\gamma < / > 1.25$, the second/first factor dominates, resulting in less/more forward-face concaved center-plane profiles.

The side-wall profiles (Fig. 15.36(b)) show the wave breaking there of the $\gamma = 0.5$ case. The concentration of energy here results in much higher crest/tip than the two-dimensional overturning wave. The large t^* also results in a more forward profile position. For larger $\gamma(> 0.5)$, the side-wall profiles are lower and non-breaking.

The role of wave energy in the development of wave overturning can be better understood by examining the ratio between the kinetic-energy increase ΔE_k and the potential-energy increase ΔE_p (from the initial time). Figure 15.37 plots the results at the time t^* as a function of γ. It is seen that $\Delta E_k/\Delta E_p$ of the three-dimensional overturning wave is smaller than the two-dimensional result with $\Delta E_k/\Delta E_p$ increasing with γ and approaching the two-dimensional value for large γ. Thus the three-dimensional wave breaks with a larger potential energy increase but is less kinetically energetic relative to the two-dimensional case. This is consistent with earlier results that the three-dimensional breaking wave has larger wave height but smaller tip velocity than the two-dimensional wave.

One notes that the above characteristics of three-dimensional overturning waves are obtained for a particular class of such waves, namely those obtained with a short-duration artificial surface pressure forcing specified by a three-dimensional parameter γ. The features and conclusions found above can also be obtained for deep-water overturning waves generated via other mechanisms. One such mechanism is the steepening to breaking of a (transversely modulated) large-amplitude wave given initially by (linear) Airy theory (Schultz et al., 1994). The similarity of the overall features are confirmed by systematic simulations also of that case (see Xue, 1997 for details).

15.7.5 Application to Steep Crescent Waves

The phenomenon of regularly-distributed crescent-shaped wave patterns (also called "horseshoe" waves) has been observed in the open ocean (Kinsman, 1984; Shrira et al., 1996) and in laboratory basins (Su et al., 1982; Su 1982). Mechanisms for the development of such three-dimensional steep waves have only recently become more conclusive. Su et al. (1982) speculated that such waves result from three-dimensional (class II) instability of Stokes waves; while Saffman and Yuen (1980) and Meiron et al. (1982) assumed the crescent wave patterns to be steady three-dimensional bifurcations of Stokes waves. Recently, Shrira et al. (1996) added non-conservative effects into the model Zakharov equation and obtained a qualitative prediction of the persistent asymmetric pattern. In any event, since these theories are based either on linear stability analysis or on weakly-nonlinear model equations, it is not clear that quantitative comparisons to crescent waves in experiments (which tend to be quite steep) can be obtained. Recently,

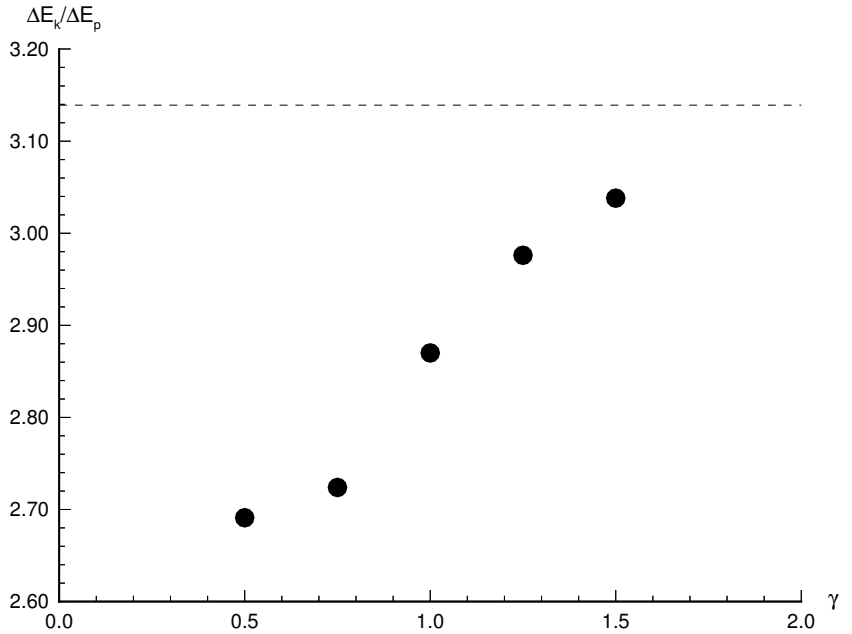

Figure 15.37: Ratio between the increases in the kinetic and potential energies ΔE_k and ΔE_p at the instant t^* of the three-dimensional overturning wave as a function of γ. The two-dimensional result is also plotted (- - -) (from Xue et al., 2001, *J. Fluid Mech.* Reproduced by permission of Cambridge University Press).

Xue et al. (2001) carried out direct simulations, using QBEM MEL approach, of three-dimensional crescent waves by following the evolution of steep two-dimensional Stokes waves with small initial class II (three-dimensional) unstable perturbations (according to Mclean, 1982). Following the fully-nonlinear evolutions, they found that, depending on the initial perturbations, fully-featured 1:2 sub-harmonic (L_2) and 1:3 sub-harmonic (L_3) crescent waves arise naturally from such nonlinear evolutions. Significantly, detailed crescent features and geometry from the simulations compare quantitatively well with experimental wave basin measurements. These simulations indicate that the formation of crescent waves is directly (and possibly solely) a result of fully-nonlinear three-dimensional evolution of unstable Stokes waves.

In this section, we follow the study of Xue et al. (2001) to elucidate the mechanism for the generation and development of three-dimensional steep crescent waves using direct MEL simulations. We start the simulations with a train of exact plane Stokes wave (Schwartz, 1974), propagating in the $+x$ direction, with fundamental wavelength $L = 2\pi/k$, steepness kA, and phase such that the maximum elevation is at $x = 0$ at $t = 0$. We then consider initial three-dimensional perturbations in the free-surface elevation and velocity potential (ζ' and ϕ') given by a single sinusoidal wave component:

$$\zeta' = \epsilon A \sin(k_x x + \beta) \cos k_y y \,, \tag{15.7.38}$$

$$\phi' = -\frac{\epsilon A}{(k_x^2 + k_y^2)^{1/4}} \cos(k_x x + \beta) \cos k_y y \exp[(k_x^2 + k_y^2)^{1/2} z] \,, \tag{15.7.39}$$

on $z = \bar{\zeta}$, where ϵ is the small parameter measuring the amplitude of the disturbance and $\bar{\zeta}$ is the free-surface elevation of the undisturbed Stokes wave. Here the wavenumbers $(k_x, k_y) = (p + k, q)$, where p and q are the longitudinal and transverse perturbation wavenumbers (cf. McLean, 1982). In the above, β is the phase of the perturbation.

We set $k = 1$ for the Stokes wave. For MEL computations, we use a rectangular domain given by $x \in [0, L/p]$ and $y \in [-L/(2|q|), 0]$ (due to transverse symmetry of the problem, only half of the y domain is needed). Based on convergence tests and the required resolution for the crescent wave features, we employ 40 nodes (corresponding to 20 quadratic elements) per wavelength in both longitudinal and transverse directions. For time integration, dynamic stepping with Courant number $C_n = 0.4$ is used. With

these numerical parameters, the total energy is conserved to $O(0.01\%)$ in the simulations.

Development of L_2 crescent waves

To simulate a L_2 crescent wave case, we choose $kA = 0.33$ (for this steepness, the fundamental period is $T \cong 5.951$) for the Stokes wave; and $\epsilon = 0.16$, $(k_x, k_y) = (1.5, 1.23)$ ($k_x = 1.5$ corresponds to $p = 1/2$), and $\beta = 0$ for the initial three-dimensional perturbation. According to McLean (1982), the latter corresponds to the dominant component of the most unstable ($p = 1/2$ sub-harmonic class II) mode for this kA.

Figure 15.38 shows a representative sequence of free-surface profiles during the nonlinear evolution. Figure 15.38(a) shows the initial perturbated Stokes wave profile. With $\beta = 0$, the elevation perturbation is zero at the crests but is discernible (though very small) elsewhere. As will be shown later, the choice of β does not affect the overall development of the L_2 crescent wave. At $t \sim T/2$, Fig. 15.38(b), clear three-dimensional wave features have developed. At this stage, the largest wave slope obtains on the back faces of the Stokes wave.

At $t \sim T$, Fig. 15.38(c), distinct crescent shape of the waves can be observed. Along the Stokes wave crest line, forward fronts of the crescents have sharper crest angles than the edges (where two crescents meet). Even at this early stage, the staggered row-shift crescent pattern has already been formed. As the evolution continues, the crescent shape becomes more rounded. Interestingly, the crescent pattern are seen to subsequently weaken a bit at $t \sim 2T$, Fig. 15.38(d).

At $t \sim 3T$, Fig. 15.38(e), the crescent wave development regains strength, the crescent trough now becomes deeper, and the crescent crest becomes sharper. Meanwhile, the edges of the crescent lines are seen to extend further in the $-x$ direction. At $t \sim 4T$, the development appears to reach a quasi-steady state. This steady state lasts for about two periods (Figs. 15.38(f), (g) at $t/T \approx 4.3$, 5.0 respectively). At this state, the sharp-crested round semi-circular and staggered row-shifted crescent crests are well formed.

As the evolution continues further, the quasi-steady state of $t/T \sim 5$ with the rounded crescent wave pattern is lost. The crescent crest sharpness is diminished and the deep trough regions flatten up. Meanwhile, steep triangular "Delta" (Δ) regions appear in front of the crescent forward fronts. The flattening of the trough and rising of the Delta region eventually cause

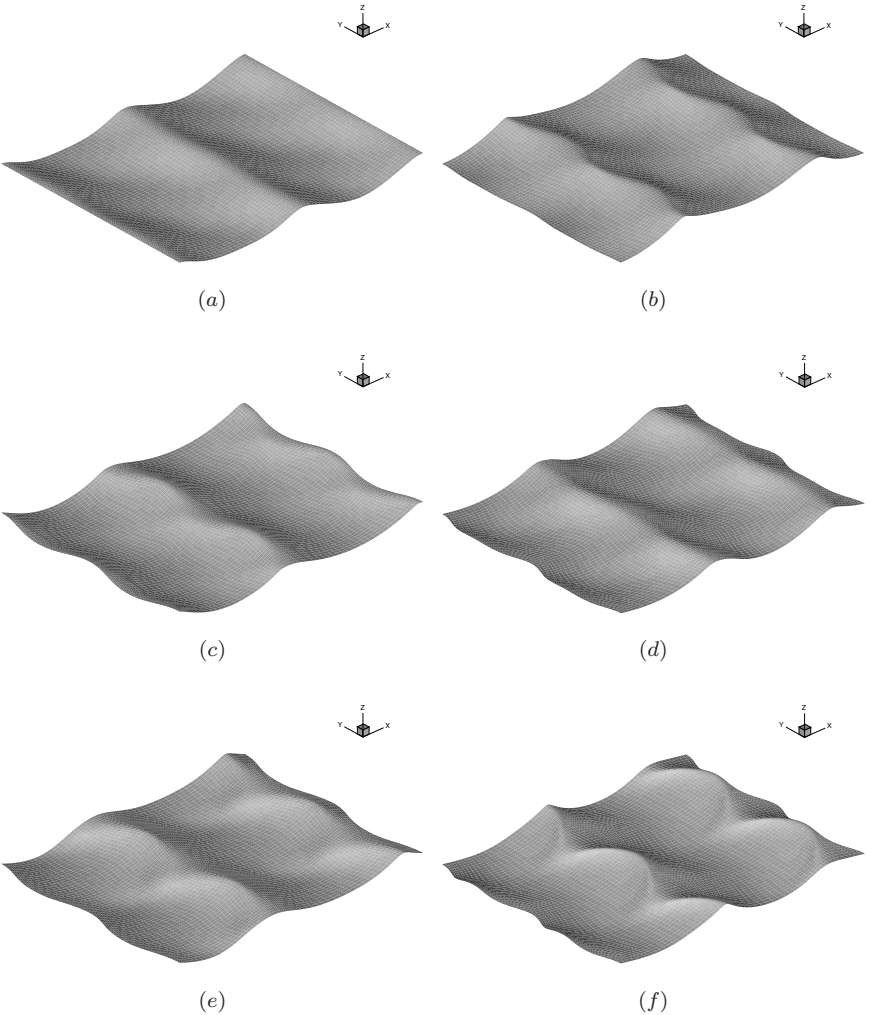

Figure 15.38: Free-surface patterns during the nonlinear evolution of a plane Stokes wave of steepness $kA = 0.33$ (fundamental period $T = 5.951$), with three-dimensional initial disturbance given by $\epsilon = 0.16$, $(k_x, k_y) = (1.5, 1.23)$ and $\beta = 0$ at time $t/T =$: (a) 0; (b) 0.635; (c) 1.078; (d) 2.002; (e) 3.172; (f) 4.338; (g) 4.955; and (h) 5.641 (from Xue et al., 2001, *J. Fluid Mech.* Reproduced by permission of Cambridge University Press).

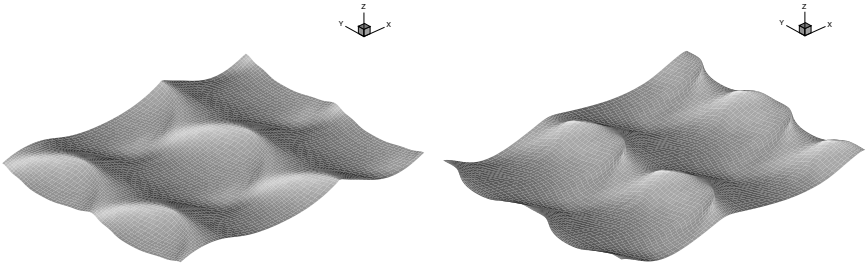

(*g*) (*h*)

Figure 12.38 (*Continued*)

(*a*)

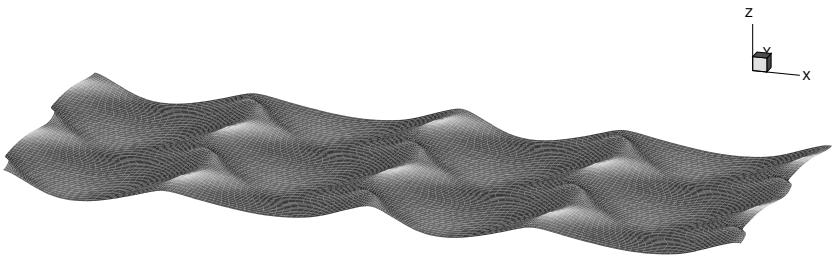

(*b*)

Figure 15.39: Comparison of a L_2 crescent wave train observed in a wave basin (*a*) (Fig. 17 of Su et al., 1992, *reproduced with permission*); and in simulation (*b*) (at $t/T \approx 5.641$, cf. Fig. 15.38(*h*) (from Xue et al., 2001, *J. Fluid Mech.* Reproduced by permission of Cambridge University Press).

the crescent crests to break in the form of spilling waves on the shoulders of the crescent wave. Figure 15.38(h) shows a typical L_2 crescent wave pattern just before breaking.

The qualitative features in Fig. 15.38 compare extremely well with observed crescent waves in experiments. Figure 15.39 compares a wave basin aerial photograph of a L_2 crescent wave (Fig. 17 of Su et al., 1982) with the simulated result in Fig. 15.38(h) (at $t/T \approx 5.641$). For the sake of comparison, the simulation result is rotated to match the perspective of the wave basin photograph. The resemblance is quite remarkable. The simulated L_2 crescent wave possesses all the notable features observed in the

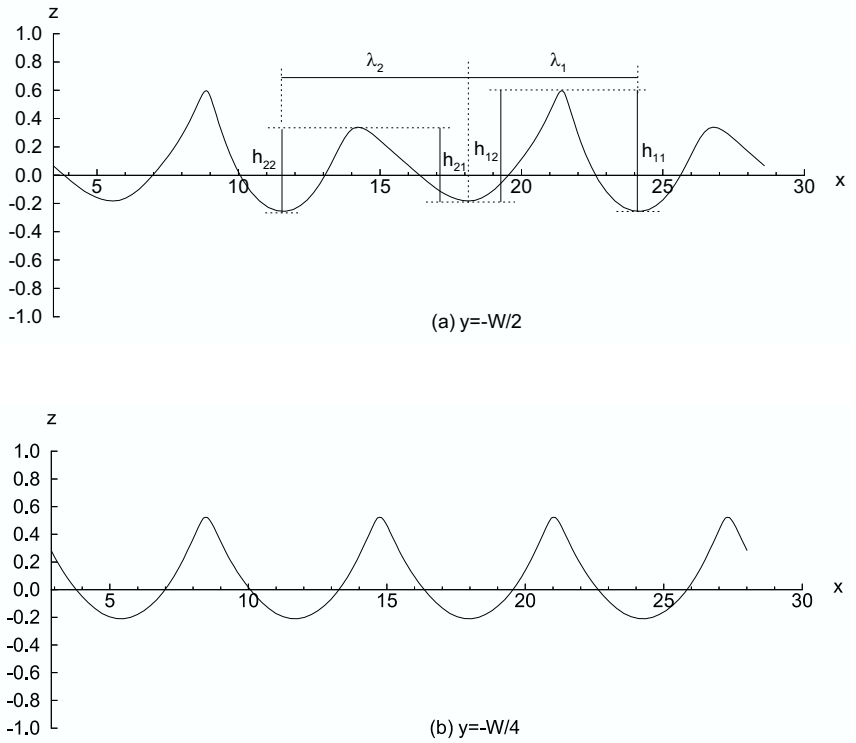

Figure 15.40: Longitudinal profiles of the L_2 crescent wave on the planes $y = (a)\ -W/2$ and $(b)\ -W/4$ at $t/T = 4.338$ obtained from simulation ($kA = 0.33$, $\epsilon = 0.16$, $\beta = 0$, and $(k_x, k_y) = (1.5, 1.23)$). Characteristic length and height parameters according to Su (1982) are labelled in (a) (from Xue et al., 2001, *J. Fluid Mech.* Reproduced by permission of Cambridge University Press).

basin experiment, including the fully-extended semi-circular crests, staggered row-shift crescent pattern, flattened troughs, rising Deltas, and steep crescent wave shoulders. Remarkably, although the (initial) disturbance in the simulation most likely differs from that in the physical experiment, the time durations required for the full development of the L_2 wave with the distinct crescent wave features in both simulation and experiment are quite close ($t/T \sim 5$).

For quantitative comparisons of the crescent wave features to experiment, Fig. 15.40 shows longitudinal surface profiles (at $y = -W/2$ and $y = -W/4$ at $t/T = 4.338$) wherein the characteristic length and height parameters (according to Su, 1982) are also labelled. (Here W denotes the width of the computational domain, i.e. period in the transverse direction of the crescent wave.) Figure 15.40(a) shows typical L_2 feature of alternating peak and trough, while Fig. 15.40(b) on $y = -W/4$ displays a (steepened) Stokes-wave-like regular profile.

Table 15.8 shows comparisons of the characteristic crescent wave geometric parameters at four representative times in the simulation with $t/T \in (3, 5)$ during which quasi-steady state approximately obtains. The agreements between simulation results and experimental measurements of Su (1982) are remarkably good for the wave height ratios h_{11}/h_{12}, h_{21}/h_{22}, and h_{11}/h_{21}, and the maximum local wave steepness $s_{\max}$. The comparisons

Table 15.8: Comparisons of geometric parameters of L_2 crescent waves between the MEL QBEM simulation ($kA = 0.33$, $\epsilon = 0.16$, $\beta = 0$, and $(k_x, k_y) = (1.5, 1.23)$) and the experimental measurements of Su (1982).[a]

	Experiment	Simulation			
	Su (1982)	$\frac{t}{T} = 3.171$	$\frac{t}{T} = 4.338$	$\frac{t}{T} = 4.955$	$\frac{t}{T} = 5.150$
$\frac{\lambda_2}{\lambda_1}$	1.28	1.05	1.07	1.03	1.17
$\frac{h_{11}}{h_{12}}$	1.10	1.18	1.09	1.18	1.26
$\frac{h_{21}}{h_{22}}$	0.88	0.81	0.88	0.80	0.75
$\frac{h_{11}}{h_{21}}$	1.66	1.49	1.64	1.63	1.60
$s_{\max}$	0.65	0.45	0.64	0.69	0.51

[a] From Xue et al. (2001).

are particularly good at $t/T = 4.338$ and $t/T = 4.955$ when the L_2 crescent features are fully developed. The comparison of the wavelength ratio λ_2/λ_1 is acceptable but not as good as the other parameters. The reason is not clear but may be due to a lower accuracy in measuring wavelengths in the experiments.

As expected from physical reasoning, the development of the L_2 crescent waves depends on physical parameters of the problem such as the precise phase β of the initial disturbance, the initial disturbance amplitude ϵ, and the longitudinal direction of propagation of the initial disturbance relative to the underlying Stokes waves. This is confirmed by simulations (for details, see Xue et al. (2001).

Development of L_3 crescent waves

In Su (1982), under natural conditions, it is reported that of the crescent wave observed, L_2, L_3 and L_4 configurations occur, respectively, approximately 90%, 10% and 1% of the time. The preceding results suggest these other crescent wave configurations may obtain as a result of similar instability mode development mechanisms.

As a demonstration, we obtain L_3 crescent configuration by nonlinear simulation of a Stokes wave with initial three-dimensional disturbance

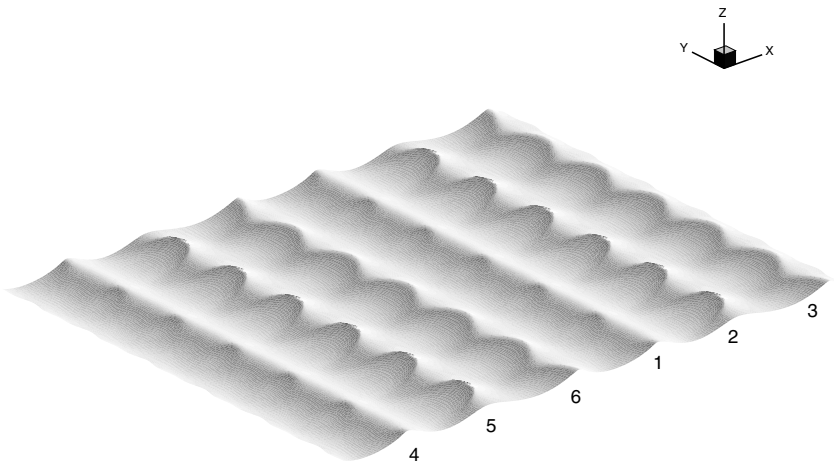

Figure 15.41: Free-surface wave pattern at $t/T = 4.198$ during the fully-nonlinear evolution of a Stokes wave ($kA = 0.33$, $T = 5.951$) with an initial three-dimensional disturbance ($\epsilon = 0.12$, $(k_x, k_y) = (1.33, 1.23)$, $\beta = 0$). The consecutive crest rows corresponding to the original Stokes wave are labelled (from Xue et al., 2001, *J. Fluid Mech.* Reproduced by permission of Cambridge University Press).

corresponding to (linearly) unstable sub-harmonic mode with $p = 1/3$ (i.e. $k_x = 4/3$). Figure 15.41 plots a representative stage in the development of L_3 crescent waves of such a case ($kA = 0.33$, $\epsilon = 0.12$, $(k_x, k_y) = (1.33, 1.23)$, $\beta = 0$). The three-row staggered structure of the L_3 crescent wave pattern is clearly shown, which obtains qualitative comparison to observations of such waves in the tank (e.g. Su, 1982 Fig. 11). The simulations indicate that, unlike the L_2 crescent pattern, such an L_3 pattern is non-stationary relative to the Stokes carrier. Furthermore, the L_3 configuration is characterized by different crescent crest shapes at different rows. This is indicated by the "high-high-low" (HHL) pattern of wave crest amplitudes in Fig. 15.41. All these features match well experimental observations of L_3 crescent waves (Su, 1982).

The results in this section using direct QBEM MEL simulations show that nonlinear evolutions of (linearly) unstable three-dimensional (class II) modes co-propagating on a steep Stokes wave train provide the sufficient mechanism for the development of crescent waves. This is confirmed by qualitative and quantitative comparisons to the physical measurements of crescent waves.

15.7.6 Application to Free-Surface Flow Over an Impulsively Started Point Sink

We consider the fully-nonlinear MEL simulation of the incompressible irrotational axisymmetric flow caused by an impulsively started point sink beneath a free surface (Xue and Yue, 1998). This example illustrates an application of the MEL approach to a vertically axisymmetric problem (using a ring-source Green function) and the use of the matching technique to achieve far-field closure. These two techniques in the context of the MEL method were first developed in Dommermuth and Yue (1987b).

The fluid "withdrawal" problem has been the subject of many investigations in recent years because of its fundamental scientific interest and engineering importance in applications such as optimal pumping from storage tanks, ocean thermal power plants, cooling and solar ponds, as well as water quality control in reservoirs and lakes. The bulk of the studies of this problem are for the two-dimensional case assuming steady flow (Peregrine, 1972; Vanden-Broeck et al., 1987; Tuck and Vanden-Broeck, 1984; Sahin and Magnuson, 1984; Hocking, 1985; Collings, 1986; Vanden-Broeck and Keller, 1987; Hocking, 1988; King and Bloor, 1988; Mekias

and Vanden-Broeck, 1989; Mekias and Vanden-Broeck, 1991; Mekias and Vanden-Broeck, 1993). For infinite depth, stagnation-point solutions, those characterized by a stagnation point at the free surface directly above the sink, are found for Froude number $\mathcal{F}_r$ (based on the volume flux rate and submergence) below a critical value. Above this value, steady-state solutions have not been found, except for a cusp solution (the free-surface profile is a downward facing cusp with its tip above the sink).

A notable exception to these steady solutions is Tyvand (1992) who focused on the initial evolution of the free surface for the two-dimensional problem using a small-time expansion. Arguing that nonlinear free-surface effects are exactly cancelled by gravitational effects for a particular Froude number, he finds the critical value of $\mathcal{F}_r \equiv Q/2\pi(gh^3)^{1/2} = 1/3$ for the formation of a center dip, where Q is the volume flux rate of the sink, h its submergence with respect to the far-field/initial free surface, and g the gravitational acceleration. This value is much lower than the upper limit of $\mathcal{F}_r = 1.42$ of Hocking and Forbes (1991) based on a steady-state analysis.

Investigations of the three-dimensional problem are fewer with the exception of linear analyses (e.g. Wehausen and Laitone, 1960) and experiments (e.g. Lubin and Springer, 1967; and Miloh and Tyvand, 1993). The salient feature of the experimental observations is the formation of a dip on the surface above a critical Froude number. Assuming steady state and a stagnation point at the surface above the sink, Forbes and Hocking (1990) used a boundary-integral-equation (BIE) computation as well as a small-Froude-number analysis to show that such a steady stagnation-point solution exists for small Froude numbers, in this case $\mathcal{F}_r \equiv Q/4\pi(gh^5)^{1/2} < 0.509$. Above this value of $\mathcal{F}_r$, their calculation fails to give a steady-state solution. Whether the unsteady withdrawal flow with a cusp pointing towards the sink is the only permissible outcome for large Froude number remains unclear. Zhou and Graebel (1990) performed numerical simulations of drainage from a cylindrical basin using a nonlinear axisymmetric BIE method. Their results of the unsteady problem show two different phenomena depending on the drain rate. For relatively large Q, a dip forms at center of the free surface which is rapidly drawn into the drain. For small Q, they observe an upward jet depending on the drain size. In their problem, the Froude number is defined with respect to the tank radius. Since this is not the only physically important parameter, the precise dependence on $\mathcal{F}_r$ for this problem is not established.

More recently, Miloh and Tyvand (1993) extended the small-time perturbation analysis of Tyvand (1992) to axisymmetric flow and identified the corresponding critical Froude number to be $\mathcal{F}_r = 15^{-1/2} \approx 0.258$. Presumably, a dip forms on the free surface and eventually collapses towards the sink only for $\mathcal{F}_r$ greater than this value. This analysis depends only on the third-order (leading order of gravitational effect) time derivative of the center surface elevation at time $t = 0$, and its validity for the long time evolution of the actual physical problem is unclear. Using direct fully-nonlinear computations, Xue and Yue (1998) obtained a complete quantification of the solution of this problem. They found that, depending on $\mathcal{F}_r$, there are three distinct flow regimes: (i) $\mathcal{F}_r < \mathcal{F}_{r1} \approx 0.1924$: a "sub-critical" regime marked by a damped wave-like behavior of the free surface which reaches an asymptotic steady state; (ii) $\mathcal{R}_{r1} < \mathcal{F}_r < \mathcal{F}_{r2} \approx 0.1930$: the "trans-critical" regime characterized by a reversal of the downward motion of the free surface above the sink, eventually developing into a sharp upward jet; (iii) $\mathcal{F}_r > \mathcal{F}_{r2}$: a "super-critical" regime marked by the cusp-like collapse of the free surface towards the sink. In the following, we outline the approach and some of the key results of Xue and Yue (1998).

We consider the unsteady fully-nonlinear free-surface flow in deep water above a submerged three-dimensional point sink started abruptly from rest to a constant volumetric withdrawal rate Q. The problem is governed by a single dimensionless physical parameter, the Froude number $\mathcal{F}_r \equiv Q/4\pi(gh^5)^{1/2}$. We computationally map out the entire solution of the problem, systematically varying $\mathcal{F}_r$.

We assume that the fluid is inviscid and incompressible, and the flow is irrotational. Surface tension is ignored. For simplicity, we choose time, length and mass units such that the depth h, the gravitational acceleration g, and the fluid density ρ are all unity. For numerical solution of the initial-boundary-value problem, we adopt the fully-nonlinear mixed Eulerian-Lagrangian (MEL) approach. We further assume axisymmetry, and for the solution of the field equation (i.e. BVP) we use an axisymmetric (ring-source) BIE technique (Dommermuth and Yue, 1987b). For computation, the domain in deep water is simply closed at some large constant depth $z = -H$. For far-field closure in the horizontal plane, we match the fully-nonlinear inner MEL solution to a general time-dependent linearized outer wavefield at a fixed radius on a matching cylinder: $r = R_0$. Since the far-field wave amplitude must necessarily decay with radius in three dimensions, for a suitably chosen matching radius R_0 (based on nonlinearity only), fully-nonlinear inner simulations can be carried indefinitely in

time (Dommermuth and Yue, 1987b). This is especially important for the present problem where the approach to asymptotic steady state (or not) is a central question. Details on the implementation of the matching can be found in Dommermuth and Yue (1987b) where the validity and efficacy of this (matching) scheme are demonstrated.

For the numerical solution of the axisymmetric BIE problem, the trace of the free surface, bottom, and matching boundary is approximated by cubic splines over (Lagrangian) nodes, and Φ and Φ_n are represented by linear basis functions based on arclength between adjacent nodes. To maximize stability of the time integration, for which we employ a consistent fourth-order Runge-Kutta scheme, the nodes on the free surface are maintained at equal arclength spacing via a regridding procedure after each time step. To track the rapid cusp-like development of the free surface, dynamic time stepping based on (15.7.32) is adopted.

The computational method for this problem is validated systematically through convergence tests with varying the panel length $\Delta\ell$, the depth of the computational domain H, the matching radius R_0, and the maximum and minimum time-step sizes, $\Delta t_{\max}$ and $\Delta t_{\min}$, which are the upper and lower bounds of the time step Δt in the dynamic time integration scheme. The details can be found in Xue and Yue (1998). Systematic tests confirm the generally quadratic and fourth-order convergence rates of the absolute error with $\Delta\ell$ and Δt, respectively. Based on convergence tests for the full range of $\mathcal{F}_r$ we consider, we choose for all our computations: $\Delta\ell = 0.05$, $\Delta t_{\max} = 0.032$, $\Delta t_{\min} = 0.001$, and $R_0 = 6$. The expected error in the free-surface elevation is less than $O(1\%)$ in all cases shown below.

Sub-critical regime: $\mathcal{F}_r < \mathcal{F}_{r1} \approx 0.1924$

In this sub-critical regime, the flow is marked by a damped wave-like behavior of the free surface which eventually tends to an asymptotic steady state. Figure 15.42 shows the time-histories of the free-surface elevation at specific radii. At each r, the free surface behaves like a damped oscillator eventually reaching an asymptotic steady state. The free surface near the origin initially goes down, reaches a minimum value, then rises and settles towards an asymptotic value in an oscillatory manner emitting outwardly propagating radial waves in the process. Note that with the use of the matching boundary, we are able to continue simulations to well beyond $O(10)$ characteristic time (limited only by computational effort).

For sufficiently small $\mathcal{F}_r$, one may apply linearized free-surface boundary conditions throughout, and the solution of the linearized problem can be

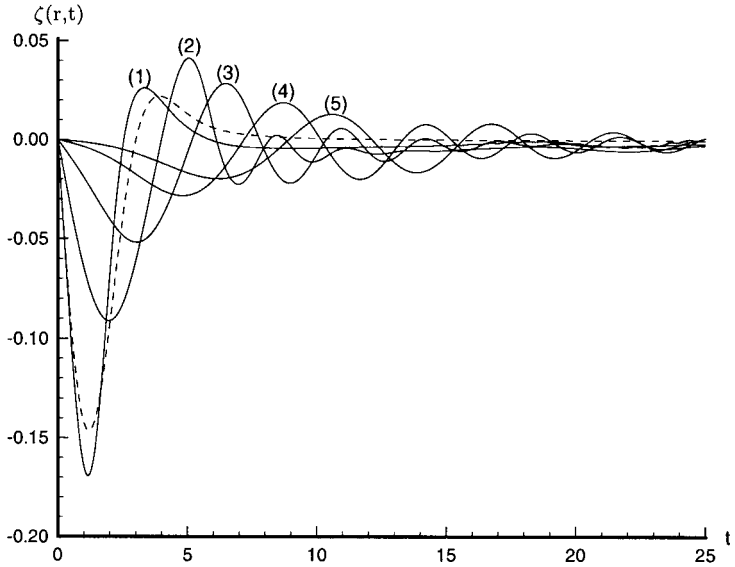

Figure 15.42: Time histories of the free-surface elevation for sub-critical $\mathcal{F}_r = 0.1$ at different radii $r =$ (1) 0; (2) 1; (3) 2; (4) 4; (5) 6. The dashed line is the elevation at $r = 0$ from linear theory according to Eq. (15.7.40) (from Xue and Yue, 1998, *J. Fluid Mech.* Reproduced by permission of Cambridge University Press).

written in closed form (Wehausen and Laitone, 1960). The corresponding free-surface elevation is given by

$$\zeta(r,t) = -2\mathcal{F}_r \int_0^\infty k^{1/2} \sin(k^{1/2}t) \mathrm{e}^{-k} J_0(kr)\, \mathrm{d}k\,. \tag{15.7.40}$$

It is easy to see (e.g. using integration by parts) that the integral terms in (15.7.40) vanish with increasing time for any finite r, so that the linearized result does predict asymptotic steady state. In Fig. 15.42, we plot the linear solution of the free-surface elevation at the origin $\zeta(0,t)$. It is seen that the linear solution behaves similarly to the fully-nonlinear result.

Super-critical regime: $\mathcal{F}_r > \mathcal{F}_{r2} \approx 0.1930$

For $\mathcal{F}_r$ greater than a critical value of $\mathcal{F}_{r2} \approx 0.1930$, the solution is characterized by a rapid cusp-like collapse of the free surface towards the sink. The decrease of the surface elevation is everywhere monotonic in time. We are able to compute well after the cusp is developed, limited by the spatial discretizations and minimum temporal increment we use. Eventually, as the free surface approaches the sink, the velocity asymptotically

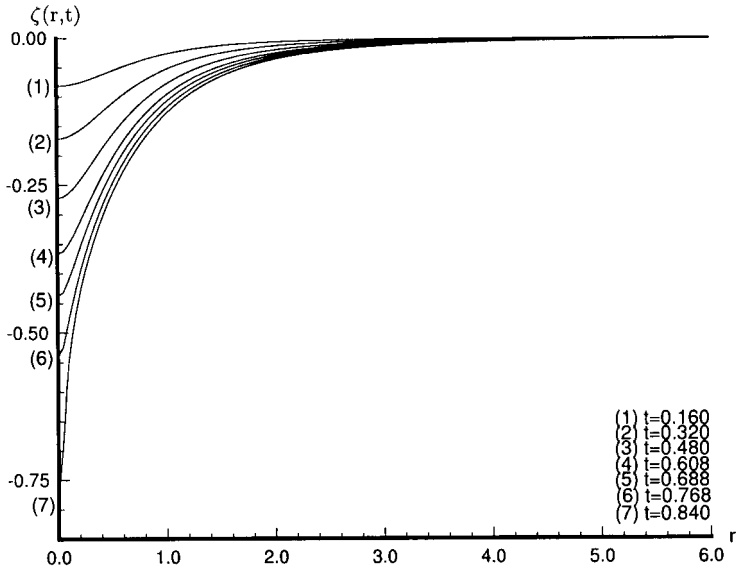

Figure 15.43: Free-surface profiles at different times for super-critical $\mathcal{F}_r = 0.24$. The horizontal and vertical scales are different, and the sink is at $z = -1$ (from Xue and Yue, 1998, *J. Fluid Mech.* Reproduced by permission of Cambridge University Press).

develops an inverse square singularity, and the simulations finally break down.

Figure 15.43 shows typical super-critical results for the case of $\mathcal{F}_r = 0.24$ for the instantaneous free-surface profiles $\zeta(r, t)$ at different times of the development of the center dip. The decrease in elevation is everywhere monotonic in time and monotonically increasing with decreasing radial distance for all time, eventually developing a cusp-like profile. Such a solution behavior for the super-critical regime can be expected from physical arguments at least in the limiting case. As $\mathcal{F}_r$ increases, the effect of the sink eventually dominates that of gravity, and the solution then resembles that of a single point sink.

The overall dynamics can be elucidated by examining the pressure field (e.g. Zhou and Graebel, 1990). Figure 15.44 plots the pressure contours at three instants corresponding to early, intermediate and late stages of the free-surface collapse. At an early time (Fig. 15.44(a)), there are two zero pressure lines: the free surface, and an another line inside the fluid domain around the sink. There exist then a region of positive pressure and a

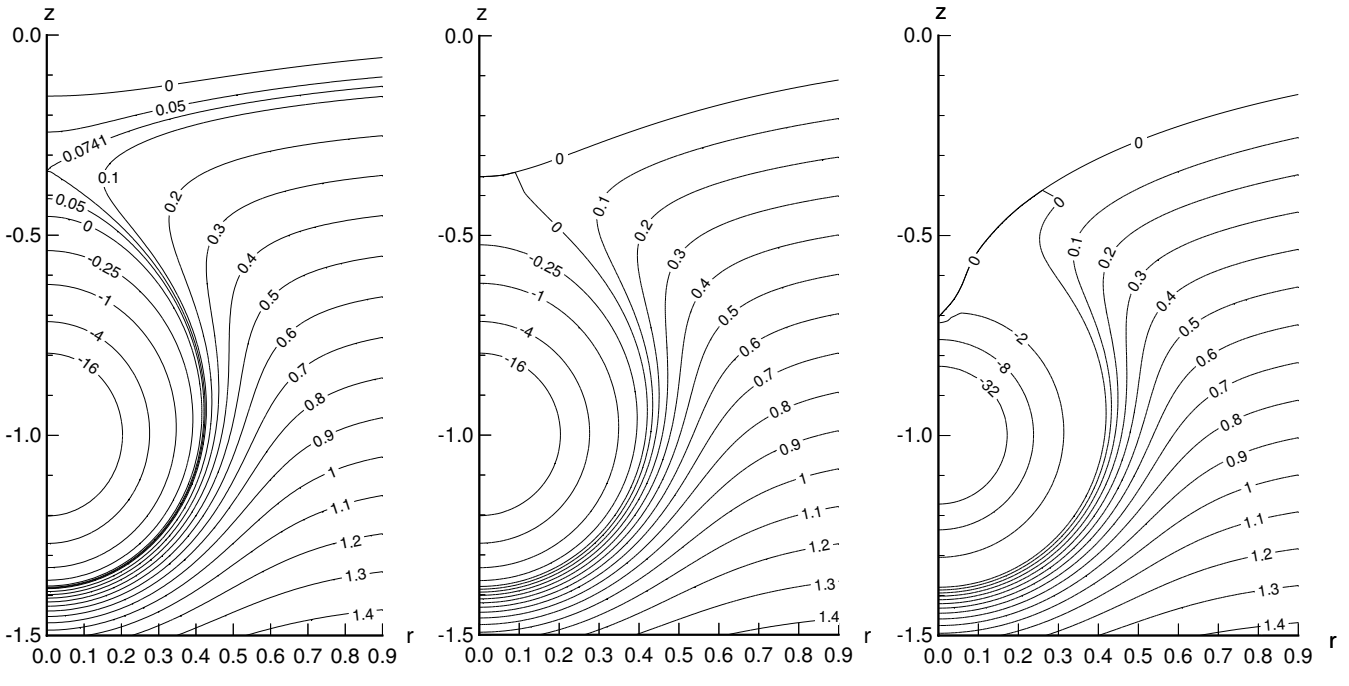

(*a*) (*b*) (*c*)

Figure 15.44: Constant pressure contours for super-critical $\mathcal{F}_r = 0.24$ at three stages of the evolution at $t =$ (*a*) 0.288; (*b*) 0.592; (*c*) 0.828. The vertical and horizontal scales are different (from Xue and Yue, 1998, *J. Fluid Mech.* Reproduced by permission of Cambridge University Press).

pressure maxima above the sink below the free surface. As time progresses (Fig. 15.44(b)), the interior zero pressure line connects to the free surface, eliminating the positive pressure region above the sink. The pressure gradient on the centerline above the sink obtains a single sign (directed from the sink to the free surface). This pressure gradient increases rapidly as the free surface drops closer to the sink (Fig. 15.44(c)). The simulation eventually breaks down when the free surface reaches the location of the sink.

Trans-critical regime: $0.1924 \approx \mathcal{F}_{r1} < \mathcal{F}_r < \mathcal{F}_{r2} \approx 0.1930$

As we pointed out, the sub-critical solution behavior (with an asymptotic steady state) is suggested, at least for small $\mathcal{F}_r$, from linear theory, while the super-critical solution (with a developing center dip) can be anticipated from physical arguments, at least in the limit of very large $\mathcal{F}_r$. Careful and systematic search of the solution space, however, reveal clearly a small but distinct trans-critical regime.

The solution in this trans-critical regime is characterized by a sharp reversal near the origin of the initially downward motion of the free surface eventually developing into a sharp upward jet immediately above the sink. Such an upward jet has some resemblance to that observed in Zhou and Graebel (1990) for a tank with small draining rate. Similar jets are also often observed when the cavity in a bubble collapses or when steep gravity waves approach a vertical sea-wall or a ship's hull (Longuet–Higgins and Oguz, 1997).

A plot of the flow field after the free-surface reversal reveals clearly the flow structure. This is shown in Fig. 15.45 at $t = 1.38$ which is in the final stage of the upward jet development. The most prominent feature is the presence of a stagnation point above the sink (at $z \sim -0.52$) similar to that in the case of sub-critical withdrawal. A dividing streamline emanating from this stagnation point and becoming almost parallel to the free surface some distance away divides the flow field into two regions. In the lower region, the flow converges smoothly towards the sink. In the region above the dividing streamline, the velocity is tangent to the free surface some distance away forming a slightly downward converging jet-like sheet. As this radial jet converges towards the center, the velocity is directed upwards over a very small distance, reaching large magnitudes at the origin near the free surface below a sharp upward jet.

We remark that the present results are for an abrupt start-up of the sink. For the effect of gradual start-up, the reader is referred to Xue (1997)

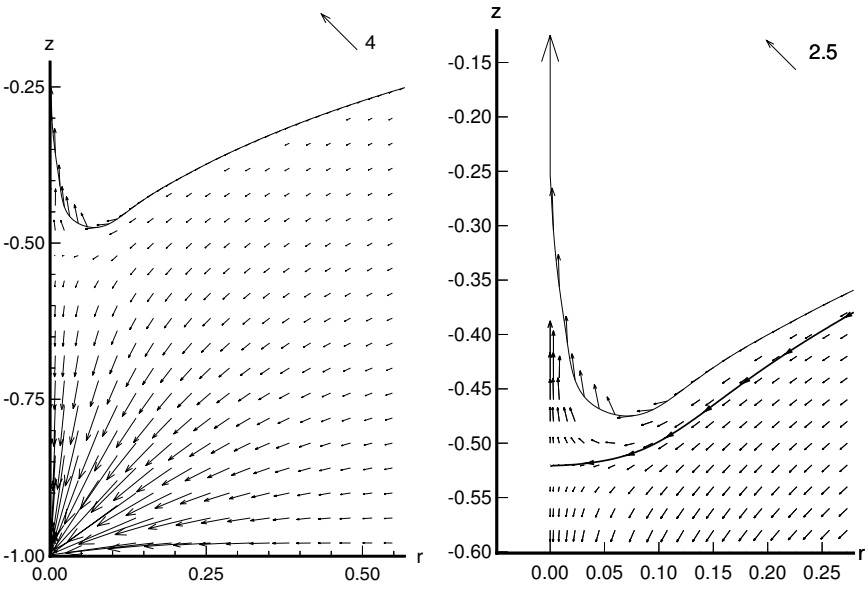

(*a*) (*b*)

Figure 15.45: Velocity field for trans-critical $\mathcal{F} = 0.1927$ at $t = 1.38$ for (*a*) "outer"; and (*b*) close-up views. In (*b*) the dividing streamline ending at the stagnation point near $(0, -0.52)$ is also plotted. The sink is at $z = -1$ and the vertical and horizontal scales are equal in each case. Reference vectors are given above (from Xue and Yue, 1998, *J. Fluid Mech.* Reproduced by permission of Cambridge University Press).

and Xue and Yue (1998). The problem considered here of a fixed sink and constant volume flux rate is also a special case. The computational method used here is, in fact, general and can be extended in straightforward ways to account for effects such as a sink in motion, time varying drain rates, and the presence of boundaries.

15.7.7 Application to Plunging Wave Impact on a Vertical Wall

Large pressures and loads associated with breaking wave impact on sea walls, ships, and offshore structures are important subjects in ocean engineering. The magnitudes of the impact pressure maxima are related to the type of breaking waves, among which plunging breakers usually produce the largest impact pressures on the structures. In this section, the impact of a plunging breaker on a rigid vertical wall is considered.

Both field measurements (Miller et al., 1974; Blackmore and Hewson, 1984; Führböter, 1986; Whillock, 1987) and model experiments (Bagnold, 1939; Hayashi and Hattori, 1958; Kirkgöz, 1990, 1991; Schmidt et al., 1992; Oumeraci et al., 1993; Hattori et al., 1994, for impact of shallow-water breaking waves; Chan and Melville, 1988, Chan, 1994, for impact of deep-water breaking waves) have shown that the impact pressure history due to a plunging breaker striking a vertical wall is of high intensity ($10 \sim 100$ kPa) and short duration ($10^{-1} \sim 10^{-3}$ sec.). One mechanism responsible for the generation of high pressure intensities is attributed to the direct collision of the fluid body in the region of the plunger tip and the wall surface (Lundgren, 1969; Schmidt et al., 1992). Another mechanism is related to the effect of an air cushion trapped between the concave boundary of the plunger surface and the wall (Bagnold, 1939; Hayashi and Hattori, 1958; Chan and Melville, 1988; Hattori et al., 1994). These studies also show that the measured magnitude and rise time of the impact pressure maxima are marked by large scatter and lack of repeatability, even under nearly identical experimental conditions. Furthermore, they are highly sensitive to local impact conditions, such as the inclination angle and position of the wall relative to the approaching breaker (e.g. Whillock, 1987; Kirkgöz, 1990, 1991; Chan and Melville, 1988).

Significantly, effective scaling laws for extrapolating from model to prototype scales are as yet unavailable (e.g. Führböter, 1986), in large part due to the lack of understanding of mechanisms associated with the trapped air. Bagnold (1939) presented a piston model to approximate the trapped-air impact process as an adiabatic compression of a column of fluid mass in an air-filled rigid cylinder. His model correlates the impact pressure maxima to the ratio of the length of the column of the 'kinetic mass' of water to the thickness of the air pocket. Führböter (1986) pointed out that different parameters, and hence scaling laws, must be employed in different flow regions in the impact process. Stive (1984) indicated that the parameter $P_0/\rho U^2$ must be scaled if the deceleration of the water after impact is governed by the compression of the enclosed air. Here, P_0 is the initial air (atmospheric) pressure in the air pocket, ρ the fluid density, and U the (initial) impact velocity of breaking waves normal to the wall. A number of other scaling criteria have also been proposed in wave impact and water-entry problems (Whiteman and Pancione, 1973; see also summaries in Hayashi and Hattori, 1958; Stive, 1984; Blackmore and Hewson, 1984).

Although there are many experimental studies on breaking wave impact, few corresponding analytical and numerical studies are available. The

essential physics involved in the impact process however can be captured in the simplified theoretical framework of potential flow. Compressibility of the fluid is ignored in view of the fact that the impacting plunging breaker is wedge-like as it strikes the wall and that the impact velocity is much less than the speed of sound in the fluid (Korobkin and Pukhnachov, 1988). Furthermore, viscosity and surface tension effects can be neglected since inertia forces are dominant during the impact (Cooker and Peregrine, 1991).

In this context, numerical simulations were performed by Vinje and Brevig (1980, 1981) who employed a MEL boundary-integral method to calculate the forces on solid bodies due to plunging breaker impact. Due to difficulties in evaluating the impact pressures, particularly at the initial stage of the impact, the forces were obtained by calculating the time derivative of the pressure impulse. Using classical impulse theory (Lamb, 1932) and the MEL boundary-integral method of Dold and Peregrine (1986), Cooker and Peregrine (1992, 1995) obtained the pressure impulse due to a breaking wave striking a vertical wall. Their theory was used by Chan (1994) to compare with experiments, and it was extended by Topliss (1994) to cases involving waves sloshing in a container, and wave impact with entrained air and its effect on a flexible wall. Since these studies rely on the impulse theory, they do not provide a complete description of the impact process and require ad hoc parameters to estimate the size of the impact area and the duration of the impact.

Despite recent progress, a number of important questions associated with the plunging wave impact problem remain unresolved. For instance: (1) How can the initial stage of the plunger impingement on the wall be properly characterized and simulated? (2) What are the most important scaling parameters governing the trapped-air wave impact process? (3) How do the maximum value and duration of the impact pressure scale with these parameters? To assist in answering these open questions, Zhang et al. (1996) performed a numerical study of the impact of a two-dimensional plunging wave on a rigid vertical wall in the context of potential flow. The plunging wave generated by a piston wavemaker is simulated using a MEL-BIE scheme (described in Section 15.6.1). The initial stage of the impact is characterized by an oblique impact of a liquid wedge on the wall and described by a similarity solution. Following the initial impact, the simulation with a trapped air pocket is continued using MEL with the trapped air described by polytropic gas law. Based on systematic MEL simulations (sixty in all) and direct comparisons to experiments, they concluded that the maximum wall impact pressure can be well scaled by the local parameters of

the breaker at the instant of impact: U, the horizontal impact velocity; h, the depth of the plunger tip; ℓ and H, the width and height of the air cushion; and P_0 the initial air pocket pressure (atmospheric pressure). Among these, the dimensionless parameters $P_0/\rho U^2$ and ℓ/h are found to be most important, and provide the scaling laws for the maximum impact pressure, $P_m/\rho U^2$, and the rise time of this pressure, $T_r U/\sqrt{H\ell}$. In the following, we briefly outline their simulation procedure and present representative results of the free-surface profiles and maximum impact pressure on the wall during impact.

Simulation scheme

The simulation of a plunging wave impacting a vertical wall can be divided into three stages: (i) the generation of the plunger to the point just before the impact ($0 \le t < t_I$); (ii) the initial stage of the impact from the instant $t = t_I$ when the plunger tip touches the wall, to the instant $t = t_I + \Delta t_I$ just after the converging plunger jet tip converts into a diverging jet spreading along the wall; and (iii) the subsequent evolution ($t > t_I + \Delta t_I$) involving a trapped air pocket. In the present approach, the direct MEL simulations are carried out for the stages before and after the initial impact, and a similarity solution is derived and used for the initial impact stage (ii).

Definition sketches corresponding to stages (i) and (iii) are shown in Figs. 15.46(a) and 15.46(b), respectively. The fluid flow in a rectangular numerical tank of length L_0 and initial water depth h_0 is described by Cartesian coordinates (x, y) and time t. The origin of the coordinate system is located at the intersection between the still water level ($y = 0$) and the y-axis which is directed vertically up. A piston wave maker, S_L, is located at $x = 0$ initially, and a rigid wall, S_R, is on the right end of the tank at $x = L_0$. The bottom of the tank and the free surface are denoted as S_B and S_f, respectively. Unless otherwise noted, we non-dimensionalize the problem, hereafter (in this section), by selecting mass, length and time units such that the fluid density $\rho \equiv 1$, the gravitational acceleration $g \equiv 1$, and initial tank depth $h_0 \equiv 1$.

At $t = 0$, the piston wave maker S_L moves abruptly from rest to a constant velocity U_0. It travels a distance L_1 and then stops. Due to the phase focusing of the different frequency components, a plunging breaker is created towards the far wall. To provide an additional adjustment of the characteristics of the resulting breaking wave, a channel of length L_e and height h_e at the bottom of S_R is opened at $t = 0$, maintained up to the instant of impact t_I, and is closed thereafter. For definiteness, we

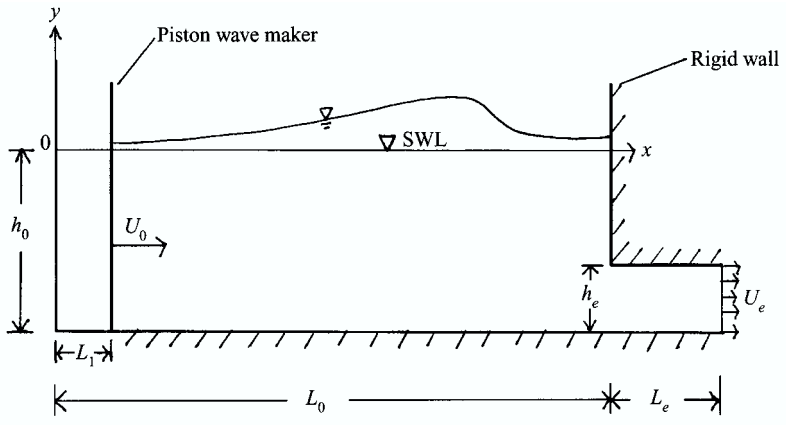

(*a*)

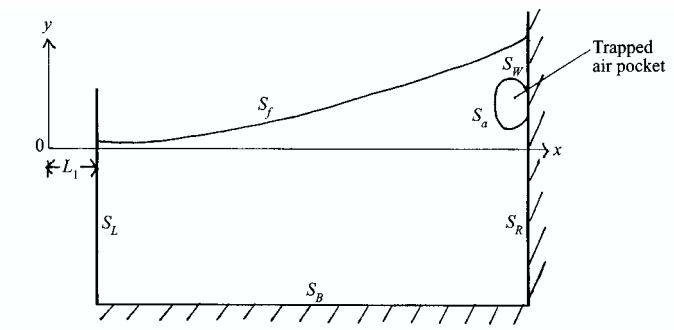

(*b*)

Figure 15.46: Definition sketches for a plunging wave impact on a vertical wall in a numerical tank for (*a*) before impact; and (*b*) after impact (from Zhang et al., 1996, *J. Fluid Mech.* Reproduced by permission of Cambridge University Press).

fix $L_e = L_0/5$, and set the horizontal exit velocity in the channel to be uniform given by $U_e = \sqrt{10 y_R}$, where y_R is the height of the water line on S_R. The channel height h_e is left as a parameter of the simulation to be adjusted. This is a convenient procedure to create trapped air pockets of different sizes and at different locations on the wall. Different breaking wave profiles and kinematics are obtained by numerical testing and adjusting the parameters L_0, L_1, U_0 and h_e. Typically, a plunging breaker impacts S_R in the form of an oblique wedge. After impact (see Fig. 15.46(*b*)), this plunger

tip spreads out into a wetted area S_W on the wall, trapping an air pocket below between the interior free surface of the breaker, S_a, and the wall.

During the short period of the initial stage of impact, $t_I \le t \le t_I + \Delta t_I$, the effect of the trapped air represented by its volume change is negligible, and a local solution can be obtained by modeling the jet tip as a liquid wedge moving with uniform constant velocity towards the plane wall. A similarity solution for the case of non-symmetric oblique impact of a liquid wedge can be obtained using the method of Borisova et al. (1959) who considered the case of symmetric normal impact.

For $t > t_I + \Delta t_I$, the trapped air significantly affects the impact process, especially the maximum impact pressure. On S_a, as a dynamic boundary condition, the (water) pressure equals the trapped air pressure $P_a(t)$. Assuming an adiabatic process in the air pocket, P_a is modelled using a polytropic gas law (e.g. Cole, 1948),

$$\frac{P_a(t)}{P_0} = \left(\frac{V_0}{V_a(t)}\right)^{\gamma_a} \tag{15.7.41}$$

where $V_a(t)$ is the instantaneous volume (area) of the air pocket, V_0 its initial value at impact, and γ_a the polytropic gas constant. For air, $\gamma_a = 1.4$ is used in the simulations. One simple way to account for air leakage effects is to adjust the value of γ_a.

The MEL simulations for the plunging wave impact on a vertical wall are carried out starting from rest ($t = 0$) until the time of impact at $t = t_I$. During the initial stage of the impact, $t_I < t < t_I + \Delta t_I$, the similarity solution of oblique impact of a liquid wedge on a wall is applied. At $t = t_I + \Delta t_I$, the numerical solution at a small horizontal distance from the wall is then matched to the similarity solution. The numerical simulations are continued again with a trapped air pocket for $t > t_I + \Delta t_I$. Such a patching allows a smooth continuation of the MEL simulation and a convergent pressure history. With appropriate treatment of the spray roots (e.g. Zhao and Faltinsen, 1993), the MEL simulations can be carried out through a number of oscillations of the air pocket.

Direct comparison with experiments

To assess the validity and usefulness of the simulation scheme, a direct simulation of and comparison to the experiment of Chan and Melville (1988) is performed for the impact of a deep-water breaking wave against a vertical wall. The specific case considered corresponds to case "(b)" of Chan and Melville (1988). The numerical simulation duplicates exactly the

experimental conditions in terms of the vertical wall location, $L_0 = 11.75$, and the paddle motion of the wave maker (Dommermuth et al., 1988). In the experiments, the physical still water depth is $h_0 = 0.6$ m, and for comparison to the measurements, the density of water ρ, gravity g and atmospheric pressure P_0 are set at 10^3 kg/m^3, 10 m/s^2 and 10^2 kN/m^2, respectively.

Figure 15.47 shows the free-surface profiles before and after impact at different time instants obtained from nonlinear MEL simulations and from

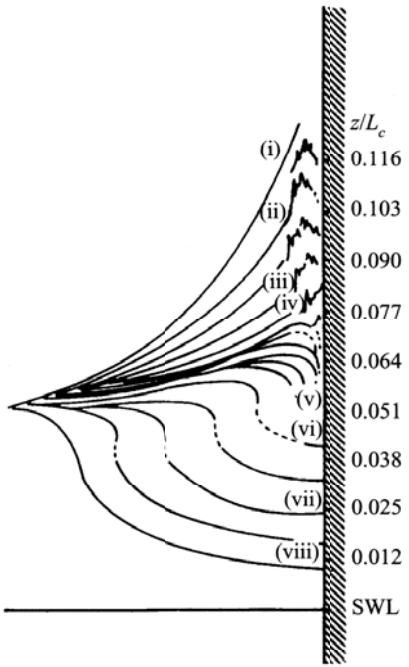

(a)

Figure 15.47: (a) Surface profiles of the experiments of Chan and Melville (1988) obtained from high-speed films at *ca.* 1100 frames per second. The time from the start of the wave maker in seconds for each profile are: (i) 17.014; (ii) 17.004; (iii) 16.984; (iv) 16.979; (v) 16.968; (vi) 16.964; (vii) 16.944; and (viii) 16.924. Elevations relative to still water level (SWL) are also indicated. The parameters of the experiment are: $h_0 = 0.6$ m, $L_0/h_0 = 11.755$, and characteristic incident wave period $T_c = 1.136$ s and wavelength $L_c = 1.936$ m. Free-surface profiles from nonlinear MEL simulations before impact (b) at $t - t_I = -0.134$ (— ·· —); -0.072 (— · —); -0.053 (——); -0.017 (- - - -); -0.001 (——); and during impact (c) at $t - t_I = 0$ (——); 0.017 (- - - -) ; 0.026 (— · —); 0.039 (— — —); 0.054 (— ·· —) (from Zhang et al., 1996, *J. Fluid Mech.* Reproduced by permission of Cambridge University Press).

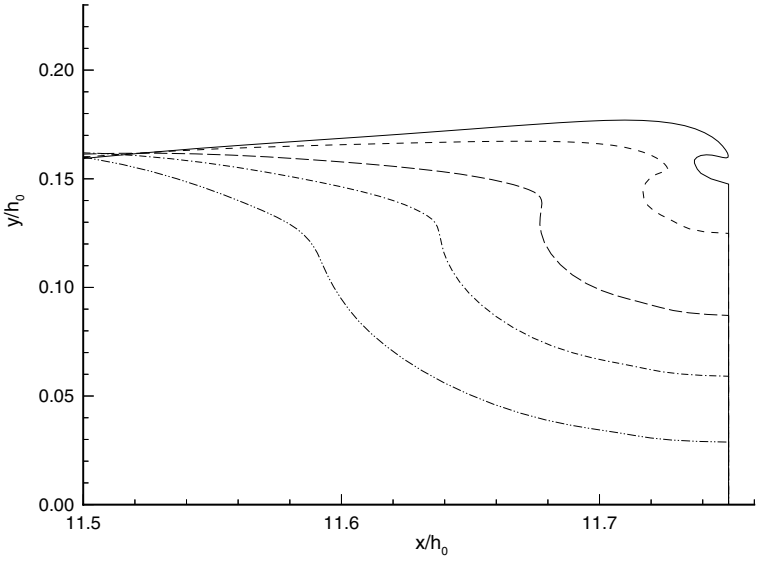

(*b*)

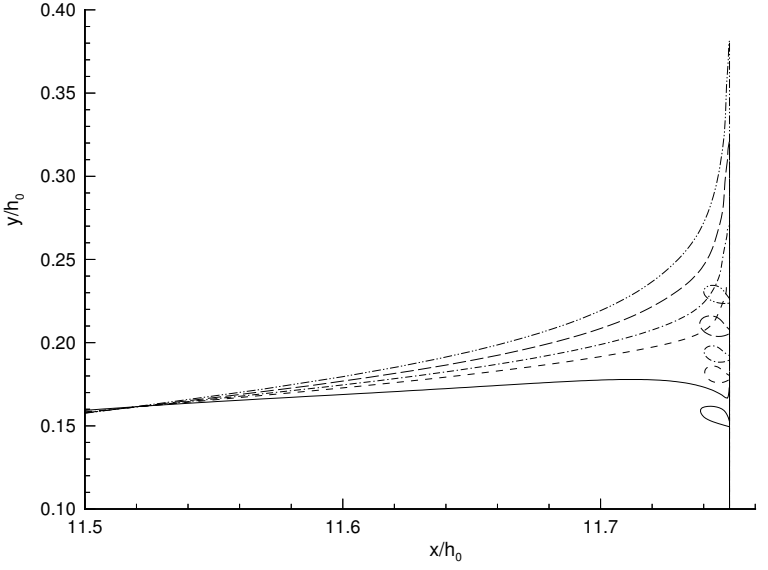

(*c*)

Figure 15.47 (*Continued*)

experiments of Chan and Melville (1988). Before impact, at $t-t_I \approx -0.053$, as the contact point on the wall ascends to about $y = 0.08$, the computed height of the plunger tip is 0.14. The corresponding value from the experiment (cf. profile (vii) in Fig. 15.47(a) is about 0.15 (the conversion factor from the experiment is $L_c/h_0 \simeq 3.23$). At the instant of impact, the height of the computed impact point is approximately 0.16, while this value in the experiment is between $0.17 \sim 0.20$. The time of impact is $t_I \simeq 51.18$ from the calculation, while the estimated value from the experiment is between $51.15 \sim 51.19$. As for the size of the air pocket at impact, an accurate reading from the experiment is difficult, although a qualitative estimate is still possible. From Fig. 15.47(a), if one measures the vertical distance between $z/L = 0.051$ and 0.064 and estimates the actual pocket dimension at the instant of impact to be approximately half that distance, one obtains a value of $H \approx \ell \approx 0.021$. This is to be compared with calculated values of $H = 0.016$ and $\ell = 0.013$. The qualitative agreement is still reasonable.

In the experiment of Chan and Melville (1988), the maximum horizontal crest speed of the breaking wave is measured in the absence of the vertical wall to be about 2 m/s ($U \simeq 0.82$), but no impact velocity at the instant of the impact is given. The numerical simulation shows a horizontal velocity of the plunger tip, U, increasing from ~ 1.0 at an instant $t - t_I \simeq -0.07$ before impact to ~ 1.37 at the instant of impact. The upward vertical tip velocity of the spreading jet on the wall just after impact at $y = 0.17$ and $t - t_I \simeq 0.0012$ is about 5.4. From Fig. 10(j) of Chan and Melville (1988), the vertical velocity of the jet tip at a similar stage is estimated to be about 4.9. Overall, the simulation of the impact wave profile and velocities agree with the experimental values to within about 10%.

Figure 15.48 compares the computed and measured maximum impact pressures on the wall. The simulation results, Fig. 15.48(a), give the wall pressure distribution at the instant, T_r, when P_m is reached. Our simulations show that the maximum pressures in the vicinity of P_m (close to the air pocket) are also reached at approximately the same time instant. Thus the pressure profile(s) in Fig. 15.48(a) near P_m can be considered to be also the maximum wall pressures at these locations. Far from P_m, this is no longer true, and the value there should not be considered to be the maxima reached. The main interest, of course, is in P_m and values in its vicinity.

For comparison, the measured peak pressures at seven locations from repeated runs of Chan and Melville (1988) (see also Chan, 1986) are plotted

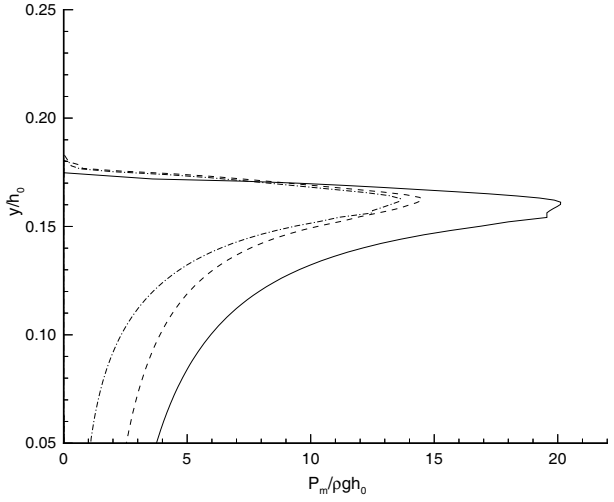

(*a*)

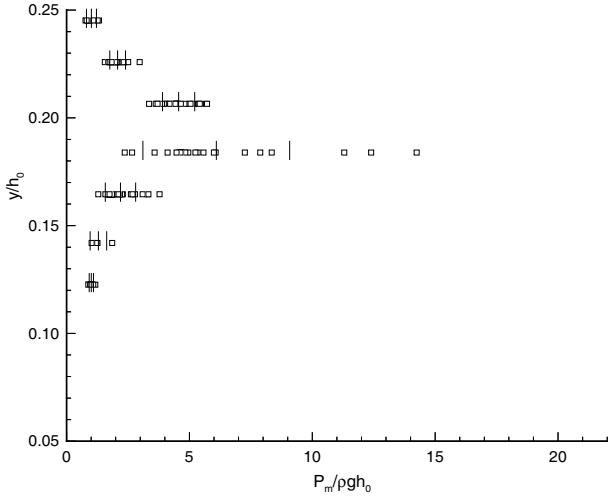

(*b*)

Figure 15.48: Wall impact pressure profile at the instant P_m is reached. (*a*) Numerical simulations for: $\gamma_a = 1.4$ (at $t - t_I = 0.003$) (——); $\gamma_a = 0.5$ (at $t - t_I = 0.004$) (- - -); and $\gamma_a = 0.5$ for an elastic wall (at $t - t_I = 0.004$) (— · —). (*b*) Experimental measurements of Chan (1986) and Chan and Melville (1988) in repeated runs at seven locations. The three vertical bars indicate respectively the mean value and mean plus and minus one standard deviation of the measured values (from Zhang et al., 1996, *J. Fluid Mech.* Reproduced by permission of Cambridge University Press).

on the same scale in Fig. 15.48(b). Comparing the two, we note that the computed P_m (using $\gamma_a = 1.4$) is $\simeq 20.2$ which is reached at $t - t_I \simeq 0.003$ at a location of $y \simeq 0.16$. This maximum pressure is about three times (~ 4.5 standard deviations) higher than the mean measured value of the maximum wall pressure ($P_m \simeq 6$) which is obtained at approximately the same location. Away from P_m, the measured maximum values decrease rapidly with depth and are lower than those from the computed profile. Indeed, the overall qualitative comparison would be better if the computed profile(s) can be reduced (shifted) by a constant value. For discussions on the effects of other physical factors such as spray, air leakage, and hydroelasticity, the reader is referred to Zhang et al. (1996).

15.7.8 Application to Nonlinear Wave Interaction with Floating Bodies

As a final illustration of the MEL approach, we apply the method (using QBEM) to the problem of nonlinear wave diffraction of periodic Stokes waves by a surface-piercing truncated vertical cylinder. Of particular interest is the quantification of high-order high-frequency "ringing" loads on the cylinder that have been observed in the field and measured in experiments.

Large compliant offshore structure with high-natural-frequency low-damping resonances are often observed to be excited by high-harmonic nonlinear wave loads. Such phenomena are termed "ringing" and have been reported in a number of recent studies (e.g. Davies, Leverette and Spillane, 1994; Krokstad and Stansberg, 1995; Chaplin, Rainey and Yemm, 1997). To evaluate the importance of nonlinear diffraction effects to ringing excitation, frequency-domain perturbation analysis can be extended to higher-order. The extension to second-order is now well established (e.g. Kim and Yue, 1989; Chau and Eatock Taylor, 1992[3]). The observation that ringing often occurs at the third (or even higher) harmonic of the fundamental incident frequency spurred recent perturbation analysis at the third order. These include the third-order diffraction theory of Faltinsen, Newman and Vinje (1995), who made a further assumption of long incident waves; and Malenica and Molin (1995), who solved the problem for arbitrary incident wavelength. Both theories apply (only) to the case of a vertical circular

[3]For a variation of Chau and Eatock Taylor (1992) which can be extended to a sea bed of mild slope, see Section 13.12.

cylinder in a regular (mono-chromatic) incident wave. The predictions of Faltinsen, Newman and Vinje (1995) and Malenica and Molin (1995) differ appreciably in the magnitude of the third-order force (except for very small incident frequency) and markedly in the phase of that force. In addition to expected difficulties in extending such theories to more general geometries, fully-nonlinear effects for steep waves may also limit the usefulness of such perturbation approaches. Given the analytic complexity even at third order, extension to multiple wave interactions and especially to higher orders (which may be called for in some applications) is formidable. Recently, Rainey (1995) refined Morison's formula to include third-order effects of the incident wave field. Chaplin, Rainey and Yemm (1997) showed that this simple model tends to substantially over-estimate the ringing wave excitation even for a small cylinder.

Given the physical nature of this problem, a perhaps more efficacious approach is to tackle the nonlinear wave-body interaction problem directly in time domain and then obtain the harmonic forcing of interest from the nonlinear limit-cycle force histories. In this direction, Ferrant (1996) developed a linear boundary element method based on the semi-Lagrangian formulation and applied it to study the problem of wave diffraction of mild long waves by a bottom-mounted vertical cylinder. Recently, Liu, Xue and Yue (2001) employed the MEL/BIE approach with quadratic boundary elements for a fully-nonlinear time-domain simulation of the diffraction of Stokes incident waves by a surface-piercing cylinder. Their prediction of the high-harmonic (ringing) force components compares remarkably well to available experimental measurements for the third harmonic third-order horizontal forcing on the cylinder. These results are outlined below.

We consider the fully-nonlinear three-dimensional wave diffraction by a surface-piercing body in a Stokes incident wave. To be specific, we perform fully-nonlinear three-dimensional MEL simulation of the diffraction of an exact (2D) Stokes wave train (Schwartz, 1974) by a surface-piercing vertical truncated circular cylinder radius R and (still-water) draft D. The Stokes wave has wavelength $\lambda = 2\pi/k$, fundamental period $T = 2\pi/\omega$, and steepness kA. We consider the initial-value problem (cf. Section 15.2) to obtain the nonlinear (horizontal) force history $F(t)$. The simulations are continued until (limit-cycle) steady-state $F(t)$ is obtained from which the harmonic force amplitudes and phases are extracted by Fourier analysis.

The approach to steady state of the normalized complex amplitudes of the harmonic components is monitored by using Fourier integration over moving time:

$$f^{(0)}(t) = (kA)^{-2} \cdot \frac{1}{T} \int_t^{t+T} F(\tau)\, \mathrm{d}\tau\,, \tag{15.7.42}$$

$$f^{(m)}(t) = (kA)^{-m} \cdot \frac{2}{T} \int_t^{t+T} F(\tau) \mathrm{e}^{\mathrm{i}n\omega\tau}\, \mathrm{d}\tau\,, \quad m = 1, 2, \ldots\,; \tag{15.7.43}$$

where the leading-order magnitudes of the harmonics are factored out. The amplitude of $f^{(m)}(t)$ is simply $|f^{(m)}(t)|$, while its phase (relative to the incident wave) is:

$$\theta^{(m)}(t) \equiv \frac{1}{m}\{\arg[f^{(m)}(t)] + 2n\pi\}\,, \quad m = 1, 2, \ldots\,; \quad n = 0, \pm 1, \pm 2, \ldots\,. \tag{15.7.44}$$

In the simulation, for spatial discretization, $N_c \times N_z$ QBEM nodes on the vertical cylinder surface are used. For the cylinder geometries considered, typically $N_z = N_c/2$ is used. Accounting for elements on the cylinder bottom, we thus have a total of $9N_c^2/64$ (9-node) quadratic elements on the body surface. (For a doubly-periodic computational domain of length $L/\lambda = 1$ and width $W/L = 0.6$, the total number of free-surface quadratic elements is approximately $0.006N_c^2LW/R^2$.) For time evolution, dynamic time stepping with Courant number $C_n = 0.2$ and $\Delta t_{\max} = T/100$ is employed. Due to the transverse symmetry of the problem, only half of the computational domain and cylinder are used in the simulation.

A main interest is to predict the (steady-state) harmonic force amplitudes/phases using fully-nonlinear time-domain (MEL) simulations. In particular, we seek to obtain prediction up to third harmonic $m = 3$, for which experimental (ringing force) data are available. For the regular (exact) Stokes incident waves, we study three wavelengths (relative to body dimension) given by: $kR = 0.22$, 0.29 and 0.39; and three wave amplitudes to wavelength ratios: $kA = 0.130$, 0.148 and 0.20 (A/R varies from 0.34 to 0.91).

Based on convergence tests, we use $N_c = 24$, and continue simulations up to $t_S = O(5T)$. With this t_S, a (doubly periodic) computational domain size $L = 3\lambda$ and $W = 1.5\lambda$ is found to be sufficient. With these computational parameters, for all cases, relative mass and energy are conserved

to within $O(10^{-7})$ and $O(10^{-4})$ respectively; and convergence in $f^{(m)}$ is expected to be less than $O(1\%)$ for $m = 0$, 1 and 2; and well within $O(5\%)$ for $m = 3$.

First- and second-harmonic forces

Figure 15.49 shows the approach to steady-state of the harmonic amplitudes ($m = 0, 1, 2, 3$) for the problem with $kR = 0.22$ and $kA = 0.133$. At $t/T = O(3.5)$, the coefficient $|f^{(1)}|$ has converged to less than 1%, while $|f^{(2)}|$ exhibits a small oscillation of less than 2% amplitude. Table 15.9 shows the comparisons of predicted $|f^{(m)}|$, $m = 1$, 2 (MEL) with: experimental measurements (Krokstad and Stansberg, 1995, hereafter MARINTEK); second-order frequency-domain (axisymmetric) computations (Kim and Yue, 1989, hereafter KY); and the (frequency-domain) small-body asymptotic theory of Faltinsen, Newman and Vinje (1995) (hereafter FNV). It should be pointed out that the fully-nonlinear time-domain prediction differs from frequency-domain results (even for the first harmonic) because

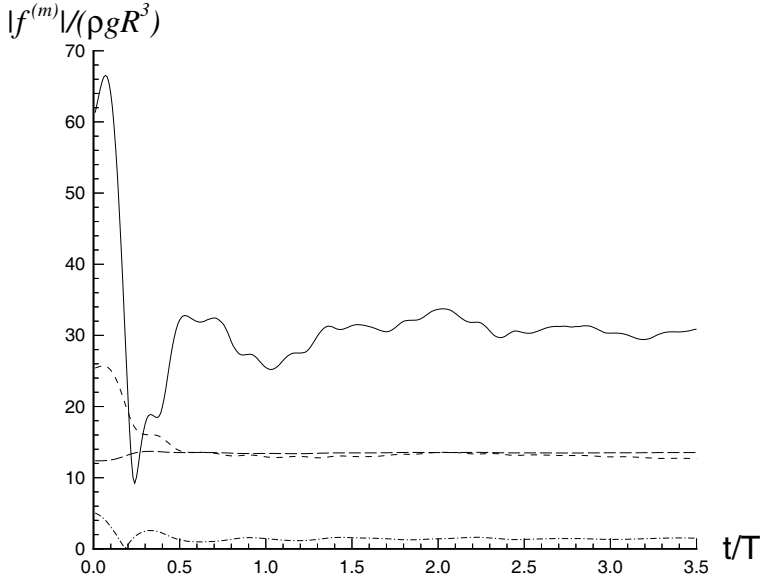

Figure 15.49: Time evolutions of the magnitude of the harmonic components, $|f^{(m)}|$, $m = 0$ (— · —), 1 (– – –), 2 (- - -) and 3 (——), of the nonlinear longitudinal force $F(t)$ on a vertical circular cylinder in Stokes incident waves ($kR = 0.22$, $kA = 0.133$, $D/R = 3$) (from Liu et al., 2001, *J. Fluid Mech.* Reproduced by permission of Cambridge University Press).

Table 15.9: Comparisons of the first- and second-harmonic force amplitude $|f^{(1)}|$ and $|f^{(2)}|$ on a truncated vertical cylinder ($D/R = 3$) among: experimental measurements (Krokstad and Stansberg, 1995, MARINTEK); fully-nonlinear (MEL) simulations; second-order frequency-domain (axisymmetric) computations (Kim and Yue, 1989, KY); and (c) (frequency-domain) small-body asymptotic theory of Faltinsen, Newman and Vinje (1995) (FNV). For MARINTEK and MEL, $kA = 0.133$ and 0.148 for $kR = 0.22$ and 0.39 respectively.[a]

	$\frac{\lvert f^{(1)}\rvert}{(\rho g R^3)}$		$\frac{\lvert f^{(2)}\rvert}{(\rho g R^3)}$	
	$kR = 0.22$	$kR = 0.39$	$kR = 0.22$	$kR = 0.39$
MARINTEK	13.64	11.07	10.85	3.04
MEL	13.41	11.18	12.97	2.87
KY	13.28	10.99	14.86	4.38
FNV	13.93	11.31	16.64	9.85

[a] From Liu et al. (2001).

the former, in general, contains all other nonlinear interactions also operating at this harmonic (Section 15.3.4). In this sense, the frequency-domain result of harmonic m is merely the *leading-order* term of the fully-nonlinear m-th harmonic amplitude. With this understanding, the differences between MEL and KY predictions are expected to increase with nonlinearity. Thus the differences between MEL and KY in Table 15.9 increase with kA and kR, as expected.

Comparing MEL to MARINTEK, the values for $|f^{(1)}|$ agree to about $1 \sim 2\%$, while for $|f^{(2)}|$ the discrepancies range from $6 \sim 19\%$. In contrast, FNV substantially over-predicts the harmonic amplitudes in all cases, with the over-prediction increasing rapidly with increasing kR. This is not unexpected since FNV is formally a low-kR and low-kA theory with a range of validity for the wavelength likely to be lower than the kR range considered here (see e.g. Malenica and Molin, 1995).

Third-harmonic force

This is the case of main interest in the context of ringing excitations. Table 15.10 compares the values of $|f^{(3)}|$ obtained from: fully-nonlinear (MEL) simulations; experiments (MARINTEK); small-body asymptotic theory (FNV); and the third-order (frequency-domain) theory of Malenica and Molin (1995) (hereafter MM). Considering that the quantities in question are third order (in wave steepness), the present MEL results compare remarkably well with the experimental measurements of MARINTEK with the differences between the two within $O(2\%)$ for the shorter incident

Table 15.10: Comparisons of the third-harmonic force amplitude $|f^{(3)}|k^3/(\rho g)$ on a truncated vertical cylinder ($D/R = 3$) among: experimental measurements (MARINTEK); fully-nonlinear (MEL) simulations; small-body asymptotic theory (FNV); and the third-order (frequency-domain) theory of Malenica and Molin (1995) (MM). For MARINTEK and MEL, $kA = 0.133$, 0.130 and 0.148 for $kR = 0.22$, 0.29 and 0.39 respectively.[a]

	$kR = 0.22$	$kR = 0.29$	$kR = 0.39$
MARINTEK	0.27	0.489	0.50
MEL	0.33	0.47	0.50
FNV	0.30	0.51	0.95
MM	0.28	0.52	0.97

[a] From Liu et al. (2001).

wavelengths $kR = 0.29$ and 0.39, and $O(20\%)$ for the longer wavelength $kR = 0.22$. In the physical experiment, the lower $kR \sim 0.22$ case has an associated Keulegan-Carpenter number $K_c \equiv \pi A/R \sim 2$, and non-potential flow effects may play a (minor) role. To assess this, we add a Morison-type quadratic drag term to $F(t)$:

$$F_D(t) = F(t) + \rho R C_D \int_{-D}^{\zeta} U|U| \, \mathrm{d}z \,, \tag{15.7.45}$$

where C_D is an empirical drag coefficient, and $U = U(z,t)$ is the (nonlinear) incident wave field velocity on the central axis of the cylinder. With $C_D = 1$, we obtain $|f_D^{(3)}|k^3/(\rho g) = 0.291$ which halves the original difference and is now $\sim 12\%$ above the measurement value. For the cases with $KR = 0.29$ and 0.39, $K_c = 1.4$ and 1.2, respectively, and non-potential flow effects are much less important.

The frequency-domain perturbation theories compare reasonably well to each other and acceptably so relative to MEL and experiments for the smaller kR cases. As kR increases, FNV and MM increasingly over-predict $|f^{(3)}|$, and for the $kR = 0.39$ case we studied they exceed measurements and fully-nonlinear computations by almost a factor of 2. As noted earlier, fully-nonlinear time-domain MEL differs from frequency-domain perturbation theories because, in addition to the leading-order term(s) perturbation theories predict, MEL contains also higher-order nonlinear contributions at a given harmonic. Such higher-order contributions increase with nonlinearity. In general, nonlinearity increases due to two independent factors: increase in the incident wave steepness kA, and increase in the (local) diffracted wave

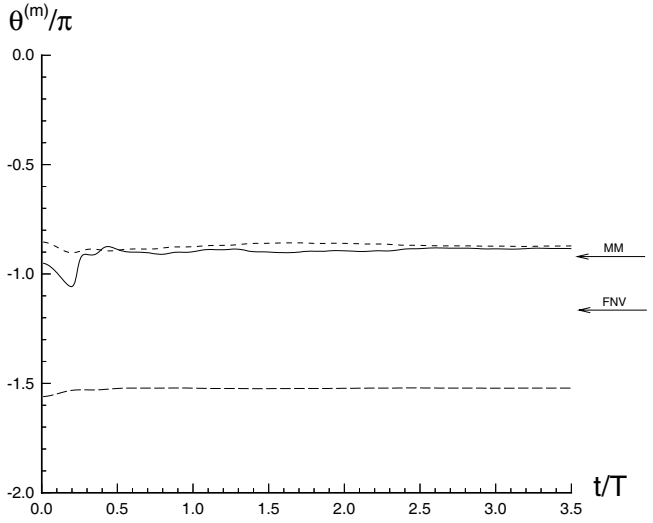

(*a*)

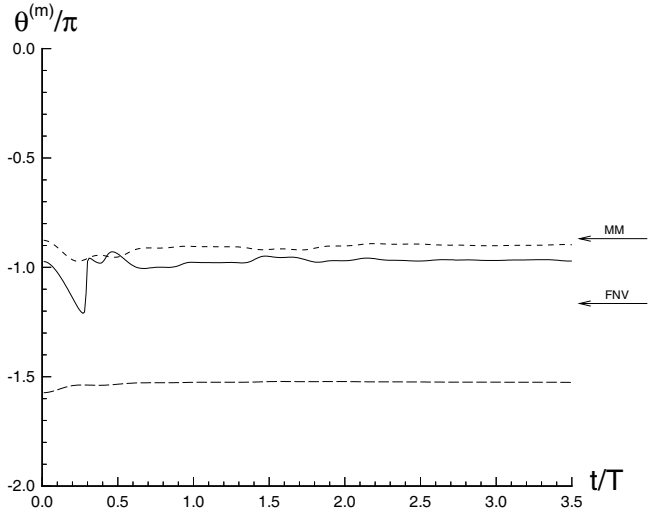

(*b*)

Figure 15.50: Phases (relative to incident wave) of the longitudinal force harmonics on a vertical circular cylinder ($D/R = 3$) in Stokes incident waves: (*a*) $kA = 0.133$, $kR = 0.22$; and (*b*) $kA = 0.130$, $kR = 0.29$. The results shown are: fully-nonlinear MEL $\theta^{(m)}(t)$, $m = 1$ (– – –); 2 (- - -); 3 (——); and frequency-domain predictions of $\theta^{(3)}$ from MM and FNV (from Liu et al., 2001, *J. Fluid Mech.* Reproduced by permission of Cambridge University Press).

steepness which generally increases with the diffraction parameter kR. Our computations and experimental measurements indicate that, for this range of kR, the latter factor is dominant. This explains the substantially larger discrepancies in the frequency-domain perturbation results for larger kR.

For the range of kR in Table 15.10, the FNV and MM predictions of $|f^{(3)}|$ agree reasonably well with each other. As shown in Fig. 15.51, appreciable differences in $|f^{(3)}|$ appear for $kR > 0.4$. This is somewhat in deviance with the results of Malenica and Molin (1995) which show a large discrepancy between FNV and MM (in the contribution associated with the product of the first- and second-order potentials) even for very small kR (50% difference for $kR \sim 0.035$). The significant difference between FNV and MM, however, is the prediction of the phase $\theta^{(3)}$ of $f^{(3)}$. According to FNV, $\theta^{(3)} = \pi/6 + 2n\pi/3$ (for some integer n) and is independent of

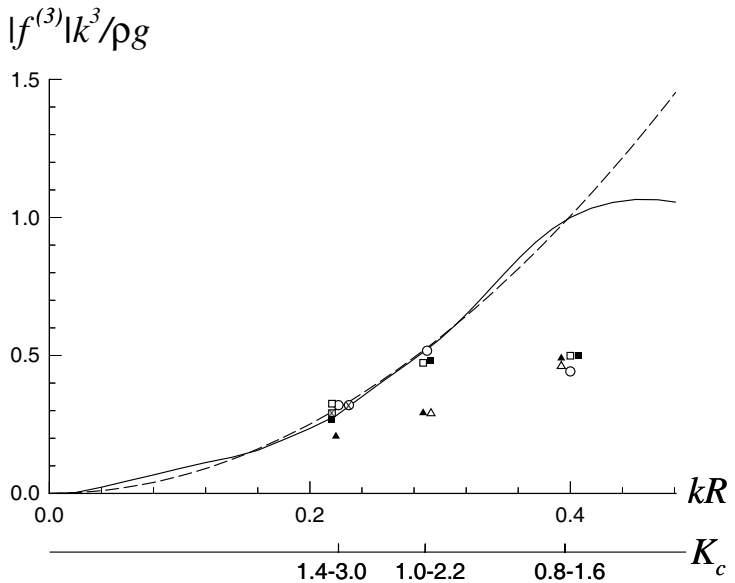

Figure 15.51: Third-harmonic "ringing" horizontal wave force amplitude $|f^{(3)}|k^3/\rho g$ for a surface-piercing vertical circular cylinder ($D/R = 3$) in Stokes incident waves of different (relative) wavelengths kR and amplitudes kA. The results shown are: experimental measurements, MARINTEK for $kA \sim 0.15$ (■) and 0.20 (▲); and fully-nonlinear MEL simulations for $kA \sim 0.10$ (⊗/◯, with/without drag correction), 0.15 (■/□, with/without drag correction) and 0.20 (△). The range of Keulegan-Carpenter numbers $K_c \equiv \pi A/R$ for the range of kA considered are indicated. For comparison, frequency-domain perturbation results of FNV (- - -) and MM (——) (which are independent of kA after the normalization in $|f^{(3)}|$) are also plotted (from Liu et al., 2001, *J. Fluid Mech.* Reproduced by permission of Cambridge University Press).

kR. As expected, $\theta^{(3)}$ from the complete (arbitrary kR) third-order MM varies with kR. Figure 15.50 shows the time histories of $\theta^{(m)}$, $m = 1$, 2, 3 from fully-nonlinear MEL simulations for two values of kR (see Xue (1997) for additional cases). For the simulation time used, the time histories have long approached their limit-cycle values. These values can be compared to the (frequency-domain) predictions of FNV and MM, which are also shown. The present fully-nonlinear predictions tend to agree with MM. The comparison is better for lower kR values (as expected from the discussions of the diffracted wave nonlinearity earlier). On the other hand, the FNV predictions differ appreciably for these values of kR.

Systematic MEL computations similar to the above are conducted for a range of incident wave parameters. The selection of parameters is guided by the experimental cases reported in MARINTEK. Figure 15.51 summarizes the comparisons for the normalized third-harmonic ("ringing") force amplitude $|f^{(3)}|$. Also plotted are the frequency-domain perturbation results of FNV and MM. As mentioned earlier, for the lower kR, flow separation effects may play a role. To provide an assessment, the Keulegan-Carpenter number $K_c \equiv \pi A/R$ (for the range of kA considered) is noted on a second horizontal axis. For the lowest $kR = 0.22$ case, the MEL result with the (Morison-type) drag correction (cf. (15.7.45)) is also shown.

Considering the fact that $|f^{(3)}|$ is a third-order quantity, the overall excellent agreement between MEL and MARINTEK is remarkable. For $kR = 0.22$, the addition of a Morison-type correction improves the comparison somewhat but the discrepancies are small in either case. In contrast, the FNV and MM predictions are acceptable only for lower kR and smaller values of kA. For the case of $kR = 0.29$, for example, perturbation results are good for $kA < 0.15$ but differ from fully-nonlinear simulations and experiments by $O(70\%)$ for $kA \sim 0.20$. As (local diffracted wave) nonlinearity increases with kR, these discrepancies increase and perturbation theories over-predict $|f^{(3)}|$ by $O(100\%)$, for example, for $kR = 0.39$, even for relatively small incident steepness of $kA \sim 0.1$.

We remark that the computational parameters for the present MEL simulations are chosen to provide reliable predictions up to $m = 3$. In theory even higher-order force harmonics $m = 4, 5, \ldots$, can be of practical interest. These can, in principle, be obtained similarly by direct fully-nonlinear MEL computations at higher resolutions.

In addition to the work we described, recent years have seen continuous active development and extensions of MEL applications to fully-nonlinear

wave and wave-body problems. Notable representative examples include the calculation of three-dimensional breaking waves on sloping beach (Grill et al., 2001), simulation of ship slamming and water impact (Zhao and Faltinsen 1993), and recent extensions to include wave overtopping and green-water on deck (Greco and Faltinsen, 2005).

Taken together, these and the recent and ongoing developments in HOS methods we described earlier, have brought the simulation of potential-flow based nonlinear wave dynamics to a relatively mature level. These help set the stage for developments into new directions and areas replete with opportunities and challenges. These developments, broadly speaking, fall into two categories. First is the extension of these simulations into large-scale applications taking advantage of modern high-performance computing capabilities. Several such developments are mentioned at the conclusion of Section 15.6. Second is the incorporation of important physics and processes not now modelled or not describable by potential-flow free-surface formulation. Basic examples of the latter include computational investigations of free-surface turbulence (e.g. Shen et al., 1999; Shen and Yue, 2001), and effects of surfactant on free-surface vortical/turbulent flows (e.g. Tsai and Yue, 1995; Shen, Triantafyllou and Yue, 2004), and air-sea coupled wave boundary layers (Liu et al. 2004). Advanced topics include simulation of breaking and post-breaking processes, and the interactions of these with bodies and bottom.

References

The numbers in square brackets refer to the page numbers where the references have been cited in the text.

Abbot, M. B. (1979). *Computational Hydraulics*, Pitman, New York. [625]

Ablowitz, M. J. and A. C. Newell (1973). The decay of the continuous spectrum for solutions of the Korteweg–de Vries equation. *J. Math. Phys.* **14**: 1277–1284. [670, 674, 775, 866]

Ablowitz, M. J., D. J. Kaup, A. C. Newell, and H. Segur (1974). The inverse scattering transform — Fourier analysis for nonlinear problems. *Studies Appl. Math.* **LIII 4**: 249–336. [670, 676, 776]

Ablowitz, M. J. and H. Segur (1981). *Solitons and the Inverse Scattering Transform*, Society Industrial and Applied Mathematics, Philadelphia. [670, 674, 775, 886]

Abramowitz, M. and I. A. Stegun (1972). *Handbook of Mathematical Functions*, Dover, New York. [708]

Agnon, Y. and A. Sheremet (2000). Stochastic evolution models for nonlinear gravity waves over uneven topography. *Advances in Coastal and Ocean Engineering* **6**: 103–131, ed. P. L.-F. Liu, World Scientific, Singapore. [878]

Akylas, T. R., (1984). On the excitation of long nonlinear water waves by a moving pressure distribution. *J. Fluid Mech.* **141**: 455–466. [718]

Akylas, T. R. (1987). Unsteady and nonlinear effects near the cusp lines of the Kelvin ship-wave pattern. *J. Fluid Mech.* **175**: 333–342. [917, 923]

Alber, I. E. (1978). The effects of randomness on the stability of two-dimensional surface wavetrains. *Proc. R. Soc. Lond. A* **363**: 525–546. [977]

Anderssen, K. H., M-L. Chbanol and M. van Hencke (2001). Dynamical models for sand ripples beneath surface waves. *Phys. Rev. E*, **63**, 066308 1–8. [527]

Annenkov, S. Y. and V. I. Shrira (2001). Numerical modelling of water-wave

evolution based on the Zakharov equation. *J. Fluid Mech.* **449**: 341–371. [876]

Aranha, J. A., C. C. Mei, and D. K. P. Yue (1982). Nonlinear waves near a cut–off frequency in an acoustic duct – A numerical study. *J. Fluid Mech.* **121**: 465–485. [769]

Armstrong, J. A., N. Bloembergen, J. Ducuing, and P. S. Pershan (1962). Interactions between light waves in a nonlinear dielectric. *Phys. Rev.* **127**: 1918–1939. [697, 703, 707]

Arthur, R. S. (1962). A note on the dynamics of rip currents. *J. Geophys. Res.* **67**: 2777–2779. [609]

Bagnold, R. A. (1939). Interim report on wave pressure research. *J. Inst. Civ. Eng.* June, 202–226. [1024]

Bagnold, R. A. (1946). Sand movement by waves: Some small scale experiments with sand of very low density. *J. Inst. Civil Eng.* **27**: 457. [542]

Banner, M. L. and D. H. Peregrine (1993). Wave breaking in deep water. *Annu. Rev. Fluid Mech.* **25**: 373–397. [989]

Bartholomeuz, E. F. (1958). The reflection of long waves at a step. *Proc. Cambridge Philos. Soc.* **54**: 106–118. [135, 138]

Batchelor, G. K. (1967). *An Introduction to Fluid Dynamics*, Cambridge University Press, London. [5, 437]

Battjes, J. A. (1972). Set up due to irregular waves. *Proc. 13th Conf. Coastal Eng. ASCE* **2**: 1993–2004. [608]

Battjes, J. A. (1974a). Computation of set-up long shore currents, run-up and overtopping due to wind generated waves. *Communications on Hydraulics*, Dept. of Civil Engineering, Delft University of Technology, Report 74-2. [570–574]

Battjes, J. A. (1974b). Surf similarity. *Proc. 14th Conf. Coastal Eng. ASCE* 466–480. [570]

Battjes, J. A. (1975). Modeling of turbulence in the surf zone. *Proc. Symp. Modeling Techniques ASCE* 1050–1061. [589]

Battjes, J. A. (1988). Surf-zone Dynamics. *Ann. Rev. Fluid Mech.* **20**: 257–293. [609]

Benjamin, T. B. (1967). Instability of periodic wave trains in nonlinear dispersive systems. *Proc. R. Soc. Lond. A* **299**: 59–75. [763]

Benjamin, T. B. and J. E. Feir (1967). The disintegration of wave trains on deep water. *J. Fluid Mech.* **27**: 417–430. [745, 760, 763]

Benjamin, T. B. and M. J. Lighthill (1954). On cnoidal waves and bores. *Proc. R. Soc. Lond. A* **244**: 448–460. [658]

Benney, D. J. (1962). Nonlinear gravity wave interactions. *J. Fluid Mech.* **14**: 574–584. [697, 858, 889]

Benney, D. J. (1966). Long nonlinear waves in fluid flows. *J. Math. Phys.* **45**: 52–63. [612]

Benney, D. J. and J. C. Luke (1964). On the interactions of permanent waves of finite amplitude. *J. Math. Phys.* **43**: 309–313. [666-670]

Benney, D. J. and A. C. Newell (1967). The propagation of nonlinear wave envelopes. *J. Math. Phys.* **46**: 133–139. [770]

Benney, D. J. and G. J. Roskes (1969). Wave instabilities. *Studies Appl. Math.* **48**: 377–385. [746, 747, 764, 765, 870]

Berger, U. and S. Kohlhase (1976). Mach reflection as a diffraction problem. *Proc. 15th Conf. Coastal Eng. ASCE* **1**: 796–814. [810]

Blackmore, P. A. and P. J. Hewson (1984). Experiments on full-scale wave impact pressures. *Coastal Eng.* **8**: 331–346. [1024]

Blondeaux, P., (1990). Sand ripples under sea waves. Part 1. Ripple formation. *J. Fluid Mech.* **218**: 1-17. [526]

Blondeaux, P., (2001). Mechanics of coastal forms. *Ann. Rev. Fluid Mech.* **33**: 339–370. [526]

Boczar-Karakiewicz, B. (1972). Transformation of wave profile in shallow water — a Fourier analysis. *Arch. Hydrotechniki* **19**: 197–210. [694, 695, 708, 709]

Bolt, B. A. (1978). *Eurrhquukes — A Primer*, Freeman, San Francisco. [688]

Boussinesq, J. (1877). Essai sur la théorie des eaux courantes. *Mém. Prés. Acad. Sci. Paris* (*Ser.* 2) **23**: 1–680. [611]

Boussinesq, J. (1878). Complement a úne étude intitulée: "Essai sur la théorie des eaux courante" et á un memoire "Sur l'influence des frottments sur leo mouvements regulier des fluids." *J. Math. Pures Appl.* **4**: 335. [688]

Bowen, A. J. (1969). The generation of longshore currents on a plane beach. *J. Marine Res.* **27**: 206–214. [549, 578, 588, 609]

Bowen, A. J. (1969). Rip currents, I. Theoretical investigations. *J. Geophys. Res.* **74**: 5467–5478. [609]

Bowen, A. J. (1972). Edge waves and the littoral environment. *Proc. 13th Conf. Coastal Eng. ASCE* 1313–1320. [609]

Bowen, A. J. and R. T. Guza (1978). Edge waves and surf beat. *J. Geophys. Res.* **83**: 1913–1920. [609]

Bowen, A. J. and D. L. Inman (1969). Rip currents II. Laboratory and field observations. *J. Geophys. Res.* **74**: 5479–5490. [609, 642]

Bowen, A. J., D. L. Inman, and V. P. Simmons (1968). Wave set-down and set-up. *J. Geophys. Res.* **73**: 2569–2577. [576, 577, 579]

Breit, S. R. (1991). The potential of a rankine source between parallel planes and in a rectangular cylinder. *J. Engng. Math.* **25**, 151–163. [984]

Bretherton, F. P. (1964). Resonant interaction between waves. *J. Fluid Mech.* **20**: 457–480. [697, 858]

Brown, E. D. S. B. Buchsbaum, R.E. Hall, J.P.Penhue, K.F. Schmitt, K. M. Watson, and D.C. Wyatt. (1989). Observations of a nonlinear soitary wave packet in the Kelvin wake of a ship. *J. Fluid Mech.* **204**: 263–293. [817]

Bryant, P. J. (1973). Periodic waves in shallow water. *J. Fluid Mech.* **59**: 625–644. [697, 701, 708, 709]

Bryant, P. J. (1983). Cyclic gravity waves in deep water. *J. Australian Math. Soc.* **25**: 2–15. [893]

Byatt-Smith, J. G. B. and M. S. Longuet-Higgins (1976). On the speed and profile of steep solitary waves. *Proc. R. Soc. Lond. A* **350**: 175–189. [658]

Byrd, P. F. and M. D. Friedman (1971). *Handbook of Elliptic Integrals for Engineers and Scientists*, Springer-Verlag. [861]

Canuto, C., M. Y. Hussaini, A. Quarteroni and T. A. Zang (1988). *Spectral methods in fluid dynamics*, Springer-Verlag. [956]

Carrier, G. F. (1966). Gravity waves on water of variable depth. *J. Fluid Mech.* **24**: 641–659. [637]

Carrier, G. F. and H. P. Greenspan (1957). Water waves of finite amplitude on a sloping beach. *J. Fluid Mech.* **4**: 97–109. [571, 632, 636, 637]

Carrier, G. F., M. Krook, and C. E. Pearson (1966). *Functions of a Complex Variable — Theoy and Technique*, McGraw-Hill, New York. [29, 263]

Carter, T. G., P. L. F. Liu, and C. C. Mei (1973). Mass transport by waves and offshore sand bedforms. *J. Waterways, Harbours Coastal Eng. Div. ASCE* **99**: 165–184. [510, 517,519, 522, 524, 525]

Chan, E. S. (1986). *Deep water breaking wave forces on structures.* Sc.D. Thesis, MIT, Dept. of Civil Engineering. [990, 1031]

Chan, E. S. (1994). Mechanics of deep-water plunging-wave impacts on vertical structures. *Coastal Engng.* **22**: 115–133. [1025]

Chan, E. S. and W. K. Melville (1988). Deep-water plunging wave pressure on a vertical plane wall. *Proc. R. Soc. Lond.* A**417**: 95–131. [1024, 1028, 1031]

Chaplin, J. R. (1984). Nonlinear forces on a horizontal cylinder beneath waves. *J. Fluid Mech.* **147**, 449-464. [947, 951]

Chaplin, J. R., R. C. Rainey and R. W. Yemm (1997). Ringing of a vertical cylinder in waves. *J. Fluid Mech.* **350**: 119–147. [1033, 1034]

Charkrabarti, S. K. (1972). Nonlinear wave forces on vertical cylinders. *J. Hydraul. Div. ASCE* **98**: 1895–1909. [826]

Charkrabarti, S. K. (1978). Comments on second order wave effects on large diameter vertical cylinder. *J. Ship Res.* **22**: 266–268. [826]

Chau, F.P. and R. Eatock Taylor (1992). Second-order wave diffraction by a vertical cyliinder. *J. Fluid Mech.* **240**: 571-599. [826, 834, 836, 1033]

Chen, M. Y. (2005) *Second-order diffraction by regular or random waves.* PhD thesis, Civil and Environmental Engineering, Mass. Inst. Tech. [826, 836]

Chen, T. G. (1961). Experimental studies on the solitary wave reflection along a straight sloped wall at oblique angle of incidence. *U. S. Beach Erosion Board Tech. Mem.* **124**. [809]

Chen, X. N. and S. D. Sharma (1995). A slender ship moving at a near-critical speed in a shallow channel. *J. Fluid Mech.* **291**: 263–285. [718, 728, 729]

Chu, V. C. and C. C. Mei (1970). On slowly varying stokes waves. *J. Fluid Mech.* **41**: 873–887. [747, 756, 771, 773]

Chu, V. C. and C. C. Mei (1971). The nonlinear evolution of stokes waves in deep water. *J. Fluid Mech.* **47**: 337–352. [746, 775, 779, 786]

Clément, A. (1996). Coupling of two absorbing boundary conditions for 2D time-domain simulations of free surface gravity waves. *J. of Computational Physics* **126**: 139. [984]

Coddington, D. A. and N. Levinson (1955). *Theory of Ordinary Differential Equations.* McGraw-Hill, New York. [964]

Cohen, B. I., K. M. Watson and B. J. West (1976). Some properties of deep water solitons. *Phys. of Fluids* **19**: 345–354. [889]

Cointe, R. (1989). Nonlinear simulation of transient free surface flows. In *Proc.*

5th Intnl. Conf. Num. Ship Hydro., Hiroshima, 239–250. National Academy Press, Washington. [948]

Colagrossi, A., M. Landrini and O. Faltinsen (2003). Sloshing in 2-D flows by the SPH method. *Proc. of 8th international conference on numerical ship hydrodynamics*, Busan, Korea. [886]

Cole, J. D. (1968). *Perturbation Methods in Applied Mathematics*, Blaisdell, Waltham, Mass. [56, 690]

Cole, R. H. (1948). Underwater explosions. *Princeton Univ. Press, Princeton, NJ*, 274. [1028]

Cole, S. L. (1985). Transient waves produced by flow past a bump. *Wave Motion* **7**: 579–587. [718, 730]

Collings, I. L. (1986). Two infinite-Froude-number cusped free-surface flows due to a submerged line source or sink. *J. Austral. Math. Soc.* B**28**: 260. [1015]

Cooker, M. J. and D. H. Peregrine (1991). Wave breaking and wave impact pressures. *Development in Coastal Engineering* (Ed. Peregrine & Loveless), University of Bristol, 47–64. [1025]

Cooker, M. J. and D. H. Peregrine (1992). Wave impact pressure and its effect upon bodies lying on the sea bed. *Coastal Eng.* **18**: 205–229. [1025]

Cooker, M. J. and D. H. Peregrine (1995). Pressure-impulse theory for liquid impact problems. *J. Fluid Mech.* **297**: 193–214. [1025]

Courant, R. and K. O. Friedrichs (1949). *Supersonic Flow and Shock Waves*, Interscience, New York. [621]

Courant, R. and D. Hilbert (1962). *Methods of Mathematical Physics II*, Interscience, New York. [621]

Crapper, G. D. (1972). Nonlinear gravity waves on steady non-uniform currents. *J. Fluid Mech.* **52**: 713–724. [120]

Crawford, D. R., B. M. Lake, P. G. Saffman, and H. C. Yuen (1981). Stability of weakly nonlinear wave in two or three dimensions. *J. Fluid Mech.* **105**: 177–191. [764, 768, 866–871, 889]

Cummins, W. E. (1962). The inpulse response functions and ship motion. *Schiffstechnik* **9**: 101–109. [442]

Dagan, G. (1972a). Nonlinear ship waves theory. *Proc. 9th Symp. Naval Hydro.*, Paris, 1697–1737. [917]

Dagan, G. (1972b). Small Froude number paradoxes and wave resistance at low speeds. *Hydronautics Tech. Report* **7103-4**. [917]

Dailey, J. W. and S. C. Stephan, Jr. (1952). The solitary wave — its celerity, profile, internal velocities and amplitude attenuation in a horizontal smooth channel. *Proc. 3rd Conf. Coastal Eng. ASCE*, 13–30. [658]

Dalrymple, R. A. (1975). A mechanism for rip current generation on open coast. *J. Geophys. Res.* **80**: 3485–3487. [609]

Davey, A. (1972). The propagation of a weak nonlinear wave. *J. Fluid Mech.* **53**: 769–781. [746, 756]

Davey, A. and K. Stewartson (1974). On three-dimensional packets of surface waves. *Proc. R. Soc. Lond. A* **338**: 101–110. [747, 760]

Davies, A. G. and A. D. Heathershaw (1984). Surface-wave propagation over sinusoidally varying topography. *J. Fluid Mech.* **144**: 419–443. [934]

Davies, K. B., S. J. Leverette and M. W. Spillane (1994). Ringing response of TLP and GBS platforms. *Proc. BOSS'94 Conference*(ed: C. Chryssostomidis), Cambridge, Massachusetts. [1033]

Dawson, C. W. (1977). A practical computer method for solving ship-wave problems. *Proc. 2nd Int. Conf. Num. Ship Hydro.*, Berkeley, 30–38. [917]

Dean, W. R. (1948). On the reflection of surface waves by a submerged circular cylinder. *Proc. Camb. Phil. Soc.* **44**, 483–491. [947]

De Best, A. and E. W. Bijker (1971). Scouring of a sand bed in front of a vertical breakwater. *Communications on Hydraulics*, Dept. of Civil Engineering, Delft University of Technology, Report 71-1. [524]

Djordjevic, V. D. and L. G. Redekopp (1978). On the development of packets of surface gravity wave moving over an uneven bottom. *J. Appl. Math. Phys.* **29**: 950–962. [808]

Doctors, L. J. and R. F. Beck (1987). Convergence properties of the Neumann-Kelvin problem for a submerged body. *J. Ship Research* **31**: 1–13. [917]

Dold J. W. (1992). An efficient surface-integral algorithm applied to unsteady gravity waves. *J. Comput. Phys.* **103**: 90–115. [986]

Dold, J. W. and D. H. Peregrine (1986). An efficient boundary-integral method for steep unsteady water waves. *Numerical Methods for Fluid Dynamics II (ed. K.W. Morton and M.J. Baines)*, Oxford University Press, 671–679. [1025]

Dommermuth, D. G., and D. K-P. Yue (1987). A higher-order spectral method for the study of nonlinear gravity waves. *J. Fluid Mech.* **184**: 267-288. [889, 890, 985-987, 1015, 1017]

Dommermuth, D. G. and D. K. P. Yue (1987b). Numerical simulations of nonlinear axisymmetric flows with a free surface. *J. Fluid Mech.* **178**: 195–219. [985–987, 1015, 1017]

Dommermuth, D. G. and D. K. P. Yue (1988a). The nonlinear three-dimensional waves generated by a moving surface disturbance. *Proc. 17th Symp. on Naval Hydro., Hague, Netherlands.* Washington DC: National Academy Press. [918, 923]

Dommermuth, D. G. and D. K. P. Yue (1988b). A high-order equation for shallow-water waves. *Proc. 3rd Intl. Wrksp. Water Waves & Floating Bodies*, Woods Hole, MA. [900]

Dore, B. D. (1976). Double boundary layers in standing surface waves. *Pure Appl. Geophys.* **114**: 629–637. [521, 535]

Dore, B. D. (1977). On mass transport velocity due to progressive waves. *Q. J. Mech. Appl. Math.* **30**: 157–173. [536, 544]

Dore, B. D. (1978). Some effects of the air–water interface on gravity waves. *Geophys. Astrophys. Fluid Dynamics* **10**: 215–230. [543, 544]

Dysthe, K. B. (1979). Note on a modification to the nonlinear Schrödinger equation for application to deep water waves. *Proc. R. Soc. Lond. A* **369**: 105–114. [865, 870, 888]

Eagleson, P. S. (1965). Theoretical study of longshore currents on a plane beach. Hydraulics Lab., Massachusetts Institute of Technology, Technical Report 82. [549]

Ertekin, R. C. (1984). *Soliton Generation by Moving Disturbances in Shallow Water* PhD Theis, Univ. Calif. Berkeley, 352pp. [718–720]

Ertekin, R. C., W. C. Webster and J. V. Wehausen, (1986). Waves by a moving disturance in a shallow channel of finite width. *J. Fluid Mech.* **169**: 275–292. [718]

Faltinsen, O. M., J. N. Newman and T. Vinje (1995). Nonlinear wave loads on a slender vertical cylinder. *J. Fluid Mech.* **289**: 179. [1033, 1034]

Feir, J. E. (1967). Some results from wave pulse experiments. Discussion of M. S. Lighthill: Some special cases treated by the Whitham theory. *Proc. R. Soc. Lond. A* **299**: 54–58. [774]

Fenton, J. (1972). A ninth-order solution for the solitary wave. *J. Fluid Mech.* **53**: 257–271. [658]

Fenton, J. (1979). A higher-order cnoidal wave theory. *J. Fluid Mech.* **94**: 129–161. [665]

Fink, P. T. W. K. Soh (1978). A new approach to roll-up calculations of vortex sheets. *Proc. R. Soc. Lond.* A **362**: 195–209. [986]

Floryan J. M. and Rasmussen (1989). Numerical methods for viscous flows with moving boundaries. *Appl. Mech. Rev.* **42**: 323–341. [885]

Forbes, L. K. and G. C. Hocking (1990). Flow caused by a point sink in a fluid having a free surface. *J. Austral. Math. Soc.* B**32**: 231. [1016]

Fornberg, B. and G. B. Whitham (1978). A numerical and theoretical study of certain nonlinear wave phenomena. *Philos. Trans. R. Soc. Lond.* **289**: 373–404. [676, 890]

Friis, A. (1990). A second order diffraction forces on a submerged body by a second order Green function method. *Fifth Intl Workshop on Water Waves and Floating Bodies*, Manchester, UK, 73–74. [948]

Führböter, A. (1986). Model and prototype tests for wave impact and run-up on a uniform 1:4 slope, *Coastal Eng.* **10**: 49–84. [1024]

Frisch, U. (1968). Wave propagation in random media. *Probabilistic Methods in Applied Mathematics*, Vol. 1, Academic.

Fu, L. L. and B. Holt, (1982). SESAT view of oceans and sea ice with sythetic aperture radar. *Jet Propulsion Laboratory Publ.* 81-120. [816, 917]

Fuhrman, D. R., P. A. Madsen and H. B.Bingham (2004). A numerical study of crescent waves. *J. Fluid Mech.* **513**: 309–341. [619]

Gadd, G. E. (1969). Ship wavemaking in theory and practice. *Trans. Roy. Inst. Naval Architects* **111**: 487–506. [917]

Galvin, C. J., Jr. (1968). Breaker type classification on three laboratory beaches. *J. Geophys. Res.* **73**: 3651–3659. [572]

Galvin, C. J. and P. S. Eaglesen (1965). Experimental study of longshore currents on a plane beach. U.S. Army Coastal Engineering Research Center Technical Memorandum 10. [582]

Gardner, C. S., J. M. Greene, M. D. Kruskal, and R. M. Miura (1967). Method for solving the Korteweg–de Vries equation. *Phys. Rev. Lett.* **19**: 1095–1096. [674, 775]

Gardner, C. S., J. M. Greene, M. D. Kruskal, and R. M. Miura (1974). Korteweg–de Vries equation and generalizations, VI: Methods for exact solution. *Comm. Pure Appl. Math.* **27**: 97–133. [670]

Gelfand, I. M. and B. M. Levitan (1955). On the determination of a differential equation from its spectral function. *Am. Math. Soc. Transl.* **1**: 253–304. [673]

Gerber, M. (1993). The interaction of deep-water gravity waves and an annular current: linear theory. *J. Fluid Mech.* **248**: 153–172. [926]

Goda, Y. (1967). Travelling secondary wave in channels. Port and Harbour Research Institute, Ministry of Transport, Japan. Report 13: 32. [694, 708]

Goda, Y. and Y. Suzuki (1976). Estimation of incident and reflected waves in random wave experiments. *Coastal Eng.*, 828–845. [933]

Gottlieb, D. and S. A. Orszag (1977). *Numerical analysis of spectral methods: theory and applications.* SIAM, Philadelphia, PA. [956]

Gradshteyn, I. S. and I. A. Ryzhik (1965). *Tables of Integrals Series and Products*, Academic, New York. [740]

Grant, W. D. and O. S. Madsen (1979b). Combined wave and current interaction with rough bottom. *J. Geophys. Res.* **84**: 1797–1808. [585]

Grataloup, G. and C . C. Mei,(2003).Localization of harmonics generated in nonlinear shallow water waves. *Phys. Rev. E*, **68**: 026314 1-9. [730]

Greco, M., O. M. Faltinsen and M. Landrini (2005). Shipping of Water on a Two-dimensional Structure. *J. of Fluid Mech.* (in press). [1042]

Greenhow, M. (1983). Free-surface flows related to breaking waves. *J. Fluid Mech.***134**: 259–275. [998]

Greenhow, M., T. Vinje, P. Brevig and J. Taylor (1982). A theoretical and experimental study of the capsize of Salter's duck in extreme waves. *J. Fluid Mech.* **118**: 221–239. [974, 990]

Grilli, S. T., P. Guyenne and F. Dias (2001). A fully nonlinear model for three-dimensional overturning waves over arbitrary bottom. *Intl. J. Numer. Meth. Fluids* **35**: 829–867. [1041]

Grosenbaugh, M. A. and R. W. Yeung (1989). Nonlinear free-surface flow at a two-dimensional bow. *J. Fluid Mech.* **209**: 57. [974]

Grue, J. (1991). Nonlinear water waves at a submerged obstacle or bottom topography. *Preprint Series of Institue of Mathematics, University of Oslo.* No **2**: 1-21. [948, 949]

Guazzelli, E., V. Rey and M. Belzons (1992). Higher-order Bragg reflection of gravity surface waves by periodic beds. *J. Fluid Mech.* **245**: 301–317. [935, 938]

Guevel, P. et al. (1977). Numerical solution of the Neumann-Kelvin problem by the method of singularities. *Proc. 2nd Intl. Conf. Num. Ship Hydro.*, Berkeley, 107–123. [917]

Guza, R. T. and A. J. Bowen (1976). Finite amplitude Stokes edge waves. *J. Marine Res.* **34**: 269–293. [642, 649]

Guza, R. T. and R. E. Davis (1974). Excitation of edge waves by waves incident on a beach. *J. Geophys. Res.* **79**: 1285–1291. [642]

Hagen, G. E. (1975). Wave-driven generator. U.S. Pat. 4,077,213. [405]

Hammack, J. L. and H. Segur (1978). Modelling criteria for long water waves. *J. Fluid Mech.* **84**: 359–373. [691, 693]

Hansen, E. A., J. Fredsøe and R. Deigaard (1994). Distribution of suspended

sediment over wave-genrated ripples. *J. Waterway, Port, Coastal and Ocean Engng.* **120**, 37–55. [527]

Hara, T., and C. C. Mei, (1987) Bragg scattering of surface waves by periodic bars. *J. Fluid Mech.* **178**: 221–241. [318, 806, 807, 930]

Hashimoto, H. and H. Ono (1972). Nonlinear modulation of gravity waves. *J. Phys. Soc. Japan* **33**: 805–811. [756, 771, 774]

Haskind, M. D. (1944). The oscillation of a body immersed i

Hasselmann K. (1962). On the non-linear energy transfer in a gravity-wave spectrum, Part I: General theory. *J. Fluid Mech.* **12**: 481. [848]

Hasselmann, K. *et al.* (1973). Measurements of wind–wave growth and swell decay during the joint North Sea wave project (JONSWAP). *Deutschen Hydrographischen Zeitschrit. Reihe* **A8**: 7–95. [789]

Hattori, M., A. Arami and T. Yui (1994). Wave impact pressure on vertical walls under breaking waves of various types. *Coastal Eng.* **20**: 79–114. [1024]

Havelock, T. H. (1908). The propagation of groups of waves in dispersive media, with application to waves on water produced by a travelling disturbance. *Proc. Roy. Soc.* **A 81**: 398–430. [916]

Hayashi, T. and M. Hattori (1958). Pressure of the breaker against a vertical wall. *Coastal Eng. in Japan* **1**: 25–37. [1024]

Heathershaw, A. D. and A. G. Davies (1985). Resonant wave reflection by transverse bedforms and its relation to beaches and offshore bars. *Mar. Geol.* **62**: 321–338. [930]

Herbers, T. H., S. Elgar and R.T. Guza, (1994). Infragravity–frequency (0.005-0.05Hz) motions on the shelf. Part I. forced waves. *J. Phy. Ocean.* **24**: 917–927. [790]

Herbers, T. H., S. Elgar and R.T. Guza, (1995a). Infragravity–frequency (0.005-0.05Hz) motions on the shelf. Part II. free waves. *J. Phy. Ocean.* **25**: 1063–1079. [790]

Herbers, T. H., S. Elgar and R.T. Guza, (1995b). Generation an propagation of infragravity waves. *J. Geophy. Res.* **100**: 24863–24872. [790]

Herbich, J. B., H. D. Murphy, and B. Van Weele (1965). Scour of flat sand beaches due to wave action in front of sea walls. *Coastal Eng.*, *Santa Barbara Specialty Conf. ASCE* 705–726. [524]

Hesegawa, A. and F. D. Tappert (1973). Transmission of stationary nonlinear optical pulses in dispersive dielectric fibers. *Appl. Phys. Lett.* **23**: 142–172. [774]

Hibberd, S. and D. H. Peregrine (1979). Surf and run-up on a beach: A uniform bore. *J. Fiuid Mech.* **95**: 323–345. [639]

Ho, D. V. and R. E. Meyer (1962). Climb of a bore on a beach, Part I. Uniform beach slope. *J. Fluid Mech.* **14**: 305–318. [639]

Hocking, G. C. (1985). Cusp-like free-surface flows due to a submerged source or sink in the presence of a flat or sloping bottom. *J. Austral. Math. Soc.* B**26**: 470. [1015]

Hocking, G. C. (1988). Infinite Froude number solutions to the problem of a submerged source or sink. *J. Austral. Math. Soc.* B**29**: 401. [1015]

Hogan, S. J., I. Gruman, and M. Stiassnie (1988). On the change in phase speed of

one train of water waves in the presence of another. *J. Fluid Mech.* **192**: 97–114. [857]

Hogben, N. (1972). Nonlinear distortion of the Kelvin ship-wave pattern. *J. Fluid Mech.* **55**: 513–528. [917]

Hovgaard, G. W. (1909). *Trans. Roy. Inst. Naval Architects* **51**: 251. [917]

Howe, M. S. (1967). Nonlinear theory of open-channel steady flow past a solid surface of finite-wave-group shape. *J. Fluid Mech.* **30**: 497–512. [917]

Howe, M. S. (1968). Phase jumps. *J. Fluid Mech.* **32**: 779–789. [917]

Houston, J. R. (1976). Long beach harbor: Numerical analysis of harbor oscillations. *U.S. Army Engineering Waterways Experiment Station*, *Vicksburg*, *MS*, Report **1**, Misc. Paper H-76-20. [199, 260]

Houston, J. R. (1978). Interaction of tsunamis with the Hawaiian Islands calculated by a finite element numerical model. *J. Phys. Ocean.* **8**: 93–102. [197, 198]

Houston, J. R. (1981). Combined refraction and diffraction of short waves using the finite element method. *Appl. Ocean Res.* **3**: 163–170. [98]

Howe, M. S. (1967). Nonlinear theory of open-channel steady flow past a solid surface of finite-wave-group shape. *J. Fluid Mech.* **30**: 497–512. [917]

Howe, M. S. (1968). Phase jumps. *J. Fluid Mech.* **32**: 779–789. [917]

Howe, M. S. (1971). On wave scattering by random inhomogeneities, with application to the theory of weak bores. *J. Fluid Mech.* **45**: 783–804. [730]

Huang, D.B. O. J. Sibul and J. V. Wehausen, (1983). Ships in very shallow water, *Institut for Schiffbau der Universitat Hanburg., Bericht Nr. 427.* 29-49. [718]

Huang, N. E. (1978). On surface drift currents in the ocean. *J. Fluid Mech.* **91**: 191–208. [545]

Huang, N. E., D. T. Chen and C. C. Tung (1972) Interactions between steady non-uniform currents and gravity waves with applications for current measurements. *J. of physical oceanography* **2**: 420–431. [926]

Hunt, J. N. (1952). Viscous damping of waves over an inclined bed in a channel of finite width. *Houille Blanche* **7**: 836–842. [478]

Hunt, J. N. and B. Johns (1963). Current induced by tides and gravity waves. *Tellus* **15**: 343–351. [509, 514, 517, 545]

Hunt, J. N. and R. E. Baddour (1981). The diffraction of nonlinear progressive waves by a vertical cylinder. *Q. J. Mech. Appl. Math.* **34**: 69–87. [826]

Huthnance, J. M. (1981). On mass transports generated by tides and long waves. *J. Fluid Mech.* **102**: 367–387. [545]

Hwang, L. S. and Y. K. Lee (eds.) (1980). *Tsunamis*. Proceedings of the National Science Foundation Work Shop, Tetra Tech Inc., Pasadena, Calif. [689]

Idelsohn, S., E. Oñate, F. Del Pin and N. Calvo. (2003). Lagrangian Formulation of the Fluid Mechanic Problems Including Free Surface and Breaking Waves. *Proc of 7th U.S. National Congress on Computational Mechanics*. [886]

Inman, D. L. (1957). Wave generated ripples in nearshore sands. Beach Erosion Board U.S. Corps of Engineers Technical Memo 100. [524, 526]

Inman, D. L., R. J. Tait, and C. E. Nordstrom (1971). Mixing in the surf force. *J. Geophys. Res.* **76**: 3493–3514. [590]

Inoue, R. and Y. Kyozuka (1984). On the nonlinear wave forces acting on submerged cylinders. *J. Soc. Nav. Arch.*, Japan, **156**: 115-127. [947]

Inui, T. and H. Kajitani (1977). A study on local nonlinear free surface effects in ship waves and wave resistance. *Proc. 25th Anniv. Coll. Inst. Schiffbau*, Hamburg. [917]

Ippen, A. T. and Y. Goda (1963). Wave induced oscillations in harbors. The solution for a rectangular harbor connected to the open-sea. Hydrodynamics Lab., Dept. of Civil Engineering, Massachusetts Institute of Technology Report 59. [258]

Ippen, A. T. and C. R. Kulin (1957). The effect of boundary resistance on solitary waves. *Houille Blanche* **12**: 401–408. [687]

Ippen, A. T. and M. M. Mitchell (1957). The damping of the solitary waves from boundary shear measurement. Hydrodynamics Lab., Dept. of Civil Engineering, Massachusetts Institute of Technology Report 23. [687]

Irribarren, C. R. and C. Nogales (1949). Protection des Ports 11. *Comm. 4*, *17th Int. Navig. Congr.*, *Lisbon* 31–80. [571]

Issacson, M. St. Q. (1976). The viscous damping of cnoidal waves. *J. Fluid Mech.* **75**: 449–457. [681]

Issacson, M. St. Q. (1977). Nonlinear wave forces on large offshore structures. *G. Waterways Port Coastal and Ocean Eng. ASCE* **101**: 166–170. [826]

Isaacson, M. de St.Q. (1982). Nonlinear–wave effects on fixed and floating objects. *J. Fluid Mech.* **120**: 267–281. [989]

Izubuchi, T. and S. Nagasawa, (1937). Experimental investigation on the influence of water depth upon the resistance of ships. *Japan Soc. Nav. Arch.* **61**: 165-206. (In Japanese). [718]

James, I. D. (1974b). A nonlinear theory of longshore currents. *Estuary Coastal Marine Sci.* **2**: 235–250. [608]

Janssen, P. A. E. M. (2003). Nonlinear four wave interactions and freak waves. *J. Phys. Oceanography* **33**: 863–884. [876]

Johns, B. (1970). On the mass transport induced by oscillatory flow in a turbulent boundary layer. *J. Fluid Mech.* **43**: 177–185. [510]

Johnson, D. W. (1919). *Shore Processes and Shoreline Development*, Hafner, New York. [547]

Johnson, R. S. (1972). Some numerical solutions of a variable-coefficient Korteweg–de Vries equation (with applications to soliton wave development on a shelf). *J. Fluid Mech.* **54**: 81–91. [678, 680]

Johnson, R. S. (1973). On the development of a solitary wave over an uneven bottom. *Proc. Cambridge Philos. Soc.* **73**: 183–203. [676, 677, 680]

Jolas, P. (1960). Passage de la houle sur un seuil. *Houille Blanche* **15**: 148–152. [696, 710]

Jonsson, I. G. (1966). Wave boundary layers and friction factors. *Proc. 10th Conf. Coastal Eng. ASCE* 127–148. [586]

Jonsson, I. G. (1990). Wave-current interactions. *Ocean Engineering.* [926]

Jonsson, I. G. and L. Arneborg (1995). Energy properties and shoaling of higher-order Stokes waves on a current. *Ocean Engineering* **22** (8): 819–857. [926]

Jonsson, I. G., O. Skovgaard, and T. S. Jacobsen (1974). Computation of longshore currents. *Proc. 14th Conf. on Coastal Eng. ASCE* 699–714. [580, 584, 589]

Kakutani, T. (1971). Effect of an uneven bottom on gravity waves. *J. Phys. Soc. Jap.* **30**: 272–276. [677]

Kaneko, A. and H. Honji (1979). Double structures of steady streaming in the oscillatory flow over a wavy wall. *J. Fluid Mech.* **93**: 727–736.

Karpman, V. I. (1975). *Nonlinear Waves in Dispersive Media*, Pergamon, 186 pp. [670]

Kaup, D. J. and A. C. Newell (1978). Solitons as particles, oscillators and in slowly changing media: a singular perturbation theory. *Proc. Roy. Soc. Lond.* , A. **361**, 413-446. [680]

Kawahara, T. (1976). Effects of random inhomogeneities on the propagation of water waves. *J. Phys. Soc. Japan*, **41**: 1402–1409. [730]

Keller, J. B. (1961). *Tsunamis... Water Waves Produced by Earthquakes*, ed. D. C. Cox, *Proc. Tsunami Meetings 10th Pacific Science Congress*, IUGG Monograph **24**: 154–166. [636]

Keller, H. B., D. A. Levine and G. B. Whitham (1960). Motion of a bore over a sloping beach. *J. Fluid Mech.* **7**: 302. [639]

Keulegan, G. H. (1948). Gradual damping of solitary waves. *J. Res. Natl. Bur. Stand.* **40**: 487–498. [681]

Keulegan, G. H. (1959). Energy dissipation in standing waves in rectangular basins. *J. Fluid Mech.* **6**: 33–50. [478]

Kim, M. H. and D. K. P. Yue, (1989). The complete second-order diffraction of waves around an axisymmetric body. Part 1. monochromatic waves. *J. Fluid Mech.* **200**: 235–262. [826, 836, 1033, 1036]

King, A. G. and M. I. G. Bloor (1988). A note on the free surface induced by a submerged source at infinite Froude number. *J. Austral. Math. Soc.* B**30**: 147. [1015]

King, C. A. M. (1959). *Beaches and Coasts*, Arnold, London. [547]

Kinsman, B. (1984). *Wind Waves*, Dover. [1007]

Kirby, J. T. (1986). A general wave equation for waves over rippled beds. *J. Fluid Mech.* **162**. 171–186. [98]

Kirkgöz, M. S. (1990). An experimental investigation of a vertical wall response to breaking wave impact. *Ocean Eng.* **17** (4): 379–391. [1024]

Kirkgöz, M. S. (1991). Impact pressure of breaking waves on vertical and sloping walls. *Ocean Eng.* **18** (1/2), 45–59. [1024]

Kitazawa, T. and M. Takagi (1976). On the second order velocity potentials of the thin ship. *SNAJ Int. Sem. Wave Resistance*, Tokyo, 255–261. [917]

Kjeldsen, S. P. and G. B. Olsen (1971). *Breaking Waves.* Film by Technical University of Denmark, Lynby, Denmark. [570]

Ko, K. and H. H. Kuehl (1978). Korteweg–de Vries soliton in a slowly varying medium. *Phys. Rev. Lett.* **40**: 233–236. [680]

Komar, P. D. (1971). Near shore circulation and the formation of giant cusps. *Geol. Soc. Am. Bull.* **82**: 2643–2650. [609]

Komar, P. D. and M. K. Gaughan (1972). Airy wave theory and breaker height prediction. *Proc. 13th Int. Conf. Coastal Eng.* 405–418. [574]

Komen, G. J., L. Cavaleri, M. Donelan, K. Hasselmann, S. Hasselmann, and P. A. E. M. Janssen (1994). *Dynamics and Modelling of Ocean Waves*, Cambridge University Press. [873]

Korobkin, A. A. and V. V. Pukhnachov (1988). Initial stage of water impact. *Ann. Rev. Fluid Mech.* **20**: 159–185. [1025]

Korteweg, D. J. and G. de Vries (1895). On the change of form of long waves advancing in a rectangular canal and on a new type of long stationary waves. *Philos. Mag.* **39**: 422–443. [611, 660]

Kothe, D. B. (1998) Perspective on Eulerian Finite Volume Methods for Incompressible Interfacial Flows, *Free Surface Flows*, Springer.[886]

Krasitskii, V. P. (1994). On reduced equations in the Hamiltonian theory of weakly nonlinear surface waves. *J. Fluid Mech.* **272**: 1–20. [851, 876]

Krokstad J. R. and C. T. Stansberg (referred as MARINTEK) (1995). Ringing load models verified against experiments. *Proc. International Conference on Offshore Mechanics and Arctic Engineering* (ed: S. K. Chakrabarti, D. Myrhaug, R. C. Ertekin and H. Maeda), Copenhagen, Denmark. [1033, 1036]

Kuehl, H. H. (1976). Nonlinear effects on mode-converted low-hybrid waves. *Phys. Fluid.* **19**: 1972–1974. [777]

Lai, R. J., S. R. Long and N. E. Huang (1989). Laboratory studies of wave-current interaction: kinematics of the strong interaction. *J. of geophysical research* **94** (C11): 16201–16214. [926]

Lake, B. M. and H. C. Yuen (1977). A note on some nonlinear water wave experiments and comparison of data with theory. *J. Fluid Mech.* **83**: 75–81. [763]

Lake, B. M. and H. C. Yuen (1978). A new model for nonlinear wind waves Part I. Physical model and experimental evidence. *J. Fluid Mech.* **88**: 33–62. [789]

Lake, B. M., H. C. Yuen, H. Rungaldier, and I. N. E. Ferguson, Jr. (1977). Nonlinear deep water waves: Theory and experiment Part II. Evolution of a continuous wave train. *J. Fluid Mech.* **83**: 49–74. [764, 778, 786, 789, 872]

Lamb, G. L., Jr. (1980). *Elements of Soliton Theory*, Wiley–Interscience, New York. [670, 674]

Lamb, H. (1932). *Hydrodynamics*, Dover, New York. [718, 816, 916, 1025]

Lamoure, J. and C. C. Mei (1977). Effects of horizontally two-dimensional bodies on the mass transport near the sea bottom. *J. Fluid Mech.* **83**: 415–431. [527, 530, 531, 545]

Landau, L. D. and E. M. Lifshitz (1958). *Quantum Mechanics* (*Non-relativistic Theory*), Addison-Wesley, Reading, Mass. [676]

Lau, J. and A. Barcilon (1972). Harmonic generation of shallow water wave over topography. *J. Phys. Ocean.* **2**: 405–410. [710]

Lau, J. and B. Travis (1973). Slow varying Stokes waves and submarine long-shore bars. *J. Geophys. Res.* **78**: 4489–4498. [523, 524]

Lax, P. D. (1968). Integrals of nonlinear equations of evolution and solitary waves. *Comm. Pure Appl. Math.* **21**: 467–490. [676, 775]

LeBlond, P. H. and L. A. Mysak (1978). *Waves in the Ocean*, Elsevier, Amsterdam. [4]

Lee, C.-H. and J. N. Newman (1991). First- and second-order wave effects on a submerged spheroid. *J. Ship Res.* **35**: 183–195. [955]

Lepelletier, T. G. (1980). Tsunamis–Harbor oscillations induced by nonlinear transient long waves. Report No. KH-R-41. Keck Laboratory, California Institute of Technology. [669, 718]

Li, Y. and P. Scalvounos, (2002). Three-dimensional nonlinear solitary waves in shallow water generated by an advcancing disturbance. *J. Fluid Mech.* **470**:383-410. [728]

Lighthill, M. J. (1949). The diffraction of blast I. *Proc. R. Soc. Lond. A* **198**: 454–470. [810]

Lighthill, M. J. (1956). River waters. *Proc. 1st Symp. Naval Hydro.*, Washington D.C., 17–44. [916]

Lighthill, M. J. (1967). Some special cases by the Whitham theory. *Proc. R. Soc. Lond. A* **299**: 28–53. [746, 917]

Lighthill, M. J. (1978). *Waves in Fluids*, Cambridge University Press, London. [763]

Lin, C. C. and A. Clark, Jr. (1959). On the theory of shallow water waves. *Tsing Hua J. of Chinese Studies*, *Special* **1**: 54–62. [611]

Lin, W. M., J. N. Newman and D. K. P. Yue (1984). Nonlinear forced motions of floating bodies. *Proc. 15th Symp. on Naval Hydro., Hamburg* (ed: O. Krappinger), Washington, National Academy Press. [980, 987]

Liu, A. K. and S. H. Davis (1977). Viscous attenuation of mean drift in water waves. *J. Fluid Mech.* **81**: 63–84. [544]

Liu, P. L. F. (1989). A note on long waves induced by short-wave groups over a shelf. *J. Fluid Mech.* **205**, 163–170. [804, 816]

Liu, P. L. F. (1989). Wave transformation. In *The Sea – Ocean Engineering Science*, **9**, Part A. 27–63. [804, 816]

Liu, P. L. F. and R. A. Dalrymple (1977). Bottom friction stresses and longshore currents due to waves with large scales of incidence. *J. Marine Res.* **36**: 357–475. [585]

Liu, P. L. F. and G. P. Lennon (1978). Finite element modeling of near shore currents. *J. Waterways*, *Port*, *Coastal Ocean Div. ASCE* **104**: 175–189. [609]

Liu, P. L. F. and C. C. Mei (1974). Effects of a breakwater on near-shore currents due to breaking waves. Parsons Lab., Dept. of Civil Engineering, Massachusetts Institute of Technology Report 192. [592]

Liu, P. L. F. and C. C. Mei (1976a, b). Water motion on a beach in the presence of a breakwater 1. waves 2. mean currents. *J. Geophys. Res.-Oceans Atmos.* **81**: 3079–3084; 3085–3094. [185, 592, 596, 599–601]

Liu, Y. (1994). *Nonlinear wave interactions with submerged obstacles with or without current.* PhD thesis. Massachusetts Institute of Technology. [935]

Liu, Y., D. G. Dommermuth and D. K. P. Yue (1992). A higher-order spectral method for nonlinear wave-body interactions. *J. Fluid Mech.* **245**: 115–136. [840, 890, 898]

Liu, Y. H. and X. S. Lu (1988). Polar coordinate transformation approach for treatment of singular integrations in boundary element analysis. *Applied Math. and Mech.* **9**(10): 899–915. [982]

Liu, Y. M. and D. K. P. Yue (1998). On generalized Bragg scattering of surface waves by bottom ripples. *J. Fluid Mech.* **356**: 297–326. [890, 931, 933, 939]

Liu, Y., M. Xue and D. K. P. Yue (2001). Computation of fully-nonlinear three-dimensional wave-wave and wave-body interactions — Part II: nonlinear waves and forces on a body. *J. Fluid Mech.* **438**: 41–66. [973]

Liu, Y., Q. Zhu and D. K. P. Yue (1999). Nonlinear radiated and diffracted waves due to the motions of a submerged circular cylinder. *J. Fluid Mech.* **382**: 263–282. [946, 955]

Lo, E. and C. C. Mei (1985). A numerical study of wate wave mudulation based on a higher-order nonlinear Schrödinger equation. *J. Fluid Mech.* **150**: 395–416. [789, 872, 889, 913]

Longuet-Higgins, M. S. (1953). Mass transport in water waves. *Philos. Trans. R. Soc.* **345**: 535–581. [509, 517, 520, 535, 536, 543]

Longuet-Higgins, M. S. (1958). The mechanics of the boundary layer near the bottom in a progressive wave. *Proc. 6th Conf. Coastal Eng.* 184–193. [510]

Longuet-Higgins, M. S. (1970a, b). Longshore currents generated by obliquely incident sea waves, 1 and 2. *J. Geophys. Res.* **75**: 6778–6789; 6790–6801. [549, 578, 580, 582, 583, 588]

Longuet-Higgins, M. S. (1970c). Steady currents induced by oscillations round islands. *J. Fluid Mech.* **42**: 701–720. [545]

Longuet-Higgins, M. S. (1974b). On mass, momentum, energy and circulation of a solitary wave. *Proc. R. Soc. Lond. A* **337**: 1–13. [658]

Longuet-Higgins, M. S. (1978a). The instability of gravity of finite amplitude in deep water I. Superharmonics. *Proc. R. Soc. Lond. A* **360**: 471–488. [767]

Longuet-Higgins, M. S. (1978b). The instabilities of steep gravity waves of finite amplitude in deep water II. Subharmonics. *Proc. R. Soc. Lond. A* **360**: 489–505. [767]

Longuet-Higgins, M. S. (1983). Paristaltic pumping in water waves. *J. Fluid Mech.* **137**: 393–407. [544]

Longuet-Higgins, M. S. and E. D. Cokelet (1976). The deformation of steep surface waves on water I. A numerical method of computation. *Proc. R. Soc. Lond. A* **350**: 1–26. [898, 902, 948, 973, 985, 989, 996]

Longuet-Higgins, M. S. and E. D. Cokelet (1978) The deformation of steep surface waves on water II. Growth of normal mode instabilities. *Proc. R. Soc. Lond. A* **364**: 1–28. [746]

Longuet-Higgins, M. S. and J. Fenton (1974). Mass, momentum, energy and circulation of a solitary wave, II. *Proc. R. Soc. Lond. A* **340**: 471–493. [658]

Longuet-Higgins, M. S. and M. J. H. Fox (1977). Theory of the almost highest wave: The inner solution. *J. Fluid Mech.* **80**: 721–742. [746]

Longuet-Higgins, M. S. and M. J. H. Fox (1978). Theory of the almost highest wave II: Matching and analytic extension. *J. Fluid Mech.* **85**: 769–786. [746]

Longuet-Higgins, M. S. and H. N. Oguz (1997). Critical jets in surface waves and collapsing cavities. *Phil. Trans. R. Soc. Lond.* A**355**: 625. [1022]

Longuet-Higgins, M. S. and R. W. Stewart (1960). Changes in form of short

gravity waves on long waves and tidal currents. *J. Fluid Mech.* **8**: 565–583. [926]

Longuet-Higgins, M. S. and R. W. Stewart (1962). Radiation stresses and mass transport in gravity waves with applications to surf-beats. *J. Fluid Mech.* **13**: 481–504. [549, 550, 576, 790]

Longuet-Higgins, M. S. and R. W. Stewart (1964). Radiation stresses in water waves; a physical discussion with applications. *Deep-Sea Res.* **11**: 529–562. [566]

dip on the surface of a liquid draining from a tank. *J. Fluid Mech.* **29**: 385. [1016]

Lundgren, H. (1969). Wave shock forces: an analysis of deformations and forces in the wave and in the foundation. *Proc. Symp. on Research in Wave Action, Delf Hydraulic Laboratory, Delf, The Netherlands*, Paper 4. [1024]

Luneberg, R. K. (1964). *Mathematical Theory of Optics*, University of California Press, Los Angeles. [69, 72, 82]

Ma, Q. W., G. X. Wu and R. Eatock Taylor (2001a). Finite element simulation of fully nonlinear interaction between vertical cylinders and steep waves. Part 1: Methodology and numerical procedure. *Int. J. Num. Meth. Fluids* **36**: 265–285. [886]

Ma, Q. W., G. X. Wu and R. Eatock Taylor (2001b). Finite element simulation of fully nonlinear interaction between vertical cylinders and steep waves. Part 2: Numerical results and validation. *Int. J. Num. Meth. Fluids* **36**: 287–308. [886]

Madsen, O. S. (1978). Mass tranport in deep-water waves. *J. Phys. Ocean.* **8**: 1009–1015. [545]

Madsen, O. S. and C. C. Mei (1969). The transformation of a solitary wave over an uneven bottom. *J. Fluid Mech.* **39**: 781–791. [619, 676, 680]

Madsen, O. S., C. C. Mei, and R. P. Savage (1970). The evolution of time-periodic waves of finite amplitude. *J. Fluid Mech.* **44**: 195–208. [676, 710]

Madsen, P. A., and Y. Agnon (2003). Accuracy and convergence of velocity formulations for water waves in the framework of Boussinesq theory. *J. Fluid Mech.* **477**: 1–30. [619]

Madsen, P. A., H. B. Bingham and H. Liu (2002). A new Boussinesq method for fully nonlinear waves from shallow to deep water. *J. Fluid Mech.* **462**: 1–30. [619]

Madsen, P. A., H. B. Bingham and H. A. Schäffer (2003). Boussinesq-type formulations for fully nonlinear and extremely dispersive water waves : derivation and analysis. *Proc. R. Soc. Lond.* A **459**: 1075–1104. [619]

Madsen, P. A. and H. A. Schäffer (1998). Higher-order Boussinesq-type equations-derivation and analysis. *Phil. Trans. Roy. Soc. Lond. Series A.* **356**: 1–59. [619]

Malenica, Š. and B. Molin (1995). Third-harmonic wave diffraction by a vertical cylinder. *J. Fluid Mech.* **302**: 203. [1033, 1037]

Mallory, J. K. (1974). Abnormal waves on the south east coast of South Africa. University of Capetown Libraries, Cape Town. [117]

Martin, D. U. and H. C. Yuen (1980). Quasi recumng energy leakage in the

two space dimensional nonlinear Schrödinger equations. *Phys. Fluids* **23**: 1269–1271. [889]

McGoldrick, L. F. (1965). Resonant interactions among capillary-gravity waves. *J. Fluid Mech.* **21**: 305–331. [848]

McGoldrick, L. F., O. M. Philips, N. E. A. Huang, and T. Hodson (1966). Measurement of resonant wave interactions. *J. Fluid Mech.* **25**: 437–456. [877]

McIver, M. and P. McIver (1990). Second-order wave diffraction by a submerged circular cylinder. *J. Fluid Mech.* **219**: 519–529. [948]

McLean, J. W. (1982). Instabilities of finite-amplitude water waves. *J. Fluid Mech.* **114**: 315–330. [877, 970, 1008]

McLean, J. W., Y. C. Ma, D. U. Martin, P. G. Saffman, and H. C. Yuen (1981). A new type of three-dimensional instability of finite amplitude gravity waves. *Phys. Rev. Lett.* **46**: 817–820. [970, 1008]

Mei, C. C. (1966b). On the propagation of periodic water waves over beaches of small slope. Technical Note 12, Hydrodynamics Laboratory, Massachussetts Institute of Technology. [637]

Mei, C. C. (1973). A note on the averaged momentum balance in two-dimensional water waves. *J. Marine Res.* **31**: 97–104. [562]

Mei, C. C. (1978). Numerical methods in water wave diffraction and radiation. *Ann. Rev. Fluid Mech.* **10**: 393–416. [885]

Mei, C. C. (1985). Resonant reflection of surface waves by periodic sandbars. *J. Fluid Mech.* **152**: 315–335. [725, 930, 934]

Mei, C. C. (1986). Radiation of solitons by slender bodies advancing in a shallow channel. *J. Fluid Mech.* **162**: 53–67. [718]

Mei, C. C. and D. Angelides (1976). Longshore currents around a conical island. *Coastal Eng.* **1**: 31–42. [604, 607]

Mei, C. C. and C. Benmoussa, (1984). Long waves induced by short-wave groups over an neven bottom. *J. Fluid Mech.* **139**: 219–235. [796, 798, 799, 801, 803, 804]

Mei, C. C. and H. S. Choi, (1987). Forces on a slender ship advancing near the critical speed in a wide channel. *J. Fluid Mech.* **179**: 59–76. [721]

Mei, C. C. and B. LeMéhauté (1966). Note on the equations of long waves over an uneven bottom. *J. Geophys. Res.* **71**: 393–400. [619]

Mei, C. C. and Y. Li, (2004). Evolution of solitons over a randomly rough seabed. *Phys. Rev. E* **70**: 016302 1-11. [730, 736, 737]

Mei, C. C. and P. L. F. Liu, (1977). Effects of topography on the circulation in and near the surf zone — Linear theory. *Estuary Coastal Marine Sci.* **5**: 25–37. [609]

Mei, C. C., P. L. F. Liu and T. G. Carter (1972). Mass transport in water waves. Parsons Lab., Massachusetts Institute of Technology Report 146: 287. [521, 535]

Mei, C. C., and M. Naciri, (1991). Note on ship oscillations ad wake solitons. *Proc. Roy. Soc. Lond.* **A, 432**, 535–546. [817, 825]

Mei, C. C. and Ü. Ünlüata (1972). Harmonic generation in shallow water waves. *Waves on Beaches*, ed. R. E. Meyer, Academic, New York, 181–202. [697, 701, 708]

Meiron, D. I., P. G. Saffman and H. C. Yuen (1982). Calculation of steady three-dimensional deep-water waves. *J. Fluid Mech.* **124**: 109–121. [1007]

Mekias, H. and J.-M. Vanden-Broeck (1989). Supercritical free-surface flow with a stagnation point due to a submerged source. *Phys. Fluids* A**1**(10): 1694. [1016]

Mekias, H. and J.-M. Vanden-Broeck (1991). Subcritical flow with a stagnation point due to a source beneath a free surface. *Phys. Fluids* A**3**(11): 2652. [1016]

Mekias, H. and J.-M. Vanden-Broeck (1993). Free-surface flow due to a source submerged in fluid of infinite depth with two stagnant regions. *J. Austral. Math. Soc.* B**34**: 368. [1016]

Melville, W. K. (1980). On the mach reflexion of a solitary wave. **98**: 285–297. [810]

Melville, W. K. (1982). The instability and breaking of deep-water waves. *J. Fluid Mech.* **115**: 165–185. [872]

Melville, W. K. (1983). Wave modulation and breakdown. *J. Fluid Mech.* **128**: 489–506. [872]

Melville, W. K. and K. R. Helfrich, (1987). Transcritical two-layer flow over topography. *J. Fluid Mech.* **178**: 31–52. [719]

Mercer, G. N. and A. J. Roberts (1992). Standing waves in deep water: their stability and extreme form. *Phys. Fluids* A **4**(2): 259–269. [961, 967]

Meyer, R. E. and A. D. Taylor (1972). Run-up on beaches. *Waves on Beaches*, ed. R. E. Meyer, Academic, New York, 357–412. [639]

Miche, R. (1944). Mouvements ondulatoires de la mer en profondeur constante ou décroissante form limte de la houle lors de son déferlement. Application aux digues maritimes. *Ann. Pontes Chaussées* **114**: 25–78, 131–164, 270–292, 369–406. [639]

Miche, R. (1951). Le pouvoir reflechissant des ouvrages maritime exposés á l'action de la houle. *Ann. Ponts Chaussées* **121**: 285–319. [573]

Miles, J. W. (1957). On the generation of surface waves by shear flows. *J. Fluid Mech.* **3**: 185–204. [745]

Miles, J. W. (1962). Transient gravity wave response to an oscillating pressure. *J. Fluid Mech.* **13**: 145–150. [61, 63]

Miles, J. W. (1976). Damping of weakly nonlinear shallow water waves. *J. Fluid Mech.* **76**: 251–257. [681]

Miles, J. W. (1977). Diffraction of solitary waves. *J. Appl. Math. Phys.* **28**: 889–902. [810]

Miles, J. W. (1979). On the Korteweg–de Vries equation for a gradually varying channel. *J. Fluid Mech.* **91**: 181–190. [680]

Miles, J. W. (1980). Solitary waves. *Ann. Rev. Fluid Mech.* **12**: 11–44. [680]

Milgram, J. H. (1987). Theory of radar backscatter from short waves generated by ships, with application to radar (SAR) imagery. *J. Ship. Res.* **32**: 54–69. [917]

Miller, R. L., S. Leverette and J. O'Sollivan (1974). Field measurements of impact pressures in surf, *Proc. 14th Int. Conf. Coastal Eng.* **3**: 1761–1777. [1024]

Miloh, T. (1980). Irregularities in solutions of nonlinear wave diffraction problem

by vertical cylinder. *J. Waterways, Port Coastal Ocean Eng. Div. Proc. ASCE* **106**: 279–284. [826]

Miloh, T. and G. Dagan (1985). A study of nonlinear wave resistance using integral equations in Fourier space. *J. Fluid Mech.* **159**: 433–458. [917]

Miloh, T. and P. A. Tyvand (1993). Axisymmetric nonlinear unsteady free-surface flow due to a submerged Sink: The drainage Problem. *Phys. Fluids* A**5**(6): 1368. [1016, 1017]

Minzoni, A. A. (1976). Nonlinear edge waves and shallow water theory. *J. Fluid Mech.* **79**: 369–374. [649]

Minzoni, A. A. and G. B. Whitham (1977). On the excitation of edge wave on beaches. *J. Fluid Mech.* **79**: 273–287. [643]

Miura, R. M. (1974). The Korteweg–de Vries equation: A model equation for nonlinear dispersive waves. *Nonlinear Waves*, eds. S. Leibovich and A. R. Seabass, Cornell University Press, Ithaca, New York, 212–234. [670]

Miura, R. M. (1976). The Korteweg–de Vries equation — A survey of results. *SIAM Rev.* **18**: 412–459. [670]

Miyata, H., G. Khalil, Y-G. Lee and M. Kanai (1988). An experimental study of the Nonlinear forces on horizontal cylinders. *J. Kansai Soc. N. A.*, Japan, **209**, 11–23. [947, 953]

Molin, B. (1979). Second order diffraction loads upon three-dimensional bodies. *Appl. Ocean Res.* **1**: 197–202. [826]

Mollo-Christensen, E. and A. Ramamonjiariosa (1978). Modeling the presence of wave groups in a random wave field. *J. Geophys. Res.* **83**: 4117–4122. [789]

Moore, D. (1970). The mass transport velocity induced by the free oscillation of a single frequency. *Geophys. Fluid Dynamics* **1**: 237–247. [545]

Moore, D. W. (1983). Resonances introduced by discretization. *IMA J. Appl. Math.* **31**: 1–11. [986]

Moraes, C.deC. (1970). Experiments of wave reflection on impermeable slopes. *Proc. 12th Conf. on Coastal Eng. ASCE* 509–521. [571]

Munk, W. H. (1949a). The solitary wave and its application to surf problems. *N.Y. Acad. Sci.* **1**: 376–424. [574]

Munk, W. H. and M. Wimbush (1969). A rule of thumb for wave breaking over sloping beaches. *Oceano.* **9**: 56–59. [571]

Murty, T. S. (1977). *Seismic Sea Waves/Tsunamis*, Bulletin 198, Fisheries and Environment, Ottawa, Canada. [688]

Naheer, E. (1978). The damping of solitary waves. *Int. J. Hydraul. Res.* **16**: 235–249. [687]

Nakos, D. E., D. C. Kring and P. D. Sclavounos (1993). Rankine panel methods for transient free surface flows. *Proceedings of the 6th International Conference on Numerical Ship Hydrodynamics*, Iowa City, IA. [984]

Nayfeh, A. H. and D. T. Mook (1979). *Nonlinear Oscillations* John Willey & Sons, New York. [972]

New, A. (1983). A class of elliptical free-surface flows. *J. Fluid Mech.* **130**: 219–239. [998]

New, A. L., P. McIver and D. H. Peregrine (1985). Computations of overturning waves. *J. Fluid Mech.* **150**: 233–251. [989]

Newman, J. N. (1970). Recent research on ship waves. *Proc. 8th Symp. Naval Hydro.*, Pasadena, CA. [917]

Newman, J. N. (1971). Third-order interactions in Kelvin ship-wave systems. *J. Ship Res.* **15**: 1–10. [917, 918, 923]

Newman, J. N. (1977). *Marine Hydrodynamics*, MIT Press. Cambridge. [718, 818]

Newman, J. N. (1986). Distribution of sources and normal dipoles over a quadrilateral panel. *J. of Engng Math.* **20**: 113–126. [979]

Newman, J. N. (1992). The Green function for potential flow in a rectangular channel. *J. Engng. Math.* **26**: 51–59. [984]

Ng, C. O., (2004) Mass transport in geavity waves revisited. *J. Geophy. Res.* **109**: C04012 1-11. [537]

Nielsen, A. H. (1962). Diffraction of periodic waves along a vertical breakwater for small angles of incidence. University of California–Berkeley IER Technical Report HEL 1–2. [810]

Noda, E. K. (1974). Wave-induced nearshore circulation. *J. Geophys. Res.* **79**: 4097–4106. [609]

Noda, H. (1968). A study on mass transport in boundary layers in standing waves. *Proc. 11th Conf. Coastal Eng. ASCE* 227–235. [524] ‘

Ochi, M. K. (1998). *Ocean Waves — A Stochastic Approach*, Cambridge University Press. [839]

Ochi, M. K. and C. H. Tsai (1984). Prediction of impact pressure induced by breaking waves on vertical cylinders in random seas. *Applied Ocean Research* **6** (3): 157–165.

Ogawa, K . and K. Yoshida (1959). A practical method for a determination of long gravitational waves. *Records Oceangraphic Works Jap.* **5**: 38–50. [153]

Ogilvie, T. F. (1960). *Propagation of Waves Over an Obstacle in Water of Finite Depth*, University of California–Berkeley, Inst. Eng. Res. Report 82-14. [135]

Ogilvie, T. F. (1963). First and second order forces on a cylinder submerged under the free surface. *J. Fluid Mech.* **16**: 451–472. [405, 947, 951]

Ogilvie, T. F. (1964). Recent progress toward the understanding and prediction of ship motions. *Proc. 5th Symp. Naval Hydrodyn.*, Office of Naval Research 3–97. [442, 446]

Ogilvie, T. F. (1968). Wave resistance — the low speed limit. *Dept. Naval Arch., U. Michigan*, Ann Arbor, Rep. 002. [917]

Ono, H. (1972). Wave propagation in an inhomogeneous anharmonic lattice. *J. Phys. Soc. Jap.* **32**: 332–336. [676, 680]

Onorato, M., A. R. Osborne, M.Serio and S Bertone, (2001). Freak waves in random oceanic sea states. *Phys. Rev. Lett.* **86** : 5831-5834. [117]

Orszag, S. A. (1971). Numerical simulation of incompressible flows within simple boundaries: accuracy. *J. Fluid Mech.* **49**: 75–112. [899]

Ostrovsky, L. A. and E. N. Pelinovskiy (1970). Wave transformation on the surface of a fluid of variable depth. *Atmos. Oceanic Phys.* **6**: 552–555. [679]

Ott, E. and R. N. Sudan (1970). Damping of solitary waves. *Phys. Fluids* **13**: 1432. [681, 683]

Oumeraci, H., P. Klammer and H. W. Partenscky (1993). Classification of break-

ing wave loads on vertical structures. *J. Waterway, Ports, Coastal and Ocean Eng.* **119** (4): 381–397. [1024]

Özhan, E. and H. Shi-igai (1977). On the development of solitary waves on a horizontal bed with friction. *Coastal Eng.* **1**: 167–184. [687]

Palm, E. (1991). Non-linear wave reflection from a submerged circular cylinder. *J. Fluid Mech.* **233**: 49–63. [948, 949]

Peregrine, D. H. (1967). Long waves on a beach. *J. Fluid Mech.* **27**: 815–827. [612, 619, 680, 710]

Peregrine, D. H. (1972). A line source beneath a free surface. Mathematics Research Center, Univ. Wisconsin, Technical Summary Report No. 1248. [1015]

Peregrine, D. H. (1976). Interaction of water waves and currents. *Adv. Appl. Mech.* **16**: 10–117. [926]

Perroud, P. H. (1957). The solitary wave reflection along a straight vertical wall at oblique incidence. University of California–Berkeley IRE Technical Report 99-3. [809]

Peters, A. S. (1949). A new treatment of the ship wave problem. *Comm. Pure App. Math.* **2**: 123–148. [916]

Phillips, O. M. (1957). On the generation of waves by turbulent wind. *J. Fluid Mech.* **2**: 415–417. [745]

Phillips, O. M. (1960). On the dynamics of unsteady gravity waves of finite amplitude Part I. *J. Fluid Mech.* **9**: 193–217. [697, 745, 847, 849, 889, 931]

Phillips, O. M. (1977). *Dynamics of the Upper Ocean*, 2nd ed., Cambridge University Press, London. [550, 554, 560, 745]

Piedra-Cueva, I., (1995). Drift velocity of spatially decaying waves in a two-dimensional viscous system. *J. Fluid Mech.* **299**: 217–239. [537]

Pierson, W. J., Jr. (1962). Perturbation analysis of the Navier–Stokes equations in Lagrangian form with selected linear solutions. *J. Geophys. Res.* **67**: 3151–3160. [538]

Putnam, J. A., W. H. Munk, and M. A. Traylor (1949). The prediction of longshore currents. *Trans. Am. Geophys. Union* **30**: 337–345. [548]

Radder, A. C. (1979). On the parabolic equation method for water wave propagation. *J. Fluid Mech.* **95**: 159–176. [185]

Rainey, R. C. T. (1995). Slender-body expressions for the wave load on offshore structures. *Proc. R. Soc. Lond.* A**450**: 391–416. [1034]

Raman, H. and P. Venkatanarasalah (1976). Forces due to nonlinear waves on vertical cylinders. *J. Waterways Harbor, Coastal Engineering Div. ASCE* **102**: 301–316. [826]

Rapp, R. J. (1986). *Laboratory measurements of deep water breaking waves.* Ph.D. Thesis, MIT, Dept. of Ocean Engineering. [990]

Rapp, R. J. and W. K. Melville (1990). Laboratory measurements of deep-water breaking waves. *Phil. Trans. R. Soc. Lond.* A**331**: 735. [989]

Rasmussen, J. H. (1998). Deterministic and stochastic modelling of surface gravity waves in finite depth. Ph.D. Thesis, ISVA, Denmark, *Series Paper* **68**, 245 pp. [877]

Rasmussen, J. H. and M. Stiassnie (1999). Discretization of Zakharov's equation. *Eur. J. Mech. B/Fluids* **18**: 353–364. [877]

Rayleigh, L. (1883). On the circulation of air observed in Kundt's tubes, and some allied acoustical problems. *Philos. Trans. R. Soc. London* **175**: 1–21. [509]

Riabounchinsky, D. (1932). Sur L'anologue hydraulique des mouvements dun fluid compressible. Institut de France Academic des Sciences. *Comptes Rendus.* **195**: 998. [620]

Rienecker, M. M. and J. D. Fenton (1981). A Fourier approximation for steady water waves. *J. Fluid Mech.* **104**: 119–137. [893]

Riley, N. (1967). Oscillatory viscous flows: Review and extension. *J. Inst. Math. Appl.* **3**: 419–434. [532]

Roberts, A. J. (1983). A stable and accurate numerical method to calculate the motion of a sharp interface between fluids. *IMA J. Appl. Math.* **31**: 13–35. [986]

Rockliff, N. (1978). Finite amplitude effects in free and forced edge waves. *Math. Proc. Cambridge Philos. Soc.* **83**: 463–479. [643, 650]

Roger, S. E. and D. Kwak (1991). An upwind differencing scheme for the incompressible Navier-Stokes equations. *Applied Numerical Mathematics* **8**: 43–64. [886]

Rogers, S. R. and C. C. Mei (1978). Nonlinear resonant excitation of a long and narrow bay. *J. Fluid Mech.* **88**: 161–180. [669, 710, 715–717]

Romate, J. E. (1989). The numerical simulation of nonlinear gravity waves in three dimensions using a higher panel method. PhD thesis, University of Twente, Enschede, The Netherlands. [989]

Romate, J. E. (1989). The numerical simulation of nonlinear gravity waves. *J. Computational Phys.* **99**: 135-145. [989]

Rosales, R. R. and G. C. Papanicolaou (1983). Gravity waves in a channel with a rough bottom. *Stud. Appl. Math.* **68**: 89–102. [730]

Roskes, G. (1969). Wave Envelopes and Nonlinear Waves, Ph.D. Thesis, Dept. of Mathematics, Massachusetts Institute of Technology. [757]

Russell, J. S. (1838). Report of the Committee on Waves. *Rep. Meet. Brit. Assoc. Adv. Sci. 7th*, Liverpool, 1837, John Murray, London, 417–496. [681]

Russell, R. C. H. and J. D. C. Osorio (1957). An experiment investion of drift profiles in a dosed channel. *Proc. 6th Conf. Coastal Eng. ASCE* 171–193. [760]

Saad, Y. and M. H. Schultz (1986). GMRES: A generalized minimal residual algorithm for solving nonsymmetric linear systems. *SIAM J. Sci. Stat. Comput.* **7**: 856–869. [982]

Sahin, I. and A. H. Magnuson (1984). A numerical method for the solution of a line source under a free surface. *Ocean Engng.* **11**(5): 451. [1015]

Salter, S. H., D. C. Jeffrey and J. R. M. Taylor (1976). The architecture of nodding duck wave power generators. *The Naval Arch.* 21–24. [947]

Sammarco, P., H. Tran and C. C. Mei (1997a) Subharmonic resonance of Venice storm gates in waves. I. Evolution equation and uniform incident waves. *J. Fluid Mech.* **349**: 295–325. [655]

Sammarco, P., H. Tran, O. Gottlieb and C. C. Mei (1997b). Subharmonic resonance of Venice storm gates in waves. II. Sinusoidally modulated incident waves. *J. Fluid Mech.* **349**: 327–359. [655]

Sammarco, P., C. C. Mei and K. Trulsen (1994) Nonlinear resonance of free surface waves in a current over a sinusoidal bottom– a numerical study. *J. Fluid Mech.* **279**: 377–405. [770]

Satsuma, J. and N. Yajima (1974). Initial value problems of one-dimensional self-modulation of nonlinear waves in dispersive media. *Suppl. Progr. Theor. Phys.* **55**: 284–306. [776–778]

Sauvage de Saint Marc, M. G. and M. G. Vincent (1955). Transport littoral formation de fleches et de tombolos. *Proc. of 5th Conf. Coastal Eng. ASCE* 296–328. [591]

Scardovelli, R. and S. Zaleski (1999). Direct numerical simulation of free-surface and interfacial flow. *Annu. Rev. Fluid Mech.* **31**: 567–603. [885]

Schmidt, R., H. Oumeraci and H. W. Partenscky (1992). Impact loads induced by plunging breakers on vertical structures. *Proc. 23rd Int. Conf. Coastal Eng.* ASCE, Venice, 1545–1558. [1024]

Schwartz, L. W. (1974). Computer extension and analytic continuation of Stokes' expansion for gravity waves. *J. Fluid Mech.* **62**: 553–578. [573, 746, 902, 928, 1034]

Schwartz, L. W. and J. D. Fenton (1982). Strongly nonlinear waves. *Ann. Rev. Fluid Mech.* **14**: 39–60. [885]

Sclavounos, P. D. and D. E. Nakos (1990). Ship motions by a Rankin panel method. *Proc. 18th Symp. Naval Hydrodyn.* Ann Arbor. [818]

Scott, A. C., F. Y. F. Chu, and D. W. McLaughlin (1973). The soliton: A new concept in applied science. *Proc. IEEE* **61**: 1443–1483. [670, 771]
e Vries equation and water waves. Solution of the equation: Part I. *J. Fluid Mech.* **59**: 721–736. [674]

Sethian, J. A. and P. Smereka (2003). Level set methods for fluid interfaces. *Annual Review of Fluid Mech.* **35**:341–372. [886]

Shemer L. and M. Stiassnie (1985). Initial instability and long-time evolution of Stokes waves. *The Ocean Surface*, *Wave Breaking*, *Turbulent Mixing*, *and Radio Probing*, eds. Y. Toba and H. Mitsuyasu, 51–57. [870]

Shen, M. C. and R. E. Meyer (1963a). Climb of a bore on a beach — Part II. Nonuniform beach slope. *J. Fluid Mech.* **16**: Part I, 108–112. [639]

Shen, M. C. and R. E. Meyer (1963b). Climb of a bore on a beach — Part III. Run-up. *J. Fluid Mech.* **16**: Part I, 113–125. [639]

Shen, L., G. S. Triantafyllou and D. K. P. Yue (2004). Effects of surfactants on free-surface turbulent flows. *J. Fluid Mech.* **506**, 79–115. [1042]

Shen, L., X. Zhang, D. K. P. Yue and G. S. Triantafyllou (1999). The surface layer for free-surface turbulent flows. *J. Fluid Mech.* **386**, 167–212. [1042]

Shepard, F. P. and H. R. Wanless (1973). *Our Changing Coastlines*, McGraw-Hill, New York. [547]

Shimano, T. M. Hom-ma and K. Horikawa (1958). Effect of a jetty on nearshore currents. *Coastal Eng. Japan* **1**: 45–58. [601]

Shrira, V. I., S. I. Badulin and C. Kharif (1996). A model of water wave 'horseshoe' patterns. *J. Fluid Mech.* **318**: 375–404. [1007]

Shyu, J. H. and O. M. Phillips (1990). The blockage of gravity and capillary waves by longer waves and currents. *J. Fluid Mech.* **217**: 115–141. [926]

Shyu, J. H. and C. C. Tung (1999). Reflection of oblique waves by currents: analytical solutions and their application to numerical computations. *J. Fluid Mech.* **396**: 143–182. [926]

Smith, R. (1975). The reflection of short gravity waves on a non-uniform current. *Math. Proc. Camb. Phil. Soc.* **78**: 517–525. [926]

Sonu, C. J. (1972). Field observation of nearshore circulation and meandering currents. *J. Geophys. Res.* **77**: 3232–3247. [609]

Stansby, P. K. and A. Slaouti (1983). On non-linear wave interaction with cylindrical bodies: a vortex sheet approach. *Appl. Ocean Res.* **6**, 108–115. [648]

Stiassnie, M. (1984). Note on the modified nonlinear Schrödinger equation for deep water waves. *Wave Motion* **6**: 431–433. [865]

Stiassnie, M. (2001). Nonlinear interactions of inhomogeneous random water wave. ECMWF Report of the Workshop on Ocean Waves Forecasting, Reading, July 2–4, 2001, 39–52. [877]

Stiassnie, M. and U. I. Kroszynski (1982). Long-time evolution of an unstable water-wave train. *J. Fluid Mech.* **116**: 201–225. [787]

Stiassnie M. and L. Shemer (1984). On modifications of the Zakharov equation for surface gravity waves. *J. Fluid Mech.* **143**: 47–67. [889]

Stiassnie M. and L. Shemer (1987). Energy computation for evolution of class I and class II instabilities of Stokes waves. *J. Fluid Mech.* **174**: 299–312. [876]

Stive, R. J. H. (1984). Wave impact on uniform steep slopes at approximately prototype scale. *Symposium on scale effects in modelling hydraulic structures, Esslingen am Neckar, Germany* (Ed. H. Kobus), 7.11-1–11.7. [1024]

Stoker, J. J. (1957). *Water Waves*, Interscience, New York. [620, 621, 625, 629, 639, 718, 818]

Stokes, G. G. (1847). On the theory of oscillatory waves. *Trans. Cambridge Philos. Soc.* **8**: 441–455. Reprinted in *Math. Phys. Papers*, Cambridge University Press, London, Vol. 1, 314–326. [745]

Stuart, J. T. (1966). Double boundary layers in oscillatory viscous flow. *J. Fluid Mech.* **24**: 673–687. [532, 535]

Su, M. Y. (1982a). Evolution of groups of gravity waves with moderate to high steepness. *Phys. of Fluids* **25**: 2167–2174. [902, 912, 913, 1013, 1014]

Su, M.-Y. (1982b). Three-dimensional deep-water waves. Part I. Experimental measurement of skew and symmetric wave patterns. *J. Fluid Mech.* **124**: 73–108. [902, 912, 913, 1013, 1014]

Su, M.-Y., M. Bergin, P. Marler and R. Myrick (1982). Experiments on nonlinear instabilities and evolution of steep gravity-wave trains. *J. Fluid Mech.* **124**: 45–72. [1007]

Susbielles, G. and Ch. Bratu (1981). *Vagues et Quvrages Pétroliers en Mer* Editions Technip 27, Paris. [387]

Svensen, I. A., and U. Putrevu (1996). Surf-zone Hydrodynamics. *Advances in*

Coastal adn Ocean Engineering, **2**: 1–78. Edited by P. L-F. Liu, World Scientific, Singapore. [609]

Tam, C. K. W. (1973). Rip currents. *J. Geophys. Res.* **78**: 1937–1943. [609]

Tappert, F. D., (1977). The parabolic approximation. *Wave Propagation and Underwater Acoustics*, 224–287, eds. J. B. Keller and J. S. Papadakis, Springer-Verlag, Berlin. [181]

Tappert, F. D. and N. J. Zabusky (1971). Gradient-induced fission of solitons. *Phys. Rev. Lett.* **27**: 1774–1776. [676, 680]

Tatsuno, M., S. Inoue and J. Okabe (1969). Transfiguration of surface waves. *Rep. Res. Inst. Appl. Mech. Kyushu University* **17**: 195–215. [967]

Tayfun, M. A., R. A. Dalrymple and C. Y. Yang (1976). Random wave-current interactions in water of varying depth. *Ocean Engineering* **3**: 403–420. [929]

Tezduyar, T. E. (2003). Computation of moving boundaries and interfaces and stabilization parameters. *Numerical Simulations of Incompressible Flows* (ed. by M. M. Hafez), World Scientific. [886]

Thiews, J. G. and L. Landweber, (1935). The influence of shallow water on the resistence of a cruiser model. *US Exp. Model Basin, Navy Yard, Washington DC, Rept. no. 414*. [718]

Thomas, G. P. (1990). Wave-current interactions: an experimental and numerical study. Part 2. Nonlinear waves. *J. Fluid Mech.* **216**: 505–536. [926, 927]

Thornton, E. B. (1970). Variation of longshore current across the surf zone. *Proc. 12th Coastal Eng. Conf. ASCE* 291–308. [549, 578, 589]

Topliss, M. E. (1994). Water wave impact on structures. Ph.D thesis, School of Mathematics, University of Bristol, U.K. [1025]

Trulsen, K. and K. B. Dysthe (1990). frequecy downshift through self-modulation and breaking. *Water-Wave Kinematics* eds. A. Torum and O. T. Gumestad, 561-572, Kluwer Academic. [789]

Trulsen, K. and K. B. Dysthe (1992). Action of wind stress and breaking on the evolution of a wave train. *Breaking Waves*: *IUTAM Symp. Sydney, Australia, 1991*, eds. M. L. Banner and R. H. J. Grimshaw, 243–249, Springer-Verlag. [872]

Tryggvason, G., B. Bunner, A. Esmaeeli, D. Juric, N. Al-Rawahi, W. Tauber, J. Han, S. Nas and Y.-J. Jan (2001). A front-tracking method for the computations of multiphase flow. *J. of Computational Physics* **169**: 708–759. [886]

Tryggvason, G., B. Bunner, A. Esmaeeli and N. Al-Rawahi (2003). Computations of multiphase flows. *Advances in Applied Mech.* **39**: 81–120. [887]

Tsai, W. and D. K. P. Yue (1987). Numerical calculation of nonlinear axisymmetric standing waves in a circular basin. *Phys. Fluids* **30**: 3441–3447. [963]

Tsai, W. and D. K. P. Yue (1993). Interactions between a free surface and a vortex sheet shed in the wake of a surface-piercing plate. *J. Fluid Mech.* **257**: 691–721. [974, 986]

Tsai, W. T., and D. K-P. Yue (1995). Computation of nonlinear free-surface flows. *Ann. Rev. Fluid Mech.*, **28**: 249-278. [1042]

Tsai, W. and D. K. P. Yue (1996). Computation of nonlinear free-surface flows. *Ann. Review of Fluid Mech.* **28**: 249–278. [885, 888]

Tuck, E. O. (1966). Shallow-water waves past slender bodies. *J. Fluid Mech.* **26**: 81-95. [722]

Tuck, E. O. and L. S. Hwang (1972). Long wave generation on a sloping beach. *J. Fluid Mech.* **51**: 449–461. [641]

Tuck, O. E. and J.-M. Vanden-Broeck (1984). A cusp-like free-surface flow due to a submerged source or sink. *J. Austral. Math. Soc.* B**25**: 443. [1015]

Tucker, M. J. (1950). Surf beats: Sea waves of 1 to 5 min. period. *Proc. R. Soc. Lond. A* **202**: 565–573. [789]

Tulin, M. P. (1978). Ship wave resistance — a survey. *Proc. 8th U.S. Nat. Cong. App. Mech.*, Los Angeles, CA, 217–244. [917]

Tulin, M. P. and T. J. Waseda (1999). Laboratory observations of wave group evolution including breaking effect. *J. of Fluid Mech.* **378**: 197-232. [916]

Tung, C. C. (1992). Wave spectrum in adverse current, Proceedings of the Second International Offshore and Polar Engineering Conference, San Francisco, 14–19 June 1992, Vol. III. [926]

Turpin, F. M., C. Benmoussa, and C. C. Mei (1983). Evolution of finite amplitude surface waves over slowly varying depth and current. *J. Fluid Mech.* **132**: 1–23. [809]

Tyvand, P. A. (1992). Unsteady free-surface flow due to a line source. *Phys. Fluids* A**4**(4): 671. [1016, 1017]

Ünlüata, Ü. and C. C. Mei (1970). Mass transport in water waves. *J. Geophys. Res.* 7611–7618. [536, 537]

Ursell, F. (1950). Surface waves on deep water in the presence of a submerged circular cylinder. *Proc. Camb. Philo. Soc.* **46**: I: 141-152, II, 153-158.

Ursell, F. (1952). Edge waves on a sloping beach. *Proc. R. Soc. Lond. A* **214**: 79–97. [174]

Ursell, F. (1953). The long wave paradox in the theory of gravity waves. *Proc. Cambridge Phil. Soc.* **49**: 685–694. [611]

Ursell, F. (1960). On Kelvin's ship-wave pattern. *J. Fluid Mech.* **8**: 418–431. [916, 923]

Ursell, F. (1964). The decay of the free motion of a floating body. *J. Fluid Mech.* **19**: 305–319. [449]

Ursell, F. (1981). Irregular frequencies and the motion of floating bodies. *J. Fluid Mech.* **105**: 143–156.

Ursell, F., R. G. Dean and Y. S. Yu (1959). Forced small-amplitude water waves: a comparison of theory and experiment. *J. Fluid Mech.* **7**: 33–52. [990]

Vanden-Broeck, J.-M. and J. B. Keller (1987). Free surface flow due to a sink. *J. Fluid Mech.* **175**: 109. [1015]

Varisco, D., (1992). Interaction between flap gates and tidal current and waves. *Proc. 23rd Int. Conf. Coastal Eng.*, Am. Soc. Civil Engrs. [426]

Vesecky, J. F. and R. H. Stewart (1982). The observation of ocean surface phenomena using imagery from the Seasat synthetic aperture radar — an assessment. *J. Geophys. Res.* **87**: 3397–3430. [917]

Vinje, T. and P. Brevig (1980). Numerical simulation of breaking waves. *3rd Int. Conf. Finite Elements Water Resources*, Univ. of Miss., Oxford, Miss. USA. [902]

Vinje, T. and P. Brevig (1981a). Numerical simulation of breaking waves. *Advances in Water Resources* **4**: 77–82. [746, 902, 906, 948, 989, 1025]

Vinje, T and P. Brevig (1981b). Nonlinear ship motions. *Proc. 3rd Int. Conf. Num. Ship Hydro., Paris, France*, 257–266. [989]

Vinje, T. and P. Brevig (1981c). Numerical calculation of forces from breaking waves. *Proc. Int. Symp. Hydro. Ocean Eng.*, Trondheim, Norway. [746, 902, 906, 948, 989, 1025]

Vinje, T., X. Maogang and P. Brevig (1982). A numerical approach to nonlinear ship motion. In *Proc. 14th Symp. on Naval Hydro.* (Chairman: I. F. Ogilvie): 245–278. Washington: National Academy Press. [985]

Vitale, P. (1979). Sand bed friction factors for oscillatory flows. *J. Waterways, Port Coastal Ocean Div. ASCE* **105**: 229–245. [489]

Vittori, G., and P. Blondeaux, (1990). Sand ripples under sea waves. Part 2. Finite-amplitude development. *J. Fluid Mech.* **248**: 19–39. [526]

von Kerczek, C. and S. H. Davis (1975). Calculation of transition matrices. *AIAA Journal* **13** (10): 1400–1403. [963]

Wang, C. Y. (1968). On high-frequency oscillatory viscous flows. *J. Fluid Mech.* **32**: 55–68. [532]

Wehausen, J. V. (1980). Perturbation methods in diffraction. *J. Waterways Port Coastal Ocean Eng. Div.* **2**: 290–291. [826]

Wehausen, J. V. and E. V. Laitone (1960). *Handbuch der Physik*, ed. W. Flügge, Vol. 9, pp. 446–778. Springer-Verlag, Berlin. [669, 718, 745, 816, 823, 1016]

West, B. J., K. A. Brueckner, R. S. Janda, M. Milder and R. L. Milton (1987). A new numerical method for surface hydrodynamics. *J. Geophys. Res.* **92**: 11803–11824. [889]

West, B. J., K. M. Watson and A. J. Thomson (1974). Mode coupling description of ocean wave dynamics. *The Phys. of Fluids* **17**: 1059–1067. [889]

Whillock, A. F. (1987). Measurements of forces resulting from normal and oblique wave approaches to small scale sea walls. *Coastal Eng.* **11**: 297–308. [1024]

Whitham, G. B. (1967). Nonlinear dispersion of water waves. *J. Fluid Mech.* **27**: 399–412. [746, 756]

Whitham, G. B. (1974). *Linear and Nonlinear Waves*, Wiley–Interscience, New York. [109, 670, 736, 747, 810, 917, 926]

Whitham, G. B. (1976). Nonlinear effects in edge waves. *J. Fluid Mech.* **74**: 353–368. [649]

Whitman, A. M. and M. C. Pancione (1973). A similitude relation for flat-plate hydrodynamic impact. *J. Ship Res.*, 38–42. [1024]

Wiegel, R. L. (1960). A presentation of cnoidal wave theory for practical application. *J. Fluid Mech.* **7**: 273–286. [663, 664]

Wiegel, R. L. (1964). *Oceanographical Engineering*, Prentice-Hall, Englewood Cliffs, N.J. [809]

Wu, D. M. and T. Y-T. Wu (1982). Three-dimensional nonlinear long waves due to moving surface prssure. In *Proc. 14th Symp. Naval Hydrod.* 103–129. [718]

Wu, G. (2004). Direct simulation and deterministic prediction of large-scale Non-

linear ocean wave-field. Ph.D Thesis, Massachusetts Institute of Technology, USA. [890, 915, 972]

Wu, G. X. (1991). On the second order wave reflection and transmission by a horizontal cylinder. *Appl. Ocean Res.* **13**, 58-62. [948]

Xia, F. and L. Larsson (1986). A calculation method for the lifting potential flow around yawed surface-piercing 3-D bodies. *Proc. 16th Symp. Naval Hydro.*, Berkeley. [917]

Xue, M. (1997). Three-dimensional fully-nonlinear simulations of waves and wave body interactions. Ph.D. thesis, Massachusetts Institute of Technology, USA. [1022]

Xue, M. and D. K. P. Yue (1998). Nonlinear free-surface flow due to an impulsively started submerged point sink. *J. Fluid Mech.* **364**: 325–347. 985, 1015, 1017, 1018, 1023]

Xue, M., H. B. Xü, Y. Liu and D. K. P. Yue (2001). Computations of fully-nonlinear three-dimensional wave-wave and wave-body interactions, Part I: three-dimensional steep waves. *J. Fluid Mech.* **438**: 11–39. [973, 989, 990, 1008]

Xü, H. (1992). Numerical study of fully nonlinear water waves in three dimensions. Ph.D. thesis, Massachusetts Institute of Technology, USA. [982, 983]

Xü, H. and D. K. P. Yue (1992). Computations of fully-nonlinear three-dimensional water waves. *Proc. 19th Symposium on Naval Hydrodynamics*, Seoul, Korea. [980, 983, 987]

Yamaguchi, M. and Y. Tsuchiya. (1974). Non-linear effect of waves on wave pressure and wave force on a large cylindrical pile. *Proc. Civil. Eng. Japan* **229**: 41–53 (in Japanese). [826]

Yao, Y., P. Wang and M. P. Tulin (1994). Wave groups, wave-wave interactions and wave breaking: results of numerical experiments. In *Proc. 20th Symp. on Naval Hydrodynamics*, Santa Barbara, USA. [989]

Yeung, R. W. (1975). A hybrid integral equation method for time-harmonic free surface flow. *Proc. 1st Int. Conf. Num. Ship Hydrodyn.* David Taylor Naval Ship Research and Development Center 581–607. [403]

Yeung, R. W. (1982). Numerical methods in free-surface flows. *Ann. Rev. Fluid Mech.* **14**: 395–442. [387, 403, 885, 899]

Yu, J., and C. C. Mei, (2000a). Do longshore bars protect the shore? *J. Fluid Mech.* **404**: 251–268. [930]

Yu, J., and C. C. Mei, (2000b). Formation of sand bars under surface waves. *J. Fluid Mech.* **416**: 315–348. [526, 930]

Yue, D. K. P. (1980). Numerical theory of Stokes wave diffraction at grazing incidence, Sc.D. Thesis, Department of Civil Engineering, Massachusetts Institute of Technology. [778, 780, 782, 784–786, 816]

Yue, D. K. P. and C. C. Mei (1980). Forward diffraction of Stokes waves by a thin wedge. *J. Fluid Mech.* **99**: 33–52. [810, 813–815]

Yuen, H. C. and B. M. Lake (1975). Nonlinear deep water waves: Theory and experiment. *Phys. Fluids* **18**: 956–960. [776]

Yuen, H. C. and B. M. Lake (1980). Instabilities of waves on deep water. *Ann. Rev. Fluid Mech.* **12**: 303–334. [810, 813–815]

Yuen, H. C. and B. M. Lake (1982). Nonlinear dynamics of deep-water gravity waves. *Advances in Applied Mechanics* **22**: 67–229. [839, 889]

Yuen, H. C. and W. E. Ferguson, Jr. (1978a). Relationship between Benjamin–Feir instability and recurrence in the nonlinear Schrödinger equation. *Phys. Fluids* **21**: 1275–1278. [789]

Yuen, H. C. and W. E. Ferguson, Jr. (1978b) Fermi–Pasta–Ulam recurrence in the two space dimensional nonlinear Schrödinger equation. *Phys. Fluids* **21**: 2116–2118. [787]

Yuen, H. C. and B. M. Lake (1975). Nonlinear deep water waves: Theory and experiment. *Phys. Fluids* **18**: 956–960. [776]

Yuen, H. C. and B. M. Lake (1980). Instabilities of waves on deep water. *Ann. Rev. Fluid Mech.* **12**: 303–334. [746]

Zabusky, N. J. and M. D. Kruskal (l965). Interaction of solitons in a collisionless plasma and the recurrence of initial states. *Phys. Rev. Lett.* **15**: 240. [670]

Zakharov V. E. (1968). Stability of periodic waves of finite amplitude on the surface of a deep fluid. *J. Appl. Mech. Tech. Phys.* (Eng. transl.) **2**: 190–194. [746, 756, 768, 847, 864, 888–890]

Zakharov, V. E. and A. B. Shabat (1972). Exact theory of two-dimensional shelf-focusing and one-dimensional self modulation of waves in nonlinear media. *Sov. Phys. JETP* **34**: 62–69. [676, 746, 771, 775, 888]

Zaroodny, S. J. and M. D. Greenberg (1973). On a vortex sheet approach to the numerical calculation of water waves. *J. Comp. Phys.*, **11**: 440–446. [948]

Zenkovich, V. (1967). *Processes of Coastal Development*, Oliver and Boyd, London. [526, 547, 601, 608]

Zhang, J., K. Hong and D. K. P. Yue (1993). Effects of wavelength ratio on wave-mode modeling. *J. Fluid Mech.* **248**: 107–127. [890]

Zhang, S., D. K. P. Yue and K. Tanizawa (1996). Simulation of plunging wave impact on a vertical wall. *J. Fluid Mech.* **327**: 221–254. [1025]

Zhou, Q. N. and W. P. Graebel (1990). Axisymmetric draining of a cylindrical tank with a free surface. *J. Fluid Mech.* **221**: 511. [1016, 1020, 1022]

Zhu, Q., Y. Liu and D. K. P. Yue (2003). Three-dimensional instability of standing waves. *J. Fluid Mech.* **496**: 213–242. [956]

Zhu, Q., A. A. Tjavaras, Y. Liu, D. K. P. Yue and M. S. Triantafyllou (1999). Mechanics of nonlinear short-wave generation by a moored near-surface buoy. *J. Fluid Mech.* **381**: 305–335. [890, 943, 955]

Zienkiewicz, O. C. (1971). *Finite Element Method in Engineering Science*, McGraw-Hill, New York. [186]

This page intentionally left blank

Subject Index